AD-A271 638

9th International Conference on High-Power Particle Beams

Beams 92

Washington, DC
May 25–29, 1992

N00014-91-J-1955

DTIC
ELECTE
OCT 27 1993
S D
A

VOLUME I

This document has been approved for public release and sale; its distribution is unlimited

Invited Papers
Pulsed Power

93-25565

Edited by
David Mosher
and
Gerald Cooperstein

93 10 21 151

Spirit

Beams 92

Proceedings of the
9th International Conference on High-Power Particle Beams

Washington, DC
May 25 - 29, 1992

Edited by

David Mosher and Gerald Cooperstein
Naval Research Laboratory

Volume I

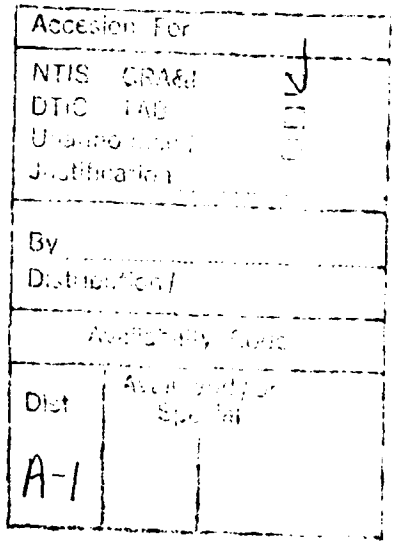

Beams 92

Proceedings of the
9th International Conference on High-Power Particle Beams

NTIS PB92-206168

Copies of these proceedings can be ordered from the National Technical Information Service (NTIS).

NTIS
PO Box 1425
Springfield, VA 22151
(703) 487-4690

Beams 92

9th International Conference on High-Power Particle Beams

was organized by

Naval Research Laboratory
University of Maryland

with U.S. government support provided through

Air Force Office of Scientific Research
Air Force Phillips Laboratory
Defense Advanced Research Projects Agency
Defense Nuclear Agency
Department of Energy
Harry Diamond Laboratory
Lawrence Livermore National Laboratory
Los Alamos National Laboratory
Naval Research Laboratory
Naval Surface Warfare Center
Office of Naval Research
Sandia National Laboratory
Strategic Defense Initiative Organization

and private organizational support provided by

Maxwell Laboratories, Inc.
Physics International Co.

Conference Organization

T. Coffey, *Honorary Chairman*
G. Cooperstein and **V. Granatstein**, *Co-Chairmen*
D. Mosher, *Scientific Secretary*
D. Quinn, *Conference Secretary*

International Advisory Committee

G. Cooperstein*, USA
V. Granatstein*, USA
A. Blaugrund , Israel
H. Doucet, France
G. Kessler, Germany
A. Kolb, USA
G. Mesyats, Russia
S. Nakai, Japan
D. Ryutov, Russia
V. Smirnov, Russia
C. Stallings, USA
R. Sudan, USA
P. VanDevender, USA
K. Yatsui, Japan

National Steering Committee

T. Coffey*, NRL
F. Agee, HDL
R. Barker, AFOSR
J. Benford, PI
A. Drobot+, SAIC
C. Fenstermacher, LANL
B. Godfrey, PL
R. Gullickson+, DNA
D. Hammer, Cornell
D. Hinshelwood, Jaycor
B. Hui, DARPA
S. Humphries, UNM
V. Kenyon, NSWC
N. Luhmann, UCLA
N. Pereira, BRA
D. Prosnitz, LLNL
M. Reiser+, UMD
C. Roberson+, ONR
N. Rostoker, UC Irvine
P. Rustan, SDIO
M. Sluyter, DOE
I. Smith, PSI
I. Vitkovitsky+, RDA
A. Wilson, MLI
G. Yonas, SNL

Local Organizing Committee

D. Mosher*, R. Commisso, D. Hinshelwood, M. Lampe+, B. Levush, J. Neri, S. Ossakow+, R. Parker+, D. Quinn, J. Sethian, and C. Striffler

**Chairman and Local Paper Selection Committee member*
+Local Paper Selection Committee member

Table of Contents

Volume I

Dedication 1
Introduction 3
Paper Index 7
Invited Ion Beam Papers 29
Invited Electron Beam, Bremsstrahlung, and Diagnostics Papers 97
Invited Radiating Z-Pinch Papers 157
Invited Microwave Papers 183
Invited Free Electron Laser Papers 245
Invited Advanced Accelerator Papers 271
Invited Beam and Pulsed Power Applications Papers 321
Invited Pulsed Power Papers 373
Contributed Pulsed Power Papers 417
Author Index 695

Volume II

Paper Index 711
Contributed Ion Beam Papers 733
Contributed Electron Beam Papers 1007
Contributed Beam Diagnostics Papers 1335
Author Index 1409

Volume III

Paper Index 1425
Contributed Microwave Papers 1447
Contributed Free Electron Laser Papers 1707
Contributed Advanced Accelerator Papers 1781
Contributed Beam Applications Papers 1893
Contributed Plasma Discharge Papers 1977
Author Index 2075
Registrant List 2085

Dedication

On August 13th of 1992, Professor Winfried Schmidt of the University of Karlsruhe and the Kernforschungszentrum, Karlsruhe, Germany died at the age of 60 in a traffic accident. The editors wish to dedicate these proceedings to the memory of this close friend. He will be sorely missed by his many colleagues for both his scientific contributions and personal qualities.

Professor Schmidt began his career at Karlsruhe in 1964 with theoretical work in high energy physics. Beginning in 1979, he headed the Office of Future Tasks for the KfK Board of Directors. We first became acquainted with him at this time when he joined the Beams community by introducing KfK research on intense ion beams and their interactions with matter. Our friendship with him and his family deepened during his two-year, Washington DC based tenure as KfK Liaison Officer in the mid 1980's when we had ample opportunity to learn of his deep love of science, be exposed to his wide-ranging ideas on many subjects, and be charmed by the warmth, intelligence, and talents of his wife and daughters. To Beams conference attendees, he may be best known as Scientific Secretary of Beams '88 and editor of those proceedings. His excellent organization of that conference provided a model for those that followed and substantially eased our similar efforts with regard to Beams 92. Beginning in 1989, Prof. Schmidt headed a numerical physics group at KfK. One part of this work was code development and comprehensive modeling of light ion diodes that lead directly to impressive improvements in the focusing performance in subsequent KfK experiments. His last effort was coordination between KfK and the University of Karlsruhe in preparation for a super-computing facility in Karlsruhe.

Winfried Schmidt will be long remembered by his colleagues for his important scientific contributions. His friends will miss him most for the infectious enthusiasm he brought to his research and other interests, and for his penetrating wit. We mourn the passing of this good friend and fine scientist.

Introduction

The 9th International Conference on High-Power Particle Beams was held in Washington D.C. from May 25th to May 29th, 1992, and was hosted by the Naval Research Laboratory and the University of Maryland. Previous conferences were held in Novosibirsk, Russia (1990, 1979), Karlsruhe, Germany (1988), Kobe, Japan (1986), San Francisco, California (1983), Paris, France (1981), Ithaca, New York (1977), and Albuquerque, New Mexico (1975). Over 400 invited and contributed papers were presented making it the largest conference of the series. The 423 registered attendees represented 16 countries and included 65 scientists from the former Soviet Union (FSU). A breakdown of the attendance and contributions by country can be found at the beginning of the Registrant List in the third volume of these proceedings.

The purpose of Beams 92 was the exchange of new ideas and results associated with the science and applications of high-power particle beams in the following areas.

- **Physics and Technology of High-Power Particle Beams** including the generation, focusing, and propagation of electron, light-ion, heavy-ion, and cluster-ion beams

- **New Developments in Pulsed-Power Technology and High-Power Accelerators** including capacitive, inductive, and rep-rated pulsed-power generators, opening-switch technology, induction and cyclic accelerators, and coherent-wave accelerator concepts

- **High-Power Particle Beam Experiments and Diagnostics**

- **Particle-Beam Interactions with Matter** including bremsstrahlung, stopping phenomena, plasma heating, and high-energy-density target plasmas

- **Physics of Pulsed-Power-Driven Discharges** including high-power imploding-plasma and plasma-focus research, fiber-generated pinches, compact toroids, and discharge-plasma heating and radiation

- **Applications to Coherent Radiation Generation** including gigawatt single-pulse microwave generators, fast-wave oscillators and amplifiers, and free-electron lasers

- **Technical and Industrial Applications** including ion-beam ICF, x-ray and neutral-beam sources, x-ray lasers, electron-beam-pumped lasers, radiography, x-ray lithography, materials processing, and pollution control

The program was divided into eight topical invited oral sessions with 20- and 30-minute presentations, seven topical poster sessions, and a summary session. The 304 papers contained in these proceedings represent approximately 90% of the invited oral

talks and 73% of the contributed poster papers. Volume I contains all of the invited oral papers and the contributed Pulsed Power papers. Volume II contains the contributed Ion Beam, Electron Beam, and Beam Diagnostics papers. Volume III contains the Microwave, Free Electron Laser, Advanced Accelerator, Beam Applications, and Plasma Discharge papers.

Gerold Yonas, who initiated this series of conferences with Beams '75 in Albuquerque, New Mexico, gave a stimulating keynote address entitled "Beams 2020" where he looked backward and forward approximately 20 years. The summary session was ably represented by J. Pace VanDevender of the USA reviewing advances in Ion Beams and ICF, Dmitri Ryutov of Russia reviewing Electron Beams, Henri Doucet of France reviewing Microwaves and Free Electron Lasers, Gennady A. Messyats of Russia reviewing Pulsed Power and Accelerator Technology, and Ravi Sudan of the USA reviewing Applications and Z-Pinches. Although the texts of the keynote address and summary papers are not included in these proceedings, each of these sessions is recorded on VHS video tape along with the other eight invited oral sessions. Copies of the video tapes, along with limited extra copies of these proceedings, will be available from Maxwell Laboratories, Inc., host of the Beams '94 Conference to be held in San Diego California, June 20-24, 1994. (See future Beams '94 announcements, or contact Roger White, Beams '94 Co-chairman for details.)

The Beams 92 Conference was special for several reasons. The scientific papers were of high quality and, taken together, represented a complete picture of the world effort in the field of high-power particle beams. The large number of domestic and international attendees represented almost every research effort in this field. A most important feature of this conference arose from its timing as the first major international conference in our field following the collapse of the Soviet Union. This provided the opportunity for extended technical exchanges, in some cases for the first time, with an extraordinarily large contingent of colleagues from the FSU. Many of these technical discussions concerned future international collaborations with FSU laboratories that hold promise for rapid progress in our field. Beams 92 hosted 65 representatives from the FSU that presented 124 papers, including many reports on subjects not previously available to western scientists. This group included an impressive number of Academicians among whom was A.I. Pavlovskii from Arzamas-16 who presented one such important report entitled "Linear Accelerators with Radial Lines." The Beams community suffered a great loss when Dr. Pavlovskii passed away this year.

The venue for Beams 92 included a number of evening social events to which all attendees were invited. These events provided opportunities for extending technical discussions begun during formal conference sessions, for strengthening old friendships, and for forming new ones.

We look forward to Beams '94 and are certain that it will prove as successful and rewarding as Beams 92.

Paper Index

Paper Index - Volume I

Invited Ion Beam Papers

PROGRESS IN LITHIUM BEAM FOCUSING AND BEAM-TARGET INTERACTION EXPERIMENTS AT SANDIA NATIONAL LABORATORIES, T.A. Mehlhorn, L.D. Bacon, J.E. Bailey, D.D. Bloomquist, G.A. Chandler, R.S. Coats, D.L. Cook, M.E. Cuneo, M.S. Derzon, M.P. Desjarlais, R.J. Dukart, A.B. Filuk, T.A. Haill, D.L. Hanson, D.J. Johnson, R.J. Leeper, T.R. Lockner, C.W. Mendel Jr., L.P. Mix, A.R. Moats, J.P. Quintenz, T.D. Pointon, T.J. Renk, G.E. Rochau, S.E. Rosenthal, C.L. Ruiz, D.B. Seidel, S.A. Slutz, R.W. Stinnett, W.A. Stygar, G.C. Tisone, R.E. Olson, J.P VanDevender, D.F. Wenger **31**

EXTRACTION GEOMETRY ION DIODE PHYSICS: THEORETICAL MODELING AND EXPERIMENTAL RESULTS, J.B. Greenly, C.K. Struckman, B.R. Kusse, W.A. Noonan **43**

FOCUSING PROPERTIES OF A STRONGLY INSULATED APPLIED BR-PROTON DIODE WITH A PREFORMED ANODE PLASMA SOURCE, H. Bluhm, P. Hoppe, M. Althaus, H. Bachmann, W. Bauer, K. Baumung, L. Buth, H.U. Karow, H. Laqua, D. Rusch, E. Stein, O. Stoltz **51**

TRANSPORT AND FOCUSING CONSIDERATIONS FOR LIGHT ION ICF SYSTEMS, P.F. Ottinger, D. Mosher, J.M. Neri, D.V. Rose, C.L. Olson **60**

HYDRODYNAMIC TARGET EXPERIMENTS WITH PROTON BEAMS AT KALIF: DIAGNOSTICS OF THE ABLATION PRESSURE BY LASER DOPPLER INTERFEROMETRY; GENERATION OF MULTI-MBAR PRESSURES BY ABLATIVE FOIL ACCELERATION AND IMPACT, K. Baumung, H.U. Karow, V. Licht, D. Rusch, J. Singer, O. Stoltz, H. Bachmann, W. Bauer, H. Bluhm, L. Buth, B. Goel, M.F. Goez, H. Guth, P. Hoppe, H. Lotz, C.D. Munz, G.I. Kanel, A.L. Ni, A. Shutov, O.Yu. Vorobjev **68**

MULTISTAGE ION ACCELERATOR FOR INERTIAL FUSION ENERGY, K. Imasaki, C. Yamanaka, S. Miyamoto, K. Yasuike, N. Shirai, S. Nakai, T. Aoki, S. Kawata **76**

INTENSE ION BEAM RESEARCH AT LOS ALAMOS, D.J. Rej, R.R. Bartsch, H.A. Davis, R.J. Faehl, D.C. Gautier, J.B. Greenly, I. Henins, T.W. Linton, R.E. Muenchausen, W.J. Waganaar **88**

Invited Electron Beam, Bremsstrahlung, and Diagnostics Papers

CHARGED PARTICLE BEAM PROPAGATION STUDIES AT THE NAVAL RESEARCH LABORATORY R.A. Meger, R.F. Hubbard, J.A. Antoniades, R.F. Fernsler, M. Lampe, D.P. Murphy, M.C. Myers, R.E. Pechacek, T.A. Peyser, J. Santos, S.P. Slinker **99**

RADLAC II HIGH CURRENT ELECTRON BEAM PROPAGATION EXPERIMENT, C.A. Frost, S.L. Shope, M.G. Mazarakis, J.W. Poukey, J.S. Wagner, B.N. Turman, C.E. Crist, D.R. Welch, K.W. Struve **109**

GENERATION, CONTROL, AND TRANSPORT OF A 19-MEV, 700-KA, PULSED ELECTRON BEAM, T.W.L. Sanford, J.A. Halbleib, J.W. Poukey, D.R. Welch, R.C. Mock, P.J. Skogmo, K.A. Mikkelson **119**

RECENT RESULTS ON THE GOL-3 DEVICE, A.V. Arzhannikov, A.V. Burdakov, V.V. Chikunov, A.F. Huber, A.V. Karyukin, V.A. Kapitonov, V.S. Koidan, S.V. Lebedev, K.I. Mekler, P.I. Melnikov, A.A. Nikiforov, V.S. Nikolaev, V.V. Postupaev, D.D. Ryutov, E.P. Semenov, S.L. Sinitsky, M.A. Shcheglov, S.G. Voropaev, M.V. Yushkov **127**

INNOVATIVE BREMSSTRAHLUNG RESEARCH AT PHYSICS INTERNATIONAL COMPANY, S.L. Wong, J.C. Riordan, J.S. Meachum **136**

SPECTROSCOPIC STUDIES OF PULSED-POWER PLASMAS, Y. Maron, R. Arad, G. Dadusc, G. Davara, R.E. Duvall, V. Fisher, M.E. Foord, A. Fruchtman, L. Gregorian, Ya.E. Krasik, C. Litwin, L. Perelmutter, M. Sarfaty, E. Sarid, S. Shkolnikova, R. Shpitalnik, L. Troyansky, A. Weingarten, R.E.H. Clark, A. Fisher, C. Litwin **143**

Invited Radiating Z-Pinch Papers

A REVIEW OF Z-PINCH RESEARCH AT PHYSICS INTERNATIONAL, C. Deeney, P.D. LePell, T. Nash, B. Failor, S.L. Wong, R.R. Prasad, M. Krishnan, K.G. Whitney, J.W. Thornhill, F.L. Cochran, M.C. Coulter, J.L. Giuliani, Jr., J.P. Apruzese, F.C. Young, D.D. Hinshelwood, J.D. Sethian **159**

RADIATIVE Z-PINCH COUPLING TO AN INDUCTIVE GENERATOR, J.L. Giuliani, Jr., M. Mulbrandon, R. Terry, P.F. Ottinger, R.J. Commisso, C. Deeney, P.D. LePell **167**

THE LOS ALAMOS FOIL IMPLOSION PROJECT, J. Brownell, J. Parker, R.R. Bartsch, J. Benage, R. Bowers, J. Cochrane, P. Forman, J. Goforth, A. Greene, H. Kruse, J. Ladish, H. Oona, D. Peterson, R. Reinovsky, N.F. Roderick, J. Trainor, P.J. Turchi **175**

Invited Microwave Papers

GYROKLYSTRON RESEARCH FOR APPLICATION TO TEV LINEAR COLLIDERS, W. Lawson, V.L. Granatstein, B. Hogan, U.V. Koc, P.E. Latham, W. Main, H.W. Matthews, G.S. Nusinovich, M. Reiser, C.D. Striffler, S.G. Tantawi **185**

NANOSECOND RADAR SYSTEM BASED ON REPETITIVE PULSED RELATIVISTIC BWO, B.V. Bunkin, A.V. Gaponov-Grekhov, A.S. Eltchaninov, F.Ya. Zagulov, S.D. Korovin, G.A. Mesyats, M.L. Osipov, E.A. Otlivantchik, M.I. Petelin, A.M. Prokhorov, V.V. Rostov, A.P. Saraev, I.P. Sisakyan, A.V. Smorgonsky, V.A. Suvorov **195**

HIGH POWER MICROWAVE GENERATION AT HIGH REPETITION RATES, N. Aiello, J. Benford, N. Cooksey, B. Harteneck, J. Levine, D. Price, R. Smith, D. Sprehn, M. Willey **203**

RELATIVISTIC MULTIWAVE CERENKOV GENERATOR, V.I. Kanavets, A.S. Nifanov, A.I. Slepkov .. **211**

HIGH POWER MICROWAVE GENERATION IN VIRCATORS, A.N. Didenko, V.I. Rashchikov **219**

THE EXPERIMENTAL AND THEORETICAL DEVELOPMENT OF A ONE GIGAWATT, REPETITIVELY PULSED, ONE MICROSECOND PULSE LENGTH, HIGH CURRENT RELATIVISTIC KLYSTRON AND MODULATOR, M.V. Fazio, B.E. Carlsten, R.J. Faehl, W.B. Haynes, R.F. Hoeberling, T.J.T. Kwan, D.G. Rickel, R.M. Stringfield, F.W. VanHaaften, R.F. Wasierski, A. Erickson, K. Rust **227**

HIGH PEAK POWER TUBES AND GATE EFFECT KLYSTRONS, N. Gerbelot, J.M. Buzzi, M. Bres, G. Faillon **237**

Invited Free Electron Laser Papers

THE ETA II LINEAR INDUCTION ACCELERATOR AND IMP WIGGLER: A HIGH-AVERAGE-POWER MILLIMETER-WAVE FREE-ELECTRON LASER FOR PLASMA HEATING, S.L. Allen, E.T. Scharlemann **247**

IREB TRANSPORT IN A FOCUSING WIGGLER AND FEL EXPERIMENTS AT JAERI, S. Kawasaki, T. Kobayashi, K. Sakamoto, Y. Kishimoto, A. Watanabe, S. Musyoki, H. Oda, S. Tokuda, Y. Nakamura, T. Nagashima, M. Shiho **255**

SELF-CONSISTENT NONLINEAR SIMULATIONS OF HIGH-POWER FREE-ELECTRON LASERS, H.P. Freund, R.H. Jackson **263**

Invited Advanced Accelerator Papers

LINEAR ACCELERATOR WITH RADIAL LINES - LIA-30, A.I. Pavlovskii, V.S. Bossamykin, A.I. Gerasimov, V.A. Tananakin, A.S. Fedotkin, K.A. Morunov, V.F. Basmanov, G.M. Skripka, A.D. Tarasov, A.V. Grishin, V.P. Gritzina, V.Ya. Averchenkov, O.N. Syutin, S.A. Lazarev, V.S. Gorkunov, V.P. Veresov **273**

TECHNOLOGY DEMONSTRATION FOR THE DARHT LINEAR INDUCTION ACCELERATORS, M. Burns, P. Allison, J. Downing, D.C. Moir, G. Caporaso, Y.J. Chen **283**

SLIA THEORY REVIEW, J.J. Petilio, A.A. Mondelli, C. Kostas, K.T. Tsang, D.P. Chernin **291**

STUDY OF RECIRCULATING INDUCTION ACCELERATOR AS DRIVERS FOR HEAVY ION FUSION, H.D. Shay, J.J. Barnard, A.L. Brooks, F. Coffield, F. Deadrick, L.V. Griffith, H.C. Kirbie, V.K. Neil, M.A. Newton, A.C. Paul, L.L. Reginato, W.M. Sharp, J. Wilson, S.S. Yu, D.L. Judd **297**

LOW EMITTANCE ACCELERATOR CAVITY DESIGN TO MINIMIZE AMPLIFICATION OF BEAM BREAKUP MODES, M.L. Sloan, J.R. Thompson, C.S. Kueny **305**

OPTICAL GUIDING AND ELECTRON ACCELERATION IN THE LASER WAKEFIELD ACCELERATOR, P. Sprangle, E. Esarey, J. Krall, G. Joyce, A. Ting **313**

Invited Beam and Pulsed Power Applications Papers

CURRENT STATUS OF PULSE-POWER TECHNOLOGY AND APPLICATIONS AT LBT, NAGAOKA, K. Yatsui, W. Masuda, K. Masugata, W. Jiang, Y. Sekimoto, G. Imada, T. Sonegawa, X.D. Kang **323**

INITIAL RESULTS FROM THE RHEPP MODULE, H.C. Harjes, K.J. Penn, K.W. Reed, C.R. McClenahan, G.E. Laderach, R.W. Wavrik, J.L. Adcock, M.E. Butler, G.A. Mann, G.E. Pena, G.J. Weber, D. VanDeValde, L.E. Martinez, D. Muirhead, P.D. Kiekel, D.L. Johnson, E.L. Neau **333**

APPLICATIONS OF HIGH POWER MICROWAVES, J. Benford, J. Swegle **341**

X-PINCH SOFT X-RAY SOURCE FOR MICROLITHOGRAPHY, S.C. Glidden, D.A. Hammer, D.H. Kalantar, N. Qi **349**

MAGNETIC FUSION WITH HIGH ENERGY SELF-COLLIDING ION BEAMS, N. Rostoker, F.J. Wessel, B. Maglich, A. Fisher **357**

PRACTICAL APPLICATIONS OF HIGH-POWER ION BEAMS, G.E. Remnev, V.A. Shulov **365**

Invited Pulsed Power Papers

MICROSECOND-CONDUCTION-TIME POS EXPERIMENTS, B.V. Weber, J.R. Boller, R.J. Commisso, P.J. Goodrich, J.M. Grossmann, D.D. Hinshelwood, J.C. Kellogg, P.F. Ottinger, G. Cooperstein **375**

INDUCTIVE ENERGY STORE (IES) TECHNOLOGY FOR MULTI-TERRAWATT GENERATORS, P.S. Sincerny, S.R. Ashby, F.K. Childers, C. Deeney, D. Kortbawi, J.R. Goyer, J.C. Riordan, I.S. Roth, C. Stallings, L. Schlitt **385**

HIGH CURRENT PULSED POWER GENERATOR GIT-16. STATE OF PROJECT. EXPERIMENTAL RESULTS, S.P. Bugaev, A.M. Volkov, A.A. Kim, V.N. Kiselev, B.M. Kovalchuk, N.F. Kovsharov, V.A. Kokshenev, G.A. Mesyats, A.P. Huseev **394**

PULSED POWER INDUCTIVE ENERGY STORAGE IN THE MICROSECOND RANGE, W. Rix, A.R. Miller, J. Thompson, E. Waisman, M. Wilkinson, A. Wilson **402**

A LONG CONDUCTION TIME COMPACT TORUS PLASMA FLOW SWITCH, R.E. Peterkin,Jr., D.E. Bell, J.H. Degnan, M.R. Douglas, T.W. Hussey, B.W. Mullins, N.F. Roderick, P.J. Turchi **408**

Contributed Pulsed Power Papers

ACCELERATORS WITH VACUUM INSULATED MARX GENERATORS, E.N. Abdullin, S.P. Bugaev, A.M. Efremov, V.B. Zorin, B.M. Kovalchuk, S.V. Loginov, G.A. Mesyats, V.S. Tolkachev, P.M. Schanin, A.A. Chistov **419**

ELECTRON BEAM GENERATORS AT ANGARA-5 FACILITY, V.V. Bulan, E.V. Grabovsky, A.N. Gribov, O.G. Egorov, V.V. Zajivikhin, E.P. Kojokhin, K.V. Kurbatov, I.N. Kukharenko, V.G. Lujnov, V.E. Pichugin, O.A. Smolenkova **425**

PROGRESS IN TECHNOLOGY OF THE MICROSECOND E-BEAM GENERATORS WITH ENERGY CONTENT IN THE RANGE 100 - 500 KJ, A.V. Arzhannikov,V.T. Astrelin, V.B. Bobylev, V.S. Koidan, V.S. Nikolaev, M.A. Shcheglov, S.L. Sinitsky, A.V. Smirnov, R.P. Zotkin **431**

HIGH-CURRENT ACCELERATOR "SIRIUS" WITH ELECTRON BEAM CURRENT OF 2 KA, ELECTRON ENERGY OF MEV-RANGE AND PULSE DURATION OF 50 MCSEC, V.I. Engelko, N.G. Beruchev, V.V. Ershov, O.L. Komarov, V.G. Kovalev, O.P. Pechersky, A.A. Petukhov, Yu.M. Saveljev, L.V. Smirnov, K.I. Tkachenko **436**

INDUCTIVE PULSED POWER SOURCE FOR PLASMA RADIATOR, B.D. Yankovskiy **443**

SUPER-POWER ACCELERATOR FOR MICROWAVE ELECTRONICS, G.I. Batskikh, L.N. Kazansky, A.A. Oreshin, P.A. Samarsky, V.D. Seleznev, A.V. Sinelshikov, A.I. Khomenko, S.P. Bugaev, B.M. Kovalchuk, V.I. Koshelev, G.A. Mesyats, M.I. Petelin **449**

IGUR-3 - POWERFUL BREMSSTRAHLUNG RADIATION PULSE GENERATOR, V.S. Diyankov, A.I. Kormilitsin, V.P. Kovalev **455**

HEAVEN-LIGHT II INTENSE PULSED ELECTRON BEAM ACCELERATOR, N. Zeng, R. Zhao, D. Yang, X. Jiang, X. Wang **462**

THE EXPERIMENTAL RESEARCH OF A FIELD-ENHANCED MULTICHANNEL OIL SWITCH, R. Zhao, N. Zeng, D. Yang, X. Jiang, X. Wang **468**

THE MAGPIE PROJECT: CURRENT STATUS, I.H. Mitchell, P. Choi, J.P. Chittenden, J.F. Worley, J.M. Bayley, A.E. Dangor, M.G. Haines **474**

OPTIMISATION OF THE POWER COUPLING IN THE MAGPIE 4-WAY JUNCTION USING A 1/6TH SCALE MODEL, I.H. Mitchell, P. Choi, J.P. Chittenden, J.F. Worley **480**

NEW HALF VOLTAGE AND DOUBLE PULSE OPERATION OF THE HERMES III LINEAR INDUCTION ACCELERATOR, K.A. Mikkelson, R.L. Westfall, S.M. Neely, V.J. Harper-Slaboszewicz.. **486**

APPLICATION OF MAGNETICALLY INSULATED TRANSMISSION LINES FOR HIGH CURRENT, HIGH VOLTAGE ELECTRON BEAM ACCELERATORS, S.L. Shope, M.G. Mazarakis, C.A. Frost, J.W. Poukey, B.N. Turman **492**

MODELLING PULSED-POWER TRANSMISSION LINES, C.W. Mendel, Jr., D.B. Seidel, W.A. Johnson, S.E. Rosenthal **499**

PULSED POWER ELECTRON ACCELERATORS WITH THE FORMING SYSTEMS BASED ON STEPPED TRANSMISSION LINES, V.S. Bossamykin, V.S. Gordeev, A.I. Pavlovskii, A.P. Klement'ev, O.N. Syutin, A.V. Budakov, V.F. Basmanov, A.P. Gridasov, V.O. Filippov, G.A. Myskov **505**

NEW SCHEMES FOR HIGH-VOLTAGE PULSED GENERATORS BASED ON STEPPED TRANSMISSION LINES, V.S. Bossamykin, V.S. Gordeev, A.I. Pavlovskii **511**

DEVELOPMENT OF MICROSECOND GENERATORS WITH PLASMA CURRENT INTERRUPTING SWITCH IN I. V. KURCHATOV INSTITUTE OF ATOMIC ENERGY: FREQUENCY OPERATION OF GENERATORS, V.M. Babykin, R.V. Chikin, G.I. Dolgachev, Yu.P. Golovanov, Yu.I. Kovalev, A.G. Ushakov, L.P. Zakatov **517**

EXPERIMENTAL RESEARCH OF MICROSECOND PLASMA INTERRUPTING SWITCH (PCIS): CANAL CONCEPT OF PCIS OPERATION, G.I. Dolgachev, L.P. Zakatov, A.G. Ushakov **523**

EXPERIMENTAL STUDIES OF A MICROSECOND PLASMA OPENING SWITCH IN THE POSITIVE POLARITY REGIME, V.M. Bystritskii, I.V. Lisitsyn, Ya.E. Krasik **529**

NUMERICAL SIMULATIONS OF PLASMA DYNAMICS IN A MICROSECOND PLASMA OPENING SWITCH, V.M. Bystritskii, I.V. Lisitsyn, A.A. Sinebryukhov **535**

A PLASMA OPENING SWITCH WITH A RETAINED PLASMA, V.L. Gumennyj, Yu.A. Zhdanov, I.N. Naugol'nyj, A.V. Pashchenko, Yu.V. Tkach **541**

ANTHEM SIMULATIONAL STUDIES OF THE PLASMA OPENING SWITCH, R.J. Mason **547**

TWO-DIMENSIONAL STUDIES OF CURRENT CONDUCTION IN PLASMA OPENING SWITCHES, D. Parks, E. Waisman, R. Ingermanson, E. Salberta **553**

ELECTRON AND ION MAGNETOHYDRODYNAMIC EFFECTS IN PLASMA OPENING SWITCHES, J.M. Grossmann, C.R. DeVore, P.F. Ottinger **559**

A SELF-CONSISTENT THEORY OF PLASMA FILLED DIODES AND PLASMA OPEN SWITCHES, L.I. Rudakov **565**

OPENING SWITCH MODEL WITH VORTEX STRUCTURES, N.B. Volkov, T.A. Golub, N.A. Gondarenko, A.M. Iskoldsky **575**

COMPACT GENERATOR WITH PLASMA FLOW OPENING SWITCH, B.A. Kablambajev, V.A. Poskonin, N.A. Ratakhin **581**

THE INFLUENCE OF THE B-THETA FIELD ON MPOS PERFORMANCE, A.A. Kim, D.V. Getman **586**

POS USE EFFICIENCY IN MULTIMODULE ACCELERATOR WITH SELF-MAGNETIC INSULATION, V.V. Zajivikhin **592**

EXPERIMENTS ON MICROSECOND CONDUCTION TIME PLASMA OPENING SWITCH MECHANICS, W. Rix, M. Coleman, A.R. Miller, D. Parks, K. Robertson, J. Thompson, E. Waisman, A. Wilson **598**

DENSITY MEASUREMENTS OF MICROSECOND-CONDUCTION-TIME POS PLASMAS, D.D. Hinshelwood, B.V. Weber, R.J. Commisso, P.J. Goodrich, J.M. Grossmann, J.C. Kellogg **603**

MICROSECOND PLASMA OPENING SWITCH EXPERIMENTS ON HAWK WITH AN E-BEAM DIODE LOAD, P.J. Goodrich, R.C. Fisher, D.D. Hinshelwood, J.R. Boller, R.J. Commisso, B.V. Weber **609**

PLASMA OPENING SWITCH FOR LONG-PULSE INTENSE ION BEAM, H.A. Davis, R.J. Mason, R.R. Bartsch, J.B. Greenly, D.J. Rej **615**

LONG CONDUCTION TIME PLASMA OPENING SWITCH EXPERIMENTS AT SANDIA NATIONAL LABORATORIES, M.E. Savage, W.W. Simpson, G.W. Cooper, M.A. Usher **621**

PLASMA EROSION OPENING SWITCH USING LASER-PRODUCED PLASMA, H. Akiyama, T. Fukuzawa, S. Ihara, S. Katsuki, S. Maeda **627**

SPECTROSCOPIC INVESTIGATIONS OF A PLASMA OPENING SWITCH USING A NOVEL GASEOUS PLASMA SOURCE, M. Sarfaty, Ya.E. Krasik, R. Arad, A. Weingarten, S. Shkolnikova, Y. Maron, A. Fisher **633**

THE AURORA ACCELERATOR'S TRIGGERED OIL SWITCH, D.M. Weidenheimer, N.R. Pereira, D.C. Judy, K.L. Stricklett **640**

HIGH-PRESSURE GAS SWITCH FOR A WIDEBAND SOURCE, P.A. Pincosy, P. Poulsen, W.R. Cravey **646**

PREDICTION OF ELECTROMAGNETIC PULSE GENERATION BY PICOSECOND AVALANCHES IN HIGH-PRESSURE AIR, D.J. Mayhall, J.H. Yee **652**

HYDROGEN SPARK SWITCHES FOR REP-RATED ACCELERATORS, S.L. Moran, M.G. Grothaus, L.W. Hardesty **659**

SIMPLE METHODS OF SQUARE PULSE GENERATION BY INDUCTIVE PULSE FORMING LINES AND A FIELD EFFECT TRANSISTOR AS AN OPENING SWITCH, M.J. Rhee, B.N. Ding **665**

HIGH REPETITION RATE MEGAVOLT MARX GENERATORS, Yu.A. Kotov, S.N. Rukin **670**

150 KEV INTENSE ELECTRON BEAM ACCELERATOR SYSTEM WITH HIGH REPEATED PULSE, Q. Zhang, T. Li, H. Tang, N. Xia, Z. Wang, B. Zheng **676**

QUICK CHARGING BLUMLEIN PFL, K. Masugata, S. Tsuchida, H. Saitou, K. Shibata, M. Shigeta, Y. Sekimoto, K. Yatsui **682**

THE DEVELOPMENT OF A ONE MICROSECOND PULSE LENGTH, REPETITIVELY PULSED, HIGH POWER MODULATOR AND A LONG-PULSE ELECTRON BEAM DIODE FOR THE PRODUCTION OF INTENSE MICROWAVES, R.M. Stringfield, R.J. Faehl, M.V. Fazio, R.F. Hoeberling, T.J.T. Kwan, D.G. Rickel, F.W. VanHaaften, R.F. Wasierski, A. Erickson, K. Rust **688**

Paper Index - Volume II

Contributed Ion Beam Papers

NEW RESULTS FROM EXPERIMENTAL AND NUMERICAL INVESTIGATIONS OF THE SELF-MAGNETICALLY B-THETA-INSULATED ION DIODE, W. Bauer, H. Bachmann, H. Bluhm, L. Buth, P. Hoppe, H.U. Karow, H. Lotz, D. Rusch, Ch. Schultheiss, E. Stein, O. Stoltz, Th. Westermann **735**

GENERATION OF STRONG RADIAL MAGNETIC INSULATION FIELDS IN HIGH POWER ION DIODES IN EXTRACTION GEOMETRIES, P. Hoppe, H. Bluhm, H. Laqua, O. Stoltz **741**

ION BEAM GENERATION WITH INHOMOGENEOUS ANODE AND CATHODE PLASMAS, V. Fedorov, W. Schmidt, Th. Westermann **747**

ION DIODE SIMULATION FOR PULSED POWER GENERATORS WITH STATIONARY CODES, M. Alef, V.T. Astrelin, L. Feher, St. Illy, M. Kuntz, W. Schmidt, R. Schuldt, D. Seldner, E. Stein, Th. Westermann **756**

SIMULATION OF A BR ION DIODE, R.J. Faehl, D.J. Rej **762**

ION BEAM DIVERGENCE FROM UNSTABLE FLUCTUATIONS IN APPLIED-B DIODES, R.N. Sudan, D.W. Longcope **769**

QUICKSILVER SIMULATIONS OF APPLIED-B EXTRACTION DIODES, M.P. Desjarlais, T.D. Pointon **775**

OPERATION OF A HIGH IMPEDANCE APPLIED-B EXTRACTION ION DIODE ON THE SABRE POSITIVE POLARITY LINEAR INDUCTION ACCELERATOR, D.L. Hanson, M.E. Cuneo, P.F. McKay, J.E. Maenchen, R.S. Coats, J.W. Poukey, S.E. Rosenthal, W.E. Fowler, D.F. Wenger, M. Bernard, J.R. Chavez, W.F. Stearns **781**

LIF ION SOURCE PERFORMANCE ON PFBA II, R.W. Stinnett, T.A. Green, D.J. Johnson, T.R. Lockner, T.A. Mehlhorn, J.E. Bailey, A.B. Filuk, L.P. Mix, J. Panitz, P. Schwoebel **788**

SPECTROSCOPIC CHARACTERIZATION OF LEVIS ACTIVE ION SOURCE ON PBFA II, A.B. Filuk, J.E. Bailey, K.W. Bieg, A.L. Carlson, T.J. Renk, G.C. Tisone, Y. Maron **794**

LASER FORMATION OF LITHIUM PLASMA ION SOURCES FOR APPLIED-B ION DIODES ON THE PBFA-II ACCELERATOR, G.C. Tisone, T.J. Renk, D.J. Johnson, R.A. Gerber, R.G. Adams **800**

FORMATION PROCESS OF NEGATIVE IONS IN A MAGNETICALLY INSULATED DIODE, K. Horioka, Q. Yu, K. Kasuya **806**

MAGNETICALLY INSULATED H- DIODES, A. Fisher, V.M. Bystritskii, E. Garate, R. Prohaska, N. Rostoker **812**

ANODE DISCHARGE TO FACILITATE CATHODE PLASMA FORMATION FOR GENERATION OF H-, C-, F-, I-, AND PB- IONS, A.G. Mozgovoy, V.A. Papadichev **818**

H- GENERATION USING AN EXTERNALLY APPLIED PREPULSE, A.G. Mozgovoy, V.A. Papadichev **824**

LASER PLASMA PRODUCTION AND LASER DIAGNOSTICS FOR PULSED ION SOURCES, K. Kasuya, K. Horioka, T. Hushiki, N. Matsuura, T. Miyoshi, K. Nakata, Y. Miyai, Y. Kawakita, E. Ohshita **829**

IMPROVED FLASH-BOARD FOR PLASMA INJECTION DIODE, K. Kasuya, K. Horioka, H. Hayase . **835**

PRODUCTION OF PULSED F- BEAMS, A. Kitamura, K. Takahashi, A. Shinmura, Y. Furuyama, T. Nakajima **841**

CHARACTERISTICS OF HIGH POWER ION DIODE WITH REAL CATHODE, H. Sugimura, E. Chishiro, T. Tachibana, K. Masugata, K. Yatsui **847**

CHARACTERISTICS OF ION BEAM AND ANODE PLASMA IN "POINT PINCH DIODE", K. Masugata, T. Tazima, K. Yatsui **853**

POINT FOCUSING OF INTENSE ION BEAM BY SPHERICAL "PLASMA FOCUS DIODE", W. Jiang, T. Sakagami, K. Masugata, K. Yatsui **859**

CHARACTERISTICS OF THE INTENSE ION BEAMS GENERATED WITH THE POINT PINCH DIODE, M.Sato, T. Tazima **865**

EXPERIMENTAL STUDY OF THE PINCH-BEAM DIODE WITH THIN, UNBACKED FOIL ANODES, S.J. Stephanakis, J.R. Boller, G. Cooperstein, B.V. Weber, F.C. Young **871**

EXPERIMENTS ON GENERATION OF HIGH POWER ION BEAM IN PLASMA-FILLED DIODE, V.M. Bystritskii, A.V. Kharlov, G.A. Mesyats, A.V. Mytnikov, A.A. Sinebryukhov **878**

LIGHT ION DRIVER RESEARCH FOR INERTIAL FUSION, S. Miyamoto, K. Yasuike, S. Nakai, K. Imasaki, C. Yamanaka **884**

FAST MAGNETIC FIELD PENETRATION INTO AN INTENSE NEUTRALIZED ION BEAM, R. Armale, N. Rostoker **890**

DIVERGENCE IN INTENSE ION BEAMS CAUSED BY INCOMPLETE CHARGE NEUTRALIZATION, C.L. Olson, J.W. Poukey **897**

SPECTROSCOPIC STUDIES OF INTENSE ION BEAM PROPAGATION IN THE PBFA-II GAS CELL, J.E. Bailey, A.L. Carlson, D.J. Johnson, E.J. McGuire, T. Nash, C.L. Olson, J.J. MacFarlane, P. Wang **903**

BALLISTIC FOCUS LIGHT ION BEAMS FOR AN INERTIAL CONFINEMENT FUSION REACTOR, R.R. Peterson **909**

ION BEAM TRANSPORT AND FOCUSING EXPERIMENTS, J.C. Olson, B.R. Kusse **915**

FOCUSING OF INTENSE ION BEAMS WITH A PLASMA-FILLED SOLENOIDAL MAGNETIC LENS INCLUDING SELF-FIELDS, B.V. Oliver, R.N. Sudan **921**

ION BEAM MODELING USING ARGUS, J.J. Petillo, A.A. Mondelli, A. Mankofsky, C.L. Chang **927**

ESQ FOCUSING FOR AN INTENSE, HIGH-BRIGHTNESS H- BEAM: EMITTANCE GROWTH AND ITS REMEDY, S.K. Guharay, C.K. Allen, M. Reiser **933**

ORION PROJECT: ACCELERATION OF CLUSTER IONS AND HIGHLY CHARGED BIOMOLECULES FROM 10 MEV TO 1GEV, S. Della-Negra, Y. Le Beyec, A. Brunelle, D. Gardes, B. Waast, E. Parilis, P. Hakansson, B.U.R. Sundquist **939**

ION BEAM TRANSPORT IN A PREIONIZED PLASMA CHANNEL, S.P. Slinker, R.F. Hubbard, M. Lampe, G. Joyce, I. Haber **945**

STEERING ALGORITHMS FOR A HEAVY-ION RECIRCULATING ACCELERATOR, W.M. Sharp, J.J. Barnard, S.S. Yu **951**

GENERATION OF ULTRA HIGH PRESSURE WITH LIGHT ION BEAMS, B. Goel, O.Yu. Vorobjev, A.L. Ni **957**

TARGET EXPERIMENTS WITH LIGHT-ION BEAMS AT KALIF: MEASUREMENTS OF THE DYNAMIC STRENGTH AND SPALLATION THRESHOLD OF METALS AT HIGH STRAIN RATES, H. Bachmann, K. Baumung, G.I. Kanel, H.U. Karow, V. Licht, D. Rusch, J. Singer, O. Stoltz **963**

GENERATION OF EXTREME STATES IN CONDENSED MATTER BY HIGH-POWER ION BEAMS, V.E. Fortov, V.A. Skvortsov, V.V. Kostin, O.Yu. Vorobjev, I.V. Lomonosov, A.L. Ni, I. Hofmann, B. Goel **969**

PULSED-ION-BEAM DRIVEN ABLATION OF MATERIAL NEAR ITS SUBLIMATION ENERGY, A. Kitamura, T. Asahina, Y. Furuyama, T. Nakajima **976**

CHARGE FLUCTUATIONS, ENERGY STRAGGLING, AND MULTIPLE SCATTERING IN INTENSE ION BEAM-TARGET INTERACTIONS, Z. Zinamon, E. Nardi **982**

PARTICLE DRIVEN INERTIAL FUSION THROUGH CLUSTER ION BEAM, C. Deutsch, N.A. Tahir .. **988**

AN ANALYSIS OF CLUSTER-DRIVEN INERTIAL CONFINEMENT FUSION, M. Piera, S. Eliezer, J.M. Martinez-Val **995**

SMALL-SCALE TARGETS FOR HEAVY-ION DRIVEN INERTIAL CONFINEMENT FUSION EXPERIMENTS, J.M. Martinez-Val, G. Velarde, P. Velarde, M. Piera, M. Perlado, E. Minguez, J.J. Honrubia, J.M. Aragones **1001**

Contributed Electron Beam Papers

THEORETICAL EVALUATION OF THE ANGULAR SPREAD OF THE ELECTRON BEAM GENERATED IN A GUIDING MAGNETIC FIELD, D.D. Ryutov **1009**

NEW RESULTS ON MICROSECOND E-BEAM GENERATION FOR PLASMA HEATING EXPERIMENTS, Yu.I. Deulin, V.V. Filippov, A.V. Karyukin, S.V. Lebedev, M.A. Shcheglov, S.G. Voropaev **1015**

BREMSSTRAHLUNG PRODUCTION BY MICROSECOND E-BEAM FROM THIN FOIL IN A MIRROR TRAP, V.V. Filippov, V.S. Koidan, S.V. Lebedev, P.I. Melnikov, M.A. Shcheglov, S.G. Voropaev **1021**

FOILLESS INJECTION OF REB INTO A DENSE PLASMA, I.V. Kandaurov, Eh.P. Kruglyakov, O.I. Meshkov **1027**

FREQUENCY REGIME OF HIGH CURRENT RELATIVISTIC ELECTRON BEAMS INTERACTING WITH VARIOUS GASEOUS MEDIA, N.A. Kondratiev, V.I. Smetanin, Yu.P. Usov, V.E. Kulbeda..... **1033**

SPECTRA OF LANGMUIR TURBULENCE EXCITED BY HIGH-CURRENT REB, I.V. Kandaurov, Eh.P. Kruglyakov, M.V. Losev, O.I. Meshkov, A.L. Sanin, L.N. Vyacheslavov **1037**

ELECTRIC FIELD STRENGTH MEASUREMENTS IN A MEGAVOLT VACUUM DIODE USING LASER INDUCED FLUORESCENCE OF AN ATOMIC BEAM, B.A. Knyazev, V.V. Chikunov, P.I. Melnikov **1043**

TWO-STAGE DENSE PLASMA HEATING BY 100 KJ E-BEAM, A.V. Burdakov, V.V. Chikunov, A.F. Huber, A.V. Karyukin, V.S. Koidan, S.V. Lebedev, K.I. Mekler, P.I. Melnikov, A.A. Nikiforov, V.V. Postupaev, M.A. Shcheglov, S.G. Voropaev **1049**

SOFT X-RAY MEASUREMENTS OF MICROSECOND-E-BEAM-HEATED PLASMA, A.V. Burdakov, V.V. Postupaev, V. Piffl **1055**

ULTRAVIOLET FLASH LAMP ON THE NOBLE GAS DIMERS EXCITED BY AN E-BEAM, V.I. Klimov, G.P. Mkheidze, A.A. Savin **1061**

CONDUCTIVITY OF PLASMA CREATED BY REB IN ARGON, V.I. Klimov, G.P. Mkheidze, A.A. Savin **1067**

MICROWAVE GENERATION AND CHARGED PARTICLE ACCELERATION BY HIGH CURRENT RELATIVISTIC ELECTRON BEAMS, Yu.V. Tkach, I.F. Kharchenko, V.A. Balakirev, V.V. Dolgopolov, Yu.V. Kirichenko, S.M. Latinsky, E.M. Lats'ko, E.A. Lisenko, V.E. Novikov, A.O. Ostrovsky, A.V. Pashchenko, E.A. Prasol, S.S. Romanov **1073**

ELECTRON BEAM DIODES USING FERROELECTRIC CATHODES, J.D. Ivers, L. Schachter, J.A. Nation, G.S. Kerslick **1081**

THE NSWC MICROCHANNEL ELECTRON SOURCE PROGRAM, K.A. Boulais, J.Y. Choe, S.T. Chun, A. Krall, K. Irwin, S.E. Saddow, M.J. Rhee **1087**

LONG PULSE, PLASMA CATHODE E-GUN, D.M. Goebel, R.W. Schumacher, R.M. Watkins..... **1093**

CONTROLLING THE EMISSION CURRENT FROM A PLASMA CATHODE, S.P. Bugaev, V.I. Gushenets, P.M. Schanin **1099**

FORMATION OF INTENSE CONVERGENT PARTICLE BEAMS IN A GAS-DISCHARGE-PLASMA-EMITTER DIODE, N.V. Gavrilov, Yu.E. Kreindel, G.A. Mesyats, O.A. Shubin **1105**

FORMATION AND TRANSPORTATION OF A MICROSECOND HIGH CURRENT ELECTRON BEAM IN A PLASMA-ANODE GUN, M.Yu. Kreindel, E.A. Litvinov, G.E. Ozur, D.I. Proskurovsky **1111**

RIBBON REB RESEARCH ON 0.7 MJ GENERATOR U-2, A.V. Arzhannikov, V.B. Bobylev, V.S. Nikolaev, S.L. Sinitsky, M.V. Yushkov, R.P. Zotkin **1117**

HIGH BRIGHTNESS HOLLOW CATHODE ELECTRON BEAM SOURCE, G. Kirkman, N. Reinhardt, B. Jiang, M.A. Gundersen, T.Y. Hsu, R.L. Liou, R.J. Temkin **1123**

HIGH-CURRENT-DENSITY CATHODE OPERATION AND BEAM TRANSPORT WITH STEADY-STATE AND PULSED CATHODE HEATING METHODS, W.D. Getty, K.D. Pearce, M.E. Herniter **1129**

HIGH GRADIENT ACCELERATION IN A 17 GHZ PHOTOCATHODE RF GUN, S.C. Chen, B.G. Danly, J. Gonichon, C.L. Lin, R.J. Temkin, S. Trotz, J.S. Wurtele **1135**

BEAM GENERATION WITH THE 4-MV RLA INJECTOR AND ACCELERATION THROUGH THE ET-2 POST-ACCELERATING CAVITY, M.G. Mazarakis, D.L. Smith, J.W. Poukey, P.J. Skogmo, L.F. Bennett, M. George, W.R. Olson, M.J. Harden, B.N. Turman, S.A. Moya, J.L. Henderson, K.W. Struve **1141**

DESIGN AND EVALUATION OF THE XBT DIODE, E.L. Wright, A. Vlieks, K. Fant, C. Pearson, R. Koontz, D. Jensen, G. Miram **1147**

THE PHYSICS OF "VACUUM" BREAKDOWN, F. Schwirzke, M.P. Hallal, Jr., X.K. Maruyama **1153**

SIMULATIONS OF A PLASMA-FILLED PINCHED ELECTRON BEAM DIODE, S.B. Swanekamp, J.M. Grossmann, P.F. Ottinger, S.J. Stephanakis, B.V. Weber, J.C. Kellogg, G. Cooperstein **1159**

ONE-DIMENSIONAL NUMERICAL SIMULATION OF PLASMA FILLED PLANAR DIODE, I.V. Glazyring, V.S. Diyankov, A.A. Kondratyev, A.I. Kormilitsin, A.P. Yalovets **1165**

NONLINEAR DYNAMICS IN A REFLEX DIODE, M.S. Litz, J. Golden **1170**

POST ACCELERATION OF A PSEUDOSPARK-PRODUCED HIGH-BRIGHTNESS ELECTRON BEAM, B.N. Ding, M.J. Rhee **1176**

TIME-RESOLVED BEAM ENERGY MEASUREMENT OF SHORT ELECTRON BEAM BUNCHES WITH A LONGITUDINAL VELOCITY TILT, D.X. Wang, J.G. Wang, M. Reiser **1182**

THE EFFECTS OF BEAM PARAMETERS ON BREMSSTRAHLUNG EXPOSURE ANGULAR DISTRIBUTION, S. Jiangjun, M. Qian **1188**

BREMSSTRAHLUNG RADIATION ON THE SNOP FACILITIES, A.V. Luchinsky, V.K. Petin, N.A. Ratakhin, N.A. Smirnov, V.F. Fedushchak **1194**

THEORY OF THE BREMSSTRAHLUNG CONVERTER FOR RAISING ENERGY EXTRACTION IN THE RANGE 10-100 KEV, V.V. Ryzhov, A.A. Sapozhnikov **1199**

HIGH-INTENSITY FLASH X-RAY PRODUCTION BY REB, V.F. Zinchenko, V.V. Timofeyev, V.D. Shiyan **1205**

HARMONIC EMISSION IN A DIELECTRIC MEDIUM WITH A UNIFORM MAGNETIC FIELD, J. Soln **1211**

BREMSSTRAHLUNG RISETIME SHORTENING BY DIODE GEOMETRY RECONFIGURATION, M. Bushell, R. Fleetwood, D.C. Judy, G. Merkel, M. Smith, D.M. Weidenheimer **1215**

APPLICATION OF A SMALL ANGULAR SPREAD BEAM IN THE REFLECTED REB REGIME ON REBEX MACHINE, V. Piffl, V. Bohacek, M. Clupek, J. Raus, P. Sunka, J. Ullschmied **1221**

AN EXPERIMENTAL STUDY OF STRONG TURBULENCE DRIVEN BY AN INTENSE RELATIVISTIC ELECTRON BEAM, M. Masuzaki, R. Ando, M. Yoshikawa, H. Morita, J. Yasuoka, K. Kamada **1227**

INTENSE ELECTRON BEAM RADIUS-TAILORING EXPERIMENT FOR PROPAGATION STUDIES, D.J. Weidman, J.D. Miller, K.T. Nguyen, M.J. Rhee, R.F. Schneider, R.A. Stark **1233**

THEORY OF WAKEFIELD AND JXB DRIFT EFFECTS OF A RELATIVISTIC ELECTRON BEAM PROPAGATING IN A PLASMA, H.S. Uhm **1239**

RELATIVISTIC ELECTRON BEAM PROPAGATION IN HIGH PRESSURE GASEOUS MEDIA, J.A. Antoniades, M.C. Myers, D.P. Murphy, R.F. Hubbard, T.A. Peyser, R.F. Fernsler, R.E. Pechacek, J. Santos, R.A. Meger **1245**

TRANSPORT OF HIGH CURRENT, RELATIVISTIC ELECTRON BEAMS USING ACTIVE-WIRE B-THETA CELL TECHNIQUES, D.P. Murphy, R.E. Pechacek, M.C. Myers, J.A. Antoniades, T.A. Peyser, R.F. Fernsler, R.F. Hubbard, J. Santos, R.A. Meger **1251**

IFR TRANSPORT EXPERIMENTS ON THE SUPERIBEX ACCELERATOR, M.C. Myers, J.A. Antoniades, T.A. Peyser, D.P. Murphy, R.E. Pechacek, R.F. Hubbard, R.A. Meger **1257**

BEAM PROFILE DIAGNOSTICS ON THE NRL SUPERIBEX EXPERIMENT, T.A. Peyser, M.C. Myers, R.E. Pechacek, D.P. Murphy, J.A. Antoniades, R.A. Meger **1263**

ASYMPTOTIC AND NONLINEAR EVOLUTION OF THE ELECTRON-HOSE INSTABILITY OF A REB PROPAGATING IN THE ION-FOCUSED REGIME, M. Lampe, G. Joyce, S.P. Slinker, D.H. Whittum **1270**

THEORY AND SIMULATION OF THE RESISTIVE HOSE INSTABILITY IN RELATIVISTIC ELECTRON BEAMS, R.F. Fernsler, S.P. Slinker, R.F. Hubbard, M. Lampe **1276**

ELECTRON BEAM PROPAGATION IN THE ION-FOCUSED AND RESISTIVE REGIMES, R.F. Hubbard, M. Lampe, R.F. Fernsler, S.P. Slinker **1282**

CONDITIONS FOR STABLE OPERATION IN A HELICAL QUADRUPOLE FOCUSING ACCELERATOR, C.M. Tang, J. Krall **1288**

A HIGH-ORDER MOMENT SIMULATION MODEL, K.T. Tsang, C. Kostas, D.P. Chernin, J.J. Petillo, A.A. Mondelli **1294**

REFINED DEFINITION OF THE BEAM BRIGHTNESS AS THE ARITHMETIC MEAN OF THE DISTRIBUTION FUNCTION, T.J. Myers, K.A. Boulais, M.J. Rhee **1300**

ELECTRON BEAM TRANSPORT, Yu.V. Rudjak, V.B. Vladyko **1306**

GENERATION AND CHARACTERISTICS OF HIGH POWER LONG PULSE ELECTRON BEAM (PROPAGATION IN VACUUM WITH DIFFERENT PRESSURE), G.I. Alexeev, A.M. Bishaev, A.A. Golubev, V.A. Gudovich, A.H. Kadimov, G.I. Klenov, V.P. Larionov, O.I. Radkevich, O.V. Shterbina **1312**

GENERATION OF MICROWAVE OSCILLATIONS IN AN ELECTRODYNAMIC SYSTEM WITH PLASMA-BEAM INTERACTION, V.I. Perevodchikov, M.A. Zavialov, V.F. Martynov, L.A. Mitin, V.N. Tskhai, A.L. Shapiro **1318**

CYCLOTRON RADIATION OF AN REB INJECTED INTO INCREASING MAGNETIC FIELD, B.A. Alterkop, V.M. Mikhailov, A.A. Rukhadze, V.P. Tarakanov **1322**

LONG PULSE ELECTRON BEAM PROPAGATION, J.R. Smith, I.R. Shokair, K.W. Struve, P.W. Werner, S. Hogeland, P.D. Kiekel, I. Molina, B.N. Turman, R.B. Miller **1328**

Contributed Beam Diagnostics Papers

FAST H-ALPHA LINE BROADENING DURING THE 100 NS REB INJECTION INTO A PLASMA, K. Kolacek, M. Ripa, J. Ullschmied, K. Jungwirth, P. Sunka **1337**

THE BEAM CURRENT DIAGNOSING IN LARGE AREA DIODES, D. Huang, W. Ma, X. Wang, N. Zeng, Y. Shan, Y. Wang, D. Zhang **1343**

THE STRENGTH CALCULATION FOR A FOIL COAXIAL SHUNT, D. Huang **1349**

AN OFFSET MODEL RADIATION CALORIMETER, S. Fu, Y. Chen, K. Hu **1354**

INTRABAND RADIOLUMINESCENCE OF DIELECTRICS: PROPERTIES AND APPLICATIONS TO HIGH POWER BEAM DIAGNOSTICS, D.I. Vaysburd, B.N. Syomin **1360**

COMPUTER ASSISTED DIAGNOSTICS ON A HIGH-POWER MICROWAVE SYSTEM, M.T. Crawford, M. Kristiansen, L.L. Hatfield, S.E. Calico **1367**

SQUEEZED STATES OF HIGH-CURRENT ELECTRON BEAM IN A SYSTEM WITH VIRTUAL CATHODE, A.V. Fedotov, A.M. Ignatov, V.P. Tarakanov **1373**

ELECTRON BEAM DEFLECTION DIAGNOSTIC, M.T. Ngo, J.A. Pasour **1379**

ELECTRON BEAM POTENTIAL MEASUREMENTS ON AN INDUCTIVE-STORE, OPENING-SWITCH ACCELERATOR, J.C. Riordan, J.R. Goyer, D. Kortbawi, J.S. Meachum, R.S. Mendenhall, I.S. Roth **1385**

A NEW TIME-RESOLVED ENERGY-FLUX GAUGE FOR PULSED ION BEAMS, S.H. Richter, D.V. Keller **1391**

THEORETICAL SPECTROSCOPIC ANALYSIS OF INTENSE ION BEAM-PLASMA INTERACTION IN THE PBFA II GAS CELL, P. Wang, J.J. MacFarlane, G.A. Moses, J.E. Bailey **1397**

MULTI-DIMENSIONAL DIAGNOSTICS OF HIGH POWER ION BEAMS BY ARRAYED PINHOLE CAMERA SYSTEM, K. Yasuike, S. Miyamoto, N. Shirai, T. Akiba, S. Nakai, K. Imasaki, C. Yamanaka **1403**

Paper Index - Volume III

Contributed Microwave Papers

OPTIMIZATION OF THE OUTPUT CAVITY FOR A THREE CAVITY X-BAND GYROKLYSTRON AMPLIFIER, W. Main, S.G. Tantawi, P.E. Latham, B. Hogan, W. Lawson, C.D. Striffler, V.L. Granatstein **1449**

THEORETICAL INVESTIGATION OF ANOMALOUSLY HIGH EFFICIENCY IN A THREE CAVITY GYROKLYSTRON AMPLIFIER, P.E. Latham, U.V. Koc, W. Main, S.G. Tantawi **1455**

HIGH EFFICIENCY, LOW MAGNETIC FIELD GYROKLYSTRON AMPLIFIERS, P.E. Latham, G.S. Nusinovich, B. Levush **1461**

MODE-PRIMED OPERATION OF AN 85 GHZ QUASIOPTICAL GYROKLYSTRON, R.P. Fischer, A.W. Fliflet, W.M. Manheimer **1467**

LARGE ORBIT GYROKLYSTRON DEVELOPMENT AT LOS ALAMOS, R.M. Stringfield, R.M. Wheat, D.J. Brown, M.V. Fazio, J. Kinross-Wright, B.E. Carlsten, G. Rodenz, R.J. Faehl, R.F. Hoeberling **1473**

THE NRL 11.4 GHZ MAGNICON AMPLIFIER EXPERIMENT, S.H. Gold, C.A. Sullivan, B. Hafizi, W.M. Manheimer, W.M. Black **1479**

HIGH PERFORMANCE 33.2 GHZ GYROKLYSTRON, J.D. McNally, M.P. Bobys, D.B. McDermott, N.C. Luhmann, Jr. **1485**

HARMONIC GYRO-TWT AMPLIFIER FOR HIGH POWER, Q.S. Wang, D.B. McDermott, N.C. Luhmann, Jr., A.T. Lin, C.S. Kou, K.R. Chu **1491**

STABILITY AND NONLINEAR DYNAMICS OF GYROTRONS AT CYCLOTRON HARMONICS, G.P. Saraph, G.S. Nusinovich, T.M. Antonsen, Jr., B. Levush **1497**

PROSPECTS FOR DEVELOPMENT OF POWERFUL, HIGHLY EFFICIENT, RELATIVISTIC GYRODEVICES, G.S. Nusinovich, V.L. Granatstein **1503**

DEPRESSED COLLECTORS FOR MILLIMETER WAVE GYROTRONS, A. Singh, V.L. Granatstein **1508**

COHERENT FAST WAVE RADIATION FROM SPATIOTEMPORALLY MODULATED GYRATING RELATIVISTIC ELECTRON BEAMS, J.L. Hirshfield, A.K. Ganguly **1514**

CYCLOTRON AUTORESONANCE MASERS: RECENT EXPERIMENTS AND PROJECTS, V.L. Bratman, G.G. Denisov, S.V. Samsonov **1520**

CYCLOTRON AUTORESONANCE MASER (CARM) AMPLIFIER EXPERIMENTS AT 17 GHZ, W.L. Menninger, B.G. Danly, S. Alberti, C. Chen, D.L. Goodman, E. Giguet, J.L. Rullier, J.S. Wurtele, R.J. Temkin **1526**

CYCLOTRON AUTORESONANCE MASER (CARM) OSCILLATOR EXPERIMENT AT 28 GHZ, G. Gulotta, S. Alberti, B.G. Danly, T. Kimura, W.L. Menninger, J.L. Rullier, R.J. Temkin **1532**

THE ELECTRODYNAMICS OF A CO-AXIAL PLASMA SLOW-WAVE STRUCTURE OF A PLASMA CHERENKOV AMPLIFIER DRIVEN BY A HIGH-CURRENT REB IN FINITE MAGNETIC FIELD, I.A. Selivanov, A.G. Shkvarunets, V.P. Tarakanov **1538**

EXPERIMENTAL STUDY AND PIC-SIMULATION FOR THE PCM OPERATION, P.S. Strelkov, A.G. Shkvarunets, V.P. Tarakanov **1545**

INFLUENCE OF CATHODE PLASMA UPON THE RADIATION PULSE DURATION OF VACUUM MICROSECOND RELATIVISTIC MICROWAVE GENERATOR, O.T. Loza, P.S. Strelkov, S.N. Voronkov **1550**

THE "HOSE TYPE" INSTABILITY OF REB AND MICROWAVE GENERATION IN A WAVEGUIDE, A.A. Rukhadze, P.V. Rybak, V.P. Tarakanov **1556**

ON SOME PRACTICAL CONSIDERATION OF THE ELECTRON BEAM BREAKUP TRANSIT TIME OSCILLATOR, T.J.T. Kwan **1562**

EXTERNAL QUASI-OPTICAL FEEDBACK SYSTEM FOR NARROWING RADIATION BAND, V.A. Bogachenkov, V.A. Papadichev, I.V. Sinilshikova, O.A. Smith **1568**

RELATIVISTIC MAGNETRONS: OPTIMIZATION OF PARAMETERS AND MODELLING OF PHASE LOCKING PROCESSES, D.V. Alexandrovich, S.V. Baranov, A.N. Didenko, N.M. Filipenko, G.P. Fomenko, A.S. Maidanovskii, S.S. Novikov, V.V. Pozdeev, A.S. Sulakshin **1574**

THE NONUNIFORM-PHASE-VELOCITY RELATIVISTIC BWO, S.D. Korovin, S.D. Polevin, V.V. Rostov, A.M. Roitman **1580**

THE STATE OF ART OF INVESTIGATIONS OF RELATIVISTIC MULTIWAVE MICROWAVE GENERATORS, A.N. Bastrikov, S.P. Bugaev, I.A. Chernyavsky, M.P. Deichuli, P.A. Khryapov, V.I. Koshelev, V.V. Lopatin, N.S. Sochugov, K.N. Sukhushin, A.N. Zakharov, V.I. Kanavets, V.M. Pikunov, A.I. Slepkov **1586**

CHERENKOV MICROWAVE GENERATOR OF HIGH-CURRENT RELATIVISTIC ELECTRON BEAMS, N.F. Kovalev **1592**

MULTIWAVE RELATIVISTIC ELECTRON DEVICES: PROGRESS AND PROSPECTS, V.A. Cherepenin **1596**

HIGH POWER X-BAND MICROWAVE AMPLIFIERS AND THEIR APPLICATION FOR PARTICLE ACCELERATION, T.J. Davis, J.D. Ivers, G.S. Kerslick, E. Kuang, J.A. Nation, M. Oppenheim, L. Schachter **1601**

RECENT RESULTS FROM THE UNIVERSITY OF MARYLAND OVERMODED BWO AND MWCG PROGRAM, D.K. Abe, T.M. Antonsen, Jr., Y. Carmel, B. Levush, S.M. Miller, A. Bromborsky **1607**

THEORY OF RELATIVISTIC BACKWARD WAVE OSCILLATORS OPERATING NEAR CUTOFF, S.M. Miller, T.M. Antonsen, Jr., B. Levush, A. Bromborsky **1613**

THEORY OF RELATIVISTIC BACKWARD WAVE OSCILLATORS OPERATING NEAR CYCLOTRON RESONANCE, A. Vlasov, G.S. Nusinovich, B. Levush, A. Bromborsky **1619**

DIELECTRIC CHERENKOV MASER AS A POWERFUL AMPLIFIER WITH SUPERWIDE BANDWIDTH, A.S. Shlapakovskii, K.A. Chirko **1625**

EXPERIMENTAL STUDY OF A PLASMA-FILLED BACKWARD WAVE OSCILLATOR, X. Zhai, E. Garate, R. Prohaska, A. Fisher, G. Benford **1631**

PASOTRON HIGH-ENERGY MICROWAVE SOURCE, J.M. Butler, D.M. Goebel, R.W. Schumacher, J. Hyman, J. Santoru, R.M. Watkins, R.J. Harvey, F.A. Dolezal, R.L. Eisenhart, A.J. Schneider..... **1637**

THEORY OF THE INTERACTION OF ELECTRON BEAMS WITH THE WAVES IN PLASMA FILLED WAVEGUIDES, N.I. Karbushev, Yu.A. Kolosov, Ye.I. Ostrenskiy, A.I. Polovkov, A.D. Shatkus, L.A. Mitin, I.L. Volokitenkova, V.A Balakirev, G.V. Sotnikov..... **1643**

RESEARCH ON A 1.3 GHZ ANNULAR ELECTRON BEAM POWERED MULTI-GIGAWATT MICROWAVE AMPLIFIER, K.J. Hendricks, W.R. Fayne, L.A. Bowers, C.E. Davis, M.D. Haworth, R.C. Platt, R.W. Lemke, M.C. Clark **1649**

APPLICATION OF HIGH-CURRENT ACCELERATORS WITH INDUCTORS, BASED ON DISTRIBUTED PARAMETER LINES FOR GENERATION OF HIGH-POWER MICROWAVE PULSES, A.I. Pavlovskii, V.D. Selemir, V.V. Ivanov, I.V. Konovalov, I.G. Prikhod'ko, V.G. Suvorov, K.V. Shibalko, V.G. Kornilov, V.Y. Vatrunin, V.S. Zhdanov..... **1655**

EFFECT OF INTENSE SPACE CHARGE IN RALATIVISTIC KLYSTRON AMPLIFIERS, B.E. Carlsten, R.J. Faehl, M.V. Fazio, T.J.T. Kwan, D.G. Rickel, R.D. Ryne, R.M. Stringfield..... **1661**

A PROPOSED EXTENDED CAVITY FOR COAXIAL RELATIVISTIC KLYSTRONS, L. Schachter, T.J. Davis, J.A. Nation..... **1667**

RELATIVISTIC HIGH POWER KLYSTRONS, A.N. Sandalov, V.M. Pikunov, V.E. Rodiakin, A.A. Stogov..... **1673**

A NONLINERAR THEORY OF ENERGY AND CURRENT MODULATION IN RELATIVISTIC KLYSTRON AMPLIFIERS, H.S. Uhm **1679**

THE TIME ENERGY COMPRESSION OF PULSE MICROWAVE VIRCATOR RADIATION, P.Yu. Chumerin, G.V. Melnikov, S.A. Novikov, S.V. Razin, Yu.G. Yushkov, A.G. Zcherlitsin, A.N. Didenko **1685**

FREQUENCY CONTROL OF VIRCATOR MICROWAVE RADIATION, A.N. Didenko, M.Yu. Antoshkin, G.P. Fomenko, V.P. Grigoryev, T.V. Koval, G.V. Melnikov, V.I. Tsvetkov, A.G. Zherlitsin..... **1690**

NUMERICAL SIMULATION AND EXPERIMENT STUDY OF VIRCATOR, Z.X. Wang, Y.Q. Chen, Y.S. Chen, R.Y. Fan **1696**

EXPERIMENTAL STUDY OF VIRTUAL CATHODE OSCILLATOR IN UNIFORM MAGNETIC FIELD, K.G. Kostov, N.A. Nikolov, I.P. Spasovsky, R. Atanassov **1700**

Contributed Free Electron Laser Papers

NONLINEAR SIMULATION OF A HIGH-POWER COLLECTIVE FREE-ELECTRON LASER, H.P. Freund, A.K. Ganguly **1709**

ANALYSIS OF THE ELECTRON DYNAMICS IN A RAMAN FREE ELECTRON LASER WITH REVERSED AXIAL GUIDE MAGNETIC FIELD, G. Spindler, G. Renz, M.E. Conde, G. Bekefi **1715**

HELICAL SMALL PERIOD WIGGLER FOR THE RAMAN FREE ELECTRON LASER OF SIOFM, M.C. Wang, B. Feng, Z. Wang, Z. Lu, L. Zhang **1721**

DEVELOPMENT OF A HIGH POWER MILLIMETER WAVE FREE-ELECTRON LASER AMPLIFIER, S.W. Bidwell, Z.X. Zhang, T.M. Antonsen, Jr., W.W. Destler, V.L. Granatstein, B. Levush, J. Rodgers, H.P. Freund **1728**

A KIND OF MICRO-FEL DEVICE WITH SUPER-HIGH GAIN, W. Ding **1734**

OPTICAL GUIDING AND SUPERRADIANCE EFFECTS IN FREE ELECTRON LASERS, N.S. Ginzburg **1740**

NONLINEAR ANALYSIS OF A GRATING FREE-ELECTRON LASER, B. Hafizi, P. Sprangle, P. Serafim, A. Fisher **1746**

EUPHROSYNE, A PULSED ELECTRON GENERATOR FOR FEL APPLICATION, C. Bonnafond, J. Bardy, H. Bottollier-Curtet, A. Devin, J. Gardelle, G. Germain, J. Labrouche, J. Launspach, P. Le Taillandier, J. de Mascureau **1752**

FEL PROJECT FOR INDUSTRIAL APPLICATIONS IN JAPAN, K. Imasaki, S. Sato, Y. Miyauchi, T. Keishi, A. Kobayashi, A. Koga, E. Nishimura, K. Saeki, I. Bessho, M. Okano, S. Abe, A. Nagai, T. Tomimasu **1758**

A FREE ELECTRON LASER AT P. N. LEBEDEV INSTITUTE, Accelerator Physics Laboratory Staff **1764**

FREE ELECTRON LASER -FEL- BASED ON MSU RM-100 RACE-TRACK MICROTRON, V.K. Grishin, B.S. Ishkhanov, A.N. Sandalov, V.I. Shvedunov **1770**

HIGH CURRENT CERENKOV FREE ELECTRON LASER-CFEL AT FAR INFRARED WAVELENGTHS, V.K. Grishin, C.M. Cricket, I.F. Lenski **1776**

Contributed Advanced Accelerator Papers

MODEL OF CAVITY COUPLING FOR BEAM BREAKUP CONTROL, D.G. Colombant, Y.Y. Lau, D.P. Chernin **1783**

EXPERIMENTS ON THE EXCITATION AND COUPLED-CAVITY SUPPRESSION OF BEAM-BREAKUP-INSTABILITY IN LONG-PULSE ELECTRON BEAM TRANSPORT, R.M. Gilgenbach, P.R. Menge, M.T. Walter, C.H. Ching, J. Foster, P.L.G. Ventzek **1789**

ELECTRON FLOW IN POSITIVE-POLARITY MULTIGAP INDUCTIVE ACCELERATORS, B.W. Church, R.N. Sudan **1795**

SIMULATIONS OF MULTISTAGE INTENSE ION BEAM ACCELERATION, S.A. Slutz, J.W. Poukey **1801**

PROSPECTS OF CYCLOTRON RESONANCE LASER ACCELERATION, C. Chen **1807**

NUMERICAL SIMULATIONS OF DENSITY CHANNEL GUIDING AND RELATIVISTIC OPTICAL GUIDING OF LASER PULSES IN A PLASMA, J. Krall, G. Joyce, P. Sprangle, E. Esarey **1813**

TWO-BEAM VIRTUAL CATHODE ACCELERATOR, W. Peter **1819**

EXPERIMENTAL STUDIES OF BEAM ACCELERATION WITH A SHORT PULSE X-BAND ELECTRON CYCLOTRON MASER, K. Kamada, T. Kanazawa, M. Sakamoto, N. Matsumura, F. Tamagawa, R. Ando, M. Masuzaki, S. Kawasaki **1825**

COLLECTIVE ACCELERATION OF LIGHT ION BEAMS IN KALI-200, T. Vijayan, P. Roychowdhury, S.K. Iyyengar **1831**

MODELING HIGH-POWER RF ACCELERATOR CAVITIES WITH SPICE, S. Humphries, Jr. **1837**

SUPERFISH POST-PROCESSOR FOR IBM-PC COMPATIBLE COMPUTERS, S. Humphries, Jr. **1843**

SIMULATION STUDIES OF BEAM QUALITY IN HIGH-GRADIENT ACCELERATORS, G. Joyce, J. Krall **1849**

CLIA - A COMPACT LINEAR INDUCTION ACCELERATOR SYSTEM, S.R. Ashby, D. Drury, P.S. Sincerny, L. Thompson, L. Schlitt **1855**

THE LELIA INDUCTION INJECTOR: FIRST RESULTS, J. Bardy, P. Anthouard, P. Eyharts, P. Eyl, M. Thevenot, A. Roques, D. Villate **1861**

HIGH-CURRENT LINEAR ACCELERATOR, A.G. Mozgovoy **1867**

RECENT ADVANCES IN INDUCTION ACCELERATION AND POSTACCELERATION OF HIGH-CURRENT BEAMS AT TOMSK NUCLEAR PHYSICS INSTITUTE, V.V. Vasiljev, I.B. Ivanov, G.G. Kanaev, O.N. Tomskikh, Yu.P. Usov, E.G. Furman **1870**

A 3.4 MEV LINEAR INDUCTION ACCELERATOR, C. Nianan, S. Zhang, Z. Tao **1876**

BEAM MATCHING INTO THE DARHT LINAC, T.P. Hughes, D.C. Moir, R.L. Carlson **1881**

HITMI: EXPERIMENTS WITH AN ELECTRON-BEAM DRIVEN VACUUM LINEAR INDUCTION ACCELERATOR, C. Ekdahl, S. Humphries, Jr., W. Rix, C. Warn **1887**

Contributed Beam Applications Papers

FOCUSING AND PROPAGATION OF PROTON BEAM AS DRIVER OF ICF, K. Niu **1895**

LIBRA-LITE, A BALLASTIC FOCUS LIGHT ION INERTIAL CONFINEMENT FUSION REACTOR, R.R. Peterson, D. Bruggink, R.L. Engelstad, G.L. Kulcinski, E.G. Lovell, J.J. MacFarlane, E.A. Mogahed, G.A. Moses, S. Rutledge, M.E. Sawan, I.N. Sviatoslavsky, G. Sviatoslavsky, L.J. Wittenberg **1901**

IONIZATION OF A HIGH ENERGY NEUTRAL BEAM PROPAGATING IN THE IONOSPHERE, S.T. Lai **1907**

LARGE AREA ELECTRON BEAM GENERATION AND PROPAGATION FOR KRF LASERS, C.J. Pawley, J.D. Sethian, S.P. Obenschain, S.J. Czuchlewski **1912**

DEVELOPMENT OF A 100 JOULE LEVEL XECL LASER PUMPED BY INTENSE RELATIVISTIC ELECTRON BEAM, J.R. Liu, R.F. Sun, A.C. Qiu, X. Yuan, Y.G. Gan, X.H. Wang, Y.M. Zhang, X.Q. Zhao, S.Q. Ren, L. Nie, D.S. Yao, L.G. Wang, M. Zhang, Y.M. Wei, L.H. Wang **1918**

REB PUMPED SYSTEMS WITH MULTIPOLE MAGNETIC FIELD WALL SHIELDING, G.P. Mkheidze, A.A. Savin, F.B. Trintchouk **1924**

LARGE-APERTURE E-BEAM PUMPED EXCIMER LASERS FOR ICF, E.P. Bolshakov, V.A. Burtsev, M.A. Vasilevsky, V.M. Vodovosov, V.V. Jeremkin, V.E. Kuznetsov, V.A. Ovsyannikov, O.P. Pechersky, V.F. Prokopenko, R.F. Fidelskaya, K.I. Finkelstein, V.I. Chernobrovin, V.I. Chetvertkov, V.Yu. Baranov, A.P. Streltsov **1930**

PULSE HEAT TREATMENT OF MATERIAL SURFACE BY HIGH-CURRENT ELECTRON BEAM, V.I. Engelko, A.V. Lazarenko, O.P. Pechersky **1935**

DISSIPATION OF STRESS WAVE ENERGY AND STRUCTURAL MODIFICATION OF STEELS IRRADIATED BY A LOW-ENERGY HIGH-CURRENT ELECTRON BEAM, V.I. Itin, Yu.F. Ivanov, S.V. Lykov, G.A. Mesyats, G.E. Ozur, D.I. Proskurovsky, V.P. Rotshtein **1942**

ACTION OF A NANOSECOND MEGAVOLT HIGH-CURRENT ELECTRON BEAM ON METALS AND ALLOYS, I.M. Goncharenko, A.M. Efremov, Yu.F. Ivanov, V.I. Itin, B.M. Kovalchuk, S.V. Lykov, A.B. Markov, V.P. Rotshtein, A.A. Tukhfatullin **1948**

HIGH ENERGY ELECTRON BEAM MATERIALS PROCESSING, R.A. Stark, R.F. Schneider, E.E. Nolting, M. Skopec, J.C. Danko, C.D. Lundin, T.T. Meek **1954**

ENHANCEMENT OF METAL PROPERTIES BY IRRADIATION WITH INTENSE, HIGH-ENERGY ELECTRON BEAMS, K.W. Struve, A.C. Smith, E.L. Neau **1960**

HIGH-RATE DEPOSITION OF THIN FILMS BY HIGH-POWER ION BEAM, I.F. Isakov, G.E. Remnev, A.N. Zakutayev **1966**

QUICK PREPARATION OF THIN FILMS AND CHARACTERISTICS OF ABLATION PLASMA PRODUCED BY ION-BEAM EVAPORATION, T. Sonegawa, X.D. Kang, H. Hoshino, M. Ohashi, Y. Shimotori, S. Furuuchi, K. Masugata, K. Yatsui **1971**

Contributed Plasma Discharge Papers

ELECTROTHERMAL PLASMA SOURCE AS A HIGH HEAT FLUX SIMULATOR FOR PLASMA-FACING COMPONENTS AND LAUNCH TECHNOLOGY STUDIES, M. Bourham, J. Gilligan, O. Hankins, W. Eddy, J. Hurley **1979**

PLASMA DYNAMICS AND HOTSPOTS STUDIES FROM A PLASMA FOCUS DEVICE, C.C. Tzeng, C.K. Yeh, Y.J. Yu, Y.Y. Kuo, M. Wen, W.S. Hou, T.R. Yeh **1984**

DEUTERIUM-FIBER-INITIATED Z-PINCHES: SIMULATION COMPARED TO EXPERIMENT, P. Sheehey, I.R. Lindemuth, R.H. Lovberg, R.A. Riley, Jr. **1990**

RADIATIVE COLLAPSE OF A DENSE PLASMA, H.U. Rahman, N. Rostoker, F.J. Wessel..... **1996**

GOLD Z-PINCHES ON SATURN, R.B. Spielman **2002**

DIFFERENT STABILIZATION PROCESSES IN Z-PINCH PLASMA EXPERIMENTAL APPROACH, B. Etlicher, A.S. Chuvatin, L. Veron, F.J. Wessel, C. Rouille, S. Attelan, P. Choi **2008**

HIGH POWER IMPODING PLASMA FOR THE X-RAY LASER, R.B. Baksht, I.M. Datsko, V.A. Kokshenev, A.A. Kim, A.V. Luchinsky, V.V. Loskutov, V.I. Oreshkin, A.G. Russkich **2014**

MULTICHANNEL X-RAY SPECTRAL MEASUREMENT OF HOT PLASMA EVOLUTION IN NITROGEN-PUFF Z-PINCH, A. Krejci, J. Raus, V. Piffl, A.V. Golubev, Yu.Ya. Platonov, E. Krousky, O. Renner **2020**

INVESTIGATION OF INTENSE XUV EMISSION OF NITROGEN-PUFF Z-PINCH WITH SMAL ENERGY INPUT, J. Raus, A. Krejci, V. Piffl..... **2026**

TIME RESOLVED INTERFEROMETRY OF PLASMA RADIATION SOURCE LOADS, E.J. Yadlowsky, R.C. Hazelton, J.J. Moschella, T.B. Settersten..... **2032**

MAGNETIC PICKUP LOOP ANALYSIS OF AN EXPLODING WIRE Z-PINCH, J.J. Moschella, E.J. Yadlowsky **2038**

PHENOMENOLOGICAL MODELING OF ARGON Z-PINCH IMPLOSIONS, K.G. Whitney, J.W. Thornhill, C. Deeney, P.D. LePell, M.C. Coulter **2044**

RADIATION HYDRODYNAMICS OF AN IMPODING ARGON PUFF GAS PLASMA, J. Davis, F.L. Cochran..... **2050**

ANOMALOUS RESISIVITY IN A Z-PINCH SYSTEM, P.E. Pulsifer, K.G. Whitney..... **2056**

A NUMERICAL STUDY OF THE STAGNATING COMPACT TOROID AND ITS APPLICABILITY AS A RADIATION SOURCE, M.R. Douglas, R.E. Peterkin, Jr., T.W. Hussey, D.E. Bell, N.F. Roderick.... **2062**

HYDRODYNAMICS OF A STAGNATING RING-PUFF PLASMA, R.W. Clark, J. Davis, J. Les..... **2068**

Invited Ion Beam Papers

Donald L. Cook, *Session Chairman*

PROGRESS IN LITHIUM BEAM FOCUSING AND BEAM-TARGET INTERACTION EXPERIMENTS AT SANDIA NATIONAL LABORATORIES

T.A. Mehlhorn, L.D. Bacon, J.E. Bailey, D.D. Bloomquist, G.A. Chandler, R.S. Coats, D. L. Cook, M.E. Cuneo, M.S. Derzon, M.P. Desjarlais, R.J. Dukart, A.B. Filuk, T.A. Haill, D.L. Hanson, D.J. Johnson, R.J. Leeper, T.R. Lockner, C.W. Mendel, L.P. Mix, A.R. Moats, J.P. Quintenz, T.D. Pointon, T.J. Renk, G.E. Rochau, S.E. Rosenthal, C.L. Ruiz, D.B. Seidel, S.A. Slutz, R.W. Stinnett, W.A. Stygar, G.C. Tisone, R.E. Olson, J.P. VanDevender, D.F. Wenger

Sandia National Laboratories, Albuquerque, New Mexico

Abstract

Significant progress in the generation and focusing of ion beams generated by PBFA II has enabled us to begin experiments in ion beam coupling and target physics. Data from these experiments indicates that we can reproducibly deliver ~50 KJ of 5 MeV protons at an average power intensity of 3.5 TW/cm^2 to a 6 mm diameter by 6 mm tall cylindrical target. The implosion of spherical exploding pusher targets and the radiation production from foam-filled cylindrical thermal targets were studied in these experiments. They demonstrated that high quality target data can be obtained on PBFA II. Specific deposition rates of about 100 TW/g were achieved in these experiments. This deposition rate marks the boundary between the regime where enhanced ion deposition and equation-of-state (EOS) physics are studied (10-100 TW/g) and the regime where radiation-conversion and radiation-transport physics are studied (100-1000 TW/g). Experiments in the radiation-conversion regime are now of primary importance in our program because these experiments will test the target physics basis for ion-driven ICF.

Experiments using a thin film LiF source have produced an intensity of 1 TW/cm^2 of lithium ions. This beam has a potential specific deposition rate of 300-400 TW/g in hydrocarbon foams. However, radiation conversion experiments will require an increased total energy content of this beam in order to overcome the specific internal energy of the foam. Further increases in ion beam intensity and energy content are being pursued in a multi-pronged attack. Understanding and controlling ion beam divergence is the highest program priority. Present understanding indicates that instabilities in the electron sheath cause significant ion beam divergence. Our understanding suggests that this contribution to the ion divergence can be decreased by operating the diode at a low enhancement through the use of high applied magnetic fields or by modifying the electron distribution near the anode via electron limiters. The new 9 cm radius "Compact Diode" has the capability of generating ≥8 T applied magnetic fields which will enable divergence experiments in the low-enhancement, high-B regime. Experiments with the LEVIS (Laser Evaporation Ion Source) lithium source have demonstrated the existence of a preformed plasma, as determined by visible-emission spectroscopy of the anode plasma. Work on improving lithium purity with this source is in progress. This active anode plasma will be used in experiments testing the effectiveness of electron limiters in controlling ion beam divergence. We are also working to understand the interrelation between accelerator coupling, diode physics, and ion beam focusing in order to optimize the diode configuration to maximize the power intensity on target. Success in these experiments will provide an adequate lithium beam for performing target experiments exploring radiation conversion and radiation transport physics in ion-driven ICF.

Light Ion Beams for ICF

Intense beams of light ions are being developed to drive inertial confinement fusion (ICF) targets[1]. The study of the technology of high intensity light ion beams began about 1975 with pioneering work at Cornell[2], Sandia[3], and the Naval Research Laboratory (NRL)[4]. This has expanded into an international effort that now includes research in Germany, Japan, and the former Soviet Union. The list of laboratories performing this international research includes: the Nuclear Research Center, Karlsruhe; the Institute for Laser Engineering, Osaka; Tokyo Institute of Technology, Yokahama; the Technological University of Nagaoka; The Institute for High Current Electronics, Tomsk; The Institute of Nuclear Physics, Novosibirsk; and the Institute of Electrophysics, Ekaterinburg. The University of Wisconsin also participates in the engineering design of light ion facilities.

Before performing target physics experiments, it has been necessary to first develop this technology to produce and focus ion beams to the sufficient energies and intensities. In 1989, a proton beam was focused to an intensity of 5 TW/cm^2 averaged over the surface of a 6 mm diameter sphere[5]. In 1991, proton beams were used to perform the first series of target experiments aimed at contributing to the knowledge base of ICF science. Ongoing research in the understanding, development, and focusing of light ion beams is aimed primarily at the generation of lithium ion beams which will be superior in their target-drive characteristics. The first series of target physics experiments using lithium ion beams is planned for 1992.

At present, the key technical challenges for the light ion program are reducing ion divergence, increasing ion beam intensity, and conducting well-designed and well-diagnosed experiments at higher ion beam intensities.

The Physics of Indirectly-Driven Light-Ion Targets

A generic sketch of an indirectly-driven light-ion target is shown in Figure 1.

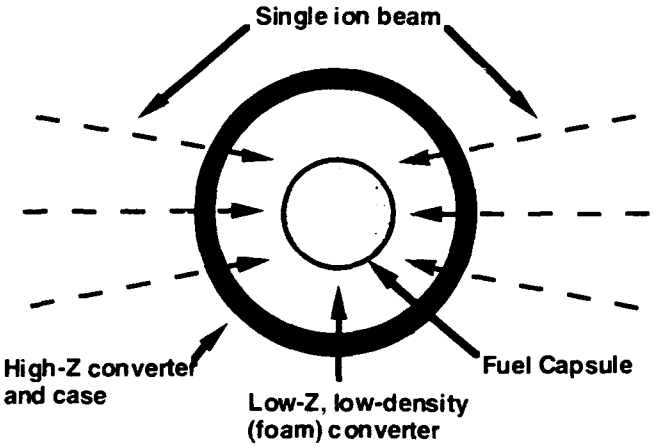

Figure 1. Generic sketch of an indirectly-driven light-ion inertial confinement fusion target.

The fusion capsule is embedded within a foam-filled hohlraum. Ions penetrate the external shell and volumetrically deposit their energy in the low-density foam, which converts the ion beam energy into x-rays. The radiation, in turn, bathes the fusion capsule and provides the drive for the capsule implosion. The principal reason for converting ion energy into x-ray energy is to achieve radiation smoothing of unacceptably large perturbations in the initial drive in order to achieve a symmetric implosion of the fuel capsule.

In a well-designed target, the target absorbs all of the incident ion energy with the low-density foam absorbing about 70% of the energy and producing a thermal electron spectrum. The absence of holes in the case minimizes energy loss from inside the hohlraum and increases the overall target efficiency. The volumetric deposition characteristic of ion beams provides initial smoothing of beam non-uniformities and radiation smoothing provides the final symmetrization. This smoothing during deposition and x-ray generation also makes the target less sensitive to the time-dependent symmetry of the drive. Volumetric deposition minimizes the density and temperature gradients in the target which decreases the opportunity for instabilities to occur in the deposition region. Energy conversion into hydrodynamic motion of the converter material is also minimized in a light-ion hohlraum. The unique and favorable deposition and hohlraum physics of light ions make these targets attractive for achieving ICF in the laboratory.

Deposition Intensities and Radiation Conversion

The peak ion beam intensity on target, the total energy delivered to the target within a hydrodynamically acceptable time, and the ion beam range in the target are among the parameters that most directly affect the performance of an ion-driven target. The ion beam intensity (TW/cm^2) divided by the ion beam range (g/cm^2) determines the specific power deposition (TW/g) in the target. The energy density (MJ/cm^2) divided by the range gives the specific energy deposition (MJ/g). The magnitude and uniformity of the specific power and energy provide the proper figures of merit for judging the performance of an ion-driven hohlraum for driving a capsule. At present, the divergence of our ion beams[7] limits the specific power and energy deposition in the target because it limits the amount of the beam that reaches the target.

The x-ray conversion efficiency depends on the ion species and energy, and on the target material. Figure 2 demonstrates that the ion beam conversion efficiency to radiation is predicted to increase as the beam intensity is increased. This efficiency estimate is based on a simple time-dependent model that balances deposited beam energy with material heat capacity and blackbody radiation losses[6]. Note that hydrodynamic motion and electron thermal conduction are ignored in this model and that these efficiencies probably reflect upper bounds. We see that this model predicts that a 10 TW/cm^2 Li beam with an energy of 10 MeV will be ~80% efficient in converting ion energy into x-rays. The conversion efficiency into x-rays is predicted to approach 90% at 100 TW/cm^2 for 24 MeV lithium.

Present Beam Focusing Capabilities

The specific deposition rates that are consistent with the present beam focusing capabilities of the ion diode on the PBFA II accelerator are summarized in Table I.

Table I: Present PBFA-II specific deposition rates and energies into a cold CH foam for a 15 ns ion beam pulse.

Ion	Ion Energy (MeV)	Range (mg/cm^2)	Intensity (TW/cm^2)	Energy on Target (KJ)	Specific Deposition (TW/g)	Specific Energy (MJ/g)
Proton	5	32	3.5	52	110	1.65
Proton	5	32	5	75	157	2.35
Lithium	9	2.6	1	15	380	5.7

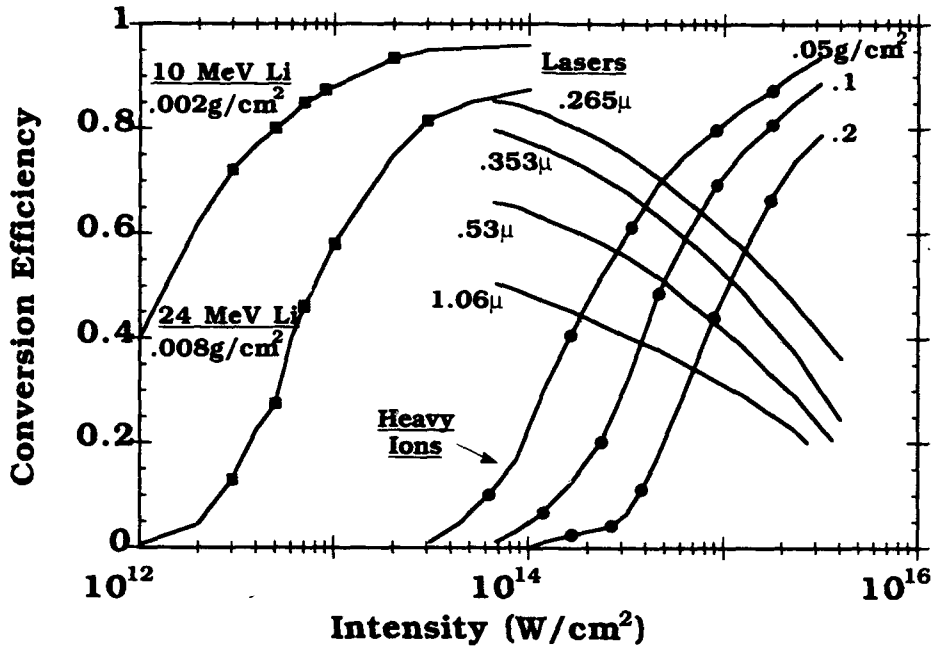

Figure 2. X-ray conversion efficiency as a function of intensity for lasers of varying wavelengths and ions of varying ranges[8].This graph has been modified to include the predicted conversion efficiency of shorter range light ions[6] assuming a 20 ns beam pulse into a carbon target.

Proton beams of up to 5 TW/cm^2 have been generated on PBFA II[5]; the 3.5 TW/cm^2 value is more representative of the average performance on a complex target experiment. A lithium beam of 1 TW/cm^2 has been generated on PBFA II[9]. Table I illustrates the role of both ion intensity and ion range in determining the target performance. Although the intensity achieved with lithium beams is less than that of protons, the specific power deposition in TW/g is larger for the lithium beams. This means that the lithium beams are actually more effective at heating the target material than the proton beams because their range is so much shorter. The more favorable deposition properties of lithium beams as compared to protons is part of the rationale for selecting lithium as the baseline ion in Sandia's ICF program.

Experiments Along the Path to Ignition

As Sandia's beam generation and focusing capability increases, the range of target experiments that can be performed with these beams increases. Figure 3 is a modification of a plot from a recent GSI report[10] that shows anticipated temperatures generated in gaseous and solid targets as a function of the specific deposition power of an ion beam. The plot indicates that ion deposition and equation of state (EOS) experiments can be appropriately performed at specific powers of 10-100 TW/g, radiation physics experiments can be conducted between 100 and 1000 TW/g, while implosion studies become possible at 1000 TW/g. Superimposed on this plot are three regions that have already been explored, or will be explored in the near future using light ion beams. The lowest specific deposition region labeled "Stopping Power Experiments" spans the specific depositions that have been realized in previous light-ion stopping power experiments both at Sandia and NRL. The next higher region labelled "PBFA-II Proton Experiments" refers to the recent proton target series; those experiments achieved specific deposition powers of approximately 100 TW/g in a hydrocarbon foam and will be the subject of the next two sections. These proton experiments generated the first data on x-ray production and radiation physics from targets in a

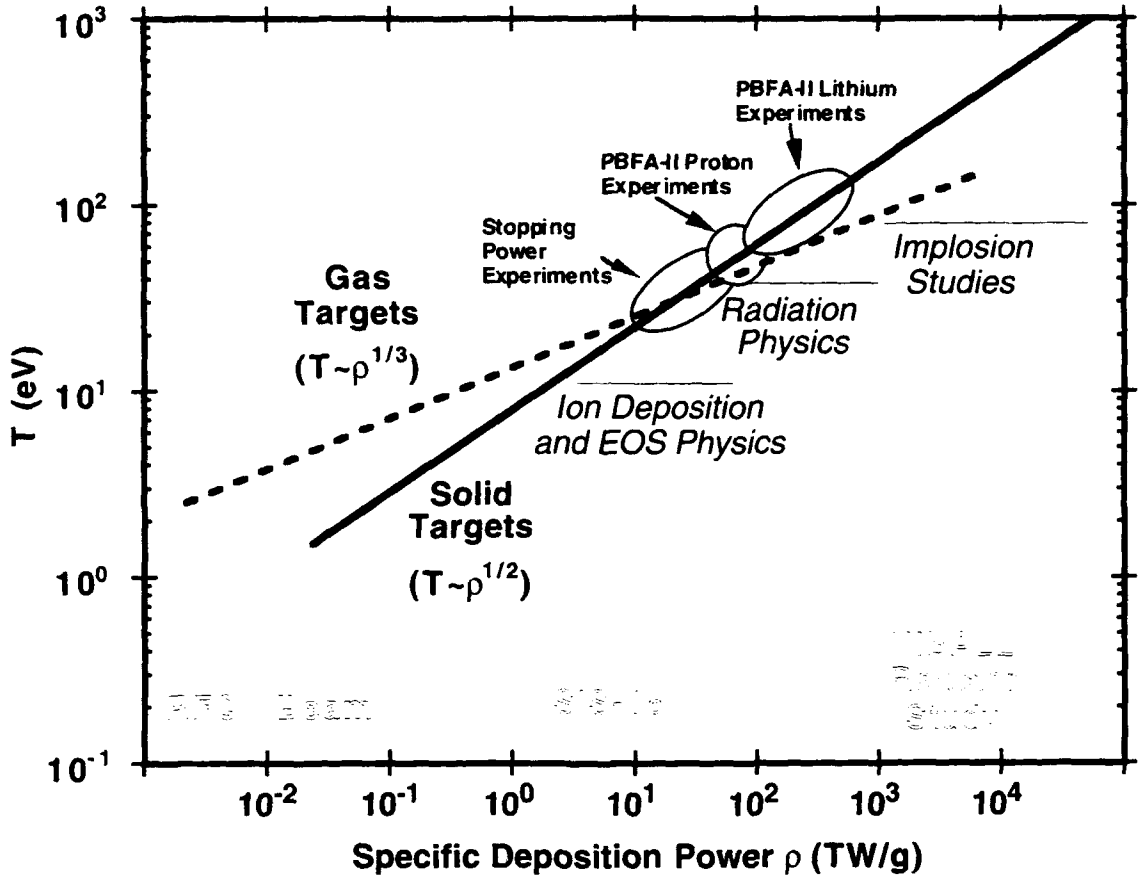

Figure 3. ICF target physics issues that can be studied by ion beams of increasing specific deposition power and associated increasing target temperature. Present and projected capabilities of light- and heavy-ion machines are noted. The original figure, found in Reference 10, has been modified to include the light ion capabilities

hohlraum-like geometry. Information on ignition-size targets was also obtained with direct-drive exploding pusher targets. The highest shaded region labeled "PBFA-II Lithium Experiments" shows the specific powers that should be available using lithium beams in 1992. This figure also indicates that target physics experiments on the PBFA II accelerator are generating important data for both the Light and Heavy Ion Programs. Target experiments in the radiation-conversion regime are now of primary importance to the program because these experiments will test the target physics basis for ion-driven ICF.

Direct-Drive Implosion Experiments

Although exploding pusher target performance does not scale to ignition conditions, these targets can provide useful target physics data. Furthermore, since exploding pusher targets are less sensitive to drive uniformity than ablative targets, they can be studied using direct-drive by the ion beam. The pie diagram in Figure 4a shows a cross sectional view of the targets that were used in these experiments.

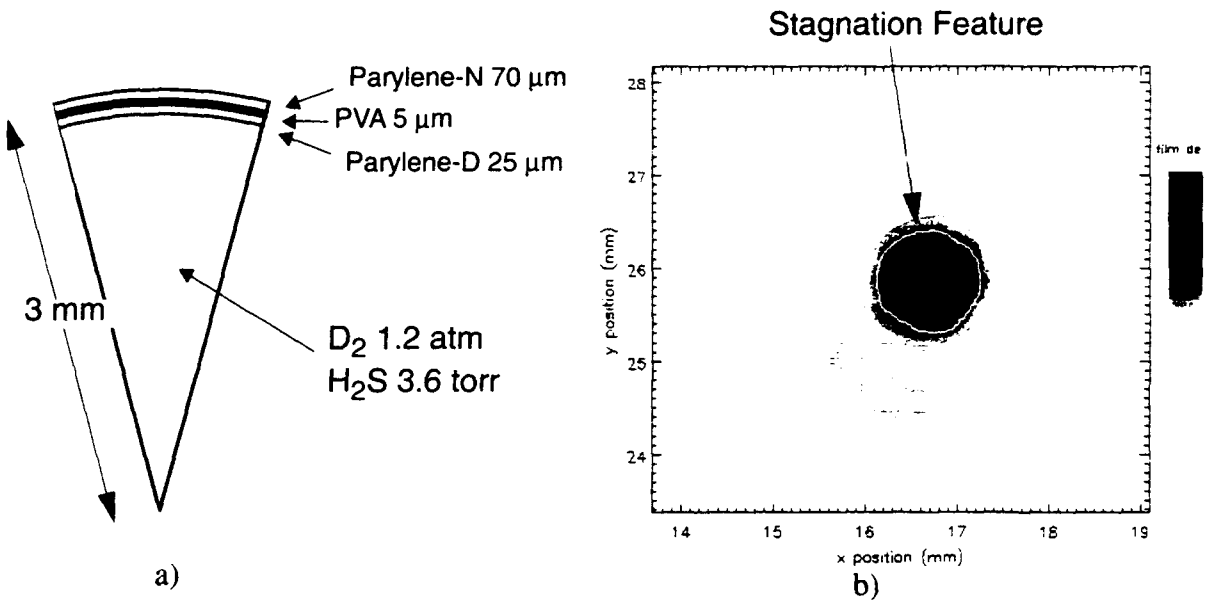

Figure 4. a) Pie diagram of a direct-drive exploding pusher target fielded on PBFA II and b) time-integrated x-ray image of the imploded target as viewed through a ~2 keV x-ray filter in the coordinate system of the film plane. Note the prominent central stagnation feature.

The target consisted of a thin plastic shell, doped with a chlorine layer on the inner surface, filled with 1.2 atmospheres of deuterium. The target shell was designed to be about 60% of an ion range thick so that ions would deposit energy on both their inward and outward trajectories in order to symmetrize the primary drive (~15-20% azimuthal nonuniformity at the target equator, the pole-to-equator asymmetry can be larger due to the difference between the spherical geometry of the target and the cylindrical geometry of the beam).

The significant results of these experiments include the following: 1) chlorine K_α radiation produced by ion impact ionization was sufficient to provide an x-ray time-history of the shell motion, 2) the target compression was about 5:1, in good agreement with hydrodynamic predictions, and 3) there were distinct differences between filled and unfilled targets as predicted by hydrodynamic simulations.

Hohlraum-Like Target Experiments

In these experiments, a cylindrical version of an ion-driven hohlraum was used to study radiation and hohlraum physics issues. Since the specific deposition power of our proton beams have reached the 100 TW/g levels which was noted in Figure 3 as being consistent with the beginnings of radiation physics experiments, and since the indirect-drive approach that the light ion program has embraced is critically dependent on radiation physics, these experiments were extremely important.

Figure 5a shows a cross sectional view of the targets used in these experiments. A low-density hydrocarbon foam was placed within a gold cylinder, approximating a cylindrical hohlraum. The exterior gold cone was part of the beam characterization and energy accounting diagnostics on these experiments while the 5 Torr of argon was used to provide space charge and current neutralization of the ion beam during transport to the target. The vacuum barrier excluded the argon from the x-ray diagnostic line-of-sight to allow viewing of the thermal emission from the target.

The foam was heated to approximately 35 eV in these experiments. An analysis of filtered XRD and bolometer signals indicates similar brightness temperatures across many spectral cuts. This is consistent with the generation of a Planckian x-ray spectrum which indicates that at this specific deposition level the ion beam coupling is indeed into a thermal spectrum. A sample x-ray pinhole camera image of the target as viewed from below is shown in Figure 6b.

Other important conclusions that can be drawn from the data include: 1) the foam was heated and reached the optically thin state necessary for radiation transport, 2) the radiation output was increased by the presence of the foam, and 3) the foam retarded the motion of the gold case.

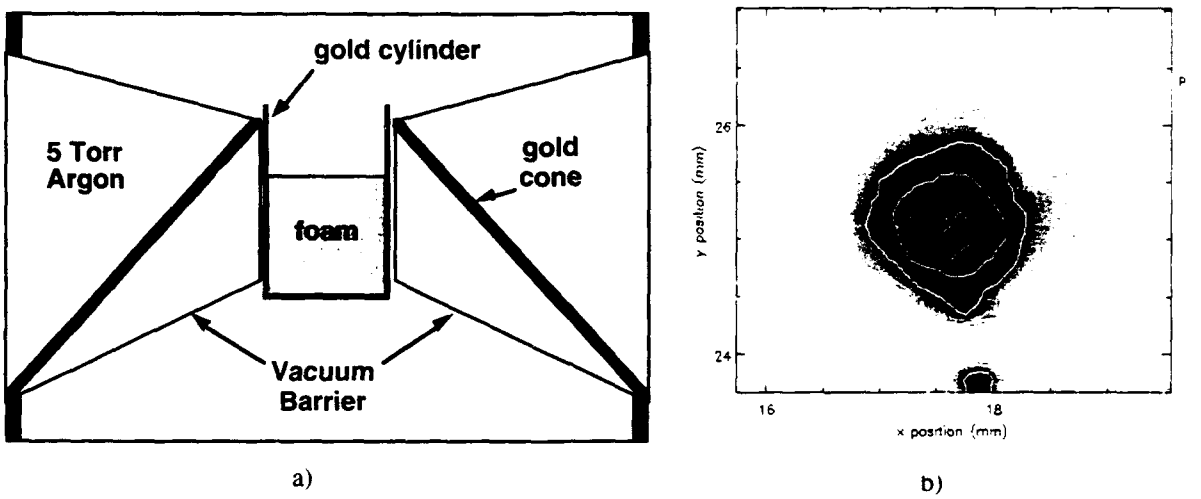

Figure 5. a) Cross sectional view of cylindrical hohlraum-like target and b) time-integrated x-ray image of the thermal emission from the central foam region of the target in the coordinate system of the film plane.

Future Beam Capabilities and Target Experiment Plans

Now that we have performed the first target experiments aimed at developing a path to ignition for light ion beams on PBFA II we are planning the future. Table II shows our present ion beam capabilities and charts a path of increasing beam intensity and specific deposition towards ignition. The superiority of lithium beams to protons for studying target physics is clear. The specific deposition power of a 9 MeV lithium beam is 10 times that of a 5 MeV proton beam for the same focal intensity. This table indicates that near-term lithium-driven hohlraum experiments can fully explore the radiation physics and hohlraum physics regimes, and achieve the conditions necessary to perform initial hydrodynamic experiments. It is interesting to note that present ignition target designs call for 24-30 MeV lithium ions at intensities of between 100 and 120 TW/cm^2. This translates to specific deposition powers of between 5000 and 10000 TW/g. We see, therefore, that a 10 TW/cm^2 lithium beam having a specific deposition rate of almost 4000 TW/g will be testing ion beam deposition and radiation conversion at near-ignition levels. Such experiments will give us an early indication of the validity of our deposition and radiation conversion models and should indicate whether non-linear processes in ion deposition or radiation conversion will be a problem for ignition targets.

Our near term strategy is to increase the lithium beam intensity up to 10 TW/cm^2 while holding the ion energy relatively constant. As the lithium intensity is increased to 20-35 TW/cm^2, modest increases in voltage become advantageous for increasing the total beam energy delivered to the target. Our present

belief is that we can achieve intensities up to 35 TW/cm^2 on PBFA II without an energy upgrade. However, reaching the 120 TW/cm^2 that is required to achieve ignition will require a substantial energy increase.

Table II: Present and future PBFA-II specific deposition rates and energies into a cold CH foam for a 15 ns beam pulse.

Ion	Ion Energy (MeV)	Range (mg/cm^2)	Intensity (TW/cm^2)	Energy on Target (KJ)	Specific Deposition (TW/g)	Specific Energy (MJ/g)
Present PBFA-II parameters						
Proton	5	32	5	50	157	1.57
Lithium	9	2.6	1	15	380	5.7
Increase specific power deposition to > 1000 TW/g at constant ion energy						
Lithium	9	2.6	5	75	1900	28.5
Lithium	9	2.6	10	150	3800	57
Increase ion energy and intensity to increase total energy on target						
Lithium	12	4.0	20	300	5000	75
Lithium	15	6.0	35	525	5800	87
Ignition level beam - requires upgrade of PBFA II						
Lithium	30	19.5	120	1800	6200	93

Status of Lithium Ion Beam Production

We are presently pursuing two thin-film approaches to generating lithium ions: 1) LiF, a ~0.6 μm vacuum-deposited coating on a stainless-steel anode, and 2) LEVIS[11], a laser-heated, laser-ionized source based on vacuum-deposited LiAg films. Visible emission spectroscopy of the accelerating gap between the anode and the cathode has provided detailed information about the physics of each of these sources. Some of this information, along with that obtained from Faraday cups, an energy-filtered ion pinhole camera, and electrical diagnostics is summarized in Table III.

Table III: Comparison of LiF and LEVIS lithium ion sources.

Property	LiF	LEVIS
Ion emission surface	Anode surface	Expanding plasma
Emission mechanism	Field emission?	Ion extraction from plasma
Purity	~100% Li^{+1}, little H+C	H+C impurities if unheated > 90% Li if DC-heated ≥5 hrs @120° C Sensitive to YAG laser power?
Ion emission delay	~24 ns	~24 ns
Early Child current?	None observed	None observed

Table III: Comparison of LiF and LEVIS lithium ion sources.

Compatible with limiter?	Unknown. Might require electrons to turn-on?	Yes
Lithium beam energy	80-140 KJ	≥100 KJ
Divergence at source	<17 mrad	≤12 mrad
Focal spot size (horiz)	8-9 mm	9-10 mm

Spectroscopic data shows a high electric field (E~8MV/cm) at the anode surface for the LiF source. The electric field drops in magnitude as the diode voltage drops. This behavior is consistent with field emission of lithium ions from the LiF film on the anode surface. The LiF source appears to have high lithium purity. Furthermore, recent experiments where the LiF coating height was varied from 1.5 to 14 cm show that the lithium beam duration increases with increasing LiF coating height as shown in Table IV. Specifically, the previously reported 15 ns duration of the lithium beam from LiF has been increased to 25-30 ns by this means. One theory suggests that this behavior is related to slower diode impedance collapse

Table IV: FWHM of Faraday cup and PIN diode lithium signals with LiF coating height.

Coating Height (cm)	Signal FWHM (ns)
1.5	8
5	15
9	20
14+	25-30

with decreasing current enhancement (over Child-Langmuir) due to increasing source area. Another suggests that uncoated portions of the anode emit protons, which changes the diode impedance, and that extending the LiF coating height suppresses this proton emission. Experiments are planned to attempt to determine the physics behind this data.

LEVIS uses a Nd:YAG and a tuned dye laser to form a lithium plasma. Spectroscopic data from LEVIS indicates that a preformed plasma has been generated that shields the physical anode surface from the electric field. Lithium ions are accelerated from the preformed plasma. Hydrocarbon surface contamination has limited the purity of the lithium beam from LEVIS when the anode is unheated. A recent experiment has shown >90% lithium purity when a LiAg-coated anode was DC-heated ≥5 hours at 120° C. The lithium purity of the beam also appears to be sensitive to the YAG laser power. In-situ deposition of lithium metal is also being tested for producing pure lithium beams using LEVIS.

The delay of ion current with respect to the diode current appears to be identical for both sources, although the expectation has been that the preformed source would generate an ion beam sooner. Surprisingly, Faraday cup data have shown that there is no low-level Child current early in time for either the LiF or the LEVIS source. We speculate that this is related to the virtual cathode dynamics of the diode. The preformed plasma from a LEVIS source is definitely compatible with electron limiters for controlling ion divergence. LiF has yet to be tested with an electron limiter and might not be suitable if it requires significant electron deposition to activate ion emission.

The lithium beam energies generated using LiF have been higher than those for LEVIS. However, we believe that operational difficulties associated with fielding LEVIS on PBFA II, rather than diode physics, is limiting the lithium energy for LEVIS. The source divergences in Table III are determined from spectral

line widths of light emitted near the anode and do not allow one to conclude that LEVIS has a lower divergence because the LiF value is only an upper bound due to electric field gradients contributing to the spectral line broadening. Note that the visible spectrometer used in these measurements is observing emission from neutral lithium (Li I) and that the Li^{+1} behavior is inferred from the Li I data. Finally, the horizontal focal spot observed by the ion pinhole camera is quite similar for LiF and LEVIS, indicating that they do indeed have similar overall beam divergences. Both sources continue to be used and developed.

Lithium Beam Focusing Strategy

The achievable lithium beam intensity on PBFA II is primarily determined by three factors: 1) the amount of power coupled from the accelerator to the ion beam, 2) the lithium beam purity, and 3) the lithium beam divergence. The present PBFA-II parameters for proton and lithium beams are summarized in Table V. We see that the power coupling of the accelerator to the ion beam is better for protons than for lithium. This is due partly to the increased ion turn-on delay (ion current with respect to diode current) for lithium as compared to protons that puts the current and voltage further out of phase. Beam purity presently favors lithium ions, however, the poor lithium beam divergence more than compensates for this advantage. Lithium beam focusing experiments are planned to deal with these issues. Ideas that will be tested include: 1) a "mesa anode" which elevates the ion source by 2-3 mm from the surrounding anode surface, 2) increased ion area to achieve lower enhancement and improve impedance and power coupling, and 3) vertical focusing experiments where special care is given to vertical alignment, under-insulation at the diode midplane, and top/bottom power balance in order to assure that we are performing midplane-symmetric beam focusing. These experiments will help determine the role of enhancement in diode impedance collapse. In particular, the mesa anode experiments will help determine whether source enhancement or impurity emission outside the lithium coating height play a dominant role in lithium diode power coupling and impedance.

Table V: Comparison of present PBFA-II proton and lithium beam parameters as related to ion beam focusing.

Species	Ion Power (TW)	Ion Emission Delay (ns)	Species Purity (%)	Divergence (mrad)	Focused Intensity (TW/cm^2)
protons	~18	~10	50-60	~16	5
lithium	5-12	~24	~100	~32	1

Ion Beam Divergence

Ion beam divergence has a quadratic effect on the achievable beam intensity. As seen in Table V, increased lithium beam divergence is the dominant factor in limiting the presently achievable lithium beam intensity. Therefore, understanding and controlling lithium beam divergence is our highest priority.

Simulations using the 3-D electromagnetic particle-in-cell (PIC) code QUICKSILVER have identified an early-time diocotron instability in the electron flow in the diode[12]. Analytic calculations[13], which include a charge-neutral region in the diode following the beam acceleration gap, produce a calculated growth rate for the diocotron instability in good agreement with the simulations. In the QUICKSILVER simulations, the high-frequency diocotron instability evolves during the pulse to a low-frequency "ion mode" instability due to the interaction of the ion beam with the electron sheath. The frequency of the ion mode instability is related to the time it takes for an ion to cross the sheath. Since our lithium beams have

lower ion velocities than our proton beams, the ion mode frequency is lower for lithium than for protons. Wave-particle coupling of the sheath instability to the ion beam will increase the beam divergence and energy spread as the ions traverse the sheath. The transverse momentum and energy spread of an ion beam interacting with the electron sheath are minimized for high-frequency instabilities and short ion transit times (high ion velocities).

Ion beam divergence can come from many sources: 1) divergence at the ion source, 2) electromagnetic fluctuations, 3) beam non-uniformities, 4) variations in canonical angular momentum at the gascell foil, 5) multiple scattering, and 6) transport effects. Experimental data, QUICKSILVER simulations, and analytic stability analysis indicate that electromagnetic fluctuations can dominate beam divergence growth. The dominance of electromagnetic fluctuations in divergence is particularly clear for proton beams where data from microwave measurements, the magnetic spectrometer, the ion movie camera, ultra-compact ion pinhole cameras, and visible spectroscopy strongly corroborate this assertion. In particular, divergence measurements at the source (by spectroscopy), at the gascell foil (by pinhole cameras), and at the focus (by the movie camera) of C IV ions in the beam show < 10 mrad divergence at the source and ~25 mrad at both the gascell and focal positions. This indicates that the largest contribution to divergence for these beams comes from the region between the source and the gascell where the electron sheath is located. The protons in the beam are assumed to follow the same pattern. Therefore, it appears that divergence from electromagnetic fluctuations is dominant for proton beams. We are presently attempting to determine whether this is also the case for lithium beams.

Our theoretical understanding of these electromagnetic instabilities has matured to the point where they can also be used to suggest means of controlling and reducing ion beam divergence. A trend of decreasing ion beam divergence with decreasing ion current enhancement over the Child-Langmuir value is found in the simulations. By providing better control over the evolution of the electron density in the anode-cathode gap, the simulations show that the low divergence phase can be extended by increasing the duration of the high-frequency phase of the electron sheath instabilities. Specific solutions for reaching this condition include providing the electron control with an increased magnetic field (~5.8 T for protons and ~6.3 T for lithium), and using an electron limiter to limit the electron density near the anode.

Preliminary data on divergence with electron limiters has recently been obtained with extraction diodes on the KALIF accelerator at Karlsruhe and the LION accelerator at Cornell University. Experiments with electron limiters and higher magnetic fields are planned for PBFA II and SABRE beginning in June. The PBFA-II experiments will use both the standard 15 cm radius ion diode and the newly developed 9 cm "compact diode" to study high fields and limiters. SABRE is a new extraction geometry machine that uses the "HELIA" inductive cavity adder technology to provide accelerating potentials of up to 10 MV. Data on divergence in 2-stage extraction diodes have been obtained on the REIDEN-IV SHVS generator at ILE, Osaka.

Planned lithium target experiments

We plan to integrate the results of our lithium beam generation, beam focusing, and divergence reduction experiments for application to preliminary lithium-driven target experiments this summer. These target experiments will be similar to the previously discussed hohlraum-like target experiments that we performed using proton beams. The targets for these experiments will be optimized for the range and deposition characteristics of 8-9 MeV lithium ions. The higher specific deposition rate of lithium beams should allow us to achieve higher foam temperatures in these experiments.

Summary

The first complex ICF target experiments to be performed on an ion accelerator have been successfully fielded on PBFA II. These experiments obtained time-integrated, time resolved, imaging, and spectral diagnostic information from an extensive array of instruments. The target data has shown that we can cou-

ple ion beam energy to ignition-size spherical targets. The data has also shown that we can couple energy into a foam-filled hohlraum, produce an optically-thin foam, and generate an x-ray yield which is consistent with a Planckian spectrum. Lithium beams will have higher specific deposition rates that will allow us to increase the temperature of our targets. Both LiF and LEVIS sources are being developed for providing a pure lithium beam. Lithium beam generation and focusing experiments are being fielded to drive further target experiments. Progress in the theoretical understanding of ion beam divergence indicate that electromagnetic instabilities are a dominant source of divergence. Experiments are being performed to attempt to control ion beam divergence and increase the power density on target. The results of our beam generation, focusing, and divergence experiments will be integrated and applied to lithium-driven target experiments.

References

1. J.P. VanDevender and D.L. Cook, Science, **232**, 831 (1986).

2. S. Humphries, Jr., J.J. Lee, and R.N. Sudan, J. Appl. Phys. **46**, 187 (1975).

3. D.J. Johnson, G. W. Kuswa, A.V. Farnsworth, Jr., J.P. Quintenz, E.J.T. Burns, and S. Humphries, Phys. Rev. Lett. **42**, 610 (1979).

4. S.J. Stephanakis, D. Mosher, G. Cooperstein, J.R. Boller, J. Golden, and S.A. Goldstein, Phys. Rev. Lett. **37**, 1543 (1976).

5. D.J. Johnson, et al. Proc. 7th IEEE Pulsed Power Conference, Monterey, CA, June 11-14, 1989.

6. J.K. Rice and T.W. Hussey, Sandia National Laboratories, private communication of the results of calculations for light ion beams based on radiation conversion model discussed in Reference 8.

7. J. P. Quintenz, et al. IAEA Technical Committee Meeting on Drivers for Inertial Confinement Fusion, Osaka Japan, April 15-19 1991, to be published in IAEA-TECDOC series.

8. Figure from, J.D. Lindl, R.O. Bangerter, J.W-K Mark, and Yu-Li Pan, Heavy Ion Inertial Fusion AIP Conference Proceedings, **152**, 89 (1986).

9. L.P. Mix, W.A. Stygar, R.J. Leeper, J.E. Maenchen, and D.F. Wenger, "Time-resolved measurements of the focused ion beams on PBFA II", to be published in Rev. Sci. Instr., October 1992.

10. R. Bock, "Status and Perspectives of Heavy Ion Inertial Fusion", GSI-91-13 (1991)

11. G.C. Tisone, K.W. Bieg, and P.L. Dreike, Rev. Sci. Intr. **61**, 562 (1990).

12. M.P. Desjarlais, T.D. Pointon, D.B. Seidel, R.S. Coats, M.L. Kiefer, J.P. Quintenz, and S.A. Slutz, Phys. Rev. Lett. **67**, 3094 (1991).

13. S.A. Slutz and W.A. Johnson, to be published in Phys. Fluids B, May 1992.

Funding has been provided by the U.S. Department of Energy under contract DE-AC04-76-DP00789.

EXTRACTION GEOMETRY ION DIODE PHYSICS: THEORETICAL MODELING AND EXPERIMENTAL RESULTS*

J. B. Greenly, C. K. Struckman, B. R. Kusse and W. A. Noonan
Laboratory of Plasma Studies, Cornell University

May 25, 1992

Abstract

The LION accelerator has been used to perform a series of experiments to investigate the operation of magnetically insulated extraction diodes. These diodes produce annular beam with an outer radius of 11.3 cm and an inner radius of 8.6 cm. The beam voltages were typically 1-1.25 MV with a 40 nsec ion beam current of approximately 250 KA 8. The diodes were normally operated at $B/B^* \approx 1.5$ and typical enhancements over Child-Langmuir of 15 to 25. Both active and passive anode plasma sources have been investigated. The effects of modifying the magnetic field gradient in the diode will be discussed and a theoretical model presented. Techniques for cleaning the anode surface for the production of Li beams will be described.

Introduction

Extraction geometry, magnetically insulated diodes will be the sources of intense ion beams for future light ion inertial confinement fusion drivers as well as for other applications such as material surface modification. These diodes are insulated by an applied magnetic field nearly parallel to the anode in the (r, z) plane. They produce annular ion beams accelerated perpendicular to the anode, in the z-direction if the anode is flat or focused to the axis if the anode surface is conical. This insulating field necessarily introduces radial gradients that influence the magnetically insulated electron flow and can cause nonuniform radial distribution of ion current and electron loss. In an attempt to better understand the operation of these diodes we have carried out an experimental study of these extraction diodes and also deveioped a theoretical model to account for radial and axial electron dynamics. The model suggests several effective means of controlling the radial dynamics which have been confirmed by experiments. Experiments have been performed using both passive "flashover" anodes and active EMFAAPS exploding foil anodes driven by the LION accelerator. In addition, a series of experiments was performed to investigate methods of removing protons from the accelerated ion beam. Cleaning techniques have been developed for use on a LiF EMFAAPS anode that reduce the proton content in the lithium beam.

Experimental Apparatus

The extraction diode used for these experiments is shown in Figure 1. Inner and outer cathode coils were used to produce the radially directed insulating magnetic field. Shunts on these coils allowed the magnetic field gradient to be adjusted, modifying the radial variation of

B/B^*. Inner and outer cathode tips were placed typically 6 mm from the anode surface. The inner and outer radii of the anode were 8.6 and 11.3 cm respectively. The anode surface was positioned at a 15° angle for geometric focusing. Passive and active anodes were used for these experiments. The passive anodes were constructed with epoxy filled grooves in aluminum. The active anodes were the EMFAAPS type[1] with a 0.1 μ evaporated aluminum foil. For producing lithium beams a 1.5 μ layer of LiF was vapor deposited over the aluminum foil. The anode was isolated from the high voltage pulsed power supply by a thin insulator that flashed over during the high power pulse but allowed the anode to be driven negative with respect to ground for the discharge cleaning.

Typical operating parameters can be summarized as follows: The diode voltage ranged from 1.0 to 1.25 MV resulting in an ion current of approximately 250 KA for 40 nsec. The insulating magnetic field parameter, B/B^*, varied with radius and its gradient was adjusted by the shunts for some of the experiments but was typically in the neighborhood of 1.5. Ion current density enhancements of 15-25 were observed. Both d.c. and 60 Hz a.c. discharge cleaning were employed. These power supplies were operated at approximately 300 V and 100 mA.

Theoretical Model

A satisfactory theoretical model of extraction diodes must be at least two-dimensional, taking into account the radial as well as axial electron dynamics. The most basic features of such a model can be deduced by considering the character of the electron flow in an idealized diode.

It has long been understood[2] that the peaking of ion current density toward the outer edge of the diode radius in a simple extractor is caused by the relative underinsulation there due to the 1/r dependence of the insulation field. In a simple flat diode with constant rA_θ(magnetic flux surfaces), this leads to a "tilt" of the edge (d*) of the electron layer toward the anode with increasing radius as shown in Figure 2. This picture follows from arguments assuming conservation of electron energy, and conservation of canonical momentum in the symmetry (θ) direction. Further arguments under this assumption, taking into account the axial electrostatics (Poisson's equation must integrate to the full gap voltage across the gap at any radius), lead to the conclusions that the (d*) surface is in fact more "tilted" than are the surfaces of constant A_θ. The equipotential surfaces are tilted less than constant A_θ, but more than the magnetic flux surfaces. The important inferences are that there must be a radial gradient in the electron density in the gap, and a non zero component of the gap electric field parallel to the magnetic flux surfaces, that is in the radial direction for a flat anode.

It is impossible that this (radially varying) parallel electric field component will be coincidentally exactly correct to bring the electrons into a static force balance condition in the radial direction. Consider the terms in the radial component of the drift approximation:

$$d^2r/dt^2 = v_r^2/r + (e/m)(E_r + v_\theta B_z - v_z B_\theta) + v_\perp^2/2r.$$

Here B_z is non zero in a conical focusing geometry, and $v_\perp$ is the perpendicular (cyclotron) component of the electron velocity in the magnetic field. The terms represent, respectively, the "centrifugal", electrostatic, applied magnetic tilt, self-pinch, and grad-B effects. Usually the inward forces other than E_r are small compared to the outward centrifugal and grad-B terms. However, the E_r required to balance these terms is of order

$$E_r/E_z = v_\theta/r\omega_c$$

which is typically less than 10^{-2}. The E_r implied by the tilt of the equipotentials is generally much larger. Thus the electrons in real diodes must "reflex" radially, bouncing off potential wells at the radial edges of the ion space charge in the gap. This radial motion must be self-consistent with the radial density gradient required by the axial electrostatics. Thus the coupling between radial dynamics and axial electrostatics in these diodes is strong, and complicated.

Nevertheless, some features and implications of the simple picture of Figure 2 have been observed in experiments. Rondeau (1) observed that an electron "collector" connected to the anode, at a radius smaller than the inner edge of the ion-emitting annulus and projecting partway across the gap, was able to "drain off" the electron space charge approaching the anode at the outer edge of the annulus and so produce nearly radially uniform ion current density. Indeed, the tilt of the (d*) line should be reduced if such a collector imposes an additional radial electric field component, producing increasing v_r for electrons in orbits closer to the anode surface. This collector was actually located 2 cm inside the inner radius of the emitting anode area, so for it to have had an influence on the electron flow within the ion-filled gap, the electron orbits must have "reflexed" and sampled the field outside the ion-filled region.

Another implication of the idealized picture is shown in Figure 3. Slutz(2) realized that the tilt of (d*) could be compensated by a reverse tilt of the applied flux surfaces, as shown in figure 3a. This scheme has the advantage of producing uniform V_{crit}, the maximum voltage at which the gap is marginally insulated, to all radii of the anode. This is an advantage when running a diode near minimum applied-B strength. Figure 3b shows another way of doing this compensation that preserves the anode as a flux surface, which is advantageous for focusing applications. This method of changing the gradient of the applied field has been used in at least three experiments, by Fedorov[3], by Bluhm et al.[4] at Kernforschungszentrum Karlsruhe, and by the present authors on the Lion extractor diode at Cornell.

∇B Studies on a LION Extractor

A series of experiments was performed on the extraction diode shown in Figure 1 to investigate the effects of modifying the radial gradient of the insulating magnetic field. A proton beam was generated by using a passive, epoxy filed, grooved anode. The ratio of the magnetic field at the outer cathode to the magnetic field at the inner cathode was varied from 0.34 to 1.0 by using current shunts on the cathode coils. The results are summarized in Figures 4-6. Figure 4 shows the current flow to the inner and outer cathodes as measured by Ragowski coils. The transfer of current from the outer cathode to the inner cathode with increasing B_{outer}/B_{inner} occurs when this ratio is approximately 0.55. Figure 5 shows that the ion current is most uniform with respect to radial variation near this crossover, when this ratio was approximately 0.5. Figure 6 shows an interesting result of this uniform emission situation. At this particular value of the field ratio, the ion current and diode efficiency peaked. It is of interest to note that equal ampere turns in the inner and outer cathode coils would produce a field ratio of approximately 0.66. This means that the uniform ion emission condition was reached by increasing the magnetic field at the inner cathode. This is in agreement with the theoretical model discussed in the previous section.

Extractor Diode Cleaning Studies

One of the first problems encountered when one uses active anodes to generate intense beams of light ions, like lithium, is proton contamination. This contamination arises from hydrogen or hydrocarbons on the anode and is a particular problem for EMFAAPS type anodes. These anodes are constructed by vacuum evaporation of the conducting foil and of the dielectric ion source material. This process traps hydrogen and water vapor in the foil and dielectric. In addition these diodes require an insulating substrate which previously had been a hydrocarbon epoxy.

To rid the diode of hydrogen, the epoxy substrate was replaced by glass and discharge cleaning was performed after the anode was attached to the pulse generator and pumped down. The discharge cleaning study proceeded in two steps. First an EMFAAPS anode with just the conducting 0.1 μ aluminum foil was discharge cleaned. For this situation a d.c. discharge was struck by applying approximately 300 V from the anode to ground. For these discharges the diode was backfilled with 100-300 mTorr of Argon or Nitrogen. The anode was isolated by a thin insulating strip which flashed over during the high power pulse. The discharge was run for 5-10 minutes with a current density of approximately 500 $\mu A/cm^2$. A second series of measurements was performed with an anode which had a 1.5 μ LiF layer evaporated over the aluminum foil. In this case a d.c. discharge could not be used because the insulating properties of the LiF effectively introduced a capacitor in the circuit for the discharge. A 60 Hz a.c. discharge appeared to work well.

The results of the cleaning study are summarized in Table 1. A Thompson parabola and filtered Faraday cups were used to measure the hydrogen content of the beams. The d.c.

Table 1. Cleaning Results

Anode	Cleaning Duration (min.)	Firing Delay (min.)	Beam Composition (%)					
			H	Al	C	O	Li	F
Grooved Epoxy	0	-	60 ± 15	2 ± 2	30 ± 10	7 ± 5	-	-
Al Foil on Epoxy	0	-	80 ± 20	9 ± 5	8 ± 5	3 ± 3	-	-
Al Foil on Epoxy	5 DC Ar^+	3	60 ± 25	23 ± 15	12 ± 10	5 ± 5	-	-
Al Foil on Glass	0		65 ± 20	29 ± 15	5 ± 5	1 ± 2	-	-
Al Foil on Glass	5 AC Ar^+	3	40 ± 20	50 ± 20	5 ± 5	5 ± 5	-	-
Al Foil on Glass	5 DC Ar^+	3	25 ± 20	60 ± 15	9 ± 5	6 ± 5	-	-
Al Foil on Glass	5 DC Ar^+	15	55 ± 20	40 ± 15	2 ± 2	3 ± 3	-	-
Al Foil on Glass	5 DC H^+	3	85 ± 15	13 ± 10	1 ± 2	1 ± 2	-	-
Al Foil on Glass	10 DC H^+	3	70 ± 10	17 ± 10	11 ± 10	2 ± 2	-	-
LiF on Al Foil on Glass	0	3	55 ± 25	6 ± 5	14 ± 10	4 ± 4	20 ± 15	1 ± 2
LiF on Al Foil on Glass	5 AC Ar^+	3	15 ± 15	19 ± 5	0 ± 2	1±10	65 ± 15	2 ± 2

discharge cleaning of aluminum foil over glass reduced the hydrogen content from approximately 65% to roughly 25%. Each entry in this table represents the range of values

for several shots. The a.c. cleaning of the LiF anode resulted in a reduction of the hydrogen content of the beam from 55% to 15%. In both situations waiting 15 minutes after terminating the discharge cleaning resulted in recontamination of the surfaces.

Rapid Rate Ion Diode Experiment

Since Beams '90, the Rapid Rate Ion Diode Experiment (RRIDEX)[5] has undergone several improvements and currently generates 120 keV beams of several tens of kiloamperes at 90 Hz in bursts of up to ten shots. It can produce beams from any gas and has employed hydrogen, nitrogen, argon and acetylene. This diode can also pulse at one shot per minute indefinitely. This feature provides a unique opportunity to perform difficult experiments requiring many data points or even to conduct experiments on a statistical basis. In particular, this capability is being exploited in an attempt to study virtual cathode formation.

In this study we backfill the diode with a low pressure of helium and observe the line radiation that He neutrals emit when they are collisionally excited by the electrons in the virtual cathode. The population dynamics of the helium neutrals is simplified by two factors. First, since we are investigating cathode formation, we are interested in only the first 0-30 nsec of the voltage pulse, which is on the same order as all of the radiative transition times between the excited states. Second, virtually all of the helium is in the ground state initially. These two factors taken together imply that the intensity of an emission line is approximately proportional to the collisional excitation rate from the ground state to the initial state of the emission line. In turn, the collisional excitation rate is proportional to the virtual cathode electron density and also proportional to $(\ln v)/v^2$, where v is the electron velocity. Thus by monitoring several lines it should be possible to extract the spatial and temporal dependence of both the density and velocity of the virtual cathode electrons. This model assumes that the virtual cathode is a cold fluid so that all of the electrons within the same small volume have the same velocity.

There are several complicating factors, however. First the helium neutrals can also be excited by collisions with the beam ions. We are attempting to quantify this problem. At present we are using a beam of massive argon ions which traverses the gap in ≥ 15 nsec and will therefore not compete much with the electrons at early times. Second, the signal to noise ration is rather low, so we must signal average. It is here that the high pulse rate and good pulse-to-pulse reproducibility become invaluable.

*Work supported by Sandia National Laboatories

1. G. Rondeau et al., Proc. 7th Int. Conf on High-Power Particle beams, W. Schmidt and W. Bauer eds., (Karlsruhe, Germany) p. 528. G, Rondeau et al., Proc. Int. Conf. on High Power Particle Beams, B. Brelzman and B. Knyazev, eds., (Novosibirsk, USSR 1990) p. 449.

2. S.Slutz and D. Seidel, J. Appl. Phys., 59, 2685 (1968).

3. P.P. Deichuli and V.M. Fedorov, Proc. 8th Int. Conf. on High Power Particle Beams, B. Brelzman and B. Knyazev, eds., (Novosibirsk, USSR 1990) p. 469.

4. H. Bluhm et al., op. cit., p.451.

5. J.B. Greenly et al., op. cit., p. 199.

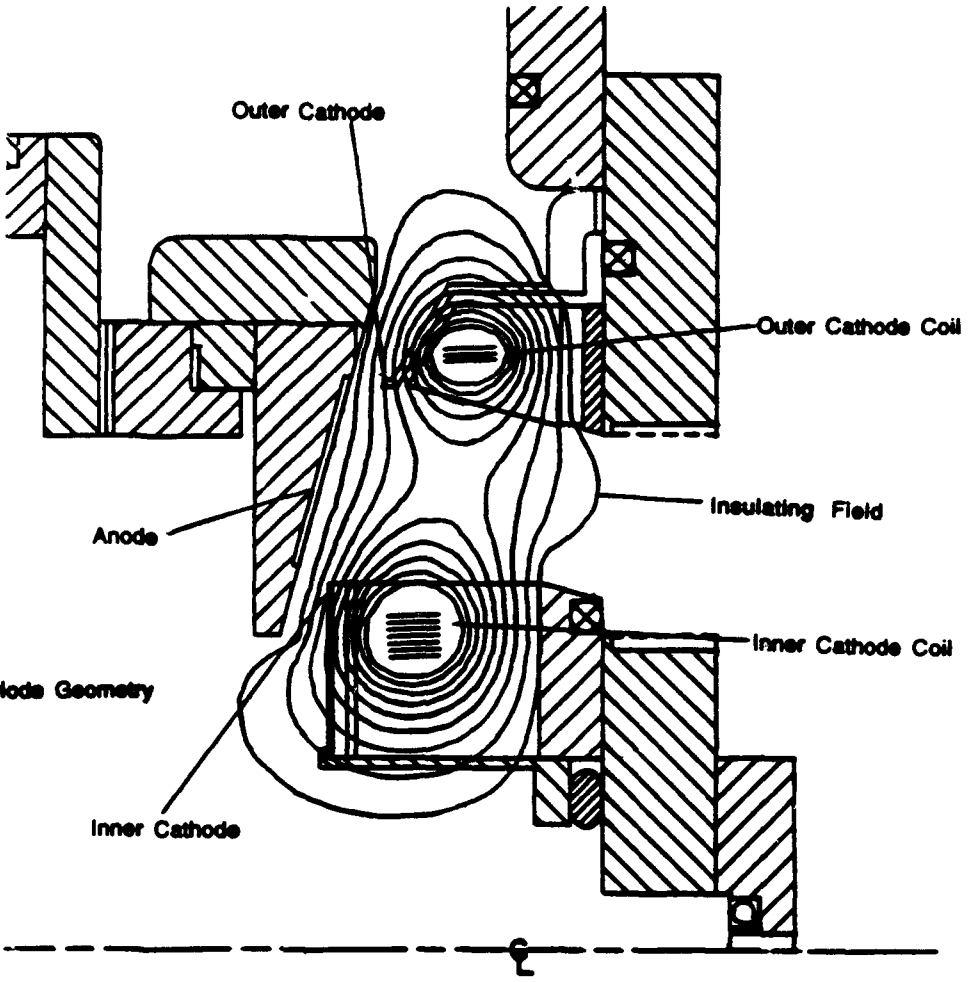

Figure 1. The Extraction Diode Geometry

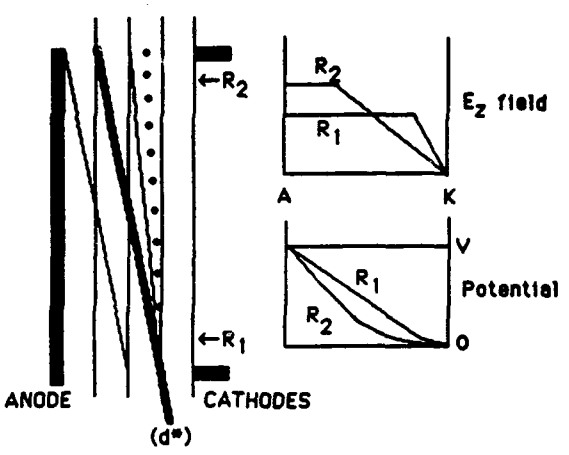

Figure 2. Relation between surfaces of constant magnetic flux (rA_θ) (vertical thin lines); surfaces of constant A_θ (tilted thin lines); the ideal limiting surface of the electron layer (d^*); and equipotential surfaces (dotted line). Electric field and potential are plotted as a function of position across the gap at two indicated radii.

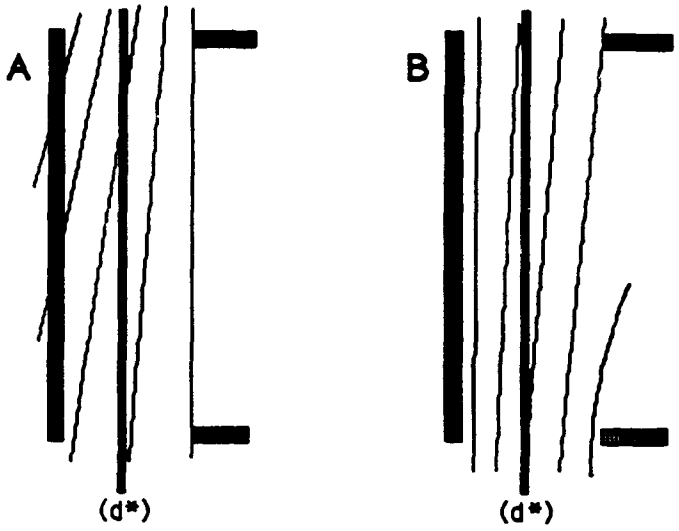

Figure 3. (A) Slutz uniform insulation with both cathodes still connected by a single flux surface, anode intersecting multiple flux surfaces.
(B) uniform ion current with anode conforming to a flux surface but inner cathode overinsulated.

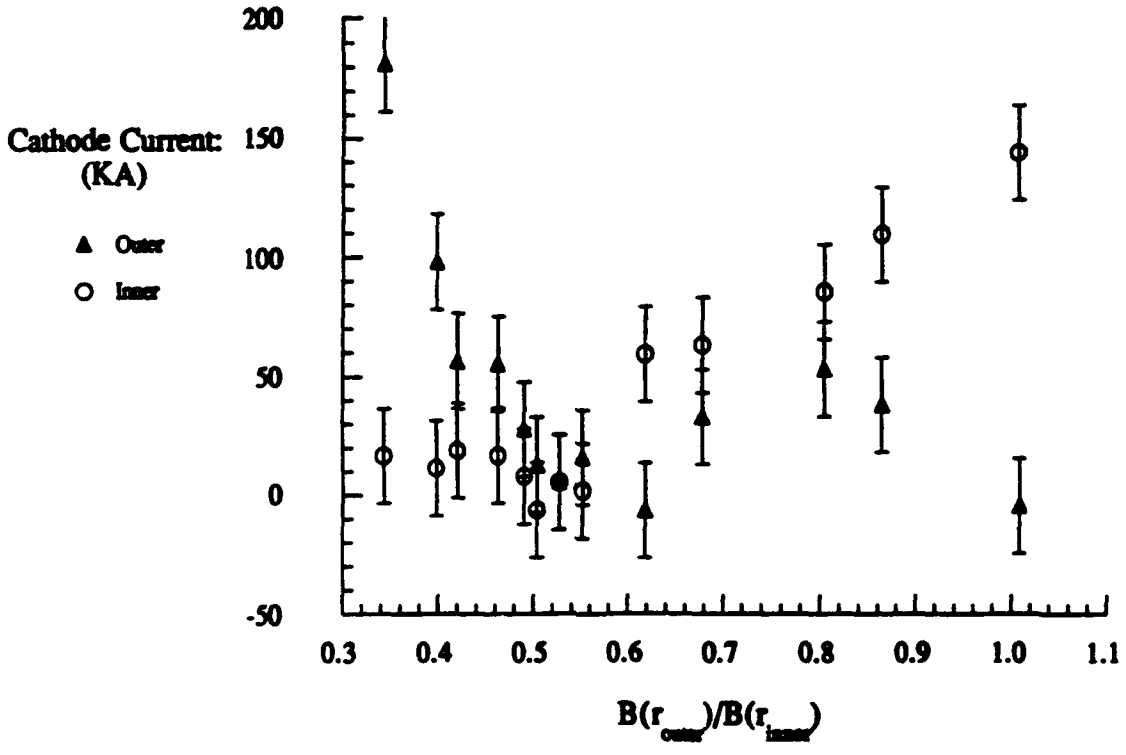

Figure 4. Cathode Currents. Ragowski measurements made on a passive epoxy filled, grooved anode as the insulating field gradient is modified.

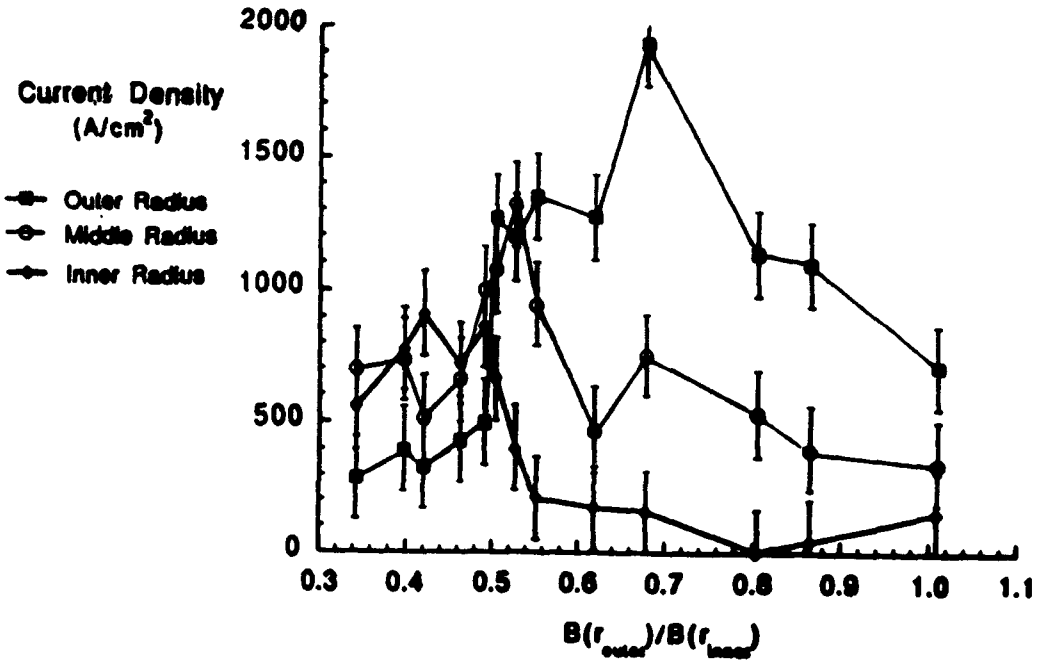

Figure 5. Ion Current Density. Faraday cup measurements on a epoxy filled, grooved anode at three radial positions near the virtual cathode as the insulating field gradient is modified.

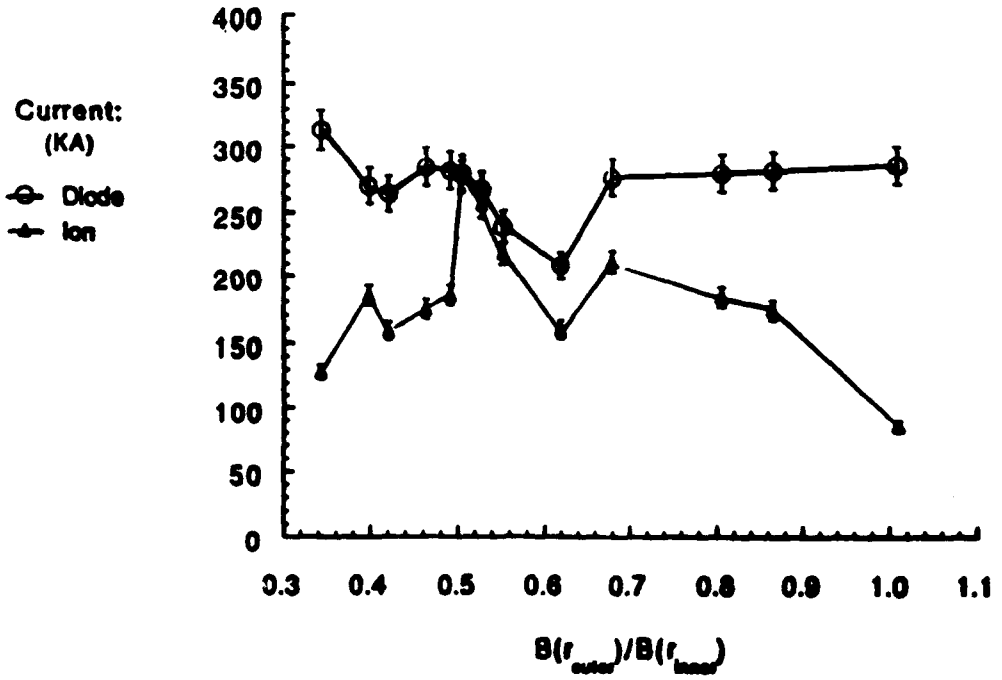

Figure 6. Total Electron and Ion Currents. Ragowski measurements of the currents as the field gradient is modified.

FOCUSSING PROPERTIES OF A STRONGLY INSULATED APPLIED B_r-PROTON DIODE WITH A PREFORMED ANODE PLASMA SOURCE

H. Bluhm, P. Hoppé, M. Althaus,H. Bachmann, W. Bauer, K. Baumung, L. Buth,
H.U. Karow, H. Laqua, D. Rusch, E. Stein, O. Stoltz
Kernforschungszentrum Karlsruhe
Institut für Neutronenphysik und Reaktortechnik
P.O. Box 36 40
W-7500 Karlsruhe

Abstract

In the paper we describe a magnetically insulated proton diode in extraction geometry developed for the high voltage pulse generator KALIF which produces a 40 kJ proton beam pulse at a power level of greater than 0.65 TW. This is very close to the optimum for the parameters of KALIF and was reached through a high diode coupling efficiency (80 %), a high ion production efficiency (90 %), and a high beam purity (80 - 90 %). The key elements of the diode are an active proton source based on a thin Ti-hydride film covered by a thin layer of Pd and a strong insulating magnetic field ($V_{crit} / V \geq 3.0$).

A microscopic divergence of about 1.0 ° and a total divergence of 1.4 ° for the complete system have been measured. It has been found that an electron limiter at the anode significantly reduces the microscopic divergence of the beam.

Focussing to proton power densitites of 1 TW / cm^2 has been achieved by eliminating most of the chromatic aberrations and by correcting for the spherical aberrations.

Introduction

The proton beam extractor diode developed for the 1.5 TW, 1.7 MV pulse power generator KALIF is based on the simultaneous application of an actively produced anode plasma source and of a strong insulating magnetic field. Its main design characteristics have been described previously [1, 2] and will only briefly be summarized here. The diode hardware is shown in Fig. 1. The anode plasma is created from a thin layer of Ti-hydride covered by a protective layer of Pd. The Ti and Pd-films of respectively 300 - 500 Å and 100 - 200 Å thickness were deposited on a 0.5 mm thick insulating layer of epoxy which covered the active area of the anode. At their inner and outer edges the films were contacted to the bulk aluminum anode by 1 µm thick and 2 mm wide deposited Al-rings. Early in the generator pulse part of the generator current is diverted through the Ti-Pd-film with the help of a bypass plate and 6 plasma opening switches (POS). By this current flow the films are resistively heated to melting temperatures and hydrogen is desorbed rapidly from the Ti-store.

As the resistance and therefore the voltage drop across the films is rising too, an electrical discharge occurs in the desorbed gas layer as soon as a critical thickness necessary for the development of electron avalanches is exceeded. Thus before the POS opens and before any voltage occurs in the diode an anode plasma has been formed. Further details on this ion source may be found in [3, 4].

The strong insulating field is produced by two compact concentric coils interconnected in series. A detailed description of the coil design is given in another paper included in these proceedings [5].

In the experiments presented in this paper a mean insulating field of 2 T was applied at the position of the cathode tip. Its strength varied by less than 22 % over the anode emission zone, reaching a minimum at an intermediate radius of 7 cm.

The cathode was a hollow truncated stainless steel cone of 0.5 mm wall thickness. At its top a 3 - 5 mm long edge projected into the direction of the anode. We define the geometric gap by the distance from the anode that a fictitious plane passing through the cathode tip maintains. In most experiments this gap was 8.5 mm.

Assuming that the virtual cathode is distributed along the magnetic field line crossing the cathode tip we obtain a critical voltage of typically 4.9 MV and 6.6 MV at the outer and inner edge of the ion emitting zone respectively.

A 1.5 µm thick Mylar foil 1.4 cm distant from the anode separated the diode vacuum region from the drift space which was filled with 5 mbar of Argon.

Basic requirements

In case of an ideal focussing system with no aberrations the maximum possible proton beam power density is given by

$$L_f \leq \frac{P_p}{\pi f^2 \delta^2} \cdot g$$

where P_p is the proton beam power in the diode, δ is the half angle of the cone with which a beamlet is emitted from a point at the exit of the diode (divergence angle), f is the focal length of the ion optics and g is a geometric factor, determined by the polar angles $\phi 1$, $\phi 2$ limiting the diode emission zone. Therefore, a prerequisite for achieving a high power density in a focus is a large proton beam power in the diode, a small divergence of the beam, and a short focal length of the optics.

It has been argued previously that there exists a lower practical limit for the focal distance of an applied-B extractor diode [2]. For the parameters of KALIF this has been estimated to be around 12 cm. The attainable proton beam power Pp is limited by the electrical power coupled to the diode, by the ion production efficiency and by the purity of the beam. Due to the large inductance of 65 nH connected with the vacuum feed of KALIF the available electrical power is below 1 TW. Of this up to 0.9 TW have been coupled to the ion diode. Applying a large magnetic insulation field ($V_{crit} / V_{operation} \geq 3$) it has been possible to achieve an ion production efficiency of greater 90 %, and with the metal hydride

anode plasma source a beam purity of between 80 and 90 % protons has been reached. Therefore, the proton power delivered by the diode was between 0.64 and 0.72 TW.

There are three main sources contributing to the ion beam divergence δ: the anode plasma, the electron sheath, and small angle scatterings in the driftspace. An inhomogeneous anode plasma covering the active area of the anode incompletely and a rough plasma surface have long been considered as the most important causes for ion beam divergence. From time resolved luminosity investigations during the early turn on phase we infered that our Pd covered Ti-hydride ion source produced a uniform covering of the anode. This conclusion was supported by the observation that generally all aperture holes of a shadow-box gave an image on the detector. However, we cannot exclude that a rough or wavy surface also occurs with our plasma source.

Electromagnetic fluctuations in the diode electron sheath are considered to be another important contributor to beam divergence. These fluctuations result from instabilities that develop in the electron sheath. It has been found by linear stability analysis that a high frequency diocotron type and a low frequency ion mode instability can develop in an ion diode with virtual cathode [6]. Since the inverse frequency of the ion mode instability can be of the order of the ion transit time in the gap its effect on beam divergence is much more severe. It has also been found by fully electromagnetic particle in cell code calculations that the ion mode instability is suppressed as long as the less destructive diocotron instability dominates [7]. Consequently, there may be two strategies to decrease the beam divergence: The first is to reduce the growth rate of any instability by a strong magnetic field. It has been demonstrated by PIC-code results that such a reduction occurs but it is presently unknown which field strength might be necessary to suppress the growth for the complete pulse duration. Nevertheless, in our experiments we mainly tried to achieve a low divergence beam by applying strong magnetic fields. The second strategy is to conserve the less destructive high frequency instabilities. It has also been found in the PIC-code calculations [7] that this possibly can be achieved with the help of an electron collector ring on the anode. We shall describe later in this paper the effect of an electron collector on beam divergence in our diode.

To focus a beam one has to apply a suitable ion optical system and to determine and eliminate its aberrations. However, with a high power diode we are not completely free in the choice of the optical system but always have to cope with a combination of different elements. Some of these elements are magnetic by nature (either self- or applied magnetic) and therefore show strong chromatic aberrations. Since it is impossible to correct these aberrations it is necessary to avoid them. This is best achieved if we have both a square pulse in the diode voltage and in the diode current. Therefore, in our experiments we strived for a common plateau in voltage and current. The degree of phase uniformity that has been achieved is shown in Fig. 2. In this shot the plateau lastet for a period of about 50 ns. Nevertheless, we may still have some chromatic aberrations due to an ion energy spread caused by instabilities or by charge exchange processes in the anode plasma [8, 9].

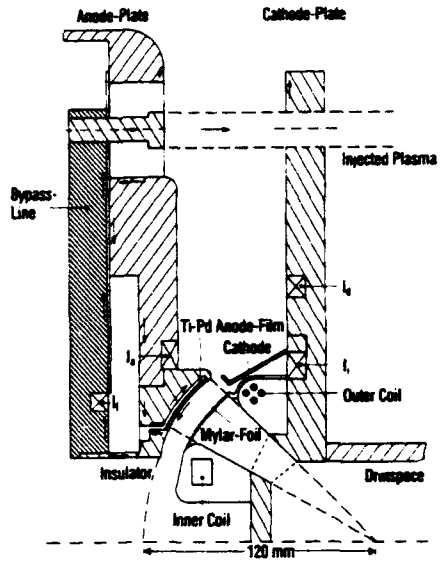

Fig.1. Schematic diagram of the KALIF $B_{appl.}$-extractor diode

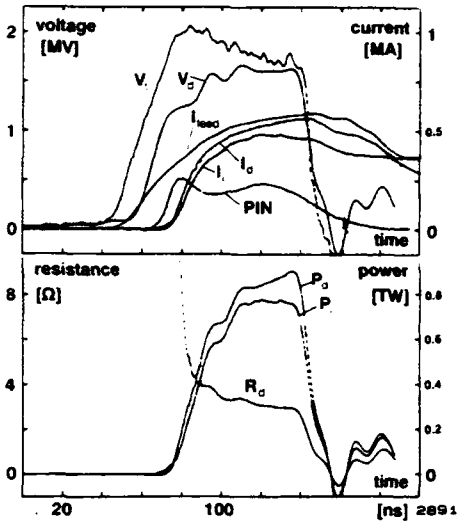

Fig. 2 Current and voltage wave forms. V_d = diode voltage, I_{feed} = generator current, I_i = ion current, I_d = diode current, PIN = hard x-ray-signal

All focussing elements effective in our diode show some spherical aberrations. However, given a high degree of reproducibility in the diode operation they can be eliminated completely if they have been measured with sufficient accuracy. This will be discussed in the next sections.

The remaining aberrations result from the nonzero canonical angular momentum of the ion beam due to the diffusion of the insulating magnetic field into the anode. Again this focussing error can theoretically be corrected completely by the superposition of a slow field. In practice however, this is complicated by the expansion of the anode plasma across the magnetic field lines during the pulse.

The focussing system

There are three possibilities to focus the beam: by external or selfmagnetic fields and by electrostatic fields.

For the ion energies produced in our diode it is difficult to construct a suitable magnetic lens with short focal distance. One can roughly approximate the focal length f of a solenoid by

$$f = \frac{4 r_g^2}{l}$$

where r_g is the gyroradius of the ions to be focused and l is the length of the solenoid. In a 1 Tesla magnetic field the gyroradius of 1.7 MeV protons is 18 cm. Therefore, it seems to be difficult to base our focussing system on a magnetic lens. Another disadvantage of a magnetic lens is its strong chromatic aberration.

Focussing by selfmagnetic fields also suffers from chromatic aberrations and in addition is difficult to control and needs a high degree of reproducibility both in voltage and current density.

The best solution for an ion optical system with short focal length is an electrostatic lens integrated into the diode which in ion optics is known as an immersion lens. The focussing effect of this lens is

based on the curvature of the equipotential surfaces in the diode gap. Since it is free from chromatic aberrations it is reasonable to make the immersion lens the main focussing element.

Unfortunately it is presently impossible to precalculate the diode lens with sufficient accuracy. In addition the effect of the self- and external magnetic fields on the ion trajectories are not negligible. Therefore, we have to determine the ion trajectories experimentally and to iterate an improved anode curvature from these measurements.

Diagnostics

The type of shadow-box that was used in our experiments to determine the ion trajectories at different positions along the driftpath consists of a 0.1 mm thick stainless steel aperture mask containing 16 holes 0.7 mm diameter each distributed over 4 radial and 16 azimuthal positions. The beamlets selected by the aperture are Rutherford scattered by a 2.5 µm Ni foil. The scattered ions are imaged with a pinhole camera onto a CR-39 ion sensitive film covered by a 10 µm thick Al-foil. Therefore, only protons with energies above 1.2 MeV resulted in visible tracks. After etching the CR-39 films were evaluated with a fully automatic nuclear track recording system.

With the aperture positioned closely behind the window-foil (i.e. 17 mm from the anode) the same arrangement was used to measure the ion beam divergence.

To determine the proton power-density L_F in the focus we must know the current density distribution at the focal spot and the ion energy E_p. The current density distribution measurement has been divided into two steps: In the first step we measure the relative distribution f(r) in the focus and in the second we determine the amplitude I_m of this distribution:

$$L_F(r) = I_m f(r) E_p$$

All parameters are evaluated for the time of maximum power in the diode. E_p is determined from the voltage trace. f(r) is found with the help of the nuclear reaction p (B^{11}, α) 2α in which three isotropically emitted α-particles with energies between 2 and 6 MeV are produced per reaction. Compared to Rutherford scattering this reaction has the advantage that ions with different entrance angles approximately produce the same α-particle yield. Differences do only occur because of the different ion path lengths in the reaction foil. The emitted α-particles are imaged with a pinhole camera onto a CR-39 film.

Using a 14 µm Al attenuation foil in front of the 6 µm B-foil and another 15 µm Al-foil in front of the CR-39 film this method can also be made proton energy selective [10]. With the described arrangement only protons having energies above 1.2 MeV contribute to the focus image.

The amplitude I_m of the current density distribution is determined with the ablation proof two step LiF-Cu activation method developed by R. Leeper [11]. The final activation product in this method is the β^+-emitter Cu^{62} with a halflife of 9.74 min. From the activation measurement and the measured diode voltage we obtain a weighted proton current $\langle I_p \rangle_a$:

$$\langle I_p \rangle_a \int y_p^* (E_p(t))\, dt = e\,(C - B) \exp.(-\lambda t_1)/(1 - \exp(-\lambda T))$$

where y^*_p (Ep) is the activation yield corrected for the contribution by deuterons of natural abundance. C is the number of counts recorded in a time period T beginning at time t_1 after the pulse. B is the number of background counts, and λ is the decay constant of Cu^{62}.

We also calculate a weighted ion current $<I_i>$ from the electrical measurements:

$$<I_i> \int y^*_p(E_p(t))dt = \int I_i(t) y^*_p(E_p(t))dt$$

The value of $<I_i>$ is always appreciably larger than $<i_p>_a$ because of losses at the vanes holding the inner field coil in place and because of the coaxial interconnection between the coils. Altogether this reduces the free cross section by a factor of 0.76. In addition we may have losses at the walls and some ions can miss the activation target. Apart from this $<I_i>$ is smaller than $<I_p>_a$ because of the nonprotonic component of the beam (up to 20 %). Since we are interested in the peak power density we use $<I_i>$ to determine a correction factor M which is the ratio of the electrically measured ion current at peak power to the weighted current $<I_i>$ defined above.

Finally we approximate the current density distribution by a circular Gaussian distribution and use the following formula to determine the maximum proton power density:

$$L_F = \frac{M \ln 2 \; <I_p>_a \; E_p}{\pi \; r^2_{1/2}}$$

where $r_{1/2}$ is the half width at half maximum of the Gaussian distribution fitted to the experimental data.

Results

In a previous series of experiments anodes with a spherical shape and a radius of curvature of 12 cm were used [2]. We anticipated a strong defocussing effect of the diode lens because we expected the virtual cathode following the magnetic field lines to bend away from the anode between the coils. This expectation was supported by earlier results of PIC-code calculations.

However, experimentally we found an annular focus at the position of the vanes that hold the inner field coil in place. Anodes with a radius of curvature of 15 cm used subsequently did not sufficiently shift the annular focus towards the axis. The next iteration led to a conical anode with a slope of 53 ° to the axis. With this shape the beam trajectories reached a common waist at a mean position of 12.2 cm from the anode with a diameter of 5 - 7 mm. Only the outermost rays did not reach the focus (Fig. 3).

From the results of the activation measurements we infered that about 0.45 TW of the available 0.64 TW proton beam power had reached the focal plane. The relative current density distribution was determined in a subsequent number of shots in which the position of the target was shifted stepwise along the axis. In the shot which gave the highest concentration the distribution was somewhat nonsymmetrical. Therefore, we fitted a twodimensional Gaussian distribution to the data whose variances were calculated from the fwhm of two cuts perpendicular to each other through the experimental distribution. The two fwhm's were found to be 5.3 and 7.2 mm respectively. Using these data we calculat-

ed a proton beam power density of 1.05 TW / cm^2. To the author's knowledge this is the highest ion beam power density ever obtained with an extractor diode.

To get an improved understanding of the ion trajectories we must know the position and the shape of the ion emitting surface and of the virtual cathode. Because of the large ratio between magnetic pressure and thermal pressure anode plasma expansion is possible only if the magnetic field penetrates into it. A rough estimate of the position of the plasma surface can therefore be obtained from a measurement of the canonical angular momentum of the ions in a field free region close to the focus. This measurement is best done with a set of two scattering foils separated by a few centimeters. From its minimum approach to the axis we can determine for each trajectory how much flux was lost through the emitting surface. If we take as a basis the original magnetic field distribution in the diode gap we can find an upper limit for the plasma expansion at the trajectory origin. The position of the ion emitting surface derived through this procedure is shown in Fig. 4 together with the original distribution of the magnetic field. As one would expect, the expansion is somewhat bigger at the edges of the plasma region than in the middle. The derived expansion of the plasma of between 2.0 - 2.5 mm at peak diode power is an upper limit because due to the diamagnetic effect the flux may have been compressed in a smaller interval.

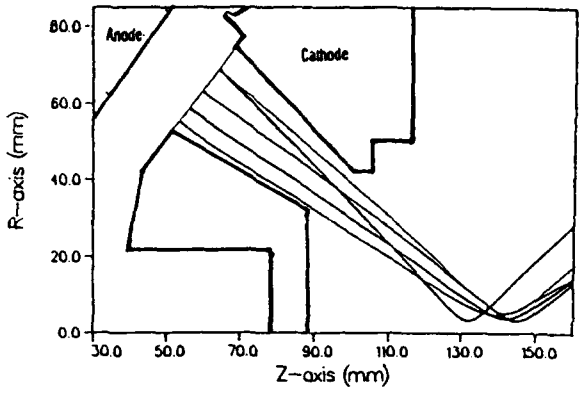

Fig. 3 Measured ion trajectories for a conical anode (extrapolated with a PIC drift space code)

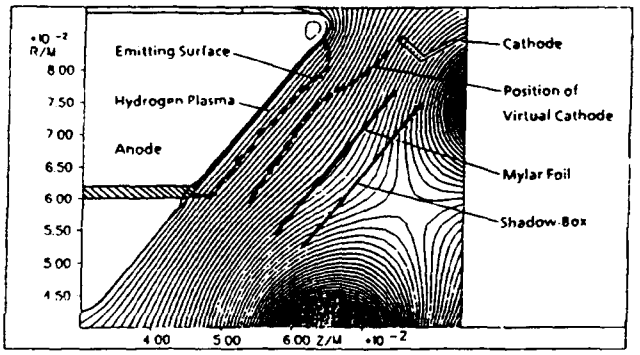

Fig. 4 Experimentally derived shape of the ion emitting anode plasma surface and of the virtual cathode

A simple estimate of the position of the virtual cathode relative to the ion emitting plasma surface can be obtained from Child Langmuirs' law if we know the ion current density as a function of position

$$j = \varepsilon\, 50.4\, \frac{U^{3/2}}{d_{eff}^2} \qquad (U \text{ in MV}, d_{eff} \text{ in cm}, j \text{ in A/cm}^2)$$

where ε is an enhancement factor due to the electron charge distribution alone (we took $\varepsilon = 5.5$ assuming a constant charge density in the gap). A value for j, time averaged over the duration of the voltage plateau, has been obtained by integrating the shadow-box traces. These values are used to determine d_{eff} as a function of position. The resulting shape of the virtual cathode presented in Fig. 4 gives at least a good qualitative description of the equipotential distribution in our diode gap. It does explain the over-focussing of the ion trajectories in case of a spherical anode. Moreover, the strong inward bending of trajectories from the outer edge of the emission zone, even observed with the conical anode (see Fig. 3) becomes understandable.

The microscopic divergence including contributions from processes in the diode and in the drift space has been measured to be between 1.1 ° and 1.3 ° for a conical anode and a strong magnetic insulation ($V_{crit} / V_{operation} \geq 3.2, B = 2$ T). From this we deduced a microscopic divergence singly due to diode effects of 0.9 ° to 1.1 °. To estimate the theoretically achievable proton power density we need the macrospcopic divergence too. This has been determined from the mean radial and azimuthal deviations from an average position of corresponding beamlet patterns. Adding the microscopic and macroscopic divergences quadratically we obtained a total divergence of about 1.4 °. Using this value the maximum possible proton power density achievable with our diode is estimated to be 1.9 TW / cm^2.

It has been pointed out earlier that contributions to the beam divergence due to electromagnetic fluctuations in the electron sheath possibly can be reduced by an electron collector ring on the anode. To investigate this effect we conducted a series of experiments at lower magnetic insulations (0.93 T - 1.6 T) where we expected electromagnetic fluctuations to make important contributions to the divergence. The electron collector was positioned about 11 mm below the active anode area. Comparing analogous shots with and without electron collector we observed the following general trends : Depending on the height of the collector the divergence angle due to diode effects was 20 - 30 % smaller with than without collector. The larger reduction being obtained with the greater height (6 mm). The effect seemed to be larger at larger anode radii and the variance of the divergence angles was always greater in shots without than with the limiter.

We therefore think that there is a noticeable reduction of beam divergence if an electron collector is used on the anode.

Summary

We have found that an extraction diode using a preformed anode plasma and a strong magnetic insulation field ($B/B_{crit} \geq 2.5$) can produce uniform focusable ion beams with efficiencies greater than 90 %. An electrical discharge through a thin Ti-Pd-hydride film creates a uniform hydrogen plasma layer from which an ion beam with a proton fraction of greater 80 % can be extracted. Focussing of this beam to high power densities was achieved by minimizing the chromatic aberrations through a common plateau in diode voltage and current and by correcting the spherical aberrations of the active focussing elements iteratively. Thus it has been possible to reach power densities of 1 TW / cm^2.

A shape of the ion emitting plasma surface has been derived from measurements of the canonical angular momentum. From an evaluation of the ion current density we have determined this effective acceleration gap and thus the position of the virtual cathode. These equipotential boundary surfaces are consistent with the observed ion trajectories. Using the experimental value of 1.4 ° for the total beam divergence we calculated a maximum possible power density of 1.9 TW / cm^2. Taking into account the transparency of the drift space a value of 1.5 TW / cm^2 seems more realistic. To achieve this power density we must further reduce the imaging errors of our focussing elements and especially must diminish the canonical angular momentum. This may be either achieved by an improved compensation of the diffused magnetic field or by a higher degree of ionisation in the anode plasma.

A further enhancement of the power density in the focus requires a reduction of the beam divergence. It has been shown that an electron collector on the anode has a certain potential to achieve that goal.

Acknowledgement

The authors thank G. Keßler for his continued support and encouragement to this work. They also thank H. Guth for doing the image processing of the CR-39 films and V. Fedorov and W. Schmidt for valuable discussions on the interpretation of the data. Finally we thank the operational staff of KALIF, H. Lotz and G. Westenfelder for their technical assistance.

References

1. H. Bluhm, P. Hoppé et al. in Proc. of the 8th Intern. Conf. on High Power Particle Beams (Beams '90), Novosibirsk, USSR, July 2 - 5, 1990, p. 451.
2. H. Bluhm, P. Hoppé, H. Laqua, D. Rusch accepted for publication in Proceedings of the IEEE Transactions, 1992.
3. H. Bluhm, H. Laqua, K. Baumung, L. Buth, P. Hoppé, Proc. of the 8th Intern Conf. on High Power Particle Beams (Beams '90), Novosibirsk, USSR, July 2 - 5, 1990, p. 927,
4. H. Bluhm, H. Laqua, L. Buth, P. Hoppé, D. Rusch, Proc. of the XVth Int. Symp. on Discharges and Electrical Insulation in Vacuum, Darmstadt, September 6 - 10, 1992.
5. P. Hoppé, H. Bluhm, H. Laqua, O. Stoltz, Generation of Strong Radial Magnetic Insulation Fields., these proceedings
6. S. Slutz, Proc of the 8th Intern Conf. on High Power Particle Beams (Beams '90), Novosibirsk, USSR, July 2 - 5, 1990, p. 511.
7. M.P. Desjarlais et al., Phys Rev. Lett. 67, 3094 (1991).
8. E. Ott et al., Phys. Fluids 28, 1948 (1985).
9. T. Pointon, J. Appl. Phys. 66, 2879 (1989).
10. A. Klumpp, H. Bluhm, KfK 4130 (1986).
11. R.J. Leeper et al., Proc. NATO Advanced Study Institute on Fast Electrical and Optical Diagnostic Principles, Vol. 1, eds., J.E. Thompson, L.H. Luessen (M. Nijhoff, The Netherlands (1986)), p. 263.

TRANSPORT AND FOCUSING CONSIDERATIONS FOR LIGHT ION ICF SYSTEMS+

P.F. Ottinger, D. Mosher, J.M. Neri, and D.V. Rose*
Plasma Physics Division, Naval Research Laboratory
Washington, DC USA 20375

C.L. Olson
Sandia National Laboratories, Albuquerque, NM USA 87185

Abstract

The Laboratory Microfusion Facility (LMF) has been proposed for the study of high-gain, high-yield ICF targets. A number of transport and focusing schemes are being considered for LMF. The schemes which have been studied most extensively include ballistic transport with solenoidal lens focusing, z-discharge channel transport and wire-guided transport. Transport efficiency η_t has been calculated as a function of various system parameters so that point designs can be developed for each scheme. The analysis takes into account target requirements and realistic constraints on diode source brightness, packing, and beam transport. The effect on η_t of voltage ramping for time-of-flight bunching has also been considered. Results show that transport efficiencies of > 50% can be obtained for all three systems with diode-microdivergence (5-10 mrad), diode-radius (10-15 cm), and diode-ion-current-density (2-10 kA/cm^2) values which seem achievable.

I. Introduction

A multimodular light-ion inertial-confinement-fusion (ICF) system directs energy from about 10 to 30 intense ion beams onto a target for implosion. Each beam is focused and transported over a distance of a few meters from the ion diode to the target. This standoff allows for packing the pulsed power generators around the target chamber. It also provides for isolation of the diode hardware from the target explosion and for power compression by time-of-flight (TOF) bunching.

The Laboratory Microfusion Facility (LMF) has been proposed for the study of high-gain, high-yield ICF targets.[1] A number of transport and focusing schemes are being considered for LMF.[2] The baseline approach is ballistic transport with solenoidal lens focusing[3,4] (BTSF), and alternate approaches include z-discharge channel transport[5] (ZDT), wire-guided transport[6] (WGT), and self-pinched transport[7]. Because they have been most extensively studied, this paper will concentrate on BTSF, ZDT, and WGT.

Transport efficiency is defined to be the ratio of ion energy which is delivered to the target to the total ion energy produced in the diode. Transport efficiency has been calculated as a function of various system parameters for each scheme so that LMF point designs can be de-

veloped The analyses take into account target requirements and realistic constraints on diode source brightness, packing, and beam transport. Results show that transport efficiencies of > 50% can be obtained for all three systems with diode-microdivergence (5-10 mrad), diode-radius (10-15 cm), and diode-ion-current-density (2-10 kA/cm^2) values which seem achievable. Not included in the analysis is waveform efficiency and beam energy losses. The waveform efficiency accounts for energy in the head and tail of the power pulse which is not usable. Beam energy losses, which are typically on the order of 10%, are due to beam ion deceleration in the self-consistent electric fields and the collisional stopping power of the background gas.

II. Ion Source Model

For LMF, lithium ions will be extracted from an applied-B diode.[8] It is assumed that the ion current density is uniform across the annular anode surface which extends from a radius of R/2 to R. Ions orbits are bent toward the axis in the diode vacuum region by the self-magnetic field of the beam. For small bending angles, $\Theta_b(r,t) = \omega_c \Delta/v$, where ω_c is the beam ion cyclotron frequency associated with the self-magnetic field in the diode region, v is the ion speed, and Δ is the distance from the anode to a transmission foil which separates the diode vacuum region and the gas-filled, charge- and current-neutralized transport region. There is no bending at the inner edge of the annular beam, where the self-magnetic field is zero. Anode shaping is used to compensate for the magnetic bending in the diode to provide a forward directed, parallel beam for BTSF or a focused beam for ZDT and WGT. Beam ions are stripped from Li^{+1} to Li^{+3} as they pass through the transmission foil. Ions are assumed to leave the diode region distributed uniformly in a cone of half angle Θ_μ about the average angle $\Theta_d = \Theta_b(r,t)+\Theta_s(r)$, where Θ_μ is the source microdivergence and $\Theta_s(r)$ results from the anode surface shaping. Since Θ_b varies in time as $I/V^{1/2}$, where I is the beam current and V is the accelerating voltage, Θ_s can only compensate for Θ_b at one point in time. This time is chosen to be when the average voltage, V_o, is reached. Assuming here that the diode current scales[9] as $I(t) = I_o[V(t)/V_o]^2$ and that V increases in time for TOF bunching, it is seen that Θ_s over-compensates for Θ_b early in time and under-compensates late in time. This will lead to an inward sweeping of Θ_d as a function of time. This model assumes changes in Θ_s in time due to anode plasma motion are negligible.

The bunching factor is defined as $\beta = \tau_o/\tau_t$, where τ_o is the beam pulse duration at the diode, and τ_t is the beam pulse duration at the target. If D is the total path length for the beam from the diode to the target, then the ideal voltage ramp for TOF bunching[10] is given by

$$V(t) = \frac{V(0)}{\left(1 - \frac{t}{T}\frac{\beta - 1}{\beta}\right)^2} \quad , \qquad (1)$$

where T = D/v(0). For these calculations, $V_o \equiv [V(0)+V(\tau_o)]/2$ = 30 MeV, D = 400 cm, and τ_t = 15 ns is set by pellet design requirements for a 10 MJ total beam energy. Setting the total beam energy per module,

$$E_T = \int_0^{\tau_o} IV\, dt = \frac{I_o}{V_o^2} \int_0^{\tau_o} [V(t)]^3\, dt \quad , \qquad (2)$$

to (10/N) MJ specifies I_o for given values of $\tau_o = \beta\tau_t$ and N, where N is the number of modules. For LMF, bunching factors of β = 2 - 4 will be required for ion pulse durations of 30 - 60 ns at the diode. The required diode ion current density is derived from $J_o = 4I_o/3\pi R^2$ with R on the order of 10 cm.

III. Ballistic Transport With Solenoidal Lens Focusing

For BTSF, the beam is extracted from the diode parallel to the axis and is propagated about 250 cm at large radius. The solenoidal lens then focuses the beam over a distance F = 150 cm onto a target of radius r_t = 1 cm. Since $F = r_t/\Theta_\mu$, it is chosen as the smallest practical target chamber radius in order to maximize allowable Θ_μ values. Beam-induced breakdown of the background gas provides beam charge and current neutralization[11], which is assumed to be complete. This system is illustrated in Fig. 1. A 30-cm long (L_s), 30-cm radius (R_s) solenoid is used with 25-cm radius flux excluding shields on either side to confine the field to the vicinity of the lens. The solenoid radius is limited by packing constraints in the target chamber wall. The magnetic field strength of the lens is adjusted to provide a 150-cm focal length at V_o and is typically about 20 kG on axis at the center of the solenoid. The code ATHETA[12] is used to create the solenoidal magnetic field map used for the transport efficiency calculations. The diode region is protected from the target blast by a center plug in the solenoid (not shown in Fig. 1). The outer radius of this plug is determined by the line-of-sight from the center of the target chamber to the outer edge of the diode. Ions at small radius are removed from the beam if they strike this plug.

The diode and solenoidal lens parameters can be matched to minimize chromatic effects due to the TOF voltage ramp. For the BTSF system discussed here, this results in the

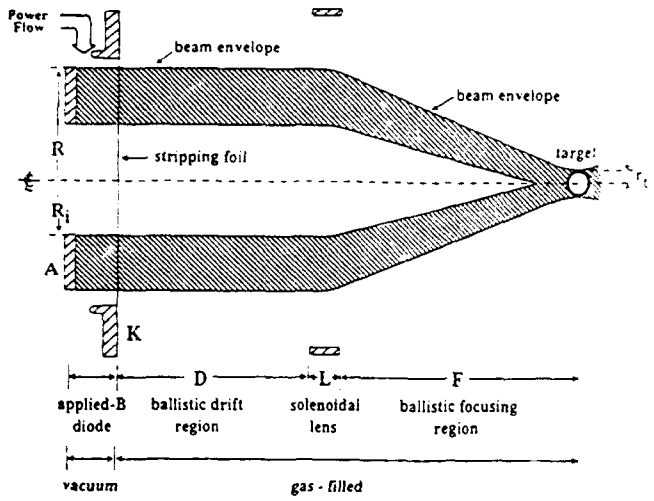

Figure 1. Schematic of BTSF system.

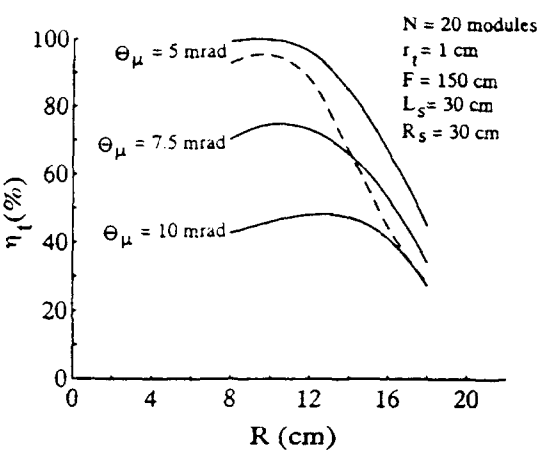

Figure 2. Plot of η_t vs. R for BTSF without focus sweeping (solid curves) and with focus sweeping (dashed curve).

condition $\Delta = 0.047R^2/I_0(MA)$, where I_0 changes with the choices of β and N [see Eq. (2)]. For ZDT and WGT, Δ is fixed independently of R or I_0. Because the BTSF system is nearly achromatic, the reduction in η_t due to focus sweeping should be less for BTSF than for either ZDT or WGT. Constraints on the stripping foil placement due to beam ion angular momentum considerations in an extraction diode[13] are not considered here, but will be investigated in the future.

The solid curves in Fig. 2 show the calculated transport efficiency η_t as a function of diode radius R for BTSF without including focus sweeping due to the TOF voltage ramp. Results are shown for N = 20 and show a decrease in η_t at R = 10 cm from about 100% to about 50% as Θ_μ increases from 5 mrad to 10 mrad. The fall off in η_t for large R is caused by the increasing gradient in the magnetic field away from the center of the solenoid.[4] This gradient causes ions at different radii to focus at different axial locations. The dashed curve shows η_t for Θ_μ = 5 mrad including focus sweeping with β = 2. The TOF voltage ramp reduces η_t at R = 10 cm from about 100% to about 95%. At larger R, the increasing gradient in the solenoidal magnetic field (i.e., non-ideal lens effects) causes a larger reduction in η_t. Within the constraints of packing, high efficiency could be extended to larger R by increasing the radius of the solenoid. For all three transport

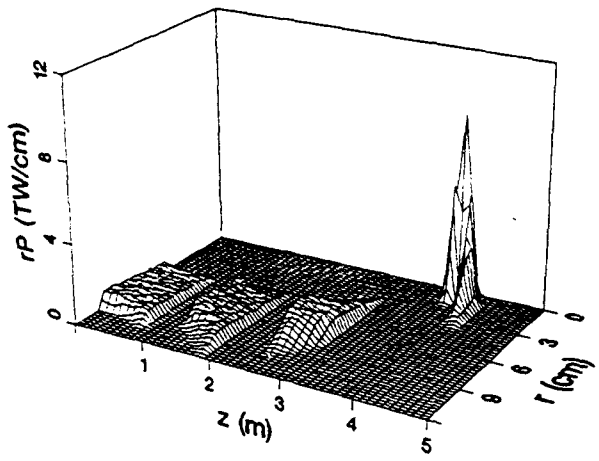

Figure 3. Plot of rP(r,z) at four points in time during transport for BTSF.

schemes discussed here, larger values of β further reduce η_t. Figure 3 shows rP(r,z) (i.e., the beam power density multiplied by r) at four times during transport for the case with N = 20, Δ = 8 cm, R = 10 cm, Θ_μ = 5 mrad and β = 2. For BTSF, P increases rapidly near the target where the beam both bunches and focuses.

IV. Ballistic Focusing With Z-Discharge Transport

For ZDT, the anode is shaped to ballistically focus the beam onto the aperture of the transport channel located a distance F from the diode. Inside the channel, the magnetic field associated with the discharge current radially confines the ions. Once focused, the beam then propagates down the channel with a small radius on the order of the target size. At the exit, the beam expands slightly over the pellet standoff distance d. The ZDT system is illustrated in Fig. 4. The low-mass current return wall provides stability for the discharge and results in a small but tolerable amount of debris for LMF.[14] The aperture radius is chosen to be $r_a = F\Theta_\mu$ so that at V_o the full beam enters the channel. Because of the time dependance of Θ_d, the focus sweeps inward in time so that early and late in the pulse some ions will strike the aperture and be lost. To allow for trapping of the expanding portion of the beam[5], the channel radius is chosen so that $r_c^2 = 2r_a^2$. Unlike the BTSF case where F is restricted by the target chamber size, F is allowed to decrease for ZDT as Θ_μ increases to maintain a channel size on the order of the target size. Consequently, $F = r_t/2^{1/2}\Theta_\mu$ with $r_c = r_t$. Finally, a typical channel current of I_c = 40 kA is chosen. For these calculations, the discharge current density is assumed to be uniform and complete beam charge and current neutralization is assumed in both the gas-filled ballistic focusing region and in the transport channel. Packing considerations determine a

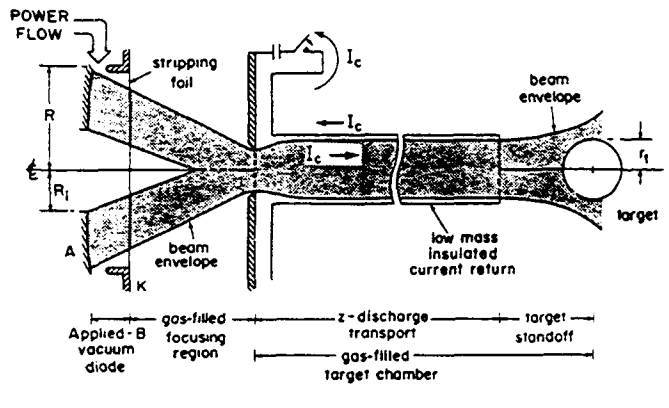

Figure 4. Schematic of ZDT system.

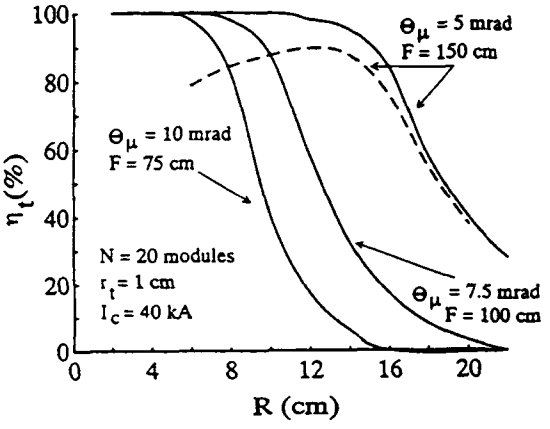

Figure 5. Plot of η_t vs. R for ZDT without focus sweeping (solid curves) and with focus sweeping (dashed curve).

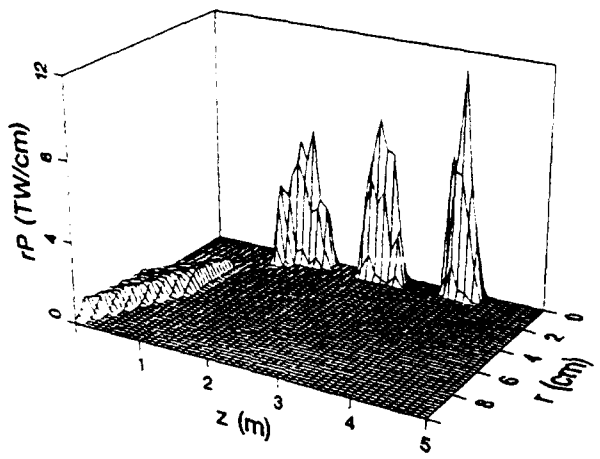

Figure 6. Plot of rP(r,z) at four points in time during transport for ZDT.

standoff distance of $d = r_t(N/2)^{1/2}$ between the channel exit and the target.[5] The length of the transport channel is given by D - F - d and is on the order of about 250 cm.

The solid curves in Fig. 5 show η_t versus R for ZDT without including focus sweeping. Results are shown for N = 20 and Δ = 4 cm, and show a decrease in η_t at R = 10 cm from about 100% to about 40% as Θ_μ increases from 5 mrad (F = 150 cm) to 10 mrad (F = 75 cm). For ZDT, the fall off in η_t for large R (at fixed I_c) is caused by increased ion losses to the channel wall as ions enter the channel at larger angles. This ion entrance angle scales roughly as R/F. High efficiency can be extended to larger R by increasing I_c (to reduce losses to the wall), however, more rapid beam expansion in the stand-off region eventually limits this.[5] The dashed curve in Fig. 5 shows η_t for Θ_μ = 5 mrad (F = 150 cm) including focus sweeping with $\beta = 2$. The TOF voltage ramp reduces η_t at R = 10 cm from about 100% to about 87%. Because Θ_b scales as R^{-1} for fixed Δ, the reduction in η_t due to focus sweeping decreases as R increases. Figure 6 shows rP(r,z) at four times during trans-port for ZDT with N = 20, Δ = 8 cm, R = 10 cm, Θ_μ = 5 mrad and $\beta = 2$. Unlike the BTSF case, here P increases first near the channel aperture where the beam focuses and continues to increase as the beam bunches approaching the target.

V. Ballistic Focusing With Wire-Guided Transport

The WGT system is illustrated in Fig. 7. Here, the magnetic field associated with the current flowing in the gas-embedded central guide wire provides the radial confinement of the ions. The focal distance and aperture size are chosen for a given Θ_μ in the same way as for ZDT so that $r_a = F\Theta_\mu = r_t/2^{1/2}$. The wire radius is set at r_w = 0.035 cm and a wire current of I_w = 40 kA is chosen.[6] For WGT, there is no confining wall and the transported beam radius[6] is given by $r_b = F\Theta_\mu \exp(vR^2/2v_wF^2)$ where $v_w = 2ZeI_w/m_ic^2$, Ze and m_i are the ion charge and mass, and c is the speed of light. Beam-induced breakdown of the gas in the ballistic focusing region and in the gas surrounding the guide wire again results in beam charge and current neutralization during transport. Return-current wires are placed around the central guide wire at a radius of about $1.4r_b$ in order to minimize losses due to chaotic orbit effects while maintaining

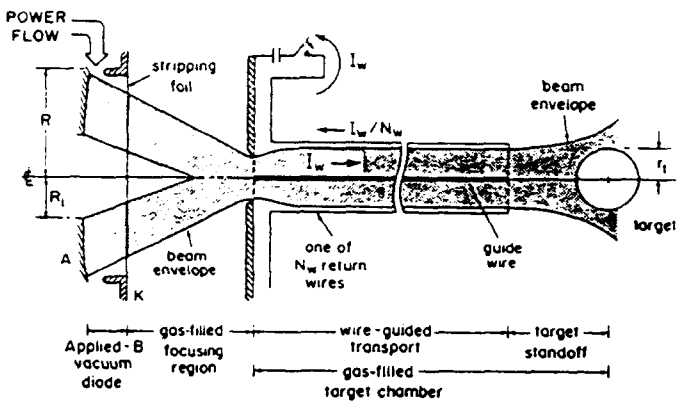

Figure 7. Schematic of WGT system

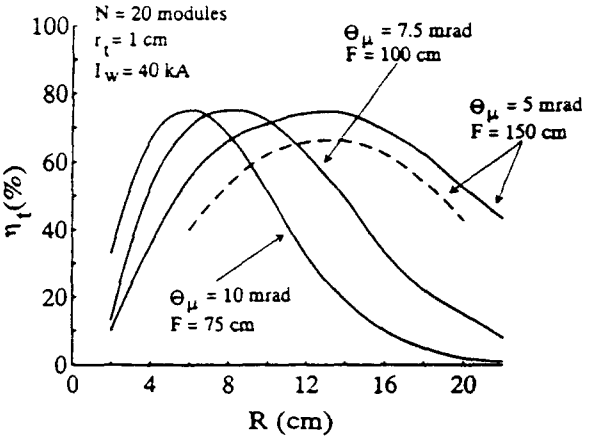

Figure 8. Plot of η_t vs. R for WGT without focus sweeping (solid curves) and with focus sweeping (dashed curve).

as compact as possible WGT system radius for packing.[6] Because the return wires are placed at $1.4r_b$, the standoff distance becomes $d = r_b N^{1/2}$ for WGT.

The solid curves in Fig. 8 show η_t versus R for WGT without including focus sweeping. Results are shown for N = 20 and Δ = 4 cm, and show a range in η_t at R = 10 cm from about 55% to about 75% for Θ_μ between 5 mrad (F = 150 cm) and 10 mrad (F = 75 cm). For WGT, the fall off in η_t for small R is caused by ions with small angular momentum hitting the central guide wire. The fall off in η_t for large R (at fixed I_w) is caused by an increase in the beam radius (beyond the target size) as ions enter the channel at larger angles. Here again, this ion entrance angle scales roughly as R/F. Losses are bigger for WGT than for ZDT because of the larger standoff distance and more rapid beam expansion in the standoff region. The more rapid expansion is a result of larger average transverse ion energies because of the larger average magnetic field with the centrally located current in WGT than with the distributed current in ZDT. Because of this more rapid expansion in the standoff region, increasing I_w for WGT is not as effective as increasing I_c for ZDT in extending high efficiency to larger R.[6] The dashed curve in Fig. 8 shows η_t for Θ_μ = 5 mrad (F = 150 cm) including focus sweeping with $\beta = 2$. The TOF voltage ramp reduces η_t at R = 10 cm from about 70% to about 60%. Aside from accounting for somewhat lower η_t and showing more rapid beam expansion in the target standoff region, the beam power density P(r,z) for WGT is similar to that shown for ZDT in Fig. 6.

VI. Summary

Transport efficiency has been calculated as a function of various system parameters so that LMF point designs can be developed for BTSF, ZDT, and WGT schemes. The analysis

takes into account target requirements and realistic constraints on diode source brightness, packing, and beam transport. Focus sweeping due to voltage ramping for TOF bunching has been considered. Because the BTSF system is nearly achromatic, the focus sweep effect reduces η_t the least for BTSF (when $R \leq R_s/3$). Results show that reasonably high transport efficiency (> 50%) can be obtained for all three systems with diode-microdivergence (5-10 mrad), diode-radius (10-15 cm), and diode-ion-current-density (2-10 kA/cm^2) values which seem achievable. Initial point design values are Θ_μ = 5 mrad, R = 15 cm, and J_i = 2 kA/cm^2. High η_t can be extended to larger R than displayed in Figs. 2, 5 and 8 by increasing R_s for BTSF,[6] I_c for ZDT[5] and I_w for WGT[4]. Eventually this is limited by packing constraints for BTSF and more rapid beam expansion in the target standoff region for ZDT and WGT. For the ZDT and WGT analyses presented here, the beam was focused onto the aperture at F near the midpoint of the voltage pulse (at the time of average voltage). Future work will investigate optimizing η_t by adjusting the aperture size r_a and focal length F to minimize the focus sweep effect for ZDT and WGT. Minor adjustments of the solenoidal lens field strength will be studied to optimize η_t for BTSF with focus sweeping. Waveform efficiency and beam energy losses during transport have not been considered and will reduce the overall efficiency. The sensitivity of the transport efficiency on the beam microdivergence model also needs to be studied.

References

+Work supported by US DOE through Sandia National Laboratories.
*JAYCOR, Vienna, VA 22182.

1. J.J. Ramirez, et al., Fusion Tech. 15, 350 (1989).
2. D. Mosher, et al., Proc. of the 8th Inter. Conf. on High-Power Particle Beams, (Novosibirsk, USSR, July 1990), p. 26.
3. C.L. Olson, Proc. of the 1988 Linear Accel. Conf., (Newport News, VA, Oct. 1988), p. 34.
4. P.F. Ottinger, et al., J. Appl. Phys. 72, 395 (1992).
5. P.F. Ottinger, et al., J. Appl. Phys. 70, 5292 (1991).
6. J.J. Watrous, et al., J. Appl. Phys. 69, 639 (1991).
7. R.F. Hubbard, et al., Part. Accel. 37-38, 161 (1992).
8. D.L. Hanson, et al., IEEE Trans. Plasma Sci. 19, 831 (1991).
9. D.L. Johnson, et al., Proc. of the 1989 Part. Accel. Conf. (Chicago, IL, March 1989), p. 1017.
10. F. Winterberg, Plasma Phys. 17, 69 (1975).
11. C.L. Olson, Proc. of the 1990 Linear Accel. Conf. (Albuquerque, NM, September 1990), LANL Report LA12004-C, p. 396.
12. J.P. Quintenz and D.B. Seidel, Sandia Nat. Lab. Report SAND84-1336 (June 1984).
13. S.A. Slutz and D.B. Seidel, J. Appl. Phys. 59, 2685 (1986).
14. D.D. Hinshelwood, et al., 1990 IEEE Inter. Conf. on Plasma Sci. (Oakland, CA, May 1990), p. 143.

HYDRODYNAMIC TARGET EXPERIMENTS WITH PROTON BEAMS AT KALIF
Diagnostics of the Ablation Pressure by Laser Doppler Interferometry; Generation of Multi-Mbar Pressures by Ablative Foil Acceleration and Impact

K.Baumung, H.U.Karow, V.Licht, D.Rusch, J.Singer, O.Stoltz, H.Bachmann, W.Bauer, H.Bluhm, L.Buth, B.Goel, M.F.Goez, H.Guth, P.Hoppé, H.Lotz, C.D.Munz
Kernforschungszentrum Karlsruhe (KfK)
P.O.Box 3640, D-W7500 Karlsruhe, Germany
and
G.I.Kanel, A.L.Ni, A.Shutov, O.Yu.Vorobjev
High Energy Density Research Center
IVTAN, Russ. Academy of Sciences, Moscow, 127 412, Russia

The hydrodynamic response of plane targets to the ablative pressure impulse induced by high-power proton beams has been investigated experimentally at the KALIF facility using time-resolved laser Doppler interferometry. With this KALIF-ORVIS diagnostics system, it has been possible to measure the complete wave form of the ablation pressure pulse, $p_{abl}(t)$, generated in aluminum at the boundary to the condensed target matter. In another class of experiments, the ablative acceleration of plane target foils to hypervelocities has been investigated. The proof-of-principle experiments have been performed at KALIF using a 20 cm-B_Θ extraction diode delivering an axial proton beam of 0.2 TW/cm^2 power density on target. Ablation pressure amplitudes of 0.3 Mbar have been determined, and 1-dimensional foil acceleration at $>10^{11}$ g up to 13 km/s final velocity has been achieved. Using these ablation flyer foils, impact experiments have been performed and diagnosed. Dynamic pressure states of 5 Mbar have been generated by impact of Al flyer foils with W targets. The experiments are being continued using the KALIF applied B extraction diode which delivers 50 kJ-proton beam pulses with 1 TW/cm^2 power density on target.- In a third class of beam-target experiments at KALIF, the tensile strength of solids (Al, Mo single crystals) has been investigated up to the highest strain rates so far achieved in dynamic matter research.

Introduction; Measurement of the ablation pressure

At the KfK KALIF facility (i.e. the Karlsruhe Light-Ion Facility), proton beam pulses are generated with an energy content of up to 50 kJ, with ≤ 1.7 MeV kinetic energy, and with pulse lengths of ≤ 50 ns. In 1992, axial proton beam pulses have been focussed to a circular focus spot of r $\approx$ 0.5cm delivering 1 TW/cm^2 of peak power on a plane target and depositing ≈ 150 TW/g in target matter of near-solid density.[1] This bulk energy deposition rises the temperature in the beam-heated deposition zone to about 10^2 eV and its pressure to ≥ 1 Mbar. The hot target matter ablates towards the outside. The transient ablation pressure state propagates as a 1-dimensional pressure wave into the condensed target matter. The dynamic response of both the ablated matter and the condensed target matter, the transient ablation pressure state and its propagation through the condensed target matter are subjects of the experimental beam-target investigations presently performed at KALIF.

A fundamental problem in beam-matter interaction physics concerns measuring in quantitative terms of the ablation pressure at the interface to the cold condensed target matter. No detector exists which would be capable to make a quantitative and time resolved measurement "in situ". It has been possible to solve this difficult diagnostics problem by measurement of the "kinematic variables-of-state" of the ablation pressure wave propagating through the interface into the cold condensed matter of the target.

For observation of the dynamic target response, and for measuring of kinematic quantities-of-state, an ORVIS type laser-Doppler-velocity interferometer[2] has been set up at the KALIF facility. With this KALIF-ORVIS diagnostics system[3], the particle (or mass) velocity $u_p(t)$ at the rear target surface of optically reflecting targets can be recorded with high accuracy (up to 1 %) and with very good time resolution (up to 200 ps). The associated thermodynamic variables-of-state - in particular the ablation pressure - can be determined by means of the Hugoniot equations which provide the necessary thermodynamic-kinematic relationship.[4] Of particular importance is the Hugoniot equation $p = p(u_p)$ which links the pressure state p of matter to its particle or mass velocity u_p.

Although the Hugoniot relations rely on the propagation of discontinuous pressure waves (shock waves), the Hugoniot equations can be equally applied to the case of ablation pressure waves with finite wave fronts, $p_{abl}(t)$, as long as the pressure amplitudes are not excessively high or the matter is not excessively compressed. This precondition is fulfilled for metal targets up to the 1 Mbar range. (The compression of matter - starting from the initial density 100% - in that case reaches levels of up to about 140%.)

The searched ablation pressure profile $p_{abl}(t)$ can be determined in principle from a time resolved measurement of the particle velocity $u_p(t)$ in the range of pressures up to 1 Mbar and above provided that a target material with known Hugoniot equation is used. However, such a thin target has to be used in the measurement that the pressure wave $p_{abl}(t)$ does not noticeably change (steepen) on its propagation path to the rear target surface where the kinematic measuring quantity $u_p(t)$ is diagnosed. This means that the non-ablated condensed target layer should be only a few μm thick. However, in such a thin layer of matter the pressure front is reflected several times back and forth during the duration of the ion beam pulse. (For illustration: The mean sound velocity u_s of the ablation pressure front, e.g. in an Al -target, is about 7 km/s or 7 μm/ns, respectively.) The back-and-forth reflected waves superimpose the original ablation pressure pulse and cause changes in the velocity profile $u_p(t)$ of the target surface.

It has been possible to avoid this fundamental problem by the following trick: The thin ablation target is tamped with a thick layer of matter which has the same Hugoniot equation of state as the thin target. Such a substance which, in addition, is optically homogeneous and transparent to the light beam of the laser-Doppler interferometer up to sufficiently high pressure states allows the particle velocity profile in a thin ablation target to be measured without producing disturbing reflections at the rear target surface. Then the searched ablation pressure pulse $p_{abl}(t)$ is obtained directly and unfalsified from the measured $u_p(t)$ profile.

Such a material combination free from pressure wave reflection at its interface actually exists - e.g. with aluminum as the ablation target and an LiF crystal as the window. In ablation experiments performed at KALIF 25 μm thick plane Al-targets were used; in these experiments the non-ablated Al-material layer was only some few μm thick. The thin ablation targets were in mechanical contact with a thick LiF monocrystal (about 5 mm in thickness). With the target taylored in this manner and with the KALIF-ORVIS velocity interferometer it was possible for the first time to determine - quantitatively and time-resolved - the ablation pressure $p_{abl}(t)$ which is generated by a high intensity ion beam pulse in solid state matter. The proof-of-principle experiments were performed with proton beam pulses of 0.15 TW/cm^2 power density using the B_Θ-extraction diode.[5]

Fig. 1 shows an example of these first quantitative ablation pressure measurements. The extremely fast rise of the ablation pressure wave $p_{abl}(t)$ is real (and not caused by steepening of the pressure wave on its path to the rear target surface). The recorded steep pressure front is rather a result of beam bunching along the 15 cm long flight path to the target. The deposition of the steep beam front causes the pressure to rise at an extremely fast rate. At 25 GPa (0.25 Mbar) a pressure drop occurs when the beam-heated target layer expands (i.e., ablates) or, in the language of shock wave physics, when the first rarefaction wave has passed through the ablation layer and reaches the condensed target matter. After this "rarefaction dip" the beam power density . The ablation pressure in the target matter increases again, attains its maximum at 28 GPa (0.28 Mbar) and subsequently decreases - on account of decreasing beam power and expansion of the ablated matter. Thus, the measured ablation pressure profile comprises both the temporal profile of the incident power density and the hydrodynamic reaction of the target matter.

The ablation pressure maximum measured in these experiments, i.e. 0.3 Mbar in Al at 0.15 TW/cm^2 of incident beam power density, approximately resembles the theoretical prediction. It has not been possible initially to verify the measured temporal pressure profile by computer simulation of the experiment [10], the reason probably being that two essential input parameters have to be known more accurately: the ion beam current density on target (focus current density) and - a theoretical problem - the equation of state of the hot and dense ablation plasma. On the other hand, the KALIF-ORVIS experiments have verified that the time-resolved diagnostics of the dynamic target response provides a new and sensitive diagnostics tool for the ion beam voltage wave form (stopping range) and the focus current density (power density) with time, - in particular for diagnosing details of the ion beam front and the rising part of the beam pulse[6]. - The ablation pressure wave compresses the condensed target matter far above its "elastic limit". The condensed target layer becomes a thin fluid layer. In ablation experiments with thicker targets it was even possible to measure the fluidity (viscosity) of the target matter. In targets of 0.1 - 0.2 mm thickness the 0.3 Mbar ablation pressure wave steepened and developed into a perfect shock wave. The time resolution of the KALIF-ORVIS system proved to be so good that the finite thickness of the steep shock front could be measured: its duration was 600 ps. Using a theoretical model of elastic-plastic material behavior[7], the viscosity of the target fluid was estimated to be 80 Poise. This result can be illustrated as follows: The Al-target matter compressed by the ablation pressure wave of several 100 kbar is as "liquid" as glycerol under normal conditions.

There is ongoing preparatory work to ablation pressure measurements at KALIF with beam power densities up to 1 TW/cm^2 and deposited power densities up to 150 TW/g, respectively - using the applied B-extraction diode as the axial proton beam source.

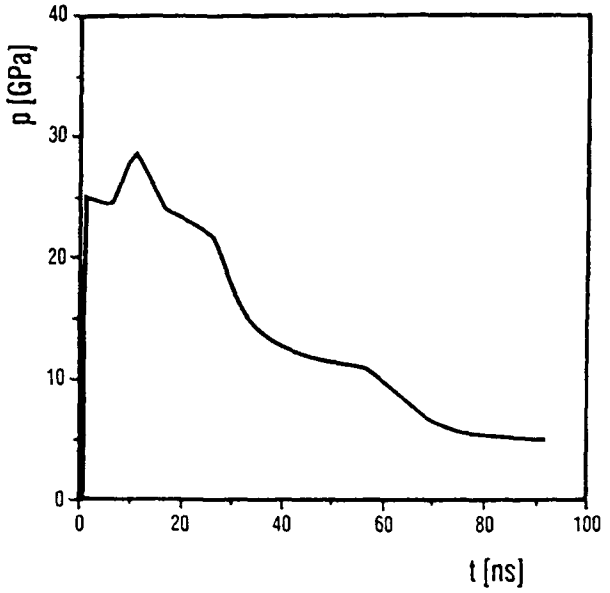

Fig. 1 Ablation pressure profile evaluated from KALIF-ORVIS recordings

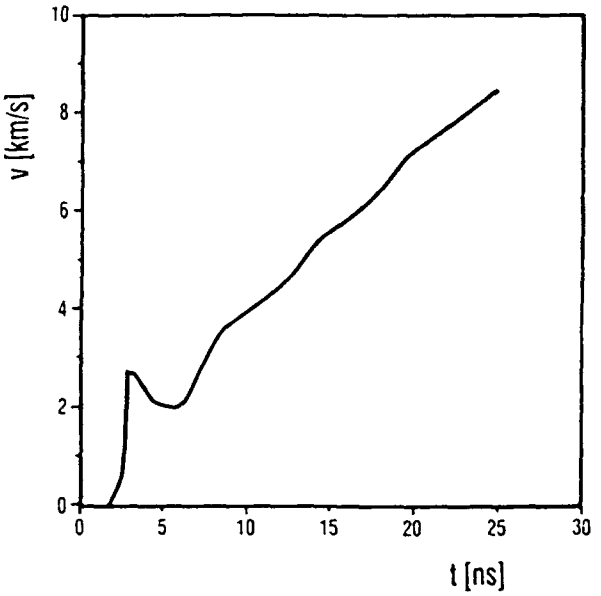

Fig. 2 Velocity profile of flyer foil measured with KALIF-ORVIS

Ablative acceleration of matter up to hypervelocities

In the KALIF ablation experiments described above the thin ablation targets were tamped with a massy layer of window material. No significant acceleration of the entire target can occur. The target dynamics undergoes dramatic changes when self-supporting thin ablation targets are used. Fig.2 shows as an example the ablative acceleration of a plane 15 μm-thick Al-foil of about 8 mm diameter which was accelerated by ablation using a proton beam of 0.15 W/cm^2 power density. (The total thickness of the Al target inclusive of the ablated layer of matter was 33 μm. The resulting acceleration and velocity profile is characterised, on the one hand, by the ablation pressure pulse $p_{abl}(t)$ acting on the target (see Fig. 1; note the different time scales) and, on the other hand, by the pressure and expansion waves moving back and forth in the thin target. The extremely fast acceleration at the beginning, within 1 ns, is caused by the steep front of the ablation pressure pulse. Also the "rarefaction dip" is reflected in the velocity profile and the subsequent pressure rise up to its maximum after about 10 ns. Thereafter, the accelerated ablation pressure decreases and a reflection pattern can be seen in the velocity profile. The limit velocity attained after 70 ns was 12.6 km/s (not seen in the ORVIS recording interval represented). Achieving such an extreme acceleration of matter - more than 10^{11} g (!) - and such a high velocity of matter in a one-dimensional configuration means a record which is of fundamental importance in matter research.

Hypervelocities of matter above 20 km/s can be anticipated at KALIF by means of one-dimensional ablative foil acceleration applying the proton beam of the applied B-extraction diode with 1 TW/cm^2 power density and 50 kJ pulse energy as the driver. (The relevant experiments are being prepared.) It is a fundamental question to which extent the thin target foils remain stable and plane in fluid dynamics terms at the extreme acceleration levels. In this context also the question of possible beam filamentations arises. In order to answer these questions it is envisaged to extend the KALIF-ORVIS diagnostic system for observing the target kinematics simultaneously in several neighbouring measuring points.

Impact experiments with flyer foils accelerated by ablation

The acceleration of matter to extremely high velocities is of paramount importance in dynamic matter research. If one makes a plate moving at high velocity - in terms of shock wave physics a flyer plate - hit a target at rest, a much higher dynamic pressure state is generated in the shocked matter than is achieved directly by ablation or by other dynamic drivers.

Pressure multiplication under the flyer plate principle is illustrated in Fig.3: If a layer of Al-matter accelerated to the limit velocity u_G hits a W-target at rest, a pressure state p_3 is generated in the zone of impact of the two layers of matter which exceeds by a multiple the ablation pressure level p_1 at which the Al-flyer plate was previously accelerated. The pressure state which can be attained by this type of pressure multiplication is limited solely by the final velocity u_G of the flyer plate prior to the impact. If the flyer plate and the target are made of the same material - as in case of the Al-on-Al impact - the relevant Hugoniot diagram is mirror symmetric; consequently, the mass velocity after the impact is $u_2 = 1/2\ u_G$; the pressure state of the shocked Al is p_2. - The duration of the dynamic pressure state generated in an impact experiment equals twice the travel time of the shock wave through the impactor. Within this short time span the variables-of-state of matter must be recorded using suitable short-time diagnostics.

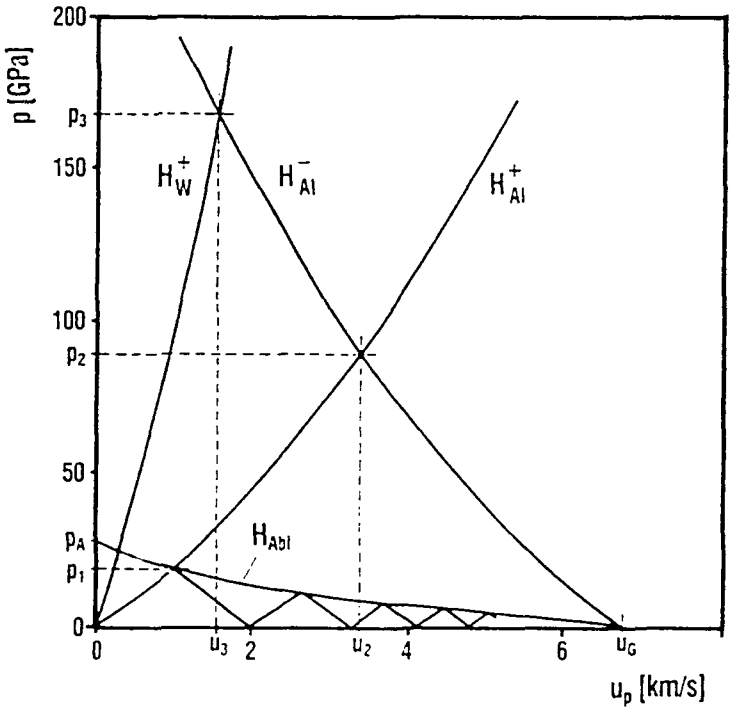

Fig. 3
Generation of very high pressure states by impact of a "flyer plate" with a target.

It has been demonstrated in basic experiments performed at KALIF and diagnosed with KALIF-ORVIS that maximum pressure states can be generated in matter using extremely thin flyer foils accelerated by ion beam ablation. To give an example: Aluminum foils of about 30 μm thickness (initial thickness 50 μm) and about 8 mm diameter were accelerated to approx. 6.5 km/s using a proton beam pulse of 0.2 TW/cm^2 power density; at the end of an acceleration and flight path of 230 μm length this foil hit a 30 μm thick tungsten target. The KALIF-ORVIS laser interferometer recorded the surface velocity of the W-target. The evaluated impact pressure of the target material was 1.68 Mbar. The thinnest Al foils (15 μm after ablation) accelerated by 0.2 TW/cm^2 beam power attained the final velocity u_G = 12.6 km/s and hence in impact experiments with W-targets pressure states of almost 5 Mbar have been generated!

In the target experiments presently prepared using the KALIF applied B-extraction diode it is envisaged to achieve hypervelocities of plane target foils of 20 km/s. If the target fluid layer remains stable during its ablative acceleration in terms of fluid dynamics, it should be possible to attain impact pressure states of 10 Mbar and above. The energy density of the shocked matter will attain > 10^4 J/g; the compression of matter attains a multiple of its solid state density and the thermodynamic state of matter is above its critical state. This range of states in which matter constitutes a high density "metallic" plasma is only imperfectly understood in theory and has almost been inaccessible in experiments by the methods of research into matter previously available[8]. In this extreme range the thermodynamic equation-of-the state (EOS) of matter is mostly unknown. For determining the unknown EOS of a target material in the multi-Mbar range two kinematic variables-of-state have to be measured in the experiments. In case of optically transparent target matter we succeeded in measuring in one single experiment both the velocity of the flyer foil prior to impact (u_G) and the velocity of the shocked matter (u_p). It was possible - actually for the first time in flyer plate experiments - to measure by interferometry also the velocity of the shock wave (u_s). In that experiment the impact target consisted of plexiglass which had been "shocked" to more than 1 Mbar by the impacting foil.

Measurement of the Dynamic Tensile Strength of Matter

In the experiments with thin targets described above the wave train of the compressive pressure wave propagating through the target matter is longer than the target thickness. In the opposite case of thick targets the dynamics changes. If under these conditions the compressive pressure front reaches the rear free target surface, the rarefaction wave traveling behind the pressure plateau superimposes within the target the release wave returning from the rear side of the target. Superposition of the two oppositely moving rarefaction waves generates dynamic tensile stresses in matter; the related deformation rate (strain rate) of matter is determined by the height and width of the original compressive pressure wave.

If the tensile stress exceeds the inner tensile strength of the target material, matter gets "spalled" at the respective point. The tensile strength of matter undergoing dynamic tensile stresses - as a function of the strain rate - is an important topic in dynamic matter research and in materials science. According to theoretical considerations the dynamic tensile strength

of matter gradually increases with increasing deformation rate - starting from its static value - and, ultimately, reaches the theoretical limit of material strength as defined in atomistic and solid state physics theories, respectively.

In case of one-dimensional dynamic strain the strain rate is defined as $(\Delta x/x_0)/\Delta t$ (dimension: s^{-1}). Previous measurements of the dynamic tensile strength of condensed matter have been possible only up to maximum strain rates of 10^{-6} s^{-1}. In ablation experiments and in flyer foil experiments, respectively, carried out with pulsed proton beams at KALIF, spalling of matter at one-dimensional strain rates up to 10^{8} s^{-1} has been generated and the dynamic tensile strength of matter has been measured (see paper #PB-43 of this conference[9]). In the ongoing experiments at KALIF various materials of interest are being studied: single crystals and polycrystalline samples of metallic and non-metallic materials like Mo, Nb, sapphire, etc.

Résumé

The beam-target experiments described above originally have been undertaken to measure the ablation pressure generated by pulsed high-power light-ion beams in solid target matter. Investigation of the dynamic target response has been the diagnostic approach to reach this goal. In addition, the target response experiments are giving diagnostic access to relevant parameters and properties of the ion beam like beam front profile, stopping range, deposited power and current density, lateral beam profile, etc.

Wave form details to be studied:	Material properties to be derived:
elastic precursor	dynamic yield stress
plastic wave rise time	viscosity at highest strain rates
phase transition	pressure and kinetics of phase transition
elastic unloading	sound velocities and elastic modules
reverse phase transition	pressure and kinetics of reverse phase transition
spall pulse	dynamic tensile strength

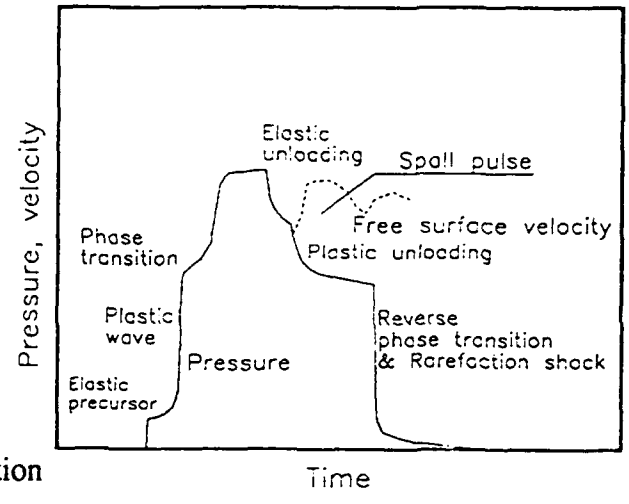

Fig. 4 Capability of material response experiments which can be performed with KALIF-ORVIS

Beyond, these proof-of-principle experiments have verified that today's pulsed light-ion beams with their high pulse energies are a new and powerful tool in dynamic matter research. By applying advanced diagnostics to the dynamic response of target matter, new and challenging research problems can be addressed now: the equations-of-state (EOS) and thermo-radiational properties of matter in a wide range of temperatures and pressures (T up to 1 MegaKelvin, p up to 10 Megabars and above), including the critical point of the elements. This wide range of thermodynamic states is not accessible at present by other laboratory techniques relying on quantitative measuring methods. In addition, mechanical properties, phase transformations, and chemical transitions of materials can be studied under conditions characterised by fastest deformations and shortest loadings. Fig. 4 summarizes the capability of target response experiments which can be performed with a high-power light-ion pulse generator as the loading driver.

Acknowledgement

The described beam-target experiments have been possible only by the excellent work done by the KALIF operation team under W. Ratajczak.
The authors would like to express their special thanks to Academician Prof. Vladimir Fortov, Moscow, for major stimulations to apply high-intensity particle beams in the field of dynamic matter research.
The German Federal Ministry for Research and Technology and the Russian Ministry for Education and Science have supported financially research stays of scientists participating in these experiments.

References

[1] H. Bluhm, P. Hoppé, H. Bachmann, W. Bauer, K. Baumung, L. Buth, H.U. Karow, H. Laqua, D. Rusch, E. Stein, O. Stoltz, BEAMS'92 - 9th Int. Conf. on High-Power Particle Beams, Washington DC, May 1992. Invited Paper no. OA-3.

[2] D.D.Bloomquist, S.A.Sheffield, J. Appl. Phys. 54, 1717 (1983)

[3] W. Bauer, K. Baumung, H.J. Bluhm, H.U. Karow, KfK Nachrichten 24/1, 19 (1992)

[4] R. Courant, K.O. Friedrich, Supersonic Flow and Shock Waves, Heidelberg (1976), ISBN 0-387-90232-5
L.D. Landau, E.M. Lifschitz, Lehrbuch der theoretischen Physik, Band 6, Hydrodynamik, Berlin (1966)

[5] W.Bauer, H.Bachmann, H.Bluhm, L.Buth, P.Hoppé, H.U.Karow, H.Lotz, D.Rusch, Ch.Schultheiß, E.Stein, O.Stoltz, Th.Westermann, BEAMS'92 - 9th Int. Conf. on High-Power Particle Beams, Washington DC, May 1992. Contrib. Paper no. PB-01.

[6] K. Baumung, G.I. Kanel, H.U. Karow, D. Rusch, V. Licht, A. Utkin, to be submitted to Laser and Particle Beams

[7] J.W.Swegle, D.E.Grady, J.Appl.Phys. 58, 692 (1985)

[8] G.A. Mesyats, V.E. Fortov, Phys. Bl. 46/10, 383 (1990)
V. Fortov, Thermophysical Properties of Hot Dense Plasmas, Stuttgart (1991), ISBN 3-8154-3010-0

[9] H. Bachmann, K. Baumung, G.I. Kanel, H.U. Karow, V. Licht, D. Rusch, J. Singer, O. Stoltz, BEAMS'92 - 9th Int. Conf. on High-Power Particle Beams, Washington DC, May 1992. Contrib. Paper no. PB-43

Multistage Ion Accelerator for Inertial Fusion Energy

K. IMASAKI and C. YAMANAKA[1],
1) Institute for Laser Technology, 2-6 Yamada-oka, Suita, Osaka.
S. MIYAMOTO, K. YASUIKE, N. SHIRAI, S. NAKAI[2],
2) Institute of Laser Engineering, Osaka University, 2-6 Yamadaoka, Suita, Osaka.
T. AOKI[3],
3) Tokyo Institute of Technology, Nagatsuta, Midoriku, Yokohama.
S. KAWATA[4].
4) Nagaoka University of Technology, Nagaoka, Ni-igata, Japan

Abstract

Recent results of two stage diode experiment are on Reiden-SHVS reviewed. Instability of the ion beam current and the stabilization, evidence of charge stripping and anomalous emittance reduction are discussed. The feasibility of this scheme for commercial reactor driver is briefly noted.

1. Introduction

An important milestone of the inertial fusion energy research is to achieve the ignition and high gain, which will be realized by the high power laser such as NOVA or/and GEKKO or particle beam machine as PBFA in the decade. The next milestone is to develop the reactor driver with a sufficient efficiency, a low cost, a long life and a high repetition. Then the ignition driver might not meet the requirements of the driver for commercial reactor.

From this point of view, LD pumped solid state laser and heavy ion beams have been proposed and discussed their feasibility. Super high voltage source (SHVS) based on the pulsed power technology shown in Fig. 1 has been also proposed for the candidate of the reactor driver.[1]

Characteristics of the SHVS are as follows. 1) Voltage of tens MeV per stage can be generated by adding the inductive voltage of each unit with magnetic insulation. Although the voltage in each unit will be less than 1MeV. So the conventional pulsed power technology will be applicable.[2] 2) The waveform of the voltage can be shaped to the bunching of the ion beam by controlling the voltage waveform of each unit.[2] 3) Heavier ion such as C, Na and

so on can be accelerated to the required energy sufficiently. Especially, using the charge stripping, the acceleration gradient will be taken very high, which implies the compact and lower cost of the driver.[3] This will be an essential advantage for the reactor driven comparing with others.

In this paper, we review the recent results of two stage diode on Reiden SHVS and discuss the feasibility for the reactor driver.

2. Study on two stage diode

2.1 Experiments on Reiden-SHVS

Figure 2 shows a schematic diagram of two stage ion diode with charge stripping.[4] The energetic ions accelerated at the first diode are injected into the second diode through a charge stripping thin foil. The injected ions are stripped to higher charge state which are determined by the energy obtained in the first stage and are accelerated in the second diode efficiently.

The potential distribution in the ion beam injected diode is different from the conventional diode with a stationary anode plasma ion source. Figure 3 shows the potential profiles in the ion beam injected diode. Energetic ions are injected from left side. Figure 3(a) shows a potential profile for simple Child-Langmiur space charge limited current.

The analogy of the electron tube analyses shows the existence of three specific current densities, J_{10}, J_{20} and J_{r0} for a gap with a potential deference V_2, fixed width d_2, and an injected beam energy ZeV_1.[5] J_{10} is the current density when its space charge becomes to form an electric field which deccelerates the beam in the accelerating gap. (Fig. 3(b)) J_{20} is the maximum steady-state current that can be transmitted through the second diode gap. (Fig. 3(c)) J_{r0} is the transmittable current density through the second diode with the maximum virtual anode potential. (Fig. 3(d)) These critical currents are calculated by a monopolar steady-state analyses.

The ion beam of $J < J_{10}$ generates the electric field that tends to extract the ion beam from the injection side of the second stage diode. In this condition, a significant portion of the accelerated beam will be extracted from this surface. This suggests to operate the diode with $J > J_{10}$ to avoid accelerating the undesirable ions generated from the anode electrode of second stage. The ion beam of $J > J_{20}$ induces the space charge instability[6], which make the virtual anode potential and its position oscillation. A part of ions is reflected back to the injection side.

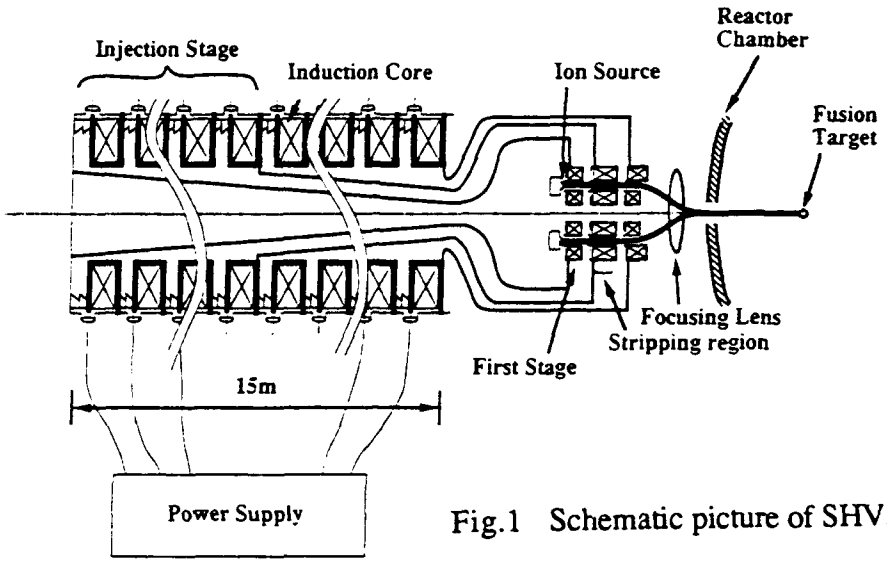

Fig.1 Schematic picture of SHVS

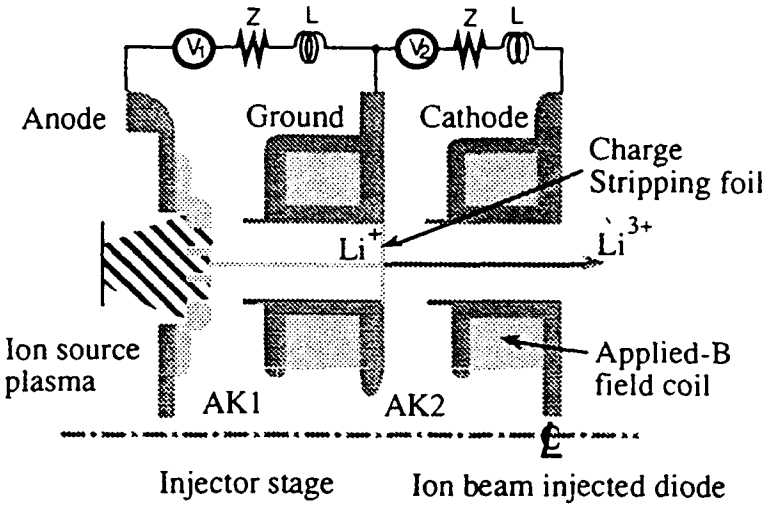

Fig.2 Schematic picture of two stage diode with charge stripping foil

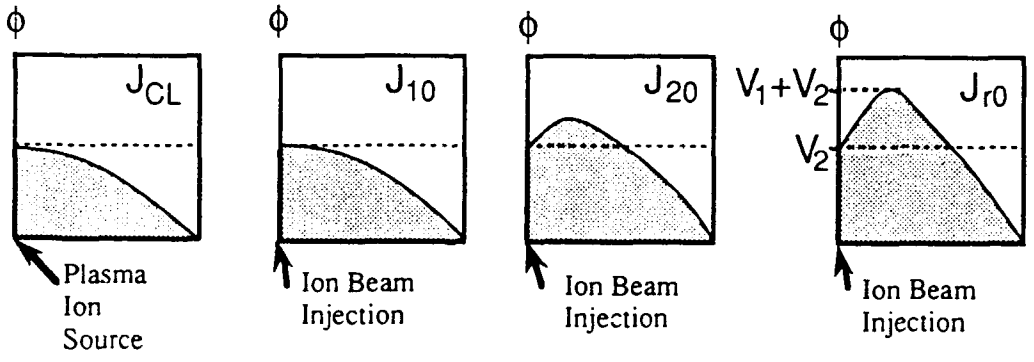

Fig.3 Potential profile of the ion beam injected diode

The ions generated from the stripping foil degrade the beam purity. The virtual anode works also to avoid the undesirable ions accelerated from the stripping foil. We denote this effect as a virtual anode filter. Then the desirable operation regime is $J_1 < J < J_2$.

Experiments have been performed on Reiden-SHVS induction adder accelerator.[7] Figure 4 shows a configuration of the induction adder section of Reiden-SHVS. It consists of eight induction adder unit. Reiden-SHVS has a capability to provide 4~6MV, 40kA, 100ns pulse to the single diode or to the two stage diodes. Positive and negative center electrodes are extended from both side. The typical operation voltages and currents of each diode were 0.5 MV, 20kA, in the carbon beam experiments and 1MV, 30kA in the proton beam experiments. The diodes are located at the center of the machine. The ground electrode connects the cathode of first diode and an anode of second diode. Each diodes are powered by four induction cavities.

The anode electrode of first stage diode is made of aluminum to exclude the insulation magnetic field. Two types of ion sources, a carbon flashboard plasma injection source located behind the anode and a pallafin grooves anode, are used. Paraffin groove anodes are used to generate the proton beams in the experiments to measure the beam trajectories and divergences. The outer and inner radius of active anode area 8 cm and 5.7 cm, respectively, The beam cross section is $100cm^2$. The diode gap and insulation field are d_1=0.9 cm and B_1=7kG in first diode. In second diode, $d_2(B_2)$ is from 0.83 cm (9kG) to 3.5 cm (6kG). Diode currents are measured by B-dot probes. Ion current densities are measured by biased charge collectors behind the second stage diode. Beam trajectories and divergences are measured by shadow boxes which have 5×3 pinhole arrays and are located just behind the cathode of each diode.

Figure 5 shows measured B-dot signals of the first stage diode and it Fourier spectrum. Shot #C107 is a reference shot which is operated without applied B-field and shows no oscillation on the signal. The oscillations on the B-dot signals of the first diode is caused by a space charge instabilities in the second stage diode through reflected ions from the large oscillating virtual anode. Data plot on V1/Vc vs. V2/Vc chart shows the shot #C114 and #C145 are in the unstable region. The oscillation frequency and its dependence on the AK gap of the second diode are in agreement with the predictions from the electron beam simulation.[6] By decreasing the AK gap of the second diode, the stable operation is achieved (shot #C119).

Charge stripping diodes are tested using carbon flash-board ion sources. Thomson parabola traces are shown in Fig. 6. The AK gap of second diode is 3.3cm. Former foil of approximately 0.1μm thickness is used as a stripping foil. Without stripping foil, the maximum energy of C^+ and C^{2+} ions are same value of about 1.1 MeV. An increment of higher ion energy component are observed obviously in the results obtained by the diode with

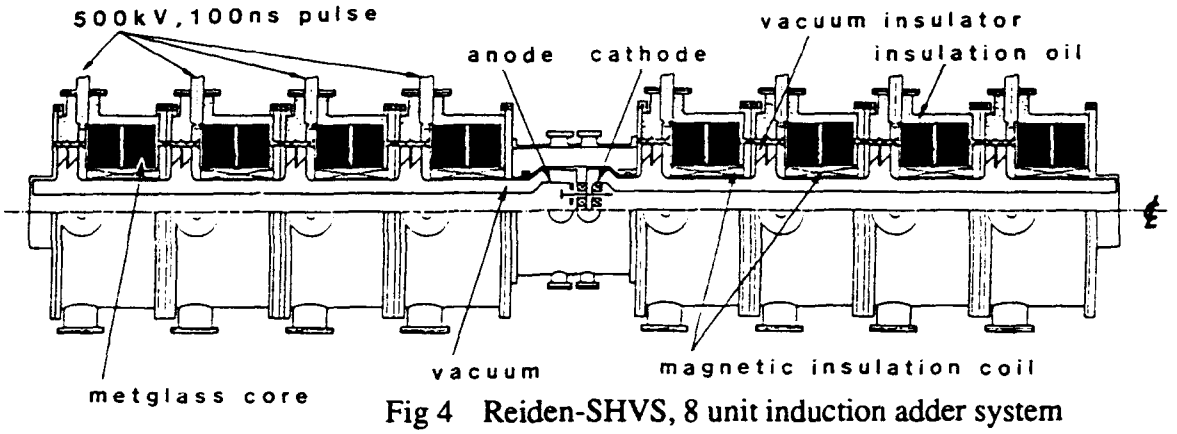

Fig 4 Reiden-SHVS, 8 unit induction adder system

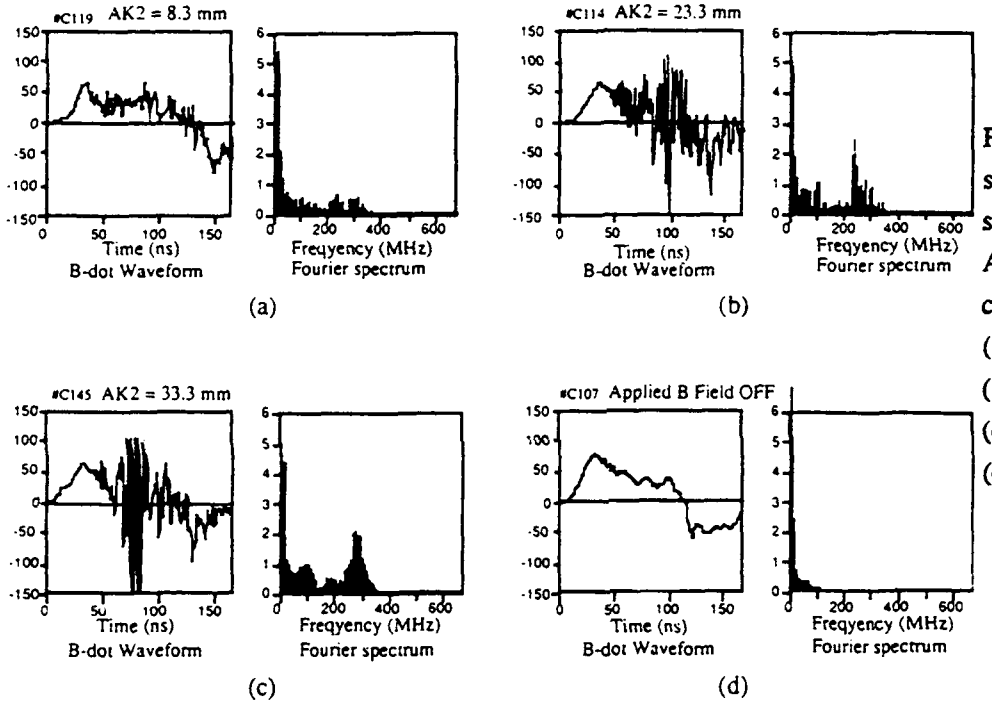

Fig.5 B-dot probe signal and its Fourier spectrum for various A-K gaps and diode condition.
(a) d_2=0.83cm
(b) d_2=2.33cm
(c) d_2=3.33cm
(d) no applied B field

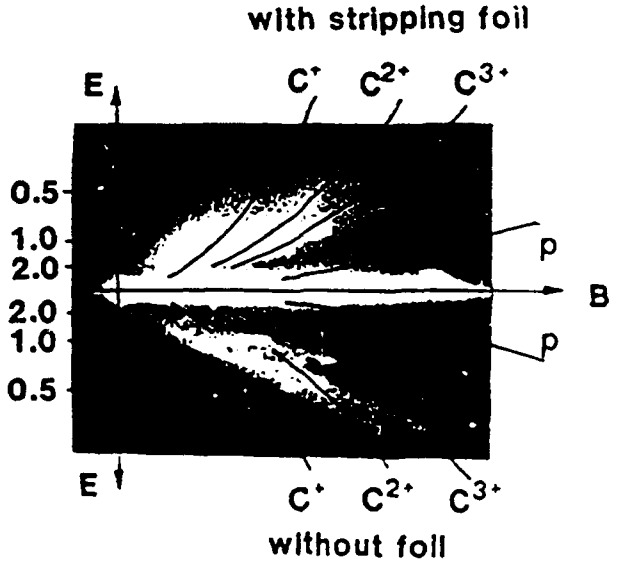

Fig. 6 Thomson parabola traces of the ion beam, with (a) and without (b) the charge stripping foils

stripping foil. The charge state equilibration of ions passing through a stripping foil is calculated from the charge stripping and the charge recombination cross section. The carbon ions C^+ and C^{2+} are stripped (or partially recombined) after acceleration at the first stage diode (V1 =0.6MV) and subsequently the acceleration energy are multiplied by the charge state times of the voltage of second diode (V2 = 0.5MV). The maximum energy edge of each ion parabola traces are in agreement with the calculation. The lower energy part of ions (<0.5 MeV) in stripping foil case are less than the case without stripping foil. This indicates a virtual anode filtering effect.

Beam divergence and trajectories are measured using paraffin filled grooves anode. Figure 7 shows ion damages in shadow boxes. (a) and (b) are obtained in the same shot. The spreads of damages in azimuthal direction are caused by the sum of a beam divergence and a magnetic deflection The parameters in this shot are as follows, the transmitted ion current density of 60 A/cm^2 with first and second stage diode voltage of 0.6MV and 1.2MV, respectively. The second diode gap is 10mm in the case of (a), (b), and 35mm in the case of (c). The instability is induced only in the case (c).

Decreases of the damage size at second stage diode indicates large improvement of beam divergence by the second acceleration. Figure 8 shows the emittance plot of this shot, when the radical beam divergences are considered. The improvement of emittance is better than the value predicted from the conservation of normalized beam emittance as,

$$\varepsilon_1 / \varepsilon_2 = 3.5 > \gamma_2\beta_2 / \gamma_1\beta_1 = 2.2$$

Emittance of the first stage diode may be strongly influenced by the nonuniformity of anode ion source which is implied from the nonuniform damage of paraffin filled grooves anode. Two-stage diode may have an effect like an emittance filter and a beam smoothing.

In case (c), the ion damages are divided into two parts. Small humps are observed at upper left side of the damages. Beam trajectory calculations indicate that this ion damages may be due to reflected ions at large virtual anode in the second stage diode. Even in this unstably large virtual anode condition, the rest part of ion damages, this is due to the unreflected ions, are less affected by the virtual anode. This is interesting to use the virtual anode operation in second stage diode without a beam degradations or deflections.

2.2 Simulations of two stage diode

The simulations of the two stage diode is performed. The code is PIC 1.5D with a nonlinear circuit model for ion emission. The results corresponds quite well to the experiments

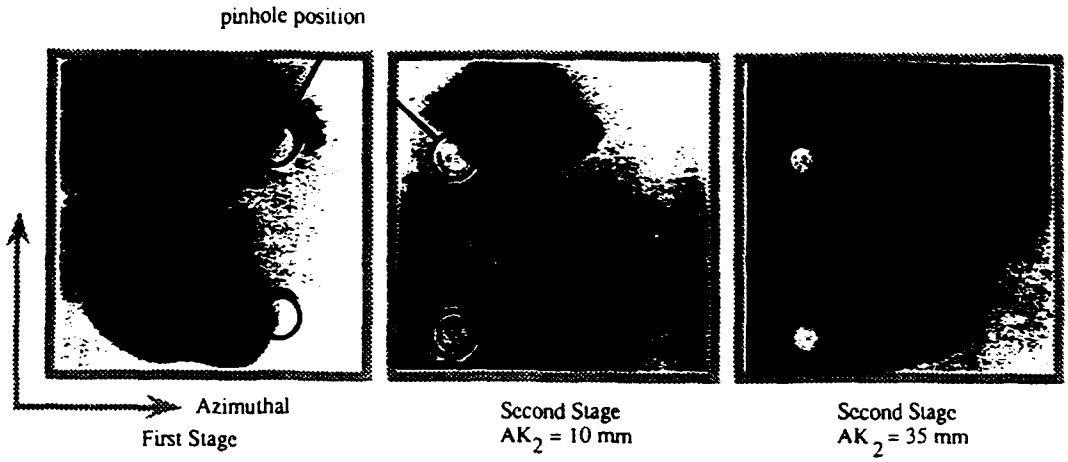

Fig. 7 Ion damages in the first (a) and second (b) stage at stable ion diode condition. (c) is the damage of untable condition

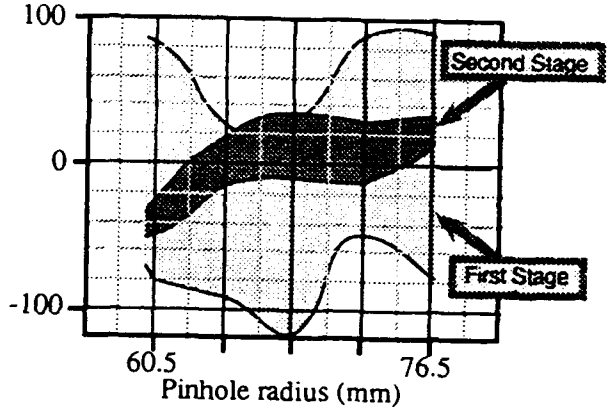

Fig. 8 Emittance plot of radial beam divergence in the first and second stage of two stage diode

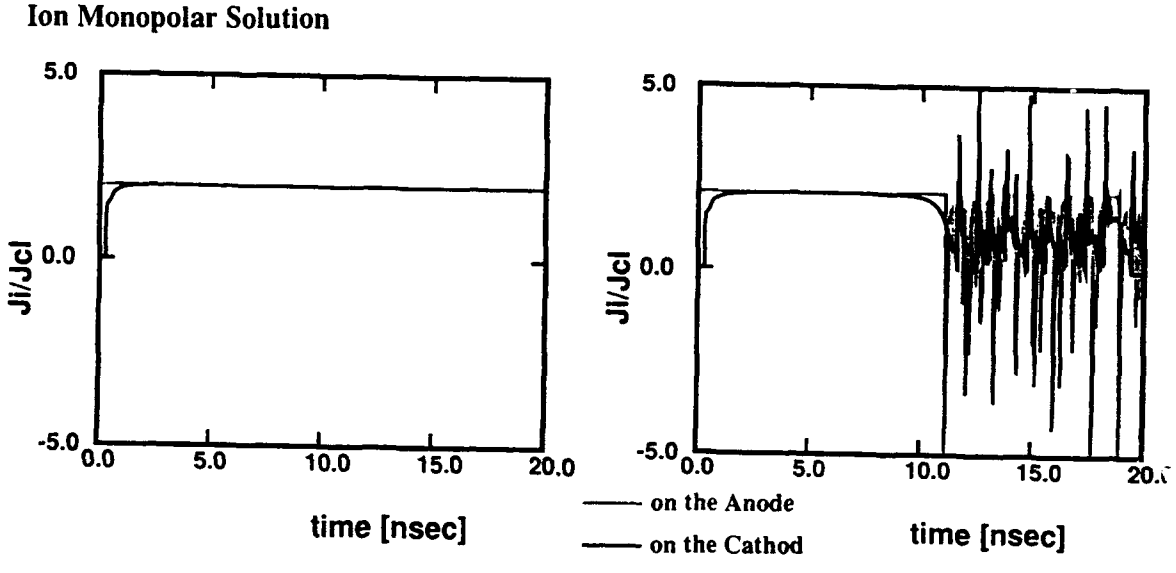

Fig. 9 Simulation of ion current density in ion ijected diode.
a) $J_i=1.0J_{10}$ b) $J_i=1.05J_{10}$

as shown in Fig. 9. The oscillation of the ion beam current in the simulation is observed when the $J_i < 2J_{10}$ which is observed in the experiment as shown in Fig. 5. The simulation code are now developing to include electron motion and sheath dynamics.

3. Prospects for IFE driver

The energy being required to compress and heat the fuel in general case is estimated by the sum of heating energy W_h (Joule) = $38.2M_{DTh}(mg)T_i(eV)$ and the pressure work to compress the fuel, which is derived from the perfect-degenerate gas equation of state. Here M_{DTh} is a part of fuel $M_{DT}(mg)$. This part is heated up to T_i and its radius is assumed to be 3 times of the radius at which a produced alpha particles stop. The pressure work is $W_p(Joule) = 114(k^{2/3})M_{DT}$, where k is the compression ratio. In our estimation ρ_R = 3g/cm^2, the implosion efficiency 5%, η_b = 20%, M=1.1, f_a = 0.1 and η_t=45%. Finally we obtain the relation between k and E_b, which is shown in Fig. 10. Figure 11 presents the pellet gain versus E_b. Figure 9 suggests us that there will be several implosion modes in IFE. In rather small size reactor-size pellet, the DT mass is about a few mg and the compression ratio is about 1000. On the other hand, in a huge pellet for example the DT mass is about 1000mg and the compression ratio is about 100, though the input energy is about 100(MJ).

One of the most important problems is to find a way to implode a fuel pellet in a spherically symmetric manner[8]. In the ion-beam-pellet implosion the ion beams introduce the nonuniformity of the physical quantities. The nonuniformity leads to the nonuniform implosion, the Rayleigh-Taylor(R-T) instability [9-12] and degrades the fusion energy output. In a reactor-size pellet the radiation is also important and can affect the growth of the R-T instability. In addition, the ion deposition layer is rather thick (usually several hundreds μm, although it depends on the particle energy and the material) and the peak of the pressure appears in a rather deep part of the deposition layer. Therefore the density valley is formed in the energy absorber. This cause the confinement of the radiation and the smoothing of the beam nonuniformity[13].

In general the beam nonuniformity introduces the source of perturbation including the nonuniformity of acceleration itself. In a reactor-size pellet the nonuniformity-smoothing effect of the radiation transportation is investigated by a 2-dimensional numerical simulation. The following valuable results are obtained by the analysis[13]. 1) The nonuniform acceleration field in space does not affect the growth rate(γ) of the R-T instability. However this nonuniformity of the acceleration can suppress the growth itself of the R-T instability, when the phase of R-T instability is different from that of the nonuniformity of the acceleration. 2) The

radiation can reduce the growth rate(γ). 3) The numerical simulation implies that the radiation can smooth out the nonuniformity introduced by the driver ion beam. For example, the initial nonuniformity of 6% is smoothed down to 0.07% during the implosion phase.

The conceptual diagram of the reactor system is shown in Fig.12. In this system, power flow can be described as

$$\eta_D G_t M \eta_g = \left(P_{out} + P_{reci} + P_a\right) / P_{reci}$$

Where η_D is the efficiency of energy driver. G_t is a target gain and is a function of the drivers energy. M is a multiplication factor of produced nuclear power in the reactor. When we use Li waterfall, M is to be 1.1 ~ 1.3. η_D is a conversion efficiency. Pout is an output power of the electricity of the power plant. Preci is a recirculating power to operate the energy driver. Pa is an auxiliary power to run the reactor system. Here, we assume Prec << Pa.

The cost of electricity Γ per MWeh in this system can be written as

$$\Gamma = \left\{ \left[A\varepsilon_b R_{rep}^{1/2} + B\left(\eta_g \varepsilon_b M G_t R_{rep}\right)^{1/3} \right] \left(f R_{op} \tau \cdot 365 \cdot 24\right)^{-1} + 3600 R_{rep} C \varepsilon_b^{1/3} \right\} \left[\eta_g \varepsilon_b R_{rep} M G \left(1 - \frac{1}{G_t \eta_D \eta_g} \right) \right]^{-1}$$

A is drivers system cost per $MJHz^{1/2}$, ε_b is a ion beam energy in MJ. B is a reactor system cost per $(MWe)^{1/3}$. C is the cost of a target per $MJ^{1/3}$ which includes the initial cost of the target fabrication factory, the fuel cost and the fabrication cost. Here we estimate the cost of the driver system and the reactor system increase with $\varepsilon_L R_{rep}^{1/2}$ and $(\eta_g \varepsilon_L M G_t R_{rep})^{1/3}$, respectively. R_{rep} is a repetition rate of the energy driver. f is a fraction of a capital cost in the electricity cost. Rop is an average operational rate in the plant life time τ (year).

Figure 13 shows a relation between Γ and ε_b for several cases listed in Tab.1. The gain is estimated by the gain curve[14]. We choose $\eta_D \approx$ 0.3 to 0.1. A and C are estimated from update technology. B is estimated from the cost of nuclear power plant system.

The results show that we need high repetition rate, low cost, high efficient and long life driver. Cheap target is also strongly required. The cost of the driver is restricted to be less than 2×10^4 yen/J, which can be found out from Fig. 13. The cost of P-SHVS is 3×10^4 yen/J. It will not be difficult to overcome the cost restriction by this driver, and this is the most important point in the commercial case. The efficiency of 30% will be also not so difficult to achieve in

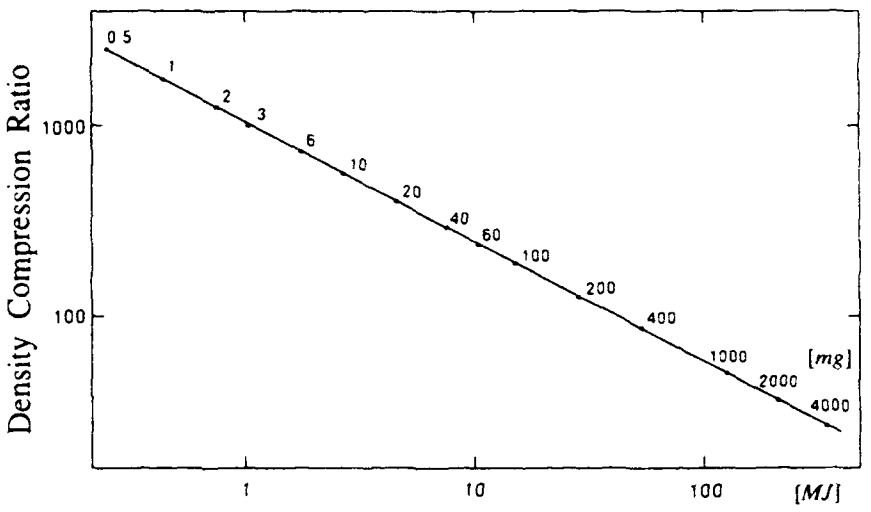

Fig. 10 Density compression ratio to input energy

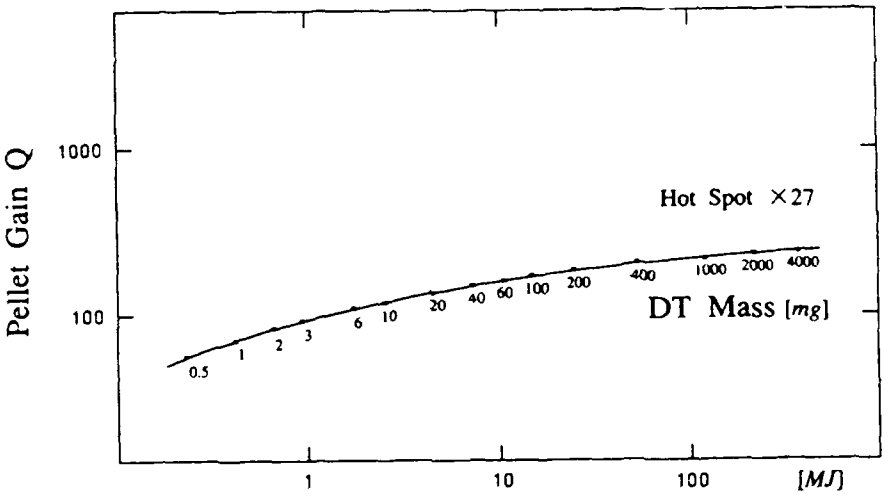

Fig. 11 Target gain to input energy

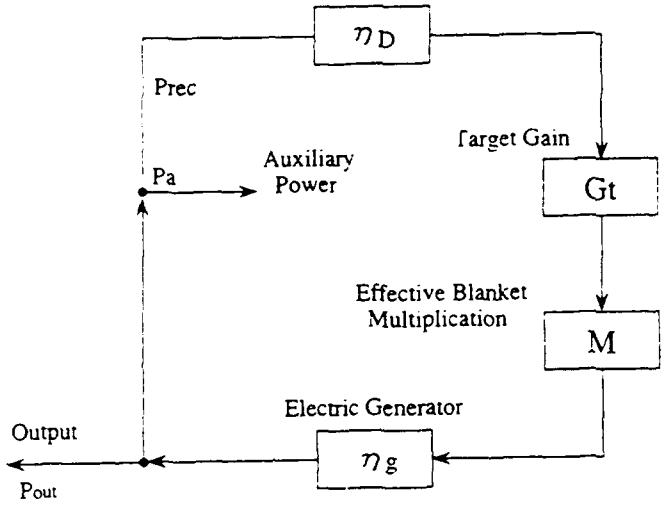

Fig. 12 Schematic diagram of energy flow in IFE reactor

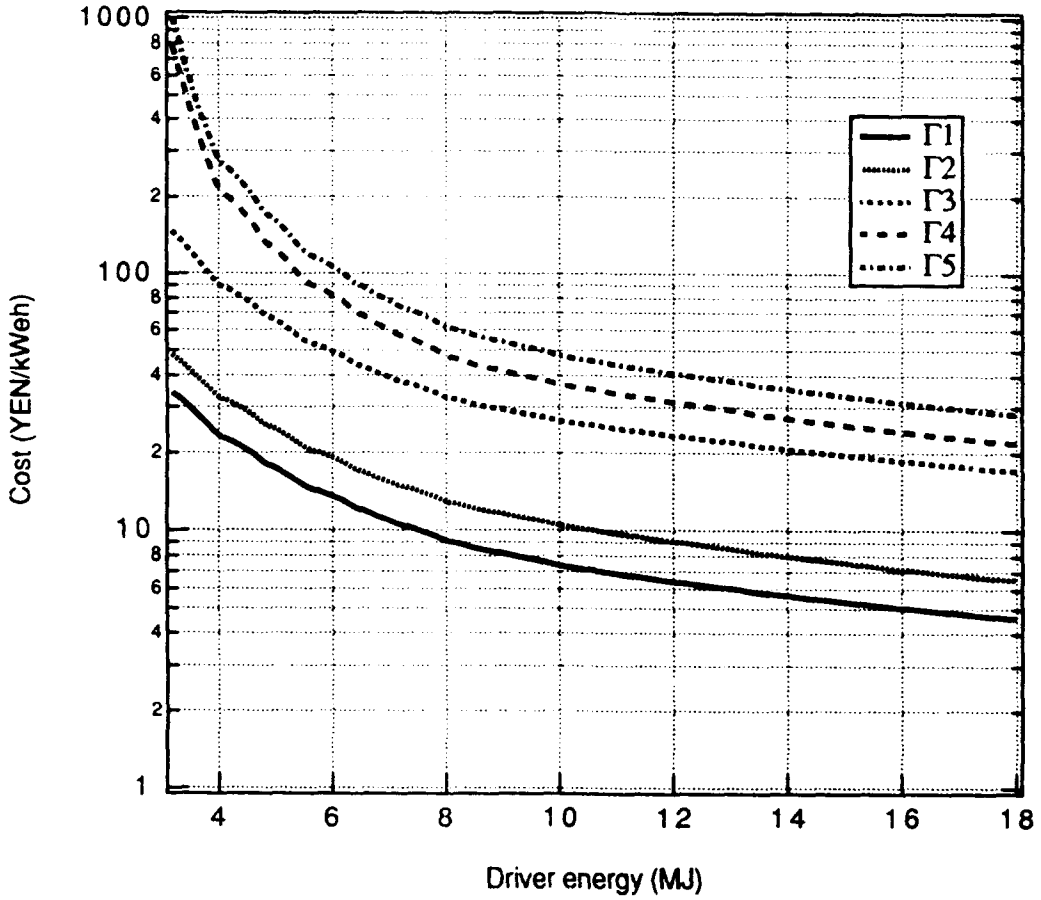

Fig. 13 Relation of electric power cost to driver energy for various parameters indicated in Tab. 1

Tab. 1 Parameters for IFE reactor

case	A	B	C	R_{rep}	η_g	η_D
1	2×10^{10} yen	3×10^{10} yen	50 yen	10 Hz	0.4	0.3
2	2×10^{10} yen	3×10^{10} yen	50 yen	5 Hz	0.4	0.3
3	5×10^{10} yen	3×10^{10} yen	100 yen	5 Hz	0.3	0.2
4	5×10^{10} yen	5×10^{10} yen	100 yen	5 Hz	0.3	0.2
5	5×10^{10} yen	5×10^{10} yen	100 yen	5 Hz	0.3	0.1
R_{op}=0.7 f=0.3 t=20years M=1.2						
Convervative Gain Curve to Driver Energy						

this scheme. Comparing with the other driver, this system is very compact, which will be an additional advantages of the location of the power plant.

The important issues are beam focusing and transport in the reactor chambers. The more investigations are required to these in the next step theoretically and experimentally.

4. Summary

Experiments have been performed on the induction adder accelerator "Reiden-SHVS". The ion beam current oscillation due to the space charge instability is observed and is studied to stabilize. A charge stripping is demonstrated to obtain higher acceleration gradient. The virtual anode filtering is observed, which makes the significant improvement of the emission.

Preliminary studies of the requirements of the IFE driver are performed. The SHVS will be able to meet the cost and efficiency requirement, which are the most important issues for the commercial reactor.

References

[1] IMASAKI, K. et al., J. Phys. Soc. Japan 51 (1988) 2233

[2] MIYAMOTO, S. et al., Laser & Particle Beams 7 (1989) 687

[3] MIYAMOTO, S. et al., IEE Japan EP-91-55 (1991)

[4] MIYAMOTO, S., Proc. 8th Int'l Conf. on High Power Particle beams, Novosibirsk, USSR, (1990)190.

[5] SLUTZ, S.A. et al., J. Appl. Phys. 67 (1990) 6705.

[6] BIRDSAL, C.K. et al., J. Appl. Phys. 3212 (1961) pp.2611-2618.

[7] AKIBA, T., et al., Nuclear Instrum. and Methods in Phys. Research A259 (1987)115.

[8] KAWATA, S. NIU, K., J. Phys. Soc. Japan 53 (1984) 3416

[9] ABE, T., NIU, K., Jpn. J. Appl. Phys. 20 (1981) 91

[10] TAKABE, H., et al, Phys. Fluids 28 (1985) 3676

[11] MUNRO, D. H., Phys. Rev. A38 (1988) 1433

[12] KAWATA, et al., Proc. of 8th Int'l. Conf. on High-Power Particle Beams, Novosibirsk, (1991)795

[13] KAWATA, S., ibid, 783

[14] UCRL 50021-80 Livermore Laser Program Annual Report (1980)

INTENSE ION BEAM RESEARCH AT LOS ALAMOS

D. J. Rej, R. R. Bartsch, H. A. Davis, R. J. Faehl, D. C. Gautier, J. B. Greenly*, I. Henins, T. W. Linton, R. E. Muenchausen, W. J. Waganaar

Los Alamos National Laboratory
Los Alamos, NM 87545, USA

ABSTRACT

Two new interdisciplinary programs are underway at Los Alamos involving the physics and technology of intense light ion beams. In contrast to high-power ICF applications, the LANL effort concentrates on the development of relatively low-voltage (50 to 800 kV) and long-pulsewidth (0.1 to 1 μs) beams. The first program involves the 1.2 MV, 300-kJ *Anaconda* generator which has been fitted with an extraction ion diode. Long pulsewidth ion beams have been accelerated, propagated, and extracted for a variety of magnetic field conditions. The primary application of this beam is the synthesis of novel materials. Initial experiments on the congruent evaporative deposition of metallic and ceramic thin films are reported. The second program involves the development of a 120-keV, 50-kA, 1-μs proton beam for the magnetic fusion program as an ion source for an intense diagnostic neutral beam. Ultra-bright, pulsed neutral beams will be required to successfully measure ion temperatures and thermalized alpha particle energy distributions in large, dense, ignited tokamaks such as *ITER*.

I. Introduction

Over the last two decades, there has been remarkable progress in the understanding and development of intense light ion beams. While a primary application driving the development of this technology is ICF energy research,[1] additional applications such as magnetic fusion energy (MFE), beam-solid interactions, and materials processing continue to be explored. Several of the latter applications could be enhanced by the development of relatively long beam pulsewidths, greater than the 10-100 ns needed for ICF. Indeed, microsecond beams have been generated for MFE ion ring applications.[2-3] In this paper, we report on two new interdisciplinary programs at Los Alamos involving long-pulsewidth intense light ion beams generated with applied-B_r extraction diodes. This technology is being developed for two specific applications: materials processing and magnetic fusion diagnostics.

* Permanent Address: Laboratory of Plasma Studies, Cornell University, Ithaca, NY 14853, USA

II. Ion Beam Generation

An ion diode has been installed on the Los Alamos *Anaconda* facility. *Anaconda* is a 10-stage Marx generator with a 300-kJ output at 1.2 MV. The diode is connected directly to the Marx generator through a stacked ring oil-vacuum interface. There are no output switches or pulse-forming lines, although a plasma opening switch has been constructed for future experiments to shape the diode voltage pulse. The combined source inductance of the Marx/interface/diode configuration is approximately 3 μH. A 1.6-Ω series resistance is installed between the Marx output and the vacuum interface to limit the output current after A-K gap closure. An applied-B_r extraction diode is used. This symmetric diode geometry is desirable for good electron confinement, which can enhance the ion emission and delay gap closure. Another attractive feature of the extraction diode is that its axisymmetric geometry can be readily modelled with two-dimensional particle-in-cell (PIC) simulations.[4]

The diode design is shown in Figure 1. The dielectric "flashover" anode consists of a Lucite annulus, 194-mm i.d., 292-mm o.d., 6.4-mm thick, mounted concentrically onto an aluminum high-voltage electrode. Both solid and perforated (with 712 evenly-spaced, 0.8-mm diameter holes) anodes have been used. The cathode consists of two concentric cylinders constructed from Ti-8Al-1Mo-1V alloy, each 102-mm long and 0.8-mm thick with diameters of 186 mm and 298 mm. For these experiments, the anode-cathode gap spacing is 20 mm. The B_r field is produced by two concentric magnets, R= 77 mm, N=18 turns (inner) and R= 161 mm, N= 7 turns (outer), positioned midway between the anode and an aluminum plate on which the magnets and cathode electrodes are mounted. The magnets are independently powered by 10-kV, 500-μF capacitors. The coil current risetimes are 170 μs (outer) and 250 μs (inner), which are sufficiently long for fields to penetrate the cathode electrodes, but short enough to prevent significant penetration into the aluminum anode electrode. Initial experiments have been performed at a reduced Marx voltage of 600 kV. Diagnostics used in these initial experiments include voltage and total current monitors located at the oil-vacuum interface, and a radial array of four unbiased, magnetized Faraday cups placed near one

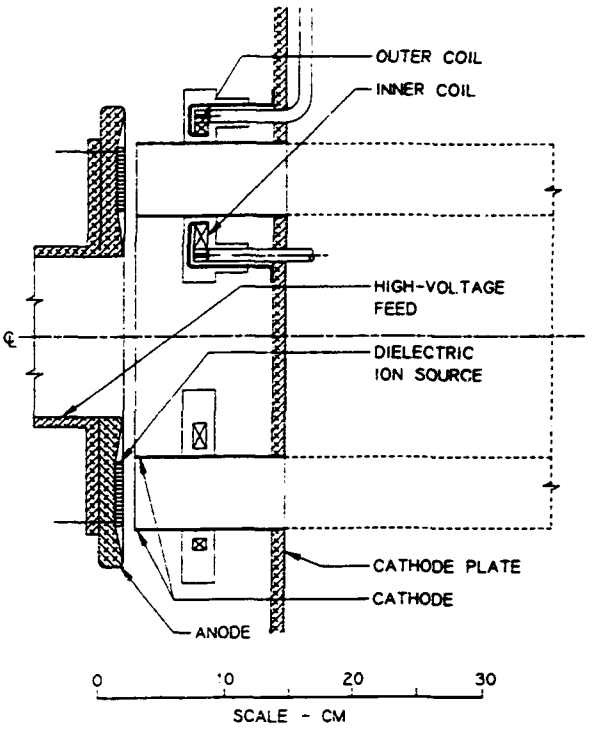

Fig. 1: Ion diode geometry.

azimuthal location at an axial position 138 mm from the anode.

Typical voltage and current waveforms for a single shot are shown in Figure 2. Initially, the diode impedance is high, resulting in a voltage risetime of less than 100 ns. Faraday cup traces are plotted in Figure 3 for the same shot. Ions are detected for approximately 0.6 μs starting 0.2 μs after application of the high-voltage. The total ion current I_i is inferred from the product of the anode area and the radially-weighted average of the Faraday cup signals. As illustrated in Fig. 2, I_i reaches a maximum of 33 kA and then falls to zero when A-K gap closure short-circuits the diode.

The influence of the magnetic field on diode performance has been assessed. The data plotted in Figures 4 through 6 have been obtained for the case where the vacuum magnetic flux across the anode surface is nearly constant. This situation is produced with equal currents in the two magnets. A critical field B_{cr} of 0.13 T is required to insulate 400-kV electrons in a 2-cm gap. The corresponding critical magnet current needed to generate B_{cr} at the outer edge of the gap is approximately 2.8 kA. This magnetic insulation threshold is clearly illustrated in Figure 4, in which the maximum ion current density j_m and integrated ion fluence $q = \int j\,dt$ measured at radius r = 129 mm are plotted *vs* magnet current. In Figures 4 through 6, the data points represent averages of 112 separate shots, while the error bars denote standard deviations. As B_r is increased past the threshold, the ion emission remains relatively constant, while the average diode voltage during ion emission steadily rises (Fig. 5). The observed j_m of 135 A/cm^2 corresponds to an enhancement of 55 over the Child-Langmuir limit computed for protons in the vacuum A-K gap. The average diode impedance at this time varies between 5 and 10 ohms. As illustrated in Fig. 2, ions can account for a majority of the total current. Insulated diode efficiencies I_i/I_{tot} between 0.5 and 0.8 are inferred (Fig. 6).

Average radial profiles j(r) and q(r) for about 100 shots are plotted in Figure 7a, for three magnetic field configurations. Ion emission is greatest at larger radii where the insulation

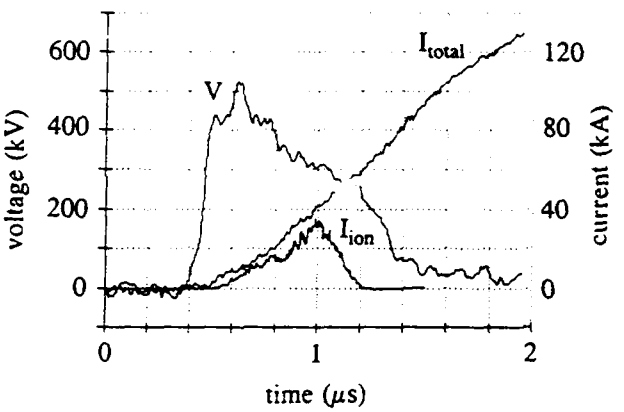

Fig. 2: Typical diode voltage and current waveforms.

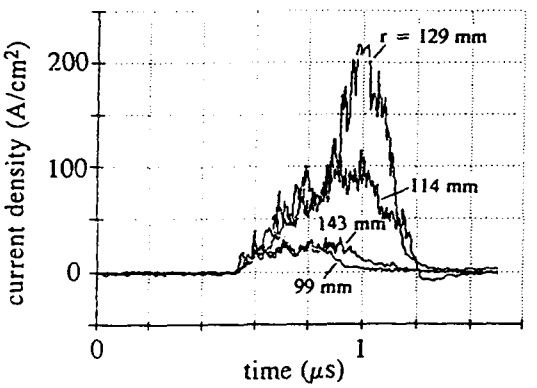

Fig. 3: Faraday cup signals at four different radii.

field is relatively low. This result is consistent with higher Child-Langmuir enhancements due to the broader electron sheath in this region. The ion current density on the inside is observed to increase when one lowers the outer magnet flux; conversely, emission on the outside is enhanced by lowering the inner magnet flux. These result are consistent with recent experiments at Cornell.[5] The use of the perforated anode did not appreciably change the output characteristics of the ion beam (Fig. 7b), although the j(r) profile is somewhat more peaked for the constant current case.

Further experiments are needed to better characterize the ion beam. Upcoming studies will concentrate on azimuthal and axial variations in the power and energy flow, divergence, composition, energy distribution, and A-K gap closure phenomenon. Parametric dependences on gap spacing, diode voltage, and anode material also need to be assessed.

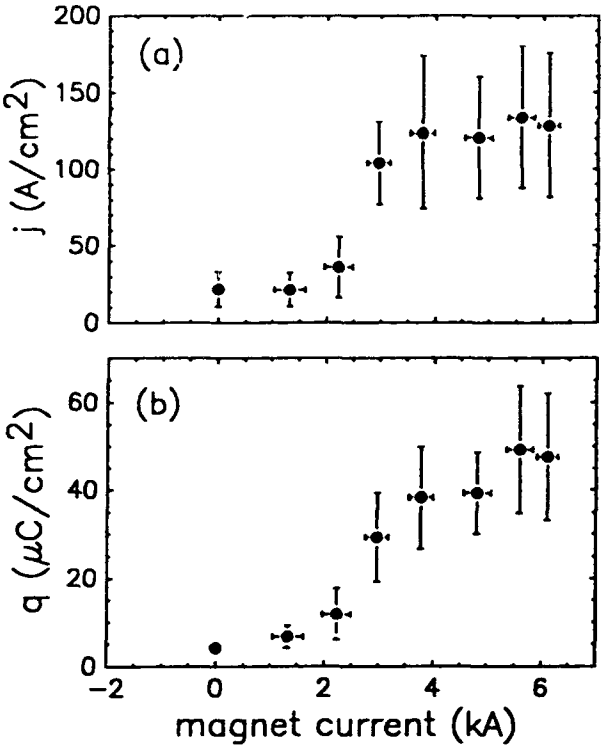

Fig. 4: Average (a) maximum ion current density and (b) integrated ion charge density obtained from the Faraday cup at r= 129 mm.

III. Thin Film Deposition Experiments

Several intriguing materials processing applications with intense ion beams have emerged recently. Because of the short range of ions in matter, applications usually involve the surface modification of materials, *e.g.*, implantation,[6] alloy mixing,[7,8] defect formation,[9] and thin film deposition.[10,11] The congruent evaporative deposition of polycrystalline thin films appears especially well suited for intense ion beams. The basic process pioneered by Yatsui[10] is illustrated in Figure 8. The beam is propagated into a solid

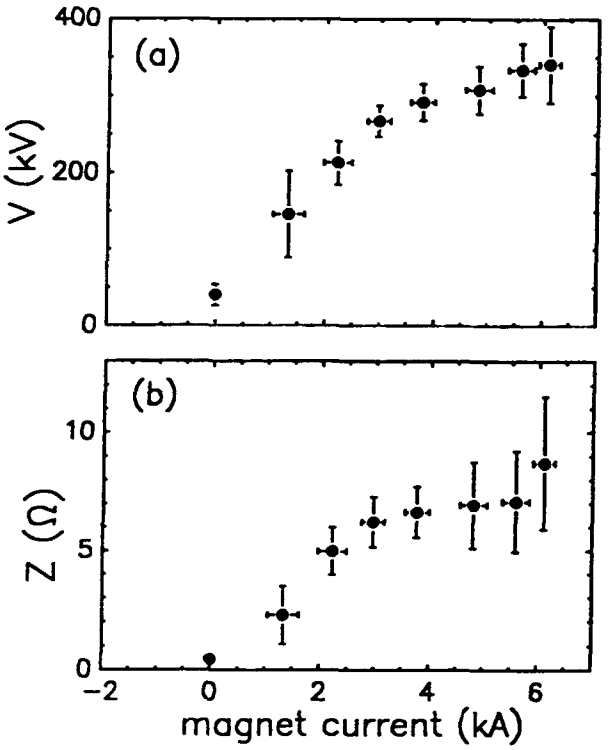

Fig. 5: Average diode (a) voltage and (b) impedance during ion emission.

target resulting in the evaporation and ionization of a substantial amount of target material. For example, an energy fluence of 1 kJ/cm^2 deposited over a 5 μm ion range will heat the target surface about 5×10^5 K or approximately 40 eV per atom. The ablated plasma is then deposited at record rates onto an adjacent substrate as a crystalline film. Long ion pulsewidths are desirable, provided thermal conduction into the target during the beam pulse is low. For most materials and sub-MeV beam energies, microsecond-long pulses are optimum.

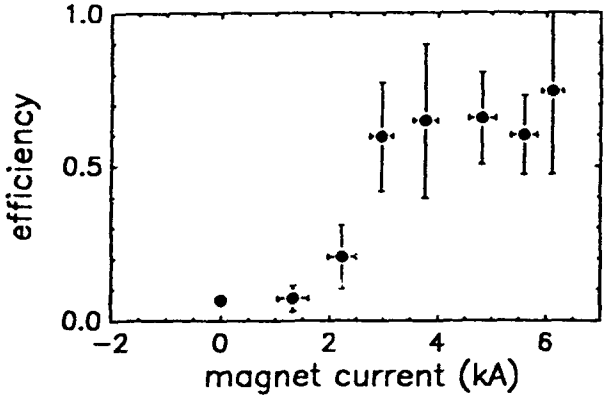

Fig. 6: Diode efficiency Ii/Itot inferred from radially-weighted peak $j_m(r)$ data.

Pulsed ion beam deposition is similar to that used with high-intensity pulsed lasers.[12,13] As with lasers, there are significant advantages: (1) target material stoichiometry is preserved (*i.e.*, the evaporation/deposition is congruent); (2) relatively high-energy (~ 1 eV) evaporated particles needed for high-quality films are produced; (3) crucibles and filaments used in thermal evaporation are unnecessary; (4) sequencing with multiple targets is possible; and (5) high deposition rates minimize contamination problems.

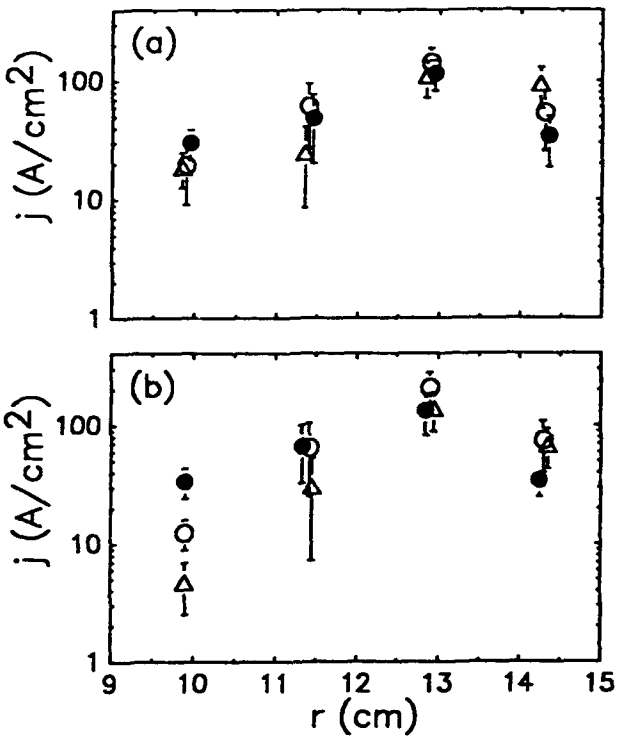

Fig. 7: Current density profiles for (a) solid and (b) perforated anodes, and 3 B-field configurations (o: inner coil I= 6 kA, outer coil I= 6 kA; •: I_{in}=6, I_{out}=3 kA; Δ: I_{in}=3, I_{out}=6 kA).

Intense ion beams offer many advantages over lasers. Ion beams penetrate deeper than laser light, thereby allowing unprecedented instantaneous evaporation and deposition rates of 1 cm/sec or more.[10] Ions penetrate the surface plasma better than laser light. Deleterious particulate phenomena ("splashing"), often attributed to preheated surface electrons, should not exist with ion beams. Metallic targets, which generally reflect laser light, readily absorb ion beams, allowing the

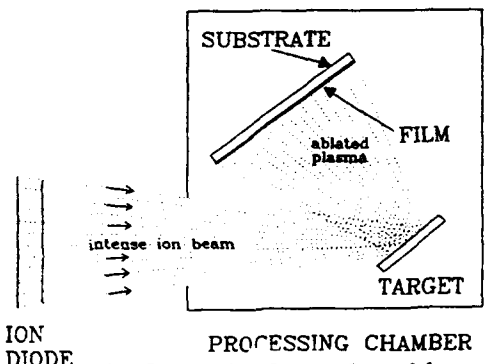

Fig. 8: The ion beam deposition process.

efficient production of metallic and intermetallic coatings. Ion beam accelerators are efficient, and, consequently, orders of magnitude less-expense (per unit energy) than commercial lasers.

Initial deposition experiments have been performed at relatively low energy fluences of 10 to 20 J/cm^2 on target using a small portion of the *Anaconda* ion beam. Approximately 1% (*i.e.*, 5 cm^2) of the beam is sent into a processing chamber containing a target-substrate assembly. The first experiment involved the deposition of copper-oxide ceramic films, which are of interest for high-temperature superconductor applications. $YBa_2Cu_3O_{7-\delta}$ films have been deposited onto a variety of room-temperature crystalline substrates, including Be, Si, and $NdGaO_3$. Rutherford backscattering (RBS) analyses of the films indicate a deposition rate of 50 nm/pulse, which is orders of magnitude higher than typical laser deposition rates. RBS analyses also indicate congruent evaporation with the 1:2:3 target stoichiometry preserved in the thin film to within 10% (Figure 9). A 50 nm/pulse deposition rate is also observed when depositing bimetallic compounds such as brass.

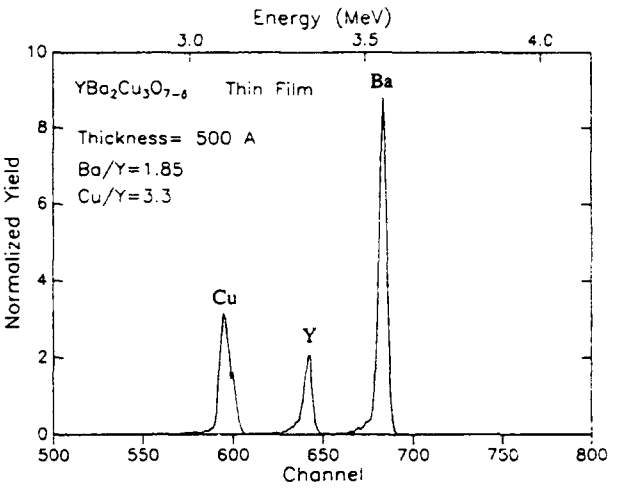

Fig. 9: RBS profile of a Y-Ba-Cu-O film on Si produced by intense ion beam deposition.

In the future, higher-power deposition will be examined. The entire beam will be focussed onto a 50-cm^2 target area. Significant evaporation and ionization (up to 100 mg/pulse) is anticipated. Despite high deposition rates, target contamination from matter ejected from the flashover anode poses a serious problem, especially for high-purity films used in electronic applications. Furthermore, dielectric anodes are incompatible with high-repetition-rate, long-lifetime diodes needed for bulk deposition applications over large areas. To address these problems, reproducible and relatively pure ion sources, such as the plasma anode,[14] will be necessary.

IV. Intense Diagnostic Neutral Beam

Over the last decade, diagnostic neutral beam (DNB) spectroscopy has emerged as a powerful diagnostic technique for tokamak plasmas.[15] Applications include local measurement of: (1) ion temperatures, plasma rotation, and fully-stripped impurity densities by charge-exchange recombination spectroscopy (CHERS); (2) density fluctuations; (3) current density profiles by motional Stark polarimetry. Furthermore, DNB spectroscopy will be needed to

measure the confined alpha particle densities and energy distributions in upcoming large burning plasma experiments such as the *International Thermonuclear Experimental Reactor* (*ITER*). Present-day low-current, long-pulse neutral-beam technology, however, will be insufficient in providing the required intensities in *ITER*. Specifically, large-radius, high-density plasmas pose two basic problems: (1) they prevent beam penetration; and (2) they reduce the signal-to-noise ratio S/N since the signal intensity rises linear with n while the background bremsstrahlung increases as n^2a. Simulations[16] for a 1-MW, 100-keV neutral hydrogen beam in *ITER* ($R = 5.8$ m, $a = 2.2$ m, $n = 1.1\times10^{20}\,[1-(r/a)^2]^{1/2}$ m^{-3}, $T = 10\,[1-(r/a)^2]$ keV, $Z_{eff} = 2$) reveal significant beam attenuation, while the anticipated charge-exchange-recombination emission drops several orders of magnitude below the background bremsstrahlung level over the first meter from the plasma edge. Improved deposition may be obtained at higher beam energies; however, high-energy beams lead to unacceptable S/N for CHERS because of the charge-exchange reaction rates which decrease significantly with beam energy. To provide adequate signals at energies matched to the charge-exchange reaction cross sections, relatively low-energy (about 100 keV/amu), high-current-density beams with short signal integration times are needed.

To address this problem, we are developing an intense diagnostic neutral beam (IDNB) which could offer significant improvements in beam current density over conventional technologies. This program is similar to the Livermore *IPINS* work of the 70's,[17] but it takes advantage of recent advances in intense ion beam physics. The prototype IDNB under construction consists of a low-inductance, 120-kV, 125-kJ capacitor bank configured to power a 300-cm^2 area, applied-B_r extraction diode. Pure proton and deuteron sources, such as cryogenic[18] and gas-loaded metallic foil anodes,[19] or a plasma anode,[14] will be required. The beam may be focussed ballistically, by conically configuring the diode. Ions are converted into neutrals in a puff gas charge-exchange cell located downstream.

To produce neutral beams, positive ion sources are useful at low energies only, typically $E < 100$ keV/amu, because of the rapid decrease of the neutral conversion efficiency with E. This decrease, however, is offset by the $E^{3/2}$ dependence of the enhanced ion current density. An operating window is evident, as illustrated by the calculation shown in Fig. 10 for protons in a 1-cm gap with Child-Langmuir enhancement of 100, and a thick H_2 neutralizer cell.

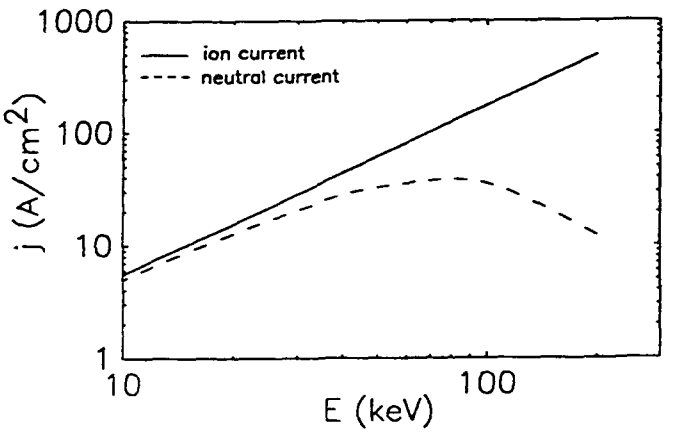

Fig. 10: Calculated IDNB current densities.

Technical issues to be addressed in upcoming proof-of-principal experiments include: the beam energy distribution, current density, pulse length, divergence, propagation, reproducibility, maintenance, and impurity content. An overall assessment of the technology's suitability for beam spectroscopic measurements on tokamaks will be made.

Acknowledgments

The authors are grateful to Prof. H. H. Fleischmann (Cornell University) for useful discussions on beam physics, and to Dr. K. M. Young (Princeton Plasma Physics Laboratory) for information on *ITER* DNB requirements. This research is funded by the USDOE Office of Fusion Energy and by the Los Alamos LDRD Program.

References

1. T. A. Melhorn *et al.*, these proceedings.
2. S. C. Luckhardt and H. H. Fleischmann, Appl. Phys. Lett. **30**, 182 (1977).
3. D. A. Hammer, J. B. Greenly, P. D. Pedrow, E. Schamiloglu, R. N. Sudan, in *Proc. 6th Intern. Conf. on High-Power Particle Beams*, BC. Yamanaka, Editor (Osaka Univ., Osaka, Japan, 1986), p. 391.
4. R. J. Faehl and D. J. Rej, these proceedings.
5. J. B. Greenly, C. K. Struckman, B. R. Kusse, W. A. Noonan, these proceedings.
6. W. Chu, S. Mader, E. Gorey, J. Baglin, R. Hodgson, J. Neri, D. A. Hammer, Nucl. Instr. and Meth. **194**, 443 (1982).
7. R Fastow, J. W. Mayer, J. Appl. Phys. **61**, 175 (1987).
8. Y. Nakagawa, T. Ariyoshi, H. Hanjo, S. Tsutsumi, Y. Fujii, M. Itami, A. Okamoto, S. Ogawa, T. Hamada, F. Fukumaru, Nucl. Instr. and Meth. **B39**, 603 (1989).
9. A. N. Didenko, A. I. Rjabchikov, G. P. Isaev, N. M. Arzubov, Yu. P. Sharkeev, E. V. Kozlov, G. V. Pushkareva, I. V. Nikonova, A. E. Ligachev, Mat. Sci. and Eng. **A115**, 337 (1989).
10. Y. Smimotori, M. Yokoyama, H. Isobe, S. Harada, K. Masugata, K. Yatsui, J. Appl. Phys. **63**, 968 (1988).
11. O. I. Goncharov, I. F. Isakov, V. N. Kolodii, V. M. Matvienko, M. S. Opekunov, G. E. Remnev, Yu. P. Usov, and A. N. Zakutayev, in *Proc. 8th Intern. Conf. on High-Power Particle Beams*, B. N. Breizman, B. A. Knyazev Editors (World Scientific Publishing Co., Teaneck, NJ, 1991), Vol. II, p. 1243.
12. J. T. Cheung, H. Sankur, CRC Crit. Rev. in Solid State and Mat. Sci. **15**, 63 (1988).
13. Bulletin Materials Research Society, Vol. XVII (February 1992). Special issue on pulsed laser deposition.
14. J. B. Greenly, M. Ueda, G. D. Rondeau, D. A. Hammer, J. Applied Physics **63**, 1872 (1988).
15. R. J. Fonck, D. S. Darrow, K. P. Jaehnig, Phys. Rev. A **29**, 3288 (1984).
16. D. J. Rej, I. Henins, R. J. Fonck, Y. J. Kim, Rev. Sci. Instr. (in press).
17. D. S. Prono, H. Ishizuka, R. J. Briggs, in *Proc. 2nd Intern. Conf. on High-Power Electron and Ion Beams*, J. Nation and R. Sudan, Editors (Cornell Univ., Ithaca NY, 1977), p. 145.
18. K. Kasuya, K. Horioka, T. Aso, Y. Saito, H. Iida, K. Nakata, Y. Kawakita, S. Kato, *op cit.* Ref. 11, Vol. I, p. 543.
19. H. Bluhm, H. Laqua, K. Baumung, L. Bluth, P. Hoppe, *op cit.* Ref. 11, Vol. II, p.927.

Invited Electron Beam, Bremsstrahlung, and Diagnostic Technique Papers

Brendan Godfrey, *Session Chairman*

Charged Particle Beam Propagation Studies at the Naval Research Laboratory*

R.A. Meger, R.F. Hubbard, J.A. Antoniades, R.F. Fernsler, M. Lampe, D.P. Murphy,
M.C. Myers, R.E. Pechacek, T.A. Peyser,[a] J. Santos,[b] S.P. Slinker

Plasma Physics Division, Naval Research Laboratory, Washington, DC 20375-5000

The Plasma Physics Division of the Naval Research Laboratory has been performing research into the propagation of high current electron beams for 20 years. Recent efforts have focused on the stabilization of the resistive hose instability. Experiments have utilized the SuperIBEX e-beam generator (5-MeV, 100-kA, 40-ns pulse) and a 2-m diameter, 5-m long propagation chamber. Full density air propagation experiments have successfully demonstrated techniques to control the hose instability allowing stable 5-m transport of 1-2 cm radius, 10-20 kA total current beams. Analytic theory and particle simulations have been used to both guide and interpret the experimental results. This paper will provide background on the program and summarize the achievements of the NRL propagation program up to this point. Further details can be found in other papers presented in this conference.

I. INTRODUCTION: The Naval Research Laboratory has been performing experimental and theoretical research into the propagation of relativistic electron beams (REB) in the atmosphere for a number of years. Recently the work has focused on the study of self-pinched propagation of intense electron beams in uniform air and on developing techniques for conditioning the beam in order to stabilize instabilities. NRL has combined a number of techniques developed by the propagation community in order to successfully demonstrate beam propagation in uniform density backgrounds. This paper will provide an overview of the NRL program with emphasis on the experimental program. Further details will be found in the accompanying papers.[1-5]

II. PROPAGATION IN THE ATMOSPHERE: Self-pinched propagation of intense relativistic electron beams in dense gases is subject to a variety of processes which may degrade the beam. The beam undergoes a slow expansion due to collisions with the neutral gas[6] which produces energy loss and increases perpendicular energy. The characteristic propagation scale length for this process (e-fold expansion of the radius) is the Nordsieck length $L_N = 6.1(I_n\gamma)^{0.93}/P$ cm where γ is the electron relativistic factor, I_n is the net current (kA) in the vicinity of the beam, and P (atms) is the background pressure. The front of the beam is also subject to a continuing erosion process driven by inductive axial electric fields which extract energy from the beam electrons. This leads to the pulse shortening accompanied by rise time sharpening. The beam will also be degraded if it is injected into the air with a transverse temperature much different from the equilibrium temperature. A poorly "matched" beam entering the air will result in additional beam expansion and/or loss of electrons throughout the pulse. Under most circumstances these processes are secondary to the growth of instabilities.

A. Resistive Hose Instability: The most threatening instability for beam propagation in high-density gas is the resistive hose instability.[5] The resistive hose is a macroscopic m = 1 kink mode which causes transverse displacements of the beam to grow as the beam propagates in z. It is the result of an interaction between the beam current and the beam generated background conductivity distribution. To get a physical understanding of the hose instability assume that a beam is propagating in a conductive background plasma distribution and that all return currents have decayed to zero. (Hose motion does not require the presence of monopole return currents generated when the beam first enters the gas.) Now assume that the beam is given an instantaneous lateral kick at a point in the beam frame (frame moving with the beam) somewhere behind the beam head. The perturbation is of finite length in the beam frame (greater than the beam radius and much less than the beam length) and moves the beam radially out of the initial beam channel a distance which is small relative to the beam radius. Since the background plasma is conductive a plasma current will be driven in the original beam channel, trying to preserve the original magnetic axis of the beam. Likewise plasma currents will be driven in the displaced beam channel, masking the presence of the displaced beam current. The circulating plasma current forms a dipole field (shaded region in figure 1) which preserves the original magnetic field distribution. The attractive force between the plasma current driven in the original beam channel and the displaced beam electrons results in the hose oscillations.[7] If the plasma conductivity were infinite then the magnetic axis of the beam would be frozen in place and the central force would produce an oscillation of the beam about the magnetic axis. For a resistive plasma the dipole field will decay away on a dipole decay time scale, $\tau_d = \pi a_b^2/2\rho c^2$ sec where ρ is the plasma resistivity. An estimate of the dipole decay time can be made using $\tau_d \cong \int I_b dt/25$ sec where I_b is the beam current (kA) giving $\tau_d \leq 10$ ns late in the beam pulse.[8] The dipole decay time will be short when ρ is large early in the pulse and will increase later in the pulse. The decay of the dipole field will result in the magnetic axis shifting toward the beam centroid. This shift introduces a phase lag between the beam and magnetic axis which leads to growth of the oscillations. The largest hose growth occurs at the betatron frequency which is the natural oscillation frequency of the beam electrons. This is characterized by the wavelength of the oscillatory electron

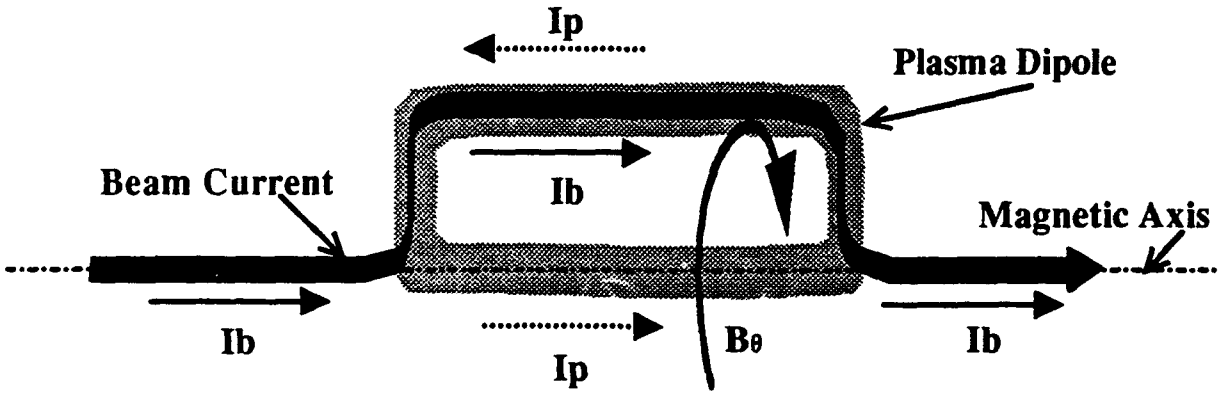

Figure 1. A displacement of the beam current leads to the formation of a plasma dipole current distribution. Resistivity in the plasma leads to decay of the dipole current and growth of the resistive hose instability.

motion known as the betatron wavelength, $\lambda_\beta = 2\pi a_b(I_A\gamma/I_n)^{1/2}$, where I_n is the net current ($I_n=I_b-I_p$ where I_p is the plasma current and I_A=17 kA). A measure of hose stability is the number of betatron wavelengths the beam can propagate without large hose growth relative to the scattering scale length, L_N.

The resistive hose is a rapidly growing instability. Under normal experimental circumstances it results in a rapid loss of the entire beam after a few meters of propagation. In several betatron wavelengths the amplitude of the instability can grow by orders of magnitude. It is triggered at a point in the beam where the dipole decay time is comparable to the perturbation frequency (higher frequencies phase mix out before the plasma channel can respond and lower frequencies result in a translation of the beam). At the point in the beam frame where the instability is triggered the amplitude of the local betatron oscillations grow rapidly. The plasma currents, which are stationary in the lab frame, excite the hose in successive slices of the beam as they move through the perturbed region. Thus, in the beam frame, the instability appears to be constantly growing and convecting toward the tail. In general, at a given location in the beam frame the hose amplitude will grow until phase mixing effects smear out the coherent beam oscillations and convert the motion into beam temperature. At a given location in the lab frame, one would see increasing amplitude radial motion of the beam as it moved past. In the beam frame, hose motion at a given location would grow in amplitude until phase mixing smears out the coherent motion and the beam quiets down again.

The hose instability cannot be eliminated for beams propagating in high pressure neutral gas. There are, however, several techniques which could minimize its effects. First the convection of the instability from one location in the beam frame backwards depends on how well one beam slice couples to the next. This coupling is dependent on the spectrum of betatron frequencies in any given slice. Since peak growth of the instability occurs near the local betatron frequency, any change in this frequency with position in the beam frame decreases the coupling. A change in the local betatron frequency can be introduced by continually changing the radius of the beam from the front to the back in the beam frame. In high pressure gas this corresponds to changing the emittance of the beam from head to tail. Ideally one would like to start with a fat beam and taper the radius down to a small radius near peak current to ensure maximum energy density on target. A second knob is the control of initial perturbations which trigger the instability. These can be externally introduced (e.g., beam sweep or BBU from the accelerator) or can be random noise on the beam. By decreasing the amplitude of the perturbations the magnitude of the instability can be reduced. Introducing the emittance tailoring to the beam and damping out initial perturbations are the basis of beam "conditioning" which has recently been the main focus of the NRL propagation effort.

B. Beam Conditioning Techniques: NRL's approach for reducing hose growth has been to employ post accelerator beam conditioning techniques.[1,2,3] Beam conditioning generally has two primary goals: (1) to introduce a head-to-tail taper in the beam radius to detune the instability, and (2) to center the beam and damp transverse perturbations on the beam which seed the instability.

1. Emittance tailoring: Beam tapering in SuperIBEX is accomplished with an ion-focused regime (IFR) transport cell.[9] When an electron beam is injected onto a plasma channel whose density is less than the beam

density, it will assume an equilibrium based on the beam current and the local space charge density. If the beam is highly relativistic ($\gamma >> 1$), the repulsive force from the beam's radial electric field is nearly canceled (to order $1/\gamma^2$) by the self-pinching magnetic field $B\theta$. A small amount of background ionization, produced by an external source such as a laser or directly by beam ionization of the low density background gas, can decrease the space charge forces, allowing the beam to pinch. By adjusting the gas pressure to allow for the pulse length and cell geometry in the beam ionized case, one can introduce a radius taper to the beam profile on the beam time scale. This radius tailoring can then be converted to emittance tailoring with a scattering foil at the end of the IFR cell.

2. Damping of Beam Perturbations: A variety of techniques have been used on SuperIBEX and other devices to reduce the perturbations which "seed" the hose instability.[1,2,3] Initial experiments used a small diameter, high pressure IFR cell to center the beam. More recent experiments have focused on the use of an externally powered, current-carrying wire cell known as a $B\theta$ cell.[10] In this system a fraction of the beam current is driven down a multi-betatron wavelength long cell with or without a gas fill. The anharmonic potential well produced by the wire current pulls the beam toward the wire and smears out coherent radial motion due to phase mixing within the beam.

III. EXPERIMENTAL APPARATUS: See figure 2.

A. Beam Generation: The beam used for these propagation experiments was produced by the SuperIBEX accelerator. SuperIBEX is a single-shot electron beam device capable of producing a 5-MeV, 40 nsec FWHM pulse with peak currents of up to 100 kA. SuperIBEX is designed to give a 10-nsec rise time with essentially zero prepulse. For these experiments a 0.3 cm radius flat cathode was used with a nominally 3-cm vacuum gap to a 2.5 μm thick Ti anode foil. For these experiments the diode was mismatched to give only 50 kA at the full 5-MV voltage. In order to improve beam quality the beam was then passed through an emittance selector consisting of a

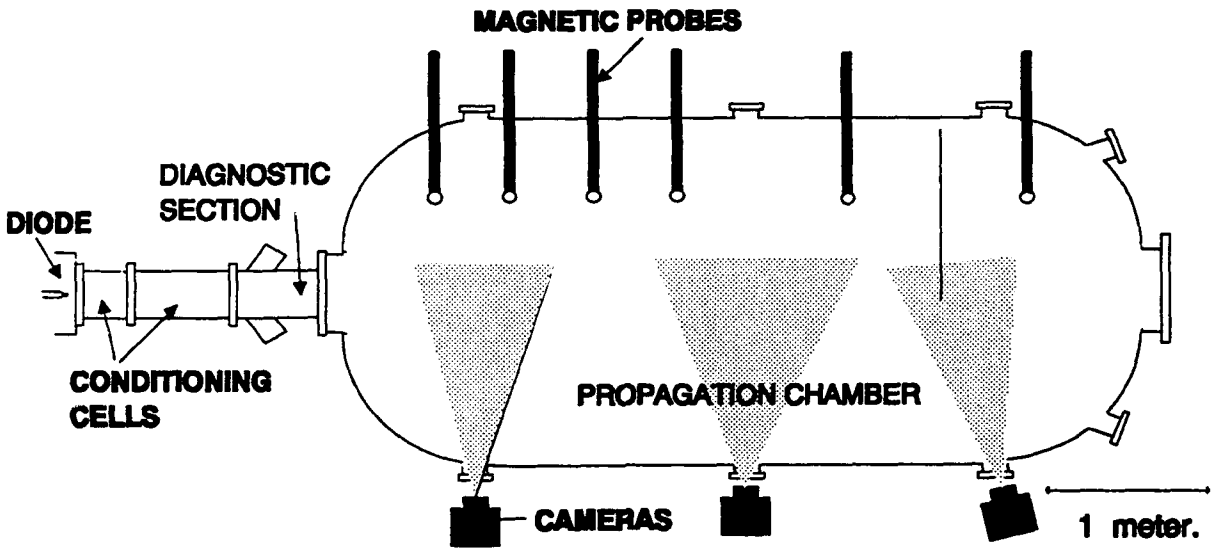

Figure 2. Schematic representation of the SuperIBEX propagation apparatus.

5 cm long, 0.9-1.1 cm radius stainless steel tube with a second foil at its exit. The thickness of this foil could be adjusted to control beam emittance. Voltage and current were monitored at various locations in the diode region.

B. Conditioning Cells: After exiting the emittance selector the beam entered the first of two conditioning cells. A 40 cm long, 10 cm diameter IFR cell was used to provide radius tailoring for the beam. IFR pressures ranging from 3-20 mTorr of Argon were used in the cell. A 40-125 μm thick Ti foil ended the IFR cell. Input and output current monitors were used to measure the beam transport in the IFR cell. Downstream of the IFR cell was a 1.2 m long, 20 cm diameter Bθ cell with a 125-200 μm wire strung along the axis. Pulsed wire current of 2-10 kA, 20 μs duration from a 58 μF bank were driven along the wire. The chamber could be evacuated or run at full density air pressure. A beam current and position monitor was located at the downstream end of the cell. A 40 μm Ti foil was used to separate the end of the Bθ cell from full density air when low pressure was used in the cell. The two conditioning cells were followed by a 80 cm long, 20 cm diameter full density air transport cell used for optical diagnostics.

C. Large Diameter Propagation Chamber: Downstream of the optical diagnostic cell was a 2m diameter, 5m long propagation chamber. Sets of 4 magnetic probes protruded in 0.5 m from the walls at half meter increments along the chamber. The probes could be summed to give net currents or opposite pairs subtracted to give radial displacement of the magnetic axis. Since the probes were located 50 cm off axis, they integrate displacements over 1-2 betatron wavelengths of beam propagation. Open shutter cameras were deployed along the propagation chamber to record gas light from air propagation experiments.

D. Beam Profile Diagnostics: One of the key issues for beam propagation is the measurement of the beam condition at different locations.[4] This requires time dependent measurements of both the beam radial position and the beam current density profile. Magnetic probes were used extensively to locate the beam or net current axis. A segmented Faraday cup[11] was used to give the beam profiles as a function of time. Framing and streak camera optical diagnostics were used to give both position and current density profiles. Streak camera images provided ns resolution of Cerenkov light from a chord of the beam passing through an FEP Teflon foil. Framing camera images of the same Cerenkov foil provided up to 120 ps resolved 2-D images of the beam at 4 arbitrary times. Figure 3 shows a radius profile of the SuperIBEX beam just downstream of the IFR conditioning cell as measured by the segmented Faraday cup with a number of framing camera measurements superimposed. Time integrated optical diagnostics were used in the propagation chamber and provided averaged information on the beam profile as it propagated in the atmosphere.

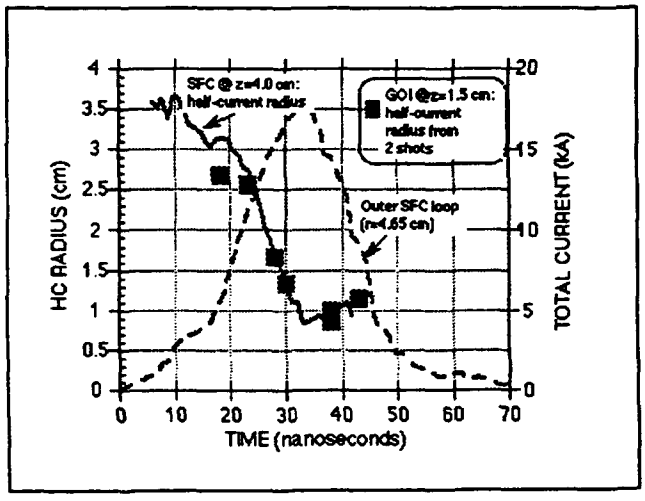

Figure 3. Beam radius as measured by the segmented faraday cup and the GOI framing camera.

IV. RADIUS TAILORING EXPERIMENTS: The amount of radius tailoring necessary to minimize hose growth is very dependent on the particular beam parameters. The local spectrum of betatron frequencies, which to a large degree determines how well a given hose perturbation couples backward in the beam, depends on the local beam emittance, net current, and beam energy at that particular location in the beam. Beams with simultaneous ramps on all three parameters may require a different radius tailoring profile than one with constant current and voltage. In addition the parameters may be changing with propagation due to nose erosion, energy loss, etc. Analytic theory has identified a scaling law for hose growth as a function of the beam radius taper.[12] The scaling law uses $a_b \propto (\zeta)^{-k}$ where ζ is the location of the beam slice relative to the beam head and k is a parameter ≤ 1. Small k values would have flat radius profiles. SARLAC simulations and the analytic model show a factor of 20 larger hose amplitude growth for k = 0.2 vs 0.7. Relatively small changes in k can lead to large changes in the hose growth. This suggests that the key to radius tailoring is establishing control of the beam radius profile and then using this control to minimize the hose growth. This must all be done with the understanding that the highest possible current density for the beam is desirable. A well tailored low current density beam may be stable but not very useful.

SuperIBEX experiments have focused on the use of a beam-generated IFR transport cell to provide radius tailoring for the beam. There are several "knobs" that can be turned experimentally to control the beam radius tailoring. These include, assuming a given injected beam voltage and current profile, the injected emittance, IFR gas pressure, cell wall radius, and cell length. Experiments have been performed varying the first three of these parameters as well as for a variety of injected beam currents. Details of these experiments can be found in an

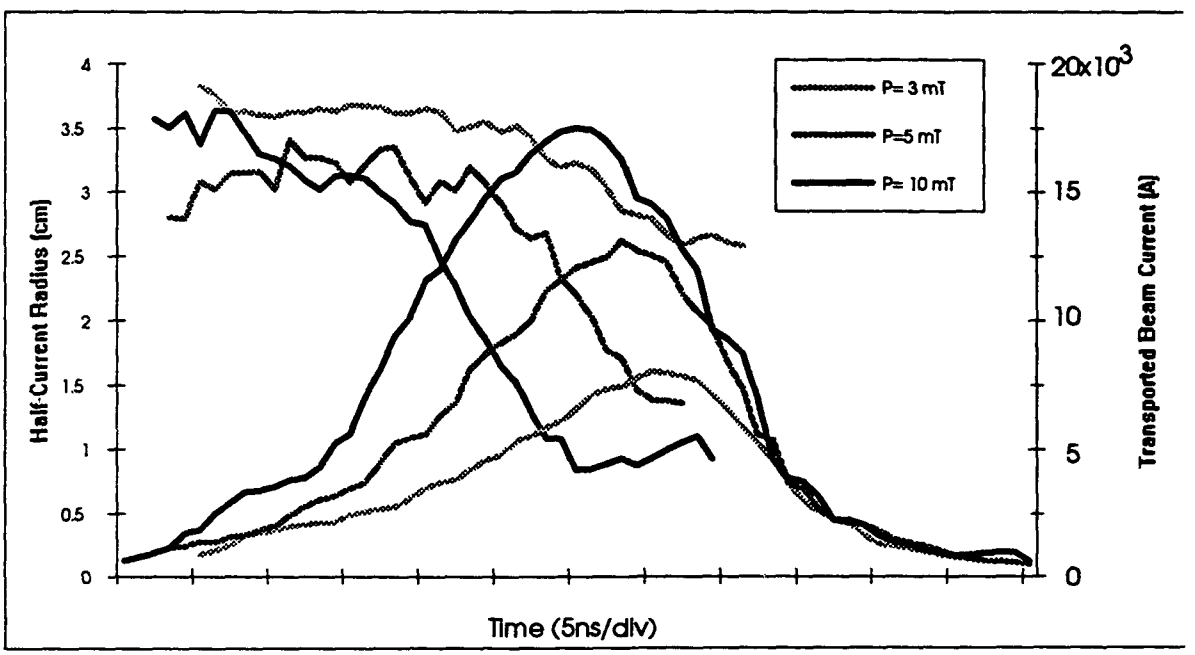

Figure 4. Beam half-current radius and transported current measured downstream of the IFR cell for 3, 5, and 10 mT IFR pressures.

accompanying paper.[2] In general the radius tailoring generated by the cell used in these experiments was very sensitive to the gas pressure used in the cell. Figure 4 illustrates this point. Gas pressures of 3, 5, and 10 mTorr of Argon were used in the cell. At low pressure (3 mTorr) the beam half current radius is limited early on by the 10 cm IFR cell diameter. The beam radius starts to decrease close to peak current but never pinches down to a small radius beam. The 10 mTorr case shows the radius tailoring to begin much earlier in the pulse and to pinch down to less than 1 cm radius. This represents greater than a factor of 6 increase in current density. In terms of the radius tailoring parameter this represents a factor of nearly 3 change in k value. The results illustrated in figure 4 agree well with analytic predictions by Fernsler[13] and with FRIEZR code simulations of the SuperIBEX beam.[14]

Experiments were also performed to test the effect of input emittance on the IFR cell radius tailoring. Increasing the input foil thickness from 40 to 80 μm Ti significantly increased the minimum radius of the beam and delayed the tailoring. Details of this experiment can be found in an accompanying paper.[2] Experiments with a 20 cm diameter IFR cell revealed the presence of a current halo surrounding the central core.[4] The 10 cm diameter cell appeared to scrape off this portion of the current distribution. Although the origin of the core-halo distribution is not well understood, it is suspected that the distribution is related to foil focusing effects at the input end of the IFR cell. The halo appears to represent <20% of the current injected into the IFR cell. Further investigations of this phenomenon are in progress.

The radius tailoring imposed on the beam by the IFR cell is converted to an emittance tailoring with a scattering foil located at the end of the cell. Ideally one would like to match the beam radius in the IFR cell to that in the air downstream of the cell. The scattering foil will increase the emittance proportional to the beam radius when it hits the foil. Larger radius beams will end up with higher emittance. If too little scattering is provided the beam will come out of the IFR cell too cold. The sudden neutralization of the space charge as it enters the full density air downstream of the foil will lead to a rapid heating of the beam, destroying the tailoring profile imposed by the IFR cell. Likewise too thick of a foil will overheat the beam and lead to rapid expansion of the beam as it propagates in the air. Usually one tries to pick the foil thickness to maintain the beam radius near peak current. 60 μm Ti appears to match the beam radius for the SuperIBEX beam. Fine tuning of the emittance conversion process awaits detailed beam measurements.

V. Bθ CELL OPERATION: Damping of the various perturbations which lead to hose growth is an important factor in beam conditioning. The frequency of the most dangerous perturbations changes as a function of position in the beam frame. Early in the pulse, when τ_d is still relatively short ($\tau_d << 1$ ns) very high frequency perturbations will couple to the beam. Later in the pulse ($\tau_d \cong 5$ ns) lower frequency perturbations will couple. In both cases the hose growth will appear near the local betatron frequency where the perturbation was first initiated. The active Bθ cell has the advantage that it will damp out high frequency perturbations even in the beam head. Schemes that depend on a feedback between the beam current and the wall (e.g., high pressure IFR cells[2]) do not damp out the head perturbations efficiently.

Experiments were performed using both full density air and vacuum Bθ cells with currents ranging from

2-10 kA.[1] To lowest order both cells appeared to center the beam. After 1.2 m of transport in the cell the beam showed very little sweep. The radius tailoring introduced by the IFR cell, with one exception, also appeared to be maintained by the cell. 24 kA, 25 ns FWHM beams injected into the Bθ cell were transported with 80% efficiency for the vacuum case and 60% efficiency for the gas filled case. The gas filled cell showed a pulse shortening down to 20 ns. The beam radius appeared to increase from 1.5 cm just downstream of the IFR cell to nearly 2 cm downstream of the gas Bθ cell. This is consistent with radius growth due to scattering off the gas background (1.2 m is nearly 1/3 of a Nordsieck length). The increased loss in the gas filled case is hypothesized to be the result of scattering beam electrons into the loss cone represented by beam electrons striking the wire. There is evidence that scattering is important from optical data taken at the output end of the cell.[4] Particularly in the gas filled case there is a hollowing of the current density profile seen. The decreased transport efficiency for the gas cell may in part be due to this increased scattering effect. There also appear to be dependencies on the wire diameter and the current driven in the cell.[1]

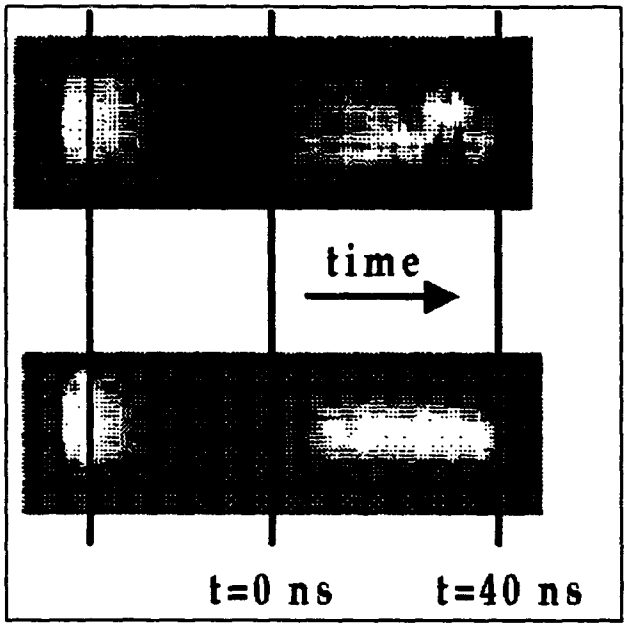

Figure 5. Streak photos of Cerenkov light produced by the SuperIBEX beam. Upper shows large beam sweep, lower almost no sweep.

Despite losses the centering cell does damp out radial motion of the beam. Figure 5 shows streak photographs from Cerenkov foils located just downstream of the exit of the Bθ cell from two SuperIBEX beams. The upper beam (without Bθ centering) shows large amplitude motion of the beam while the lower (with Bθ centering) shows almost no radial motion. Such large amplitude motion is deadly for triggering hose motion as the beam propagates. Further experiments are in progress to optimize the Bθ cell operation. There is evidence that operating at an intermediate pressure in the cell may decrease the beam loss to the wire while still damping the beam's radial motion.

VI. BEAM PROPAGATION IN THE ATMOSPHERE: The ultimate goal of beam conditioning is to stabilize the beam as it propagates in the atmosphere. From background scattering alone the radius of a relativistic beam will e-fold in one Nordsieck length. This represents a decrease of a factor >7 in current density, and therefore energy density, delivered to a target. After propagating one Nordsieck length the beam has lost most of its energy delivering capability. Likewise the hose instability growth scale length is represented by the betatron wavelength of the beam. Without conditioning a beam will either disrupt or increase in diameter in a small number of betatron wavelengths. This suggests that a figure of merit for measuring the stable propagation

of a beam could be the distance a beam propagates in units of betatron wavelengths out to a maximum of one Nordsieck length. In reality the betatron wavelength is increasing as the beam increases in radius so one must correct the figure of merit for scattering. Using initial values for the scale lengths gives a zero-order estimate of the figure of merit. This leaves undefined what constitutes "stable" propagation. For energy delivery applications a relevant measure of stability could be hose growth of less than a beam radius.

The SuperIBEX propagation experiments were performed in a 5-m long, 2-m diameter propagation chamber. At full density air pressure the Nordsieck length for the SuperIBEX beam (5 MeV, 15 kA beam current) is 4-5 m. The injected beam betatron wavelength for the SuperIBEX beam is 20-30 cm, depending on its radius. With both the IFR radius tailoring and the Bθ centering cells, stable propagation was observed for the full 5-m length of the chamber. Figure 6 shows side view pictures for open shutter cameras of the beam as it propagates. Scanning of the photographs and correction for lens effects showed that the beam diameter expanded slightly faster than the predicted Nordsieck expansion rate. After 5 m of propagation the beam had expanded out to 8-10 cm diameter rather than the expected 5-6 cm from Nordsieck expansion. The additional expansion could be a function of the open shutter camera diagnostic which measures background gas light. Plasma return currents in the beam channel tend to broaden the envelope of the light giving an overestimate of the beam cross section. High frequency hose motion or possibly phase mixed hose motion from the beam head could also broaden the beam profile. Magnetic probe measurements of the beam centroid motion along the propagation chamber showed stable beams with less than 2.5 cm radial motion over the duration of the current pulse.[3] Relatively minor changes in the "tuning" of the conditioning cells could alter the beam propagation from grossly unstable with disruption by 1-2 m of propagation, to "banana" orbit beams which followed a curved trajectory, to straight beam propagation. For a given tuning of the conditioning cells the beam propagation was very reproducible. The stable propagation shots for the full 5 m length of the chamber represent a figure of merit of between 15 and 25 for the beam. This is as large of a figure of merit as any previous experiments.

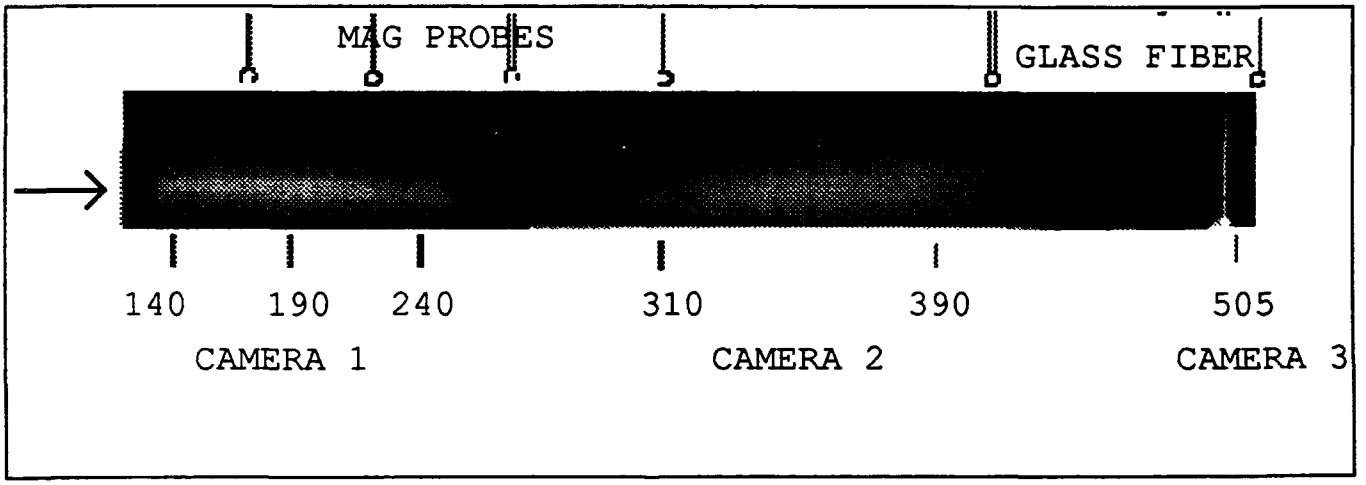

Figure 6. Open shutter pictures of the SuperIBEX beam propagating in full density air.

VIII. SUMMARY: A physical picture of the origins of the resistive hose instability was presented. The case for both radius tailoring and beam perturbation damping was made and the operation of conditioning cells to perform these functions outlined. Further information can be found in accompanying papers. Successful propagation of NRL's 5 MeV, 10-20 kA SuperIBEX beam using these techniques was reported.

IX. ACKNOWLEDGMENTS: Conversations with G. Joyce, and technical assistance from W. Dolinger, G. Littlejohn, A. Noll, J. Picciotta, J. Czarnaski are gratefully acknowledged.

*Work supported by the Office of Naval Research.

[a]Science Applications International Corporation, McLean, VA 22102

[b]Sachs/Freeman Associates, Inc., Landover, MD 20785

REFERENCES:

[1]D.P. Murphy, et al., "Transport of High Current, Relativistic Electron Beams using Active-Wire Bθ Techniques, these proceedings.

[2]M.C. Myers, et al., "IFR Transport Experiments on the SuperIBEX Accelerator," these proceedings.

[3]J.A. Antoniades, et al., "Beam Conditioning and Lead Pulse Propagation Experiments on SuperIBEX," these proceedings.

[4]T.A. Peyser, et al., "Beam Profile Diagnostics on the NRL SuperIBEX Experiment," these proceedings.

[5]R.F. Fernsler, et al., "Theory and Simulation of the Resistive Hose Instability in Relativistic Electron Beams," these proceedings.

[6]T.P. Hughes, B.B. Godfrey, Phys. Fluids 27, 1531 (1984)..

[7]S. Humphries, Jr., Charged Particle Beams, (John Wiley & Sons, New York, 1990), p.645.

[8]M. Lampe, W. Sharp, R.F. Hubbard, E.P. Lee, and R.J. Briggs, Phys. Fluids 27, 2921 (1984).

[9]K.W. Struve, E.J. Lauer, F.W. Chambers, in proceedings 5th Inter. Topical Conf. on High-Power Particle Beams (LLNL, Livermore, CA, 1983), p. 408.

[10]C.A. Frost, S.L. Shope, G.T. Leifeste, D. Welch, Bull. Am. Phys. Soc. 35, 933 (1990).

[11]T.A. Peyser, et al., Rev. Sci. Instrum. 62, 2895 (1991).

[12]M. Lampe, R.F. Fernsler, R.F. Hubbard, and S.P. Slinker, Bull. Amer. Phys. Soc 34, 1996 (1990).

[13]R.F. Fernsler, R.F. Hubbard, and S.P. Slinker, NRL Memorandum Report 7110 (in press), submitted to Phys. Fluids B.

[14]R.F. Hubbard, S.P. Slinker, R.F. Fernsler, M. Lampe, and G. Joyce, NRL Memorandum Report 6983 (in press), Submitted to J. Appl. Phys.

RADLAC II HIGH CURRENT ELECTRON BEAM PROPAGATION EXPERIMENT

C. A. Frost, S. L. Shope, M. G. Mazarakis, J. W. Poukey,
J. S. Wagner, B. N. Turman, C. E. Crist
Sandia National Laboratories, Albuquerque, NM 87185
and
D. R. Welch, K. W. Struve
Mission Research Corporation, Albuquerque, NM 87106

Abstract

The resistive hose instability of an electron beam was observed to be convective in recent RADLAC II experiments for higher current shots. The effects of air scattering for these shots were minimal. These experiments and theory suggest low-frequency hose motion which does not appear convective may be due to rapid expansion and subsequent drifting of the beam nose.

Introduction

The recent RADLAC II[1] experiments studied propagation of a high current relativistic electron beam (REB) propagating in the atmosphere, and confirmed the convective nature of the hose instability. The unique combination of high beam current and extremely small initial perturbation, allowed saturation of the hose instability to be observed for the first time. Data at higher currents were needed to study current scaling of the instability. It was important to collect data at atmospheric pressure to ensure that subtle air chemistry effects such as avalanche did not distort the experiment.

As a REB propagates through the atmosphere, the gas is ionized, quickly neutralizing the beam charge with current only partially neutralized. Thus, the beam undergoes betatron oscillations in the residual magnetic field with a wavelength λ_β. The beam emittance increases with distance due to elastic collisions with the atmosphere increasing beam radius exponentially every Nordsieck length, L_N. Analytic theory and extensive computer simulations indicate that the primary parameter of interest for a REB hose experiment is the number of betatron wavelengths occurring within a L_N ($\chi = L_N/\lambda_\beta$).[2]

The RADLAC II accelerator used a magnetically-insulated stalk adder similar to that of Hermes III.[3] This configuration demonstrated beam voltages of 10-12 MV, beam currents of 50-100 kA, and an annular beam of about 1-cm radius and 1-2 mm annular width. With no further conditioning, we found that the beam, extracted through a thin foil for propagation, quickly became unstable to high frequency hose oscillations. For propagation experiments, we conditioned the beam with a 3-m B_θ wire cell, which used an externally driven current on a thin axial wire to center the beam. This reduced the amplitude of initial transverse motion and produced a modest head to tail radius variation and produced reasonable propagation stability. Due to the high current, values for χ ranged from 10-40.

Experimental Configuration

Figure 1 shows the hardware set-up for the experiment. Initially, the 1-cm thin annular beam was not stable in the B_θ cell. Based on IPROP and MAGIC simulations of the problem, we switched to a solid beam produced by a 1.5 cm radius bullet cathode in a reduced solenoidal B_z field of 0.5 Tesla. The beam

was heated by a scattering foil to match the acceptance of the B_θ cell. Optimum tuning gave a well-damped 2-cm solid beam inside the B_θ cell which expanded to a freely propagating beam with equilibrium radius R_{equib}=3-4 cm in the propagation range at Z=1.5 m where Z is the distance from the B_θ cell exit.

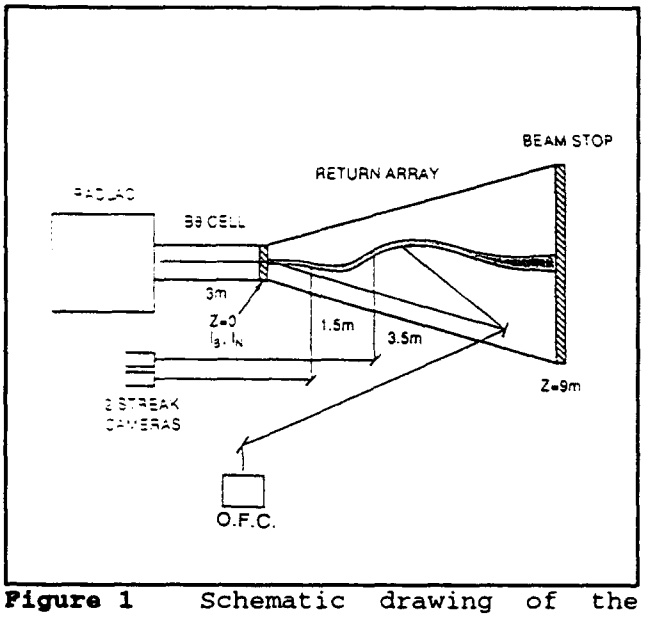

Figure 1 Schematic drawing of the RADLAC propagation experiment.

The Rogowski monitors and dielectric foil beam current monitors allowed time resolved measurements of net current (I_N) and beam current (I_B), respectively. The propagation range consisted of a conical wire cage array which expanded from the 15-cm radius B_θ cell exit monitor to a 1 m radius aluminum tank extending from Z= 7-9 m where the beam was dumped. The 9 m length of the range limited propagation to 10-15 λ_β. A time-resolved beam equilibrium radius measurement was made with an optical streak camera viewing air fluorescence at Z=1.5 m. Time-resolved beam centroid and radius data were recorded with 3 optical frame cameras viewing air fluorescence in the entire region from Z=1-5 m, giving 3 beam slice histories on each shot. Several time-integrated cameras viewed air fluorescence in the region from Z = 0-9 m. Geometric reconstruction of the entire beam path was possible by mapping the images from multiple cameras to the object space. The array of diagnostics allowed us to characterize both the injected beam parameters $I_N(t)$, $I_B(t)$ and R(t) (beam half-current radius), and the parameters $R_{EQUIB}(t)$ $X_{bar}(t)$, and $Y_{bar}(t)$ of the propagating beam on a single shot. This was essential since each machine shot had different characteristics.

Experimental Results

Many of the high current shots exhibited only a few cm of hose motion. We attribute this relative hose stability to the combination of high-current, modest radius tailoring and very low initial perturbation produced by the B_θ cell. Some shots, however, had larger initial perturbation and showed fast hose growth followed by damping. Table I summarizes a number of high quality shots which have been analyzed in detail. The minimum radius column corresponds to the minimum measured radius of the three optical cameras (streak, framing, or time integrated). Theoretical values were calculated assuming a peak beam energy of 10 MeV. All the listed shots have $\chi > 20$ and, therefore hose growth is not artificially suppressed by air scattering.

Table I. Peak current data and theory.						
Shot	beam current (kA)	net current (kA)	Minimum Radius (cm)	exp. L_N (m)	theory L_N (m)	theory χ
2181	52	28	3.8	25	32	37
2183	34	24	3.7	25	26	29
2193	54	30	3.6	NA	35	44
2200	34	24	4.2	NA	26	26
2203	42	27	3.3	37	30	40
2204	37	24	4.0	NA	26	27

Hose growth rates and saturation amplitudes have been measured for these shots and compare well with IPROP simulations. The details of data analysis and comparison to theory are described in the next section. Shots 2203 and 2204 are the best examples of saturation at low amplitudes. The initial perturbations were very small for these shots. Shot 2193 is interesting because the larger amplitudes could lead to nonlinear saturation. Figure 2 displays a typical measurement of I_B and I_N. The RADLAC II data with I_B of 30 to 50 kA is clearly in the high current regime with significant plasma return currents as seen in the figure where I_N is approximately half of I_B. The net current displays typical high current behavior in reaching peak near the end of the beam pulse and then dropping slowly as the plasma currents decay. Figure 3 displays processed streak data showing the beam current and equilibrium radius from air fluorescence measured at Z = 1.5 m. The two traces are inherently time tied since the beam current is computed from the same streak image as the radius and centroid. The beam equilibrium radius varies less than a factor of 2 during the current rise and is almost constant during the body of the pulse.

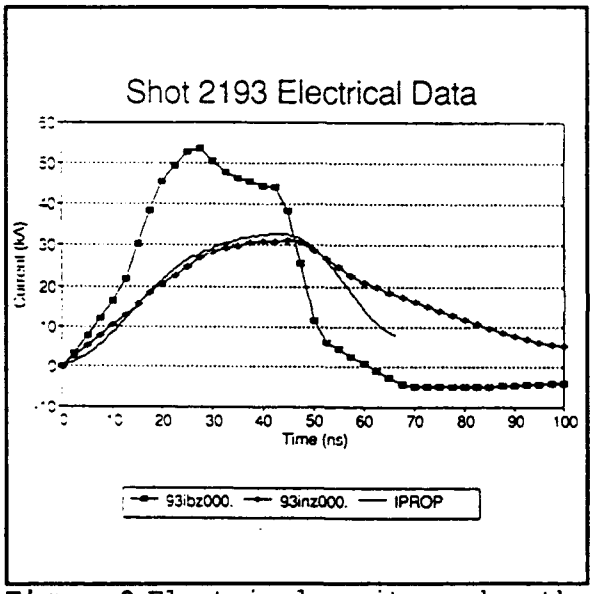

Figure 2 Electrical monitors show the net current peaks near the end of the beam current pulse in agreement with IPROP simulations.

Figure 4 displays histories of half-current radius R(Z) and the centroid $X_{bar}(Z)$ for a beam slice near peak current for shot 2203. The data is derived from a single optical frame with 3-ns gate time. This data shows a clear Nordsieck expansion consistent with calculated Nordsieck range. Three slice histories derived from shot 2193 are plotted in Figure 5 showing the growth of

the hose instability in time and space. Each of the 3 curves is obtained from a separate frame image with time delay of 7.5 ns between frames. The data at the right of the figure suggests saturation as the rate of growth decreases with time. The frame cameras only viewed the propagation range from Z= 1-5 m, so they could not record saturation occurring beyond Z = 5 m.

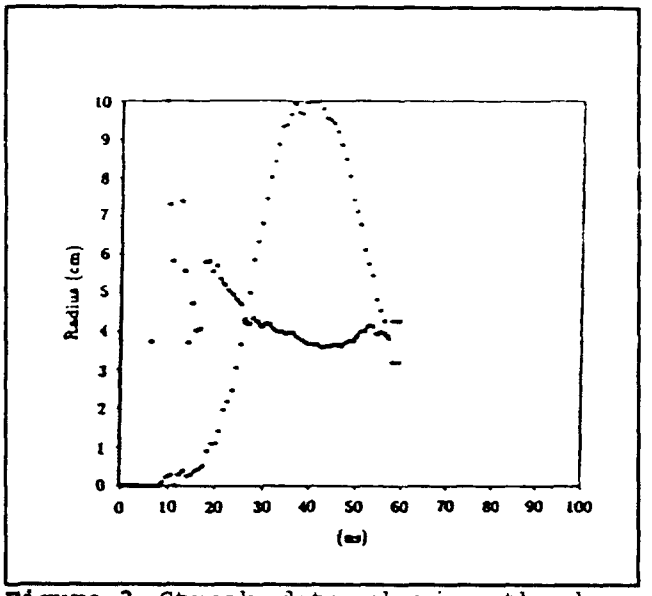

Figure 3 Streak data showing the beam radius and beam current at Z = 1.5 m indicates modest radius tailoring.

Data on stability over the entire 9-m propagation range was obtained from time-integrated photographs of air fluorescence resulting from beam propagation. The apparent distances on the photographs are distorted by camera perspective, but was eliminated by geometric correction. We digitized 2 orthogonal views and generated beam centroid tracks in 3 space. The results of this process are shown in Figure 6 where the total beam offset $(x_{bar}^2+y_{bar}^2)^{1/2}$ from the center line is plotted as a function of distance. This plot showing shot 2203 is the best example of saturation where oscillations grow to maximum amplitude near Z = 5 m and then damp. The beam offset from the centerline is less than 2 cm after 9 m of propagation. This represents an aiming accuracy of 2 mrad which is comparable to the alignment of the B_θ guide wire. Figure 7 also show damping of high frequency hose by the Z = 5 m point but also may show growth of lower frequency modes or aiming error associated with alignment of the B_θ guide wire. Shot 2204 had a smaller value of χ than 2203 which may have permitted the beam nose to drift.

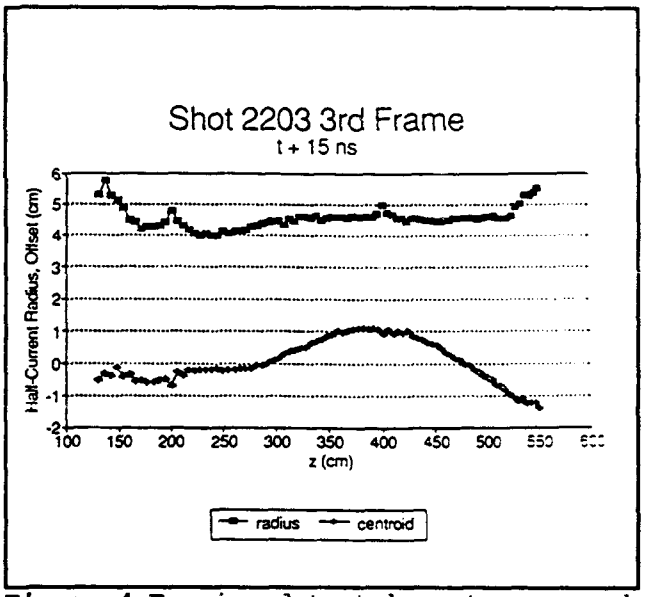

Figure 4 Framing data taken at near peak current for shot 2203 shows the beam centroid and radius as a function of Z.

Implications for Hose Dynamics

The most dangerous instability associated with propagation is the resistive hose instability.[4,5,6,7] This is a m=1 mode associated with finite scalar conductivity, σ. In the beam body with a Bennett[8] beam and conductivity radial

profile and negligible plasma return current, Lee[5] found the instability to be convective not absolute, with small displacements growing from head to tail. The convective nature of the hose instability, due to the anharmonic nature of the Bennett confining potential, made possible the 9-m propagation of the RADLAC II beam The situation is complicated by the dynamics in the beam head where parameters are changing rapidly (χ<1) in time and space. For low beam energy and current, the dynamics in the electrostatic region of the beam, where the charge neutralization time τ_c (=1/4$\pi\sigma$) > R/c and magnetic effects are small, are also important.

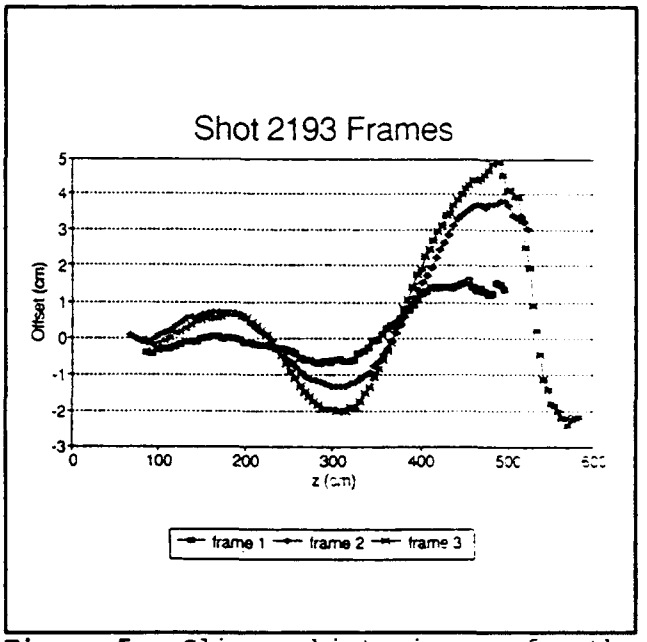

Figure 5 Slice histories of the propagating beam show growth of the hose instability in time and space.

A self-pinched REB propagating in the atmosphere expands due to elastic collisions with background nuclei. For the high currents produced by the RADLAC II accelerator, inelastic collisions which tend to shrink the beam radius are also important. These collisions act to slow down a relativistic electron, removing momentum along the electron trajectory (the finite angle scattering from these collisions is already included in the Nordsieck calculation). Accounting for these effects, the Nordsieck length becomes

$$L_N = \frac{L_{Nel}}{1 - \gamma_{ie} L_{Nel}/2\gamma} \qquad (1)$$

where γ_{ie} is the rate of change in beam γ due to inelastic collisions (ignoring bremsstrahlung emission roughly .006 1/cm-atm). L_{Nel} (≈60$\nu_n\gamma$, where ν_n is the net current normalized by 17 kA) is the Nordsieck length due to elastic collisions only. Eq.(1) shows that for sufficiently high ν_n, the beam radius will actually decrease with distance (negative L_N). For the RADLAC II parameters(ν_n = 1-2), the inelastic collision term enhances the

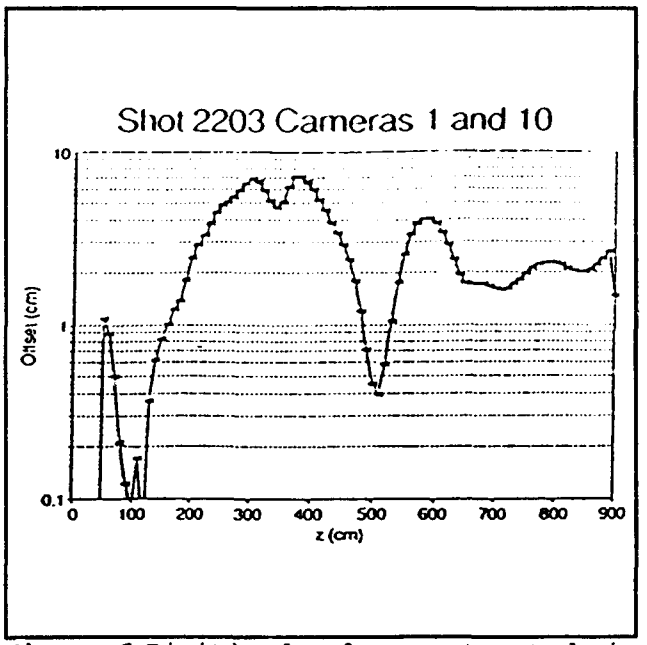

Figure 6 Digitized and reconstructed air fluorescence data shows growth and damping for shot 2203.

Nordsieck length 20-50%.

Beam expansion can have stabilizing or destabilizing effects on the resistive hose instability. A given hose mode is effectively detuned by the rapidly changing beam frequency caused by Nordsieck expansion. From Eq.(1), χ is given approximately by

$$\chi = \frac{10 v_n^{1.5} \gamma^{0.5}}{R\rho(1-0.18v_n)} \qquad (2)$$

where ρ is the pressure in atmospheres. For $\chi >> 10$, air scattering has little impact on the hose dynamics since the beam λ_β changes little on the time scale of an oscillation. For typical RADLAC II shots, the beam body has a $\chi > 20$, however, χ varies from the beam nose to the body with scattering becoming increasingly important near the beam nose.

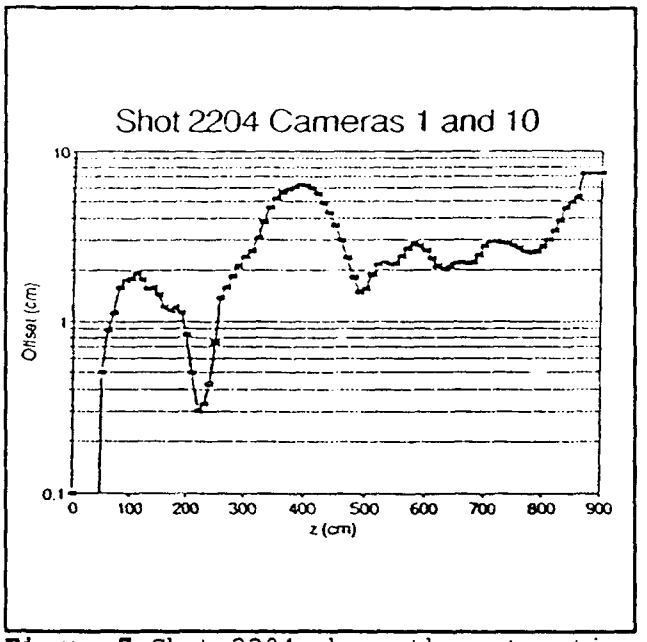

Figure 7 Shot 2204 shows the saturation of high-frequency hose with some low-frequency growth late in z.

In the past several years, we, and others, have noted low-frequency laboratory-frame oscillations which did not saturate for lower energy beams in experiment and simulation despite the prediction of convective behavior from classical hose theory. Initial IPROP[9] three-dimensional simulations of a RADLAC II beam with 5-Mev energy in the beam front and a 20-MeV maximum, a 30-kA maximum current and a minimum 1.5-cm radius, we noted that a very low frequency oscillation, which did not saturate, dominated the classical high-frequency hose behavior. These oscillations originated in the beam nose where the effects of air scattering were significant (χ < unity). This behavior suggested that hose can be re-excited by a coupling to the expanding beam head. Increasing the energy in the beam nose, as well as higher currents, were seen to produce hose saturation as predicted in classical theory. Furthermore, simulations of the 100-kA HERMES II beam with energy ramping up from 0 to 10 MeV in 100 ns and a 7-10 cm minimum radius showed remarkable stability despite the 200-ns pulse duration. We observed hose growth as low as a factor of 5 compared with 100-400 for the RADLAC II case. In the HERMES II case, $\chi < 0.2$ in the beam nose but as high as 20 in the body. The rapid blow off of the head eliminated the coupling to hose seen in the RADLAC II simulations.

Essentially, if a beam slice near t_e, defined as the time at which $\tau_c = R/c$, has χ near unity, the beam nose will drift due to a rapidly decaying transverse restoring force. Hence, the entire beam will experience a growing oscillation with a frequency characteristic of the beam nose. In order to test

this theory, we must determine $\chi(t_e)$. $\chi(t_e)$ may be estimated from known beam parameters by assuming the beam has a linearly rising current, dv/dt, and has a time dependent radius profile $R(t)=(Rt)_e/t$, where $(Rt)_e$ is the product of radius and time at t_e. Since return current is small for $t < t_e$, $\nu_n(t_e) \approx \nu(t_e)$, thus, we only need determine t_e. In the beam head for pressures near 1 atmosphere, the conductivity production rate is proportional to the current density $J_b=4\nu/R^2$ (a 4π factor is included). As a function of t, τ_c^{-1} is then given by

$$\tau_c^{-1}=c\int_0^{t_e}\lambda J_b(t)\,dt, \tag{3}$$

where λ = 0.466 for a 10 MeV beam from Bethe's electron energy loss formula[10] and assuming all the energy is deposited locally into ionization. Integrating Eq.(3) and assuming that t_e is determined precisely when $\tau_c(t_e)$ = R/c (shown to be a good approximation[11]) yields,

$$t_e=\left[\frac{c^2(Rt)_e}{\lambda d\nu/dt}\right]^{1/3} \tag{4}$$

which gives $\nu_n=((d\nu/dt)^2(Rt)_e/(c\lambda))^{1/3}$. We may now use this expression for ν_n in Eq.(2) to determine $\chi(t_e)$. For all these shots, the maximum radius measured with streak camera at 1.5 m is 5.5-6.2 cm. Using $(Rt)_e$ = 15 cm-ns gives $R(t_e)$ of this order with $t_e \approx$ 2-2.5 ns. We note, however, the model results are relatively insensitive to $(Rt)_e$ and use this value in the model for all shots. The experimental data and model results for six RADLAC II shots are given in Table II. We first note the strong correlation between $\chi(t_e)$ and the observation of hose saturation. For $\chi(t_e) < 1$, the hose does not appear to saturate. Shots 2193, 2203, and 2204 demonstrate the most classical behavior. We see good agreement between the observed oscillation wavelengths of these three shots (3-4 m) and those calculated in the model. For the other three shots, the oscillation wavelengths were quite long, > 5m, suggesting that the beam nose is indeed drifting as we predicted.

Table 2. Experimental data, simulation and model results.

Shot	$R(t_e)$ (cm)	dv/dt (ns^{-1})	$\nu_n(t_e)$	$\chi(t_e)$	$\lambda_\beta(t_e)$ (m)	Comments
2181	6.2	0.075	0.18	0.85	3.7	Ambiguous
2183	5.6	0.060	0.16	0.69	4.0	No saturation
2193	5.9	0.102	0.22	1.14	3.3	Saturation nonlinear?
2200	NA	0.072	0.18	0.82	3.8	Ambiguous
2203	6.0	0.138	0.24	1.30	3.2	Strong saturation
2204	NA	0.087	0.20	0.98	3.8	Saturation

sim1	6.3	0.219	0.37	2.12	3.0	10 MeV min. energy. Saturation
sim2	7.3	0.219	0.37	1.35	2.4	5 MeV min. energy. Weak saturation
sim3	8.4	0.088	0.20	0.48	3.7	20 ka peak current. No saturation

We have seen hose behavior similar to the RADLAC II experiment in IPROP simulations with various energy and current temporal profiles. IPROP is a three-dimensional particle-in-cell code which is Fourier analyzed in the azimuthal direction. The conductivity is calculated with an air chemistry package which self-consistently models effects such as ionization and recombination with rate equations. The relativistic electron beam was given a sinusoidal offset perturbation in the x plane with 45 MHz frequency and a 0.005-cm amplitude at injection. The current and energy linearly ramped to maximum in 13 ns. The radius was injected with the temporal profile, $R(t)=3.7(1+\exp(-t/13\ ns))$ cm. The normalized emittance was held constant such that the beam body was injected in equilibrium. The three simulations, the first with a 10 MeV minimum energy and 50 kA peak current, the second with 5 MeV minimum energy and 50 kA, and the third with a 5 MeV minimum energy and 20 kA peak current, are summarized in Table II.

As in the experiment, we determine the hose behavior by following individual slices of beam and calculating offsets as a function of Z. The growth of perturbation is seen to plateau in the IPROP simulation with little growth observed beyond 12 ns into the pulse. Beyond 12 ns, the beam remains essentially frozen at a given offset due to the large σ and hence large magnetic decay length in the beam body. Thus, the beam energy deposition in the gas which produces measurable air florescence essentially marks the maximum beam displacement. For this reason, the open shutter camera images were quite useful in the experiment for determining hose saturation.

The most classical hose behavior (χ = 2 from the model) was observed in simulation sim1 which had the faster rising current and energy. As seen in Figure 8, the offset of 20-ns beam slice grows until roughly z = 550 cm and damps at greater Z in rough agreement with shots 2193, 2203 and 2204. The dominant wavelength for the hose motion is 4 meters, close to that seen in the experiment. A 90 MHz perturbation was calculated to require a longer distance to saturate. This behavior suggests that high-frequency perturbations in the RADLAC II experiment were small. The sim2 and sim3 simulations had reduced beam parameters with χ = 1.35 and 0.48, respectively. The hose growth of the sim2 and sim3 simulations is plotted in Figure 9 for the 17-ns slice. In sim2, the growth in the beam offset saturates weakly with some residual low-frequency motion dominating the high-frequency motion by Z = 7 m. This prevents obvious damping of the offset at late Z. The low current (sim3) simulation showed the least classical behavior with a > 5 m wavelength oscillation growing for all Z. The

IPROP simulations follow the same trend as the experiment, confirming that a sufficiently rapid beam current rise and energy are required to observe classical hose convection.

Conclusions

The RADLAC data demonstrates the predicted stability of high current beam propagation through the atmosphere. On some shots we observed saturation of the resistive hose instability confirming the convective nature of the instability. It is significant that the experiments were performed in a large diameter tank and at atmospheric pressure. Although the beam radius was 3-4 cm, the stabilizing the effects of air scattering were insignificant since the high net current gave $\chi > 20$.

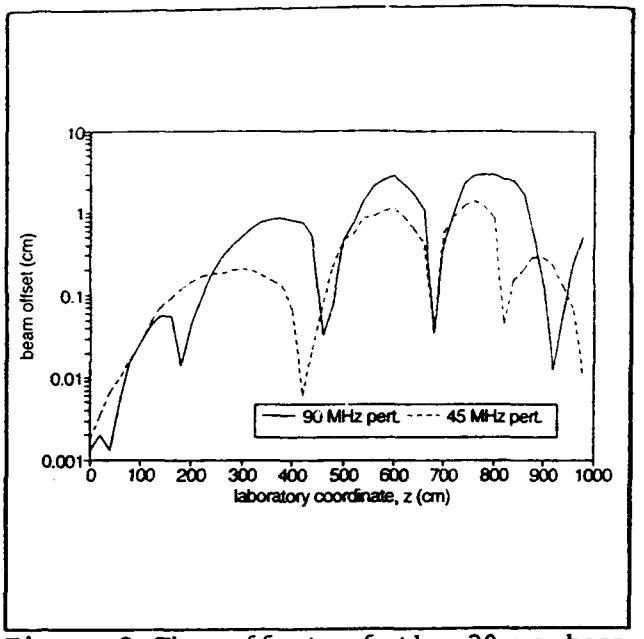

Figure 8 The offset of the 20-ns beam slice in sim1 is plotted as a function of distance for 45 and 90 MHz perturbations.

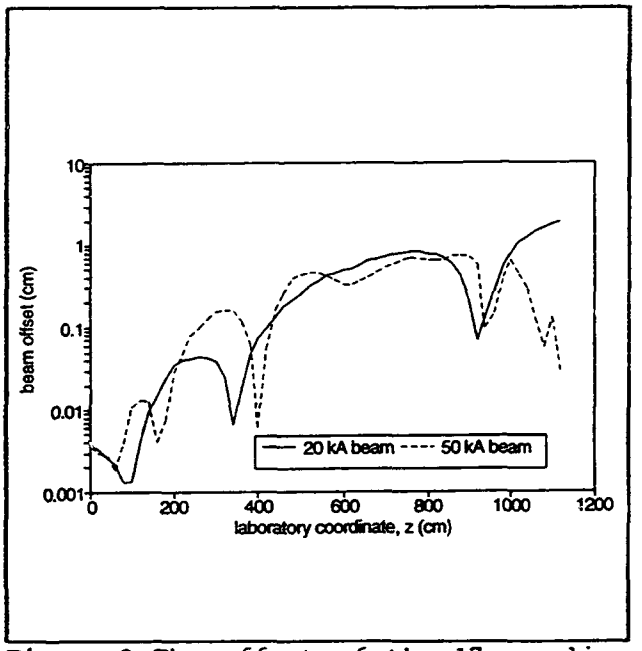

Figure 9 The offset of the 17-ns slice for sim2 and sim3 simulations are plotted versus distance. The results are for the 45-MHz perturbation.

Acknowledgements

The authors owe a sincere debt of gratitude to the RADLAC operations crew for years of dedicated service above and beyond the call of duty which made this difficult experiment successful, and to Ken Prestwich and Pace VanDevender for their advice, encouragement, and steadfast support throughout this endeavor.

*This work performed at Sandia National Laboratories supported by the U. S. Department of Energy under contract DE-AC04-76DP00789.

References

1. M.G. Mazarakis, et al., "SMILE: A Self Magnetically Insulated Transmission Line Adder for the 8-Stage RADLAC II Accelerator," *Proceedings of the 8th International Pulsed Power Conference*, IEEE91CH3052-8, P.89.

2. M. Lampe, "Propagation of Charged Particle Beams in the Atmosphere," NRL Memo Report 6159, 1988.

3. J.J. Ramirez, K.R. Prestwich, E.L. Burgess, J.P. Furaus, R.A. Hamil, D.L. Johnson, T.W.L. Sanford, L.O. Seamons, L.X. Schneider and G. A. Zawadzkas, *Digest of Technical Papers of the 6th IEEE Pulse Power Conference*, edited By B. H. Bernstein and P. J. Turchi (IEEE, New York, 1987), IEEE Catalogue No. 87CH25221, pp. 294,299.

4. M. N. Rosenbluth, Phys. Fluids **3**, 932 (1960).

5. C. S. Weinberg, J. Math. Phys. **5**, 1371 (1964).

6. E. P. Lee, Phys. Fluids **21**, 1327 (1978).

7. H. S. Uhm and M. Lampe, Phys. Fluids **23**, 1574 (1980).

8. W. H. Bennett, Phys. Rev. **45**, 890 (1934).

9. B. B. Godfrey and D. R. Welch, "The IPROP Three-Dimensional Beam Propagation Code," *Twelfth Conference on the Numerical Simulation of Plasmas*, (Lawrence Livermore Laboratory, San Fransisco, CA), 1987.

10. R.D. Evans, The Atomic Nucleus (McGraw-Hill, New York, 1955), Ch. 18, Sec. 2g. H. A. Bethe, Z. Physik **76**, 293 (1932).

11. T.W.L. Sanford, J. A. Halbleib, W.H. McAtee, K.A. Mikkelson, R.C. Mock, J.W. Poukey and D.R. Welch, J. Appl. Phys. **70**, 1778 (1991).

GENERATION, CONTROL, AND TRANSPORT OF A 19-MeV, 700-kA PULSED ELECTRON BEAM*

T. W. L. Sanford, J. A. Halbleib, J. W. Poukey, D. R. Welch†, R. C. Mock††, P. J. Skogmo, and K. A. Mikkelson

Sandia National Laboratories
Albuquerque, NM 87185-5800

Abstract

We show experimentally and theoretically that the generation of the 13-TW Hermes III electron beam can be accurately monitored, and that the beam can be accurately directed onto a high-Z target to produce a wide variety of bremsstrahlung patterns. This control allows the study of radiation effects induced by gamma rays to be extended into new parameter regimes. Finally, we show that the beam can be stably transported in low-pressure gas cells.

Introduction

Hermes III[1] is an electron accelerator that generates a 19-MeV, 700-kA, 25-ns electron beam for the study of radiation effects induced by bremsstrahlung that is produced when the beam interacts in a high-Z target. Hermes III represents a new generation of accelerator design that combines 1-MV pulsed-power technology with linear-induction and magnetically-insulated vacuum line (MITL) technology to obtain an electron beam having a fast rise time and short pulse width at both high kinetic energy (KE) and high current. In this paper, we review the generation, control, and transport of this beam. This research was motivated by the need to provide radiation fields that can be varied from uniform exposure over large areas to intense exposure over small areas.

The electron beam is generated and controlled with either an extended planar-anode (EPA) (Fig. 1A),[2] a gas-cell (Fig. 1B),[3] or a compound-lens diode (Fig. 1C).[4] The EPA and compound-lens diodes are used as injectors into short (Fig. 1B)[3] and long (Fig. 1C)[5] gas cells filled with N_2 at pressures suitable for efficient beam transport. For these diodes and gas cells, we have extensively studied the behavior of the beam when incident on a multi-element calorimeter[5] and on bremsstrahlung targets.[2] These targets, in combination with thermoluminescent dosimeter (TLD) arrays, Compton diodes, Cherenkov photo diodes, and a fast-framing x-ray pinhole camera, are used to measure the radial and angular distribution, temporal dependence, and total energy of the incident beam.[2] Sets of current shunts located in the anode at IA1, IA2, ..., IA4, and in the cathode at IC1 measure the current flowing in the diodes and gas cells. The diode voltage (Fig. 2A) is estimated by combining the current measurements at IA1 and IC1 (Fig. 2B) with parapotential flow theory.[6] CR-39 plastic film placed behind various thicknesses of aluminum measures the range of H^- ions accelerated across the radial anode-cathode (AK) gap and enables an independent bound to be placed on the peak voltage (V_p).[7]

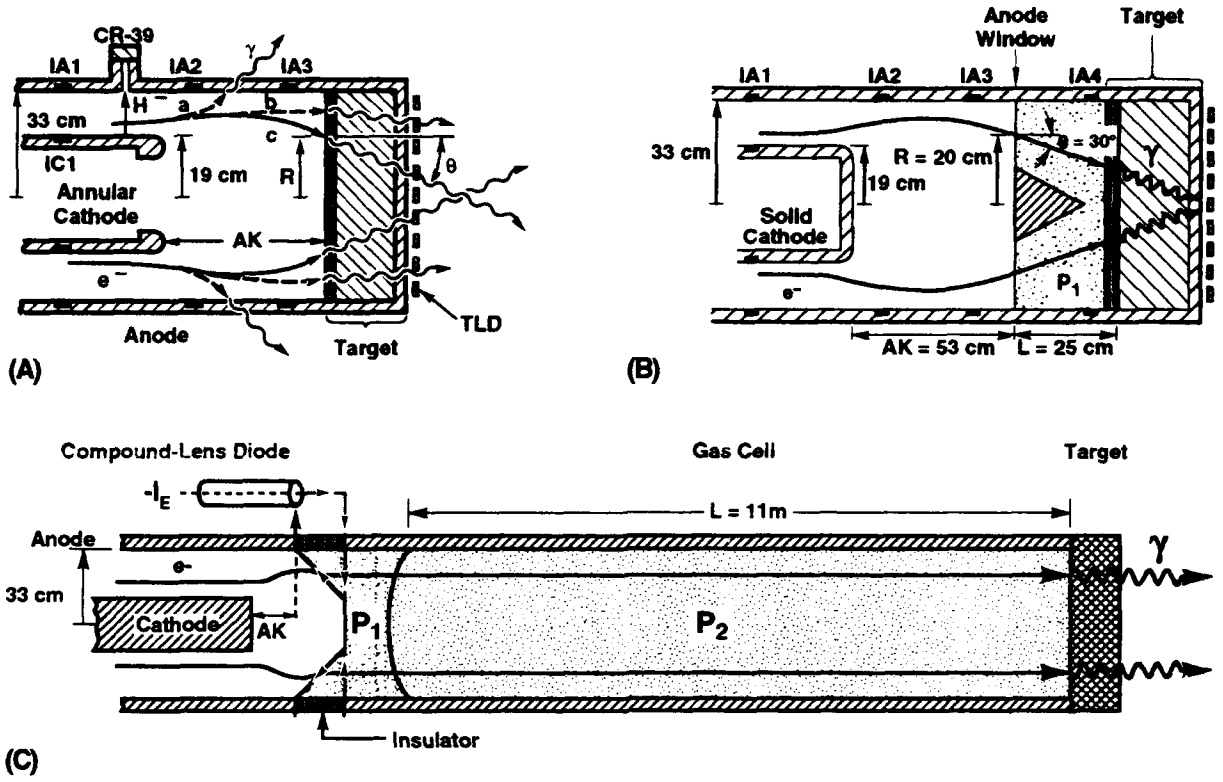

Figure 1. Schematic of (A) EPA diode[2] (showing beam at (a) early or late time, (b) midway through voltage rise or fall, and (c) peak voltage), (B) gas-cell diode[3] in high-intensity configuration,[12] and (C) compound-lens diode[4] used as injector to 11-m long gas cell.[5]

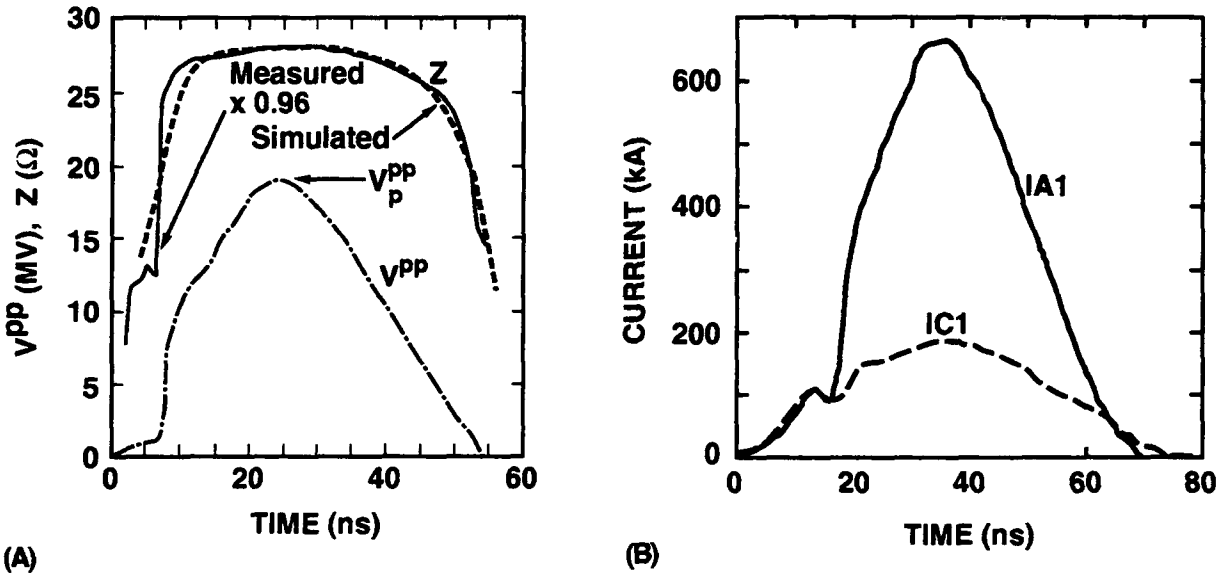

Figure 2. (A) Estimated voltage and impedance at IA1, (B) measured current at IA1 and IC1.

Beam behavior, including detector response, is modeled[2] using the estimated voltage waveform (Fig. 2A) as input to a set of interlinking computer codes: MAGIC,[8] IPROP,[9] IVORY,[10] and CYLTRAN.[11] MAGIC, IVORY, and IPROP are time-dependent, electromagnetic particle-in-cell codes. MAGIC has a 2-D field solver and is used to simulate the electron beam in the coaxial vacuum AK gap of the diode. IVORY has a 3-D vacuum-transport field solver with elastic and inelastic scattering options, including ionization subroutines, and is used to simulate the subsequent beam transport in the gas cells for pressures below 100 mTorr. IPROP has, in addition, a 3-D collisional-transport field solver, including gas chemistry subroutines, which allows for the self-consistent calculation of a tensor conductivity for pressures above 1 torr. It is used to simulate the beam transport in the gas cells above this pressure. CYLTRAN is a 2-D, time-integrated, electron-photon, Monte Carlo transport code from the ITS system, which is used to simulate the electromagnetic shower and radiation detector responses, once the beam has interacted in the target. This numerical modeling gives predictions that are in qualitative agreement with the measurements and provides insight into the underlying dynamics of the beam generation, control, and transport, which we now discuss.

Generation

The 20 induction cavities of Hermes III feed power along the length of a tapered MITL that adds the cavity outputs to generate the total power pulse.[1] The output of this adder MITL is delivered to the electron-beam diode,[2] located inside a shielded test cell, by an extension to the adder MITL. The cathode of the combined MITL is a single cantilevered shank that extends for the 16-m length of the system. MAGIC simulations and measurements (Fig. 2B) show that 75% of the beam electrons in the diode originate from this shank when the diode is matched in impedance to the MITL. Once the electron sheath forms above the cathode, the sheath flow, together with emission near the tip of the cathode, leads to a well-defined annular ring of electrons (current loss front), which then moves toward the diode and target. The notch in the leading edge of the total current pulse measured at IA1 corresponds to this loss front that sweeps down the MITL before magnetic insulation sets in (Fig. 2B). As the voltage and associated current ramp up, this annular ring sweeps radially inward at the target, attains a minimum radius near the time of V_p, and then sweeps radially outward as the voltage ramps down, owing to the time variation of the magnetic pinching force in the AK gap (Fig. 3).

For axial AK gaps larger than the radial AK gap (as is the case for all diodes discussed here), the diode runs in a line-dominated impedance mode.[2] Under this condition, the simulated impedance is in excellent agreement with that obtained by dividing the estimated voltage by the measured current at IA1 (Fig. 2A). This measured impedance of $29.4 \pm 0.3\,\Omega$ at V_p corresponds closely to the 30.6-Ω minimum-current impedance of the MITL from parapotential flow theory, indicating that the diode impedance is matched to the line-limited MITL. For voltages less than the peak voltage, the lower impedance shown in Fig. 2A is due to an increase in the radial extent of the electron flow in the radial AK gap. That the estimated voltage at its peak (VPP_p) corresponds to the peak diode voltage is confirmed when VPP_p is compared with that obtained from either the measured radiation output or with $V_p{}^{H^-}$ obtained from the range of H^- ions (Fig. 4). The excellent correlation shown in Fig. 4 gives additional credibility to using parapotential flow theory to extract diode voltage.

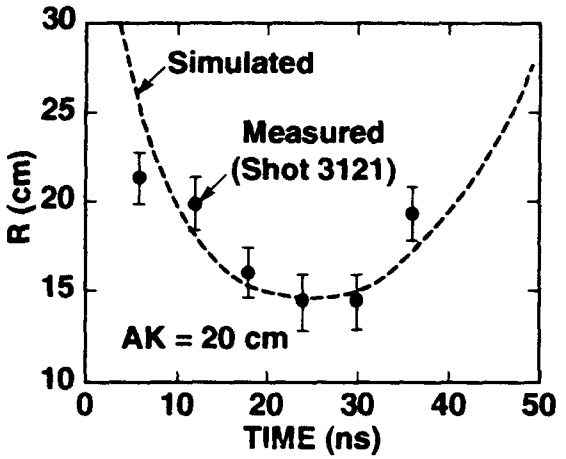

Figure 3. Radius of annular beam at conical anode window of the compound lens versus time for Fig. 1C configuration.

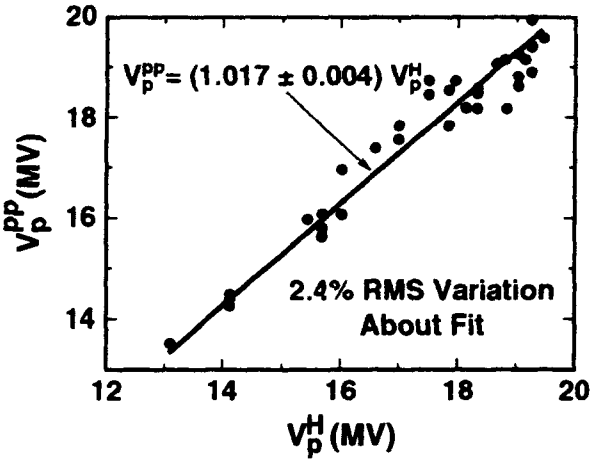

Figure 4. Comparison of peak voltage (Fig. 2A) obtained using parapotential flow theory (VPP_p) with that obtained from H^- range ($V^H_{p)}$.[7]

Control

EPA Diode: The time-averaged radius R and angle θ of the annular beam generated in the EPA diode (Fig. 1A) are correlated at the target. Adjustment of the AK gap over the range 15 to 100 cm enables the annular beam to impact the target over the range R = 11 cm and θ = 45° to R = 30 cm and θ = 8°, respectively (Fig. 5). The practical range, however, is limited to AK gaps between about 40 cm and 70 cm. Below 40 cm, the energy deposition on the surface of the target approaches that which can form an anode plasma, causing the beam to collapse radially and damage the target. Above 70 cm, the beam begins to be lost to the side anode wall and the intensity at the target decreases. For this range, a peak dose rate of 6×10^{12} rad/s over a useful area (area where dose exceeds 50% of the peak dose) of 700 cm^2 down to 3.5×10^{12} rad/s over 1800 cm^2 can be produced at the downstream face of the bremsstrahlung target.

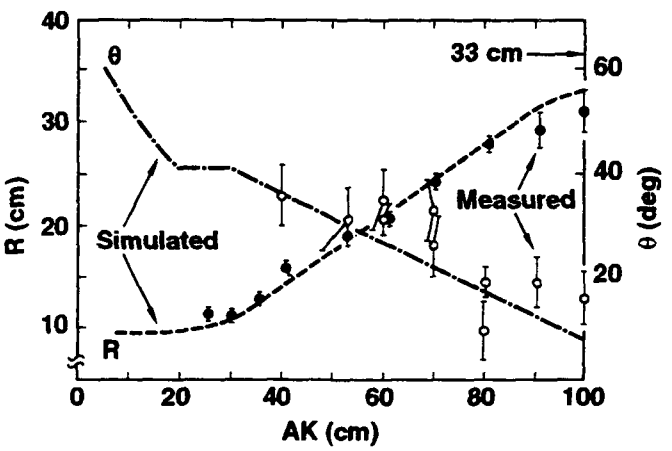

Figure 5. R and θ versus AK gap for Fig.1A configuration.[2]

Gas Cell: By injecting the beam through a thin anode window into a N_2-filled gas cell (Fig. 1B), the R-θ correlation can be changed. At pressures near 3 torr, rapid avalanche breakdown of the gas limits the net current (the beam current minus the plasma current) to 4 to 7% of the injected current near V_p.[3] Owing to the radial distribution of the net-current density, the trajectory of the beam is effectively ballistic at this pressure. Thus, by varying the length (L) of the gas cell, the beam can be made to impact the target at a desired radius (Fig. 6A), for a given incident angle (i.e., for a given AK gap). For example, for the geometry shown in Fig. 1B, the radiation is made to focus at the downstream target face producing a peak dose rate of ~3.5 x 10^{13} rad/s over 80 cm^2 without target destruction, in agreement with predictions (Fig. 7).[12] The cone shown as the shaded structure in Fig. 1B helps stabilize the beam, when operating in this high-intensity configuration. Alternatively, by increasing the gas pressure, the net current and associated azimuthal magnetic field are increased, and the beam can be made to focus in a shorter axial distance (Fig. 6B).

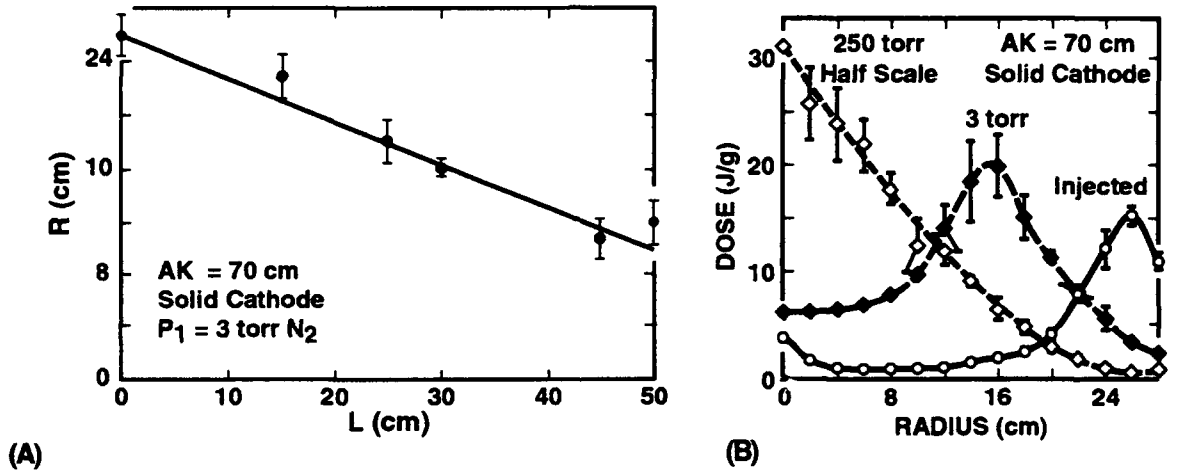

Figure 6. (A) Measured R versus L at exit and (B) comparison of measured radial electron distribution at injection and at L = 30 cm when gas pressure equals 3 torr and 250 torr, for Fig. 1B configuration.[3]

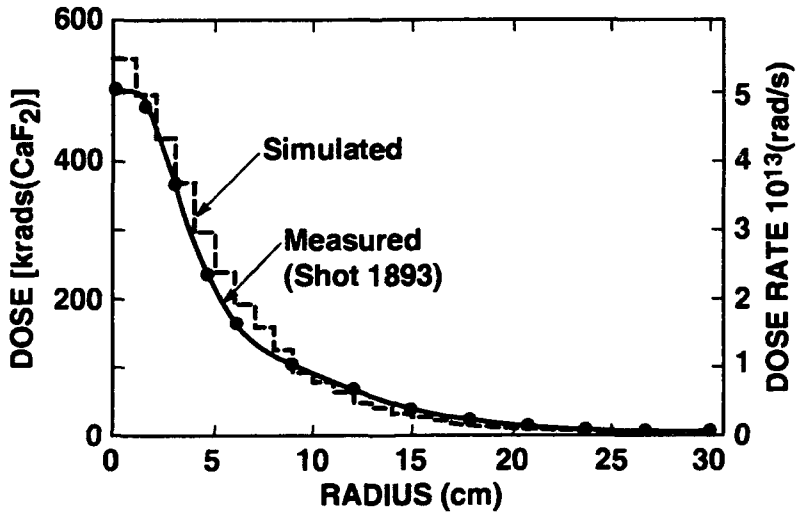

Figure 7. Radial radiation dose profile at downstream target face, for Fig.1B configuration.[12]

Compound Lens: In the above example, the radial pinch is used to generate the intense source. In general, however, the pinch (which restricts the angle of incidence to values greater than about 20°) degrades the uniformity of the radiation with depth that can be achieved with the EPA diode. Reducing the pinch angle of the beam at the target for a given radius of impact is the key to improving the radiation uniformity with depth. By introducing the compound-lens diode, the beam can be turned through any angle (without current loss to the side anode wall by the time V_p is reached). Excellent uniformity is achieved when the angle is made normal to the target.[4]

The operation of this diode is illustrated in Fig. 1C. In the diode, the beam is incident on a thin conical anode foil followed by a low-pressure gas cell and bremsstrahlung target. N_2 gas at 3 torr provides rapid charge and current neutralization of the incident beam, as in the above short gas cell. When an external current (I_E) is applied as shown in Fig. 1C, an azimuthal magnetic field is generated. By adjusting I_E, the beam can be made to impact the target at the desired angle (Fig. 8). Because the applied magnetic field decreases inversely with the radial distance from the axis, the curvature of the electron trajectories at smaller radii is greater than at larger radii. Additionally, the angle of the electrons at the anode increases with radial distance from the axis. By angling the entrance window (anode) of the gas cell as shown, the electrons at larger radii remain in the magnetic field longer, and the simultaneous effects of the decrease in field strength and higher injection angles at large radii are partially compensated. Also, the electrostatic force generated in the diode with the conical anode surface reduces the pinch angle at the anode. Because of the two-component mechanism for controlling the beam (electrostatic from the orientation of the conical surface and magnetic from I_E), the diode is called the compound lens. As with the EPA diode, adjustment of the AK gap permits selection of the desired radial impact position .

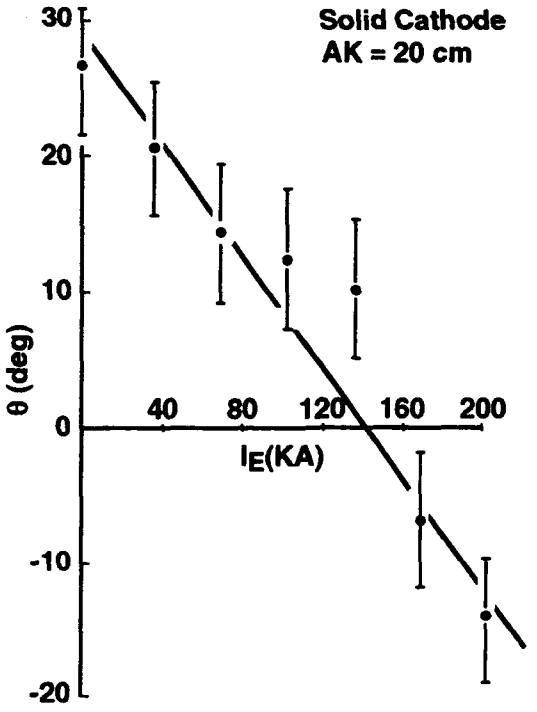

Figure 8. Measured θ versus I_E for compound-lens diode of Fig. 1C.

Transport

As has also been demonstrated with lower-power electron beams,[13] measurements and IPROP simulations show that a substantial fraction of beam can be transported in long gas cells (Fig. 1C), and that potential resistive instabilities such as hose, hollowing, and filamentation do not increase the beam emittance to the degree where prohibitive losses to the side wall occur. Specifically, when using the EPA diode as an injector to a 11-m long cell, a 70-cm AK gap and 100 torr maximizes the energy transport efficiency at 71 ± 2.4% (Fig. 9).[5] The optimum at 70 cm is a result of a balance between improving the transport efficiency by minimizing the injection angle into the cell versus minimizing the losses to the side anode wall of the diode just upstream of the entrance window. The optimum at 100 torr is a result of a balance between improving the trapping efficiency due to the magnetic pinch force generated by the residual net current after the beam passes through its first axial focus in the cell and minimizing the energy loss due to inelastic collisions and instabilities.

By replacing the EPA diode with the compound lens, we can achieve normal injection angles. Under these conditions, a pressure of 20 torr maximizes the transport efficiency at 90 ± 8% (Fig. 9). This improved efficiency is the result of being able to reduce the gas pressure and the associated net current and self-magnetic field necessary to contain the decreased dispersion of the beam. The reduction results in decreased collisional and inductive losses and improved beam stability. Under these conditions, an annular beam is often observed at the target (Fig. 10A) in agreement with that predicted by the MAGIC-IPROP simulations. The annulus is the result of an enhancement of the plasma return current near the axis, which repels the beam from that region. This enhancement is due to strong electron avalanche driven by induced electric fields that peak on axis.

By reducing the pressure further, a second transport window is found between 1 and 100 mTorr (Fig. 9). MAGIC-IVORY simulations show that this window is due to transport in the ion-focused regime.[14] Here, the beam remains near the entrance foil until sufficient ionization of the gas has taken place and the plasma electrons have been expelled, enabling the beam to begin to propagate. Further propagation is allowed by production of an ion column dense enough so that the magnetic pinch force dominates the electric repulsion due to beam charge minus ion charge. In this regime, the radial beam profile at the target (Fig. 10B) is that of a pinched beam, because the target shorts out the radial electric field.

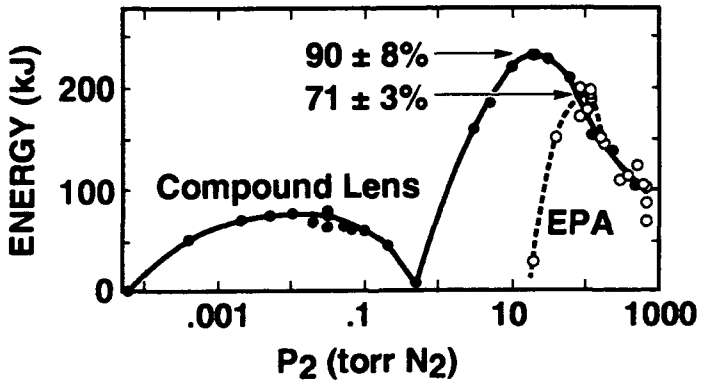

Figure 9. Energy transported in 11-m gas cell versus gas pressure and injection diode.

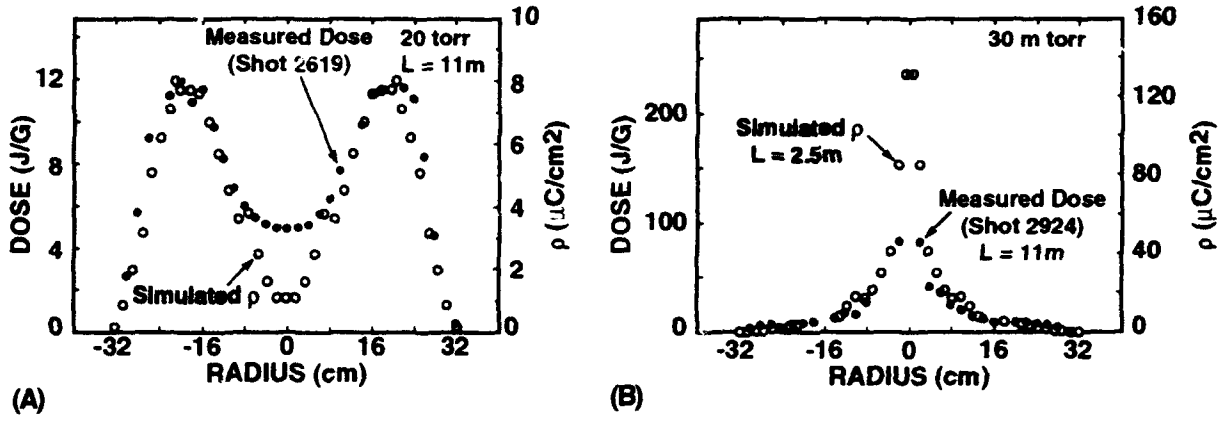

Figure 10. Radial electron profiles at target of the Fig. 1C configuration for gas pressure equal to (A) 20 torr and (B) 30 mTorr.

Summary

The modeling and diagnostic tools developed here enable the generation of high-power electron beams to be accurately monitored. The beam control developed enables peak dose rates to be generated from as high as 3.5 x 10^{13} rad/s down to 3.5 x 10^{12} rad/s over useful areas ranging from 80 cm^2 up to 1800 cm^2 at the downstream target face, respectively, without target destruction. Lastly, this research shows that gas cells provide a relatively simple and efficient method for focusing or transporting high-power electron beams.

References

1. J. J. Ramirez, et al, *Proceedings of 7th International Conference on High-Power Particle Beams*, Karlsruhe, Germany, edited by W. Bauer and W. Schmidt (Kernforschungszentum, Karlsrule, 1988), 148.
2. T. W. L. Sanford, Phys. Fluids **B3**, 2386 (1991) and references therein.
3. T. W. L Sanford, J. W. Poukey, R. C. Mock, and D. R. Welch, J. Appl. Phys. **71**, 472 (1992).
4. T. W. L. Sanford, J. A. Halbleib, W. H. McAtee, K. A. Mikkelson, R. C. Mock, and J. W. Poukey, J. Appl. Phys. **69**, 7283 (1991).
5. T. W. L. Sanford, J. A. Halbleib, W. H. McAtee, K. A. Mikkelson, R. C. Mock, J. W. Poukey, D. R. Welch, J. Appl. Phys. **70**, 1778 (1991).
6. J. M. Creedon, J. Appl. Phys. **46**, 2946 (1975); **48**,1070 (1977).
7. T. W. L. Sanford, et al, *9th Topical High-Temp. Plasma Diagnostics Conf.*, Santa Fe, NM (March 15-19,1992), in press Rev. Sci. Instru. (Oct. 1992).
8. B. Goplen, et. al, Mission Research Corp. MRC/WDC-R-068, (1983).
9. B. B. Godfrey and D. R. Welch, *12th Conf. on Numerical Simulation of Plasmas*, Lawrence Livermore National Laboratory, San Francisco, CA (1987).
10. M. M. Cambell, B. B. Godfrey, and D. L. Sullivan, Mission Research Corp., AMRC-R-454 (1988).
11. J. A. Halbleib and T. A. Melhorn, Nucl. Sci. Eng. **92**,338 (1986).
12. T. W. L.Sanford, J. A. Halbleib, D. E. Beutler, W. H. McAtee, R. C. Mock, and, D. P. Knott, IEEE Trans. Nuc. Sci., **NS-38**,1195 (1991).
13. R. B. Miller, *An Introduction to the Physics of Intense Charged Particle Beams* (Plenum, New York, 1982), Chap. 5.
14. W. E. Martin, G. J. Caporaso, W. M. Fawley, D. Prosnitz, A. G. Cole, Phys. Rev. Lett. **54**, 685(1985)

†Mission Research Corp., Albuquerque, NM.
††Ktech Corp., Albuquerque, NM.

*This work was performed under U.S. Dept. of Energy Contract No. DE-AC04-76DP00789.

RECENT RESULTS ON THE GOL-3 DEVICE

A.V.Arzhannikov, A.V.Burdakov, V.V.Chikunov, A.F.Huber, A.V.Karyukin, V.A.Kapitonov, V.S.Koidan, S.V.Lebedev, K.I.Mekler, P.I.Melnikov, A.A.Nikiforov, V.S.Nikolaev, V.V.Postupaev, D.D.Ryutov, E.P.Semenov, S.L.Sinitskij, M.A.Shcheglov, S.G.Voropaev, and M.V.Yushkov

Budker Institute of Nuclear Physics, 630090, Novosibirsk, Russia

ABSTRACT. The review of activity on the GOL-3 program is presented. The first part of the results is concerned with the experiments on the uniform plasma heating by a 100 kJ E-beam. Heating of the bulk plasma electrons up to 1 keV at 10^{15} cm^{-3} density is achieved. The second group of experiments deals with so-called "two-stage" dense plasma heating. The 10^{16}- 10^{17} cm^{-3} hydrogen bunches of 0.5-3 m length are produced by gas-puffing. High efficiency of the conversion of the energy, delivered by E-beam to 10^{15} cm^{-3} background plasma occupying the rest of the device, to the dense plasma bunches, is demonstrated. Last part of the paper describes activity on the microsecond ribbon E-beam of 4x140 cm^2 cross section and of 200 kJ energy content on the U-2 generator. The transportation of such a beam at 2 m distance in a slit vacuum channel and its shape transformation to a circular one is achieved.

I. INTRODUCTION

The GOL-3 device is designed for the study of dense (10^{15}-10^{17} cm^{-3}) plasma heating by high-power relativistic electron beams of a microsecond duration, and also for subsequent studies on multimirror confinement of a dense hot plasma [1].

The plasma that can in principle be obtained in this device after raising the beam energy content up to design value 0.5 MJ is of interest for the broad spectrum of applications, like controlled fusion, pulsed neutron sources, X-ray flash lamps, UV lasers etc. Presently the experiments are carried out at the first stage of the device with the beam energy content up to 100 kJ. First results of these experiments were presented at BEAMS-90 conference at Novosibirsk [2]. Main progress in the GOL-3 experimental program since that conference has been made in three directions:

i) more comprehensive experimental analysis of collective interaction of the electron beam with a uniform plasma of 10^{15} cm^{-3} density with direct measurements of the most important plasma parameters;

ii) realization of the earlier suggested so-called two-stage heating scheme [3] of the much denser (10^{16}-10^{17} cm^{-3}) plasma that allowed to considerably increase plasma energy density;

iii) development of the second beam generator based on the principle of extraction of a ribbon beam from the foilless diode with its successive transformation to the circular, thus approaching to 0.5 MJ beam energy content.

II. GOL-3 DEVICE AND DIAGNOSTICS

The first stage of the GOL-3 facility is described in previous papers [1,2]. Fig.1 shows the schematic of the experiments on this device. It consists of an electron beam generator U-3 (see [4]), a plasma chamber [5] inside a solenoid with 6 T field in the 7-m-long homogeneous section and 12 T in the single mirrors at the ends [6]. It also comprises a 10 MJ capacity storage for energy supply of the solenoid [7], and systems of control, monitoring and diagnostics. In the present experiments the electron beam (energy 0.8-0.9 MeV, maximum current density ~1 kA/cm^2, diameter 6 cm, duration 3-5 μs, total beam energy content of 20-90 kJ) was injected into a column of hydrogen plasma of 8 cm diameter and 10^{14}-10^{17} cm^{-3}

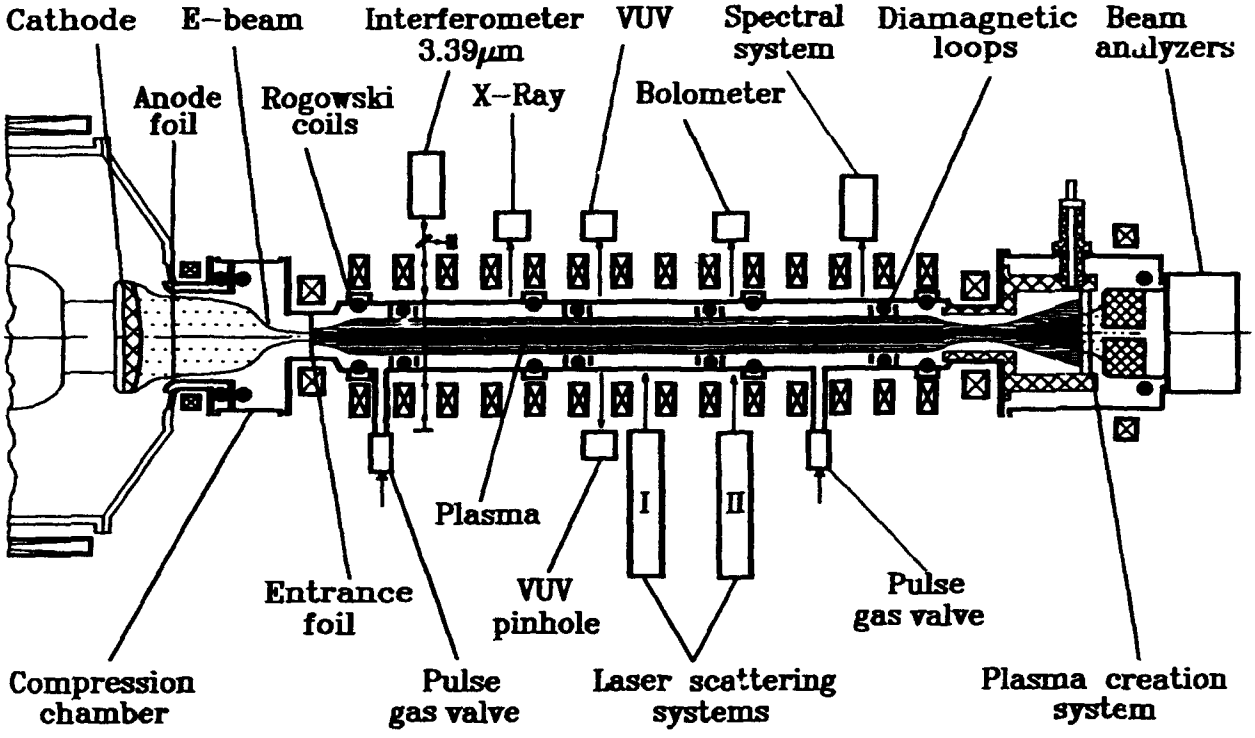

Fig. 1. Layout of the GOL-3 experiment.

density in magnetic field of 5.5 T. Plasma density can be either uniform over the device length or strongly nonuniform in the two-stage heating experiments.

Diagnostics covered a wide set of techniques for both beam and plasma measurements and studies on collective plasma-beam interactions and plasma heating. In the experiments described, the earlier developed diagnostics (see, e.g., [1,2,8-10]) were complemented by two systems of 90° -Thomson scattering of the ruby laser light. One of them at Z=270 cm was intended to measure the density and temperature of the heated electron component in the center of plasma column [11], while the second (at Z=360 cm) was used to measure the radial profile of plasma density.

III. HEATING OF HOMOGENEOUS PLASMA

This part of our work was directed to more detail study of the heating of 7 m long homogeneous plasma column by microsecond E-beam. In previous experiments performed at the GOL-3 device [1,2] it has been shown that the beam can release up to 25% of its energy in plasma under optimal conditions. The diamagnetic measurements have indicated, that some portion of the energy lost by the beam is transferred in plasma heating, the energy in the plasma being confined for rather long time even after the beam injection.

The attention in the performed series of experiments was basically paid to the study of the plasma electron bulk [12]. The energy distribution of the E-beam-heated electrons which was experimentally studied at the previous generation facilities INAR, GOL-1 (see, e.g., [13,14]), is complicated. Together with the bulk Maxwellian electrons there exist suprathermal non- Maxwellian electrons, which may contain a major part of the energy lost by the beam in the plasma. At large beam durations (up to 5 μs in GOL-3 experiments) fast electrons may leave the plasma during the beam injection time, and thus carry away a considerable part of the energy lost by the beam. Nevertheless, the value of the energy left in the plasma by the beam is of special interest, both in its absolute and relative (as compared to the REB energy) value.

The experiments showed that after the beginning of the beam injection the plasma electron temperature increased from 1-3 eV up to 0.5-1 keV. The plasma density in these experiments was 10^{15} cm^{-3}.

Fig. 2 shows the typical time evolution of the effective plasma temperature, obtained from the diamagnetic measurements. The temperature obtained from laser measurements (Z = 270 cm) is shown to be 0.6±0.2 keV in the heating maximum at $(1\pm0.2)\cdot10^{15}$ cm^{-3} density, and the values of the "laser" and the "diamagnetic" temperatures coincide within the measurement accuracy (20%). This allows to suppose, that at other distances from the entrance foil the measured value of the "diamagnetic" temperature is also basically determined by the Maxwellian electrons. In this case, in the vicinity of the device entrance the plasma electron temperature in the heating maximum should be 0.8-1 keV at the given above density.

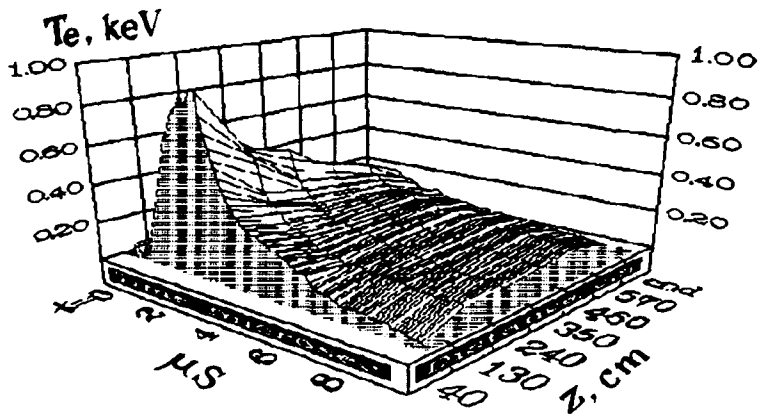

Fig.2. Time evolution of the electron temperature along the device.

An information about suprathermal electrons was obtained mainly by X-ray measurements (see [15]). It was determined that the high-energy "tail" of electron distribution have the mean energy of at least 10 keV and density of these electrons is several percent of plasma one to the end of heating pulse. The instantaneous concentration of suprathermal electrons in the plasma is much less than total amount of such electrons generated during the heating pulse due to non-classical nature of their

scattering (see later) and short transit time. It means that hot electrons can receive a major part of the energy, lost by the beam. Such a situation is favorable for the development of the two-stage scheme of dense plasma heating (see next part).

Axial distribution of the plasma temperature (Fig.2) remains strongly nonuniform during the beam duration. The calculations of heat transport in the plasma [16] show that the experimentally observed pressure distribution cannot be explained by classical heat conductivity. High temperature gradients in the relatively long-lived sub-keV plasma can be maintained if scattering rate of plasma electrons is sufficiently higher than classical one. The heat conductivity suppression in the plasma region near the device entrance should reach a factor of 100-1000 to the beam pulse end (details see in [16]). This anomalous heat conductivity can be accounted for plasma bulk electron scattering on high-level non-resonant Langmuir turbulence.

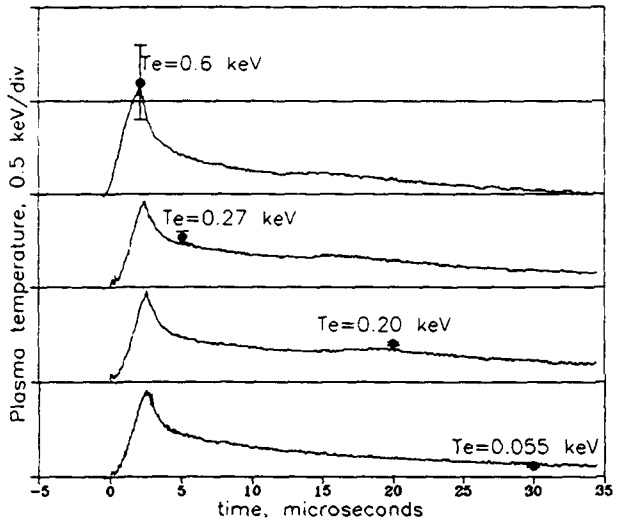

Fig.3. Electron temperature vs. time

After the end of heating pulse the level of plasma turbulence and additional electron scattering decreases rapidly. Thus plasma heat conductivity becomes classical after short time since the beam end. Fig.3 shows the time evolution of the "diamagnetic" electron temperature and Thomson scattering one. This data was compared with the plasma temperature decay calculations based on the classical heat conductivity. In the vicinity of the plasma central cross section the temperature time evolution follows the classical dependence:

$$T = T_{max}/(1+\alpha t)^{2/5},$$

with $\alpha = f(n, Z_{eff})$ calculated for the given point of the device. The measured decay rate of the plasma temperature allows to estimate Z_{eff}, which should be 1.2 - 2 to fit the experimental data.

IV. TWO-STAGE DENSE PLASMA HEATING

Our main goal on the GOL-3 facility is the heating and confinement of a dense ($n_p \sim 10^{17}$ cm^{-3}) plasma so the important part of our researches is to study the two-stage scheme of plasma heating. At the previous conference [2] we have presented the first results of "model" experiments with the use of thin organic foils placed inside plasma column as a "dense" target. The increase of the local energy deposition was observed in these experiments.

Here we present new results on the two-stage heating of plasma with the using of the short but dense (10^{16}-10^{17} cm^{-3}) gas clouds in the long but rare enough (10^{14}-10^{15} cm^{-3}) background plasma column. Detailed discussion of these experiments can be found in [17,18]. Such dense hydrogen clouds were produced by the gas-puffing. For these experiments fast gas valves were installed at 12, 45, 270 and 575 cm distances from the entrance foil (see Fig.1).

The major part of the experiments was performed at a density of background homogeneous plasma of $(3\text{-}5)\cdot10^{14}$ cm^{-3} at which E-beam interacts effectively with plasma. Upon filling the chamber with hydrogen the magnetic field and then pulse gas valves were switched on. After the formation of preliminary plasma by linear discharge the electron beam was injected into the chamber. The gas cloud length, its density and position could be varied.

The measurements by the exit calorimeter and two beam energy analyzers show that the total beam energy losses are up to 20-25% in these experiments that for different shots corresponds to the absolute losses of 10-15 kJ.

Under the conditions of an optimum beam-plasma interaction the bulk plasma electrons of $\sim10^{15}$ cm^{-3} density are heated up to the temperature of 1 keV in the region of maximum energy deposition.

The effect of two-stage heating of the gas bunch is illustrated by Fig.4. The initial gas density distribution is also shown on the Figure. The plasma pressure nT at the point Z=40 cm (near the maximum of cloud density) becomes 3-4 times higher compared to that of homogeneous plasma. With the cloud length of ~50 cm the pressure achieves its maximum of $nT=2.7\cdot10^{18}$ eV/cm^3 at local plasma density of $\sim2\cdot10^{16}$ cm^{-3}.

With the change of the initial cloud length the region of maximum pressure follows the cloud boundary siding with background "rare" plasma. The plasma pressure inside the cloud is lower but always it exceeds substantially the pressure obtained with the direct beam-plasma interaction at such cloud density. A substantial increase of plasma cooling time inside the cloud is also observed. This is apparently related to a decrease of electron thermal conductivity to the ends because of the plasma density growth and decreasing of its temperature.

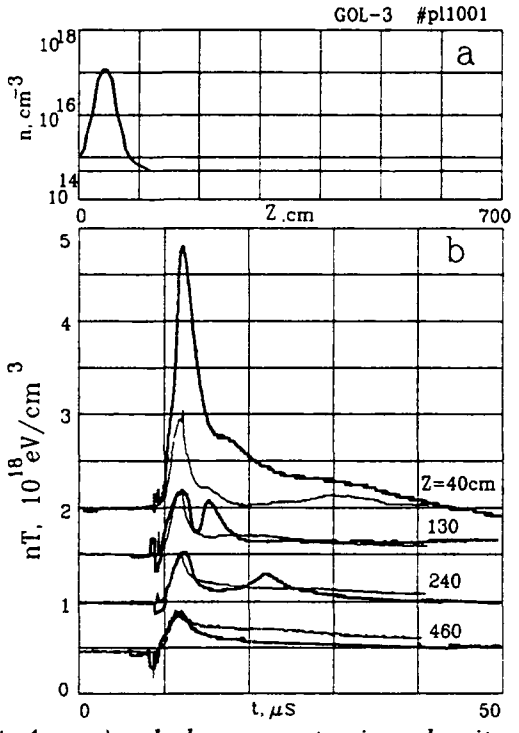

Fig.4. a) hydrogen atomic density distribution over the device length for short cloud; b) plasma pressure over the plasma column length. Thin lines mark the case of injection into homogeneous plasma

Fig.5 shows the plasma parameters both in the dense bunch and homogeneous plasma obtained from the diamagnetic and Thomson scattering measurements. For the given case of long cloud the peak electron temperature T_e reaches ~0.2 keV at $6\cdot10^{15}$ cm^{-3} density at the point of laser measurements (Z=270 cm). Changing the initial density distribution the electron temperature can be obtained from 0.1 to 0.3 keV with 10^{16} cm^{-3} to $3.5\cdot10^{15}$ cm^{-3} density in this point. The electron and ion temperatures are supposed to be equal in the denser cloud regions with $n_e>10^{16}$ cm^{-3}.

The background plasma density was also varied. If it exceeds 10^{15} cm^{-3}, the energy transfer to the cloud sharply falls down due to the decrease of the efficiency of beam interaction with the background plasma (see Fig.6).

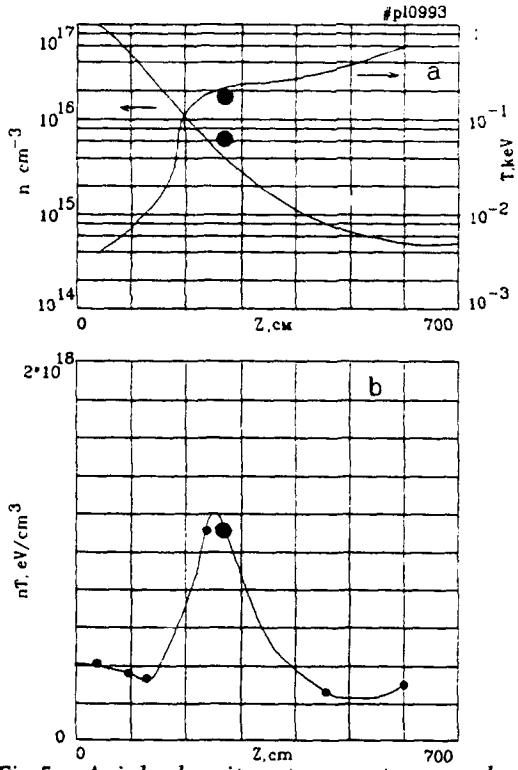

Fig.5. Axial density, temperature and plasma pressure distributions. Dots - Thomson scattering data.

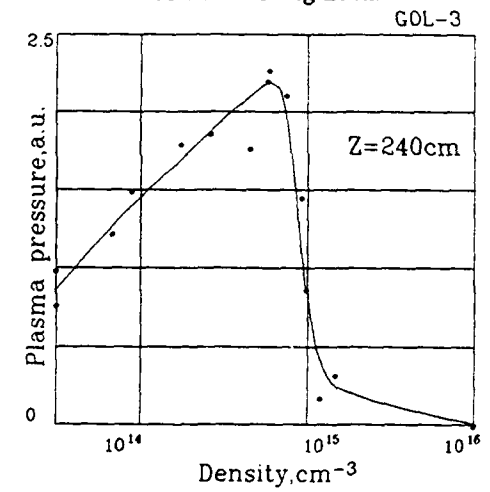

Fig.6. Plasma pressure inside the cloud vs. background plasma density.

When the initial cloud fills in a substantial part of the chamber the region of effective interaction becomes small. The heating efficiency falls down and consequently, the lower fraction of the beam energy is transferred to the cloud by the hot plasma electrons.

In the experiments with single dense cloud a substantial part of the energy lost by the beam leaves the trap during the beam pulse through the output mirror without dense plasma bunch.

Let us consider shortly dynamics of dense plasma bunch. The expansion rate of the gas cloud substantially changes with the start of heating. A complex picture of the plasma flow and pressure waves generation with the secondary maxima on the diamagnetic signals is observed after the beam injection ending (Fig.7).

Analysis of experimental data shows that several waves are generated in the dense plasma. Two waves propagate from the region with the peak pressure, one into the cloud depth (toward increasing density) and other into the region of background plasma (toward decreasing density). One more wave moves from the device entrance into the dense plasma.

The complete two-stage heating scheme was realized with two dense plasma bunches near the device ends. Fig.8a shows axial gas density distribution for this case. The beam deposits its energy in a middle part of plasma column with $5 \cdot 10^{14}$ cm^{-3} density. Than energy delivered by the beam to the hot plasma electrons is absorbed by the dense plasma clouds (Fig 8b).

Thus, the feasibility of the two-stage heating of dense plasma has been experimentally demonstrated in the experiments with the dense plasma bunches.

V. RIBBON BEAM RESEARCHES

This activity on the U-2 machine is directed to the development of physics and technology of the generation, transport and conversion of a high-power ribbon beams. Such beams have large energy content and permit to realize a successive injection into GOL-3 facility at the total energy content up to 0.5 MJ (see [1]). In the previous conference we have reported about the generation of the 150 kJ ribbon beam [2,19].

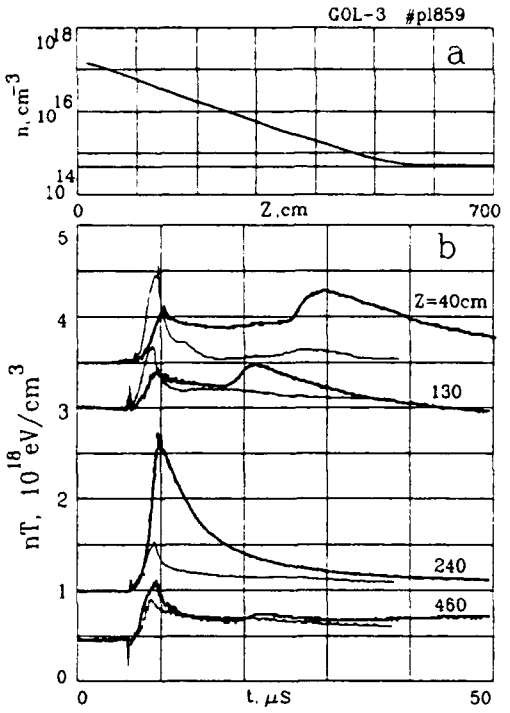

Fig.7. a) hydrogen atomic density distribution over the device length for long cloud; b) plasma pressure over the plasma column length. Thin lines mark the case of injection into homogeneous plasma.

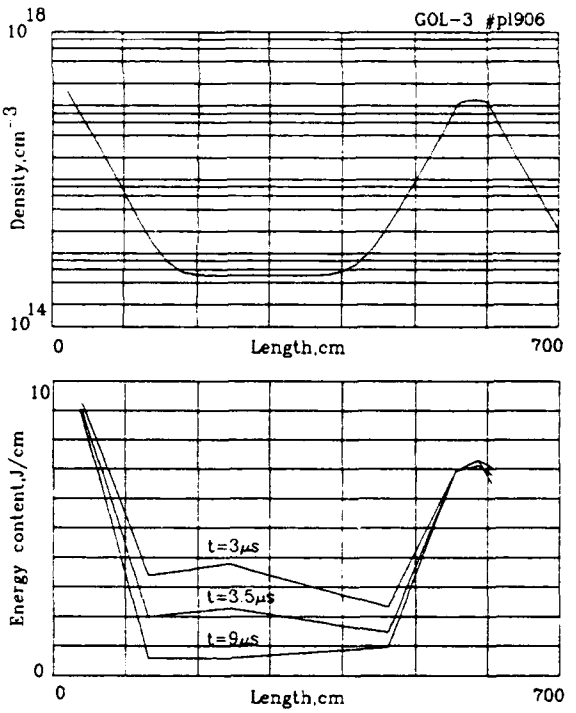

Fig.8. Experimental results with two dense clouds: a) hydrogen atomic density distribution over the device length; b) plasma energy content along the device.

Schematic of U-2 experiments may be described in the following way (see [20]). A strongly elongated cathode made of fibrous graphite material has the length 140 cm and the width 4.5 cm. A slit with sizes 5 by 140 cm sawn in a graphite plate, is operated as an anode of a magnetically insulated diode. An electron flow emitted from the cathode, comes through the anode and passes to a slit vacuum channel with inner sizes 6 by 145 cm. A residual gas pressure in the vacuum channel is about $4 \cdot 10^{-3}$ Pa. The magnetic field strength in a homogeneous part of the slit transport channel may be varied from 0 to 0.5 T. The total beam energy in various parts of the device are calculated by integration over the time of a product of the diode voltage and an appropriate current. In addition, the total energy of the beam at the exit of the channel is measured by a collector-calorimeter.

In the first series of the experiments the electron beam passed only through the slit vacuum channel with the length 2 m. When capacitors of the pulse generator accumulates the electric energy 185 kJ, the energy picked out in the accelerator diode was ~150 kJ and the beam energy at the exit of the channel measured by the calorimeter was ~120 kJ. As a result the efficiency of the U-2 device at the ribbon beam generation and transportation was about 60%.

After the experiments which have shown the high efficiency of the large ribbon beam generation and transport, we have placed on the U-2 setup a special transforming unit and a beam compression system. Magnetic coils of the transforming unit provide the necessary transformation of the magnetic flux cross section. The process of the beam cross section transformation has been checked by the imprints of the beam on the plastic films placed in various points along the beam trajectory. These imprints have shown that in the slit channel with the magnetic field 0.3 T the beam cross section has 3.5x130 cm dimensions,

after transforming the cross section shape is close to a rectangle with dimensions 13.5 by 23 cm, and then after the compression it looks like an ellipse with the largest dimension about 9 cm in the magnetic field 4.5 T. The total energy of the compressed beam is about 100 kJ.

Besides the total beam energy, the current density and the angular spread of the beam electrons are important for plasma heating experiment. Measurements of these parameters have been carried out by a microhole probe [21], which is placed at the exit of the compression system in a special solenoid providing the homogeneous magnetic field 0.5 T. These measurements show that at least in the central region of the beam cross section the angular spread of the beam electrons in the guiding magnetic field 0.5 T is close to $2\text{-}3^{\circ}$. We may state that in the magnetic field 5 T the angular spread should be about $7\text{-}10^{\circ}$, which is good enough for the plasma heating experiments. According to the measurements by the microhole probe, the local beam current density in the magnetic field 0.5 T is about 0.1 kA/cm^2. After compression this current density becomes suitable for the plasma heating experiments.

To increase the energy content of the beam, second pulse generator have been added to the operated one, and as a result of this the total stored energy in both generators was tripled. According to the computer calculations the electrical connection between the pulse generators should allow one to produce the ribbon beam with the total energy up to 0.5 MJ in the described above diode (see [19]). Nevertheless, to achieve such large energy content in our experiments one need to neutralize the space charge of the beam electrons in the vacuum chamber where the beam is transforming and compressing. For this purpose the appropriate (about $1.5 \cdot 10^{-2}$ Pa) gas pressure in this chamber is needed. Fig.9 shows a set of waveforms for the shot with the beam total energy in the diode of 310 kJ and the energy of the compressed beam of 230 kJ. With about 500 kJ energy stored in the capacitors, 65% of this energy were delivered to the beam in the accelerator diode and about 50% to the compressed beam.

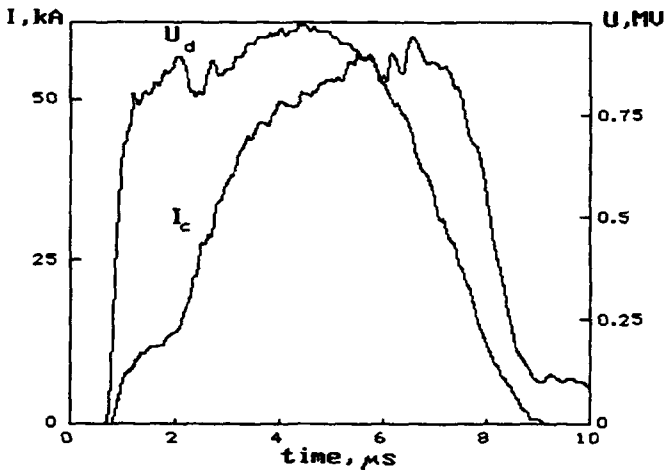

Fig.9. Ribbon beam parameters.

VI. CONCLUSIONS

1. Electron temperature of 1 keV is achieved at GOL-3 device during the heating of 7-m-long 10^{15} cm^{-3} plasma by a 100 kJ E-beam.

2. Cooling of this plasma after the heating is determined by the classical electron heat conductivity along the magnetic field to the device ends.

3. Feasibility of the two-stage heating of 10^{16}-10^{17} cm^{-3} plasma is experimentally demonstrated in the experiments with the dense plasma bunches. The three-fold increase in the plasma energy density with respect to the case of a uniform plasma is obtained.

4. Microsecond beam with total energy content of 230 kJ is obtained on the U-2 machine. The work on further increase of this parameter is in progress.

5. Presently the GOL-3 facility is being upgraded by the increasing solenoid length to 14 m and improving E-beam generator parameters.

REFERENCES

1. *Arzhannikov A.V., Burdakov A.V., Kapitonov V.A. et al.* Plasma Phys. and Contr. Fusion (Proc. 15th Europ. Conf., Dubrovnik, 1988) - 30, p.1571.
2. *Arzhannikov A.V., Burdakov A.V., Chikunov V.V. et al.* Proc. 8th Intern. Conf. on High-Power Particle Beams, Novosibirsk, 1, 14, 1990.
3. *Arzhannikov A.V., Breizman B.N., Burdakov A.V. et al.* Plasma Phys. and Contr. Fusion (Proc. 7th Europ. Conf., Innsbruck, 1978) - 2, p.623.
4. *Deulin Yu.I., Filippov V.V., Karyukin A.V. et al.* - this Cohference.
5. *Burdakov A.V., Dranichnikov A.N., Koidan V.S. et al.* Preprint INP 91-105, Novosibirsk, 1991 - *in Russian.*
6. *Deulin Yu.I., Lebedev S.V., Nikolaev V.S., Semenov E.P.* Preprint INP 90-141, Novosibirsk, 1990 - *in Russian.*
7. *Zotkin R.P., Kapitonov V.A., Koidan V.S. et al.* Sov. Phys. - Voprosy (ser. Thermoyadernyj Sintez), No.1, p.50, 1990 - *in Russian.*
8. *Burdakov A.V., Kapitonov V.A., Koidan V.S. et al.* Proc. 1989 Intern. Conf. on Plasma Physics, New Delhi, 3, p.973, 1989; *ibid*, p.969.
9. *Burdakov A.V., Koidan V.S., Piffl V. et al.* Proc. 19th Intern. Conf. on Phenomena in Ionized Gases, Belgrade, 1, 319, 1989.
10. *Burdakov A.V., Karyukin A.V., Koidan V.S. et al.* Proc. 17th Europ. Conf. on Contr. Fusion and Plasma Heating, Amsterdam, 14B, pt.2, p.614.
11. *Burdakov A.V., Postupaev V.V., Semenov E.P.* Preprint INP 91-33, Novosibirsk, 1991 - *in Russian.*
12. *Burdakov A.V., Voropaev S.G., Huber A.F. et al.* Preprint INP 92-8, Novosibirsk, 1992 - *in Russian.*
13. *Arzhannikov A.V., Burdakov A.V., Burmasov V.S. et al.* Proc. 3rd Intern. Topical Conf. on High Power Electron and Ion Beam Research and Technology, Novosibirsk, 1, p.29, 1979.
14. *Burmasov V.S., Vyacheslavov L.N., Kandaurov I.V. et al.* Proc. 8th Intern. Conf. on High-Power Particle Beams, Novosibirsk, 1, 233, 1990.
15. *Burdakov A.V., Postupaev V.V., Piffl V.* - this Conference.
16. *Burdakov A.V., Postupaev V.V.* Preprint INP 92-9, Novosibirsk, 1992 - *in Russian.*
17. *Burdakov A.V., Chikunov V.V., Huber A.F. et al.* - this Conference.
18. *Burdakov A.V., Voropaev S.V., Huber A.F. et al.* Preprint INP 92-12, Novosibirsk, 1992 - *in Russian.*
19. *Arzhannikov A.V., Astrelin V.T., Bobylev V.B. et al.* Proc. 8th Intern. Conf. on High-Power Particle Beams, Novosibirsk, 2, 849, 1990.
20. *Arzhannikov A.V., Bobylev V.B., Nikolaev V.S. et al.* - this Conference.
21. *Arzhannikov A.V., Koidan V.S., Loginov S.V.* Sov. Physics - Pribory, No.4, p.36, 1983 - *in Russian.*

INNOVATIVE BREMSSTRAHLUNG RESEARCH AT PHYSICS INTERNATIONAL COMPANY

S. Wong, J. Riordan, and J. Meachum

Physics International Company
2700 Merced Street
San Leandro, CA 94577

Abstract

For bremsstrahlung diodes optimized for X-ray production below 2 MeV, the area-weighted mean dose in the near-field is controlled by the atomic number, Z, of the converter material, and the electrical power, P, into the diode, scaling approximately as ZP. However, given the constraints of a fixed electrical power pulse from a generator, one can still vary the end-point voltage of the bremsstrahlung radiation without significant sacrifice in X-ray dose, or sharpen the risetime of the X-ray pulse without sacrificing the average dose-rate. In this paper, we will review the design of a triple series diode on the Double-EAGLE generator which reduces the end-point voltage of the bremsstrahlung source from 1.5 MV dow to 0.3 MV. In addition, we will discuss pulse sharpening of the radiation from a pinched beam diode by optimizing the dimension of the tantalum converter. Also, we will review some recent work on a linear bremsstrahlung diode which in principle can form part of a large-area bremsstrahlung source for a multi-module pulsed power generator.

Triple Series Diode

For bremsstrahlung diodes optimized for X-ray production below 2 MeV, the area-weighted mean dose in the near-field scales approximately as the power P across the electron beam diode.[1] For low end-point voltage operation, the dose then essentially decreases as V^2 For Double-EAGLE, fixing the diode configuration while decreasing the generator voltage to reduce the voltage in the diode from 1.5 MV to 300 kV will decrease the electrical efficiency, or equivalently the dose, to 0.04 of that at 1.5 MV diode voltage. A better way is to maintain the generator voltage but reduce the diode impedance to reduce the diode voltage. Such a method will mismatch the diode to the generator and will result in a drop to 35% electrical efficiency. Putting two diodes in series and adjusting the diode impedance will improve the electrical efficiency from 35% to 65%. Increasing the number of series diodes to three will further increase the electrical efficiency to 85% while operating the diodes at 300 kV end-point voltage.

The concept of the series diode[2] has been demonstrated on Double-EAGLE and at other facilities since the late 1970's. The triple series diode is an extension of the series diode work. To optimize the performance of the triple series diode, one can optimize the peak voltage by varying the diode gap of each diode. The series converters are separated laterally to minimize self-shielding. As the end-point voltage decreases and the bremsstrahlung radiation softens, the

converter thickness also needs to be reduced to optimize for X-ray production. As a tri-plate machine, Double-EAGLE is ideally suited for the ring and series diodes. A layout of the triple series diode on Double-EAGLE is shown in Figure 1. In terms of actual operation, the two "floating" rings forming the second and third cathodes are hung in place with retractable pins. The pins are retracted a few milliseconds prior to the shot to prevent the second and third cathodes from shorting to ground. Figure 2 shows an X-ray pinhole photograph of the triple series diode. The pinhole photo shows three rings with equal intensities, indicating balanced impedances and equal voltage division. Two filters with different thicknesses placed on the X-ray film also show approximately equal attenuation, thus confirming qualitatively the division of voltage equally among the three rings. In addition, a differentially-filtered spectral end-point monitor system, as shown in Figure 3, confirms that the triple series diode has an end-point voltage being equal to one-third of the applied voltage. Comparing the bremsstrahlung output from the ring diode, the two-ring series diode and the triple series diode, Table I, one can note that the end-point voltage of the bremsstrahlung radiation from Double-EAGLE can be reduced to 400 kV while maintaining a substantial fraction of the dose-area product. We have also demonstrated substantial bremsstrahlung output at 300 kV end-point voltage with an un-optimized converter. By optimizing the converter thickness, we can expect further improvement in does at the 300 kV end-point voltage.

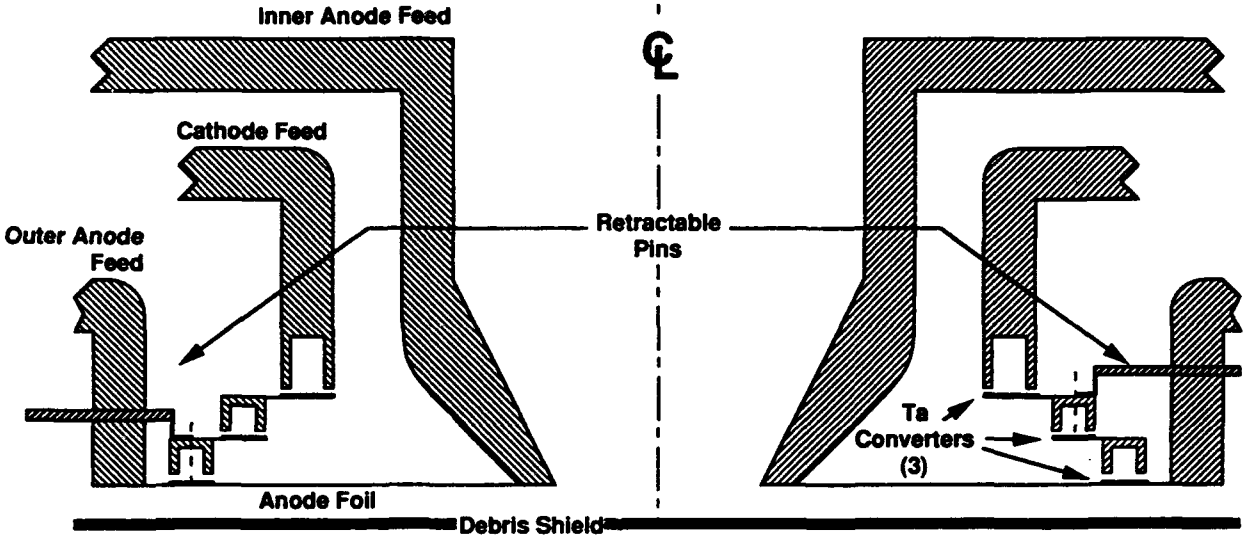

Figure 1. High spectral fidelity triple series diode on Double-EAGLE.

- Equal intensities averaged around rings on the radiograph indicate balanced impedances and equal diode voltage division.

- Filters aid comparison of ring intensities and provide qualitative indication of spectrum.

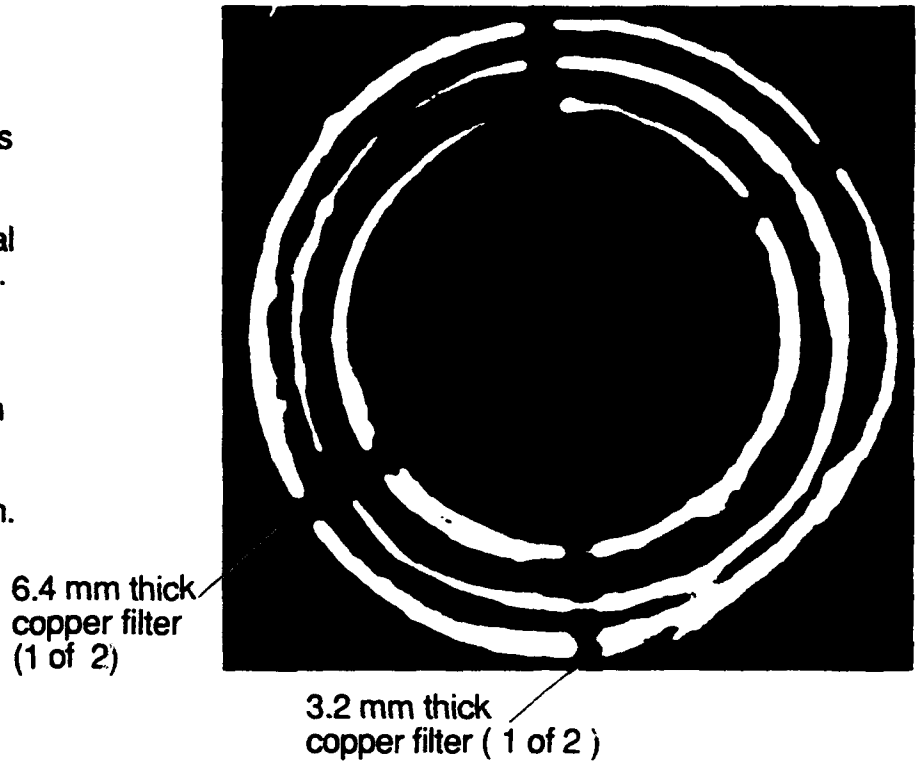

Figure 2. The Double-EAGLE triple series diode provides reliable, symmetric dose distributions.

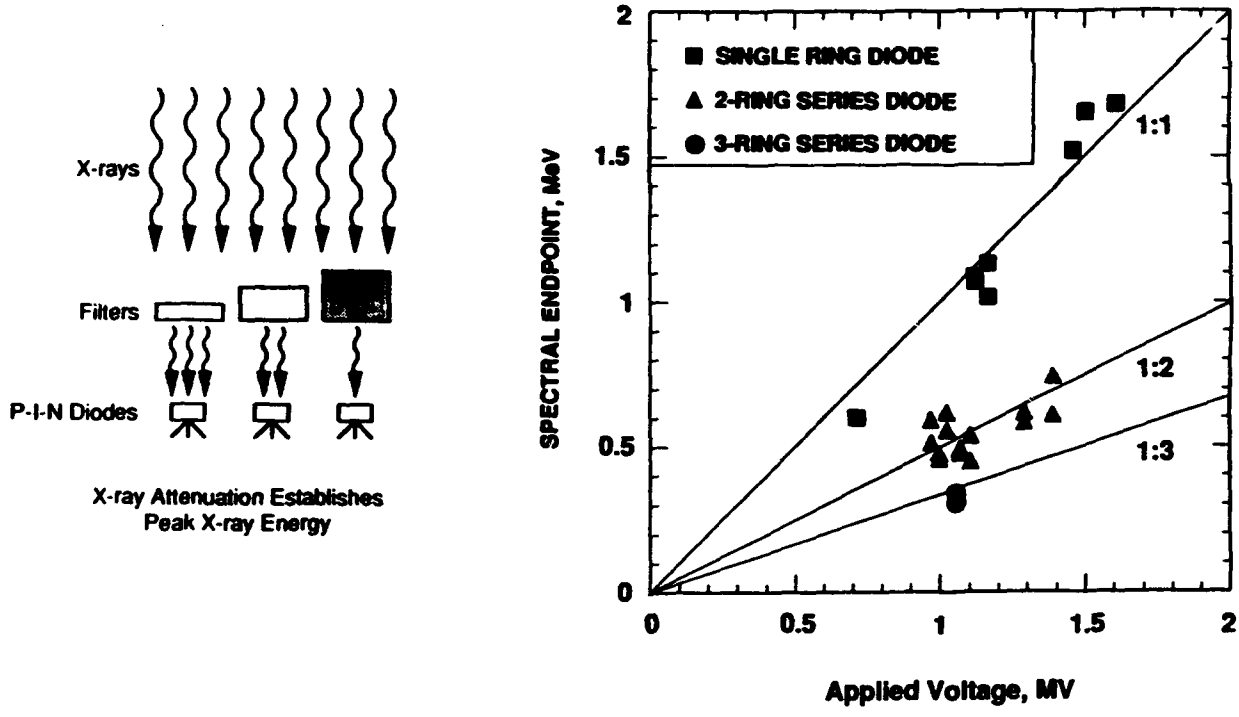

Figure 3. A spectral endpoint monitor confirms equal division of applied voltage.

Table I. The Double-EAGLE Triple Series Diode Maximizes Output at Low End-Point Voltages

	Single Ring	Two Ring Series	Triple Series Diode	
Endpoint Voltage (MV)	1.2	0.6	0.4	0.3
Area for 2:1 Uniformity (cm^2)	1600	2000	1800	
Mean Dose (krad(Si))	12	6	5	3
X-ray FWHM (ns)	43	34	42	38

Pulse Sharpening in the Pinched Beam Diode

Bremsstrahlung radiation is produced when an electron beam impacts the anode/converter. Bremsstrahlung production depends linearly on the atomic number of the anode/converter material. Thus, by tailoring the atomic number of the anode/converter as a function of radius in a pinched beam diode, the rate of bremsstrahlung production will also change with radius. As the E-beam pinches on axis with high velocities, sweeping from the low Z to high Z regions, a fast risetime bremsstrahlung pulse can be produced.

The fact that electrons pinches with high radially velocities in a pinched beam diode[3,4,5,6] has been demonstrated in many experiments during the 1970's. Current risetimes of a few nanoseconds have been observed near the axis. Thus, if we can reduce bremsstrahlung production at large radii by using a low Z anode, and let the fast risetime E-beam impact on a high Z converter near the axis, a bremsstrahlung pulse with a few nanosecond risetime can be produced. Figure 4 shows an overlay of three shots on PITHON with three different sizes of tantalum converters, showing progressively faster risetimes with smaller converter diameters. A 6 ns risetime pulse, excluding prepulse, has been demonstrated on PITHON with a 7.6 cm diameter converter. The prepulse is due to electrons impacting on the low Z anode as the beam pinches. Thus, by reducing the Z of the anode and backing it with X-ray shielding except at the high Z converter area, the prepulse in the bremsstrahlung pulse can be reduced. As shown in Figure 5, we can reduce the prepulse from 40 ns to 7 ns by using an aluminum anode instead of a stainless steel anode and by using 0.5" of lead shielding behind the aluminum anode.

Linear Diode

Ring diodes are typically used in the pulsed power community to generate a large-area bremsstrahlung radiation source. For a multi-module generator, this would require a post-hole convolute with its associated complexities. Alternately, one can also obtain a large-area bremsstrahlung source with the use of an array of linear diodes, with one linear diode driven by one module of the multi-module generator.

A linear diode[7] has been fielded on PITHON to study the X-ray dose uniformity of such a configuration. A photograph of a linear diode on PITHON is shown in Figure 6. The configuration consists of a blade-on-cone cathode. Push-pull mechanisms allows some variation of the anode-cathode gap along the tip of the blade. By varying the ratio of the A-K gap between the middle and the ends of the linear diode, we were able to obtain 2:1 dose uniformity over 90% of the length of the diode, as shown in Figure 7. Figure 8 shows the isodose contours of the radiation for the same shot. Based on the results from PITHON, we can project that operating an array of such diodes can give substantial doses over larger areas. Such an arrangement can serve as an alternative to the ring diode for the generation of a large-area, high-uniformity bremsstrahlung source on a multi-module pulsed power generator.

Figure 6. Photograph of the PITHON linear diode cathode and anode assembly.

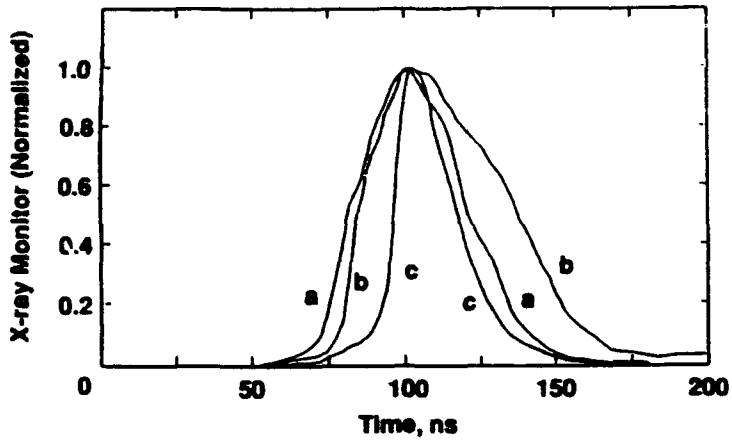

Trace	Shot No.	Ta Dia. (cm)	10-90% RT (ns)	FWHM (ns)
a	5074	25.4	22	38*
b	5073	20.3	20	54
c	5072	7.6	6**	26

* Early tube flash

** Excluding prepulse

Figure 4. Reducing the tantalum converter diameter delays x-ray production and reduces the pulse risetime

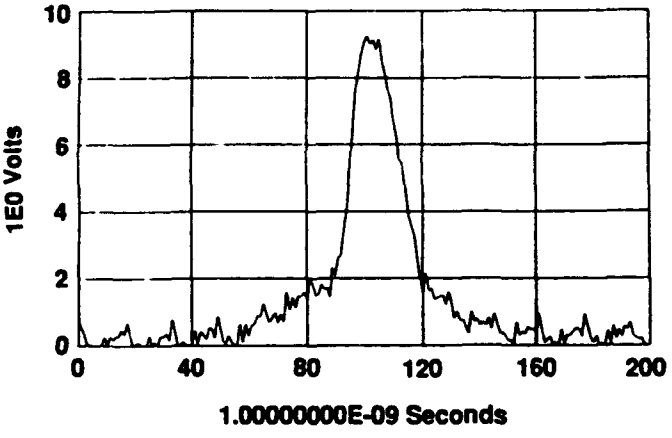

PITHON Shot 5066

Ta over stainless steel,
no Pb shielding.
40 ns precursor

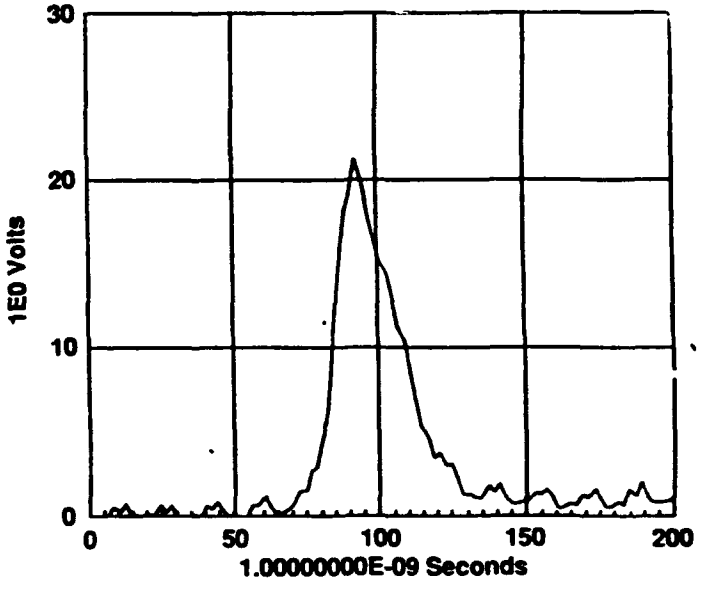

PITHON Shot 5103

Ta over aluminum,
0.5" Pb shielding.
7 ns precursor

Figure 5. Reducing the precursor in the x-ray pulse by x-ray shielding and low Z anode.

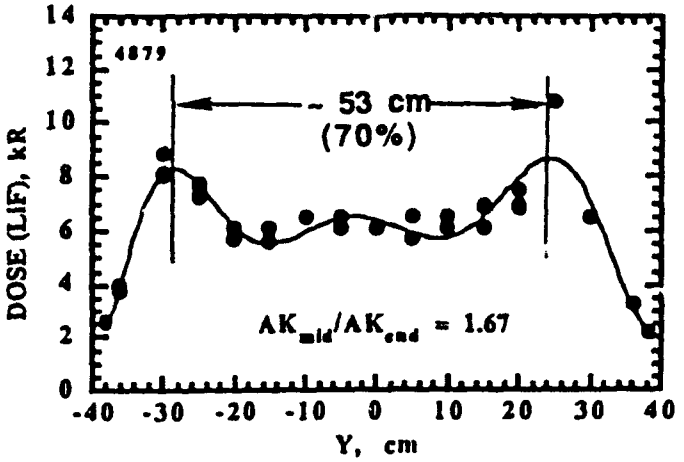

Figure 7. The long axis dose distribution is controlled by diode gap profiling.

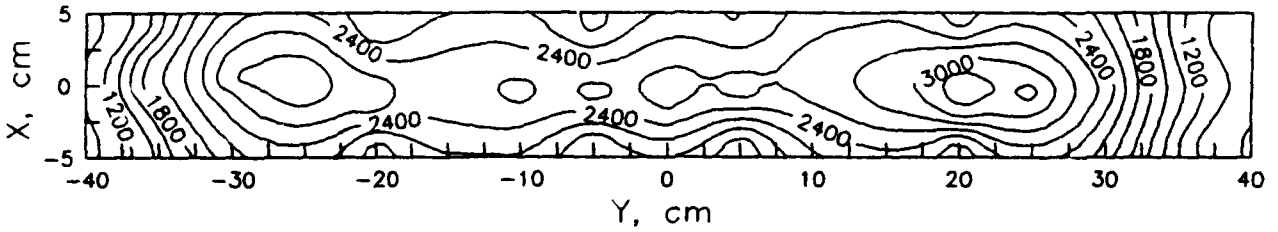

Figure 8. Isodose contours 5 cm from the PITHON linear diode.

Conclusion

To summarize, we have demonstrated the operation of a triple series diode at 300 kV end-point voltage. A simple modification of the converter of the pinched beam diode resulted in a substantial reduction in risetime. A high-uniformity linear diode has also been demonstrated at Physics International, providing the building block for a larger area bremsstrahlung source on a multi-module pulsed power generator.

References

1. "Dose-voltage dependence of coaxial Bremsstrahlung diodes," T. Sanford, et al., Nucl. Inst. and Methods in Phys. Res. B34 (198) 347-356 North-Holland, Amsterdam.
2. "Series Diode X-ray Source," I.D. Smith, L.J. Demeter, K.E. Nielson, US Patent No. 4359660 (1982).
3. "Intense Focusing of Relativistic Electrons by Collapsing Hollow Beams," A.E. Blaugrund and G. Cooperstein Phys. Rev. Lett., 34, 461 (1975).
4. "Relativistic Electron Beam Pinch Formation Processes in Low Impedance Diodes," A.E. Blaugrund, G. Cooperstein, and Shyke A. Goldstein, Phys. Fluids 20, 1185 (1977).
5. "Experimental Investigation of high-current relativistic electron flow in diodes," M. Di Capua, J. Creedon and R. Huff, J. Appl. Phys. Vol. 47, No. 5, 1887 (1976).
6. "Relativistic Electron-Beam-Focusing Experiments Employing Axial Loads," R. Genuario, K. Triebes, P. Spence, and H. Kishi, J. Appl. Phys. Vol. 48, No. 11, 4503 (1977).
7. "High-Power Linear Diode Bremsstrahlung Source Development,"J.S. Meachum, F.K. Childers, and J.C. Riordan, Proc. 8th IEEE Pulsed Power Conference, p. 571 (1991).

SPECTROSCOPIC STUDIES OF PULSED-POWER PLASMAS

Y. Maron, R. Arad, G. Dadusc, G. Davara, R.E. Duvall, V. Fisher, M.E. Foord, A. Fruchtman, L. Gregorian, Ya. Krasik, L. Perelmutter, M. Sarfaty, E. Sarid, S. Shkolnikova, R. Shpitalnik, L. Troyansky, and A. Weingarten.

Department of Physics, Weizmann Institute of Science, Rehovot 76100, Israel

R.E.H. Clark
Department of Physics, Los Alamos National Laboratory, Los Alamos, NM, USA

A. Fisher
Naval Research Laboratories, Washington D.C., USA

C. Litwin
Department of Nucl. Eng., University of Wisconsin at Madison, WI, USA

Recently developed spectroscopic diagnostic techniques are used to investigate the plasma behaviour in a Magnetically Insulated Ion Diode, a Plasma Opening Switch, and a gas-puffed Z-pinch. Measurements with relatively high spectral, temporal, and spatial resolutions are performed. The particle velocity and density distributions within a few tens of microns from the dielectric-anode surface are observed using laser spectroscopy. Collective fluctuating electric fields in the plasma are inferred from anisotropic Stark broadening. For the Plasma Opening Switch experiment, a novel gaseous plasma source was developed which is mounted inside the high-voltage inner conductor. The properties of this source, together with spectroscopic observations of the electron density and particle velocities of the injected plasma, are described. Emission line intensities and spectral profiles give the electron kinetic energies during the switch operation and the ion velocity distributions. Secondary plasma ejection from the electrodes is also studied. In the Z-pinch experiment, spectral emission-line profiles are studied during the implosion phase. Doppler line shifts and widths yield the radial velocity distributions for various charge states in various regions of the plasma. Effects of plasma ejection from the cathode are also studied.

I. Introduction

Detailed high-resolution investigations of the plasma behaviour in pulsed-power systems are important for understanding the operation of these systems. In this report we describe the use of spectroscopic diagnostic methods to study the plasma behaviour in three pulsed-power experiments: a planar Magnetically-Insulated-Diode, an annular gas puffed Z-pinch, and a cylindrical Plasma Opening Switch. In the measurements, spontaneous emission, laser-induced fluorescence, and resonant laser absorption are used to determine as a function of time in a single discharge the particle velocity distributions[1,2], the electric-field fluctuations in the plasma[3], the electron density[1,3], the particle density distributions[2,4],

and the electron energy-distribution[5,6]. For analyzing the line intensities for these nonequilibrium plasmas, we use our time-dependent collisional-radiative calculations[7]. In Sec. II we summarize the main features of our diagnostic systems and recent results from the MID experiment are given in Sec. III. In Secs. IV and V, respectively, we describe the experimental systems for the Plasma Opening Switch and Z-pinch configurations, together with electrical measurements and spectroscopic observations.

II. Diagnostic Systems

Fig. 1 presents the various features of our diagnostic systems used for the various experiments, shown here in reference to the diode experiment. In brief, light is directed from the plasma onto 1-m or 1.3-m spectrographs. For each spectrograph, a profile of a spectral line is observed in a single discharge by optically dispersing the spectral line at the output of the spectrograph, projecting its image on a rectangular array of 12 fibre-bundles, and measuring the light signal transmitted in each fibre by a photomultiplier-tube and a digital oscilloscope. The temporal resolution in these systems is $\lesssim 5$ ns. Alternatively, the spectrograph exit window is streaked by a fast U.V. camera to allow for the observation of spectral profiles of a few lines in a single discharge with a nanosecond temporal resolution.

The spectrographs are equipped with 2400 grooves/mm gratings allowing for a spectral resolution down to 0.05 Å. The spatial resolution is determined by the input optics and it can be varied from tens of microns to a few millimeters.The fused-silica optics, the photo-multiplier tubes, and the streak camera allow for sensitivity in the range 2000-7000 Å. Absolute calibration of the systems over the entire spectral range provides the absolute emission line intensities, thus allowing the absolute atomic level populations in the plasma to be obtained.

For the diagnostics we also use a high-power pulsed (6 ns) dye laser pumped by a Q-switched Nd:Yag laser equipped with a unit that extends the wavelength range to 2160-9000 Å. Using this laser system, high-spatial-resolution measurements based on resonant laser absorption are obtained, as described in Sec. III.

Time-dependent collisional-radiative models of many atomic systems, such as carbon[7], magnesium[3], and silicon[3] have been constructed in order to interpret the absolute and relative spectral line intensities. These calculations are especially important for diagnosing short-lived pulsed-power plasmas whose level populations are far from being in a steady state.

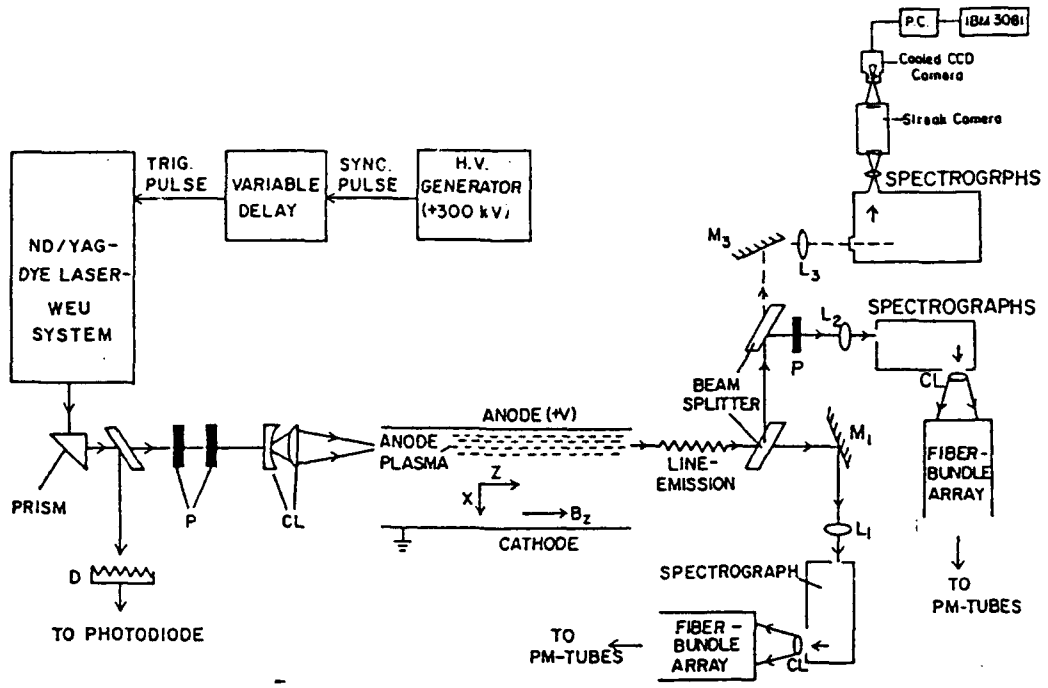

Fig. 1. The laser system and the diagnostic arrangement. WEU, D, Cl and M denote a wave extending unit, a diffuser, a cylindrical lens, and a mirror, respectively. The laser light, synchronized with the diode voltage pulse, can be directed into the diode in the x and y directions. Laser light, induced fluorescence, and spontaneous emission can be collected in various directions by the two spectroscopic systems. The polarizers P are used for the polarization spectroscopy. For cylindrical plasmas the line-emission is imaged on a cylindrical fibre array. For observing the spectral line profile as a function of time in a single discharge either a fibre-bundle-photomultiplier-tube-digitizer system or a fast streak camera system are used.

III. High-Power Diode Experiment

We report on studies that follow our recent investigations of the anode plasma in the planar Magnetically Insulated Diode. In these studies the magnetic field penetration into the anode plasma was observed as a function of time throughout the 100-ns-long voltage pulse from line Zeeman splitting[8]. From the fast field penetration a plasma resistivity higher than the classical one was inferred. This led us to search for collective electric fields in the plasma that could be associated with the anomalous conductivity. The amplitude, direction, and frequency range of anisotropic fluctuating collective electric fields in the anode plasma were investigated by the use of polarization spectroscopy of the Stark broadened hydrogen lines[3], as was used for longer duration plasmas in a mirror machine[9]. In our experiments, the spectral profiles of H_α and H_β were measured for two lines of sight and for two different polarizations[3]. The data were analyzed using calculations of the Stark

broadening for these lines under the combined influence of the collective fields and the isotropic particle fields in the plasma. Fluctuating electric fields with an amplitude of $\simeq$8 kV/cm dropping to zero at the end of the pulse were inferred[3], as shown in Fig. 2. The fields point mainly perpendicular to the anode surface, denoted here as the x direction. Using the observed ion velocity distribution a lower bound of $\simeq 10^9$ sec^{-1} for the field frequency was obtained. Recently, we suggested[10] that the ion flow observed in the plasma[1] in the x direction leads to an instability that can grow during the pulse. The predictions of this model are consistent with the direction and the size of the observed field amplitudes. Furthermore, this model suggests that the field amplitude should decrease with the ion drift velocity. Indeed, the electric field amplitude was found to decrease in time during the pulse (see Fig. 2), similarly to the ion flow velocity given in Ref. 1.

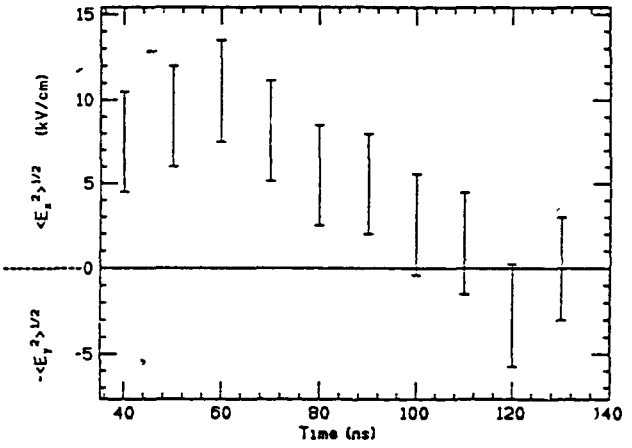

Fig. 2. Mean amplitude of the electric field $\langle \epsilon_x^2 \rangle^{1/2}$ inferred as a function of time. Here, the plasma density was assumed to be 10^{15} cm^{-3} and the Doppler broadening was so chosen to provide an agreement between the calculated widths and the measured ones for each time instant. For the data point at 120 ns the width for the x-polarization was smaller than for the y-polarization (parallel to the anode and perpendicular to the applied magnetic field B_z), which is inconsistent with the assumption of a one-dimensional field in the x-direction. For this point the same analysis is used to obtain a field in the y-direction with an amplitude $\langle \epsilon_y^2 \rangle^{1/2}$, as shown in the Figure.

In a previous study[4], we determined the fluxes of particles injected from the anode surface into the plasma and found that these fluxes are considerably affected by the plasma properties at the immediate vicinity of the anode surface. Here, we report on the use of laser absorption and laser-induced fluorescence to directly determine the particle ground-state densities and the particle velocities within $\simeq$30 μm near the surface[2]. Fig. 3 gives a sample of our measurements and Fig. 4 shows the inferred ground state and excited-state

densities. The densities of the MgII ground and first-excited states and of the LiI ground state were observed to drop considerably within $\simeq$50 μm from the anode surface. The MgII Doppler broadened absorption profile showed that a significant fraction of the MgII velocities seen in the anode plasma[1] is acquired by the ions within $\simeq$30 μm from the anode surface. From these results electric fields $\simeq$5 kV/cm in this region near the surface are concluded. This is a complement to our previous data[4] which suggested that the ion kinetic energies in the plasma result from the presence of electric fields at the immediate vicinity of the anode surface.

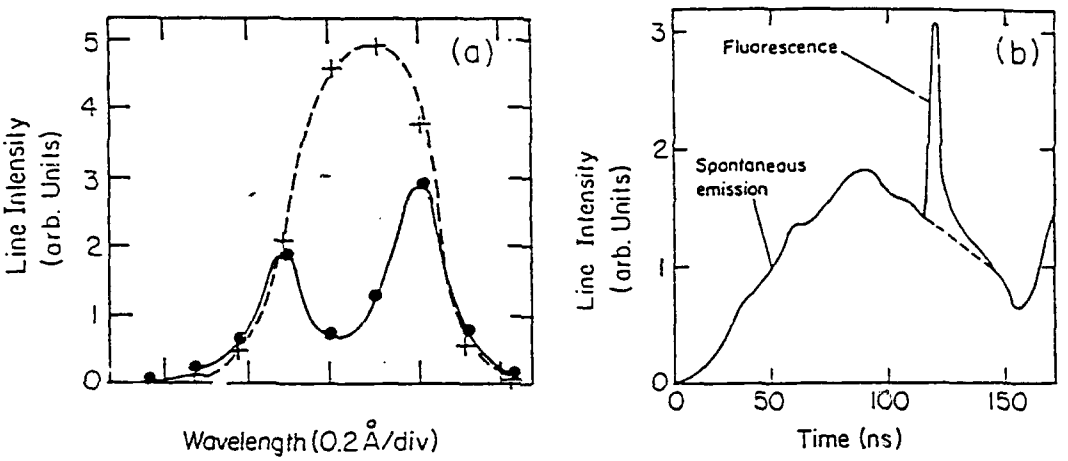

Fig. 3. (a) Typical spectral profile of the laser light transmitted through the anode plasma for the light wavelength λ=2795.53Å corresponding to the MgII $^3P_{3/2} \rightarrow ^3S_{1/2}$ transition (solid curve). Also shown is the spectral profile with no plasma in the diode (dashed curve); (b) Spontaneous emission of the $^3P_{3/2} \rightarrow ^3S_{1/2}$ transition together with the fluorescence resulting from the same transition induced by the laser saturated excitation. Here, the observation distance from the anode surface was 0.1 mm.

The observed particle velocity and density distributions are used to obtain estimates of the rate of particle ionizations near the surface and for the electron density and temperature within a few tens of μm near the anode surface[2]. The inferred values are compared to those estimated from the ratio between the ground and the first-excited level densities. This ratio can also give information on the material release from the surface into the adjacent plasma layer.

It has been suggested that the ionization of an expanding layer of neutral atoms near the anode surface makes a major contribution to the initial plasma formation[11]. Sev-

eral theoretical models are currently being used to study the general problem of ion flow through an ionizing layer and the resulting plasma buildup and screening of the electric field[12]. Our analysis indicates that the rate of electron leakage from the plasma to the anode has a major effect on the rate of electric field screening. Possible mechanisms for this electron flow include cross field drifts and losses parallel to the applied magnetic field[12]. For each mechanism there corresponds a range of possible electron flow rates. Therefore, comparison to time resolved measurements of the electric field in the diode gap will allow us to estimate the dominant mechanisms of electron flow from the anode plasma.

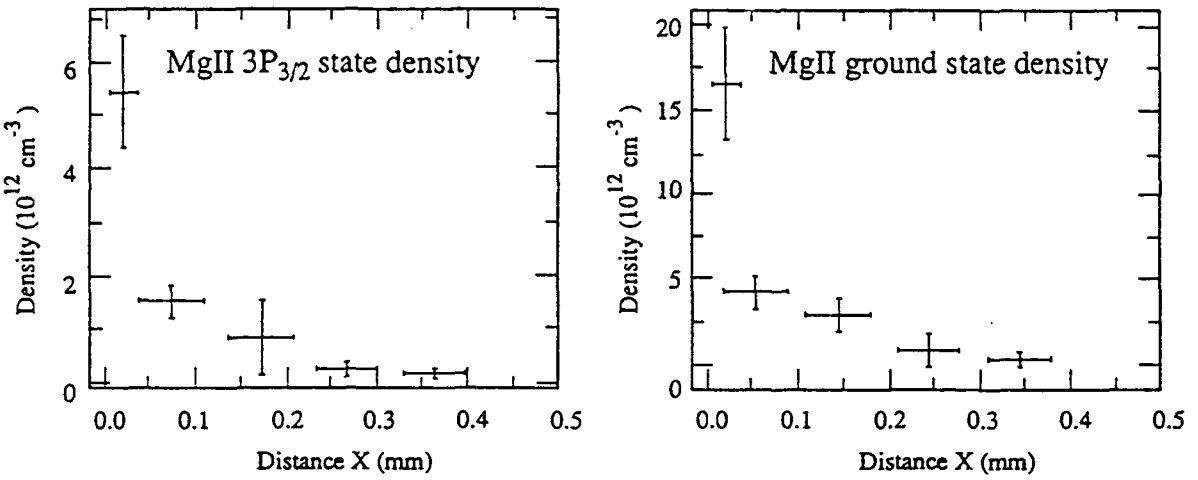

Fig. 4. (a) The MgII ground state density as a function of the distance x from the anode surface obtained from the laser absorption at 2795.53-Å for t=55 ns after the start of the diode voltage pulse. The spatial resolution near the anode surface is $\simeq$30 μm; (b) Similar to (a) for the density of the MgII excited state, $^3P_{3/2}$, obtained from the laser absorption at 2798-Å.

IV. The Plasma Opening Switch Experiment

The POS concept is relevant to various pulsed-power applications. Although considerable progress in the use of plasma switches has been made in the recent years, experimental investigations are still essential for the examination of the various underlying models. Knowledge of the distribution of the magnetic field, the electron density, the particle flow, and the electron energy distribution in the switch plasma is of major importance. We are studing these phenomena in our newly built experiment. We developed a novel gaseous plasma source that allows for satisfactory control of the plasma species and for seeding the plasma with various elements as required for the spectroscopic observations. The plasma

source is based on forming gas discharges in many capillaries drilled in the wall of a hollow tube. The discharge current, of density of a few kA/cm^2 in each capillary, produces highly ionized plasma that flows to the outside of the capillaries. Another feature of our experiment is that the plasma source is mounted inside the high-voltage cylindrical inner electrode, injecting the plasma radially outward into the spacing between the two electrodes.

The operation of the plasma source has been optimized and characterized by examining the effects of the source length, the number of capillaries, the hollow tube dimensions, and the various gases and pressures. The plasma electron density and temperature were measured simultaneously by three sets of double floating probes placed in various locations. In addition, two negatively-biased collimated charge collectors were used to measure the time dependent plasma ion density and uniformity along the axial, azimuthal, and radial dimensions. The plasma axial density distribution shows that the plasma density is uniform over $\simeq$40 mm and drops to zero at each side over $\simeq$ 20 mm. The plasma source reproducibility inferred from electric probes and light intensity signals is $\pm$20%. The plasma electron density and temperature measured in the inter-electrode gap, using various gases and discharge currents, ranged between 10^{13}–10^{14} cm^{-3} and 10-20 eV, respectively. The plasma radial propagation velocity was found to be 1.0–4.0 cm/μs.

The plasma properties were also studied spectroscopically. We used measurements of H_α and H_β line profiles from which the Doppler and Stark line broadenings were unfolded self-consistently to yield the electron density and the axial hydrogen kinetic energy. The electron density at 2 mm from the capillaries was found to be $6 \pm 2 \times 10^{14}$ cm^{-3}, and the hydrogen kinetic energy 3 ± 1 eV.

The marx-water-line generator (1.5 kJ, 300 kV, 1 Ω) can charge the inner electrode positively or negatively. In the positive mode it delivers a 90-ns-long current pulse with a peak value of 160 kA. Discharges were made for Ar, CO_2 and CH_4 as source gases. In these experiments, line intensities of various charge states were observed axially for four radial locations. The time-dependent electron kinetic energies during the switch operation are studied by observing line-emission from various excited levels and from various charge states between 1 to 5. Fig. 5 shows an example of line intensities for CII and CV observed in the axial direction. The lines become $\simeq$100$\times$ more intense when the cur-

rent flows through the plasma. The excitation of the CV upper level of this line (2271 Å) requires electron energies >300 eV, while for that of the CII level energies of ≃10eV would be sufficient. The high electron kinetic energies can be associated either with the flow of the switch current through the plasma or, if the magnetic field does not penetrate the plasma, with the flow of the return current. The charge-flow density can be estimated from the switch current and the area of the fast-electron region found to be ≃ 2 cm long. Using v_e corresponding to 300 eV gives an estimate for the fast-electron density $n_e = J/ev_e \simeq 3 \times 10^{13} cm^{-3}$, which is comparable to the plasma electron density.

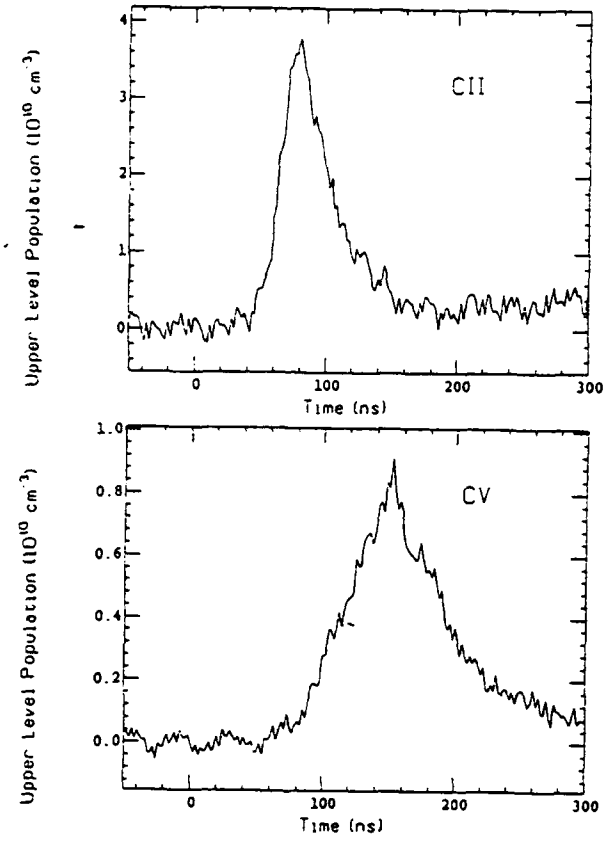

Fig. 5. Time dependent absolute populations of the CII $2p^3\ ^2D_{5/2}$ level and the CV $2p^3P_2$ level at 5 mm from the anode obtained from the intensities of the 2512-Å and the 2279-Å lines, respectively. t=0 is the start time of the upstream current.

Using other various spatially resolved time-dependent line intensities we are presently studying the current channel distribution in the plasma, hoping to compare it in the future to that obtained from the B-field measurements based on Zeeman-splitting observations.

The ion velocity distributions in the axial and radial directions were studied from Doppler broadenings and shifts. Fig. 6 shows the drift velocities of CII and CV. The velocities are seen to rise and to drop in some correlation with the current through the plasma.

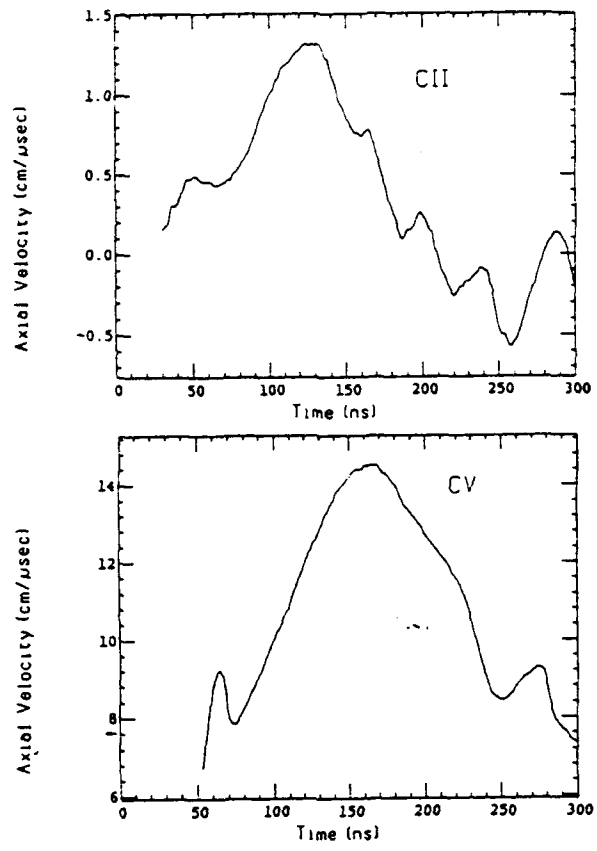

Fig. 6. Time dependent axial velocities of CII and CV at 5 mm from the anode obtained from the Doppler shifts of the 2512-Å and the 2271-Å lines, respectively. t=0 is the start time of the upstream current.

Similar observations were made for CIII, CIV, OII–OIV ions, and ArII–ArIV ions. The drift velocities in the axial direction were found to be higher for higher charge states. The CV axial velocity approaches the estimated Alfven velocity while for the other ions the velocities are much lower. Presently, we are considering an explanation to the near proportionality of the ion drift velocities to the charge state by assuming electric fields in the plasma that accelerate the various charge-state ions over similar periods of time. The magnitude of the ion drift velocities and their dependence on the charge state are also being presently used to study the magnetic field distribution in the plasma.

Doppler broadenings gave the width of the ion velocity distributions. This component, denoted here by the ion kinetic energy, is shown in Fig. 7 for CII and CV. For each ion species the kinetic energy was found to be comparable to the drift energy, and to be higher for higher charge states.

Besides the investigation of the plasma during the switch operation we also studied the plasma that forms at the electrodes and reach the middle of the A-K gap at $t > 500$ ns. Knowledge of the density, composition, and velocity of the plasma ejected from the elec-

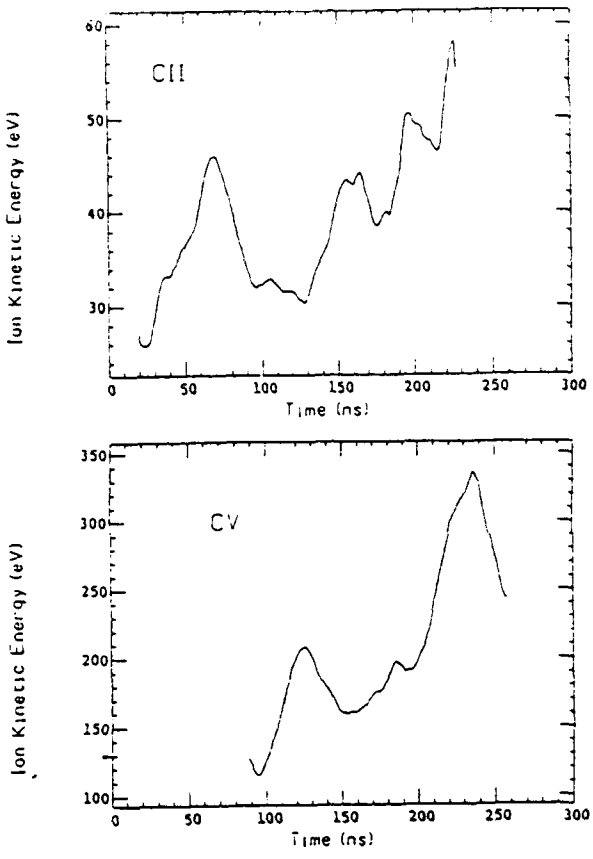

Fig. 7. Time dependent mean kinetic energies of CII and CV at 5 mm from anode obtained from the Doppler broadenings of the 2512-Å and 2271-Å lines, respectively. t=0 is the start time of the upstream current.

trodes is important for the development of long time Plasma Opening Switches. The main component of this secondary plasma was found to be carbon and hydrogen ions, which could be reliably studied in our system since it could be discriminated against ions originating from the plasma source by using a no-carbon-component gas at the plasma source. The secondary plasma was found to originate from both the anode and the cathode surfaces. At $t \simeq 1\mu s$, the electrode plasma was found to dominate the gaseous-source plasma. Based on the time delay of the secondary light signals for various distances from the electrodes, a flow velocity of $\simeq$1 cm/μs for the plasma injected from both the anode and the cathode surfaces is inferred. Further details are given in Ref. 13.

V. THE Z-PINCH EXPERIMENT

The Z-pinch plasma has many important applications such as in controlled fusion[14], and for sources of intense X-ray and VUV radiation used in material testing, lithography, and microscopy studies[15]. The dynamics of plasma pinches are very complicated involving processes such as ionization, plasma acceleration, heating, and magnetic field penetration. The main goal of this work is to study the implosion phase of the pinch which is impor-

tant for understanding the dynamics of the pinching and its influence on the final state of the plasma and is also believed to contribute in general to the understanding of the flow of ionizing plasmas under strong magnetic fields.

A gas-puff Z-pinch experiment has been constructed which produces a 400 kA, 1 μs current pulse[16]. Gas, with pressure up to 6 atm is released into an annular nozzle, producing a well collimated gas shell extending between the anode and cathode. Voltage up to 35 kV is then switched across the electrodes initiating the breakdown. The pinch occurs approximately 600 ns after the beginning of the curent rise.

Line emission from the z-pinch plasma is observed for many transitions in singly, doubly, and triply charged ions throughout the UV-visible wavelength region during most of the discharge[14]. Using CO_2 as the injected gas, line emissions from oxygen and carbon ions are observed in the radial direction with spatial resolution of 500 μm. The time-dependent radial velocity distribution of these ions are determined from their Doppler split line profiles resulting from the opposite shift in the far and near sides of plasma shell. The distribution of the radial velocity is obtained from the line widths. Measurements were performed at different z locations. The radial velocities thus obtained are given in Fig.8, showing that the radial velocity of OIII increases in time and reaches approximately 5×10^6 cm/s near the pinch time. Fig. 8 also demonstrates a velocity dependence on z. This "zippering" phenomenon may be due to non-uniformities in the injected gas profile, and is being investigated further.

CIV ions were observed to have similar radial velocities during the implosion. However, line emission from singly charged oxygen and carbon ions during the same period have significantly smaller radial velocities. OIII ions are found to have velocities larger than singly charged ions but approximately 50% less than those of CIV and OIV. We are presently developing theoretical models, based on time dependent ionizations of the various ions as they are accelerated radially by the radial electric fields, to better understand the ratios between the radial velocities of the various ions. Presently, we are also measuring the ionic velocity distribution in the axial direciton. These measurements will also give the radial density distributions, and together with the planned magnetic field measurements will enable us to gain better understanding of the current distribution and the particle flow.

We also studied the plasma ejected from the cathode by observing the line intensities and velocities of carbon ions originating at the cathode in experiments in which argon gas was used. The flow of the electrode particles away from the cathode was studied. Their radial velocities were found to be relatively low. Their effect on the pinching plasma is being

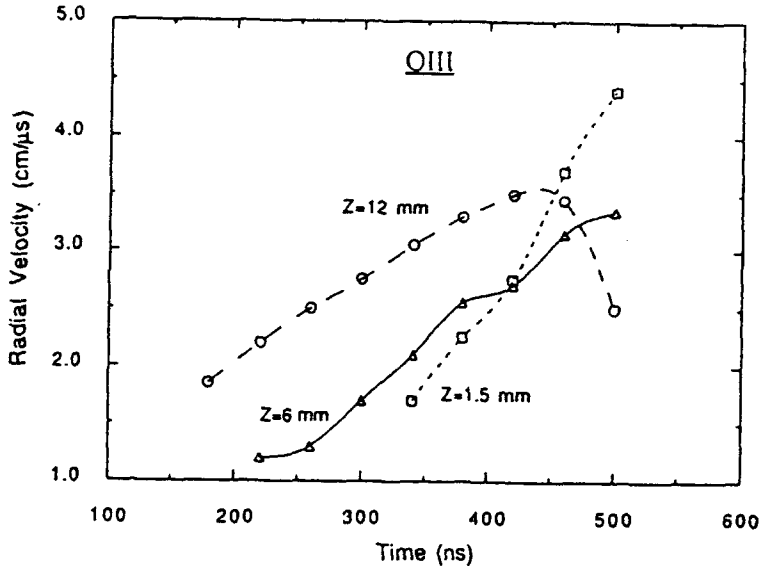

Fig. 8. Time evolution of the radial velocity of OIII from Doppler measurements of the OIII 3047-Å ($2p3s^3P_2 - 2p3p^3P_2$) line at z=1.5 mm, 6 mm, and 12 mm from the cathode. The velocity of ions at t=200-400 ns is slower near the cathode but increases to comparable values near t=500 ns. t=0 is the start time of the current.

studied. Further details of these results are given in Ref. 17.

VI. SUMMARY

Spectroscopic diagnostic methods are being used to investigate the plasma behavior in an intense Ion Diode, a Plasma Opening Switch, and a Z-pinch. In the diode experiment, the magnetic field, turbulent electric fields in the plasma, and the particle density and velocity distributions at the immediate vicinity of the anode surface were observed using emission-line Zeeman splitting, polarization spectroscopy of Stark broadened lines, and Doppler effects in laser spectroscopy, respectively. In the Plasma Opening Switch experiment, a gaseous plasma source was developed and characterized. The time dependent line intensities and velocity distributions of various charge-state ions and the electron energy during the switch operation are studied. In the Z-pinch experiment, Doppler profiles yielded the particle velocity distributions of the imploding plasma shell. Differences in the velocity distributions between various charge-states ions are being investigated.

Acknowledgment

The authors are grateful to Dr. Y. Shiloh for valuable discussions and to P. Meiri, Y. Macabi, and D. Liram for their skilled technical assistance.

References

1. Y. Maron, E. Sarid, O. Zahavi, L. Perelmutter and M. Sarfaty, Phys. Rev. A., **39**, 5842 (1989).
2. L. Perelmutter, G. Davara, and Y. Maron, "Spectroscopic investigations of particle velocities and densities on a dielectric surface undergoing flashover", 14th Int. Symp. on Discharges and Electrical Insulation in Vacuum, Sante Fe, New Mexico, USA, Sept. 17-20, 1990; L. Troyansky, M.Sc. Thesis.
3. E. Sarid, Ph.D. Thesis, Feinberg Graduate School, The Weizmann Institute of Science, Rehovot, Israel (1991); E. Sarid, L. Troyansky, C. Litwin and Y. Maron, Bull. Am. Phys. Soc. **35**, 2006 (1990).
4. Y. Maron, L. Perelmutter, E. Sarid, M.E. Foord, and M. Sarfaty, Phys. Rev. A. **41**, 1074 (1990).
5. Y. Maron, M. Sarfaty, L. Perelmutter, O. Zahavi, M.E. Foord and E. Sarid, Phys. Rev. A **40**, 3240 (1989).
6. M. Sarfaty, M.E. Foord, L. Troyansky, Y. Maron and R.E.H. Clark, Proceedings of the 9^{th} Int. Conf. on High Pow. Part. Beams, Washington, D.C. May 1992.
7. M.E. Foord, Y. Maron, and E. Sarid, J. Appl. Phys. **68**, 5016 (1990).
8. Y. Maron, E. Sarid, E. Nahshoni, and O. Zahavi, Phys. Rev. A., **39**, 5856 (1989).
9. E.K. Zavoiskii, Yu.G. Kalinin, V.A. Skoryupin,V.V. Shapkin and G.V. Sholin, JETP Lett. **13**, 12 (1971).
10. C. Litwin, E. Sarid, and Y. Maron, Bull. Am. Phys. Soc. 35, 2120 (1990).
11. C. Litwin and Y. Maron, Phys. Fluids **B1**, 670 (1989).
12. R.E. Duvall, C. Litwin, and Y. Maron, to be published.
13. M. Sarfaty, Ya.E. Krasik, R. Arad, A. Weingarten, S. Shkolnikova, Y. Maron, and A. Fisher, to be published in Beams '92, Proceedings of the 9th Int. Conf. on High Pow. Part. Beams, Wash. D.C., May 1992.
14. M.G. Haines, M. Coppins, and I.D. Culverwell, *Dense Z-pinches*, AIP Conf. Proc., AIP, NY., Edited by N.R. Pereira, **195** 203 (1989).
15. N.R. Pereira, J. Davis, J. Appl. Phys. **64** (3) R1 (1988).
16. M.E. Foord, G. Davara, Y. Maron, and A. Fisher, Bull. Am. Phys. Soc. **36** (9), 2398 (1991).
17. M.E. Foord, G. Davara, L. Gregorian, and Y. Maron, to be published in Beams '92, Proceedings of the 9th Int. Conf. on High Pow. Part. Beams, Wash. D.C., May 1992.

Invited Radiating Z-Pinch Papers

Leonid I. Rudakov, *Session Chairman*

A REVIEW OF Z-PINCH RESEARCH AT PHYSICS INTERNATIONAL

C. Deeney, P. D. LePell, T. Nash,* B. Failor, S. L. Wong,
R. R. Prasad,† and M. Krishnan†
Physics International Company
2700 Merced Street
San Leandro, CA 94577

K. G. Whitney, W. Thornhill, F. L. Cochran, M. C. Coulter,
J. Giuliani, J. P. Apruzese, F. C. Young,
D. Hinshelwood, and J. D. Sethian
Naval Research Laboratory
4555 Overlook Avenue, SW
Washington, DC 20375

Abstract

Z-pinch implosions have been studied on the Double-EAGLE generator to optimize x-ray yields, to understand basic Z-pinch phenomena, to compare experiments to numerical calculations, and to demonstrate the sodium-neon x-ray laser scheme.

Introduction

Z-pinches have been studied for many years because of their ability to produce high temperature (T_e >100 eV), high density (> $10^{18}cm^{-3}$) plasmas. Recently, Pereira[1] and Davis reviewed a significant fraction of Z-pinch research, especially relating to the Z-pinches as an x-ray source. In fact, the x-ray emission characteristics of Z-pinches have been the main reason for their study at Physics International (PI) over the past fifteen years. Much of the pioneering work performed at PI has been covered in Reference 1; and furthermore, Z-pinch research at PI up to 1989 was reviewed by Krishnan et al.[2] In this paper, we will discuss the experimental and collaborative theoretical work that has been performed at PI since 1989.

In recent years, Z-pinch experiments at PI have been motivated by three main goals: (1) to increase the x-ray yields from the 4-MA Double-EAGLE generator, (2) to demonstrate the sodium-neon photo-pumped x-ray laser scheme and (3) to understand the basic physical processes that determine the radiation efficiency of a Z-pinch.

Increasing the X-ray Yields from the Double-EAGLE Generator

Double-EAGLE[3] is a two-module, triplate waterline pulsed power generator which produces a 3.5 to 4.0 MA current pulse with a 110-ns time to peak current. When a Z-pinch load (either wire array or gas puff) is imploded with this current pulse, kilovolt x-ray yields of tens of kilojoules are produced for 1 to 2 keV photon energies and up to 5 kJ of 3 keV photons. Although these x-ray yields are acceptable to study x-ray material interactions, it is worthwhile to increase the yields further. The first technique that was applied to increase the kilovolt yield was radius scaling. This concept was first developed by workers at NRL[4] and Maxwell Laboratories,[5] who found that by decreasing the initial diameter of either neon gas puffs or

*Present address: Sandia National Laboratory
†Present address: Science Research Laboratory

aluminum wire arrays, while maintaining the same implosion time, the k-shell x-ray yield increased. Neither of these experiments, however, decreased the initial diameter enough to observe the actual optimum diameter; i.e., the yields were not seen to decrease below a certain diameter.

We performed an initial radius scan for nickel wire arrays and aluminum wire arrays, as shown in Figure 1. Wire array diameters of 6 through 25 mm were tested with 12 wires per array, and the arrays were 2 cm in length. The details of these experiments are described in detail in References 6 and 7. In the case of the nickel wire array, previous experiments at PI had usually employed 9-mm diameter loads, which produce some 10 to 15 kJ of nickel L-shell radiation. By performing the scan in initial diameter, we found that 15-mm diameter arrays produced the optimum radiated kilovolt yield. A similar initial diameter scan of aluminum wire arrays showed a similar trend. Our spectroscopic analysis (which will be discussed in Section 4) indicated that aluminum implosions with diameters less than 12.5 mm did not produce plasmas that had a high enough electron temperature to permit the bulk plasma to be ionized into the K-shell.[7] Diameters larger than the optimum produce plasmas with sufficient temperature; however, their densities were lower since less mass was imploded hence the radiated yield decreased. A similar explanation[6] was proposed for the nickel results, but with an L-shell radiator the analysis is not so straightforward.

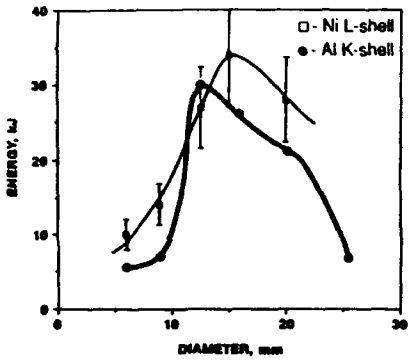

Figure 1. The x-ray yields for nickel L-shell and aluminum K-shell x-rays, as functions of the initial load diameter.

Another interesting challenge was to increase the radiated K-shell yield from argon gas puff implosions. Typically 5 to 7 kJ of argon K-shell x-rays were produced by Double-EAGLE when a 2.5-cm diameter, straight nozzle[8] as shown in Figure 2(a) was used. Time-resolved x-ray[9,10] pinhole photography indicated that a strong zipper was occurring and the plasma uniformity was not good. These measurements will be discussed in greater detail in Section 4. Our experience with tilted nozzles for neon-like krypton x-ray laser experiments suggested that the inwardly tilted nozzles produced a tight (~ 5 mm diameter), uniform pinch. Based on these observations, we tested a 4-cm diameter, ten-degree inwardly tilted nozzle, as shown in Figure 2(b). The measured x-ray yields increased to 10.5 ± 1.0 kJ when the tilted nozzle was used.[11] Figure 3 shows examples of the current pulses and K-shell pulses for both a tilted and straight nozzle. The pinch tightness and uniformity also improved. In addition, we applied the radius scaling technique described above, and we found that a 2.5-cm diameter nozzle with the ten degree inward tilt increased the yield to 12.5 kJ.

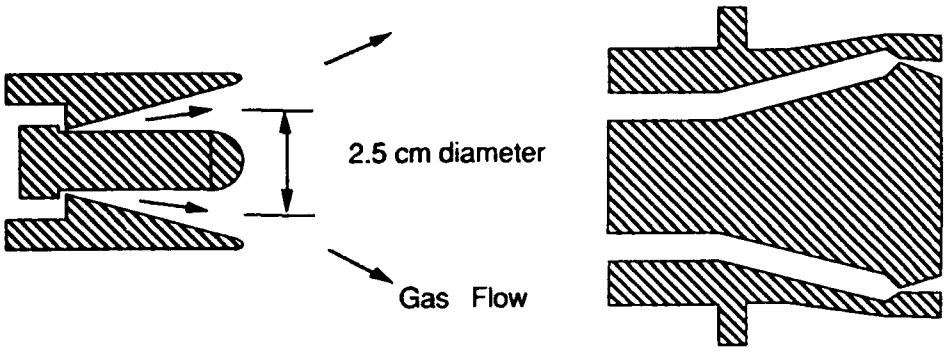

Figure 2. Cross-section of the two nozzles that we have tested: (a) is a Mach 4, 2.5 cm-diameter nozzle with a 8 mm exit width and (b) is a Mach 4, 4.0-cm-diameter nozzle with a 4mm exit width and a ten degree inward tilt. Nozzle (a) produces 5 kJ of argon K-shell x-rays whereas nozzle (b) produces 10 kJ.

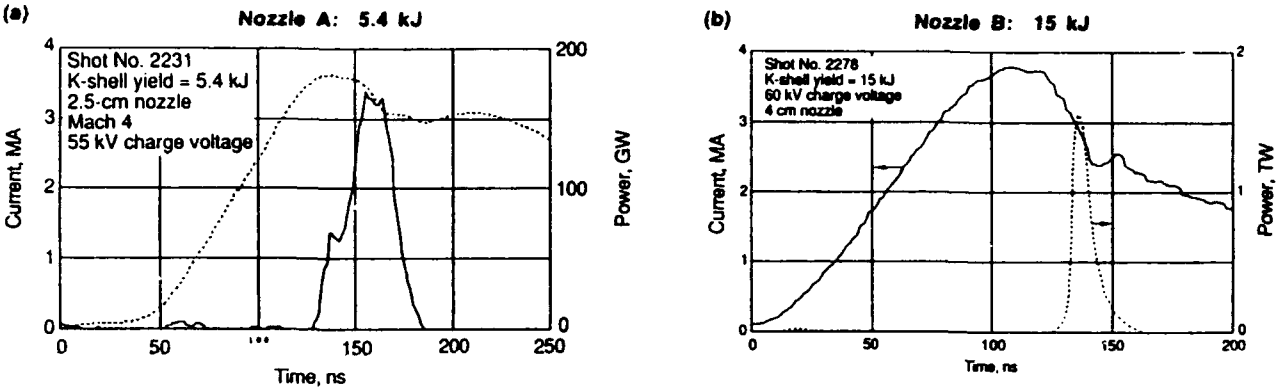

Figure 3. Current and K-shell power waveforms for Nozzle A and B.

Another well known method to increase the x-ray yield from a Z-pinch is to increase the driver current(I). Experiments[12,13] on generators at less than 3 MA showed that the K-shell yields from various elements like neon and argon scaled as I^4, and simple theoretical explanations for this behavior have been proposed.[14] Recent theoretical work has suggested that this I^4 scaling should transition to I^2 at a high current levels due to opacity effects. By operating Double-EAGLE at 10% higher voltage, therefore 10% higher current, the argon K-shell emissions increased from 12.5 to 18 ± 2 kJ, which is consistent with I^4 scaling; and indeed our x-ray measurements suggest that the argon plasma is not heavily trapped and therefore I^4 should be observed. In summary, we have found that radius scaling techniques and zipper elimination can increase x-ray emission from pulsed power driver Z-pinches.

Sodium-Neon X-ray Laser Research

The field of pulsed power driver x-ray lasers has recently been reviewed by Davis and Apruzese.[15] One approach to demonstrating gain on pulsed power Z-pinches is the sodium-neon photopump scheme.[16] In this concept, an intense sodium plasma should radiate > 100 GW in the Na X $1s^2$ - 1s 2p ^1P line at 11Å. This transition is resonant with the n = 1 to 4 transition in helium-like neon. If the neon plasma can be produced at the optimum temperature (T_e~40 eV) and density (~10^{18}cm^{-3}) either by a separate Z-pinch,[17] a photo-heated neon gas bag[18] or maybe

by a laser plasma,[19] then gain should be observed for a 2-cm pump-lasant separation. A limitation to this scheme has been the lack of an intense sodium pinch due to the difficulties in producing a sodium load for a Z-pinch. Workers at NRL developed a NaF capillary discharge[20] in which current flows in a NaF capillary placed behind a nozzle as shown in Figure 4. This results in a high pressure NaF plasma forming which ejects a plume into the diode anode-cathode gap. This source, when imploded on the Gamble II generator, produced up to 35-GW peak power in the pump line.[21] An upgraded source with a peak driver current of 200 kA was tested on Double-EAGLE, and we obtained 130 GW of peak power in the sodium pump line, as discussed by Young et al.[22] and as shown in Figure 5.

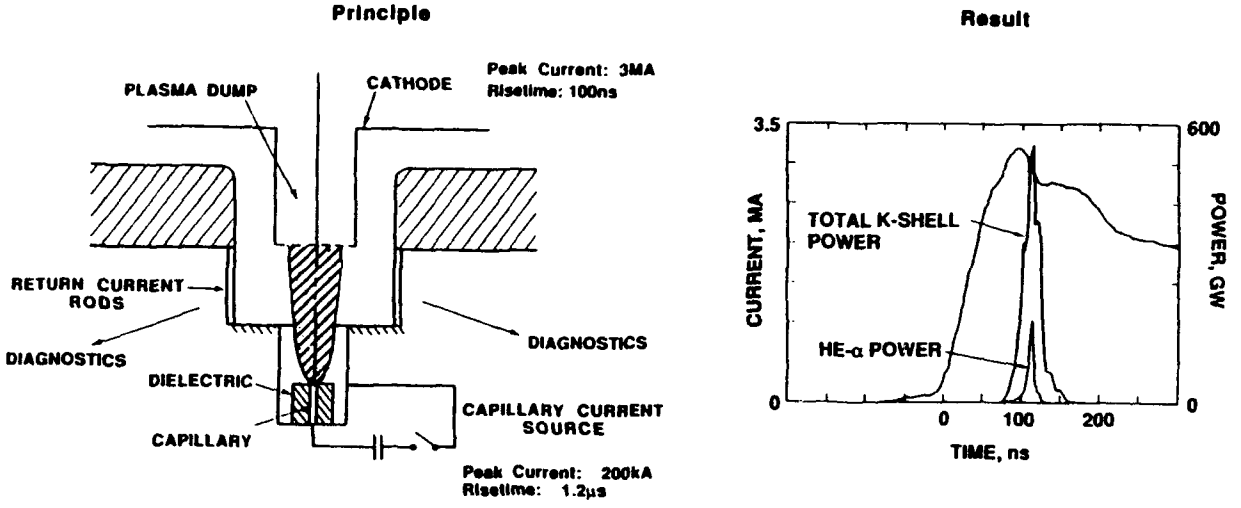

Figure 4. A schematic of the NRL NaF capillary discharge source fielded on Double-EAGLE. The plots show the measured K-shell and He-α power pulse overlayed on the current waveform. This source produces 130 GW in the sodium pump line.

At PI, we developed an alternate approach based on extruded sodium wires.[23] Figure 5 depicts the principle of the extruder and the results obtained. A high pressure ram was used to extrude sodium out through a set of pinholes which produced a wire array in-situ on Double-EAGLE. This array then formed the load for the generator. When these arrays were imploded, up to 170 GW of peak power in the pumpline was produced.[24] These first experiments had poor reproducibility, but subsequently J. Porter et al.[25] have improved the extrusion technique and on the 10-MA Saturn generator, around 250 GW can be obtained. Future experiments should now involve optimizing the neon plasma as has been discussed by Deeney et al.[26]

Basic Z-pinch Physics

Understanding of the physical processes in Z-pinches requires a combination of systematic experiments, diagnostics and theoretical calculations. We have applied these to our Z-pinch implosions on Double-EAGLE in two key areas: Z-pinch heating processes and the effect of implosion stability.

In the simplest model, an annular Z-pinch can be considered as a two stage process: the acceleration (implosion) phase where kinetic energy is stored in the collapsing shell, and the assembly phase where this kinetic energy is first thermalized and then radiated. Now, the question arises whether other heating processes, (pdV work due to instabilities or ohmic heating) contribute to the radiated energy. Whitney et al.[27] have studied the radiation efficiency behavior

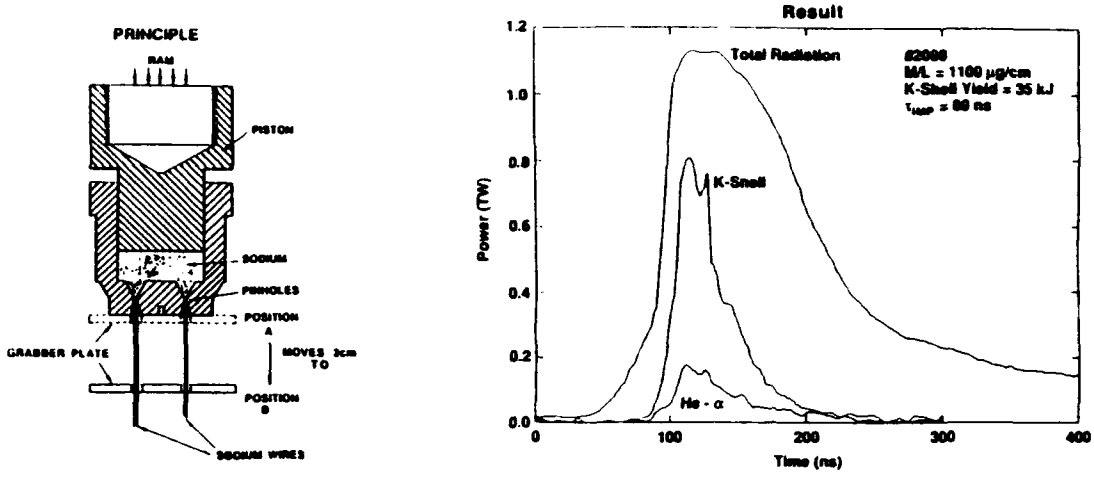

Figure 5. A schematic of the PI sodium wire array extruder and an example of the best performance. This source produced up to 170 GW in the pump line.

using a one dimensional (1D) laminar MHD code, with full radiation transport, under the condition that the kinetic energy is the only energy input to the system. This was ensured by turning off the current when the collapsing shell reached a radius of 10% of the initial radius. Subsequently, the shell would continue to the axis where thermalization and radiation would occur. Results of these calculations for our exact aluminum experimental conditions have been performed.[7]

We show a comparison of the measured K-shell x-ray yield versus the predicted K-shell yield based solely on kinetic energy input, in Figure 6. This comparison indicates that for the optimum conditions, the measured x-ray yields exceed those predicted by solely kinetic energy input. In addition, the 1D laminar calculations collapse to sub-millimeter dimensions which increase their density and probably result in the calculations somewhat overestimating the K-shell yields. We therefore interpret these results as indications of additional heating processes during the pinched phase of the plasma. There is supporting evidence for this additional heating based on our time-resolved x-ray measurements. We have analyzed our time-resolved x-ray spectra[28] based on the technique proposed by Coulter et al.[29] Figure 8 shows the estimated plasma radius (for the K-shell emitting plasma), K-shell radiating mass, plasma electron temperature and plasma ion density. From Figure 7, it is apparent that as the plasma expands, the electron temperature is also increasing. This suggests that there are additional heating processes occurring while the plasma is pinched on the axis. Giuliani et al.[29] found that with a zero dimensional code, they could predict the measured K-shell yields by artificially increasing the Spitzer resistivity. Thornhill et al.[30] have also found that by increasing the artificial viscosity and the resistivity (both mimic micro-turbulence effects) that 1D codes could be brought into agreement with the experimental parameters including plasma sizes, temperatures, densities and pulsewidths. The challenge to experimentalists is to try to measure the parameters to define the actual transport properties.

As we discussed in Section 2, we discovered that removing the zipper effect from our argon gas puffs resulted in a significant increase in the K-shell x-ray yield. Now, the zipper effect[31] is known to decrease the radiated power from a Z-pinch due to the increased axial thermalization time; however, it was not clear as to why the yield would be lower with the

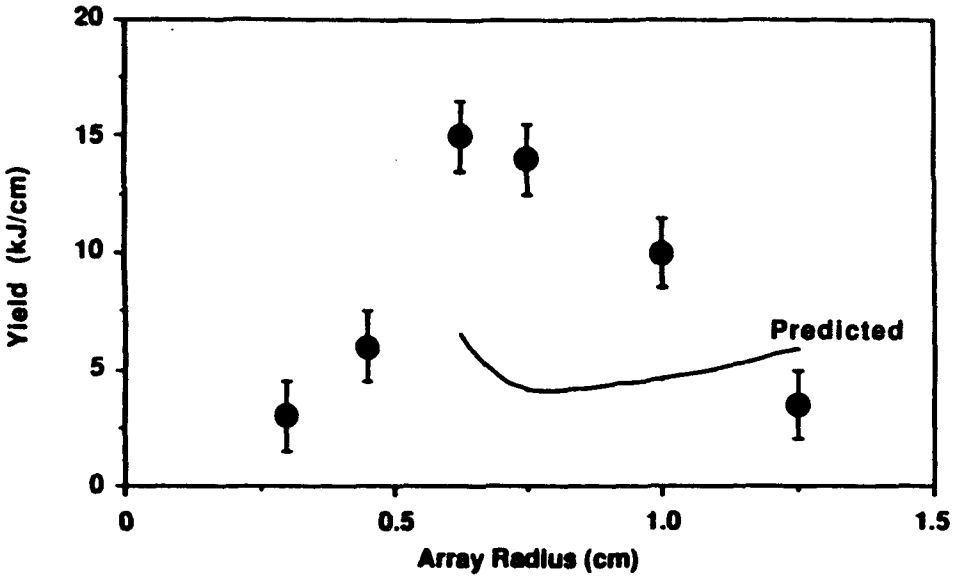

$\frac{\phi}{cm}$	η
0.3	0.5
0.45	0.8
0.625	1.6
0.75	2
1.0	3
1.25	5

Figure 6. A comparison between the measured aluminimum K-shell x-ray yields and those predicted by a 1D MHD code that only has kinetic energy input.

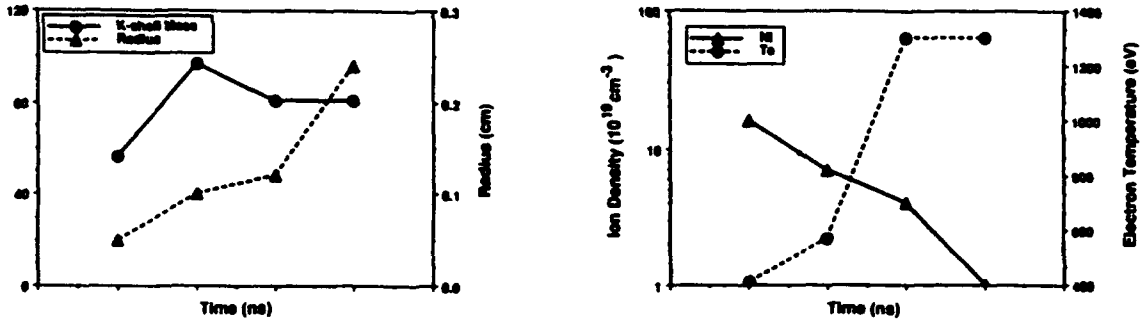

Figure 7. The measured k-shell radiating mass (mk), plasma radius (r_k), electron temperature (T_e) and ion density n_i for a 15 mm diameter aluminimum array.

zipper. We employed a 2D MHD code[33] without radiation transport, to simulate the implosions both with a zipper and without. Figure 8 shows examples of the 2D plots for the straight nozzle at 105 ns and 110 ns. At 105 ns, the shell has pinched at z=0 (the nozzle). By 110 ns, the pinch has migrated along about 1 cm of the shell's length. The 110-ns plot also shows the formation of an axial jet which is propagating along the axis as the remaining shell is imploding. We conjectured that this plasma and axis was probably limiting the compression of the rest of the shell as it implodes onto the axial plasma. To confirm this we compared the two values:

$$\frac{dQ}{dt} = \int n_e n_i \, dV$$

which is the volume integral of the electron-density-ion-density product and

$$Q = \int \int n_e n_i \, dv \, dt$$

which is the integral of dQ/dt in time. If the plasma is optically thin, Q should be related to the yield. Figure 9 shows the dQ/dt and Q traces for a 2.5-cm diameter nozzle with a 4-mm wide exit for three tilts: 0, -7.5 and -10 degrees. Clearly, the straight nozzle has a lower density, and its radiated power and yields should therefore be lower.

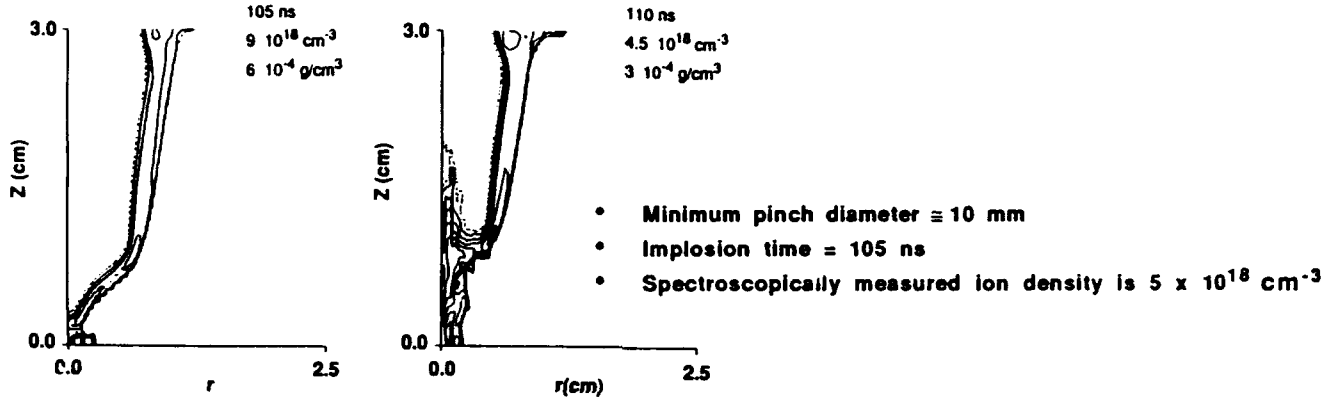

Figure 8. Density contour plots produced by a 2D MHD code for a zippering plasma with an initial mass loading of 50 μg/cm.

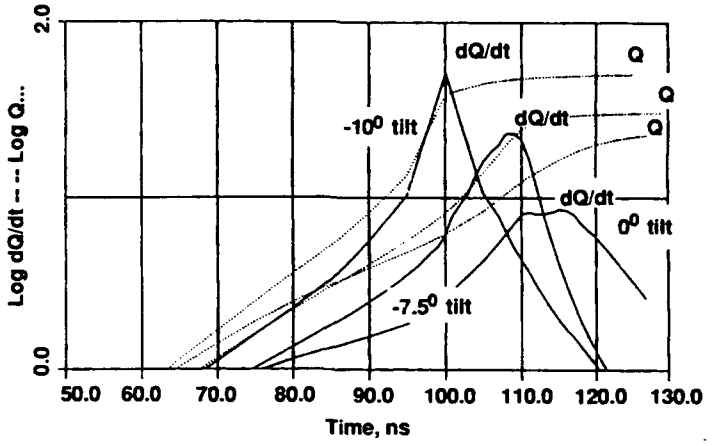

Figure 9. Curves of the volume integrated electron-ion-density product and its integral in time. These should be proportional to the radiated power and yield for an optically thin plasma.

Summary

In conclusion, we have made significant progress in increasing the x-ray emission from Z-pinches and in understanding the radiation process. We have also tested new sodium plasma sources which have allowed us to demonstrate >100 GW in the Na He-a line, which should be adequate to demonstrate gain in the sodium-neon scheme if a properly prepared neon plasma can be produced. Future experiments and theory will be aimed at improving the performance of present and future Z-pinches based on our increased understanding. We will also develop more innovative loads based on our results to hopefully increase the K-shell x-ray yields from higher atomic number.

We would like to acknowledge the technical support of Norm Knobel, the Double-EAGLE crew and Susan Green. Dwight Duston is thanked for the support of our x-ray laser work and Jack Davis' encouragement and guidance on our x-ray laser and Z-pinch research are also appreciated.

References

1. N. R. Pereira and J. Davis, J. Appl. Phys. 64(3), R1, (1988).
2. M. Krishnan, et al., AIP Conf. Proc. 195, 17, (1989).
3. P. Sincerney, et al., Proc. of the 5th IEEE Pulsed Power Conference, 151, (1985).
4. S. J. Stephanakis, et al., NRL Plasma Tech-Note 85-51, (1985).
5. M. Gersten, et al., Phys. Rev. A 33(1), 477, 91986).
6. C. Deeney, et al., JQSRT, 44(5,6), 457, (1990).
7. C. Deeney, et al., Phys. Rev. A 44(10), 6726, (1991).
8. R. S. Smith, W. O. Doggett, I. Roth, and C. Stallings, Appl. Phys. Lett. 43, 572, (1982).
9. T. Nash, et al., JQSRT 44(5,6), 485, (1990).
10. T. Nash, et al., Rev. Sci. Instrum. 61(10) Part II, 2807, (1990).
11. P. D. LePell, et al., submitted to Phys. Rev. Lett.
12. S. J. Stephanakis, et al., Appl. Phys. Lett 48(13), 829, (1986).
13. S. Wong (Private Comm.)
14. J. P. Apruzese and J. Davis, NRL Memo Report 5406, (1984).
15. J. P. Apruzese and J. Davis, Proc. of the Intl. Conf. on Lasers, 89, p7, (1989).
16. J. P. Apruzese, et al., J. Appl. Phys. 53, 4020, (1982).
17. C. Deeney, et al., OSA Proc. on Short Wavelength Coherent Radiation Generation, Volume 2, 157, (1988).
18. J. Porter and R. Spielman (Private Communication).
19. M. Krishnan (Private Comm.)
20. B. L. Welch, et al., J. Appl. Phys. 65, 2664, (1989).
21. F. C. Young, et al., Appl. Phys. Lett 50, 1053, (1987).
22. F. C. Young, et al., J. Appl Phys. 69(11), 7520, (1991).
23. C. Deeney, et al., Rev. Sci. Instrum. 61(5), 1551. (1998).
24. C. Deeney, et al., Appl. Phys. Lett. 58(10), 1021, (1991).
25. J. Porter, et al., Phys. Rev. Lett. 68(6), 796, (1992).
26. C. Deeney, et al., Proc. of the Second Intl. Colloquium on X-ray Lasers, IOP Press. (1991).
27. K. G. Whitney, et al., J. Appl. Phys. 67, 1725, (1990).
28. T. Nash, et al., Rev. Sci. Insrum. 61(10) Part II, 2804.
29. J. Giuliani, et al., JQSRT 44(5,6), 471, (1990).
30. J. W. Thornhill, et al., submitted to the Journal of Radiation Effects.
31. T. W. Hussey, et al., J. Appl. Phys. 58(8) 2677, (1986).
32. W. W. Hsing and J.L. Porter, Appl. Phys. Lett. 50(22), 1572, (1987).
33. F. L. Cochran and J. Davis, Phys. Fluids B 2(6), 1238, (1990).

Radiative Z-Pinch Coupling to an Inductive Generator

J.L. Giuliani, Jr., M. Mulbrandon, and R. Terry
Radiation Hydrodynamics Branch
Plasma Physics Division
Naval Research Laboratory, Washington DC 20375-5000

P. Ottinger and R. Commisso
Pulsed Power Physics Branch
Plasma Physics Division
Naval Research Laboratory, Washington DC 20375-5000

C. Deeney and P.D. LePell
Pulsed Power & Plasma Physics Dept.
Physics International Co., San Leandro CA 94577-0599

Abstract

The utility of inductive generators and existing results from Z-pinch experiments using a plasma opening switch (POS) are reviewed. The research then focuses on a systems study of the power flow coupling between a particular inductive generator with a POS and an imploding Z-pinch load. An end-to-end numerical simulation model for the generator, switch, and dynamic load is used to predict the K-shell radiation arising from a neon puff gas implosion. The feedback of the load on the switch impedance and the dependence of the high energy radiation on various switch opening models is discussed.

I. Introduction

As pulsed power generators are asked to deliver ever higher currents to a load, inductive store designs have become the focus for the next generation of high power machines. Papers from Physics International,[1] Maxwell Labs,[2], the High Current Electronics Institute[3], and Sandia National Laboratory[4] each describe new high power inductive machines which will supplement existing water line capacitive generators. The advantages of an inductive store generator over a capacitive one are (i) a smaller space requirement, which readily translates to cost, and (ii) lower voltage stresses on the circuit components. An intermediate storage inductor can provide a higher energy density at a lower voltage than a capacitive store element. Hence for a given energy, both the intermediate element and the Marx bank can be made smaller for an inductive generator. The disadvantage of such a generator is the requirement for a plasma opening switch (POS) that can conduct for hundreds of nsec, but open in tens of nsec. While the technology for closing switches used on capacitive generators is well developed, the physics

of the long conduction time POS is still current research, as evidenced by the many papers on this topic in the opening switch section of this conference proceedings.

Many theoretical and experimental studies have looked at the power coupling between a POS and a diode load. The first opening switch, with conduction time < 50 nsec, was used on a capacitive generator for prepulse current suppression into a diode.[5] Recent experimental work on the POS-diode coupling issue for a long conduction time POS were presented by Goodrich *et al.*[6] and Commisso *et al.*[7] for the HAWK inductive generator. Their results indicate that the switch plasma opens to a gap size of a few percent of the cathode radius.

For the coupling between a POS and a Z-pinch load there has only been a few reports. The initial work was also done on capacitive generators and for short conduction times. Stringfield *et al.*[8] found a shorter risetime for the load current and a more uniform plasma implosion on PITHON. Later Stephanakis *et al.*[9] further demonstrated a larger neon K-shell radiation production at a given current on GAMBLE II. Some analytic scaling arguments for the kinetic energy coupling on an ideal circuit composed of an inductive store, resistive shunt switch, and a shorted load, were presented by Reinovosky *et al.*[10], but no radiation effects were included. Mosher and Commisso[11] also developed some scaling laws for a similar circuit and modeled the radiation production with a gas bag model and a phenomenological radiation transfer. In a forthcoming paper Deeney *et al.*[12] have experimentally demonstrated an increase in the neon K-shell yield when a POS is added to the inductive generator FALCON.

The objective of this paper is to present a systems analysis of the energy coupling in a realistic machine from the Marx bank, through a long conduction time POS, to the Z-pinch K-shell radiation production. The chosen circuit is similar to inductive generator designs currently under development. The analysis is accomplished with an end-to-end simulation model, which includes a transmission line code for the circuit, an opening switch model, and a multi-zone magnetohydrodynamic code for the imploding neon Z-pinch. For the present switch model we find that the switch impedance Z_{POS} can vary dramatically in time due to the changing motional inductance of the load. Although the time average of Z_{POS} and the total energy transferred to the load monotonically increase for larger mass loadings, the neon K-shell production displays a particular maximum versus load mass as a result of atomic physics considerations. Finally, simulations for various switch gap size to cathode radius, d/R_c, and opening times, Δt, are compared.

II. Simulation Model

The transmission line circuit for the driving generator is shown schematically in Fig.1. The circuit, a mixture of capacitive and inductive generator components, is based on machine

designs developed by Physics International[1] and Sandia[4]. A Marx bank with an internal resistance first charges a water dielectric capacitor which is incorporated to obtain current pulse compression. After 1 μsec the transfer switch fires and current begins to flow in the storage inductor. The POS switch, represented by the time varying resistive shunt to ground, conducts for 0.5 μsec and then opens transferring current to the magnetically insulated transmission line (MITL). The circuit is bi-modular being joined at a convolute. The Z-pinch length is 3 cm with 2.5 nH initial inductance.

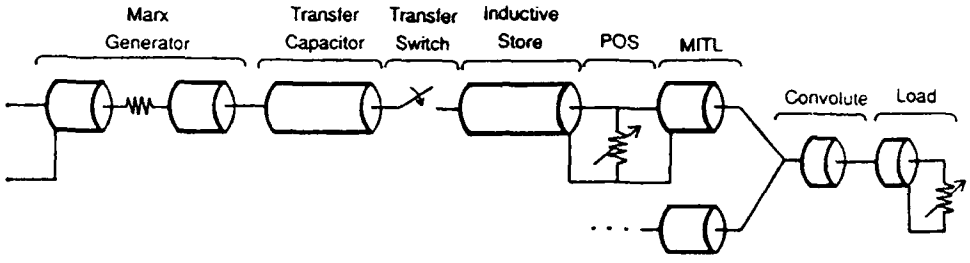

Fig.1 Bi-modular transmission line schematic of the generator circuit in the numerical simulations. The POS is treated as a time varying resistive shunt to ground.

The power flow along the circuit is calculated using rightward and leftward moving voltage waves. Transmission and reflection coefficients at the junctions determined from Kirchhoff's laws provide relations for the waves at the right and left boundaries of each element.[13] Since the load is dynamic the timestep in the calculation varies and a high order advection transport algorithm is used to advance the voltage waves within each element.

In the adopted opening switch model the shunt resistance of the POS is negligibly small during the conduction phase. The fiducial time taken to mark the beginning of the opening phase is $t = 0$. The switch gap size, d, is specified by a linear rise from 0 over a time Δt to a maximum value, d/R_c with R_c the cathode-plasma radius. We vary d/R_c from 2% to 5%, and Δt from 70 to 140 nsec. The gap size openings were chosen as reasonable values based on the data from Commisso *et al.*[7]. For $t > 0$ we require that the upstream current entering the switch must exceed the critical current for electron insulation which depends upon the voltage drop across the switch V_{POS}.[14] Once the electron flow becomes insulated in the switch, the shunted current through the switch, I_{POS} is given by ion Child-Langmuir flow.

The dynamics of the imploding gas puff is modeled with a 1-D, multi-zone Lagrangian hydromagnetic code with thermal conduction, resistive heating, and radiative losses in the internal energy equation. The induction equation for the magnetic field uses Spitzer resistivity. The coupling between the transmission voltage waves and the Z-pinch dynamics is handled implicitly to ensure total energy conservation throughout the circuit-POS-load system. The

ionization dynamics is calculated from a collisional-radiative equilibrium model[15] for neon including the ground states of all ionization stages and 95 excited levels spread throughout the stages. For the radiation transport a total of 60 emission lines are followed with a probability-of-escape method while the bound-free edges and free-free continuum are done with multi-frequency transport.

III. Results

Let us first discuss the interaction of the POS and load dynamics for the standard switch parameters. Figure 2 presents the time development of various circuit, POS, and load quantities. As the switch begins to open ($t > 0$) one clearly sees in Fig.2a the decrease in the current across the switch and the concomitant increase in the current transferred to the downstream MITL.

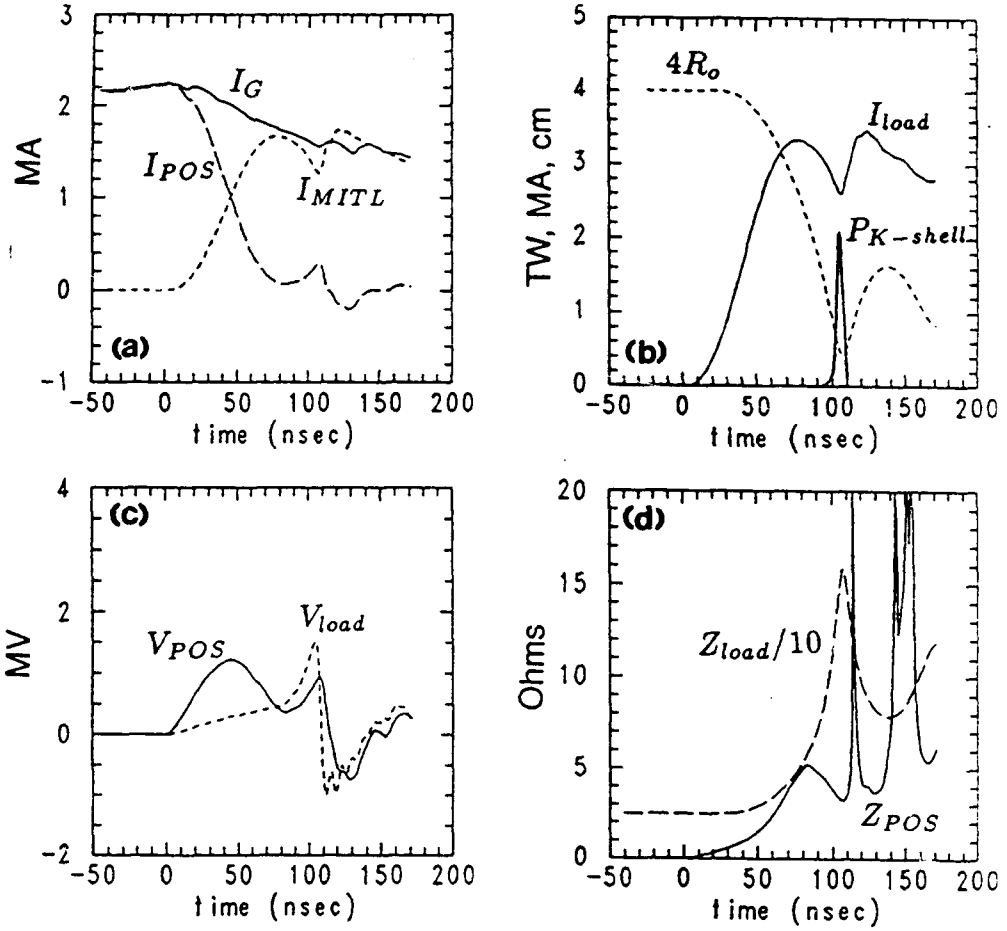

Fig.2 POS and load dynamics for a 1 mg neon gas puff implosion starting at an outer radius R_o = 1 cm with the standard opening switch parameters d/R_c = 5% and Δt = 70 nsec. (a) Generator current I_G immediately upstream of the POS, shunted current I_{POS} across the POS, and transferred current I_{MITL} for one of the modules. $t = 0$ corresponds to the opening of the switch. (b) Combined current into the load I_{load}, the outer radius of the plasma R_o, and the K-shell radiation pulse from the implosion. (c) The load and POS voltage. (d) The impedance of the load Z_{load} and across the switch Z_{POS}. Note the irregular behavior of the latter.

Figure 2b shows that the implosion time, t_{imp}, corresponding to the minimum pinch radius, occurs 105 nsec after the switch opens. The implosion marks the time of the K-shell radiation pulse and the notch in the load current due to the large motional inductance of the pinch. After the gap of the POS fully opens, the switch voltage tracks the load voltage in Fig.2c, except for a few nsec time delay. When the pinch rebounds, V_{load} reverses sign due to the now negative motional inductance, and energy is driven back upstream of the load region. Subsequently, V_{POS} goes negative and stays so as long as the plasma re-expands after the initial bounce. Since the switch can only dissipate energy, I_{POS} is also negative and I_{MITL} exceeds the generator current I_G between 115 and 140 nsec. Note that the switch impedance in Fig.2d displays an irregular spike and trough behavior. This behavior is quite different from that of a diode load wherein Z_{POS} monotonically increases in time. From ion Child-Langmuir flow, the impedance of the opened switch is proportional to $d^2/\sqrt{V_{POS}}$. Thus whenever V_{POS} is small and the gap d is opened, such as at ~85 nsec, ~115 nsec, and around 150 nsec, the switch impedance becomes large. From the discussion above, it is the motional inductance term of V_{load} which causes V_{POS} to decrease and/or cross zero. Note that the K-shell pulse occurs at the maximum load impedance and in the first trough of Z_{POS}.

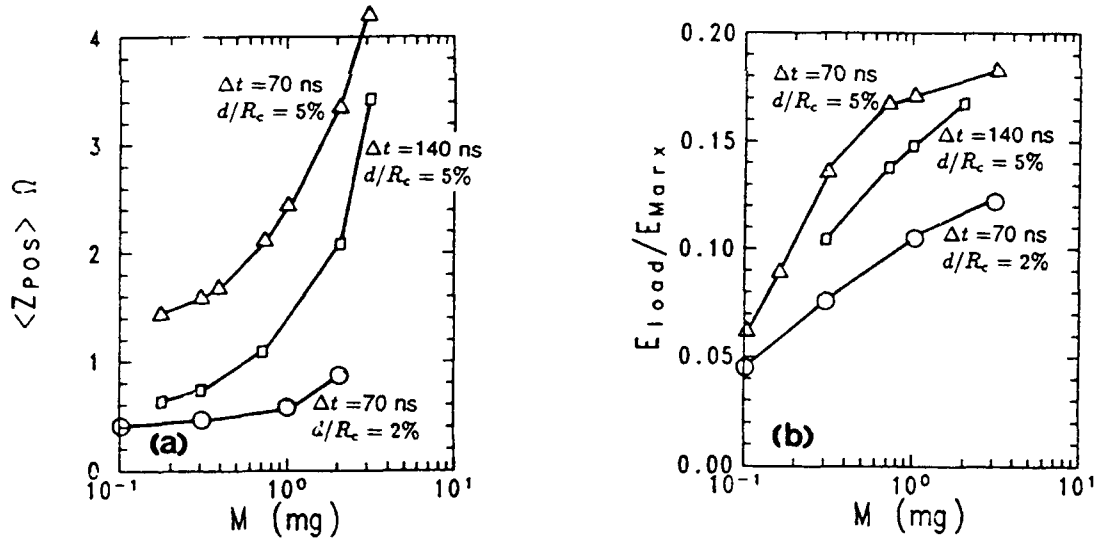

Fig. 3 Coupling properties between the circuit and load as a function of the load mass for different switch models characterized by the opening time Δt and maximum switch gap d/R_c. (a) Time averaged value for the switch impedance Z_{POS}. (b) The total energy into the load cage, including magnetic energy, work done in compression, and resistive heating, normalized by the energy initially stored in the Marx bank.

Unpublished analysis of POS current and impedance on the FALCON generator also indicate (i) a spike and trough behavior for Z_{POS}, (ii) a K-shell pulse at the first trough, and

(iii) a POS current reversal between two spikes in Z_{POS}. Although such measurements are rather difficult since they involve an inductive correction to the measured insulator voltage and the subtraction of the measured generator and load currents, it is encouraging to note the similar behavior between simulation and tentative measurements.

One can compare the POS coupling to the load by time averaging Z_{POS} for different load masses and the same initial R_o = 1 cm. Figure 3a shows this result for three different time histories of d/R_c. The total load energy coupling is presented in Fig.3b. For each switch model the larger the load mass, *i.e.*, the longer the implosion time, the more efficient is both the switch operation and the energy transferred to the load. However, comparing the individual models shows that the POS and energy coupling is particularly sensitive to the gap size. For small load masses where $t_{imp} < \Delta t$, the coupling efficiency is also reduced, but as t_{imp} becomes larger than Δt, the coupling approaches that of the standard case.

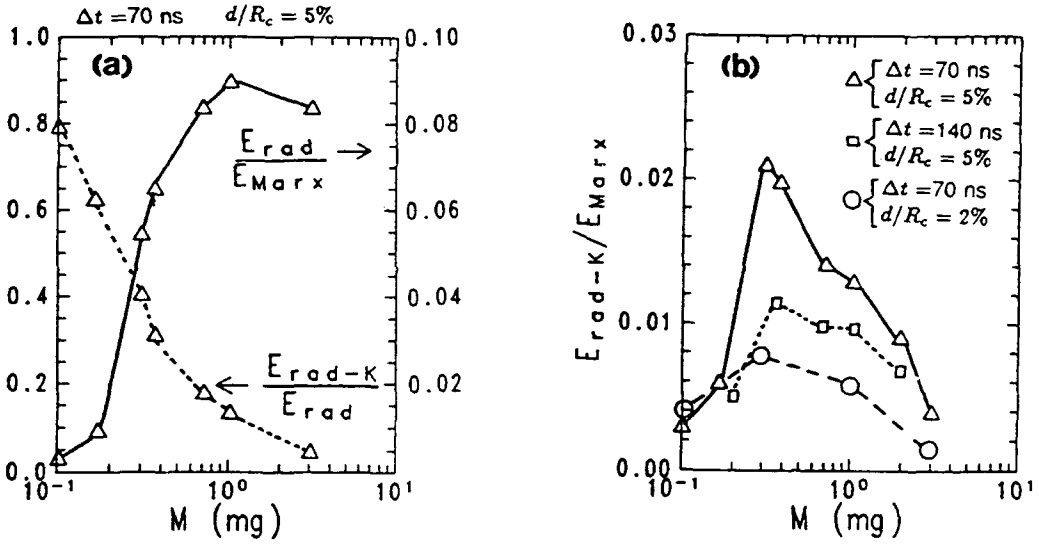

Fig. 4 Radiation coupling between the circuit and the load as a function of the load mass.
(a) For the standard switch parameters, the fraction of the Marx energy emitted as radiation over the whole spectrum E_{rad}/E_{Marx}, and the fraction of the radiation which is from the K-shell (above 900 eV) E_{rad-K}/E_{rad}.
(b) The K-shell production efficiency for different switch models.

Finally we turn to the radiation coupling problem. Figure 4a displays the total radiation versus mass loading and the fraction of that radiation which emerges in the K-shell range (> 900 eV) for the standard switch parameters. The rise in the total radiation with load mass reflects improved load energy coupling from Fig.3b as well as the increase in the number of radiators. The monotonic decrease in E_{rad-K}/E_{rad} indicates a smaller imparted energy per particle at implosion time for larger masses. According to Whitney *et al.*[16], it requires ~4.8 keV per

atom for the imploding neon to be thermalized to the helium and hydrogen-like stages. At the lowest mass the velocity of the imploding nuclei is large enough to strip most of the atoms, and the only radiation that can emerge is recombination to the bare nuclei. For the largest mass load, the energy carried per particle is too small to reach the K-shell.

Figure 4b shows the efficiency of the K-shell radiation versus load mass again for the three switch models. The peak of the K-shell radiation for the standard case is nearly three times that of the small gap size switch, and twice that of the slower opening switch. As in Fig.3 note that the case with Δt = 140 nsec approaches the radiation efficiency of the standard case for loads with the longest implosion times.

IV. Discussion

Experimental progress on the energy coupling between a generator with a POS and the radiative production from an imploding Z-pinch has not significantly advanced since the early work on the capacitive machines PITHON and GAMBLE II a decade ago. With the advent of several new inductive generators this situation will hopefully change in the near future. As a prelude to the experimental work we have presented end-to-end simulation models of a realistic generator driving a neon gas puff Z-pinch load. The numerical results indicate that the large motional inductance of an imploding and bouncing Z-pinch will induce large oscillations in the POS impedance. Measurements of Z_{POS} could be used to evaluate models of the current flow across the switch once the gap opens. We have also found that the coupling, as measured by the time averaged Z_{POS} and the total energy into the load region, becomes more efficient as the load mass, *i.e.*, implosion time, increases. However, the K-shell radiation production is dominated by atomic physics processes and displays a definite peak over the load mass. For the given POS model the results suggest that the gap size d/R_c is a more significant factor in controlling both the total energy coupling and the K-shell radiation than is the opening time Δt. Increasing d/R_c from 2% to 5% nearly tripled the maximum K-shell radiation. If the implosion time is less than Δt then the switch never fully diverts current to the load and the radiation production is also reduced.

We have used a limited switch model and further analysis using more intricate models is called for. For instance, it would be useful to know if the load behavior can also affect the gap size. There are other issues that need to be considered in a complete model. First, the insulation of the transmission line between the POS and the load would affect the power flow problem,[17] especially if switch plasma is blown toward the load. In a multiple modular generator the impact of jitter[18] between the different modules may affect the POS behavior. One long standing problem in Z-pinch simulations is the calculated short pulse widths compared to measurements

for both the total and K-shell radiation. Davis and Cochran[19] suggest that 2-D zippering effects could be the problem. Finally, implosion models with moderate Z materials often require an enhanced resistivity to match the data. This issue is discussed by several papers in this conference.[20], [21], [22]

Acknowledgements

The first author would like to thank J. Davis for many discussions and continued encouragement during the work. The research was sponsored by the Defense Nuclear Agency.

References

[1]P. I. Sincerny, F. K. Childers, C. Deeney, D. Kortbawi, J. Goyer, J. Riordan, I. Roth, C. Stallings, and L. Schlitt, in this conference proceedings.

[2]W. Rix, A. R. Miller, J. Thompson, E. Waisman, M. Wilkinson, and A. Wilson, in this conference proceedings.

[3]B. M. Koval'chuk, S. P. Bugaev, A. M. Volkov, A. A. Kim, V. N. Kiselev, N. F. Kovsharov, V. A. Kokshenev, G. A. Mesyats, and A. P. Huseev, in this conference proceedings.

[4]M. E. Savage, G. W. Cooper, W. W. Simpson, and M. A. Usher, in this conference proceedings.

[5]W. Mendel, Jr. and S. A. Goldstein, *J. Appl. Phys.*, 48, 1004 (1977).

[6]P. J. Goodrich, J. R. Boller, R. J. Commisso, D. D. Hinshelwood, J. C. Kellogg, B. B. Weber, *Proceedings 8th IEEE Int. Pulsed Power Conf.*, San Diego, CA, p.515 (1991).

[7]R. J. Commisso, P. J. Goodrich, J. M. Grossmann, D. D. Hinshelwood, P. F. Ottinger, and B. V. Weber, *Phys. Fluids B*, July issue (1992).

[8]R. Stringfield, R. Schneider, R. D. Genuario, I. Roth, K. Childers, C. Stallings, and D. Dakin, *J. Appl. Phys.*, 52, 1278 (1981).

[9]S. J. Stephanakis, J. P. Apruzese, P. G. Burkhalter, J. Davis, R. A. Meger, S. W. McDonald, G. Mehlman, P. F. Ottinger, and F. C. Young, *Appl. Phys. Lett.*, 48, 829 (1986).

[10]R. E. Reinovosky, D. L. Smith, W. L. Baker, J. H. Degnan, H. P. Henderson, R. J. Kohn, D. A. Kloc, and N. F. Roderick, *IEEE Trans. on Plasma Sc.*, **10**, 73 (1982).

[11]D. Mosher and R. J. Commisso, *NRL Memorandum*, 6427 (1989).

[12]C. Deeney, P. D. LePell, I. Roth, T. Nash, L. Warren, R. R. Prasad, C. McDonald, P. Sincerny, M. C. Coulter, and K. Whitney, submitted to *J. Appl. Phys.* (1992).

[13]D. D. Hinshelwood, *NRL Memorandum*, 5185 (1983).

[14]P. F. Ottinger, S. A. Goldstein, and R. A. Meger, *J. Appl. Phys.*, 56, 774 (1984).

[15]D. Duston, R. W. Clark, J. Davis, and J. P. Apruzese, *Phys. Rev. A*, 27, 1441 (1983).

[16]K. G. Whitney, J. W. Thornhill, J. P. Apruzese, and J. Davis, *J. Appl. Phys.*, 67, 1725 (1990).

[17]C. W. Mendel, Jr., D. B. Seidel, W. A. Johnson, and S. E. Rosenthal, in this conference proceedings.

[18]P. I. Sincerny, F. K. Childers, C. Deeney, J. Goyer, D. Kortbawi, P. D. LePell, J. C. Riordan, and I. S. Roth, in this conference proceedings.

[19]J. Davis and F. L. Cochran, in this conference proceedings.

[20]J. W. Thornhill, K. G. Whitney, C. Deeney, M. C. Coulter, P. E. Pulsifer, F. L. Cochran, and J. L. Giuliani, Jr., in this conference proceedings.

[21]P. E. Pulsifer, K. G. Whitney, and J. W Thornhill, in this conference proceedings.

[22]R. B. Spielman, in this conference proceedings.

THE LOS ALAMOS FOIL IMPLOSION PROJECT

J. Brownell, J. Parker, R. Bartsch, J. Benage, R. Bowers,
J. Cochrane, P. Forman, J. Goforth, A. Greene, H. Kruse, J. Ladish,
H. Oona, D. Peterson, R. Reinovsky, N. Roderick*, J. Trainor, P. Turchi**

Los Alamos National Laboratory
Los Alamos, NM 87545, U. S. A.

Abstract

The goal of the Los Alamos foil implosion project is to produce an intense (>100 TW), multi-megajoule, laboratory soft x-ray source for material studies and fusion experiments. The concept involves the implosion of annular, current-carrying, cylindrical metallic plasmas via their self-magnetic forces. The project features inductive storage systems using both capacitor banks and high explosive-driven flux compression generators as prime energy sources. Fast opening switches are employed to shorten the electrical pulses. The program will be described and activities to date will be summarized.

Introduction

The goal of the Los Alamos foil implosion project is the development of an intense (>100 TW) source of soft x-rays and hot plasma produced from the thermalization of 1 to 10 MJ of plasma kinetic energy. With a pulse duration of 10's of nanoseconds this source will be used for the study of material properties and fusion conditions. The source is formed by passing a large current through a thin cylindrical metallic foil, thus producing a plasma that implodes under the action of its self-magnetic force and stagnates on axis to produce a hot, radiative plasma that calculations indicate will have a blackbody temperature of several hundred electron volts. This concept has also been studied at other laboratories including the Phillips Laboratory[1], Maxwell Laboratories[2], Physics International[3], Sandia National Laboratory[4], and the Kurchatov Institute[5] using capacitor banks.

At Los Alamos both capacitor bank facilities and explosive flux compression generators (FCG) are being used in the research. An FCG uses explosive energy to do work on a conducting shell which encloses an initially emplaced magnetic field. The field is compressed, and the magnetic energy is amplified. Since the FCG operates on a long time scale (50 to 300 μs) compared to the implosion time ($\sim$ 300 - 600 ns), substantial pulse compression is required.

One or more opening switches provide this pulse compression with the final switch transferring the stored electrical energy in 300 - 600 ns to a load that consists of a very thin (typically a few thousand angstroms) cylindrical metallic foil. The foil vaporizes in a few tens of ns to form a plasma that implodes under the **jxB** force and stagnates to produce radiation. The overall power compression from FCG to radiation output may be as much as 40000. The overall efficiency of the system (explosive energy to radiation) is potentially as high as 1%. FCG's offer system flexibility at very large electrical energies, and they allow the feasibility of the concept to be examined with a small capital investment.

In this paper we shall briefly review the history of the project, detail current activites in explosive pulsed power, fast opening switches, and plasma implosion physics, and, finally, outline our plans for the future.

History

Early in the project it was decided to use inductive storage systems instead of high voltage water-line technology because of the potential for economical scaling to very high energy output. Research has focused on pulsed power development, both experimental and calculational. Three experimental FCG systems at increasing energies have been completed, and a fourth is now underway. In addition, opening switch and implosion experiments have been performed at our capacitor bank driven inductive storage facility.

A. Trailmaster and Pioneer

The first FCG system, designated Trailmaster, demonstrated that explosively driven inductive storage systems constituted a viable approach. The second system, designated Pioneer, utilized a circuit consisting of a plate-type flux compression generator, a plasma compression opening switch (planar version of the Pavlovsky switch)[6], and an integral transmission line and foil diode.[7] A high quality implosion was achieved and 20 kJ of x-rays were emitted from a 30 ev plasma with a pulse width of approximately 250 ns. One and two dimensional MHD calculations predicted the dynamics, the radiation pulse width, and the plasma temperature. Pioneer demonstrated the principle of an FCG-driven x-ray source and laid the foundation for the design of megajoule coaxial systems.

B. LAGUNA

The third experimental FCG system, designated Laguna, had the goal of producing a plasma kinetic energy of 100 kJ. Several components of this system were prototypes for

our planned megajoule system, including the helical Mark-IX FCG, an explosively-formed fuse opening switch (EFF), vacuum power flow channel, and diode load.

The Mark-IX FCG has an initial inductance of about 7.2 μH that is charged by a capacitor bank to 430 kA in about 150 μs. After a run-time of 200 μs it has generated 12 MA in a 120 nH load.[8] The EFF, a robust, long conduction time opening switch, was developed to carry the output of the Mark-IX and open in about one microsecond, thus compressing the pulse duration by a factor of more than 300.[9] The Laguna EFF developed a higher resistance than expected and produced a higher voltage (250 kV) than the rest of the system was designed to handle. As a result Laguna had to be operated below the design current. Even so a current of 4 MA was driven through the load foil (5cm initial radius, 2 cm long, 2500 $\AA$ thick aluminum foil). Visible framing camera pictures and an x-ray pinhole picture were obtained of the plasma pinch. A bolometer measurement indicated 80 kJ of x-radiation was produced. These measurements are consistent with post-shot calculations based on the measured current profile.

Current Activities

A. Procyon

The Procyon FCG system utilizes the experience obtained from Pioneer and Laguna to address plasma implosions at the megajoule level. Subsystems of Procyon are currently being tested. Implosion experiments are scheduled to be performed next year.

The energy source for Procyon is the same Mark-IX used in Laguna, but in this design it generates 22 MA in a 70 nH storage inductor. To circumvent the problem of high voltages that are generated in a single-stage opening switch at high current, Procyon uses two stages of switching.

The first stage opening switch is a flux conserving EFF (or FCEFF), a variation of the EFF that trades higher efficiency for somewhat slower operation. The FCEFF transfers 16.5 MA into a plasma flow switch (PFS) in 4.6 μs. The PFS is the second stage opening switch in Procyon.[10] The PFS consists of an annular plasma that is formed from a mass-graded (to maintain planarity) wire array plus a mylar barrier film. The combined plasma is accelerated axially towards the load slot by self-magnetic pressure; current is switched into the imploding foil load as the trailing edge of the plasma crosses the slot. The PFS switches about 15 MA into the load chamber in less than 500 ns. The complete Procyon

system is contained in a cylinder that is about 0.7 meters in diameter by 4 meters in length.

The advantage of the PFS is that commutation is accomplished without generating large voltages. However, one must deal with instabilities that arise from the switch plasma's interaction with the load. Preliminary 1-D calculations of PFS operation have been performed with the Lagrangian MHD code RAVEN. These first-principles calculations of PFS performance start with room temperature aluminum and carry it through its solid, liquid, and vapor phases into the plasma phase.

Using the 1-D results as a starting point, self-consistent 2-D radiation-MHD calculations have been performed to study switching efficiency and the effect of switch plasma on implosion quality. These calculations are considered to be a baseline determination of system performance because they assume a planar (i.e. unperturbed) PFS profile at a point that is 0.5 cm before the load slot. The switch plasma interacts with the imploding plasma, and severe perturbations that are the magnetic analog of the Rayleigh-Taylor instability grow as the implosion proceeds. The calculations predict a double peak radiation pulse. The first pulse is produced when a bubble of low-density plasma with an internal energy of 0.2 MJ stagnates on axis in 14 ns. The second pulse results when about 75% of the initial mass, with a kinetic energy of 0.5 MJ, thermalizes in 30 ns. These calculations are preliminary; the design will be optimized when the PFS and its interaction with the load foil are more fully understood.

B. Pegasus

Although our main thrust has been explosive pulsed power, we have also developed a laboratory capability based on capacitor bank driven inductive energy storage. We are currently using the 1.5 MJ, 216 μF, 6.5 MA Pegasus bank for PFS and plasma implosion experiments.

1. Plasma Flow Switch

The current carrying capacity of the opening switch for a future 10 MJ system must be approximately 50 MA with a conduction time $\leq$ several microseconds and an opening time of less than 0.5 μs. Development of a PFS to provide this performance is an important goal of the Los Alamos project. The main issues that are being studied include: current shunting due to the formation of a boundary layer on the surface of the inner PFS conductor, the interaction of the switch plasma with the load, and the switching of current to the load.

Plasma located near the inner and outer coaxial conductors of the PFS is cooled by thermal conduction and forms a higher density perturbation that grows and distorts the sheath Because of the finite conductivity of the conductors current exits the surface at an acute angle, and the resulting jxB force has a radial component that presses the plasma toward the surface. Both of these processes contribute to forming a boundary layer. When the switch plasma crosses the load slot, the boundary layer also flows across and greatly impedes the movement of flux into the load slot. An MHD calculation of switching into a fixed load is shown in Fig. 1. The experimental curve shows that the load current does not reach the level of the driving current[11]. Based on these experimental and computational results a "plasma trap" was designed to catch the boundary layer flow just before the load gap[12]. As shown in the calculation of Fig. 2, this trap effectively removes the layer and allows efficient movement of flux into the gap. The experimental curve in Fig. 2 shows that complete switching of the driving current is obtained into a fixed load, as predicted by the calculation.

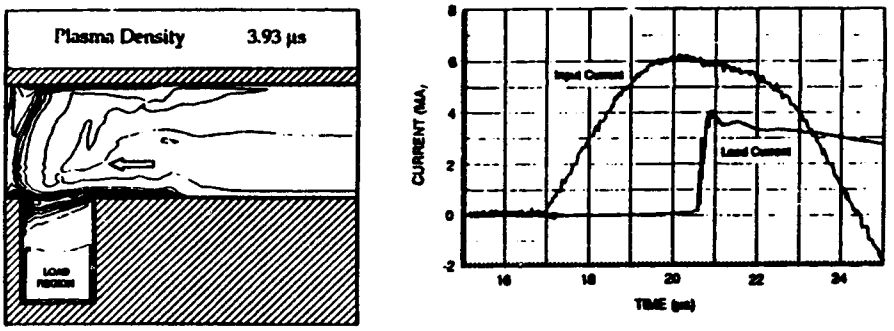

Fig. 1 Boundary layer causes incomplete switching.

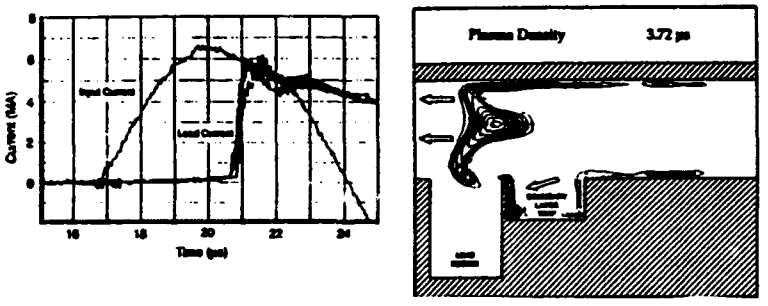

Fig. 2 Plasma trap catches boundary layer and improves switching performance.

When the fixed load is replaced by a dynamic load, the plasma trap PFS is less effective. Fig. 3. shows the source and load currents for a PFS (initiated from a $1/r^2$ wire array) transferring current into a 40 mg Al foil. Fig. 3a shows that the load current measured just

outside the initial position of the load foil approaches but does not equal the driving current. We believe that the difference in the two currents is due to the resistance that occurs when the load fuses. Through switching and initiation of the load foil the performance of the plasma trap PFS is quite good and is similar to results obtained at the Phillips Laboratory. Fig. 3b also shows the load current just outside the initial foil position and at several points inside the initial foil position (4, 3, 2, and 1 cm from the axis). The current reaching these positions decreases monotonically with radius. We believe that this is due to break-up of the imploding plasma from instability growth initiated by wrinkles in the foil and/or low density plasma filaments behind the plasma that entrain magnetic flux. Further study and development will be necessary to obtain efficient switching.

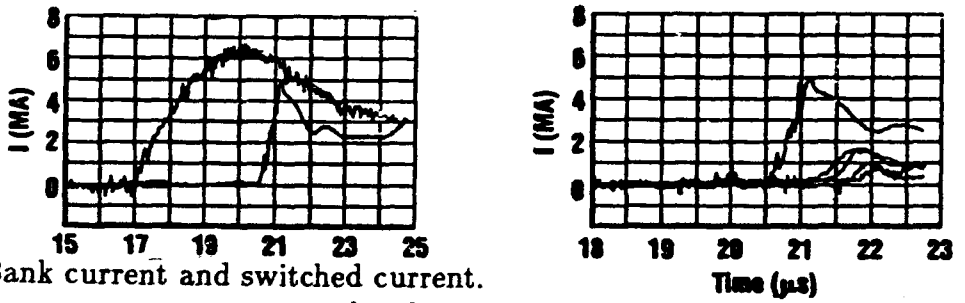

a. Bank current and switched current.

b. Switched current and current measured in load slot.

Fig. 3 Load probe measurements indicate not all switched current drives load implosion.

2. Implosion Physics

To maximize the power compression of the system, plasma stagnation must occur very quickly. This requires that the imploding plasma be as thin and symmetric as possible. To study instablity growth and its effect on the radiation pulse width, we have conducted imploding foil direct drive experiments (i.e. without an opening switch) using the Pegasus bank. Fig. 4 compares the implosion of a 4.2 mg foil to that of a 12.6 mg foil at the same radius. The visible framing camera pictures show that the heavier foil is much less disrupted than the lighter foil. The experiment was modeled with a 2^{n} MHD code assuming that the imploding plasma has an initial average random density perturbation of 10%. The behavior of the 4.2 mg foil agrees with the calculation until late in the implosion but eventually develops three dimensional structure and breaks up. The 12.6 mg foil stays intact through stagnation. The calculated density contours of the imploding plasma at the same position as that of the framing camera pictures show qualitative agreement with

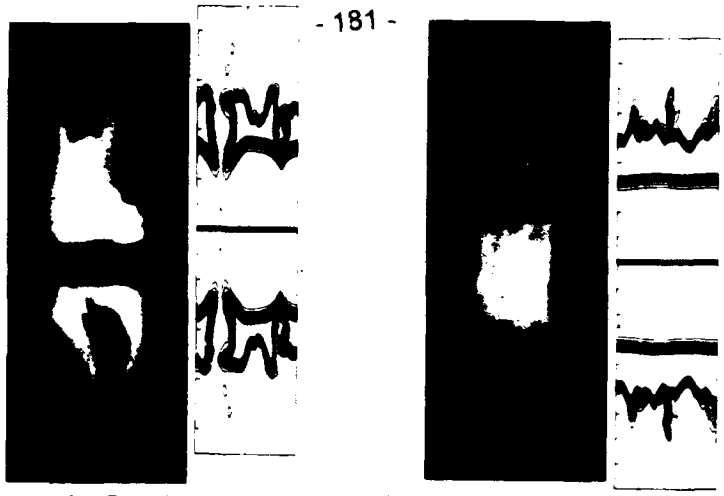

Fig. 4 Visible image and 2D MHD mass distribution for two direct drive experiments. 4.2 mg load (left figure) disrupts during implosion; 12.6 mg load (right figure) retains cylindrical symmetry throughout implosion; 2D MHD simulations reproduce observed scale of instabilities.

the experiment and reproduce the observed amplitude and wavelength of the instabilities. Fig. 5 shows the agreement between the measured and calculated current and the emitted x-radiation waveforms for the same assumed 10% initial density perturbation for the 4.2 mg foil implosion. The MHD calculation reproduces the shape of I(t), the relative timing of the peaks of I(t) and x-ray output, and the x-ray pulse width. Note that the experimental and calculated pulses are significantly wider than the 1D MHD result because of instabilities.

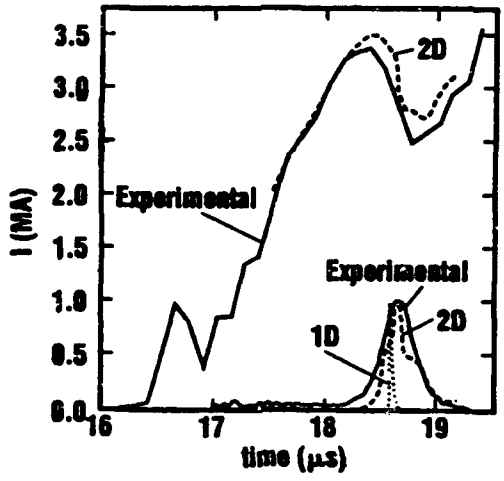

Fig. 5 Perturbed 1D and 2D MHD calculation compared to direct drive data of implosion current and XRD response.

Future Activities

To increase the relevance of our capacitor bank driven experiments to the high energy program, the Pegasus bank will be upgraded this summer to 4.3 MJ stored energy and a peak current of 13 MA. In addition, development has started on a new class of FCG that will operate in 5 μs and drive a PFS directly. This system will have only one switching

stage, generate 15 MJ of electrical energy, and deliver 5 MJ to an imploding load. FCG driven plasma implosion x-ray sources have been demonstrated at the 100 kJ level. The program is presentlv engaged in development of the Procyon system to produce plasma energies near one megajoule. To go beyond this level will require new developments in the areas of HE-driven generators, fast high-current opening switches, high power-density flow channels, and an improved understanding of implosion physics. We plan to address each of these topics in our future work.

Work supported by U.S. Department of Energy
*University of New Mexico, Albuquerque, NM, USA
**Ohio State University, Columbus, OH, USA

References

1. R. E. Reinovsky , J. H. Degnan, G. F. Kiuttu, R. A. Nuttelman, and W. L. Baker, "Megagauss Physics and Technology," P. J. Turchi ed. Plenum Press, New York, 1980. p. 313.
2. J. Pearlman, et al., Fourth Inter. Conf. on High-Power Electron and Ion-Beams, Palaiseau, 1981, p. 271.
3. C. Gilman, et al., Ref. 2, p. 287.
4. J. Van Devander, et al., Ref. 2, p. 725.
5. S. G. Alikhanov, L. I. Rudakov, V. P. Smirnov, I. R. Yampol'skii, Sov. Tech. Phys. Lett. 5, 587 (1979)
6. A. I. Pavlovskii, V. A. Vasyukov, and A. S. Russkov, Sov. Tech. Phys. Lett. 3, 320 (1977).
7. J. Brownell, et al., IEEE Inter. Conf. on Plasma Science, Pittsburgh, 1985.
8. C. M. Fowler and R. S. Caird, Proc. of Seventh IEEE Pulsed Power Conf., Monterey, CA, 1989.
9. J. H. Goforth, A. H. Williams, and S. P. Marsh, Proc. Fifth IEEE Pulsed Power Conf. Arlington, VA, 1985.
10. J. H. Degnan, et al., IEEE Trans. on Plasma Science, Vol. PS-15, No. 6, Dec. 1987.
11. D. L. Peterson, R. L. Bowers, J. H. Brownell, A. E. Greene, N. F. Roderick, Proc. of the Eighth IEEE Pulsed Power Conf., San Diego, CA, 1991, p. 614.
12. J. C. Cochrane, et al., Ref. 11, p 618.

Invited Microwave Papers

Martin P. Reiser, *Session Chairman*

GYROKLYSTRON RESEARCH FOR APPLICATION TO TEV LINEAR COLLIDERS

W. Lawson, V. L. Granatstein, B. Hogan, U. V. Koc, P. E. Latham, W. Main, H. W. Matthews, G. Nusinovich, M. Reiser, C. D. Striffler, and S. Tantawi

Laboratory for Plasma Research
University of Maryland
College Park, MD 20742 USA

Abstract

X-Band and K-Band gyroklystrons are being evaluated for possible application to future linear colliders. So far we have examined ten different two- and three-cavity configurations. We have achieved a maximum peak power of 27 MW in ~ 1 μs pulses at a gain of 37 dB and an efficiency exceeding 32 %. The nominal parameters include a 430 kV, 150-200 A beam with an average perpendicular to parallel velocity ratio near one. In this paper, we detail our progress to date and describe our plans for future experiments that should culminate in amplifier outputs in excess of 100 MW.

Introduction

An international effort is underway to develop amplifiers in the 10 - 30 GHz range with peak powers in excess of 100 MW for driving future multi - TeV electron positron colliders [1]. At the University of Maryland, we are concentrating on the use of gyrotron amplifiers to achieve the required parameters. At the time our project first got underway, the state-of-the-art power for gyroklystrons hovered near 50 kW due in part to limitations imposed by spurious oscillations [2]. As an intermediate step toward the 100+ MW goal, we constructed and tested a system which was designed to surpass the 50 kW level by a factor of 500 [3]. We have achieved our goal [4], in part by increasing the power capability of the standard gyrotron electron gun [5] and by developing improved microwave absorbers to enhance stability [6].

A schematic of our experimental facility is shown in Fig. 1. A 1 - 2 μs, 500 kV, 400 A line-type modulator provides the required beam power with a maximum repetition rate of 4 Hz. A resistive divider shunts half the current and provides the intermediate voltage required for the double-anode magnetron injection gun (MIG). The MIG is designed to have a space-charge limiting current of 400 A and an axial velocity spread under 7% at the nominal current of 160 A with an average perpendicular to parallel velocity ratio of α = 1.5. Considerable flexibility in the magnetic field profile is achieved by using four independent supplies to power eight water-cooled pancake coils. The design magnetic field is 0.047 T at the cathode and 0.565 $\pm$ 0.005 T

for 25 cm in the circuit region, but the magnetic field can be varied along the axis to optimize performance.

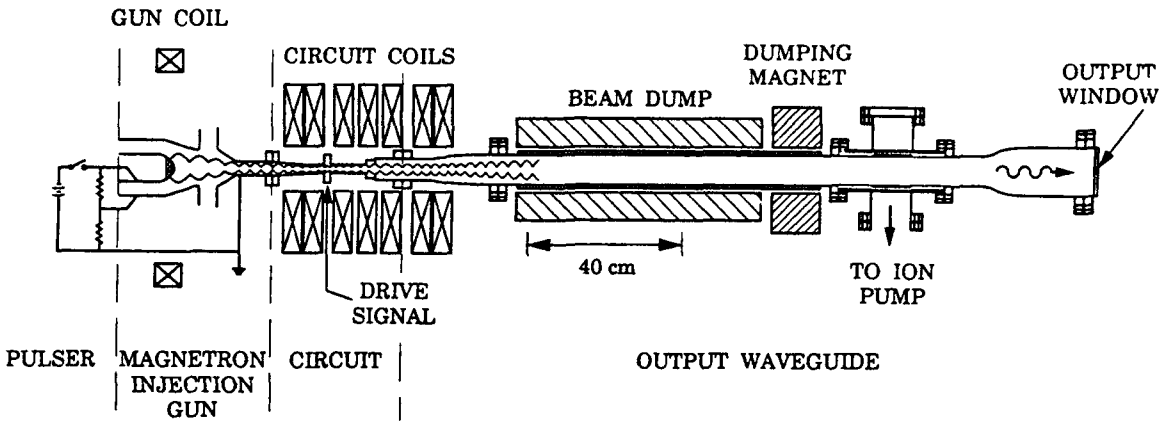

Figure 1. A schematic view of the gyroklystron experimental facility.

An enlargement of the circuit region for the last two-cavity tube is shown in Fig. 2. The downtaper is lined with lossy dielectrics, which are indicated in black. The tapered ceramics are a non-porous mix of 20% SiC in 80% BeO. The other ceramics are made in-house from carbon-impregnated alumino-silicate. Most of the drift tube is also lined with lossy ceramics to suppress instabilities. A partially self-consistent code which includes realistic rf field profiles [7] and AC space-charge effects [8] is used to design the microwave circuit dimensions and predict amplifier performance. Power is injected from a 2 μs, 100 kW magnetron through a slit in the radial wall into the input cavity. Control over the quality factor (Q) in the input cavity is obtained from losses in a thin ceramic ring placed against the sidewall. The output cavity Q is predominantly due to diffractive losses from the cavity's output lip. The Q factors have spanned the range 125 - 500 in the various tubes, but the resonant frequencies have always been derived from TE_{01} modes at 9.85 GHz.

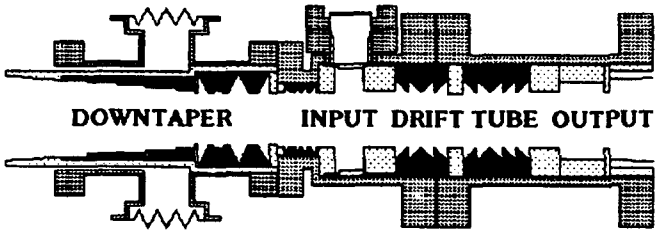

Figure 2. The two-cavity microwave circuit configuration.

The output waveguide is shown in Fig. 1. A short 2° linear taper is followed by a non-linear taper which brings the waveguide radius to a value suitable for the copper beam dump. A cross-guide magnetic field at the end of the dump prevents high-energy electrons from traveling through the second non-linear taper and impinging on the five inch diameter half-wavelength BeO output window.

Two types of microwave diagnostics can be attached to the output waveguide. An anechoic chamber uses an open-ended piece of X-band waveguide as a receiving antenna to estimate

output power and mode purity via far field measurements. The horn can be rotated by 90° and remotely swept transverse to the z-axis over one meter. The signal is split into several different size waveguides for instantaneous frequency estimates and is fed to an HP 8566B spectrum analyzer for time-averaged frequency resolution. Calibration measurements have been in good agreement with an uncertainty less than ± 1 dB. The second diagnostic involves an overmoded directional coupler and a liquid calorimeter. The coupler provides the microwave power envelope and gives an additional peak power estimate. The calorimeter consists of a methanol - water mixture flowing between two 17° conical pieces of polyethylene. Bench test measurements against a 20 W CW signal have given similar agreement for these diagnostics.

Experimental Results

A total of six two-cavity and four three-cavity gyroklystron tubes have been tested. A summary of the progress toward achieving high peak power is shown in Fig. 3. The saturated gain at each power level is also indicated. The first two tubes were plagued by a multitude of instabilities, produced power levels below the state of the art, and had signal gains less than 0 dB. These results occurred at a beam voltage of 183 kV, a current of 55 A, and a velocity ratio of $\alpha \approx 0.45$. The instabilities could be classified into four groups. Modes in the first class existed mainly in the output waveguide in frequency ranges where the window was a good reflector. These modes required good post-output cavity beam quality and were suppressed by amplifier operation. The second class existed in the output waveguide adjacent to the output cavity and required significant reflections from the first non-linear taper. Whole tube modes comprised the third class and had their energy mainly in the drift tube with reflections provided by the cavities. The final mode class included instabilities in the downtaper.

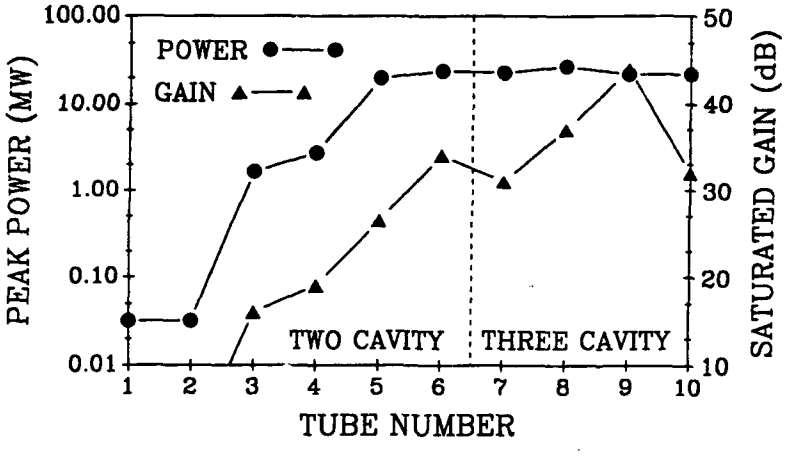

Figure 3. Summary of tube peak power performance.

Instabilities in classes 3 and 4 were the most troublesome and usually involved modes with one azimuthal variation. These modes can be controlled by the introduction of loss into the downtaper and drift tube. Figure 4a shows the total single pass attenuation of the TE_{11} mode through these regions in Tube 1 in the most troublesome frequency range. The downtaper had

only a few thin lossy rings and very little attenuation. The drift tube consisted of alternating rings of copper and ceramic (1% SiC in 99% MgO) in nearly equal amounts. Though there were some highly absorptive resonances, there was a large frequency range with negligible loss. In contrast, Fig. 4b shows the TE_{11} attenuation for the Tube 6. This attenuation was sufficient to allow operation at the parameters listed in the abstract.

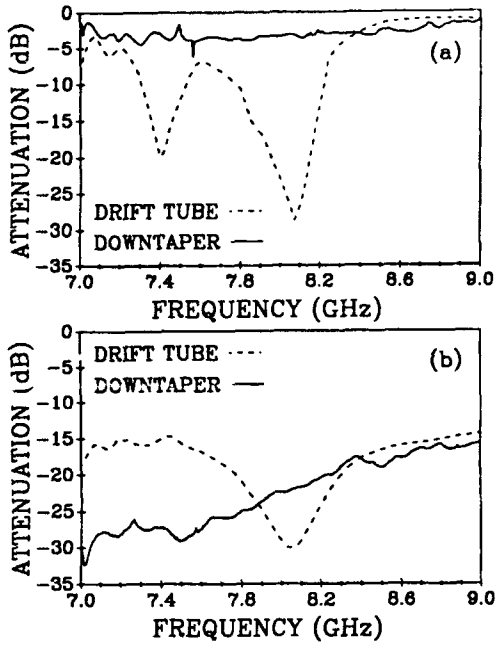

Figure 4. TE_{11} attenuation vs. frequency in the downtaper and drift tube regions: (a) for Tube 1 and (b) for Tube 6.

Tube 3 incorporated a downtaper and drift tube with attenuations near the final values of Fig. 4b. This allowed significant beam power to be used for the first time and resulted in a one and a half order of magnitude increase in output power. The input and output cavity Q's were 175 and 145, respectively. In a flat magnetic field of 0.452 T, a peak power above 1.5 MW was produced at 9.866 GHz when the beam voltage was 305 kV and the current was 108 A. Parameter space for amplification was limited by a class 2 instability near the amplifier frequency. We determined that the mode was the TE_{121} operating near cutoff in a constant radius waveguide section immediately following the output cavity. This mode could not be suppressed by amplifier operation but was eliminated in Tubes 4 and beyond by introducing a linear wall taper after the output cavity lip. With this modification, Tube 4 produced peak powers near 2.7 MW with a 427 kV, 130 A beam in a constant magnetic field of 0.537 T. Maximum efficiencies of both Tubes 3 and 4 were approximately 5%.

The final order of magnitude increase in power was achieved with Tube 5, which had additional loss in the downtaper and a higher Q in the output cavity (224). The primary performance increase came not from the circuit modifications but rather from the introduction of magnetic field tapering. A careful search of parameter space showed that the optimal input cavity field was 0.545 T while the best output cavity performance occurred at 0.474 T. Figure 5

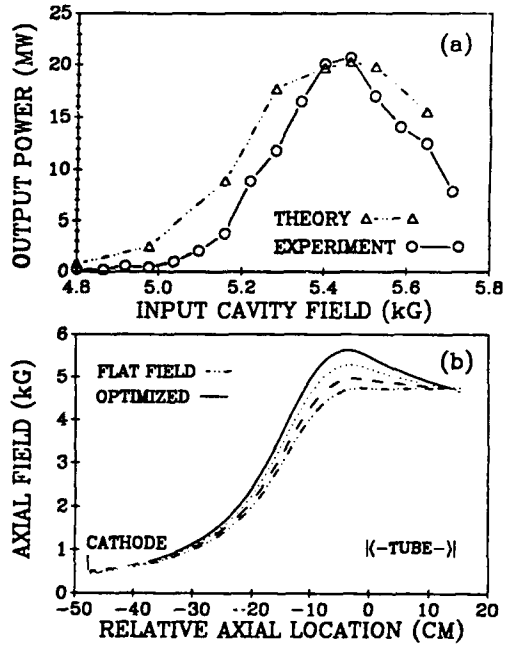

Figure 5. (a) Peak measured and theoretical output power vs. input cavity magnetic field, (b) axial field profile.

reveals the dependence of peak power on input cavity magnetic field when the output cavity field is fixed at the optimal value. The beam voltage and current were 425 kV and 150 A, respectively. The simulated velocity ratio was $\alpha \approx 0.98$ in the output cavity and varied adiabatically with the magnetic field. At the optimum level, $\alpha \approx 1.15$ at the center of the input cavity. The efficiency at the maximum was 31% and the gain exceeded 26 dB. (Assuming no exchange of axial energy, the perpendicular conversion efficiency was 74%.) The average relativistic mass factor was 16% lower after energy extraction occurred. The drop in the ideal magnetic field profile was 15% so that the 'final' cyclotron frequency was nearly equal in both cavities. The input power was limited to 45 kW due to breakdown at the input window and the drive curve indicated that Tube 5 was not saturated. An increase in the input cavity Q to ~500 in Tube 6 allowed saturation to be examined. Theory predicted this Q to be 80% of the required start oscillation value and oscillations were in fact observed in the input cavity at some points. The optimal amplified power occurred with the same 15% field profile, but the flat field peak power improved to 12.5 MW. Two distinct points were examined. The first was the maximum efficiency point, where 22 MW was produced at 9.871 GHz with an efficiency of 34% and a gain of 34 dB. The beam voltage and current were 425 kV and 150 A, respectively. Figure 6 shows the time dependence of the cathode voltage and output power as measured by a calibrated crystal detector. The second point had a maximum power level of 24 MW at 9.875 GHz for the same field profile and beam voltage but with a current of 190 A.

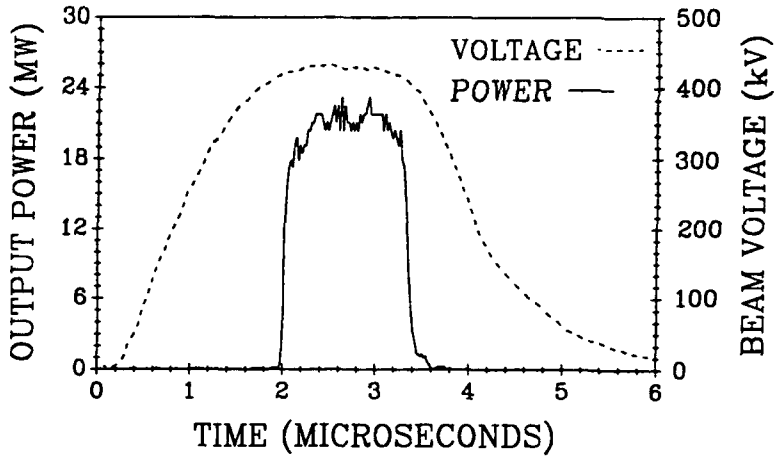

Figure 6. Time dependence of the output power and the beam voltage at the maximum efficiency point.

The three-cavity tubes had three distinct departures from the two-cavity designs. The first, of course, was the introduction of the penultimate cavity whose Q (~270) was defined solely by an alumino-silicate ring on the outer wall. Two metal rods with rounded ends provided remote-controlled tunability of $\pm$ 90 MHz by adjustment of their insertion length. No breakdown problems of any kind were observed. The second change was to use exclusively alumino-silicate in the drift tubes (Tubes 7 and beyond) and downtaper (Tubes 8 and beyond). The inner radius of these ceramics was determined by the beam and the outer radius was adjusted (via a theoretical code) to maximize attenuation. The TE_{11} attenuation was always superior to their non-porous counterparts, the

TE_{01} attenuation was adequate for cavity isolation at 9.85 GHz, and no outgassing problems were observed. The third difference was to use a lossy dielectric on the radial wall of the input cavity and modify the coupling slit. Both input cavities performed well; no noticeable advantages of either design were discerned during the amplifier studies. The output cavity Q in Tubes 7 and 8 were 200 and 350, respectively.

The power performance of the two- and three-cavity tubes was similar at the 15% tapered field profile. The gain was typically improved, with a maximum saturated gain of 50 dB occurring at an operating point that produced 21 MW. The improved gain also resulted in a considerable increase in total pulse energy (wider output pulses). Optimal performance occurred, however, when a 33% decrease in the output cavity magnetic field was introduced. A maximum peak power of 27 MW was obtained with an efficiency of 32%. Several interesting phenomena were observed that are still being investigated. First, the operation was quite sensitive to the load. The anechoic chamber, with its low reflection, worked best with the high-Q output cavity of Tube 8 while the more reflective calorimeter worked best with the earlier tube. Second, the velocity ratio in the output cavity was low ($\alpha \approx 0.8$) and thus significant axial energy conversion must have occurred. This was reasonable given the high voltage (large axial velocity) and short cavity (large axial wave number) and has been observed in preliminary theoretical modeling [9]. Finally, investigations with magnetic field adjustment suggest that a significant part of the interaction could have occurred after the output cavity.

The final three-cavity tubes are described elsewhere in these proceedings [10] and are mentioned only briefly here. In an attempt to explore this extended interaction, both tubes employed considerably longer output cavities. Tube 9 expanded its length by 90% via a reduced radius to achieve a significant fraction of the start oscillation requirement. Tube 10 utilized a TE_{012} mode to increase its length by 125%. Both tubes surpassed 20 MW of peak power, but neither improved upon the upper limit of Tube 8. Experimental investigation of Tube 10 was still underway at the time this paper was written.

Future Experiments

With the success of the intermediate experiment, we are now contemplating our approach to a 100+ MW device. The high power requirement places several constraints on the electron gun and the microwave circuit. To produce a higher power MIG, we must either increase the beam voltage, increase the peak electric field in the gun, enlarge the average beam radius, or decrease the applied magnetic field [11]. The new microwave circuit must continue to be stable to spurious modes, provide inter-cavity isolation, and dissipate a fair amount of average power. Our options will be explored by performing cold test studies, constructing and testing additional

tubes with the existing beam parameters, and designing MIGs and microwave circuits for 300 - 400 MW beams.

1. Near term plans

While the low repetition rate of our facility doesn't allow an examination of the system's average power considerations, the only unique gyroklystron feature of potential concern is the power dissipated in the lossy ceramic of the penultimate cavity. We are initiating a study of the effects of temperature rise and means of cooling via a cold test mockup of the buncher cavity. The available power in our 2.5 kW CW klystron is considerably higher than the current estimate of penultimate cavity energy deposition.

One way to lower magnetic field is to inject at the fundamental and extract at the second harmonic. We will test this concept by replacing the output cavity of Tube 6 with the 19.7 GHz TE_{02} cavity shown in Fig. 7. Several of the key dimensions are indicated in the figure. The small cavity radius insures that the TE_{01} cannot exist at 9.85 GHz. The adiabatic wall transitions are designed to minimize mode conversion to the TE_{01} at 19.7 GHz. A cold cavity design code indicates that the power flowing into the drift tube is 50 dB lower than the power extracted at the end of the system. Simulations of amplifier stability and operation have been performed assuming the nominal experimental beam parameters. The design quality factor of 780 exceeds the start oscillation requirement for magnetic fields above 0.545 T. Efficiencies of at least 25% have been predicted by the large signal code.

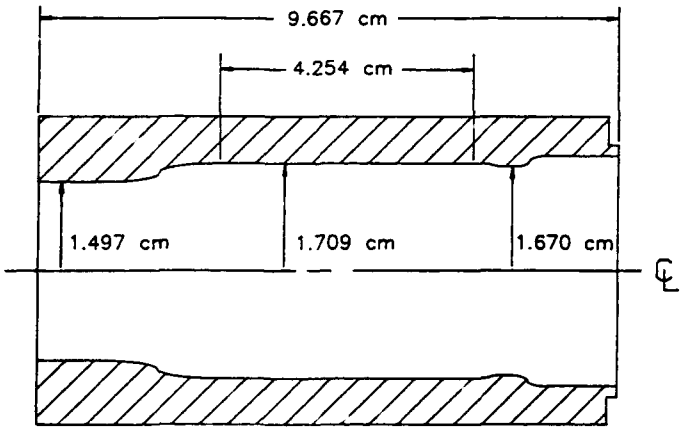

Figure 7. The output cavity for the second harmonic experiment.

The output cavity has been constructed and cold tested. The measured parameters are f=19.64 GHz and Q=685. The existing non-linear tapers are inadequate in terms of TE_{01} - TE_{02} mode conversion, so new tapers with Dolph-chebychev profiles and theoretical mode conversion under 45 dB have been designed and are being electroformed. Also under construction are a 60 dB overmoded TE_{02} directional coupler and mode converters from TE_{10} rectangular to TE_{01} circular and from TE_{01} to TE_{02} in circular waveguide.

Three additional experimental configurations are under consideration. The first is simply a shorter output cavity to be used if spurious oscillations in the output cavity become a problem. The only potential drawback is an increase in the 19.7 GHz TE_{01} mode content. A single short cavity filter before the output cavity can potentially increase isolation.

The other two approaches are aimed at improving efficiency. First, an inner conductor will be inserted into the second harmonic tube. The 2 mm radius will increase isolation between cavities. In the downtaper, the insert radius will be increased and lossy dielectrics will be added in an attempt to further suppress class 4 modes. Because of the electric field distribution of the TE_{11} mode, we anticipate a significant improvement in attenuation in the section closest to the gun. This should result in a higher attainable velocity ratio which the non-linear code predicts will translate into better efficiency.

If the velocity ratio cannot be improved, an alternative approach to higher efficiency and lower magnetic field is to operate at the fundamental with a large Doppler shift $k_z v_z$. We are currently designing a traveling wave output section (gyro-twistron) which would replace the output cavity of Tube 6. Though the design is not yet completed, initial indications are that efficiencies of 40% are possible with the existing experimental beam parameters.

Finally, two alternative concepts which could be tested on the existing facility are also being explored. A second harmonic output traveling wave section can be used to eliminate the backward TE_{01} component and insure isolation. The second approach is to use non-symmetric modes to enhance beam - microwave coupling at the second harmonic.

2. Long term plans

The approach to a 100+ MW system is dependent on the current and near term experiments and the selection of the optimal amplifier frequency. To conform to conventional modulator and emitter technology, we assume the new system's maximum beam voltage and cathode loading will be 500 kV and 8 A/cm^2, respectively. This implies that higher current, probably with a larger guiding center radius, gives the required approach to higher powers. As the guiding center is increased, one must either (1) use an extremely lossy lining (~15-20 dB per wavelength), (2) choose a mode with a higher cutoff, or (3) use a coaxial insert in order to maintain cavity isolation. Even if a material could be found that satisfies (1), the required heat load would probably be prohibitive. Approach (2) would require suppression of the lowest radial mode with the same azimuthal index (m) as the operating mode or a large increase in m. Either approach would probably entail a new input cavity scheme. The third approach is viable provided that TE_{0n} modes are used.

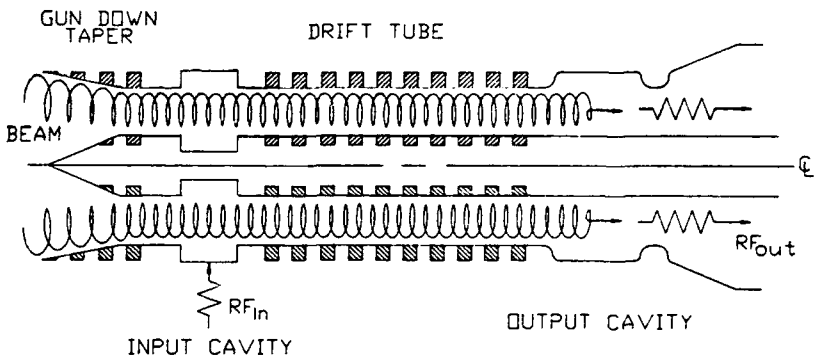

Figure 8. A coaxial second harmonic two-cavity circuit.

We have considered MIG designs at 11.424 GHz

and 19.7 GHz for fundamental and second harmonic devices with 300 MW beams in coaxial geometry. All designs appear feasible with the fundamental 19.7 GHz design being the most difficult. In the following paragraphs, we detail only a scenario for a second harmonic experiment at 11.424 GHz. Other scenarios are receiving similar scrutiny.

A schematic for a system that utilizes a 5.712 TE_{01} input cavity and a second harmonic TE_{02} output cavity is shown in Fig. 8. Tentative parameters for such a system are given in Table I. The current will be supplied by doubling the number of PFNs in the modulator and decreasing the repetition rate. The longer magnetic field region required for the interaction will be achieved by adding two field coils. The same supplies can be used as the magnet power requirement is considerably reduced at the lower field. Scaling the current beam from 200 A to 600 A requires a three-fold increase in guiding center radius. The inner conductor will be supported at the end of the beam dump and will include lossy ceramics to enhance stability. The output cavity radius is selected to preclude fundamental TE_{01} operation but may have to be increased if spurious modes become a problem. Initial large-signal modeling has predicted efficiencies above 27%; we expect this value to increase significantly when the design is optimized.

Table I. Nominal system parameters

Beam Voltage	500 kV
Beam Current	600 A
Velocity Ratio	1.5
Magnetic Field	3.28 kG
Input Cavity	
Length	2.30 cm
Q	70
Output Cavity	
Length	4.20 cm
Q	368
Drift Tube	
Length	18 cm
Inner Radius	1.6 cm
Outer Radius	3.9 cm

A MIG which provides the required beam parameters is shown in Fig. 9. Its single anode configuration reduces its overall size and complexity and eliminates compensation problems associated with the resistive divider. Simulations are performed with the EGUN [12] code. The average cathode radius is 7.13 cm and the magnetic field compression is 7.55 at α = 1.5. The peak electric field is less than 90 kV/cm on the cathode and 30 kV/cm on the anode. The

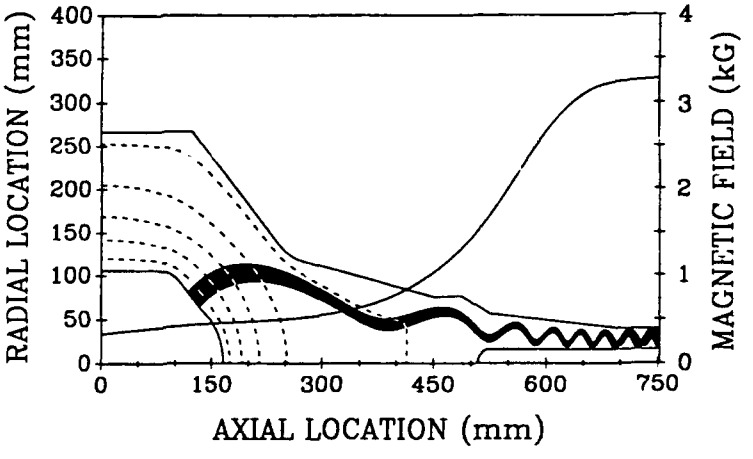

Figure 9. Electrode design and ray trajectories for the 300 MW MIG.

nominal current is only 26% of the space-charge limiting value. The simulated beam thickness allows only 1.1 mm clearance between the beam and the drift tube walls.

The emitter strip is slightly curved to reduce velocity spread with an average half-angle of 46°. The dependence of axial velocity spread on current is shown in Fig. 10 [13]. The magnetic field at the cathode is adjusted to maintain $\alpha = 1.5$. Near the design current, the beam is not fully mixed by the input cavity. This accounts for the difference in spread between the two cavities. The design can operate over an 800 A range with a velocity spread below 10% due to the laminar flow of electrons throughout much of the gun. This extended range will facilitate the study of high efficiency amplification in the 100+ MW regime.

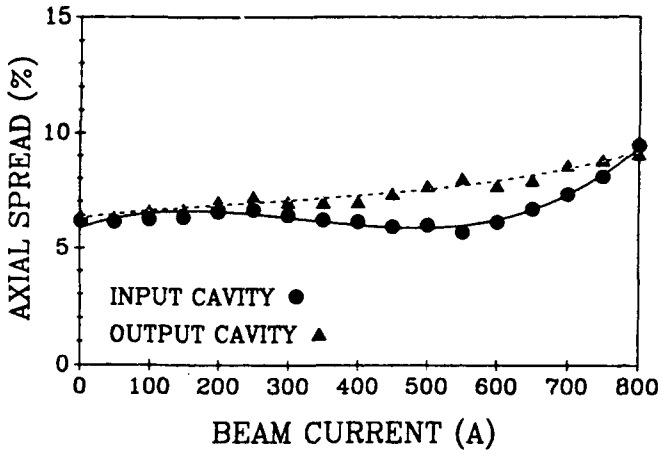

Figure 10. The dependence of axial velocity spread on current.

Acknowledgment

This work was supported by the United States Department of Energy.

References

1. Proc. Int. Workshop on the Next Generation Collider, SLAC Report-335, Dec. 1988.
2. W. M. Bollen, *et al.*, *IEEE Trans. Plasma Sci.* Vol. PS-13, p. 417 (1985).
3. K. R. Chu, *et al.*, *IEEE Trans. Plasma Sci.* Vol. PS-13, p. 424 (1985).
4. W. Lawson, *et al.*, *Phys. Rev. Lett.* Vol. 67, p. 520 (1991).
5. W. Lawson, *et al.*, *Int. J. Electron.* Vol. 61, p. 969 (1986).
6. J. P. Calame and W. Lawson, *IEEE Trans. Electron Dev.* Vol. 38, p. 1538 (1991).
7. J. Neilson, *et al.*, *IEEE Trans. Microwave Theory Tech.* Vol. MTT-37, p. 1165 (1989).
8. P. E. Latham, *IEEE Trans. Plasma Sci.* Vol. 18, p.273 (1990).
9. P. E. Latham, *et al.*, in these Proceedings.
10. W. Main, *et al.*,, in these Proceedings.
11. W. Lawson, *IEEE Trans. Plasma Sci.* Vol. 16, p. 290 (1988).
12. W. B. Herrmannsfeldt, SLAC Report-226, Nov. 1979.
13. W. Lawson and V. Specht, submitted to *IEEE Trans. Electron Dev.*, May 1992.

NANOSECOND RADAR SYSTEM BASED ON REPETITIVE PULSED RELATIVISTIC BWO

B. V. Bunkin, A. V. Gaponov-Grekhov, A. S. Eltchaninov, F. Ya. Zagulov, S. D. Korovin, G. A. Mesyats, M. L. Osipov, E. A. Otlivantchik, M. I. Petelin, A. M. Prokhorov, V. V. Rostov, A. P. Saraev, I. P. Sisakyan, A. V. Smorgonsky, V. A. Suvorov

Russian Academy of Sciences, Tomsk, Russia

Abstract - The paper presents the results of studies of a nanosecond radar system based on repetitive pulsed relativistic BWO. A pulsed power repetitive accelerator producing electron beams of electron energy 500-700 keV and current 5 kA in pulses of duration 10 ns with a repetition rate of 100 pps is described. The results of experiments with a high-voltage gas-filled spark gap and a cold-cathode vacuum diode under the conditions of high repetition rates are given. Also presented are the results of studies of a relativistic BWO operating with a wavelength of 3 cm. It is shown that for a high-current beam electron energy of 500-700 keV, the BWO efficiency can reach 35%, the microwave power being 10^9 W. A superconducting solenoid creating a magnetic field of 30 kOe was used for the formation and transportation of the high-current electron beam. In conclusion, the outcome of tests of a nanosecond radar station based on a pulsed power repetitive accelerator and a relativistic BWO is reported.

I. Introduction

The information potential of a radar system (RS) depends on the transmitter average power as well as on the character of modulation of the microwave radiation. The very short, high-repetition-rate high-power pulses allow one to determine the distance to the object and the object velocity highly accurately even when no account of the Doppler effect is taken [1, 2]. Up to now, pulses were shortened, mainly, in the input lines of RS by letting the freguency modulated pulses to pass through optimally compressing filters [3]. However, applicability of this method is limited by the complexity of considerable pulse compression and by the fact that the correlation function of the signals can give an information about the position of the object, which can hardly be interpreted.

That is why it is more preferable to produce powerfull electromagnetic pulses directly in the transmitting unit of the RS. This, first, permits one to simplify the whole radiotechnical scheme of the station (freguency modulation becomes unnecessary and compressing filters are not required); second, it eliminates false signals; and, finally, reduces the dead zone in front of the RS and considerably increases its noise immunity.

A study has been carried out aimed at the creation of a nanosecond radar system with radiation wavelength $\lambda \simeq 3$ cm, microwave power $P \sim 10^9$ W, pulse

independent of the ferromagnetic material properties and only dependent on its geometrical parameters. For the accelerator version illustrated by Fig. 1, the efficiency of forming line charging is determined by the expression

$$\eta \simeq 1 - \frac{\pi^2}{3} \left(\frac{r_1}{l_L}\right)^2 F(\beta)\ ln\beta,$$

where $\beta = r_1/r_2$, l_L is the length of the coaxial line, r_1 and r_2 are the outer and the inner radius, respectively, $F(\beta) \sim 1$. Thus, for $l_L >> r_1$ we have $1-\eta << 1$. Actually, $\eta \simeq 0.8$ is the case. Note that the integration of the Tesla transformer with the forming line has made it possible not only increased the efficiency of line charging but also decreased the overall dimensions of the whole system and to make its operation much more rediable.

In choosing the pulse-forming line parameters, taken into account were the energy loss in its charging, the requirement of high electric strength for its main units under the conditions of high pulse repetition rates, and the need of matching the pulse-forming line with the vacuum diode. Under the experimental conditions, the line wave resistance was 20 Ω and the maximum electric field at its elements was about 180 kV/cm. For insulation, the line was filled with transformer oil. The pulse-forming line and the vacuum diode were matched using a long adiabatic transmission line playing the role of a wave transformer. Using such lines allows matching a pulse-forming line, capable of storing large amount of energy and showing long lifetime, to the vacuum diode producing an electron beam with parameters optimal for the operation of the BWO.

One of the main problems that had to be resolved under the experimental conditions was to make the electron beam parameters as reproducible as possible. The spread in these parameters is mainly dependent on the fluctuations of the voltage at which the gas-filled spark gap operates and on the variation of the vacuum diode impedance. As the experiment has shown, forced circulation of the working gas in the spark gap (nitrogen at 20 atm) makes the operating voltage reproducible within ~ 2-3 % at a pulse repetition rate of 100 pps. The minimum gas circulation rate is proportional to the radius of the gas spark gap electrodes [4]. Using trigatron triggering decreased the spread in pulse amplitudes to 0.5 - 1%.

Trigatron triggering of the spark gap switch was realized using a compact pulsed power source allowing one to control the switch breakdown voltage and providing for its low-jitter operation.

Experiments with the magnetically insulated coaxial vacuum diode have shown that, at high pulse repetition rates, the fluctuations of the electron beam parameters are considerably affected by the cathode material. The best results have been obtained for thin cylindrical cathodes made of graphite. The effect of cathode material on the stability of cathode operation seems to be related to the fact that the number of emission centers on its surface is not large. The number of emission centers can be increased by using materials showing short time delays of

duration $t \simeq 5 \times 10^{-9}$ s, and repetition rate $f_r = 100$ pps at relatively low instability levels for the radiation amplitude and freguency. Using a BWO with the above parameters in radar systems allows one to identify objects with a spatial resolution of $\sim 10^2$ cm at a distance of up to $\sim$ 100 km, and efficiently select moving object on the background of signals reflected from stationary objects.

An outline is given to the pulsed power accelerators used in the experiment as electron sources for the relativistic oscillators. The attention is focused on repetitive pulsed accelerators based on open-core Tesla transformers. The results of studies of explosive-emission cold cathodes and high-voltage gas-filled spark gaps, which have made it possible to produce electron beams with the electron current and the energy reproducible within less than 1%, are given (Section 2). Section 3 describes the results of a study of a relativistic nanosecond BWO with a wavelength $\lambda \simeq 3$ cm. It has been demonstrated that the BWO efficiency at a high-current beam electron energy of 500-700 keV can reach 35%, the microwave power being $\sim 10^9$ W. This, however, requires that the magnetic field necessary for the beam transportation would be high enough ($H \simeq 30$ kOe). This leads to the need of using super-conducting solenoids. Section 4 gives the main out-come of a test of a radar station based on a pulsed power repetitive accelerator and a relativistic BWO.

II. The Pulsed Power Accelerator

For experimental studies of high-power microwaves, repetitive pulsed power accelerators of the Sinus series have been developed for some years at the Institute of High Current Electronics (Tomsk, Russia). Figure 1 illustrates a typical schematic diagram of the Sinus accelerator. Its principal elements are a Tesla transformer, a pulse-forming line, a high-voltage gas-filled spark gap, a transmission line, and a cold-cathode vacuum diode.

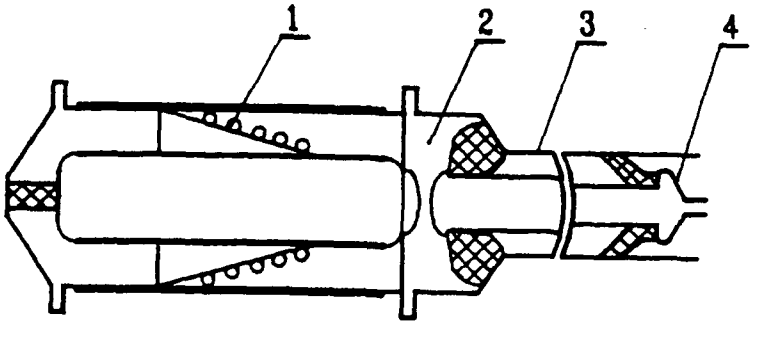

Fig. 1. Accelerator configuration: 1 - Tesla transformer; 2 - gas-filled spark gap; 3 - transmission line; 4 - cathode.

The Tesla transformer is used to charge the pulse-forming line. The primary energy store and forming line charge voltages are, respectively, < 500 V and < 800 kV. The use of an open ferromagnetic core in the Tesla transformer allowed us to reach high coupling coefficients between the transformer windings ($1-k \ll 1$). In this case, the efficiency of energy exchange between the windings was

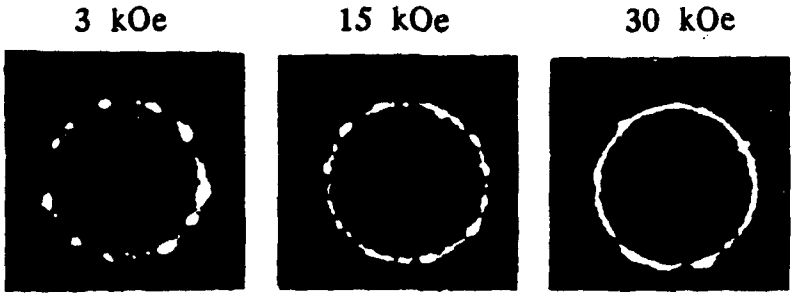

Fig. 2. Photographs of the cathode.

micropoint explosions [5] and by properly choosing the cathode geometry. In the experiment, the number of emission centers on the cathode surface was affected by the external magnetic field used for the electron beam formation and transportation. Figure 2 shows photographs of the cathode taken at different values of magnetic field in the vacuum diode. The magnetic field dependence of the number of emission centers can be associated, on the one hand, with the screening effect, when the appearance of emission centers on the cathode surface is hindered on the scale of the Larmor radius of the electrons near the cathode. On the other hand, this can be associated with the instability of the emission surface in such vacuum diodes. The latter, in particular, is indicated by the fact that, when the *total current through* the vacuum diode was reproducible enough, there existed a characteristic, rather small, electron beam cross section for which the value of beam current varied in a random manner.

III. The relativistic BWO

The relativistic backward wave oscillator is a source of short pulses of electromagnetic radiation. Theoretical and experimental studies of various types of devices with relativistic electron beams have shown that the BWO - type oscillators have a number of advantages in this region of energies, since they are simple in their design, easily adapted, and highly efficient in operation [6, 7].

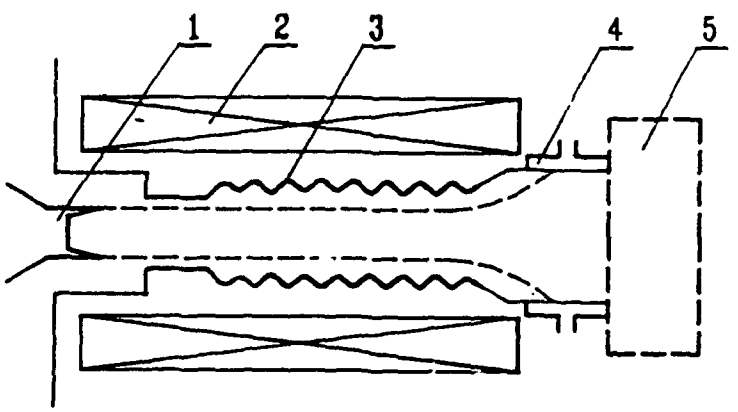

Fig. 3. Schematic diagram of the BWO: 1 - cathode; 2 - magnetic coil; 3 - electrodynamic system; 4 - collector; 5 - mode converter.

A schematic diagram of a typical BWO is given in Fig. 3. Used for slowing down the electomagnetic wave in the experiment were lightly corrugated waveguides. The waveguide diameter, the corrugation spacing and height were chosen so that the electron flow would interact with the first backward harmonic of the TM_{01} -type wave. Then we have

$$\omega + h v_e \simeq h_o v_e ,$$

where $\omega = 2\pi c/\lambda$, c is the velocity of light, λ is the radiation wavelength, v_e is the longitudinal electron velocity, $h_o = 2\pi/d$, d is the corrugation spacing. For the interaction length and the synchronous wave field we have, respectively, $L \sim \lambda\gamma^2$ and $E \sim mc^2/(e\lambda\gamma)$, where γ is the particle relativisic factor, m end e are the electronic mass and charge, respectively. The radiation was extracted from the oscillator using the electromagnetic wave reflected from the beyond-cutoff neck at the system inlet. Just behind the electron beam collector, a mode converter transforming the TM_{01}-type wave to the TE_{11}-type one was placed.

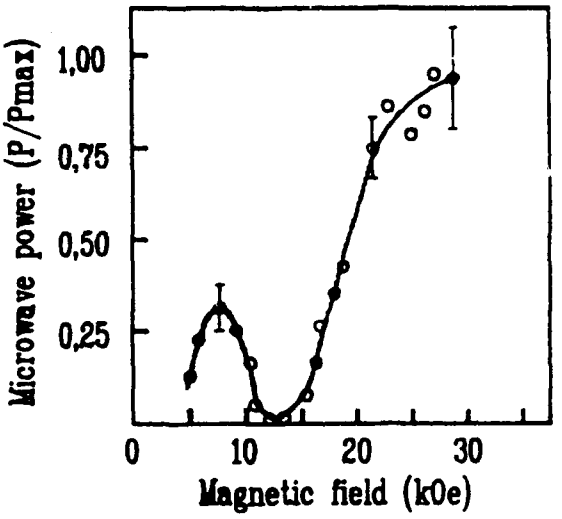

Fig. 4. Microwave power versus focusing magnetic field.

Figure 4 shows a typical curve of the magnetic field dependence of the BWO microwave power, having a characteristic dip in the region of resonant magnetic fields, $H_r \simeq mcv_e h_o \gamma/e$. For $H \simeq H_r$, in addition to the Cherenkov resonance condition, the magnetobraking resonance condition $\omega + h v_e \simeq \omega_H$, where $\omega_H = eH/(mc\gamma)$, is satisfied. With this condition satisfied, a fast cyclotron wave is excited in the electron beam and the electromagnetic wave energy is absorved [8]. The existence of the nonmonotonic P(H) dependence leads to the need of using strong magnetic fields which, for $\gamma \sim 2$, $I \sim 5$ kA, and $\lambda \simeq 3$ cm, should be in excess of 20 kOe. This is why all high-pulse repetition-rate experiments were carried out with the use of superconducting solenoids.

In the single-pulse mode (f_r < 0.1 pps), the microwave power of 500-600 MW was obtained. For a pulse repetition rate of 100 pps, the output power level was somewhat lower, 300 MW.

In experiments aimed at increasing microwave power, a BWO with inhomogeneous coupling impedance was used. The coupling impedance increased toward the end of the interaction space. The generator had two sections with different corrugation heights.

The maximum power produced in the experiment was 10^9 W, the efficieincy being ~ 35%. For f_r = 100 pps, the pulsed power was somewhat lower, 500 MW [8].

In the high pulse repetition rate mode, the BWO operation was stable, both in output power and microwave frequency, during a long period. Owing to this, the relativistic BWO could be used in testing a nanosecond RS.

IV. Conclusion

Figure 5 shows a schematic diagram of a radar station based on a pulsed power repetitive electron accelerator and a relativistic BWO operating with $\lambda \simeq 3$ cm. The microwave power and pulse duration were, respectively, 500 MW and 5×10^{-9} s. The spread in microwave power was no more than a few percents, the microwave frequency beihg reproducible within $df/f < 10^{-3}$.

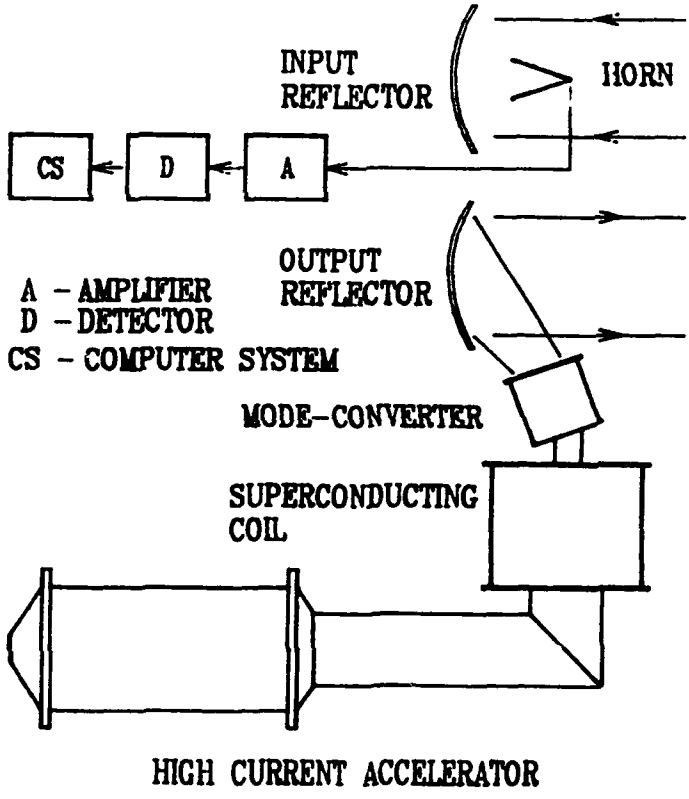

Fig. 5. Schematic diagram of the RS.

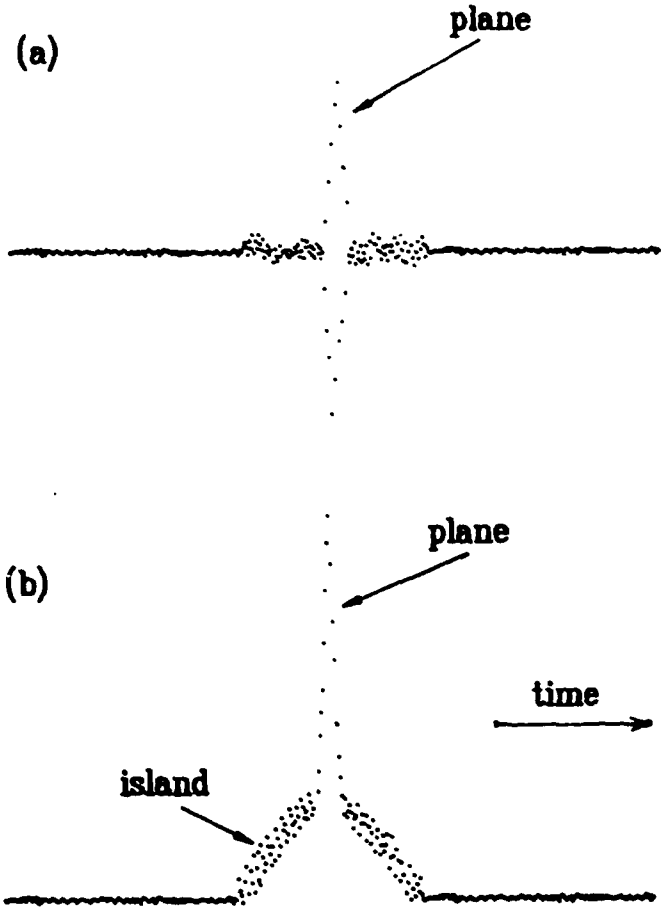

Fig. 6. Typical radar signals.

Field tests have demonstrated that the RS operation was reliable and efficient. Such object as river boats (including small ones) were clearly detectable in the water/shore background from distances ranging from some tens of meters to some tens of kilometers. Location of airplanes from the same distances in the background of clouds and lining surface, when they moved near to the horizont, provided clear images of the moving objects. For more reliable detection of objects with small effective reflecting surface, a system for moving-target selection (MTS) has been developed, whose operation is based on transperiodic subtraction of reflected signals. The reflections from local objects (trees, bushes, clouds) were so small, at the distances of more than several kilometers, that the RS could be operated without MTS. However, trans-periodic subtraction of the signals reflected from the objects to be located permitted us to take images of the objects situated close to the radar (individual trees, special control reflectors, etc.).Figure 6 shows typical detected radar signals: (a) the signal reflected from an island and an AN-2 plane flying at 100 m over the island surface (MTS pocessed) and (b) the same signals not MTS processed. The time interval between two neighboring points in Fig. 6 is 5 ns.

It can be concluded that the radiolocation application of microwave oscillators with relativistic electron beams, which produce powerful short microwave pulses, opens a new line in radar science, and, to our opinion, is rather promising.

REFERENCES

[1] V. E. Dulevich, A. A. Korostelev, Yu. A. Melnik, et al. Theoretical Basis of Radaring, Moscow, Sov. Radio, 1964. - 760 pp. (in Russian).

[2] M. I. Skolnik. Handbook on Radaring, Moscow, Sov. Radio, 1976, v. 1,-360 pp. (in Russian).

[3] Foreign Radioelectronics. Radaring (Methods of Compressing and Processing Pulses). Special Issue, 1987, N 1. (in Russian).

[4] N. M. Bykov, V. P. Gubanov, A. V. Gunin, et al. - In: Relativistic Microwave Electronics, Gorky, v.5, 1988, pp. 101 - 124. (in Russian).

[5] G. A. Mesyats. Generation of High-Power Nanosecond Pulses, Moscow, Sov. Radio, 1974. - 256 pp. (in Russian).

[6] A. V. Gaponov-Grekhov, M. I. Petelin Vestnik AN SSSR, 1979, N 4, pp. 11 - 23. (in Russian).

[7] V. I. Belousov, B. V. Bunkin, A. V. Gaponov-Grekhov, et. al. Pisma J. Eksper. Teor. Fiz., 1978, v. 4, N 23, pp. 1443 - 1447. (in Russian).

[8] S. D. Korovin, V. V. Rostov, A. V. Smorgonsky. Izv. Vyssh. Uchebn. Zaved., Radiofizika, 1986, v. 29, N 10, p. 1278 - 1280. (in Russian).

HIGH POWER MICROWAVE GENERATION AT HIGH REPETITION RATES

N. Aiello, J. Benford, N. Cooksey, B. Harteneck, J. Levine, D. Price, R. Smith, D. Sprehn and M. Willey

Physics International Company
2700 Merced Street
San Leandro, CA. 94577

Generation of microwaves at high power has progressed largely with single shot devices. Yet applications require repetitive operation at substantial repetition rates, implying high average power. This requires operation in a new domain for microwave devices. The technical challenge is to achieve very high electric fields in the source on a repetitive basis. We describe experiments on CLIA, a Compact Linear Induction Accelerator, generating 750 kV, 10 kA using magnetic switching to produce 60 ns pulses. We describe experiments with relativistic magnetrons and klystrons in the 1 GW,100 Hz domain. As a first application we used CLIA to drive a water-cooled L-band magnetron at repetition rates as high as 250 Hz with no breakdown or pulse shortening. This gave 6.3 kW average power. A short burst at 1 kHz operated at ≈25 kW. In this regime operation is not limited by gas build-up, electrode erosion or microwhisker depletion. We are now operating on CLIA with relativistic klystrons of both the high current and low current varieties. Beams with modulated current powers of ≈1 GW have been generated at 200 Hz for bursts as long as 1000 pulses.

Introduction

The generation of microwaves at high power (> 100 MW) has progressed largely on single shot devices. Yet many applications will require repetitive operation at substantial repetition rates[1], implying high average power. Only a few repetitive high power experiments have been conducted. In most the pulse duration was < 50 ns, with average powers less than a kilowatt. Conventional microwave tubes have operated at high average power, but peak power has been low.

The technical challenge of achieving both high peak and high average power is that repetitive operation may 1) evolve material from surfaces which raise the pressure, causing breakdown in the high electric fields (≈100 kV/cm) of successive pulses and 2) prevent emission of electron beams from cold cathode surfaces by evaporating monolayers (of gas, oil, water, *etc.*) and firing again before they can recondense. [It has been suggested that monolayers are the seat of plasma formation from cold cathodes, rather than plasma formation from exploded metal micro-projections.] The vacuum poisoning issue can be addressed by better high vacuum techniques, but only by actually operating at high peak power (> 100 MW) and high repetition rates (> 100 Hz) can the practical limitations be found.

A particularly attractive pulsed power system for such experiments is the hard-core (i.e., central cathode shank, not e-beams) linear induction accelerator (LIA), first used in high power microwave research[2] by the Tomsk group. They operated an S-band relativistic magnetron at 300 MW, 60 ns, 50 Hz, for an average power of 0.5 kW. The system is compact, which is an advantage for most applications. The basic reason for the compactness is that voltage from individual sections is added in vacuum so that the peak voltage appears only on the load. The system we describe here, CLIA (Compact Linear Induction Accelerator), is an LIA using magnetic pulse compression for switching. This technology has inherent long lifetime, eliminating the erosion problems of spark gaps.

The first microwave source tested on CLIA was an L-band relativistic magnetron. Our goal was to produce a pulse train of 100 shots at 100 Hz, each with peak power of 1 GW. This greatly extends the experience of 1–10 Hz sustained operation,[3,4] 50 Hz continuous operation[2] and the three shot bursts at 100–160 Hz[5] previously reported at lower powers, producing high peak and average microwave power simultaneously. We are now operating relativistic klystrons on CLIA.

Repetitive Magnetron

We modified our L-band magnetron[6] for repetitive operation for this experiment. It has six cavities, with cathode, anode and vane radii of 1.27, 3.18, and 8.26 cm, respectively, and oscillated in the π-mode at 1.1 GHz. This magnetron had produced 3.6 GW when connected to Marx bank/water line drivers.

The modifications for repetitive operation consisted of cooling the anode vanes (via water channels) and the downstream surface where the axial current emitted from the cathode tip is collected. We paid particular attention to creating good electrical contact between parts and avoiding virtual leaks. We also used a cryo-pump for our vacuum system to eliminate possible contamination from backstreaming oil. Base pressure was 4×10^{-6} torr. Previous single shot experiments have shown that peak power is increased by lowering base pressure.[7]

As shown in Figure 1, the microwaves were extracted from two opposing resonators which were connected to WR650 waveguide through quarter-wave transformers and absorbed by dummy loads, all in vacuum. Power samplers (≈80 db coupling) allowed for power, pulse shape and frequency diagnostics. The signal was viewed two ways: by the response of a crystal detector recorded on each pulse and directly on a high speed oscilloscope on one pulse (not necessarily the first) within the burst. The only electrical diagnostic used was a Rogowski coil measuring the total current into the magnetron. The voltage was determined from the current, the CLIA charge voltage and a measured load line.

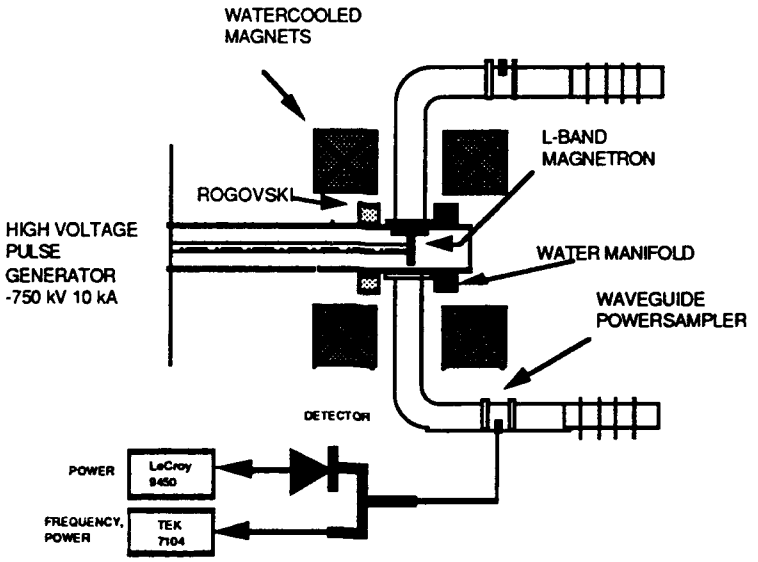

Figure 1. L-Band magnetron CLIA.

At a repetition rate of 100 Hz, we produced pulse trains of 1.0 GW, 50 ns FWHM pulses with 44 J each yielding 4.4 kW average power. Figure 2(a) shows the current and microwave pulse trains (each spike is a separate pulse; the data acquisition system does not record during the time between pulses) for a 50 shot burst, Figure 2(b) is an expanded view of one pulse in the middle of the burst. The recorded microwave signal is the crystal output on one of two extraction arms. This

produces the nonlinear scale for power. To determine total extracted power we double the power measured on one arm since we know, from other measurements, that the two extraction arms have nearly identical powers.

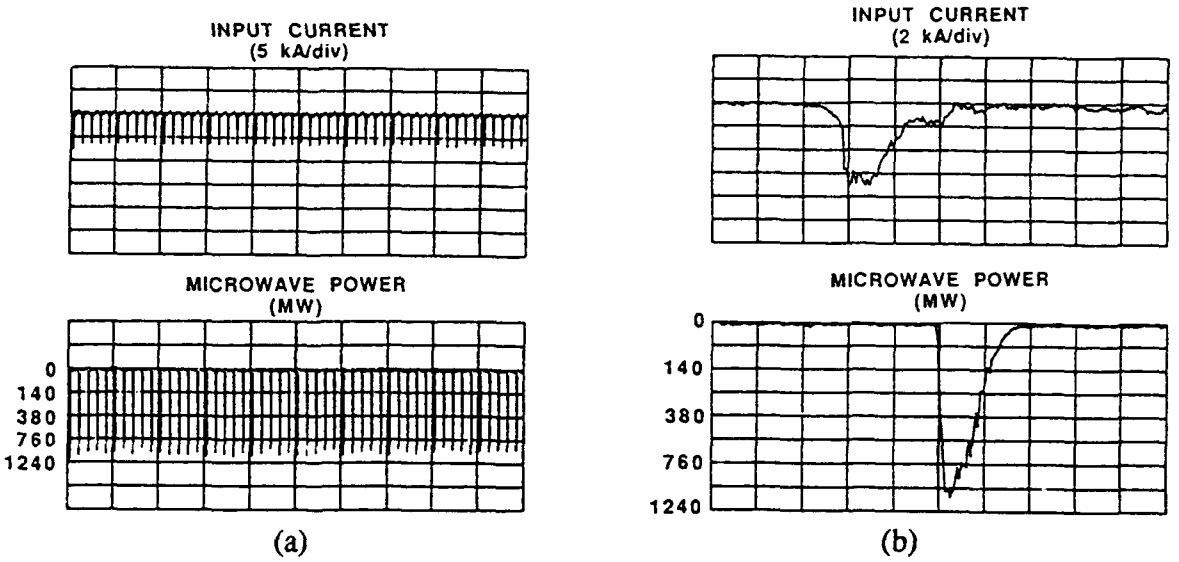

Figure 2. Current and microwave power for (a) a 50 shot burst at 100 Hz and (b) an expanded view of one pulse within the burst.

As can seen from Figure 2, the pulses are nearly identical. The microwave pulses last as long as the current pulse, *i.e.* there is no indication of impedance collapse or shifting of the operating point off resonance (effects conjectured to limit the pulse length in other relativistic magnetron experiments). A significant feature of magnetron operation on CLIA is that the pulse duration of the microwaves (50 ns) is only slightly less than that of the electrical pulse (60 ns). In many previous relativistic magnetron experiments, the ratio is typically 1/3.[8]

The first few pulses are slightly more powerful because there is slightly more current. This is due to the time it takes to establish a steady state within the CLIA power conditioning system. This effect becomes more obvious as the repetition rate is increased, causing a decrease in the peak power even though the average power is still increasing. As shown in Figure 3, at 200 Hz the typical peak power dropped to 700 MW while the average power rose to 6.0 kW. At 250 Hz, the trend continued to yield 600 MW peak power and 6.3 kW average power. We tested the system with a 5 shot burst at 1000 Hz (far beyond the average current specification for CLIA) to see if there was a minimum recovery time between pulses. The magnetron operates at 1000 Hz even though CLIA is capable of only a few pulses. Therefore, evolved gas clearing time is < 1 msec. Based on the third pulse, we estimate the average power would be ≈25 kW, with a peak power of 600 MW. These results are summarized in Table I.

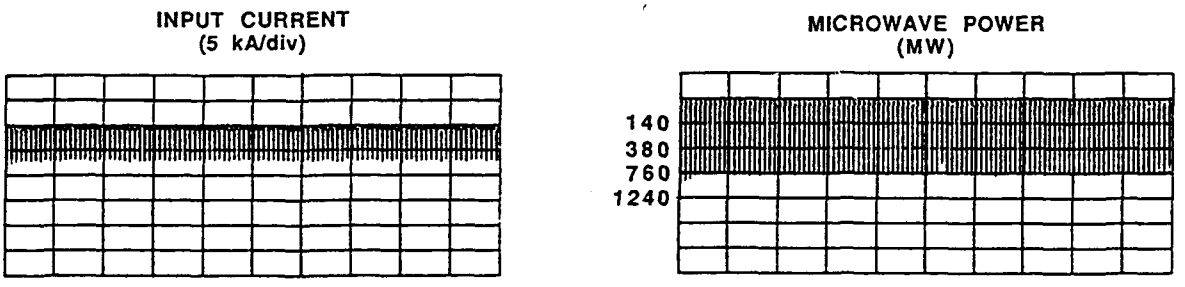

Figure 3. Current and microwave power for a 100 shot burst at 200 Hz.

Table I. Summary of magnetron peak and average power as a function of repetition rate.

Repetition Rate (Hz)	Peak Power (MW)	Average Power (kW)	Number of Shots
100	1000	4.4	50
200	700	6.0	100
250	600	6.3	100
1000*	600	25	5

* based on third shot of 5 shot sequence

In the magnetron, beam emission, RF generation and beam collection all occur in the same space. The problems of repetitive operation are much more difficult in the magnetron because of the proximity of these three functions. The linear beam devices (such as the relativistic klystron, travelling wave tube, backward wave oscillator and free electron maser), are very different because these functions are well separated.

Repetitive Relativistic Klystron Amplifier

Another microwave source, capable of producing GW power levels in the GHz range, that has seen substantial single-shot development but little repetitive development, is the high-current relativistic klystron amplifier.[9] We have undertaken to extend this technology to the repetitive regime at the level of 1 GW peak power for 100 pulses at 100 Hz.

In order to propagate the very high current in the high-current RKA, the on-axis, pencil-beam typically found in klystrons is replaced with a thin, annular electron beam with a radius almost equal to the drift tube radius. Even so, the beam has a significant fraction of its total energy stored in the electrostatic potential produced by its space charge. The interaction of the beam with a intense RF field thus has the possibility for a strong nonlinear effect, as the decelerated beam is brought near to space-charge limited flow.[10] This provides for short bunching lengths, even with relativistic electron beams.

In our experiment, a 5 kA, 500 kV annular electron beam, 1.8 cm mean radius by 0.2 cm thick, is emitted by a graphite cathode from a foilless diode energized by CLIA. The beam propagates through a two cavity RKA buncher,[10] supplied by M. Friedman and V. Serlin of the Naval Research Laboratory, as shown in Figure 4, below. The drift tube radius is 2.38 cm. A 500 kW L-band magnetron provides the input signal at 1.32 GHz. The input cavity is $3\lambda/4$ long; the radial wires are placed at a null at the input frequency and therefore have no effect on it, but load down the fundamental mode. (These wires have been removed, as explained below.) An axial magnetic guide field, 6–10 kG, is required for beam transport. The current modulation on the beam is measured with a B-dot probe mounted in a section of the drift tube.

Our initial efforts have been directed at optimizing the cavity positions for maximum beam modulation and determining if there are any inherent limitations in the design for repetitive operation that had not been resolved in the previous single-shot development. As we report below, we have successfully met (and exceeded) our goals for repetitive operation, and are presently constructing RF extraction hardware.

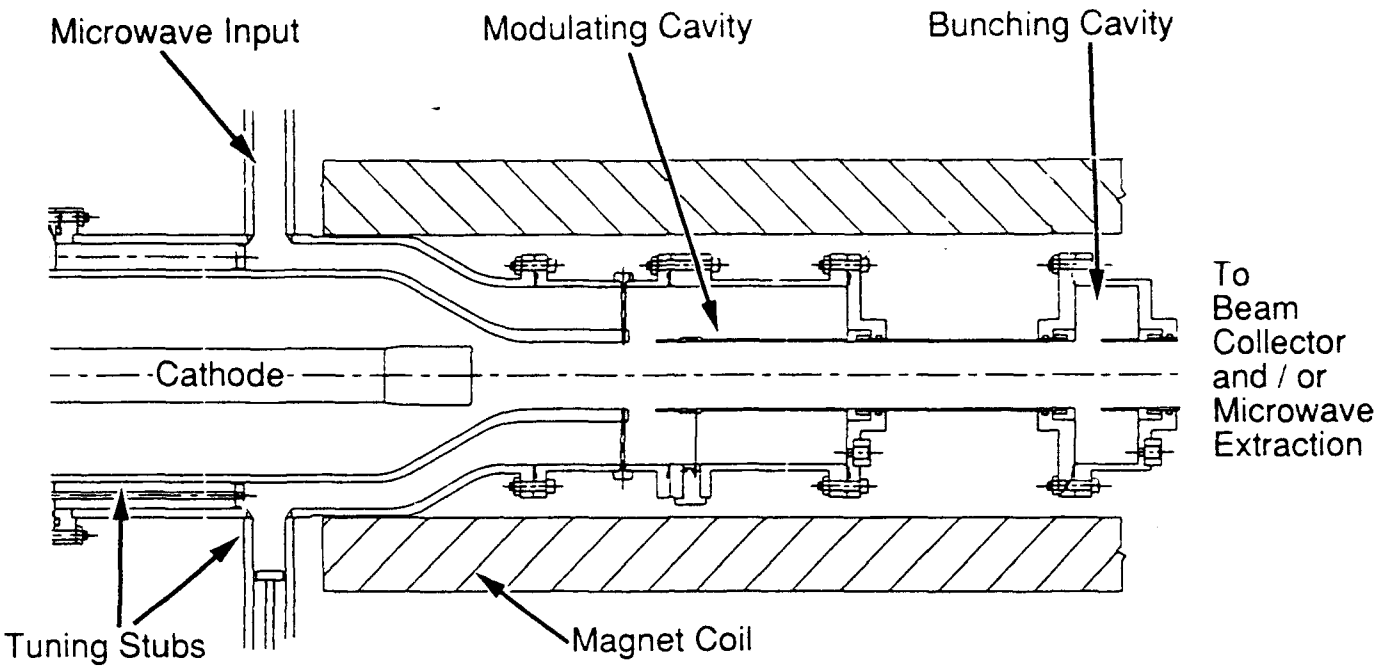

Figure 4. Annular cathode and RKA bunching section in magnetic solenoid.

Since repetitive operation requires a vacuum system that has a low base pressure before not just the first but also the n^{th} shot in a burst, one of the main considerations in the design of the RKA was simply good vacuum technique. Copper gaskets are used wherever practical; where the flexibility provided by O-rings is required, viton O-rings are used to allow moderate bake-out. Trapped spaces are eliminated by pump-out holes. Good electrical contact between pieces is also required to prevent arcing. As a result, we are able to obtain a base pressure of 1.0×10^{-8} torr.

The electron beam collector used in the single-shot RKA is a flat graphite disk in the drift tube just downstream of the output cavity.[10] For repetitive operation, we instead collect the beam on the inner surface of a 15 cm diameter stainless steel tube, which can be cooled with liquid nitrogen. To make the transition from the drift tube to the collector, a taper was designed that took account of the magnetic field profile and the electron beam parameters. The taper angle was chosen to be large enough to allow the beam to expand along the magnetic field lines without hitting the walls, but not so large that the beam exceeds the local space-charge limited flow condition (by having a radius less than the critical radius), creating a virtual cathode. [The critical radius is proportional to the drift tube radius, with the constant of proportionality determined by the beam energy and current (500 kV and 5 kA)].

Another element of the single-shot design that has proven to be unsuitable for repetitive operation is the use of radial wires in the input cavity (see Figure 4) for mode selection.[10] During the rising and falling edges of the current pulse, these wires carry the beam return current due to the inductance of 20 nH represented by the remainder of the cavity (10 kV would be generated at the location of the wires at the dI/dt of 5×10^{11} A/s typical of our experiment). The resultant heating causes outgassing, embrittlement and eventual failure of the wires. The broken wires can then become a source of arcing and electrical; breakdown. The net result is that the input microwave signal, as measured in the first cavity, gets progressively shorter during a burst. Luckily, we have been able to remove the wires without noticeable degradation to the bunched beam.

The position of the cavities are optimized for microwave production within the constraints of the electrical parameters of the pulsed power source (5 kA and 500 kV chosen for this experiment even though CLIA can operate at both higher current and voltage) and the magnetic field parameters of the solenoid (10 kG peak field, 1 m long x 11 cm radius bore).

The optimum position of the second cavity, relative to the input cavity, is determined as the point of peak bunching. This aspect of the RKA is well modeled by linear theory,[10] as confirmed by previous[10] and the present research. It is a strong function of the beam radius in the parameter regime of interest . We chose a 1.8 cm radius electron beam and a 33 cm gap separation, for reasons explained below. Given the profile of the magnetic field produced by our solenoid, we could control the beam radius by shifting the position of magnet with respect to the cathode (when the beam is emitted at lower magnetic field, it compresses more as it enters the drift tube), which was easier in practice than changing the cathode itself to control the electron beam radius.

We have measured peak modulation at 10 cm downstream of the second cavity and have designed an RF extraction cavity for this position. (It just barely fits within the magnet before the collector taper. The length constraint imposed by the solenoid was the determining factor in choice of beam radius.) The length of the drift tube between cavities is easily changed so we will have some limited flexibility to further optimize the system while measuring the extracted RF power instead of the beam modulation.

The modulated beam current is measured with a B-dot probe in a section of drift tube. The signal is filtered with bandpass filters to restrict the signal to the input RF frequency, and recorded directly on a high frequency oscilloscope (6 GHz bandwidth Tektronix 7250) and, using a diode detector, on a slower digital oscilloscope (350 MHz bandwidth LeCroy 7200/7242) The two measurements are in excellent agreement. As shown in Figure 5, we have measured 2.5 to 3.0 kA of modulated current, out of a total injected current of 4.5 kA. The RKA is well optimized with the chosen gap spacings.

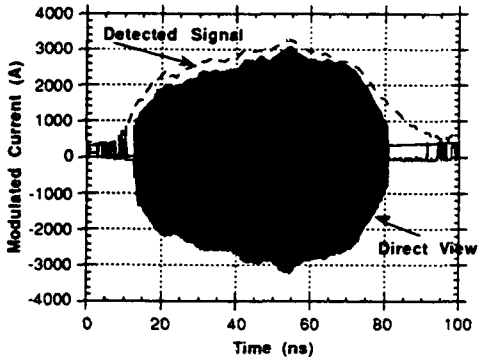

Figure 5. Modulated current, measured directly and with a crystal detector, on a 4.5 kA shot.

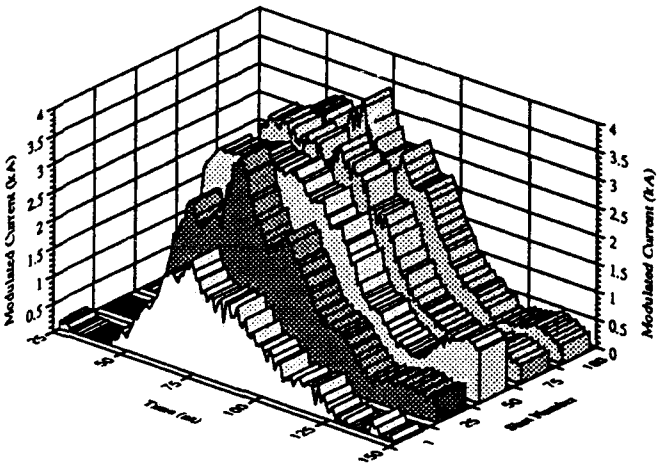

Figure 6. Amplitude of the modulated current for selected shots in 100 shot burst taken at 100 Hz. The total current was 4.5 kA.

Extending these results to repetitive operation has proven to be relatively straight-forward. Figure 6 shows the modulated current on selected shots in a 100 Hz, 100 shot burst at 4.5 kA total current. After some transient behavior in the first ≈ 20 shots, the output becomes quite

reproducible, with 3.0 – 3.5 kA modulation. (This data is from the crystal detector view of the B-dot probe; the direct view oscilloscope can record only 15 shots total, at 10 Hz.)

We have successfully increased the number of shots by a factor of ten (to 1000) and the shot rate by a factor of two (to 200 Hz), simultaneously, with highly reproducible results. The modulated current was 2.0–2.5 kA, out of 3.5 kA total current. The decrease in the modulated current, as compared with Figure 6, is due to the decrease in the cathode voltage, and thus the total current, at the higher repetition rate (since we chose not to increase the storage capacitor voltage for this test).and to a decrease in the efficiency of modulation because the position of the gaps was not optimized for these beam parameters. The data do, however, clearly demonstrate that there are no inherent limitations (at the beam modulation stage, at least) to long bursts of high repetition rate pulses with the RKA.

Discussion

These results extend the envelope of high average and high peak powers for microwave sources, as shown in Figure 7. What may be most notable about these results are the things that do not limit operation:

- There is no problem of gas build-up in the magnetron and klystron that could produce impedance collapse or interfere in other ways, though a vacuum system with a base pressure in the low 10^{-6} torr range seems to be required for consistent repetitive operation.
- There is no noticeable erosion of the anode vanes of the magnetron or the klystron cathode, even after several hundred shots on single-pulse generators and several thousand shots on CLIA. This is very different from our S- and X-band magnetrons.
- There is no diminution of cold cathode emission after 5000 shots, consistent with the result of Buttram[11] that at least 100,000 shots are required to show diminished emission.

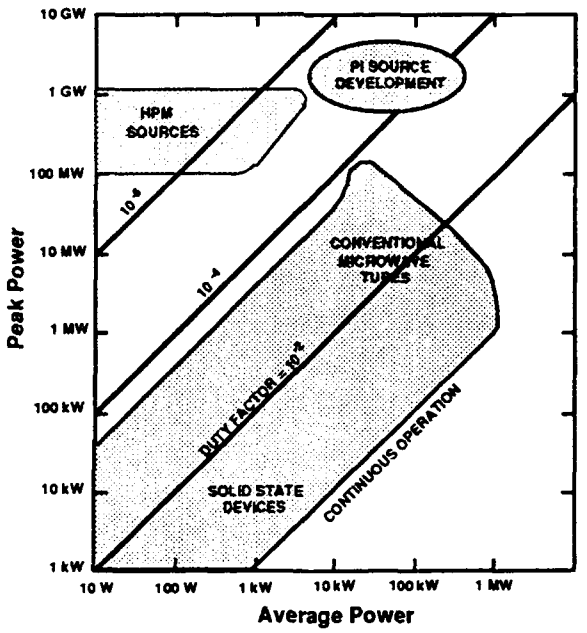

Figure 7. Peak versus average power domains for conventional and HPM sources. The domain of our program is indicated.

CLIA can be upgraded to extend the pulse length beyond the present capability. Since the microwave pulse lasts as long as the current pulse, there is clearly no impedance collapse and furthermore there must be relative insensitivity to the applied voltage. Thus, there is cause for optimism that these sources would generate longer microwave pulses.

One result of this experiment, that 250 Hz, 100 shot bursts and 1000 Hz, 5 shot bursts can be achieved reproducibly, indicates that much higher average powers should be achievable in the magnetron and other high peak power devices at repetition rates in excess of a kilohertz.

Acknowledgements

This work was supported by the Defense Nuclear Agency and the Strategic Defense Initiative Office under a contract managed by the Harry Diamond Laboratory. The RKA bunching section was supplied by NRL under SDIO contract.

References

1 See for example, Chapter 2 of *High Power Microwaves,* J. Benford and J. Swegle, Artech House, Boston, 1992. See also Benford and Swegle, Proceedings of this Conference.

2 V. V. Vasil 'yev, I. I. Vintizenko, A. N. Didenko, Ye. I. Lukonin, A. S. Sulakshin, G. P. Fomenko, and E. G. Furman, "Relativistic Magnetron Operating in the Mode of a Train of Pulses," *Sov. Tech. Phys. Letts.*, **13**, 762 (1987).

3 D. Phelps, M. Estrin, J. Woodruff, R. Sprout, and C. Wharton, "Observations of a Repeatable Rep-Rate IREB HPM Tube," Proc. Seventh Intl. Conf. on High-Power Particle Beams, Karlsruhe, 1347, 1988.

4 S.T. Spang, D.E. Anderson, K.O. Busby, K.D. Claborn, S.P. Manning, A.K. Milakovic, J.J. Prochazka, D.M. Rexroad, E.P. Scannell, T.K. Seybold, R.J. Williams, Jr. and D.A. Woodyard, "Relativistic Magnetron Development For Use in a Lightweight, Repetitively Pulsed, Portable HPM Transmitter," *IEEE Trans Plasma Sci.*, **18**, 586 (1990).

5 A.N. Didenko, G.P. Fomenko, E.G. Furman, E.I. Lukonin, A.S. Sulakshin, V.V. Vasil 'yev, and I.I. Vintizenko, "Pulse-Periodic Relativistic Magnetron," Proc. Seventh Intl. Conf. on High-Power Particle Beams, Karlsruhe, 1380, 1988.

6 R. R. Smith, J. Benford, B. Harteneck, and H. Sze, "Development and Test of An *L*-Band Magnetron," *IEEE Trans. Plasma Sci.*, **19**, 628 (1991).

7 R. Smith, J. Benford, N. Cooksey, N. Aiello, J. Levine and B. Harteneck, "Operation of an L-Band Relativistic Magnetron at 100 Hz," *Intense Microwave and Particle Beams II*, Howard E. Brandt, ed., SPIE **1407**, 83, 1991.

8 J. Benford and J. Swegle, "Crossed-Field Devices," Chapt. 6 of *High Power Microwaves*, Artech House, Boston, 1992.

9 M. Friedman, V. Serlin, Y. Y. Lau and J. Krall, "Relativistic Klystron Amplifier I – High Power Operation," *Intense Microwave and Particle Beams II,* Howard E. Brandt, ed., Proc. SPIE **1407**, 2, SPIE, Bellingham, 1991.

10 M. Friedman, J. Krall, Y. Y. Lau and V. Serlin, "Externally modulated intense relativistic electron beams," *J. Appl. Phys.*, **64**, 3353 (1988).

11 M. T. Buttram, "Repetitively Pulsed Electron Beam Diode Lifetime and Stability," Proc. 2nd IEEE Pulsed Power Conference, Lubbock, 61, 1979.

RELATIVISTIC MULTIWAVE CERENKOV GENERATOR

Kanavets V.I., Nifanov A.S., Slepkov A.I.

Moscow State University, Moscow

Abstract- The general physical processes in Multiwave Cerencov Generator are considered. The feature of beam-field interaction, field structure and "electron" mode forming are discussed.

1. Inroduction

For the last years the great attention was payed to the investigation of directional radiation of relativistic electron beams in the superdimensional waveguide. The exsperiments with two sectional systems was the most successful. The radiation field of generators is multiwave. This type of microwave sources are promising to obtain the radiation in mm and sm range of wavelengths of the 1-100 GWt power level with 10ns-1mcs puls duration.

The experiments, caried out in MSU [1] and Institute of high curent electronics [2,3] have shown the Cerenkov mechanism of radiation perspective. The interaction of the beam and the field of the frequency range near passband cuttoff of surface wave ("π"-mode) was found effective for the mode selection. This selection was determined by a significant role of the "π"-mode interaction in traditional microwave electronics, and the first of all in coupled cavity TWTs [4].

For space-development relativistic Cererнkov devices, as the relativistic surface wave generator (RSWG)[1] and the multiwave Cerenkov generator (MWCG)[2,3], this principle was used in condition, when the electromagnetic fields are localised near surface and completely determined by resonans properties of periodic sistem. Characteristics of radiation field and feedback are determined by volume fields.

A following experiments have shown the perspectivity of the device sectionalisation when the first section is a modulator and at the second take a place the radiation of bunching beam.

In repo t the analysis of basic physical proceses in MWCG is present. Results are obtained with the following methods:

- the variation method based on description fields with waveguide network;

- the nonlinear nonstationary method based on a discret model of electron beam and impulse voltage consideration;

- matrix multimode method based on field decomposition on a series cylindrical waveguide modes [6,7].

The typical scheme of MWCG is shown on fig.1. Generator contains two sectional periodic waveguide, vacuum-tube diode, hollow electron beam, output window. Relativistic beam is focused by longitudinal magnetic field of solenoid. The spot of radiation is represent wide ring out the window.

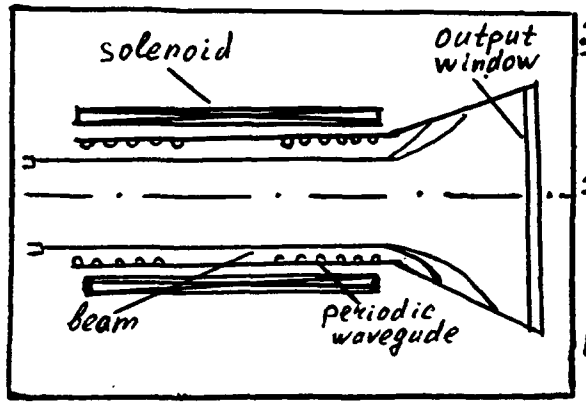

Fig.1 Two-sectional MWCG

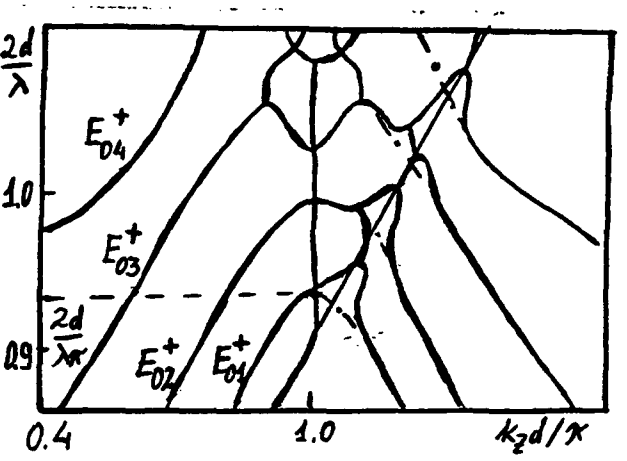

Fig.2 Dispersion characteristics

For numerical analysis the typical shape of each section for MWCG [4] was selected. Accelerating voltage changed from 0.5 to 2.0 MV, beam current: 1- 30 kA.

2. Waves in a periodical waveguide with an electron beam

We consider dispersion characteristics of the periodical waveguide, that is presented at fig. 2 (k_z - is a longitudinal wave number, d - period, λ-wavelength). The unbroken inclined line corresponds to the kinematic characteristics of an electron beam. The greatest connection is achieved at synchronism with surface waves near triplets points. This points are high frequency boundaries of a bandwidth ("π"-mode, "2π"-mode).

The waves of field modes $E_{01}, E_{02}, E_{03}, E_{04}$ are propagated in "cold" (without electron beam) periodical system at the same parameters and λ=3 sm. The lowest mode is a slow wave, its field is located near the waveguide surface. The other modes is volume

waves, their field structures are similar to a mode structures of a cylindrical waveguide.

At fig. 2 the dispersion characteristics of waveguide with electron beams are shown at the high value of the focusing magnetic field. The typical gapes are observed at the frequency over "π"-cutoff. It is caused by the connection of fast space-charge wave and slow one with the axially-symmetrical periodical waveguide modes of highest type. The "electron" "π"-cutoff frequency shift to longer wavelengths is detected. The eigenwave structure of waveguide, loaded by an electron beam depends on the signal frequency. The results applied to frequency of "π"-mode oscillations of "cold" system are presented at fig.3. The irregularity of curves is determined by the connection between different periodical waveguide waves, caused by the electron beam introduction.

The eigenwaves structure, propagating without an amplification from the left to the right with the $k_z d/\pi=1,04$ are not distinguish. They are like to a surface wave (fig.3, curv.1). The interaction this waves and an electron beam is characterized by a periodic energy transfer (Im $k_z d/\pi=0$). The phase velocities of this waves differ from the average beam velocity. The electromagnetic field is forced out the beam area therefore the longitudinal field component in beam region has a minimum (fig.3).

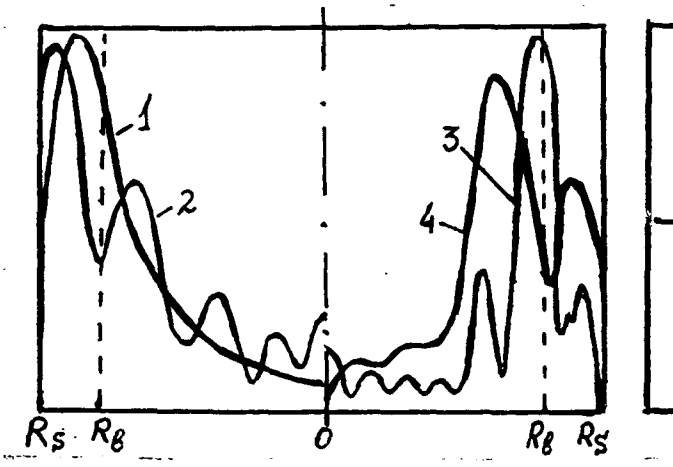

Fig.3 Eigenwaves of periodic waveguide with electron beam

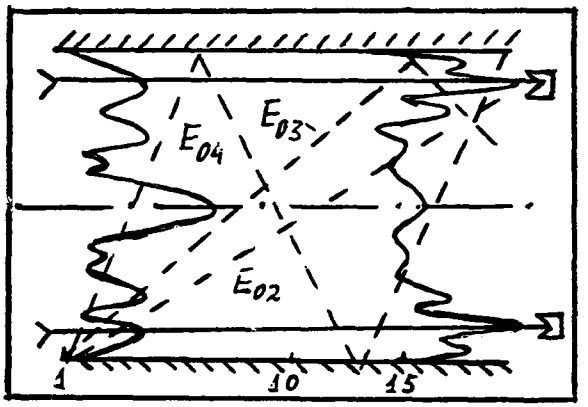

Fig.4 The field structure in section of MWCG

The different field distribution along the radius is observed for increasing and attenuating waves (fig.3,curv.3,4).

These waves have identical field structures. The increasing wave propagating from the left to the right of the wave number $k_z d/\pi = 0,98$ causes the most interest. The phase velocity of this wave is near an electron velocity. The electromagnetic field is located in a beam area and decreases with removing from it. The longitudinal component has a sharp maximum (fig.3 curv.3), but transverse component changes sign in the beam area(curv.4). At the same system parameters the increasing wave correspond to drawn vortex field . For a sufficiently long system (amplification section) the increasing wave dominates at the simultaneous excitation of a various eigenwaves and determines an amplification character. Generally, this situation is similar to the amplification of an increasing wave in intermediate section unrelativistic coupled-cavity TWT. However, for super dimensional waveguides the variation of the transverse component of the electromagnetic field takes place in influencing of the electron medium.

3. Volume and surface fields in sections

Near "π"-cutoff frequency and higher an amplifiers range transits to decreasing. Oscillator regimes and wave ones are connected. Hence it is necessary to consider boundary conditions. Analyzing the interaction of the beam and the field in short sections we used "cold" impedance matching in the input and the output of a section.

We consider the amplitude of forward waves are known. At fig.4 the longitudinal component of vortex field in dependence on the radius in input and output of the section of the Cerenkov amplifier , consisting of 17 cells, is presented at fig.4. A vortex fields, localized near a waveguide surface and in a beam region, are the most important. Since the section length is less than surface wave forming length, a disconnecting vortex field from surface takes place, and that is a reason of forming volume radiation flows. This is used for determine feedback and the output of the microwave energy.

The total power of surface and volume vortex field at the output of the system as a function of a section length is complicated. Main maximums correspond to longitudinal

resonances, which are caused by connection of a forward increasing wave and backward surface one. Volume resonances has an auxiliary role in "hot" case as it was in a "cold" one. They provides processes synchronization and take part in a forming output field structure.

Volume field resonances, arising in a short section, may be considered by using Brilluen diagrams. The directions of a volume modes propagation is shown on fig.4 (dotted line). In considering case (a section length is 17 cells) the fields of E_{02} and E_{03} modes are not settled. The resonant condition of excitement are kept for E_{04}-mode only. The cylindrical wave, corresponding to this mode, undergoes integer number of reflections and has a strong influence on a volume field structure . In particular, the volume field structure at the input corresponds to this mode structure. The interference picture is observed along the system. This is determined by summarisation of the forward wave and a backward one of E_{04}-mode, partially reflected from the input and the output.

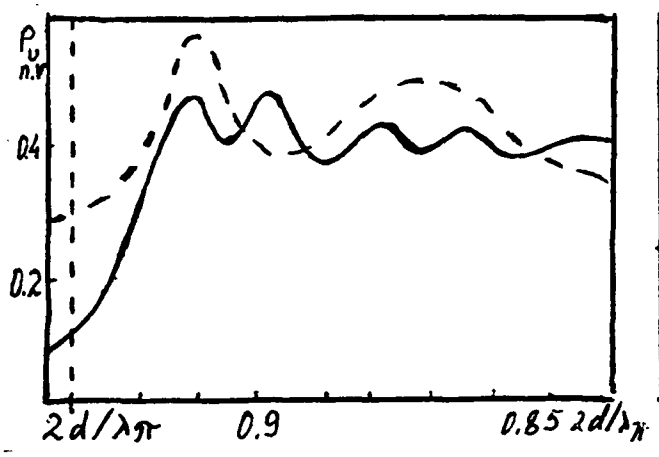

Fig.5 Amplitude-frequency characteristics of "cold" system.

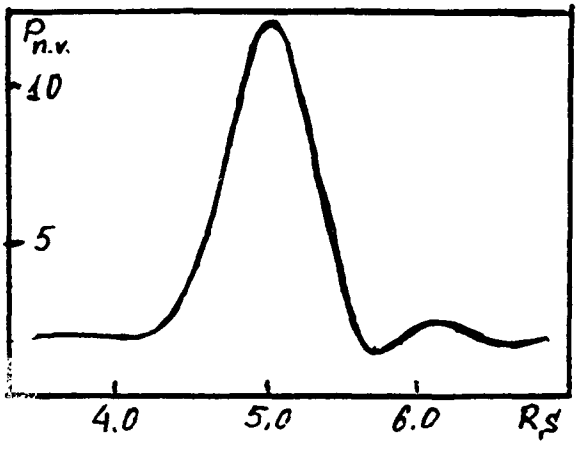

Fig.6 The dependence of output power from beam's radius.

The peculiarity of the two section structure acting is illustrated on fig.5. The system is considered system without the beam, and the amplitude wave at the input is known. The dependence of output signal amplitude on the frequency for individual section (fig.5, dotted line) is determined by surface resonances mainly. The connection of two sections results in a bifurcation of the number of maximums (unbroken line), that

is a typical for an amplitude-frequency characteristic of the two-contour oscillating system. The beams introducing complicates this dependence. However, the resonances of the fields, localized near the surface and at the beam region, are so significant as in the former case. The importance of this resonances is confirmed by the presence of an acute maximum in the $P_o(R_b)$ dependence (fig.6), where P_o - is an output power in normalized values, R_b -is a beams radius. The extreme value of P_o is detected in passing the beam through the range of the surface field concentration of a short section.

4. The "electron" mode of a generator. The settling of oscillation.

The Cerenkov's generator dispersion characteristics area corresponding to surface waves is perturbing near "π"-cutoff. Since the connection between a beam and a surface field dominates, the field structure of radiation keeps sufficiently good and provides the stable operation of the device. We can assume, that the "electron (hot)" mode excites. Its structure depends on the beam and insignificantly varies on changing the system parameters.

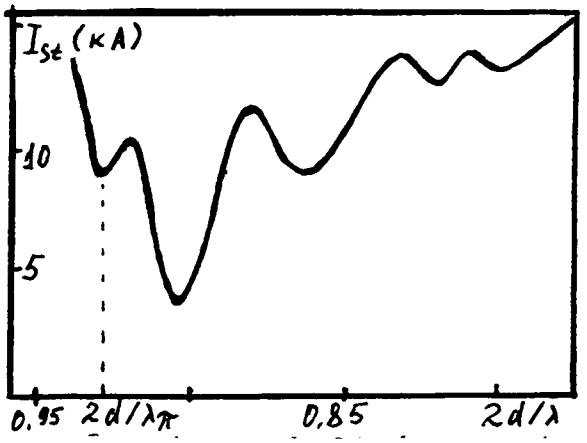

Fig.7 The dependence of starting current on a frequency

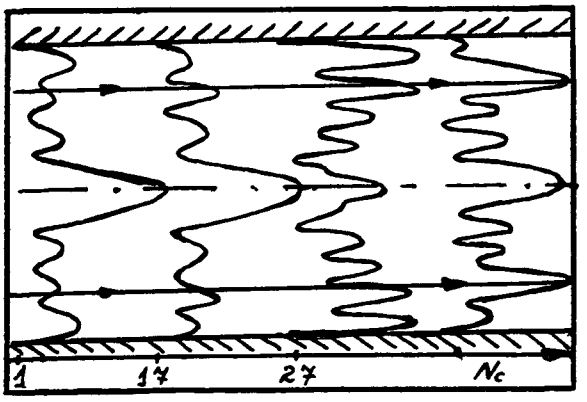

Fig.8 Field structure in MWCG

This results are confirmed by means of the computation, carried out by matrix multiwave method. The iterative procedure was used to analyze two section systems. The starting conditions of the system are satisfied if iteration begin to diverge. The dependence of starting currents on the frequency is presented

on fig.7. The generation condition are satisfied at the frequency near the bandwidth boundary. The analysis have shown that the vortex field structure varies weakly in the device in changing the frequency. The assumption of the "electron" mode stability is confirmed also by the coupled two-part network method, when only a surface wave with the varying longitudinal structure is considered.

The analysis of generation settling processes in MWCG was carried out by the equivalent two-port network [8]. The scattering field was considered by means of series of electromotive forces, introducing in the theory.

The numerical analysis results are corresponded to ones of stationary methods. The velocity modulation of an electron beam takes place in the first section, the effective energy exchange between the beam and the field takes place in the second one . The analysis performed is suitable for relativistic generators and amplifiers of the Cerenkov's type. This devices have the stable structure of an "electron" mode.

The analysis of settling oscillations was carried out to one-section and two-section systems. The process of settling oscillation is shown to one section system, consisting of 36 identical cells. On fig.9 the parameter τ is normalizing time $\tau=\omega_0 t$. The rise of field amplitude along the section is observed at small times. The presence of the feedback results in the change of field structure during the time period and at $\tau>500$ the field distribution corresponds to the basic longitudinal mode.

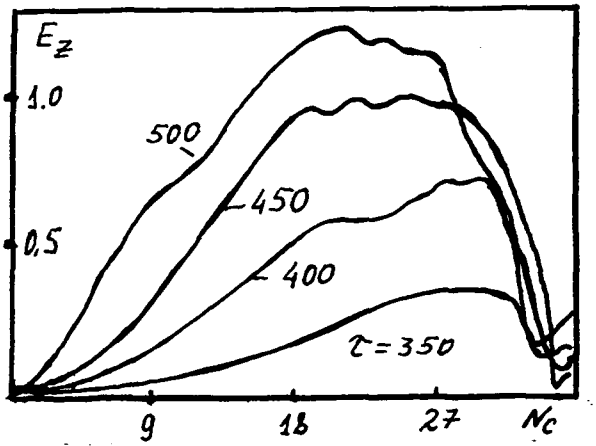

Fig.9 Variation of field destribution along the system with the time

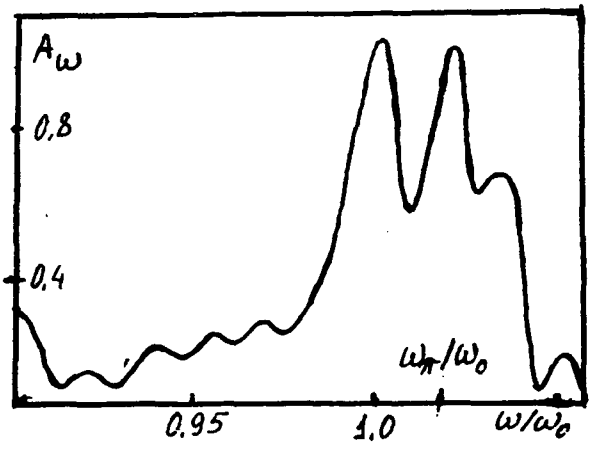

Fig.10 Typical spectrum of radiation field of MWCG

The process of an oscillation rise in two sectional system has more complex nature. The field distribution along the first section is near to basic longitudinal mode, the distribution isn't identified by any mode in the second section. This shows that the processes of the electron bunches emission dominates. The emission of an electron beam isn't monochromatic for discussing version of generators (fig.10). The greatest emission occurs at frequency, that is near to point of synchronization of the beam and the surface wave in the system. In this case it is near to the "π"-cutoff frequency (ω_π/ω_o=1,01).

5. Conclusion

The characteristics of processes in MWCG are determine by interaction of the electron beam with surface wave of the structure in the main. Complete field structure is connected with the short sections length and the field scattering on the edges of sections. Beam and field interaction in MWCG led to forming stable "electron" mode.

Literature

[1] Alexandrov A.F., Afonin A.M., Galuso S.Ju. at al.// Relativistic Highfrequency Electronics. Gor'ky. Ins.App.Ph. 1983. p.145-169.

[2] Bugaev S.P., Kanavets V.I., Klimov A.I. at al.// The Relativistic Highfrequency Electronics. Gor'ky. Ins.App.Ph. 1984. p.79-103.

[3] Bugaev S.P., Kanavets V.I., Klimov A.I. at al.// The Relativistic Highfrequency Electronics. Gor'ky. Ins.App.Ph. 1988. p.78-100.

[4] Grigorenko L.P., Kanavets V.I., Koreshkov E.N. at al.//The Electronics Technology. The Microwave electronics. 1979. No 8. p.27-40. p.79-103.

[5] Bugaev S.P., Kanavets V.I., Klimov A.I. at al.// Radioengineering and Electronics. 1987. V. 32. No 2. p.1488-1494.

[6] Garutsa N.A., Kanavets V.I., Slepkov A.I. // The Radioengineering and Electronics. 1988. No 4. p.783-795.

[7] Kanavets V.I., Nifanov A.S., Slepkov A.I. // Vestnik Moskovskogo Universiteta. Physics. Astronomy. 1990. V. 31.No 5. p.34-41.

[8] Kanavets V.I., Kaeva N.S., Slepkov A.I. // Proc. of seminar "Physic and Application of Microwaves". Moscou State University. 1991. V. 1. p. 22-25.

HIGH POWER MICROWAVE GENERATION IN VIRCATORS

A.N.Didenko, V.I.Rashchikov

Moscow Engineering Physics Institute

Vircator as high-power microwave source has recently become an intensive area of research. It is the device in which own beams fields dominate.Triod with reflex cathode investigated by H.Barkhausen and K.Kurz has been considered as low current analog of vircator .It is shown that such analogy is not correct, but parametric amplifier which based on triod with reflex cathode is real analog of vircator. The theory of vircator is developed for broad range of electron velocities.

Generation of electromagnetic oscillations in virtual cathode systems draws attention due to absence of current limitation in these systems because of space charge field available in familiar vacuum generators, a possibility for propagating into region of great powers and enhance of radiation efficiency. The ability for generating electromagnetic oscillations when electron beam currents are higher than vacuum limit current and conditions of a virtual cathode formation are carried out is a distinguished feature of a virtual cathode systems (VC). Therefore one can produce new powerful high-current relativistic devices on the basis of virtual cathode system. These devices may generate the centimeter and millimeter wavelength ranges and have such advantages as frequency retuning, formation of durable electromagnetic pulses, structural simplicity and small size (it's possible not to have the focusing magnetic fields and its power sources).

The first investigations on generating in these systems [1-5] showed a possibility for producing powerful high frequency pulses and stimulated an experimental research of dependencies of basic radiation characteristics upon electrical and geometric paramerters of various generating devices. One of

the most important problems in all VC system is to define a radiation frequency.

Two mechanisms have been proposed to explaine the microwave generation process in vircators. The first deals with electrons reflexing between the real and virtual cathodes, and the second with virtual cathode oscillating as a whole [6].

To determine the frequency of electron oscillation around the anode , it is necessary to solve relativistic Poisson equation, from which we will obtain the folloving expression for current density:

$$j=\frac{8}{9}\cdot\frac{I_o}{4\pi d^2}\cdot\frac{(\gamma_a-1)^2}{\sqrt{\gamma_a^2-1}}F^2 \quad . \qquad (1)$$

where F- hypergeometrical row whose value vary from 1 to 3/2 with γ_a varying from 1 to ∞, $I_o=\frac{m_o c^3}{e}=17kA$, and transit time of cathode-anode gap spacing:

$$t_{c-a}=\int_o^t dt'=\frac{1}{c}\int_o^d\frac{\gamma}{\sqrt{\gamma^2-1}}\frac{dz}{d\gamma}d\gamma=\frac{1}{c}\int_o^{\gamma_a}\frac{1}{(8\pi j/I_o)^{1/2}}\frac{d\gamma}{(\gamma^2-1)^{3/4}}=$$

$$=\frac{2(\gamma_a^2-1)^{1/4}}{c(8\pi j/I_o)^{1/2}}=\frac{3}{2\cdot F}\left[\frac{\gamma_a+1}{\gamma_a-1}\right]^{1/2}\cdot\frac{d}{c}=\frac{3}{2\cdot F}\frac{\gamma+1}{\gamma}\frac{d}{v_{max}} \quad . \qquad (2)$$

Thereby radiation frequency of the electrons oscillating around the anode equals:

$$\Omega=2\pi f=\frac{2\pi}{4t_{c-a}}=\frac{\pi F}{3}\frac{\gamma}{\gamma+1}\frac{v_{max}}{d} \quad . \qquad (3)$$

From the other hand frequency of virtual cathode oscillations which is obtained from experiments (especially from experimental investigation of reditron) is defined by following relation $\omega_{vc}=2.5\ \omega_p=2.5(4\pi ne^2/m_o\gamma)^{1/2}$.

This expression can be transformed by substituting n from (1) and taking into the account that j=envv:

$$n=\frac{8}{9}\cdot\frac{1}{4\pi ed^2}\cdot\frac{1}{v_{max}}\frac{(\gamma_a-1)^2}{\sqrt{\gamma_a^2-1}}F^2 \quad . \qquad (4)$$

Then

$$\omega_{vc}=2.5\sqrt{2}\,\frac{2}{3}\,F\left[\frac{(\gamma_a^2-1)^2}{\gamma^2-1}\right]^{1/2}\cdot\frac{c}{d}=\frac{5\sqrt{2}}{3}\cdot F\frac{\gamma_a}{\gamma_a+1}\,\frac{v_{max}}{d}\,. \qquad (5)$$

More accurate calculation gives $1.92\,\omega_p \leqslant \omega_{vc} \leqslant 2.31\,\omega_p$. Comparison (3) with (5) shows, that virtual cathode oscillation frequency approximately twice biger than Ω. In that case virtual cathode oscillations play the role of external force which excites parametric resonance in this system.

This fact, that both this frequencies depend on gap spacing d and particle energy γ in the same manner allows to make conclusion that vircator not only parametric generator, which operates in autogeneration regime, but the device, in which parametric resonance conditions are satisfied in the broad band of parameters [7].

It is known that parametric amplifiers have a low noise coeficient compare with all other types of amplifiers. Investigation shows that for vircator which operates as amplifier with input signal frequency equal Ω, noice coeficient can be reduced essentially by decreasing initial electron beam temperature.

Based on this parametric resonance between virtual cathode and electron oscillation frequencies we may now develop the vircator theory. Let us take into consideration only the electron oscillations in cathode-virtual cathode region, because virtual cathode play the role of external force. During this oscillations electrons change their velocities from zero to light velocity. It is difficult to obtain analytical solution in this case,becouse not easy to find small expantion parameter. Nevetheless it will be shown that this problem can be solved by corresponding chose of variables.

To describe the movement of oscillating electrons we use square amplitude of electron oscillation in steady state a^2 and fase $\phi=\Omega t+\phi_0$ [8]. Kinetic equation for distribution function for this case is given by:

$$\frac{\partial f}{\partial t} + \left[\Omega + F_z^{(1)} \frac{\sin\phi}{am_o\gamma\Omega}\right]\frac{\partial f}{\partial\phi} + F_z^{(1)} \frac{2a\cos\phi}{m_o\gamma\Omega} \frac{\partial f}{\partial(a^2)} = 0, \qquad (6)$$

where $F_z^{(1)} = -eE_z^{(1)}$ - force from the fields, which deals with density and current perturbation, Ω-steady state oscillation frequency. In common case Ω depends on amplitude of oscillations. Nonlinearity deals with relativistic effect and nonparabolic form of potential well.

Using for determination of perturbation fields the method of cavity eigenmodes expansion and expanding perturbation of oscillating electrons to harmonics $e^{i(e\phi-\omega t)}$, we obtain the following dispersion relation [8]

$$1 = \sum_{k_z} \frac{m_o c^2 \omega_p^2}{2}\, iZ(\omega) \int_o^\infty \frac{\partial f_o/\partial(a^2)}{(\omega - l\Omega)\Omega}\, I_l(k_z a)\, d(a^2). \qquad (7)$$

The impedance is given by:

$$Z(\omega) = \sum_\nu Z_\nu^{(b)}(0) \frac{\omega + i\alpha_\nu}{\omega_\nu^2 - \omega^2 - i\alpha_\nu\omega} + Z_\nu^{(k)}(0)\cdot 1/\omega,$$

where $Z_\nu^{(b)}(0) = -4i \dfrac{4\varepsilon_m k_1^2\, r_b^2\, d|\rho_1|^2}{hk^2R^2J_n'^2(k_1R)}$ - the impedance, which deals with rf fields, $Z_\nu^{(k)}(0) = -Z_\nu^{(b)}(0)\dfrac{k_z^2}{k_1^2}$ - the impedance, which deals with space-charge fields, $\alpha_\nu = (1-i)\dfrac{\sqrt{\omega\cdot\omega_\nu}}{Q_\nu}$; $k_z = \dfrac{\pi m}{h}$, $m = 0, 1, 2..$;

$\omega_\nu = ck = c(k_1^2 + k_z^2)^{1/2}$; Q_ν-cavity quality factor for frequency ω_ν;

$$\varepsilon_m = \begin{cases} 1/2, & \text{if } m=0 \\ 1, & \text{if } m\neq 0 \end{cases}; \quad \rho_1 = \int \rho(r,\theta) J_n(k_1 r) e^{-in\theta} r\, dr\, d\theta = \frac{2\rho_o}{k_1 r_b} J_1(k_1 r),$$

when $\rho(r,\theta) = \rho_o = \text{const}$ and $n = 0$.

$$I_l(k_z a) = \frac{1}{(2\pi)^2} \left[\int_o^{2\pi.} \frac{2\gamma}{c} \cos(k_z a) e^{il\phi} d\phi\right]\left[\int_o^{2\pi.} \frac{z}{\gamma c} \cos(k_z a) e^{-il\phi} d\phi\right].$$

For monoenergetic beam dispersion relation becomes:

$$1+\Lambda A c^2 \sum_{k_z} iZ(\omega)\left\{\frac{1\dfrac{\partial\Omega}{\partial(a^2)}\, I_l(k_z a)}{(\omega-l\Omega)^2}+\frac{\dfrac{\partial I_l(k_z a)}{\partial(a^2)}}{(\omega-l\Omega)}\right\}_{a=a_o}=0, \qquad (8)$$

where

$$\Lambda=\frac{\omega_p^2}{2\pi\gamma_o\Omega_o^2}\ ;\quad A=\left[1-\frac{1}{2\pi\gamma_o}\int_o^{2\pi}\frac{eU(a_o^2,\phi)}{m_o c^2}d\phi\right]^{-1};\quad \Omega_o=\Omega(a_o^2);\quad \gamma_o=\gamma(U_o).$$

Thus, there are two particles bunching mechanisms: the first is described by $d\Omega/d(a^2)$ and deals with oscillators nonlinearity, and the second $dI_l(k_z a)/d(a^2)$ with linear oscillator interaction. For strong nonuniform fields instability rise. For resonant system when perturbation frequency is equal to one of eigenmode $\omega \approx l\Omega_o \approx \omega_\nu$, and $(\omega_\nu - l\Omega_o) \ll \omega_\nu$, $(\omega - l\Omega_o) \ll \omega_\nu$, instability increases, if

$$|K|=\frac{c^2}{\Omega_o^3}\left|(\partial\Omega/\partial(a^2)\right|_{a=a_o} \geq \frac{1}{9\cdot 2^{1/3}Q_\nu}\,\frac{\left[\dfrac{c^2}{\Omega^2 I_l(k_z a)}\,\dfrac{\partial I_l(k_z a)}{\partial(a^2)}\right]_{a=a_o}}{1+\dfrac{2^{2/3}}{9Q_\nu}\,\dfrac{Z^{(k)}(0)}{Z^{(b)}(0)}\left[\dfrac{(\partial\Omega/\partial a^2)}{|\partial\Omega/\partial a^2|}\right]_{a=a_o}} \qquad (9)$$

If $\dfrac{Z^{(k)}(0)}{Z^{(b)}(0)}\,\dfrac{1}{Q_\nu} \ll 1$ space charge forces may be neglected, but not for low quality factor cavity. Under this conditions (9) maximum increment will be:

$$\xi=\frac{\sqrt{3}}{2}\left\{\frac{1}{2}\Lambda A i Z^{(b)}(0) I_l(k_z a)|K|1\right\}^{1/3}\Bigg|_{a=a_o}\cdot\Omega_o-\frac{l\Omega_o}{6Q_\nu} \qquad (10)$$

For nonmonoenergetic beam with Lorents distribution we will obtain following expression for threshold current

$$I_{cr}=\frac{\pi r_b}{a_o^2}\,\frac{\Delta K\,\dfrac{\Delta a^2}{a_o^2}l^2\left[\Omega_o^2\dfrac{a_o^2}{c^2}\right]^2}{2AiZ^{(b)}(0)Q_\nu I_l(k_z a)}\,\Psi I_o \qquad (11)$$

where $\Psi=\begin{cases}2, \text{if } 1/Q_\nu \gg 4\Delta K;\ |\tilde{\delta}_\nu|;\\ 2(Q_\nu \Delta K)^{1/2}, \text{if } |\tilde{\delta}_\nu| \ll 1/Q_\nu \ll 4\Delta K;\\ 4|\tilde{\delta}_\nu|Q_\nu, \text{if } Q_\nu \to \infty,\end{cases}$ $\Delta K=\frac{a_o^2\Omega_o^2}{c^2}K\ \frac{\Delta a^2}{a_o^2}$; $\tilde{\delta}_\nu=\frac{\delta_\nu}{l\Omega_o}$.

Thus threshold current increases with cavity quality factor decreasing and beam energy spread rising. Because of electromagnetic wave radiation beam energy spread increases until Δa^2 reach the threshold value,which is given by (11). After that instability is stabilized.

Let us make some quantitative analysis. Using parabolic approximation of potential well $U(z)=U_o\left(\frac{z-d}{d}\right)^2$ for weakly relativistic case $\Omega(a^2)\equiv\Omega_o\left[1-\frac{3}{16}\frac{\Omega_o^2a^2}{c^2}\right]$ and in optimal case, when $\Omega_o \sim \omega_p$ and $I_l(k_z a)=\frac{\cos^2(k_z a)}{4}$ for monoenergetic azimutally symmetric beam oscillating in high quality factor cavity $Q_\nu \to \infty$, we obtain for maximum increment:

$$\xi=\frac{\sqrt{3}}{2}\ \frac{\lambda}{2\pi R}\left\{\frac{3}{2\gamma_o}\frac{d}{\lambda}\frac{R}{h}\ \frac{J_1^2(k_1 r_b)}{J_1^2(k_1 R)}\right\}^{1/3}\Omega_o\ . \qquad (12)$$

Now we can make following conclusions from (12):

1.Increment decreases with decreasing of ratio of wavelength generated to cavity radius.

2.Increment decreases with decreasing of injected beam radius.

For typical vircator parameters $\xi=(0.1\div0.01)\Omega_o$. It means that 10 cm wavelength instability time equals (0.5-5)ns. Approximatelly the same rf pulse shortening with respect to pulse current duration occurs in experiments. Space charge limiting current (11) in case of electron beam with energy spread $\frac{\Delta a}{a}=\frac{\Delta\varepsilon}{\varepsilon}$ becom-

$$I_{cr}=\frac{3\pi}{16}\left(\frac{2\pi R}{\lambda}\right)^2\frac{r_b^2}{a_o^2}\left(\frac{a_o^2\Omega_o^2}{c^2}\right)^3\left(\frac{\Delta\varepsilon}{\varepsilon}\right)^2\frac{hl^2\Phi(Q)}{dAQ\cdot 2\varepsilon_m I_l(k_z a)}\frac{J_1^2(k_1R)}{J_1^2(k_1r_b)}I_o. \quad (13)$$

Taking into account that $(a_o\Omega_o/c)\sim 1$; $I_l(k_z a)\simeq 1/4$; $\varepsilon_m=1$ for $l\neq 0$; $J_1^2(k_1R)\simeq 0.25$,.and for thin beams $J_1(k_1r_b)\simeq\frac{k_1r_b}{2}$, we obtain following expression for space charge limiting current (l=1):

$$I_{cr}=1.2\left(\frac{\Delta\varepsilon}{\varepsilon}\right)^2\frac{V_c}{V_b}\frac{1}{Q}\Phi(Q)I_o,$$

where V_c and V_b volumes of the cavity and beam in the cavity respectively. In our case $\Phi(Q)\simeq 2$; $Q\simeq 10$; $(V_c/V_b)\simeq 10^2-10^3$, and $I_{cr}\simeq 2.5(10^{-2}-10^{-3})I_o$ for $(\Delta\varepsilon/\varepsilon)=0.01$ and $I_{cr}=(10^{-1}-10^{-2})I_o$ for$(\Delta\varepsilon/\varepsilon)=0.02$. This results are in a good agreement with the experimental data.

It is evident from results above that space charge limiting current in vircators and noice coefficient in virtual cathode amplifiers are strongly depend on the value of electron beam energy spread. Computer simulations shows that beam spread of less than 3% in energy reduce the microwave generation by an order of magnitude. Thus small value of electron beam energy spread is very essential for virtual cathode generators and amplifiers.

Hence we can make the conclusion that suggested theory is accurate enough to describe the physics in vircators

REFERENCES

1. A.N.Didenko, A.G.Zherlitsyn, V.I.Zelentsov, G.P.Fomenko, Yu.G.Shtein, Yu.G.Yushkov. Proc.Int.Top. Conf.on Electron Beam Research and Technology. Albuquerque,1975,V.2,p.424.
2. R.A.Mahaffe y , P.Sprangle, J.Goldek and C.A.Kapetanakos. Phys.Rev.Lett. 39.p.843 (1977).
3. H.E.Brandt, A.Bromborsky, H.B.Burks and R.A.Kehs. Proc. 2nd Int.Top.Conf.on High Power Electron and Ion Beam Research and Technology (Cornell

University, Ithaca, N 4, p.649,(1977).

4. A.N.Didenko, Ya.E.Krasik, S.F.Perelygin, G.P.Fomenko. Pisma Zh.Tekh.Fiz.,321 (1979).
5. A.N.Didenko, A.G.Zherlitsyn, A.S.Sulakshin, G.P.Fomenko,V.I.Tsvetkov, Yu.G.Shtein. Pisma Zh. Tekh.Fiz. 9,1510 (1983).
6 .A.N.Didenko, V.I.Rashchikov, Reports of the Academy of Science. V.312, p.597, 1990.
7 .A.N.Didenko Reports of the Academy of Science. V.321,1991,p.442.
8 .V.P.Grigoryev, A.N.Didenko. Radiotech. and Elect. V.33, p.353, 1988.

THE EXPERIMENTAL AND THEORETICAL DEVELOPMENT OF A ONE GIGAWATT, REPETITIVELY PULSED, ONE MICROSECOND PULSE LENGTH, HIGH CURRENT RELATIVISTIC KLYSTRON AND MODULATOR

M.V. Fazio, B.E. Carlsten, R.J. Faehl, W.B. Haynes, R.F. Hoeberling,
T.J.T. Kwan, D.G. Rickel, R.M. Stringfield, F.W. VanHaaren,
R.F. Wasierski, A. Erickson*, K. Rust**

Los Alamos National Laboratory, MS-H851, Los Alamos, NM 87545
* Mission Research Corp., ** Superconducting Supercollider Laboratory

Abstract

A research effort is underway with the goal of obtaining an energy of one kilojoule per pulse, with a 5 Hz pulse repetition frequency, from a high current relativistic klystron amplifier (RKA). The pulse length is one microsecond (1 GW peak power) with a microwave frequency of 1.3 GHz. This paper focuses on three areas: the theory, modeling, and experimental development of the microwave tube; the 1-μs-pulse-length field-emission diode electron gun developed for the RKA; and the BANSHEE pulsed power modulator that powers the RKA.

This research builds on the pioneering work done by Friedman and Serlin [1] on the RKA at the ~100 ns pulse length. The one microsecond pulse length is almost an order of magnitude beyond what has been achieved with an RKA. Achieving a peak power approaching 1 GW for 1 μs requires a well behaved electron beam on that time scale, and an optimized extraction efficiency in the output cavity. The microwave tube design was guided by theory and particle-in-cell (PIC) code modeling that relate output cavity extraction efficiency to the amplitude of the beam harmonic current modulation and output cavity shunt impedance. The output cavity has adjustable tuning, loading, and output gap length to allow experimental optimization of the coupling between the modulated beam and the output cavity. An electron beam diode is used that delivers a peak current of 4 to 5 kA for a pulse duration exceeding 1 μs, at a beam kinetic energy above 600 keV.

BANSHEE is the high voltage modulator designed for use as an electron beam driver for high power microwave tube development. The BANSHEE output pulse design parameters are 1 MV and 10 kA, with a 1 μs pulse width at a repetition rate of 3-5 Hz, driving a load of impedance of 100 Ω. BANSHEE is a thyratron-switched line-type modulator with a pulse transformer output stage. The modulator design is pushing the state of the art in thyratron technology and capacitor lifetime. The results of the BANSHEE modulator testing are described.

Theory and Modeling

In this section, we review basic relativistic klystron amplifier physics. We show how the power extraction from the device depends on both the harmonic current content of the beam and also on its excess kinetic energy, which is difference between the actual kinetic energy and the minimum required to transport the beam. We will show that as the beam is bunched, the kinetic energy is decreased, and there exists an optimum amount of bunching which leads to the maximum power extraction. For devices operating on time scales of 1 μs, the optimum harmonic current is only about 75%, leading to a dc-beam to microwave efficiency of less than 35%. The theory and modeling results, briefly summarized here, are treated much more extensively in references [2] and [3].

First, we will discuss the basic RKA theory, including the definition of harmonic current and power extraction. Next, we will review the basic physics of intense space-charge beams, emphasizing the partitioning of energy due to the space charge. We will also include a discussion of PIC simulations showing the tradeoff between higher harmonic current and excess kinetic energy.

Work supported and funded jointly by the DoD Office of Munitions and the DOE Defense Programs through the joint DoD/DOE Munitions Technology Development Program, and by the Army Harry Diamond Laboratories and Missile Command.

In our RKA, an annular, intense (5 kA), mildly relativistic (500 keV) electron beam passes through three cavities. The first cavity is externally driven and impresses an axial momentum variation on the initially uniform beam. Current modulation grows as the beam travels, as the momentum variation causes variations in the beam's axial density. We can describe the beam current in terms of its Fourier components

$$I(t,z) = I_0 + I_1(z)\cos(\omega t + \phi_1) + I_2(z)\cos(2\omega t + \phi_2) + \ldots \tag{1}$$

The product $I_1 V_0/2$ is often referred to as the beam rf power, where V_0 is the beam kinetic voltage. The fundamental current component, I_1, is typically on the order of $0.05 I_0$ at the idler cavity. This cavity is driven by the harmonic current and the cavity's gap voltage is given by

$$V_{gap} = Z_{cav}\, I_{ind} \tag{2}$$

where Z_{cav} is the cavity shunt impedance and I_{ind} is the induced current. The induced current is the average beam harmonic current at the cavity, times transit time and field coupling factors. The gap voltage induced in the idler cavity is typically near the beam kinetic voltage, resulting from the large harmonic current (250 A or so). The idler cavity rf fields further modulate the beam momentum and provide harmonic current at the output cavity close to the DC beam current. The maximum harmonic current possible, for a delta function bunch of current, is twice the DC current. The fundamental current I_1 is typically around $1.4\, I_0$ for conventional klystrons. For an RKA, the harmonic content is usually $\leq 1.0 I_0$. The output cavity is resonantly tuned, so the rf fields induced in it decelerate the beam. Ramo's theorem gives the microwave power which is extracted from the beam,

$$P(t) = \int_V \mathbf{J}(\vec{r}, t) \cdot \mathbf{E}(\vec{r}, t)\, dV \tag{3}$$

where J is the beam current density and E is the rf electric field. We see from Eq. (3) that only the beam's kinetic energy can be extracted; and since $E \sim e^{j\omega t}$, we can only extract power from the fundamental harmonic component. It is clear that we must simultaneously maximize I_1 and extract the maximum kinetic energy from the beam in order to have the highest microwave power. From Eq. (3) we can write this expression for the efficiency of conversion from beam power to rf power:

$$\eta = \frac{m_o c^2 (\Delta\gamma)\, I_1}{e V_{inj}\, I_o}\, \kappa$$

where $\Delta\gamma$ is the maximum allowed decrease in the relativistic factor as the electrons are decelerated and κ is related to the efficiency of extraction, usually better than 0.9.

At this point, we wish to understand how $\Delta\gamma$, the maximum kinetic energy we can extract from the beam, depends on I_1. The amount of available energy is the difference between the injection energy (the depressed kinetic and potential energy) and the minimum injection energy (again summing the kinetic and potential energies) required

to transport the bunched beam. Two effects are occurring as the beam is bunched and then decelerated in the output cavity. First, as the beam is bunched, the kinetic energy is depressed and the beam velocity decreases because more energy is required in the space-charge fields. Additional conversion from kinetic to potential energy is required in the output cavity as the bunch velocity is decreased further. As the bunched beam current is increased, we see that the kinetic energy available for extraction is decreased by both the larger potential depression requirement and by the larger minimum kinetic energy needed for transporting the higher current beam.

For a given injection diode voltage, the voltage associated with an annular beam's kinetic energy is less because some potential energy is required to set up the Coulomb fields within the cylindrical pipe. The potential of an annular beam injected at radius r_b with initial gamma γ_{inj} into a conducting cylinder of radius r_w must satisfy

$$\phi(r) = \frac{I_o}{2\pi\varepsilon_o v_o} \ln\frac{r}{r_w} \qquad r_b < r < r_w$$

$$\phi(r) = -\frac{I_o}{2\pi\varepsilon_o v_o} \ln\frac{r_w}{r_b} \qquad r \le r_b$$

where the beam velocity is

$$v_o = c\sqrt{1 - \left(\gamma_{inj} + \frac{e\,\phi(r_b)}{m_o c^2}\right)^{-2}} \quad .$$

The beam potential at $r=r_b$ must thus satisfy ($\phi_b = \phi(r_b)$)

$$\frac{e\phi_b}{m_o c^2}\sqrt{1 - \left(\gamma_{inj} + \frac{e\phi_b}{m_o c^2}\right)^{-2}} = \frac{e}{2\pi\varepsilon_o m_o c^3} I_o \ln\frac{r_w}{r_b} = \frac{I_o}{8.5\,\text{kA}} \ln\frac{r_w}{r_b} \quad .$$

We can define a convenient normalized threshold current I_s to be

$$I_s = \frac{2\pi\varepsilon_o m_o c^3}{e \ln\frac{r_w}{r_b}} = \frac{8.5\,\text{kA}}{\ln\frac{r_w}{r_b}} \quad .$$

The conservation of energy, including that from the magnetic field, becomes (where the small circles denote the DC beam energy)

$$\gamma_{inj} = \gamma_o + \frac{I_o}{I_s \beta_o} \quad .$$

The largest permissible beam current, I_{max}, corresponds to a beam potential energy increase (and kinetic energy decrease) of

$$e\phi_b = \left(\gamma_{inj} - \gamma_{inj}^{\frac{1}{3}}\right) m_o c^2 \qquad \text{so} \qquad I_{max} = \frac{2\pi\varepsilon_o m_o c^3}{e} \frac{\left(\gamma_{inj}^{\frac{2}{3}} - 1\right)^{\frac{3}{2}}}{\ln\frac{r_w}{r_b}} \quad .$$

We see that the kinetic energy drop is not the injection voltage and that there is residual kinetic energy. One might think that since some kinetic energy remains, additional current can be pushed through the cylinder. However, removal of any additional kinetic energy drops the beam velocity v_o, which in turn increases the charge density and requires more increased potential energy from the beam than was given by the drop in the kinetic energy. This nonlinear slowing of the bunch as it forms aids its growth, and can be responsible for significant harmonic beam currents (greater than 1.0 I_o). If the beam current is near the threshold current I_{max}, and is increased slightly, a significant reduction in the beam's kinetic energy (and velocity) is possible. At the threshold current, a majority of the injection energy is partitioned into the potential energy fields; in Fig. 1 we see the partitioning of the total energy into kinetic and potential energy parts as a function of the injection gamma, γ_{inj}, and the beam current.

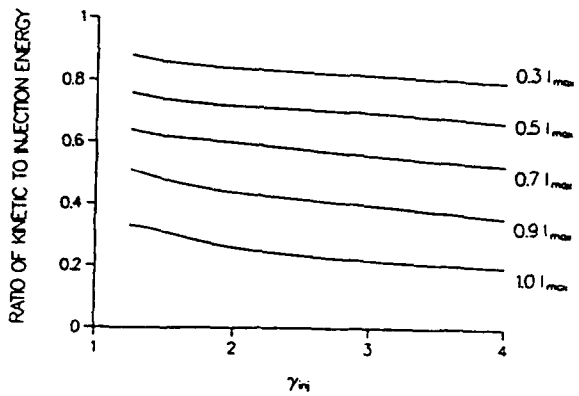

Fig. 1. Partitioning of total energy into kinetic and potential components for different injection energies and beam currents.

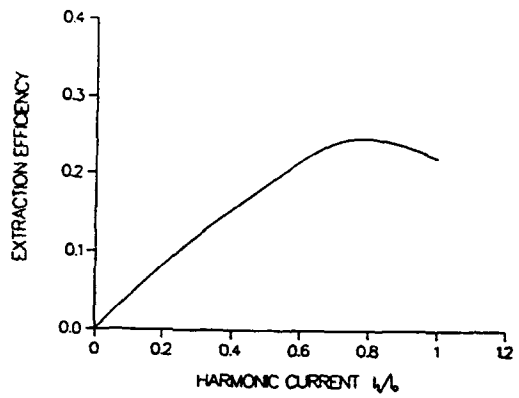

Fig. 2. Extraction efficiency versus harmonic current for a 500 kV, 5 kA beam with radius of 3.2 cm and wall radius of 3.65 cm. Best extraction is for 65% harmonic current.

We can rewrite the energy conservation statement to calculate the minimum total beam energy for a given beam current. Solving for the minimum potential and kinetic energy we get

$$\gamma_{min}^{\frac{2}{3}} = \left(\frac{PE + KE}{m_o c^2} + 1\right)^{\frac{2}{3}} = \left(\frac{I_{peak}}{8.5\ \text{kA}} \ln \frac{r_w}{r_b}\right)^{\frac{2}{3}} + 1 \quad .$$

For a given peak current, I_{peak}, the difference between γ_{inj} and γ_{min} is the available kinetic energy for conversion to microwaves. The maximum power extraction possible is

$$P_{out,max} = \frac{1}{2} I_1 (511\ \text{kV}) (\gamma_{inj} - \gamma_{min}) \quad .$$

It is clear we want to simultaneously generate as much beam harmonic current as possible while minimizing γ_{min}. If the beam was collected by a conducting surface within the output cavity, this limitation would no longer be valid, since the beam's potential energy would be reconverted into kinetic energy. However, the plasma generated will become too large for microsecond pulse lengths.

Although a smaller beam radius leads to more harmonic current, we found that the maximum extraction occurs at the minimum beam-to-wall spacing possible. For a beam pipe radius of 3.65 cm and beam at 500 keV and 5 kA, the maximum extraction for a beam radius of 3.2 cm occurs with a harmonic current of 70% (dc beam to microwave efficiency of 25%), and for a beam radius of 3.4 cm with a harmonic current of 75% (efficiency of 30%). In both cases, beam harmonic current could easily exceed 100%. In Fig. 2 we plot extraction efficiency versus harmonic current for a 5 kA beam at a radius of 3.2 cm. We see that the maximum extraction, 25%, occurs at a fundamental current component of only 70%, far below the maximum current we can generate.

Experimental Tube Development

The first generation RKA has been constructed and operated on the BANSHEE pulsed power modulator. These results are described in detail elsewhere [4, 5], but are briefly summarized here. The RKA design consists of a field emission diode producing a hollow beam that passes through the coaxial quarter-wave input cavity and idler cavity, and on to the rectangular waveguide output coupler placed transversely to the beam. The RKA drift pipe diameter is 7.3 cm. The rf drive to the input cavity is 5 kW and is coupled to the input cavity through a loop. The annular electron beam is supplied by a 6.35 cm-diameter circular stainless-steel field-emission cathode. Guiding of the electron beam is accomplished by a pulsed, strong uniform magnetic field (0.5 to 1.0 T) along the electron beam axis. For rf beam modulation measurements, a linear array of eleven B-dot loops were placed 5 cm apart along a section of drift pipe. Annular beam thickness is 2 to 4 mm.

Early RKA work produced a modulated electron beam for 1 μs with a peak rf current (I_1) of 1 kA and a voltage of 350 kV. Some experimental configurations produced beam modulation in excess of 2 μs which was the full width of the pulsed-power modulator pulse driving the RKA. The dc beam current was about 2.5-3 kA giving approximately a 30% beam modulation ($I_1/I_0 = 0.3$). The component of beam power at the microwave drive frequency (1.3 GHz) was approximately 175 MW. Approximately 50-70 MW was coupled into rectangular waveguide and gains of 20-40 dB were measured. The modulated-beam power to microwave output power coupling efficiency was ~30%. The low output coupling efficiency was due primarily to the inability to adjust the output gap tuning and shunt impedance.

A second generation RKA design, currently being tested, has incorporated the following three major design improvements: (1) The nominal input beam voltage and current produced from the field emission diode electron gun and transported through the RKA has been increased from 350 kV and 2.5 kA, to over 600 kV and 5 kA with a pulse duration of 1 μs. (2) A measurement of the output power dependence on input power level gave no hint of saturation up to the maximum available 5 kW drive level, indicating that a higher input drive would give a larger output power. A 500 kW magnetron source has replaced the 5 kW input drive amplifier previously used. (3) The theory and modeling indicate the sensitivity of output power on output gap shunt impedance, tuning, and Q. A new output cavity has been built with variable tuning, loading, and shunt impedance to allow adjustments of these parameters for optimal conversion efficiency of modulated-beam power to microwave output power.

1 μs Pulse-Length Field-Emission Diode Electron Gun

A major part of the recent experimental effort was directed toward obtaining a stable beam with the desired beam parameters of 500 kV and 5 kA for a 1 μs pulse. The specific details of this electron gun work are discussed in another paper at this conference [6] and in [5]. Significant beam current loss (40-50%), due to backstreaming along diverging magnetic field lines and anode interception, and low beam energy (350 keV) dictated a critical reexamination of the design of the explosive field emission diode to improve the amount of beam current injected into the RKA from 2.5 kA to 5 kA and to raise the injection energy.

With a combination of particle-in-cell code simulations and experimental testing we arrived at a diode design that placed the tapered cathode (small diameter end faces downstream) in the converging magnetic field region of the magnet, and shaped the cathode surface so that it approximately followed the curvature of the magnetic field lines. This design resulted in much improved transmission characteristics. The converging magnetic field causes the beam to shrink to a smaller overall diameter with a smaller annular beam thickness. Electrons emitted from the cathode at radial positions larger than the drift tube radius converge to a smaller radius as they are guided into the drift tube by the converging magnetic field.

Since the RKA microwave tube modeling results indicated that we should operate at a somewhat higher voltage and lower current (lower perveance) to improve overall tube efficiency by reducing the kinetic energy lost to the beam's space charge potential energy, we increased the A-K gap to raise the diode impedance. Representative waveforms for modulator voltage and current injected into the drift pipe are shown in Figs. 3 and 4. We were able to achieve voltages in excess of 650 kV and currents up to 5 kA during the pulse. The longer A-K gap also resulted in a slightly longer pulse length due to the increased time before diode closure.

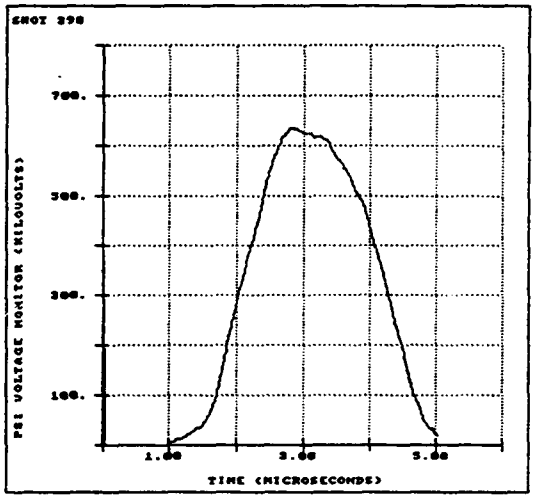

Fig. 3. Diode voltage with final diode configuration. Voltage exceeds 650 kV for 1 μs.

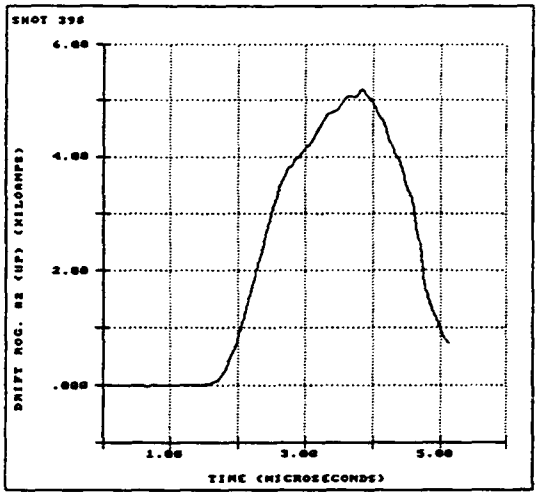

Fig. 4. Electron beam current measured in the drift pipe from final diode configuration. Current increases from 3.5 to 5 kA during the time that the voltage is at its peak value.

Input Cavity

The new cavity was needed because the microwave input drive was increased from 5 kW to 500 kW by the installation of a high power magnetron. Power was coupled to the original cavity through a loop fed by 0.5 in coaxial cable. Since this scheme was inadequate for the new 500 kW power level, a new input cavity was designed that is fed through an iris by reduced-height rectangular waveguide. The stainless steel cavity is a quarter-wavelength coaxial line, shorted at one end and capacitively loaded by the gap at the other end. The loaded Q of the cavity, at low power without beam, was measured to be 20. The customary copper plating is unnecessary because the beam loading is so heavy (cavity Q with full beam loading is ~10, compared to an unloaded Q of ~400) that resistive losses in the cavity walls are negligible compared to the power absorbed by the beam. This is seen by comparing the beam impedance, which is 2000 to 4000 ohms, to the cavity shunt impedance which is around 100,000 ohms. Since the magnetron driver must be matched to the cavity at full beam loading for efficient power transfer, the cavity, without beam, had to be strongly overcoupled to the magnetron. This condition results in a VSWR (looking into the cavity from the input waveguide) of 27 without beam. The VSWR approaches 1 with full beam loading.

Figs. 5-7 show the beam current pulse overlaid with the magnetron reflected power, the modulated beam current envelope 25 cm downstream from the input cavity gap, and the frequency downconverted mixer IF signal of the modulated beam current. The salient features that should be noted are that: 1) the reflected magnetron power goes to zero as the beam current increases from zero indicating good coupling to the beam loaded cavity, 2) the rf pulse length of the modulated beam is about 2.5 μs, and 3) the rf current on the beam is about 8% with 50 kW of rf drive. Only about 5 % modulation is needed from the first cavity for the RKA to operate as we have designed it.

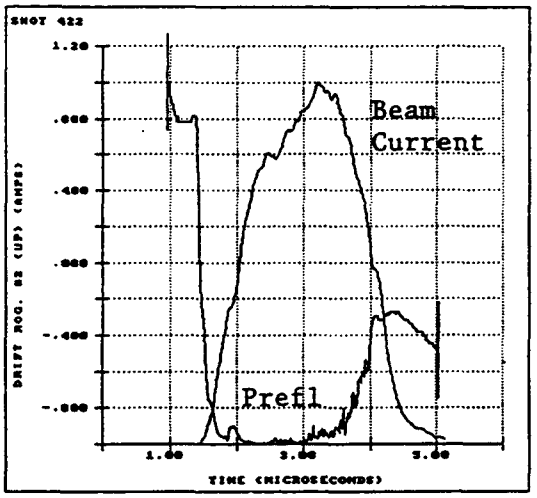

Fig. 5. Beam current overlaid on magnetron reflected power signal showing how the impedance change due to beam loading leads to a matched condition between the input waveguide and the input cavity. (Scale on vertical axis is arbitrary.) Peak beam current is 4.5 kA.

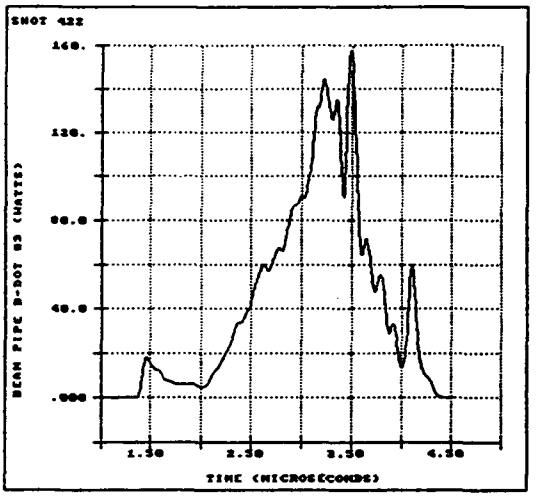

Fig. 6. Detected signal from B-dot loop located 25 cm downstream from the input cavity gap. This B-dot loop measures the 1.3 GHz current modulation on the beam. The rf modulation imparted to the beam by the input cavity with 70 kW of input power is about 8% or $I_1/I_0 = 0.08$.

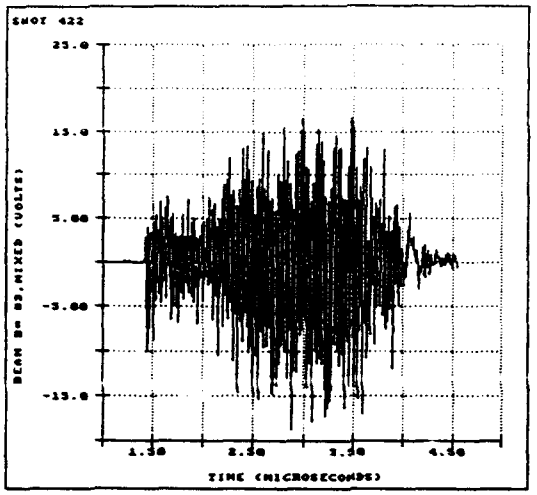

Fig. 7. Frequency downconverted mixer signal (IF) from the same B-dot loop as in Fig. 6. Note that the duration of the rf modulation of the beam is 2.5 μs, which corresponds to almost the full width of the modulator pulse.

Output Cavity

The modeling has resulted in a new output cavity design that optimizes the efficiency of the coupling of microwave energy from the modulated beam to the output cavity and transmission line. The output cavity must be made resonant and matched to the beam to provide the gap voltage that extracts all the available kinetic energy. Because efficient beam to cavity coupling depends sensitively on matching the cavity shunt impedance to the beam impedance, the output cavity is designed with frequency tuning, output loading, and output gap length that are all adjustable. The output cavity assembly is shown in Fig. 8. The cylindrical TM_{010} output cavity is iris coupled to a low impedance coaxial transmission line. A tapered impedance transformer transitions to standard 50 Ω, 6-in-diam coaxial line dimensions. In this 50 Ω section of line is a calibrated directional coupler for accurate power measurement of the microwave energy travelling in the TEM mode. The 50 Ω line is terminated with a matched coaxial dummy load. Careful attention to the vacuum aspects of the design has resulted in enough pumping ports for a turbopump and several cryopumps.

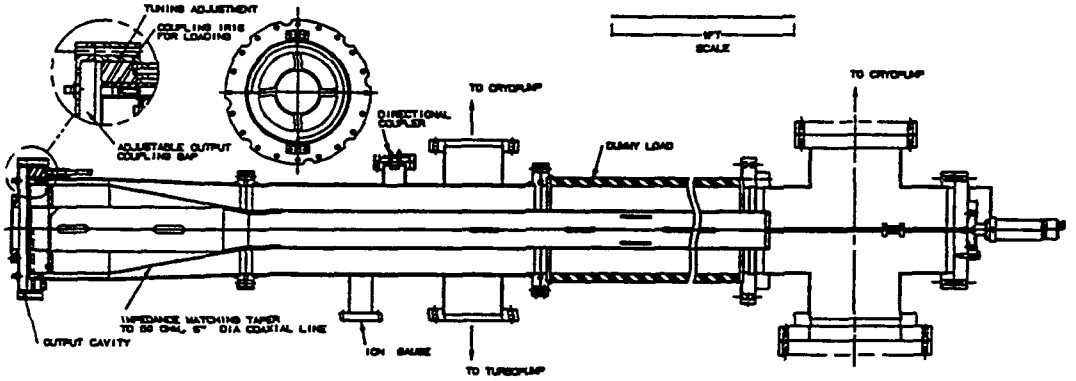

Fig. 8. Output cavity and coaxial transmission line assembly.

After the output cavity and transmission line assembly has been tested and tuned for high power operation, the dummy load will be replaced with a yet to be designed coaxial line to rectangular waveguide mode converter which

will be designed to present a 50 Ω impedance to the mating 6 in-diam coax line section that contains the directional coupler. The modularity of this design allows us to swap the coaxial dummy load with a waveguide load without changing the tuning and loading of the output cavity. The output cavity and transmission line assembly is being characterized at low power and will soon be tested on the RKA.

Repetitively Pulsed Modulator Development

BANSHEE is the repetitively pulsed, high voltage modulator used to produce a high current relativistic electron beam for high power microwave tube development at microsecond pulse lengths. The design goal for BANSHEE is to achieve a 1 MV, 10 kA pulse, with a 1 μs flat-top, driving a load impedance in the range of 100 Ω at a pulse repetition frequency of 5 Hz. The long term goal is a prf of 100 Hz. With BANSHEE, thyratron-switched line-type modulator technology is being extended to the megavolt and multi-kiloampere level. Performance to date has achieved 600 kV at 6 kA for 1 μs at a 1 Hz prf [6]. A prf of 5 Hz has been also been achieved.

A block diagram of BANSHEE is shown in Fig. 9. The prime power source is a 90 KW, variable-voltage dc power supply. An intermediate capacitive energy storage bank of 37.5 μF is used with a small thyratron to command resonantly charge the main pulse forming Blumlein system. The Blumlein system consists of four lumped element Blumleins. The four Blumleins each consists of two six-stage PFNs. Each set of two Blumleins is switched by a newly-developed 120 kV, hollow anode thyratron (EEV CX-1812). The CX-1812 is designed for 100 kA peak current, 10 μs pulse width, and a 500 Hz prf. The Blumleins are discharged through a 10:1 step-up iron core transformer to achieve 1 MV at the 100 Ω load. This modulator design is possible because of the ability of the CX-1812 thyratron to hold off 100 kV and conduct a peak current of 100 kA with a di/dt of over 10^{11} A/s. The design of the CX-1812 will allow operation of the BANSHEE modulator at 1 MV and 10 kA for a 1 μs pulse length at an ultimate prf of 500 Hz. It must be emphasized that the CX-1812 is still an experimental tube under development, and it has not been tested to its full specifications.

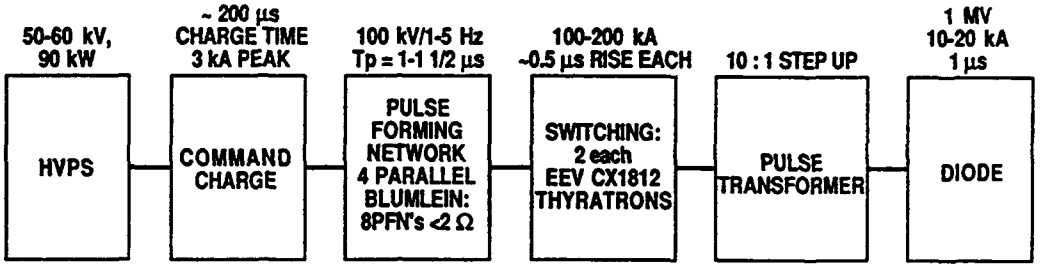

Fig. 9. Block diagram of the BANSHEE modulator.

In the initial modulator testing, four lumped element PFNs were connected in parallel and switched by a single CX-1812 thyratron. Operating at 1 Hz prf for 16 hrs, an output voltage pulse of 455 kV into 100Ω was attained before tube performance began to deteriorate and the test was halted. The CX-1812 peak anode voltage

was 80 kV and the switched current was 42 kA. Later analysis by EEV personnel determined that welding problems at the metal-metal joints in the tube envelope, done by vendors to EEV, had contributed to very small vacuum leaks to the outside atmosphere. EEV has now corrected this problem.

Meanwhile the CX 2593 was substituted as the main switch tube, while the CX-1812 was undergoing design improvements. The CX-2593 has a similar peak voltage rating to the CX-1812, but has a lower peak current rating, and is designed for lower peak and average powers. The modular nature of BANSHEE allows us to operate only one-half of the modulator consisting of one pair of Blumleins switched by one thyratron. Using a single CX 2593 tube, we achieved 73 kV and 77 kA at 1 Hz prf for over 10,000 shots with a dummy load in place of the the output pulse transformer primary. These numbers would correspond to about 700 kV and 7.5 kA with the full-up modulator (4 Blumleins with two thyratrons) driving the output pulse transformer with a 100 Ω load. During the same test period, BANSHEE was operated at a 5 Hz prf for 60,000 shots at 60 kV and 55 kA, which corresponds to 600 kV and 5 kA in the full-up modulator configuration.

The most recent testing utilized the full-up modulator configuration of four Blumleins with two thyratrons. Each CX-2593 thyratron switched two parallel Blumleins. These tests achieved 600 kV at 6 kA for 1 μs at a 1 Hz prf into a dummy load. This accomplishment demonstrates the successful operation of two state-of-the-art high power thyratrons in parallel, at a voltage, current, and pulse length appropriate for 1 μs, repetitive-pulse development of the RKA.

Summary

We have described our RKA experimental results and our second generation RKA design that is currently being tested. We have added to the understanding of RKA physics with the importance of the role of intense space charge in limiting the efficiency of the device because of the beam potential depression that reduces the kinetic energy available for conversion to microwaves. We have produced a stable 650 kV, 5 kA annular beam of microsecond duration from an explosive field emission cathode. Repetitively pulsed, 1 μs pulse-length RKA operation is possible because of the capability of the BANSHEE thyratron-switched line-type modulator. Rep-rate RKA development awaits the availability of a dc magnet for beam transport through the klystron.

References

[1] M. Friedman, J. Krall, Y.Y. Lau, and V. Serlin, "Externally Modulated Intense Relativistic Electron Beams," J. Appl. Phys., 64 (7), 3353 (1988).

[2] B.E. Carlsten, M.V. Fazio, R.J. Faehl, T.J.T. Kwan, D.G. Rickel, R.M. Stringfield, "Theory and modeling of a relativistic klystron amplifier with high space charge for microsecond applications," Proc. SPIE 92 Intense Microwave and Particle Beams III, Los Angeles, Ca., Jan. 1992, **1629**, p. 57-68.

[3] B.E. Carlsten, R.J. Faehl, M.V. Fazio, T.J.T. Kwan, D.G. Rickel, R.D. Ryne, R.M. Stringfield, "Effect Of Intense Space Charge In Relativistic Klystron Amplifiers," Proc. 9th Intl. Conf. on High Power Particle Beams, Washington, D.C., May 1992, to be published.

[4] D.G. Rickel, M.V. Fazio, B.E. Carlsten, R.J. Faehl, T.J.T. Kwan, R.M. Stringfield, "Experimental Progress on a Microsecond Pulse-Length Relativistic Klystron Amplifier," Proc. SPIE 92 Intense Microwave and Particle Beams III, Los Angeles, Ca., Jan. 1992, **1629**, p. 51-56.

[5] D.G. Rickel, , M.V. Fazio, B.E. Carlsten, R.J. Faehl, T.J.T. Kwan, R.M. Stringfield, R.F. Wasierski, "Development of a Long-Pulse 1.3 GHz Relativistic Klystron Amplifier," IEEE Trans. on Plasma Science Special Issue on High Power Microwave Generation, to be published, June 1992.

[6] R.M. Stringfield, R.J. Faehl, M.V. Fazio, R.F. Hoeberling, T.J.T. Kwan, D.G. Rickel, F. VanHaaften, R.F. Wasierski, A. Erickson, K. Rust, "The Development of a One Microsecond Pulse-Length, Repetitively Pulsed, High Power Modulator and a Long Pulse Electron Beam Diode For the Production of Itense Microwaves," Proc. 9th Intl. Conf. on High Power Particle Beams, Washington, D.C., May 1992, to be published.

HIGH PEAK POWER TUBES AND GATE EFFECT KLYSTRONS

N. GERBELOT - J.M. BUZZI* - M. BRÈS - G. FAILLON

THOMSON TUBES ELECTRONIQUES - VELIZY FRANCE
* PMI/CNRS - ECOLE POLYTECHNIQUE PALAISEAU FRANCE

INTRODUCTION

The conventional microwave tubes such as TWTs, Magnetrons, Klystrons... deliver the very high peak powers which are required by radar transmitters but more especially by many particle accelerators. In the range of a few hundred MHz to about 10 GHz, some dozen of MWs per unit are currently obtained and commercially available, according to the frequency and the pulse lengths.

But peak power requirements are ever increasing, especially for the expected new linear particle accelerators, where several hundred MWs per tube would be necessary. Also some special military transmitters begin to request GW pulses, with short pulse lengths - of course - but at non negligible repetition rates.

Therefore several laboratories and microwave vacuum tube manufacturers have engaged - for several years - studies and development in the field of very high peak microwave power (HPM) toward two main directions :

* extended operation and extrapolation of the conventional tubes and devices

* development of new concepts, among which the most promising are likely the high-current relativistic klystrons - that we also call gate effect klystrons.

CONVENTIONAL KLYSTRONS

Fig. 1 shows the state of the art in narrow band tubes. The TH 2100 and TH 2132 that deliver 45 MW peak over 4.5 μs at 3 GHz and the SLAC 5045 that delivers 67 MW over 3 μs at 2856 MHz are the present capabilities of the high power klystrons. In X band - 11.4 and 14 GHz - the developments are difficult and still disappointing : 72 MW - 100 ns in US and 50 MW - 700 ns or less in Russia.

The three main reasons which limit the peak power capabilities of klystrons are by order of decreasing importance :
. HV breakdowns, which occur mainly in the gun and in the output cavity
. cathode loading
. thermal dissipation.

Arcing is characterized by a strong dependence of the peak power with respect to the pulse length.

As far as arcing in the gun is concerned, the curves of Fig. 2 show this dependence on 2 types of very similar guns - in L and S bands - The high voltage is of course applied during all the pulse and the arcs occur especially between the focus electrode and the anode i.e. between metallic surfaces in a vacuum of 10^{-7} torr. Based on the preliminary evaluations made by L. Cranberg [1], an analytical study [2] on the theorical maximum permissible electric field between metallic electrodes shows that the maximum peak power P_M varies approximately with the pulse length τ as $\tau^{-0.4}$, between $\simeq$ 1 μs and 1 or 10 ms. Above, P_M does not vary any more and below, P_M increases more abruptly than

predicted. The maximum field at 300 kV is about 12 - 15 kV/mm with a pulse length of about 5 μs, according to the temperature of the focus electrode, the barium deposition and the pressure and composition of the residual gases.

RF breakdowns in the output cavity are as dangerous as the previous ones : they occur mainly across the gap(s) and in the window(s) , and - excepted the arcs brought on by the multipactoring effects - they appear with electric fields in the range of 50 to 70 kV/mm, values slightly lower than what exists in the accelerators' RF structures. This difference can be explained by the strong deceleration of the electron bunches in the gap of a klystron output cavity which leads to an interception by the lips of the drift tubes Even with only a few °/oo of the beam power, this interception gives rise locally to X rays and above all to high temperatures and therefore outgassing and ionizations or surface perturbations. Therefore they increase the probability of arcing by increasing the local electric fields.

The second fundamental limitation of pulsed power klystrons is cathode loading i.e. the current density which the cathode has to generate. Values of 50 to 60 A/cm^2 during 4-μs pulses have been obtained by Thomson with MM and CMM cathodes, and experimental studies are still in progress in this area [3].

Finally the third limitation is thermal. Even if the requirements in average power tend to increase, duty cycles remain quite low, in order of 1 °/oo. But under special conditions - high efficiencies, mismatched loads - drift tube noses in the output cavity can be heated above 300°C. Such temperatures become unacceptable on conventional OFHC copper because of recrystallizations, dislocations and - after a few thermal cycles - leakages. Therefore the choice of another material and of the geometry is in this respect of utmost importance. But in any case these thermal difficulties have a moderate influence on high peak power tubes.

To take into accouont these three limitations, we have analysed all the relations between the different electrical and geometrical parameters of the klystrons. Fig. 3 gives two examples of power versus frequency diagrams, where arcing appears as the main limitation. The conclusion is the feasibility of a conventional S band 200 MW peak klystron at 1 μs - 600 kV x 750 A - with a single output cavity. To go further, the arcing limit can be perhaps pushed by using a multigap standing or travelling wave output structure.

PULSE COMPRESSORS

To get very high peak output powers, energy pulse compressors can also be used as the SLED at Stanford, the LIPS at CERN [4] and the CIDR manufactured at Thomson TTE [5].

These compressors are passive structures, which are located after the high pulsed power klystrons ; they store the electromagnetic energy for a couple of μs and release it for typically .5 to 1 μs.

The principle is given on Fig. 4. The basic elements of such a system are :

- A 3 dB waveguide coupler which is able to withstand, without arcing, the very high peak powers and fields considered. Such a coupler, which gives a one way phase shift of π/2 (π on the backward wave) safely protects the klystron.

- Two resonant cavities with an unusually high Q_o factor ($Q_o \simeq 1.9\ 10^5$ in our CIDR). They are therefore highly overmoded (TE_{038}). A fine retuning system must be implemented to adjust the mode, even with a temperature regulation within ± .5 or 1°C.

- A very fast 0-π phase shifter in the RF driving circuit of the klystron, 50 ns in our case. This shifter is activated after the cavities are filled and it triggers on their rapid emptying through the coupling holes.

On Fig. 4 we present the general shape of the output signal of the CIDR. The peak output power is given by $P = P_{klystron}\left(1+\frac{2Q_T}{Q_x}\right)^2$ and after the phase shift, this power decays in exp $(-2\pi F/Q_t)$. Q_O is the internal quality factor, Q_X is the coupling factor and Q_t the total quality factor : $\frac{1}{Q_t}=\frac{1}{Q_o}+\frac{1}{Q_x}$.

Q_O is usually larger than Q_X and with ideally $Q_O \gg Q_X$, the multiplication ratio could be 9 in power.

Regarding Thomson CIDR, we obtain more than 210 MW peak power and 155 MW averaged over .8 μs at 3 GHz.

GATE EFFECT KLYSTRONS

To overcome conventional klystron limitations, a new klystronlike amplifier, using a relativistic high-current electron beam, has been developed by M. Friedman and co-workers at the US Naval Research Laboratory. The physics of the NRL relativistic klystron amplifier has been extensively investigated [6] and we will only report the main features of interest here. Beam bunching and power generation in such high-current klystrons differ from the classical picture because of fundamental properties due to the intense space charge of the beam, which is essentially annular in shape :

a) In a hollow drift tube of radius r_w, the energy of an electron is split between kinetic and potential energies, according to the relationship

$$\gamma_{inj} = \gamma_o + \frac{I_o}{\beta_o}\,\frac{eLn\,r_w/r_b}{2\pi\epsilon_o m_o c^3} = \gamma_o + \frac{I_o}{I_s\beta_o}$$

Where $(\gamma_{inj}-1)m_oc^2 = eV_{inj}$ is the total energy at injection, $(\gamma_o-1)m_oc^2$ is the kinetic energy with corresponding normalized drift velocity $\beta_o=\frac{v_o}{c}$, I_O and r_b are respectively the beam current and radius. The potential energy is all the more important as the beam current is large and as the distance between the beam and the drift tube wall increases. This equation leads to a maximum current level $I_{scl} = I_s(\gamma_{inj}^{2/3}-1)^{3/2}$, and associated minimum kinetic energy $(\gamma_{inj}^{1/3}-1)m_oc^2$, beyond which the beam propagation is disrupted by the formation of a virtual cathode. Thus in a cavity gap, it is possible that the kinetic energy of the beam, the retarding dc potential and the rf voltage across the gap be all of the same order of magnitude, and that the propagating speed be reduced below the critical speed during the decelerating portion of the rf cycle. This results in an effect similar to a periodic gate and in strong current modulation.

b) Regarding high power generation, based on this new bunching mechanism, intense beams offer the remarkable possibility of providing electrical insulation against vacuum breakdowns at the gaps, because their self fields can modify the electric field configuration in the gap regions.

We at Thomson, and in collaboration with the Ecole Polytechnique, have engaged two experiments based on this concept of "gate effect" klystron amplifier.

The 1st one concerns the development of a beam of 30 kV x 200 A over a few μs, which in a future phase is intended to supply 1.5 to 2 MW peak power. The cathode is an impregnated thermoelectronic one with a density of 30 A/cm^2. This cathode is annular and the convergent gun has a special conical inner electrode at ground potential.

The 2nd experiment is currently underway at PMI Laboratory, Ecole Polytechnique, and is aiming toward X-band operation in small diameter - below cut-off - hollow drift tube geometry. As a first step, we conducted an experiment of intense beam production and propagation in a smooth drift tube, using a foilless diode on the pulsed power capability of PMI Lab. (20 -ns pulse length). We have obtained a 16-kA, 500-keV, highly annular electron beam, generated by a graphite explosive field effect cathode, and confined in the 20-mm inner diameter stainless steel tube by a 18-kG magnetic field. As can be seen on Fig 5, the beam mean diameter is 17 mm and its thickness remains less than 1 mm over a distance greater than 150 mm. Then an azimuthal (diocotron) instability develops, which was expected for this high-current, small diameter, hollow beam ; this results in a thickening of the beam and in a loss of current after 300 mm.

But such an intense beam with only 500 keV at injection is not suitable for driving an X-band RKA in this geometry, for we could observe significant spontaneous microwave emission when we inserted the first cavity into the device and had the beam pass through the passive gap. This was probably due to the formation of an oscillating virtual cathode in the gap region. Hence in a second step of our experiment, we reduced the current by changing the cathode geometry, until the spontaneous microwave emission disappeared, and we started the modulation experiment with a 7-kA, 500-keV beam.

The modulating cavity was tuned to 9.5 GHz and was driven by a 100 kW magnetron. Since our usual oscilloscopes and beam diagnostics didn't allow us to measure any high frequency modulation, a second cavity was inserted downstream at various distances from the 1st cavity : it was coupled to a 60-m delay line, so that beam pre-modulation, if any, could be diagnosed by recording some power excited at the right frequency in this idler cavity. Both cavities were equipped with an uncalibrated electrostatic probe to detect the electric field, and the idler cavity was strongly damped to reduce field intensity and to enlarge its bandwidth, in case of detuning if the 1st cavity by the beam.

With the 7-kA beam, we obtained significant levels of excited power in the idler cavity, as well as parasitic power peaks in the first cavity. Fig. 6 shows the signal of the electrostatic probe in the 1st cavity : sometime during the 800-ns magnetron pulse, the beam was launched through the drift region and we can observe the corresponding abrupt drop in the probe signal as the beam passes through the gap and absorbs energy ; but the narrow high peak that can be seen then indicates some parasitic phenomenon, perhaps monotron effect. Even when the magnetron was switched off, we recorded some power in both cavities, which lead us to further reduce the current to 5 kA.

With such a 5-kA current level, no power is excited when the magnetron is switched off. When the magnetron injects microwave energy into the 1st cavity, no parasitic peak appears on the probe signal (Fig. 6), while well defined power peaks at 9.3 to 9.5 GHz propagate in the delay line from the idler cavity. Fig. 7 displays the variation of the probe signal in the idler cavity versus the distance between the two cavities. The first distance is the closest location allowed by the geometry. Although the signal level could vary from shot to shot while keeping the same distance, a maximum appears around 230 mm, which would correspond fairly well to the second maximum of modulation predicted by the small signal theory of NRL RKAs [6] for our beam parameters.

Very recently, we could obtain simulation results with the particle in cell code PRIAM [7] for our one-cavity geometry. Fig. 8 shows kinetic energy plots versus propagation distance for the 7-kA and 5-kA cases : according to previous simulations performed at NRL, these plots would indicate that gate effect occurs at the 1st gap in the 7-kA case (existence of a population of slow electrons) while the 5-kA case gives rise to a pre-modulation of the beam.

CONCLUSION

By carefully extending the technology, the peak power of the klystrons can be higher than the usual 50 to 60 MW. Moreover, thanks to the present development of the pulse compressors, peak power is also increased toward the range of 200 to 300 MW.

The gate effect klystron seems to be one of the best candidate for GW pulses. These tubes use low impedance - 20 to 100 Ω - intense annular electron beams. They are compact not only because of reduced high voltages but also because the cavities are few in number and the drift tubes almost non existent. These very high power tubes ($\geq$ GW) are amplifiers and not oscillators like their competitors, the relativistic magnetrons or the vircators.

Nevertheless some difficulties must be overcome to go beyond the laboratory stage :
- Instabilities of intense hollow beams.
- Coupling of the output cavity to the external waveguide(s).
- Design of guns with field emission cathodes ($\simeq$ kA/cm^2 for 10 to 50 ns) or thermoelectronic cathodes like the 100 to 200 A/cm^2 for 0.1 to 1 μs, currently being studied by Thomson TTE.

We would like to express our special thanks to G. Le Meur at Laboratoire de l'Accélérateur Linéaire, Orsay, and to S. Attelan and C. Rouillé at PMI Laboratory, Ecole Polytechnique.

BIBLIOGRAPHY

[1] J. Appl. Phys. Vol 53 n° 5, May 1952, L. Cranberg.

[2] Thomson Tubes Electroniques - internal report 636, 4 oct 91, A.J. Durand.

[3] Review of Dispenser cathode, A. Shroff. Revue technique Thomson CSF, Dec 91.

[4] Design considerations. Construction and performance of a SLED-type RF pulse compressor using very high Q cylindrical cavities. A. Fiebig et al., 1987 Particl Acc. Conf., Washington DC.

[5] Progress report on 3π/4 Backward TW accelerating module for the Elettra 1.5 GeV Electron injector - EPAC 92 - Berlin Mars 92 - P. GIRAUD et Al... (CGR).

[6] M. Friedman, J. Krall, Y.Y. Lau, V. Serlin, J. Appl. Phys. Vol 64, 3353 (1988). M. Friedmann, J. Krall, Y.Y. Lau and V Serlin, Rev. Sci. Instrum. Vol 61, 171 (1990).

[7] G. Le Meur, F. Touze "Priam : a self-consistent finite element code for particle simulation in electromagnetic fields". Proc. of the 2nd European Particle Accelerator Conference, Nice 1990. Ed. Frontières.

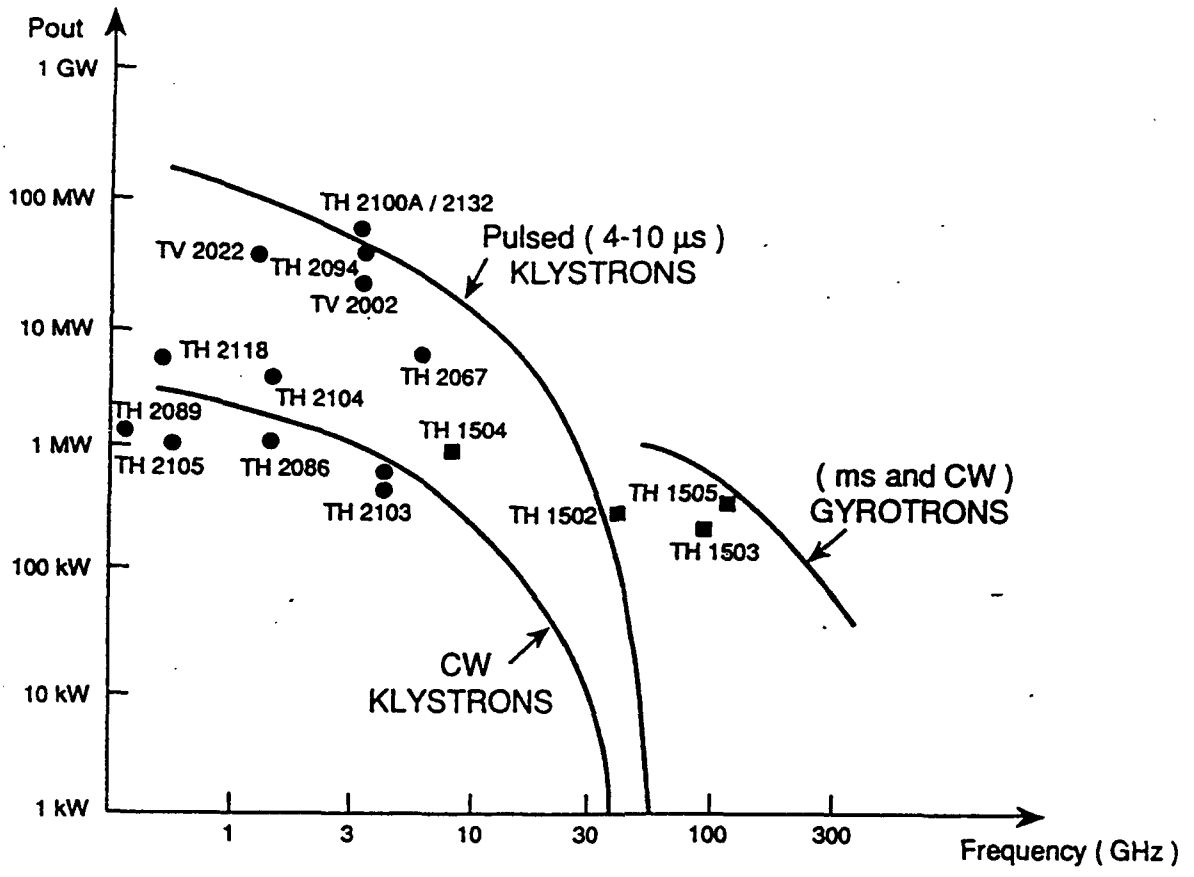

Fig.1 PRESENT TECHNOLOGY FOR PULSED AND CW HIGH POWER µW TUBES

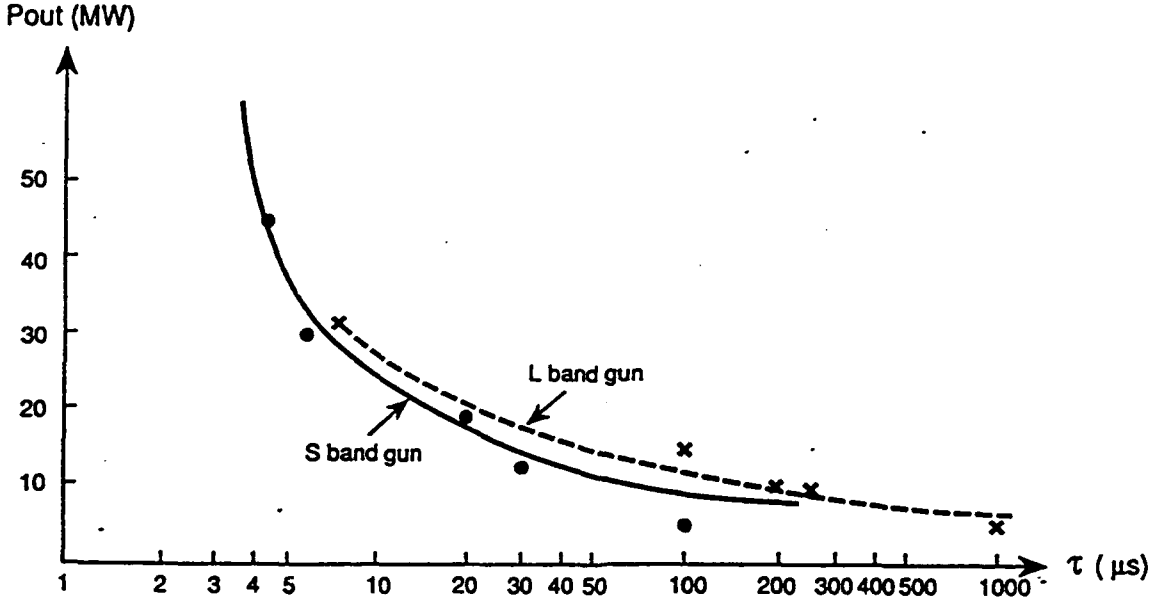

Fig.2 KLYSTRONS GUNS BREAKDOWN LIMITATIONS

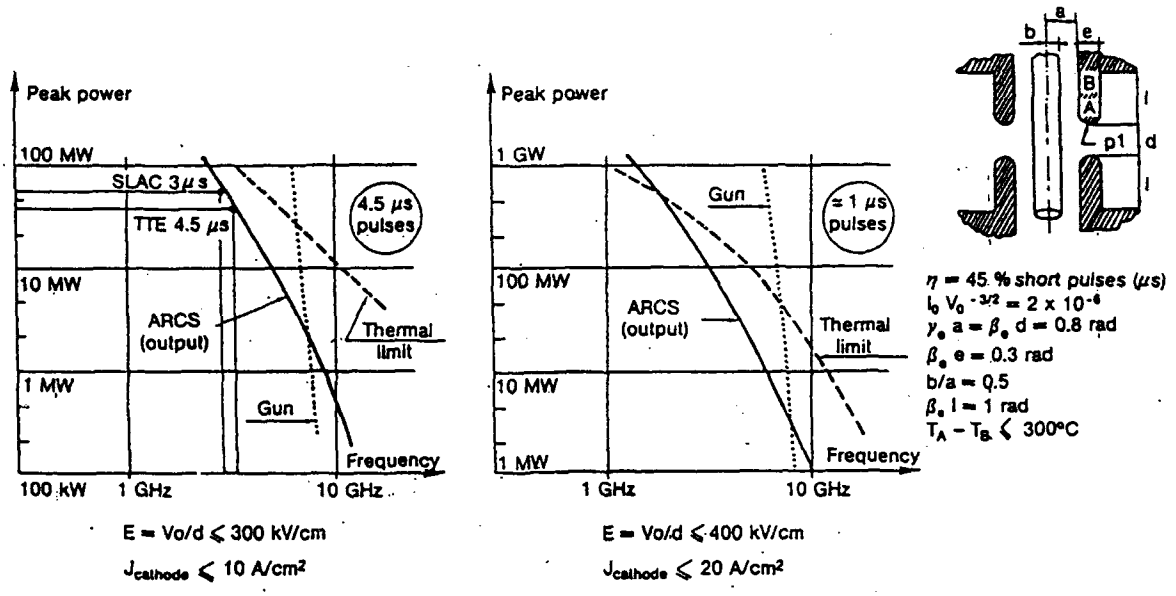

FIG.3 : POWER, FREQUENCY AND COMPUTED LIMIT DIAGRAMS FOR KLYSTRON

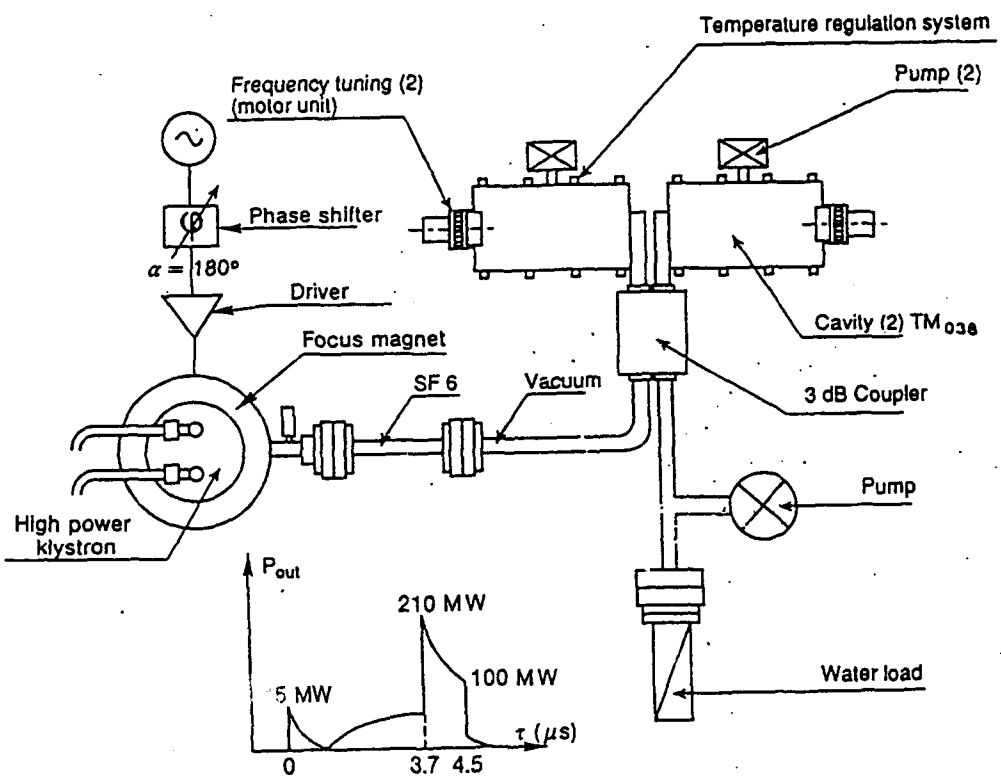

Fig. 4 : PULSE COMPRESSOR

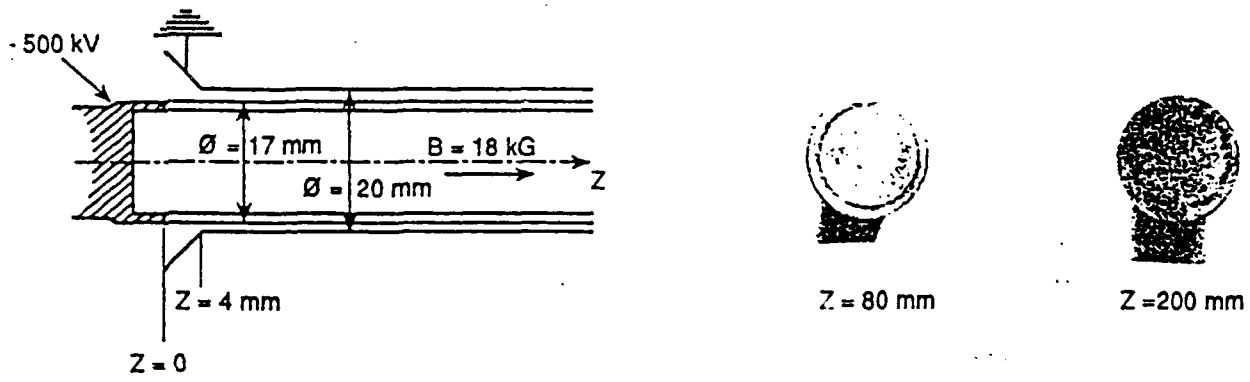

Fig. 5 : 16-kA HOLLOW BEAM TRANSPORTATION

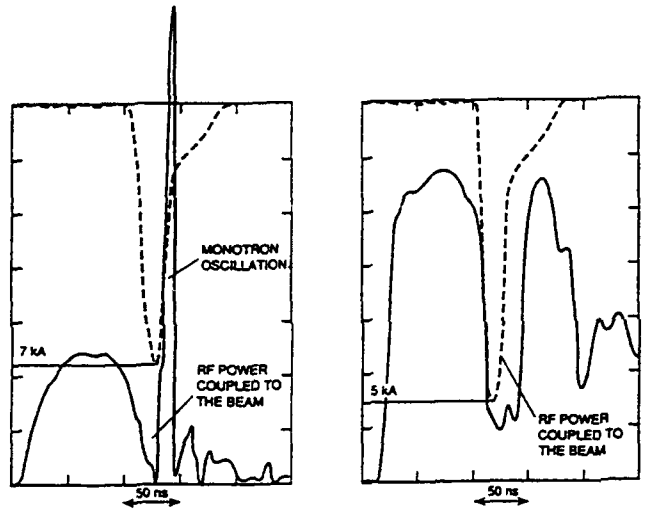

Fig. 6 : BEAM CURRENT (---) AND RF POWER (——)
IN THE FIRST CAVITY (MAGNETRON 9.5 GHz ON)

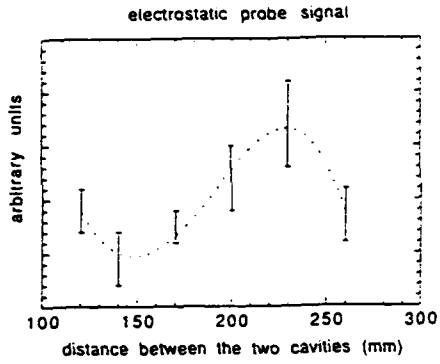

Fig. 7 :
POWER EXCITED IN THE SECOND CAVITY

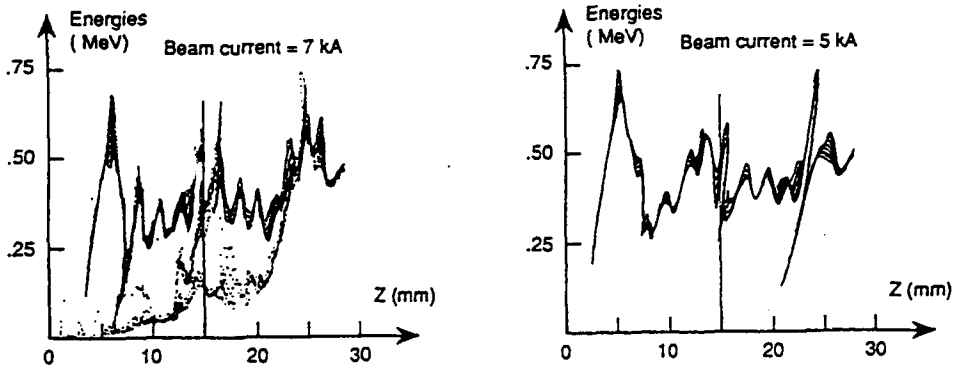

Fig. 8 : ELECTRON ENERGY (PIC) CALCULATIONS (7 kA AND 5 kA)

Invited Free Electron Laser Papers

Robert Parker, *Session Chairman*

THE ETA–II LINEAR INDUCTION ACCELERATOR AND IMP WIGGLER: A HIGH-AVERAGE-POWER MILLIMETER-WAVE FREE-ELECTRON LASER FOR PLASMA HEATING

S.L. Allen and E.T. Scharlemann
for the
MTX and ETA-II Experimental Teams and the Beam Research Program[1]
Lawrence Livermore National Laboratory
Livermore, CA 94550

Abstract

We have constructed a 140-GHz free-electron laser to generate high-average-power microwaves for heating the MTX tokamak plasma. A 5.5-m steady-state wiggler (Intense Microwave Prototype–IMP) has been installed at the end of the upgraded 60-cell ETA-II accelerator, and is configured as an FEL amplifier for the output of a 140-GHz long-pulse gyrotron.

Improvements in the ETA-II accelerator include a multicable-feed power distribution network, better magnetic alignment using a stretched-wire alignment technique (SWAT), and a computerized tuning algorithm that directly minimizes the transverse sweep (corkscrew motion) of the electron beam. The upgrades were first tested on the 20-cell, 3-MeV front end of ETA-II and resulted in greatly improved energy flatness and reduced corkscrew motion. The upgrades were then incorporated into the full 60-cell configuration of ETA-II, along with modifications to allow operation in 50-pulse bursts at pulse repetition frequencies up to 5 kHz. The pulse power modifications were developed and tested on the High Average Power Test Stand (HAPTS), and have significantly reduced the voltage and timing jitter of the MAG 1D magnetic pulse compressors. The 2-3 kA, 6-7 MeV beam from ETA-II is transported to the IMP wiggler, which has been reconfigured as a laced wiggler, with both permanent magnets and electromagnets, for high magnetic field operation. Tapering of the wiggler magnetic field is completely computer controlled and can be optimized based on the output power.

The microwaves from the FEL are transmitted to the MTX tokamak by a windowless quasi-optical microwave transmission system. Experiments at MTX are focused on studies of electron-cyclotron-resonance heating (ECRH) of the plasma.

We summarize here the accelerator and pulse power modifications, and describe the status of ETA-II, IMP, and MTX operations.

1. Introduction

Tokamak magnetic fusion devices achieve high plasma temperatures with a combination of ohmic heating (i.e., the current in the plasma times its resistivity) and direct heating of ions or electrons. The Microwave Tokamak Experiment (MTX) focuses on methods of electron cyclotron resonance heating (ECRH). The frequency of the incident microwave beam is equal to the electron gyrofrequency in the plasma, f_C/B_T=28 GHz/T, where B_T is the toroidal field of the tokamak. Heating of high-field tokamaks, with B_T=5-10T, requires f_C to be 140-280 GHz. Generation of high power microwaves in this frequency regime is possible either with gyrotrons or

FEL's. The present discussion focuses on the details of the FEL experiments; Ref. 2 presents details of heating experiments on MTX with a 400 kW, ~100 ms gyrotron pulse.

Generation of high power microwaves for tokamaks with an FEL can have several desirable features: 1) the output (for tapered operation) is expected to be a simple TE_{11} mode which couples directly to the plasma (as opposed to high order gyrotron modes, e.g., $TE_{15,2}$, which must be converted), 2) the FEL does not require an output window, which can be susceptible to breakdowns at high power, 3) the FEL is a broad-bandwidth amplifier [3], so that frequency sweeping during a tokamak shot is feasible by sweeping a low-power driving source, and 4) it is feasible to build an FEL with large average power output (10-20 MW), rather than combining many low power sources.

There are five major parts to the experiment: the ETA-II linear induction accelerator, the electron beam line, the IMP wiggler, a quasi-optical microwave transport system, and the MTX tokamak. The last two systems are described in detail in Ref. 4-5; we focus here on the FEL system. The overall goals of the experiment are to generate microwave pulses greater than 1 GW at 140 GHz (where the absorption physics in the MTX plasma becomes nonlinear), and to generate ECRH heating power comparable to the MTX ohmic input power of 300-600 kW (using a burst of pulses at 5 kHz). We have used the two-dimensional FEL simulation code FRED [6] to estimate the beam parameters necessary for these goals. This code has been benchmarked with previous FEL results at 35 GHz [7] and 140 GHz [8]. For a tapered IMP wiggler configuration with a beam energy of 7.35 Mev, 2 kA of beam current, and 50 W of drive power, the calculated output power is about 5 GW[9]. This estimate includes a ±0.1 cm beam displacement, a ±1% energy sweep, and a 0.1% error in the wiggler magnetic fields. Table I presents the sensitivity of the output power to these parameters.

Table 1 Predictions from FRED indicating sensitivity of FEL output power at 140 GHz to input parameters and expected ETA-II and IMP parameters. Achieved quantities (single pulse, 1 Hz operation) are denoted with a star *.

Parameter	Variation	Output Fraction	Expectation
Beam Energy	7.5 to 6 Mev	0.5	6^*-7.5 Mev
Beam Current	2.5 to 2 kA	0.6	2-2.5^* kA
	2.0 to 1.5 kA	0.17	
Brightness	1 to 0.2×10^8 A $m^{-2}r^{-2}$	0.6	$>10^{8*}$
Energy Sweep	±1% to ±2%	0.8	±1%*
Beam Motion			±1 mm*
Wiggler Error			0.2% RMS*

The parameters in Table 1 determine the beam quality required in the ETA–II accelerator. The improvements to the accelerator required to achieve this operation are presented in Section 2, along with a description of the electron beam line. The IMP wiggler, the measurement of the magnetic errors, and the microwave system are described in Section 3. The status of the experiment is discussed in Section 4, followed by a conclusion.

2. The ETA-II Linear Induction Accelerator

The ETA-II accelerator consists of an electron beam injector (up to 3 kA, 1.5 Mev) and 60 acceleration cells (~100 kV per gap) driven by pulsed power supplies. Several systems were first tested on a 20 cell version of the accelerator, and then were installed on the whole 60 cell ETA-II for FEL operations.

The ETA–II injector uses a thermionic, osmium-coated dispenser cathode that is 12.7 cm in diameter. One of the MAG-1D (MAG) magnetic pulse compressors [11] drives the injector in a diode configuration [10]. The cathode operates in a space-charge-limited mode to produce 2-3 kA of beam current at ~1-1.5 Mev. We are currently operating the injector at 2.5 kA; most of this current is transported through the 60 cells of the ETA-II accelerator. The measured normalized brightness of the cathode alone on a test stand was ~10^{10} $\mathcal{A}$ [10] ($\mathcal{A}$=A/m^{2}rad^2); acceleration and transport reduce the brightness. The measured brightness for 20-cell experiments was ~10^9 $\mathcal{A}$ for individual beamlets, and ~4 x 10^8 $\mathcal{A}$ for the whole beam[12]. Measurements on a previous 60-cell version of ETA-II (before modifications) yielded a brightness of 6 x 10^8 $\mathcal{A}$[13]. All of these values equal or exceed the FEL brightness requirements of ~10^8 $\mathcal{A}$.

The ETA-II accelerator is made up of six blocks of ten cells; each pulsed power system drives twenty cells. Each system uses a MAG to provide an output pulse of 80-120 kV for 70 ns. The MAG output at a given beam current (the beam load is the largest load on the MAG) and the voltage holding capability of the insulators in the accelerator gaps determine the ultimate energy of the beam. Previous versions of ETA-II used alumina insulators; we are now using Rexolite insulators that have been tested to over 120 kV/gap.

Efficient FEL operation (Table 1) relies on control of the beam energy sweep and transverse motion. Solenoidal magnets transport the beam through the accelerator; the equations of motion for propagation beyond a solenoidal channel of length L at an angle α are:

$$x = L\,(1-\cos\alpha)\,\sin(k_C z), \text{ and } \quad y = L\sin\alpha\,\sin(k_C z)) \qquad (1)$$

where $k_C = eB/(m\gamma\beta c^2)$. The angular misalignments α are due to tilts and offsets in the solenoidal magnets. Any variations in the energy of the beam will cause k_C to be time dependent, and hence different parts of the beam will rotate with different cyclotron frequencies. The result is a

helical or "corkscrew" motion of the beam; magnetic errors determine the amplitude of this motion, and the energy sweep sets the phase.

We have implemented a special multi-cable power distribution system to minimize the energy sweep[14]. A pair of 20-ohm cables feeds two cells; a distribution system connects 20 cables to each MAG. This system ensures good impedance matching and transit-time isolation between the cells. Operation during the 20-cell checkout experiment and the 60-cell experiment has shown that the applied accelerating voltage is similar for each cell in a cell block. The optimized impedance matching has also minimized voltage reflections that can damage the insulators. During operations, a protection system measures the peak (overvoltage protection) and integral (arc protection) of the applied voltage on each gap; values out of range will stop the accelerator.

The lengths of the feed cables determine the timing of the applied voltage pulse within a twenty-cell system (one MAG). A computerized timing compensation system dynamically controls the timing between MAGs; optimum values to minimize corkscrew phase are determined experimentally. This system has compensated for slow drifts up to 20 ns caused by power line variations during a run day. The measured shot-to-shot timing reproducibility of each MAG is typically less than 0.5 ns; we normally observe good pulse-to-pulse reproducibility during accelerator operations.

We use an energy compensation scheme in the accelerator to reduce the energy sweep during the beam pulse, as the injector current waveform (and therefore voltage as $V \propto I^{2/3}$) is not flat[15]. The MAG operating voltage determines its output pulse shape[16]. Therefore, cells at the beginning of the accelerator use a slightly rising waveform to compensate for the (normally) falling energy of the injector pulse. The rest of the cells then use a flatter accelerating pulse. A magnetic analyzer measures the energy variations during the beam pulse. We have obtained a 35 to 40-ns interval of the beam pulse with $\Delta T/T \leq \pm 1\%$, both in the 20-cell checkout at 2.7 Mev[17], and for initial 60-cell operation at 6.3 MeV. As 7.5 MeV is the calculated optimum operating point for the 60 cells, we expect even longer energy flatness as we increase the energy.

We use two techniques to minimize the magnetic errors and hence the corkscrew amplitude: a stretched wire alignment technique during construction, and a computerized minimization of the corkscrew motion during operations with electron beam. Each cell block is carefully assembled using a new vertical assembly technique designed to minimize offsets. A Stretched Wire Alignment Technique (SWAT) [18] then verifies the construction accuracy. In the SWAT measurement, a current pulse is propagated down a wire that is stretched through the axis of the solenoidal magnets. A photodetector at the end of the wire measures the displacement of the wire; deviations from the original pulse shape indicate the presence of tilts or offsets. We

also use SWAT during assembly of the six cell blocks and the electron beam line; mechanical adjustments of the support structures minimize the offsets.

Trim magnets, which are dipole coils wrapped coaxially around the solenoid magnets, are used to null magnet tilts. Initial values are determined during the SWAT alignment procedure. A computerized system (MAESTRO) minimizes the corkscrew directly during beam operations by adjusting the (120) trim coils. Theoretical models [19] and experiments [20] have shown that a certain value of trim current in each coil minimizes the corkscrew amplitude A calculated from the x and y position:

$$A^2 = \int_{t_1}^{t_2} (x^2 + y^2)\, dt \quad . \qquad (2)$$

MAESTRO calculates the x and y positions from signals on return-current monitors. We normally define x relative to the mean to emphasize corkscrew minimization in the accelerator; the system usually converges in one pass. In the beam transport section, we use the absolute x to minimize offsets. MAESTRO evaluates the integral over the FWHM of the pulse; we have also concentrated on the central 40 ns of the pulse.

The MAESTRO computer system performs the corkscrew minimization algorithm automatically: it first sets the trim current power supply, it next acquires the beam position data, and then the computer calculates the corkscrew amplitude A. MAESTRO completes this cycle between accelerator pulses at 1 Hz. When the scan of a trim coil is completed, the computer determines and sets the current for the minimum corkscrew. MAESTRO can tune one cell block (10 cells) in about 15 minutes; 60 cells require about 1-2 hours. In some cases, convergence of the procedure requires a second pass. The measured corkscrew motion for the 20-cell experiment was less than ±0.6 mm for 40 ns of the pulse[20]. As shown in Fig. 1, the 60-cell experiment, running at the 6.3 MeV (not optimized) condition has yielded corkscrew amplitude of ±1-1.5 mm for 40 ns, sufficient for the requirements discussed in Table 1

Another source of beam motion is the Beam Break-Up Instability (BBU), studied previously both on ETA-II and ATA [21]. The growth length is proportional to $Z/I/B$, where Z is the transverse impedance of the cell, I is the beam current, and B is the focusing field. The BBU growth decreases with B, while the corkscrew phase advance increases with B. We have added metal rings [22] to lower the cell impedance at the resonance frequency of ~300 MHz. With B~800 G, we have seen only small-amplitude high-frequency beam motion at 2400 A and 6.3 Mev.

A beam line transports the beam to the wiggler; it consists of a matching section, a transport lattice with slits, and a matching section into the wiggler. The first matching section can be either a solenoidal or quadrupole system; the quadrupole system is energy selective, so that if

the accelerator fails, the beam is dumped ... the beam line rather than the wiggler. Water-cooled carbon slits after each magnetic lens in the lattice serve as beam dumps. An optical foil and gated camera are used to measure the beam size out of the accelerator; good quality beams with a diameter of 1.5-2 cm have been observed. As shown in Fig. 2, the beam passes through a microwave sidecoupler just before the wiggler; at this point, another optical system measures the beam size, which again is about 1.5-2 cm. The beam is matched into the wiggler with a final pair of solenoid magnets.

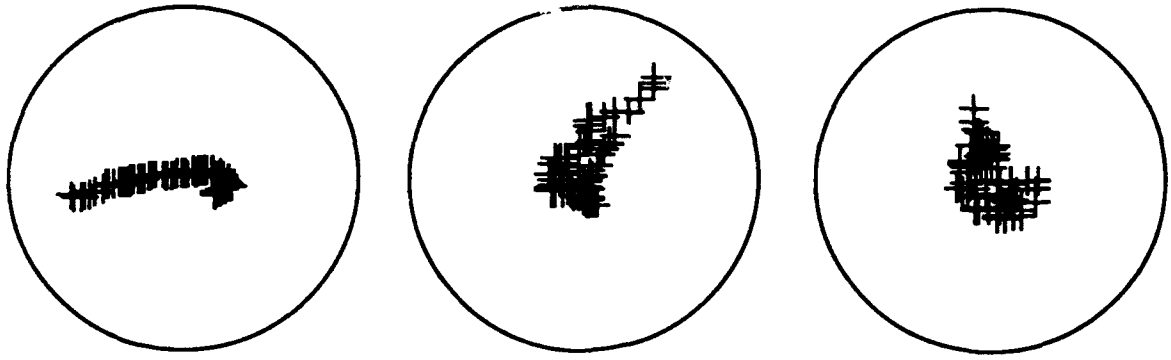

Fig. 1 Beam motion at three locations from the 60-cell experiment every 0.4 ns for 40 ns, the circles are 2 mm in radius.

2. The Microwave System and IMP Wiggler

The overall FEL microwave system is shown in Fig. 2. The master oscillator (MO) for the FEL is a 140-GHz, high-power gyrotron (also used for plasma heating experiments). A waveguide couples the (primarily) $TE_{15,2}$ mode output from the gyrotron to a Vlasov launcher that converts it into a gaussian mode. The MO power is then transmitted with a quasi-optical transport system of mirrors to the side coupler. The side coupler consists of a large mirror that focuses the microwave beam to the input of the wiggler waveguide. The electron beam passes through a 4-cm diameter central hole in the mirror.

The IMP wiggler is described in detail in ref. 4. Briefly, it is a ~5.5-m steady-state wiggler with a 10 cm period, and uses a combination of both electro- and permanent magnets. The magnetic field is adjustable in the range of 2.7-5.5 kG in the first 2.2 m, and 0.6-4.1 kG in the region from 2.2-5.5 m. Detailed measurements of the magnetic field profile with a computer-controlled Hall probe have been obtained. The RMS wiggler errors (i.e., the deviations from a fit of B(z) to a Fourier series) were 0.1% for electromagnets alone, and 0.2% for the whole wiggler. Careful selection and alignment of the permanent magnets were required to obtain the final value. The MAESTRO system controls the field in the 30 power supplies; angle and offset coils are used for steering at the input of the wiggler. As MAESTRO also acquires the microwave output power,

it can be used to tune the wiggler magnetic field and thereby find the resonance magnetic field and optimum taper.

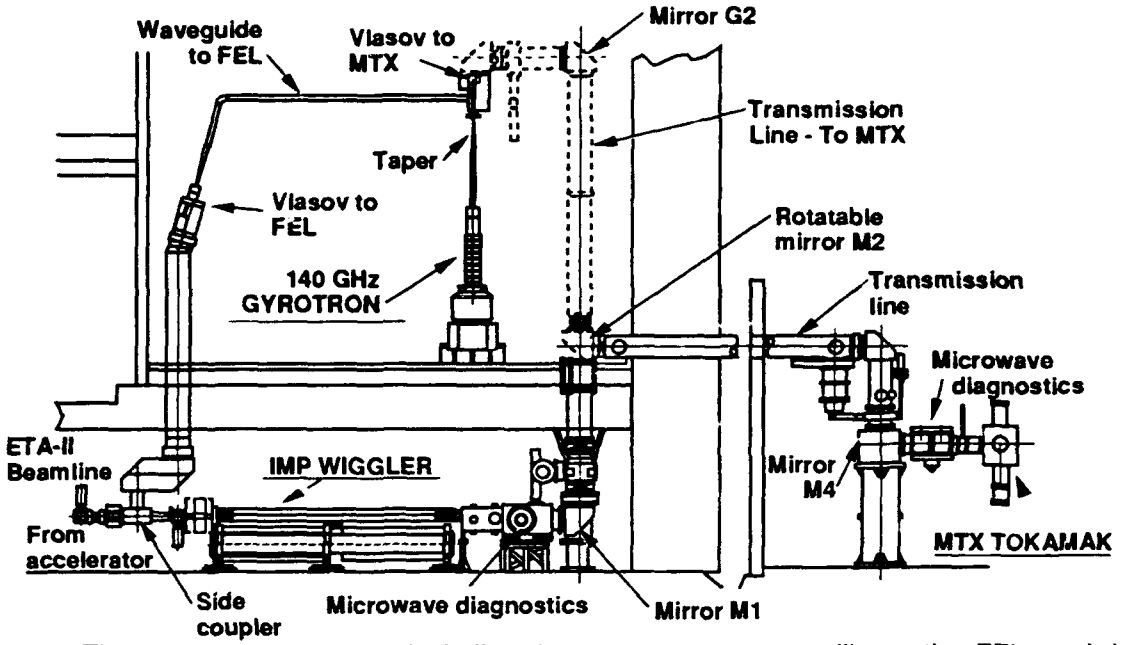

Fig. 2. The microwave system, including the gyrotron master oscillator, the FEL, and the transport system to the MTX tokamak. The direct connection between the gyrotron and the tokamak is also shown (dotted lines).

The beam transport in the IMP wiggler has also been checked during electron beam operations. A moveable optical target was viewed from the end of the wiggler by a gated camera. The beam size was observed to be about 0.4 cm in radius, near the optimum. The wiggler motion was observed, with the proper period of 10 cm. Most importantly, the wiggle amplitude was on the order of 0.5 cm, again in agreement with theoretical models. No evidence of strong beam steering or abnormal growth in beam size was observed.

The microwave output power is measured at a diagnostic station near the end of the wiggler, as shown in Fig. 2; this contains microwave receivers, diodes, and a calorimeter. A moveable mirror is used to direct the FEL output through the quasi-optical transport system to the MTX tokamak. A second diagnostic station and calorimeter are located at the input to the tokamak.

3. FEL Status and Summary

As discussed above, nearly all of the required beam parameters have been achieved from the ETA-II accelerator. The IMP wiggler operation has been checked with magnetic measurements and with electron beam operations. The gyrotron provides 1-10 kW of MO power to the input of the wiggler. We have checked out the whole FEL system at low electron beam current with single pulses at 1 Hz. Clear evidence of FEL gain has been observed: the microwave output power decreases sharply when the MO is turned off, and the power increases

sharply at the resonant wiggler magnetic field. The microwave pulse width is between 20-50 ns; experiments are in progress to determine if any of this signal results from reflections within the transport system. As expected, the microwave power during these checkout operations is low, in the 10-100 MW range.

We are currently starting wiggler tuning at the full electron beam current to increase the output power. We plan to first carry out single pulse microwave heating experiments with MTX, and then proceed to burst-mode checkout.

We would like to acknowledge the fundamental FEL work done by previous ETA-II, ELF, and Beam Research staffs at LLNL that made this work possible. This work is performed by LLNL for USDOE under Contract W-7405-ENG-48.

References

1. The members of the MTX, ETA-II, and Beam Research Groups are: S.L. Allen, D. Behne, H. Bell, J. Bowman, M. Brown, D. Butner, J. Burris, T. Casper, R. Cavitt, F. Chambers, Y.J. Chen, T. DaCosta, M. DeLong, F. Deadrick, J. Dunlap, W. Edmondson, B. Felker, M. Fenstermacher, W. Ferguson, S. Fields, J. Foote, G. Garcia, D. Garner, R. Geer, D. Hathaway, S. Hibbs, C. Holmes, E. B. Hooper, K. Hoshino, T. Hubbard, S. Hulsey, D. Lager, D. Lang, C. Lasnier, M. Jackson, J. Jolly, G. Mattson, M. McDaniel, M. Makowski, M. Marinak, R. Miller, J. Moller, W. Meyer, D. Nilson, K. Oasa, T. Oda, K. Odajima, T. Ogawa, C. Ollis, A. Paul, A. Payne, D. Pendleton, F. Penko, D. Petersen, D. Podestra, D. Prosnitz, V. Renbarger, D. Rogers, B. Rice, S. Sampayan, L. Schlander, D. Seilhymer, P. Souza, B. Stallard, R. Stever, T. Scharlemann, K. Thomassen, J. Watson, C. Wendland, W. Weiss, R. Wood. Previous members J. Clarke, R. Jong, W. Nexsen, A Throop, and W. Turner were of great assistance.
2. E. B. Hooper, et al, Bull. Amer. Phys. Soc. **36** (1991) 2312.
3. T.J. Orzechowski, et al, Nucl. Instrum and Methods in Physics Res **A250** (1986) 144.
4. B Felker and S.W. Ferguson, Proceedings of the 14th IEEE-NPSS Fusion Eng. Symposium, San Diego, 1991, p 132.
5. D.D. Lang, S.L. Allen, H.H. Bell, Processing of the 14th IEEE-NPSS Fusion Eng. Symposium, San Diego, 1991, p 174.
6. E.T. Scharlemann, Laser Handbook, Vol 6, (North-Holland, New York, 1990) 291.
7. E.T. Scharlemann, et al, Nucl. Instr. and Meth in Phys. Res. **A250** (1986) 150. and T.J. Orzechowski, et al, Phys. Rev. Lett **57** (1986) 2172.
8. S.L. Allen, et al, in Proc. 13th Int. Conf. on Phys. and Cont. Nuclear Fusion Res., Washington, D.C., 1990, Vol 1 (IAEA, Vienna, 1991) 783.
9. R. A. Jong, et al, Nucl Instrum. Meth. in Phys. Res. **A285** (1989) 379, also private communications, April 1992.
10. W.C. Turner, et al, Proceedings of 1989 Part. Accel. Conf. (Chicago, 1989) 996.
11. S.E. Sampayan et al, Proc. 1991 IEEE Part. Accel Conf (San Francisco, 1991) 3097.
12. A. Paul, et al., Proc. 1991 IEEE Part. Accel. Conf. (San Francisco, 1991) 3106.
13. Y.-J. Chen, et al., Proc. 1990 Lin. Accel. Conf. (Albuquerque, 1990) 414.
14. S.E. Sampayan et al, in Proc. of 1990 Lin Accel. Conf (Albuquerque, 1990) 417.
15. Y.J. Chen, Nucl. Instrum. and Meth. in Phys. Res. **A292** (1990) 455.
16. W.C. Turner, et al, *Critical System Issues and Modeling Requirements-the Problem of Beam Energy Sweep in the Electron Linear Accelerator,* in proceedings of Int. Mag. Pulse Comp. Workshop, Lake Tahoe, CA, February 1990.
17. W.E. Nexsen et al, Proc. 1991 IEEE Part. Accel Conf (San Francisco, 1991) 3103.
18. F.J. Deadrick, et al, Proc. 1990 Lin Accel Conf (Albuquerque, 1990) 423.
19. W.C. Turner, et al, Proc. 1990 Lin Accel Conf (Albuquerque, 1990) 435.
20. S.L Allen, et al, Proc. 1991 IEEE Part. Accel Conf. (San Francisco, 1991) 3094.
21. G.J. Caporaso et al, Proc. 5th Int. Cof. on High Power Beams, (San Francisco, 1983) 427.
22. G. Craig, private communications, 1990.

IREB TRANSPORT IN A FOCUSING WIGGLER AND FEL EXPERIMENTS AT JAERI

S. Kawasaki and T. Kobayashi*
Department of Physics, Faculty of Science, Saitama University
255 Shimo-ohkubo, Urawa, 338 JAPAN
and
K. Sakamoto, Y. Kishimoto, A. Watanabe, S. Musyoki, H. Oda,
S. Tokuda. Y. Nakamura, T. Nagashima and M. Shiho
Department of Fusion Engineering, Japan Atomic Energy Research Institute, Naka-machi, Ibaraki, 311-01 JAPAN

* Present address: Toshiba Corporation, Tsurumi Works, 2-4 Suehirocho, Tsurumi, Yokohama 230 JAPAN.

Abstract

An experiment of Raman mm wave FEL was carried out using a planar focusing wiggler and an additional axial magnetic field. An IREB (0.9 MeV, 2 kA, 100 μs) was generated by a field emission gun drived with inductive acceleration units and flowed into the wiggler. The beam transmission up to 85% through the whole wiggler length(1.5 m) was realized at its best, though the axial magnetic field was kept very low. The particle orbits in the wiggler were to be in the "group I". There appeared a pattern showing effect of higher modes of the resonance between the *electron cyclotron* frequency in the axial field and the frequency associated with the wiggler field. The results were compared with the simulation made by a newly developed code. Strong superradiant emission was found several sharp peaks with a very narrow width, separated by 6-8 GHz in the frequency spectrum in the range between 30-65 GHz. The radiation power as well as the spectrum were correlated to the radial distribution of the particles in the cross section of the beam. At the amplifier mode of the FEL operation, rf pulse of 45 GHz was injected at the entrance of the wiggler, and amplified along the beam flowing in the wiggler from the power level of 100 W at the input, to finally 6 MW at the saturated state, at a spatial growth rate of 50-56 db/m. The amplification process observed was also consistent with the analyses by 3D simulations.

Introduction

Raman FELs are usually operated with an intense axial guide magnetic field Bz to avoid the beam divergence due to the space charge field of the beam in the wiggler. The presence of the guide field however, necessarily makes the FEL operation quite complex due to the effects of magneto-resonce[1] and particle drift caused by the intrinsic inhomogeneity of the field, especially in the case of a planar wiggler. A focusing wiggler was

suggested first by Phillips[2] to furnish the beam an efficient focusing force even without Bz, and later Scharleman analysed the particle motion in it in relation to the FEL and found that the wiggler field by the parabolic pole face would not degrade the coherent characteristics of the radations coming from each electron[3]. This paper reports the results of the experimental FEL study at JAERI, where an IREB generated with an induction linac LAX-1, was injected into the focusing field of a newly installed wiggler of Scharleman type[4]. The beam transport in the wiggler was investigated in detail for various operation parameters such as the particle energy and additional low axial magnetic field, which was applied to study the effect of Bz on the beam transmission and the FEL characteristics. It should be noticed that the axial field takes a crucial role on the other hand in the transition area between the anode of the diode and the wiggler entrance for keeping the beam stable in the orbit.

We have found intense superradiant emissions in certain cases to have several sharp peaks separated regularly by some GHz in the frequency range observed, contray to the prediction of the FEL theory. The spectrum does depend on Bz very slightly.

Also investigated and reported here is the FEL experiment in the amplification mode where an rf pulse of 45 GHz was injected and grown up along the beam in the wiggler. The parameters of the operation were set so as to get a good transmission in the wiggler. The result is also discussed, being compared with a 3D simulation.

Experimental Arrangements

Fig. 1 shows the schematic of the experimental setup. A four stage induction accelerating unit generates an IREB (0.8 MeV, 2 kA, 100 ns). The details of the hardwares were described elswhere[5]. On the central plane of the device, placed is a field emission diode consisting of a tungsten mesh anode and a metal cathode, the surface of which is covered with velvet. The beam is guided to the wiggler with an axial magnetic field of 1 - 2 kG. The wiggler has 33 periods over the whole length of 1.5 m and the unit pitch length is 4.5 cm. It consists of permanent magnets (Nd-Fe-B), the pole surface of which is shaped to be

parabolic(Fig. 2)[3]:

$$y = (1/k_y)\sinh^{-1}(C_0/\cosh k_x x).$$

Corresponding to the wiggler field Bw = 1.8 kG, it was taken that $k_x = k_y = k_w/2^{1/2}$ and $k_w = 2\pi/\lambda$ as, and $C_0 = 1.57$.

The beam enters an adiabatic taper section of 5 pitches in the wiggler at first. The taper was designed to optimize the beam trapping efficiency. An axial magnetic field Bz can be applied in the wiggler region in addition to Bw, which enabled us to study FEL mechanism in the transition between the axial field-free operation and the Bz dominated one. It also gives a smooth beam transfer from the diode to the wiggler area. In the wiggler+axial fields, the beam propagates inside a metal drift tube of 40 mm radius, radiates spontaneously and/or amplifies rf pulse externally injected along the beam at the entrance of the wiggler. The resulted spontaneous and stimulated radiations are going forward to pass through a microwave window located at the end of the device, and then are frequency-analysed with use of the filters of various bandwidths

IREB Transmission in Focusing Wiggler

The introduction of the taper section in the wiggler improved the transmission efficiency remarkably in comparison with our previous result(Fig. 3)[6]. At the best condition, 85% of the beam could propagate until the wiggler end, even in the case of no axial field inside the most area of the wiggler. This means the wiggler works well for focusing the beam. The result is in good agreement with the simulation of the particle code.

The effect of Bz on the transmission was studied in detail. It is summarized in an intensity map of the transmitted beam as illustrated in Fig. 4. It is found that the increase of Bz from zero generally detriorated the beam transmission and an stop band was formed in the pattern. In Fig. 5 one example of the analyses with particle simulation codes is shown. The stop band corresponds with the second cyclotron resonance and we reached the conclusion that we observed the effect of the higher modes of the magnetoresonance between the electron motions in Bz and Bw, which was never observed experimentally

so far. We also calculated the particle orbits for the helical wiggler either, and the result was similar to the case of the planar one.

Superradiant Radiation

Spontaneous radiations by the beam were detected and analysed in their frequency spectrum with narrow band microwave filters. Fig. 5 gives the observed spectrum, where several very sharp peaks appear regularly, separated 6-8 GHz and show a complex feature of the radiation, although the absolute level of the radiated power calibrated was not very high (about 10 KW). This kind of the spectrum has not been found in the case of simple planar wiggler. The width of the each peak was estimated to be 0.1-0.2 GHz. The position of the peak slightly depends on Bz (possibly also on Bw). The exact origin of the mechanism causing the spectrum remains still unsolved. From the regular space between the peaks, we speculate that they could be the higher harmonics of a certain fundamental frequency associated with FEL, the effect of which was known to be large for the focusing wiggler[7].

Amplifier Experiment

Fig. 6 shows the output power of the FEL amplified rf. Bz and the beam intensity at the end were 0.75 kG and 250 A respectively. The output power levels were measured and presented for the interaction length normalized with the unit wiggler pitch. The interaction length was controlled by interrupting halfway the beam propagation with a kicker magnet placed at prescribed locations. The input rf pulse was supplied from a klystron and injected through an entrance port near the wiggler entrance. The power was varied at the level of 10-300 W. A linear dependence of the amplified intensity on the initial power was seen in the range. The spatial growth rate of 50-56 db/m and the total gain of 50-52 db over the whole wiggler were obtained. When the input power was increased up to 200 W, the satuaration occurred at z = 28 units. The maximum power attained was 6 MW, corresponding to 3 % of the conversion efficiency. The observed gain of the amplification and the saturation level are well

explained with the analytical estimation and also with the 3 D simulation. It was found that the electrons going through the peripheral region in the radial cross section of the beam could enhance the FEL radiation considerably. The numerical study is being continued.

Conclusive Remarks

We can make some conclusions as follows:

1)The focusing wiggler works well for confining the electron on the orbit in the wiggler, and the transmission up to 85 % was realized.

2)We observed the effect of the higher harmonic modes of the magnetoresonance, which formed stop bands in the transmission map.

3)Superradiant radiation has a complex structure in the frequency spectrum. It seems characteristic for the use of the focusing wiggler. The mechanism is to be studied.

4)Amplification experiment was carried out succesfuly with the focusing wiggler. The output power of 6 MW was obtained at 45 GHz.

References

[1] H.P.Freund, Phys. Rev. 27 1977(1983).
[2] R.M.Phillips, IRE Trans. Electron Devices ED-7, 231(1960).
[3] E.T.Scharleman, J. Appl. Phys. 58 2154 (1985).
[4] M.Shiho, K.Sakamoto, S.Maebara, A.Watanabe, Y.Kishimoto, H.Oda, S.Kawasaki, T.Nagashima and H.Maeda, Nucl. Instr. and Methods in Phys. Res. A304 141(1991).
[5] M.Shiho, S.Maebara, K.Sakamoto, A.Watanabe, S.Kato, S.Nakajima, K. Yamauchi and T.Iimura, Proc. Intren. Workshop on Magnetic Compression, Tahoe City, CA, Feb. 1990.
[6] K.Sakamoto, S.Maebara, A.Watanabe, Y.Kishimoto, H.Oda, S. Kawasaki, T.Nagashima, H.Maeda and M.Shiho, JAERI-M 91-036 March 1991.
[7] H.Bluem, H.P.Freund and C.L.Chang, Nucl. Instr. and Methods in Phys. Res. A272 579(1988).

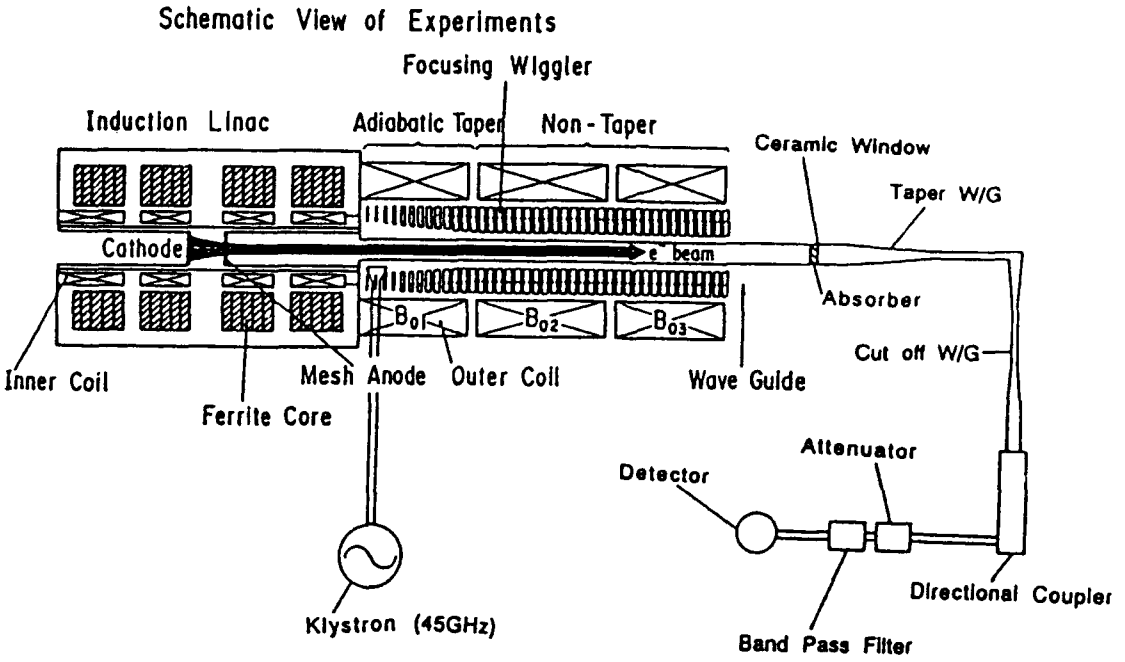

Fig. 1. Schematic of experimental Setup.

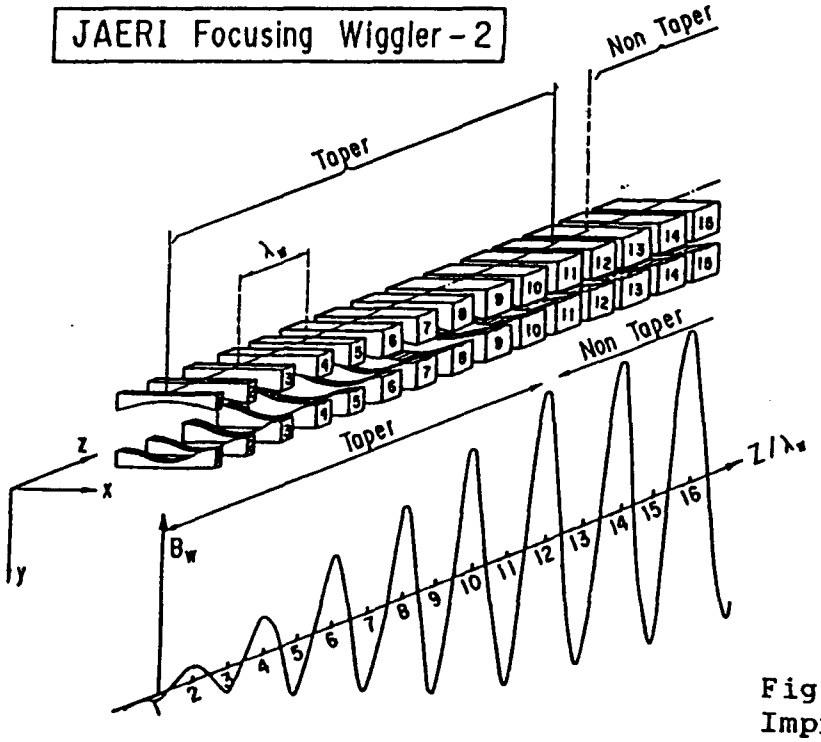

$$y(x) = \frac{1}{k_x} \sinh^{-1}\left(\frac{C_0}{\cosh k_x x}\right)$$
$$\cosh k_x x \cdot \sin k_y y = C_0$$
} No. 1 ~ No. 30

Fig. 2.
Improved focusing wiggler and coordinate system.

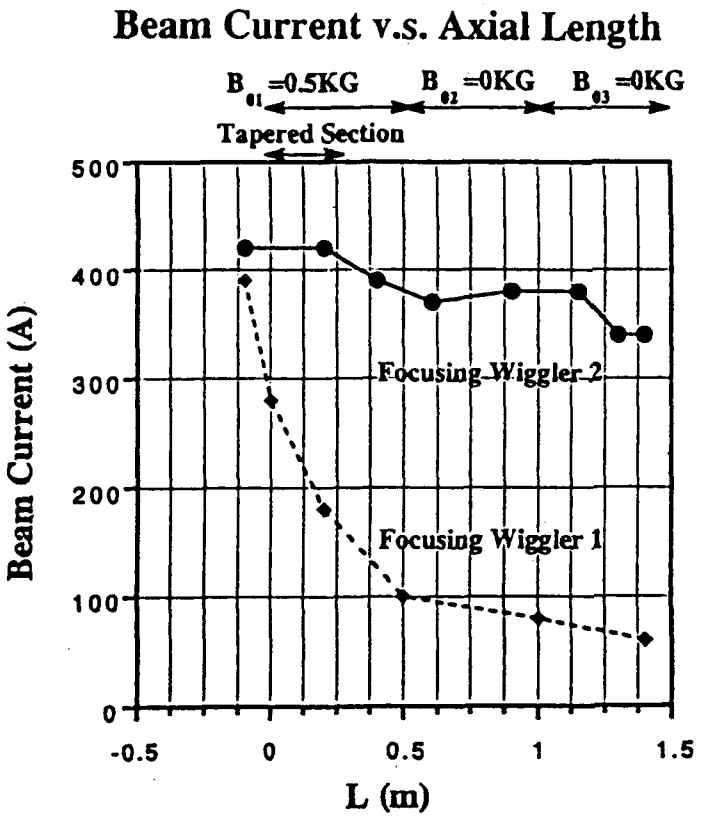

Fig. 3.
Beam transmission.
Beam current vs.
axial length.

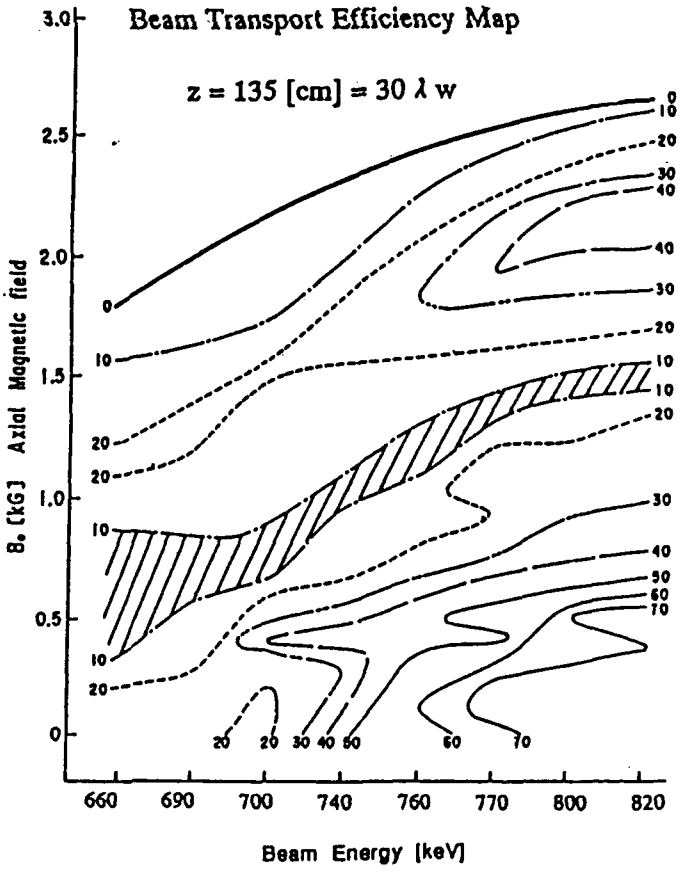

Fig. 4.
Beam transmission
efficiency map.

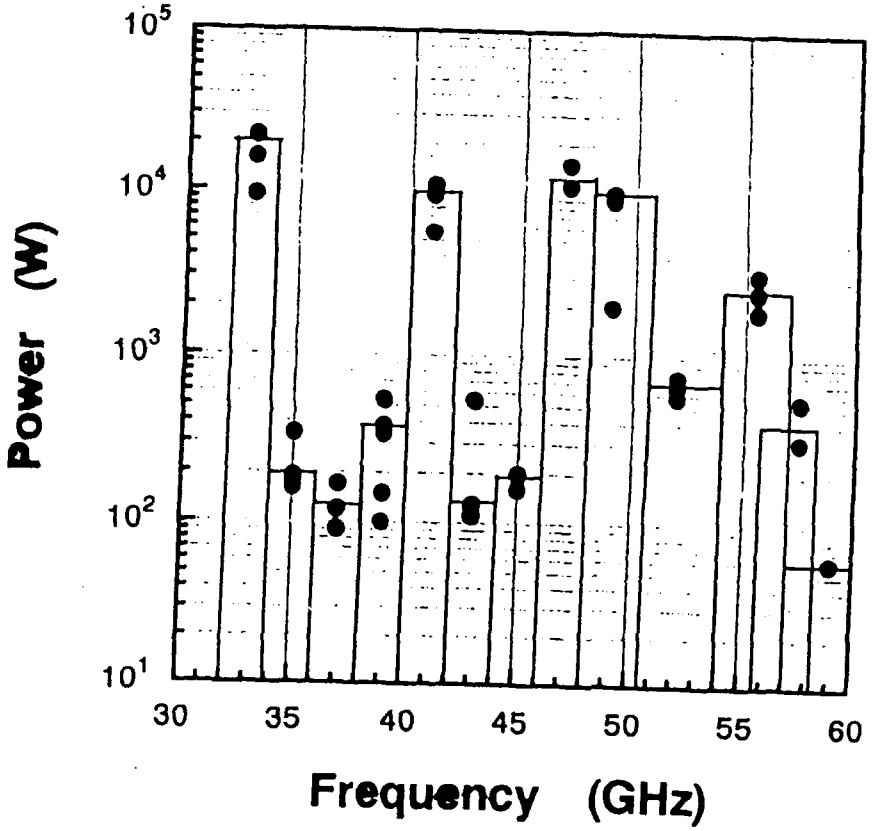

Fig. 5.
Frequency spectrum of spontaneous radiation.

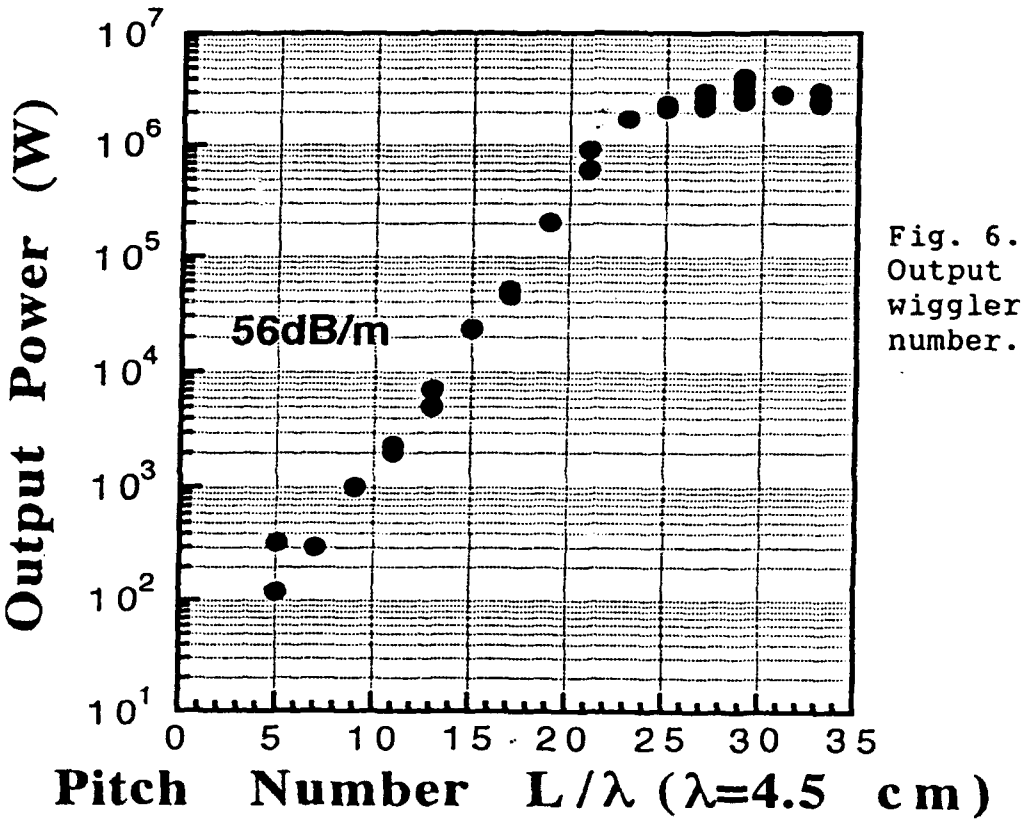

Fig. 6.
Output power vs. wiggler pitch number.

SELF-CONSISTENT NONLINEAR SIMULATIONS OF HIGH-POWER FREE-ELECTRON LASERS

H.P. Freund† and R.H. Jackson
Naval Research Laboratory, Washington, D.C. 20375

ABSTRACT

Two 3-D nonlinear formulations of FEL amplifiers are described which treat both planar and helical wiggler geometries. For convenience, we refer to the planar (helical) formulation and simulation code as WIGGLIN (ARACHNE). These formulations are slow-time-scale models for FEL amplifiers in which the electron dynamics are treated using the complete 3-D Lorentz force equations without recourse to a wiggler period average. The application of these codes to the description of a collective reversed-field FEL experiment and to random wiggler field errors is described.

I. INTRODUCTION

Free-Electron Laser (FEL) experiments typically employ wiggler magnets with either helical or planar symmetry. Most helical wiggler-based FELs operate in the Raman regime with high current beams, and use axial magnetic fields for enhanced focusing. In contrast, planar wiggler-based FELs have generally not operated in the Raman regime, and space-charge forces have been negligible . Hence, it is important for most helical wiggler designs to include the effects of both a guide field and space-charge fields on the interaction. In contrast, the simulation of most planar wiggler designs can be accomplished with the inclusion of only the electromagnetic fields.

The present paper is concerned with the theoretical description of both planar and helical wiggler configurations in three-dimensions. To this end two related formulations and simulation codes have been developed. For convenience, we refer to the 3-D formulation and code used for helical (planar) wiggler configurations as ARACHNE[1-6] (WIGGLIN[7-9]). Both formulations represent slow-time-scale analyses of FEL amplifiers in which the electron dynamics are treated using the complete 3-D Lorentz force equations. We emphasize that the Lorentz force equations are not averaged over a wiggler period in these formulations. The treatment of the electron dynamics is the most important aspect of these formulations since it permits the self-consistent inclusion of effects such as the injection of the beam into the wiggler, bulk wiggler motion, Larmor motion, wiggler inhomogenieties [i.e., Betatron motion, guiding-center drifts, velocity shear effects, orbital instabilities, and etc.], random wiggler errors, and harmonic interactions. Specific applications of these codes to the description of a recent high-power reversed-field FEL amplifier experiment[10,11] and to the treatment of random wiggler errors are described.

II. THE THEORETICAL FORMULATION

We summarize the essential properties of the formulation, and refer the interested reader to the original papers[1-9] for a complete discussion. ARACHNE and WIGGLIN are 3-D slow-time-

scale descriptions of FEL amplifiers. Single frequency propagation is assumed and Maxwell's equations are averaged over a wave period. This results in two numerical simplifications: (1) the fast-time-scale oscillation disappears and only the slow-time-scale growth of the wave must be resolved, and (2) only a *beamlet* of electrons entering the wiggler within one wave period needs to be included. For an idealized beam [i.e., zero energy spread] only 1000 electrons are needed and run times are typically 20-40 seconds on a CRAY-2 supercomputer. For a realistic beam with a nonvanishing energy spread 9600 electrons are needed and run times are typically 5-10 minutes.

The electromagnetic field is represented as a superposition of the propagating TE and TM modes of the vacuum waveguide. A cylindrical waveguide model is used in ARACHNE, and a rectangular waveguide model is used in WIGGLIN. In addition, a model of the collective Raman interaction is included in ARACHNE through the interaction of the beam with the electrostatic field. This space-charge field in ARACHNE is represented as a superposition of the Gould-Trivelpiece modes for a completely filled waveguide.[12] Since both the electromagnetic and electrostatic fields are at the same frequency, the dynamical equations for both cases can be averaged over the wave period in order to obtain the equations for the slow variations.

Electron dynamics in both WIGGLIN and ARACHNE are treated by integration of the 3-D Lorentz force equations in the complete set of electrostatic, magnetostatic, and electromagnetic fields. The generality of this formulation of the orbits is crucial, and permits the description of the primary wiggler oscillation, Larmor effects, Betatron oscillations and guiding-center drifts due to the wiggler inhomogenieties, orbital instabilities, and harmonic interactions. This is critical in the simulation of both wiggler errors and the field-reversed configuration.

The initial conditions describe the beam upon entry into the wiggler, and the effect of an axial energy spread is included by means of a pitch angle spread. The wiggler field model in both ARACHNE and WIGGLIN is 3-D and includes an adiabatic entry taper, and the codes describe the self-consistent injection of the beam into the wiggler. This has a practical advantage, since it is easier to characterize the beam prior to injection. Random wiggler field errors have been incorporated into WIGGLIN through the use of a randomly generated set of variations in the wiggler amplitude from pole-to-pole with a continuous mapping between them. The initial conditions imposed on the TE and TM modes are that the initial amplitude of each mode is chosen to reflect the injected power into the system, and the initial wavenumber corresponds to the vacuum value appropriate to the mode. Initialization of the Gould-Trivelpiece modes in ARACHNE is accomplished by evaluation of the appropriate initial phase averages of the beam.

ARACHNE and WIGGLIN self-consistently integrates the dynamical equations for the field amplitudes and phases in conjunction with the Lorentz force equations for the electrons. Since the complete Lorentz force equations are used, this permits the self-consistent description of the injection of the beam into the wiggler, the bulk wiggler motion, Larmor motion, wiggler

inhomogenieties [i.e., Betatron motion, guiding-center drifts, velocity shear effects, orbital instabilities, and etc.], random wiggler errors, and harmonic interactions.

III. WIGGLER ERROR ANALYSIS

The wiggler configuration employed in WIGGLIN to treat the effects of a random wiggler variations is that of a planar wiggler with parabolic pole faces which can be represented as

$$\mathbf{B}_w(\mathbf{x}) = \left[B_w(z) + \Delta B_w(z)\right]\left\{\cos k_w z \left[\hat{\mathbf{e}}_x \sinh\left(\frac{k_w x}{\sqrt{2}}\right) \sinh\left(\frac{k_w y}{\sqrt{2}}\right) + \hat{\mathbf{e}}_y \cosh\left(\frac{k_w x}{\sqrt{2}}\right) \cosh\left(\frac{k_w y}{\sqrt{2}}\right)\right] - \sqrt{2}\,\hat{\mathbf{e}}_z \cosh\left(\frac{k_w x}{\sqrt{2}}\right) \sinh\left(\frac{k_w y}{\sqrt{2}}\right) \sin k_w z \right\} , \quad (1)$$

where k_w denotes the wiggler wavenumber for a wiggler period λ_w, $B_w(z)$ and $\Delta B_w(z)$ denote the systematic [*i.e.*, non-random] and random variations in the amplitude respectively. The systematic variation in the wiggler amplitude is assumed to be

$$B_w(z) = \begin{cases} B_w \sin^2\left(\dfrac{k_w z}{4N_w}\right) & ; 0 \le z \le N_w\lambda_w \\ B_w & ; N_w\lambda_w < z \end{cases} . \quad (2)$$

which describes the adiabatic entry taper over N_w wiggler periods.

The random component is chosen at regular intervals using a random number generator, and a continuous map is used between these points. Since a particular wiggler may have several sets of pole faces per wiggler period, the interval is chosen to be $\Delta z = \lambda_w/N_p$, where N_p is the number of pole faces per wiggler period. Hence, a random sequence of amplitudes $\{\Delta B_n\}$ is generated, where $\Delta B_n \equiv \Delta B_w(n\Delta z)$. The only restriction is that $\Delta B_w = 0$ over the entry taper region to ensure a positive amplitude. The variation in $\Delta B_w(z)$ between these points is given by

$$\Delta B_w(n\Delta z + \delta z) = \Delta B_n + \left[\Delta B_{n+1} - \Delta B_n\right] \sin^2\left(\frac{\pi}{2}\frac{\delta z}{\Delta z}\right) , \quad (3)$$

where $0 \le \delta z \le \Delta z$. Note that it is possible to model the effects of pole-to-pole variations in specific wiggler magnets with this formulation.

The configuration under study is one in which a 3.5 MeV/850 A beam with an initial radius of 1.0 cm propagates through a rectangular waveguide [$a = 9.8$ cm, $b = 2.9$ cm] in the presence of a wiggler with $B_w = 3.72$ kG, $\lambda_w = 9.8$ cm, and $N_w = 5$. This corresponds to an experiment at LLNL,[13,14] and comparisons between WIGGLIN and the experiment show good agreement without recourse to inclusion of space-charge forces.[7,8] Interaction occurs with the TE_{01}, TE_{21} and TM_{21} modes at frequencies of 30-40 GHz, and the efficiency decreases across this band. For an ideal beam and wiggler [*i.e.*, $\Delta\gamma_z = 0$ and $\Delta B_w = 0$], the efficiency falls off from a maximum 12.38% at 30 GHz to a minimum of 3.58% at 40 GHz. A frequency of 34.6 GHz with an

efficiency of 8.57% is selected for the comparison. The efficiency decreases gradually with the axial energy spread for $\Delta\gamma_z/\gamma_0 \leq 3\%$, at which point the efficiency falls to 5.45%.

Random wiggler fluctuations can take many different forms for a fixed rms value. It is most natural to consider a random fluctuation which is relatively uniform over the interaction region [*i.e.*, $\langle \Delta B_w \rangle = 0$]; however, other configurations are possible. For example, fluctuations where $\langle \Delta B_w \rangle > 0$ or $\langle \Delta B_w \rangle < 0$ are possible, as is one in which ΔB_w is very large over a small range and zero elsewhere. These are only limited examples, and a thorough analysis necessitates a large number of simulation runs with different random wiggler fluctuations to obtain adequate statistics. In practice, we find that 35 runs provide convergence to within ≈ 1%.

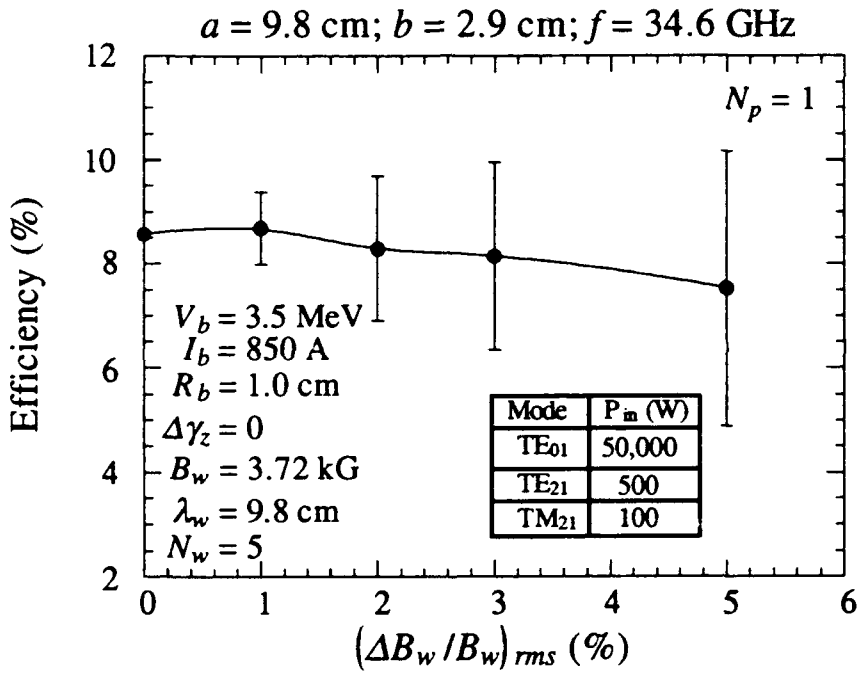

Fig. 1 Variation in the efficiency as a function of rms wiggler error for $N_p = 1$.

The effect of random wiggler errors is shown in Fig. 1 where the efficiency is plotted versus the rms wiggler error for $\Delta\gamma_z = 0$ and $N_p = 1$. The dots represent the average efficiency over the *ensemble* of random fluctuations, and the error bars denote the standard deviation. The average efficiency is relatively insensitive to wiggler errors for $(\Delta B_w/B_w)_{rms} \leq 5\%$, although the standard deviation increases with the rms error. For this example, the effect of a given $(\Delta B_w/B_w)_{rms}$ is much more benign than for a comparable $\Delta\gamma_z/\gamma_0$. Particle loss was not found to be a problem. In addition, the statistical distribution of the efficiency differs from the normal distribution, and the standard deviation must be used with some caution. For example, the

distribution for $(\Delta B_w/B_w)_{rms} = 3\%$ exhibits a skewness ≈ -0.41 and a kurtosis ≈ 0.92 indicating a distribution skewed below the mean and more peaked than the normal distribution

Observe that the efficiency increases relative to the ideal wiggler case for some particular wiggler error distributions. There are several mechanisms by which this can occur. First, note that the efficiency varies across the frequency band. This tuning can also be accomplished by variations in the wiggler magnitude, and an increase (decrease) in $\langle \Delta B_w \rangle$ can be expected to result in an increase (decrease) in the efficiency. Second, the error distribution can affect the efficiency is if the field exhibits a bulk taper either upwards or downwards over the interaction region. A downward (upward) taper can be expected to increase (decrease) the efficiency. It is the latter cause which appears to be responsible for the largest increases or decreases in the efficiency.

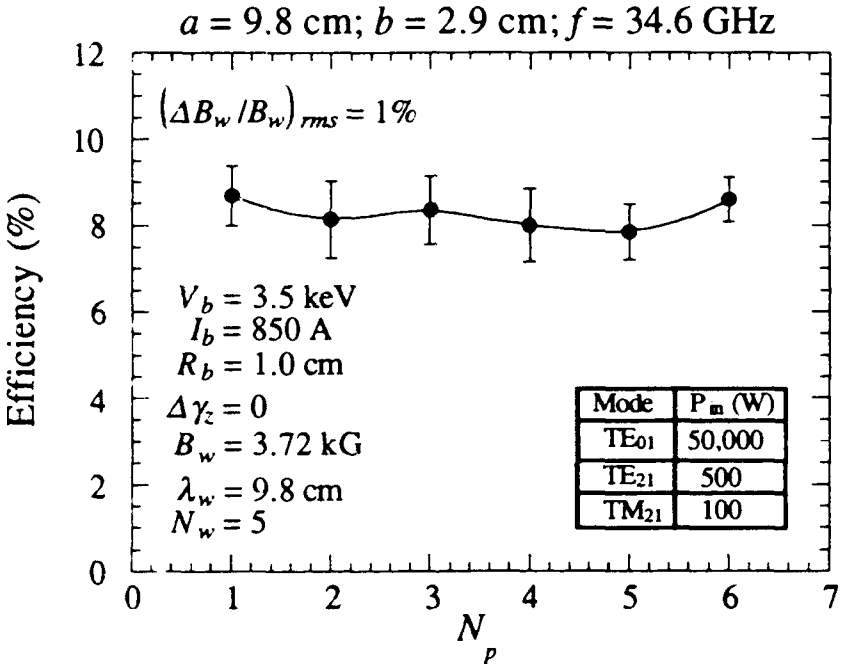

Fig. 2 Variation in the efficiency as a function of N_p for a 1% rms wiggler error.

The effect of variations in the spacing of the random fluctuations is shown in Fig. 2 in which we plot the efficiency as a function of N_p for $(\Delta B_w/B_w)_{rms} = 1\%$. In practice, the variation in the spacing between the random wiggler fluctuations is governed by the number of pole faces per wiggler period in a specific wiggler design. Note also that wiggler designs with more than 4 pole per wiggler period are unlikely, and that we have gone beyond this range in the figure merely to test the parameter space. In view of this, it is evident from the figure that the results are not extremely sensitive to the spacing of the random errors, although there appear to be minima in the

efficiency for N_p = 2 and 4. Observe that for a fixed length system, increases in N_p imply an increase in the number of random jumps in the wiggler amplitude.

IV. THE REVERSED-FIELD FEL

The reversed field experiment[10,11] was an amplifier in which the beam is injected into a cylindrical waveguide of 0.51 cm radius in the presence of both a helical wiggler and a guide field. The helical wiggler had a period of λ_w = 3.18 cm, a length of $50\lambda_w$, and a six period entry taper. The wiggler amplitude was adjustable up to an amplitude of ≈ 1.8 kG. The guide field could be adjusted up to a maximum of ≈ 12 kG. The interaction is with the TE_{11} mode at 33.39 GHz, which is the frequency of the drive magnetron. The magnetron produces ≈ 17 kW (±10%) in a linear polarization corresponding to 8.5 kW in the circular polarization capable of interacting with the helical wiggler geometry. The beam energy was 750(±50) keV, and beam quality was controlled by scraping the beam with a shaped graphite anode. The beam radius was 0.25 cm [the anode aperture radius], and the axial energy spread was $\Delta\gamma_z/\gamma_0 \approx 1.5\%$. The current at the wiggler entrance was 300(±30) A. However, the propagating current varied with the orientation and magnitude of the guide field. The current generally increased with increases in the guide field, except when the Larmor and wiggler periods were comparable. In the field-reversed case in which the wiggler and guide fields were anti-parallel, the increase in the propagation current leveled off when the Larmor and wiggler periods were comparable [i.e., the *anti-resonance*]. The anti-resonant effect is important for beams big enough that electrons far from the axis experience a varying wiggler field which results in an anti-resonant enhancement in orbital perturbations.

Peak efficiency occurred at a power of 61 MW [for an efficiency of 27%] for wiggler and axial field magnitudes of ≈ 1.47 kG and 10.92 kG respectively. The propagation current for these fields was near the maximum of 300 A. The output power for the field-reversed configuration also showed a sharp decrease in the vicinity of the anti-resonance, dropping by more than three orders of magnitude. The power observed when the guide field was parallel to the wiggler [≈ 4 MW] was much less than for the field-reversed configuration.

The experiment has operated with the guide field oriented both parallel and anti-parallel with the wiggler, and we shall limit the discussion here to the field-reversed orientation. A more complete discussion of the comparison is given in ref. 15. We use the actual experimental parameters in ARACHNE; specifically, a waveguide radius of R_g = 0.51 cm, a wiggler period of λ_w = 3.18 cm, a wiggler entry taper of N_w = 6 wiggler periods, and a beam energy and initial radius of 750 keV and 0.25 cm. In all cases, we use the measured beam current for the given values of the guide field. The initial power of the TE_{11} mode is chosen to be 8.5 kW. The only Gould-Trivelpiece modes which interact in this case have an azimuthal mode number of $l = 0$, and only the lowest order radial mode is required to give reasonable agreement with the experiment.

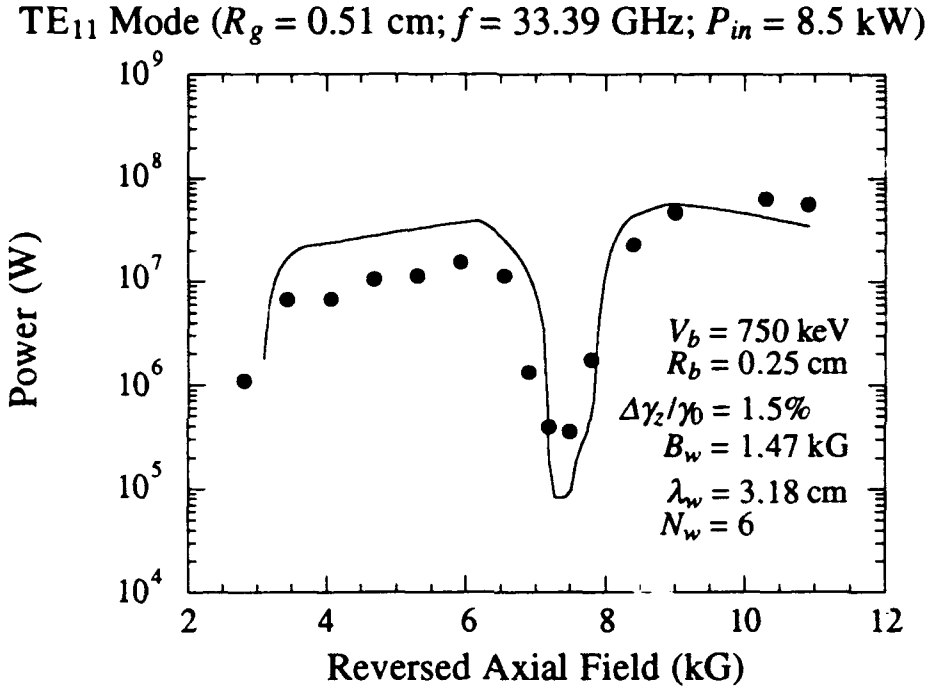

Fig. 3 The variation in the output power versus the magnitude of the reversed axial field as measured in the experiment (dots) over an interaction length of 150 cm and with ARACHNE.

The variation in the power over a length of 150 cm as a function of the reversed magnetic field is shown in Fig. 3. The dots represent the measured power and the curve is from ARACHNE. The current used in the simulation for each value of the axial field corresponds to the measured current.[10,11] Agreement between the experiment and theory is good across the entire range studied. Of particular note, however, is the sharp decrease in the output power in the vicinity of the anti-resonance at axial field magnitudes between approximately 7-8.5 kG.

The source of the anti-resonant decrease in the interaction efficiency is the irregularity introduced in the electron trajectories by the transverse wiggler inhomogeniety.[15,16] For this example, the radius of the wiggler-induced motion is $\approx$ 0.04 cm. However, the beam radius is 0.25 cm. As a consequence, the electrons at the outer regions of the beam are quite sensitive to the wiggler inhomogeniety, and experience a sinusoidally varying wiggler field during the course of their trajectories. The effect of this sinusoidal variation is to act as an anti-resonant harmonic driver to the electron orbits which distorts the wiggler motion and degrades the interaction.

V. SUMMARY AND DISCUSSION

In this paper, we have presented the application of two 3-D nonlinear formulations, ARACHNE and WIGGLIN, to realistic problems in FEL design and operation. ARACHNE deals

with a helical wiggler model, and shows substantial agreement with a high-power Raman FEL using a helical wiggler/guide field in a reversed-field configuration. Two significant new results are represented by this comparison. The first is the near-30% efficiency with a uniform-wiggler. While efficiencies of this magnitude are expected on the basis of both simple phase-trapping arguments and detailed numerical simulations, this is the first time such efficiencies have been demonstrated in the laboratory. The second, is the existence of the anti-resonant degradation in the operating efficiency. This had been previously unsuspected, and the experimental demonstration of the effect has been instrumental in pointing the way toward a theoretical reexamination of the orbital dynamics in this regime. WIGGLIN deals with planar wiggler configurations, and has been applied to the self-consistent treatment of random wiggler errors. For the specific parameters under study, the results indicate that the effects of random wiggler errors are relatively benign. Indeed, some error configurations chosen at random were found to result in efficiency enhancements due to effective increases. It is important to note here that experimental quantification of these issues is difficult to obtain. While measurements for $(\Delta B_w/B_w)_{rms}$ are possible to achieve with some accuracy, there is always a greater uncertainty as to beam quality. Hence, it is difficult to determine the relative importance of wiggler errors in the laboratory. The results of the present work, however, suggest that wiggler errors may not constitute a serious issue for FEL design.

ACKNOWLEDGMENTS

This work was supported by ONR and the ONT. We would like to thank G. Bekefi and M.E. Conde for providing us with the experimental data.

REFERENCES

†Permanent Address: Science Applications International Corp., McLean, VA 22102.
[1]A.K. Ganguly and H.P. Freund, Phys. Rev. A **32**, 2275 (1985) .
[2]H.P. Freund and A.K. Ganguly, Phys. Rev. A **33**, 1060 (1986).
[3]H.P. Freund and A.K. Ganguly, Phys. Rev. A **34**, 1242 (1986).
[4]H.P. Freund and A.K. Ganguly, J. Quantum Electron. **QE-23**, 1657 (1987).
[5]A.K. Ganguly and H.P. Freund, IEEE Trans. Plasma Sci. **16**, 167 (1988).
[6]A.K. Ganguly and H.P. Freund, Phys. Fluids **31**, 387 (1988).
[7]H.P. Freund, H. Bluem, and C.L. Chang, Phys. Rev. A **36**, 2182 (1987).
[8]H.P. Freund, Phys. Rev. A **37**, 3371 (1988).
[9]H.P. Freund and R.H. Jackson, Phys. Rev. A (in press).
[10]M.E. Conde and G. Bekefi, Phys. Rev. Lett. **67**, 3082 (1991).
[11]M.E. Conde and G. Bekefi, IEEE Trans. Plasma Sci. (this issue).
[12]N.A. Krall and A.W. Trivelpiece, *Principles of Plasma Physics* (McGraw-Hill, New York, 1973), p. 202.
[13]T.J. Orzechowski *et al.*, Phys. Rev. Lett. **54**, 889 (1985).
[14]T.J. Orzechowski *et al.*, Phys. Rev. Lett. **57**, 2172 (1986).
[15]H.P. Freund and A.K. Ganguly, IEEE Trans. Plasma Science (in press).
[16]K.R. Chu and A.T. Lin, Phys. Rev. Lett. **67**, 3235 (1991).

Invited Advanced Accelerator Papers

Charles Roberson, *Session Chairman*

LINEAR ACCELERATOR WITH RADIAL LINES - LIA-30

A.I.Pavlovskii, V.S.Bossamykin, A.I.Gerasimov, V.A.Tananakin,
A.S.Fedotkin, K.A.Morunov, V.F.Basmanov, G.M.Skripka,
A.D.Tarasov, A.V.Grishin, V.P.Gritzina, V.Ja.Averchenkov,
O.N.Sjutin, S.A.Lazarev, V.S.Gorkunov, V.P.Veresov

Experimental Physics Research Institute
Arzamas-16, Nizhny Novgorod Region, 607200 RF

Multimodule linear induction 40 MeV accelerator on radial lines with distributed parameters, a powerful generator of bremsstrahlung radiation, is briefly described. More than 2000 controlled spark switches commutate low-impedance inductor lines according to a specified program at nanosecond accuracy. The electron beam of to 100 kA current is transported in the external longitudinal magnetic field over the beamline 25 m long. Some research results in optimization of the conditions for annular electron beam transportation and feasibility of various acceleration regimes are noted.

Introduction

From middle 60^{ties} the authors have been working at ironless linear induction accelerators (LIA). In 1967 the first accelerator of this type was accomplished at 2 Mev energy and 2 kA current per 40 ns pulse [1]. It united all the elements of the primary circuit of a pulsed transformer into an uni-turn coil toroidal oscillatory contour-inductor. Different schemes of toroidal contours were analyzed, namely the possible application of powerful energy sources - magnetocumulative generators [2]. In 1968 a new LIA type on radial lines with distributed parameters was suggested (A.I.Pavlovskii, V.S.Bossamykin) [3,4]. It combines the capability for acceleration energy increase with growth of an accelerating system length and high current peculiar to the direct discharge in low-impedance lines. Various inductors were considered which employed the forming lines where the necessary for acceleration energy is stored [2,5,6]. Beginning with the late 70^{ties} new schemes based on stepped lines with capacitive and inductive energy storage were analyzed and implemented [7]. In 1977 the first accelerator on radial lines of series modular structure for an accelerating system - LIA-10 [8] was put into operation at 14 Mev energy and 50 kA current per 20 ns pulse. The acceleration rate was 1.7 Mev/m. A new technology was created based on 500 kV elements and multimodule accelerating system employing

hundreds of spark switches operating according the specified program at nanosecond accuracy, methods for high current electron beam shaping and conduction, etc. were developed. Alongside with LIA-10 creation and operation, a new accelerator, LIA-30, was under design. In 1985 its main units were tested, and in 1989 it become operative. LIA-30 is the electron accelerator to 40 Mev energy at 100 kA beam current per 20 ns pulse. It is a powerful bremsstrahlung radiation generator providing $5 \cdot 10^{11}$ rad/s (TLD) intensity and to 10^4 rad (TLD) dose at one meter from the target. On 500 cm^2 area the maximal radiation intensity has been achieved 10^{13} rad/s and the dose - 10^5 rad. Two bremsstrahlung pulses can be generated with a lower boundary energy. If a U^{238} target is used, photoneutron pulse of 10^{14} n/pulse total yield and 10^{22} n/s intensity can be achieved. With comparatively simple and safe multiplying systems, the high pulse intensity can provide fission neutron pulses of 10^{16}-10^{17} n/pulse total yield at 1-10 μs generation.

The current report briefly describes LIA-30 and some results of its investigations.

Accelerator Design

LIA-30, which general view is presented in fig. 1, comprises of an injector, accelerating system, an output device and Marx type pulsed voltage generators (PVG) to charge the inductor forming lines, a synchronization system for accelerator units, a condenser storage of energy to create a longitudinal magnetic field in the beamline and output device. Technological and auxiliary equipment provides its normal operation regime, and the automated control and monitor system - its control. The accelerator dimensions are: length - 25 m, width - 9.5 m, height - 4 m. The acceleration rate is 1.7 MeV/m.

LIA-30 accelerator concept is based on inductors employing non-uniform radial lines with distributed parameters [2]. Each inductor comprises of two radial lines formed by a central disc electrode and a grounded toroidal cavity opened in its inner diameter. In radial lines energy is accumulated when disc electrode capacitances are quickly charged by a pulsed generator.

When a ring commutator closes a gap in the inner diameter of one of the radial lines, an accelerating voltage appears on the second radial line gap. The first voltage pulse duration approximately equals the wave transit time in the forming line formed by two radial lines. The acceleration regime can be achieved at the second voltage pulse which lasts the

double transit time of a current wave in the forming line.

In LIA-30 ~40 MeV accelerating voltage is generated in the pre-axial volume of the accelerator by 144 inductors included in the injector and accelerating system. As a dielectric, high specific resistance water (~10 MOhm.cm) is used in the radial lines. The inductors in the injector and the accelerating system are of the same design and differ in diameters and voltage pulse width, wave resistance and energy store correspondingly. At 500 kV charging voltage the gap in the radial lines is 5 cm long for all inductors. Shielding rings reduce the electric field concentration at the edges of the disc electrode.

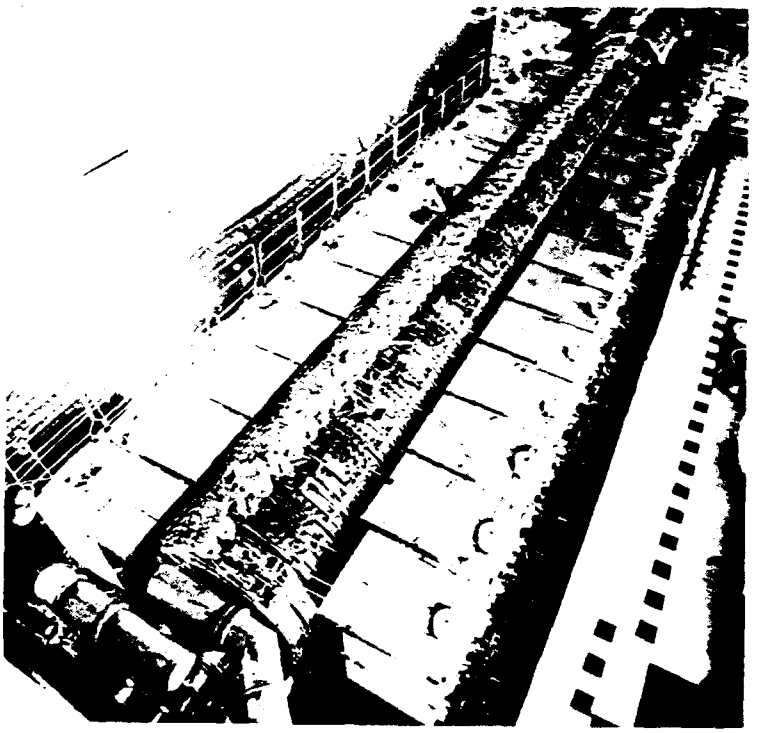

Figure 1 General view of LIA-30 accelerator.

This design unites each four inductors in the inductor unit with a common accelerating tube. Between inductors there are technological cavities for cables and gas trunks leading to the switches located at the inner diameter of the radial lines. Thus, the acceleration tempo is reduced approximately by 25%. Two inductors are coupled in the charging circuit in each unit and are charged with one pulsed generator.

Separate spark-gap switches of a trigatron type are employed for annular commutation of low-impedance radial lines. Minimal number of spark-gap switches was determined by the forming conditions for a cylindric current wave, time discrimination of spark channels as well as by commutated energy and current. In the injector units the radial lines are commutated by 24 switches and in the accelerating ones - by 16 switches. All in all, LIA-30 employs 2432 spark-gap switches operating at a nanosecond accuracy according to the specified time program. This is the most critical component of the accelerator as it

works under ultimate electric fields, static and shock affects. As the space for this switch location is rather limited (5 cm), there was a difficulty in the development of a highly reliable and accurate switch. Vast researches were demanded including tens of thousands of bench tests and experiments with separate inductors and inductor units to create a reliable switch for 500 kV voltage which can be placed in the radial line gap. The characteristics mentioned are true for the switch included in the radial line. The electric field is uniformly distributed along the dielectric casing of the switch due to the relevant choice of a shield geometry in the region of switch coupling with the line disc electrode. Thus, the maximal electric field strength does not exceed 80 kV/cm. The design concept of the switch fixing to the grounded electrode of line provides a relatively low electric field strength, ~30 kV/cm, in the metal-dielectric contact region. In the switch placed in caprolone casing two main electrodes 4 cm in diameter and a trigger electrode manufactured of the tungsten alloy are located. With the chosen electrode geometry and switch filling with 20% SF_6 + 80% N_2 mixture the electric strength resource is 100% over spark gap (2.5 cm) at 1.2 MPa pressure. The switching-on accuracy ±1 ns is achieved when a 50 kV, 5 ns voltage pulse is fed on the trigger electrode. The switch lifetime is 10^4 times of switching-on when ~500 J energy and 70 kA current are commutated.

The lines are charged to 500 kV in pulses in 0.75 μs with PVG. The PVG's used for charging the radial lines of the inductors for the injector and the accelerating system differ in energy store as well as in some schemes and switches number. The PVG's charging lines of two inductors of injector units store 32.5 kJ and those for the accelerating units - 20 kJ. Five-cascade PVG's are employed with two parallel discharge circuits mounted in metal casings, filled with transformer oil. The capacitors charged to 100 kV are commutated by gas-filled (40% SF_6 + 60% N_2) spark switches of the trigatron type. The commutation accuracy is ±5 ns at ~100% resource of spark-gap electric strength. This switch operation lifetime is 10^4 commutations at 30 kJ commutated energy and 120 kA discharge current. 72 PVG's of LIA-30 accelerator contain 668 switches of this type.

Fig. 2 presents the schematic cross-section of LIA-30 injector. An annular electron beam is formed in a foilless diode magnetically insulated by longitudinal magnetic field. The voltage from four inductor units are summed in the diode formed by a cylindric part of the cathode and anode electrodes. The electron beam diameter can vary from 0.1 to 0.3

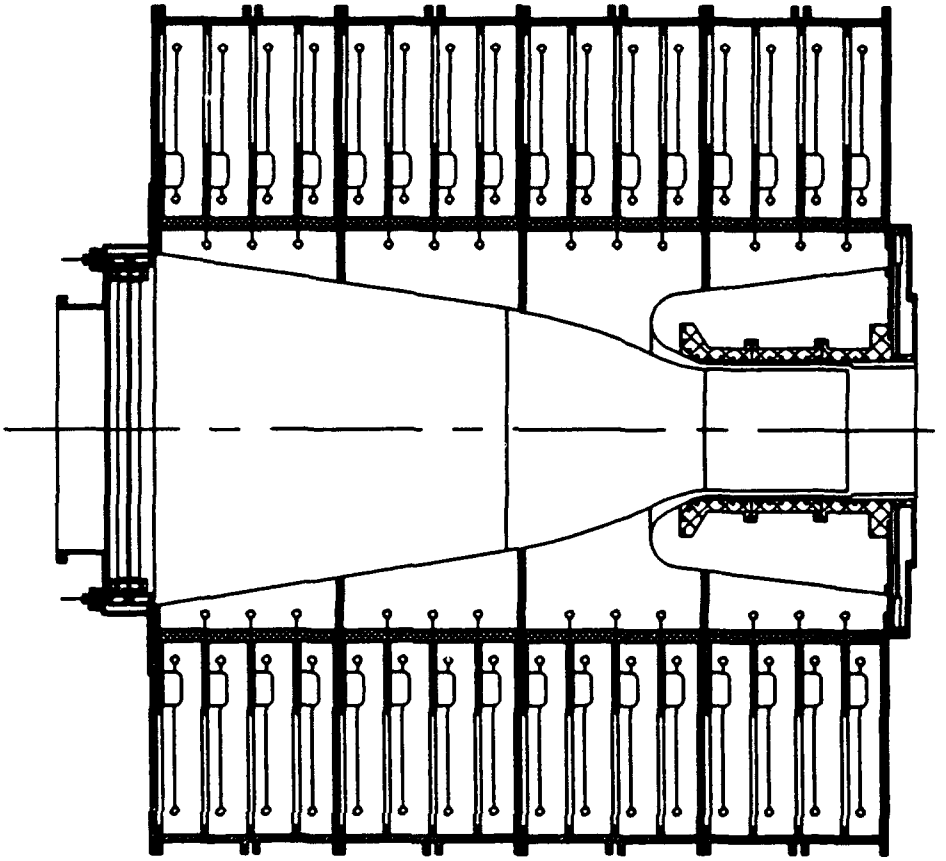

Figure 2 Schematic cross-section of LIA-30 injector.

m with the change in the diameters of the emitting part of the cathode and anode electrodes. The longitudinal magnetic field to 6 kOe is produced by a solenoid placed inside the anode. The cathode electrode 2 m long and 1.7 m in base diameter as well as the anode are manufactured of sheet stainless steel. They have polished external surfaces. The cathode electrode conical part angle is determined under the condition of electric field strength constancy along its surface, and the transient and cylindrical parts - under the condition on magnetic insulation. The injector unit inductor diameters are 3 m, the line wave resistance - 0.4 Ohm. The energy store of radial lines for four inductor units is 250 kJ. The accelerating tube in each unit contains polyethylene rings 1.2 m in inner diameter and 1.4 m in outer diameter and the gradient electrodes. The chosen design concept provide

minimal electric field strength at metal-dielectric contacts and its uniform distribution along the insulator surfaces. Thus, the maximal electric field strength does not exceed 35 - 40 kV/cm. LIA-30 injector allows to shape 4 MeV, 200 kA annular electron beam 0.3 m in diameter in a 35 ns pulse.

Fig. 3 is a schematic cross-section of one of 32 inductor units in LIA-30 accelerating system. In the radial lines of this accelerating system 1.2 MJ energy is accumulated, the unit diameter being 2 m. The electron beam is transported in ~6 kOe uniform longitudinal magnetic field. It is produced by 64 solenoids having thick-wall metal shields. The voltages from each two inductors are concentrated in the gaps between the solenoid shields. The non-uniformity of the magnetic field at 0.3 m diameter does not exceed 2% at 1 ms rise time of the magnetic field and the specified shield thicknesses and solenoid coil pitch. The energy source for magnetic field production in the beamline and the output device is 6 MJ condenser bank.

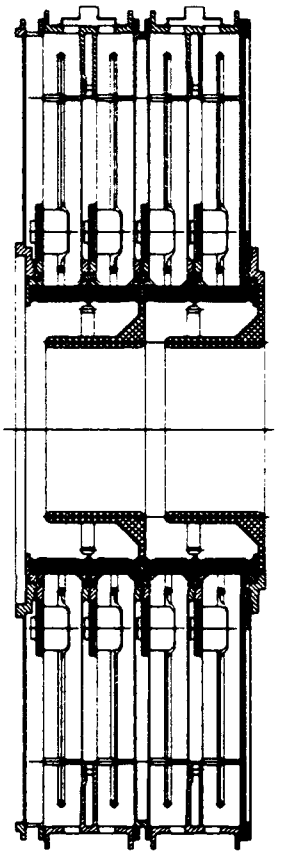

Figure 3 Schematic cross section of an accelerator unit.

The output device assists in transporting the accelerated electron beam for 4 m from the accelerating system end, then it is compressed in the growing along the axis longitudinal magnetic field.

The target for bremsstrahlung radiation generation is fabricated of the tungsten-based composite and is transparent for the slowly growing magnetic field. Thus it can be located in the magnetic field used for beam transportation without path perturbations of the electrons impinging on the target.

LIA-30 synchronization system provides the nanosecond accuracy of switching-on according to the specified time sequence for radial line commutators (two switches are triggered by one pulse), 72 PVG's charging pulsed line and some other devices. Triggering pulses of 100 kV amplitude and 5 ns rise-time are produced by the generators (19 pieces) of multichannel commutation of low-impedance lines with the pulsed charging. The reliable

operation of accelerator synchronization and commutation systems is achieved due to the duplication of trigger pulse channels for radial line switches, commutators of intermediate and output triggering pulses generators as well as the generators themselves. If only one channel is switched on, it provides triggering of one half of switches in each radial line.

LIA-30 automated control and monitor system is a structure comprising the manual control devices with local automatics and a three-level computer complex with communication means at the monitored object. It records and controls nearly 2000 various signals, namely with 40 ns discrete intervals, and generates 200 control and block commands. This system is an open one and can evolve both by adding to the number of control and monitor channels and by new subsystem introduction. The control and monitor system can provide for the absolutely automated regime of experiments according to the specified scenario at one operator command.

Diagnostics

The operation of main accelerator components and units is monitored in each shot. Thus the following is measured:

- current pulses charging inductor lines by 72 pulsed voltage generators;
- voltage for line charging in inductors;
- current pulses in 80 solenoids producing a longitudinal magnetic field;
- triggering pulse parameters and synchronization system generator switching time of ±1 ns accuracy;
- current in the injector and its output;
- accelerated electron current in 12 points along the beamline;
- pulse voltage in 6 acceleration gaps.

Images of electron beam cross-section are recorded with color film dosimeters employing low-energy electron absorption filters. The information on high-energy electron distribution in the accelerated beam cross-section is received from activation measurements of metal foils having 11-18 Mev range of photonuclear reaction thresholds.

Thermoluminescence dosimeters record bremsstrahlung radiation doses near the target, a dose field of a directed radiation flux and an output electron beam. Ten recording channels of 0.3-1.5ns time resolution reliably measure bremsstrahlung radiation dose rate.

Wide range measurements of radiation intensity are done with Compton, diamond, scintillation and semiconductor detectors of radiation.

The boundary energy and bremsstrahlung radiation spectrum are determined by time-of-flight measurements of photoneutron energies. The numerical simulation techniques are developed for wave transient processes in non-uniform concentrated component lines. The computations were tested according to experimental data accounting loading characteristics, real losses in electric circuits, probable azimuthal current non-symmetry in multichannel commutators. The calculation models account the peculiar interactions of high-current electron beams with the accelerating system. Nowadays, it is possible to describe electric processes of electron beam formation in the injector and the subsequent acceleration in multi-unit inductor system being computated at the statistic jitter relatively to the specified time sequence. A beam configuration is considered specified, nevertheless, the computation satisfactorily describes the processes of energy gain and successive generation of bremsstrahlung radiation.

Some Research Results

By gradual augmentation of the number of accelerating inductor units, LIA-30 accelerator was put into the projective operation. Thus, the following basic problems were solved:

- determination of the conditions for a annular beam formation in a magnetically insulated diode at the minimal transversal particle energies in the region of a virtual cathode;
- optimization of a switching-in program for the accelerating inductor units at the initial stage of acceleration when a beam front velocity is less than the light velocity, and its successive correction to match a beam current gain rate and an accelerating field rate;
- determination of the conditions for effective transportation of an electron beam to a target;
- optimization of bremsstrahlung radiation output in a dose and dose rate.

In the course of investigations a beam diameter varied from 0.15 m to 0.25 m, as well as an injection energy, a form and duration of injection pulse via the programmed switching of injector inductor units. The experiments were conducted with a magnetically insulated injection system comprising four injector units and four accelerating units of inductors being

switched on according to the definite time program. The voltage was summed up at the diode with conical cathode electrode 5 m long which formed a annular beam 0.25 m in diameter. At the output of such injection system a 180 kA, 7 MeV beam was obtained. However, for a considerable current beam portion transversal particle energies happened to be too big for effective transportation along LIA-30 beamline.

Various accelerator operation regimes were studied. Bremsstrahlung radiation pulse can be varied in 5-24 ns range, and the leading front - 2-10 ns. The experiments were done to study the transportation of electron beam 0.15 m in diameter at injection energy along the beamline. At the output a substantial variation in current pulse duration and shape was noted. The efficiency of a charge passing is 0.9, not less. The generation regime of two gamma-pulses with a < 0.5 ms interval was realized. In the first pulse the electrons are accelerated by a system of 15 inductors including injector units. The cathode diameter is 15 cm. The rest part of the accelerator is employed to produce the second pulse. As an injector, a diode served with a thin-wall hollow cathode 25 cm in diameter where voltages of two accelerating inductor units were summed up. The first beam was shot through it. Thus, three autonomous acceleration regimes were accomplished at 15 MeV, 25 Mev and to 40 MeV electron energies.

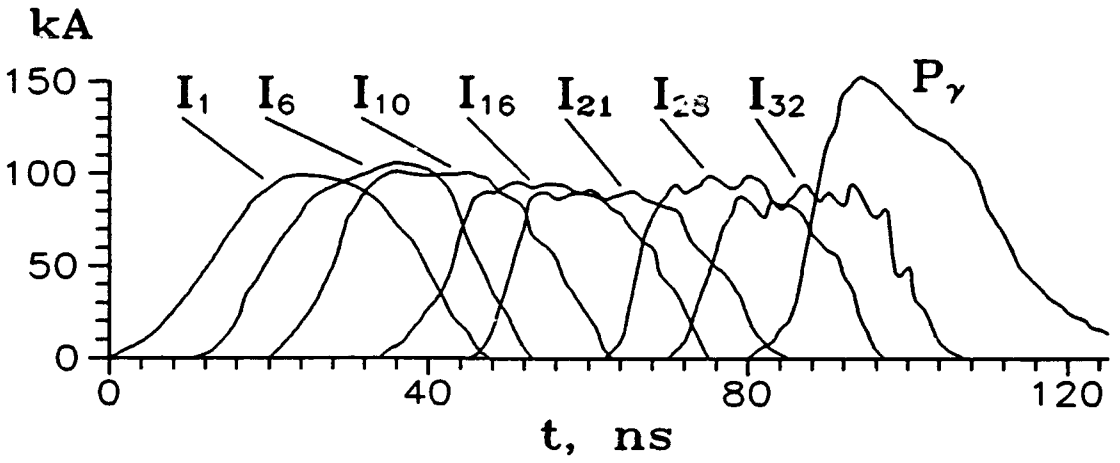

Figure 4 Pulsed current oscillograms recorded in the inductor unit along the beamline and the oscillogram of bremsstrahlung radiation pulse P_γ, generated from the target located in the output device.

In one-pulse generation regime at maximal dose and dose rate, the injector with the cathode 15 cm in diameter is employed, and a beam is formed in the anode region. Figure 4 presents the current pulse oscillograms recorded along the beamline in the effective beam transport regime, and the bremsstrahlung pulse. The efficiency of a charge transportation to a target is usually 0.7-0.8. The transversal thickness of an electron layer on the target grows till 8 cm at a dose half-height, the average radius remaining 15 cm. The rotation of a beam as a whole is absent at the accelerator output. Minimal total divergence angle is 20° for bremsstrahlung radiation flux at intensity half-height. It grows at magnetic field variation in the target area.

In conclusion it should be noted that LIA-30 facility provides the accelerated electron energy which is record for this class of accelerators that enlarges the application field for high-current accelerators. The stable operation of multimodule accelerating system is achieved by high reliability of its components and units. The research of possible acceleration regimes has not been completed. There are grounds for a hope to further increase in beam current at LIA-30 output.

References

1. A.I.Pavlovskii, A.I.Gerasimov, D.I.Zenkov et al. "Ironless Induction Accelerator", AE, t. 28, vyp. 5, s. 432-437 (1970).
2. A.I.Pavlovskii, V.S.Bossamykin "Ironless Linear Induction Accelerator", AE, t. 37, vyp. 3, s. 228-232 (1970).
3. A.I.Pavlovskii, V.S.Bossamykin, G.D.Kuleshov et al. "Multielement Accelerator on Radial Lines", DAN SSSR, t.222, No.4, s. 817-820 (1975).
4. A.I.Pavlovskii, V.S.Bossamykin, V.A.Savchenko et al, "Powerful Electron Accelerator, LIA-10", DAN SSSR, t.250, No.5, s. 1118-1122 (1980).
5. V.S.Bossamykin, V.S.Gordeev, A.I.Pavlovskii, "New Schemes of Pulsed High-Voltage Generators Based on Stepped Lines", this Proceedings.

TECHNOLOGY DEMONSTRATION FOR THE DARHT LINEAR INDUCTION ACCELERATORS

M. Burns, P. Allison, J. Downing, D. Moir
Los Alamos National Laboratory, Los Alamos, NM 87545

G. Caporaso, Y.J. Chen
Lawrence Livermore National Laboratory, Livermore, CA 94550

Abstract

The Dual-Axis Radiographic Hydrodynamics Test (DARHT) facility will employ two 16-MeV, 3-kA Linear Induction Accelerators to produce intense, bremsstrahlung x-ray pulses for flash radiography. Technology demonstration of the key accelerator sub-systems is underway at the DARHT Integrated Test Stand (ITS), which will produce a 6-MeV, 3-kA, 60-ns flattop electron beam. We will summarize measurements of ITS injector, pulsed-power, and accelerator cell performance. Time-resolved measurements of the electron beam parameters will also be presented. These measurements indicate that the DARHT accelerator design is sufficiently advanced to provide the high quality electron beams required for radiography with sub-millimeter spatial resolution.

I. Introduction

The DARHT facility at Los Alamos will generate intense bremsstrahlung x-ray pulses for radiography using two linear induction accelerators (LIA). Each LIA will produce a 3-kA, 16- to 20-MeV, 60-ns flattop, high-brightness electron beam using a 4-MeV injector and a series of 250-kV induction cells. The facility's mission requires radiographic spatial resolution of less than 1 mm through very dense objects moving rapidly in explosively driven experiments. The primary radiographic machine characteristics required for this application include the production of large x-ray dose (greater than 300 R one meter from the source) in short bursts (less than 100 ns) from a very small source size (1.2 mm). Detailed considerations of detector response, test object transmission, and the bremsstrahlung spectrum limit maximum electron-beam energy to 20 MeV. The high dose and short pulse width specifications thus require high peak current. LIA technology is the best choice for high current at modest energy while also producing the excellent beam quality required to achieve a small focal spot on the bremsstrahlung conversion target.

Existing LIAs have not been shown to possess characteristics to fully meet the DARHT requirements. Thus, important accelerator development has been completed and the Integrated Test Stand (ITS) constructed to demonstrate the key accelerator systems before construction of DARHT. The ITS consists of a large, 4-MeV pulsed-power injector, a 2.5-m drift section to match the electron beam into the accelerator, and an assembly of eight, 250-kV induction cells, referred to as the cell-block (Fig. 1). The test stand has been assembled in a step-by-step manner, with detailed measurements of electron-beam parameters and radiation production as each step has been completed.

In this paper we will discuss representative measurements made to date on the ITS. Section 2 will summarize injector performance and Section 3 will discuss the accelerator cells. In Section 4, we will cover accelerator pulsed power and will finish, in Section 5, with a description of upcoming work.

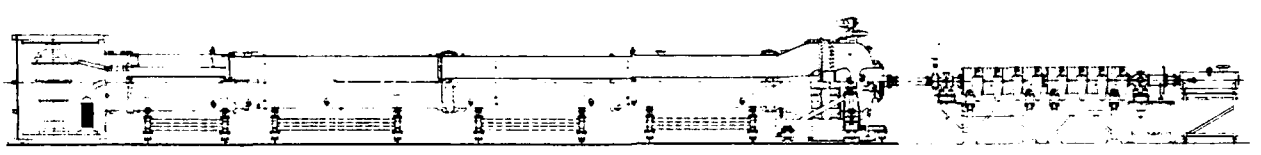

Figure 1. The DARHT ITS layout showing pulsed-power injector, accelerator cell block and diagnostic tank.

II. Injector

The ITS injector, developed from an earlier prototype [1] of a low-energy flash x-ray source, is shown in Fig. 2. The injector prime power supply consists of a 2.8-μF capacitor bank charged to 114-kV dc, and switched through the primary of a 1:15 Stangenes iron-core pulse transformer by a single gas-blown spark gap. A glycol Blumlein, consisting of a 7.65-Ω line and a 7.3-Ω line, is pulse-charged to 1.5-MV in 4.6 μs. The Blumlein is switched with four, parallel, laser-triggered spark gaps (measured jitter of 1.16 ns over 1050 pulses). The output pulse traverses an adjustable L-C filter, which converts the initially sharp-rising pulse to a [1-cos(ωt)] shape, with a 10-90% risetime of 20 ns. Three output lines transform the output pulse from 1.8 MV to 4.0 MV on the diode. A more complete description of the injector pulsed power has been given by Downing, *et. al.* [2].

A simplified cross-section view of the diode, with calculated equipotential lines, is shown in Fig. 3 [1]. A 76.2-mm-diam velvet emitter, centered on the cathode shroud, produces 3.8 kA at 3.9 MeV. Velvet turn-on is shown in Fig. 4, with space-charge-limited emission beginning about 1.75 MeV across a 198.4±0.5-mm A-K gap. The output current, delivered to the accelerator cell-block as well as that transported through the cell-block, is shown in Fig. 5. Peak current is reduced as expected through the non-achromatic transport of the matching section, thus approaching the design accelerator current of 3.0 kA, without discrete apertures. A complete description of ITS transport is provided at this conference by Hughes, *et.al.* [3].

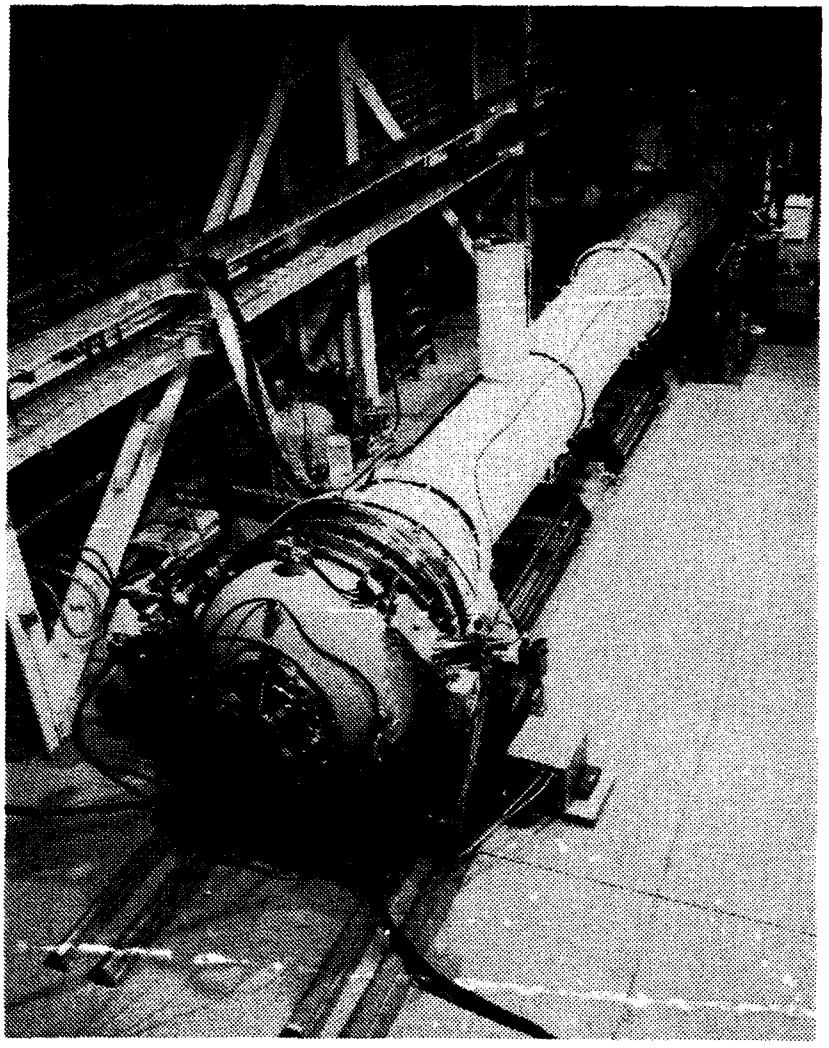

Figure 2. The ITS injector during installation.

The electron beam energy has been measured with a magnetic spectrometer whereby the beam is collimated entering the magnet and bent approx. 45° through an adjustable slit onto a Farady detector. The injector has demonstrated excellent reproducibility so that energy-spread measurements may be made over several shots. A current-weighted average of the detector signal provides the beam energy vs. time data shown with exaggerated scale in Fig. 6. Average energy during the 60-ns flattop is 3.92 MeV ± 0.7 %. DARHT requires an energy variation of <1%.

Emittance measurements of the electron beam are performed using a range-thick mask (typically a row of 1-mm-diam holes spaced 10 mm apart), which creates a series of beamlets that expand in a field-free region onto a scintillator and are viewed by a streak camera. Complete calibration of film response and camera and optics characteristics allow

detailed, time-resolved analysis of the hard-film record to produce an emittance measurement as described by Hughes [4] and also by Kaupilla [5]. Observation of the beam emittance at a point 2.4 meters downstream of the injector results in a measurement of 0.07±0.01 πcm-rad. Numerical studies of the DARHT accelerator and final focus set a baseline specification of 0.1 πcm-rad.

A photomultiplier tube mounted on the injector diode has noted insulator flashover on occasion. This time-resolved diagnostic detects light microseconds after the primary pulse. Prompt insulator flashover occurs on the next shot. Fig. 7 is a trace of the diode potential during and after the primary pulse and shows a long-duration, reverse polarity post-pulse approx. 2 μs after the primary pulse. Carlson [1] has shown the vulnerability of the radial insulator design to such a reverse-polarity post-pulse. Installation of a 50-Ω liquid resistor in series with the Blumlein charging inductor has decreased the amplitude of the long-duration post-pulse without greatly affecting other operation. This has resulted in a decrease in the number of insulator flashovers, although they still occur. We are now investigating possible charging of the aluminum grading rings imbedded in the insulator (Fig. 3).

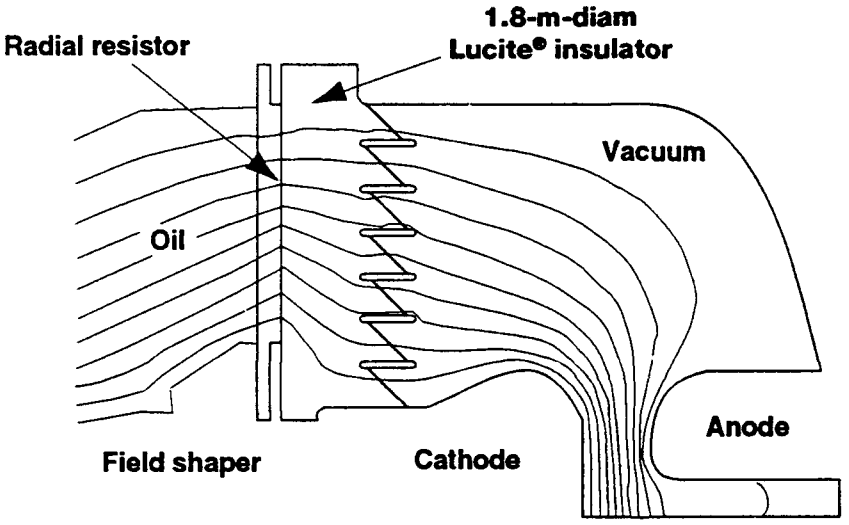

Figure 3. Schematic of ITS injector diode with equipotential lines.

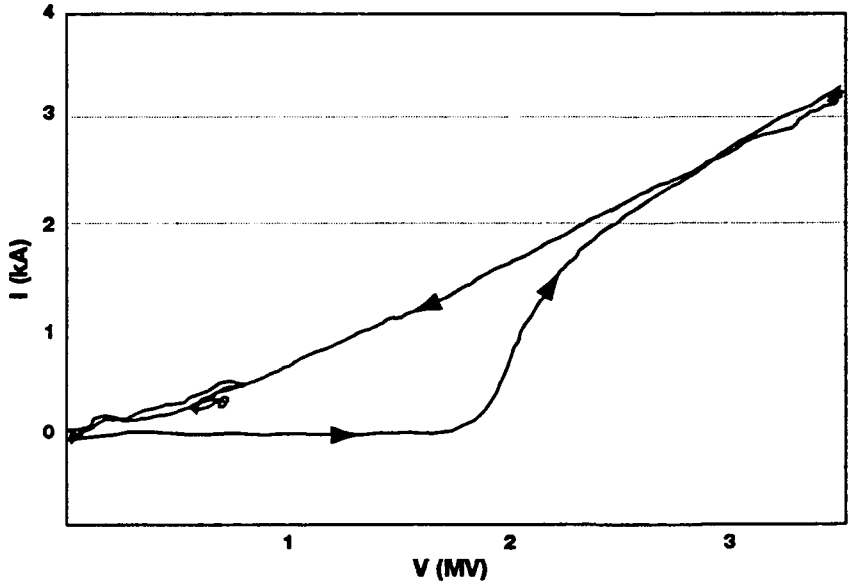

Figure 4. Time-aligned A–K current vs. voltage.

III. Accelerator Cells

The accelerator cell development process has been discussed earlier [6] and included the design, fabrication, and testing of three prototype cell configurations. The final configuration features a 148.2-mm-diam bore, 19.1-mm accelerating gap, 11 oil-insulated TDK PE11B ferrite toroids (237-mm ID, 503-mm OD, 25.4-mm thick), a low-dielectric-constant REXOLITE insulator, and a quadrufilar-wound solenoid magnet with iron homogenizer rings and two cosine-wound dipole trim magnets. Fig. 8 is a cross-section of the DARHT/ITS accelerator cell.

To minimize the growth of the BBU instability, the DARHT accelerator cell is designed for low transverse impedance. The two-dimensional, finite-difference, time-domain electromagnetic simulation code AMOS [7] was used to design each cell iteration. Measurements of transverse impedance were then carried out on full-sized test cells [8]. These measurements indicated that the high-voltage feed to the cell split the rf

modes substantially. Solenoid focusing causes the beam to rotate and interact with both horizontal and vertical modes. The average of the impedance measurements in both planes has been shown to be the important parameter in predicting BBU growth for DARHT [9]. The average impedance of the DARHT/ITS cell is shown in Fig. 9. The peak value of 670 Ω/m ±20% meets DARHT requirements and results in a miximum calculated BBU gain of <20 through a 20 MeV accelerator.

Accelerator cell magnet design is of great importance to minimize BBU and corkscrew instability. When compared to previous LIA solenoid magnets, the DARHT design used on the ITS greatly reduces transverse magnetic field errors by combining multifilar winding with iron homogenizer rings and dipole trim magnets [10]. The parameter used to judge the effectiveness of the magnet design for these 2 kG (peak) magnets is the magnetic-axis tilt, defined as the dipole field measured on axis divided by the local axial field. Fig. 10 shows such a measurement for a representative magnet used on the ITS. Placing the magnet into the accelerator cell and welding the cell shut results in mechanical fit tolerances which increase the magnetic axis tilt.

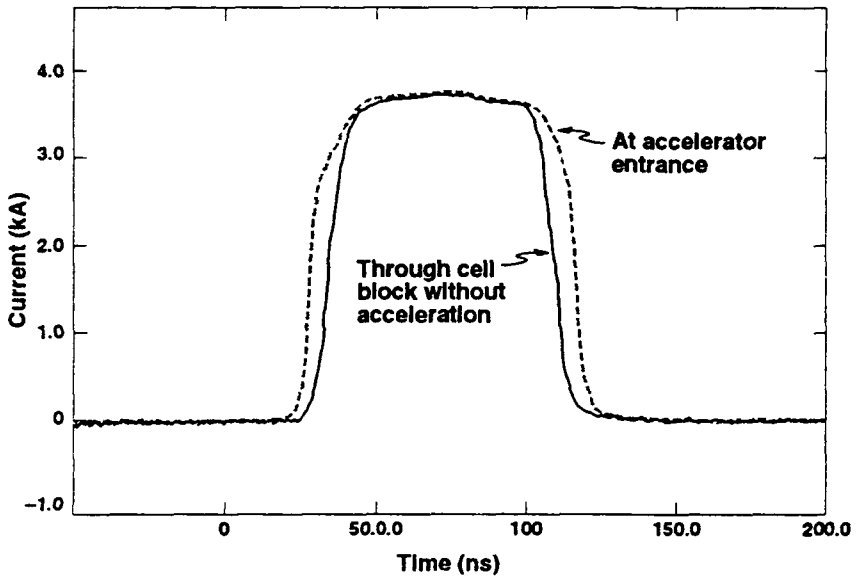

Figure 5. Beam current transported to and through cell block.

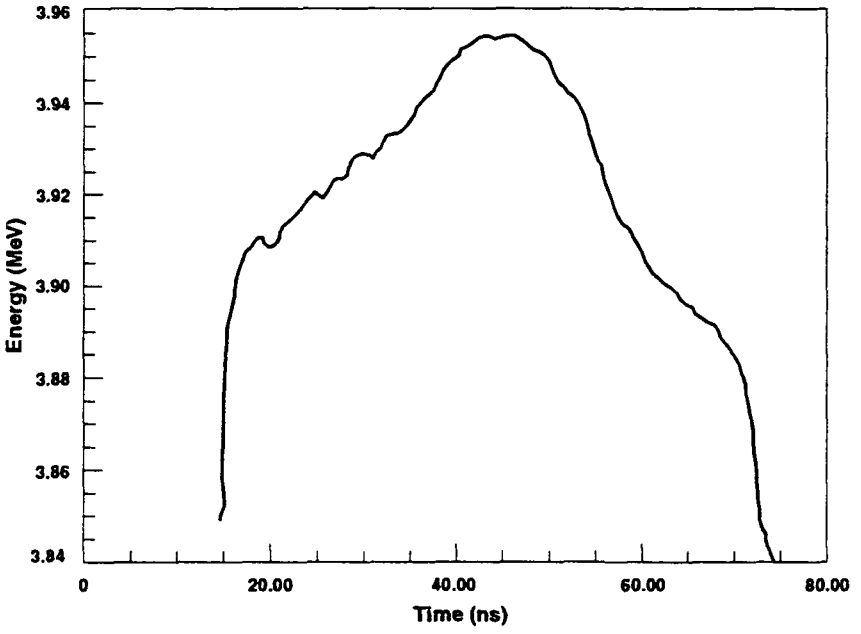

Figure 6. Beam energy vs. time at the end og the matching section. Pulsewidth is 60 ns, with ±0.7% energy spread.

Keeping BBU and corkscrew motion to acceptable levels requires limiting random magnetic axis tilts to 1 mrad and offsets to 250 microns for a full DARHT accelerator. After precision assembly of the ITS cell-block sections in a vertical tooling dock, mechanical alignment was completed by using a remotely controlled cart which moved through the accelerator bore and measured the alignment of the bore with respect to a twin-beam HeNe laser using lateral effect photodiodes [11]. Measurement accuracy was approx. 40 microns. Final magnetic-axis alignment is done by pulsing a 100-micron CuBe wire threaded through the center of the accelerator and observing the motion induced on the wire due to the Lorentz force generated by misaligned solenoids and the wire current [12]. Two dipole-wound cosine trim magnets on each solenoid allow for the correction of

installation tilts. Final tuning with the electron beam and beam position monitors [13] ensure the reduction of BBU and corkscrew to acceptable limits. Fig. 11 shows the upstream end of the cell block during installation.

Initial transport of a 3.9 MeV beam through the unpowered ITS cell-block is shown in Fig. 5. The peak current remains constant but the pulse width is reduced, though the total transported charge exceeds DARHT requirements. Shock excitation of the unpowered accelerator cavities by the beam results in a longitudinal rf mode that modulates the beam energy as shown in Fig. 12. The high voltage connections to the accelerating gap were shorted to ground and the electric field induced across the gap by the beam was monitored with capacitive probes within the cell.

IV. Accelerator Pulsed Power

The Induction Cell Pulsed Power (ICPP) for the ITS consists of four water-insulated, 12-Ω Blumleins with coaxial midplane-trigger switches based on the ATA design [14] and operating in pure SF_6. A single Blumlein is connected to two accelerator cells. Each Blumlein has a separate charging unit which uses two 1.2-μF Maxwell primary capacitors charged to 28kV. Two EEV CX 1722 thyratrons are used in parallel to switch the primary capacitors into a 1:11 step-up Stangenes iron-core transformer that charges the Blumlein to 250 kV in 5 μs. An independently controllable trigger unit is connected to each Blumlein. Each trigger unit is housed in a separate, oil-insulated steel enclosure and consists of two 15-nF, 70-kV primary capacitors switched by a EEV CX 1725 thyratron into a Stangenes 1:4 step-up auto-transformer that drives a magnetic-pulse compressor. This reduces the risetime of the required 200-kV output pulse to less than 10 ns into the trigger cable, in turn resulting in a risetime of 20 ns at the Blumlein spark-gap trigger electrode. Fig. 13 shows the installed ITS ICPP, discussed in more detail by Downing, *et. al.* [2].

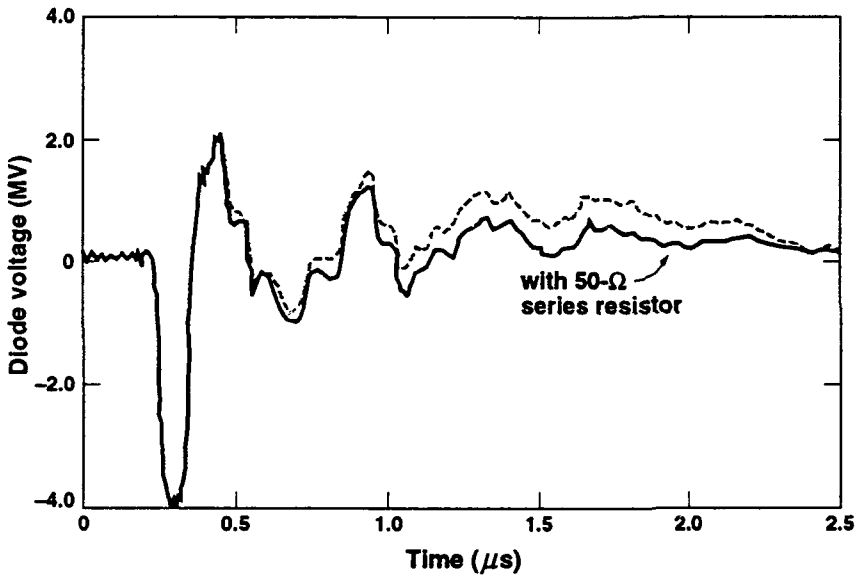

Figure 7. Diode voltage during and after the primary pulse. Injector pulsed-power modifications have reduced the number of observed diode insulator flashovers.

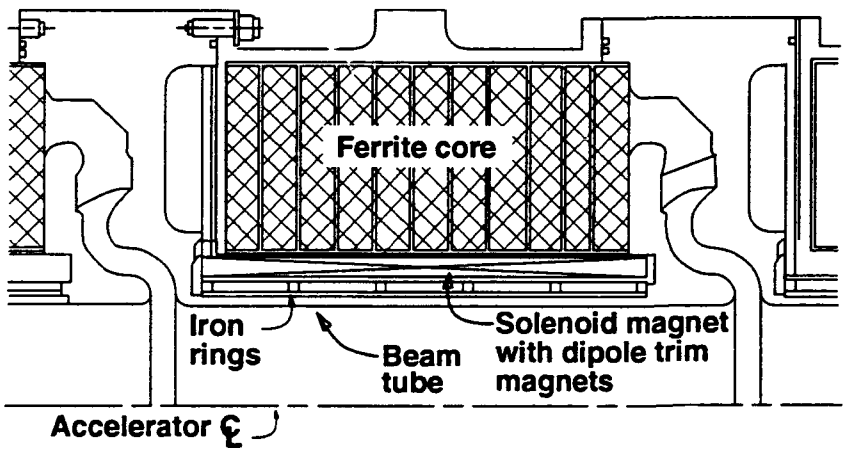

Figure 8. Cross-section schematic of the DARHT ITS accelerator cell.

The measured pulse width delivered to the accelerating cells at 250 kV is >70 ns, with a fluctuation of ±1%. Trigger system per-

formance has exceeded requirements by demonstrating a peak output voltage of 225 kV with a 13-ns risetime, measured into the output cable. System jitter has been measured at 0.6 ns (3 σ).

V. Future Work

Experiments transporting the electron beam through powered accelerator cells (6-MeV beam) are beginning as of the date of this conference. In addition, a variable-frequency, beam-excited rf cavity will be inserted into the beamline between the injector and accelerator section. This will induce a known transverse oscillation onto the beam and the growth of this oscillation through the cell-block will be measured. We have placed an abrupt transverse deflection onto the ITS beam and have shown that present diagnostics have sufficient sensitivity to clearly see BBU growth through only eight cells. Results of this experiment will validate the BBU growth projections for a complete DARHT accelerator made as a result of rf testing of prototype cells.

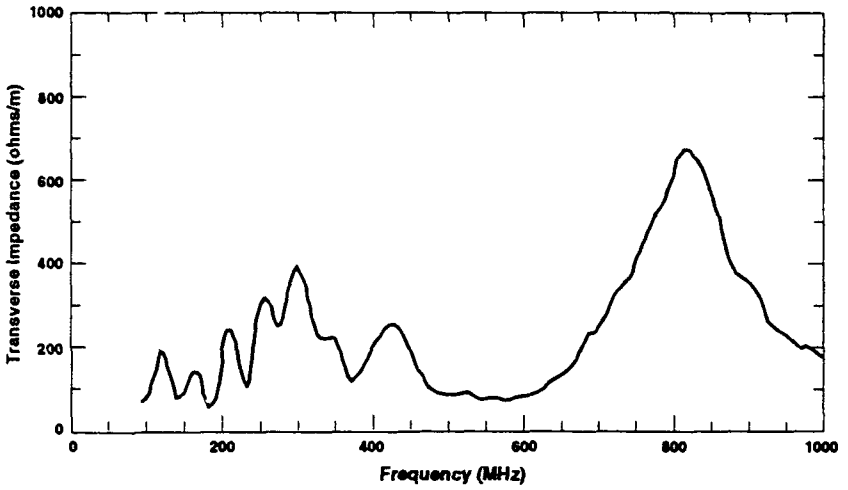

Figure 9. Average of horizontal- and vertical-plane transverse-impedance for the DARHT ITS cell. Oscillation at low frequency is due to slight calibration error.

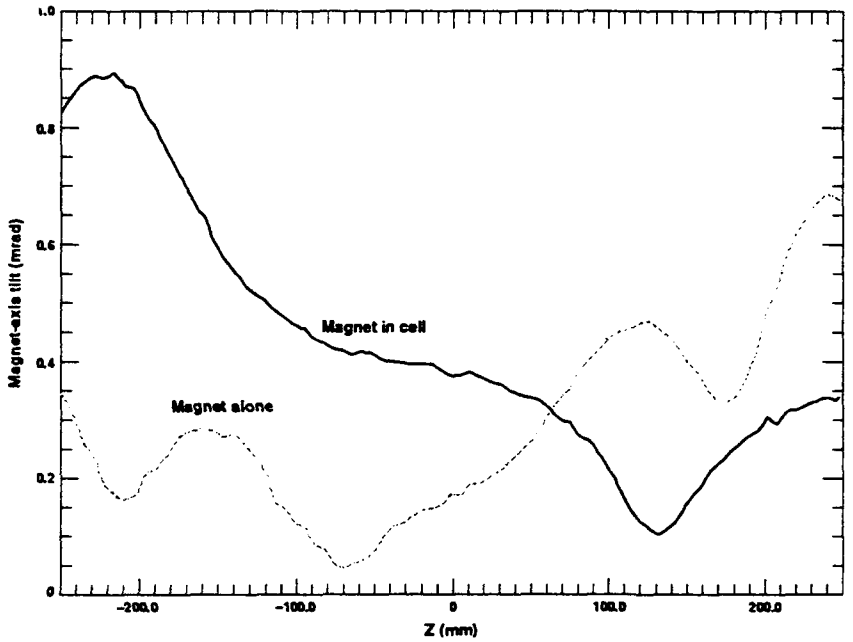

Figure 10. Magnet-axis tilt of a DARHT ITS solenoid before and after assembly into the cell. Magnet is 324-mm-long, centered at Z=0. Magnet leads are near −160 mm.

The ITS injector has performed at levels that meet DARHT specifications. The electron beam has been transported to and through an unpowered section of eight induction cells, with parameters that meet DARHT specifications for the electron beam at those locations. Accelerator design has met specifications for accelerating-gap, high-voltage stand-off, transverse impedance, magnet design, and alignment-system design. Accelerator pulsed-power systems have been fabricated which meet or exceed all requirements measured to date. Completion of experiments now underway will result in complete technology demonstration of the DARHT accelerators and will provide confidence that DARHT's accelerators will function as required to meet a pressing national need.

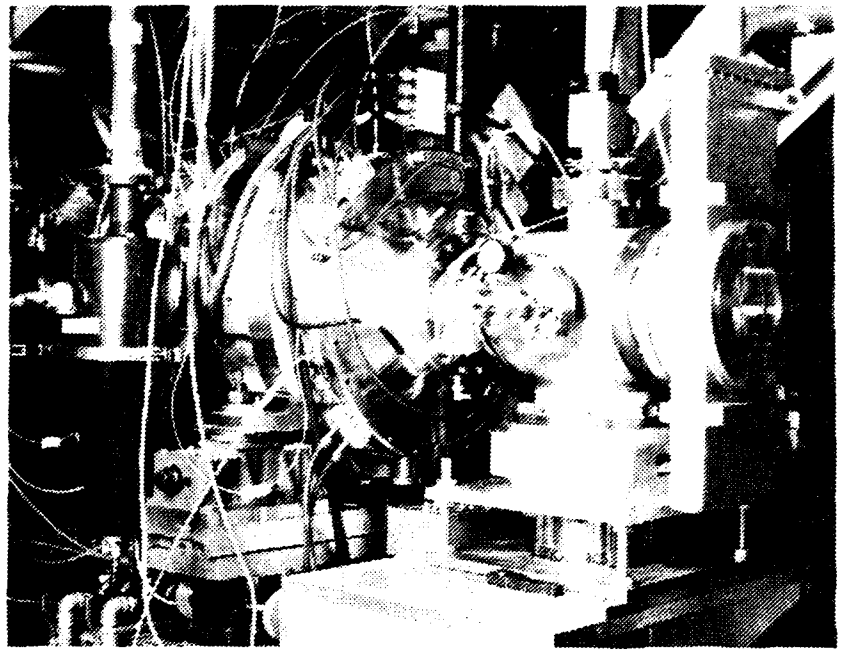

Figure 11. Upstream end of 8-cell ITS cell block during installation.

References

[1] R.L. Carlson, T.J. Kauppila, R.N. Ridlon, "REX: A 5-MV Pulsed-Power Source for Driving High-Brightness Electron Beam Diodes", *IEEE 1991 Particle Accelerator Conference*, San Francisco, CA, May 1991.

[2] J.N. Downing, et. al., "Pulsed Power Systems for the DARHT Accelerators, *IEEE 1991 Particle Accelerator Conference*, San Francisco, CA, May 1991.

[3] T.P. Hughes, R.L Carlson, D.C. Moir, "Beam Matching into the DARHT Linac", these proceedings.

[4] T.P. Hughes, R.L. Carlson, D.C. Moir, "High-Brightness

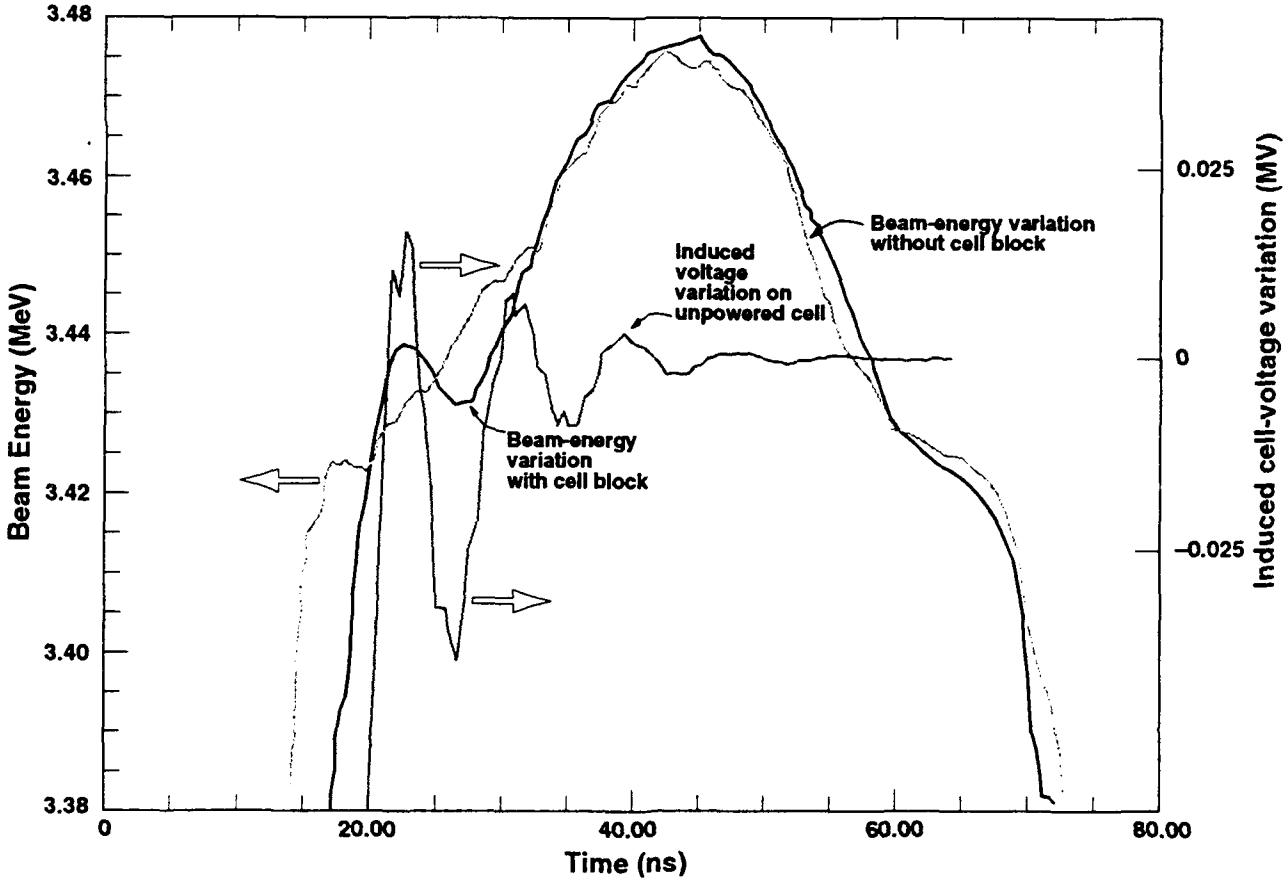

Figure 12. Overlay of measured accelerating-gap voltage variation in an unpowered cell and the beam-energy spectrum with and without the cell block. Shock-excited longitudinal rf modes modulate the beam energy on the leading edge. Injector is operating near 3.5 MeV.

tron Beam Generation and Transport", *J. Appl. Phys.*, 68 (6), Sept. 1990.

[5] T.J. Kauppila, R.L. Carlson, D.C. Moir, R.N. Ridlon, "Time-Resolved Emittance Measurements of an Excimer-Laser Driven Metal Photocathode", *IEEE 1991 Particle Accelerator Conference*, San Francisco, CA, May 1991.

[6] M.J. Burns, et. al., "Cell Design for the DARHT Linear Induction Accelerators", *IEEE 1991 Particle Accelerator Conference*, San Francisco, CA, May 1991.

[7] J.F. DeFord, G.D. Craig, R.R. McLeod, "The AMOS Wakefield Code", *Workshop on Accelerator Computer Codes*, Los Alamos, NM, Jan. 1990.

[8] L. Walling, et. al., "Transverse Impedance Measurements of Prototype Cavities for a Dual-Axis Radiographic Hydrotest (DARHT) Facility", *IEEE 1991 Particle Accelerator Conference*, San Francisco, CA, May 1991.

[9] P. Allison, M.J. Burns, G.J. Caporaso, A.G. Cole, "Beam-Breakup Calculations for the DARHT Accelerator", *IEEE 1991 Particle Accelerator Conference*, San Francisco, CA, May 1991.

[10] M.J. Burns, et. al., "Magnet Design for the DARHT Linear Induction Accelerators", *IEEE 1991 Particle Accelerator Conference*, San Francisco, CA, May 1991.

[11] R. Schamaun, "Mechanical Alignment of the ITS Cell-Block", *DARHT Technical Note No. 23* (LANL), May 1992.

[12] F.J. Deadrick, L.V. Griffith, "Progress in ETA-II Magnetic Field Alignment Using Stretched Wire and Low Energy Electron Beam Techniques", *1990 LINAC Conference*, Albuquerque, NM, Sept. 1990.

[13] W.C. Turner, "Control of Energy Sweep and Transverse Beam Motion in Induction Linacs", *IEEE 1991 Particle Accelerator Conference*, San Francisco, CA, May 1991.

[14] L.L. Reginato, et. al., "Advanced Test Accelerator (ATA) Pulse Power Technology Development", *IEEE Trans. on Nuc. Sci.*, NS-28 (3), June 1981.

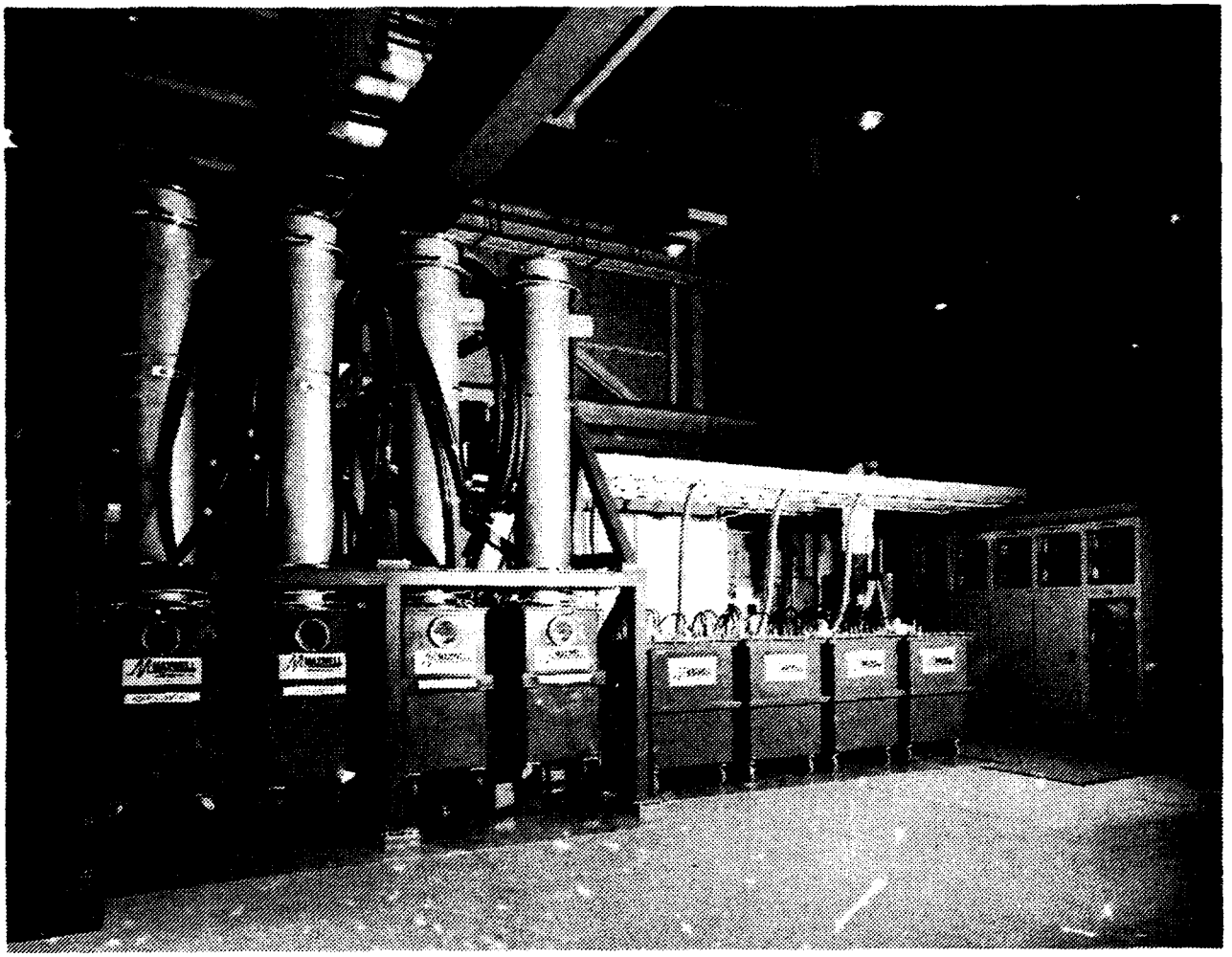

Figure 12. Accelerator pulsed power installed on the ITS.

SLIA THEORY REVIEW

J.J. Petillo, A.A. Mondelli, C. Kostas, K.T. Tsang, and D.P. Chernin

Science Applications International Corporation
1710 Goodridge Drive
McLean, Virginia 22102 U.S.A.

This paper describes the design of a proof-of-concept experiment (POCE) currently being constructed at Pulse Sciences Incorporated (PSI). The POCE is designed to accelerate a 10 kA, 3.5 MeV electron beam to 9.5 MeV after four passes through two sets of 1.5 MeV induction modules (each module incorporating 5 cells). The issues related to beam instabilities and beam transport, as well as cavity and gap modeling for the acceleration module are presented.

Introduction

The Spiral Line Induction Accelerator (SLIA) is a high-current (multi-kiloampere) recirculating induction electron accelerator that incorporates stellarator windings to provide strong-focusing quadrupole fields on the recirculating bends.[1] The SLIA is an open-ended device that consists of a spiral racetrack configuration, with linear induction acceleration modules on the straight sections. A single spiral beamline guides the beam into the device, recirculates and threads through the induction modules several times, and then guides the beam out. The induction modules are reused several times, and can be reset between passes using branched magnetic switches. The effective energy gain per unit length, which is typically ≤1 MeV/m in a linear induction accelerator, is multiplied in the SLIA by the number of passes through the acceleration module. Beam injection and extraction are greatly simplified by the open-ended geometry of the SLIA, while the spiral geometry allows the use of static beam transport fields on each bend as the beam is accelerated.

Proof-of-Concept Experiment

The PoCE consists of a 20-gap accelerator, with an energy gain of 300 keV per gap, for a total energy gain of 6 MeV during acceleration. The 20 gaps (or cells) are traversed in two passes through a 10-cell accelerator, with five cells in each of two acceleration modules. The spiral beamline passes twice through each module. The modules are located on the two straight sections of a racetrack configuration.

The induction modules are energized for the entire beam transit in the PoCE; i.e., branched-magnetic switches planned for the SLIA will not be employed to reset the modules between passes. The modules must therefore provide sufficient flux swing (Volt-seconds) to accommodate the entire beam transit through two passes. This constraint forces a small radius bend and a minimal dead time between passes. In the PoCE the bends have a major radius of 80 cm, and the beam head of the second pass enters each acceleration gap as the tail of the first pass leaves it. The beam is 35 ns long. The beamline minor radius in the bends is 3 cm.

Known equilibrium solutions for a beam in a toroidal stellarator field have been used to construct design parameters for each bend. Parameters are chosen so that the beam trajectory (position and slope) at the exit of the bend is identical to that at the entrance. Several parameter choices satisfy this condition at the design energy for each bend. The parameter set that displays the smallest chromatic effect near the design energy, and that satisfies constraints required for beam stability with practical limits on fields and aperture, has been chosen. Table 1 displays the equilibrium parameter set chosen for each of the three bends of the PoCE. The beam injector is a 3.5 MeV accelerator. At 10 kA the space-charge depression is approximately 1 MeV, yielding an input energy of 2.5 MeV. Each pass through a five-

Bend #	Kinetic Energy [MeV]	Axial Field [G]	Quad Gradient [G/cm]	Quad Pitch [cm]	Major Radius [cm]	Minor Radius [cm]
1	4.0	5481.	254.5	62.8	.866	.559
2	5.5	5327.	208.4	83.8	.934	.556
3	7.0	5476.	183.1	126.	1.12	.525

Table 1 PoCE Parameters.

cell module then adds 1.5 MeV to the energy. In the stellarator bends, the equilibrium beam profile is an ellipse, with major and minor radii shown on the table.

Beam Break-Up (BBU) Instability

The BBU instability[2] is perhaps the most serious scaling issue for the SLIA. The SLIA will require that the transverse impedance of the accelerating cells be $\leq 10\ \Omega/cm$. Based on impedance measurements at PSI, and simulations by MRC and LLNL, the PoCE is expected to be relatively insensitive to the BBU. It will have a limited ability to detect the instability if the growth rate is enhanced by either increasing the beam current, reducing the focusing field, or using a tickler to increase the initial beam offset.

Calculations at NRL indicate that the coupling between cavities should dramatically reduce the growth of the BBU.[3] Recent simulations at MRC, however, show the potential for only a modest reduction of the transverse impedance for coupled cavities, compared with uncoupled cavities.

Electromagnetic Three-Wave Instability

The SLIA is subject to a three-wave instability that occurs at a resonance between a waveguide mode of the vacuum chamber, a negative-energy beam mode, and the helical stellarator field (a zero-frequency mode with a wavelength equal to the pitch length)[4].

The helicity of the stellarator field can be parallel or anti-parallel to that of the electron trajectory in the axial field. When it is parallel, the beam cyclotron mode is the negative energy mode, and the three wave coupling will be stable at low energy. Since the cyclotron frequency scales as the inverse of the beam energy, the instability will unavoidably occur at high energy, but its growth rate there is significantly weaker. With the parallel choice of beam helicity, the PoCE is theoretically stable to this instability.

Beamline Design

Identity Transformation: Matched particle orbits in a stellarator-focused bend are given by a superposition of betatron oscillations at four different frequencies, and may be expressed as

$$\zeta(\theta) \equiv x + iy$$

$$= e^{im\theta/2}\left[A_+ e^{i\nu_+\theta} + \sigma_+ A_+^* e^{-i\nu_+\theta} + A_- e^{i\nu_-\theta} + \sigma_- A_-^* e^{-i\nu_-\theta}\right],$$

where m is the number of stellarator periods on a 360° bend, and $m/2 \pm \nu_\pm$ are the four betatron frequencies. These orbits will return to their initial transverse coordinates and momenta at $\theta=\pi$ if $m = 2N_m$, $\nu_+ = N_+ \equiv 2N_{++} - N_m$, and $\nu_- = N_- \equiv N_m - 2N_{--}$. If N_m is an (even, odd) integer, then $N_\pm$ must be an (even, odd) integer also. This gives an identity transformation only at the matched energy, because $\nu_\pm$ are functions of energy.

Envelope Matching: The beam propagates in a solenoidal field through the straight sections and enters a stellarator field on the bends. In the transition, the beam envelope must be matched from a round envelope in the solenoid field to an elliptical beam envelope in the stellarator field. The beam matching strategy illustrated in Figure 1 was suggested by M. Tiefenback at PSI and developed at SAIC. It has been generalized to allow thick focusing elements, to include the fringe fields of the

stellarator and vertical field coils, and to permit the matching section to be displaced from the mouth of the bend. Using this technique, it is now possible to match any solenoid-stellarator transition in SLIA. A feature of this three element matching section, is that it allows tuning and flexibility that may not otherwise be available using less elements, although less elements are sufficient at times.

Centroid Correction: Beam offset occurs in straight solenoids due to fringe fields. Correction dipoles are used to force the beam centroid back on axis. A schematic of the coil configuration is shown in Figure 2. The vertical and horizontal correction coils are adjusted so that the centroid trajectory meets the axis with zero slope at the reference plane. With no correction coils the centroid trajectory may cross the reference plane at $\{x_0, y_0, x_0', y_0'\}$. With a current of 1 A in the jth correction coil and no current in the other correction coils, the centroid orbit switches to $\{x_j, y_j, x_j', y_j'\}$. With current I_j in the jth coil, the trajectory may be written by linear superposition as

$$x - x_0 = \sum_{j=1}^{4} I_j (x_j - x_0).$$

This equation can be solved for the I_j's that satisfy $x=y=x'=y'=0$ at the reference plane.

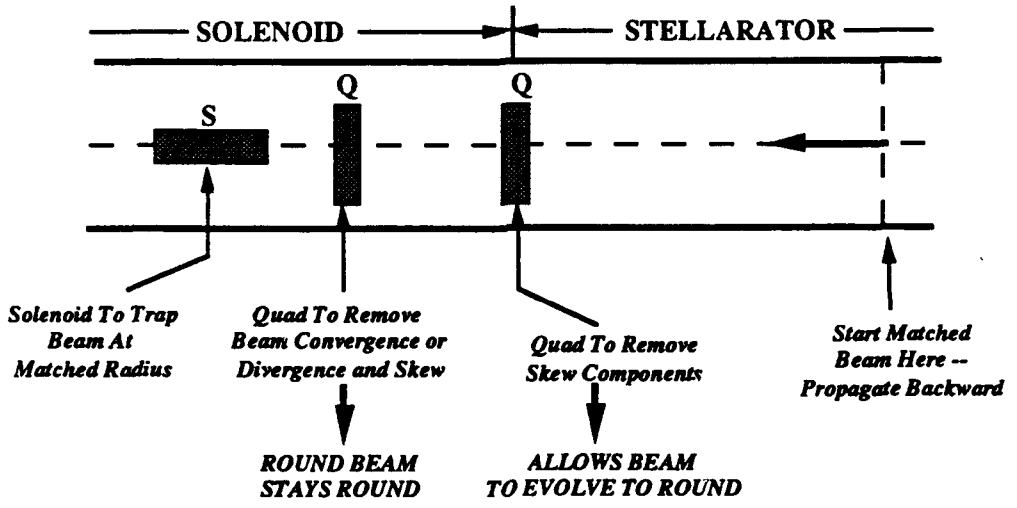

Figure 1. Beam Envelope Matching Scheme for the Solenoid-Stellarator Transition.

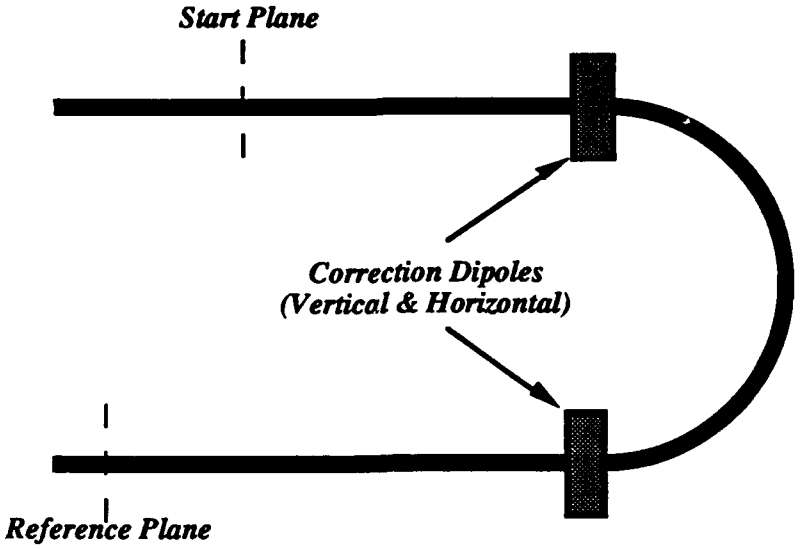

Figure 2. Centroid Orbit Correction Coil Scheme.

Three-Turn PoCE Simulation: To carry out the three-turn simulation for the PoCE, the individual bends were first matched and corrected, as described above, in three separate simulations, using an envelope code (ABBY) that was specifically developed for the SLIA project. The simulations included the acceleration term (γ'/γ) as well as the axial and radial electric field components in the accelerating gaps. Since the longitudinal magnetic field is slightly different in the three bends (see the table of equilibrium solutions above), that field component is ramped in the straight sections, and the radial magnetic field component associated with the ramped axial component in the straight sections is included in the simulation.

A planar PoCE configuration has been modeled as a test case to verify the efficacy of the envelope matching and centroid correction coils used in the PoCE design. The results for a matched injection, shown in Figure 3, indicate that the beam will return to the reference orbit (axis) in the straight section after each bend, with zero slope.

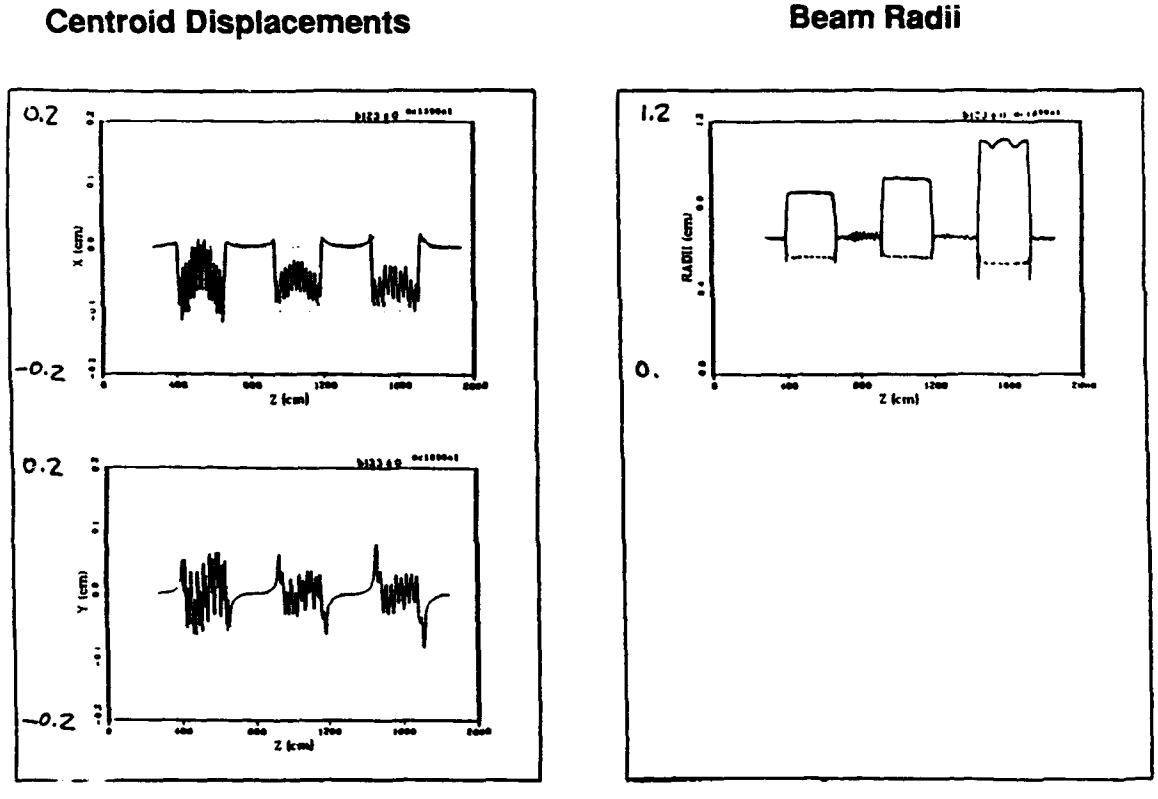

Figure 3. Planar ABBY Simulation of the Three-Turn PoCE.

Bend-to-Bend Coupling: The first and third bends of the PoCE are separated vertically by approximately 30 cm, and the fringe fields from one bend will act as field errors on the electron orbits in the other bend. The effect of bend-to-bend coupling in the PoCE is similar to a 10% mismatch. Most of this effect can be removed by retuning the vertical field on the bend to compensate for the average field error. The residual centroid error can be removed by making a small adjustment in the centroid correction coils. The beam envelope is very insensitive to the bend-to-bend coupling. These results indicate that magnetic

shielding of the bends in the PoCE will not be needed.

Coil Tolerances: Studies of the sensitivity of the beam centroid and envelope equilibria to the accuracy with which the stellarator winding is set indicate that random and semi-random winding errors of ±30 mils have no effect. PSI has designed and wound the stellarator coils to ±5 mils.

"Straight-Bend" Experiment: As a preliminary experiment, PSI has constructed a straight system consisting of a solenoid-stellarator transition, thus simulating the fields in the bends without curvaure. This experiment was carried out at an energy of 850 keV and a beam current of 200 A. The results of simulations of this experiment using the ABBY code are shown in Figure 4. Using the Lawson-Penner emittance (ε=.0374 rad-cm), the computed beam envelope undergoes five betatron oscillations over the length of the system. The experiment gives four betatron oscillations. Using experimental data to correct the emittance to ε=.0177 rad-cm brings the computed betatron frequency into agreement with the measurements.

NRL has carried out an extensive program of simulating this experiment. Their results indicate that the beam has a "core-halo" distribution. With this distribution they reproduce not only the betatron frequency, but also the damping of the betatron oscillations due to phase mixing and emittance growth.[5] The damping effect cannot be captured with a linear envelope model, such as ABBY. Experiments at PSI have detected the presence of a beam halo.

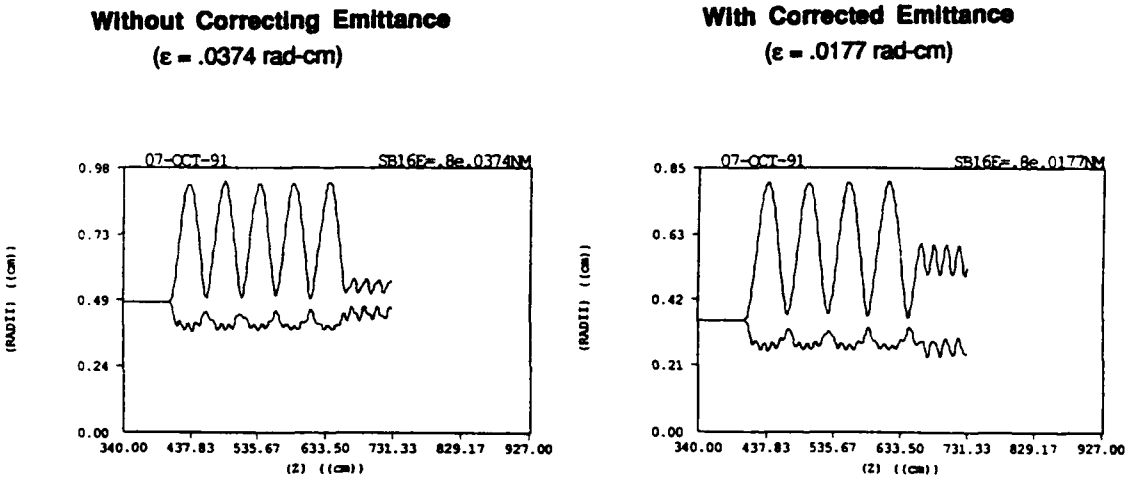

Figure 4. ABBY Simulations of PSI's "Straight-Bend" Experiment.

High-Order Envelope Model

A new, nonlinear envelope model is under development to include energy spread, nonlinear fields, high-order correlations and emittance growth, and time-dependent effects. The current implementation of this model includes terms up to fourth order, as well as nonlinear space-charge effects, in a straight geometry.

The formulation of the model is based on taking transverse spatial averages of the moments of the relativistic Vlasov equation to obtain a system of partial differential equations in z and t. The z coordinate is discretized and a system of ordinary differential equations in time is solved in each cell from specified initial conditions.

Acknowledgment

This work has been supported by DARPA/NSWC under Contract No. N60921-91-C-0148.

The SLIA PoCE design effort has been carried out by a collaboration between PSI, SAIC, MRC, NRL, and LLNL. It is a pleasure to acknowledge many fruitful discussions with all the members of this design team.

References

1. V. Bailey, L. Schlitt, M. Tiefenback, S. Putnam, A. Mondelli, D. Chernin, and J. Petillo, *An Experimental Program to Investigate the Strong Focussed, Spiral Line Recirculating Accelerator*, Proc. 1987 IEEE Part. Accel. Conf., Vol. 2, p. 920.

2. V.K. Neil, L.S. Hall, and R.K. Cooper, *Further Theoretical Studies of the Beam Breakup Instability*, Part. Accel. **9**, 213 (1979).

3. D.G. Colombant, Y.Y. Lau, and D. Chernin, *Reduction of Beam Breakup Growth by Cavity Cross-Couplings in Recirculating Accelerators*, Part. Accel. **35**, No. 4 (1991).

4. T.P. Hughes and B.B. Godfrey, *Electromagnetic Instability in a Quadrupole Focusing Accelerator*, Phys. Fluids **29**, 1698 (1986).

5. J. Krall, S. Slinker, M. Lampe, and G. Joyce, *Numerical Modeling of Intense Electron Beam Transport in the Spiral Line Induction Accelerator*, submitted to Phys. Rev. A.

STUDY OF RECIRCULATING INDUCTION ACCELERATOR AS DRIVERS FOR HEAVY ION FUSION

by

H.D. Shay, J.J. Barnard, A.L. Brooks, F. Coffield, F. Deadrick, L.V. Griffith, H. C. Kirbie, V.K. Neil, M.A. Newton, A.C. Paul, L.L. Reginato, W.M. Sharp, J. Wilson, and S.S. Yu, Lawrence Livermore National Laboratory, P.O. Box 808, Livermore, CA 94550; and D.L. Judd, Lawrence Berkeley Laboratory, 486 Cyclotron Rd., Berkeley, CA 94720

Introduction

Two years ago, Lawrence Livermore National Laboratory (LLNL) began a study of the viability and relative utility of recirculating induction accelerators as drivers for Heavy Ion Fusion (HIF). The final draft of the report detailing the results in 284 pages was completed in September, 1991 [ref 1]. As well as broadly involving the collaboration of many researchers from several groups at LLNL, it also benefited from contributions from several individuals in the HIF program at Lawrence Berkeley Laboratory (LBL) and from others in the HIF community nationwide. This presentation summarizes the key findings given in that report.

From its inception, the HIF community has pursued three driver options: the RF linac, the induction linac, and the synchrotron. The RF linac has the most mature technology and, while the most expensive, is the principal driver candidate in the European HIF programs. The induction linac has a simple configuration, but has less mature technology - it is the principal candidate in the U.S. The synchrotron, while the cheapest, was rejected long ago because of the long residence time of the beam, about one second, which is intolerable because of beam loss. The recirculating induction accelerator, or recirculator, has features in common with induction linacs and synchrotrons. It has the high current accelerating capability associated with induction cores. Like a synchrotron, it is circular and so "reuses" components in accelerating a given collection of ions, but, unlike the synchrotron, it has a short residence time, of the order of a millisecond. Since the beginning of serious consideration of HIF, a number of researchers [ref 2-6] have advanced concepts that have, in some measure, been incorporated into the designs presented here.

The key notion of the recirculator is the extension of the induction-linac technology with significant potential for cost reduction. The most expensive components of an induction linac are the induction cores, the focusing magnets, the pulsers, and the structure. At the expense of adding pulsed dipole bending magnets, the recirculator can reduce cost drastically by decreasing the number of needed components, since the circumference of a recirculator can be as low as 20% of the length of the comparable induction linac. Furthermore, the induction cells of the

recirculator can have a lower voltage per pass than those of the linac. Consequently, the induction cores can be much smaller and cheaper.

Study Methodology

During the study, we first sought to identify and to evaluate the major physics issues and, thereby, to focus upon feasible accelerator configurations. We then derived system requirements and identified the major engineering issues. We could then conduct system tradeoffs of limited scope and could estimate the cost and expected efficiencies for several recirculator designs. The last several steps, the systems-engineering studies, were conducted with a recirculator-systems model based on physics and engineering design relationships. We calculated feasible system parameters for wide variety of configurations. Approximate costs were determined with algorithms based on "bottom-up" estimates of specific designs, and system efficiencies were determined from component designs. Although system tradeoffs were investigated, we had no full fledged optimization capability.

In all these studies, we assumed as given a specific input from the injector, a given performance of the final focus and target chambers, and a given set of fusion target requirements. These assumed parameters are listed in Table 1. This study focused on the design of the HI accelerator itself. A complete system study would certainly conduct an end-to-end optimization, from the injector to and including the target.

Table 1. Systems Parameters Assumed for Target and Reactor Requirements.

Total Pulse Energy	4 MJ
Final Heavy Ion Energy	10 GeV
Heavy Ion Atomic Mass	200
Charge State of Heavy Ions	+1
Total Electrical Charge in Ion Pulse	400 μC
Main Pulse Duration at Target	10 ns
Target Stopping Range	0.15 gm cm2
Final Spot Radius on Target	1.5 mm
Final Normalized Emittance	0.001 cm-rad
Final Momentum Spread	0.004
Repetition Rate	10 Hz
Accelerator Efficiency times Target Gain	≥ 10
Accelerator Efficiency	≥ .20
Power Plant Lifetime	30 years

There are a large number of "physics" issues which place constraints on possible recirculator designs. The dipole fields must be ramped accurately, and the dipole field energy must be recovered very efficiently. Beam optics in the space-charge-limited regime and the maximum magnetic field place limits on the number of rings. At the highest energy, the high angular velocity of the beam stresses the repetition rate of the induction cell pulsers, and some designs require that these pulsers have a turn-to-turn variable format to maintain the appropriate schedule of pulse compression. Because the residence time is longer than in an induction linac, greater care must be taken to avoid excessive beam loss through beam-beam charge exchange; consequently, limits on the current density must be observed, and this places a minimum on the beam radius. Such considerations as the maximum feasible quadrupole field and the cost of large bore quadrupoles imply that the charge must be transported in several space-charge-limited beams, not one. Likewise, because the beam passes through the same spot repeatedly, there must be stringent vacuum requirements to avoid excessive beam loss through ion-neutral collisions and ion-wall interactions. As in the case of induction linacs, care must be taken to avoid stimulating beam instabilities; beam break-up and longitudinal instabilities seem to be controllable. In each accelerating ring, there must be a straight injection/extraction section. Since the geometry of the beams may be different in the ring than in the injection/extraction section, there may be beam manipulations entering and exiting it. Throughout the entire accelerator, emittance must be preserved so that the beam may be focused to a small spot on the target.

Our approach has been to develop point designs. Since a broad range of design philosophies were possible, we selected three different point designs, listed in Table 2. This approach allowed us to present the trade–offs for different design goals and priorities.

Model "T" (for technology) is our baseline design. Our goal was to establish a firm and believable foundation for cost estimates. Thus we chose to use only today's technology at today's prices. This allowed us to make a concrete tally of the components at verifiable costs. This approach also allowed us to perform a first engineering study of individual components and subsystems. It was gratifying to find that a recirculator driver system could be constructed with no large technological extrapolations. This, however, was not a fully optimized recirculator design. In order to establish a well-founded data point, a similar linear driver system (which is also not fully optimized) was designed, and a component–by–component comparison was made, using the same costing algorithms to the extent possible. In this particular comparison, the recirculator (based on Model "T") was shown to reduce the cost by a factor of 2.7.

The philosophy of "today's technology" underlying the "T" model constrained us quite severely in our design parameter space. As a consequence, the cost and efficiency results were expected to be far from the best achievable driver system to be constructed several decades from now. This motivated us to pursue the "C" model ("C" for "cost" reduction). The approach here

Table 2. Some Comparisons of the "T", "C", and "P" Designs.

	"T"	"C"	"P"
Description	Today's Technology	Low cost , adv. tech.	Low physics risk
Risk			
Number of rings	4	3	3
Number of Beamlines	4	4	1
Number of Beamlines per core	4	4	1
Induction module pulsers in HER	Line type modulator	FET switches	FET switches
Dipole magnetic field temporal ramp	Sinusoidal	Linear	Linear
Superconducting dipole bias field in HER?	No	Yes	No
Number of laps per ring	50	100	50
Circumference of HER	3553 m	1934 m	4231 m
Linear buncher section after HER?	No	Yes	No
Acceleration schedule	constant pulse duration	continuous bunch compression	continuous bunch compression

was to make reasonable extrapolations of the cost of several critical components, with the presumption that the need for fusion drivers would stimulate manufacturing R&D in industries. These cost assumptions have allowed us to employ components that would otherwise be too costly for the design of a much more efficient recirculator driver. The projected total cost of a Model "C" driver is less than $500M in today's dollars, with the high-technology components of the main accelerator (induction cores, pulsers, focusing and bending magnets) accounting for roughly one third of the total cost. The other two–thirds goes to facilities, prime power, administration, installation, auxiliary systems and various special subsystems. The projected efficiency of the Model "C" is about 35%.

In our recirculator designs, much of the physics risk is associated with multiple beams in a circular geometry. These risks can be eliminated if a recirculating accelerator with several beams (as is the case with both Model "T" and "C") is replaced by several independent recirculators each with one beam only. This was the motivation behind Model "P" ("P" for "physics" risk minimization) which was constructed to demonstrate the trade–off between

physics risks and cost and efficiency gains. Model "P" has 20% efficiency, but its cost is slightly more than a factor of two over the lowest cost version.

Sample Point Design

Figure 1 shows the geometry of the "C" design; and Table 3 lists some of its parameters. Because of the limited dynamic range on the cell pulsers and dipole magnets, there are three rings to cover three energy ranges: the LER (low energy range), the MER (medium), and the HER (high). The upper limit on the number of laps in each ring is essentially established by residence time and pumping rate requirements. Within each ring, there are four separate beams, each carrying 100μC. To reduce component cost, these beams are arranged in a two by two matrix pattern and share quadrupoles and dipoles. In each ring there is a short injection/extraction section in which the beams may be either be introduced or removed from the ring. Because of the geometry of the Panovsky quadrupoles (ref 7) and the kicker dipoles in these sections, the

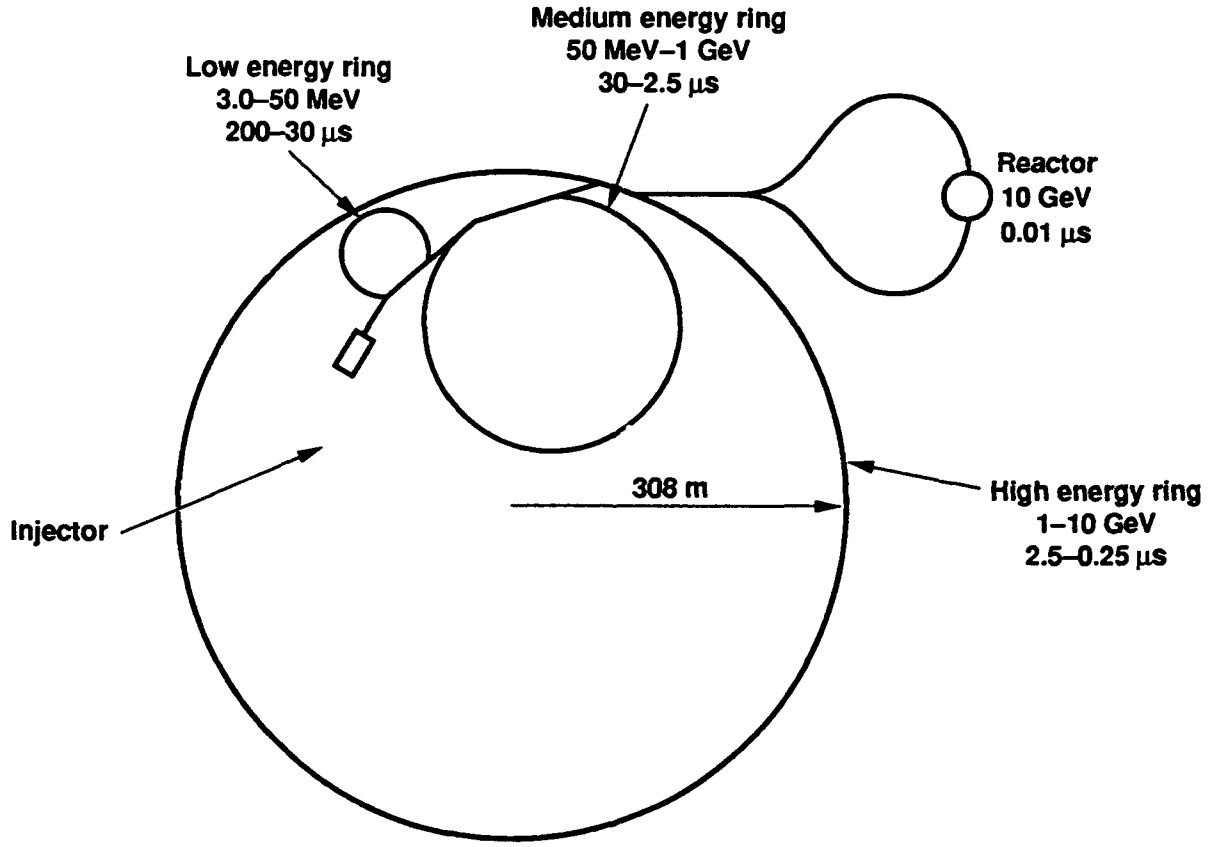

Figure 1. Schematic geometry of "C" HI accelerator design.

Table 3. Some parameters for the C design recirculator.

	LER	MER	HER
Initial energy (GeV)	0.003	0.05	1.0
Final energy (GeV)	0.05	1.0	10.0
Initial pulse duration (μs)	200	30	2.5
Final pulse duration (μs)	30	2.5	0.25
Circumference (m)	700	885	1934

beams were arranged in a vertical 1 x 4 pattern. The beam optics between the 2 x 2 and 1 x 4 patterns have been carefully designed to prevent objectionable growth of emittance.

Each of the "physics" issues mentioned above was examined in the context of the point designs. The code CIRCE was written for the Cray X/MP and Y/MP computers to design the lattice and the acceleration schedule and to examine the effects of misalignments and field errors. A quasi-static theory has been developed to determine the upper limit on emittance growth in each ring, and has subsequently (after the completion of the report) been substantiated by detailed 3D PIC WARP simulations. (ref 8) Analytic theories and numerical solutions have examined the growth rates of all known beam instabilities and the pumping rate requirements.

The study has included a systematic conceptual engineering designs of all systems, most notably, the bending magnets and their pulsers, the accelerating cells and pulsers, and the focusing systems. Questions of costs and system efficiency have been paramount. Because of the large energy stored in the peak field of the bending magnets, viz., about 36 MJ in the HER of the "T" design (and 76 MJ total), it was necessary to devise a system which has an energy recovery efficiency of over 95%. In the "C" design, significant energy efficiencies and cost reductions were realized by the use of dipole bending magnet design in which the superconducting bias magnet was used to decrease the excursions needed in the ramped field, and a compensating alternator was used to provide a nearly linear drive and to reduce, thereby, the peak field required. Likewise, the peak angular frequency in the HER ring prompted the design of modulators which could sustain peak repetition frequencies of 50 kHz. All of the relations governing the performance and cost of the recirculator were programmed into a spreadsheet, which was used for trade-off studies during the development of the three point designs. The cost model included installation and commissioning costs and the administrative and engineering expenses. Table 4 shows the division of costs and power budgets for the final "C" design, which has a total cost of about $500M and a driver efficiency of about 35%. Note that cost reduction has reached a point of diminishing returns since the cost of the accelerator subsystems (focusing, bending, induction cells, and cell pulsers) is only 34% of the total cost while items like prime power and

Table 4. Relative costs and power consumption in the "C" design. Total cost is $497M and the total beam power is 40 MW.

	Fractional Cost
Focusing	9%
Bending	6%
Induction cores	8%
Pulsers	26%
A&E, installation	23%
Prime power & facilities	20%
Auxiliary	29%
	Fractional power consumption
Beam	35%
Dipoles	24%
Acceleration Modules	28%
Miscellaneous	12%

the cost of installation, which have mature technologies, predominate the costs. Likewise, the system energy budget is very efficient - the bending dipoles, with the superconducting bias and compensating-alternator pulsers, consume 25% of the energy budget, and the losses in the induction cells are 28%, so that the total efficiency of power transfer to the beam is 35%.

Conclusions

This study has sharpened the focus for future recirculator studies. Future system studies should include end-to-end optimization, including the performance of the target, so that the beam energy and the ion mass, charge state, and final velocity all become optimization variables. Collision cross-sections and sputtering rates were estimated here and should be confirmed by careful measurements. Beam dynamic issues such as the growth rates of instabilities and of the transverse emittance all merit more study. Because the success of the more advanced designs hinges on high repetition rate modulators driving the induction cells, prototypes of increasing power and repetition rate should be tested. Likewise, the bending dipoles with compensating alternator pulsers and superconducting bias fields should also be prototyped.

The fundamental conclusions are that recirculators are feasible, that, for comparable technology, they are significantly cheaper than linear induction heavy ion accelerators, and that, with the cost associated with maturing technologies, a recirculator suitable for driving a fusion power plant can cost about $500M.

References

[1]J. J. Barnard, A. L. Brooks, J. P. Clay, F. E. Coffield, F. J. Deadrick, L. V. Griffith, A. R. Harvey, D. L. Judd (Lawrence Berkeley Laboratory), H. C. Kirbie, V. K. Neil, M. A. Newton, A. C. Paul, L. L. Reginato, G. E. Russell, W. M. Sharp, H. D. Shay, J. H. Wilson, and S. S. Yu, *Study of Recirculating Induction Accelerator as Drivers for Heavy Ion Fusion,* UCRL-LR-108095, Lawrence Livermore National Laboratory (1991).

[2]T. F. Godlove, *ERDA Summer Study of Heavy Ions for Inertial Fusion* (1976).

[3]A. Faltens and D. Keefe, *Proceedings of the HIF Workshop* (1977).

[4]A. Faltens and D. Keefe, *Proceedings of the HIF Workshop* (1979).

[5]T. F. Godlove, *Workshop of the HIFSA Study* (1984).

[6]A. Warwick, L. Smith, and T. Fessenden, *HIFAR: "Next Step"* (1985).

[7]L. N. Hand and W. K. H. Panovsky, *Rev. Sci. Instrum.* **30**, 927 (1959).

[8]J. Barnard, H. D. Shay, S. S. Yu, A. Friedman, and D. P. Grote, "Emittance Growth in Heavy Ion Recirculators," *Proceedings of the 16th International LINAC Conference,* Ottawa, Ontario, August 23-28, 1992 (in preparation).

LOW EMITTANCE ACCELERATOR CAVITY DESIGN TO MINIMIZE AMPLIFICATION OF BEAM BREAKUP MODES

M. L. Sloan, J. R. Thompson, C. S. Kueny
Austin Research Associates, Austin, Texas 78746

Abstract

Theoretical analysis and computer simulation have been applied to obtain cavity designs that dramatically reduce cumulative beam breakup amplification for solenoidally focused, high current, relativistic electron beam multiple gap induction accelerators. Specific use is made of low emittance, long gap designs which provide phase cancellation and attendant reduced beam-eigenmode coupling; an effect the usual short gap,or impulse, approximation cannot address. Specific comparison with a standard short gap cavity design for a 50 MeV, 10 kA induction accelerator illustrates the significant improvement in beam breakup suppression that obtains with the low emittance long gap accelerator cavity designs.

I. Introduction

Beam breakup instability processes have been found to pose significant problems for high current, multi-MeV induction electron accelerators [1,2], particularly the cumulative type B instability [3]. Some improvement in performance has been gained by utilization of gas focusing or similar increase in focusing strength [4]; however, persistent beam breakup problems have often precluded operation of such accelerators at full design goals.

Over the past several years a new class of impedance matched induction accelerator gap geometries have been developed which provide significant improvement in maintenance of beam brightness at high beam currents [5]. These new geometries are characterized by long, adiabatic accelerating gaps and TEM power feed structures, as illustrated in Figure 1. Although initial conjectures that such structures might be immune to beam breakup [2] were shown under subsequent analysis to be incorrect [6], intensive investigation during the past 12 months has demonstrated that such structures can be configured to significantly reduce beam breakup well below levels achievable with conventional accelerating cavity geometries.

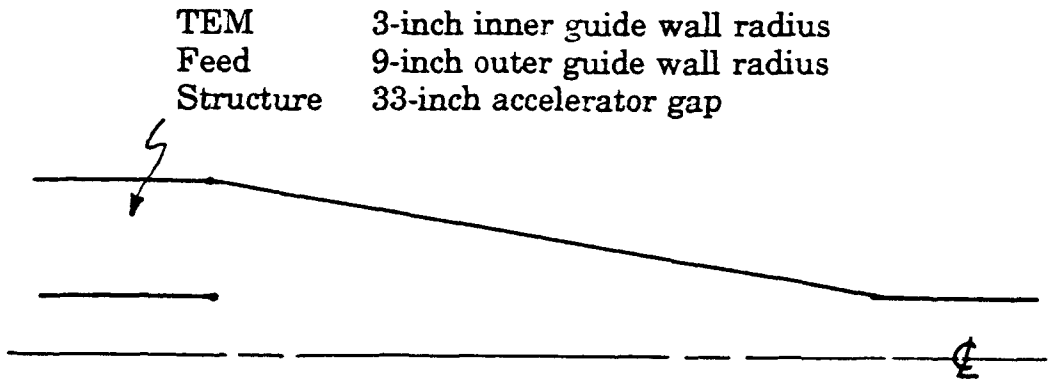

Figure 1. High brightness accelerating cavity.

II. Procedures for Investigation of Beam Breakup

Using the single mode approximation, the cumulative beam breakup gain per gap for a solenoidal magnetic field guided relativistic electron beam may be expressed [6]:

$$G = 2.5\,\frac{QI}{\omega^2 B}\,\frac{\left|\int_0^L dz\,\left[\partial_r E_z - (\partial_z - i\omega)\,E_r\right]_{r=0}\,\exp\left[-i\,(\omega+\Omega)\,z/c\right]\right|^2}{\int d^3x\;|\boldsymbol{E}|^2} \qquad (1)$$

where I is the beam current in kiloamperes; B, the magnetic guide field in kilogauss; ω, the frequency of the cavity resonance; Ω, the relativistic cyclotron frequency; Q, the resonant cavity quality factor; L, the accelerator gap length; and $\mathbf{E}(r,z)$, the electric field of the cavity resonance.

For a conventional small gap accelerating cavity (i.e., $L \rightarrow 0$) of volume $\pi R^2 L$ dominated by a TM E_z field, Equation (1) yields the conventional beam breakup gain scaling:

$$G \sim \frac{QIL}{BR} \qquad (2)$$

Given that cavity geometry, beam current and focusing strength are often fixed by other considerations, the usual procedure employed to mitigate beam breakup is to

devise dissipative loading of accelerating cavity structures to reduce Q. This procedure is effective up to a point; in practice the overall minimum attainable Q is usually of the order of 2 - 10.

However, in addition to Q spoiling of the accelerating cavity, Equation (1) indicates a further approach offered by the high brightness, wide gap cavity designs; namely, phase cancellation between the propagating negative energy beam eigenmode and the cavity fields, as indicated by the overlap integral in the numerator of Equation (2). Specifically, if the cavity eigenmode is sufficiently extended in z [e.g., of the form exp (-z/ℓ)] and the focusing wavelength sufficiently short [$\Omega\ell/c = B\ell/1.7\gamma > 1$], significant phase cancellation may occur resulting in a reduced gain of the form:

$$G \sim \frac{QI\ell}{BR} \frac{1}{(1+0.35B^2\ell^2/\gamma^2)} \qquad (3)$$

In order to determine whether such improvements can be realized with the high brightness gap designs, a relativistic electron beam, cumulative beam breakup simulation code, BREAKUP, has been developed and benchmarked against known analytic solutions. This simulation code determines the beam breakup amplification factor over a specified frequency band for acceleration gap structures of arbitrary axisymmetric design and arbitrary resistive loading. Using BREAKUP, conventional high current, multi-MeV electron accelerator cavity structures as well as the high brightness structures have been examined and the resulting total amplification factors compared. One specific comparison is noted below.

III. Comparison of Conventional and High Brightness Cavity Structures

Typical of conventional accelerator cavity design is the structure shown in Figure 2, which is modeled after an ATA design [7]. By appropriate loading, the Qs of this cavity can be brought in line with quoted values [7] and the resulting beam breakup amplification calculated by BREAKUP. As noted, the third TM resonance appears to dominate beam breakup [7]. This is borne out by the

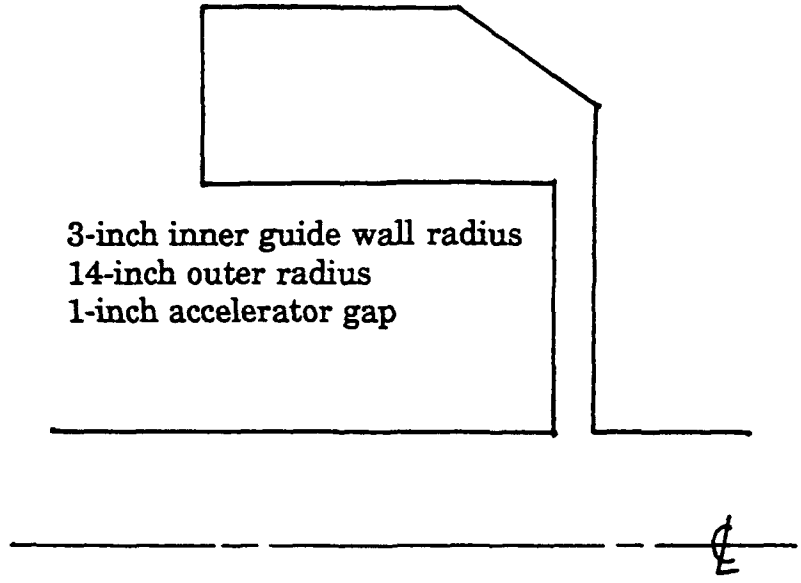

Figure 2. Conventional accelerator cavity.

BREAKUP simulation data shown in Figure 3 which spans the frequency space of the second and third cavity resonances. The peak gain value for this cavity is calculated by BREAKUP to be

$$G = \frac{I}{18B} \qquad (4)$$

Similarly, the beam breakup characteristics of the high brightness accelerating cavity of Figure 1 have been examined. An exhaustive search was conducted to determine the best achievable Q spoiling of the cavity. This will not be detailed here; suffice it to say that cavity loading dominated by a relatively simple 50 Ohms per

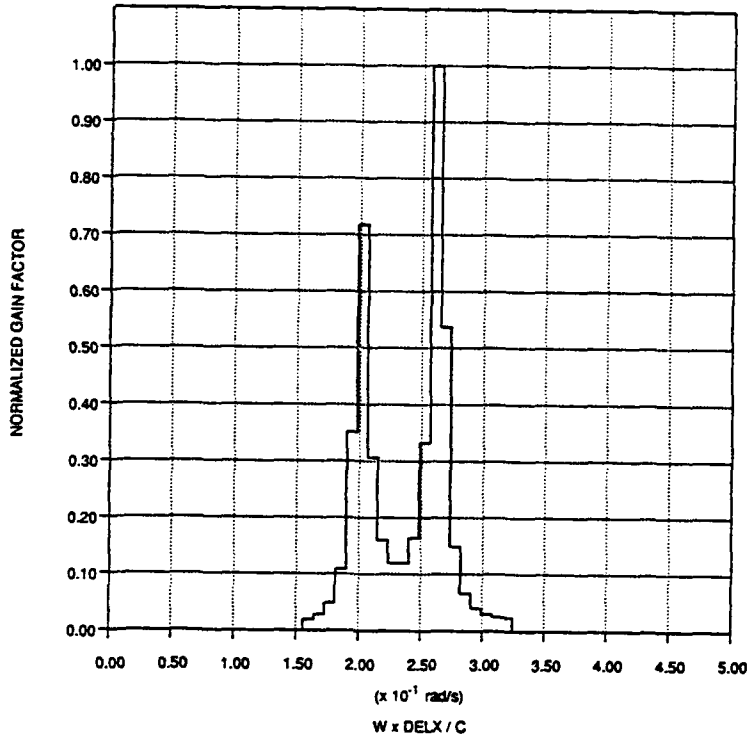

Figure 3. Conventional cavity gain curve.

square resistive sleeve insert in the TEM power feed line proved optimum. The BREAKUP-computed gain curve for this cavity is shown in Figure 4, with a peak gain given by

$$G = \frac{I}{34\,B} \qquad (5)$$

We note, however, that the above BREAKUP simulations were carried out for very small magnetic field values, in the range of $10^{-2}\,\gamma$ kilogauss. If we raise the value of the magnetic guide field a factor of 10, the narrow gap amplification formula remains unchanged; however, the high brightness cavity gain as computed by BREAKUP simulation code shows a lower numerical value G = I/(59 B), indicating the onset of phase cancellation reduction. With another factor of 10 increase in magnetic field, the gain curve shown in Figure 5 is obtained, exhibiting little of the original resonance structuring of Figure 4, with a marked decrease in gain to G = I/(5000 B). These lower values are consistent with the phase cancellation reduction factor of Equation (3). Indeed, a good fit to the Equation (3) scaling obtains for an ℓ = 25 cm, allowing the high brightness cavity gain to be expressed.

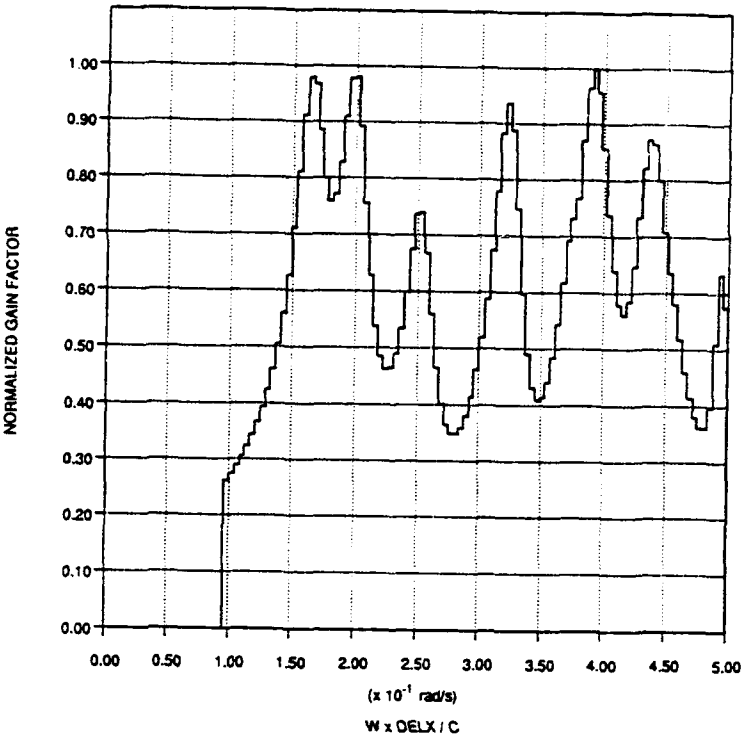

Figure 4. High brightness cavity gain curve.

$$G = \frac{I}{34\,B}\;\frac{1}{(1+230\,B^{2}/\gamma^{2})} \qquad (6)$$

The gain formula for the standard narrow gap cavity of course shows no such reduction.

In order to calculate the total gain through an accelerator, the gains given by Equations (4) and (6) may be cumulatively summed over the number of accelerating cavities, starting with $\gamma = 1$ up to the final desired γ. For acceleration of a 10 kA electron beam to 50 MeV energy, utilizing 200 250 kV/gap accelerating cavities, the overall gain for the standard cavity design is given by

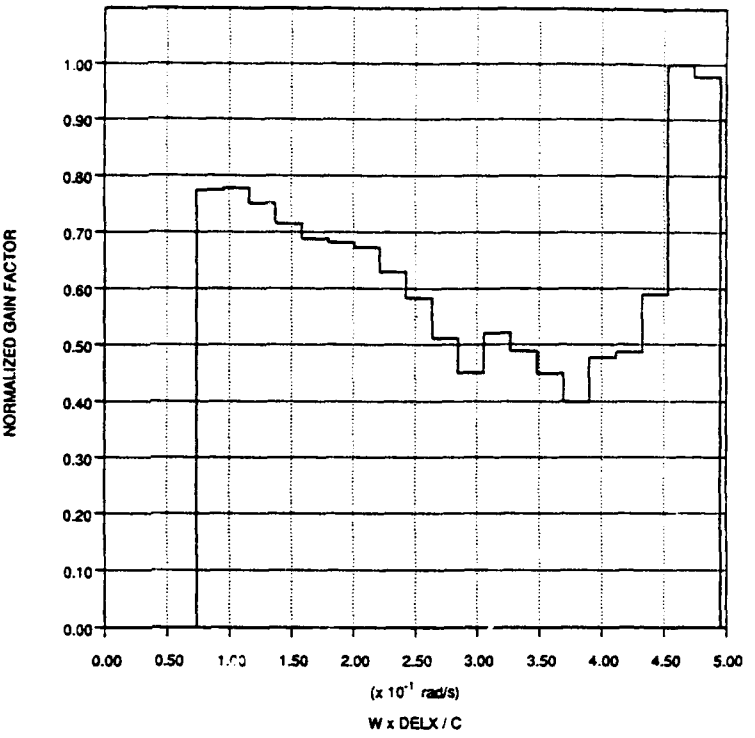

Figure 5. High brightness cavity gain curve showing phase cancellation reduction.

$$G = \exp\left(\frac{111.}{B}\right) \tag{7}$$

while the cumulative gain for the high brightness cavity may be expressed (allowing the replacement of the sum with an appropriate integral)

$$G = \exp\left[\frac{58.8}{B}\left(1 + 0.15B \arctan\left(\frac{1}{0.15B}\right)\right)\right] \tag{8}$$

The comparison of the number of e-folds of beam breakup for the two different cavities is shown in Table 1 for magnetic fields ranging from 1.0 to 10.0 kilogauss.

TABLE I

NUMBER OF E-FOLDS

B[kG]	STANDARD DESIGN	HIGH BRIGHTNESS DESIGN
1.0	110.	46.
2.0	56.	18.
3.0	37.	9.5
4.0	28.	5.6
5.0	22.	3.6
6.0	19.	2.4
7.0	16.	1.7
8.0	14.	1.2
9.0	12.	0.91
10.0	11.	0.69

The ATA literature [8] clearly indicates the desirability of limiting beam breakup amplification to less than 10 total e-folds down the accelerator. With the conventional cavity, this would require a rather large 10 kilogauss magnetic guide field, while the high brightness cavity would allow such reduced e-folds to be achieved with about 1/3 that value. Or stated another way, with a nominal 6.0 kilogauss guide field, the conventional cavity accelerator would exhibit some 19 e-folds, or an overall gain of some 2×10^8, while a high brightness cavity accelerator would suffer a total overall beam breakup gain of only 11.

IV. Summary

The large accelerating gap inherent to the high beam brightness cavity structures provides a means of significant reduction of cumulative beam breakup gain through phase cancellation between the negative energy beam eigenmode and the attendant cavity eigenmodes. Follow-on experimental investigation of such

designs to confirm their inherent beam breakup suppression, as well as high brightness advantages, should be carried out.

V. References

1. G. J. Caporaso, A. G. Cole, and K. W. Struve, "Beam Breakup Instability Experiments on ETA and Predictions for ATA," IEEE Trans. Nuc. Sci., Vol. NS-30, 1983, p. 2507.

2. R. B. Miller, B. M. Marder, P. D. Coleman, and R. E. Clark, J. Appl Phys. 63 (4), 997 (1988).

3. Y. Y. Lau, Phys. Rev. Lett. 63, 1141 (1989).

4. G. J. Caporaso, F. Rainer, W. E. Martin, D. S. Prono, and A. G. Cole, "Laser Guiding of Electron Beams in the Advanced Test Accelerator," Phys. Rev. Lett., Vol. 57, 1986, p. 1591.

5. J. R. Thompson, M. L. Sloan, J. R. Uglum, and B. N. Moore, "Beam Handling and Emittance Control," Proc. SPIE, Microwave and Particle Beam Sources and Directed Energy Concepts, Vol. 1061, 454 (1989).

6. M. L. Sloan and James R. Thompson, "Beam Breakup in Low Emittance Accelerator Cavities," Proc. SPIE, Intense Microwave and Particle Beams, Vol. 1226, 447 (1990).

7. R. J. Briggs, et al., IEEE Trans NS-28, 3360 (1981).

8. D. S. Prono, "Recent Progress of the Advanced Test Accelerator," IEEE Trans. Nuc. Sci., Vol. NS-32, 1985, p. 3144.

VI. Acknowledgement

This research was carried out under ONR Contract N00014-88-C-0542.

OPTICAL GUIDING AND ELECTRON ACCELERATION IN THE LASER WAKEFIELD ACCELERATOR

P. Sprangle, E. Esarey, J. Krall, G. Joyce and A. Ting

Beam Physics Branch, Plasma Physics Division
Naval Research Laboratory, Washington, DC 20375-5000

Abstract

The laser wakefield acceleration concept is studied using a general 2D formulation based on relativistic fluid equations. Simulations of an intense laser pulse propagating in a plasma address both optical guiding and wakefield generation issues. It is shown that relativistic guiding is ineffective in preventing the diffraction of short pulses and long pulses are broken up into beamlet segments due to wakefield effects. The use of preformed plasma density channels or tailored pulse profiles allows intense laser propagation over many Rayleigh lengths. The ponderomotive force associated with the laser pulse envelope generates large amplitude accelerating and focusing wakefields over long distances to achieve electron trapping, acceleration and focusing.

Introduction

The possibility of utilizing the fields of intense laser beams to accelerate particles to high energies has attracted a great deal of interest.[1-4] The fundamental motivation for studying laser driven accelerators is the ultra-high fields associated with high intensity pulsed lasers. The laser transverse electric field in units of TV/m is given by

$$E_L(\mathrm{TV/m}) = 2.6 \times 10^{-9} I_L^{1/2}[\mathrm{W/cm^2}] = 3a_L/\lambda[\mu\mathrm{m}],$$

where I_L is the laser intensity in W/cm^2, λ is the laser wavelength in μm and a_L is the unitless laser strength parameter. Recent developments in compact laser systems[5-8] has resulted in laser intensities of $I_L \sim 10^{18}$ W/cm^2($a_L \gtrsim 1$) for $\lambda = 1$ μm. The transverse electric field associated with these lasers is typically, $E_L \gtrsim 3$ TV/m. The various laser acceleration concepts involve transforming a small fraction of the transverse laser field into an effective longitudinal accelerating field.

A laser driven plasma wave accelerator that has a number of attractive features is the laser wakefield accelerator[9-17] (LWFA). In the LWFA, a short (~ 1 psec) intense ($a_L \sim 1$) laser pulse propagates through an underdense plasma, $\lambda^2/\lambda_p^2 \ll 1$, where $\lambda_p = 2\pi c/\omega_p$ is the plasma wavelength and $\omega_p = (4\pi e^2 n_o/m_o)^{1/2}$ is the plasma frequency. If the laser pulse length, $c\tau_L$, is approximately equal to the plasma wavelength, $c\tau_L \approx \lambda_p$, the ponderomotive force associated with the laser pulse envelope, $F_p \sim \nabla a^2$, can generate a trailing large amplitude plasma wave (wakefield) with phase velocity equal to the laser pulse group velocity by expelling electrons from the region of the laser pulse. The accelerating gradient and transverse focusing field associated with the wakefield can accelerate and focus a trailing electron beam. The ratio of the accelerating field to the laser field in the LWFA is given by[13-16]

$$E_{acc}/E_L = 1.6 \times 10^{-11} (n_o[\mathrm{cm^{-3}}])^{1/2} \lambda[\mu\mathrm{m}] \frac{a_L}{(1+a_L^2/2)^{1/2}},$$

where n_0 is the ambient plasma density in cm^{-3}. For $n_0 = 10^{17}$ cm^{-3}, $a_L = 1$ and $\lambda = 1$ μm, the accelerating field is $E_{acc} \simeq 12$ GeV/m, which is 0.4% of the laser field E_L (~ 3 TV/m). In the LWFA, the plasma serves a dual purpose, it acts as a medium which i) transforms a fraction (~ 1%) of the laser field into an accelerating field and ii) modifies the refractive index to optically guide the laser pulse.

In the absence of optical guiding, the major limitation of laser acceleration schemes is the limited acceleration distance, due to diffraction,[11,12] which is given by $L_{int} \simeq \pi Z_R$, where $Z_R = \pi r_{L0}^2/\lambda$ is the vacuum Rayleigh length and r_{L0} is the minimum waist. The maximum energy gain of the electron beam in a single stage is $\Delta W \simeq E_{max} L_{int}$ which, in the limit $a_L^2 << 1$, may be written as

$$\Delta W[\mathrm{MeV}] \simeq 580 (\lambda/\lambda_p) P_L[\mathrm{TW}].$$

As an example, consider a $\tau_L = 1$ psec linearly polarized laser pulse with $P_L = 10$ TW, $\lambda = 1$ μm and $r_L = 30$ μm ($a_L = 0.72$). The requirement that $c\tau_L \simeq \lambda_p$ implies a plasma density of $n_0 = 1.2 \times 10^{16}$ cm^{-3}. The wakefield amplitude is $E_{acc} = 2.0$ GeV/m and the interaction length is $L_{int} = 0.9$ cm. Hence, a properly phased trailing electron bunch would only gain an energy of $\Delta W = 18$ MeV in a single stage without optical guiding. The interaction length and consequently the electron energy gain, may be greatly increased by optically guiding the laser pulse in the plasma. In plasmas, nonlinear and relativistic effects associated with intense laser fields can significantly modify the propagation characteristics of the laser.[11-28] Optical guiding in plasmas can be achieved by relativistic effects,[11-26] preformed density channels[15-17] or tailored laser pulse profiles.[15,17]

Nonlinear Formulation

A fully nonlinear, relativistic, two-dimensional axisymmetric laser-plasma propagation model is formulated and numerically evaluated for laser pulses of ultra-high intensities and arbitrary polarizations.[17] The formulation has a number of unique features which allow for numerical simulations to be carried out over extended laser propagation distances. The appropriate Maxwell-Fluid equations are recast into a convenient form by i) performing a change of variables to the speed of light frame, ii) applying the quasi-static approximation[13,14] (QSA), iii) expanding in two small parameters (which are independent of the laser intensity) and iv) averaging over the fast spatial scale length, i.e., the laser wavelength.

The plasma is modelled using relativistic cold fluid equations. The momentum and continuity equations are $d\mathbf{u}/dt = c\nabla\phi + \partial\mathbf{a}/\partial t - c\mathbf{u} \times (\nabla \times \mathbf{a})/\gamma$ and $\partial(\rho\gamma)/\partial t + c\nabla\cdot(\rho\mathbf{u}) = 0$, respectively, where $\mathbf{a} = |e|\mathbf{A}/m_0c^2$ and $\phi = |e|\Phi/m_0c^2$ are the normalized vector and scalar potentials, respectively, $\mathbf{u} = \mathbf{p}/m_0c$ is the normalized fluid momentum, $\rho = n/\gamma n_0$, n is the electron density, n_0 is the ambient density, $\gamma = (1 + u^2)^{1/2}$ is the relativistic factor, and $-|e|$ and m_0 are the electron charge and rest mass, respectively. In the following, the Coulomb gauge is used ($\nabla\cdot\mathbf{a} = 0$), the ions are assumed stationary and thermal effects are neglected.[13,14]

The full set of equations are recast into speed of light coordinates by changing variables from z,t to $\zeta = z - ct$ and $\tau = t$, where z and t are laboratory frame variables denoting the distance along the laser propagation axis and time, respectively. The QSA[13,14] is then applied. The resulting equations are expanded to first order in the parameters $\epsilon_1 = 1/kr_L << 1$ and $\epsilon_2 = k_p/k << 1$, where $k = 2\pi/\lambda$, $k_p = 2\pi/\lambda_p = \omega_p/c$, and r_L is the laser spot size.

All the fluid and field quantities are expanded in slow and fast terms, i.e., $Q = Q_s + Q_f$. The fast quantities are of the general form $Q_f = \hat{Q}_f(r,\zeta,\tau)\exp(im k\zeta)/2 + c.c.$, where $m = 1,2,3,...$ and $\hat{Q}_f$ is complex and slowly varying in ζ. Within this representation, the nonlinear fluid equations are averaged over the laser wavelength in the (ζ,τ) frame. The ζ-averaging allows for all the laser-plasma response quantities to be evaluated on the slow spatial scale, i.e., λ_p or $c\tau_L$, permitting solutions over extended propagation distances.

The resulting equations describe the slowly varying components of the fluid and field quantities:

$$\nabla_\perp^2 \underset{\sim}{a} = k_p^2 \rho \underset{\sim}{u} - \partial(\nabla\phi)/\partial\zeta, \tag{1a}$$

$$\nabla_\perp^2 \phi + \partial^2\phi/\partial\zeta^2 = k_p^2(\gamma\rho - \rho^{(o)}), \tag{1b}$$

$$\partial(\underset{\sim}{u} - \underset{\sim}{a})/\partial\zeta = \nabla(\gamma - \phi), \tag{1c}$$

$$\partial(\rho(1 + \psi))/\partial\zeta = \nabla_\perp \cdot (\rho \underset{\sim}{u}_\perp), \tag{1d}$$

where the subscript s, denoting the slow component of the quantity, has been dropped, $\rho^{(o)} = n^{(o)}/n_o$, $n^{(o)}(r)$ is the initial plasma density profile prior to the laser interaction which may be a function of radial position and $\psi = \phi - a_z$ is the wake potential. Equations (1a)-(1d) represent, respectively, the slow components of the wave, Poisson's, momentum and continuity equations.

In obtaining Eq. (1c), the identity $\nabla \times (\underset{\sim}{u} - \underset{\sim}{a}) = 0$, showing the irrotational nature of the ponderomotive flow, was used. It can be shown that the quantity $\gamma - u_z - \psi$ is an invariant which is set equal to unity, i.e., its value prior to the arrival of the laser pulse. The slowly varying component of the relativistic factor is

$$\gamma = (1 + \psi)^{-1}\left\{1 + u_\perp^2 + |\hat{\underset{\sim}{a}}_f|^2/2 + (1 + \psi)^2\right\}/2, \tag{2}$$

where a linearly polarized laser pulse with amplitude $|\hat{a}_f|$ is assumed throughout this paper. The transverse component of the laser radiation field is $a_f = \hat{a}_f(r,\zeta,\tau)\exp(ik\zeta)/2 + c.c.$, where $\hat{a}_f$ is the complex, slowly varying amplitude which satisfies the parabolic (reduced) wave equation,

$$\left(\nabla_\perp^2 + 2c^{-1}k\partial/\partial\tau\right)\hat{\underset{\sim}{a}}_f = k_p^2 \rho \hat{\underset{\sim}{a}}_f. \tag{3}$$

Within the QSA, the self-consistent, slowly varying equations in the (ζ,τ) variables, describing the laser-plasma interaction, to first order in ϵ_1 and ϵ_2, are given by Eqs. (1)-(3).

Equations (1a)-(1d) can be combined to yield a single equation for ψ in terms of $|\hat{a}_f|^2$ of the form $\partial^2\psi/\partial\zeta^2 = G(\psi, |\hat{a}_f|^2)$, where G is an involved function. The equation for ψ is obtained by noting that $\rho = (\rho^{(o)} + k_p^{-2}\nabla_\perp^2\psi)/(1 + \psi)$ and $u_\perp = \rho^{-1}k_p^{-2}\nabla_\perp\partial\psi/\partial\zeta$. Note also that the refractive index is solely a function of ψ through ρ, i.e., $\eta_R = 1 - k_p^2\rho/2k^2$. Equation (3) together with $\partial^2\psi/\partial\zeta^2 = G$ completely describe the 2D-axisymmetric laser-plasma interaction. The wake potential, ψ, is related to the axial electric field, E_z, of plasma response (wakefield) by $\hat{E}_z = -\partial\psi/\partial\zeta$, where $\hat{E}_z = |e|E_z/m_o c^2$. Equations (1)-(3) reduce to models which have been previously studied, i.e., the broad pulse limit[13,14] ($\nabla_\perp \to 0$) and the axially uniform pulse limit[23-26] ($\partial/\partial\zeta \to 0$).

LWFA Simulations Results

a) Short Pulsed Propagation

Simulations[15,17] of short pulse propagation confirm the predictions of Refs. 13 and 14 that relativistic guiding, which requires laser powers $P_L \geq P_{crit} = 17(\lambda_p/\lambda)^2$[GW], does not occur for short pulses, $c\tau_L < \lambda_p/(1 + |\hat{a}_f|^2/2)^{1/2}$. For short pulses the plasma can not collectively respond to modify the refractive index. The results are shown in Fig. 1 for the parameters $\lambda_p = 0.03$ cm ($n_o = 1.2 \times 10^{16}$ cm^{-3}), $r_L = \lambda_p$ (Gaussian radial profile), $\lambda = 1$ μm ($Z_R = 28$ cm) and $P_L = P_{crit}$. The initial axial laser profile is given by $|\hat{a}_f(\zeta)| = a_L \sin(-\pi\zeta/L)$ for $0 < -\zeta < L = c\tau_L$, where $a_L = 0.9$ for the above parameters. Simulations are performed for two laser pulse lengths, $L = \lambda_p$ ($\tau_L = 1$ ps) and $L = \lambda_p/4$ ($\tau_L = 0.25$ ps). The initial normalized laser intensity, $|\hat{a}_f|^2$, is shown in Fig. 2 for $L = \lambda_p$. The spot size at the pulse center versus propagation distance $c\tau$ is shown in Fig. 1 for (a) the vacuum diffraction case, (b) the $L = \lambda_p/4$ pulse and (c) the $L = \lambda_p$ pulse. The $L = \lambda_p/4$ pulse diffracts almost as if in vacuum. The $L = \lambda_p$ pulse experiences a small amount of initial guiding before diffracting.

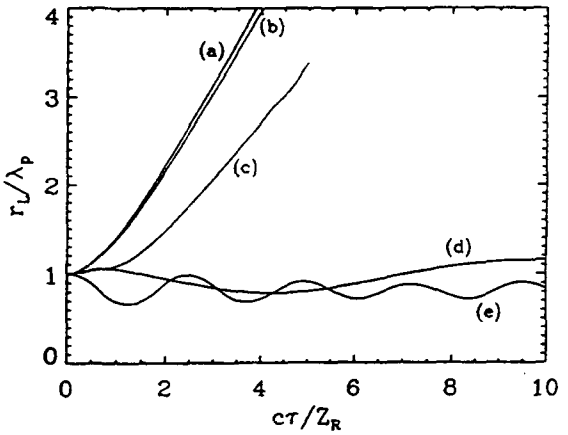

Fig. 1. Laser spot size r_L/λ_p (at $\zeta = -L/2$) versus propagation distance, $c\tau/Z_R$, for (a) vacuum diffraction, (b) pulse with $L = \lambda_p/4$, (c) pulse with $L = \lambda_p$, (d) a shaped pulse and (e) a channel-guided pulse.

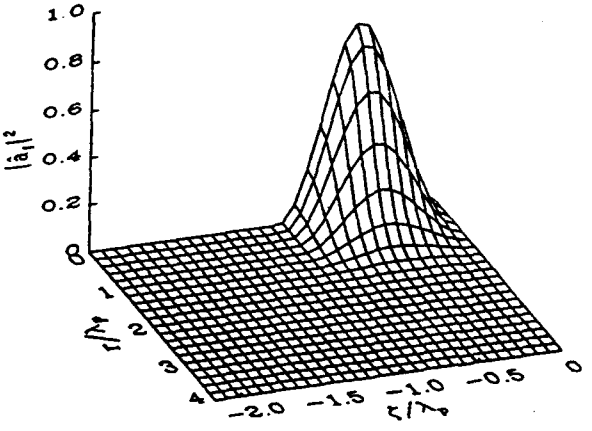

Fig. 2. Normalized laser intensity $|\hat{a}_f|^2$ in the speed of light frame (ζ,τ) at $\tau = 0$ for the parameters $a_o = 0.9$, $L = r_L = \lambda_p = 0.03$ cm and $\lambda = 1$ μm. The plasma flows from right to left.

b) Laser Pulse Modulation

The wakefield generated by the finite rise time of a long pulse can modulate the pulse structure.[15,17] Consider a long laser pulse in which the body of the pulse has a constant amplitude with $P_L = P_{crit}$ and, therefore, should be relativistically guided. The amplitude of the wakefield generated by the front of the pulse is determined by the rise time. The wakefield, which consists of a plasma density modulation of the form $\delta n = \delta n_o(r)\cos(k_p\zeta)$, modifies the plasma's refractive index.[27] In regions of a local density channel, i.e., where $\partial\,\delta n/\partial r > 0$, the radiation focuses. In regions where $\partial\,\delta n/\partial r < 0$, diffraction is enhanced.

Pulse modulation is illustrated by a simulation of a long pulse (a long rise, $L_{rise} = 5\ \lambda_p$, followed by a long flattop region, $L_{flat} = 5\ \lambda_p$) with $P_L = P_{crit}$ ($a_L = 0.09$, $r_L = 10\ \lambda_p$, $\lambda_p = 0.03$ cm and $\lambda = 1$ μm). Simulations indicate that for $P_L \geq P_{crit}$, an unstable wakefield is excited at the front of the pulse and rapidly modulates the

pulse profile. Figure 3 shows the pulse modulation, where $|\hat{a}_f|^2$ is plotted at $c\tau = 2Z_R$ for the above initial parameters. At high intensities, i.e., $a_L^2 >> 1$, the modulation is reduced.

c) Pulse Propagation in a Plasma Density Channel

A preformed plasma density channel can guide short, intense laser pulses.[15-17] In the weak laser pulse limit, $|\hat{a}_f|^2 << 1$, the index of refraction is given by $\eta_R = 1 - k_p^2\rho^{(o)}/2k^2$. Optical guiding requires $\partial\eta_R/\partial r < 0$, hence, a preformed density channel, $n^{(o)}(r) = n_0\rho^{(o)}(r)$, may prevent pulse diffraction. Analysis of the wave equation in the weak pulse limit indicates that a parabolic density channel will guide a Gaussian laser beam provided that the depth of the density channel[15-17] is $\Delta n = 1/\pi r_e r_L^2$, where $\Delta n = n^{(o)}(r_L) - n^{(o)}(0)$ and r_e is the classical electron radius.

A simulation of channel guiding is shown in Figs. 4 for a laser pulse with the initial conditions of Fig. 2 propagating in a parabolic density channel with $\Delta n = 1.3 \times 10^{15}$ cm^{-3} and $n^{(o)}(0) = 1.2 \times 10^{16}$ cm^{-3}. Figure 4 shows the laser intensity at $c\tau = 10\ Z_R$. The laser pulse shows some distortions but remains essentially guided. Guiding is confirmed by the $r_L(c\tau)$ plot in Fig. 1(e). The $r_L(c\tau)$ oscillations indicate a slight mismatch between the laser and channel parameters. This is caused by the laser pulse further reducing the plasma density in the region of peak laser intensities.

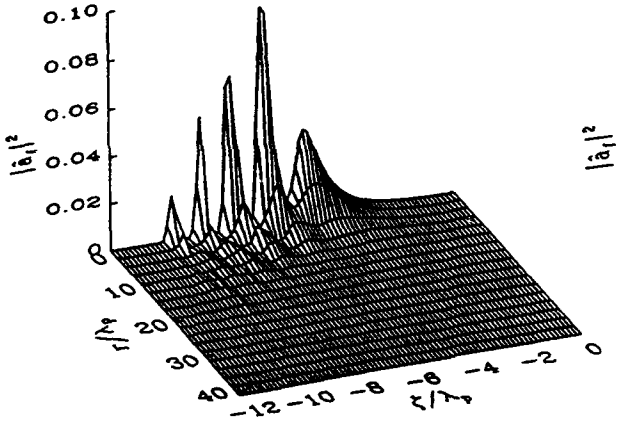

Fig. 3. Normalized laser intensity $|\hat{a}_f|^2$ at $c\tau = 2$ Z_R for a long pulse showing modulation.

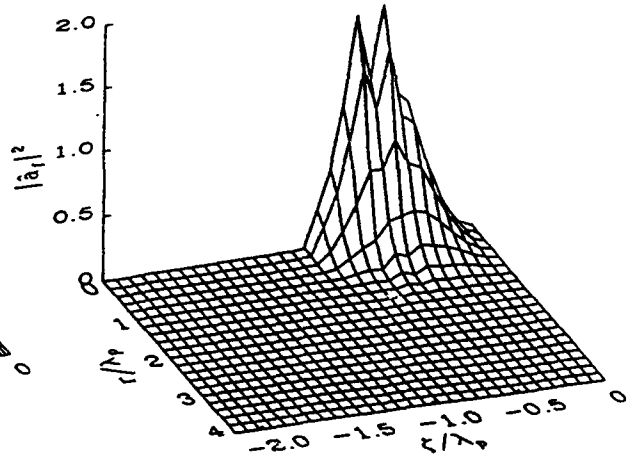

Fig. 4. Normalized laser intensity $|\hat{a}_f|^2$ at $c\tau = 10$ Z_R for the laser pulse of Fig. 2 propagating in a plasma density channel.

d) Electron Trapping, Acceleration and Focusing

The large amplitude wakefield which can be generated over extended distances in a preformed plasma density channel can trap, focus and accelerate electrons to high energy. In the following, a laser pulse is propagated in a preformed plasma density channel with $\Delta n = 3.16 \times 10^{16}$ cm^{-3} and $n^{(o)}(0) = 7.8 \times 10^{16}$ cm^{-3}. The laser pulse parameters are $P_L = 40$ TW, $a_L = 0.72$, $r_L = 0.5\ \lambda_p$ and $\lambda_p = 0.012$ cm. The laser pulse is propagated in the density channel over a distance equal to $c\tau = 20\ Z_R = 23$ cm. In this example, the electrons are

nearly totally expelled from the vicinity of the laser pulse. The maximum accelerating gradient is E_{acc} = 5.5 GV/m and the maximum transverse field at $r = r_L/2$ is E_r = 3.0 GV/m. Figure 5(a) shows the configuration space for the cylindrically symmetric injected electron beam. The initial energy and radius of the continuous electron beam is E_{inj} = 2.0 MeV and r_b = 10 μm, respectively. Figure 5(b) shows the beam after being accelerated to 1.0 GeV in a distance of $c\tau$ = 20 cm. The initially continuous beam becomes bunched and focused during the acceleration process. Approximately 70% of the initial beam electrons are trapped and accelerated. Figure 6(a) shows the energy distribution of the injected electron beam and Fig. 6(b) shows the final beam energy distribution of the accelerated beam. In this example, only three periods of the accelerating wakefield are shown.

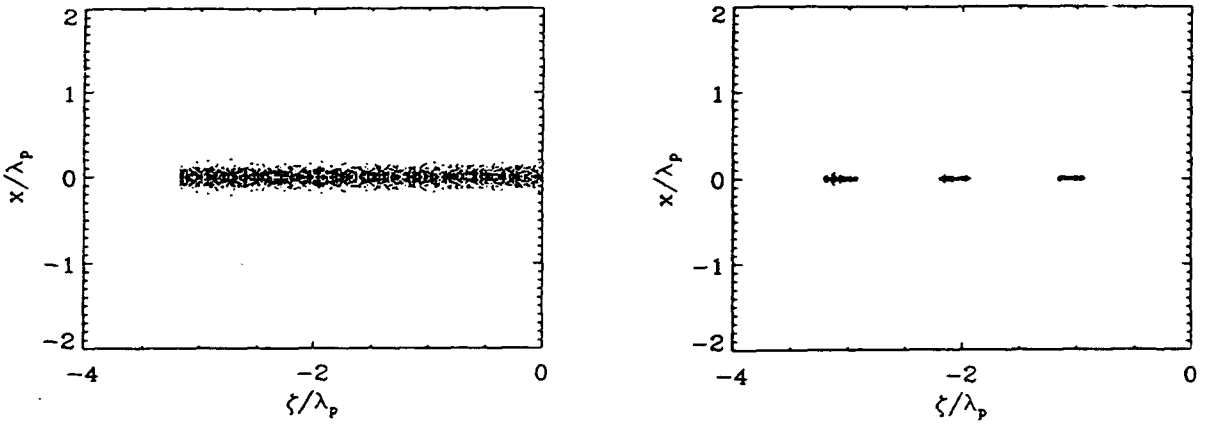

Fig. 5. Transverse and longitudinal spatial distribution of a) injected electron beam, and b) electron beam accelerated to 1 GeV in a distance of 20 cm.

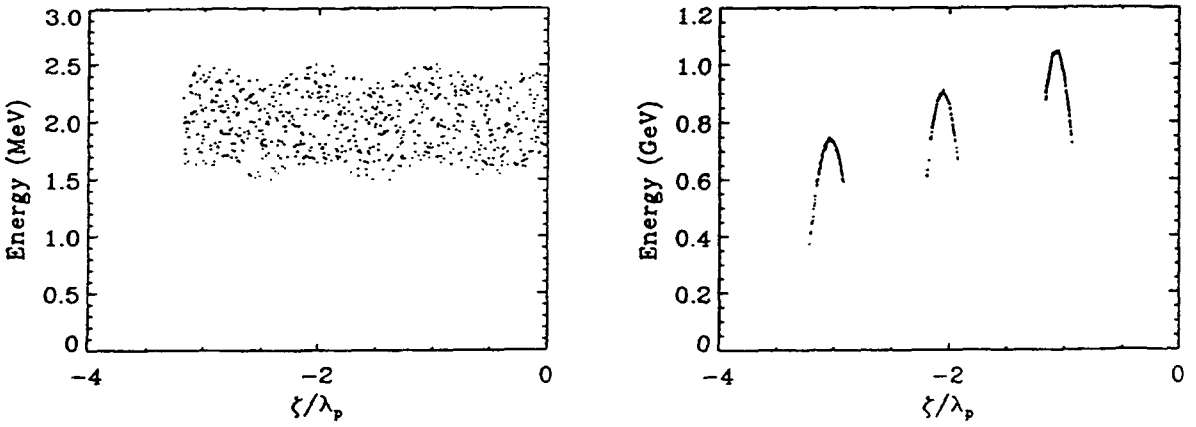

Fig. 6. Energy distribution of a) injected electron beam, and b) accelerated beam.

e) Tailored Laser Pulse

A tailored laser pulse can propagate many Rayleigh lengths without significantly altering its original profile.[15,17] Consider a long laser pulse, $c\tau_L >> \lambda_p$, in which the spot size is tapered from a large value at the front to a small value at the back, so that the laser power, $P_L \sim r_L^2 |\hat{a}_f|^2$, is constant throughout the pulse and equal to P_{crit}. The leading portion ($<< \lambda_p$) of the pulse will diffract as if in vacuum.[13,14] However, since r_L is large at the front of the pulse, the Rayleigh length is also large. Hence, the locally large spot size allows the pulse front to propagate a long distance, whereas the body of the pulse will be relativistically guided. Also, since $|\hat{a}_f|^2$ increases slowly throughout the pulse, detrimental wakefield effects are reduced.

Figure 7(a) shows the initial profile of a tailored pulse in which $|\hat{a}_f|$ increases from 0.09 to 0.9 over a length $L_{rise} = 2\lambda_p$. Here, $P_L = P_{crit}$ throughout the pulse, $|\hat{a}_f| r_L = 0.9\lambda_p$ ($\lambda_p = 0.03$ cm, $\lambda = 1$ μm), which implies a decrease in r_L from $10\lambda_p$ to λ_p. At peak intensity the vacuum diffraction length is $Z_R = 28$ cm. The effectiveness of pulse tailoring can be seen by the $r_L(c\tau)$ plot in Fig. 1(d) and in Fig. 7(b), where a plot of $|\hat{a}_f|^2$ at $c\tau = 24\ Z_R$ demonstrates that the pulse is distorted but largely intact. At $c\tau = 24\ Z_R = 6.8$ m, the peak accelerating gradient of the wakefield behind the pulse is $E_{acc} = 1.3$ GeV/m.

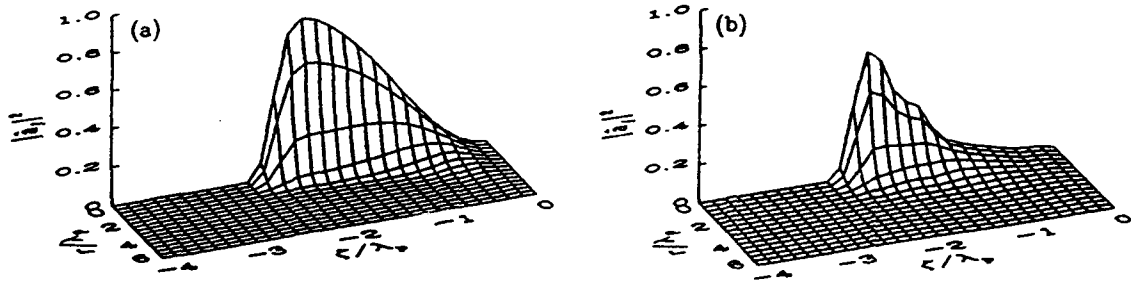

Fig. 7. Normalized laser intensity $|\hat{a}_f|^2$ at (a) $\tau = 0$ and at (b) $c\tau = 24\ Z_R$ for a tailored pulse.

Conclusions

The laser wakefield accelerator is capable of generating ultra-high accelerating and focusing fields over extended distances (many Rayleigh lengths). The ultra-high accelerating gradients and focusing fields are generated by the ponderomotive forces associated with the envelope of the laser pulse. These forces can totally expel electrons from the vicinity of the laser pulse, leaving behind an effective positive charge which sweeps through the plasma at the speed of light. It has been demonstrated that relativistic effects cannot prevent short laser pulses ($c\tau_L \lesssim \lambda_p$) from diffracting. Preformed plasma density channels or tailored laser pulse profiles can provide a means of propagating laser pulses many Rayleigh lengths. We have shown, using present-day laser technology,

that the LWFA can produce accelerating gradients in excess of of 5.5 GV/m over distances greater than 20 cm. In this example an injected uniform 4 MeV electron beam was accelerated to 1 GeV in a distance of 20 cm.

Acknowledgment

This work was supported by the Department of Energy and the Office of Naval Research.

References

1. Laser Acceleration of Particles, Edited by P. Channell, AIP Conf. Proc. No 91. (AIP, NY 1982).
2. Laser Acceleration of Particles, Edited by C. Joshi and T. Katsouleas, AIP Conf. Proc. No. 130 (AIP, NY, 1985).
3. Advanced Accelerator Concepts, Edited by F. Mills, AIP Conf. Proc. No. 156 (AIP, NY, 1986).
4. Advanced Accelerator Concepts, Edited by C. Joshi, AIP Conf. Proc. No. 193 (AIP, NY, 1986).
5. D. Strickland and G. Mourou, Opt. Commun. 56, 216 (1985).
6. P. Maine, D. Strickland, P. Bado, M. Pessot, and G. Mourou, IEEE J. Quantum Electron. QE-24, 398 (1988).
7. M. D. Perry. F. G. Patterson, and J. Weston, Opt. Lett. 15, 1400 (1990).
8. G. Mourou and D. Umstadter, Phys. Fluids B, July (1992).
9. T. Tajima and J. M. Dawson, Phys. Rev. Lett. 43, 267 (1979).
10. L. M. Gorbunov and V. I. Kirsanov, Sov. Phys. JETP 66, 290 (1987).
11. P. Sprangle, E. Esarey, A. Ting, and G. Joyce, Appl. Phys. Lett. 53, 2146 (1988).
12. E. Esarey, A. Ting, P. Sprangle, and G. Joyce, Comments Plasma Phys. Controlled Fusion 12, 191 (1989).
13. P. Sprangle, E. Esarey, and A. Ting, Phys. Rev. Lett. 64, 2011 (1990); Phys. Rev. A 41, 4463 (1990)
14. A. Ting, E. Esarey, and P. Sprangle, Phys. Fluids B 2, 1390 (1990).
15. P. Sprangle, E. Esarey, J. Krall and G. Joyce, presented at the Ultra High Field Symposium, APS-DPP Meeting, Tampa, FL, Nov, 1991.
16. P. Sprangle and E. Esarey, Phys. Fluids B, July (1992).
17. P. Sprangle, E. Esarey, J. Krall and G. Joyce, submitted for publication in Phys. Rev. Lett. (1992).
18. A. G. Litvak, Sov. Phys. JETP 30, 344 (1970).
19. C. Max, J. Arons, and A. B. Langdon, Phys. Rev. Lett. 33, 209 (1974).
20. P. Sprangle, C. M. Tang, and E. Esarey, IEEE Trans. Plasma Sci. PS-15, 145 (1987).
21. E. Esarey, A. Ting, and P. Sprangle, Appl. Phys. Lett. 53, 1266 (1988).
22. W. B. Mori, C. Joshi, J. M. Dawson, D. W. Forslund, and I. M. Kindel, Phys. Rev. Lett. 60, 1298 (1988).
23. G. Z. Sun, E. Ott, Y. C. Lee, and P. Guzdar, Phys. Fluids 30, 526 (1987).
24. T. Kurki-Suonio, P. J. Morrison, and T. Tajima, Phys. Rev. A 40, 3230 (1989).
25. P. Sprangle, A. Zigler, and E. Esarey, Appl. Phys. Lett. 58, 346 (1991).
26. A. B. Borisov, A. V. Borovskiy, O. B. Shiryaev, V. V. Korobkin, A. M. Prokhorov, J. C. Solem, T. S. Luk, K. Boyer, and C. K. Rhodes, Phys. Rev. A 45, 5830 (1992).
27. E. Esarey and A. Ting, Phys. Rev. Lett. 65, 1961 (1990).
28. X. Liu and D. Umstadter, submitted to Phys. Rev. Lett.

Invited Beam and Pulsed Power Applications Papers

Gunther Kessler, *Session Chairman*

CURRENT STATUS OF PULSE-POWER TECHNOLOGY AND APPLICATIONS AT LBT, NAGAOKA

K. Yatsui, W. Masuda, K. Masugata, W. Jiang, Y. Sekimoto,
G. Imada, T. Sonegawa and X. D. Kang
Laboratory of Beam Technology, Nagaoka University of Technology,
Nagaoka, Niigata 940-21, Japan

Tight focusing of an ion beam was obtained by "Plasma Focus Diode". In addition to two-dimensionally line-focusing reported previously, we achieved point focusing of the proton beam.

Quick charging Blumlein PFL was successfully developed. Using saturable cores as a charging inductor, we succeeded in the reduction of prepulse and quick charging of the Blumlein line. Output pulse of voltage ~ 580 kV and current ~ 24 kA with current rise time of less than 16 ns. Various thin films were quickly prepared by Ion-Beam Evaporation (IBE) such as ZnS, YBCO, $BaTiO_3$, BN, B, C, ITO, apatite, etc. Basic characteristics were studied of ablation plasma produced by the irradiation of ion beam on the targets.

Highly-repetitive excimer laser with subsonic gas flow is developed by Ludwieg charge tube. Basic characteristics of gas dynamics are studied by simulation. We developed a new circuit to excite highly-repetitive excimer lasers, where a saturable transformer is used in magnetic pulse compressor.

To control lightning artificially, we studied basic plasma channel produced by TEA-CO_2 lasers in air.

INTRODUCTION

Since the establishment of our university in 1978, we started R & D of pulse-power technology and its applications of charged particle beams (intense, pulsed, light ion beam (LIB) or relativistic electron beam (REB)).

In this paper, current status of our research activities is overviewed such as three-dimensional focusing of proton beam by spherical "plasma-focus diode", basic characteristics of applied B_r diodes, quickly charging Blumlein pulse forming line. Various applications of pulse-power technology are mentioned such as in materials science and laser engineering.

I. TIGHT FOCUSING OF PROTON BEAM BY SPHERICAL PLASMA-FOCUS DIODE

We have developed a spherical "plasma focus diode" (SPFD), a new self-magnetically insulated, three-dimensionally focused ion-beam diode. Figure 1 shows the basic structure of SPFD. It consists of two spherical electrods,

anode (50-mm I.D.) and cathode (40-mm O.D.) with the gap length of 5 mm. The basic principle of SPFD is similar to the coaxial, two-dimensional focusing "plasma focus diode" reported elsewhere.[1,2]

The experimental results of Rutherford scattering pinhole camera have shown that the ion beam is toghtly focused toward the central axis. Figure 2 shows the cross-sectional profile of the ion-beam obtained by the pinhole camera. Results obtained at different axial positions have shown that the focusing area is ≧ 1 mm long near the geometrical center. We have also used shodow-box to measure the deflection angle of the ion beam. We have found that average azimuthal diflection angle is very small (~ 1°) and that the average deflection in ψ direction is relatively large (≧ 5°) especial at the upstream of the electron flow. From the data of both pinhole camera and shadow-box, we believe that ions is mostly focused into a small cylindrical volume with 0.5 mm in diameter and 2.5 mm in length. Using four biased ion collectors (BIC), we measured the ion-beam current distribution on the anode surface. Figure 3 shows the typical waveforms of ion-beam current at four positions. We see that the average ion-beam current density on the anode surface is ≧ 2 kA/cm^2. With the above results, we have calculated the ion-beam current density ~ 680 kA/cm^2 and the power density at the focusing area ~ 0.54 TW/cm^2 at the beam voltage of ~ 0.8 MV.

Ⅱ. DEVELOPMENT OF QUICK CHARGING BLUMLEIN PFL

A compact, high voltage, discharge-switch free Blumlein PFL has been developed for pulse-power applications. Figure 4 shows the schematic of the PFL. In the PFL, we have utilized a saturable inductor of amorphous metallic cores as a charging inductor (CI). As a result, quick charging of PFL becomes possible with low prepulse level. In addition, using CI as a step-up transformer in the output phase, twice of the output voltage of the PFL is applied to the load. As a Blumlein switch, magnetic switch (MS) is utilized to obtain a repetitive operation of PFL. Since the switching speed of MS is almost propotional to the charging time, high-speed switching is obtained in the quick charging BL.

Figure 5 shows the typical waveforms. We see PFL is charged to + 290 kV by a fast Marx generater in ~ 220 ns. After the charging, MS of amorphous

core is saturated and the output of -290 kV, 50 kA, 60 ns is generated. The output pulse is doubled in the volage in CI and the pulse of - 580 kV, 24 kA is applied to the load with current rise time less than 16 ns. The energy transfer efficency (output energy/charging energy of PFL) is estimated to be more than 92 %.

Ⅲ. HIGH POWER DENSITY ION DIODES

Ⅲ-a) Evaluation of the Effect of Prepulse

In a high-power short gap-length diode, pre-formation of anode or cathode plasma produced by a prepulse strongly affects the diode operation. To evaluate the effect, self-magnetically insulated plasma-focus diode (PFD) is used with vacuum flashover prepulse switch (VPS) on the pulse power generator, "ETIGO-II".

Experimental setup is shown in Fig. 6. VPS of twelve discharge gaps is installed in vacuum chamber. Before the experiment, the prepulse voltage is evaluated by using a dummy load of inductor, from which it is reduced by VPS to be less than 1/3 of that without VPS. PFD used has A-K gap of 5 mm and length of ~ 40 mm, and is constructed of a cyrindrical anode with epoxy filled grooves (inner diameter = 33 mm), and a cathode of outer diameter of 23 mm.

With VPS, PFD is operated at relatively high impedance of ~ 10 Ω with diode voltage ~ 1 MV and diode current ~ 100 kA. In contrast to the above, PFD is short circuited in evely shots in the absence of VPS.

Ⅲ-b) Evaluation of Gas Produced in the Diode Operation

In the shot of high power ion diode, a lot of morecules are released mainly from anode. These molecules will be the source of anode plasma, which affects the diode operation, such as the gap closure. To evaluate the mechanism of production of molecules, species and quantity of these moleculers are evaluated.

The diode used is a PFD with epoxy anode. The main elements of the gas are found to be H_2 (more than 70 %) and hydrocarbons. The quantity of the gas is estimated to be $(2 \sim 3) \times 10^{21}$ molecules/shot. The souce of the gas seems to be molecules absorved on the anode surface.

Ⅲ-c) Development of High-Power B_r Diode

To obtain an ion beam of high current density of ~ 10 kA/cm² on the anode, we are developing a new type of B_r-magnetically insulated diode with real cathode. The diode is a small size (effective anode area ~ 20 cm²) with short gap length (~ 3 mm). To realize a high-voltage operation, strong magnetic field coil has been developed to produce B_r field more than 5 T. The coil is constructed of a flat copper wire with Kevlar fiber immersed in epoxy resin.

Using a capacitor bank of 800 μF, coil current rises to 35 kA in ~ 100 μs, where we have observed B_z ~ 35 T on the axis of the coil without destruction. Using this coil, it becomes possible to obtain insulating B_r field of more than 5 T in the diode gap. As a pilot study of the developement of high power B_r diode, characteristics of conventional B_r diode is evaluated. The diode is constructed of a pair of coaxial blade cathodes (inner and outer cathode diameters are 50 mm and 100 mm, respectively) and an aluminium flat anode. The diode is well reproducebly operated at gap length ~ 5.0 mm, diode voltage ~ 700 kV, diode current ~ 120 kA. We have found the beam divergence ~ 50 mrad, current density on the anode ~ 1 kA/cm², total ion current ~ 50 kA and brightness of the ion beam ~ 0.5 MA/cm²/sr.

Ⅳ. APPLICATIONS OF PULSE-POWER TECHNOLOGY

Ⅳ-a) Materials Science[3)]

Using high-density (~ 10^{20} cm^{-3}), high-temperature (a few eV) "ablation" plasma which is produced by the irradiation of LIB onto solid targets, we have succeeded in the prepartion of various thin films at low temperature by intense, pulsed, ion-beam evaporation (IBE) such as of ZnS, ZnS:Mn, boron, carbon, indium-tin-oxide (ITO), oxide superconductor ($YBa_2Cu_3O_{7-x}$), $BaTiO_3$, boron nitride (BN), yittria stabilized zirconia (YSZ), apatite, and so on.

The features of IBE are summarized as follows:

1) The instantaneous deposition rate is very high (~ 4 cm/s).
2) Most atoms to be deposited are ions with energies of more than a few eV.

An experimental arrangement of IBE is shown schematically in Fig. 7. The LIB is extracted from a magnetically-insulated diode (MID)[1)], which is connected to a pulse-power machine, "ETIGO-I" (1.2 MV, 240 kA, 50 ns) or

"ETIGO-II" (3 MV, 460 kA, 50 ns). A flashboard (polyethylene) is stuck to the anode as an ion source. The cathode works as an one-turn theta-pinch coil, producing transverse magnetic field (~ 1 T). The gap length is 10 mm. The anode and cathode are shaped spherically, and the radii of the sphere are 160 mm and 150 mm, respectively. The beams are mainly composed of protons (> 80 %). The vacuum chamber is pumped to ~ 10^{-4} Torr. The taget (35 mm in diameter, 5 mm thick) is placed at z = 140 mm from the anode by an angle of 45° with respect to the beam axis. The substrate is located parallel to the target surface at the distance of 30 or 40 mm. We do not heat the substrate during the experiment.

Figure 8 shows the resistivity vs. temperature of the thin film prepared on $SrTiO_3$ (100) by IBE. Here, the target was Y : Ba : Cu : O = 1 : 2.0 : 3.1. The thickness of the film is typically ~ 1 μm/shot. We see clearly that after being annealed the superconductive thin films are prepared, which shows $T_{c\ onset}$ ~ 70 K, and $T_{c\ zero}$ ~ 15 K.

Ⅳ-b) Laser Engineering

Ⅳ-b-1. Highly-Repetitive, Discharge-Pumped Excimer Laser with High-Speed Gas Flow by Ludwieg Tube[4)]

We have developed a new facility, "LUCE", Ludwieg Charge-tube Experiment, for the highly-repetitive, discharge-pumped excimer lasers. Figure 9 shows the outline of LUCE. The length, volume, and pressure of charge tube are 10 m, 0.5 m^3, and 447 kPa, respectively. Figure 10 shows the flow parameters at the test section. We have succeeded in achieving high-speed gas flow, u_t (velocity) = 204 m/s, M_t (Mach number) = 0.65, P_t (pressure) = 293 kPa, and t_t (flow duration) ~ 48 ms (in dry air). As a result of expansion cooling, in addition, T_t (temperature of gas flow) is lowered to be ~ 254 K.

The high-speed, excimer-laser flow is also simulated. The density profile in the discharge region at 30 μs after the excitation discharge is shown in Fig. 11. The flow parameters simulated are as follows: buffer gas is neon, velocity, pressure and density of the flow are 200 m/s, 294.2 kPa and 2.74 kg/m^3, respectively. A large density perturbation appears in the discharge region when the main discharge occurs and/or the gas heated by the upstream preionization discharge arrives at the discharge region.

Ⅳ-b-2. All-Solid-State Magnetic Pulse Compressor with Saturable Transformer to Excite Excimer Lasers[5)]

To reduce loads for switching devices in the excimer-laser excitation circuits, we have successfully developed a new type of all-solid-state excitation circuit using a magnetic pulse compressor (MPC) with a saturable transformer (ST). Figure 12 shows its basic circuit. Since ST has two functions, i.e., step-up transformer and magnetic switch (magnetic compressor), we are able to obtain both the voltage gain and current gain. We have optimized (maximized) the winding ratio of ST, and developed ST with the winding ratio of 1:7. One gate-turn-off thyristor (GTO) has been utilized as a switching device.

The exiperimental results of this circuit are summerized in Table I.

Ⅳ-b-3. Laser-Triggered Lightning

To control the lightning artificially, we have studied laser-induced breakdown characteristics in the atmosphere. When TEA-CO_2 laser (10.6 μm, energy ~ 8 J, pulse width ~ 200 ns, cross section ~ 20 × 20 mm^2) is focused by ZnSe lens (f = 200 mm), we have obtained the plasma channel of ~ 15 mm in length around the focal point. Optical-breakdown threshold (P_{OB}) is estimated to be ~ 0.5 GW/cm^2. The focused laser beam is introduced into the discharge gap. Figure 13 shows breakdown probability η (number of discharge induced/number of optical breakdown) vs. V/V_{SB} (applied voltage/self breakdown voltage). At d (discharge-gap distance) = 15 mm and V/V_{SB} = 50 %, we have found η ~ 90 % when the laser beam is focused on the axis of the gap (z = 200 mm). If the focal point moves 5 mm further from the discharge gap axis (z = 195 mm), η increases to ~ 100 %. At z = 205 mm, however, η significant reduces to ~ 70 % probably due to the lack of plasma channel in the gap.

Effect of microparticles diffused in the atmosphere for the optical-breakdown plasma channel has also been studied. Using 3-μm-diam. aluminum particles (density ~ 1 mg/m^3) and ZnSe lens (f = 500 mm), P_{OB} is lowered to 15 MW/cm^2. The length of the plasma channel produced has been found to elongate to ~ 200 mm.

CONCLUDING REMARKS

Recent progress has been quickly overviewed on pulse-power technology and its applications at LBT, Nagaoka. Although our project originally started in inertial confinement fusion research, there are recently growing and wide interests in applications in material science or laser engineering. Very promising and fruitful achievements can be expected in the future since it is able to obtain extremely high power density even in a very short time.

ACKNOWLEDGEMENTS

This work was partly supported by the grant-in-aid from the Ministry of Education, Science, and Culture of Japan.

References

1) K. Yatsui, et al., Proc. 12th Int'l Conf. on Plasma Phys. & Controlled Nucl. Fusion Res., IAEA, 3, 153 (1989).
2) K. Masugata, et al., Laser and Particle Beams, 7, 287 (1989).
3) K. Yatsui, Laser and Particle Beams, 7, 733 (1989).
4) G. Imada, et al., Proc. 2nd Int'l Conf. on laser Advanced Materials Processing, Nagaoka, Japan (1992).
5) K. Kurihara, et al., Rev. Sci. Instrum. 63, 2138 (1992).

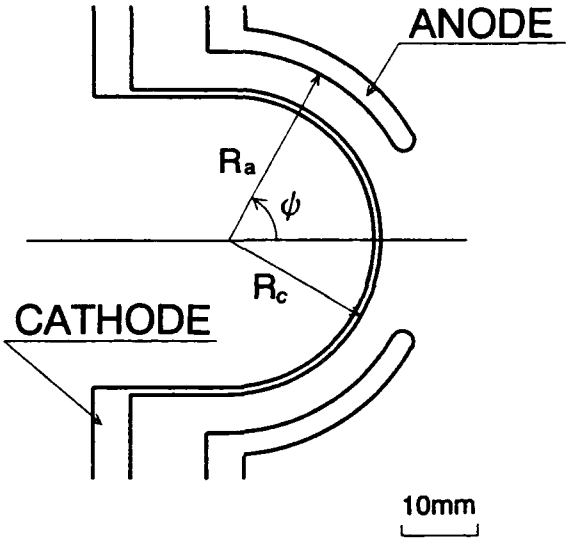

Fig. 1 Basic structure of SPFD.

Table I Summarized results of MPC with ST.

$C_0/C_1/C_2/C_p$ (nF)	950/20/16/16
Input voltage, V_0 (kV)	5.5
Peak value of initial current, I_{0p} (kA)	1.7
Pulse width of initial current, τ_0 (ns)	5.2
Peak value of dI_0/dt (kA/μs)	1.0
Peak value of output voltage, V_{pp} (kV)	32.7
Energy-transfer efficiency, η (%)	59.5
Pulse compression ratio	54
Voltage amplification factor	6.0
Current amplification factor	5.1

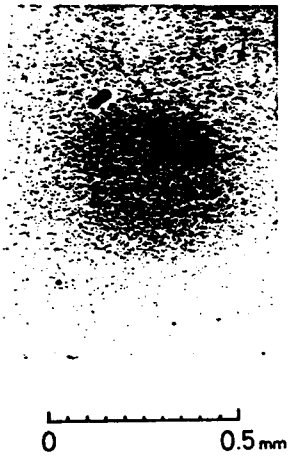

Fig. 2 Cross-sectional profile of ion beam obtained by pinhole camera.

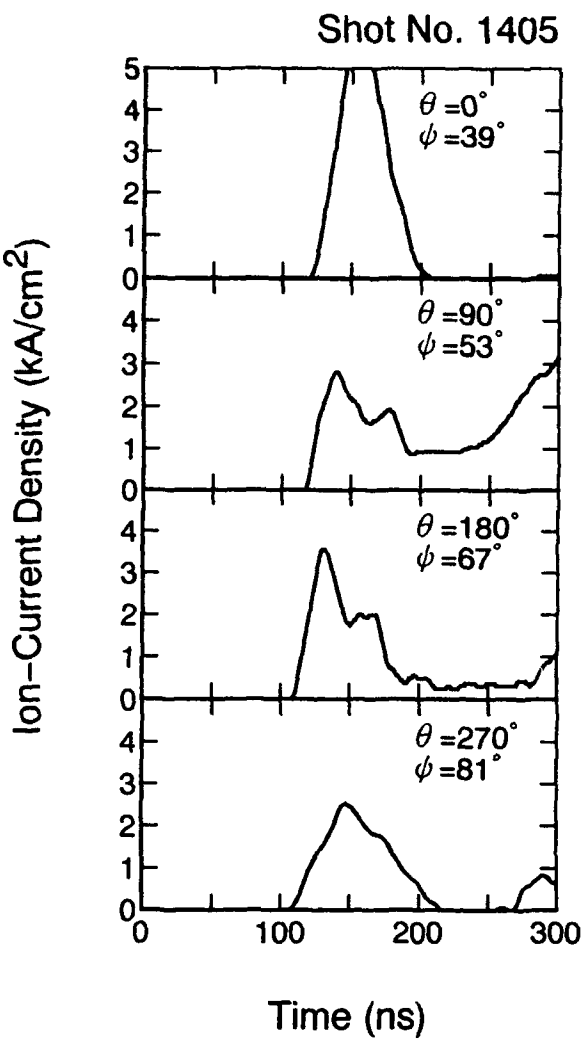

Fig. 3 Typical waveforms of ion-current on anode surface.

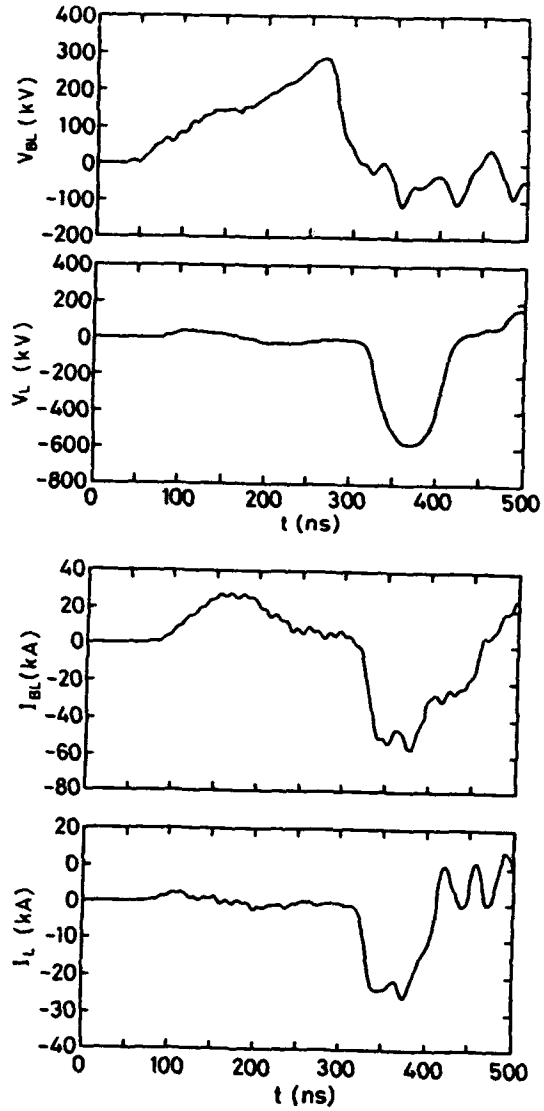

Fig. 5 Typical waveforms of quick charging PFL.

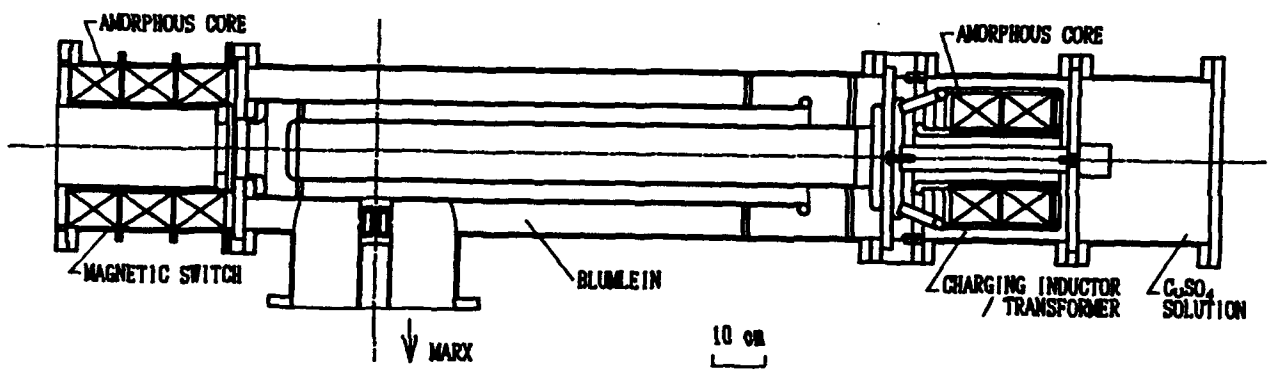

Fig. 4 Schematic of quick charging PFL.

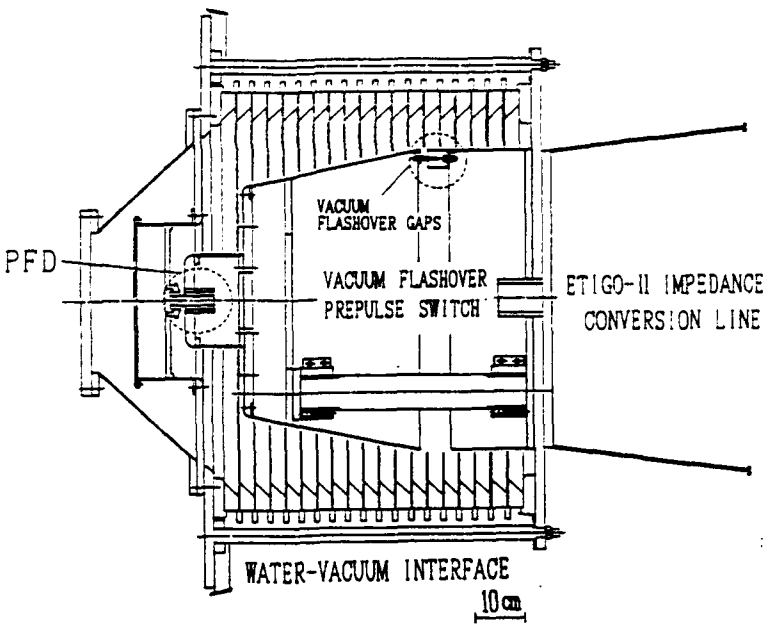

Fig. 6 Experimental setup of VPS.

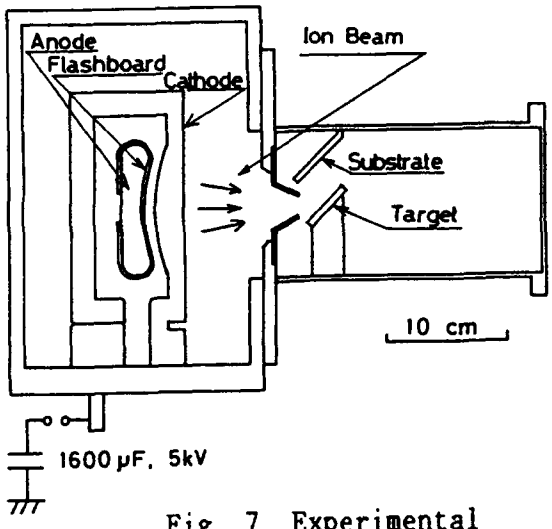

Fig. 7 Experimental arrangement of IBE.

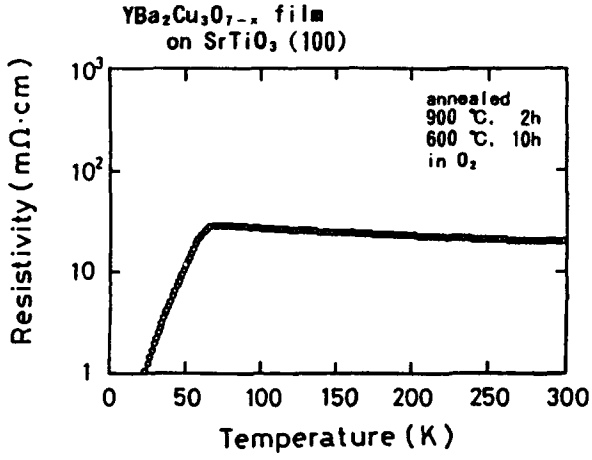

Fig. 8 Resistivity vs. temperature of YBaCuO thin film prepared on $SrTiO_3$.

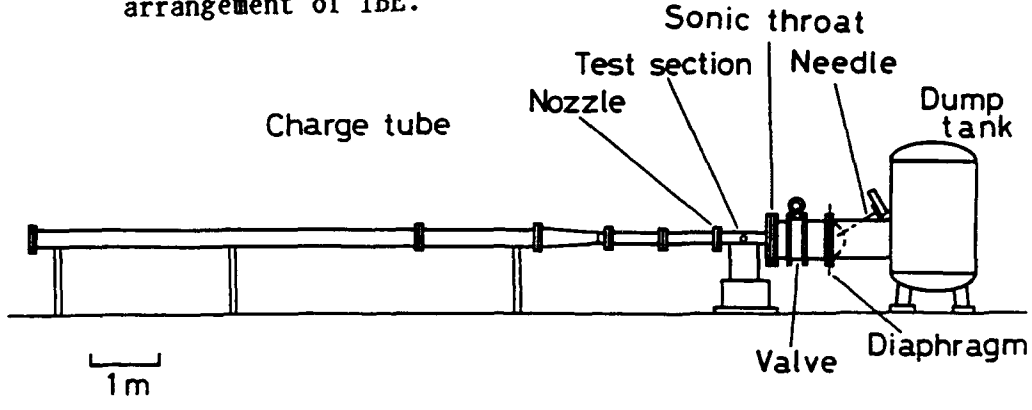

Fig. 9 Outline of LUCE.

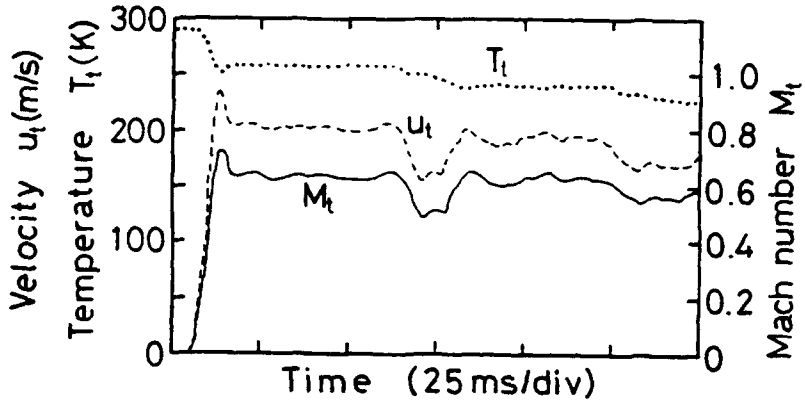

Fig. 10 Flow parameters at test section.

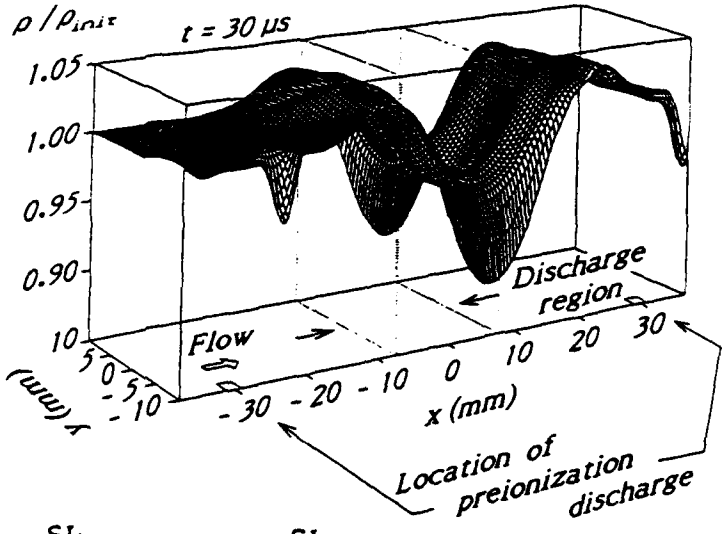

Fig. 11 Simulation results of density profile in discharge region at 30 μs after excitation discharge.

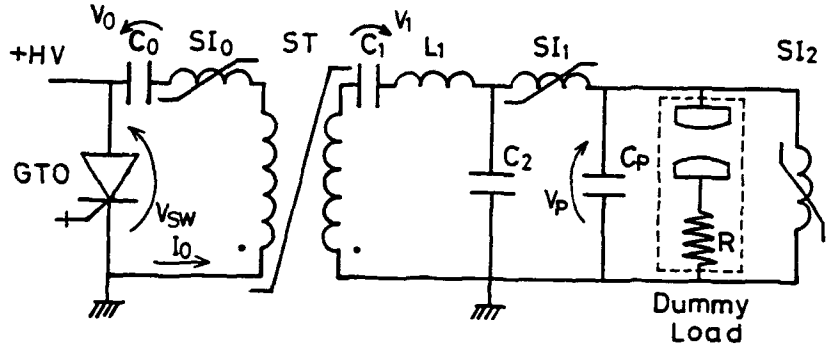

Fig. 12 Basic circuit of MPC.

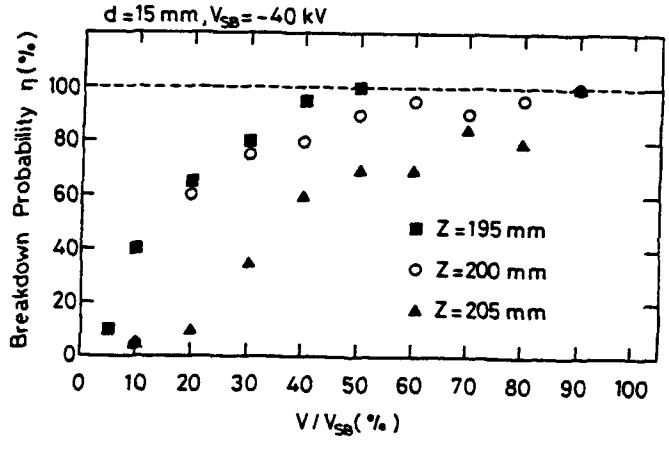

Fig. 13 Breakdown probability η vs. V/V_{SB}.

INITIAL RESULTS FROM THE RHEPP MODULE

H. C. Harjes, K. J. Penn, K. W. Reed, C. R. McClenahan, G. E. Laderach, R. W. Wavrik
J. L. Adcock, M. E Butler, G. A. Mann, G. E. Pena, G. J. Weber, D. VanDeValde
L. E. Martinez, D. Muirhead, P. D. Kiekel, D. L. Johnson, E. L. Neau

Sandia National Laboratories
Albuquerque, NM 87185

Abstract

Several potential applications such as medical waste treatment, chemical waste treatment, food treatment, and flue gas cleanup have been identified for high average power electron beam systems. In the RHEPP (Repetitive High Energy Pulsed Power) project, the technology for such a system is being developed. The RHEPP module consists of a magnetic pulse compressor driving a linear induction voltage adder with an e-beam diode load. It has been designed to operate continuously, delivering 350 kW of average power to the diode in 60-ns FWHM, 2.5-MV, 2.9-kJ pulses. The module is presently under construction with the first phase scheduled for completion in the summer of 1992. In the first phase, four of ten adder stages are being built so that testing can begin with a 1-MV, 160-kW diode with the balance of the power from the compressor diverted to a resistive load. A description of the system and test results from the initial stages of the compressor will be presented.

Introduction

The large pulse power accelerators developed during the late 60's through the late 80's set the background for a new family of high average power accelerators[1]. This type of accelerator, with output powers of 100's of kW to MW, is based on multiple stages of pulse compression to furnish output pulses ten's of nanoseconds wide at voltages of up to 20 MV. DC machines such as the Dynamitron can furnish up to 200-kW at 5 MV and may be fitted with a high Z target fo. x-ray output[2]. Special pulsed, high-voltage transformer systems also deliver megavolt outputs for use in 10's to 100's kW average power facilities[3,4]. High average power machines may use spark gap switches in the pulse compression stages but are increasingly relying on semiconductor and magnetic switches to achieve high reliability and long lifetimes[5]. Cooling of components, such as switches and transformers, is a design consideration in systems with output powers of 100 kW or more. Work on repetitive systems was carried out in parallel with the evolution of the large single-shot machines but only recently have applications for high average power systems developed through changes in government regulations, an increasing public awareness of environmental pollution issues, and studies showing the beneficial effects of x-ray

This work supported by the U.S. Dept. of Energy under contract no. DE-AC04-76DP00789 and by SDIO.

treatment in a number of applications. These applications span the range from food processing, to sterilization of infectious medical waste, and destruction of chemical pollutants. Irradiation with Cobalt-60 is coming into acceptance in the marketplace but has the drawbacks associated with radioactive sources[6]. Pulsed power e-beam or x-ray sources have the benefit of being able to be turned off, with no residual radiation. The system output voltage should be as high as allowed by regulations, usually up to 10 MV for electron accelerators, to permit deep penetration of the desired product. A bremsstrahlung x-ray converter can be fitted to an electron accelerator when more depth penetration is required, at the expense of efficiency. The maximum acceleration voltage is limited to 5 MV by FDA regulations and the Codex Alimentarius[6] in the x-ray mode. Pulsed power irradiators, because of the number of large components, tend to be high in capital cost thereby requiring high volume throughput applications to achieve adequate return on investment. Several such markets appear to be on the near horizon, if supported by adequate and timely technology development.

New component technologies will be needed to gain marketplace acceptance of pulsed-power based irradiators. High-voltage capacitors are perhaps the only system component with an adequate history of development because of the requirements of the power industry. The key high-average-power component is the large area, uniform current density, repetitive diode/converter required to treat large volumes of material being irradiated. Switches for pulse compression, long-life high-electric-field pulse-forming lines, and high-voltage pulse transformers will also be required. The RHEPP system is being designed for an average power output of more than 350 kW at 2.5 MV to address these component issues and is shown as a scale model in Fig. 1. The status of design, construction, and testing of each of these components will be reviewed in the following sections.

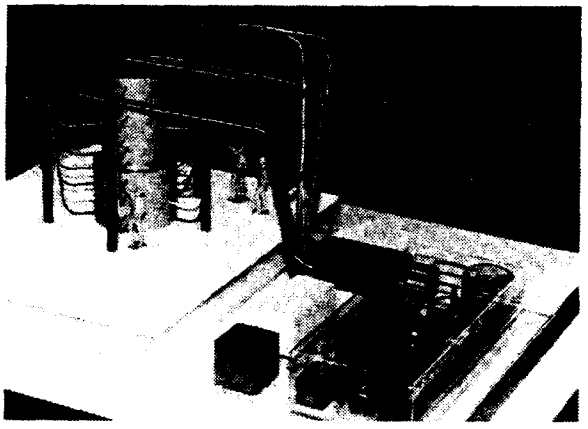

Fig. 1. Scale model of the RHEPP facility.

Pulse Compression System

The pulse compressor has been designed to deliver unipolar, 250-kV, 15-ns risetime, 60-ns FWHM, 4-kJ pulses at a rate of 120 Hz to the linear induction voltage adder. The pulse compressor circuit is shown in Fig. 2. The power source for the system is a Westinghouse motor driven, 600-kW, 120-Hz alternator[7]. During operation, the alternator will deliver 3200 V rms and 210 A rms at a power factor of about 0.88. Magnetic switches (i.e. saturable reactors) are

used exclusively in the compressor because they have the potential of satisfying system lifetime requirements (10^9 to 10^{11} pulses). Detailed descriptions of the circuit operation and magnetic switch theory are in the literature[8].

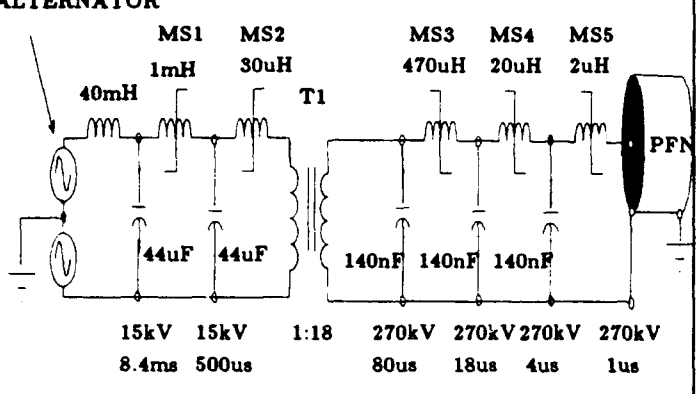

Fig. 2. Pulse compressor circuit.

To operate in a unipolar mode, reset circuits (not shown in Fig. 2) are required to reset the switch cores between pulses. The first loop in the circuit is resonant with the source so that the voltage on C1 rings up to 15 kV. The first switch then saturates and launches a 15-kV pulse down the compression chain. The transformer steps the pulse voltage up to 270 kV and the 5th stage delivers a 1.2-μs risetime, (1-cosωt) pulse to the PFN. The operation of the compressor has been demonstrated in a 5-kW benchtop model[9] whose topology is the same as Fig. 2.

Detailed designs of the compressor components are complete and construction is expected to be completed this summer. The first two switches (MS1 & MS2) and the transformer (T1) are finished and preliminary testing is underway. A summary of design data and measured data is given in Table I. Photographs of MS1 and T1 are shown in Figs. 3 and 4. The transformer is the result of a cooperative effort between Sandia National Laboratories and Westinghouse Research and Development Center. The transformer was designed by Westinghouse and constructed by Sandia. Low cost conventional silicon steel magnetic cores are used because the magnetization rates are low enough that core losses are acceptable. All subsequent magnetic cores in the compressor will be wound from 2605CO METGLAS. The coils on MS1 and MS2 are wound from Litz wire to keep the current distributions in the coil wire cross sections uniform for low losses. In previous switches with sheet copper coils, nonuniform current distributions were induced in the coils

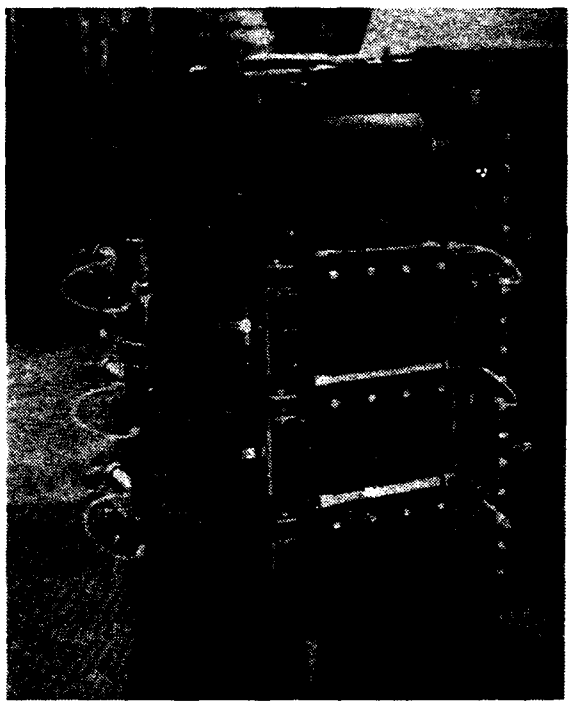

Fig. 3. Photograph of Magnetic Switch 1

Fig. 4. Photograph of Transformer T1.

by the magnetic flux that escapes the core upon saturation. Coil losses were higher (by a factor of 2-3) than expected. The compressor is immersed in transformer oil which is continuously circulated through a heat exchanger. Thermal management of losses was one of the key technical issues considered in switch designs. Codes were used predict temperature distributions and cooling channels were designed into the switches to keep temperatures within acceptable ranges.

Initial testing of the compressor through the transformer was performed in a single-shot mode. The measured values for volt-second products and saturated inductances are given in Table I. Measured load voltage wave form and the corresponding wave form from a computer circuit simulation agree within measurement accuracy. Future tests will be conducted to determine efficiency. The components through MS2 have also been tested at a average power level of about 200 kW. The transformer can not be included in such a test until MS3 is available due to T1 core saturation concerns. Figure 5 shows typical wave forms from a test, whose duration was about 5 minutes.

The thermal management calculations for the cores consisted of steady state computer

Table I. Summary of Data on Compressor Components

Device	Core Mat.	Mag. Area (m^2)	Core Mass (kg)	Coil Turns	Cal. VS	Cal. L sat (mH)	Meas. VS	Meas. L sat (mH)
MS1	9 mil Si-Steel	0.07	760	83	22	1000	23	900
MS2	2 mil Si-Steel	0.07	760	13	2.9	20	3.0	30
T1	2 mil Si-Steel	0.038	720	prim 9 sec 162	1.1	-	-	-
MS3	Metglas 2605-CO	0.027	400	90	8.3	470	-	-
MS4	Metglas 2605-CO	0.027	400	20	1.9	20	-	-
MS5	Metglas 2605-CO	0.027	400	4	0.42	2	-	-

analyses to determine the maximum temperatures in the cores and windings and a heat balance to determine the required coolant flow rates. It was desirable to maintain winding temperatures below 110° to 120° F in order to limit the resistive losses in the Litz wire. A finite element heat transfer program (NISA) was used both in the heat transfer as well as the combined thermal and flow analyses.

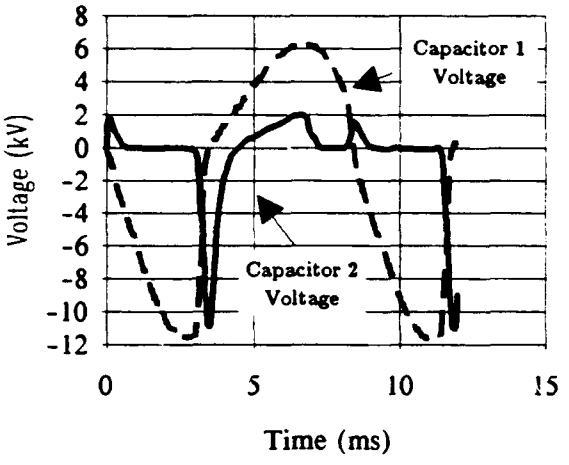

Fig. 5. Capacitor voltages from initial test.

A convective heat transfer coefficient for forced convection was used for the heat transfer analysis of the windings. Thermal conductivity of the Litz wire stack was calculated using a parallel path heat flow through the wire. Using these values and estimated resistive loss as a heat load, the maximum temperatures in the Litz wire stacks for all the switches was 110° F. In order to maintain this temperature, coolant flow of 3 gpm (or less depending upon the switch) will be required to maintain a 20° F bulk coolant temperature rise.

Cooling of the cores was analyzed using the same methods. Forced cooling of the laminated steel cores was done on the core edge only, using thermal conductivity based upon parallel flow in the stack. The METGLAS cores were analyzed assuming that the cores were coated (i.e., no polycarbonate interleaves) and flow was across the edge rather than the face of the METGLAS resulting in a highly efficient mode of conductive heat transfer. Since the coolant flow would be, in effect, confined within a small channel, an alternative analysis using a combined fluid flow and thermal code was used. The flows were adjusted to maintain core temperatures at 110° to 120° F.

RHEPP Pulse Forming Line

A triaxial water insulated pulse forming line (PFL), Fig. 6, following the 1-μs pulse compressor provides two stages of additional pulse compression and converts the input LC charge wave form to a flat-top trapezoidal pulse. The intrinsic voltage doubling in this design delivers a voltage pulse to the matched 0.88-Ω linear induction voltage adder (LIVA) equal in magnitude to the original charge voltage from the 1-μs switch tank. The PFL uses 2605CO METGLAS in the output switch, the inversion switch, and the charge blocking core. The inversion stage compresses the 1.2-μs, 270-kV LC wave form to a 180-ns, 500-kV LC wave form, and the output stage compresses the 180-ns LC wave form to a 12-ns, 10-90% risetime,

60-ns FWHM, 250-kV trapezoidal pulse. Two adjacent cores wound from 22-μm thick 2605CO METGLAS ribbon form the output switch, each of which is 5-cm wide wrapped on a common 11-cm wide sheet of 12-μm thick polycarbonate insulator film. The windings have axial cooling channels uniformly distributed in the build with a net stacking factor of 0.44. Oil serves as both an insulator and a flowing coolant in the PFL cores. Calculations based on B-H data taken at Sandia, and data obtained from Allied Signal, indicate that the overall efficiency of the PFL will be 90% or better. Static, frequency domain and time domain analyses were conducted with the EMAS[11] finite element code. These models predict peak stresses of 90 kV/cm over small areas at the ends of the transmission lines and maximum stresses of 84 kV/cm over larger areas in the inner triaxial PFL. The JCM breakdown field in water[12] is, E_{-}=142 kV/cm. Pulses from the PFL are conveyed to the LIVA via 50 coaxial cables. A cable study conducted at Sandia considering cost, expected lifetime and ease of installation resulted in the selection of Dielectric Sciences 44-Ω, #2158 cable.

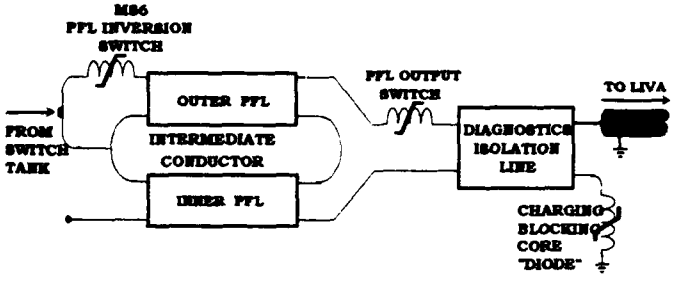

Fig. 6. Pulse Forming Line Converts 1.5 μs Raised Cosine Charging Wave form to a 60 ns FWHM Trapezoidal Pulse with a 12 ns Risetime.

RHEPP Linear Induction Voltage Adder

Pulses from the PFL are combined in the LIVA, Fig. 7, to generate 900-kV, 60-ns FWHM voltage pulses with a 15-ns rise and fall time into the 35-Ω diode load. Each of the four 250-kV LIVA cavities are fed symmetrically around their circumference by five cables. Each cavity contains a single 17-cm wide core wound from 20-μm thick 2605S2 METGLAS ribbon with 12-μm thick Makrofol KG Polycarbonate insulation film. Continuous operation at 120 Hz requires 0.16-cm high cooling channels be wrapped into the core. These cooling channels are formed by winding an array of Lucite rods attached crosswise to a strip of METGLAS at 1.1-cm intervals into the core. Core temperatures are monitored at strategic locations by LUXTRON photoluminescent optical fibre probes. The $\int V dt$ of the PFL pulses is 15 mV-s and that of the LIVA cores is 50 mV-s, so a flux swing of about 1 Tesla is expected. Small core B-H measurements made at Sandia and data obtained from Allied Signal Corp.[13] indicate that the four stage LIVA will be about 80% efficient. These cores contain 4700 turns, yielding 54 volts/turn and a stress of about 16 kV/cm on the mandrel, well within the conservative

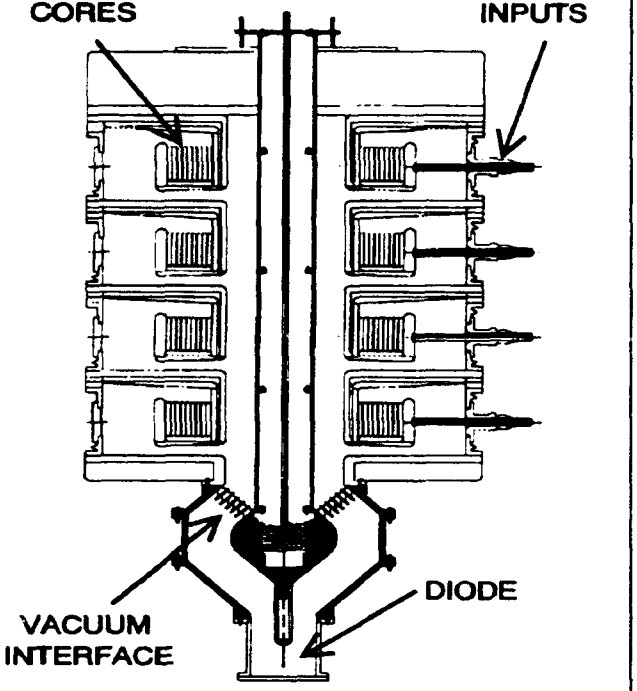

Fig. 7. Linear Induction Voltage Adder, Vacuum Interface and Vacuum Diode.

limits of other successful machines that have been published. Oil insulation was selected for use in the central transmission line, as this simplified the coolant flow to the cores and was considered to be one of the lowest risk technologies available. Electrical stress in the LIVA was limited to 100 kV/cm. J. C. Martin's single shot breakdown field[12] is E=656 kV/cm. Use of an magnetically insulated transmission line (MITL) in the central transmission line would greatly reduce the size and cost of the machine. It is not certain, however, whether an MITL would operate in a stable steady state mode when subjected to repeated pulsing. The RHEPP machine will be used to investigate the feasibility of operating a MITL in the repetitive mode.

The LIVA output is connected to the vacuum diode via a six-ring conical vacuum interface, Fig. 7. This design grades the electrical stress uniformly at 63 kV/cm ± 1.6%. Cooling water is manifolded to the surfaces where the vacuum interface contacts the outer transmission line wall and the shank bulb. An EMAS axisymmetric 3-D finite element transient model was constructed of the vacuum interface with a 35 Ω resistive load. A normalized trapezoidal input pulse with a 10 to 90% risetime of 12 ns was launched into the vacuum interface from the LIVA side and a risetime of 12.5 ns was observed at the load corresponding to a 3.5-ns risetime for the conical vacuum interface.

Diode Development

High throughput of irradiated products or waste streams may require treating areas of 0.1 to 1 m^2 with x-rays or electrons. These conditions place stringent requirements on cathodes and converters/windows for 100's kW to MW average power systems. In addition, 10^9 or more, shot lifetimes are necessary to meet operational and economic concerns.

Uniform current density, large area beams need cathodes capable of supplying greater than 100 A/cm^2. A 250-kV test bed is being operated to determine geometry and material suitability for use as cold, field emission sources. The EGUN[14] electron-optics code is being used in the design of experiments and other codes, such as MAGIC[15], are available to predict electron

trajectories and anode power dissipation levels. Preliminary experiments show encouraging results but will require additional work.

Conclusion

The RHEPP program has identified several possible applications of high average power systems based on short pulse technology. We identified key technology development areas which are being developed for the 2.5-MV, 350-kW, system to be fielded during the summer of 1993. Initial results will be obtained from a 1-MV system operating at the 150-kW level during the summer of 1992. Preliminary testing of pulse compression components is underway and other major sub-systems are being fabricated.

References

1. J. J. Ramirez, et al., "The Four Stage Helia Experiment", Proc. 5th IEEE Pulsed Power Conf., Arlington, VA, June 1985, pp. 143-146.
2. C. C. Thompson and M. R. Cleland, "High-Power Dynamitron Accelerators for X-Ray Processing", Nucl. Inst. and Methods in Physics Research B40/41, (1989), pp. 1137-1141.
3. E. A. Abramyan, "On Possibilities of Transformer Type Accelerators", Nuclear Instruments and Methods, 59, (1968), pp. 22-28.
4. G. J. Rohwein, et al., "Operation of the Tempo Machine", Proc. 6th IEEE Pulsed Power Conf., Arlington, VA, June 1987, pp. 707-710.
5. D. L. Birx, et al., "Magnetic Switching", Proc. 4th IEEE Pulsed Power Conf., Albuquerque, NM, June 1983, pp. 231-235.
6. "Dishing Up Gamma Rays", Newsweek, Jan. 27, 1992.
7. R. M. Calfo, D. J. Scott, and D. W. Scherbarth, "Design and Test of a Continuous Duty Pulsed AC Generator," Proceedings of the 8th IEEE Pulsed Power Conference, June, 1991, San Diego, CA.
8. W. S. Melville, "The Use of Saturable Reactors as Discharge for Pulse Generators." Proceedings, IEE, London, England, Vol. 98, Pt. 3, pp. 185-207.
9. H. C. Harjes, et al., "Status of the Repetitive High Energy Pulsed Power Project," Proceedings of the 8th IEEE Pulsed Power Conference, June, 1991, San Diego, CA.
10. Available from Engineering Mechanics Research Corp., Troy,MI.
11. Available from Engineering/Electromagnetics Applications, Milwaukee, WI.
12. R. J. Adler, et al., "Pulse Power Formulary", 1992 Twentieth Power Modulator Symposium, IEEE Electron Devices Society.
13. C. H. Smith and L. Barberi, "Dynamic Magnetization of Metallic Glasses", Proceedings of the 5th IEEE Pulsed Power Conference, Arlington, VA, June 1985, p.664.
14. W. B. Hermannsfeldt, EGUN - An Electron Optics Gun Design Program, SLCA-331 Stanford CA: Stanford Linear Accelerator Center, 1988.
15. B. Goplen, et al., Mission Research Corp. Report No. MRC/WDC-R-068, Alexandria, VA, Sept. 1983; T. D. Pointon, SAND88-0982 UC-28, June 1988.

APPLICATIONS OF HIGH POWER MICROWAVES

James Benford
Physics International Company
2700 Merced Street
San Leandro, CA 94577

John Swegle
Lawrence Livermore National Laboratory
P.O. Box 808
Livermore, CA 94550

Abstract

We address a number of applications for HPM technology. There is a strong symbiotic relationship between a developing technology and its emerging applications. New technologies can generate new applications. Conversely, applications can demand development of new technological capability. High-power microwave generating systems come with size and weight penalties and problems associated with the x-radiation and collection of the electron beam. Acceptance of these difficulties requires the identification of a set of applications for which high-power operation is either demanded or results in significant improvements in performance. We identify the following applications, and discuss their requirements and operational issues: (1) High-energy RF acceleration; (2) Atmospheric modification (both to produce artificial ionospheric mirrors for radio waves and to save the ozone layer); (3) Radar; (4) Electronic warfare; and (5) Laser pumping. In addition, we discuss several applications requiring high average power that border on HPM, power beaming and plasma heating.

Over the past two decades, there has been a return to vacuum electronics and the application of pulsed power technology to the generation of microwaves, a move (in terms of scale and power) counter to that in solid-state electronics. Tapping the energy of intense relativistic electron beams with accelerating voltages of the order of a megavolt and currents in excess of a kiloampere has permitted the production of pulsed microwave power levels in excess of 10 gigawatts, and gigawatt power levels at frequencies as high as 60 GHz. At these power levels, the operation is necessarily pulsed, the weight and volume of the system is large, and there are radiation and electron beam collection problems to be dealt with. In applications demanding repetitive operation, one must additionally deal with the need to dissipate excess heat and to operate a pulsed power system repetitively.

Our purpose is to outline some of the applications that justify the acceptance of these technical challenges. Applications for HPM are surveyed in detail in our recent book *High Power Microwaves*.[1] Here we describe applications for which high microwave powers either are required or offer some intrinsic improvement in system performance.

RF Accelerators

The development of a TeV electron-positron collider will demand higher accelerating gradients than those in the largest accelerators currently available. A TeV accelerator with a reasonable length will require gradients of the order of 100 MV/m or more. The lowest risk option for achieving such gradients is to raise the power and frequency of the microwave input to the accelerating sections.

Over the range of 3 to 30 GHz, breakdown limits appear to be much higher than those allowed by the Kilpatrick limit.[2] Scaling relations on the energy stored in the accelerating section, the average RF power, dissipation within the structure, the peak RF power, and the section length push for a higher RF frequency. On the other hand, the dimensions and associated fabrication tolerances of the accelerating structure become smaller in inverse proportion to the frequency. Further, undesirable wakefields in the structure grow with frequency. Overall, the effect has been to limit consideration to frequencies below 30 GHz. The microwave sources desired for future high-gradient accelerators will have power levels of the order of one to several hundred megawatts, with pulse lengths of one to several hundred nanoseconds. Phase and amplitude stability requirements have steered designers in the direction of high-power amplifiers driven by a master oscillator. At SLAC, four source options have been considered:[3] upgrades to present SLAC klystrons to 11.4 GHz and 100 MW, followed by pulse compression to further raise the power and shorten the pulse; relativistic klystrons producing the necessary power without pulse compression (a line of work also being pursued at Lawrence Livermore National Laboratory and in Russia); cluster klystrons, using a number of smaller, more economical klystrons in a common magnetic field; and crossed-field amplifiers. In addition, gyroklystrons are under consideration at the University of Maryland, and a magnicon promising high efficiency is being developed at the Institute of Nuclear Physics in Novosibirsk.

Atmospheric Modification

Some emerging applications involve controlling the atmosphere for human purposes. One set of potential applications is to long range communications and radar. For example, microwaves at power level ~ 1 GW can be beamed into the lower ionosphere around 70 km to enhance the local ionization level to ~ 10^7 electrons/cm^3. The moving microwave beam quickly paints an ionizing region and a low frequency (< 100 MHz) radar signal is bounced over the horizon from the artificial ionospheric mirror (AIM).[4] With repetitive operation the mirror can be placed so as to

survey a very large geographical area and detect targets out to 1000 km. Because the ionization patch is within the near field of the large aperture antenna, the individual sources driving the antenna must have a high degree of phase control in order to paint the mirror. At optimized frequencies, the effective radiated power is of order 150 dBW. Using a sparse antenna array 1 km^2, consisting of 36, 0.25-GW klystrons operating at a GHz, a demonstration patch of 7 m diameter at 70 km could be painted. This is a truly high power application and requires a high degree of phase and frequency control.

Another emerging application of HPM with requirements similar to AIM is ozone conservation. It is now well documented that the ozone layer is being depleted as a result of catalytic destruction of ozone through chemical reactions involving chlorine. Total ozone levels have already dropped by several percent in the northern hemisphere. It is important to note that the chlorine in not destroyed by the chemical process, but acts as a catalyst. The residence time for chlorine in the upper atmosphere is roughly a century; therefore, stopping chloroflourocarbon (CFC) production, while necessary, will not prevent continued destruction of the ozone.

Eradicating the CFC inventory by local deposition of microwave energy has been proposed by several authors.[5,6] The electrical power required is very large because the inventory already present in the atmosphere is huge. The scale of the solution is 10 GW continuous microwave power produced by individual radiators at GW peak levels. Parameters similar to the AIM numbers given above would be necessary. Several decades would be required to completely cleanse the atmosphere of CFCs. Preliminary laboratory experiments in Russia have shown that microwave beams can eliminate CFCs. Only very preliminary experiments have been conducted and only in environments not characteristic of the upper atmosphere. The detailed chemistry in the upper atmosphere is not well known. Experiments should be undertaken which accurately investigate upper atmosphere chemistry in the presence of microwaves.

The requirements on HPM technology are much the same as for AIM, (high efficiency, high average power, and reliable repetitive sources). Since the CFC problem exists at altitude lower and denser than the ionosphere, the optimum frequency is at the high end of the microwave frequencies—perhaps 35 GHz would be preferred. Therefore, FELs and multiwave Cerenkov generators are candidates for this application.

Researchers at the Institute of General Physics in Moscow have conducted plasma chemistry experiments indicating that both CFC destruction and production of oxides of nitrogen

can be caused by microwave discharges. These oxides can themselves be destructive of ozone, possibly making atmospheric modification by microwaves an environmental hazard.

Radar

There are two radar aspects of HPM. The maximum detection range scales as $P^{1/4}$, and therefore increasing radar power from a MW to 10 GW will increase detection range by an order of magnitude. If the pulse is short, it is possible to increase range resolution so that targets can be precisely located and perhaps even identified from the time-dependent return signal. Little has been done on HPM radar in the West, but the Russians have recently reported a field demonstration of an HPM radar operating in X-band at a GW peak power, 5 ns pulse duration and 100 Hz repetition rate.[7] The device used was a backward wave oscillator powered by the Sinus-4 repetitive pulse power generator, operated from vans in the Tomsk region of Russia. They report detection of aircraft at a range of 50 km with range resolution of 10 meters. Here we can see understandable technology choices: the backward wave oscillator has high efficiency and the Sinus generator series is both efficient and compact.

An unconventional radar approach is impulse or wideband radar, which uses typically 1-ns impulses at GW powers in order to produce broadband radar signals. The advantages are extreme range resolution, clutter rejection, penetration of the ground, and possible detection of low observable targets. The sources used are Hertzian pulse generators or frozen wave generators fed by light activated semi-conductor switches. A primary issue in impulse radar is the antenna; it is difficult to produce a high gain wideband antenna. There is also development needed in receiver and signal processing techniques for such pulses.

Electronic Warfare At High Power

The most direct application of electronic warfare (EW) using high power is to increase the effective range of any EW technique. Therefore deception, spoofing or jamming can be done at greater range in the same manner. Between high power jamming and burnout or lethal damage lies a new middle ground where the digital electronics can be upset, i.e., temporary loss of information so that a weapon system can become disoriented or a communication system can become confused. The fundamental reason that electronics are increasingly vulnerable to burnout or upset is that modern electronics are increasingly miniaturized. The development of smart weapons means that modern forces can be attacked through electronic vulnerabilities much more than previous generations of weapon systems. In conventional EW the techniques are extremely target specific.

The advantage of high power is that generic classes of targets can be attacked. Therefore, there is a trade-off between sophistication of the attack and the power level used.[1]

For defense classification reasons, the sources and technologies to be used in advanced electronic warfare are not widely discussed. However, a few requirements are apparent. Compactness of an HPM system is a general problem for military applications. In general, increasing the efficiency and compactness will raise the cost of a device. Military requirements will also place an emphasis on efficiency because the prime power requirement is likely to determine the overall weight. Another constraint to be taken into account in any practical military device is the limitation of onboard platform power. For example, if an airborne HPM system generates a kJ pulse and operates at 100 Hz, an average power of 100 kW is required, beyond the power available from most platforms.

Laser Pumping

Although microwaves produced either in a high-power tube or a microwave discharge have been used for some time to pump lasers, the use of a high-power source in this application remains relatively rare. The advantages of microwave pumping are the following:[8] (1) transport of the microwaves presents no serious technical difficulties; (2) absorption of the microwaves in the discharge is efficient; (3) there are none of the plasma discharge instabilities initiated by the electrodes in electric discharge lasers; (4) in the absence of the electrodes seen in discharge lasers, contamination of the lasant is reduced; and (5) high specific pump levels can be achieved. Further, the bremsstrahlung from the electron beam driving the microwave source can be used to preionize the lasant and improve the uniformity of the microwave discharge. Nevertheless, this application is being pursued by two Russian groups. One group, at the Tomsk Polytechnic Institute, has used a relativistic magnetron to pump both excimer[9] and nitrogen[10] lasers. The second group, at the Institute of Applied Physics, used a relativistic traveling wave tube to pump a nitrogen laser.[8]

High Average Power Applications

There are a number of applications demanding high average power that border on HPM and draw upon its community:

Power beaming involves the use of microwaves to transport energy from point to point through the atmosphere or space. A survey of these applications is given in Reference 1. The first application proposed was the solar power satellite (SPS), in which sunlight is converted to microwaves and beamed to earth to provide power. A key element is the *rectenna*, an antenna

which rectifies microwaves at high efficiency. A second application is satellite recharging: as the power needs of satellites grow, the solar cell becomes impractical. Beaming power from the earth using a large antenna to a relatively small antenna on the satellite can be attractive. The preferred frequency is 35 GHz for propagation and because antenna sizes are reduced.

Plasma heating is needed to reach the 10-keV temperatures required for thermonuclear fusion breakeven in magnetically-confined plasmas. Of the various methods available, the one taxing high average power technology is electron cyclotron resonance heating (ECRH). The source for ECRH will operate at frequencies of 250 GHz or 500 GHz (the first and second electron cyclotron harmonics). There are three source candidates for the task.[11] One is the gyrotron, either in a standard arrangement with the microwaves generated in a cavity arranged colinearly with the beam, or in a "quasi-optical" geometry, with the microwave cavity arranged perpendicularly to the direction of electron flow in the electron beam. The second is the cyclotron autoresonant maser (CARM), which is still largely in the developmental stage, but promises high-frequency operation at high powers using more modest values of the guiding magnetic field than in the gyrotron to reach the requisite frequencies. Third is the FEL, which can be run cw or in a repetitively-pulsed, high peak- and average-power mode.

The above applications have received considerable attention. Recently, several other possibilities have been suggested. Manheimer[12] has suggested sensing the structure of clouds and clear air turbulence and measuring relative humidity with gyrotrons. Prosnitz[13] has studied the use of FELs for high power long range radar for detection of earth intersecting asteroids.

Technical for Applications

The variety of applications is echoed in the diversity of peak power, average power, and frequency requirements. Table I gives some indication of the technical issues which will determine the utility of the applications.

Table I

Application	Technical Issues
Particle Acceleration	Breakdown at high frequency, phase control, component lifetime
Atmospheric Modification	Atmospheric chemistry, phase control
Radar	Pulse reproducibility and antenna gain
Electronic Warfare at High Power	Vulnerability and coupling, compact lightweight field technologies, efficiency
Laser Pumping	Efficiency of coupling to lasant
Power Beaming	High peak and average powers, efficiency and cost
Plasma Heating	High average power at hundreds of GHz

The wide variety of issues in the applications is a challenge to the technical community. Not all the issues focus on the microwave sources. Some applications, such as laser pumping and impulse radar, probably don't require great extrapolation beyond the present source technology state-of-the-art but require some improvements in areas beyond the source. (This is certainly true of impulse radar where the signal processing and the antenna may both be quite sophisticated.)

The primary area where substantial improvement must be made is shown in Figure 1. The duty factor displayed diagonally is a measure of the difficulty of thermal management in the applications. AIM and CFC elimination will require systems with 1-GW peak , 1-MW (duty factor 10^{-3})average capability in a single source, with the system consisting of many sources. High power microwave sources have only recently begun to develop at high average power. The present HPM state-of-the art[14] in duty factor is ~ 10^{-5}. This is about the limit of high power tubes of the conventional variety as well. Future applications will require duty factors of 10^{-3}, which will mean substantial average power handling engineering requirement. Therefore, the challenge of HPM applications will reside in handling average powers in the presence of the intense RF electric fields in HPM sources.

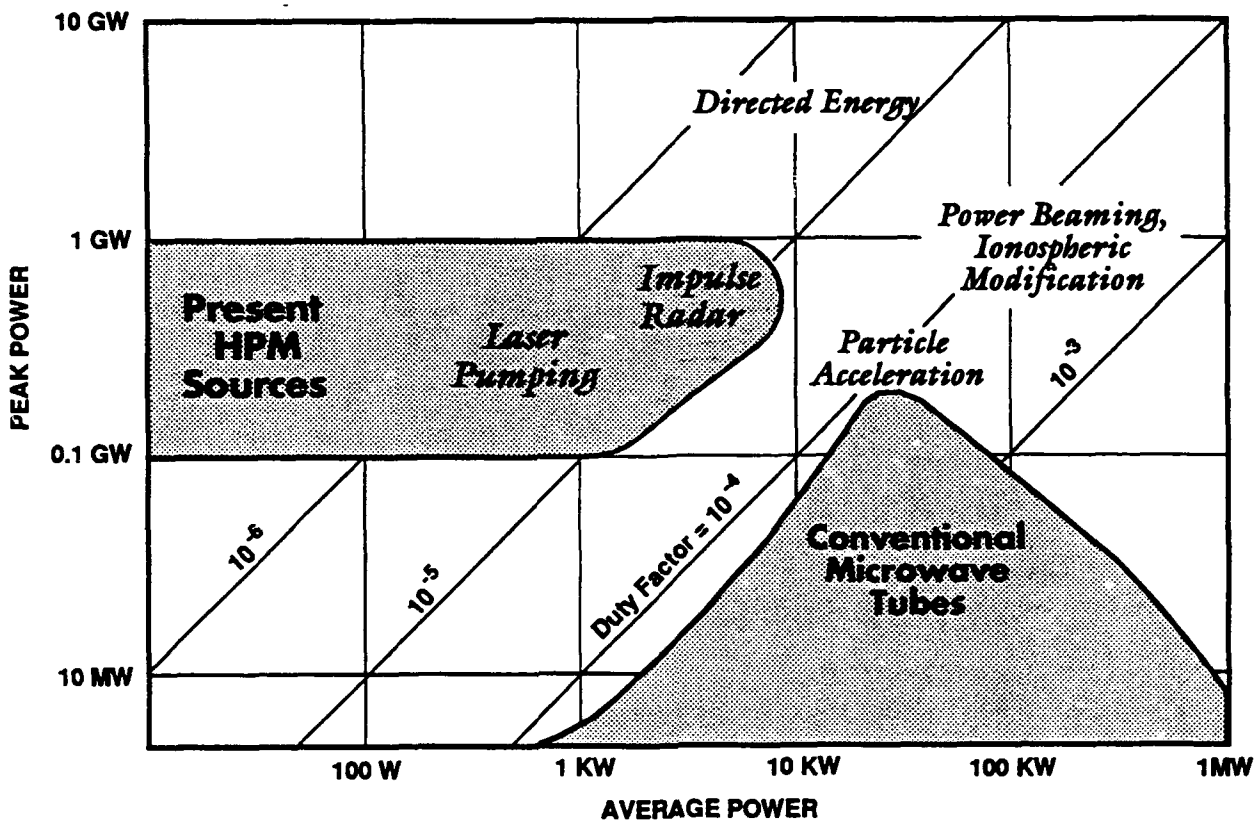

Figure 1. Power requirements of HPM applications.

The experiments by the PI group with high repetition rate magnetrons and klystrons have shown that 10 kW can be maintained at a GW power level (100's Hz)[14]. They used many techniques from the conventional tube community, such as bakeout and beam conditioning, to achieve reproducible operation at high peak powers. Widespread adoption of such techniques will be required in order to produce high average powers. In such repetitive systems, heat dissipation will be a major issue. Plasma clearing, when explosive emission diodes are used, will be a major issue at repetition rates in excess of 1 kHz; peak output power may have to be traded against the repetition rate. Avoidance of plasma formation in the device will require improvement of beam transmission systems and development of cooled depressed collectors and rf output structures that distribute the high electric fields over multiple gaps or extraction ports.

References

1. J. Benford and J. Swegle, "High Power Microwaves," Artech House, Boston, Mass., 1992.
2. W. D. Kilpatrick, *Rev. Sci. Instrum.* **28**, 824,1957.
3. B. Richter, *Part. Accel.* **26**, 33,1990.
4. R.D. Short, T. Wallace, C.V. Steward, P. Lallement, and P. Koert, "Artificial Ionospheric Mirrors for Radar Applications," *AGARD Conf. Proc.*, **455**, paper 17B, 1990.
5. A. Wong, J. Steinhauer, R. Close, T. Fukuchi and G. Milikh, "Conservation of Ozone in the Upper Atmosphere by Selective Ion Removal,"*Comments Plasma Phys. Controlled Fusion*, **12**, p. 223, 1989.
6. G. Askaryan, G. Batanov, I. Kossyi and A. Costinskii, "Microwave Discharges in the Stratosphere and Their Effect on the Ozone Layer," *Sov. J. Plasma Phys.*, **17**, p. 48, 1991.See also I. A. Kossyi, A. Yu. Kostinsky, A. A. Matveev and V. P. Silakov,"Microwave Discharge Action on the Ozone Layer," *Comments Plasma Phys. Controlled Fusion* **14**, 73, 1991.
7. Bunkin, et al., "A Radar Based on a High Power, Nanosecond Microwave Generator with a Relativistic Beam," in proceedings of this conference.
8. A. N. Didenko, V. M. Petrov, V. N. Slin'ko, A. S. Sulakshin, and S. S. Sulakshin, *Sov. Tech. Phys. Lett.* **12**, 515 ,1986.
9. V. A. Vaulin, V. N. Slin'ko, and S. S. Sulakshin, *Sov. J. Quantum Electron*, **18**, 38, 1988.
10. A. A. Babin, A. L. Vikharev, V. A. Gintsburg, O. A. Ivanov, N. G. Kolganov, and M. I. Fuks, *Sov. Phys. Tech. Phys.* **15**, 176, 1989.
11. V. L. Bratman and G. S. Nusinovich, *Proc. 7th Int. Conf. on High-Power Particle Beams (BEAMS '88)*, W. Bauer and W. Schmidt, eds. (KfK, Karlsruhe, Germany, 1988), p. 395; T. V. George, *13th Int. Conf. on Infrared and Millimeter Waves* (SPIE, Bellingham, WA), **1039**, 173, 1988.
12. W. Manheimer, "On the Possibility of High Power Gyrotrons for Super Range Resolution Radar and Atmospheric Sensing," NRL Report 6830, 1990.
13. D. Prosnitz, Private communication.
14. R. Smith, J. Benford, N. Cooksey, N. Aiello, J. Levine and B. Harteneck, "Operation of an L-band Relativistic Magnetron at a 100 Hz," *Intense Microwave & Particle Beams II*, Ed. H. Brandt, SPIE, **1407**, 83, 1991. See also Aiello et al. in this conference.

X-PINCH SOFT X-RAY SOURCE FOR MICROLITHOGRAPHY

S.C. Glidden, D.A. Hammer, D.H. Kalantar, and N. Qi
Laboratory of Plasma Studies, Cornell University, Ithaca, NY 14853
and
Applied Pulsed Power, Inc., 140 Langmuir Lab., 95 Brown Rd., Ithaca, NY 14850

Abstract

The x-pinch soft x-ray source is described for application in submicron resolution lithography. Experiments have been performed to characterize the radiation emitted from magnesium wire x-pinch plasmas using an 80 ns, ≤500 kA pulse. Yields of 14.2 J averaged over three independent calibrated diagnostics at 445 kA have been measured in magnesium K-shell radiation (predominantly 8.4 Å to 9.4 Å or 1.5 keV to 1.3 keV) from a submillimeter source, with as little as 5-10% of the yield below the 6.74 Å silicon absorption edge. A new ≤700 kA, 100 ns pulser being used for x-pinch physics experiments is described. The design of a 40 pulse per second pulsed power system and wire loading mechanism for exposing a resist in 1 second at a distance of 40 cm is presented.

I. Introduction

In this paper we describe the work at Cornell on the x-pinch plasma soft x-ray source, and the design of a compact, high repetition rate pulser at Applied Pulsed Power, Inc. (APP), for practical testing of the x-pinch for application to lithography in the microelectronics industry. A close relative to the conventional wire-array z-pinch, the x-pinch consists of two or more wires stretched between the output electrodes of a pulsed power generator in an '*X*' configuration so that they touch at a single point, as illustrated in Fig. 1. The current pulse from the pulsed power generator causes a plasma to form at the initial position of the wires in a few ns, and the self-magnetic field causes the plasma to pinch towards the axis. Because the current is shared by several wires except at the single point where they touch, only there is the plasma implosion powered by the full current, thereby generating intense soft x-ray radiation only at that point. Using magnesium (Mg) wires in the x-pinch, the radiation is mostly K-shell lines between 8.4 Å and 9.4 Å, an attractive range for x-ray lithography.[1]

Although our experiments to date[2,3] suggest that the scientific feasibility of the Mg x-pinch for microlithography is established, as described in Sections II-IV, studies are continuing to understand the physics of the x-pinch. Taking advantage of a pulser built especially for x-pinch experiments, which is described in Section V, these studies will enable us to optimize the x-pinch .for the lithography application. Considerations which led us to choosing a 40 pulses per second, 500 kA pulser for a prototype lithography system are also discussed in Section IV, and the pulser design itself is presented in Section VI.

II. Experimental Procedure

The x-pinch experiments were conducted using the LION pulsed power generator[4] to deliver up to a 470 kA, 80 ns full width at half maximum (fwhm) current pulse to the crossed wire loads. Experiments were

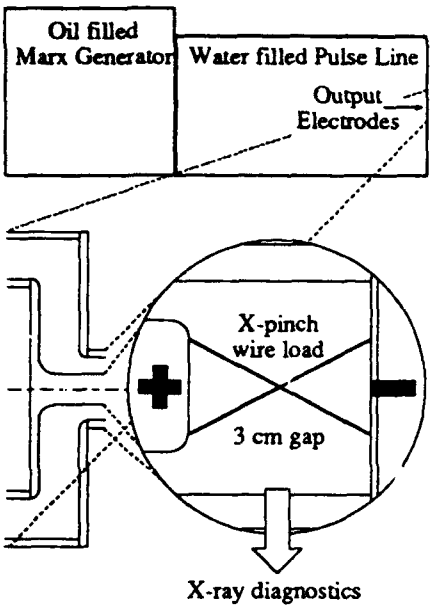

Figure 1: Schematic showing the LION pulsed power generator, output electrodes, and wire load placement.

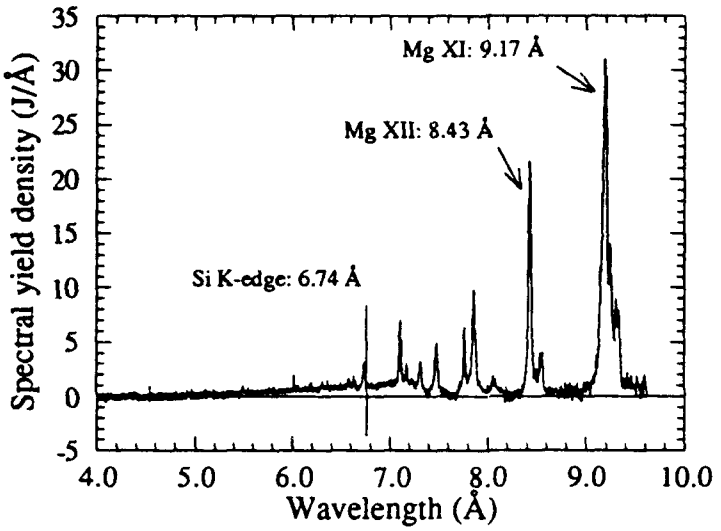

Figure 2: Magnesium spectrum for Pulse 2273 showing K-shell line radiation and free-bound continuum. The wire load consisted of four 50 μm Mg wires at 370 kA.

carried out with two to eight Mg wires, each ranging from 50 μm to 125 μm in diameter, and with two to six aluminum (Al) wires ranging from 12 μm to 100 μm in diameter. Although more tests were performed with Al wires, the useful radiation yield was higher with Mg wires, and the Mg K-shell spectrum satisfies the needs of a lithography system better than that from Al. Therefore, we will discuss mostly Mg results here.

X-ray diagnostics that were used to study the x-ray source characteristics included an x-ray curved crystal spectrograph, filtered x-ray pinhole cameras, four filtered GaAs:Cr photoconducting diodes (PCDs),[5] and Far West Technologies (FWT) dosimetry film.[6] The potassium acid phthalate (KAP) curved crystal spectrograph provided a spectrum of the soft x-ray Mg emission above 3.44 Å, the minimum defined by the absorption edge due to potassium in the crystal. Spectra were recorded with Kodak DEF x-ray film. The pinhoie cameras were filtered with 25 μm Be, 10 μm Al, 10 μm Al with 20 μm mylar, and 4-5 μm aluminized mylar filters. Using multiple filters enabled images to be recorded in different wavelength regions. All cameras held two pieces of film, so as to record the harder emission on the second film. The PCDs were filtered with 25 μm Be, 25 μm Be with 20 μm mylar, and 10 μm Al filters. The FWT dosimetry film, filtered with a combination of Be foils, mylar filters, and a Si foil, was used to measure the total K-shell yield, and to estimate the effective photon energy of the source. Several samples of x-ray resist were placed around the source at a distance of 10 cm, both with and without an x-ray mask, in order to test if an exposure was possible.

Additional x-pinch diagnostics used included a 5 ns visible light framing camera, a step filtered film detector, and a transmission grating soft x-ray spectrograph. The step filtered detector used varying thicknesses of Al and mylar foils in order to determine the effective photon energy and overall yield of any hard radiation components from the pinch. The transmission grating spectrograph provided spatially resolved, spectrally

dispersed K-shell images of the pinch plasma, allowing estimates of the x-ray source size to be made. LION output pulse voltage and current were also monitored on each pulse.

III. Results and Discussion

Within a few ns, the LION power pulse generated a plasma along the wires, and the self-magnetic fields from the current through the plasma then pinched the plasma towards the axis. XUV and soft x-ray pinhole images showed a bright spot at the cross point of the wires, indicating that the plasma had achieved a high temperature and density. While Mg L-shell radiation was observed from the full length of the wires, strong K-shell radiation was observed only from the cross region of the wires. The filtered pinhole images indicated that the harder free-bound continuum component of the radiation is emitted from spots as small as a few tens of μm at the crossing point of the wires. These are co-located with the larger sources of K-shell line radiation. The overall number and size of the distribution of these sources varies with the wire load configuration.

A sample K-shell spectrum recorded with the curved crystal spectrograph is shown in Fig. 2. The line radiation is predominantly from the 9.17 Å and 8.43 Å resonance transitions in Mg XI (helium-like Mg) and Mg XII (hydrogen-like Mg), respectively. The distribution of the radiation in lines and continuum depended on the wire load and the peak current, with 5-35% of the total energy yield was emitted as photons with wavelength below the Si K-edge at 6.74 Å. With lower mass loads, that percentage tended to be smaller.

The filtered PCDs were used to monitor the radiation yield for all the x-pinch test pulses. The energy yields measured behind the Be, Be and mylar, and Al foils were consistent with the spectral distributions recorded with the crystal spectrograph. For the Mg pinch at 370 kA, with an x-pinch wire configuration consisting of four 50 μm Mg wires (135 μg/cm), the K-shell radiation yield was approximately 20 J, of which 16 J is useful (above the 6.74 Å Si absorption edge). Increasing the current to 470 kA provided a K-shell yield as high as 25 J from an x-pinch load consisting of six 50 μm Mg wires (200 μg/cm).

Independent measurements of the K-shell yield were made on six Mg x-pinch pulses using the FWT dosimetry film, and comparisons of the measured yields from the PCDs, the spectrograph, and the dosimetry film were made. The spectral distribution obtained from the spectrograph was assumed for the analysis of the PCD and film data. For three pulses with six 50 μm Mg wires at 400 kA, the average yield per pulse was 5.7 J measured with dosimetry film. An effective radiation wavelength of 8.35 Å (1480 eV) was determined by placing samples of the dosimetry film behind a Be foil and both in front and behind a 3.2 μm Si foil, in agreement with the radiation spectrum recorded by the spectrograph. Single pulse yields from the dosimetry film were as high as 13 J for a six wire x-pinch at 430 kA and 15 J for a four wire x-pinch at 445 kA. The PCD signals provided yields of 14 J and 20 J for the same pulses. The calibrated crystal spectrograph was used to estimate 8 J for the latter pulse.

The filtered pinhole photographs show the overall size of the emission region to be as large as 1-2 mm including a diffuse halo of plasma that is weakly radiating. Figure 3 shows the source through different filters.

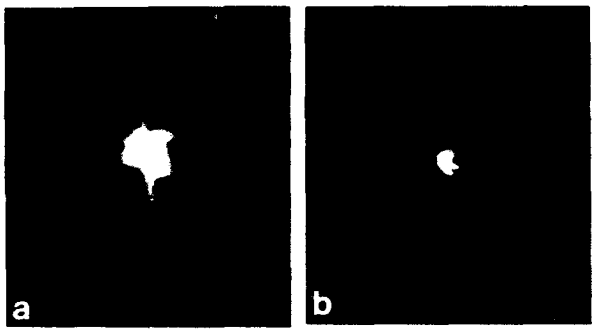

Figure 3: Filtered pinhole cameras recorded the emission in different wavelength ranges for an x-pinch load consisting of one 50 μm Al wire and one 75 μm Mg wire. a) Mg and Al L-shell XUV emission from the full length of the wires. b) Mg and Al K-shell emission from the cross point of the wires.

The second film from the pinhole cameras show that the individual regions of intense free-bound continuum radiation are a few tens of μm in size distributed over less than 0.5 mm for many pulses. The K-shell spectrum recorded by the spectrograph provides a measure of the upper limit of the soft x-ray source size from the spectral linewidths. The effective K-shell source size is estimated to be less than 0.6 mm for many pulses assuming the widths of selected lines in the spectrum are entirely due to the source size. In fact, the linewidth is affected by the crystal diffraction resolving power and line broadening due to Doppler and other effects. This implies that the K-shell source size is surely ≤0.5 mm, consistent with the overall extent of the free-bound continuum spots.

Yield measurements made with the PCDs and the dosimetry film differed by as much as a factor of two. In our lithography system discussion (Section IV), we rely on the absolute yield measurements made with the FWT dosimetry film, as only this diagnostic has been used to test other potential x-ray lithography sources.[7] When needed for data analysis, the radiation spectrum is assumed to be that recorded by the crystal spectrograph. The best LION pulse diagnosed with the dosimetry film yielded 15 J in Mg K-shell radiation at a peak current of 445 kA. For this pulse, a yield of 20 J was measured with the PCDs, whereas this diagnostic measured yields as high as 25 J for a six 50 μm Mg wire x-pinch at 470 kA on which there was no dosimetry film measurement. Therefore, the dosimetry film equivalent yield was 18.4 J for 470 kA peak current.

K-shell radiation yield measurements made for Al wire configurations on LION at 370-470 kA and on Gamble II at currents of 800 kA and 1 MA[8] provide an approximate power law scaling of the yield with current I of I^x, where x is in the range 3-4. The same scaling law is expected to apply to Mg wire yields.

A 1000 Å silicon nitride x-ray mask in contact with a high-sensitivity (IBM proprietary) resist-coated wafer was exposed to two pulses at a distance of 10 cm from the source. The radiation fluence at the resist was about 10 mJ/cm^2. Therefore, complete resist exposure was not possible and the image vanished during development. Further details of these tests are available in reference 3.

IV. Implications for Lithography

In order for the x-pinch source to be applicable to high resolution lithography with a minimum feature size of 0.25 μm or less, we must place the x-pinch at least 40 cm from the mask and wafer so that source size blurring and pattern runout are acceptable.[9] A soft x-ray intensity of about 50 mW/cm^2 is required for a production lithography system, namely to expose a high sensitivity resist in about 1 s. The yield of 18.4 J per pulse corresponds to a fluence at 40 cm of about 0.50 mJ/cm^2 through an 8 μm Be foil and a 2 μm Si

membrane. Therefore, for a production system, 100 pulses per second (pps) would be required without further optimization of the x-pinch yield per pulse. A combination of x-pinch load optimization and/or higher current to increase the yield per pulse by a factor of 2-4, together with a 25-50 pps repetition rate would also suffice. Of course, the required 0.5 mm source size must be maintained, including pulse-to-pulse position variation, as the yield per pulse is increased.

The source experiments described in this paper were conducted using a pulsed power generator (LION) that stored 90 kJ at 470 kA. Because this nominal 40 ns pulser was designed to power a 4Ω resistive load, and the power feed inductance to the 20 nH x-pinch was about 90 nH, LION was very inefficient as an x-pinch driver. In addition, because of the large inductance involved, it was not possible to determine the load voltage from electrical measurements, so that power flow into plasma implosion and resistive heating, (I dL/dt + R), where L and R are the x-pinch inductance and resistance, respectively, could not be evaluated very well. In short, we do not yet know the efficiency with which Mg K-shell radiation was produced on LION relative to the energy actually delivered to the load.

At a more fundamental level, as we do not yet understand the dynamics of the x-pinch as it implodes, assembles on axis, converting kinetic energy of implosion to ionization and thermalization, and re-expands, it is not at all clear how to optimize the radiation yield and the electrical-to-soft-x-ray radiation energy efficiency. Thus, it behooves us to carry out experiments to understand the physics of the x-pinch. We will attempt to determine the fraction of the wire material that actually participates in the pinch, whether there is a solid-density core left behind when the wire initially "explodes" which affects the ultimate conditions achieved in the x-pinch, and whether virtually all the radiated energy comes from implosion kinetic energy. The principle diagnostics for these studies will be a 1 ns nitrogen laser which we will try to use for interferometry, schlieren imaging and Faraday rotation measurements of the electron density and current density profiles of the pinch as a function of time. Both z-pinches and x-pinches will studied. A new pulser, especially built to facilitate these experiments, will be described briefly in the next subsection.

Lithography with an x-pinch must be more than just scientifically feasible. It must also be practical from an engineering standpoint and economically competitive. Pulsed power technology is already capable of generating the necessary 500-700 kA, 80-100 ns (fwhm) current pulses at a repetition rate of 25-100 pps, with 25 kJ primary storage. APP has completed the design of a 500 kA pulse power accelerator with 40 pulse per second operation, which is described in Section VI. Less obvious is that a Mg wire feeder consistent with 40 pps operation is also well within the capability of mechanical devices, as we also describe in Section VI. When those two subsystems are built and tested together, we will be capable of evaluating the engineering practicality and cost-competitive position of the x-pinch for lithography in the microelectronics manufacturing industry. We conclude this section with our reasons for choosing 40 pps operation.

Mask damage precludes delivering the 50 mJ/cm^2 soft x-ray fluence in fewer than 10 pulses. With yield scaling as I^3-I^4, it is advantageous to increase the current to achieve higher efficiency. However,

increasing current requires increased driver voltage. This leads to larger spacings and more parasitic inductance, which eventually outweighs the advantage of higher current. In addition, the cost of a high repetition rate pulser is roughly proportional to the energy per pulse and only weakly dependent on the repetition rate. Therefore, it is advantageous to increase the repetition rate rather than the energy per pulse within limits set by achieving a reasonable operating efficiency (radiation yield relative to electrical energy). A deciding factor is that a repetition rate of 40 pps is about half of the limit estimated for the mechanical wire feeder described in Section VI. Given the exploratory nature of our experiments so far, we believe that the factor of 2.5 x-pinch yield improvement required to achieve 50 mJ/cm in 1 s at 40 cm with this repetition rate should be possible with little or no increase in current. Finally, we note that with 40 pps, it should be straightforward to achieve the exact exposure desired on each resist by adjusting the current in the last few pulses of an exposure.

V. Special Purpose Pulser

The key design requirement for the x-pinch pulser is a capability to efficiently power an inductive short circuit load. A peak current capability up to 700 kA was selected (to comfortably exceed that from LION). Furthermore, we wanted a pulse duration comparable to that used on LION to avoid surprises concerning x-pinch yield and source size that might come from a significantly longer pulse. If possible, within cost constraints, we wanted the design to allow some flexibility in pulse duration. This was possible in practice because we will be able to add extra parasitic inductance to increase the pulse length, and still have LION-level or higher peak currents available. The net result is the pulser shown in Fig. 4. To summarize its operation, the Marx

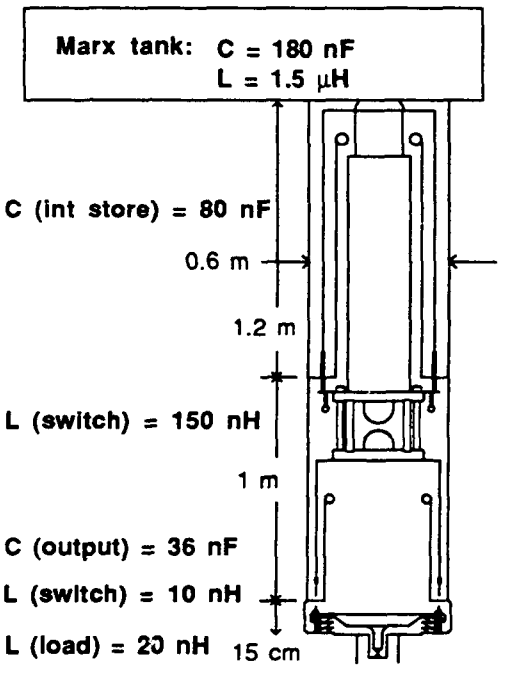

Figure 4: Schematic of the purpose built pulser showing the quadriaxial and triaxial capacitors.

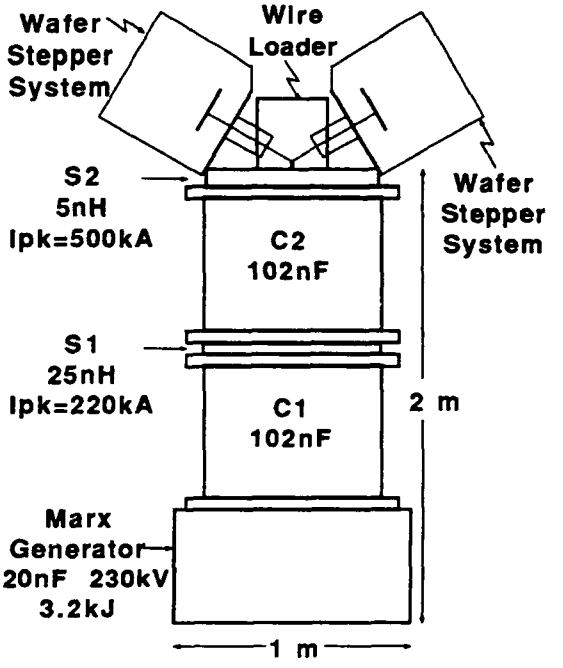

Figure 5: Schematic of an x-pinch lithography system illustrating simultaneous exposures on multiple wafer stepper systems.

Generator charges the intermediate quadriaxial water capacitor in about 900 ns to 670 kV when the Marx capacitors are charged to 54 kV. The energy then rings through the self break gas switch into the triaxial output capacitor in a time of 185 ns, charging it to 800 kV. The $CV^2/2$ energy in the output capacitor is then transferred to the load through the multichannel self-break water switch. With optimum performance of the 12 parallel switches, we expect to obtain about an 80 ns pulse with a peak current of 700 kA (at 54 kV charge). Initial x-pinch experiments are being performed using a 100 ns (fwhm) current pulse. The disadvantage of using water switches is that they are high loss switches and they create shock waves, but this is satisfactory for a one pulse per hour device.

The anticipated efficiency of this purpose built pulser is as high as a few tenths of a percent. Based on the observed current scaling of the K-shell yield as I^3-I^4 and yield improvements through optimization, 40 pps should be suitable to achieve wafer exposures in 1 second at a 40 cm source-mask distance. Using multiple pulses for a single exposure allows the number of pulses to be adjusted to ensure exposure variation of only a few percent.

VI. Lithography System Pulser

The key requirement for a high repetition rate pulser for a commercial lithography system is that it must be very reliable, with long component lifetimes. Operating at 40 pps, weekly maintenance implies intervals of $>10^6$ pulses, and major components must have $>10^8$ pulse lifetimes. To achieve long lifetimes, we have relatively low electric fields in solid dielectrics and relatively low current in Marx generator switches and we use long life, low energy density capacitors. Magnetic (saturable core inductor) switching is used in the pulse compression stages.

Because magnetic switch size (and cost) is proportional to switch gain (output current/input current) squared, it is important to minimize the required gain. Therefore, the Marx generator is actually three parallel-connected sub-Marxes to reduce the current through each spark gap to below 50 kA while achieving a low inductance. Using several techniques to extend electrode life, we believe the switches will have a $>10^6$ pulse life. Since the Marx generator can charge the first pulse compression stage in 300 ns, only two stages of pulse compression, each consisting of a water-dielectric capacitor and a magnetic switch, are required. The magnetic switches have very low inductance (when saturated), a high repetition rate capability and lifetimes of 10^9-10^{10} pulses. The output pulse is presently designed to be a 100 ns (fwhm) sine wave with a peak current of about 500 kA. Figure 5 illustrates how the system might look, and summarizes the important design parameters.

Although replacing the Mg wires in the x-pinch 40 times per second, including assuring the location of the cross point is reproducible to within perhaps 0.1 mm, may seem unreasonably fast, in fact there are many feed mechanisms that operate faster. Movie projectors operate at 48 frames/s and industrial sewing machines at 90 stitches/s. After examining several possible approaches with the assistance of mechanical engineer D.

Belongie,[10] we designed a wire feeder that works as follows: Wires from supply spools (two if the x-pinch is to be made from two wires) are threaded through tubes that have one-way inertial clamps on one end. Each tube, driven by a four-bar slider mechanism or a solenoid, moves back and forth across the electrode gap at an angle. When the tubes move forward, the inertial clamp holds the wires, transporting them across the gap into holes in the high voltage electrodes, where stationary clamps grab the ends. As the tubes begin to move backward, the inertial clamps release, leaving the wires in place in the gap. As the tubes pass out of the gap through the grounded electrode, a rotating clamp immediately behind the electrode turns, twisting the wires enough to touch in the center of the gap. This clamp also cuts the wires, leaving enough wire protruding from the tubes for the clamps in the high voltage electrode to grab on the next cycle. At 40 pps, a 1/10 horsepower motor is sufficient to drive a two- or three- wire four-bar slider mechanism. We estimate that this design is capable of operating at up to 80 pps.

Acknowledgments

Contributions to the Cornell experiments from J.R. Maldonado, Y. Vladimirsky, and K.C. Mittal are gratefully acknowledged. We wish to thank Dr. R.B. Spielman of Sandia National Laboratories for calibrating and lending us the PCDs, and Dr. P.G. Burkhalter of the Naval Research Laboratory for advice regarding the DEF film and KAP crystal calibrations. The research at Cornell was supported by NSF Grant Nos. ECS-89-19960 and ECS-91-13695, New York State Science and Technology Foundation Contract RDG 90179, and by the Plasma Physics Division, Naval Research Laboratory, under ONR contract No. N00014-90-J-2002. The x-pinch system study at Applied Pulsed Power, Inc., was supported by DARPA contract DAAH01-91-C-R028.

References

1 J.R. Maldonado, Journal of Electronic Materials **19**, 699 (1990).

2 D.A. Hammer, D.H. Kalantar, K.C. Mittal, and N. Qi, Appl. Phys. Lett. **57**, 2083 (1990).

3 D.H. Kalantar, D.A. Hammer, K.C. Mittal, N. Qi, J.R. Maldonado and Y. Vladimirsky, J. Vac. Sci. Technol. **B9**, 3245 (1991).

4 J. Maenchen, H.T. Sheldon, G.D. Rondeau, J.B. Greenly, and D.A. Hammer, Rev. Sci. Instrum. **55**, 1931 (1984).

5 R.B. Spielman, W.W. Hsing, and D.L. Hanson, Rev. Sci. Instrum. **59**, 1804 (1988); Dr. R.B. Spielman, private communication, 1990.

6 J.R. Maldonado, A. Reisman, H. Lezec, B. Bumble, C.K. Williams, and S.S. Iyer, J. Vac. Sci. Technol. B **5**, 248 (1987).

7 D.W. Peters, B.J. Dardzinski, and D.R. Kelly, J. Vac. Sci. Technol. B **8**, 1624 (1990).

8 D.H. Kalantar, L.A. Brissette, D.A. Hammer, F.C. Young, S.J. Stephanakis, P.G. Burkhalter, and D.A. Newman, Bull. Am. Phys. Soc. **35**, 2077 (1990).

9 E. Cullmann, T. Künneth, W. Neff, and K.H. Stephan, J. Vac. Sci. Technol. B **5**, 638 (1987).

10 D. Belongie, private communication.

MAGNETIC FUSION WITH HIGH ENERGY SELF-COLLIDING ION BEAMS*

N. Rostoker and F. Wessel, University of California, Irvine, CA
B. Maglich, Advanced Physics Corporation, Irvine, CA
A. Fisher, Naval Research Laboratory, Washington, DC

Abstract

Field-reversed configurations of energetic large orbit ions with neutralizing electrons have been proposed as the basis of a fusion reactor. Vlasov equilibria consisting of a ring or an annulus have been investigated. A stability analysis has been carried out for a long thin layer of energetic ions in a low density background plasma. There is a growing body of experimental evidence from tokamaks that energetic ions slow down and diffuse in accordance with classical theory in the presence of large non-thermal fluctuations and anomalous transport of low energy (10 keV) ions. Provided that major instabilities are under control, it seems likely that the design of a reactor featuring energetic self-colliding ion beams can be based on classical theory. In this case a confinement system that is much better than a tokamak is possible. Several methods are described for creating field reversed configurations with intense neutralized ion beams.

Introduction

Aneutronic reactions such as D-He^3 require a relative ion energy an order of magnitude larger than D-T reactions. For D-He^3 the maximum reactivity $\langle \sigma v \rangle$ is smaller by a factor of 4 compared with D-T so that a higher density or longer confinement time is required. Since the Rutherford scattering cross-section is inversely proportional to the square of the ion energy the confinement time should be longer by two orders of magnitude.

The observed confinement times are anomalous; in tokamaks they are 10-100 times shorter than classical predictions. The energy containment time scales with the square of the minor radius in a tokamak so that long confinement times (about 1 sec) can be obtained only with very large systems such as TFTR and JET. If the confinement were classical (determined by Rutherford scattering) it would be possible to obtain long confinement times with a small device; ion containment would be determined primarily by slowing down which is size-independent, rather than by diffusion. There is a growing body of experimental evidence that super-thermal ions in tokamaks[1] slow down and diffuse classically in the presence of the super-thermal fluctuations that cause anomalous transport of thermal ions.

*This work was presented as an invited paper at the BEAMS 92 Conference, May 25-29, 1992, in Washington, D.C.

Confinement systems are considered where the characteristic size is comparable to the ion gyroradius. The ions do not follow adiabatic particle dynamics as in tokamaks; it is well known from accelerators that non-adiabatic ions can be magnetically confined. Indeed the confinement is much better than it is for adiabatic ions in a plasma. It has been assumed that good confinement obtains only for low density. However, there have been experiments where large orbit particles (electrons,[2] or ions[3]) of high density are confined for long times in field reversed configurations.

In Fig. 1 various confinement systems for high energy ions are illustrated. Simplified physical models will be developed from self-consistent solutions of the Vlasov/Maxwell equations. Several methods for creating these configurations with ion beams are considered.

Equilibria for Confinement of High Energy Ions

1. General Solution of the Vlasov/Maxwell Equations

Consider distribution functions of the form

$$f_j(\mathbf{x}, \mathbf{v}) = n_j(\mathbf{x}) \exp -m_j[\mathbf{v} - \mathbf{u}_j(\mathbf{x})]^2/2T_j(\mathbf{x}) \; ; \tag{1}$$

different values of j correspond to electrons and various ion species. If $\mathbf{u}_j(\mathbf{x})$ and $T_j(\mathbf{x})$ are the same for all ions, ion-ion collisions will not change the distribution function and ion-electron collisions change it on a very long time scale. In order to satisfy the Vlasov equation $T_j(\mathbf{x})$ must be constant and $\mathbf{u}_j(\mathbf{x}) = (\omega_j y, -\omega_j x, 0)$ where ω_j is constant.[4] The density is determined by the following simultaneous equations

$$n_j = n_{0_j} \exp \left[\frac{m_j \omega_j^2 r^2}{2T_j} - \frac{e_i \phi}{T_j} - \frac{e_j \omega_j \psi}{c T_j} \right] \tag{2}$$

$$\frac{\partial B_z}{\partial r} = -\frac{4\pi}{c} \sum_j n_j e_j \omega_j \tag{3}$$

$$\sum n_j e_j = 0 \; . \tag{4}$$

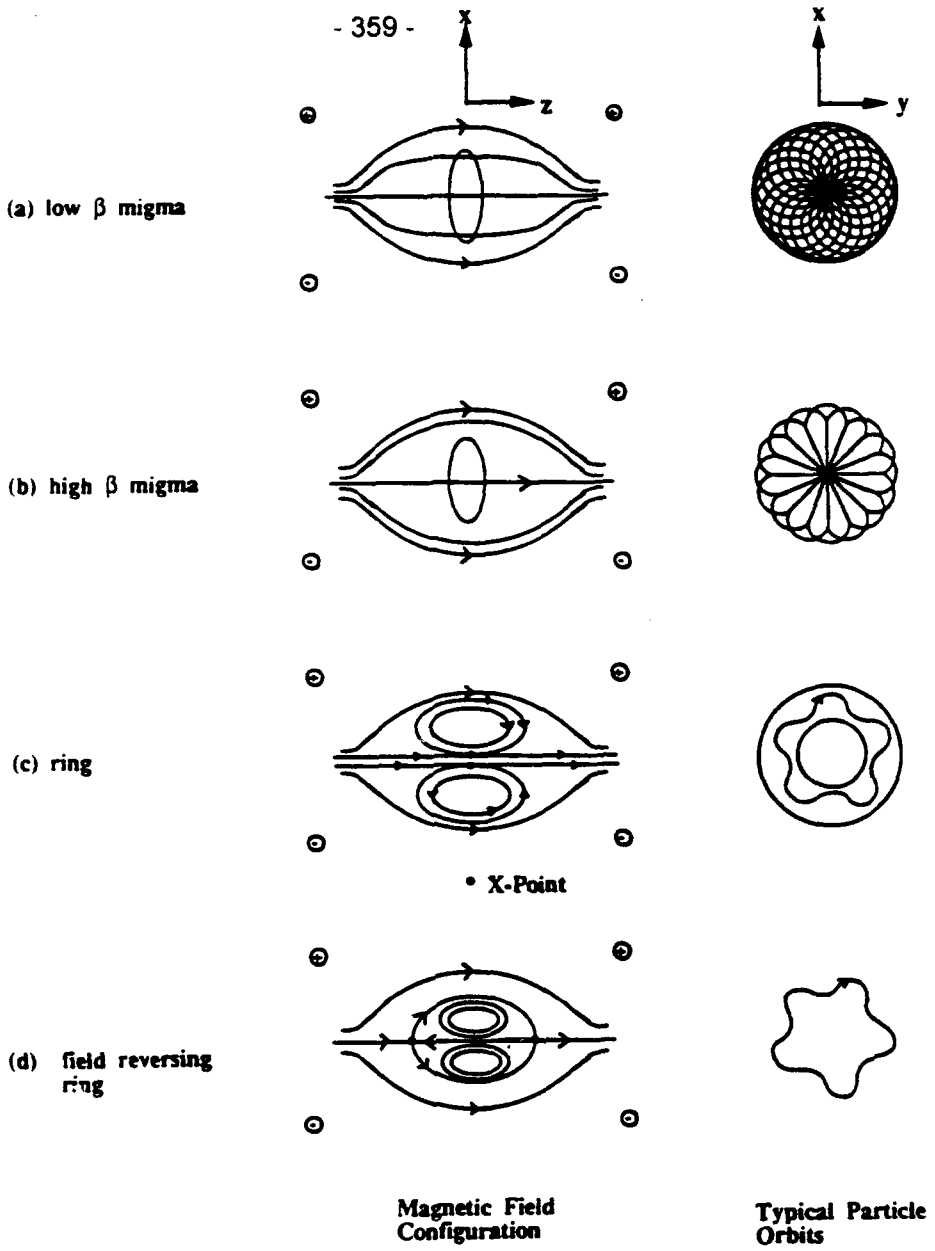

Fig. 1 Equilibria for high energy self-colliding beams

ϕ, ψ are electric and magnetic potentials. The electric and magnetic fields in cylindrical geometry are $B_z = (1/r)\partial\psi/\partial r$ and $E_r = -\partial\phi/\partial r$. Equation (4), the condition of quasi-neutrality, implies a relation between ϕ and ψ. For a single ion species Eqs. (2) to (4) combine to the nonlinear partial differential equation

$$\left\{\frac{1}{r}\frac{\partial}{\partial r}\frac{1}{r}\frac{\partial}{\partial r} + \frac{1}{r^2}\frac{\partial^2}{\partial z^2}\right\} \ln n_e = -\frac{4\pi e^2(\omega_i - \omega_e)^2 n_e}{c^2[T_e + (T_i/Z)]} \,. \tag{5}$$

Assuming $\omega_e = 0$, $Z = 1$, $\partial/\partial z = 0$, and that the density has a maximum value n_0 at r_0

(the plasma is assumed to be formed by beam injection at $r = r_0$), the solution is

$$n = n_0/\cosh^2\left(\frac{x - x_0}{\sqrt{2}}\right) \tag{6}$$

$$B_z = B_0\left[1 + \frac{1}{\sqrt{2}}\left(\frac{T_e + T_i}{W}\right)\tanh\left(\frac{x - x_0}{\sqrt{2}}\right)\right] \tag{7}$$

$$\phi = -\frac{B_0 R^2}{2c}\,\frac{\omega_i T_e}{W}\log\left[\cosh\left(\frac{x - x_0}{\sqrt{2}}\right)\Big/\cosh\frac{x_0}{\sqrt{2}}\right]\ , \tag{8}$$

where $\quad x = r^2/2\sqrt{2}\,R^2\ , \qquad W = \frac{1}{2}M(R\omega_i)^2$ and

$$\frac{1}{R^2} = \left(\frac{4\pi n_0 e^2}{T_e + T_i}\right)^{1/2}\frac{\omega_i}{c}$$

$$B_0 = \frac{cM}{e}\omega_i\ .$$

Typical data for a deuterium plasma might be $T_i = 100\,\mathrm{keV}$, $T_e = 20\,\mathrm{keV}$, $r_0 = 30\,\mathrm{cm}$, $n_0 = 10^{14}\,\mathrm{cm}^{-3}$ and $\omega_i = 2.9 \times 10^7\,\mathrm{sec}^{-1}$. For these data $(1/2)M(r_0\omega_i)^2 = 800\,\mathrm{keV}$, $B_0 = 5.9\,\mathrm{kG}$, $R = 5.2\,\mathrm{cm}$, $B_z(x = 0) = -15\,\mathrm{kG}$ and $B_z(x = \infty) = 27\,\mathrm{kG}$. Equations (6), (7), and (8) represent field reversed configurations if $x_0 > 0$ and $T_e + T_i > \sqrt{2}\,W$. If $x_0 = 0$ the peak density is on the axis. For this migma-like solution there can be no field reversal. In the limit that $\omega_i = 0$, $x_0 = 0$

$$B_z = \sqrt{8\pi n_0(T_e + T_i)}\,\tanh(x/\sqrt{2}) \tag{9}$$

$$\Phi = -(T_e/e)\log[\cosh(x/\sqrt{2})]\ . \tag{10}$$

2. Finite Boundary Conditions

A reasonable boundary condition is $\Phi(r_B) = \Phi(0) = 0$ in which case $n(0) = n(r_B) = n_B$. The previous solution satisfies these conditions if $r_B = \sqrt{2}r_0$, $r_0 \neq 0$. The solution is not yet determined. From Eq. (6)

$$n_B = n_0/\cosh^2(x_0/\sqrt{2})\ . \tag{11}$$

If (r_B, n_B) are fixed, this is a transcendental equation for n_0 because x_0 depends on n_0. If $\lambda = \sqrt{n_0/n_B}$ and

$$x_B = \frac{r_B^2}{2\sqrt{2}}\left(\frac{4\pi n_B e^2}{T_e + T_i}\right)^{1/2}\frac{\omega_i}{c}\ ,$$

the equation to be solved for λ is from Eq. (11), $\cosh \frac{\lambda x_B}{2\sqrt{2}} = \lambda$. If $x_B < 1.9$ there are two solutions for λ which can be labeled λ_D and λ_S where $\lambda_D > \lambda_S$. Since $n_0/n_B = \lambda^2$, λ_D the deep solution gives much better density contrast than λ_S, the shallow solution. As x_B approaches 1.9 the two solutions merge and for $x_B > 1.9$ there is no solution. These properties of the solution[5] are called bifurcation and $x_B = 1.9$ is the point of bifurcation. Two dimensional (r, z) equilibria have similar properties as illustrated in Fig. 2a to 2c. For fusion applications it is essential to have a low plasma density at the wall which is easily achieved with the deep solution but not with the shallow solution. It is not necessary to have $\phi = 0$ at the walls in which case the equilibria are less restrictive. However, this will involve large bias potentials which may create experimental difficulties such as breakdown.

Stability

Possible microinstabilities include drift modes, drift cyclotron modes, loss cone modes, Harris instabilities, etc. The list is long and it seems unlikely that they can all be avoided. They produce turbulence in tokamaks and anomalous transport. However, experiments in tokamaks show that high energy test-particles are insensitive to this turbulence. The probable reason is that the test-particle averages the fields so that only wavelengths long compared to the gyroradius contribute to transport. For adiabatic particles this includes much of the spectrum of field fluctuations. For high energy particles most of the spectrum is excluded. This explanation has been verified in a computer simulation study of transport.[6] It is likely that microinstabilities will not be important except for low energy particles for which a short containment time is desirable.

Of course a high density of high energy particles can produce instabilities and it is essential that long wavelength macroinstabilities be avoided. From the extensive research in FRCs[3] we know of two such instabilities: the rotational instability that has been eliminated with quadrupole windings and the tilt-mode that is stabilized by energetic particles. The rotational instability merits further study; it is conceivable that with the large gyroradii discussed here, the quadrupole windings will be unnecessary. To date there has been only one stability calculation[7] for an idealized model of a field reversed system which indicates that a long thin annular layer is susceptible to the kink instability. Techniques appropriate to the ring or the high β migma are not yet available.

Experimental Realization

A low density plasma in the migma configuration has been[8] produced by injecting 1.4 MeV D_2^+ ions that are ionized by collisions. A density of $10^{10}\,\mathrm{cm}^{-3}$ of .7 MeV $- D^+$ was

achieved with a confinement lifetime of $20 - 30$ sec. An instability was encountered and stabilized by applying a bias potential to the boundary of about 300 volts. The density could be increased by increasing the accelerator current which was only .5 milliamperes. Many other instabilities are expected before reaching $10^{14}\,\mathrm{cm}^{-3}$ and it may be possible to control them with a bias.

Another method to reach high density involves pulsed ion diodes and intense neutralized ion beams. Such a beam may cross a magnetic field without deflection in vacuum[9] if the beam density satisfies the inequality

$$\frac{4\pi n M c^2}{B^2} > \sqrt{\frac{M}{m}}\,. \tag{12}$$

The beam is polarized, the resultant field cancels the Lorentz force on the ions and makes the electrons drift with the ions. When the beam reaches a region of significant electron density electrons can freely move along the field lines and neutralize the polarization as illustrated in Fig. 3. Then the beam moves on a single particle orbit and is trapped. Preliminary successful experiments on trapping neutralized ion beams have been carried out with mirror and tokamak geometry.[10] With this method the density can be increased to $10^{14}\,\mathrm{cm}^{-3}$ in less than a microsecond so that instabilities characteristic of a low density plasma do not have time to develop. It can be used to produce migma or ring configurations by directing the beam to the axis or off-axis.

The current in a ring required for field reversal as in Fig. 1d is

$$I \cong \frac{1}{\pi}\frac{Mc^3}{e}\left(\frac{v}{c}\right) \cong 560\,kA$$

for an 800keV beam of D^+. This is within the present state of the art for pulsed power devices. A configuration with mainly closed field lines like Fig. 1c requires only about 50 kA.

The field reversed configuration could also be produced by injecting a long pulse beam of 10-100 amperes of D_2^+ or D into a pre-formed FRC made with standard techniques.[3]

Since the energetic particles have a much longer lifetime they would eventually dominate.

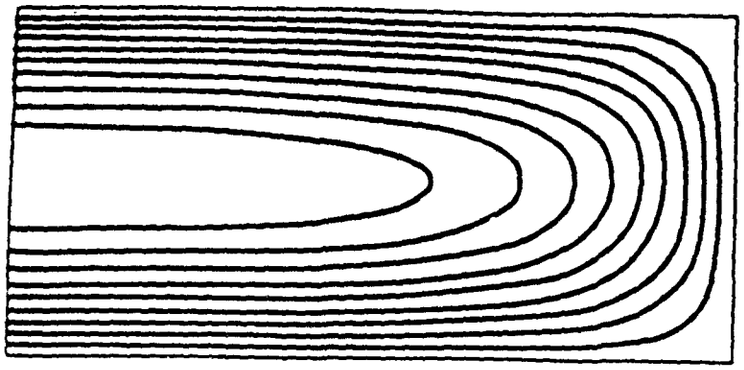

Fig. 2a Shallow solution near bifurcation $n_0/n_B = 2.23$

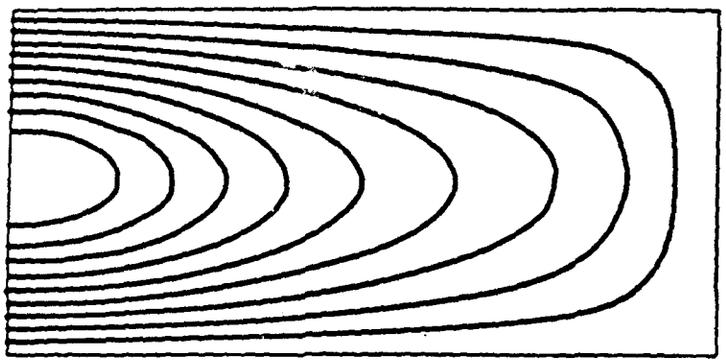

Fig. 2b Deep solution near bifurcation $n_0/n_B = 8.2$

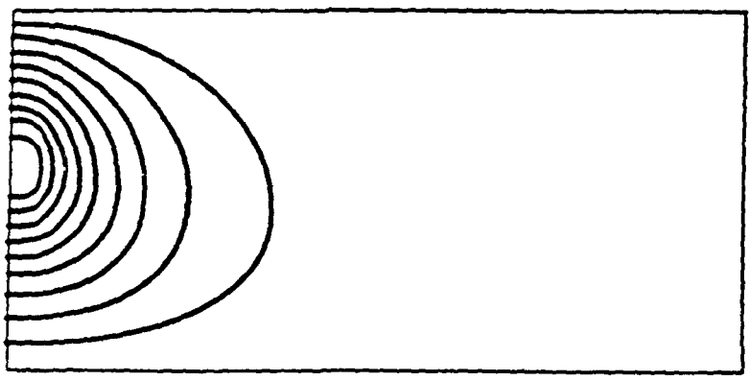

Fig. 2c Deep solution not near bifurcation $n_0/n_B = 330$

Fig. 2 Contours of constant density and/or equipotentials for conducting walls

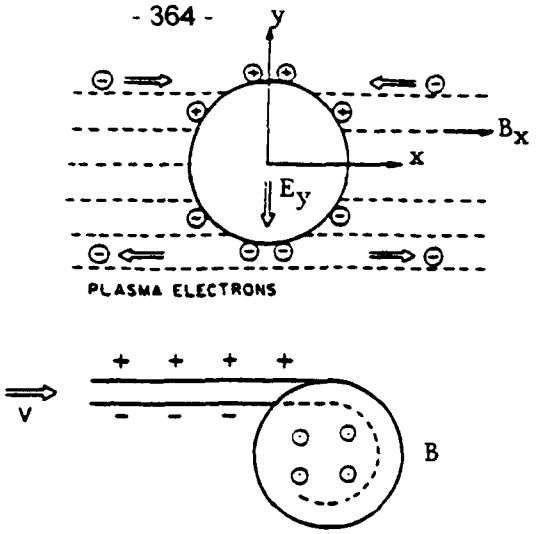

Fig. 3 Trapping of an intense neutralized ion beam

Acknowledgments

This paper was prepared at the Institute for Fusion Studies, at The University of Texas at Austin. The authors would like to express their appreciation to the IFS. N. Rostoker would like to express appreciation for useful discussions and criticism by IFS scientists, particularly H.L. Berk, T. Tajima, and H.V. Wong. The work was supported by the U.S. Department of Energy contract #DE-FG05-80ET-53088.

References

1. W. Heidbrink, J. Kim, and R.J. Groebner, Nucl. Fusion **28**, 2097 (1988); W. Heidbrink, Phys. Fluids B **2**, 4 (1990).
2. H. Fleischmann *et al.*, Phys. Fluids **17**, 2226 (1974); **19**, 728 (1976).
3. M. Tuszewski, Nuclear Fusion **28** 2033 (1988).
4. B. B. Spivey, Ph.D. thesis, University of California at Irvine, 1992.
5. B. Marder and H. Weizner, Plasma Phys. **12**, 435 (1970); D.A. Larrabee, R.V. Lovelace, and H. Fleischmann, Nucl. Fusion **19**, 499 (1979).
6. H. Naitou, T. Kamimura and J. Dawson, J. Phys. Soc. Jpn. **46**, 258 (1979).
7. H.V. Wong, H.L. Berk, R.V. Lovelace, and N. Rostoker, Phys. Fluids B **3** (11) 2973 (1991).
8. M. Salameh *et al.* Phys. Rev. Lett. **54**, 746 (1988); B. Maglich, Nucl. Instr. Meth. A **271**, 13 (1988).
9. S. Robertson, H. Isizuka, W. Peter, and N. Rostoker, Phys. Rev. Lett. **17**, 508 (1981).
10. M. Wickam and S. Robertson, Plasma Phys. **25**, 103 (1983); J. Katzenstein and S. Robertson, Proc. Compact. Torus Symposium (Bellevue, Washington, Nov. 16-20, 1982).

PRACTICAL APPLICATIONS OF HIGH-POWER ION BEAMS

G.E. Remnev, Nuclear Physics Institute, 634050 Tomsk, Russia

V.A. Shulov, Aviation Institute, 125871 Moscow, Russia

Abstract

The results of experimental investigations on the practical applications of high-power ion beams are presented. These include the use of 200-300 keV, 50-250 A/cm^2, 60 ns duration beams for modification of properties of metals and production of unique compounds in the surface layer of the target, pulse beam machining of implanted silicon hardening of cutting tools, reconditioning and cleaning machine parts

Introduction

The research into practical use of high-power ion beams (HPIB), basically in the interests of material engineering, began more than a decade ago [1, 2]. Recent years have seen great efforts made in this area by Russian, Japanese and Hungarian investigators [3-8]. These comprise implantation and annealing of semiconductor materials, modification of properties of metals, thin films deposition, formation of special resists in the surface layer of articles using convective and ion mixing of multilayer target materials. The beam power density used for these purposes ranges from 10^7 to 10^9 W/cm^2.

Practical applications of HPIB's require a fairly high shot-to-shot stability of the beam parameters (up to 20 %), a uniform beam current density distribution, the 0.1-10 Hz pulse repetitionrate and high reability of all the accelerator units. The beam composition is important for implantation and annealing of semiconductor materials.

The object of this paper is to report the results obtained by different workers using high-current ion accelerators developed and built at the Nuclear Physics Institute. In particular, the problems pertaining to the increase of wear resistance of cutting tools, hardening of high-temperature titanium alloys, reconditioning and cleaning of articles and thin film deposition are discussed. Schematic diagrams of diode systems of the accelerator employed to that effect are given.

Specific Features of the Mechanism Responsible for the HPIB - Material Interactions

HPIB's used in the applied research generally have the following parameters:
ion energy 10^5-10^6 eV, current density 10^1-10^4 A/cm^2, pulse duration 10^{-8}-10^{-6} s.

The exposure of the materials to HPIB's results in such major processes as heating, melting, liquid-phase mixing of components and evaporation; vapor-plasme flame formation, intense mixing and plasma expansion at rates between 10^5 and 10^6 cm/s; compression and shock wave excitation; fast cooling of the near-surface target layer after the axposure ($dT/dt > 10^6$ K/s), condensation of sputtering species into the environment and on the irradiated target.

These processes cause specific changes in the surface chemistry and formation of the fine crystalline structure. The resulting changes, in turn, alter physicomechanical properties and, consequently, performance characteristics of the articles.

HPIB's have advantages over other kinds of concentrated energy fluxes in the high-efficiency beam-target interaction, fairly uniform depth of penetration of the absorbed energy and high beam cross section (10^1 - 10^3 cm^2).

HPIB Sources

We have studied the beam-material interactions using TONUS and VERA accelerators [2, 3, 7] and specially developed TEMP accelerator [9] whose parameters meet, to some extent, the specific requirements. The accelerator comprises a seven-stage Marx generator, a double pulse shaping circuit, a vacuum diode system, power supply and control unit. A general view of the accelerator is shown in Figure 1.

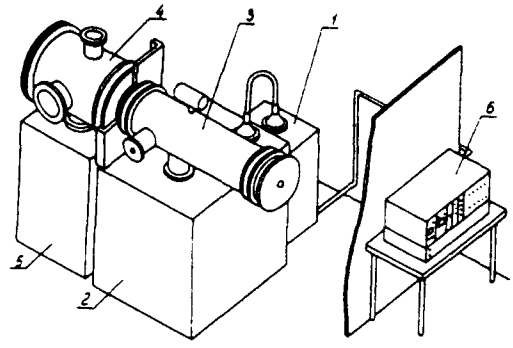

Fig. 1. Shematic diagram of TEMP accelerator. 1 - power supply system; 2 - Marx generator; 3 - pulse shaping line; 4 - vacuum chamber; 5 - vacuum pump system; 6 - control unit.

The accelerator is supplied with different magnetically-insulated diode configurations (see Fig. 2)

Fig. 2. Schematic diagrams of magnetically insulated diodes. a - strip diode; b - focusing diode.

perfectly ordered structure of the near-surface layer and the formation of carbides. All these contribute to material strengthening. The fatigue range can be increased by 12–200 % for different alloys. More than a two-fold increase in the heat-resistance is observed which is due to both the formation of perfectly ordered structure in the alloy surface layer and fine carbide precipitates.

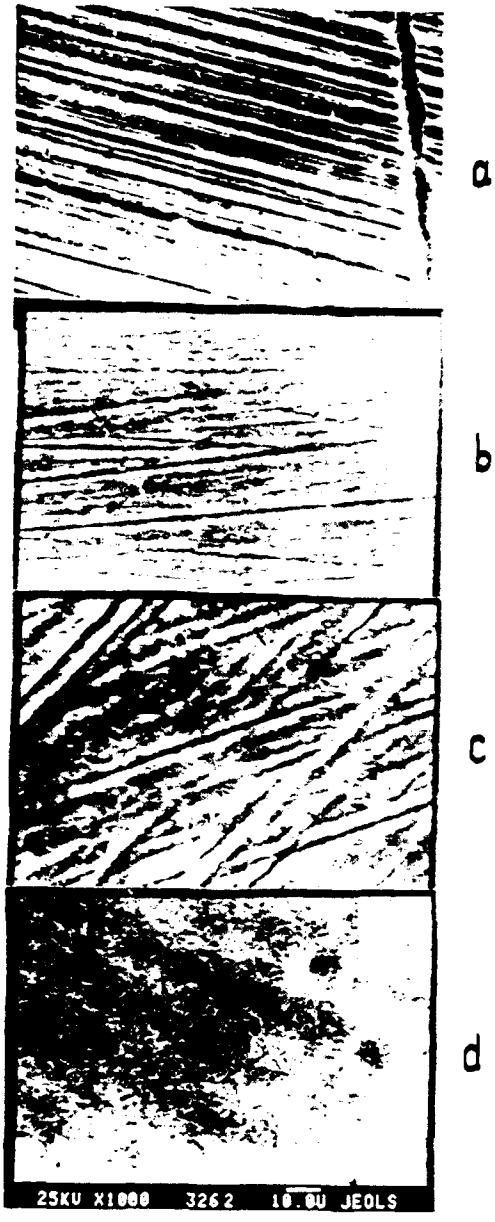

Fig. 8. HPIB-induced surface morphology of compressor blades made of VT25 titanium alloy vs pulse number: a – initial state; b – n = 1 pulse; c – n = 10 pulses; d – n = 20 pulses.

HPIB processing enhances the corrosion resistance by a factor of 6. The irradiation of titanium alloys combined with thermal treatment also increases their errosion resistance by a factor of 1.8. The errosion tests were carried out for a load of 20 mg/cm^2. To this end, quartz sand was used with a particle diameter of 40–100 μm and speed of 200 m/s.

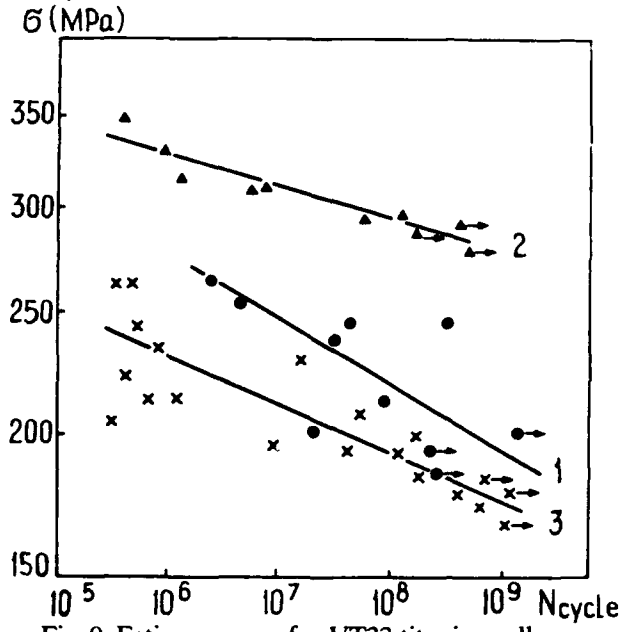

Fig. 9. Fatigue curves for VT33 titanium alloy samples: 1 – after HPIB irradiation; 2 – after diffusive annealing alone; 3 – initial state. Repeated loading is 3300 Hz and annealing temperature – 450°.

The data obtained show that HPIB technology can be used to advantage to modify the properties of articles made of heat-proof materials. It is to be noted, on the other hand, that the craters formed on the surface of the irradiated samples are the major limitations to further improvement of their performance characteristics. Therefore, gaining a deep insight into the crater formation process and developing efficient crater control techniques would benefit extensive industrial applications of the HPIB technology.

Reconditioning and Cleaning of Machine Parts
Using High-Power Ion Beams

Expensive industrial equipment and machine parts being in long-term service have to be reconditioned and cleaned from carbon deposits, oxide layers and skin inclusions. As a rule, this operation involves mechanical machining, chemical or electrochemical etching. A competitive method for the job is beam etching which is highly efficient and ecologically safe at that. For example, the HPIB technology is capable of cleaning disused gas-turbine engine blades made of high-temperature titanium alloys [10]. The oxide layer may be as thick as 40–80 μm. The HPIB machining partially or completely removes the oxide material. Moreover, fine carbide or oxycarbide precipitates are formed in the surface layer. An extra finishing thermal treatment results in fine-grained surface structure with a highly uniform distribution of α-plates. The grain size is 40–60 μm. Residual compressive stress is formed in the near-surface zone 5 μm thick. An optimum machining regime makes it possible to reduce the surface roughness from 0.30 to 0.06 μm and enhance the sample microhardness by a factor of 1.5. Figure 10 illustrates the results of fatigue tests. The fatigue curve for compressor blades of a gas-turbine engine subject to HPIB machining and diffusive annealing is seen to lie even higher than the one for new commercial blades. In addition, the resistance to dust erosion and salt corrosion can be increased at least to the level of new commercial products. The HPIB technology is applicable to machining and reconditioning of articles made of different materials and to the preliminary surface preparation for different protective coatings.

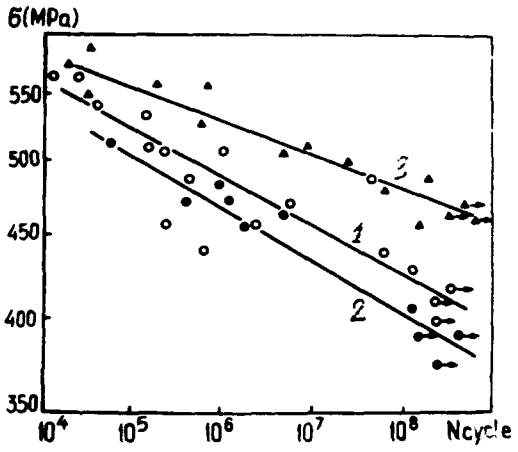

Fig. 10. Fatigue curves for VT9 titanium alloy samples after 1000 hrs service: 1 – new blade; 2 – compressor blade after 1000 hrs service; 3 – HPIB irradiation plus diffusive annealing. Repeated loading is 3300 Hz and annealing temperature – 500°C.

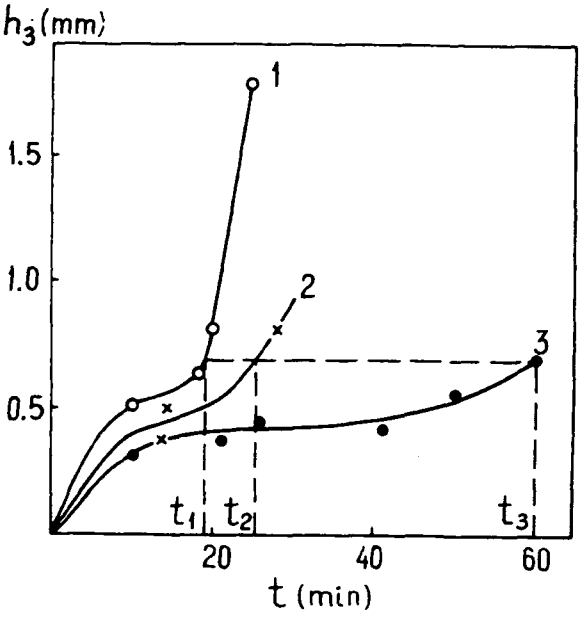

Fig. 11. Fatigue Wear, h, of tool tips as a function of service time, t: 1 – new tips; 2, 3 – HPIB-irradiated tips for different processing regimes.

HPIB processing of high-temperature alloys affects greatly their microhardness and surface roughness. As the current density is increased their microhardness first reduces from 360 to 200–280 HV and enhances to 430–700 HV for different alloys. The surface roughness can be reduced from 0.26–0.4 to 0.06–0.12 μm. In addition, the annealing of the irradiated samples promotes intense recrystallization processes in the surface layers of titanium alloys. As a result, 40 μm grains are formed with a highly homogeneous substructure.

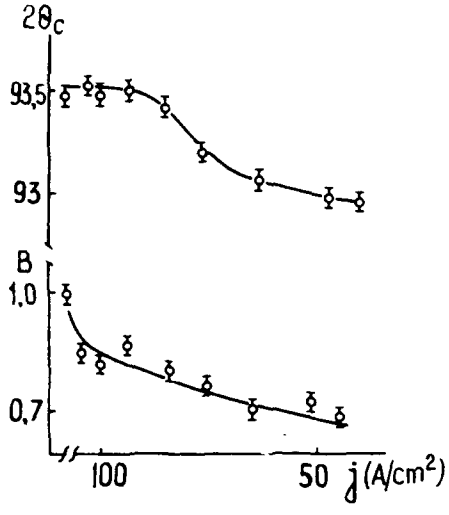

Fig. 6. (102)-α-Ti X-ray line position ($2\Theta_c$) and FWHM (B) as a function of j_i for VT18U titanium alloy samples.

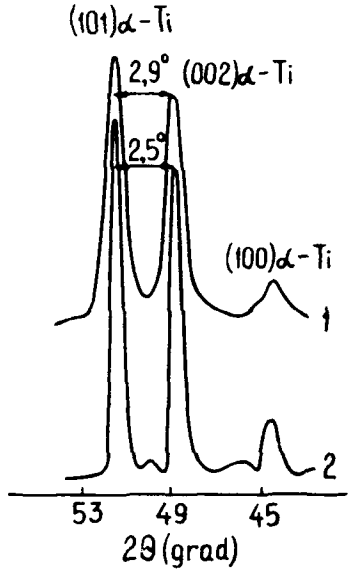

Fig. 7. X-ray line for VT18U titanium alloy sample: 1 - initial state; 2 - after HPIB irradiation and diffusive annealing alone.

The results obtained from scanning electron microscopy show the feasibility of the HPIB technique to the microrelief burnishing. Figure 8 illustrates this fact. It takes but 20 shots to scrape off the traces of the initial machining of compressor blades of a gas turbine engine.

However, high current densities result in the formation of microcraters on the surface of titanium alloys. As the current density is increased the craters grow slightly larger but their number decreases. The cross-sectional dimensions of the craters (5–80 μm) are independent of the number of shots. It is to be noted that the thermal treatment following the sample irradiation gives rise to the formation of new craters. The mechanism responsible for this effect is most probably related to purely nonlinear liquid-vapor processes which occur in the beam-target interaction zone. High-temperature titanium alloys were put to fatigue, high-temperature strength, dust erosion and salt corrosion tests. Theresults showed the improvement of their performance characteristics at certain beam parameters. Of greatest interest are the data on the fatigue properties of the irradiated alloys, Fig. 9.

Typically, the sites of breakage of samples before the exposure are sharp edges while after the exposure they are found beneath the surface (6–120 μm deep) or in craters. The enhanced fatigue strength of the irradiated samples is primarily due to the reduced size and number of macrodefects of the cutting edge, fairly

A nanosecond generator delivers two successive pulses (see Fig. 3). The first pulse induces plasma formation, while the second one accelerates the ion species. The current density of the focusing diode is controlled by varying the diode-target separation. The accelerator parameters are as follows: ion energy -up to 300 keV; current density at the target 50-200 A/cm^2; pulse duration - 50 ns; PRR - 1 pulse per 3 seconds.

A special device has been added to the vacuum chamber to provide automatic handling of samples placed in the beam path. The accelerator is capable of processing a 1 m^2 surface per hour and the treatment would require the vacuum chamber to be opened three times during an hour session.

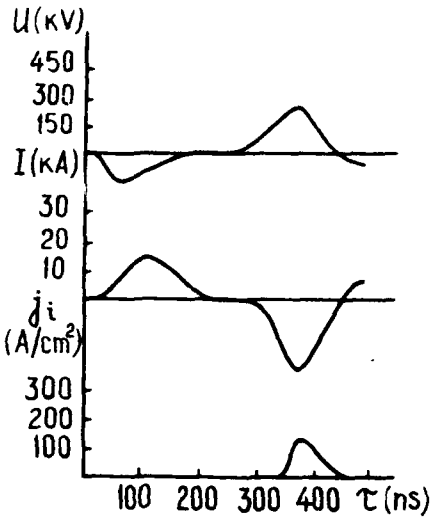

Fig. 3. Oscillogram traces of accelerating voltage (U), total diode current (I), and ion current (J_i) at the target.

Pulsed Beam Machining of Implanted Silicon

Thermal treatment of semiconductors using charged particle beams with a nanosecond or microsecond pulse duration has a number of advantages over laser machining. Beam energy deposition in a sample volume provides fast thermal treatment without any surface damage. Furthermore, the fact that the energy deposition is independent of changes in the state of aggregation of matter and optical parameters of the beam improves the machining repeatability. R.M. Bayazitov et al. [11] explored the possibility of crystallization and formation of high-alloy silicon layers using a combination of ion implantation and HPIB machining. TEMP accelerator was employed in the experiments [9]. Figure 4 shows carrier layer concentration as a function of implantation dose.

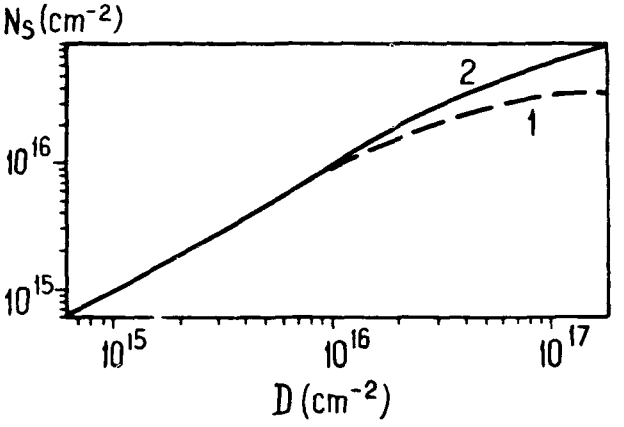

Fig. 4. P$^+$-doped silicon layer concentration as a function of irradiation dose after laser annealing (1) and HPIB annealing (2).

It is seen that high implantation doses ($2 \cdot 10^{16}$) permit higher impurity activation to be achieved (100 %) as compared t. laser annealing. High-alloy ($n_0 = 3 \cdot 10^{21}$ cm^{-3}) highly conducting silicon layers are formed. The method in question is full of potentialities since it affords an opportunity to combine the implantation of electrically active impurities with the annealing of radiation-induced defects. Work is under way now to build a short-pulse implanter with an output energy of 120 keV and average beam power up to 1 kW.

High-Temperature Resistant Titanium Alloy Modification

We have investigated HPIB-induced changes in the physico-chemical properties of the surface layers of samples and machine components made of high-temperature α-, $\alpha+\beta$-, β- titanium alloys. The analysis was done by means of Auger spectroscopy, scanning electron microscopy, X-ray diffraction technique, X-ray microanalysis, and exoelectron emission. In addition, we have measured surface microhardness and roughness, fatigue strength, resistance to dust erosion, salt corrosion and atmospheric corrosion at high temperatures. Following the irradiation, all the samples were subject to stabilizing vacuum thermal treatment.

The HPIB irradiation and thermal treatment cause drastic changes in the chemical composition of the surface layers up to 1 μm thick, Figure 5. Carbon and oxygen concentrations grow higher and carbon, zirconium, molybdenum concentrations distributions become more uniform. There appear fine carbide and oxycarbide precipitates in the near-surface layers up to 100 nm thick. X-ray diffraction analysis have shown changes in the structural composition of the near-surface layer of the irradiated samples. The layer thickness is 4-7 μm, which exceeds greatly the depth of convective mixing (~1 μm). The difference in angles of reflection $2\Theta_c$ in the diffractograms of Figure 6 before and after irradiation is the evidence of the material deformation and residual compressive or tensile microstresses. Maximum structural changes have been found after irradiation using high current densities. In this case the diffraction lines on the X-ray patterns of Figure 7 are narrower after vacuum annealing. The interplanar spacing d_{103} is reduced from 0.1335 to 0.1329 and the line separation (002) and (101) increases from 2.5 to 2.9°. It is likely to be due to a more complete relaxation of residual macrostresses in the near-surface layer after irradiation and thermal treatment.

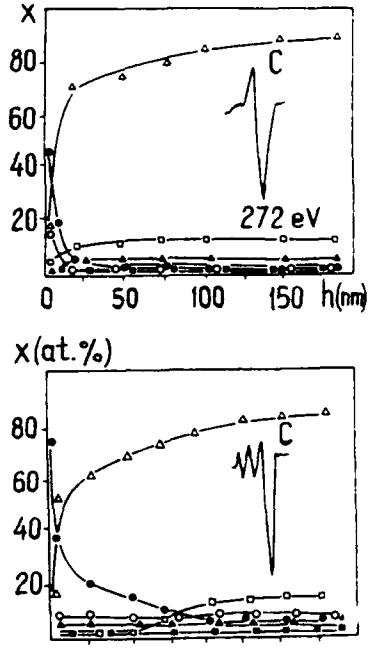

Fig. 5. Concentration profiles of Ti, C, O, Al, Mo and Zn in the surface layer (100 nm) of samples made of VT9 titanium alloy and Auger peaks of carbon. a - initial state; b - HPIB technology at E = 300 keV and j_i = 140-150 A/cm^2 and diffusive annealing at 550°C for 2 hrs (Δ -Ti; ● - C; O- O; □- Al; ■- Mo; ▲- Zn).

Hardening of Cutting Tools

The serviceability of cutting edges, i.e. surface layers 100 μm thick, is known to be critical for the tool life time. The HPIB machining of cutting tools is proposed as an alternative to plasma sputtering of wear-resistant coatings. The HPIB technology is characterized by a superior machining rate and lower specific energy input. The HPIB machining is found to improve the wear resistance of tool tips drills, cutters and taps by a factor of 2 to 8 3, 7. Figure 11 gives wear curves for VK-7 alloy tool tips employed for rough-machining of titanium alloy samples. The data were obtained using a software machining center. We are performing experiments on the combined use of HPIB's and plasma fluxes for applying different coatings.

Concluding Remarks

HPIB sources have shown good promise for a great number of practical applications. Currently, the major problem is to study the dynamic processes occuring at the interface of beam-vapor-plasma layer-liquid phase boundary-solid. Further-more, the development of efficient crater control techniques would bring about a considerable improvement of performance characteristics of articles which underwent the HPIB treatment. Unlike metal working, the application of the HPIB technology to semiconductor materials, for example, for the electrically active impurity implantation followed by defect annealing would set a more severe requirements to the beam composition, pulse duration and energy spectrum.

References

1. J.E. Baglin et al. Appl. Phys. Lett. 1980, 37, p. 187.
2. Yu.P. Usov et al. Paper Abstracts, 3d All-Union Conf. on Applications of Electron-Ion Technology in the National Economy. Tbilisi, 1991, p. 110.
3. A.D. Pogrebnjak et al. Izv. Vyssh. Uchebn. Zaved. Fiz., 1987, No 1, p. 52.
4. J. Gyulai. Modification of Material Surfaces by Ion Pulses. Proc EPM 87, Drezden, 1987.
5. A.N. DIdenko et al. The Effect of Charged Particle Beams on the Surface of Metals and Alloys. M: Energoatomizdat, 1987.
6. K. Yatsui. Laser and particle beams, 1989, vol. 7, part 4, p. 733.
7. G.E. Remnev and A.D. Pogrebnjak. Novosti Nauki i Tekhniki, M. VINITI, 1990, vol. 2.
8. A.D. Pogrebnjak et al. Nucl. Instrum. Methods, 1989, vol. 36, No 3, p. 286.
9. I.P. Isakov et al J. Vacuum, 1991, vol. 42, No 1/2, p. 159.
10. V.A. Shulov et al. Zn. Eksp. Teor. Fiz. Pis'ma Red. [JETP Lett.], 1991, vol. 17, 17, p. 38.

Invited Pulsed Power Papers

Richard Gullickson, *Session Chairman*

MICROSECOND-CONDUCTION-TIME POS EXPERIMENTS

B. V. Weber, J. R. Bolier, R. J. Commisso, P. J. Goodrich,* J. M. Grossmann, D. D. Hinshelwood,* J. C. Kellogg, P. F. Ottinger and G. Cooperstein

Plasma Physics Division
Naval Research Laboratory, Washington, DC 20375-5000
*Jaycor, Vienna, VA 22182-2270

Abstract Experiments have been performed to improve the understanding of the μs-conduction-time plasma opening switch (POS). Measurements with a He-Ne laser interferometer show that the line-integrated plasma density reaches a peak value during conduction, then decreases to a relatively small value before opening begins. During opening, the density is low over a large fraction of the electrode gap, but is relatively high at both electrodes, indicating that opening actually occurs in the middle of the electrode gap. The dependence of conduction current and conduction time on density and other POS parameters (radius, length, and current waveform) indicate that conduction is controlled by hydrodynamic displacement and distortion of the plasma, resulting in a low density region where opening occurs, possibly by erosion. Experiments with electron-beam diode loads have been performed for a variety of load and POS configurations. Assuming the POS gap at peak power equals the radial extent of the electron orbits, the calculated switch gap is about 2-3 mm over a wide range of load impedances, conduction currents, and center conductor radii. Increased load power requires increasing the (effective) gap size. Fluid and PIC codes may be suitable to simulate the conduction and opening phases, respectively, and a combined fluid/particle model could indicate promising methods for increasing the output power using a POS.

I. Introduction

Inductive-store pulsed power generators require a fast opening switch to transfer current from an energy-storage inductor to a load. One approach[1] is to use a plasma opening switch (POS) to conduct current during the discharge of a Marx generator into an inductor, which generally takes about 1 μs. After this conduction phase, the POS opens and transfers most of the current to a load. This approach to inductive-store pulsed power generators is attractive compared with conventional (capacitive water-line) generators because of decreased size and cost, and the potential to scale up to higher energy.[2]

POS experiments have been performed on the Hawk inductive-store pulsed power generator at the Naval Research Laboratory (NRL). Hawk consists of a high-current, 1-μF Marx bank[3] with a typical output voltage of 640 kV and stored energy of 0.23 MJ at 80-kV charging voltage. The discharge of the Marx into the circuit inductance, shorted by a POS, results in a sinusoidal current with peak amplitude 720 kA and quarter period 1.2 μs. When the POS opens, current is transferred to an electron-beam diode load, resulting in load power as high as 0.7 TW (450 kA, 1.6 MV).[4] The overall energy efficiency of the Hawk generator is about 20%, about two times smaller than for conventional water-line generators. (For example, the Gamble II generator at NRL is about 40% efficient and generates 1-2 TW into a load for similar stored energy.) The volume of Hawk (50 m^3) is far smaller than its conventional counterpart, (Gamble

II: 2000 m^3), making it an attractive alternative for many applications, especially if the efficiency and power could be increased.

The output power of Hawk, and of similar generators, is limited by the POS. Research on Hawk has concentrated on identifying the physical mechanisms that determine conduction and opening for the μs-conduction-time POS. This paper gives an overview of this research work. Interferometry is used to measure the distribution and evolution of the plasma density during POS operation, and to determine the dependence of conduction current and time on density and other POS parameters. Experiments with electron-beam diode loads demonstrate that the size of the vacuum gap generated in the plasma during opening is limited to about 3 mm. Understanding the gap opening mechanism and increasing its size, perhaps with the aid of computer simulations, could lead to significant improvement in output power and efficiency.

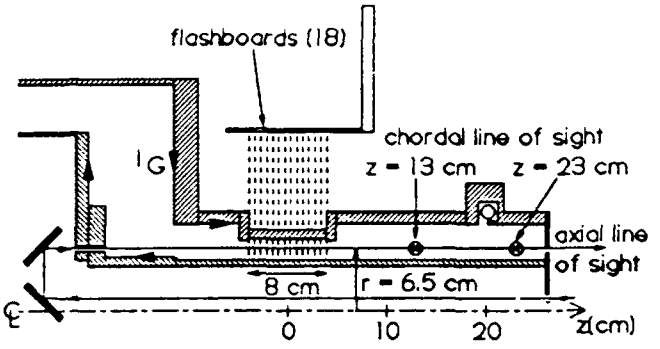

Fig. 1. Hawk POS arrangement showing axial and chordal He-Ne laser lines-of-sight for interferometry.

II. Physics of conduction based on interferometry

Measurements of plasma dynamics and conduction scaling on Hawk have been made using a He-Ne interferometer[5,6]. Details of the interferometer are given in Ref. [7]. A sketch of the POS on Hawk and sample laser lines-of-sight used for density measurements are shown in Fig. 1. The POS plasma is injected between the coaxial conductors using 18 flashboards, each driven by a capacitor circuit generating about 35 kA in 0.6 μs. Currents are measured on the generator (I_G) and load (I_L) sides of the POS. A short circuit load is used to minimize debris and prevent high voltages that could adversely affect the density measurement. The axial line-of-sight measures the line integrated electron density in the plasma injection region at a selected radial location. The length of the plasma injection aperture, l = 8 cm in Fig. 1, is used to convert the line-integrated density to more convenient density units (cm^{-3}). The precision of the density measurement using the axial line-of-sight is about 1×10^{14} cm^{-3}.

Fig. 2 shows data taken on Hawk using an r = 5 cm center conductor using the axial line-of-sight located at r = 6.5 cm, 1.5 cm from the center conductor and 0.5 cm from the outer conductor in the POS region (as shown in Fig. 1). The average density measured by firing the flashboards alone, n_{FB}, increases from about 2×10^{15} cm^{-3} at the time the Hawk current would begin (t = 0), to over 8×10^{15} cm^{-3} at the time the load current would begin (t = 0.9 μs). The density measured during the Hawk shot, n_e, follows n_{FB} for the first 0.4 μs and then decreases, becoming relatively small at the time opening begins. The decrease in density during conduc-

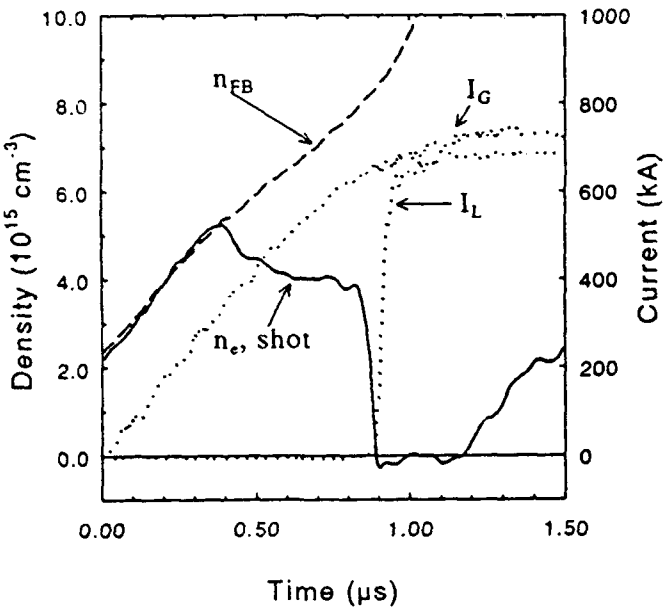

Fig. 2. Density measured in Hawk, 1.5 cm from the r = 5 cm center conductor.

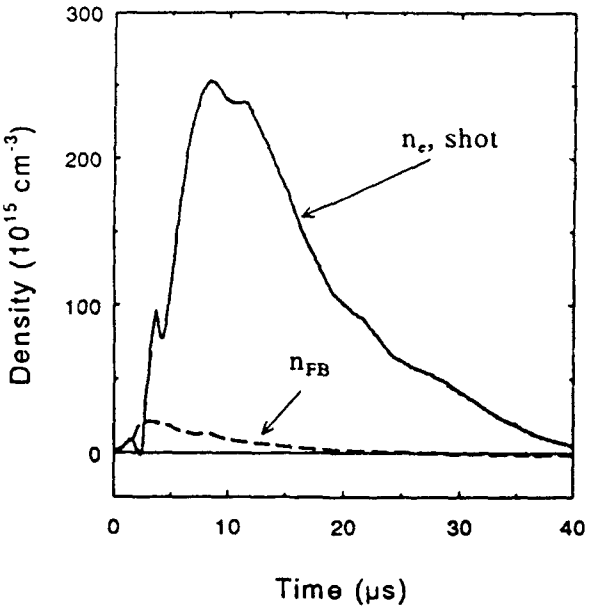

Fig. 3. Density measured on a long time scale, 1.0 cm from the r = 5 cm center conductor.

tion is typical for Hawk experiments, although the rapid decrease shown in Fig. 2 is not necessarily typical. After opening, the density is lower than the measurement limit for 0.3 μs before increasing. The density eventually exceeds 10^{17} cm^{-3}, an order of magnitude higher than the peak flashboard density, as shown in Fig. 3. The high density after switching is attributed to plasmas generated at the electrodes after bombardment by the energetic particles generated during the opening phase.

The radial dependence of the density is measured by changing the radial location of the laser line-of-sight for shots with the same nominal POS parameters. The measured density distributions at the start of conduction and during opening are shown in Fig. 4. The density distributions measured by firing the flashboards alone are indicated by dashed lines. The distribution at the start of conduction for the Hawk shots matches the flashboard-only data. The density distribution at the start of conduction shows a drastic density increase near the center conductor resulting from a plasma-surface interaction. The density is relatively constant between r = 6 and 7 cm. At a time during opening, t = 900 ns in Fig. 4, the density measured on Hawk shots has a minimum at r = 6.5 cm, and increases toward both conductors. Presumably, opening occurs in this region. For comparison, the density distribu-

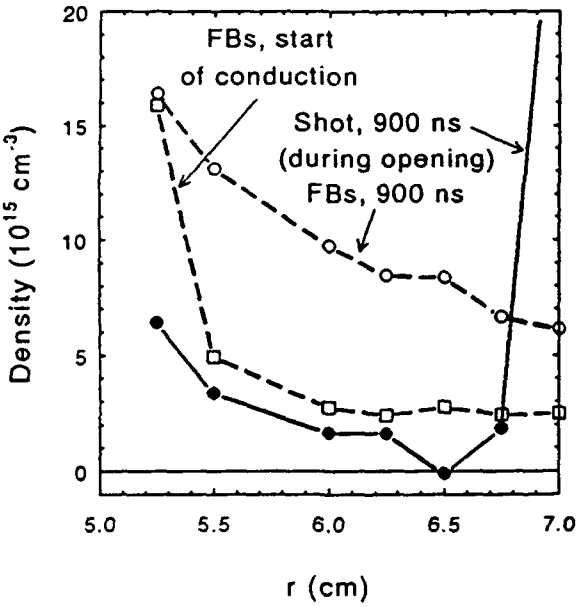

Fig. 4. Radial distribution of density at the start of conduction and during opening.

tion measured at the corresponding time but without firing Hawk is shown. The consequence of current conduction is that this additional plasma does not completely enter the switch region, and the density is redistributed by **J**×**B** forces during conduction, resulting in a rarefied region where fast opening can occur.

Measurements[8] made using other electrode radii (2.5-13 cm) and inner-outer conductor spacings (2-4.5 cm) indicate that the minimum density region during opening extends over a larger region (1-2 cm) of the gap between the conductors. In all cases, opening probably occurs between the conductors where the density is low, instead of near the cathode or anode surfaces, where the density is relatively high.

Measurements[8] using the chordal lines-of-sight shown in Fig. 1 indicate that opening occurs before plasma is displaced to these locations (9 cm and 19 cm from the edge of the plasma injection aperture). The reduction in density occurs in the switch region, without significant translation of the switch plasma toward the load.

An illustration of the physical process that could explain the density reduction is shown in Fig. 5. Here, the POS is simulated using the Anthem code[9] to model the plasma as two fluids (electrons and ions). The experimentally measured radial density distribution 300 ns after conduction begins is used in the simulation. During conduction, the plasma is compressed, and a thick "snowplow" effect is seen. The current streamlines follow the electron contours in the compressed density region, resulting in primarily radial current with a slight bow in the middle where the plasma has been displaced the farthest. At the end of conduction, the plasma has accumulated near the load end of the switch region. The axial components of the current density cause a radial displacement of plasma toward both electrodes. This forms a valley in the plasma distribution at about r = 6.7 cm, close to the location of the minimum density in the corresponding Hawk experiment (Fig. 4). The line-integrated density decreases rapidly at this location at

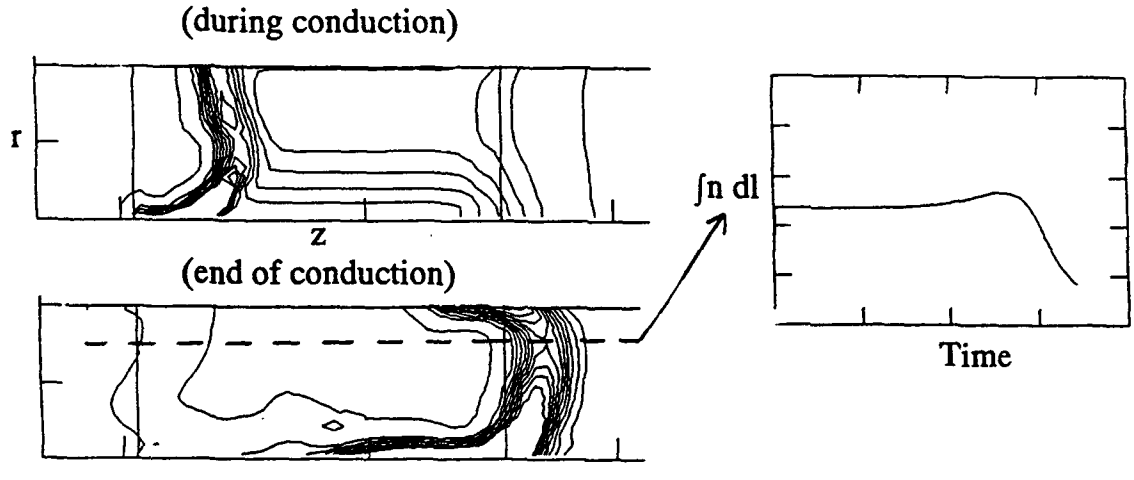

Fig. 5. Anthem simulation of Hawk POS. Electron contours are plotted during conduction (above left) and at the end of conduction (below left). Line-integrated electron density at r = 6.7 cm is plotted vs. time (right).

the end of conduction. The fluid version of the code is probably inadequate to simulate the opening phase, when it is believed particle effects (magnetically insulated electrons and enhanced erosion) dominate the physics. However, a fluid code could be sufficient to model the conduction phase and provide the input to a particle code to model the opening phase.

Interferometry was used to test the scaling of the POS conduction current (and time) with simplified predictions from theory. At least four conduction limits have been proposed: bipolar [10], modified bipolar,[11] electro-magnetohydrodynamics (EMH),[12] and magnetohydrodynamics (MHD)[13,14]. For the long conduction times considered here, only the EMH and MHD cases are expected to apply. A simple EMH limit can be derived assuming ion motion is negligible and that radial current is conducted by electrons executing **E×B** drifts. It can then be shown[15] that the azimuthal magnetic field penetrates through the plasma with an axial velocity, u, given by:

$$u = \frac{I}{2\pi enr}\left[\frac{1}{n}\frac{dn}{dr} + \frac{2}{r}\right], \tag{1}$$

where e is the electron charge, r is the radius where opening occurs and n is the density. For Hawk, penetration ($u > 0$) could occur in the region where $dn/dr \sim 0$ ($r = 0.7$ cm in Fig. 4). Opening is assumed to begin when the field penetrates the length of the plasma, $\int u\,dt = l$, resulting in the conduction limit:

$$\int I_{EMH}\,dt = \pi e r^2 l n\ . \tag{2}$$

For a linearly rising current, $I(t) \propto t$, the conduction current $I_{EMH} \propto n^{1/2}$.

The MHD limit occurs when ion motion is not negligible and the plasma is displaced or distorted by **J×B** forces. Based on empirical evidence[16,17] and the simulation results presented earlier, conduction is assumed to end when the plasma center-of-mass is displaced to the load end of the POS. This results in an MHD conduction limit:

$$\iint I_{MHD}^2\,dt^2 = \frac{100\pi^2 r^2 l^2 M_i}{Z} n, \tag{3}$$

where M_i and Z are the ion mass and charge state, respectively, and cgs units are used except for I(Amps). For a linearly rising current, $I_{MHD} \propto n^{1/4}$.

These simplified scaling laws are in general agreement with Hawk experiments. Fig. 6 shows data and scaling predictions from Eqs. 2 and 3. The horizontal axis is the peak density measured during conduction, about 1.5 cm from the center conductor. In both graphs in Fig. 6, a standard case is shown, where r = 5 cm, the Marx capacitors are charged to 80 kV, and the plasma length is 8 cm. The data (circles) match the MHD limit, both in the density scaling and magnitude. For currents less than 450 kA, the EMH limit should be reached before the MHD limit. The trend in the data suggests this may occur in the Hawk experiments. The graph on the left in Fig. 6 shows the effect of changing dI/dt by lowering the Marx voltage to 50 kV. The

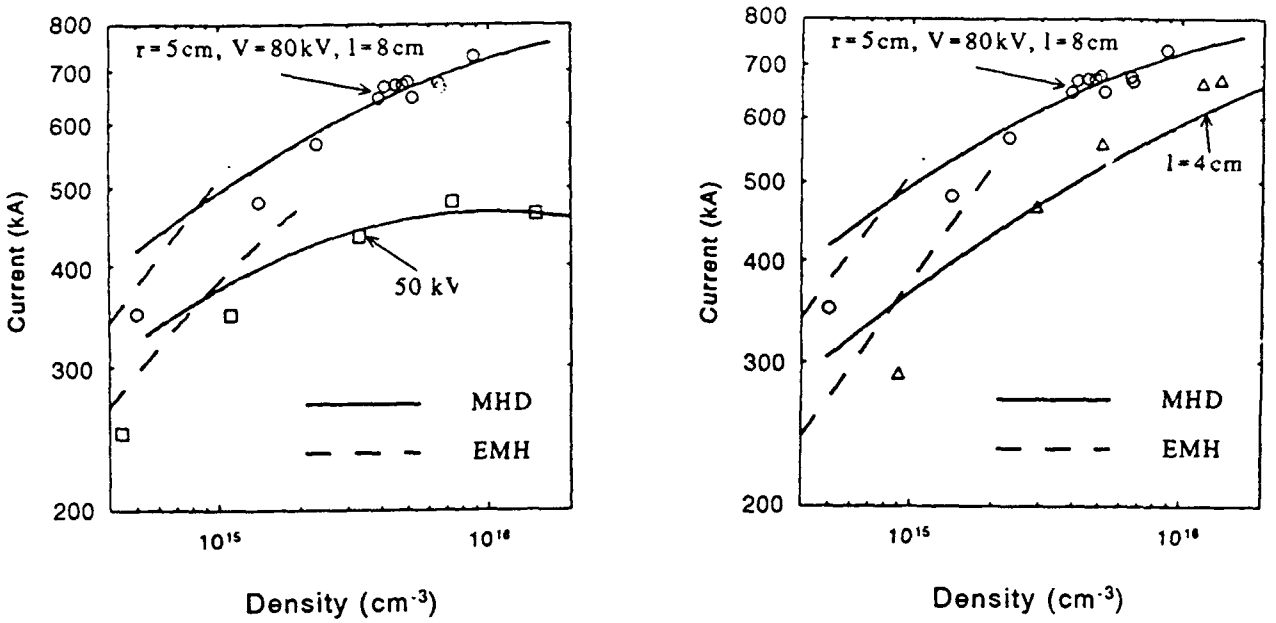

Fig. 6. Hawk conduction current scaling and comparisons with MHD and EMH scaling laws.

graph on the right in Fig. 6 shows the effect of decreasing the length to 4 cm. For both changes, the data match the MHD/EMH prediction. Similar agreement occurs for radii of 2.5, 5, and 12 cm.[8]

A striking difference between the MHD and EMH regimes is shown in Fig. 7. In the top graph in Fig. 7, load currents are shown for different plasma densities. The conduction current varies from 200 kA (#1) to 700 kA (#6). The bottom graph in Fig. 7 shows the density measured 9 cm from the load edge of the plasma aperture using a chordal line-of-sight (z = 13 cm in Fig. 1). A large plasma density, comparable to the density in the POS region, appears at this location *after* opening for cases 3-6, that is, for currents greater than 450 kA. For currents less than 450 kA, the measured densities at this location are negligible (much less than the density in the POS region during conduction). This phenomenon is consistent with the difference between the MHD and EMH limits. In the EMH case, switching occurs before the plasma is translated. Evidently, plasma motion in the axial direction is negligible compared with radial motion. In the MHD case, the plasma center-of-mass is translated a fixed distance during conduction. The measured downstream density begins later for longer conduction times.

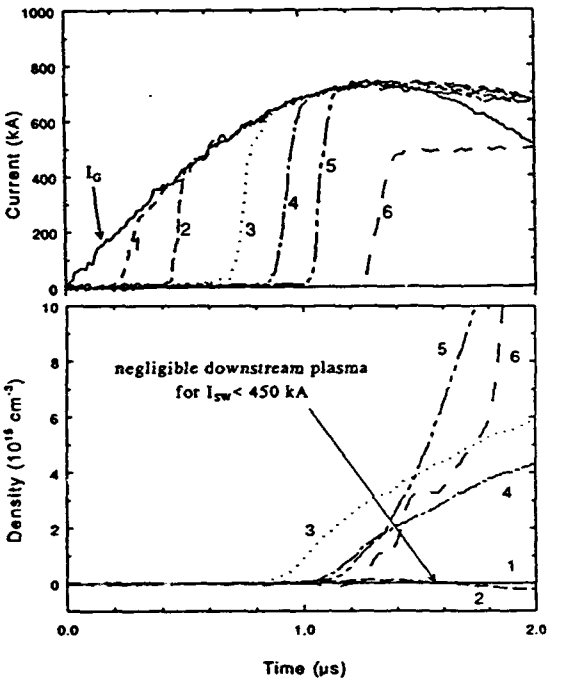

Fig. 7. Density measured using a chordal line-of-sight 9 cm from the edge of the POS (bottom) and corresponding load currents (top).

III. Physics of opening based on electrical measurements with diode loads

Experiments have been performed on Hawk using various POS configurations and electron-beam diode loads.[18,4] Results from experiments using an r = 5 cm center conductor are summarized in Fig. 8, which is a plot of peak switch voltage (essentially the same as the load voltage) as a function of the load impedance at the time of peak load power. Different symbols in this plot correspond to different conduction current ranges. The two dashed lines define "load-limited" and "switch-limited" regimes. In the load-limited regime, the load impedance determines the voltage. In the switch-limited regime, the voltage is independent of the impedance, for a given conduction current. In this case, the voltage is limited by the switch to about 900 kV, and the load current is less than the generator current (current is lost in the switch region or between the switch and load). Maximum load power occurs at the intersection of these two lines, about 0.4 TW in this case.

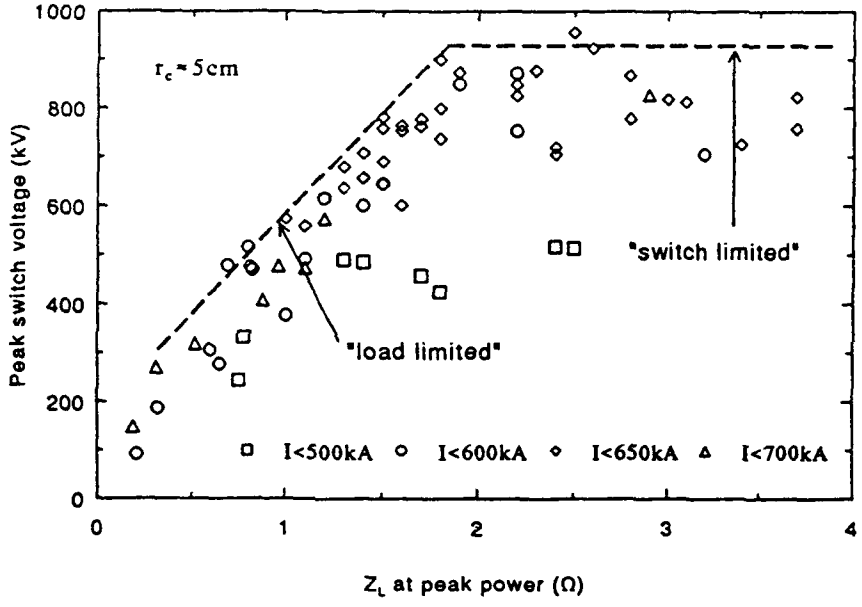

Fig. 8. Peak voltage vs. load impedance for Hawk shots using an r = 5 cm center conductor. Symbols correspond to different ranges of conduction current.

The data in Fig. 8 suggest a simple picture of the opened POS, illustrated in Fig. 9. At peak power, a vacuum gap is assumed to have formed in the POS plasma. Electron orbits are illustrated in Fig. 9 for the load-limited and switch-limited cases (see, for example, [19]). The electron flow extends a distance D from the cathode side of the POS gap. Within a numerical factor, D can be calculated from a critical current formula:

$$D = 1.6 \times 8500 \beta\gamma \frac{I}{I}, \tag{4}$$

where the factor 1.6 is a correction factor from PIC simulations, β and γ are the standard relativistic factors and I is the generator current (in Amps) at the time of peak power. The load-limited case corresponds to low load impedance, so that the electron flow extent D is less than (or equal to) the vacuum gap. The switch-limited case corresponds to high load impedance where the electron flow extends across the plasma, and current is lost across the POS. In this case, the calculated value of D using Eq. 4 will be approximately equal to the physical gap in the plasma, assuming the electron flow is in equilibrium.

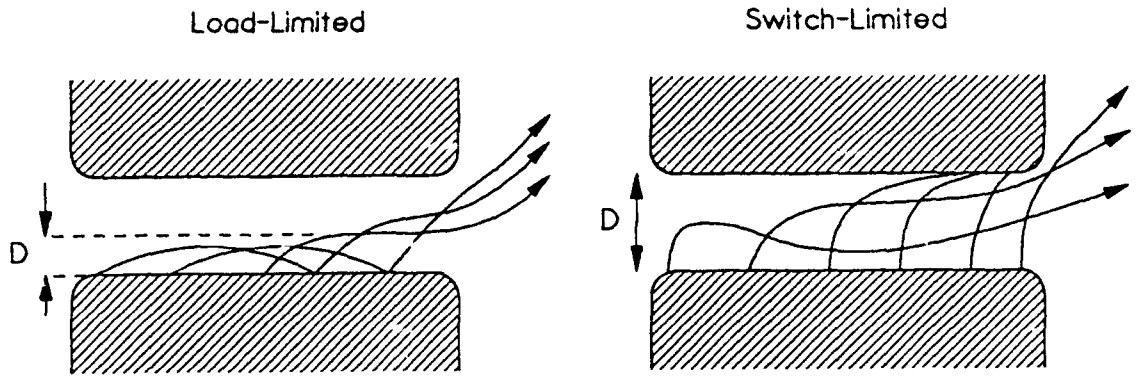

Fig. 9. Electron flow patterns across a vacuum gap in a POS for "load-limited" and "switch-limited" cases.

The calculated values of D are shown in Fig. 10 for the same shots corresponding to the data in Fig. 8. In the switch-limited regime, the calculated gap, D, is in the 2.5-3 mm range, independent of load impedance and conduction current. (For comparison, the radial distance between the POS conductors is 20 mm.) In the load-limited regime, D is independent of conduction current and an increasing function of load impedance. It is not clear whether the gap in this case is larger than D, as illustrated in Fig. 9, or if the gap generated in the plasma stops growing when the electron flow is insulated. In either case, the simple picture of a 2.5-3 mm gap forming in the plasma explains all the data in Fig. 8.

The limited gap size results in a limited load power, and determines the "matched load" impedance to maximize the load power (1.5-2 Ω in Fig. 8). If the gap size or magnetic field could be increased, the matched load impedance would be higher resulting in higher load voltage and power. Empirically, reducing the center conductor radius on Hawk results in higher voltage and a fixed gap size. Experiments[4] using an r = 2.5 cm center conductor are limited to a voltage of 1.5 MV, and the calculated gap is ≤ 3 mm. Further reduction of the center conductor radius to 1.3 cm results in the highest voltage to date on Hawk, about 2 MV, and a similar calculated switch gap. An example of data from a Hawk shot with an r = 1.3 cm center conductor is shown in Fig. 11. The conduction current is

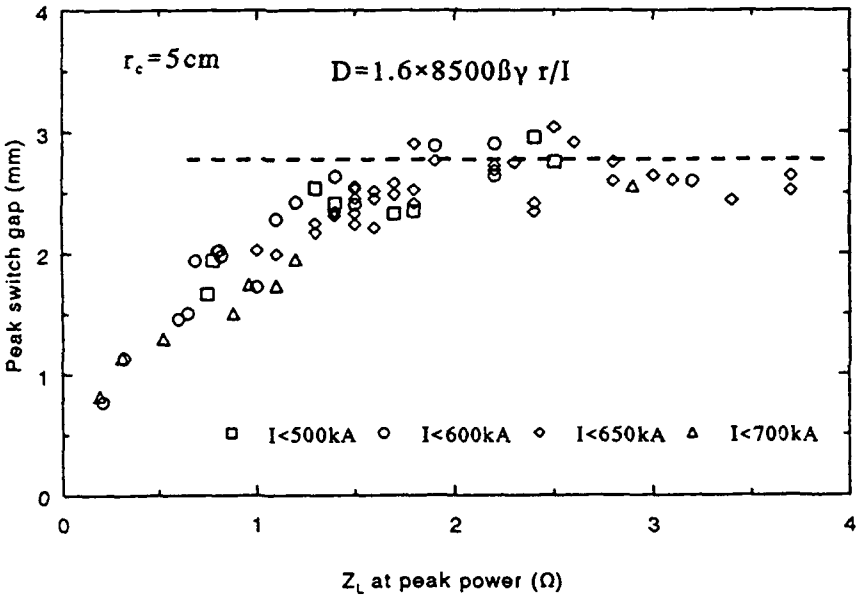

Fig. 10. Gap size, D, for the data in Fig. 8., as a function of load impedance. The gap is limited to ≤ 3 mm.

limited to lower values in this case (500 kA with r = 1.3 cm compared with 700 kA with r = 5 cm) because of the MHD scaling (Eq 3) and the limited plasma density available from the flashboards. The maximum load power obtained on Hawk, 0.7 TW, used a tapered center conductor (r = 5 cm at the generator end of the switch region to r = 1.3 cm at the load end) in an attempt to extend the conduction phase and increase the magnetic field in the region where opening occurs.[4]

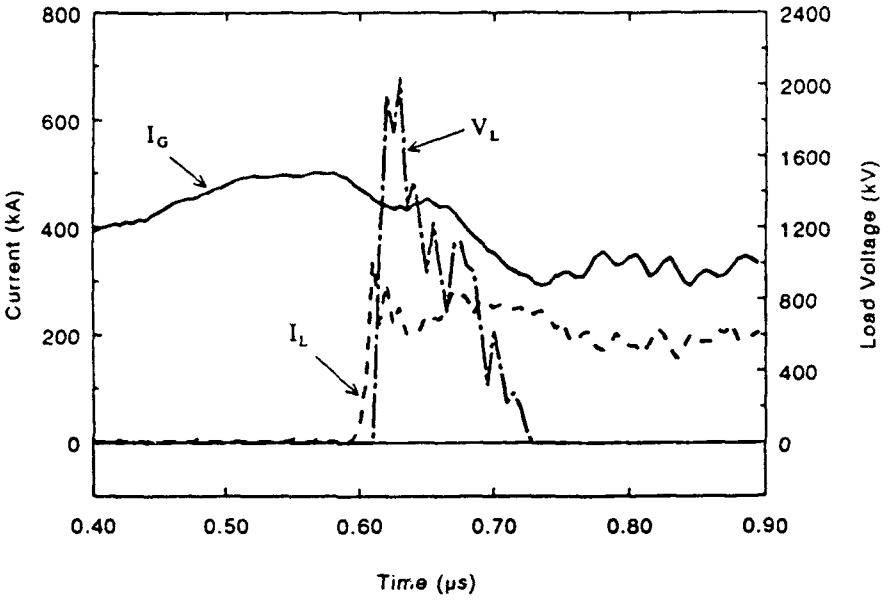

Fig. 11. Highest load voltage (2 MV) obtained on Hawk using an r = 1.3 cm center conductor.

One possible explanation of the limited gap has been deduced from PIC code simulations[20] of a low density (< 10^{13} cm^{-3}) shorter time scale (< 100 ns) POS. As mentioned before, these simulations may be applicable to the μs POS after the density has been reduced during the conduction phase. The PIC simulations show a region of net positive charge (potential hill) resulting from electron depletion. This potential hill migrates axially through the rarefied plasma, leaving behind a vacuum gap where electrons are magnetically insulated. When the ion-rich region reaches the load end of the plasma, the ions erode and the preformed gap exists along the extent of the plasma, independent of the load impedance. In simulations, the size of the gap increases by increasing the magnetic field and by decreasing the density. These results could be applied to Hawk using a density distribution determined by a fluid code. In the future, a combined fluid/particle treatment could provide a reliable modeling tool for the μs POS.

IV. Summary and conclusions

POS experiments on Hawk are leading to improved understanding of μs-conduction-time POS physics. Density measurements during Hawk shots have been the most revealing new technique. These measurements show that the density decreases during conduction, that opening occurs in the middle of the electrode gap instead of near the cathode or anode electrodes, and that the conduction current scaling can be understood from simple limits: MHD for high currents, where opening begins when the axial plasma displacement is about half the switch length, and EMH for low currents, where axial field penetration occurs before plasma displacement is significant. Experiments with diode loads indicate that the POS operates as if a ~ 3-mm vacuum

gap forms in the plasma, independent of conduction current, load impedance, and center conductor radius. Consistent with this limited gap, higher voltage is obtained when the center conductor radius is reduced. Optimizing the POS parameters to maximize the output power is a tradeoff between higher voltage generated using a small radius center conductor, and the corresponding reduction of conduction current because of the MHD limit. Fluid and particle codes may be able to simulate the conduction and opening phases, respectively, and to indicate promising methods to increase the output power, making this technique even more attractive for pulsed power applications.

It is a pleasure to acknowledge Rick Fisher for his expert technical assistance on Hawk experiments. We also benefited from many discussions of POS physics with J. Thompson and E. Waisman of Maxwell Labs and J. Goyer of Physics International Co.

References

1. G.A. Mesyats and B.M. Koval'chuk, Sov. Phys. -- Dokl. 30, 879 (1987).
2. G. Cooperstein and P.F. Ottinger, Guest Editorial, IEEE Trans. Plasma Sci. PS-15, 629 (1987).
3. P. Sincerny, D. Drury, J. Goyer, G. James, M. Krishnan, J. Levine, C. McDonald, I. Roth, in Proc. Seventh IEEE Pulsed Power Conf., B.H. Bernstein and J.P. Shannon, eds., Monterey, CA (IEEE, New York, 1989), IEEE Cat. No. 89CH2678, p. 275.
4. P.J. Goodrich, J.R. Boller, R.J. Commisso, D.D. Hinshelwood, J.C. Kellogg, B.V. Weber, these proceedings.
5. David Hinshelwood, Bruce Weber, J.M. Grossmann and R.J. Commisso, to be published in Phys. Rev. Lett., June 1992.
6. R.J. Commisso, P.J. Goodrich, J.M. Grossmann, D.D. Hinshelwood, P.F. Ottinger and B.V. Weber, to be published in Phys. Fluids B, July 1992.
7. B.V. Weber and D.D. Hinshelwood, to be published in Rev. Sci. Instrum., Oct., 1992.
8. D.D. Hinshelwood, R.J. Commisso, P.J. Goodrich, J.M. Grossmann, J.C. Kellogg and B.V. Weber, these proceedings.
9. R.J. Mason, M.E. Jones, J.M. Grossmann, and P.F. Ottinger, Phys. Rev. Lett. 61, 1835 (1988).
10. P.F. Ottinger, Shyke A. Goldstein and R.A. Meger, J. Appl. Phys. 56, 774 (1984).
11. J.R. Goyer, IEEE Trans. Plasma Sci. 19, 920 (1991).
12. K.V. Chukbar and V.V. Yan'kov, Sov. Phys. Tech. Phys. 33, 1293 (1988).
13. B.V. Weber, R.J. Commisso, G. Cooperstein, P.J. Goodrich, J.M. Grossmann, D.D. Hinshelwood, J.C. Kellogg, D. Mosher, J.M. Neri, and P.F. Ottinger, in Proc. Eighth Int'l. Conf. on High-Power Particle Beams Vol. 1, B.N. Breizman and B.A. Knyazev, eds., Novosibirsk, USSR (World Scientific, New York, 1991), p. 406.
14. W. Rix, D. Parks, J. Shannon, J. Thompson, and E. Waisman, IEEE Trans. Plasma Sci. 19, 400 (1991).
15. A. Fruchtman, Phys. Fluids B 3, 1908 (1991).
16. D.D. Hinshelwood, R.J. Commisso, P.J. Goodrich, J.M. Grossmann, J.C. Kellogg, P.F. Ottinger and B.V. Weber,in Proc. Eighth Int'l. Conf. on High-Power Particle Beams Vol. 1, B.N. Breizman and B.A. Knyazev, eds., Novosibirsk, USSR (World Scientific, New York, 1991), p. 1034.
17. B.V. Weber, R.J. Commisso, P.J. Goodrich, J.M. Grossmann, D.D. Hinshelwood, J.C. Kellogg and P.F. Ottinger, IEEE Trans. Plasma Sci. 19, 757 (1991).
18. P.J. Goodrich, J.R. Boller, R.J. Commisso, D.D. Hinshelwood, J.C. Kellogg, B.V. Weber, in Proc. Eighth IEEE Pulsed Power Conf., R White and K. Prestwich, eds., San Diego, CA (IEEE, New York, 1991), IEEE Cat. No. 91CH3052-8 p. 515.
19. C.-K. Ng and R.N. Sudan, J. Appl. Phys. 69, 137 (1991).
20. J.M. Grossmann, P.F. Ottinger, and R.J. Mason, J. Appl. Phys. 66, 2307 (1989).

INDUCTIVE ENERGY STORE (IES) TECHNOLOGY FOR MULTI-TERRAWATT GENERATORS

P.S. Sincerny, S.R. Ashby, F.K. Childers,
C. Deeney, D. Kortbawi, J.R. Goyer,
J.C. Riordan, I.S. Roth, C. Stallings

L. Schlitt

Physics International Company
2700 Merced Street
San Leandro, CA 94577

Leland Schlitt Consulting
2725 Briarwood Drive
Livermore, CA 94550

Abstract

An IES pulsed power machine has been built at Physics International Company that serves as a prototype demonstration of IES technology that is scaleable to very large TW generators. The prototype module utilizes inductive store opening switch technology for the final stage of pulse compression and is capable of driving both electron beam Bremsstrahlung loads or imploding plasma loads. Each module consists of a fast discharge Marx driving a water dielectric transfer capacitor which is command triggered to drive the inductive store section of the machine. The inductive store is discharged into the load using a plasma erosion opening switch. Data demonstrating 22% efficient operation into an electron beam diode load will be presented. The system issues addressing the combining of these modules into a very large pulsed power machine will be discussed.

Introduction

Pulsed high power machines have historically been built using Marx driven capacitive store closing switch pulse compression as the method of achieving high power. The machine discussed in this paper is unique in that it utilizes an inductive energy store (IES) switched with an opening switch (OS) as the final stage of pulse compression. The reason for developing this new IES/OS pulse compression technology is that it is more compact (higher energy density) than the capacitive store pulse compression technology. The higher energy density of the IES/OS system results in lower cost and technology that scales favorably up to higher powers.

The pulsed power machine that has been designed, built, and tested called Prototype Module 1 (PM1) is shown in Figure 1. Figure 1a shows the machine prior to final assembly, while Figure 1b shows the front-end after assembly. This module has been designed and built to be a building block of a much larger pulsed power machine by simply replicating the hardware. System requirements that facilitate combination of multiple modules into a larger facility have been incorporated into the design of PM1. These system requirements include: low (± 10 ns) command fire jitter, converging geometry for maximum diode parking efficiency, and reliable low stress component operation. This module has now been operational for 15 months and has demonstrated all single module and system performance goals.

A side view sketch of PM1 is shown in Figure 2. The principle components of this module are the Marx, a water transfer capacitor, diverters, triggered gas switches, tube, pulse forming line (PFL) MITL, plasma erosion opening switch (PEOS), and an electron beam Bremsstrahlung diode. The pulse compression time line for this machine is shown in Figure 3. The first event in the triggering of the Marx generator. The Marx charges the transfer capacitor in 1.5 μsec. Once the transfer capacitor is fully charged the transfer switches are command triggered with low ± 2 ns jitter. The command triggering of these switches provides the timing control that is required to combine several of these modules into a single large pulsed power system. Once the TC output switches are triggered the inductive energy store (current charged pulse forming line) is charged in 500 ns. The final event is the opening of the PEOS which discharges the inductive store into the electron beam Bremsstrahlung load with a 70 ns power pulsewidth.

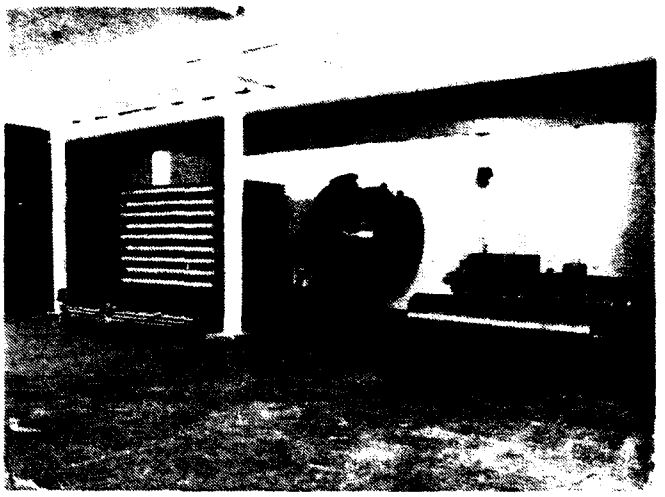

1 (a). Prototype module 1 (PM1) prior to final assembly.

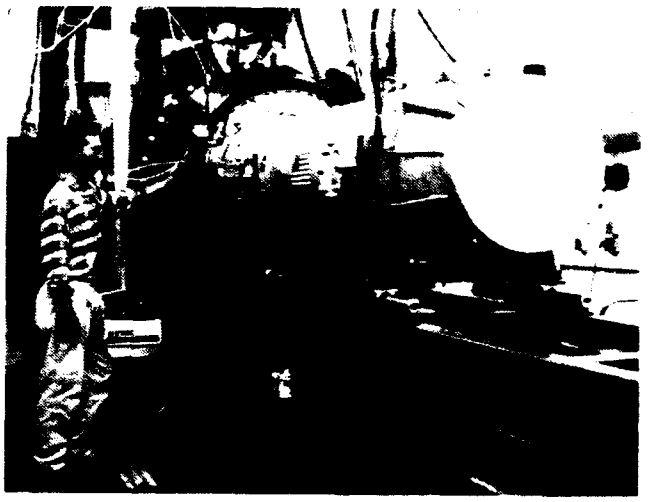

1 (b). Front end of PM1 after assembly.

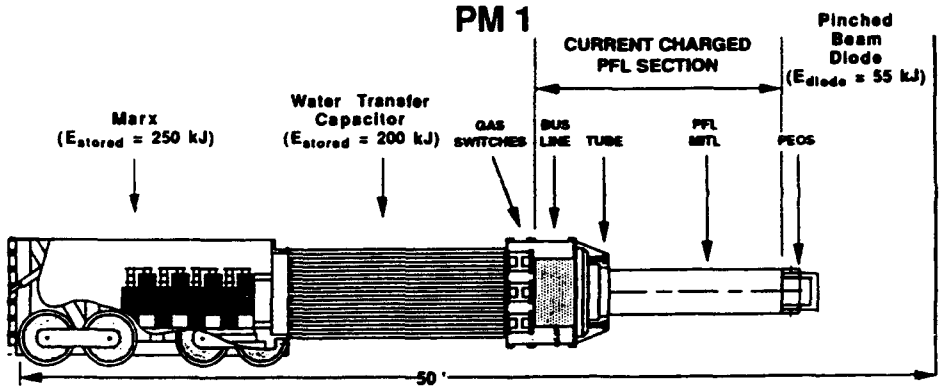

Figure 2. Side view sketch of PM1.

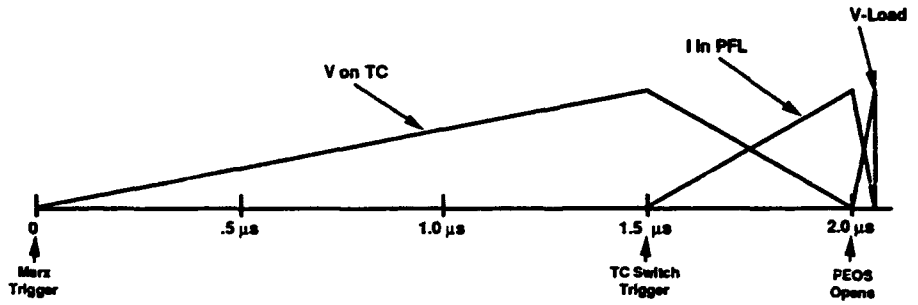

Figure 3. Pulse compression timeline. The combined transfer capacitor closing switch and IES/opening switch power amplification stages provide three stages of pulse compression which meet the source input electrical requirements.

Description of PM1

Marx: The Marx is constructed from four submarxes in parallel. The total erected capacitance is 1.1 μF and when charged to ± 84 kV the erected voltage is 670 kV for total stored energy of 250 kJ. Each of the four submarxes contains four ± 84 kV stages. The capacitors are 2.2 μF, 100 kV, 30 nH in a standard 11" x 14" x 24" casing. These capacitors have been routinely used for years in large pulsed power machines. Figure 4 shows one of the individual submarxes. The current in each submarx is measured with a current viewing resistor.

Transfer Capacitor: The transfer capacitor (TC) is shown in Figure 5. The transfer capacitor consists of 68 individual coaxial water capacitors. The transfer capacitor capacitance is 0.77 μF and when charged to 720 kV stores 200 kJ. The TC voltage is measured at the output end with a capacitive divider voltage monitor

Figure 4. One of four PM1 submarxes.

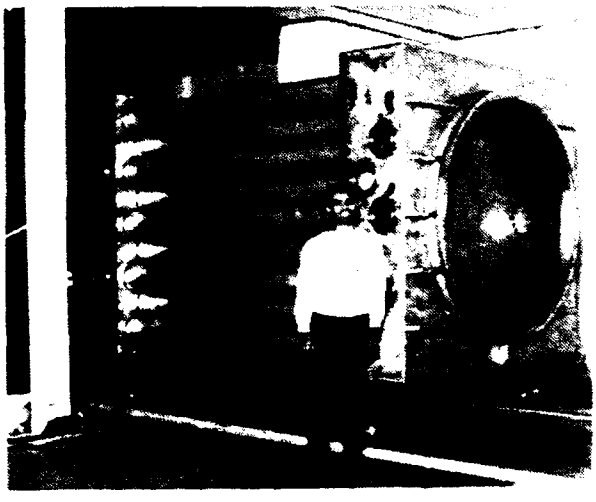

Figure 5. The transfer capacitor assembly prior to final connection to the output line.

Diverters: There are five wire resistor diverters at the Marx end of the TC. These diverters are used to reduce the voltage reversal on the TC and to remove the waste energy from the system. The diverters timing is controlled by adjusting the self-breaking water gap spacing.

Tube: The vacuum interface consists of a stacked insulator and gradient ring as shown in Figure 6. This tube is identical to tubes that have been built for other super-power generators such as PITHON, Double-EAGLE, and PHOENIX. The tube has worked flawlessly on PM1 and requires cleaning only after a few hundred shots.

Pulse Forming Line MITL: The MITL is shown in Figure 7. This is a coaxial 4.5 Ω magnetically insulated vacuum line. This line stores energy from the transfer capacitor prior to the opening of the final switch. This section of MITL has worked well on all tests and a comparison of current injected at the tube to the current delivered to the PEOS has shown no losses. The current is measured with arrays of four B-dot current monitors at various locations along the MITL.

PEOS: The PEOS consists of a 25 cm diameter cathode within a 35 cm diameter rod anode structure. The plasma sources are eight - six row flashcards each driven by 0.6 μF charged to 25 kV. The plasma is injected along a 10 cm length of A-K gap. A sketch of the PEOS and diode configuration is shown in Figure 8. The current between the diode and the load is measured with an array of four B-dot monitors equally spaced azimuthally.

Diode: The pinched beam diode geometry is shown in Figure 8. The anode to cathode spacing is adjusted to obtain the optimum impedance for maximum output power and energy. The diode current is measured with the B-dot monitors just upstream and the diode voltage is measured using a radiation end-point monitor consisting of five filtered Si pin diodes.

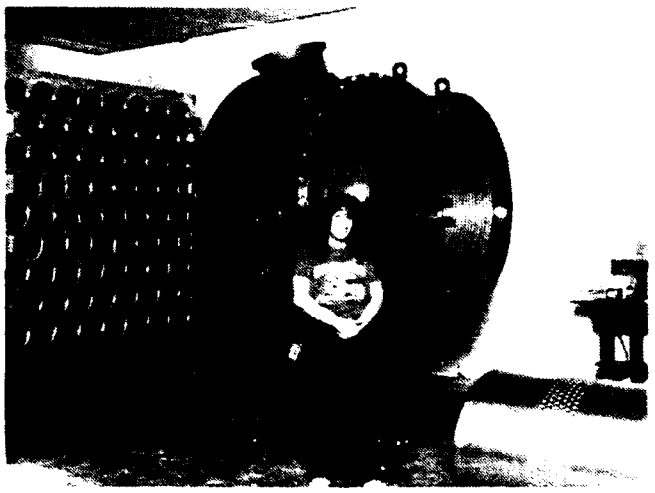

Figure 6. PM1 tube assembly prior to final installation.

Figure 7. PFL MITL sharing the cathode and anode prior to final assembly.

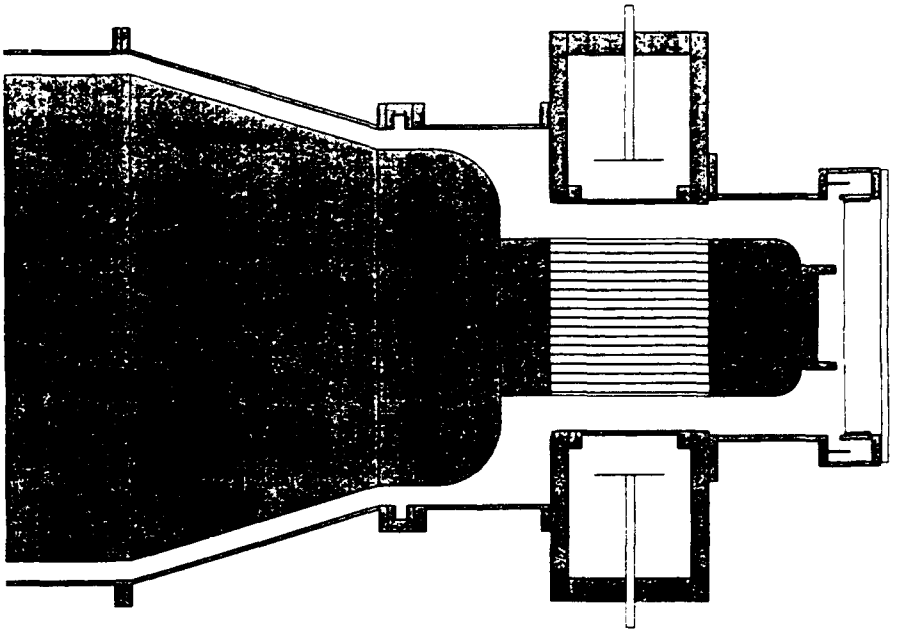

Figure 8. PEOS and pinched beam diode configuration.

Output Predictions versus Performance

An end-to-end circuit model has been developed to predict the output from the PM1. This circuit model is shown in Figure 9. Each subsystem has been carefully modeled using measured values for all individual components. The measured values were obtained by doing various pulsed power tests such as firing the TC output switches and observing the ringing frequency and amplitude between the Marx and TC. The opening switch is modeled using three measured parameters; the conductive time, the opening time, and the opened impedance. The diode is modeled as an initial impedance that collapses linearly in time once the power is delivered to the load. The initial impedance and the rate of collapse are measured quantities.

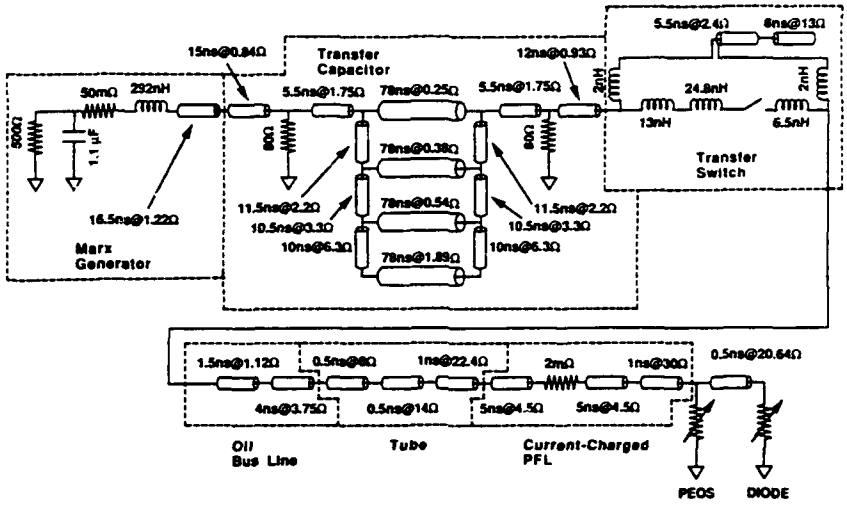

Figure 9. PM1 circuit model contains the detail required to accurately model transient electrical behavior.

Figures 10 and 11 show a comparison of the model output and measured performance. The excellent agreement is due to the fact that the circuit model parameters have been benchmarked (adjusted) to this data to obtain those results. This benchmarked circuit model is very useful for; optimizing firing time of the TC and PEOS switches for maximum load power; quantifying the effect of specific PEOS improvements, predicting the performance of larger prototype modules and minimizing the throughput timing jitter. As seen in Figure 11 the prototype module is capable of delivering up to 60 kJ of electron beam energy to the load with an end-point voltage of 1.1 MV for an overall efficiency of 22%. Table I is a summary of the electrical parameters of PM1 and the average performance achieved.

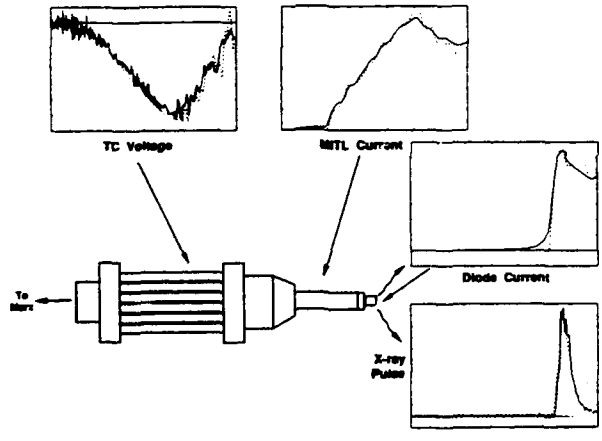

Figure 10. PM1 experimental waveforms (solid) versus modeled.

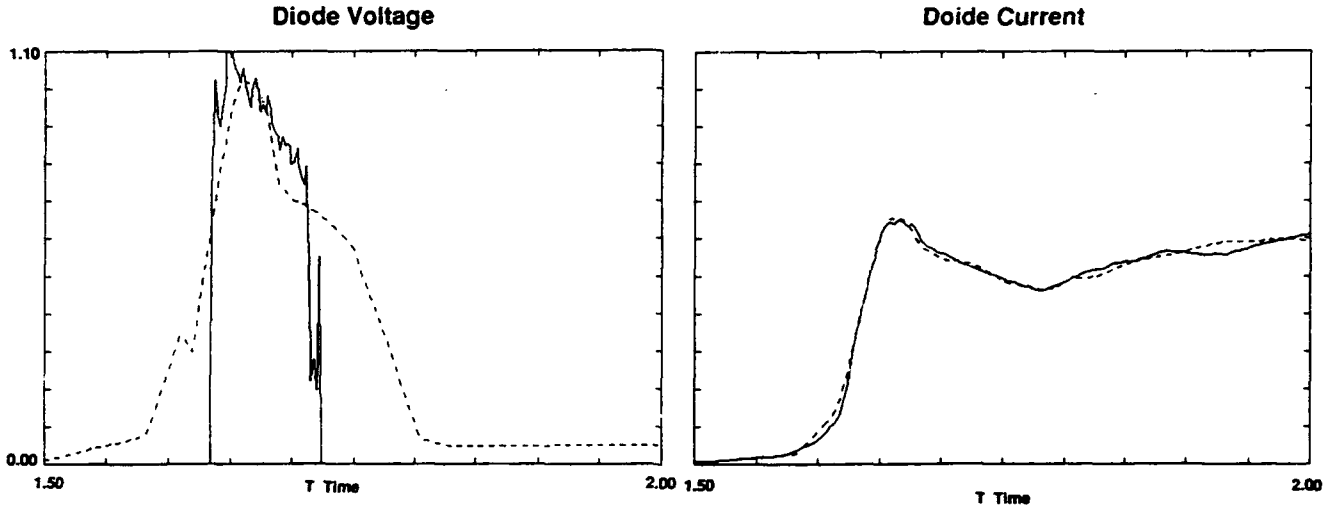

Figure 11. Experimental versus modeled waveforms continued; current, and diode voltage.

The PM1 has achieved all of the original design goals and has operated reliably and reproducible at the levels shown in Table I.

Table I. Demonstrated Performance of the Prototype Module PM1.

Electrical Parameters	PM1 Average Measured Performance
Marx Voltage, ± kV	± 84 kV
E_{Marx}, Energy Stored	250 kJ
E_{Diode}	54 ± 5 kJ
Efficiency, E_{Diode}/E_{Marx}	22%
V_{Diode}, Peak	1.2 ± 0.2 MV
I_{Diode}	0.65 ± 0.04 MA
Z_{Diode}, at Peak Power	1.9 ± 0.4 Ω
P_{Diode}	0.6 TW
τ_{Power}, (FWHM)	71 ± 5 ns
$\tau_{Radiation}$ V^2I, (FWHM)	Measured X-ray, Pulsewidth 41 ± 10 ns
Z_{PEOS},Peak Normalized to 2.2 MA	7.4 ± 20 Ω
τ_c, Conduction Time	303 ± 14 ns
τ_c, Opening Time	30 ± 10 ns
I_C, Peak Conduction Current	0.92 ± 0.03 MA
V_{PEOS}, Peak Voltage at PEOS	1.2 ± 0.2 MV
(t) Z_{PEOS}	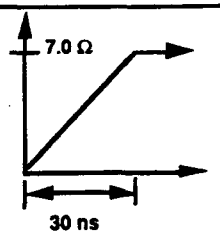

Multiple Module System Parameter Demonstration

Command Fire Control:

We have performed sequences of shots at identical control settings to obtain jitter measurements. Our procedure was to clean the flashcard plasma sources prior to each sequence and to recoat the gaps with graphite. The vacuum system was pumped out and was not vented again on two of the sequences. In these sequences, the module jitter is defined as the standard deviation of the interval measured between the command trigger of the system and the production of the x-ray pulse. We avoided using the noise-sensitive x-ray peak and defined the x-ray time as the middle of the interval of the x-ray FWHM.

Our first run of 12 data shots had a total module jitter from command trigger to x-ray pulse of 11 ns. Figure 12 overlays the twelve XRD traces. To ensure that low jitter was not peculiar to one specific operating point, we performed a second jitter run with the transfer switch trigger delayed by an additional 100 ns. For this run of nine data shots, the total module jitter was 9 ns. We observed that the mean time of the x-ray pulse was delayed 81 ns. The x-ray timing shift is not the full 100 ns delay in the transfer switch because of correlations among various other switching times.

We further performed a short run of six shots to determine if the initial shot after pump down differed significantly in timing from subsequent shots and might skew our data. The system was vented and pumped down before the first, fourth and sixth shots in the series. On this run, the jitter was only 7 ns. No trend was observed in the data that indicated special performance of the first shot after pump-down.

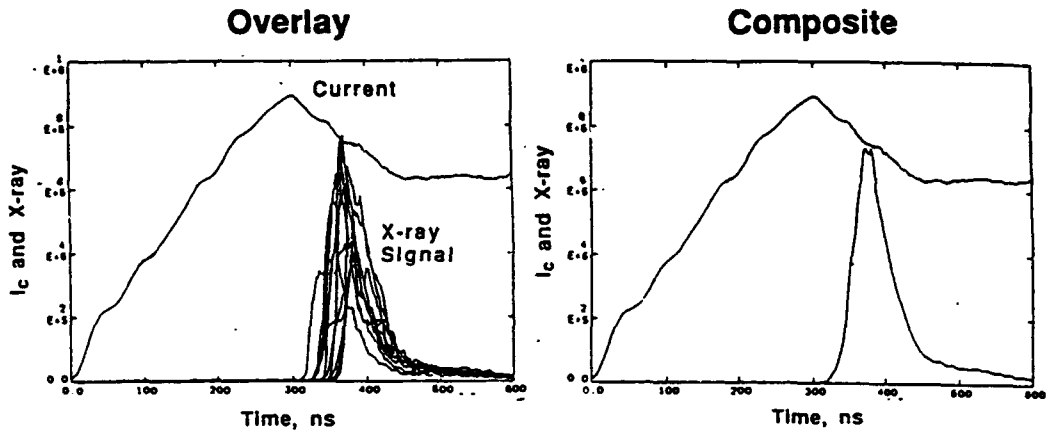

Figure 12. A sequence of 12 PM1 shots had a total module jitter (1σ) of 11 ns.

The jitter we have measured arises from the three major switching subsystems: transfer switches, Marx switches, and PEOS. The transfer switch timing determines the initiation of current in the pulse forming line (PFL). The timing difference between the Marx and transfer switches determines the rate of rise of PFL current. Our circuit model shows jitter propagation in good agreement with PM1 measurements made with the PEOS replaced by a hard short.

We have not been successful in using the circuit model to propagate the jitter through the PEOS because the rising PEOS impedance is not well enough understood for this analysis. We observe experimentally that the PEOS begins to open soon after PFL current initiation, which reduces the rate of PFL current rise and makes it impossible to separate the PEOS jitter form the other jitter sources.

Despite this difficulty, we were able to measure individual component jitters which are indicated in rectangular boxes in Figure 13. Times in circles represent cumulative jitter from the command trigger to that point in the circuit.

This data shows the ability to adjust the command fire timing of one module and attain low, ± 10 ns, throughput jitter. Therefore this module can be replicated and synchronized with other modules to produce a very high power generator system.

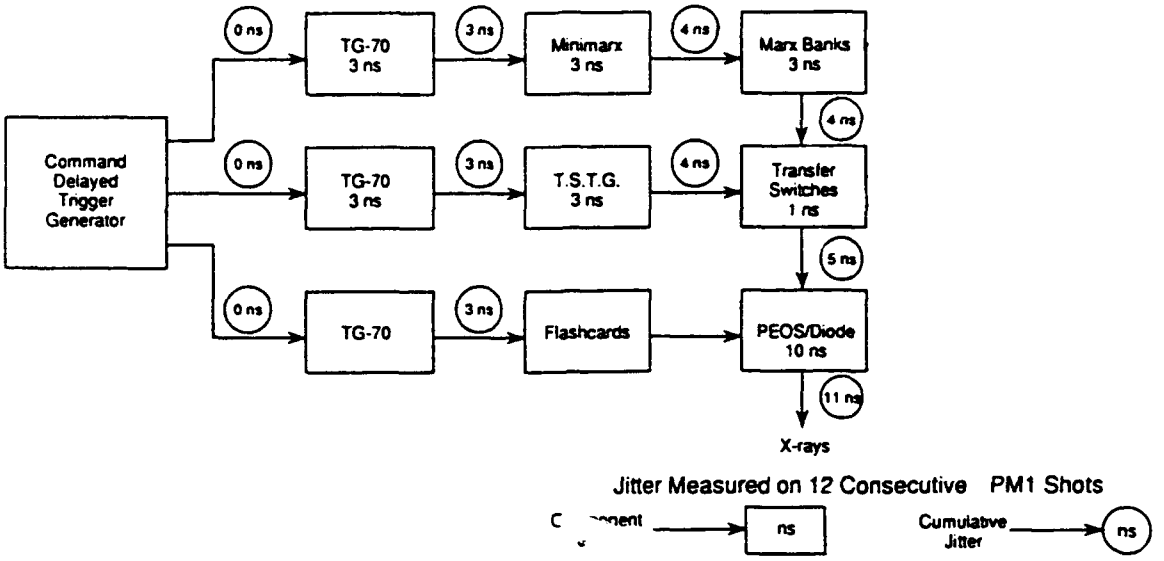

Figure 13. We have measured the switch jitter for all PM1 components.

System Reliability

System reliability has been an integral part of the design of PM1. As a consequence, many features have been incorporated into the design that assure system reliability requirements will be met. Conservative design practices have been used, maximizing design margins throughout the system. The PM1 prototype module has provided a 1300 shot data base for both component and module reliability.

The design has been engineered to be fault-tolerant. For example, the system modularity limits the energy that can be released locally by an electric arc. Also diverter switches have been incorporated in the design to limit voltage reversals on the transfer and Marx capacitors. In the event of any anomaly, system status and fault detection monitors will automatically block all trigger system command fire signals and crowbar all high-voltage components.

Marx Generator. The capacitors in the Marx are rated at 100 kV, but operate at 84 kV with a 32% voltage reversal; predicted lifetime under these conditions is over 13,000 shots (versus 10,000 shots for operation at full rating). In addition, the probability of a Marx prefire is maintained at an extremely low value. This is accomplished primarily by operation of the switch with an SF_6 gas pressure sufficiently high so that the charging voltage is approximately half (or less) of the self-break voltage for the switch; this is the practice on large simulators such as AURORA, SATURN and PBFA-II.

Transfer Capacitors. The transfer capacitor has several features that enhance reliability. Tests on PM1 show that failure-to-fire for two of the six transfer (output) switches will not adversely affect the module output. Other conservation features are that the oil/water diaphragms operate at 60% of their design limit and the diverter switches have demonstrated energy dissipation at twice their design level without damage.

Vacuum Tube. The tube insulators are coated with Limitrak^{TM} and operate at 44% of the JCM breakdown criterion. the tube on PM1 has been cleaned only when maintenance was required for the transfer switches (twice for > 1000 shots), and has shown no signs of electrical tracking.

Magnetically Insulated Transmission Lines - MITLs. The design criterion used for the inductive energy store MITL is to maintain the operating impedance at less than 1/3 of the characteristic impedance of the line; this is a conservative approach that ensures that there is no significant loss of energy in the MITL.

Auxiliary Systems. The auxiliary systems also incorporate features that aid in maintaining system reliability.

The oil system includes continuous circulation and filtering of the oil, thereby assuring that carbon particles from any electrical discharges and any other foreign materials are removed.

The water system contains a circulation and deaeration system that will dissolve any air bubbles that form.

The vacuum system utilizes cryopumps that are fast and clean, both features that have enhanced the performance of PM1.

Summary

A novel pulse power machine has been built and tested which uses inductive energy store (IES)/opening switch technology as the final pulse compression stage. The PM1 has routinely delivered up to 60 kJ into an electron beam Bremsstrahlung diode for an overall efficiency of 22%. This new machine has also demonstrated low timing jitter and very reliable operation, which along with the compactness of the IES technology facilitates scaling to much higher output power by simply replicating modules.

HIGH CURRENT PULSED POWER GENERATOR GIT-16. STATE OF PROJECT. EXPERIMENTAL RESULTS.

S.P.Bugaev, A.M.Volkov, A.A.Kim, V.N.Kiselev, B.M.Koval'chuk, N.F.Kovsharov*, V.A.Kokshenev, G.A.Mesyats**, A.P.Huseev*

High Current Electronics Institute, Tomsk 634055, Russia

*High Power Electronics SCB, Tomsk 634055, Russia

**Electrophysics Institute, Ekaterinburg 620219, Russia

Abstract

The concept of pulsed high power generator based on the direct charging of the inductive storage from Marx capacitance and the application of the microsecond plasma opening switch (MPOS) as a key element delivering the energy to the load is being studied at High Current Electronics Institute in Tomsk since 1984. The research way includes the experiments on GAMMA, MARINA and GIT-4 generators. Two months ago the next step on this way was made by putting the half of the GIT-16 (called GIT-8) into operation. The whole concept of GIT-16 as well as the last experimental results will be reported in this paper.

Introduction

There are two major goals in our MPOS research - the output power and voltage multiplication. Both of them depend on the switch performance but our experience show that there may be additional limiting factors. First we discuss some general considerations keeping in mind the scaling relations obtained previously. Than the two POS stage concept will be briefly described being useful for powerful MPOS generators. At the end the GIT-16 (GIT-8) design will be given as well as the first experimental results obtained on this machine.

Output power multiplication

Let us consider the MPOS generator equivalent circuit shown in Fig.1. Here C is the Marx output capacitance, $L=L_0+L_v$ is the total discharge circuit inductance, R_s represents the MPOS resistance by opening and R_1 is the diode type load. The peak power

regime in this scheme is realized at optimum condition

$$R_l = R_s \qquad (1)$$

with the load power P_l being equal to

$$P_l \simeq 0.25\, I_s^2 R_s,$$

where I_s is the peak switch current before opening. If the output

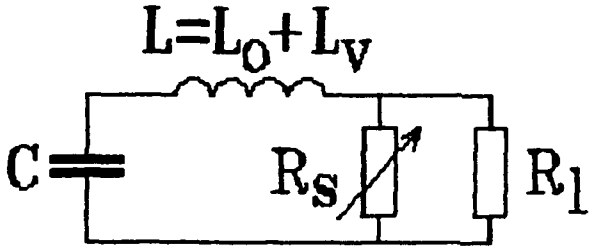

Fig.1.

Marx voltage is U_o the load power may be expressed as following

$$P_l \simeq 0.25\, \frac{U_o^2}{\rho}\, \frac{I_s R_s}{U_o} \simeq P_M\, \frac{I_s R_s}{U_o}. \qquad (2)$$

Here $\rho=(L/C)^{1/2}$, P_M - Marx peak power on the matched load $R_M \simeq 1.1\rho$. So our simple analysis shows that the peak possible power multiplication M_p due to MPOS stage inserted at the output of the Marx equals to

$$M_p = \frac{P_l}{P_M} = \frac{I_s R_s}{U_o}. \qquad (3)$$

The diode voltage in peak power regime equals to $U_l=0.5\, I_s R_s$ - a half of the maximum available one in the scheme shown in Fig.1.

Our experience shows that the MPOS resistance R_s does not depend significantly on the load resistance R_l. The value of R_s depends on many factors but the most important among them are two - the cathode radius and the discharge current. The cathode radius at given switch current must be chosen as small as possible to

obtain the peak magnetic field in the switch region for good opening. The influence of the discharge current may be explained in following way. To conduct more current one must use more switches. If each single switch keeps its resistance unchanged the total resistance of the whole switch will be decreased by a factor of current multiplication. This consideration results in a conclusion proved in experiment that the product $I_s R_s$ in Eqs.2,3 is approximately constant (and equals to (2-2.5) MV). By other words to increase the output MPOS generator power there is (at present) only one way - to increase the power of the primary storage. The last may be achieved in two ways - by increasing the Marx output voltage or by decreasing the discharge circuit impedance ρ. The multimodule concept including MARINA, GIT-4, GIT-8 and GIT-16 generators is the example of the second way.

Output voltage multiplication

The peak voltage available on the MPOS generator output appears if the load resistance is large compared to the switch one $R_l \gg R_s$. Such regime may be interesting for some special applications. As was mentioned above this peak voltage equals to $I_s R_s$ resulting in the same voltage multiplication M_V as the power one

$$M_V = M_P = \frac{I_s R_s}{U_o}. \qquad (4)$$

The GIT-4 experience shows that this peak voltage multiplication is quit difficult to obtain in experiment because of the breakdown of the vacuum insulator dividing the total secondary inductive storage into two equal parts: oil part L_o and vacuum part L_v. This insulator serves in very hard conditions because it is stressed by some hundreds kV for $\sim$ 1 μs during conduction and by some MV for $\sim$ 0.1 μs during switch opening. Moreover its surface may be exposed to strong UV radiation from the switch region during both phases. If the insulator breaks down the total inductance two times decreases preventing the further switch voltage rise and increasing the amplitude of the current flowing through

the Marx. The large current of opposite polarity may destroy the Marx condensers creating additional problems. The GIT-16 design was chosen by taken into account this difficulties. Unlike GIT-4 the GIT-16 generator has vacuum insulators at the output of each module located more than 4 m upstream from the switch region in the shade of the UV radiation. Operating in 8 module configuration (GIT-8) the vacuum insulators divide the total inductance L_1 into two approximately equal parts as well as on GIT-4 generator. In full GIT-16 version the relation L_v/L_o would equal to ~1.5 decreasing the influence of the high voltage pulse by switch opening.

Two POS stage concept

It must be noted here that due to the condition $I_s R_s \propto$ const the Eq.4 does not promise to expect the additional voltage increase on GIT-8 (GIT-16) generator compared to MARINA and GIT-4. Moreover the power increase by increasing the primary storage power leads because of the same condition to the decrease of the load resistance below ~1 Ohm in peak power regime (1) creating possible problems in application. The possible way to avoid discussed difficulties is the two POS stage concept which may be useful for powerful MPOS generators. The principal feasibility of this way is provided by ~100 times higher short conduction POS impedance rise rate by opening than that of the MPOS.

The scheme of the two POS stage generator is given in Fig.2.

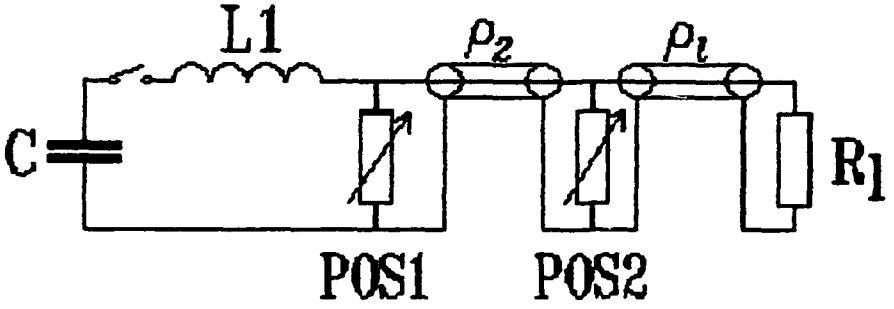

Fig.2.

The first inductive storage L_1 is shown as a lumped element because all its processes are slow compared to the EM wave transition time along its length. The switches POS1 (MPOS) and POS2 (short conduction POS) as well as the POS2 and the load R_1 are separated

double its output power. The optimized GIT-4 two POS stage design requires the load resistance to be equal to R_1=5.4 Ohm instead of R_1≈1.5 Ohm in one stage MPOS version.

Fig.3 illustrates the scheme of the last two POS stage experiment on GIT-4 with the POS2 switching current being increased up to 750 kA. The value of secondary inductive storage L_2 was equal to 130 nH, the 2.5 m long load line with cold wave impedance of 44 Ohm operated in vicinity of minimum Creedon current. Fig.4 shows

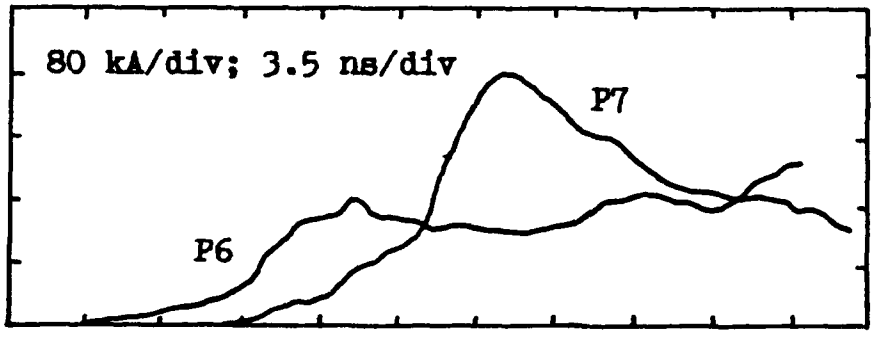

Fig.4.

that the amplitude of the propagating load current wave reaches ~160 kA in ~9 ns. This allows to estimate the hot load line wave impedance to be of ρ_1^*≈34 Ohm and the wave voltage amplitude of U≈5.6 MV. The switch resistance ~9 ns after the start of the POS2 opening rises up to R_s≈10.6 Ohm, the power in the wave propagating downstream the POS2 reaches ~0.9 TW.

GIT-16 design and first results

The GIT-16 generator is being created as a base for liner, charged particle beams as well as different kinds of radiation development and application. The basic operational principle of the machine is the direct charging of the inductive storage from Marx generators and the application of MPOS as a key element delivering the energy to the load.

The primary capacitive storage consists of 16 modules being copies of the modules developed for GIT-4 generator. Being located within a 12 meter radius the modules are connected to the central junction by 4 m long vacuum coaxial lines. The vacuum insulators are placed at the output of each module because of the reasons

discussed above. Each single unit up to the central junction has the output capacitance of 1.2 μF and the inductance of 0.65 μH. The scheme of the central junction is given in Fig.5. The main

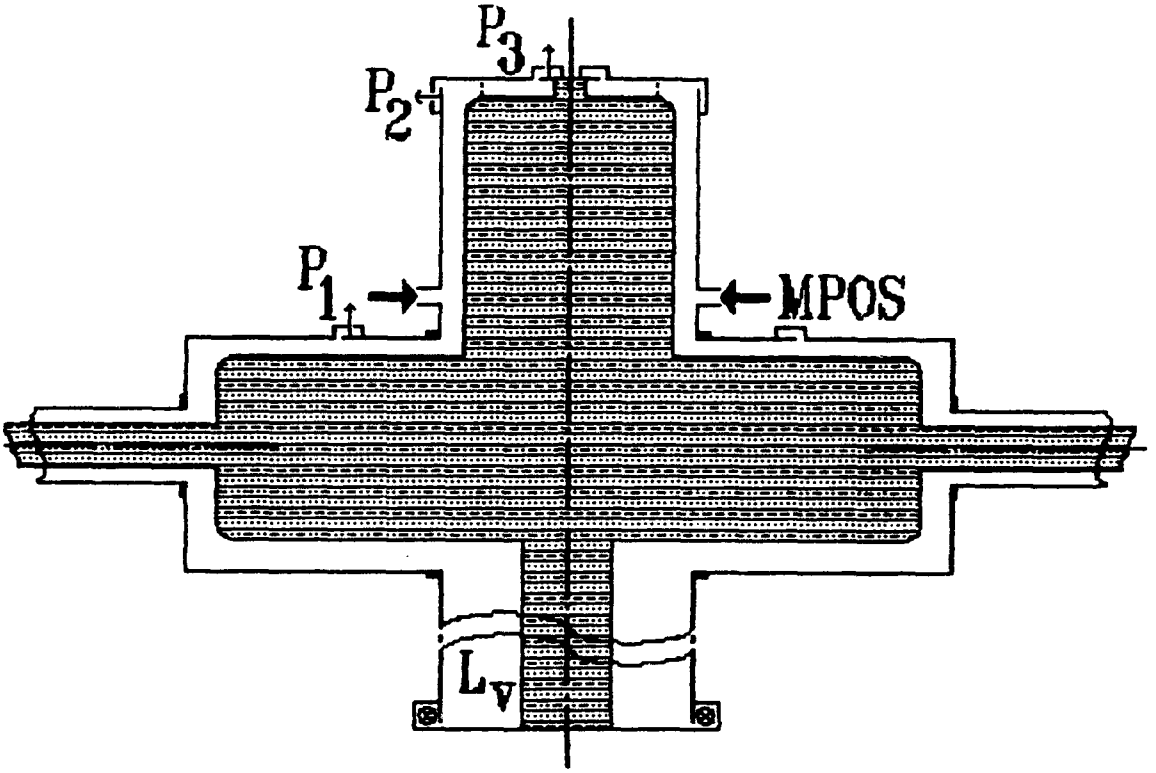

Fig.5.

collector 1580 mm diameter and 460 mm long is supported by the grounded tube operating as an inductive voltage monitor (L_V≈410 nH). At the top side of the main collector the inner MPOS electrode is mounted being 400 mm (or 300 mm) in diameter and 680 mm long. Plasma is injected radially from 505 mm diameter outer anode by 64 (32) plasma guns of capillary type developed for GIT-4 generator. The injection plane is located 285 mm from the top side of the main collector, the total inductance of the central junction up to the MPOS plane is estimated to be of 22 nH (for 400 mm diameter cathode). The current diagnostic includes Rogovsky coils at oil (M_i) and vacuum (B_i) sides of each vacuum insulator, the dB/dt-rings at the anode measuring the total switch current (P_1), the current downstream the switch (P_2) and the load current (P_3).

Two months ago the 8 module version of GIT-16 called GIT-8 was put into operation. The experiments were performed at 40 kV

by the transmission lines with impedances ρ_2 and ρ_1. In this lines the wave processes are important. The line separating the switches serves as a secondary inductive storage $L_2 = \rho_2\tau_2$.

The analysis shows that the peak power regime in two POS stage scheme requires to optimize the values of R_1, ρ_1, L_2 and τ_2. The load power would be equal to

$$P_{12} = (k_1k_2)^2 \frac{U_o^2R_2}{\rho^2} F(x) = 4 (k_1k_2)^2 P_M \frac{R_2}{\rho} F(x),$$

where $k_1(k_2) \approx 0.75$ is the relation of the expected POS1 (POS2) switching current to maximum available one, R_2 is the peak POS2 resistance by opening, $F(x) \approx (0.05-0.1)$. One may see that this power is determined by the relation of the peak POS2 impedance to the Marx discharge circuit one. The peak power of the two POS stage generator exceeds that of the one stage MPOS generator by a factor of

$$4k_1k_2^2 \frac{U_o}{I_sR_s} \frac{R_2}{\rho} F(x).$$

For example, according to GIT-4 conditions (U_o=720 kV, L_1= 200 nH, ρ = 0.2 Ohm, $I_sR_s \approx$ 2.5 MV, $R_2 \approx$ 10 Ohm, $\tau_R \approx$ 10 ns, $F(x)$ = 0.08), it is easy to estimate that the optimized second POS stage would

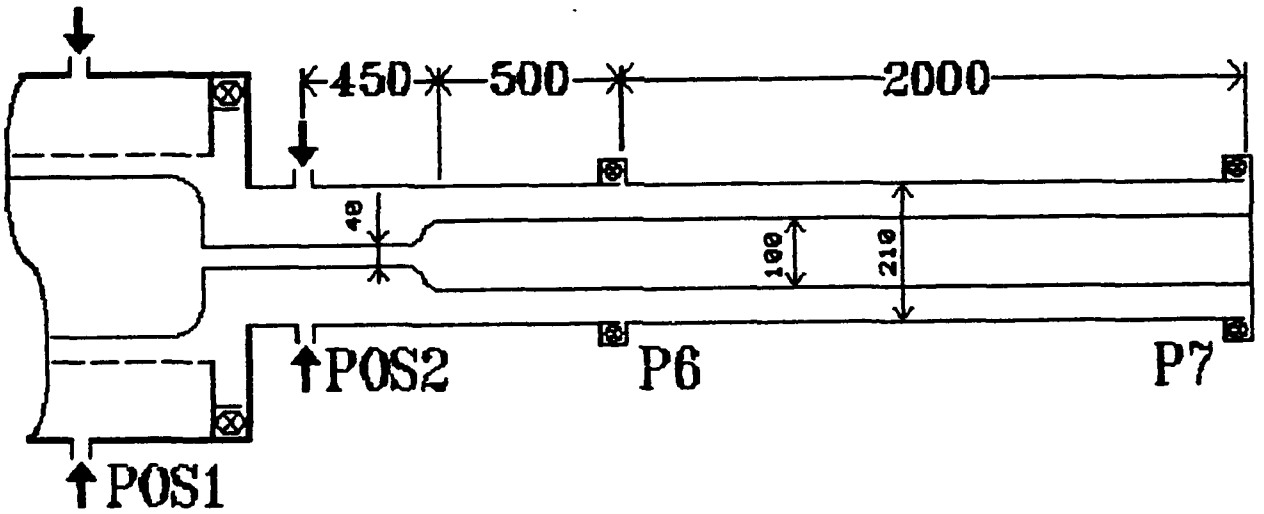

Fig.3.

Marx charging voltage resulting in 1.1 MJ stored energy. The Marx discharge circuit impedance up to the MPOS equals to ρ=0.11 Ohm with L_o=54.5 nH and L_v=63 nH. Fig.6 shows the switch upstream cur-

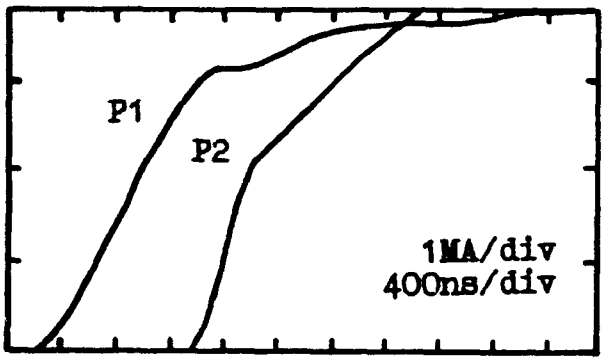

Fig.6.

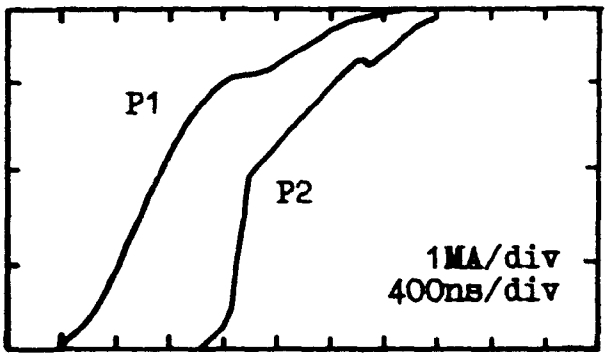

Fig.7.

rent P_1 and the switch downstream current P_2 in a shot with 64 plasma guns at 3.2 μs time delay between plasma and Marx firings. The switch downstream geometry was that shown in Fig.5 with a dashed line. The cold inductance of the load in this case equals to 22 nH. The switch current rises up to 3.15 MA in 1.3 μs. The opening occurs rather slowly, the P_2 current rises up to 2.2 MA in 400 ns before the current diagnostic fails. Fig.7 shows the traces in a shot obtained in the same conditions except of the plasma guns number. Here only 32 guns were operating. The switch current P_1 does not decrease significantly but the opening occurs more rapidly as one may see from the P_2 current trace. It rises up to 1.95 MA in ~200 ns and then the diagnostic also fails.

This year we hope to examine the machine in all operating regimes and improve the diagnostics. The switch behavior will be studied as well. To the end of the year the liner and charged particle beams experiments will be started.

PULSED POWER INDUCTIVE ENERGY STORAGE IN THE MICROSECOND RANGE

W. Rix, A.R. Miller, J. Thompson, E. Waisman, M. Wilkinson, A. Wilson

Abstract

During the past five years Maxwell has developed a series of inductive energy storage (IES) pulsed power generators; ACE 1, ACE 2, ACE 3, and ACE 4, to drive electron-beam loads. They are all based on a plasma opening switch (POS) contained in a single vacuum envelope operating at conduction times of around one microsecond. They all employ fast capacitor bank technology to match this conduction time without intermediate power conditioning. Oil or air filled transmission lines transfer capacitor bank energy to a vacuum section where the final pulse compression is accomplished.

Development of the ACE series is described, emphasizing capacitor bank and the opening switch technology for delivering high voltage, multimegampere pulses to electron beam loads.

Introduction

The ACE program at Maxwell Laboratories is concerned with scaling inductive energy storage technology to generate high power electron beams. Existing microsecond inductive storage systems operate with less than 1 TW in the electron beam. The goal of the ACE program is to use microsecond inductive energy storage power conditioning to realize the simplest, most compact pulsed power design.

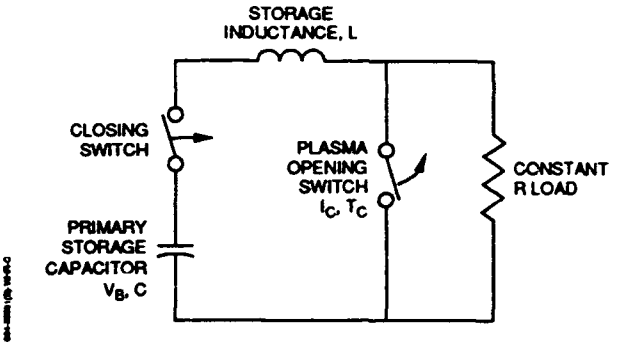

Fig. 1. Schematic diagram showing circuit elements in the ACE approach to inductive energy storage power conditioning.

The ACE conceptual approach uses only inductive storage for power conditioning. As shown in Figure 1, the concept is a very simple one requiring only circuit elements for a primary energy store, an opening switch, and an electron beam load. The ACE component configuration achieves compactness as shown in Figure 2. This approach to high power electron beam generation requires optimization of two key driver elements to realize compactness and simplicity. The primary energy store capacitor bank is constructed for high "speed density." The plasma opening switch is contained in a single vacuum envelope of minimum size. These two elements will now be discussed.

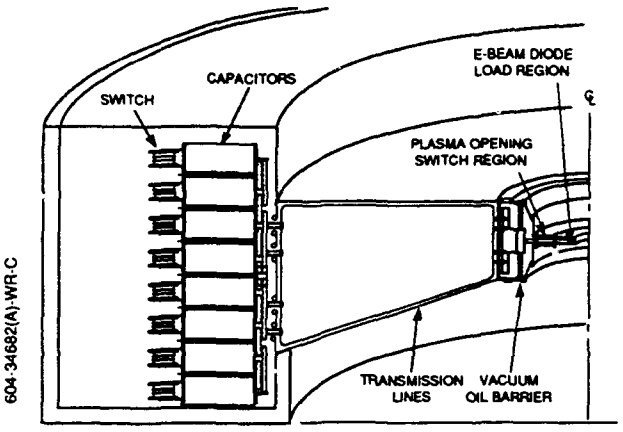

Fig. 2. Physical layout of the IES components in the ACE concept.

Capacitor Bank Design

To determine how optimized the capacitor bank is for driving fixed conduction time opening switches, "speed density" has been developed as a criteria. By "speed density" we mean the rate of rise of output power per unit volume of the bank. Any capacitor bank is constructed out of n basic elements characterized by a peak voltage, V_e, an inductance, L_e, and a volume, v_e. To create the capacitor bank the elements are arranged in s series and p parallel stages resulting in the following relationships between the bank (B) and the elements (e); $V_B = sV_e$, $L_B = sL_e/p$, $v_B = nv_e$, with $n = s \cdot p$. For an inductive energy storage system with a fixed load inductance, L_o, and a fixed opening switch conduction time, the most energy is stored when dI/dt from the capacitor bank is a maximum. Maximizing dI/dt leads to a formula for s. This in turn allows expressing the maximum dI/dt as a function of the number of elements:

$$\dot{I}_{max} = \frac{1}{2}\sqrt{\frac{n}{L_o}}\left[\frac{V_e}{\sqrt{L_e}}\right]$$

The quantity in brackets $\frac{V_e}{\sqrt{L_e}}$ can be squared and defined to be the "speed" of each element in the capacitor bank. The "speed density," $S=V^2/Lv$, can be seen to be an intrinsic figure of merit for the capacitor bank configuration:

$$S_B = \frac{V_B^2 / L_B}{v_B} = \frac{s^2 V_e^2 / sL_e / p}{nv_e} = \frac{V_e^2 / L_e}{v_e} = S_e$$

The ACE capacitor bank has been designed to have the highest practical speed density. A comparison of the ACE approach with the conventional capacitor bank technology used in BLACKJACK 5 is shown in Table 1. The ACE capacitor bank is called FASTCAP and was further improved in going from ACE 2 to ACE 4.

Plasma Opening Switch

The ACE radial POS configuration is indicated by Figure 3. The radial geometry permits the

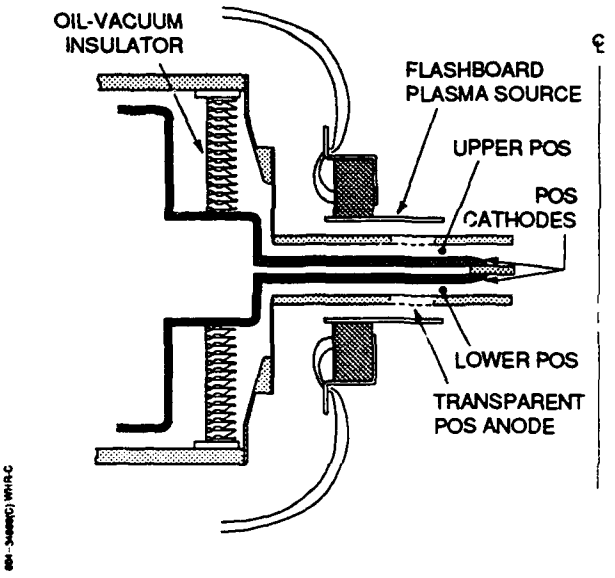

Fig. 3. The ACE radial geometry POS configuration.

TABLE 1
Speed Density Comparison for Conventional and ACE Capacitor Banks

System	V(kV)	L(nH)	Volume (m^3)	Speed Density ($GW/\mu s\text{-}m^3$)	Energy Density (kJ/m^3)
Conventional Marx technology					
BJ 5 Marx	8400	15000	74.0	63	33
ACE technology					
ACE 2-(FASTCAP 1)	720	360	8.0	>200	<120
ACE 4-(FASTCAP 3)	720	117	12.2	>350	>90

most compact and simple POS configuration for a large current POS. The POS is split into two back-to-back annuli to conserve space and this configuration can still be contained in one, compact vacuum envelope. The radial geometry also couples naturally to a high power electron beam at the center of the vacuum section, permitting reduced inductance and greater power flow.

ACE Pulser Evolution

ACE 1 and ACE 2 were constructed to demonstrate key technology capabilities. ACE 3 was the 2 MJ initial phase of ACE 4. The steps in the ACE program will now be discussed.

ACE 1

ACE 1 first demonstrated microsecond conduction time plasma opening switches could drive electron beams. Figure 4 shows the location and approximate size of the ACE 1 components. Using only inductive energy storage power conditioning out of the 100 kV ACE 1 capacitor bank output current pulse width, the electron beam had a peak voltage of 300 kV, a pulse width

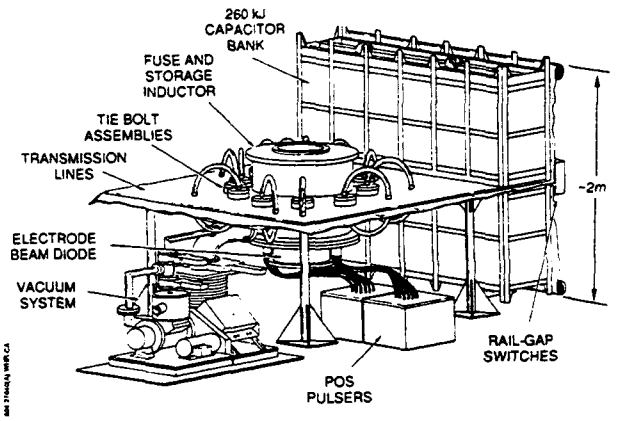

Fig. 4. Sketch of the ACE 1 pulser.

one-tenth of the capacitor bank, and over 10 percent of the bank energy was transferred to the electron beam. Typical current waveforms and the bremsstrahlung X-ray pulse produced by the electron beam are shown in Figure 5. ACE 1 demonstrated driving electron beams with inductive stored pulsed power was feasible.

ACE 2 Coaxial POS Configuration

The ACE 2 coaxial configuration demonstrated both the operation of FASTCAP high speed density components and a megampere coaxial

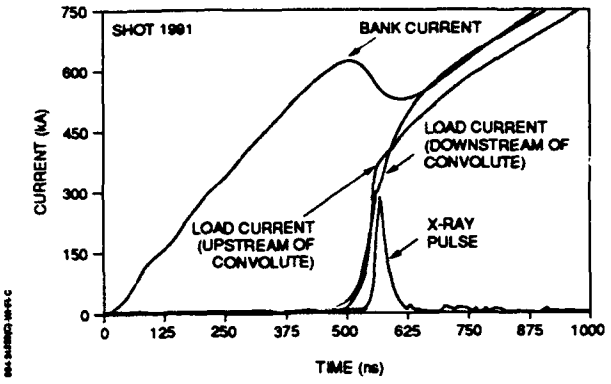

Fig. 5. Typical ACE 1 waveforms.

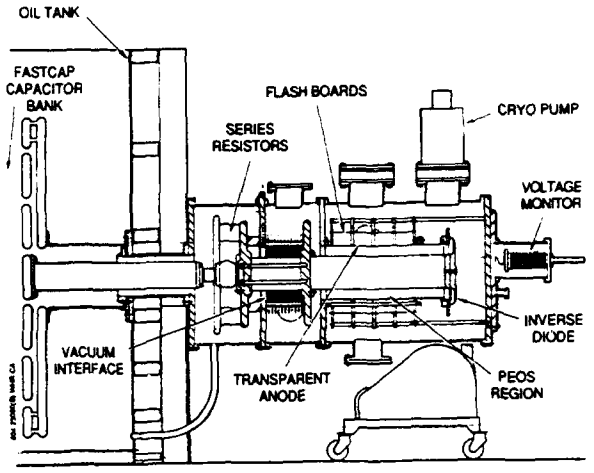

Fig. 6. ACE 2 coaxial POS configuration.

POS. Figure 6 shows the layout of the ACE 2 components. When operating at capacitor bank charge voltage of 600 kV, electron beam voltages of 1.5 MV with 45 kJ of energy in the electron beam (bank-to-beam transfer efficiency of about 6 percent) were achieved.

Representative current and electron beam load bremsstrahlung X-ray waveforms from ACE 2 coaxial POS configuration are shown in Figure 7.

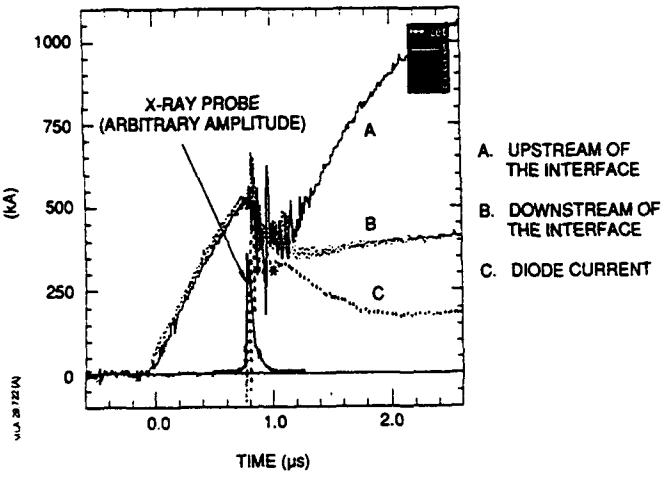

Fig. 7. Current and X-ray traces from ACE 2 coaxial POS configuration.

ACE 2 Radial POS Configuration

As designs for higher power inductive energy storage systems were developed, the advantages of a radial POS configuration for coupling to a single electron beam load in minimizing coupling inductance became clear. To test the feasibility of operating a large current, microsecond POS in the radial geometry, ACE 2 was converted from the coaxial geometry to a single-sided radial POS as shown in Figure 8.

Data from ACE 2 indicated the radial POS works like a coaxial POS. Current waveforms in Figure 9 display near microsecond conduction, rapid rise, and nearly complete current transfer into a short circuit load for the radial POS.

ACE 4

ACE 4 was designed to demonstrate all aspects of a compact, simple electron beam driver. The photograph in Figure 10 shows ACE 4. A cut-away schematic view of the major components in ACE 4 is shown in Figure 11.

ACE 4 consists of four major subsystems. Four megajoules are initially stored in the *fast capacitor*

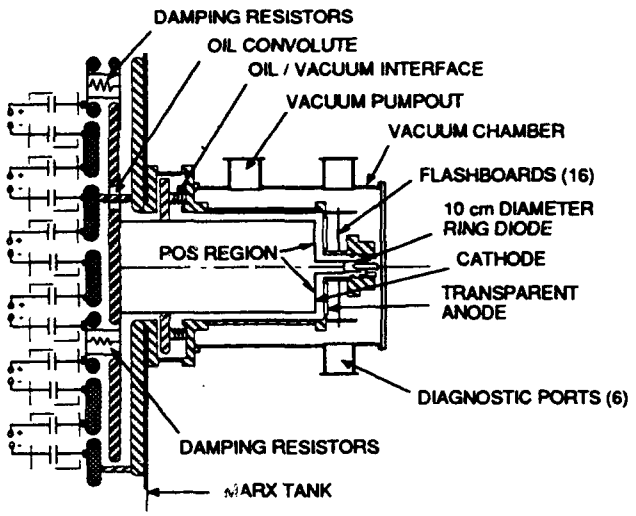

Fig. 8. ACE 2 single-sided radial POS configuration.

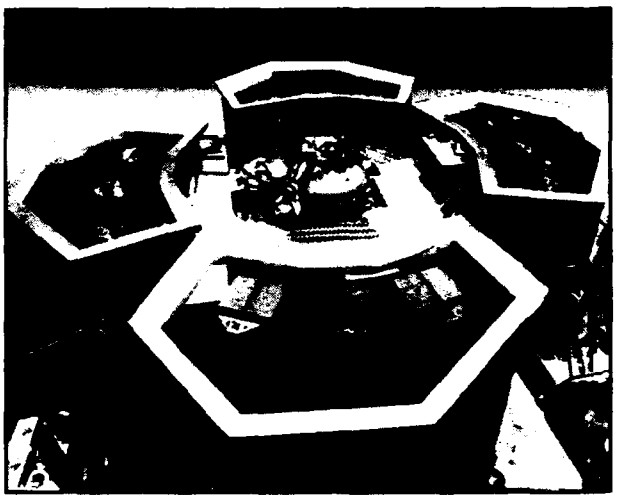

Fig. 10. Photograph of the ACE 4 pulser.

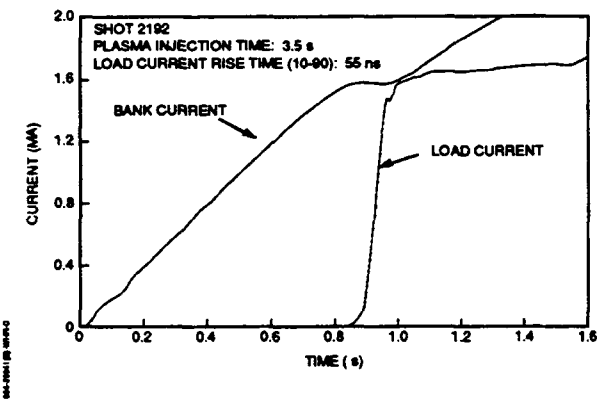

Fig. 9. Current waveforms from an ACE 2 radial POS shot.

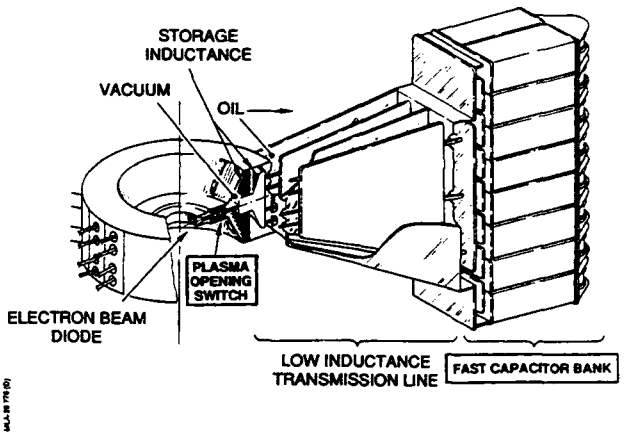

Fig. 11. Cut-away, schematic view of ACE 4 components.

bank. Low inductance triplate transmission lines are used to conduct the current from the capacitor banks at the circumference of the accelerator to the vacuum region at the center of the accelerator. In the vacuum region a *plasma opening switch* (POS) conducts the capacitor bank current for about a microsecond before opening in around a hundred nanoseconds and transferring the current into the *electron beam* diode near the axis of the accelerator. The capacitor bank and the transmission lines use transformer oil to provide insulation. The POS and diode are in vacuum. Use of a long conduction time POS eliminates the requirement for any additional stages of power conditioning such as transfer capacitors. Each of these subsystems will now be discussed.

Figure 12 is a picture of the basic building block of the ACE 4 capacitor bank. It consists of two FASTCAPS connected in parallel with a single switch to produce a 180 kV stage with a circuit inductance of 175 nH, storing 40 kJ.

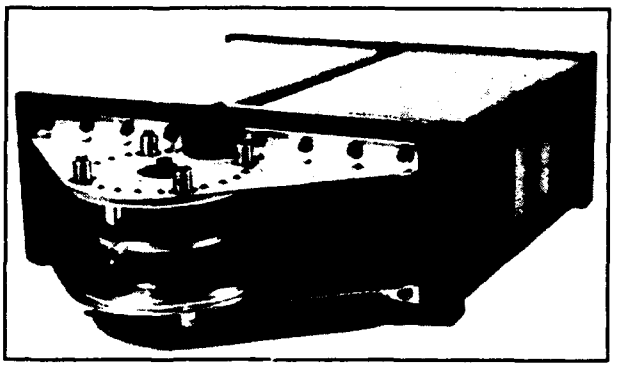

Fig. 12. An ACE 4 180 kV FASTCAP stage.

The plasma source is a crucial component of the POS. For the conduction times around a microsecond, conduction currents of several megamperes, and switch areas of around 10^4 cm^2 in ACE 4, a plasma density of 10^{14} to 10^{15} cm^{-3} is required. The plasma source selected for this application is an array of flashboards similar to those used on many other accelerators. The flashboard array shape is matched to the radial geometry of the POS. The flashboards cover the area between the inner radius of 40 cm to an outer radius of 60 cm. A flashboard array is pictured in Figure 13.

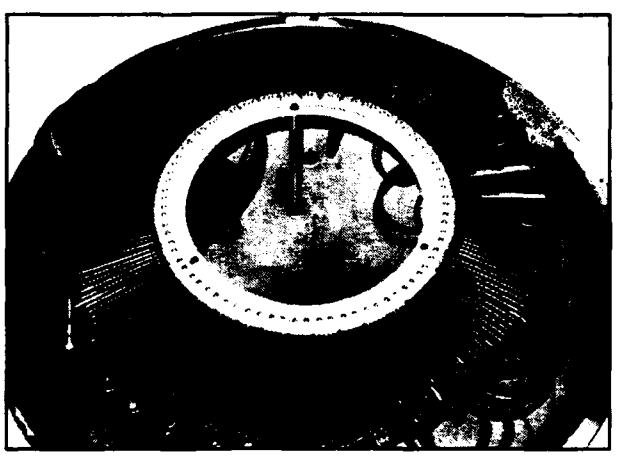

Fig. 13. ACE 4 flashboard plasma source array.

As previously discussed, to reduce the radial length of the POS (and the size of the vacuum transmission line required), the POS on ACE 4 is double-sided. The top and bottom POS are closely coupled through the common feed on the cathode and at the common load. This close coupling was designed to aid in synchronizing the opening of the two switches.

Summary

Microsecond pulsed power inductive energy storage permits simple, compact, and powerful electron beam drivers to be constructed. The ACE series of experiments has demonstrated the enabling technologies. For further details of experimental results and theoretical studies of the POS operation, see papers by Rix, et al.[1], and Parks, et al.[2], respectively in this conference.

References

1. W. Rix, M. Coleman, A.R. Miller, D. Parks, K. Robertson, J. Thompson, E. Waisman, and A. Wilson, "Experiments on Microsecond Conduction Time Plasma Opening Switch Mechanisms," these proceedings, Session PI.

2. D. Parks, E. Waisman, R. Ingermanson, and E. Salberta, "Two-Dimensional Studies of Current Conduction in Plasma Opening Switches," these proceedings, Session PI.

A LONG CONDUCTION TIME COMPACT TORUS PLASMA FLOW SWITCH

Robert E. Peterkin, Jr., David E. Bell, James H. Degnan,
Melissa R. Douglas, Thomas W. Hussey, Bill W. Mullins,
Norman F. Roderick*, and Peter J. Turchi**
Phillips Laboratory
Kirtland AFB, NM 87117-6008, USA

Experiments to form and accelerate compact toroid (CT) plasmas have been performed on the 9.4 MJ Shiva Star fast capacitor bank at Phillips Laboratory since late 1990. We investigate the possibility of employing a CT as a very fast opening switch by performing 2-1/2 dimensional magnetohydrodynamic computer simulations of a pair of axisymmetric, albeit geometrically-complex, switch designs. Both designs conduct current for ten or more μs. The first design relies on the acceleration of the CT to high speed whereas the second design does not. Although both designs hold promise for achieving a fast (less than 100 ns) opening time, the second may prove to be a preferred design because of its low impedance.

Introduction.

A switch that opens in less than 100 ns and that conducts current for longer than 1 μs would be a valuable addition to the pulsed power toolbox. For example, it could be used to power a bremsstrahlung diode or to energize a plasma radiation source. A variety of inductive store opening switches have been studied in recent years, but a long conduction time, fast opening switch so far remains an elusive goal.

One idea that holds much promise is the accumulation of magnetic energy behind a fast-moving compact torus (CT) that acts as a plasma armature in a coaxial rail gun configuration. The accumulated magnetic energy can be quickly transferred to a load as the armature moves past the end of the gun. Earlier theoretical investigations of the use of a CT plasma as a fast opening switch proved interesting[1], and that work is extended in the present paper.

The MARAUDER program is a research effort at the Phillips Laboratory to accelerate 0.5 - 1 mg magnetized plasma rings to velocities above 200 cm/μs and energies above 1 MJ with the Shiva Star fast capacitor bank. A number of interesting applications are planned; for example, high speed toroids, when crushed against a stationary wall, may be copious producers of soft x-rays.[2] The experiment is a two-stage plasma discharge in a coaxial gun with embedded

* permanent address: The University of New Mexico
** permanent address: The Ohio State University

poloidal magnetic flux. The first stage is called the formation discharge and it injects magnetic helicity into the gun and entrains plasma in a helical magnetic field to create a CT. The second discharge is called the compression discharge because it creates a magnetic piston field that pushes the CT into a compression cone. So far, the MARAUDER experimental program has successfully created rings of argon, deuterium, and nitrogen which have been driven into both cylindrical and biconic coaxial configurations. Similar experiments at lower energy have been performed at LLNL.[3] Numerical simulations of the the formation and compression processes have been performed with the 2 ½-D MHD code, MACH2.[4] The code agrees with experimental diagnostics of the magnetic field and mass density.[5] MACH2 is known to have predictive power and has been used to design a self-similar pair of compression cones that will be fielded on an upcoming series of experiments to attempt self-similar compression of a CT.

The plasma flow switch[6] (PFS) has been used extensively for pulse sharpening of relatively slow capacitively produced discharges. There is a limit to the speed to which the conventional PFS can be accelerated by a magnetic piston because of the tendency of the plasma to disrupt as the Rayleigh-Taylor instability grows. A CT plasma, however, is confined by its own helical magnetic field for which the Hamiltonian is a minimum. This implies that perturbations of the CT tend to decay rather than to grow. For this reason, it is believed that a CT can be accelerated to a much larger speed and can conduct current for a much longer time than can a conventional plasma switch.

To illustrate the concept of a CT fast opening switch, Fig. 1 shows the magnetic flux surfaces from a MACH2 computer simulation of a CT that is accelerated to 200 cm/μs as it crosses an axial gap to a virtual load. Magnetic energy is accumulated behind the CT for many μs, and is delivered to the load at a rate characterized by the speed of the low density flow behind the CT. This speed can exceed that of the higher density switch because it is produced by the same magnetic force per unit volume. The simulation predicts an opening time < 100 ns for this configuration. The axis of symmetry is a vertical line in all computer-gererated pictures; only the region of the r-z plane that is to the right of the axis is displayed.

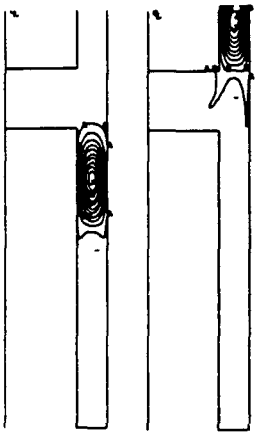

Fig. 1. A compact torus plasma flow switch moving upward as it approaches (left) and passes (right) the gap to a load.

In this paper, we investigate two designs for using compact toroid plasmas to compress a pulsed electrical discharge. The compact toroids are produced in a magnetized coaxial plasma gun, and they are moved downstream in a configuration similar to a coaxial railgun. The first design, illustrates how a CT that is formed from realistic initial conditions can be accelerated to 30—50 cm/μs while accumulating magnetic energy from a capacitor bank behind the CT. A CT armature that moves at such a speed was shown in Ref. 1 to be sufficient to improve the switch performance and implosion quality of a plasma liner beyond that achieved by

the conventional plasma flow switch. In the second design, a CT is pushed into a shallow compression bicone where the self-magnetic confinement limits the speed of the CT and hence the circuit impedance. The low speed, low impedance CT armature permits high currents to be reached by the capacitive driver and the switch opens more like a vacuum opening switch than a high-speed plasma flow switch.

Self-Similar Compression and Acceleration of a CT.

The major diameter for the CT formed with present MARAUDER hardware is nominally 1 m. The size of the CT must be made significantly smaller for most applications, including fast opening switches. One way to compress a CT is to use a pair of self-similar compression cones that maintain a constant $\delta\rho/\rho$ along the axis of the bicones. A particular self-similar compression bicone, with an additional long focusing bicone attached at the end, is shown in Fig.2. The formation gun is at the bottom of this design. The central axis of the compression bicone makes an angle of 30° with the vertical. This relatively steep bicone is presently being built and will be fielded on Shiva Star later in 1992. The focussing bicone is also self-similar and makes an angle of 5.7° with the vertical. The figure shows the poloidal magnetic flux and ion number density isocontours for a CT that is near its equilibrium configuration for this geometry (10 μs after the beginning of the formation discharge). The CT acts like a gasket in the compression region as it maintains contact with the conducting walls and keeps magnetic flux from the compression discharge behind it. The formation discharge circuit parameters are: 110 μF bank capacitance, 23 nH external inductance, and ±35 kV capacitor voltage; the compression circuit parameters are: 440 μF, 100 nH, and ±35 kV. Approximately 1 MJ of electrical energy is stored in the compression discharge which begins 7 μs after the beginning of the formation discharge.

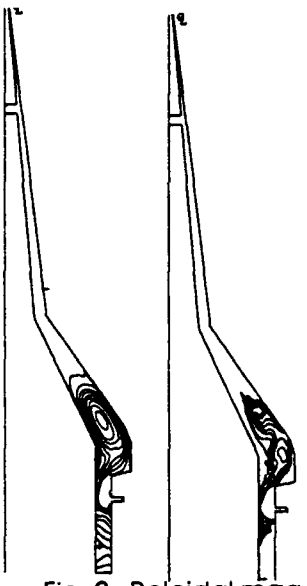

Fig. 2. Poloidal magnetic flux (left) and ion number density (right) isocontours for a CT trapped in a 30° compressionon cone.

The simulation is finely-zoned; there are 12 cells across and 128 cells along the compression and focussing bicones with many more cells in the other blocks of the problem domain The key idea in this design is that the distance between the electrodes is kept constant across the transition region between the various segments of the device This idea is implemented with a compound bicone — one transitional biconic segment is placed on each side of the main biconic compression region. The poloidal magnetic field lines of a CT that has been pushed 2/3 of the way into the

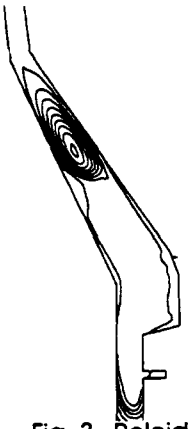

Fig. 3. Poloidal magnetic flux lines for the CT of Fig. 2 — 3 μs later.

compression bicone at 13 μs is shown in Fig. 3. The CT is prolate with the upstream end flattened by the magnetic piston that pushes it into the bicone. This gives the CT a comet-like shape. In fact, a cometary "wind," which carries mass and magnetic flux with it, emanates from the downstream end of the CT .

Compression of the CT increases the magnitude of the axial component of the magnetic induction as is shown in Fig. 4 where the time-histories of each of a sequence of magnetic field probes that are distributed along the outer electrode of the compression region at 7 cm intervals between the cylindrical radial locations ρ = 57 cm and ρ = 22 cm are plotted. As the CT is pushed into the compression bicone, the magnitude of the magnetic field should increase as its volume decreases if magnetic flux is approximately conserved — as it is for sufficiently large magnetic Reynold's number. One sees from Fig. 4 that the magnitude of the axial component of **B** increases monotonically as the CT passes probes that are further downstream in the compression bicone. The peak value at the most downstream probe, positioned at ρ=22 cm, is five times the value at the probe near the upstream end of the compression region which is at 57 cm cylindrical radius. Flux conservation for self-similar compression (i.e. compression during which the CT maintains its cross-sectional shape) would yield a compression factor of $(57/22)^2$=6.7 for B_z. That a somewhat lower value is obtained by the numerical simulation is a result of resistive flux losses and the non self-similar nature of the "wind" that carries magnetic flux with it off the front of the CT.

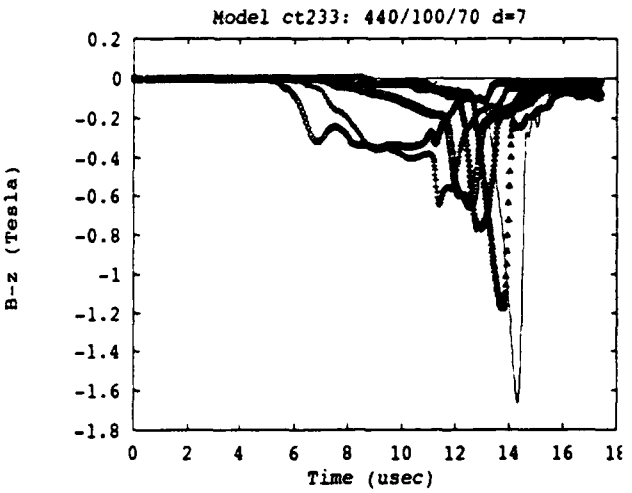

Fig. 4. The axial component of the magnetic field vs time for a sequence of 7 probes located along the outer electrode of the 30° compression cone of Fig. 2.

Snapshots of the poloidal magnetic flux lines and the ion number density are illustrated in Fig. 5 at 16 μs. The speed of the CT at this time is approximately 40 cm/μs. This is to be compared to a terminal speed of 7 cm/μs for a conventional PFS.[7] The CT, which has not yet reached the switch region that is positioned between the inner electrode and the axis of symmetry, has already conducted current since the compression discharge was fired at 7 μs. Hence, the conduction time is at least as great as 10 μs which is what we mean in the title of this paper when we promise to discuss a *long* conduction time switch.

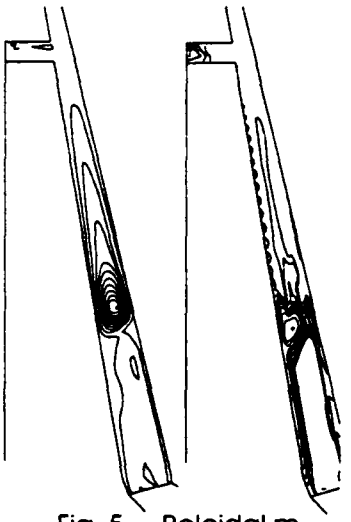

Fig. 5. Poloidal magnetic flux (left) and ion number density (right) isocontours for th CT of Fig. 2 that has been accelerated into the long focussing cone. (The scale is expanded).

There is a potential difficulty with such high-speed

plasma switches, however. Both the minor and major diameters of the electrodes must be on the order of a few cm to avoid problems with gap closure that may arise from excessive energy density. The CT has traveled proximately 1 m as it is accelerated from 0 to 40 cm/μs in approximately 5 μs. The large impedance of of such a system will decrease the fraction of driver energy that can be delivered to a load. Also, the axial spreading of the CT may have deleterious effects on the performance as a switch because toroidal magnetic flux entrained in the elongated CT may pass into the switch region over the relatively long timescale of the transit time of an elongated CT.

Self-Similar Compression of a CT *Without* Acceleration.

As magnetic energy accumulates behind a plasma armature, the armature is accelerated by the $\mathbf{J}\times\mathbf{B}$ force. When a CT moves into a region formed by converging electrodes, however, there is an additional force that resists compression: $\mathbf{F}_B = -\nabla U_B$ where U_B is the magnetic field energy which scales inversely with the spherical polar radius, r, if magnetic flux is conserved and if the compression is self-similar. We can take advantage of this additional work term to avoid the high impedance associated with a fast-moving plasma armature. Fig. 6 shows a shallow self-similar biconic compression region, the center of which makes a 60° angle with the vertical. The bicone terminates when the cylindrical radius of its central axis is 1/3 of the value of the cylindrical radius at the widest part of the bicone. For the example illustrated here, ρ_{out}=49.14 cm and ρ_{in}=16.38 cm; $r\delta\vartheta_{out}$=17.78 cm and $r\delta\vartheta_{in}$=5.93 cm. Above the compression bicone is a downstream coaxial expansion region that is wider than the 5.93 cm gap at the end of the bicone. The reason for the expanded gap will be made clear below. Somewhat above the end of the compression bicone is a 5 cm high axial gap to a load region that extends from the inner electrode to the axis.

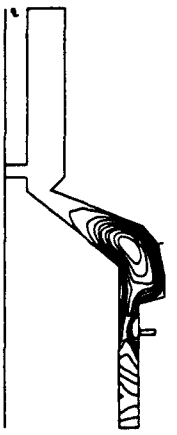

Fig. 6. Poloidal magnetic field contours for a CT trapped in a 60° self-similar compression cone.

Snapshots of the poloidal magnetic flux lines and the ion number density between 13 and 16 μs at 1 μs intervals are illustrated in Fig. 7. The formation and compression discharges are identical to those used for the previous simulation. The CT maintains the essence of its cross-sectional shape as it is pushed into the shallow compression bicone, and it remains compact.

The CT is driven into the compression bicone by the magnetic piston created by the compression discharge, I_c. This toroidal field varies with the cylindrical radius, ρ, as I_c/ρ and hence is larger near the inner electrode than near the outer one. The $1/\rho$ distribution of the accelerating field is an important effect that occurs in many coaxial plasma schemes. As the CT approaches the end of the bicone, the magnetic piston field pushes the CT aside to the outer electrode -- a process that is called "blow-by."

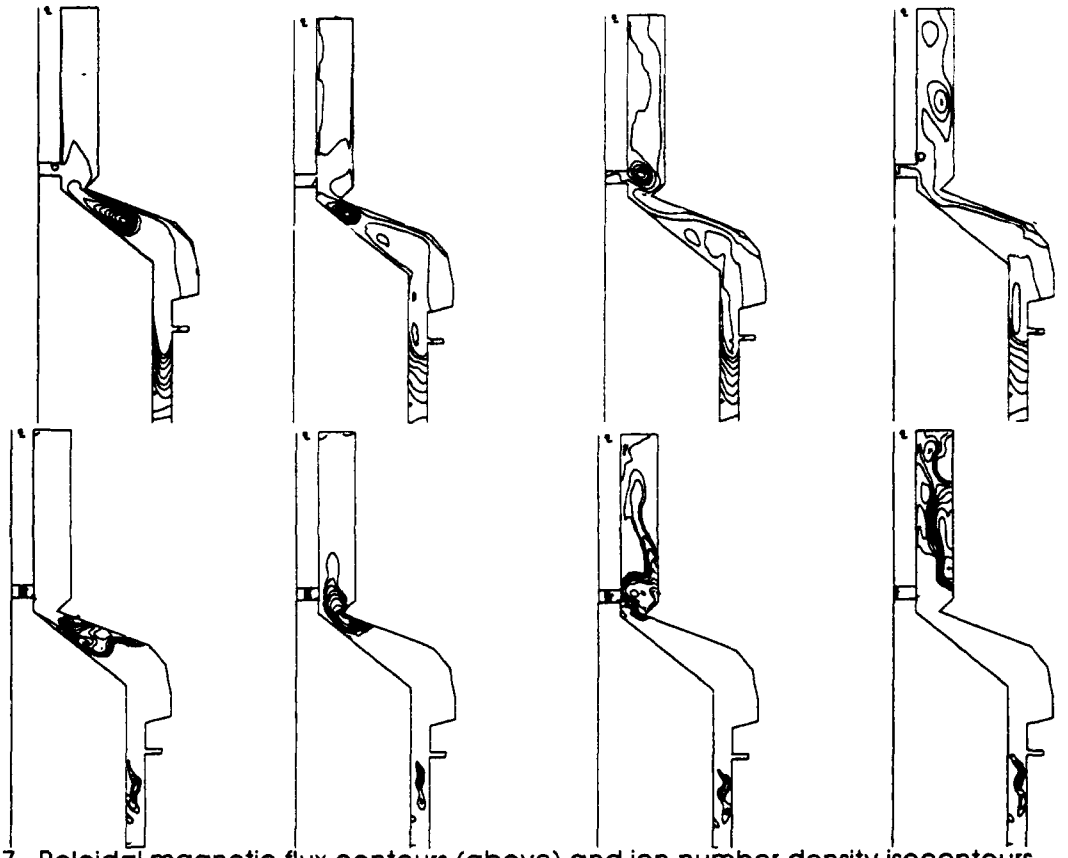

Fig. 7. Poloidal magnetic flux contours (above) and ion number density isocontours (below) at 13, 14, 15, and 16 μs (from left to right) for a low-impedance, shallow, biconic compression cone that opens to an axial gap to a load region.

In other words, the CT gasket fails. This phenomenon generally occurs when the compression field exceeds the self-field of the CT, and will occur more easily in shallow bicones than in steeper ones. Although usually thought to be a problem, "blow-by" is used in this design to our advantage.

In the present case the CT conducts current for many μs while it is pushed into the bicone toward the downstream expansion region. The cone is designed so that the CT reaches the end of the cone as the accelerator bank achieves its peak current. As the CT approaches the end of the compression region, the compression field exceeds the CT self-field and the "blow-by" phenomenon begins to push the CT toward the outer electrode. As the CT passes off the end of the cone through the wide gap into the downstream expansion region (at t~15 μs in Fig. 7), the CT looses contact with the inner electrode allowing the magnetic piston field to move quickly into the switch region that is just downstream of the wide gap. The mass density behind the CT is substantially less than the density of the CT itself. This particular design for a CT switch works more like a vacuum opening switch (POS) than a plasma flow switch. For the present case the CT behaves in a similar fashion as that which is planned for the current-toggle opening switch of Mendel and co-workers.[8]

Conclusions.

Two designs for a long conduction time, fast opening switch that use a compact toroid armature and a low voltage capacitor discharge to accumulate magnetic flux behind the CT in an inductive store are discussed in this paper. The first relies on the acceleration of the CT to a large speed. A potential problem with this scheme is that the fast CT creates a high impedance that may prevent the acceleration bank from developing the desired high current. The second design may prove to be more useful. Essentially, a shallow compression cone is used to compress a CT during the rise time of the compression discharge. The work performed by this discharge on the CT does not, however, convey kinetic energy to the CT but rather increases its self magnetic field.

We believe that it may be possible to use the "blow-by" phenomenon in which the compression discharge pushes the CT to the outer electrode to our advantage to open in a vacuum sense, similar to that of a POS, after conducting current for a long time by designing a shallow compression bicone to accumulate magnetic flux behind the CT until peak current is reached. This concept has an additional advantage that it may be efficient in extracting a large fraction of the energy from the accelerator bank. The inductive losses can be minimized if the compression is quasi-static, and compression is closer to the static case for a shallow compression bicone.

References.

[1] R. E. Peterkin, Jr., et al., "A Compact Torus Plasma Flow Switch," *Digest of Technical Papers: Eighth IEEE International Pulsed Power Conference,* 17-19 June 1991, San Diego, CA, R. White and K. Prestwich eds., p. 277. (IEEE, New York, NY, 1991.)

[2] See, for example, M. R. Douglas, et al., "A Numerical Study of the Stagnating Compact Toroid and its Applicability as a Radiation Source," these proceedings.

[3] A. W. Molvik, et al., "Quasistatic Compression of a Compact Torus," *Phys. Rev. Lett.* **66**, p. 165 (1991).

[4] J. H. Degnan, et al., "Compact Toroid Formation Experiments at the Weapons Laboratory," *Physics of Alternative Magnetic Confinement Schemes*," S. Ortolani and E. Sindoni, eds. (Societá Italiana di Fisica, Italy, 1991.).

[5] National Technical Information Service Document No. ADA 192285, (Mission Research Corporation Report AMRC-R-874 by M. H. Frese, 1987). Copies may be obtained from the National Technical Information Service, Springfield, VA 22161. The price is $14.95 plus a $3.00 handling fee. All orders must be prepaid.

[6] P. J. Turchi, et al., "Development of Coaxial Plasma Guns for Power Multiplication," *Digest of Technical Papers: Third IEEE International Pulsed*

Power Conference, 1-3 June 1981, Albuquerque, NM , T. H. Martin and A. H. Guenther, eds. (IEEE, New York, NY, 1981.)

[7] J. Buff, et al., "Simulations of a Plasma Flow Switch," *IEEE Transactions on Plasma Science,* **PS-15**, 6, p. 766 (1987).

[8] C W.. Mendel, Jr., M. E. Savage, D. M. Zagar, W. W. Simpson, P. W. Grasser, and J. D. Quintenz, *J. App. Phys.* **71**, p. 3731 (1992).

Contributed Pulsed Power Papers

ACCELERATORS WITH VACUUM INSULATED MARX GENERATORS

E.N.Abdullin, S.P.Bugaev, A.M.Efremov, V.B.Zorin,
B.M.Koval'chuk, S.V.Loginov, G.A.Mesyats*,
V.S.Tolkachev, P.M.Schanin, A.A.Chistov

High Current Electronics Institute, Tomsk 634055, Russia
*Electrophysics Institute, Ekaterinburg 620020, Russia

Abstract

The module type Marx generators developed to drive high current diodes are described. Their special feature is the air proof sectioned body. The design and parameters of the e-beam accelerators for eximer lasers based on such Marx generators will be given.

Introduction

To drive the broad beam eximer lasers the ~0.5 μs, 0.5-0.8 MV electron beams with total energy of hundreds kJ are needed. Such beams are generated in high current explosion emission diodes. Usually the water line generators are used to drive the diodes [1]. The direct Marx-diode scheme may also provide the above given e-beam parameters. The main problem on this way is the generator design with extreme low circuit inductance. The inductance decrease may be achieved in multimodule generator version providing small module firings jitter. To minimize the each module inductance its Marx column may be located inside the air proof body used also as a bushing to the diode vacuum chamber. The multymodule design allows also to section the accelerator diode excluding the e-beam focusing in the absence of the external magnetic field. All this considerations lie in a base of our research.

Module type Marx generator

The electrical scheme of the Marx module is given in Fig.1,a. It consists of 8 stages with 3 condensers/stage. The condensers in each stage are separated by the resistors. The module is charged by the direct positive voltage source through

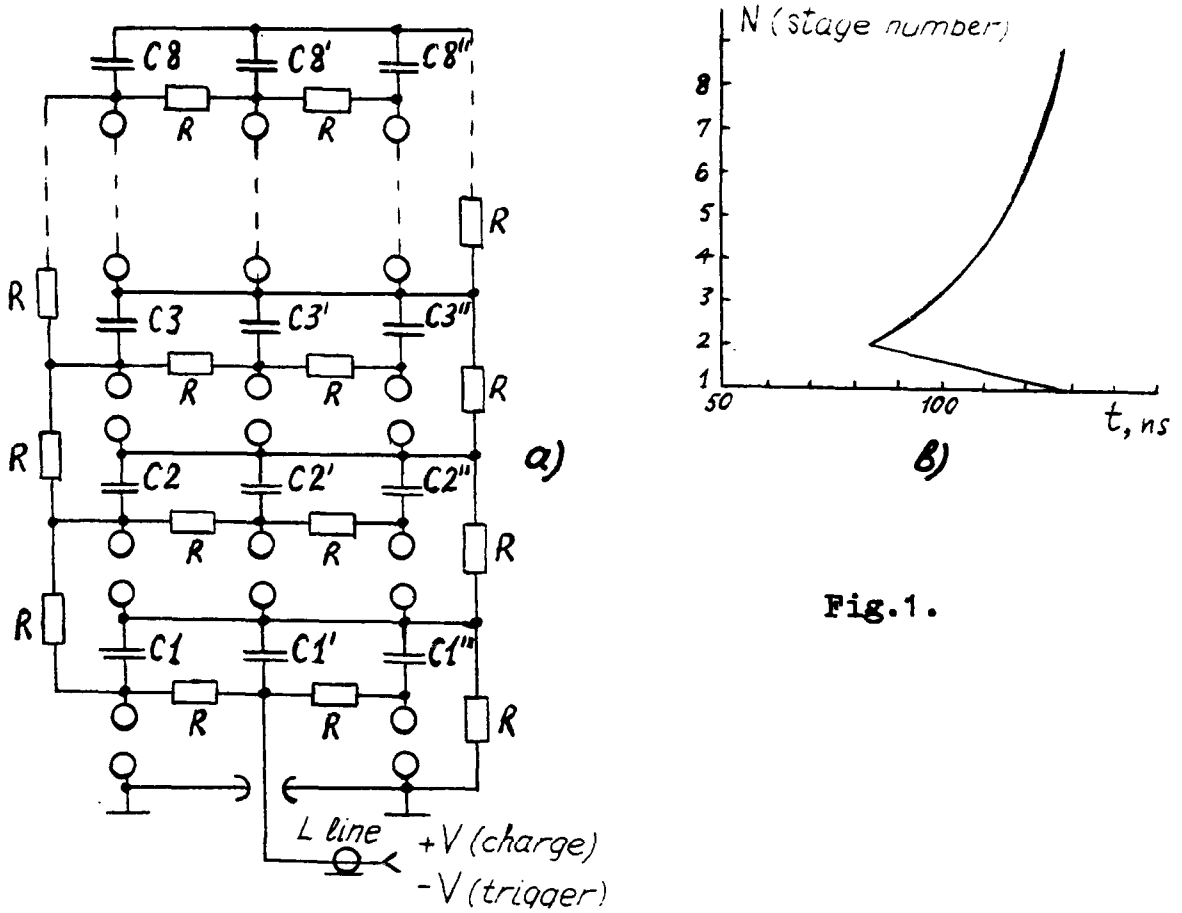

Fig.1.

the line L. The same line is used to apply the negative trigger pulse. Each module condenser is switched by its own gas discharge gap. The synchronization is provided by the gap overstress with the amplitude controlled by the trigger pulse and the gas pressure. The analysis of the transition process at the trigger pulse arrival gives the gap firings succession shown in Fig.1,b. The last gap switched is one in a first stage. This allow to control the synchronization by means of the trigger pulse.

Module construction

The sketch of the condenser used in a module is shown in Fig.2,a. It has a plastic body, the main connections are located on its opposite sides made as a semispheres. There are additional outputs used to connect the condenser to charging and separating resistors. The condenser capacitance is of 0.18 μF, the voltage of 100 kV, the inductance of 40 nH. Fig.2,b demonstrates the module construction. The storage condensers (1) are supported by

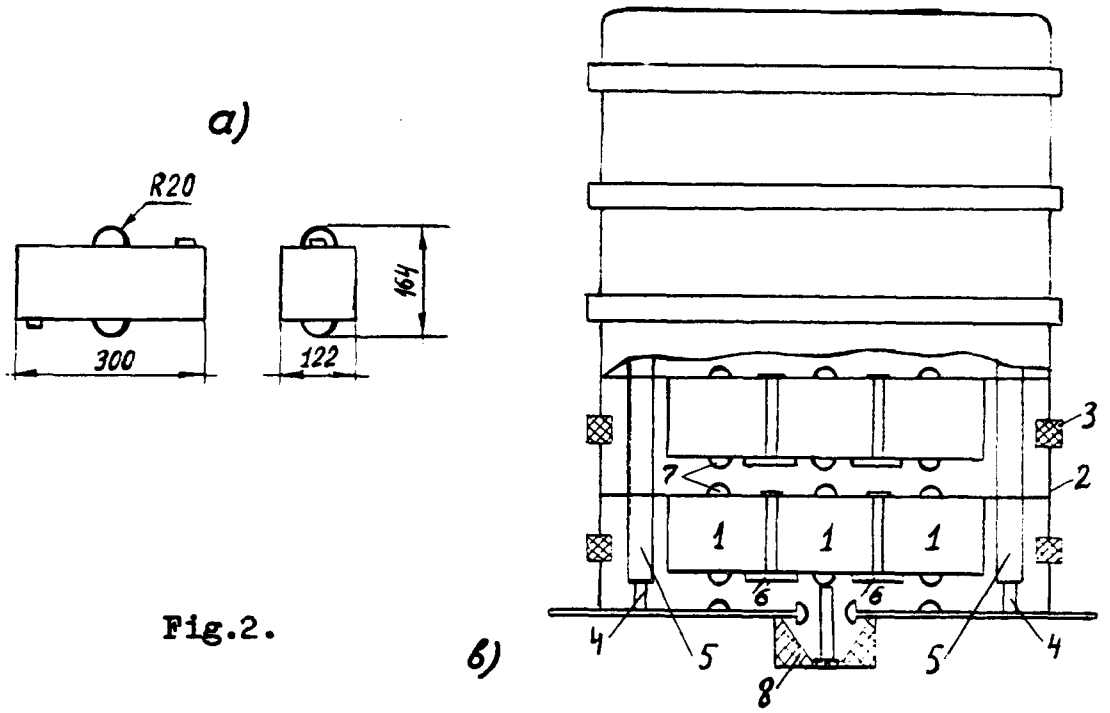

Fig.2.

the metal shields (2). The shields are separated by the polyethylene insulators (3). The shields and the insulators are drawn together by the fiberglass rods (4) with charging resistors (5). The separating resistors (6) are inserted between the neighboring condensers. The shields and the insulators form an air proof body withstanding 10^{-5} Torr outside pressure. The separated semispherical condenser connectors serve as a discharge gaps (7). The column is filled by a 30% SF_6-air mixture, the inside pressure is up to 1.5 ata. The charging voltage and the trigger pulse are applied to the electrode (8) at the grounded end of the generator. The high voltage Marx output electrode is the shield of the top stage where the diode cathode is located. Fig.2,b shows the module with rectangular cros-section. The circular modules are also developed.

The module parameters are given below:

Output capacitance	68 nF
Charging voltage	100 kV
Stored energy	22 kJ
Inductance	300 nH
Dimensions	1200x1500x200 mm^3
Weight	500 kg

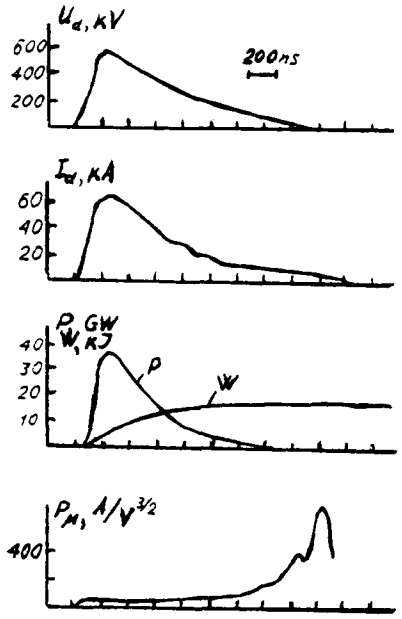

Fig.3.

Fig.3 gives the typical traces obtained in a module discharge through an explosion emission diode with cathode area of 19x81 cm^2 and A-K gap of 6 cm. The e-beam total energy equals to 16.8 kJ. More than 95% of this energy is transported by electrons with energy exceeding 200 kV.

The 301 exited volume accelerator

The accelerator scheme is given in Fig.4. The circular Marx module is located inside the 900 mm diameter chamber. Its high voltage electrode (1) is connected to the cathode stalk (2). Four cathodes (3) with dimensions 130x800 mm^2 are used in a diode. They are placed on the inner surface of the cathode stalk representing the velvet strips glued on the metal. The 200 mm diameter anode made of 50 μm thick Ti foil is located inside the cathode stalk. The diode generates the ~0.4 μs, 80 kA, 600 kV electron beam with total energy of ~16 kJ.

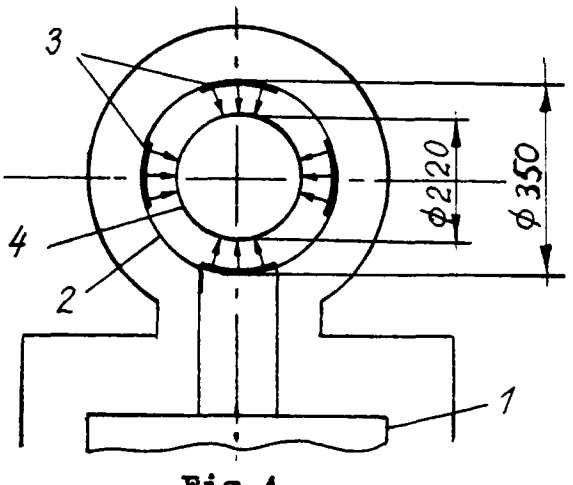

Fig.4.

The 6001 exited volume accelerator

The accelerator design consisting of 12 rectangular modules is illustrated in Fig.5. Each two modules are installed on a plate as shown in Fig.5,a. Each plate serves as a lid of the air proof accelerator chamber being shaped as a star shown in Fig.5,b. In the middle of the chamber the output window is loca-

ted separating the accelerator vacuum volume and the laser gas

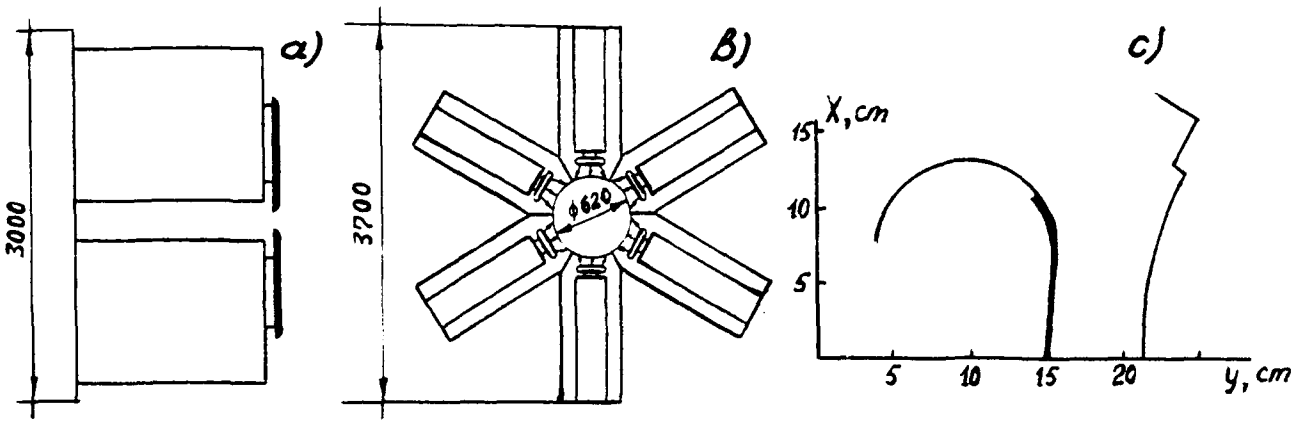

Fig.5.

cavity. The e-beam output system consists of cylindrical body with 24 removable grids (4 grids per each e-beam) supporting 40 μm thick Ti foils. The grids are bent to form a cylindrical surface at a radius of 310 mm. The grid rods are 5 mm thick. The total transparency of the output system equals to ~70%. The design provides the laser cavity gas pressure up to 3 ata. The diode cros-section corresponding to one single module is shown in Fig.5,c. The emitting cathode surface 90 cm long is made of velvet glued on the cathode stalk metal.

By operation the cathode voltage and current are measured for each of 12 diodes. This information allows to estimate the module firings jitter and the e-beams energy characteristics. The time jitter does not exceed ±50 ns. The total e-beam current is of ~700 kA, the peak electron energy of ~600 kV. The typical cathode voltage and current traces correspond to those shown in Fig.3.

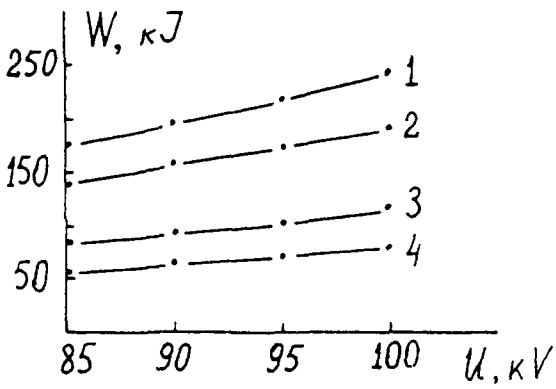

Fig.6.

The energy loss distribution of the electrons by entering the gas cavity is illustrated in Fig.6. Here the condenser stored energy (1), calculated using diode voltage and current e-beam energy (2), the energy measured by calorimeters located 3.5 cm from the output foil

in the gas (3) and the energy estimated by measuring the pressure change in the gas cavity filled by 3 ata Ar (4) are given versus generator charging voltage. The pressure change was measured by means of mechanotron.

Conclusion

The vacuum insulated Marx accelerators experience has shown that their reliability correspond to that achieved for installations of traditional type. The total accelerator dimensions are significantly diminished. Decreasing the self condenser resistance it would be possible to decrease the losses in the generator discharge circuit and to increase the e-beam power by shortening of its length. The development of the condensers with long transmission line parameters would result in the possibility to design the module forming rectangular voltage pulse in the diode.

References

1.Rosocha L.A., Riepe K.P., Fusion technology, 1987, v.11, p.576.

ELECTRON BEAM GENERATORS AT ANGARA-5 FACILITY.

V.V.Bulan, E.V.Grabovsky, A.N.Gribov, O.G.Egorov, V.V.Zajivikhin, E.P.Kojokhin, Kurbatov K.V., Kukharenko I.N., Lujnov V.G., Pichugin V.E., Smolenkova O.A..

142092, Russia, Moscow reg., Troitsk, TRINITI.

The schemes of electron beam generators developed at Angara-5 division of TRINITI are under consideration. Those generators will be used for development and testing of high power technology elements and for applications. ISTOK generator (0.5 TW,1-1.2 Ohm, 50 ns) is the test bed for some elements of Angara-5-Upgrade project. The pulse forming line of VOLNA generator (500 kV, 300-500 ns, 4-8 Ohm) is based on the wave slowing periodical structure.

Introduction.

There are a number of generators at Angara-5 division of TRINITI which give possibility to test elements of main system, to develop high-power technology elements and diagnostic systems.

TRITON generator [1] (600kV, 200 kA, 30 ns) made 20 years ago is mentioned here for fullness of picture. Mainly, it is used for testing of diagnostic systems.

VOLNA generator was designed to obtain long large aperture electron beam pulses (300-500 ns, 500 kV). To make long pulse the PFL based on the water filled periodical structure is used. The scheme, evaluation of output parameters and first experimental results are considered here. ISTOK generator (0.5 TW, 0.7 MV, 50 ns, 1-1.2 Ohm) will be used to test elements of high power technology for Angara-5-upgrade project. ISTOK and VOLNA generator use partially common synchronization system and common control/measurement system.

2. VOLNA generator.

Pulse forming line of VOLNA generator (fig.1.) is based on the scheme of the line discharging through the switch to the load. To make the pulse duration longer, the PFL of generator is made as periodical structure. The PFL consists of the disks on

the common central cylinder (diameters 98 and 9.6 cm). The capacitance of PFL is close to that of straight coaxial line and the inductance is added by the inductance of cavities located between disks. Interelectrode space is filled with deionized water. To improve mechanical stability of PFL, disks are connected by the dielectric rods. By change of the interdisk gap one can change PFL impedance from 3 to 8 Ohm (the pulse duration will change accordingly).

PFL is charged from Marx bank and is switched by the externally triggered controlled gas switch. The gas and trigger voltage are supplied through spiral inductance. The output Marx capacitance is 50 nF, output voltage under working conditions 1100 kV.

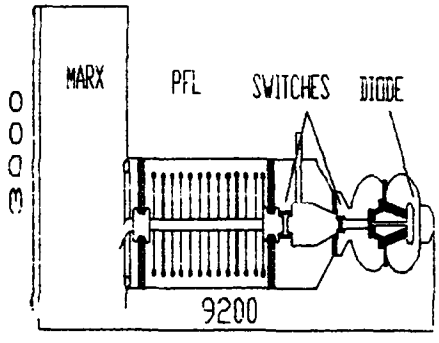

Fig.1. VOLNA generator scheme.

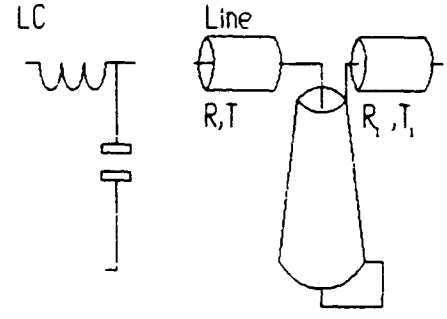

Fig.2. Simulation models of VOLNA PFL elements

At the generator output the short oil filled transmission line and shortening switch are located. The inductance of output structure - insulator and diode - is about 400 nG. Cathode area is 60 X 10 sq.cm.

The proposition of the PFL scheme was made by I.Yampolsky. Design and preparing of generator to first tests are due to O.Egorov, mainly.

3. PFL of VOLNA generator.

VOLNA PFL works as the chain of individual elements. To simulate the PFL work two models were used (fig.2). First one was the model of chain of lumped elements - inductances L and capac-

itances C. C is defined by capacitance of disk to adjacent part of external cylinder cavity. The second model is the one of serially connected straight lines and connected at one end disk lines. Disk line impedance [2]:

$$Z = iQ = i\ 60\ h/b\ \frac{Y_0(wT_b)J_0(wT_a)-Y_0(wT_a)J_0(wT_b)}{Y_0(wT_a)J_1(wT_b)-Y_1(wT_b)J_0(wT_a)} \qquad (1)$$

h - interdisk gap, b,a - disk/central cylinder radii, $T_a=a/v$, $T_b=b/v$, v-e.m.wave velocity, w - cycle frequency.

Wave resistance and delay can be found from transition matrix of voltage-current vector (eigenvalue phase and eigenvector components relation):

$$\begin{bmatrix} \cos(wT) & -iR\sin(wT) \\ -i\sin(wT)/R & \cos(wT) \end{bmatrix} \begin{bmatrix} 1 & iQ \\ 0 & 1 \end{bmatrix} \begin{bmatrix} \cos(wT) & -iR\sin(wT) \\ -i\sin(wT)/R & \cos(wT) \end{bmatrix} \qquad (2)$$

T,R are length and wave resistance of straight lines. Wave resistance and delay in w=0 limit are:

$$T_n=2T(1 + R_1T_1/2RT)^{1/2} \qquad (3)$$
$$R_n=R(1 + R_1T_1/2RT)^{1/2}$$

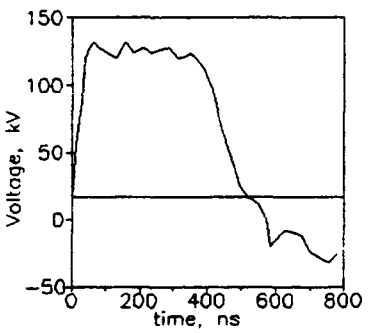

Fig.3. Voltage at VOLNA output (load 7.5 Ohm).

For the large frequencies the PFL do not works as slowing structure due to the resonances in disk line. The first resonance frequency is close to the double disk line length.

4. Test results.

During tests the external triggering of PFL switch was not used. The charging voltage was 1/4-1/3 of working value. The output voltage waveform is shown at fig.3. The load resistance was 7.5 Ohm. According to LC-model matched load resistance is 8.5 Ohm, for line model - 6 Ohm.

5. ISTOK generator scheme.

One of the main goals of the generator design was to test some elements of Angara-5-Upgrade. The proposition on the project of A-5-Upgrade was considered earlier [3].

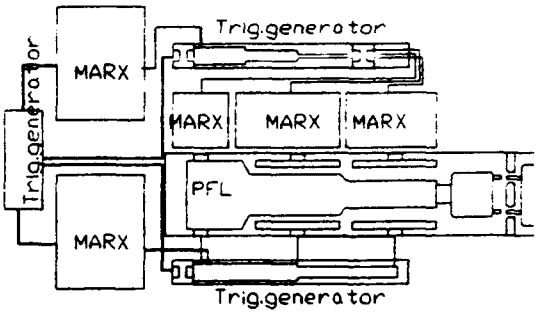

Fig.4. Synchronization system of Angara-5-Upgrade.

A-5-U consists of eight 5 TW modules. Each module consists of the 2.5-section PFL (sections sequentially add energy to output pulse) and pulse shortening section with water switches. The high voltage synchronization system (HVSS) project is based on the assumption of the usage in A-5-upgrade of analogs to the present A-5 switches. The HVSS (fig.4) consists of the similar elements - pulse forming generators with trigatron-type switches and small Marx generators. Time dependencies will be defined by L-C-diode structures [4] of first triggering generator.

There four main events: 1) triggering of Marx banks for charging of main-Marx-triggering generators, 2) triggering of main-Marx-triggers, 3) start of Marx banks for charging of main switch triggering generators, 4) start of those generators.

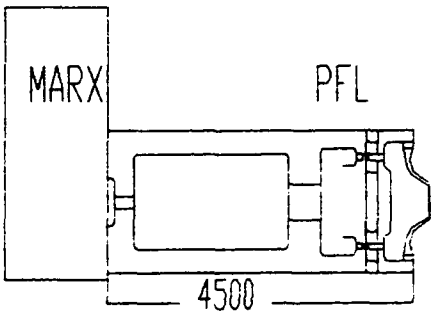

Fig.5. ISTOK generator scheme.

ISTOK generator will be used in testing of elements of HVSS (Marx banks and trigger generators) and in the simulation of shortening section.

Design of the ISTOK generator was partially defined by the usage of outer electrode

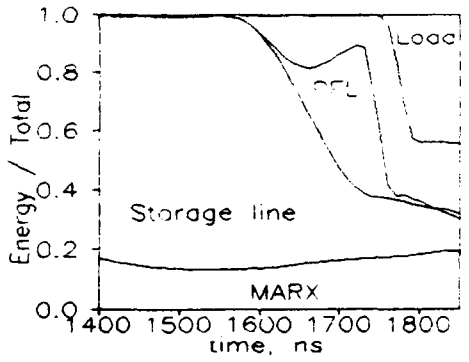

Fig.6. Energy distribution in the ISTOK generator. The width of segment is proportional to part of total energy in the subsystem. Unlabeled area is for switches and output transmission section.

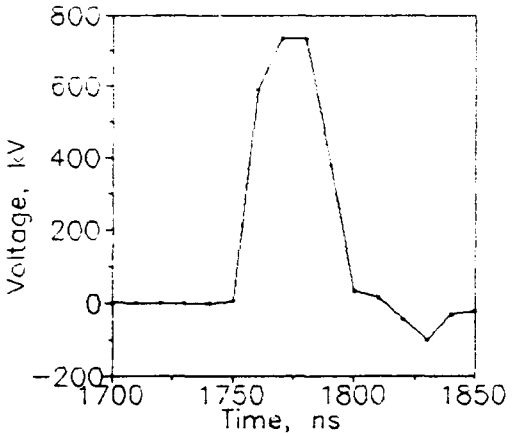

Fig.7. Calculated output voltage of ISTOK generator (1.2 Ohm load).

of the transmission line of Angara-5 module (4.5 m X 1.2 m diameter cylinder). Output capacitance is 50 nF of Marx bank. Charge voltage of storage line (3.1 Ohm,70 ns) is 1300 kV. Charge voltage of PFL (1.8 Ohm,20 ns) is 1900 kV, charging time being equaled to 150-170 ns. The storage line and PFL are divided by gas switch, and PFL and output structure by water switches. Amplitude of output pulse is 700-750 kV (load impedance 1.2 Ohm).

The output pulse parameters depend on the moment of switching of water switches and on the value of inductance of gas switch. Optimal values of time and inductance forms the narrow region at the map of output voltage and pulse forming efficiency (Fig.8). The best efficiency (from Marx to output pulse) is 40%, gas switch inductance and switching time being equaled to 350 nG and 175 ns. Fig. 6 and 7 show distribution of energy in system and calculated output voltage pulse for optimal conditions.

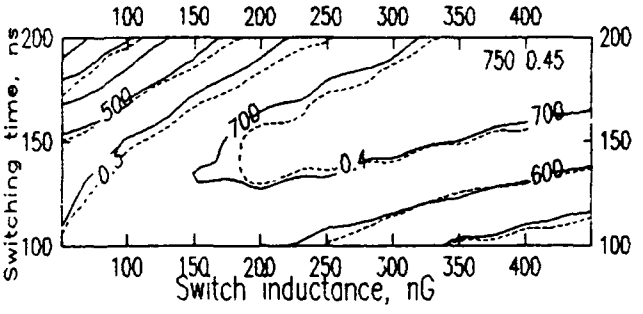

Fig.8. Marx-output energy transfer efficiency (dashed line) and output pulse voltage (solid) vs gas switch inductance and trigger time of water switches. Load impedance 1.2 Ohm.

The output power is limited due to the conditions in the PFL. For described parameters the electric field strength at outer electrode is 160 kV/cm. To enhance power it is possible to use larger charging voltage or another capacitance banks. With those improvements the output power may reach 0.7 TW.

At the present moment the Marx bank was assembled and tested at 1/4 of operational voltage.

6. Synchronization system.

ISTOK and VOLNA generators have common DC charging system and common triggering generator (made of cables) for Marx banks. Another triggering generator is used for PFL triggering of VOLNA generator. The first experiments at ISTOK are planned with selfbreakdown of gas switch. One example of triggering generator for A-5-upgrade was made. Later this generator or VOLNA PFL triggering generator can be used for triggering of ISTOK gas switch. Time dependencies are defined by L-C-diode structures of small Marx bank.

7. Summary.

There are two new generators under development at Angara-5 division of TRINITI. The ISTOK generator (0.5 TW) will be used for studies connected with Angara-5-Upgrade project. The pulse forming line of VOLNA generator (500 kV,200-300 ns) is made on the base of periodical wave slowing structure.

References:

1. V.I.Liksonov, Sidorov Yu.P., Smirnov V.P.. High current ns accelerator TRITON. Pribory i technika experimenta.-1975.-N5.-p.187-189.
2. W. Smythe. Static and dynamic electricity. N.Y.1950.-p.541 of Russ.edit..
3.V.Bulan,E.Grabovski,I.Yampolski,A multistage high voltage generator for light ion beams. Proc.of 8th Int.conf.on high-power part.beams,July 2-5,1990.World Scientific,v.1,p.207.
4. Albikov Z.A. et al., Pulse thermonuclear facility Angara-5-1, Atomnaya Energiya.-1990.-68,N1.-p.26-35.

PROGRESS IN TECHNOLOGY OF THE MICROSECOND E-BEAM GENERATORS WITH ENERGY CONTENT IN THE RANGE 100-500 kJ

A.V.Arzhannikov, V.T.Astrelin, V.B.Bobylev, V.S.Koidan
V.S.Nikolaev, M.A.Shcheglov, S.L.Sinitsky, A.V.Smirnov
and R.P.Zotkin
Budker Institute of Nuclear Physics, 630090, Novosibirsk, Russia

ABSTRACT. It is described a development of the microsecond E-beam generators U-2 and U-3 intended for the plasma heating experiments on the GOL-3 device [1]. Presented results are concerning to both an increase of energy content in the beam pulse and a rise of the beam power.

INTRODUCTION. Generators of 100-500 kJ microsecond electron beams are under development at the INP for the purpose of plasma heating in a long solenoidal trap (the GOL-3 program [1]). The microsecond E-beams with small angular spread and high current density can be also used for other applications, such as driving high power microwave generators, X-ray sources, etc. At the previous BEAMS-90 conference a paper was presented where operation of the U-1, U-2, and U-3 generators with energy content in capacitor storage about of 200 kJ was described [2,3,4]. Now we report on the increase of the energy content of both the capacitor storage and the generated electron beam.

INCREASE OF ENERGY CONTENT. The increase of the initial energy content in the high voltage pulse generator of the U-2 device is achieved due to using of capacitor banks accumulating two-fold electric energy more then ones used before and connecting the additional LC-generator in parallel with the operated one before. The electrical scheme of these generators together is shown in Fig.1. The picture of these generators is presented in Fig.2. The circuit design of the additional pulse generator is similar to that of the precedent one but the capacity of the banks of the new generator is 6 μF instead of 3 μF. Moreover, the inductance in the LC-cascades of the additional generator has been chosen

such as the voltage rise time is about 13 μs. In the precedent pulse generator (3 μF capacitor banks) the voltage rise time was 10 μs. To equalize this time with that of the new generator the inductances in the LC-cascades of the first generator have been increased. Because of two-fold increased capacity of the banks multistage switches operated in the LC- cascades have been also reconstructed. First of all it is concerning solidity of the discharge gap covers.

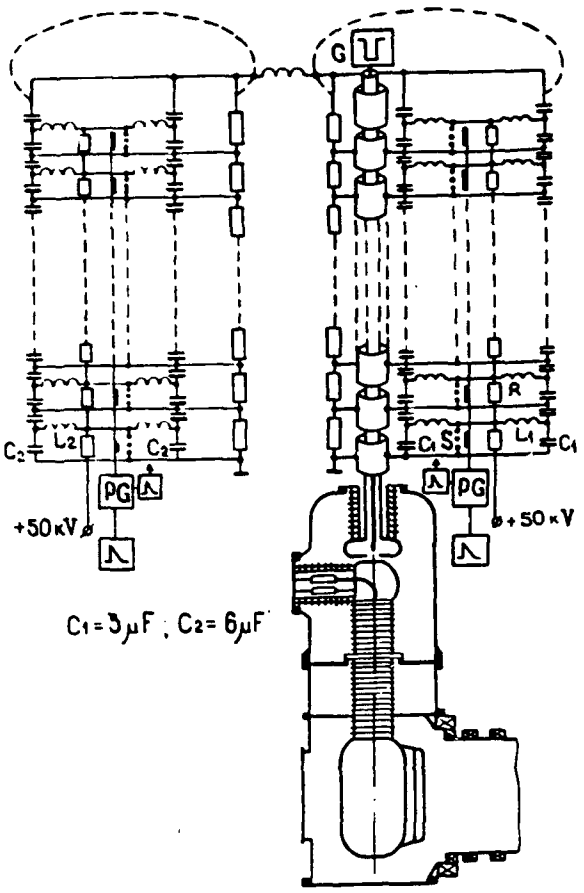

Fig.1

Design of the connections between the capacitors in a single column is shown in Fig.3. These connections have been made with a minimum inductance and as a result the rise time of the accelerator diode voltage is about 0.3 μs. The choice of the optimum(about 10 μG) inductance of the electrical connection between two pulse generators provides the diode voltage approximately unvariable during 5 μs.

Joint operation of the two LC-generators together on the single accelerating diode has been simulated by a computer and results of the simulation are given in Fig.4. The wave form of the diode voltage, the total electron current in the diode and currents flowing from the each of the pulse generators are shown in this Figure. Time behavior of the diode gap resistance for this simulation corresponds to the experience obtained in the experiments on the ribbon beam generation with the previous single generator. It is seen from the figure that at the simultaneous triggering of the LC-cascades and the same voltage rise time of ones, the diode current is mostly produced by the first generator within up to 3-4 μs. After this time the second

generator begins to transfer the energy to the diode. In the case of the optimum diode operation regime the accelerating voltage is approximately constant during 5-6 μs that gives opportunity for generation of the beam with the electron energy unvariable in the time, that is appropriated for various applications.

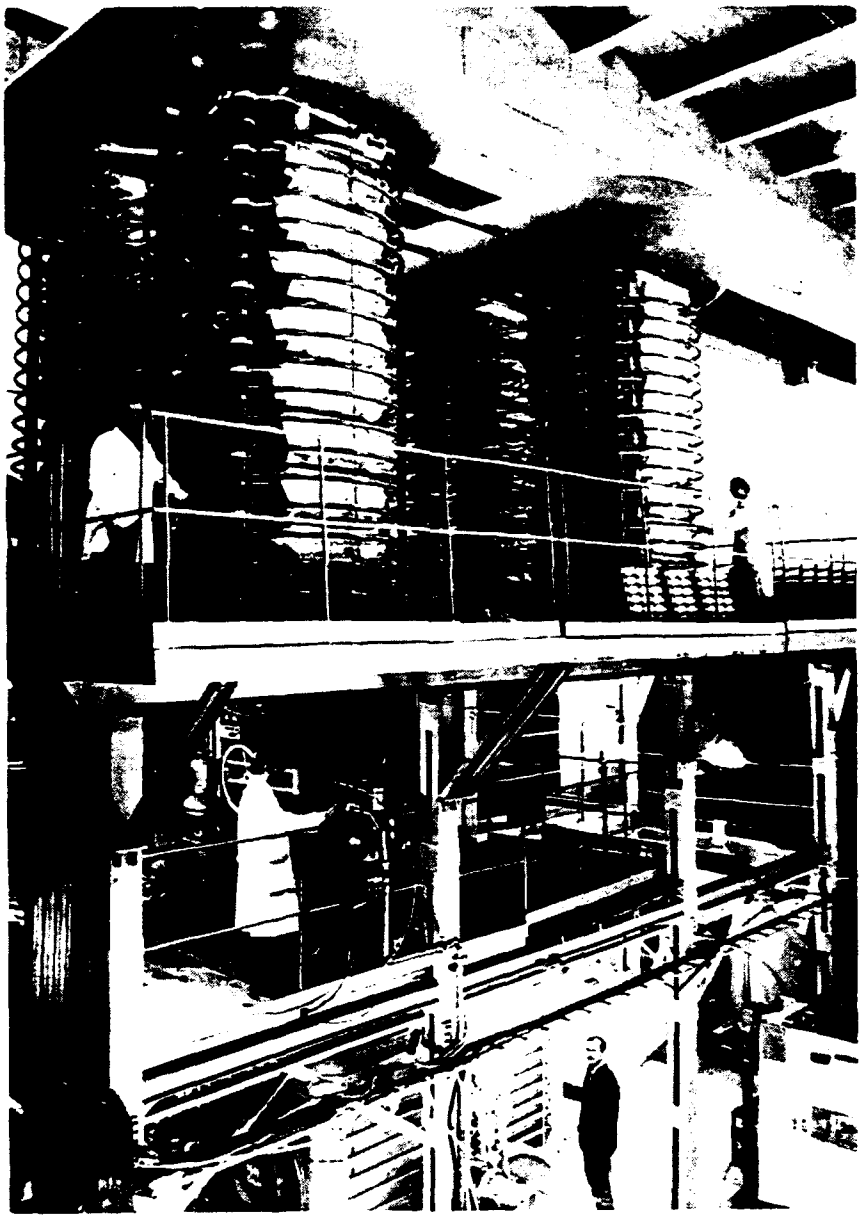

Fig.2

At present the U-2 accelerator is operated at the energy content in the capacitor storage up to 0.5 MJ. At these conditions the total energy of the ribbon beam, about 0.3 MJ has

been achieved.

INCREASE OF DIODE VOLTAGE. The design of the U-2 and U-3 devices allows to increase the accelerating diode voltage in 1.5 times. For this purpose a few of the LC-cascades should be added to the high voltage columns of the U-2 generator. As for the U-3 machine, it is necessary to replace the scheme of a statically charged column of capacitors connected in series by the pulse generator scheme (same as used in the U-1 and U-2 devices). At the increased voltage the accelerating diodes should be reconstructed so that to keep the electric field strength on the metallic elements not more then 75 kV/cm.

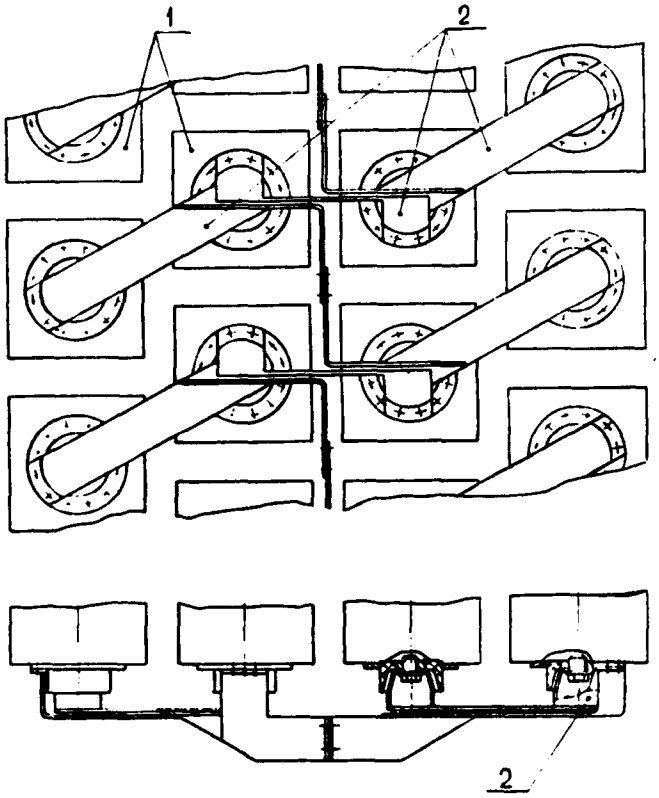

Fig.3
1-capacitor banks
2-low inductive connections

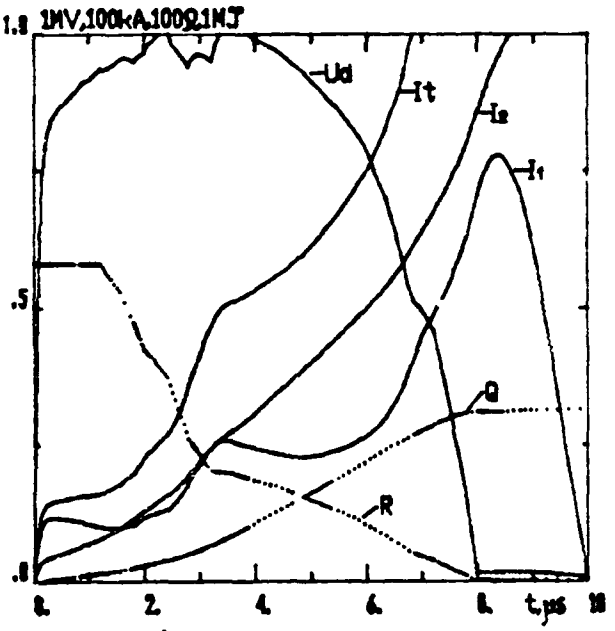

Fig.4

U_d – diode voltage; I_t – total current; I_1 and I_2 – currents of HV generators; Q-energy content in the beam pulse; R-resistance of the diode gap

It is supposed that the sectional transmit insulator with conducting electrolyte used before, should be replaced by another one with compressed insulating gas (SF_6). The voltage will be shifted along the insulator by an ohmic divider, made of

high-resistance wire. The diameters of the high voltage electrode and the vacuum chamber of the U-3 device will increase respectively up to 60 and 160 cm (at present these diameter are 42 and 100 cm). The diameters of the insulating dielectric rings and the gradient sectional electrodes should be also increased (see Fig.5). In the U-2 accelerator only the transmit insulator have to be reconstructed, because of the high-voltage electrode and the vacuum chamber have been made in advance of size mentioned above.

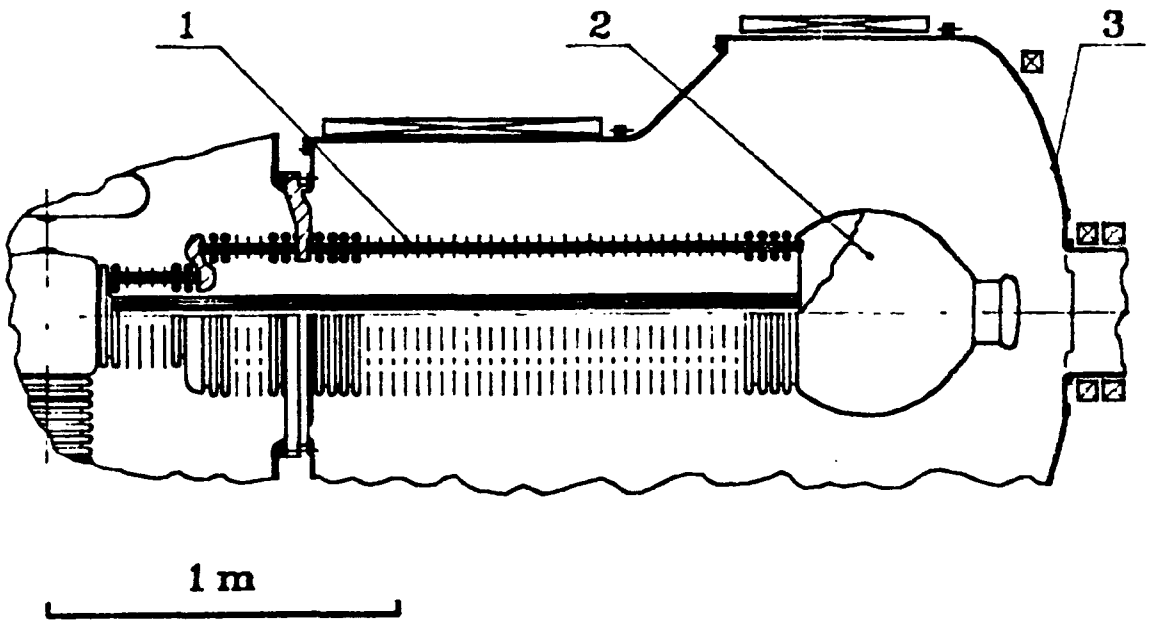

Fig.5

1-transmit insulator; 2- high-voltage electrode;
3-vacuum chamber

REFERENCES

1. *Arzhannikov A.V., Burdakov A.V., Chikunov V.V., et al.* Proc. 8th Int.Conf.on High-Power Particle Beams, Novosibirsk,1,14(1990)

2. *Astrelin V.T., Chikunov V.V., Koidan V.S., et al.* Proc 8th Int.Conf.on High-Power Particle Beams, Novosibirsk,1, 288 (1990).

3. *Arzhannikov A.V., Astrelin V.T., Bobylev V.B., et al.* Proc 8th Int.Conf.on High-Power Particle Beams, Novosibirsk,2, 849 (1990).

4. *Arzhannikov A.V., Astrelin V.T.,Gorbovski A.I.,et al.* Proc 8th Int.Conf.on High-Power Particle Beams, Novosibirsk,2, 979 (1990).

HIGH-CURRENT ACCELERATOR "SIRIUS" WITH ELECTRON BEAM CURRENT OF 2KA,ELECTRON ENERGY OF MEV-RANGE AND PULSE DURATION OF 50 MCSEC

V.I.Engelko,N.G.Beruchev,V.V.Ershov,O.L.Komarov,V.G.Kovalev, O.P.Pechersky,A.A.Petukhov,Yu.M.Saveljev,L.V.Smirnov,K.I.Tkachenko

D. V. Efremov Scientific Research Institute of
Electrophysical Apparatus
Metallostroy St. Petersburg
189631 Russia

Abstract. High-current electron accelerator "SIRIUS" being under construction now in the Efremov Institute is described. The accelerator parameters are: an accelerating voltage of idle running is 5MV and 2.5MV in the matched mode, a beam current is 2kA, a total pulse duration is 50μsec and a flat top pulse duration is about 20μsec.

1. Introduction. Already for many years Efremov Institute has been developping high-current accelerators operating in the micro-second range of pulse duration. Physical mechanismes, determining characteristics of high-current electron beams (HEB) were studied, methods for HEB production with long pulse duration were developed and high voltage generator schemes were improved. The data available for today provide in particular an information about a top pulse duration of HEB. A planar diode has a pulse duration $\tau<10\mu$sec at accelerating voltage of MeV-range. Foiless diodes inserted into nonuniform magnetic field can provide τ up to 50μsec [1]. Pulse duration >100μsec can be achieved by using multipoint explosion-emission cathodes (MEC) developed in Efremov Institute [2]. Nonetheless τ exceeding 10μsec can be obtained, applying mentioned vacuum diodes, if accelerating voltage is not more than 300kV [1]. Consequently, for production of MeV-range HEBs we need some additional accelerating structures. One of such structures enhancing the energy of a beam formed in a magnetron diode with multipoint cathode is described in [3].

In this paper an accelerator with electron energy of MeV-range, being now built in Efremov Institute, is presented.

2.General scheme of accelerator. Fig.1 shows an accelerator schematically.It consists of an electron injector,a pulse voltage generator, an accelerating tube,magnetic and vacuum systems. A high voltage structure is made in the form of a vertical column and is placed in a tank,3m in dia and 11.4m in heigt,filled with nitrogen up to 6atm. An accelerating tube is placed along the Marx generator and all the tube sections are connected with the generator stages. This allows to realize the best electrical distribution on the tube and make a sectional accelerating structure. Each accelerating section consists of one accelerating tube section of 0.85m length and four Marx generator stages (Fig.2) Marx generator consists of 8 accelerating sections and being charged to 75% of the nominal voltage provides 5MV accelerating voltage of idle running. If a load is matched to the accelerator impedance, an average voltage gradient on the accelerating tube surface is about 6kV/cm,less than the breakdown value.

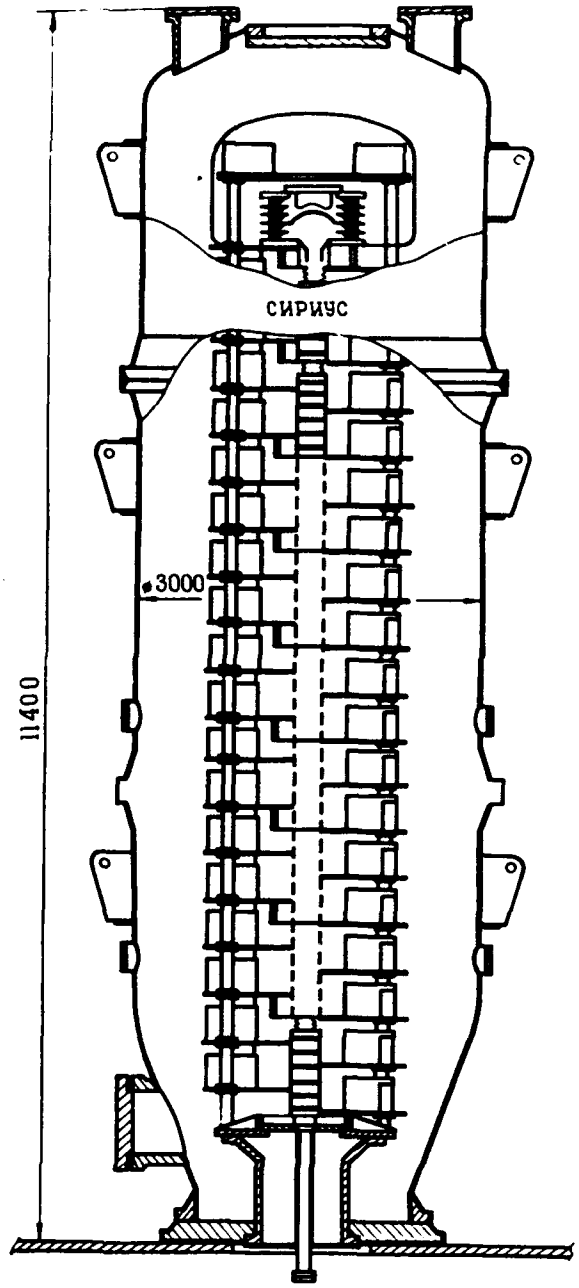

Fig.1 General scheme of the accelerator "SIRIUS"

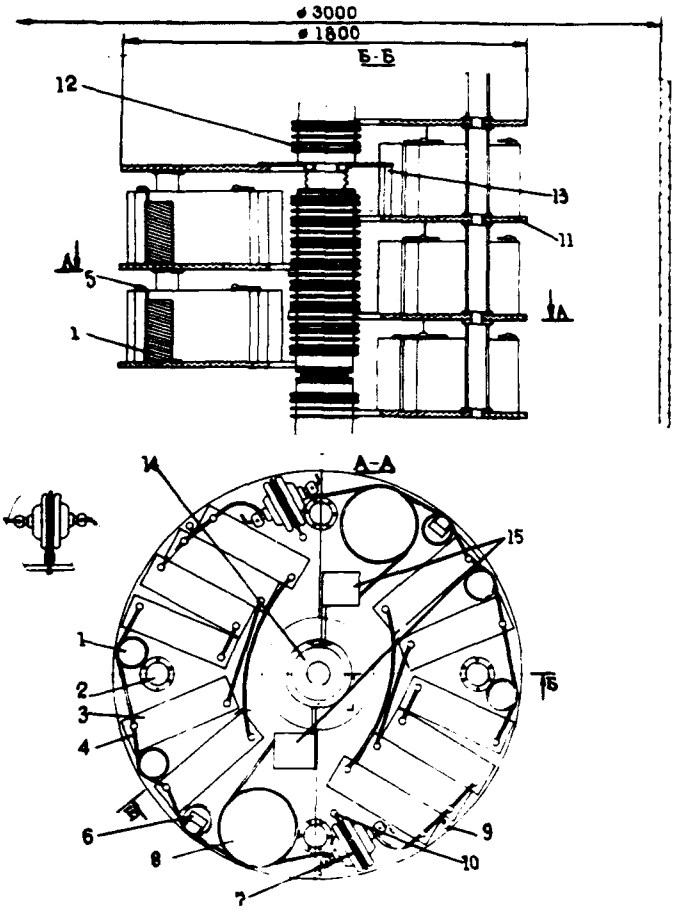

Fig.2 Accelerating section 1-inductance; 2-Marx generator stage support; 3-capacitor; 4-busbars; 5-electrostatic shield; 6-resistor; 7-spark gap; 8-decoupling inductance; 9-liquid charging resistor 10-resistor of spark gap control circuit; 11-insulator; 12-magnetic coil;13-accelerating tube support; 14-accelerating tube; 15-power supply of magnetic coils.

3.Pulse voltage generator. Marx generator is schematically shown in Fig.3. Generator stages have been made as a nonuniforme pulse forming lines to create a flat top of a voltage pulse on the nonlinear load. The load consist of an electron beam impedance,resistors of charging Marx generator capacitor circuits and inductive circuits for charging capacitors of a magnetic coil power supply. The use of 0.4μF capacitors in the Marx generator stages allows to form a high voltage pulse with a flat top duration of about 20μsec.

4.Pulse duration control device. A special device to control current beam pulse duration by falling down an injector voltage and hence stopping an electron emission from the cathode,was developed. Its operation is based on the effect of rapid change of an inductance of a choking coil with an iron core at the moment when current,flowing through the choke,reaches the value sufficient for the iron core saturation,thus causing the start-up of a cutting spark gap. A remote control of a beam current pulse duration is possible.

5.Injector. An injector with a multipoint explosion emission cathode is used for an electron beam production. Such a cathode,as

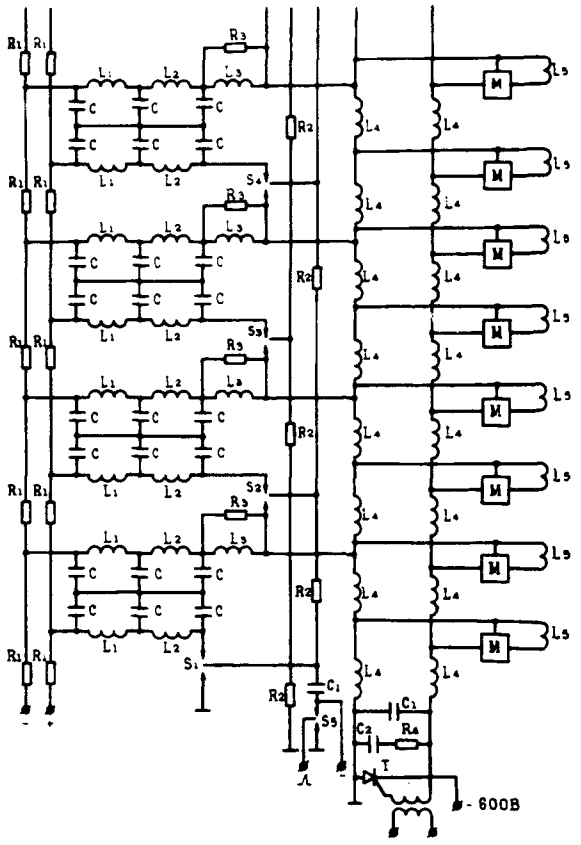

Fig. 3 Electric circuit of accelerator.

mentioned above, allows to produce electron beams with highly stable parameters in the long pulse mode. Fig. 4 shows an injector with an annular multipoint cathode and Fig. 5 shows general view of the cathode. The injector is designed as a triode, offering better cathode operation and possibility of a beam current changing at constant injector voltage. A cathode emission surface is 490cm^2. So the current density at the cathode is 2-4A/cm^2, if the beam current is 1-2kA. Highly stable operation of the multipoint cathode is well known at such current density in the cours of tens microseconds.

To form an electron beam we use electric and magnetic fields, the latter increasing in the beam propagation direction from

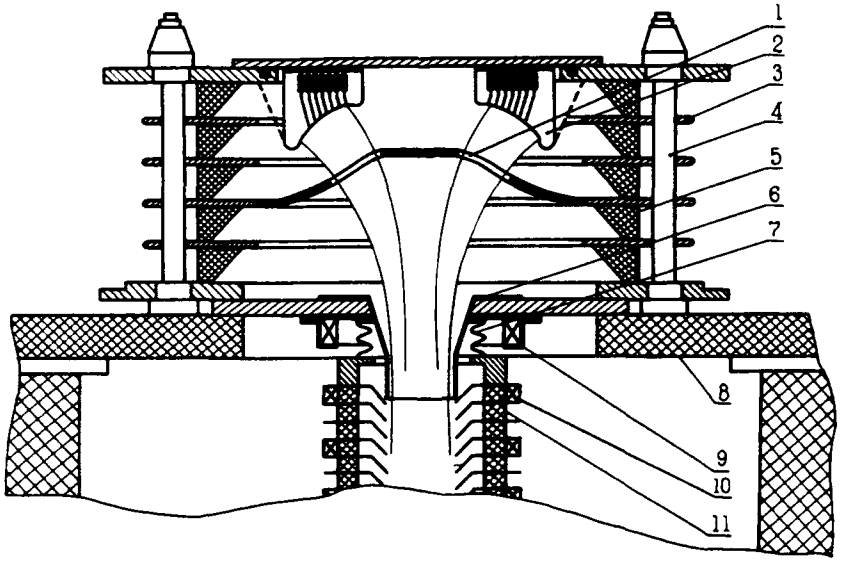

Fig. 4 Electron injector. 1-grid, 2-cathode, 3-gradient ring, 4-tightening pin, 5-annular insulator, 6-anode, 7-bellows, 8-injector support, 9 and 10-magnetic coils, 11-accelerating tube

cathode to anode. Magnetic field in the injector is generated by a series of coils placed behind the injector anode. For more effective extraction of an electron beam into an accelerating channel, a very careful choice of electric and magnetic field shapes is needed. PIC simulations of electron trajectories allowed us to solve this task. Pay attention to the fact that the beam

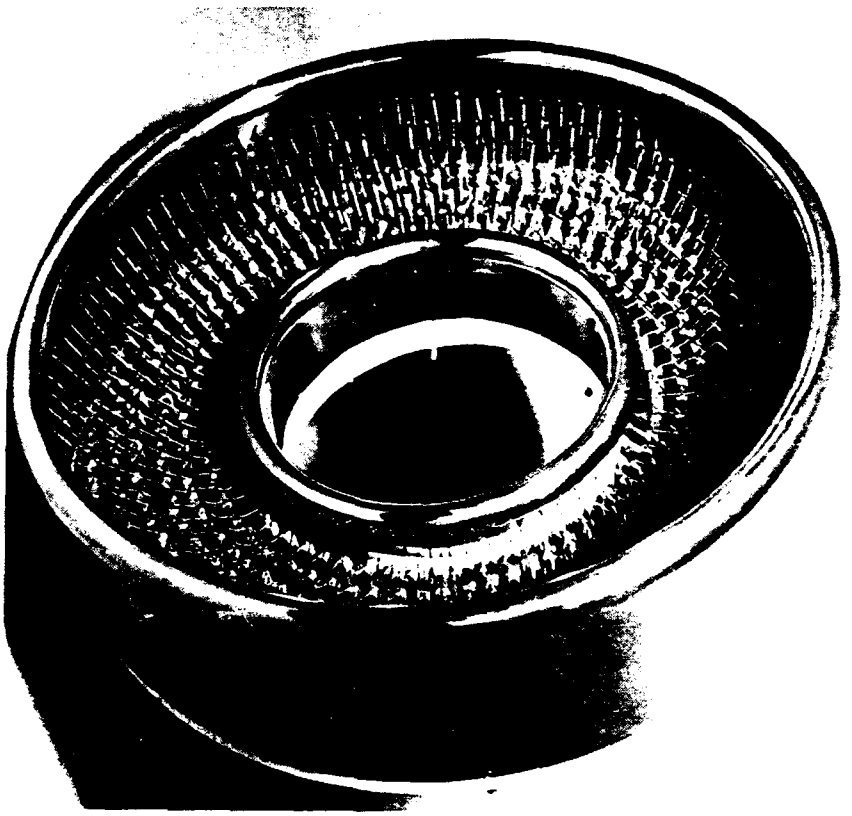

Fig. 5 Multipoint cathode general view.

formation efficiency strongly depends on magnetic field intensity. As a result of trajectory analysis, it was shown that there is no leakage of a beam current at the injector anode when the magnetic field intensity in the accelerating tube is $B_{max} > 2.5$kG and that on the cathode is $B_c > 150$G. At $B_{max} = 0.65$kG the anode current leakage reaches the value of 33% of the total beam current.

6.Magnetic focusing system. Magnetic system is used for an electron beam formation in the injector,its transport through the accelerating tube and its focusing at the end of the electron trajectory. The main peculiarity of the magnetic system is that the most part of the magnetic coils are under high accelerating voltage. So we face the problems: to provide necessary electric strength of the magnetic system elements being under high accelerating voltage; to decouple the power supplies of low voltage magnetic coils and high voltage Marx generator; to decrease the magnetic system effect on the Marx generator operation.

The analysis of alternative magnetic systems suggested that the best choice was that,consisting of a large number of magnetic coils,each having its own power supply. The coils are placed directly on the dielectric accelerating tube rings with the pitch of 75-100mm. The magnetic system originates a magnetic field >2kG on the accelerating tube axis with the field nonuniformity 3%.

An output unit is the specific part of the magnetic system. Its possible design versions depend upon the electron beam application. In particular,one of the output unit allows to transport an electron beam to the required place and compress it up to 2cm in dia on the target. The total length of the output unit is 1.7m. The magnetic field increases from 2.3kG in the uniform region to 28kG on the target. Magnetic coils are supplied from a grounded capasitor battery (3kV,4.2μF).

7.Electron beam propagation through the accelerating channel. As a result of an electron beam propagation through the long accelerating channel the effects connected with a residuel gas ionization and growing a number of different beam instabilities could be manifested. The calculations performed by now show that electron beam instabilities such a diocotron and Buneman instabilities do not appear in the beam of our accelerator. The residual gas under $5*10^{-5}$Torr can provide an ion current density of 0.03A/cm^2. Such a high current value of high energy ions and the possibility of ion focusing near the axis region [4]can strongly affect the injector operation. This negative influence can be decreased by using a multipoint cathode with annular emission surface.

8. Conclusions. At D.V.Efremov Institute a high-current electron accelerator "SIRIUS" is under construction. It is designed for an accelerating voltage of idle running of 5MV and 2.5MV in the matched mode, a beam current of 2kA, a total pulse duration of 50μsec and a flat top pulse duration of about 20μsec. A triode injector with a multipoint explosion emission cathode is used for an electron beam formation. An electron beam is accelerated in 8 accelerating sections each consisting of one sectionalized accelerating tube, four Marx generator stages and a series of magnetic coils. Each of these coils is supplied from a separate power supply positioned under a proper potential of a high voltage structure. The remote control of an electron beam pulse duration is performed by a special device that falls down an injector voltage. The high voltage structure is placed inside the tank, 3m in dia and 11.4m in height. Formed and accelerated azimuthally-uniforme electron beam, 8cm in external diameter, can be transformed depending on the application. For example, it can be compressed under magnetic field up to 2cm in dia. Preliminary tests of the injector with one accelerating section have shown a good agreement between designed and experimentally tested parameters of the accelerator.

REFERENCES

1. V.G.Kovalev et al., in Proc. of the 7 Int. Conf. on High-Power Particle Beams, Karlsruhe, Germany, v.II, pp.1037-1041, 1988.

2. M.A.Vasilevsky, I.M.Royfe, V.I.Engelko. ZhTF, v.51, No6, pp.1183-1194, 1981. (In Russian)

3. V.G.Kovalev et al., Pisjma ZhTF, v.14, No12, pp.1112-1116, 1988. (In Russian)

4. V.I.Engelko et al., in Proc. of the XIV Int. Symp. on Discharges and Electrical Insulation in Vacuum, Santa Fe, USA, p.636, 1990.

Inductive Pulsed Power Source for Plasma Radiator.

B.D.Yankovskiy
Russian Academy of Science, Institute for High Temperature
127412, Moscow, Russia

INTRODUCTION. The current feeded plasmadynamic discharges is used for generation of wide range radiation [1]. Such discharges have variable inductivity and resistivity. Therefore they require the definite power source in order to the energy transfer had high efficiency. It's known that inductive stores have the greater specific energy capacity as compare with capacitive stores and the better agreement with variable inductive load. It's associated with the facts, that the energy transfer to the variable inductive load from inductive store is defined by the ratio of them inductivities and one from capacity store is defined by the current difference of the capacitive and the load induced EMF. Therefore for feeding of the plasma flow switch based plasma radiator was designed the inductive pulsed power source with the current multiplication of sectioned inductive store and with the utilisation of the explosive switching technology.

This report deals with the description of the design and the parameters of the store and the switches and the test results of model source, in which the energy scale is 1:20.

ELECTRIC SCHEME. Multiplication of the current might be realized either by simple recommutation of inductivity from series to parallel circuit, or by transformer effect (fig.1). The first method with high multiplication coefficient requires lots of commutative equipment, and second one is fraught with high commutative overvoltage of the primary circuit during energy feeding into the load. It seems relevant to use both methods in combination (fig.2). Thus the energy source scheme has N inductivities, each of them is formed by n turns with magnetic connection. Each of N inductivities has a tap from the last turn to connect the load current shorter SS, which is common for all inductivities. During feeding by the current all inductivities are connected in series with the help of the opening switches OS1. At the current maximum the load current shorter SS is connected to n turns of each inductivities with the help of closing switches $CS1_1$

and $CS1_2$ and then opening switches OS1 break down series of inductivities. After the end of the transition process the last turns of each inductivity is connected to the load current shorter SS with the help of closing switches CS2 and opening switches OS2 commutate the current to the shorter once more. The shorter SS may connect up the load at any moment of transition process, providing for the required form of the current pulse. N inductivties may be with mutual magnetic connection. Such scheme and current multiplication process have elevated energy capacity and efficiency of energy feeding [2, 3].

INDUCTIVE STORE. The design of an inductive store should correspond to a number of specific demands of an electric scheme, energy accumulation and feeding,load and exploitation. They include the necessary mechanical strength and dynamic stability, higher time decay in the initial state, large coefficient of transformer coupling, minimal inductivity in recommutative state, high conductivity of the conductor of the store, high electric strength. According to this demands the store is designed as a toroid (fig.3), made by 16 D-shaped coils with winding of flat copper bus 70 20 mm with a central outlet of 12 mm in diameter for cooling with liquid nitrogen up to 100 K. Each coil has 4 turns isolated for the voltage 50 kV, with a tap from the last outer turn. The carrier-bandage of each coil is formed by glass-epoxy isolation. The coil are fixed on a support cylinder and are connected over the outer diameter of the toroid by dielectric distance-pieces. The inner diameter of the toroid is 600 mm, the outer one is 1800 mm, the height is 700 mm. The toroid in the volume of 2300 mm in diameter and 1300 mm in height. The leads of the coil are placed upward. With electric bridges 16 coils form 8 separate inductivities.

OPENING SWITCH OS1. The requirement to the opening switch OS1 are conditioned by the necessity of a prolonged current leakage during the energy accumulation, fast voltage generation during the breaking of series inductivities, retaining the commutative overvoltage at the primary winding under feeding energy to the load or during energy transformation in the load.

All these requirementsmust be satisfied by a two-step explosive

opening switch (fig.4), where the functions of prolonged current leakage and fast voltage generation are divided. The first function is ensured by a wall of an aluminium tube 90 mm in diameter, 200 mm long and with wall 4 mm thick squeezed between two electrodes on diametrically opposite generating lines of the tube. Inside the tube there is a dielectric cylinder with six longitudinal slots 2 mm deep and 10 mm wide for placing the linear HE charge. Outside the aluminium tube opposite and between the slots there are placed bronze knives and rests, on which the tube wall destruction is realized during the HE charges explosion. The function of voltage generation is ensured during destruction of the aluminium foil 0,3 mm thick on ribbed dielectric obstacle during the explosion of half-disc HE charge take placed with a certain delay after the destruction of an aluminium tube of the first stage. Mass of summary HE charge of this opening switch is 50 g. The proper resistance is 6-10 μOhm. Both functional stage of the opening switch are placed in an indestructible glass-epoxy cylinder with outer diameter 220 mm for protection of the outer equipment.

OPENING SWITCH OS2. This opening switch, as the second stage of the opening switch OS1. is not difficult for project, as it is already well investigated [4] with lesser current densities. The draft of the opening switch is shown on fig. 5.

CLOSING SWITCHES $CS1_1$, $CS1_2$ and CS2. Closing switches $CS1_1$, $CS1_2$ and CS2 are meant for operative switching the store inductivities to the load current shorter or the load. This is accomplished by the destruction of polyethylene isolation between potential electrodes during launching of the neutral conductor by the HE detonation products. Working conditions of all closing switches are different , but the same structure has be used (fig.6).

LOAD CURRENT SHORTER. The process supervises, that the load current shorter should sum the total current in the process of two commutations, afterwords it should quickly increase the voltage for current feeding to load. With this aim we plane to usea plasma flow switch [5, 6], modified for a more prolonged process of current multiplication. Probably, it should include several stages and be less rapid (fig.3). Anyhow, the structure of a plasma flow

switch with prolonged period of current accumulation demands a detailed research.

ENERGY SOURCE STRUCTURE. Meeting the requirements of minimal spurious inductivity the load current shorter SS is fixed on the toroidal inductive store on the coil leads collector with opening switches OS2 and closing switches $CS1_1$, $CS1_2$ and CS2, which are placed there (fig.3). 8 opening switches OS1 are placed on the periphery of the store. The overall height of the energy source is 2000 mm, diameter 2500 mm, mass 6000 kg.

MAIN PARAMETERS. The initial inductivity of the energy source is 160 μH, the final one is 150 nH, the time decay is 1 sec. Feeding current is up to 300 kA, energy capacity to 7 MJ, current in the shorter 5 MA. Voltage of current multiplication is 20 kV, time of current multiplication is about 20 μsec. The suggested voltage in the load current shorter is 100 kV, timerise is about 1 μsec.

EXPERIMENTAL MODELLING. In order to work out the conception of the energy source was created a toroidal 8-sectional inductive store with inner and outer diameters 600 and 1400 mm and 500 mm height. The store inductivity is 120 μH, time decay is 10 msec. In the recommutative state the store inductivity is 70 nH, with connected shorter one is 100 nH. The store may be accumulate of 60 kA current. For current commutation we have used explosive opening switches with arc forcing out from the electrode system by the detonation products [4] and explosive closing switches. The voltage of commutation was 5 kV. An explosive opening switch with arc compression on dielectric wall was used as a shorter. After two-stage multiplication of current we got a summary coefficient of multiplication 17. Commutation of the total current to equivalent load was realized with a voltage in the shorter 50 kV.

REFERENCES

[1] P.J.Turchi, J.F.Davis, M.L.Alma et al. - Generation of High-Energy X-Radiation Using a Plasma Flow Switch. - J. Appl. Phys. 69(4), 15 February 1991, pp. 1999-2007.

[2] E.A.Azizov, A.P.Lototskiy - Structure and Optimal Parameters

of Sectional Inductive Stores for Pulsed Feeding of Large Magnets. - "Electrichestvo", 1990, 3, pp. 25-31.

[3] O.Zucker, J.Long, K.Linder et al. - Inductive Energy Transfer Circuit Proof of Principle Experiment. - Rev. Sci. Instrum. - 1986, v. 5, N 5.

[4] B.D.Yankovskiy - Once More about Explosive Opening Switches. - in the Proceedings of the 8th IEEE Pulsed Power Conference. San-Diego, California, June 17-19, 1991

[5] G.A.Tripoli, P.J.Turchi, D.Conte, S.W.Seiler - Design and Operatin of a 0,4 MJ Current Multiplier Inductive Store with Multiple Exploding Foil Switching. - in the Proceedings of the 5th IEEE Pulsed Power Conference. Arlington, VA, 10-12 June 1985, New-York, N.Y. 1985, pp. 22-25.

[6] M.L.Alma, B.Bird, C.Boyer et al. - High Voltage Pulse Generation in 10 MA Plasma Switch Experiments. - in the Proceedings of the 6th IEEE Pulsed Power Conference. Arlington, VA, June 29 - Yuly 1, 1987. New-York, N.Y. 1987, pp. 684-687.

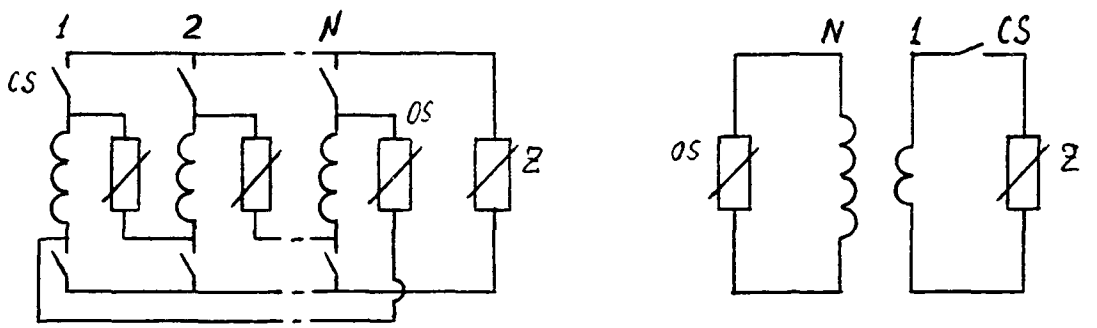

Fig.1. Possible schemes of current multiplication.

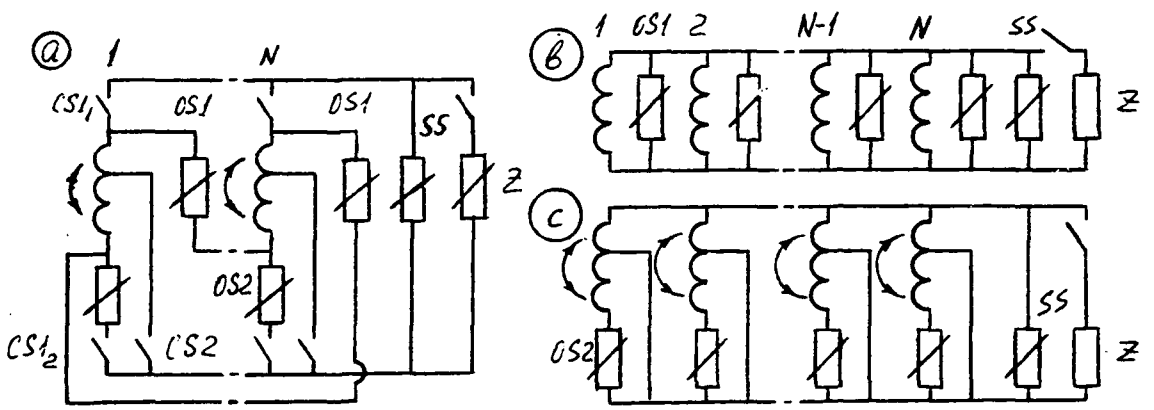

Fig.2. Electric scheme of energy source: a - general one; b - during first commutation; c - during second commutation.

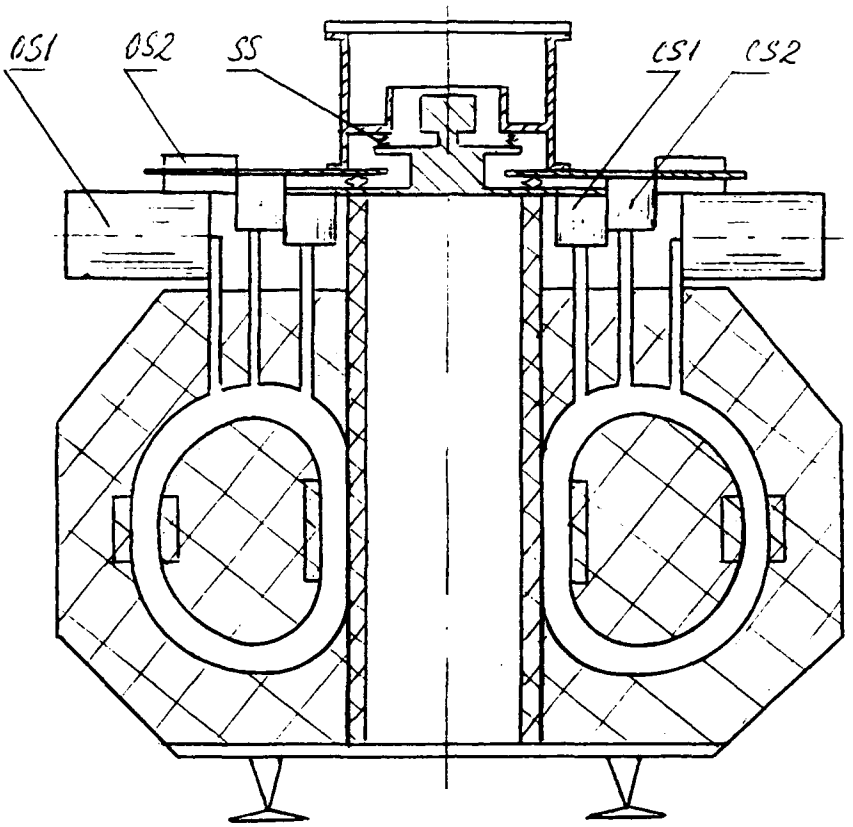

Fig.3. Draft of the inductive pulsed power source.

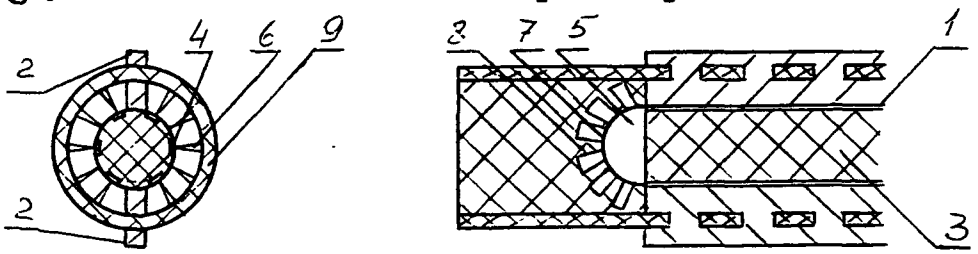

Fig.4. Draft of the opening switch **OS1**: 1-aluminium tube; 2-electrodes; 3-dielectric cylinder; 4-longitudinal slots; 5-high explosive; 6-bronze knives; 7-aluminium foil; 8-ribbed dielectric obstacle; 9-glass-epoxy cylinder.

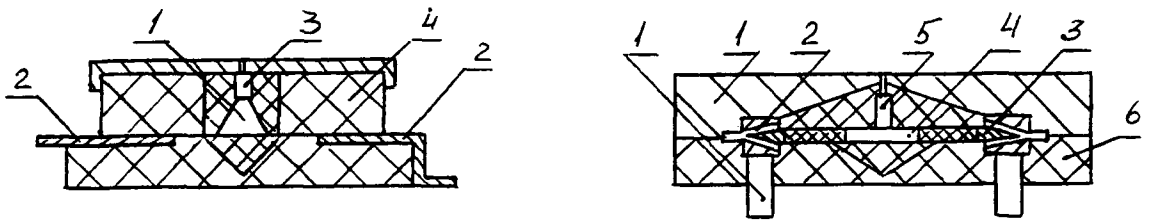

Fig.5. Draft of the opening switch **OS2**: 1-high explosive; 2-electrodes; 3-detonator; 4-body.

Fig.6. Draft of the closing switches: 1-electrodes; 2- polyethylene isolation; 3-launching conductor; 4- high explosive; 5-detonator; 6-body.

SUPER-POWER ACCELERATOR FOR MICROWAVE ELECTRONICS.

Batskikh G.I., Kazansky L.N., Oreshin A.A., Samarsky P.A., Seleznev V.D., Sinelshikov A.V., Khomenko A.I. (Moscow Radiotechnical Institute of Russian Academy of Sciences), Bugaev S.P., Kovalchuk B.M., Koshelev V.I., Mesyats G.A. (High Current Electronics Institute of Russian Academy of Sciences, Tomsk), Petelin M.I. (Institute of Applied Physics of Russian Academy of Sciences, N.Novgorod).

Abstract. High-current accelerator of Moscow Radiotechnical Institute of Russian Academy of Sciences is utilized in relativistic microwave electronics. The experimental setup is composed of high power multimodule Marx generator on 1.5 MJ, 3 MV; two electron diodes with the beam magnetic transportation channel; vacuum-technological facility with the chamber of 400 m^3 volume, 3 m in diameter and working pressure of 10^{-6} Tor. Autonomous and combined channel operation are available.

1. Introduction.

First beam channel was put into operation in 1983. Microwave radiation generated by carcinotron was transported to the vacuum chamber (Fig.1). In 1984-1986 the limiting beam parameters were obtained: 2.6 MeV, 50 kA, 1.5 μs; microwave radiation transmission and focusing were carried out into the vacuum chamber. In 1987--1991 the setup was considerably modified: the electron beam front sharping had been performed; the second beam channel was installed; the combined channel operation was provided; the microwave radiation extraction into the atmosphere was realized.

By now the microwave radiation pulses of 1.5-2,0 GW in X-band with duration of 50-60 ns were obtained.

2. Marx generator.

Marx generator has a metal tank of 10 meters in height. On top of the assembly up to 25 modules are inserted into the tank's cells. Each of modules consists of 38 cascades with the charge voltage up to 85 kV and power capacity to 55 kJ. Module is commutated with the help of three-electrode inflated dischargers.

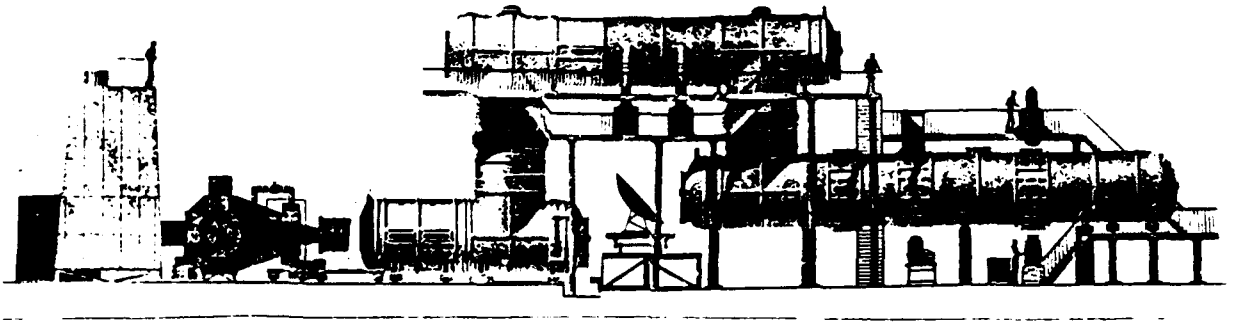

Fig.1 Experimental setup configuration.

Module construction of Marx generator provides high reliability and fast repair, enables to change discharge current, power capacity and to reduce the inductance of Marx generator.

As a rule only 8 modules (total inductance of 8 μH and shock capacity of 0.08 μF) are used for beam experiments. The characteristic pulse front duration of Marx generator voltage is about 200 ns; the shortening discharger (trigatron, 3 MV, 1 MA) comes into action in 0.5-1.5 μs. So generator formes voltage pulse of required duration with a plateau up to 3 MV.

3. Accelerating tubes and beam transportation.

The accelerating tubes of both channels are performed identically: sectional cylindrical insulators of 2.3 m in lengh with inner diameter of 1.5 m consist of 24 gradient coils. At the tube exit there is a cathode holder of 30 cm in diameter which has a conical transition to the field emission cathode.

The electron beam is transported in axial magnetic field of 1.0-3.0 Tl at a distance of 1.5-2.0 m. Both sectional and profile solenoids coiled around the drift tubes may be harnessed.

A sectional capacitor battery (9 MJ, 4.5 kV) is used for solenoids power supply. Capacitors on 5 kV, 200 μF are gathered in blocks taken 12 at a time, each of 324 blocks is commutated by the assembly of 6 tiristors. Sinusoidal pulse of the magnetic field has a duration of 10-50 ms.

4. Beam research.

The basic beam investigations has been carried out with a front duration of 150-200 ns. The forming and transportation of the beam, the transverse expansion of the cathode plasma, the cathode and magnetic self-insulation lines performance at the microsecond pulse duration have been examined.

Some basic results are as follows:

- the beam on 200 kJ and 2.6 MeV, 50 kA and 1,5μs is obtained;
- at the diode voltage more than 1.2 MV two coaxial tubular beams are observed (at the voltage more than 1.6 MV - three beams), as this takes place there are no ledges on the cathode assembly;
- at microsecond pulse durations the effective magnetic self-insulation is possible, beam current value agrees with the calculated minimum one;
- the cross-section expansion rate of the cathode plasma at the pulse front doesn't exceed the value of 0.2 cm/μs, at the pulse slope it has increased up to 2-3 cm/μs.

5. Two-channel accelerator and pulse front sharpening.

In order to increase the experimental capabilities of the setup and to provide the microwave radiation research both in vacuum and in atmosphere the two-channel alternative accelerator was designed (Fig.2,3).

Two identical channels are supplied from the same Marx generator, the transition from one channel to another is carried out by means of the mechanical switches (S1,S2) which combine the turn off with earthing of the unused channel, or by locking the sharpening SF_6 - dischargers (SD1,SD2).

Power capacity surplus of Marx generator was utilized for the beam front sharpening. Some part of Marx generator discharge current from the circuit with the inductance of 10 μH is switched to the diode, the duration of the beam front is 10-12 ns.

In order to supress the oscillations at the beam current pulse top the damped resistors are connected in series with the diode. Autonomously in each channel as well as when both channels

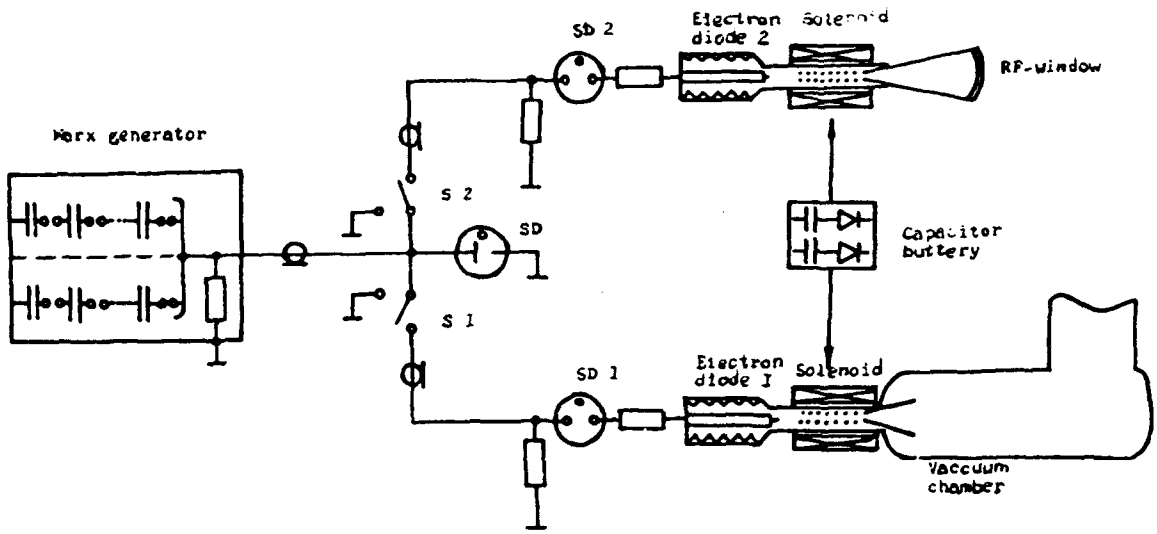

Fig.2 Two-channel accelerator scheme.

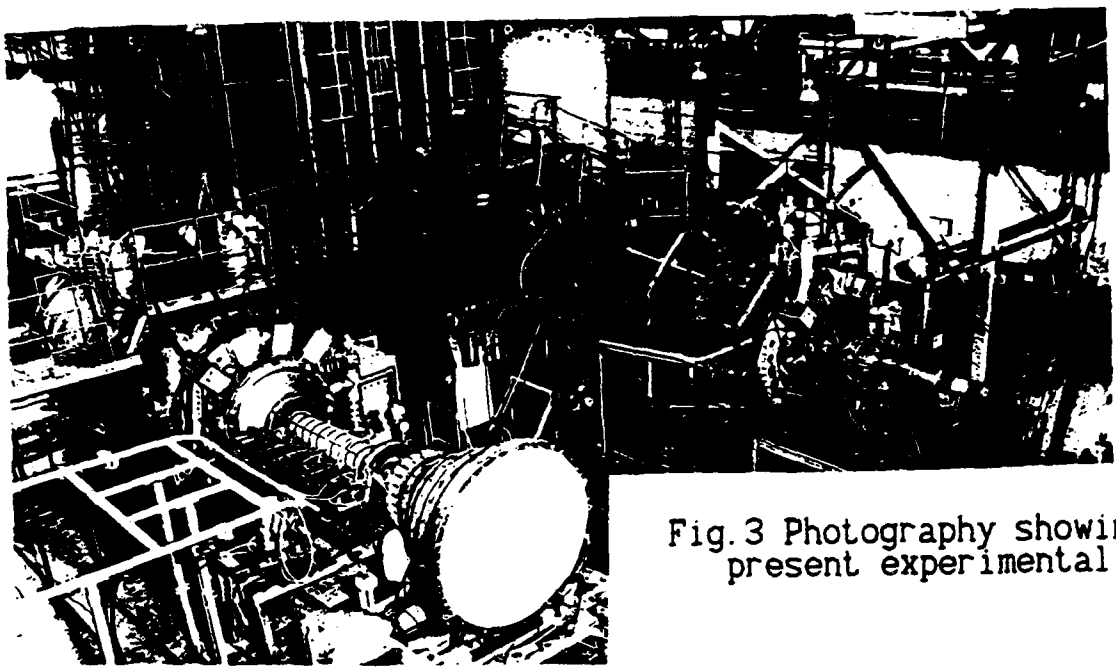

Fig.3 Photography showing the present experimental setup.

operating simultaneously the identical parameters of the electron beam and microwave generation are obtained (Fig. 4).

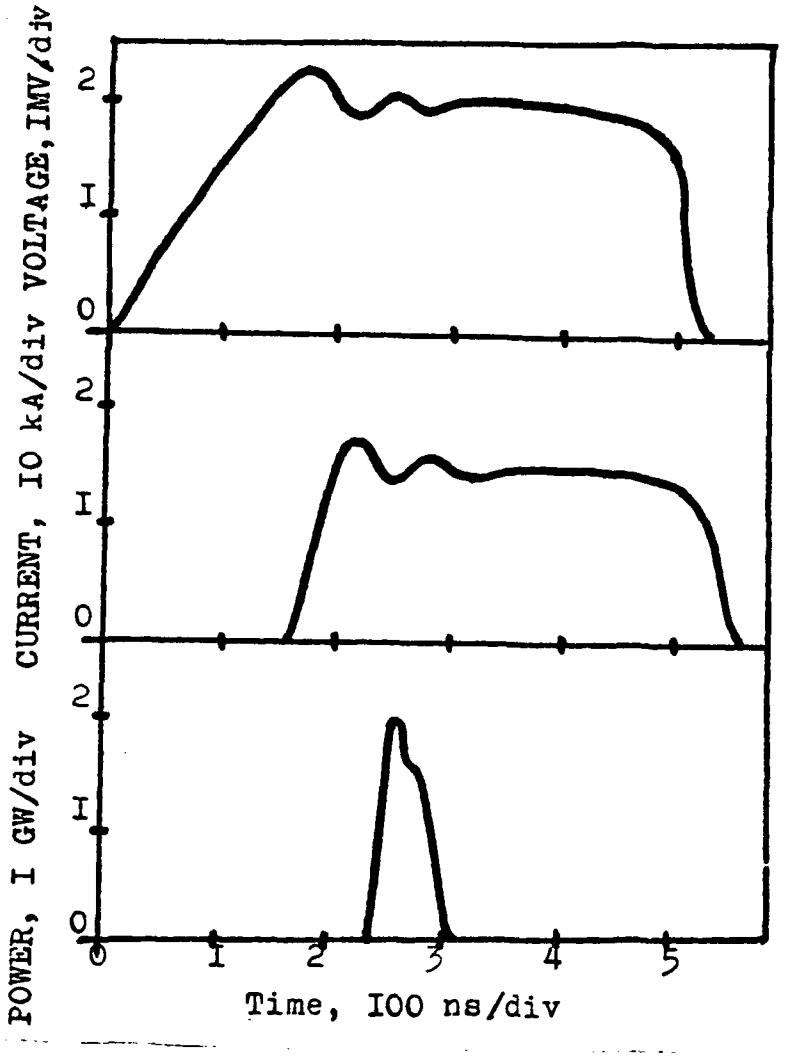

Fig 4 Supplied voltage, beam current and microwave power signals.

The conditions of channel's synchroneous operating are provided with an accuracy of better than 20 ns at the cost of the sharpening discharger steady functioning. Microwave radiation of the second channel is extracted into the atmosphere by means of a horn with exit aperture of 2.0 m closed with a spheroidal polyethylene window. The approaching magnetic coil provides the field casp preventing the electron bombardment of the window. The total current on the window is not more than 50 A. On extraction of microwave radiation (1-2 GW) with a cycle of 1000 pulses the window remains damage free.

6. Relativistic microwave generators research.

Several types of generators have been investigated: carcinotrons on the pulse power up to 2 GW in X-band with pulse duration to 100 ns; sectional cherenkov generators (1 GW, X-band, 60 ns); reditron (100 MW, X-band, 100 ns).

Some exerimental phenomena should be noted:

- in regimes of short beam front (less than 15 ns) for all the types of generators being under investigation we have observed the radiation delay at about 30-40 ns, when the beam pulse duration makes up 50 ns the generation is not observed;
- the first channel voltage modulation (voltage drop is about 15--20 %) by manner of turning on the second beam channel provides the decrease of microwave pulse duration from 10 to 60 ns, so it makes possible to control the microwave pulse duration.

By now we undertake reasearch into vircators and cherenkov generators which are functioning with high currents in multimode regime.

IGUR-3 - POWERFUL BREMSSTRAHLUNG RADIATION PULSE GENERATOR

V.S. DIVANKOV, A.I. KORMILITSIN, V.P. KOVALEV

National Institute of Technical Physics
454070, Chelyabinsk-70, P.O. Box 245, Russia

Electron accelerator IGUR-3 belongs to class of direct drive accelerators and is used for radiation investigations. Simplified electric scheme of accelerator is presented in Fig.1. Inductive energy store with wire-explosion switch is used to formation of high-voltage pulse. Accelerator IGUR-3 is located in room with sizes 24×18×12 cub. meters. Accelerator construction is drawn in Fig.2. Total high is 8.5 meters, largest diameter is 7.5 meters. IGUR-3 is the first IGUR-type accelerator in which transformer oil is used as insulator of high-voltage units. The most important units of installation are:

- Marx generator;
- pulse forming system (PFS);
- electron beam diode;

Marx generator of IGUR-3 consists of two parallel working units with the same charge scheme. Units are located symmetrically each other and PFS tank in loop-forming container. The using of two parallel units, the way of its arrangement and location in container allow to create generators with relatively small inductance.

The generator parameters are:

- capacitor charge voltage is 85 kV;
- stored energy is 320 kJ;
- number of stages are 17;
- inductance is 2 μG;
- output capacity is 0.28 μF;

The generator contains of 34 gas switches. First switch is common for two generators. It is a trigatron type. It supplies simultaneous start of the units.

Energy transmission from generator to pulse forming system is carried through passing insulator located on PFS tank (fig.2). Insulator's construction allows to work without breakdown.

PULSE FORMING SYSTEM CONSTRUCTION

PFS forms current and voltage pulses with required parameters on the load.

PFS consists of:

- stored inductance;
- wire-explosion array (wires are located in polyethylene tubes and explore in air);
- sharpening switch which consist of two electrodes with oil insulation between electrodes.

PFS is located in 2-m diameter and 8.5-m high tank. PFS construction completely satisfies to requirements as for work secure as to forming work voltage pulse.

SHARPENING SWITCH

The switch is the two electrode construction. High-voltage steel electrode is 60 mm in diameter. The plane flange is the second electrode. The switch allows to form voltage pulses with front ranging from 15 ns to 150 ns.

DIODE

The diode is located in transformer oil tank together with PFS (see Fig.4). The highest electric strength is 45 kV/cm. Diode insulator is made a sectional. It is accembled from kaprolon rings (1) with 40-mm width and from aluminum gradient rings (2) with 3-mm width. The gasket between gradient and kaprolon rings is made from oil-proof rubber. Electric breakdown probability is decreased by kaprolon ring. It has 45 degree bevel. Insulator is fixed on flange (4) by four kaprolon ties (5) 60 mm in diameter. Aligning electric potential at the diode insulator is achieved by installing shield on high-voltage electrode. The shield (6) is 1400 mm in diameter and 140 mm height. Cathode (7) is made as a cone 1595 mm height with top angle of 25 degree for inductance reducing. The diode container is 1200 mm in diameter and 600 mm height. It is made from steel 10 mm width.

The diode provides 6 MV voltage pulses with currents up to 90 kA. Longtime diode usage experience (more than 20000 pulses) with electric strength about 35...45 kV/cm on insulator surface shows a high construction reliability.

IGUR-3 accelerator is used as electron beam pulse generator with following parameters:

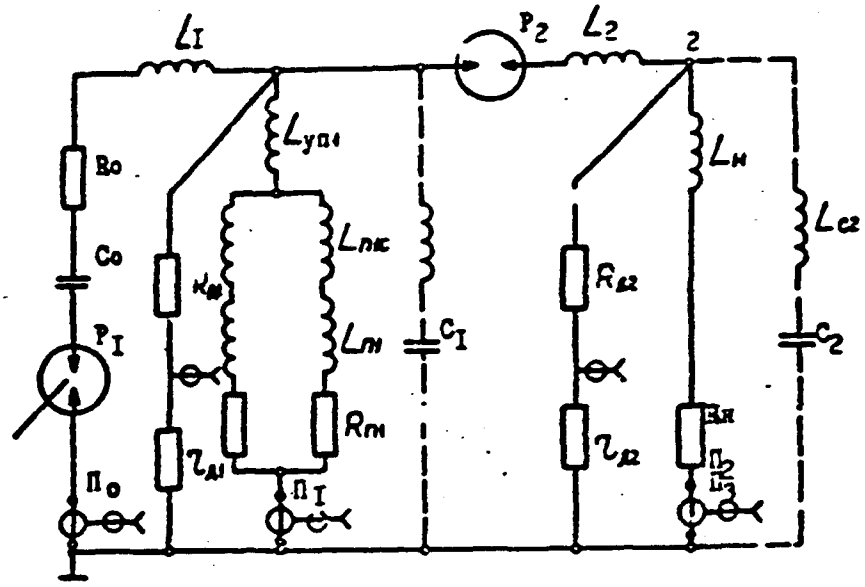

FIG.1 The principal scheme of pulse highvoltage electron accelerator IGUR-3.

C0 - shock PVG (Pulse Voltage Generator) capacitance;
C1,C2 - spurious capacitance in circuit;
L1,L2 - Exploding Conductor (EC) circuit inductance and loads;
Lnlc - inductance constant component of EC cascade;
Ln1 - EC inductance varying component;
Leg1 - inductance of EC hooking-up unit;
Ly - load inductance;
Ry - load active resistance;
Rl1,rl1,Rl2,rl2 - voltage diviver;
Rg1 - EC active resistance;
R0 - PVG circuit active resistance;
P1,P2 - commutating discharges;
G1·G2·G3·G0 - Rogovsky contures.

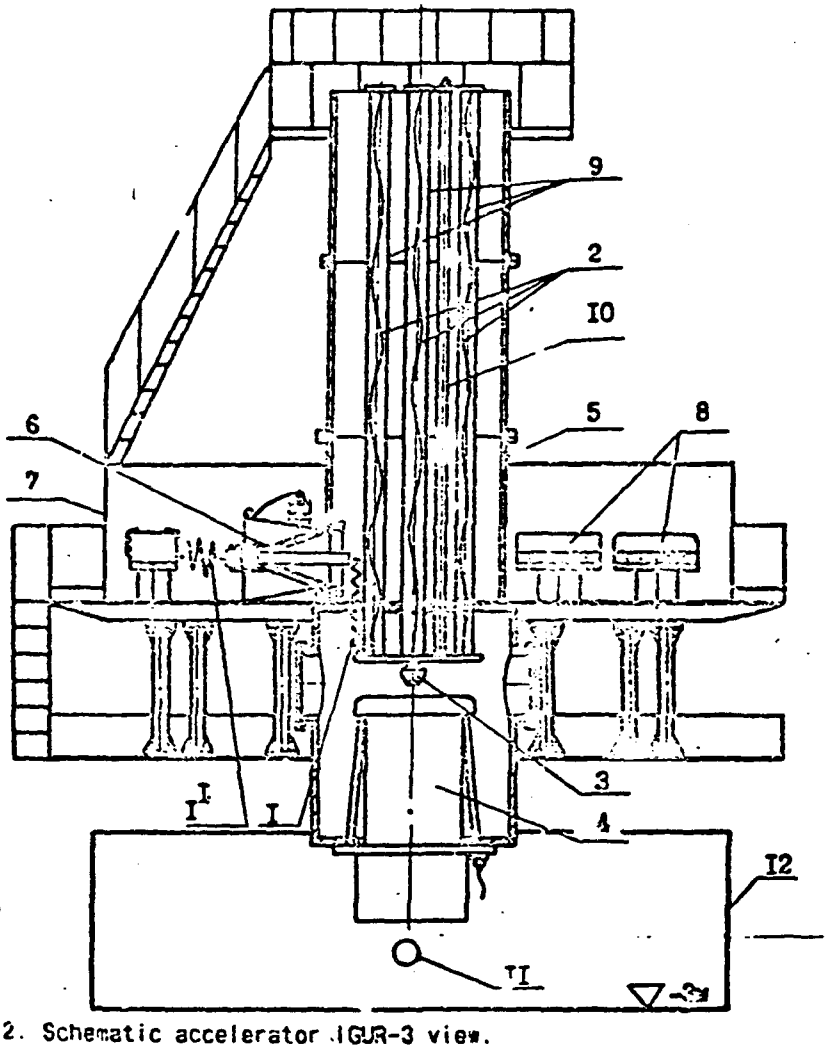

Fig.2. Schematic accelerator IGUR-3 view.

1. 1^1 - inductive store;
2 - exploding conductors;
3 - sharpen discharge;
4 - accelerating tube;
5 - PFS tank;
6 - passing insulator;
7 - PVG container;
8 - PVG;
9 - polietilen tubes;
10 - EC voltage divider;
11 - object under study;
12 - shielding box.

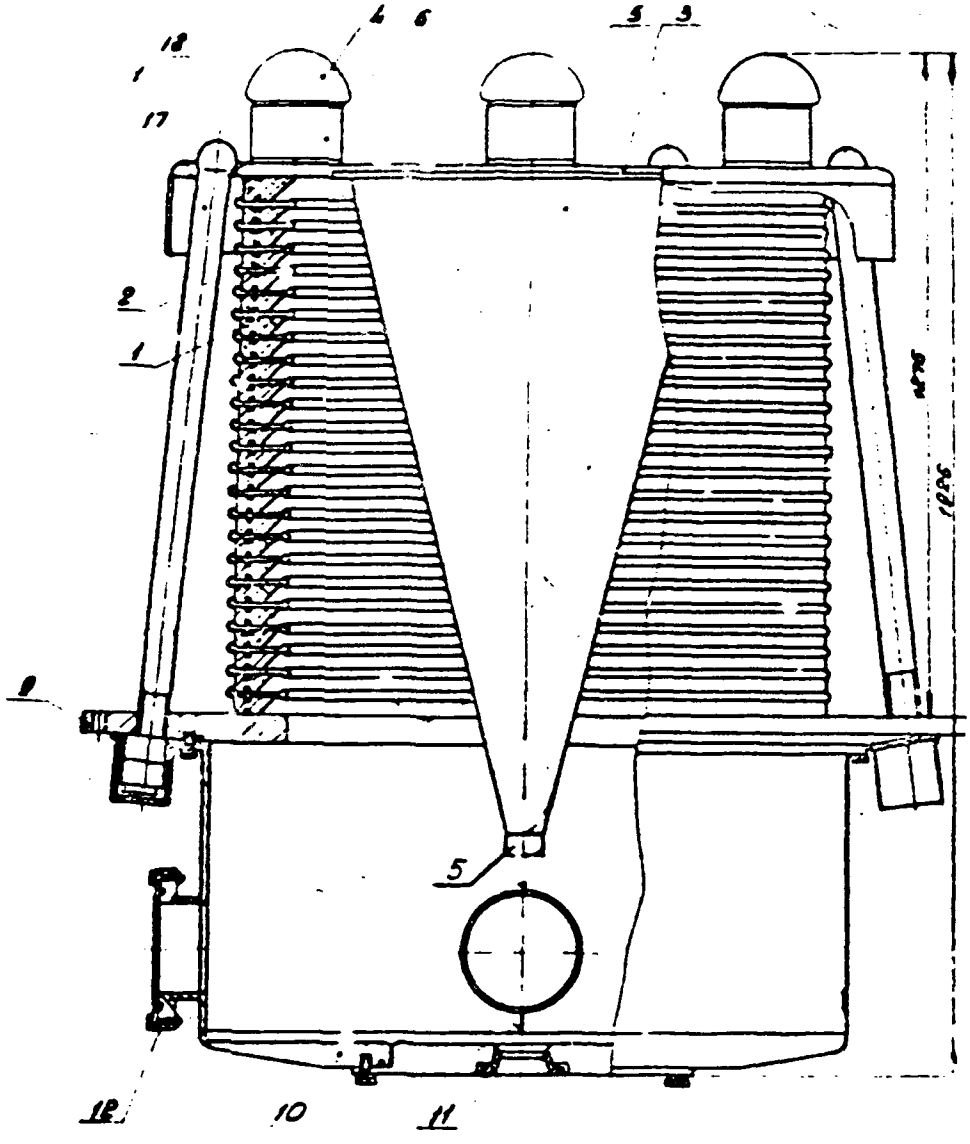

FIG 3. - accelerating tube.

- wavelength from 30 ns to 300 ns;
- total energy of electron beam taking out to atmosphere is about ~20 kJ;
- maximum energy density on the beam axis up to 300 J/cm^2.

Accelerator has following parameters in mode of gamma-ray pulse generation:

- pulsewidth 15...150 ns;
- maximum dose rate in the anode plane (S = 1 cm^2) up to 10^{13} Rads/s.

Izodoses map of gamma-ray generation is shown in Fig.4. Dose rate along beam axis vs. distance from target plane (anode) is shown in Fig.5. Accelerator is used during 14 years. High security of its construction is demonstrated for the time. High radiation characteristics for this accelerator class with good pulse reproduction are recieved.

The authors would like to express their sincere thanks to Dr. Luchinski A.V. for the large contribution of the first stage of the installation creating. Also it is necessary to note the substantial contribution of Martynov V.I. to designing and setting-up of installation.

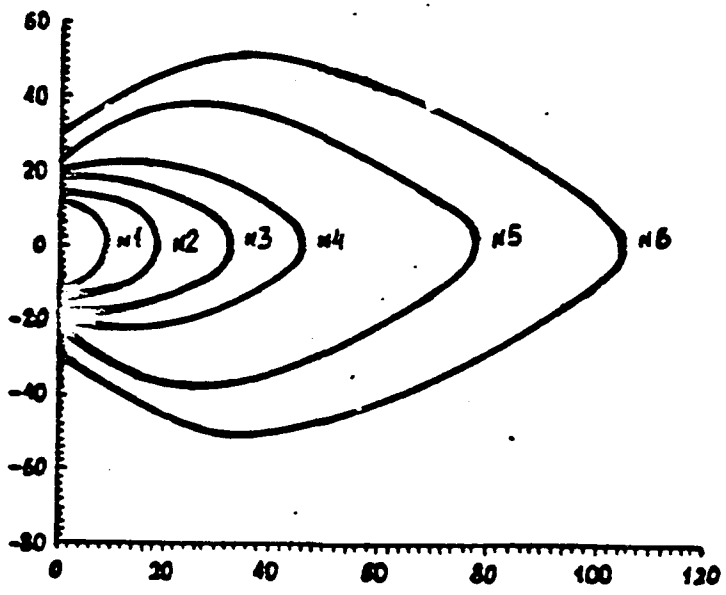

FIG.4. - izodoses in one of regimes.

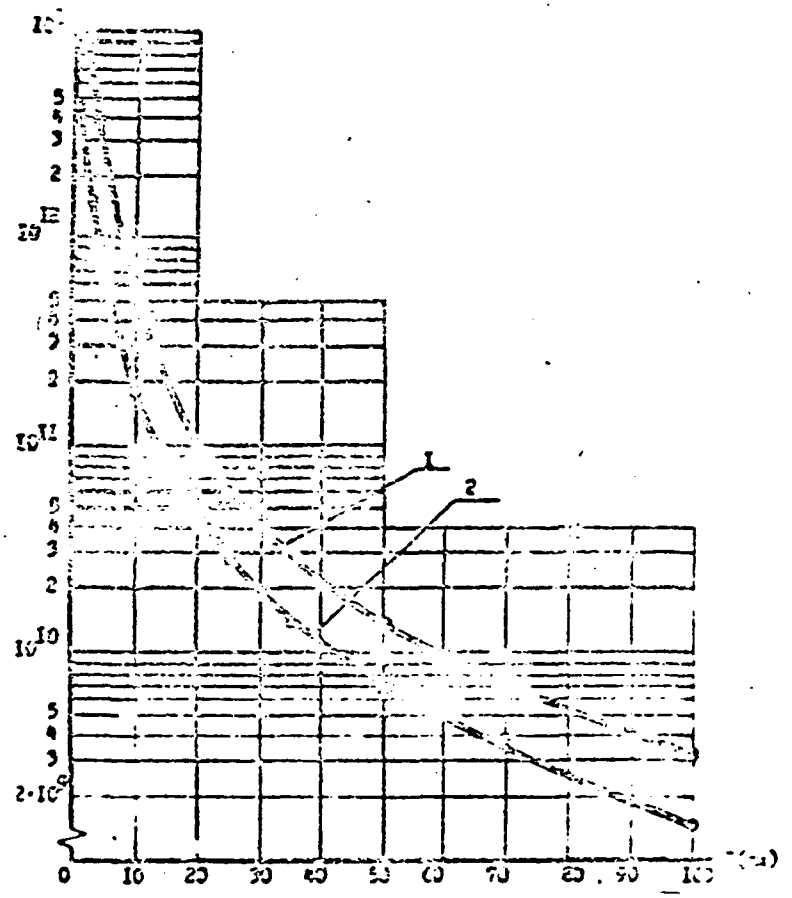

FIG.5. - dose tension along beam axis.

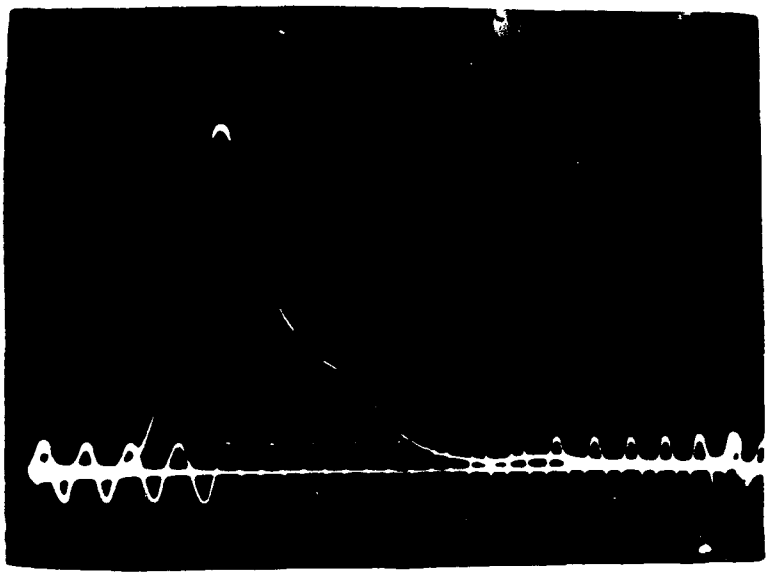

FIG.6. - brake emission pulse form in one of regimes.

HEAVEN-LIGHT Ⅱ Intense Pulsed Electron Beam Acclerator

Zeng Naigong, Zhao Rongsheng, Yang Dawei,
Jiang Xingdong, Wang Xiaojun
China Institute of Atomic Energy, Beijing, P.O. Box 275-7, 102413

Abstract
This paper describes the performance of HEAVEN-LIGHT Ⅰ intense pulsed electron beam accelerator at CIAE and the characteristics of its various component parts.

Introduction

HEAVEN-LIGHT Ⅱ is the second intense pulsed electron beam accelerator at CIAE. Its parameters are electron energy of 650keV, beam current of 150kA, and pulse duration of 40ns. This accelerator consists of Marx generator, pulse forming line, main switch, transmission line, prepulse switch, output line and diode. The coaxial lines are all water dielectric lines.A field enhanced multichannel oil switch is used as the main switch of the accelerator. The breakdown voltage stability of the switch is satisfactory and its fluctuation is less than 2%. The rise time of the output voltage pulse of the accelerator is less than 15ns. The fluctuation of the output pulse amplitude is less than 5%. Figure 1 is the schematic diagram of HEAVEN-LIGHT Ⅱ.

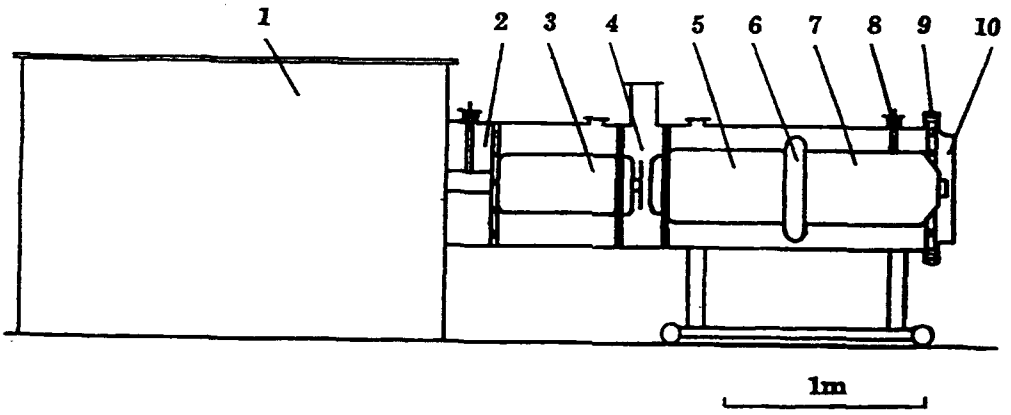

Fig.1 The schematic diagram of Heaven Light Ⅱ accelerator
1. Marx generator 2. oil chamber 3. formation line 4. main switch 5. transmission line 6. prepulse switch 7. output line 8. resistance divider 9. current shunt 10. diode

Marx Generator

Marx generator is composed of 24, 100kV, 0.1μf capacitors and 12 spark

gap switches with trigger disc. The spark gap switches are designed and made by ourselves. The switch is characterized by novel structure, small dimension, low inductance (about 80ns) , long lifetime and wide operation voltage region (from 80kV to 180kV). The capacitors and spark gap switches are connected in the form of Ω (see Fig.2) . The Marx generator is dc-charged with a variable ±100kV power supply. The first two spark gap switches are triggered by a external trigger signal from a small Marx generator. Others are triggered by overvoltage through the coupling resistance. This arrangenment is characterized by compact struture, small circuit inductance, fast voltage erection time and good stability.

The voltage waveform for Marx generator to charge the pulse forming line is shown in Figure 3. The inductance of Marx generator can be calculated according to the oscillation period of the charging voltage waveform. It is about 3.2μH.

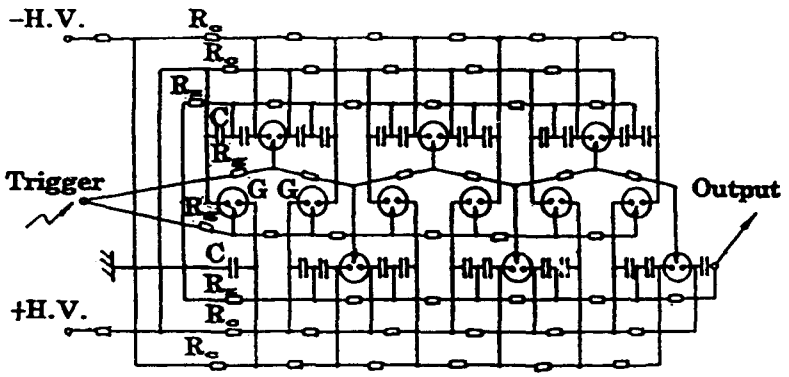

Fig.2 The circuit diagram of Marx generator
C-capacitors G-spark gap switches R_c-charge resistors
R_s-grounding resistors R_g-trigger resistors

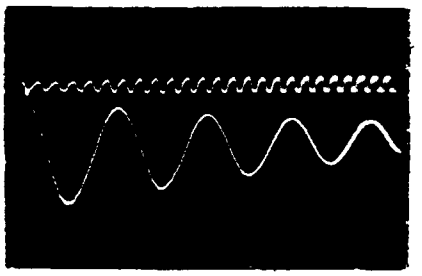

Fig.3 The charge waveform of formation line
(time scale: 88ns/period)

Pulse Forming Line, Transmission Line and Output Line

Pulse forming line, transmission line and output line are all coaxial water line. The forming line, a single line,the impedance of which is 5Ω, has a length of 67cm,an inner cylinder diameter of 28.4cm and a external cylinder diameter of 60cm. The impedances of the transmission line and output line are all 3.5Ω. Their inner cylinder and external cylinder diameters are 35.6cm and 60cm respectively.

The maximum voltage of the forming line is 1.8MV. The maximum field strength at the faces of the inner cylinder and the external cylinder can be calculated by coaxial field formula. The critical breakdown field can be calculated by J.C.Martin's formula. The ratio of the former to the latter is 0. 3. Therefore the design is safe for preventing breakdown.

The experiment on surface effect of the insulator in deionized water for microsecond pulse breakdown voltage has been carried out. The experiment indicates that the surface effect and the body effect of water are about the same as long as no bubbles exist. Water is filled into the coaxial line by means of vacuum pumping to remove the bubbles. The water resistivity can be maintained above 1MΩ · cm.

Main Switch

A field enchanced multichannel oil switch is used as the main switch of HEAVEN-LIGHT I accelerator. The schematic diagram of the switch is shown in Figure 4. It has a floating midplane trigger disc supported by a teflon rod. The field enchancement factor is decided by the position of the disc. To the right side of the disc is a selfclosing axial oil gap and a solenoid inductor. As the pulse forming line is charged to about the maximum of the charging pulse, the axial gap closes first. At this time the potential of trigger disc starts to oscillate in cosinusoidal fashion. While reverse of the potential on the disc takes place, an intense field enchancement comes true between the disc and the left electrode ring and results in the left main gap to breakdown in muitichannel fashion. After the left main gap closes, the potential of the disc will be equal to the potential of the forming line. A considerable field enhancement takes place at the right main gap and induces it to breakdown, and the whole main switch closes.

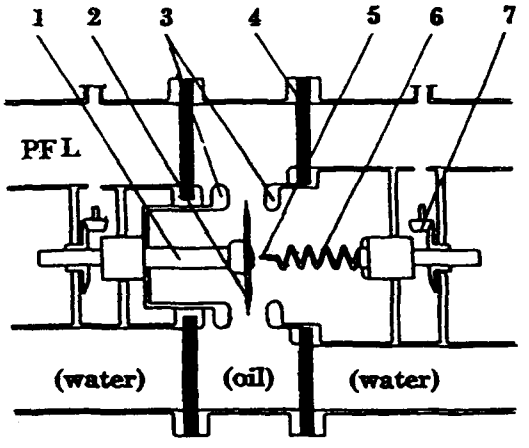

Fig.4 The schematic diagram of the main switch 1.insulator rod 2. trigger disc 3.main electrodes 4.polyurethane diaphragm 5.axial gap 6. solenoid inductor 7. adjuster

The switch has two adjusters to adjust the separation of the main gap and axial gap and the position of the trigger disc.The switch is separated by two polyurethane diaphragms at the ends of the switch from the water line. Both oil and water can be used as the breakdown medium of the switch.

The switch experiments under different parameters in oil or water as the breakdown medium have been carried out. The experiment results indicate that the operating field strength of the switch, the field enhancement factor(i.e. the position of the trigger disc) and the inductance of

the solenoid inductor in series with the axial gap have a considerable effect on the switch channel number and the output waveform of the accelerator. The oil switch has satisfactory properties when appropriate switch parameters are chosen. More than 6 channels can be formed in general. The risetime of the output voltage waveform is less than 15ns. The output waveform and the breakdown voltage of the switch have good stability. The fluctuation of the breakdown voltage is less than 2%. Fig.5 is the typical photograph of the switch spark channels and the voltage

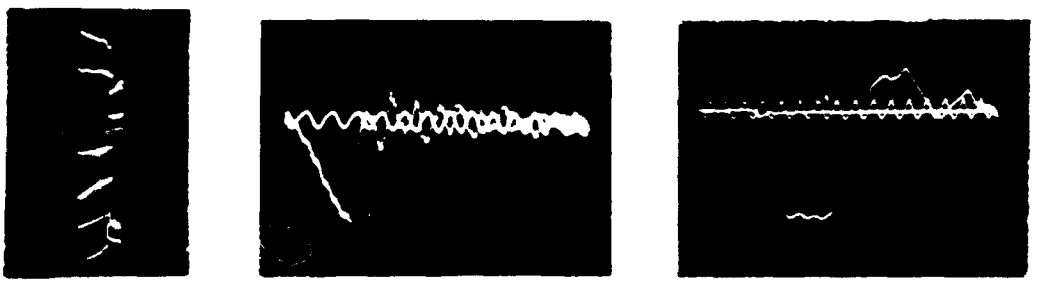

(a) (b) (c)

Fig.5 (a) spark channels of main switch (b) the voltage waveform of five-shot overlay of the formation line when the main switch breakdown (c) the output voltage waveform

waveforms of the pulse forming line and the diode. For water switch, although it is not difficult to form more channels, the output waveform and the stability of the switch are obviously not as good as that of the oil switch. In addition, oil switch feeds much lower prepulse than water switch during the pulse forming line to be charged. Consequently the oil is finally chosen as the medium of the switch. Although oil is easy to be carbonated, it dosen't influence the properties of the switch for short pulse.

Prepulse Switch

There is a pressurized tri-channel gas switch between the transmission line and the output line. Its structure is shown in Fig.6. It has a pair of circular electrodes. One of them has three convex cones. The prepulse switch forms tri-channel spark gaps simultaneously when it breakdown. The switch is filled with a mixture of gases of 20% SF_6 and 80% N_2 . The breakdown threshold of the switch depends on the pressure of the switch. The capacitance of the

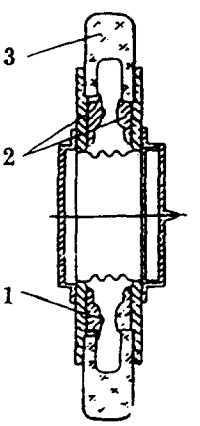

Fig.6
The cross section of prepulse switch
1. protrusion end
2. circular electrods
3. perspex case

switch is assumed to be about 40pF. One of the output line is 5.7nF. Therefore the prepulse is attenuated by a factor of 150. The prepulse is less than 100V while the output voltage of the diode is 650kV.

Diode

The diode is designed in radial insulating fashion, and has low inductance. It is favourable to get fast risetime of the output pulse. The output voltage and current waveforms measured at Marx generator's capacators to be charged to 70kV are shown in Fig.7. The peak voltage and current are 647kV and 165kA respectively, and achieve the design parameters.

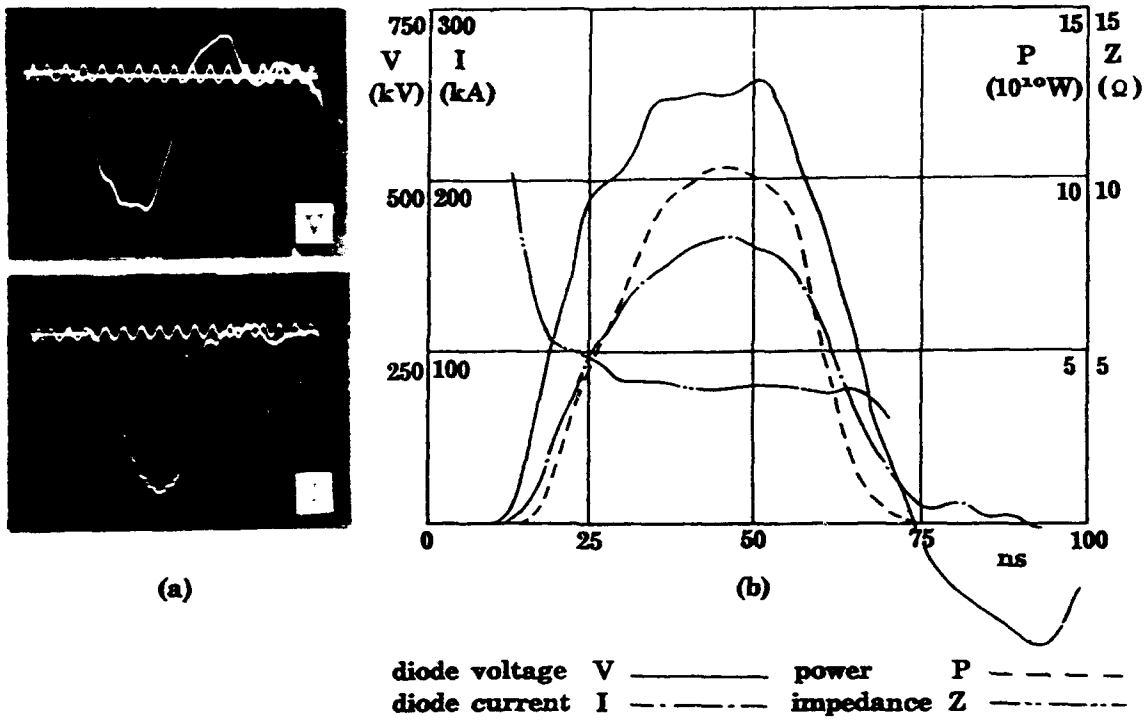

Fig7 (a) The waveforms of diode voltage and current (time scale: 10ns/period)
(b) The curves of diode voltage, current, power and impedance

The experiments of large area diode have been done for the purpose to pump KrF excimer laser. The cathode is a carbon felt of 36×6 cm ^{2}. The data obtainded for different charge voltage and gap separation of the diode are listed in table 1. For the first two situation, serious pinch takes place in short side direction. A uniform electron beam is required for pumping laser. If there is no external magnetic field, the spacing of 16mm is suitable for getting uniform electron beam. The life time test of the anode foil and the main foil has been done at diode

Table 1. The experiment data of the diode

Voltage of Marx generator (kV)	Breakdown voltage of the switch (kV)	Separation between cathode and anode of the diode (mm)	Peak output voltage (kV)	Peak output current (kA)
1430	1415	12	611	151
1430	1415	12	597	147
1430	1410	12	611	144
1320	1253	14	593	119
1320	1273	14	600	125
1320	1294	14	572	119
1210	1128	16	592	91
1210	1085	16	585	94
1210	—	16	599	91

voltage of 600kV and diode current of 90kA. When the titanium foils of 25 μm in thickness are used as the anode foil of the doide and the main foil of the laser cell, the life time is more than 100 shots . For the aluminium foil of 30 μm in thickness used as the anode foil, the life time is about 40 shots . Fig.8 is the schematic diagram of the diode and the laser cell. The unstable resonator experiment of KrF excimer laser is under progress . The laser beam with energy of 2J has been obtained.

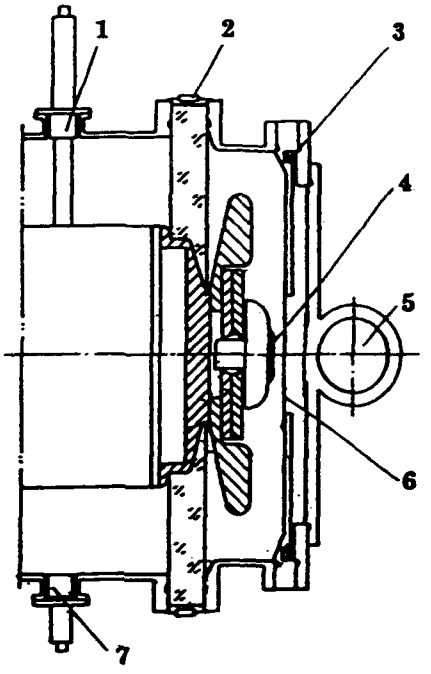

Fig.8 The diode and laser oscillator
1. resistance divider 2. current shunt
3. Rogowski coil 4. carbon felt cathode
5. laser cell 6. anode foil
7.capacitance divider

Acknowledgments

The author wish to acknowledge professor Wang Ganchang for the enthusiastically support.

The Experimental Research of a Field-Enhanced Multichannel Oil Switch

R. Zhao, N. zeng, D. Yang, X. Jiang, X. Wang
China Institute of Atomic Energy, Beijing, China, P. O. Box275-7, 102413

Abstract — This paper describes the performance of a field enhanced multichannel oil switch which is used as the main switch of HEAVEN -LIGHT Ⅱ intense pulsed electron beam accelerator at CIAE. The switch experiments have been carried out with different inductance of the solenoid inductor in series with a self - closing axial gap and position and diameter of the trigger disc.The experiments using water as a breakdown mideum of the switch have been done too to compare with oil switch. These experimental results and conclusions are presented in the paper.

Introduction

Another water dielectric pulse electron beam accelerator HEAVEN -LIGHT Ⅱ has been designed and constructed and is now in operation to pump excimer laser at CIAE. The design parameters of 650kV, 180kA, 40ns have been achieved. A field-enhanced multichannel oil switch is used as the main switch between the pulse forming line and the pulse transmission line. The switch has a floating midplane trigger disc between the main electrodes and is driven by a self -closing axial oil gap. In fact, it is a variety of general V/n switch. Its breakdown principle is same as general V/n switch. In order to get the optimal operation of the switch, it is necessary to chose appropriate position and diameter of the trigger disc and inductance of the solenoid inductor. the relevant experiments have been carried out. The experimental results indicat that these switch parameters have obvious effect on the property of the switch. The property of the switch is very satisfactory when appropriate switch parameters are chosen. Average channel number of more than 6, output voltage rise time of less than 15ns, breakdown voltage jitter of less than 2% and output voltage amplitude jitter of less than 5% are obtainded. The conclusions induced from the experiments, we believe, is suitable to general V/n switch.

Description of The Switch

The schematic diagram of the switch is shown in Figure 1. it is a cross section of the switch which is cylindrically symmetric about the axis. The total gap separation between the main electrode rings and the position of the trigger disc can be adjusted by two adjusters. The trigger disc is supported by a teflon rod. To the right of the trigger disc is a self-closing axial gap and a solenoid inductor of the trigger

circuit. The closing process of the switch is as follows: As the pulse forming line is charged to V_f and voltage is applied to the open switch , the trigger disc "floats" in potential maintaining a value egual to about Vf/n (n is the ratio of gap D to gap d_2 in Fig.1). Until the axial gap closes , there is no field enhancement at the edge of the trigger disc . Switch action starts when the axial oil gap reaches its self-breakdown field and closes. The trigger disc is now connected to the transmission line through the solenoid inductor and starts to oscillate in potential in cosinusoidal fashion. The potential of the trigger disc starts to reverse from V_f/n to $-V_f/n$ and an intense field enhancement at gap d_1 will induce the gap d_1 to breakdown. After the gap d_1 closes in multichannel fashion, the potential of the disc will change suddenly to the potential of the pulse forming line. Therefore a considerable field enhancement takes place at gap d_2 and induces the gap d_2 to breakdown, and whole the main gap closes.

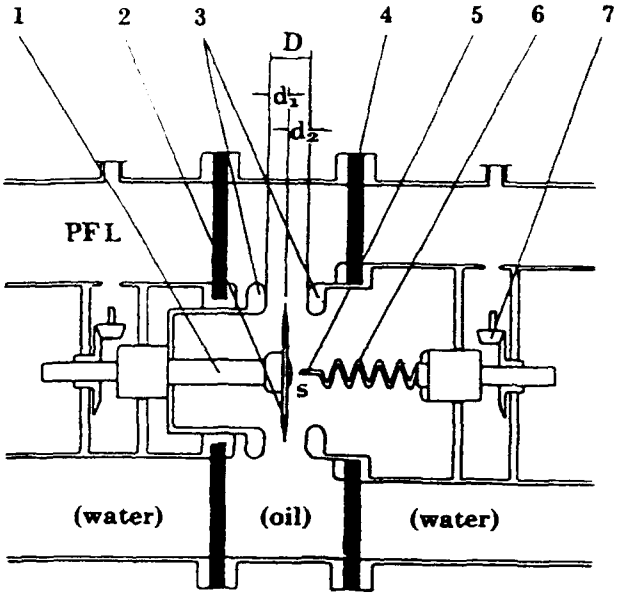

Fig.1 The schematic diagram of the main switch 1.insulator rod 2. Trigger disc 3.main electrodes 4.polyurethane diaphragm 5.axial gap 6. solenoid inductor 7. adjuster

Experiments and Results

Figure 2 is the schematic diagram of HEAVEN LIGHT-Ⅱ accelerator. The rise time of the charging pulse of the switch is 250ns. The impedance of the transmission line and output line are all 3.5 Ω. There is a window in the main switch section for taking the open shutter photograph of the switch channel. At the end of the output line there are a resistive voltage divider and a Rogowski loop to monitor the voltage and the current of the diode respectively. The charging waveform of the pulse forming line is monitored by the resistive voltage divider at the forming line section. The property of the main switch can be judged by the output waveform, the breakdown point of the switch and spark channel mumber of the switch.

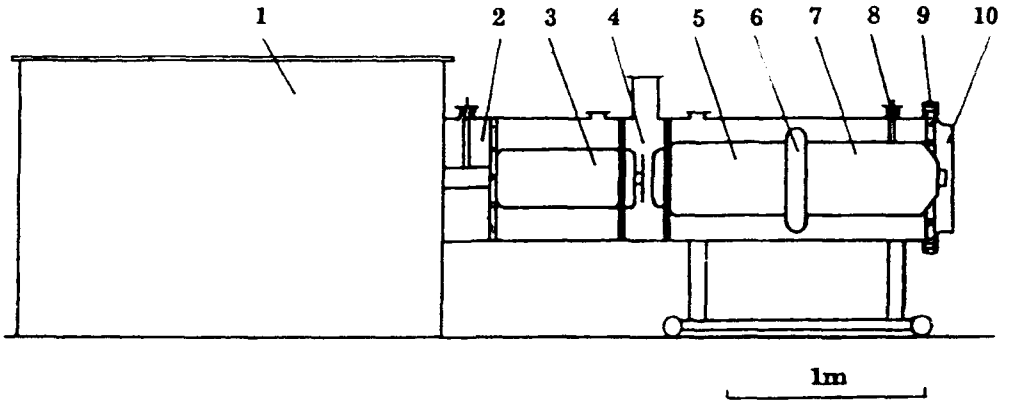

Fig.2 The schematic diagram of Heaven Light Ⅱ accelerator
1. Marx generator 2. oil chamber 3. formation line 4. main switch 5. transmission line 6. prepulse switch 7. output line 8. resistance divider 9. current shunt 10. diode

(1). Experiments with different solenoid inductor

Four solenoid inductors (0.12μH, 0, 71μH, 1. 4μH and 2. 45μH respectively) are used in our experiments. Satisfactory output waveform with fast rise time and more channels are only obtainded when the inductor of 2.45μH is used. When the lower inductor is used, the rise time of the output waveform become slower eventhough more spark channels are formed. It can be explained as follows: Before the main gap d_2 closes the self-closing axial gap s and the left main gap d_1 have already closed, and there is a discharging current passes through gap s and the soleniod inductor, i.e. the discharge of gap d_2 takes place too during gap d_2 to be charged. This discharge current makes the voltage rise rate of gap d_2 become slow and results in appreciable transit time jitter between the various channels formed in gap d_2 . For very short pulse accelerator this jitter is important contribution to the rise time. Consequently, it is necessary to limit the discharge current. Obviously, large inductance of the inductor is favourable to limit this current. But too large inductance will induce too long oscillation period of oscillating circuit consisted of gap s, the solenoid inductor and the right main gap d_2 . When this oscillation period is comparable to the rise time of the charging pulse of the switch, the full potential reverse of the trigger disc can not come true after the self closing axial gap closes, and the field enhancement of gap d_1 will be not intense enough. When the inductance is 2.45uH, the oscillation period is calculated to be about 70ns. It is appropriate to the charging pulse with a rise time of 250ns. But if water is used as the breakdown mideum of the switch, this period is about 340ns when the inductance is 2.45uH. Obviously, it is too large.

The period can not be reduced by means of reducing the inductance of the soneloid inductor because of the reason mentioned above. In addition water switch will feed through large prepulse during the pulse forming line to be charged. Therefore using water as the breakdown medium of this type of switch is not suitable for fast charge pulse. It has been proven by the experiments. The output waveform and the stability of the water switch are all obviously not as good as that of the oil switch.

(2). Experiments with Different Trigger Disc Position

The experiments with various N (is 2,3,4,5,6,7 respectively), which is the separation ratio of gap D to gap d_2, were carried out. The results indicate that larger N (i.e. smaller d_2) is favourable to obtaind fast rise time and good stability. When N is 6 or 7, the most satisfactory output waveforms are abtained. As mentioned above, gap d_2 has more appreciable transit time jitter between the various channels than gap d_1 because of having a discharge current during gap d_2 to be charged, and this jitter is a important contribution to the rise time. It is obvious that the larger N is, i.e. the smaller d_2 is, the smaller the jitter is. Consequently, fast risetime can be obtained When N is larger.

(3). Experiments With Different Trigger Disc Diameter

The inner diameter and the external diameter of the main electrode rings are 19cm and 31cm respectively. Two trigger discs, the diameter of which are 18cm and 22cm respectively, are used to test. For the former, after a few hundreds shots only small torsion, which dosen't interfere with normal operation of the switch, forms at the edge of the disc. But for the letter, after only a few tens shots it has to be replaced because large torsion forms at its edge. Since the diameter of the larger disc is larger than the inner diameter and less than the external diameter of the main electrode rings. So the streamers passing through the edge of the disc is perpendicular to the disc face. Whole the force from the streamers is effective on the torsion and seriously damages the disc. For the smaller disc, the diameter of the disc is less than the inner diameter of the main electrode rings. There is an angle between the streamers and the axis of the switch. Only the axial component of the force has an effect on the torsion of the disc, and results in light damage of the disc.

Switch Performance

Figure 3 is a typical open shutter photograph of the switch

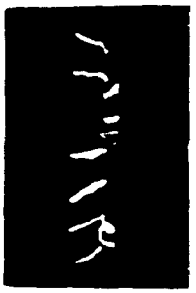

Fig.3 The open shutter photograph of the spark channel of the switch

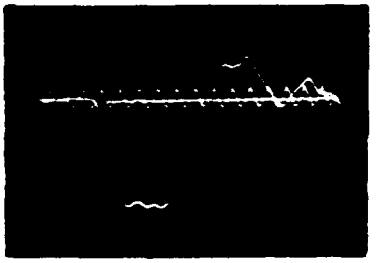

Fig.4 The output voltage waveform of the accelerator (time scale: 10ns/period)

action which is taken from one side of the switch. It dosen't include all the channels, because some of the channels formed on the another side of the switch are sheltered by the support rod of the disc and the disc itself. The channel number is more than 6 in general. Figure 4 is a typical output voltage waveform of the accelerator. 10% to 90% rise time is less than 15ns. The accelerator has very stable output waveform. Figure 5 is the output voltage and the output current waveforms of continuous shots. The jitter of the breakdown voltage of the switch is less than 2%. The jitter of the output voltage amplitude is less than 5%.

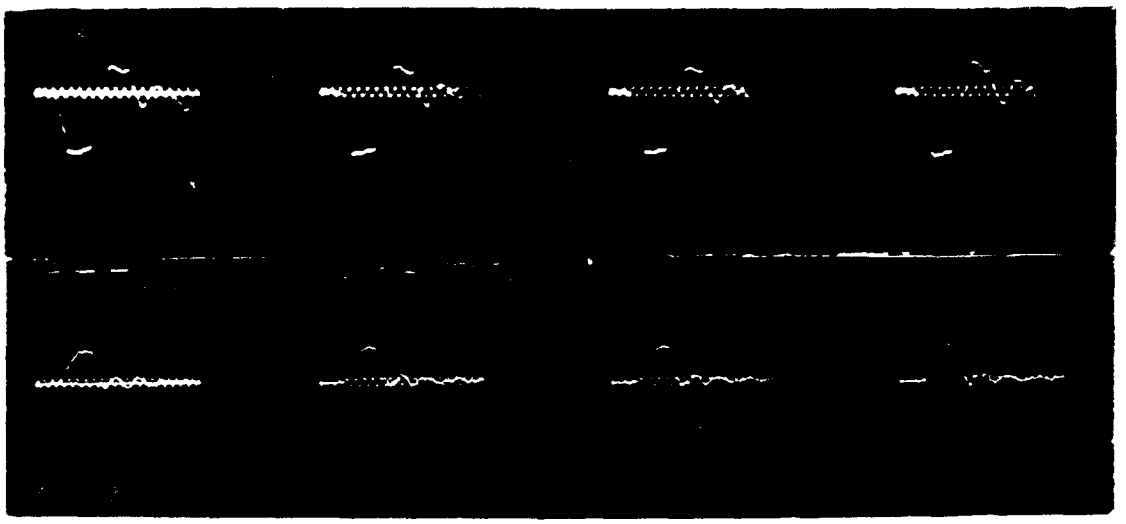

Fig.5 The output voltage (above) and current (below) waveforms of continuous shots

Conclusions

(1). The transit time jitter between the various channels of gap d_2 is a important contribution to the rise time. In order to reduce this jitter, it is necessary to chose appropriate large series solenoid inductor

and arrange larger N (6 or 7 is the best).

(2). For long trigger disc lifetime the diameter of the trigger disc should be less than the inner diameter of the main electrode rings.

(3). Water is not suitable breakdown medium to this type of switch because of large switch capacitance.

References

(1). John D. Shipman, Jr., "Design and Perpormance of the New Multichannel Oil Output Switch on the GAMBLE Ⅱ A Water Dielectri Pulse Power Generator at NRL", Inner report.

(2). J.C.Martin, "Nanosecond Pulse Techniques, " Staff Repor AWRE, SSWA/JCM/704/49 Alderaston, England, April 1969.

(3). D.L.Johnson, J.P.Vandevender, and T. H. Martin, "High Power Density Water Dielectric Switching", IEEE Trans. on Plasma Science, Vol. PS-8,No.3, September, 1980.

THE MAGPIE PROJECT : CURRENT STATUS

I H Mitchell, P Choi, J P Chittenden, J F Worley,
J M Bayley, A E Dangor, M G Haines.
The Blackett Laboratory, Imperial College, London SW7 2BZ, England

Introduction.

A Mega-Ampere Generator for Plasma Implosion Experiments (MAGPIE) is currently under construction in the Plasma Physics group at Imperial College, London. The generator is specifically designed to carry out radiative collapse experiments in hydrogen fibre Z-pinches [1]. In order to achieve this goal, MAGPIE must be capable of delivering in excess of 1.5MA into a 150nH load in under 200ns. An artist impression of MAGPIE is shown in fig.1. In the final generator, four 2.4MV Marx banks charge four 5 ohm, coaxial, 100ns single transit, water filled pulse forming lines (PFLs). The four PFLs are connected to a single coaxial vertical transfer line via four synchronously triggered trigatron switches. The vertical transfer line has an impedence of 1.25ohm and therefore represents a matched load to the four PFLs. At the top of the transfer line a graded insulator stack makes up the vacuum-water interface. A magnetically insulated transmission line section then feeds the load. The total energy stored in the banks is 336kJ making MAGPIE a multi terrawatt, long pulse generator. This paper reports on the general status of the programme and on details of the work carried out in characterising and optimising the trigatron switches.

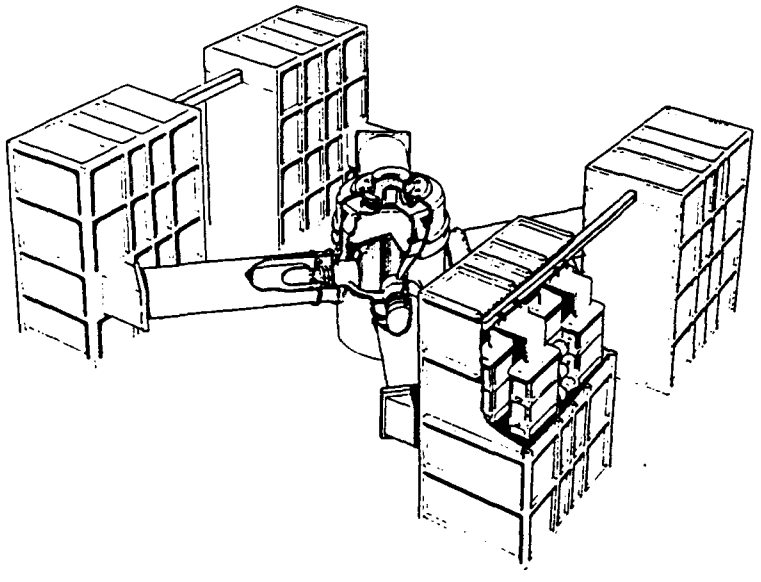

Fig.1 Artist impression of MAGPIE

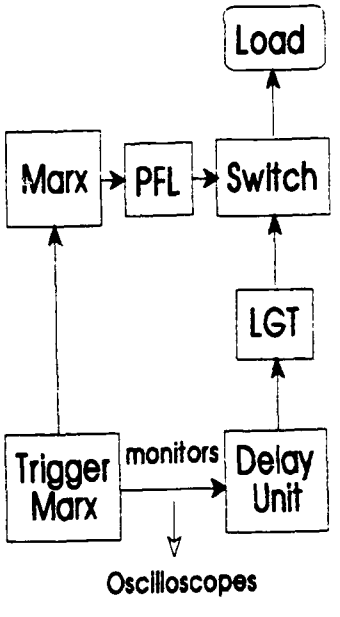

Fig.2 Block diagram of GEN1

Generator Progress

Currently, a single arm of the system, GEN1, has been assembled for detailed testing. A block diagram of GEN1 is shown in fig.2. This consists of a single 2.4MV, 84kJ Marx of the Hermes III design, the performance of which has been characterised and optimised [1]. The Marx is connected to one of the PFLs and then to a trigatron switch. The switches to be used in MAGPIE were designed at Sandia National Laboratories for operation in the megavolt regime. They have a main gap, d_g, of 95mm, and a trigger gap, d_t, of 3.1mm. The trigatron is triggered by the line gap trigger unit (LGT), the output of which can be varied from 15 to 40kV. The load has taken the form of both a simple short circuit and a parallel plate liquid copper sulphate resis tor housed in a 50cm long cylindrical section.

Various monitors are installed on the apparatus. A resistive divider monitors the trigger Marx output. The signal from this monitor is used in the screened room to trigger the oscilloscopes and is also used, via a variable delay unit, to initiate the trigatron trigger sequence. A fibre optic and photo-diode are used to monitor the light output from the final spark-gap in the Marx erection sequence. This gives a reference for the commencement of the line charging. A resistive divider positioned at the output of the LGT unit monitors the trigger volts. A capacitive monitor situated at the switch end of the PFL provides the line voltage. This is effectively the voltage, V_g, on the switch live electrode. A B-dot coil, situated at the oil-water interface between the PFL and the switch section provides, after integration, a measurement of the current through the switch. A signal from this coil is used as an indication of closure of the switch. A set of traces from a typical shot is shown in fig.2. The top trace shows the output from the trigger Marx. This pulse, typically 300kV, triggers the first five spark-gaps of the main Marx. The light emitted from gap 12, the last gap of the main Marx, can be seen to rise sharply, signaling erection of the Marx. The voltage at the switch end of the PFL, V_g, then rises as the Marx charges the line. The output voltage from the switch trigger unit, V_{LGT}, is displayed in the next trace. The pulse from this unit is launched along an 83ns, 50 Ohm cable to the switch trigger pin. The voltage doubles up at the trigger pin, giving V_t nomimally double V_{LGT}. The reflection can then be seen at the monitor after another transit time of the cable. Finally the two bottom traces show the I dot signal, which is obtained from the probe situated at the junction of the PFL and the switch section, and then its integral.

Trigatrons are known to operate in one of two distinct modes determined by the initiation path of the discharge. The voltage on the trigger pin can cause breakdown to the adjacent electrode (BAE) with the resulting UV and charged particles initiating the closure of the

main gap [2]. Alternatively the trigger voltage can create an enhanced field across the main gap, resulting in the formation of streamers directly across to the opposite electrode (BOE) [3]. It has been suggested [4] that the optimum trigger voltage for the trigatron would be obtained when both the BOE and BAE modes are operating simultaneously and this value is given by $V_t^* = -V_g d_t/(d_g-d_t)$ for opposite polarity V_t and V_g.

A series of experiments has been carried out to optimise the trigatron performance [5]. The tests were all carried out with the switch closing at approximatley 80% of self break. Three sets of data have been obtained, under different operating voltages, the first two varying the trigger voltage to locate the optimum operating point. In both these scans at least 20 shots were taken for each trigger voltage and the data from each suggested that the optimum performance was obtained with the trigger voltage closest to V_t^*. In obtaining the third set of data 200 shots were fired through the switch to test the long term drift under the optimum triggering conditions. The data from the final 160 shots of this run are shown graphically in fig.3. The running average of the delay and jitter over 20 shots are shown in fig.4. The switch performance was analysed with respect to two characteristic times, t1 and t2. t1 is the time between the arrival of the trigger voltage at the trigger pin and the fall in trigger pin voltage due to breakdown from the trigger pin to either of the other electrodes. t2 is the time between this voltage fall and a signal on from the B-dot coil, indicating conduction of the switch. The results from these tests are shown in table I.

Table I

V_g (MV)	V_t/V_g (%)	E_g (kV/cm)	E_t (kV/cm)	t1 (ns)	t2 (ns)	(t1+t2) (ns)	std dev
	3.0	107	98	59	17	75	9
1.0	5.0	108	160	12	84	96	21
	8.0	109	260	5	115	120	23
	3.3	163	161	51	9	60	7.5
1.5	1.2	161	116	76	7	83	16
	4.4	165	213	32	32	64	12.6
2.0	3.4	218	219	36	7	43	4.4

The two modes of switch operation are clearly evident in this data. For the large values of V_t/V_g, where $E_t > E_g$, t1 is much smaller than t2 which is indicative of BAE operation. For the case of V_t/V_g of 2.0% the trigger signal at breakdown, indicates that the first gap to close is that from the trigger pin to the opposite electrode which agrees with the BOE

mode of operation.

For the cases with V_t/V_g close to the optimum, which is 3.4% for the switch under tests, operation of the switch in two different regimes is again evident as shown by the two LGT output traces in fig.5. In the majority of shots, t1 is significantly larger than t2. The LGT output is observed to drop well below zero, as in fig.5a), indicating that breakdown is occurring between the trigger pin and the live electrode. For some of the shots, for example in approximately 12% of the shots in the third set of data, the LGT output does not go negative, as in fig5.b), indicating that the trigger pin has broken down to the adjacent, earthy electrode. As the fields across both the main gap and the trigger gap are similar at optimum trigger voltage, it is to be expected that breakdown will be initialized with both the BOA and BAE modes competing. As a result, the total breakdown delay is not drastically changed depending on which mode operates, in contrast to the results from the first two sets of data. It can be seen, from the first two sets of data in table I, that the minimum delay and jitter is obtained for the trigger voltage closest to V_t^*. Furthermore fig.3 and fig.4 indicates that 200 shots can be fired through the switch under these conditions with no serious effect on the switch performance.

The hydrogen fibre maker

For the intended radiative collapse experiments cryogenic hydrogen fibres with diameters down to 10 μm must be produced. A new fibre maker is being developed for this purpose as recent designs reported on pulsed power fibre pinch experiments [6,7] are limited to fibres with diameters above 30 μm. Furthermore, these designs produce deuterium fibres by first desublimating deuterium gas into a chamber at 5 K to form snow. The resulting snow is then warmed to 13 K to make it plastic and extruded through an aperture by a ram. Deuterium may not be suitable for the radiative collapse experiment as the exothermic DD fusion could prevent radiative collapse.

In designing a new device to produce hydrogen fibres it is desirable to avoid producing snow-like material. To compact the snow for extrusion the ram must apply a large pressure. Consideration of the extrusion of metals and plastics indicates that the quality of the extruded product is reduced by excessive pressure. A two temperature system was chosen in the present design. Hydrogen will be condensed in an upper chamber to the liquid phase and the vapour pressure is used to force the liquid down a capillary to a small second chamber and exit through a pinhole. Comparison of the saturated vapour pressure curve with the yield stress [8] indicates that the liquid should be at 20 K and the pinhole at 10 K.

To attain 10 K a closed cycle helium refrigerator will be used in preference to a liquid helium system. This offers lower running costs and increased robustness. The system is currently under construction.

Summary

One arm of the MAGPIE generator is assembled and is fully operational. The system, including the Marx, a pulse forming line, a switch and a resistive load, has proved to be very reliable over several hundred shots at the proposed working voltage. Experiments have been carried out to locate the optimum switch triggering voltage which has been found to be close to that which would result in simultaneous closure of the trigger and main gaps in the switch. With this optimum trigger a switch maintains a reasonable delay and jitter performance over 200 shots under MAGPIE operating conditions, with the standard deviation of the delay increasing from 2.3 ns for the first 20 shots and reaching a maximum of 5.3 ns. Optimisation of the powerflow through the junction between the four PFLs and the vertical transfer line is being carried out and the results are reported elsewhere.[9] The water vacuum interface and the diode feed section has undergone detailed design studies and a curved, tapered magnetically insulated transmission line feed terminating into a 6 cm diameter load section is being adopted for final characterization. Work has also been carried out on the design of a new fibre maker to produce hydrogen fibres. The fibre maker employs a novel liquid-solid dual reservoir design and make use of the vapour pressure above the liquid hydrogen reservoir to extrude solid hydrogen through a pinhole at the cooler reservoir.

References

[1] P. Choi, J. Chittenden, I. Mitchell, J. Worley, J. Bayley,R. Bialecki, A.E Dangor, M.G. Haines, 1991, Digest of Technical Papers, 8th IEEE Pulsed Power Conf, San Diego, California, p173.
[2] J.D. Craggs, M.E. Haine, and J.M. Meek, 1946, J. Inst. Elec. Engrs. 93A,963.
[3] T.H. Martin,1985, Digest of Technical Papers, 5th IEEE Pulsed Power Conf, Arlington, Virginia, p74.
[4] T.H. Martin,1989, Digest of Technical Papers, 7th IEEE Pulsed Power Conf, Monteray, California, p75.
[5] I.H. Mitchell, P. Choi, J.P. Chittenden, J.F. Worley, to be published in Proc. GD92, Swansea, 1992.
[6] J.D. Sethian and K. A.Gerber, 1987, Rev. Sci. Instrum. 54, p536.

[7] E.R. Grilly, J.E. Hammel, D.J. Rodriquez, D.W. Scudder and J. S. Shlachter, 1985, Rev. Sci. Instrum. 56, p1885,
[8] P.C. Souers,'Hydrogen properties for fusion energy', University of California Press, Berkley, (1986)
[9] I.H. Mitchell, P. Choi, J.P. Chittenden, J.F. Worley, this Conference.

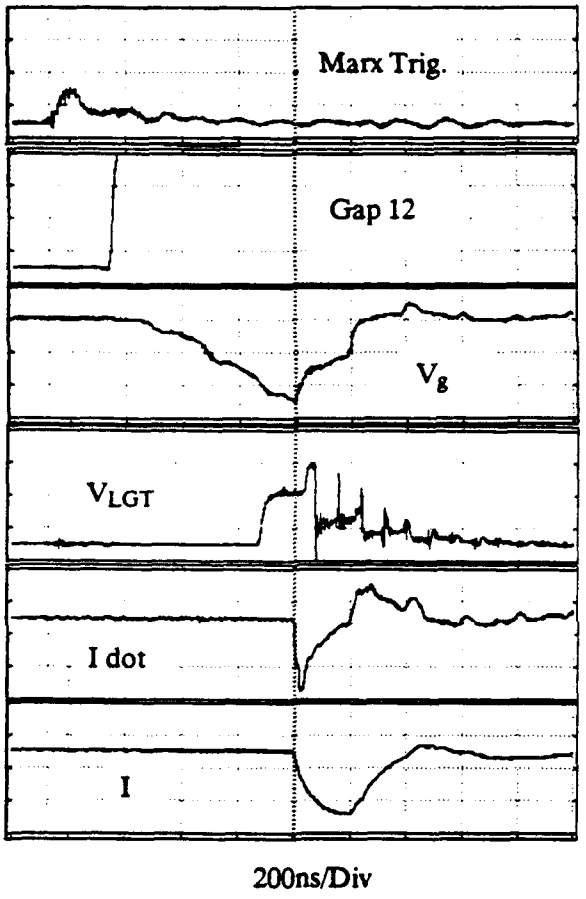

Fig.3 System voltages and currents

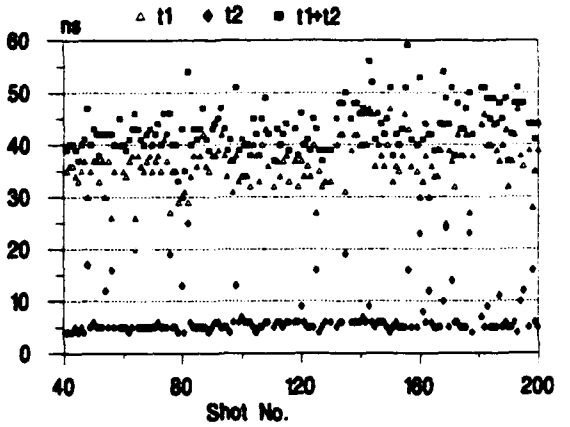

Fig.4 Breakdown delay of trigatron

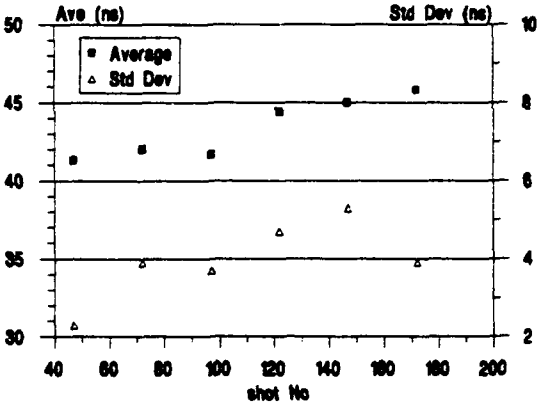

Fig.5 Running average of delay and jitter

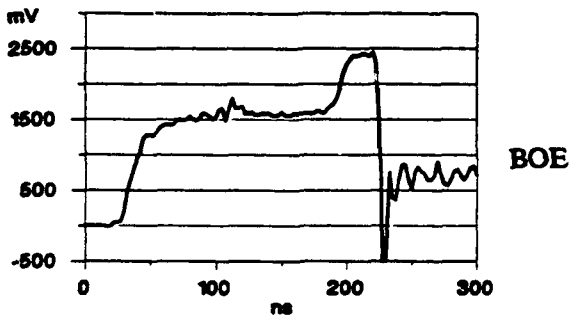

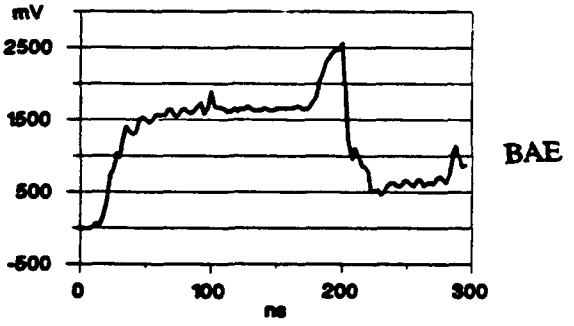

Fig.6 LGT output for the BOE and BAE mode of breakdown conditions

OPTIMISATION OF THE POWER COUPLING IN THE MAGPIE 4-WAY JUNCTION USING A 1/6TH SCALE MODEL.

I H Mitchell, P Choi, J P Chittenden, J F Worley
The Blackett Laboratory, Imperial College, London SW7 2BZ, United Kingdom.

Introduction.

A Mega-Ampere Generator for Plasma Implosion Experiments (MAGPIE) is currently under construction in the Plasma Physics group at Imperial College, London. The generator is specifically designed to carry out radiative collapse experiments in hydrogen fibre Z-pinches [1]. In order to achieve this goal, MAGPIE must be capable of delivering in excess of 1.5MA into a 150nH load in under 200ns. An artist's impression of MAGPIE is shown in fig.1. In the final generator, four 2.4MV Marx banks charge four 5 ohm, coaxial, 100ns single transit, water filled pulse forming lines (PFLs). The four PFLs are connected to a single coaxial vertical transfer line via four synchronously triggered trigatron switches. The vertical transfer line has an impedence of 1.25ohm and therefore represents a matched load to the four PFLs. At the top of the transfer line a graded insulator stack makes up the vacuum-water interface. A magnetically insulated transmission line section then feeds the load. The total energy stored in the banks is 336kJ making MAGPIE a multi terrawatt, long pulse generator. A necessary feature of the generator is the junction of the four horizontal PFLs to the single vertical transfer line. This paper reports on work being carried out to characterize the power flow through this juncion using a 1/6th size scale model.

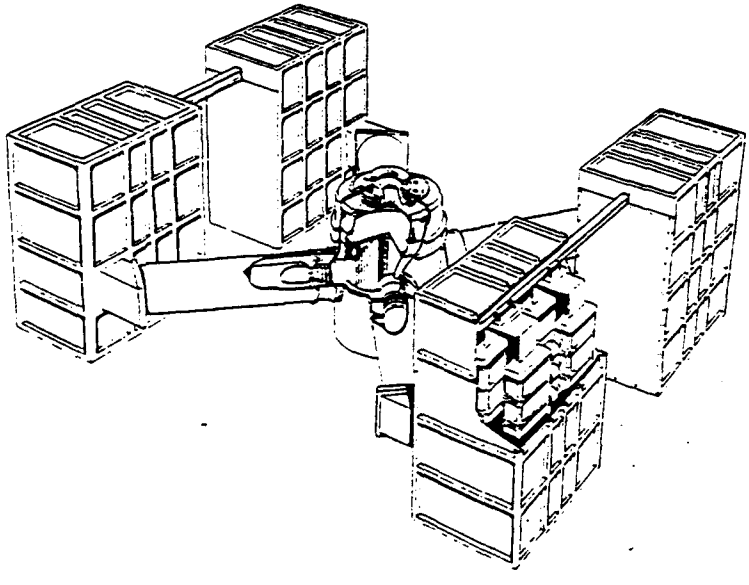

Fig.1 An artist's impression of MAGPIE

The Generator design

The MAGPIE generator was designed to enable radiative collapse experiments to be carried out with cryogenic hydrogen fibres. Radiative collapse occurs when the current in a Z-pinch exceeds the Pease-Braginskii current, I_{PB}. For hydrogen fibres of radii around 20μm, I_{PB} has a value in excess of 1.2MA. Having such a fire, 20μm in diameter, as a load introduces the problem of high inductance. MAGPIE was designed to be a long pulse generator, 200ns, in order to reach the required current without excessive high voltage. Taking a margin of 20 % on the design, a current in excess of 1.5MA with a long pulse length is sepcified for MAGPIE and a system with four PFL and four switches was chosen. The number of PFL was chosen upon the total current requirement and the technological limit of high voltage switches with ns jitter and yet long service life time. The impedance of each PFL is 4 times that of the transfer line for optimal theoretical power transfer. An additional benefit of this design is that the rise time of the voltage on the transfer line is smaller as a result of the higher impedance feeding each switch. Production of cryogenic fibres requires that the fibre is extruded vertically, therefore a vertical feed to the load is required. The long pulse required for the fibre experiments dictates that the PFLs, which are 3.3m long, need to be horizontal. Therefore a logical solution to the design problem is a single junction which combines the four horizontal PFLs to a single vertical feed to the load. However, the conversion of the voltage waves from the PFLs into an upward travelling wave on the transfer line is not a simple matter. With the geometry concerned, there is no reason why the waves launched from the PFLs should travel preferentially up the transfer line. A more probable alternative is that a wave launched from the junction travels outward in all directions.

The Scale Model

Numerical simulation of the above junction is a complex 3D problem which could prove extremely costly in terms of both time and money. An alternative route is to build an electrically accurate scale model which provides a convenient means of investigation.[2] The scale chosen for the model was 1:6.6, ie. 12" are equivalent to 2 m. The PFLs and the outer of the transfer line are made from aluminium tubing with flanges attached to the ends. This allows the lines to be filled with deionised water, as in the full generator. The inner of the transfer line is made from rolled tin sheet which allows alterations to be made easily. Scaling down of the coaxial lines therefore conserves the impedance as both the ratio of the diameters of the inner and outer conductors, and the dielectric constant of the insulating medium are conserved. In the scale model, it is necessary to scale not only the

physical dimensions, but also the characteristic timescales. Thus, inductances in the full generator are scaled down linearly which decreases the characteristic L/Z times. As the physical distances are scaled by the same factor, the integrity of the model is maintained by similarly reducing the rise time of the voltage input pulse. In the full generator, the switch forms the inner conductor of an oil-filled, coaxial section. This represents a short transit time, high impedance section. In the scale model the switch section is represented by a scaled coaxial air section. The inner of this section can be varied in diameter, therefore changing the effective inductance. In the results presented in this paper the switch section has an inductance of 12nH, equivalent to a full size switch inductance of 75nH, several times less than the measured value of the actual switch installed. This lower value enables the effects of the junction to be observed without added complications arising from the switch inductance. The voltage on the scale model can be monitored at any of twenty one different locations. A diagram of the scale model, and the location of the voltage probes, is shown in fig.2.

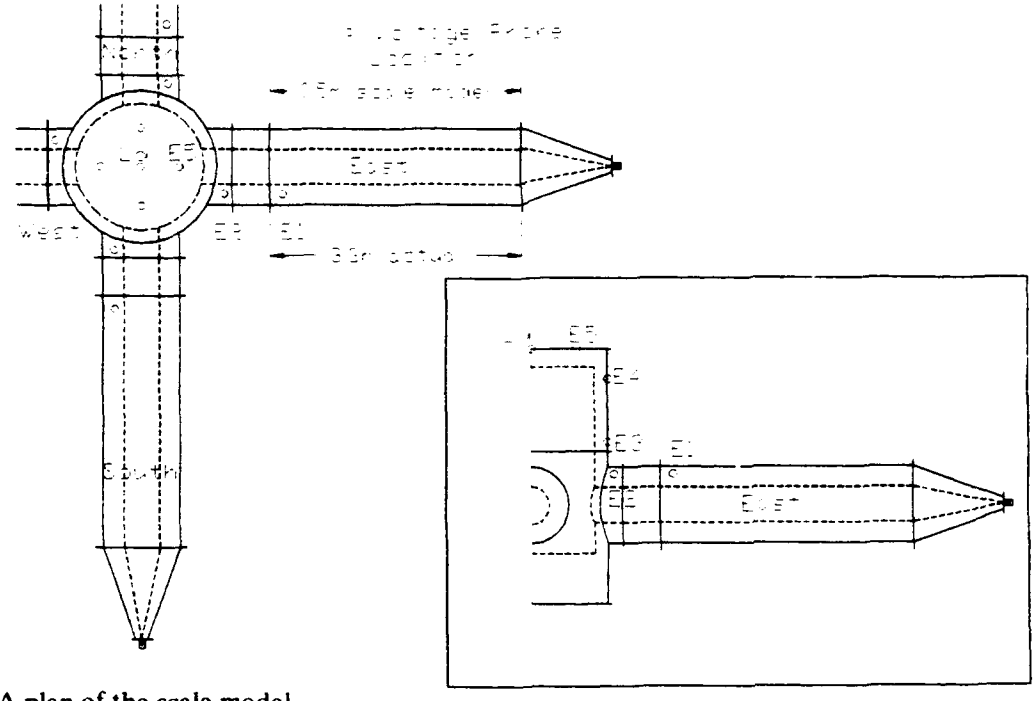

Fig.2. A plan of the scale model.

Monitoring is carried out on a HP16500A system with five 1GHz sampling rate digitizers. This results in a resolution of 3.3cm in the water sections of the model, equivalent to 22cm in the full generator. The four inputs were fed through identical 18ns double transit, coaxial cables from the same pulse generator. The resulting input pulse had a 10-90% rise time of 3ns and peak value of 220mV.

The aim of the scale model experiments is to characaterize the wave coupling across the

junction and to study the mixture of modes by altering the inner conductor of the transfer line. The resulting risetime of the voltage at the load and the effect of simulated switch jitter are also examined. To date, four different designs of inner conductor have been tried. The four designs are shown in fig.3.

Results

Evidence that the wave from the PFL is launched into all directions was found from the voltage traces in fig.4. These traces were obtained by launching a pulse into the east line only and monitoring the probes in the west arm. It is immediately obvious that the voltage wave reaches the opposite side of the transmission line. Fig.5. shows a schematic of the 'unrolled' inner conductor of the transfer line and the positions of the voltage probes. The dimensions stated are the transit times in nanoseconds. With reference to Figs.4 and 5, information about the path taken by the voltage wave can be obtained. Noticeable features of the traces in fig.4 are the double hump observed in W2 and, to a lesser extent in W3, and also the fact that the voltage magnitude peaks at W4. These features can be explained by considering two different paths that a voltage wave can take to any of the probes. Starting with W2, which is situated a few nanoseconds before the junction, two distinct peaks can be seen, seperated by approximately 11ns. This coincides with the difference in transit times of a wave travelling directly from the East junction around the inner to the west, and another travelling upwards, over the top and back down. This amounts to approximately 12ns. The relative magnitude of the two humps relates to the energy travelling in each direction. This picture is supported by the fact that the two humps are closer together at W3 since the direct wave has further to travel and the 'over the top' wave has to cover less distance. The peak value at W4 arises becauses here the waves coincide, the transit times differing by only 1.4ns. As an explanation of the voltage traces, this is obviously an over simplification. In reality the trace will be the sum of many reflected and direct components having travelled along different paths. Nevertheless it illustrates that the energy does not all propogate in the preferred, vertical direction. An effort to minimise the energy travelling around the inner was made by cutting vertical slots in inner #3 and inner #4 as shown in fig.3. This resulted in the reduction of the amplitude of the first hump, attributed to the direct voltage wave, relative to the second hump from 62% for inner #2 to 29% for #3 and 11% for #4. It should also be noted that the voltage appearing at the load increased by 5% with this inner over inner #2.

The effect of switch jitter on the peak voltage obtained was investigated for each of the

transfer line inners. The four input pulses were fed from a common pulse unit with, normally, equal cable transit times. Additional cables were added to simulate switches firing at different times. For the data presented here, a single input, south, was delayed by times equivalent to 0, 10 , 20, 30 and 40ns in the full generator. The data is presented graphically in fig.6 for inners #1,#2 and #4. The voltages quoted are normalised to the maximum voltage obtained, ie. inner #4 with equal switch times. It can be seen, as expected, that the configuration resulting in the highest peak voltage is the one most susceptible to degradation due to switch jitter. Results were also obtained with staggered inputs but the most dramatic effects were observed in the cases presented in fig.6. The trigatron switches to be used in the MAGPIE generator have been tested and optimised [3,4]. A first to last jitter of 25ns over 160 shots has been observed under the optimum triggering conditions. The present results suggest that this would result in less than a 10% loss of volts. The risetime of the voltage at the load was measured for each of the inners. The only measurable difference in rise time occurred when inner #1 was replaced by #2. The removal of the bottom section of the PFL resulted in an improvement in the 10 to 90% rise time from 10ns to 5ns.

Conclusions and Further Work.

A scale model has been built to investigate the power flow in the junction between the four horizontal pulse forming lines and the vertical transfer line in the MAGPIE generator. It has been demonstrated that the voltage wave launched into the junction does not travel only in the desired upward direction but, rather the results have been explained assuming a spherical wave is launched. This results in a fraction of the wave travelling around the transfer line. An effective way of considerably reducing these horizontal components of the wave was established by cutting vertical slots in the inner of the transfer line. This also slightly increased the voltage obtained at the load. This is to be expected as the slots prevent the voltage waves from each of the seperate PFLs from mixing. This configuration was found to be more susceptible to the simulated switch jitter. However, the jitter results from the optimised trigatron switches seem to suggest that the voltage loss is within an acceptable range. Further work on the scale model is being carried out. The effect of a switch inductance will be investigated along with the effect of switch jitter on the symmetry of the current flow.

Acknowledgement
We would like to thank Larry X. Schneider for sharing his experience on scale modelling with us while at Sandia National Laboratories.

References

[1] P. Choi, J. Chittenden, I. Mitchell, J. Worley, J. Bayley, R. Bialecki, A.E Dangor, M.G. Haines, 1991, Digest of Technical Papers, 8th IEEE Pulsed Power Conf, San Diego,California, p173.

[2] L.X. Schneider, W.A. Johnson, E.L. Neau and S.R. Babcock, 1989, Digest of Technical Papers, 7th IEEE Pulsed Power Conf, San Diego,California, p214.

[3] I.H. Mitchell, P. Choi, J.P. Chittenden, J.F. Worley, J.M. Bayley, A.E Dangor, M.G. Haines,this Conference.

[4] I.H. Mitchell, P. Choi, J.P. Chittenden, J.F. Worley, to be published in Proc. GD92, Swansea, 1992.

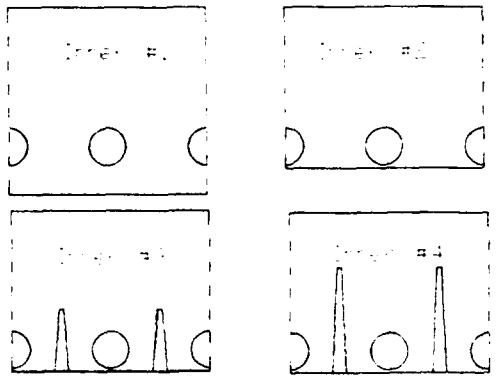

Fig.3 Schematic of the transfer line inners

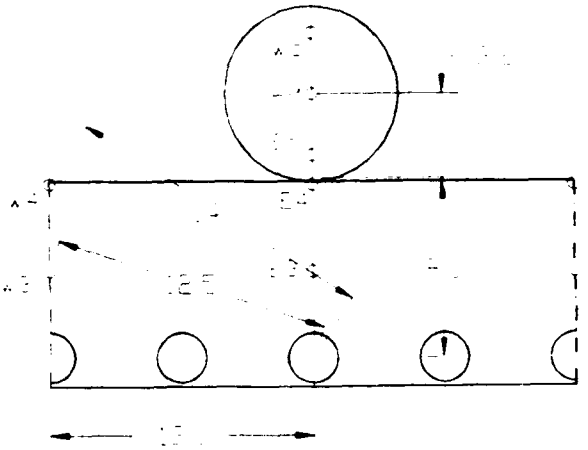

Fig.5 Schematic of the inner of the transfer line 'unrolled'

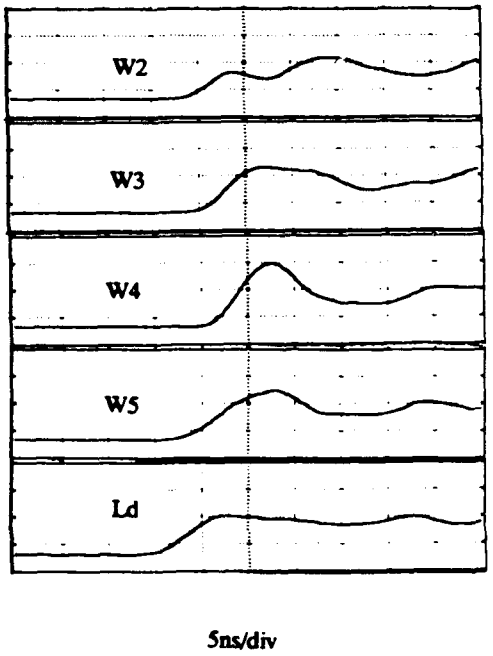

Fig.4 Voltage at various locations for E-only feed

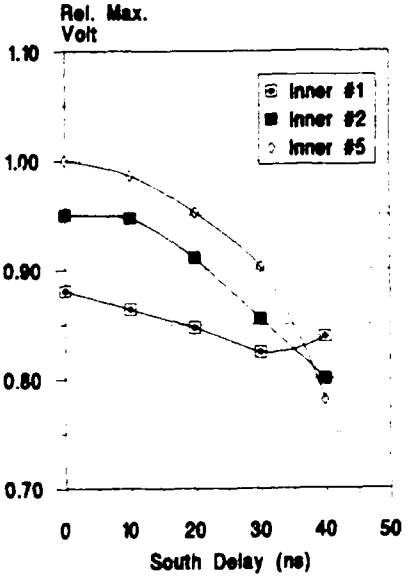

Fig.6 Effect of switch jitter on peak load volage

NEW HALF VOLTAGE AND DOUBLE PULSE OPERATION OF THE HERMES III LINEAR INDUCTION ACCELERATOR*

K. A. Mikkelson, R. L. Westfall, S. M. Neely**
V. J. Harper-Slaboszewicz

Sandia National Laboratories
Albuquerque, NM 87185-5800
**Ktech Corporation

Abstract

The standard operating mode produces bremsstrahlung with an endpoint energy of about 18 MeV. This paper describes a new mode with a 8.5 MeV endpoint energy and the same standard mode pulse characteristics achieved by operating only half of the accelerator at full charge with the advantage of minimal setup time. An extension of the new half voltage mode is to use the other half of the accelerator for delivering a second pulse at a later time using the same technique. This double pulse mode is ideal for beam generation which requires a long interpulse time in the millisecond regime. The beam characteristics of the two half voltage pulses are nearly identical with the nominal radiation pulse full width at half maximum of 21 ns and 10-90% risetime of 11 ns.

Introduction

The HERMES III accelerator [1] located at the Sandia National Laboratories is used to produce intense bremsstrahlung pulses to simulate the effects of gamma rays produced by nuclear weapons on various systems. The linear induction technology is a significant advancement in the pulsed power field, and future simulators may well incorporate this technology. HERMES III is the prime example of a flexible, modular, implementation of this technology on the 10 - 20 TW scale.

The standard operating mode produces bremsstrahlung having an endpoint energy of about 18 MeV and an average photon energy of about 2 MeV with the bremsstrahlung dose produced proportional to $V^{2.8}$[2]. The half voltage and double pulse modes have a 8.5 MeV endpoint energy, therefore these alternate modes generate about one-tenth the dose of the standard operating mode for each pulse.

Background

These new modes use a characteristic behavior of modular linear induction technology which may be important in the future design and operation. HERMES III operates very similar to many accelerators with a oil insulated energy storage section and water insulated pulse forming lines. The major difference is how the output is generated. The normal

parallel output of water transmission lines is transformed to a series output of linear induction gaps on a magnetically insulated transmission line (MITL) adder [3]. This configuration functions as a distributed transmission line transformer (Fig. 1). The same MITL is used in the half voltage mode so the impedances are fixed which implies quarter-power operation at half voltage.

A straight forward approach is to charge the Marx capacitor banks to half voltage and deliver one quarter of the energy and power. This requires changes in the accelerator setup for different water switch parameters to obtain proper performance.

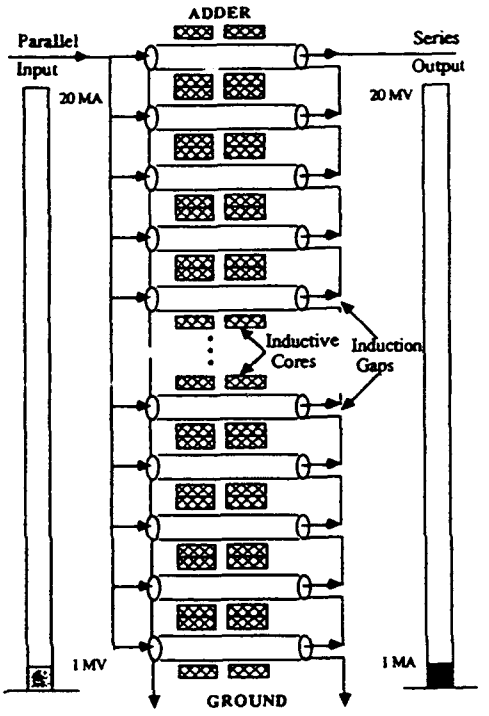

Figure 1. HERMES III transmission line transformer.

Other approaches involve using only half of the accelerator. One, is to operate only half of the induction gaps at full voltage, another approach is to operate all the induction gaps at half voltage. HERMES III is symmetrical, side-to-side, down the MITL with half of the energy storage section located in each tank, east and west.

Operating half of the accelerator at full charge delivers one half of the energy. With only a quarter of the energy required the other quarter of the energy is lost and may cause damage. If half of the induction gaps are operated the undriven induction gaps are loads in the series circuit. If all the induction gaps are operated with only half of the accelerator the undriven water transmission lines of the other half of the accelerator are loads in the parallel circuit. The disadvantage of operating only half of the accelerator is being more susceptible to poor performance because a single module is a larger fraction of the total output. The advantage of these approaches are that they allow half voltage operation at full charge with minimal setup time, so that a sequence of full voltage and half voltage shots can be taken without reconfiguring the accelerator.

Half Voltage Operation

A fault mode observed during the HERMES III development program suggested the last approach would work without damaging the accelerator. A sequence of seven shots, #2276 - #2282, were taken with key measurement points instrumented. Data shows the induction gap voltages obtained when firing each half of the accelerator (Fig. 2). The mismatch due to the undriven water line loads results in a reflection coefficient of -1/2 and only .6 MV of the nominal 1.2 MV pulse delivered to the gaps.

The corresponding diode parameters are 350 kA/125 kA for anode/cathode currents and 8.5 MeV endpoint measured with H^- using a CR-39 range filter [4]. These parameters are approximately one half the nominal 700 kA/250 kA anode/cathode currents and 18 MeV endpoint [5]. The radiation dose measured using a CaF_2 TLD cross array on the converter [2] is reduced from the nominal 80 kRad to 11 kRad (Fig. 3) with the same useful area.

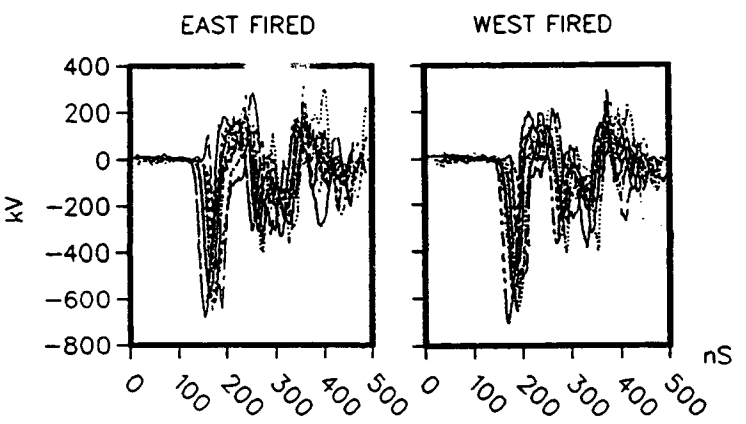

Figure 2. Induction gaps voltage waveforms firing only half of accelerator.

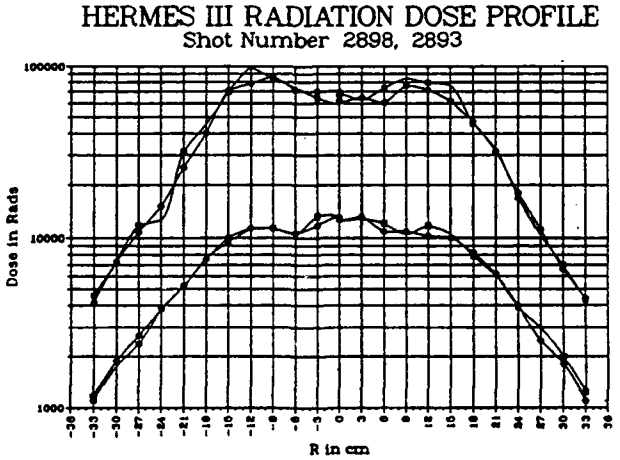

Figure 3. Dose curves for full voltage (2898) and half voltage (2893) shots.

Double Pulse Operation

An extension of the new half voltage mode is to use the other half of the accelerator for delivering a second pulse at a later time with the same technique. The accelerator requirements for double pulse mode are, separate charging of the Marx capacitor banks and a independent trigger system, for each side of the accelerator. This utilizes the redundant spares available for these systems.

Additional concerns of the double pulse mode not relevant for the half voltage mode were 1) time for the unused energy to dissipate 2) possible saturation, during the second pulse, of inductive cores which isolate the induction gaps 3) water switches being functional for second side pulse forming lines after the first pulse and 4) vacuum effects on second pulse propagation down the MITL and diode performance.

Data from the half voltage shot sequence addressed the first three concerns. Reflections from the mismatch were observed to settle in <20 us with >20 ms allowed for the double pulse test. Saturation with two .6 MV pulses in worst case (additive with no oscillations) is equal to 1.2 MV normal pulse excluding the safety margin. Pulse forming line voltages were monitored at very sensitive levels which showed only capacitive coupling across the open water switches (functional for second pulse). The fourth concern required experimental verification.

The double pulse experiment used both halves of the accelerator charged to full voltage and fired 30 ms apart driving all the induction gaps at quarter power twice to deliver two half voltage pulses to the diode with a 34 cm anode-cathode gap. A sequence of 5 shots, #2283 - #2287, were taken with the east side fired first for three shots, followed by the west side fired first for two shots. Diode currents for the first and second pulse of the last shot are shown in Figure 4. The current waveforms compared very well (amplitude and shape) indicating no problems associated with propagation down the MITL due to vacuum effects. In addition, there is no evidence of core saturation which would clip the induction gap voltages and reduce the amplitudes of diode currents.

Radiation characteristics of the two half voltage pulses were nearly identical with the nominal full width at half maximum of 21 ns and 10-90 risetime of 11 ns recorded by the same Compton diode radiation monitors [6] on instruments triggered 30 ms apart. The comparisons of the two radiation

pulses on the three radiation detectors show a 5-11% amplitude variation (Fig. 5). This close comparison indicated no beam pinching or instability due to ion formation or vacuum degradation in the diode A-K gap.

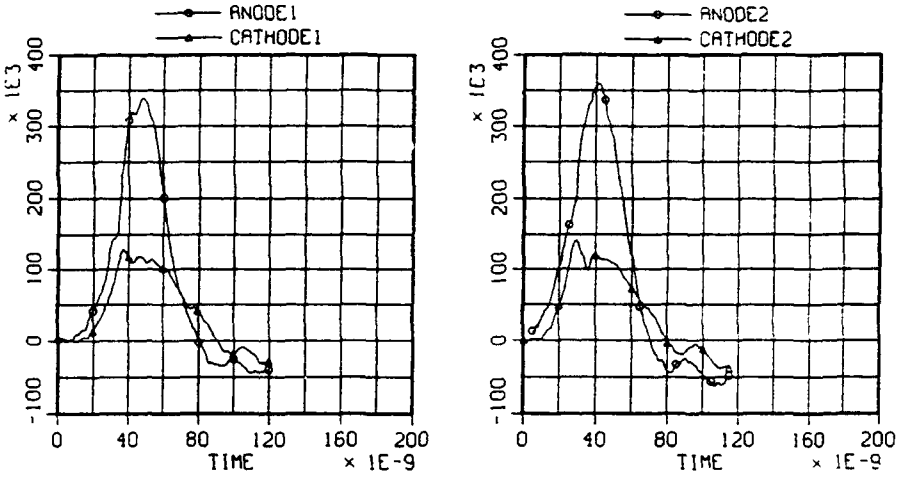

Figure 4. Double pulse diode current waveforms recorded 30 mS apart.

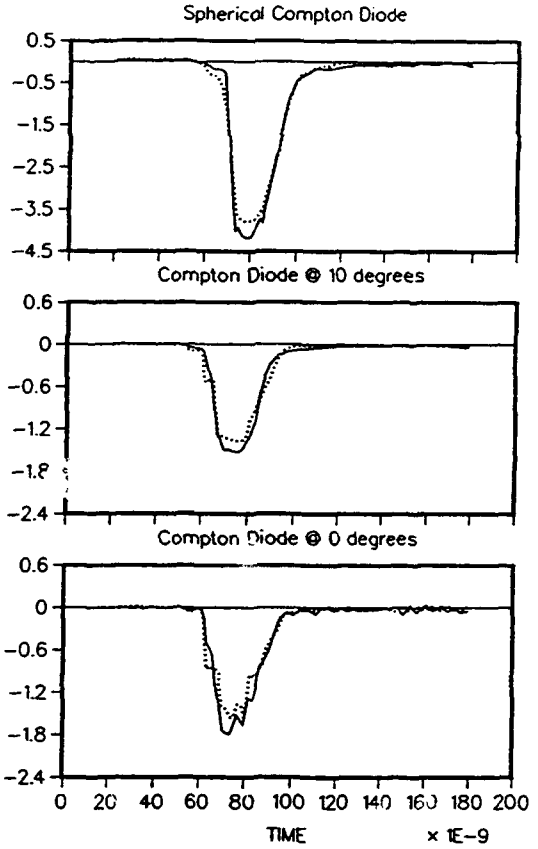

Figure 5. Radiation monitors waveforms for first and second pulse.

Summary

HERMES III with its unique and flexible modular linear induction design allows various operational modes. The half voltage mode discussed in this paper is important in its own right. First, it produces an 8.5 MeV endpoint energy comparable to the Hermes II [7] and old Aurora operating modes, which substantially reduces the activation of materials during tests and may be useful for simulation fidelity studies. Second, it allows convenient beam current (1/2) and dose (1/8) variations for some experiments. Third, it permits operation of Hermes III in a widely-spaced (millisecond regimes) double pulse mode, consisting of two half voltage pulses with equal beam and radiation characteristics, to study multiple pulse effects.

REFERENCES

[1] J. J. Ramirez, "Very High Pulse-Energy Accelerators," in *Proceedings of 1989 Particle Accelerator Conference,* Chicago, IL, March 20-23, 1989, edited by F. Bennett and J. Kopta (IEEE, NY, 1989) IEEE Catalog Number 89CH2669-0, 1446.

[2] T. W. L. Sanford, J. A. Halbleib, J. W. Poukey, D. E. Beutler, G. A. Carlson, G. T. Baldwin, T. Sheridan, R. Mock, R. S. Klingler, and D. P. Knott, "Radiation Field From an Extended Planar-Anode Diode on Hermes III," in *IEEE Transactions on Nuclear Science,* Vol. NS-36, No. 6 (Dec 1989) 1931.

[3] J. J. Ramirez, K. R. Prestwich, D. L. Johnson, J. P. Corley, G. J. Denison, J. A. Alexander, T. L. Franklin, P. J. Pankuch, T. W. L. Sanford, T. J. Sheridan, L. L. Torrison, and G. A. Zawadzkas, "Performance of the HERMES III Gamma Ray Simulator," *Digest of Technical Papers of the 7th IEEE Pulse Power Conference,* edited by R. White and B. H. Berstein (IEEE, New York, 1989), pp. 26-31.

[4] T. W. L. Sanford, J. A. Halbleib, J. W. Poukey, J. J. Ramirez, J. A. Alexander, G. Douglas, R. Mock, and T. Sheridan, "Indirect Measurement of HERMES III Voltage," in *Proceedings of 1989 Particle Accelerator Conference,* Chicago, IL, March 20-23, 1989, edited by F. Bennett and J. Kopta (IEEE, New York, 1989) IEEE Catalog Number 89CH2669-0, 1948.

[5] T. W. L. Sanford, J. A. Halbleib, J. W. Poukey, G. T. Baldwin, G. A. Carlson, W. A. Stygar, G. A. Mastin, T. Sheridan, R. Mock, J. A. Alexander, E. R. Brock, and C. O. Landron, "Dynamics of Electron Flow in Extended Planar-Anode Diode Operating at 19 MV and 700 kA," in J Appl Phys 67 (February 1990), 1700.

[6] G. A. Carlson, T. W. L. Sanford, and B. A. Davis, "A Solid Dielectric Compton Diode for Measuring Short Radiation Pulse widths," *Rev Sci Instr,* Vol. 61, p. 3447, 1990.

[7] G. A. Zawadzkas and K. A. Mikkelson, HERMES II Experimenters Manual, Revised, SAND77-0341 (Sandia National Laboratories: Albuquerque, NM, March 1983).

*Work performed under U.S. Dept. of Energy Contract No. DE-AC04-76DP00789

APPLICATION OF MAGNETICALLY INSULATED TRANSMISSION LINES FOR HIGH CURRENT, HIGH VOLTAGE ELECTRON BEAM ACCELERATORS*

S. L. Shope, M. G. Mazarakis, C. A. Frost, J. W. Poukey, and B. N. Turman
Sandia National Laboratories
Albuquerque, NM 87185

Abstract

Self Magnetically Insulated Transmission Lines (MITL) adders have been used successfully in a number of Sandia accelerators such as HELIA,[1] HERMES III,[2] and SABRE.[3] Most recently we used a MITL adder in the RADLAC/SMILE electron beam accelerator to produce high quality, small radius (r_b < 2 cm), 11 to 15 MeV, 50 to 100-kA beams with a small transverse velocity $v_\perp/c = \beta_\perp \leq 0.1$.[4] In RADLAC/SMILE, a coaxial MITL passed through the eight, 2 MV vacuum envelopes. The MITL summed the voltages of all eight feeds to a single foilless diode. The experimental results are in good agreement with code simulations.

Our success with the MITL technology led us to investigate the application to higher energy accelerator designs. We have a conceptual design for a cavity-fed MITL that sums the voltages from 100 identical, inductively-isolated cavities.[5] Each cavity is a toroidal structure that is driven simultaneously by four 8-ohm pulse-forming lines, providing a 1-MV voltage pulse to each of the 100 cavities. The point design accelerator is 100 MV, 500 kA, with a 30-50-ns FWHM output pulse.

Introduction

MITLs are efficient in performing the series addition of voltage pulses from inductively isolated cavities. When the output is used with a foilless diode, immersed in an applied magnetic field, very high current, low emittance, high brightness beams can be produced. Accelerators with MITL-adders have an advantage over conventional linear induction accelerators because there is no beam transport with associated beam instabilities through the length of the accelerator.

The success we have had with this technology prompted us to design a 100-MV, 500-kA electron beam accelerator. There are practical upper limits to this approach. One is the length of the MITL and the effects of gravitational droop in a horizontal configuration. This can be reduced by building the accelerator vertically, but again there are limits to this approach. Another constraint is the center stalk radius which is determined by the system impedance. The 100-MV system does not approach either of these limits.

Magnetic Insulation

The theory of magnetic insulation is given in several references.[6,7] We have used the criteria for self-magnetic insulation derived from Creedon's theory. In the Creedon

*This work performed at Sandia National Laboratories supported by the U.S. Department of Energy under contract DE-AC04-76DP00789.

formalism the minimum current, I_ℓ, required to establish self-limited magnetic insulation is given by:

$$I_\ell = 8500\ g\ \gamma_\ell^{2/3}\ \ell n\left[\gamma_\ell + (\gamma_\ell^2 - 1)^{1/2}\right] ,$$

$$\gamma_0 = \gamma_\ell + \left[\gamma_\ell^2 - 1\right]^{3/2}\ \ell n\left[\gamma_\ell + (\gamma_\ell^2 - 1)^{1/2}\right] ,$$

$$g = \left(\ell n\ R/r_i\right)^{-1} \text{ and } \gamma_0 = V(MV)/mc^2 + 1 = \left(1 - v^2/c^2\right)^{-1/2} .$$

The relativistic Lorentz factor, γ_ℓ, is for electrons at the boundary of the electron sheath in the minimum current case.

This formalism was successfully used in designing a MITL for the linear induction accelerator, RADLAC. The MITL eliminated the accelerating gaps and B_z transport system that had yielded unsatisfactory beam quality. The design was simulated with the PIC MAGIC code.[8] Figure 1 shows an electron map of the SMILE configuration used in RADLAC and verifies that magnetic insulation does occur. The losses near the cathode tip were expected and are due to the radial component, B_r, of the applied magnetic field of the foilless diode. Simulations of the diode region have shown that the output current is a function of the beam loss at the divergence of the applied magnetic field, the magnitude of the applied field, and the anode-cathode spacing. A diode simulation is shown in Fig. 2. Examples of the beam out of RADLAC/SMILE are shown in Fig. 3.

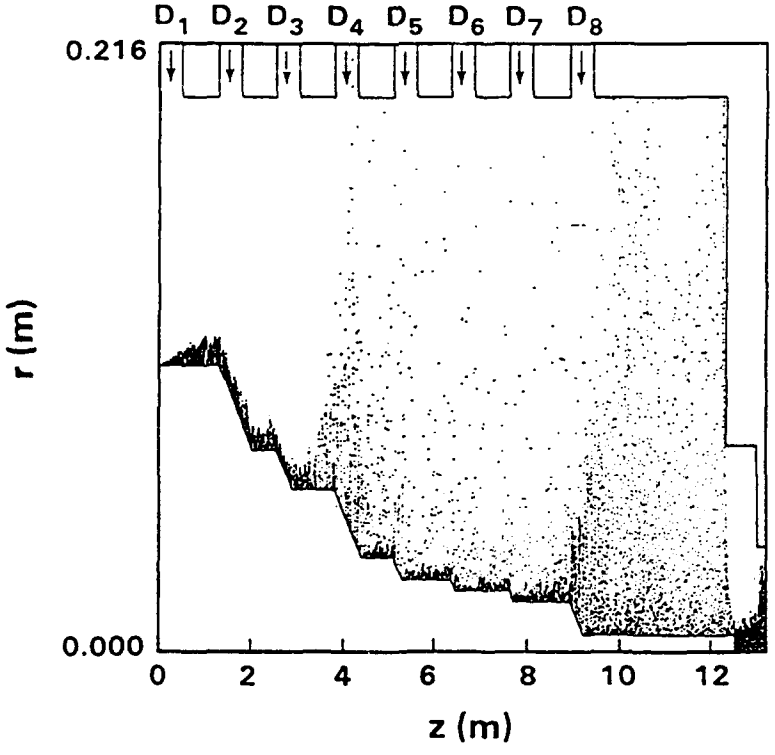

Fig. 1: Simulations showing magnetic insulation of SMILE.

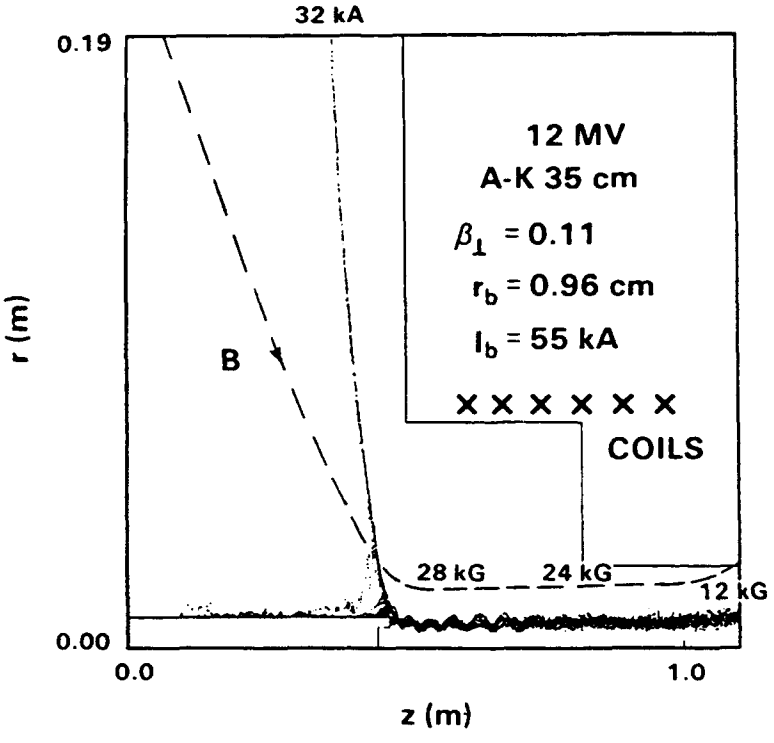

Fig. 2: Simulation of a typical SMILE foilless diode.

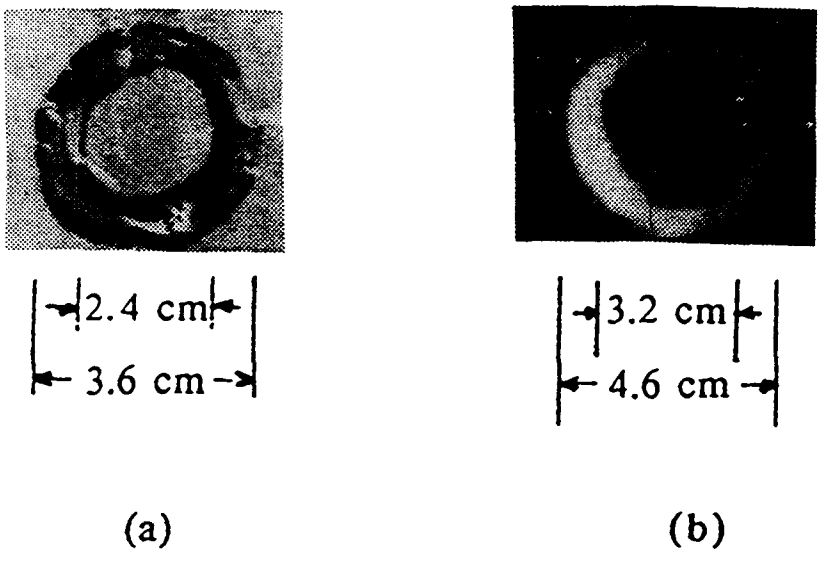

Fig. 3: (a) Witness foil of a 13-MeV, 78 kA-beam with $\beta\perp$ = 0.05.
(b) X-ray pinhole photograph of a 10-MeV, 80-kA beam with $\beta\perp$ = 0.07.

100-MV Accelerator Design

Based on the successful performance of accelerators using MITLs at Sandia National Laboratories we designed a 100-MV, 500-kA accelerator. The design has 100, 1-MV, toroidal cavities that sum the voltages of each cavity in series resulting in a 100-MV output voltage. The cavities could utilize ferromagnetic materials to provide the required inductive isolation or they could be isolated Blumleins using a liquid dielectric such as deionized water. The 100-MV accelerator can be visualized as 10 SABREs connected in series with one MITL.

For the design of the tapered MITL stalk we fixed the inner radius of the cavities at 19.1 cm and calculated the required radius of the stalk to achieve magnetic insulation. We divided the accelerator into 10 segments for this purpose. The results are shown in Table 1.

Table 1

Radius and impedances of a 10-stage tapered MITL for a 100-MV accelerator.

MITL Segment i	Segment Voltage V_i [MV]	Cathode Radius r_i [cm]	Operating Impedance Z_i [Ω]	Vacuum Impedance Z_i [Ω]
1	1	17.9	2	3.73
10	10	12.59	20	24.85
20	20	8.73	40	46.82
30	30	6.12	60	68.13
40	40	4.34	80	88.75
50	50	3.02	100	110.51
60	60	2.13	120	131.14
70	70	1.50	140	152.50
80	80	1.06	160	173.32
90	90	0.74	180	194.89
100	100	0.514	200	216.75

The MITL would start at a radius of 17.9 cm and taper to a final radius at the cathode of 0.5 cm. The length would be 58 m and weigh ~500 lbs. This could be cantilevered from one end and preloaded to compensate for gravitational droop, however, it would be preferable to build the accelerator vertically and eliminate the droop. A conceptual drawing of the accelerator is shown in Fig. 4. Since the potential on the stalk is logarithmic in R/r the alignment at the high voltage end, where radii are small, is not critical. RADLAC/SMILE produced excellent quality beams with the MITL as much as 20% misaligned.

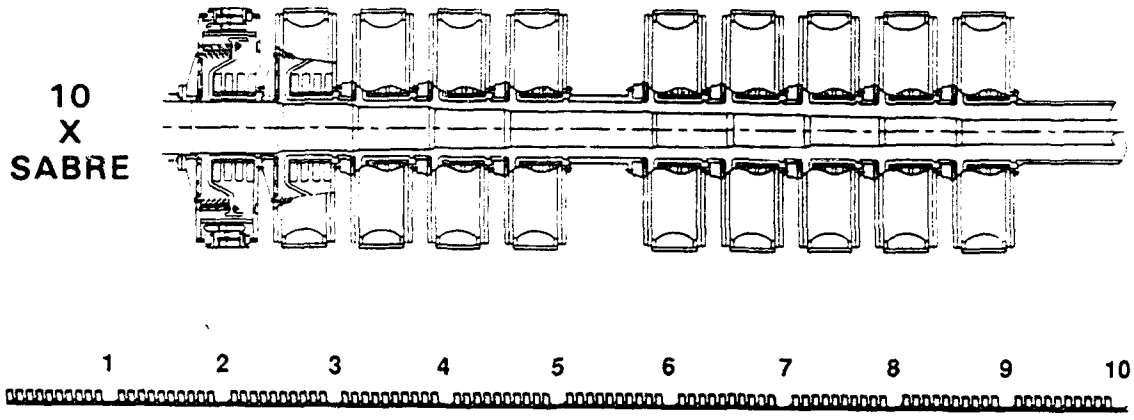

Fig. 4: Drawing of a 100-MV accelerator based on SABRE technology.

A PIC MAGIC simulation of the 100 MV, 500-kA foilless diode is shown in Fig. 5. Simulated output waveforms are shown in Fig. 6 for square and triangular inputs.

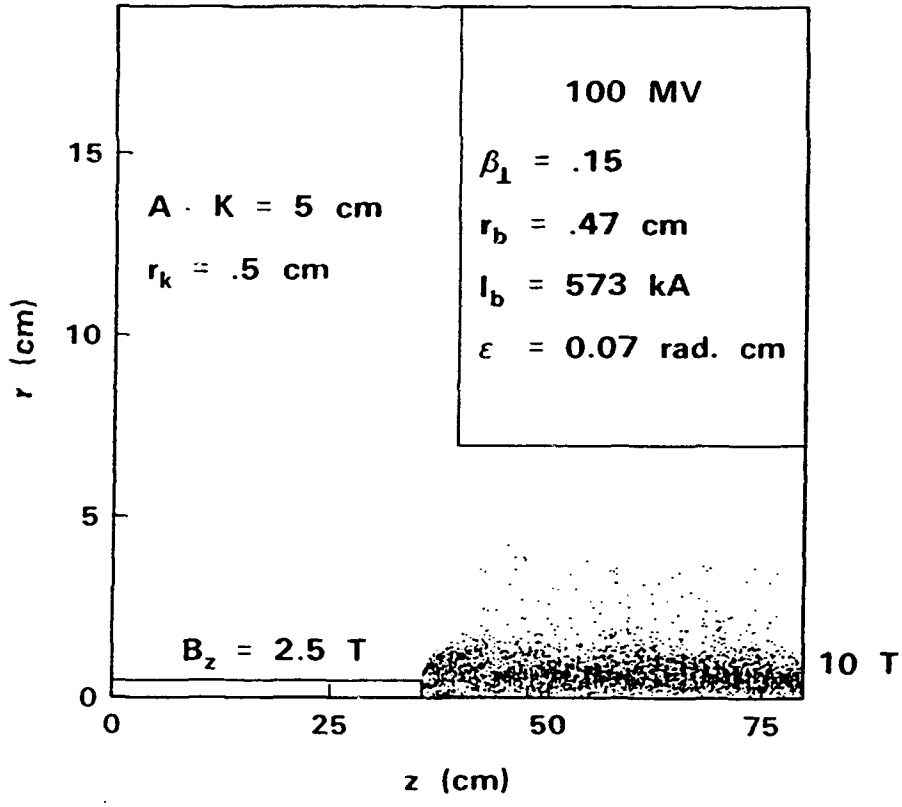

Fig. 5: Simulation of a 100-MV immersed diode and calculated output parameters.

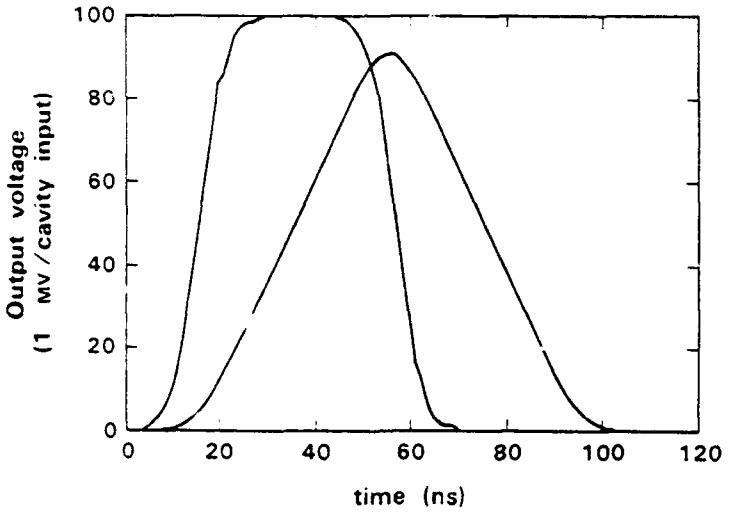

Fig. o: Calculated diode outputs for a square and triangular input.

Another interesting accelerator configuration we have looked at would be to fold the accelerator into an "S" shape, see Fig. 7. This could halve the length of the accelerator. The "S" shape is a stable configuration and would be a strong structure with extra reinforcing in the bends. Both AURORA[9] and HYDRA[10] have successfully used curved MITLs. The physical size of either concept could be reduced if fewer but higher voltage cavities were used.

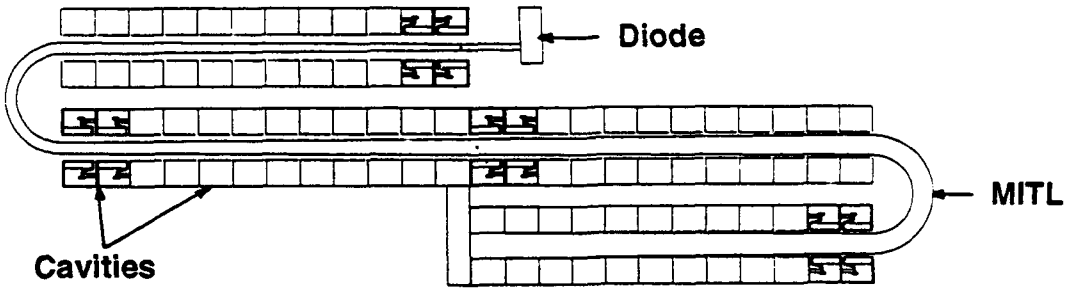

Fig. 7: Conceptual drawing of an "S" shaped accelerator.

Conclusion

We have a conceptual design of a high voltage, high current accelerator based on an extrapolation of proven technology. The design is based on SABRE and HERMES III type accelerators in series. The design is modular and could be built in stages. Low emittance, high brightness beams can be produced with magnetically immersed foilless diodes that are driven by MITLs.

References

[1] J. J. Ramirez, et al., Proc. 5th International IEEE Pulsed Power Conf., Arlington, VA, p. 143 (June 10-12, 1985).
[2] R. C. Pate, et al., Proc. 6th International IEEE Pulsed Power Conf., Arlington, VA, p. 478 (June 29-July 1, 1987).
[3] D. L. Johnson, et al., Bull. Am. Phys. Soc. 35, No. 4, 955 (1990).
[4] M. G. Mazarakis, et al., Proc. 1990 Linear Accelerator Conf., Albuquerque, NM, LA-12004-C, p. 438 (September 10-14, 1990).
[5] M. G. Mazarakis, et al., Proc. 1991 IEEE Int. Conf. on Plasma Sci., Williamsburg, VA, p. 109 (June 3-5, 1991).
[6] R. Lovelace and E. Ott, The Phys. of Fluids, 17, No. 6, p. 1263 (1974).
[7] J. H. Creedon, J. Appl. Phys. 48, p. 1070 (1977).
[8] B. Goplen, et al., "Users Manual for MAGIC/Version-Sept. 1983, MRC/WDCR/068," Mission Research Corp., Washington, D.C. (1983).
[9] B. Bernstein and I. Smith, IEEE Trans. Nucl. Sci. NS-20, 3 (1973).
[10] S. Shope, et al., J. Appl. Phys. 49, (7), p. 3675, (1978).

Modelling Pulsed-Power Transmission Lines

C. W. Mendel, Jr., D. B. Seidel,
W. A. Johnson and S. E. Rosenthal
Sandia National Laboratories, Albuquerque, NM 87185

Abstract: Transmission lines in modern pulsed-power machines such as PBFA-II operate at ten or more megavolts with multi-megampere currents. They often have series (voltage) or parallel (current) power addition. In these transmission lines the cathodes emit electrons freely. In addition, perturbations such as plasma opening switches cause additional electrons to be launched into the flow. The large magnetic field due to the transmission line current prevents these electrons from crossing the transmission line to the anode directly, but in most situations electron current flows to the anode after travelling a long distance down the transmission line. Usually these losses occur just before the load or at adder points.

Reliable modelling of these lines is important both for design purposes and for use in analyzing data. This paper presents models that can be used for these purposes. The models are primarily based upon known symmetries plus measurable parameters. Comparisons to data, particularly data taken on PBFA-II, are made.

Introduction: Figure 1 shows a schematic of an equilibrium magnetically-insulated electron flow (MIFL). Several physical parameters describing the flow are illustrated in the figure. Fortunately most of the characteristics of a MIFL can be derived exactly, or to good approximation, using only considerations of global symmetry such as pressure balance across the flow,[1] added to a few experimental observations. Because of this, these flows can be modelled without considering microscopic details of the flow.

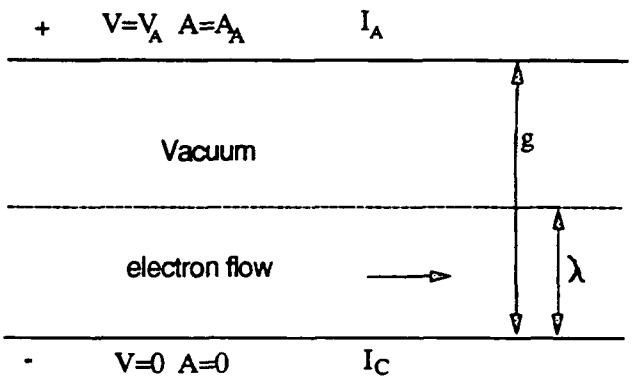

Figure 1. Schematic of a MIFL.

Table I shows several relationships between physical parameters and measurable quantities. These relationships are derived from pressure balance across the flow, Maxwell's equations, and two experimental observations. It is easily seen that pressure balance must occur at frequencies to which most diagnostics can respond. The first experimental observation is that cathodes in MIFL are space-charge-limited emitters of electrons. This has been verified in many experiments, e.g., experiments that use this assumption to calculate voltage from line currents. The second assumption is that any ion emission from electrodes is small enough that ion pressure is negligible. If this were not true,

Table I

line-charge	$q=\frac{\sqrt{I_A^2-I_C^2}}{c}$
drift velocity	$v_d=c\sqrt{\frac{I_A-I_C}{I_A+I_C}}$
line voltage	$V=Z_o\sqrt{I_A^2-I_C^2}-\frac{mc^2}{e}f(I_A/I_C)$
flow impedance	$Z_f\equiv\frac{V}{\sqrt{I_A^2-I_C^2}}$
vector potential	$Z_f<\frac{cA_A}{I_a}<Z_o$
electron density	$\rho>\rho_o=\frac{e\epsilon_o B_C^2}{m}$
sheath thickness	$\lambda\approx\lambda_o=g\frac{mc^2}{Z_o e}\frac{\sqrt{I_A^2-I_C^2}}{I_C^2}$
current ratio	$\frac{I_A}{I_C}<1+\frac{eV}{mc^2}$

Table II

front velocity	$v_f=\frac{V_A}{A_A}$
front velocity	$\frac{Z_f}{Z_o}\frac{\sqrt{I_A^2-I_C^2}}{I_A}<\frac{v_f}{c}<\frac{\sqrt{I_A^2-I_C^2}}{I_A}$
front/drift velocities	$\frac{Z_f}{Z_o}\frac{I_A+I_C}{I_A}<\frac{V_f}{V_d}<\frac{I_A+I_C}{I_A}$
front current	$I_f=I_A-\sqrt{I_A^2-I_C^2}\frac{v_f}{c}$

magnetically-insulated transmission lines (MITL) would not be efficient. There are local areas where ion emission is important, for instance plasma-opening switches (POS).

In Table I, Z_o is the transmission line vacuum impedance, V_A is the line voltage, and A_A is the line vector potential, i.e., the integral of the transverse magnetic field across the line gap. The effective gap, g, is the actual gap in the case of a stripline, or $(r_A^2-r_C^2)/2r_C$ in the case of a coaxial line. The function f in the expression for the line voltage depends upon the form of the space-charge correction, i.e., it depends upon the way electrons are distributed across the transmission line. A useful expression for f,

$$f(I_A,I_C)=(I_A^2-I_C^2)/I_C^2 \quad ,$$

is based upon the assumption that the electrons are in a constant density sheath with density given by ρ_o. The sheath thickness must then be given by λ_o. The space-charge correction term determined by f is small at high voltage (compared to mc^2/e), and becomes negligible at very high voltages (> 5 MV).

An additional assumption supported by experiment, that TEM fronts moving slower than the speed-of-light exist, leads to Table II. In addition, it can be shown that the thickness of the electron sheath and the ratio of cathode to anode current behind the front go to zero, and that the front velocity goes to c as the voltage on the transmission line voltage becomes infinite.

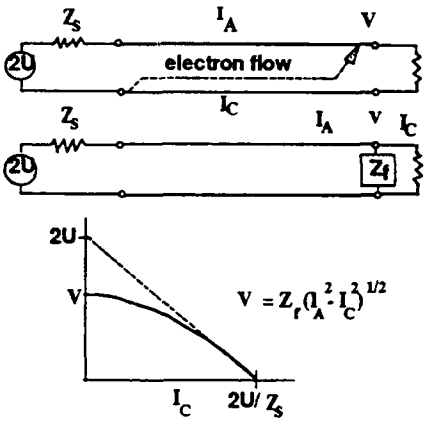

Figure 2. Flow impedance model of a MITL circuit, and the I,V characteristic.

impedance element at the end of the transmission line ,Z_f, must be less than the impedance of the TEM wave in vacuum, Z_o. At very high voltage it is often satisfactory to use the actual value of Z_o. If there are added electron losses, for example feed losses at the load, a smaller value may be required to fit the data. Figure 2 also shows the I,V characteristic of the model,

Flow Impedance Model of Transmission Lines: Figure 2 shows a MITL and a simple model that can be used with a circuit code. The flow impedance circuit element is not a simple resistor, but rather obeys the equation in Table I. The value of the flow

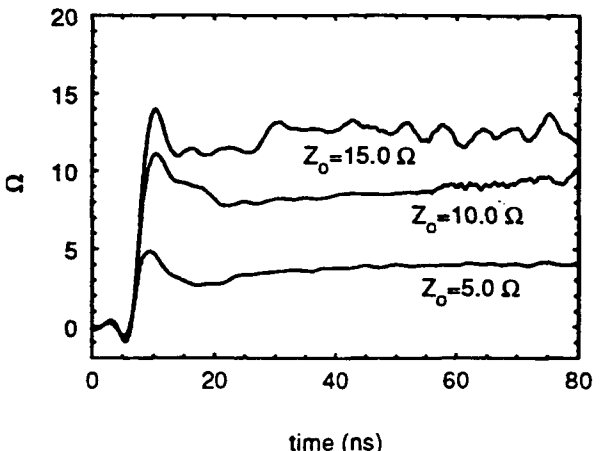

Figure 3. Flow impedance versus time for three perturbations in a MITL. The numbers by each curve are the vacuum TEM impedances of the perturbation.

showing the voltage-limiting effect. Figure 3 shows the flow impedance of feed perturbations in TWOQUICK[2] simulations of the PBFA-II ion diode. Notice that the flow impedance is essentially constant in spite of the variation of the line voltage and the diode impedance with time.

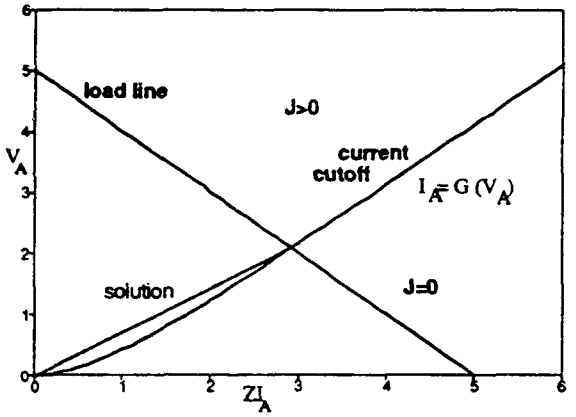

Figure 4. The loss current J in the I,V plane.

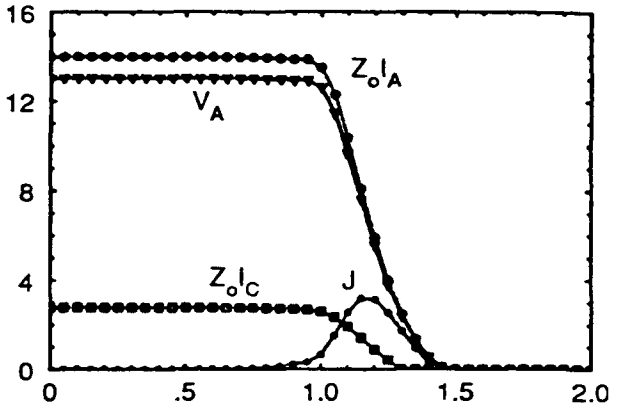

Figure 5. A moving front solution.

Modelling MITLs with Loss Fronts: In long MITLs loss fronts are important. A set of telegrapher's equations can be written for this case.

$$\frac{\partial V_A}{\partial t}=-cZ_f\frac{\partial I_A}{\partial x} \qquad \frac{\partial I_A}{\partial t}=-\frac{c}{Z_o}\left[\frac{\partial V_A}{\partial x}+J(V_A,I_A)\right]$$

The flow impedance occurs in the first equation because the displacement current to the anode depends upon the electric field at the anode, rather than the voltage divided by the gap, i.e., the average electric field. The cathode current can be calculated from V_A,I_A and the flow impedance (Table I). The loss current in the front can be modelled by the function $J(V_A,I_A)$. Figure 4 shows the I,V plane, and the behavior of J on that plane. There is some curve $I_A=G(V_A)$ to the right of which the loss current is zero. Since the front velocity is determined by the intersection of the load line with the current cutoff curve, the front velocity as a function of voltage behind the front is given by

$$v_f=V_Ac/Z_oI_A \qquad G(V_A)=I_A=V_Ac/Z_ov_f$$

and the load line of the generator. The cutoff current, G, might be determined from the usual Hull condition, but this generally gives a higher front velocity than is seen in experiments. The voltage and the current behind the front extend all the way to the input, so that the line will run at the intersection between the insulation line and the driver load line, shown schematically in Fig 4. Since the condition $v_f=V/A$ is true for every point in a moving TEM front, the solution $V(x-v_ft)$, $I(x-v_ft)$ lies along a line from the insulation line (representing all points behind the front) to the origin (representing all points ahead of the front). The voltage versus the current in the front is shown in the figure. Since the loss current, J, is zero ahead of the front and behind the front, there is a maximum between, probably close to the front.

The partial differential equations can be solved for local voltage and current. Figure 5 shows such a

solution for the case

$$J(V_A,I_A)=[G(V_A)-I_A]V_A/\chi Z_o$$

where I_A is less than F and zero elsewhere. χ is a constant and the Hull condition was used for G. This J gives an exponential behavior to the fronts. Experimental fronts tend to steepen continually, but finite difference methods will limit the solution. Generally the exact shape of the front solution is not important; consequently other dependences of J could be used.

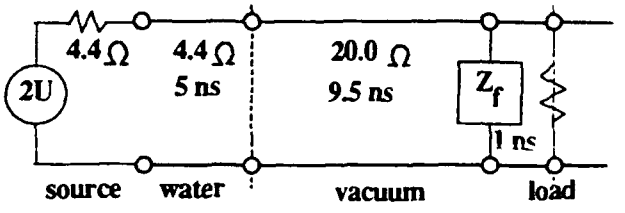

Figure 6. Model of PBFAII. It is symmetric about the load, representing top and bottom feeds.

Modelling MITLs, J=0 Case: In most experiments the MITLs are relatively short. The maximum length of the PBFA-II MITLs are less than 8 light-nanoseconds long, and since the front velocity in MITLs at PBFA-II voltages is >0.8c, the timing error due to neglecting front current is less than 2 ns which is about the timing tolerance of the data. The assumption that J=0 has an enormous effect in computational time because the equations can then be integrated to get the forward and backward waves:

$$F(x-v_f t)=[V_A(x,t)+Z_o I_A(x,t)]/2$$
$$B(x+v_f t)=[V_A(x,t)-Z_o I_A(x,t)]/2 \quad .$$

Using these equations each time step involves calculating two points for each transmission line and moving two array pointers. A model for PBFA-II which includes top and bottom water lines and two top and bottom MITLs (ergo 6 transmission lines) takes 3 seconds to calculate a solution for 500 time steps (33 MHz, 386 PC). A similar calculation with a loss front takes about ten minutes on the same computer.

Losses at adder points, POS[3], or before loads can be modelled using flow impedance circuit components. Figure 6 shows a model used to simulate PBFA-II data. The flow impedances before the load can be time-dependent to simulate the POS on experiments that have a POS, or can be constant at the line impedance of non-POS shots. Figure 7 shows the fit of a solution to PBFA-II data (top). The fit could be improved with more general functions for forward wave voltage, POS flow impedance, and load impedance, but after about 60 ns the top insulator has flashed and the model cannot be correct. The bottom data were similar.

The MITLs on PBFA-II actually each consist of four 5 Ω sections added in series per side. Early in the power pulse, before the ion diode has begun to carry current, there are losses at each adder point. The data indicate that a flow impedance model can be used to model the adder losses, but we have not made such a model yet.

We have also developed a two-dimensional quasi-TEM theory for conical transmission lines when loss current can be neglected.[4] It appears that the flow impedance model can be modified to calculate electron losses including azimuthal dependence with this model, but this work is still in progress.

Acknowledgement: This work was supported by the United States Department of Energy under Contract No. DE-AC04-76DP00789.

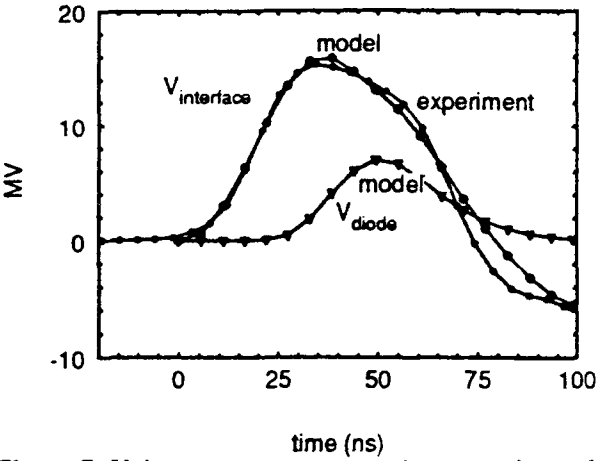

Figure 7. Voltages in the water section (experimental and model) and voltage at the diode load (model).

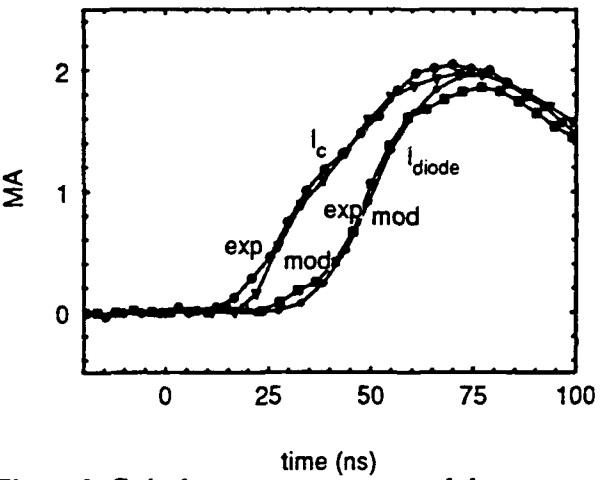

Figure 8. Cathode currents upstream and downstream of the POS.

1. C. W. Mendel, Jr., D. B. Seidel, and S. E. Rosenthal, Laser and Particle Beams 1, 311 (1983).

2. T. D. Pointon and D. B. Seidel, private communication. TWOQUICK is a 2-dimensional particle-in-cell code currently under development, based on the 3-dimensional code QUICKSILVER (D. B. Seidel, M. L. Kiefer, R. S. Coats, T. D. Pointon, J. P. Quintenz, and W. A. Johnson, Computational Physics, Edited by A. Tenner, World Sci. Publishing Co., Singapore 1991, p. 475).

3. C. W. Mendel, Jr., G. E. Rochau, M. A. Sweeney, D. H. McDaniel, J. P. Quintenz, M. E. Savage, E., L. Lindeman, J. M. Kindel, Proceedings of the Novosibirsk Opening Switch Workshop, Siberia, USSR, 1989 (to be pub). C. W. Mendel, Jr., M. E. Savage, D. M. Zagar, W. W. Simpson, T. W. Grasser, and J. P. Quintenz, J. Appl. Phys. 71, 3731 (1992).

4. W. A. Johnson, C. W. Mendel, Jr., and D. B. Seidel, J. Appl. Phys. 71, 4034 (1992).

PULSED POWER ELECTRON ACCELERATORS WITH THE FORMING SYSTEMS BASED ON STEPPED TRANSMISSION LINES

V.S.BOSSAMYKIN, V.S.GORDEEV, A.I.PAVLOVSKII,
A.P.KLEMENT'EV, O.N.SYUTIN, A.V.BUDAKOV, V.F.BASMANOV,
A.P.GRIDASOV, V.O.FILIPPOV, G.A.MYSKOV

SCIENTIFIC RESEARCH INSTITUTE OF EXPERIMENTAL PHYSICS

Arzamas-16, Nizhni Novgorod region, 607200, Russia

Last years the electron accelerators I-3000 (3.2 MV, 20 kA, 15 ns), STRAUS(2.7 MV,15 kA,40 ns) and STRAUS-2 (3.3 MV, 50 kA,40 ns) were created for pulsed bremstrahlung radiation generation and other applications. Relatively small dimensions and energy store (10-24 kJ), stable output characteristics make this devices convenient tools for systematic scientific investigations. A considerable increase in the accelerating voltage compared with the charge one (500 -700 KV) is provided by the wave processes in the stepped transmission lines. The accelerating cavity of the LIU-10M accelerator (25 MV, 50 kA, 22 ns, 3 MeV/m) being created now are based on the similair schematic design. The STRAUS-2 accelerator is employed as an injector of LIU-10M device.

Alongside with the analysis of new arrangments for powerful electric pulse production and transformation based on homogeneous and stepped lines [1,2], the authors were engaged in development of comparatively small 2-4 MeV accelerators to provide various researches. At the same time the obtained results were always considered from the point of view of further possibilities in linear induction accelerators (LIA) development, as well as their basic components - accelerating modules, injectors and other pulsed systems.

In 1981 when I-3000 facility was created on the basis of two LIU-10 modules, a dramatic increase in the accelerating voltage was realized compared to the charging one [3]. To increase the accelerating voltage generated by six LIU-10 cavities, the additional transmission line was used. This technique is often used in unipolar pulse generators. However a substantially greater effect can be obtained for the generators forming a bipolar voltage pulse. Fig.1 presents the scheme of Z_L resistive load connection to a cavity (some cavities) of Z_1 impedance via a homogeneous transmission line of Z_2 impedance and T_0 electric length.

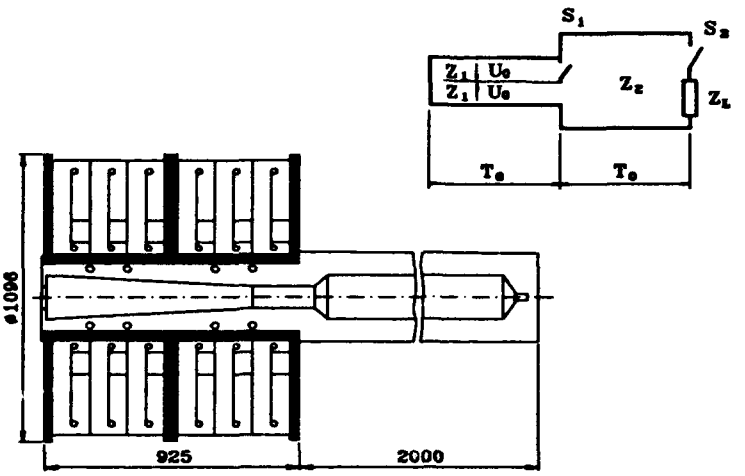

Fig.1. I-3000 concept and schematic design

At t=0, one of high voltage cavity gaps is closed by S_1 switch. For the first voltage pulse regime the load is constantly switched on to the transmission line output and for the second pulse regime it is commutated at $t=3T_0$ when the voltage changes the polarity at the line output. For the mentioned regimes optimal Z_2 impedances are the following : $Z_{21}=(Z_L Z_1)^{1/2}$, $Z_{22}=Z_1(1+(1+8Z_L/Z_1)^{1/2})/2$. Thus , the maximal load voltage is

$$U_1=2U_0 Z_L((Z_1)^{1/2}+(Z_L)^{1/2})^{-2},$$

$$U_2=4U_0 Z_L(Z_{22})^2(Z_1+Z_{22})^{-2}/(Z_L+Z_{22}).$$

The second regime provides a considerable increase in the voltage. For example, at Z_L/Z_1 = 10 and first pulse operation ($Z_{21}/Z_1=3.2$), the voltage grows in 1.15 times compared to charging one due to the transmission line , and for the second pulse operation ($Z_{22}/Z_1= 5$) - in 1.85 , i.e. the additional growth is 60%. With Z_L/Z_1 relation increase this gain tends to 100% (U_1/U_0->2, U_2/U_0->4).

Main components in I-3000 facility are two injector modules of LIU-10 accelerator with 360 mm vacuum cavity diameter , two Marx generators GIN-500, trigger generators for switches and vacuum transmission line (Z_2 = 43 Ohm) 2m long with a field-emission diod. The diod simultaneously functions as a prepulse switch cutting off the first 2 MV voltage pulse of a reverse polarity. Each module contains three cavities -1m in outer diameter, ten switches commutate the forming line of each cavity. The inner electrode of the transmission line is 240 mm in diameter , a grounded one - 510 mm , a graphite cathode - 30 mm. The maximum energy store is 12 kJ. At 95 kV GIN charge

voltage, 20 kA diode current and 16 ns pulse half-width , the peak electron energy was 3.5 MeV. At 0.8 level against the maximum of the electron energy distribution energy variates in the range 3.0-3.4 MeV. Gamma-pulse width is 12 ns. The target axis dose was $2 \cdot 10^3$ rad (TLD), at 1m distance - 8 rad. The dose rate at the target of 10 cm in diameter equals 10^{11} rad/s; at 1m distance from the target - $7 \cdot 10^8$ rad/s. I-3000 facility provided ~5% gamma-radiation output stability.

Multicascade stepped line-based pulsed facilities are characterized by a high coefficient of voltage transformation and effective energy transfer onto the load [2]. Voltage increase can be achived by one multichannel switch. To determine the facility of accelerator arrangements and possibility of monoenergetic electron beam reseaches the first accelerator named STRAUS was constructed in 1983. The generator is based on a double stepped forming line (fig. 2a) formed by five transmission line sections of equal electric length T_0 and $Z_2/Z_1 = Z_3/Z_4 = 3$, $Z_4/Z_1 = 5/4$, $Z_5/Z_1 = 15$ impedances. At t=0 the commutator is switched on closing 1 and 4 line outputs. At $t=4 \cdot T_0$, Z_L load is commutated to the transmission line output via S_2 switch. On a matched load $Z_L = Z_5 = 15 \cdot Z_1$ a single $2T_0$, $3U_0$ pulse is formed during which the energy from 1-4 lines is transferred to the load. At $Z_L >> Z_5$ the output voltage exeeds the charging one in 6 times.

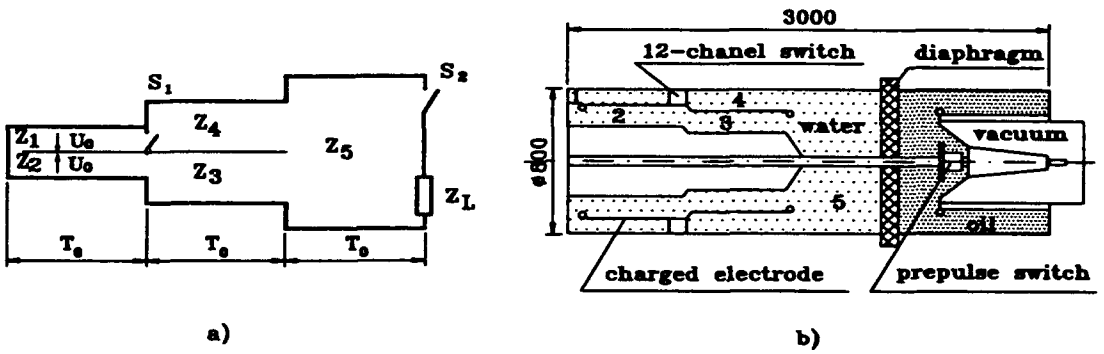

Fig.2.STRAUS concept and schematic design

Fig.2b shows the accelerator design scheme. The coaxial electrodes of stepped form are emplaced in 3m long casing 0.8m in diameter.The multichannel commutator is formed of twelve spark switches. Deionized water insulates the

lines. Line section electric length is 20 ns, the impedance values are Z_1=1 Ohm, Z_2=3.2 Ohm, Z_3=4 Ohm, Z_4=1.3 Ohm, Z_5=16 Ohm.

The accelerating tube comprises of a sectioned vacuum insulator enveloped with a tubular layer of electrolyte (NaCl water solution) and an external polyethelene tube. The electrolytic load serves for electric field levelling on the vacuum surface and for left in the lines energy absorbtion. Transformer oil fills the volume between the accelerating tube and separating diaphragm. The electron diod is commutated to the transmission line output at the desired moment, when the single-chanell triggered gas-filled prepulse switch starts operating. The DSFL is charged to 530 kV in 800 ns by one GIN-500 of 80 nF capacitance and 10 kJ energy Marx generator. At total 25 kA current (15 kA in the electron beam, 10 kA - in the electrolyte) the accelerating voltage was 2.7 MV. In the matched regime , current is 100 kA at 1.5 MV voltage. Diode current pulse is trapezi form with duration $t_{0.5}$=40 ns. The gamma pulse of the same form has $t_{0.5}$=32 ns and $t_{0.9}$=20 ns . From the point of view of gamma-radiation production ,the optimal is regime at 2.3 MV accelerating voltage and 20 kA electron current. The target axis dose was $4.5 \cdot 10^3$ rad, the one at 1m distance - 9 rad. The accelerator can produces for tens of shorts a day with well reproducing.

The experimental results obtained at STRAUS device absolutely confirmed the theoretical analisys conclusions for the stepped line devices.

In 1989 a more powerful accelerator STRAUS-2 was constructed to be used as an injector for LIU-10M upgrade and for other applications. It consists of a high-voltage pulse generator, two six-cascade Marx generators GIN-600 and other systems.

Pulse generator is also based on DSFL comprising 5 line sections with T_0=18 ns being water insulated which are optimized for electron beam injector regimes and gamma-radiation production according to the impedance relationships $Z_1:Z_2:Z_3:Z_4:Z_5$ = 1.1:1.0:2.4:4.0:22.5; the impedances values are 0.9, 0.8, 1.9, 3.2 and 18 Ohm , correspondingly. In idial case it allows to increase the voltage transformation coefficient from 6 to 7.2.

Pulse generator diameter is 1.2m , total axial dimension of the electron beam generator - 2.7m (Fig.3). DSFL is commutated by twenty switches . The pulse generator is switched to the accelerating tube via a triggered prepulse switch. DSFL is charged to -750 kV voltage in 560 ns by two GIN-600 of 130 nF capacitance (24 kJ energy).

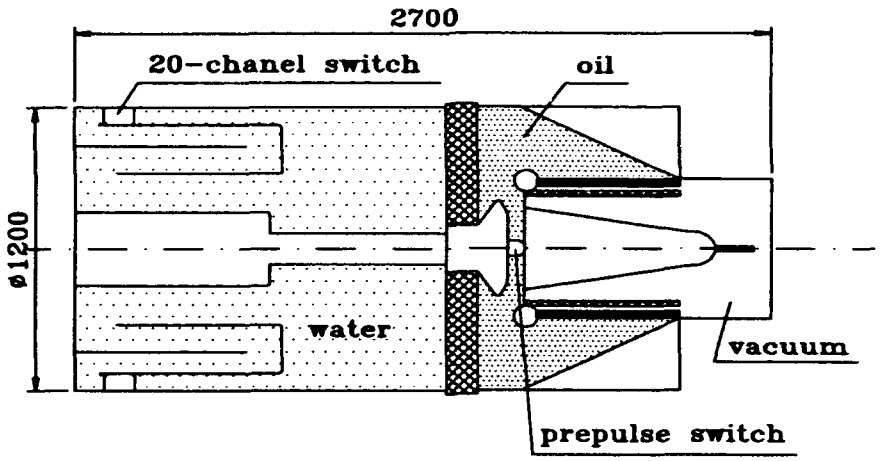

Fig.3.STRAUS-2 schematic design

Electron current pulse of 50 kA amplitude lasts $t_{0.5}$=40 ns and $t_{0.9}$=27 ns (20 kA electrolyte current). The leading front width is 12 ns. In this regime gamma-radiation dose on the target axis was 10^4 rad, in the spot 7 cm in diameter, and 25 rad - at 1m on the area 0.8 m in diameter. Gamma-pulse width $t_{0.5}$=25 ns, the dose rate 10^9 rad/s at 1m distance. When the anode-cathode gap was reduced the target dose increased to $1.8 \cdot 10^4$ rad , the dose rate grew up to $7 \cdot 10^{11}$ rad/s on the spot 5 cm in diameter. The electron peak energy was 3.3 MeV that corresponds to the maximal voltage at the open end of DSFL 4.5 MeV. Thus , the real transformation coefficient is 6.5. In the injection tests with electron beam from the foilless diode into the drift tube with the longitudinal magnetic field the problems of formation and transportation were studied at 40-70 kA currents.

LIU-10M accelerator consist of the injector and 16 accelerating modules. Fig.4 shows the accelerating cavity comprising the high-voltage pulse generator based on four-cascade DSFL and the accelerating tube with the solenoid to excite the longitudinal magnetic field. Three coaxial line sections of Z_1=0.55 Ohm, Z_2=1.65 Ohm, Z_3=3.3 Ohm impedances are implaced in series over the radius in the limit of one axial dimension. The fourth section with Z_4=1.1 Ohm is fabricated in the form of a homogeneous radial line formed by a high-voltage electrode and cavity casing. The cavity diameter is 1.1 m, the axial dimensions - 0.57 m.

DSFL is commutated by twenty spark switches. The charging to 560 kV in 850 ns is done with the five-cascade Marx generator GIN-500 (10 kJ, 80 nF).

The pilot accelerating cavity was constructed in 1987. At 100 Ohm load , the first and the second voltage pulse amplitudes were 1.2 and 2.0 MV, the full pulse durations - 30 and 34 ns, $t_{0.5}$=22 ns. The comparision of the experimental data with the numeric simulation results showed their good agreement in time and amplitude characteristics.

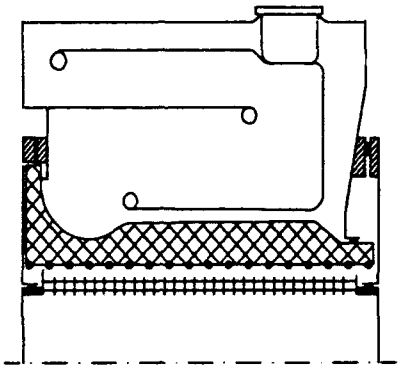

Fig.4.LIU-10M accelerating cavity schematic design

The sectioned insulator was placed inside the polyethelene tube, the solenoid being located in the electrolyte layer. The magnetic field was 5.5 kG in the vacuum cavity. At 60 Ohm electrolyte layer resistance and 50 kA electron beam current the accelerating voltage amplitude is 1.6 MV at 2.8 MeV/m accelerating gradient.

LIU-10M accelerator must have the following output parameters: ~25 MeV electron energy, ~50 kA beam current, ~22 ns current pulse width.

Nowadays the LIU-10M is being put into operation. In the tests of the 50 kA beam acceleration with the injector and four modules , 9 MeV acceleration energy was obtained during the stable transport of the annular beam 120 mm in diameter and ~10 mm thick.

In conclusion it should be noted that the data obtained in the course of the operating device creation testify about the perspective of stepped line scheme application in high-voltage and acceleration technique.

REFERENCES

1.A.I.Pavlovskii, V.S.Bossamykin. Atomnaya energiya 37, No.3 (1974) 228.
2.V.S.Bossamykin , V.S.Gorgeev , A.I.Pavlovskii New schemes for high-voltage pulsed generators based on stepped transmission lines.- in this Proceedings.
3. A.I.Pavlovskii, V.S.Bossamykin et al. Dokl.Akad.Nauk SSSR, 250(1980) 1118.

NEW SCHEMES FOR HIGH-VOLTAGE PULSED GENERATORS BASED ON STEPPED TRANSMISSION LINES

V.S.BOSSAMYKIN , V.S.GORDEEV , A.I.PAVLOVSKII

SCIENTIFIC RESEARCH INSTITUTE OF EXPERIMENTAL PHYSICS

Arzamas-16 , Nizhni Novgorod region , 607200 , Russia

Wave processes were analyzed from the point of effective energy delivery in pulsed power systems based on transmission lines. A series of new schemes for the pulsed generators based on multistage stepped transmission lines both with the capacitive and inductive energy storage was found. These devices can provide voltage or current transformation in up to 5-10 time due to wave processes if stage's characteristic impedances are in a certain correlation. The schemes suggested can be widely applied in the new powerful pulsed power accelerators. The theoretical conclusions are justified experimentally.

Single or double forming lines (SFL or DFL) are widely employed in powerful pulsed accelerators. A relatively low output voltage is their drawback. High voltage technique operates stepped transmission lines [1] however they do not realize a high transformation coefficient alongside with the effective electromagnetic energy transmission.

After LIU-10 construction in 1977 [2] the authors directed their efforts to search for new more effective schemes of pulsed generators . A series of pulsed generator arrangements was invented based on multicascade stepped forming lines (SFL) which provide the formation of rectangular pulses on the resistive load.The transient processes result in transformation of voltage and current pulses that simplifies substantially the problem of high voltage and power achivement. As we later got to know , seccessful theoretical research was done in this field by J.D.Smith [3] and D.Eccleshall [4] from the USA.

Fig.1 presents the SFL arrangement formed by connected in series n-sections (n=1,2,3...) of homogeneous lines of the same electric length T_0. At t=0 the SFL input end charged to U_0 voltage is closed by switch S_1. A wave reaching SFL output at $t=n \cdot T_0$, switch S_2 connects load Z_L. This generator has the maximum efficiency at the growing impedance choice from the relation $Z_i=Z_1 i(i+1)/2$, where i-a step number, Z_1,Z_i- impedances of the first and i-steps, correspondingly. Rectangular

voltage pulse of $2T_0$ duration and $nU_0/2$ amplitude is formed on a matched load. In 1979 the experimental testing was conducted with cable lines and water-insulated SFL's comprising three sections at Z_1=2.5 Ohm and U_0=90 kV. In accordance with calculations a 135 kV pulse was obtained at Z_L=15 Ohm (~ 90% efficiency) and 250 kV - at Z_L=250 Ohm.

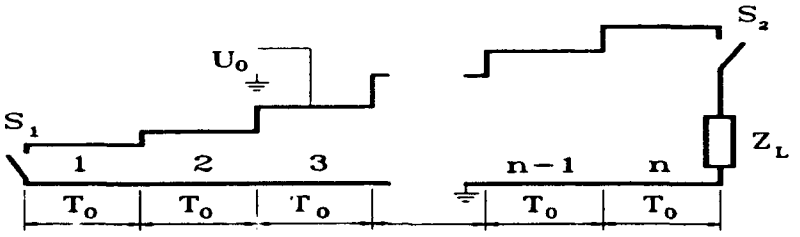

Fig.1.Stepped forming line scheme

A scheme of a double stepped forming line (DSFL) can be presented in analogy to DFL. For this purpose one must just connect a charged opened line of T_0 electric length and $Z_1 \cdot (n+1)/2$ impedance in series with a SFL output step and a load. The optimal ratio of SFL section impedances remains unchanged. The DSFL arrangement provides the same amplitude voltage pulse as in SFL case with the similar number of sections.

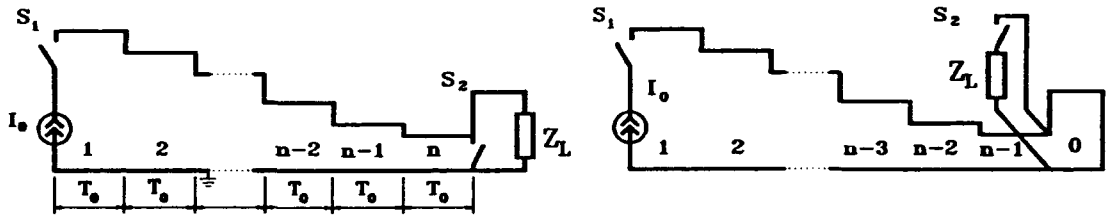

Fig.2.SFL and DSFL analogues with inductive energy

For SFL and DSFL the inductive energy store analogues are found (Fig.2).The first one is formed of n=1,2,3.. sections of T_0 electric length with decreasing $Z_i=2Z_1/i(i+1)$ impedances. In the closed contour formed with SFL electrodes and S_1,S_2 current opening switches, an external generator produces I_0 current, and the energy is stored in the magnetic field. At t=0, S_1 opening switch is turned on and at $t=nT_0$ - S_2

opening switch, a rectangular $nI_0Z_L/2$ voltage pulse being formed on the matched load at $nI_0/2$ current. DSFL with inductive energy store differs in parallel connection to the load of a shortcircuited line section of $Z_0=2Z_1/(n+1)$ impedance. In this case the second opening switch is not needed. With the same number of sections both schemes provide current pulses of the equal amplitude on the matched load. The inductive energy storage schemes are advantageous in possible substantial increase of the stored in the lines energy density. In practice such schemes are difficult to realize because of fast opening switch designing; we did not study these schemes experimentally.

For LIA cavities the capacitive energy storage schemes differ in outer current-conducting shield availability which are to be opened in the acceleration gap. All possible cavity scheme analysis showed that total energy transmission in a single $2T_0$ pulse is feasible only when a load is commutated to the cavity output with delay $t_d=2T_0$, $4T_0$, $6T_0$... relative to the moment of the first electromagnetic wave arrival. From the practical point of view the minimal delay time, $t_d=2T_0$, is of the greatest interest. For this case only the schemes with voltage increase are invented.

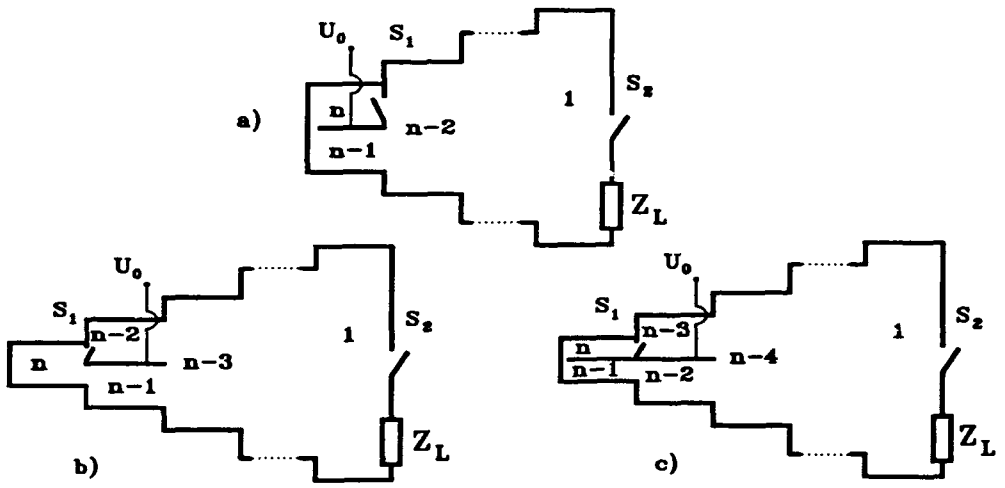

Fig.3.LIA cavity schemes based on stepped forming lines

Moreover, when a load is commutated to the forming line via stepped transmission lines, at the full energy transfer to the load their impedances must satisfy relation $Z_i=2Z_1/i(i+1)$, the step number being counted from the load.

Fig.3 shows the cavity schemes based on the forming lines of two, three and four sections. The impedances are chosen from the following relations:

-for the first case $Z_i=2Z/i(i+1)$, where i=1,2...n;

-for the second case $Z_i=2Z/i(i+1)$, where i=1,2..(n-3);

$Z_{n-2}=2\cdot Z/(n-2)(3n-5), Z_{n-1}=4Z/(n-1)(3n-5), Z_n=4Z/(n^2-1)$;

-for the third case $Z_i=2Z/i(i+1)$, where i=1,2..(n-4),

$Z_{n-3}=Z/2(n-3)(n-2)$, $Z_{n-2}=3Z_{n-3}$, $Z_n=Z/n(n-2)$,

$Z_{n-1}=3Z_n$, where Z-an cavity output impedance.

With total number of line sections, n, a rectangular voltage pulse of $2T_0$ width and $nU_0/2$, $U_0(3n-5)/4$, $U_0(n-2)$ amplitudes correspondingly is formed on the matched load. Earlier in ref.[5,6] and [8] scheme (a) for n=2 and 3 and scheme (b) for n=3 were described.

The cavity which scheme is shown in Fig.3c is of interest mostly as it is characterized by a rapid voltage growth with line section number increment. Such n=5 scheme supports the first steeped line accelerator STRAUS and more powerful accelerator STRAUS-2 [7]. Its n=4 modification is the basic in the cavity design for new LIU-10M accelerator [7], this arrangment is also described in ref. [3].

In some cases the devices are needed for high-voltage pulse parameter converting which provide variations in current, power and width of a pulse fed from the generator over a uniform transmission line of Z-impedance. Figure 4 presents two upgrades of these devices.

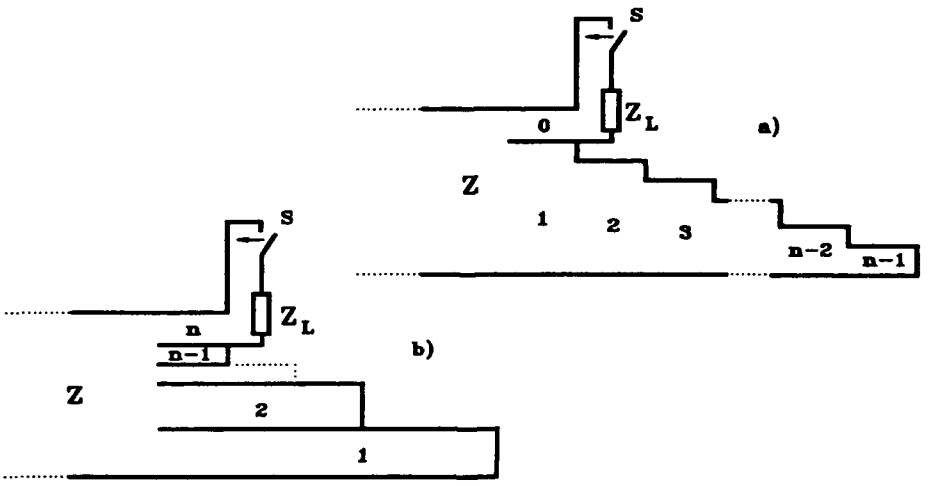

Fig.4.Pulse converter schemes

The converter consists of an opened line of Z/n-impedance and a closed stepped line formed of n-1 (n=2,3...) sections of equal electric length, $T_0=t_p/2n$, where t_p - an external generator pulse width. A matched resistive load is switched via a commutator to the opened section output being delayed compared in relation to the first electromagnetic wave arrival, $t_d=t_p(1-1/n)/n$. The stepped line impedances equal $Z_i=Z(n-i)(n+1-i)/n^2$ when the sections are numerated (i=1,2...n-1) from the converter output. Instead of the stepped line the second upgrade (fig. 4b) employes n-1 shortcircuited lines connected in series at the input. Their electric length and impedances are determined by relations $T_i=t_p 2^{-[i+1]}$, $z_i=Z\cdot 2^{-i}$, where i - a number of a shortcircuited section. The electric length and impedance of an opened line is selected equal to the analogous parameters of the last one (i=n-1) of the shortcircuited lines. A load is switched via the commutator with a delay, $t_d=t_p(2^{n-1}-1)2^{1-n}$.

For both upgrades the output voltage amplitude in the matched mode equals the voltage pulse amplitude fed by the outer generator. For the first version the current and electric power grow at the converter output and the pulse width reduces in n times; for the second one - in 2^{n-1} times. The converter parameters are selected so that during the wave processes the energy from generators is concentrated in the open line, and after switching all of it is transferred to a load in the form of a shorter rectangular pulse. The dimensions being alike, the described converters have approximately equal efficiency.

The converters considered can be connected directly or via transmission line to any generator output which forms a rectangular pulse, in some cases they can be built in the output section of the stepped line generators.When n=2, (a) and (b) schemes have similar shapes; the built-in upgrade was tested in the experiments on three-step SFL pulse conversion.

Fig. 5 shows the scheme of meander pulse conversion into a rectangular pulse. These schemes are in particular needed to design LIA fed by outer pulse generators [8].The converter is formed by shortcircuited line of Z_0 impedance and stepped line connected in parallel to the transfer line from the outer generator of Z-impedance. The stepped line is made as n-1 line sections of similar electric length

to equalling the electric length of the shortcircuited line. The line section impedances satisfy the following relations: $Z_0=nZ$, $Z_i=Zn^2/(n-i)(n+1-i)$, $i=1,2...n-1$. In this case, a rectangular voltage $2T_0, nU_0$ pulse is formed on the matched load $Z_L=Zn^2/2$ commutated to the converter output at $t_d=2T_0$. The cavity-converter scheme from ref. [8] are particular cases of n=1 and n=2 for the common scheme in fig. 5.

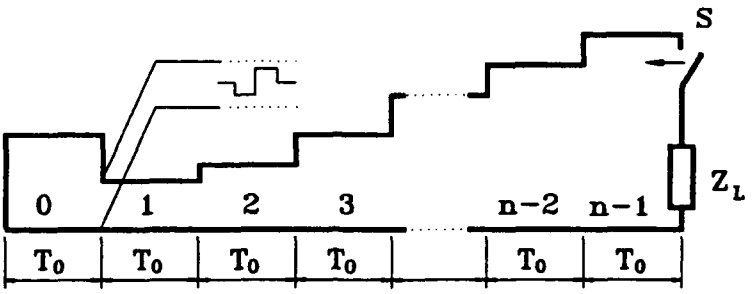

Fig.5.Meander pulse converter scheme

New schemes considerably expand the possibilities of further upgrading of powerful accelerators and their pulsed systems. They are not necessarily optimized only for effective energy transfer; the needed impedance relations can be determined to modify other accelerator characteristics, ex. to achive the maximal bremsstrahlung output.

REFERENCES

1. A.A.Morugin, G.V.Glebovich Nanosecond pulse technique (Sov.Radio, Moscow, 1964)
2. A.I.Pavlovskii, V.S.Bossamykin, V.A.Savchenko at al., Dokl.Akad.Nauk SSSR, 250 (1980) 1118.
3. I.D.Smith IEEE Conf. record of 1982 15 power modulation symposium., N.Y.,(1982),223.
4. D.Eccleshall Nucl.Instr. and Meth. in Phys. Research (1987),B24/25,801-804.
5. D.Eccleshall, J.H.Temperley J.Appl.Phys 49 (1978),3649.
6. D.Eccleshall, J.H.Temperley, C.E.Hollandsworth IEEE Trans. Nucl.Sci. NS-26 (1979),4245.
7. V.S.Bossamykin, V.S.Gordeev, A.I.Pavlovskii at al. Pulsed power electron accelerators with the forming systems based on stepped transmission lines.- this Proceedings.
8. I.D.Smith Rev.Sci.Instr. 50(1979) 714.

DEVELOPMENT OF MICROSECOND GENERATORS WITH PLASMA CURRENT INTERRUPTING SWITCH IN I.V.KURCHATOV INSTITUTE OF ATOMIC ENERGY. FREQUENCY OPERATION OF GENERATORS.

V.M.Babykin, R.V.Chikin, G.I.Dolgachev, Yu.P.Golovanov, Yu.I.Kovalev, A.G.Ushakov, L.P.Zakatov

I.V.Kurchatov Institute of Atomic Energy, 123182, Moscow, Russia

A description of major experiments on Microsecond Plasma Current Interrupting Switch (PCIS) research in I.V.Kurchatov Inst. is adduced in [1,2]. Below we represent some suggestions important for a practice and an overview of new facilities.

Charge limit through each canal (5-7 mK/gun) created by one plasma gun does not depend on place and order of guns displacement. Plasma guns of coaxial PCIS could be placed at both outer and inner electrodes. Surface charge density limit is (1-3) mK/cm^2 and this results in corresponding limit for drive current of microsecond PCIS of about 1 kA/cm^2.

A voltage obtained at PCIS is determined by ion diode impedance including electron leakages (where PCIS is ion diode). To increase PCIS impedance and voltage all methods of electron leakages suppression are developed: applied external magnetic fields, reflection systems, current pinching.

A moment of current interruption is determined by the charge value going through PCIS that allows to synchronize several switches. To provide an accuracy of two identical PCIS synchronizing at least at half of drive current amplitude level it is necessary to provide a current feedback of about 20 % (or 1% of charge redistributed among the switches).

Synchronizing allows to increase drive current with parallel PCIS operation and voltage - with consequential one. To increase power density in the load the scheme of parallel-consequential PCIS switching is proposed.

A maximum voltage increase coefficient is 15 with capacity storage voltage 40-50 kV and it drops to 3 with that of 1-1.5 MV.

Main results on microsecond PCIS operation were obtained in wide range of parameters: 20-400 kA, 0.5-4 MV, $2x10^7$-10^{12} Wt. Design of main units of facilities allows to create superpower generators for practical applications including frequency operation.

Module design (fig.1) is worked out with 1 MJ stored energy and 10 MV pulsed voltage for high-dose bursts of "gamma" radiation. An ability to switch several modules in parallel to one load is provided. Displacement of parallel generators around the insulator allows to use them as an outer electrode of coaxial vacuum line. That is why a total inductiveness could be reduced without oil insulation.

All magnetic flux is stored in vacuum volume of insulator decreasing requirements to its electrical strength. Use of air-insulated Marx voltage generator and unified units substantially decreases the cost of the facility.

The design of high-power accelerator "Tigr-3" (fig.2) intended for technology surface processing is carried out. Energy storage is 200 kJ, drive current peak - 8 MA, ion current peak - 4 MA, ion beam energy - 0.5 Mev. Ion flow is formated directly in PCIS. To increase current density and also for size decreasing 4-side PCIS feeding is proposed. So an opportunity of ion beam focusing on the central axis is provided.

The "RS-20" X-ray generator for sterilizing of agriculture production and medical equipment is designed and constructed by the contract with "CHETEK" Stock Holding Company and this device is a property of "CHETEK".

A creation of the generator enables to resolve a row of complex technical problems, they are: increase of plasma guns resource and bremsstrahlung target. Experiments were carried out at "Taina" facility [3].

PCIS scheme was equivalent to that of [4] where central PCIS axis is placed perpendicularly to that of insulator (fig.4). Plasma injectors were placed at inner electrode - PCIS cathode. This results in reducing of their feeding energy [5]. Outer electrode - PCIS anode - is connected with Marx generator high voltage output. Positive polarity at high-voltage electrode allows to avoid electron leakages on the insulator surface and to increase its electrical strength. Cathode of electron diode is placed at the butt-end of PCIS cathode. Electron beams accelerated toward the diode anode (X-ray radiator). Marx generator modules are placed around the insulator. A distance between the triggering switches of adjacent sections of the generator is equal to that of adjacent gradient rings of the insulator. It allows to use generator construction to uniform a distribution of electric potential at the insulator surface and to improve the synchronizing of generators.

Low inductive Marx generator design is proposed, it uses commutation scheme with 3-electrode minimum size triggering switches [6]. Marx generator uses specially constructed capacity banks (50 kV, $0.25*10^{-6}$ F) for frequency operation. Testing at 50 kV and 10 Gz frequency gives the resource of banks about 10^7 discharges.

To increase PCIS impedance it was proposed to use the anode with variable transparency along the axis (fig.5). With current growth through the PCIS plasma volume shifts to the area with high transparency and electrons are suppressed as it occurs in reflex triode. Diode anode is connected with the PCIS anode by thin rods. So plasma can move in radial direction and does not act on diode impedance.

Most critical PCIS element in frequency regime is dielectric surface of plasma guns because of bombardment which results in intensive gas emission. This limits operating frequency and guns resource. That is why a new scheme (fig.6) was proposed where plasma guns "shoot" along the axis. The reflector enables plasma flow to go in a radial direction and ceramic dielectric surface is protected from particle beams.

Anode thickness is chosen from maximum dose condition. The scheme and main units considered were tested at the model. Average beam power was 2 kWt with beam current - 5 kA, electron energy - 2 Mev, pulse width -10^{-7} s with 2 Gz frequency. X-ray dose at 1 m from the anode was $2x10^{-2}$ R/pulse. Maximum power density from the anode due to radiation could be estimated as 300 W/cm^2. In spite of the average power density of 20 cm^2 target slowly compressed that could be explained by a beam nonuniformity and local overheating and melting.

After $1.5*10^6$ pulses generator fully maintained its efficiency without a replacing of units.

Frequency accelerator scheme was used to construct X-ray sterilizer "RS-20" (fig.3). 4 twenty-section Marx generators were used with output voltage 1 MV. Electrical circuit parameters are: C = $0,05*10^{-6}$ F, T = $2,4*10^{-6}$ s, p= 10 Ohm. Average beam power - 20 kWt with 3 Mev energy of electron beam, electron beam current - 20 kA, pulse width - 100 ns, frequency - 4 Gz. Average power density on a target is 100 Wt/cm^2. Dose power on 1 m distance from the anode is 50 kR/hour.

Typical pinhole frames show x-ray image of the anode (fig.6) and oscilloscopes illustrate sterilizer operation (fig.7)

Thus the successful understanding of PCIS operation mechanism allows to design simple and reliable accelerators in wide range of parameters for practical use in different industrial technologies.

REFERENCES.

1. G.I.Dolgachev, L.P.Zakatov A.G.Ushakov "Experimental research of Microsecond Plasma Opening Switches ", Submitted to this conference .
2. G.I.Dolgachev, L.P.Zakatov A.G.Ushakov Sov. "Fizika plazmy", 1991, vol.17, is.10, p. 1172-83.
3. G.I.Dolgachev, L.P.Zakatov et al. Sov. "VANT", Series "Termonuclear Fusion", 1988, is.2, p.40-42.
4. Yu. P. Golovanov, G.I.Dolgachev et al.Sov. "VANT", Series "Termonuclear Fusion", 1991, is.3, p.35-38.
5. V.M.Bystritski, Ya.E.Krasik et al. Sov."Fizika plazmy", 1988, vol.14, is.1, p.61-65.
6. G.I.Dolgachev, L.P.Zakatov, A.G.Oreshko Sov. "VANT", Series "Termonuclear Fusion", 1983, is.2(12), p.97-99.

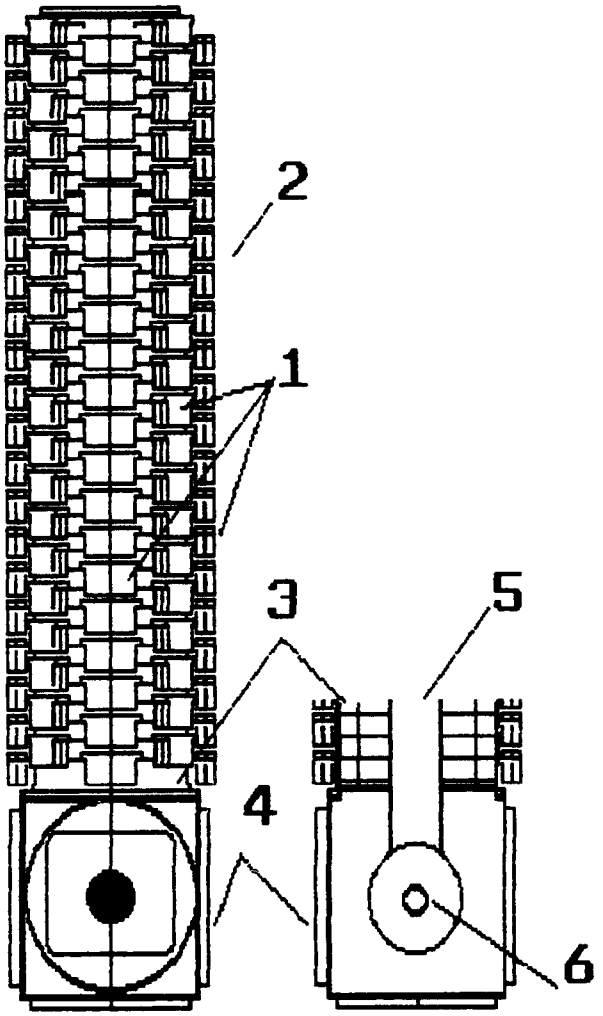

FIG.1
Scheme of facility:
1-capacitor bank,
2-pulse voltage generator,
3-high voltage insulator,
4-vacuum chamber,
5-current drive,
6-PCIS.
Total height - 9300 mm

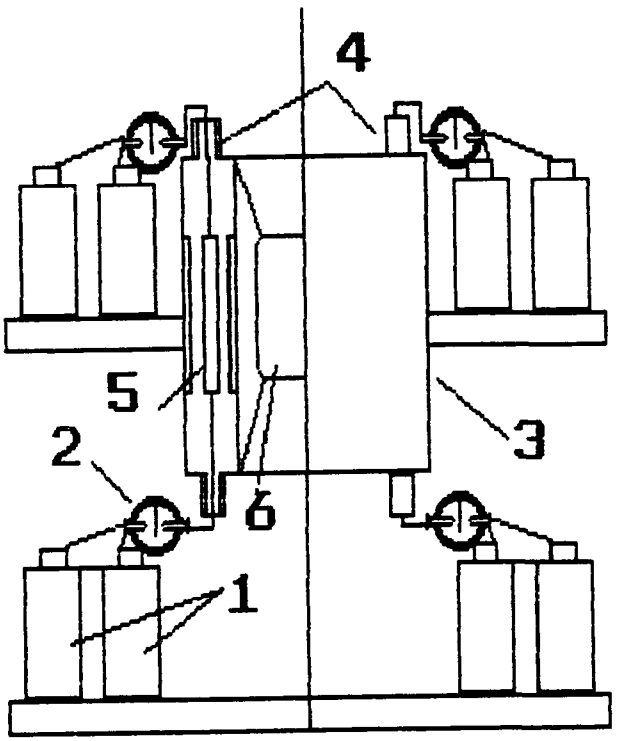

FIG.2
Scheme of "Tigr-3" facility:
1-capacitor bank,
2-triggering switch,
3-vacuum chamber,
4-high voltage insulator,
5-PCIS,
6-beam target.
Total height - 3500 mm

FIG.3
"RS-2C" generator
photograph.

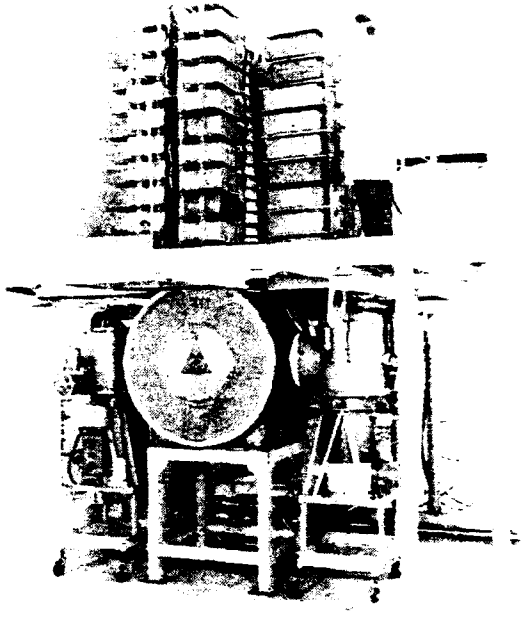

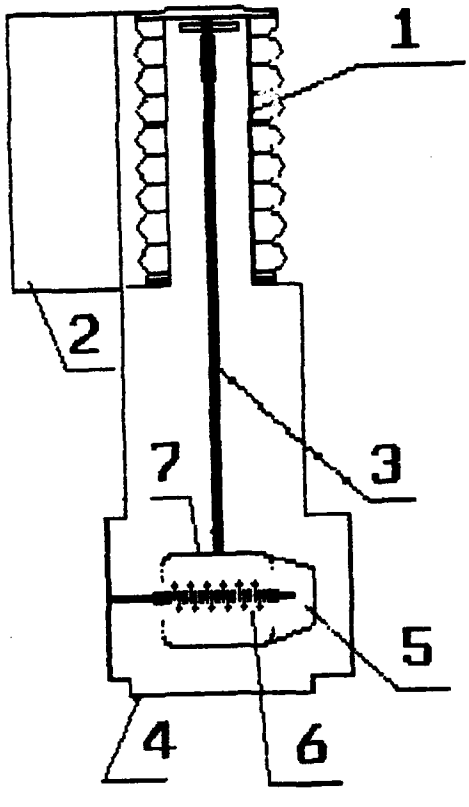

FIG.4
Scheme of generator
with PCIS.
1-insulator,
2-pulse voltage generator,
3-current drive,
4-vacuum chamber,
5-diode,
6-PCIS,
7-outer PCIS electrode.

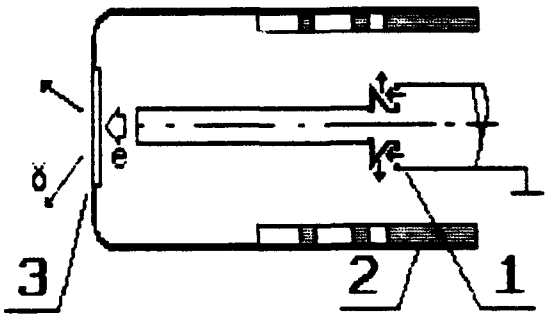

FIG.5
PCIS construction:
1 - plasma injectors, arrows show plasma movement direction, 2 - anode with nonuniform transparency, 3 - x-ray radiator - electron diode anode.

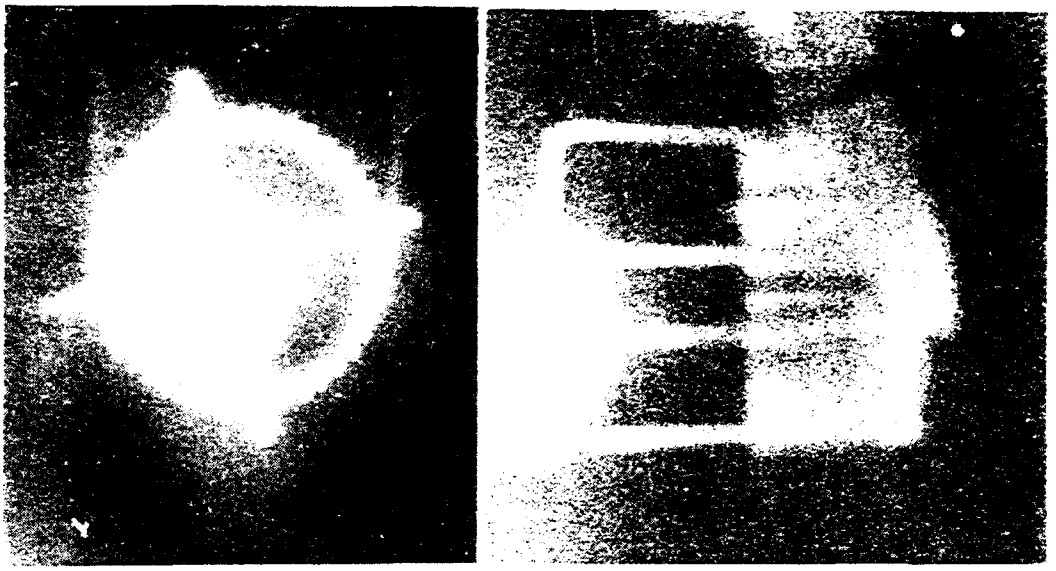

FIG.6
Time-integrated pinhole frames of anodes of PCIS and diode.

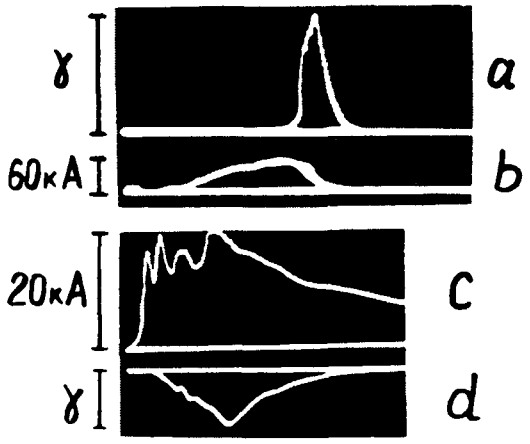

FIG.7
Characteristic oscilloscopes,
from top:
a-x-ray detector signal,
b-current through PCIS,
a,b-streak length $1*10^{-6}$ s,
c-current to the diode,
d-x-ray detector signal,
c,d-streak length
$0.5*10^{-6}$ s,

EXPERIMENTAL RESEARCH OF MICROSECOND PLASMA INTERRUPTING SWITCH (PCIS). CANAL CONCEPT OF PCIS OPERATION.

G.I.Dolgachev, L.P.Zakatov. A.G.Ushakov

I.V.Kurchatov Institute of Atomic Energy, 123182, Moscow, Russia

ABSTRACT

Main results on plasma current interrupting switch (PCIS) or plasma erosion opening switch research are reported. A canal concept allowing to compare microsecond and nanosecond generators with PCIS and a model of PCIS operation are proposed.

Plasma opening switch research [1,2] show that they are prospective for microsecond inductive energy storage systems. The scheme of high power generators including PCIS is prospective for industrial applications. From the other hand physical processes taking place in the rear plasma (concentration of (10^{12}-10^{14}) cm^{-3}) with high current (amplitude 100-1000 kA, current rising time (10-100) ns) are interesting for theoretical and experimental research. Further progress in experimental field is connected with both generalization and new results on detailed physical picture of PCIS operation appearance.

With generalization of experimental results [3,4] it is worth to outline a certain concept of PCIS operation which proposes plasma volume division onto parallel operating canals (fig.1). They have certain values of impedance on stages of erosion and current interruption and these values are determined by concrete geometry and plasma concentration. Experiments used different variants of plasma guns displacement (at inner and/or outer electrode of PCIS going along a circle or along a cylindrical surface with the length exceeding electrode diameter). It was shown that charge density limit exists and charge goes through inner surface of PCIS outer electrode - q_{lim}= (1-3) mKl/cm^2. This value limits energy flow density through plasma volume. Attempting to exceed charge density limit with concentration growth makes interruption impossible. If not to take into account plasma gun construction it is possible to divide plasma volume on parallel canals with single square on outer electrode surface. To increase charge value going through PCIS or to increase current drive amplitude or its rising time it is necessary to increase geometrical dimensions: diameter or length. In experiment with "wide" PCIS it was shown (fig.2) [4] that with current rising more and more PCIS area (and plasma canals) are captured by current. Both current and charging time growth requires more plasma canals that results in impedance decrease. If no more new canals could be created then interruption before drive current maximum occurs. The plasma canal

which permits higher current increases its impedance earlier. That results in current redistribution and equalizes the interruption time from each canal.

Voltage value at PCIS in such a scheme could be estimated:

$$U_{pcis}=I*R_{pcis},$$

where $R_{pcis}=R'/n$, n - number of canals, R' - resistance of one canal which is determined by current PCIS geometry. Full current could be written as

$$I=I'* n,$$

where $I'=q_{lim}/t_{inp}$ - current through 1 canal with a square of 1 cm^2. So the voltage could be written:

$$U=q_{lim}*R'/t_{inp}, \qquad (1)$$

q_{lim} - charge limit per canal, t_{inp} - a time from the erosion beginning to the interruption.

Fig.3 illustrates calculated curves of drive current (I), charge through PCIS (Q) and voltage (U_{pcis}) at PCIS without a load depending on interruption time. This time is determined by a number of plasma canals required for a given charge. It appears that decrease of energy input time results in voltage growth 2 times as high if the interruption takes place at the current maximum. Current interruption at the maximum is disadvantageous because PCIS resistance drops dramatically with increase of number of plasma canals required. With drive current value 0.9 the switching voltage is 1.5 times as high as that at drive current maximum. Drive current amplitude increase with the same charging time does not result in PCIS voltage increase. It is in accordance with numerical experimental results and allows to estimate the voltage obtained. It is possible to increase the voltage with consequential PCIS operation then impedance increase is equivalent to that of radial gap. The second way is reducing of energy input time that could be realized in several stage PCIS operation.

Table 1 contains parameters of several nanosecond and microsecond generators with PCIS. It is evident that PCIS with a high impedance could be realized in both cases. For different PCIS geometries ("short" and "wide") charge limit condition should be filled q_{lim}=(1-3) mKl/cm^2 that proves the concept discussed above. For nanosecond facilities this value is an order as low but the concept could be applied for them also. From a comparison of two facilities: "Gamble-2" and "Reiden-6H" with the same current charging time it occurs that in spite of drive current at "Gamble-2" is 4 time as high as that of "Reiden-6H" their voltages at interruption are practically equal i.e. drive current amplitude (and charge) increase requires more parallel canals that results in PCIS impedance decrease and does not allow voltage growth.

TABLE 1

Facil.	Ref.	Io, MA	tp, mks	q'', mKl/cm^2	R, Ohm
PBFA-2	[9]	4.0	$5x10^{-2}$	0.1	7
Gamble-2	[8]	1.0	$8x10^{-2}$	0.3	4
Calif	[10]	0.9	$6x10^{-2}$	0.34	2.2
Reiden-6H	[7]	0.25	$5x10^{-2}$	0.5	20
Angara-1	[11]	0.6	10^{-1}	0.38	1.6
SNOP-3	[12]	1.0	$6x10^{-2}$	0.47	1.5
Hawk	[6]	0.7	1	2.0	1.2
Taina	[13]	0.2	1.7	1.8	10
GI-4	[5]	1.0	1.0	2.6	1.5
Dubl'	[14]	0.24	1.2	1.3	5
Tigr-M	[4]	0.12	1.8	2.3	5

It is worth to outline that there are much experimental data [4] which give a permission to consider PCIS operation in our experiments in erosion regime. Erosion begins (fig.4) when current reaches the value I_{cr} when a condition is implemented:

$$r_{He} < r_{De} \qquad (2)$$

It could be obtained from (2) that I_{cr} is proportional to $n^{1/2}$. This connection is proved qualitatively by results of experiment (fig.5) when plasma concentration increase results in shift of H-alpha line luminescence beginning and erosion beginning. When electrons are magnetically insulated (2) most part of current is transported by ions. Estimation of plasma concentration gives a condition $n < 10^{13}$ cm^{-3}. From the other hand concentration value estimated from a total charge carried through plasma before the interruption moment T_{int} is: $n > 10^{14}$ cm^{-3}. These requirements could be met if propose neutrals ionizing with current going through PCIS. This is proved also by PCIS operation under the gas concentration 10^{13} cm^{-3}. Apparently microsecond PCIS plasma contains substantially more neutral particles. Their ionizing with current growth allows to increase charge density in comparison with nanosecond PCIS.

Ion acceleration could take place on a plasma boarder in a double layer [4] or in Holl electric field [15] arising on a plasma concentration gradient without quasi-neutralizing disturbance. On a last stage when electrons are magnetically insulated PCIS impedance is determined by ion diode geometry.

REFERENCES

1. IEEE Trans. on Plasma Science, PS-15,Dec.1987.

2. Proceedings of VIII Int. Conf on High Power Particle Beams, BEAMS '90 Novosibirsk, 1990.
3. Chikin R.V. Dolgachev G.I. et al. ref.2, vol.2, p.1022-1025.
4. G.I.Dolgachev, L.P.Zakatov, A.G.Ushakov Sov. "Fizika plasmy ', vol.17, is.10, p.1171-1182.
5. B.M.Kovalchuk, G.A.Mesyats, ref.6,vol.1, p.92-103.
6. B.V.Weber, R.J.Comisso et al. ref.6, vol.2, p.1034-1039.
7.Mijamoto S., N.Jugami et al. ref.1, p.667.
8. B.Weber, R.J.Comisso, G. Cooperstein et al., ref.2, p.406-413.
9.B.V.Weber et al., Laser and particle beams, vol.5, part 3, Aug.1987, p.537-548.
10. Bluhm H., Greenly J.B. ref.1, p.654-666.
11. Afonin I.P., Bartov A.V. et al. XIII International Symposium on Discharge and Electrical Insulation in Vacuum Paris 1988,Proceedings,p.27-30.
12.Yu.A.Glushko, Ya.E.Krasik et al. Proceedings of VIII All Union Symposium on High Current Electronics Sverdlovsk-90, part 3, p.121-123.
13. Yu.P.Golovanov, G.I.Dolgachev et al. Sov. "VANT", Series Thermonuclear, Fusion, 1988, N 2, p. 40-42.
14. V.M.Bystritski, Ya.E.Krasik et all. see 12, p.112-114.
15. Ya.L.Kalda, A.S.Kingsep Sov. "Fizika plasmy", 1989, vol.15, is.8, p.981-986.

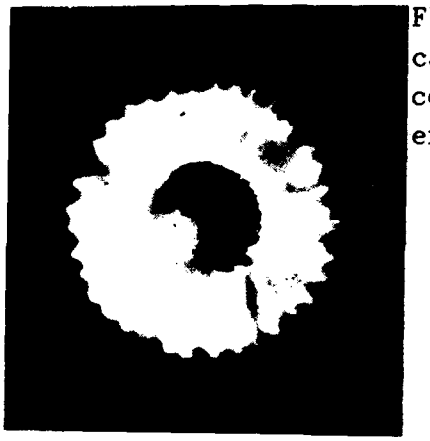

FIG.1 Optical frame of PCIS plasma canals on a stage of current rising, central electrode is cathode, exposition - 80 ns.

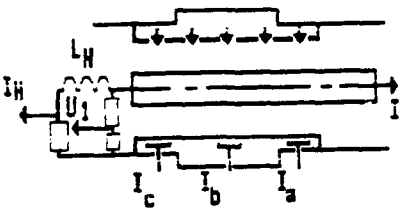

FIG.2-a Scheme of the experiment with a wide PCIS $L_H=2*10^{-7}$ Hn, U_1-PCIS voltage, a distance between neighbor Faraday cups (I_a, I_b, I_c) is 25 cm.

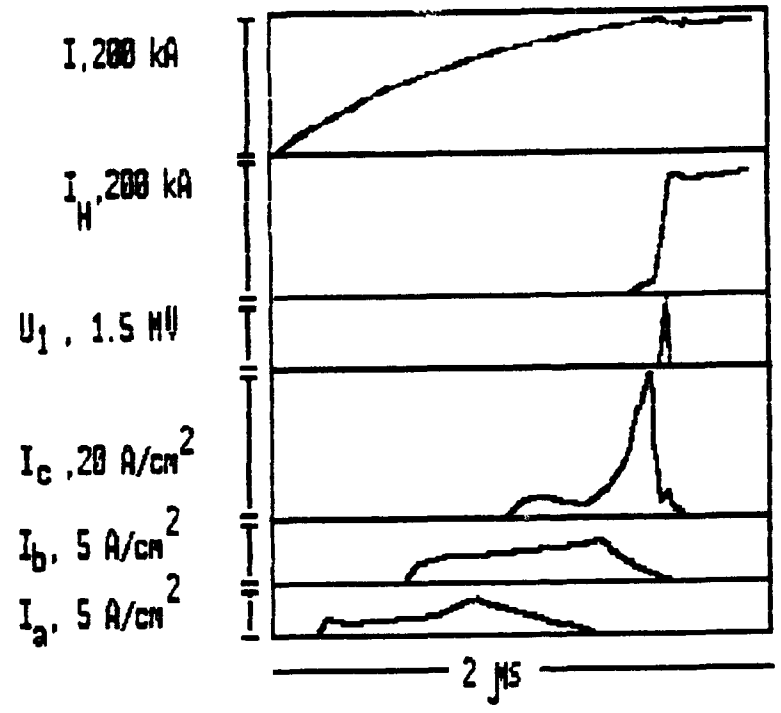

FIG.2-b
Oscilloscopes: total current-I_o, load current-I_H, PCIS voltage-U_1, currents to the anode-I_a, I_b, I_c.

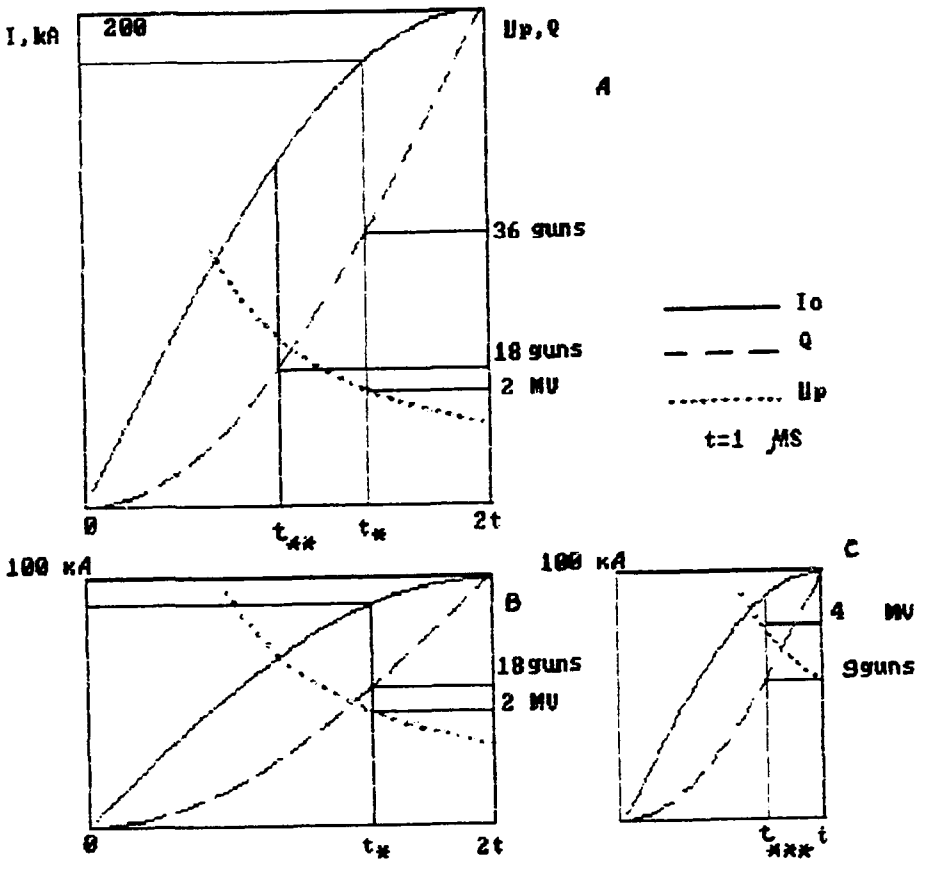

FIG.3 Calculated current (I), charge (Q), open circuit voltage (U_p) dependencies. Values at fig.3-A are corresponded to the parameters of "Taina". 3-A - charging time - $2*10^{-6}$ s, current amplitude - 200 kA. Charge is measured conventionally by plasma guns number, t_*-switching moment with 36 guns at 3-A and with 18 guns at 3-B, t_{**} - switching moment with 18 guns at 3-A, t_{***} - the same time at 3-C.

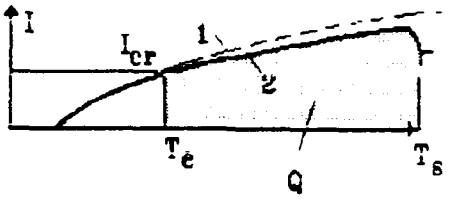

FIG.4 Erosion model illustration: 1 - short circuit current, 2 - total drive current, T_e - erosion beginning, I_{cr} - critical current, T_s - switching time, Q - charge through PCIS.

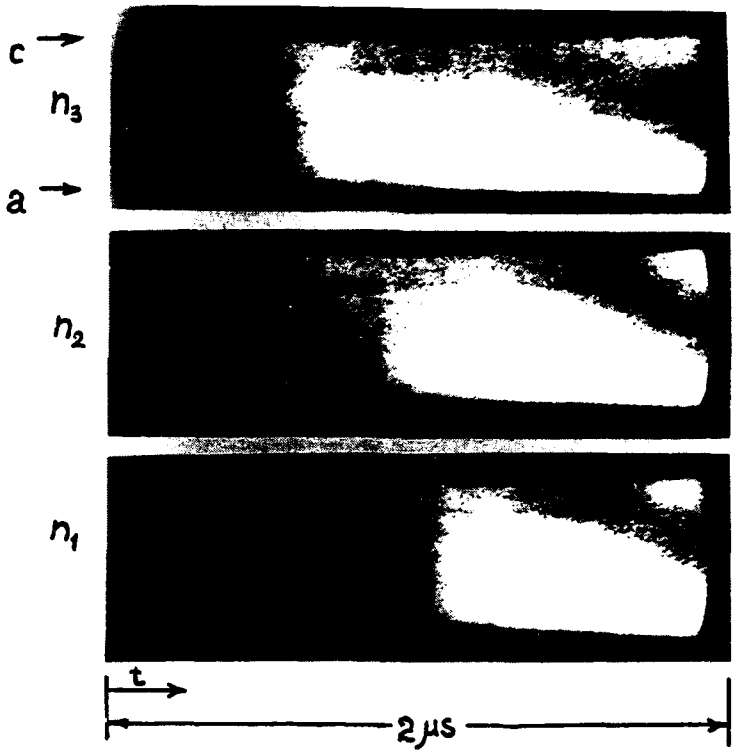

FIG.5 Hydrogen luminescence with different plasma concentration created by plasma injectors $n_1 > n_2 > n_3$.

EXPERIMENTAL STUDIES OF A MICROSECOND PLASMA OPENING SWITCH IN THE POSITIVE POLARITY REGIME

V.M.Bystritskii, I.V.Lisitsyn
Institute of Electrophysics, Ekaterinburg, Russia
Ya.E.Krasik
Weizmann Institute, Rehovot, Israel

Abstract. Positive polarity regime of microsecond plasma opening switch (MPOS) was investigated at the DOUBLE generator (480 kV, 300 kA, 1.3 μs). The measurements of the ion flow parameters showed the considerable enhancement of the ion current density over the thermal flow in the conduction phase. Ion losses reached more than 80% of the full energy losses in MPOS operating on the inductive load. The positive polarity MPOS operation proved to be more critical to the stored current amplitudes and electrode diameters. On one hand, the magnetic field strength should be more than 1 T on the outer cathode surface, on the other hand, the inter-electrode gap should be big enough to avoid the secondary plasma influence to the switch performance. The problems of MPOS-diode load coupling are discussed.

1. INTRODUCTION

The main bulk of experimental statistics and calculations on MPOS deals with coaxial geometries, where the inner high voltage electrode is of negative polarity, which is inherently compatible with electron diode load, but cannot be adjusted straightforward to the load of the extraction type ion diode. As it was pointed out in the early studies [1], the performance of MPOS significantly deteriorated after transition to the operation with positive polarity of inner electrode. The authors [1] proposed several possible mechanisms, causing this deterioration. The reasons named there to be the most critical to MPOS operation were the magnetic field strength in the near- cathode region and early strong anode sheath formation.

In the meantime, the positive polarity regime of MPOS operation is more appropriate for High Power Ion Beam (HPIB) generation in extraction type of ion diodes. Also it is worth noting that this regime provides the unique opportunity for

detailed studies of ion flow characteristics just in the MPOS, placing the diagnostics at the grounded outer cathode.

These factors stimulated the present studies devoted to investigation of ion flow dynamics and coupling of MPOS with the ion diode load.

2. EXPERIMENTAL SET UP AND DIAGNOSTICS

The experiments were carried on at the Marx generator DOUBLE [2] with the following parameters: erection capacity- 0.533 μF, output voltage 480 kV, upstream inductance- 1.3 μH. The MPOS plasma source consisted of two flashboards of 280 mm in diameter connected in parallel to feeding bank of 3 μF, 35 kV. The plasma was injected into the MPOS region through anode with a total geometric transparency of 75%. The anode slots length was 10 cm. The electrode diameters in the MPOS region used in the experiments were 64, 80 and 300 mm for the anode and 16 and 24 mm for the cathode respectively.

In the first experimental run the coaxial inductive load of 500 nH was used, in the second one the magnetically insulated extractor B- applied ion diode (MID) served for a load. The ion diode hardware was of the same characteristics as in [3]. The MID had a spherical focusing shape and passive plasma source. The insulating magnetic field was produced by a pair of coaxial coils and made up to 1.2 T in AC- gap.

The following MPOS diagnostics were used in the experiments: the electrical parameters of the MPOS were measured by active voltage divider and two Rogovsky coils placed upstream and downstream the MPOS. The additional voltage divider was installed just near the diode when a MID was used for a load.

MPOS ion flow parameters were measured by activation technique, Faraday cups array and by a time resolving Thomson parabola. The HPIB diagnostics in the ion diode included also the calorimeter.

3. EXPERIMENTAL RESULTS

The experiments with different diameters of the MPOS electrodes provide us with important information on switch operation and respective roles of different factors (interelectrode

gap, magnetic field etc.). The acceptable switching took place only for one pair of electrodes - 16 mm anode and 80 mm cathode. The voltage amplitude made up to 1.5 MV in this case for a stored current range of 170-190 kA. The other pairs of electrode diameters (16 and 64, 24 and 80, 16 and 300 for anode and cathode respectively) showed the significant deterioration of switching characteristics (at least two-fold voltage decrease). For the optimum pair of electrode diameters the stored current rise over the 190 kA value resulted in sharp decrease of generated voltage (See Fig.1). The switched current waveform displayed a presence of long current foot which appeared few hundred ns before opening. This seems to be inherent for a positive polarity plasma opening switch [1].

In the experimental run with MID only the optimum pair of electrodes (16 and 80 mm) was used. The MPOS+MID system displayed the following characteristic features:

1. Low level of stored current amplitude;
2. The presence of long foot at voltage waveform;
3. Short duration of MPOS high voltage phase (30-40 ns FWHM) in comparison with ~ 80 ns for conventional MPOS operation. This comparison is relevant with the MPOS interelectrode gap breakdown, which corresponds to the fact that the load current amplitude has never reached the generator current amplitude after switching.

The system MPOS+MID displayed strong intercoupling, resulting in MPOS voltage clamping at the level of 1.1-1.3 MV in a wide range of MID impedance so the total dissipated energy and system impedance remained constant in spite of considerable MID impedance variation.

$W_s = W_{mpos} + W_{mid}$ = const (about 10 kJ)

$Z_s = Z_{mpos} \times Z_{mid} / (Z_{mpos} + Z_{mid})$ = const (about 5.5-6 Ohm)

For optimum diode A-C gap (10 mm) the ion beam energy made up to 4 kJ with respective power of 120 GWt. The ion current amplitude reached 100 kA. The MPOS impedance was on the level 20 Ohm, which was 2.5 times higher than the diode impedance. The diode "turn-on" delay was short ~ 5-10 ns, which could be explained by the prepulse voltage foot presence prior to the high voltage phase.

MPOS ion flow measurements were performed for the case with inductive load. The ion current density waveforms, resulting ion current distribution and total ion current behavior were in good agreement with previous negative polarity MPOS studies [3]. The same two hump structure of ion density waveforms was observed. The total ion current reaches 30% of switch current already in the conduction phase. The ion losses made up 80% of total switch losses during switching.

The activation measurements of high energy protons displayed that the main part of the proton current occurs downstream of plasma source location. This means that the lightest ions (protons) control the process of plasma displacement and switch region expansion because of their highest axial velocity comparing with other ion species.

The time resolving ion spectrum measurement showed the presence of H^+, H_2^+, $C^{(1-3)+}$ ions with energy corresponding to the voltage changes in time. This fact does not contradict to the four-phase theory assumption, that the particle acceleration occur in the cathode vacuum gap.

4. DISCUSSION

The positive polarity MPOS is characterized with enhanced magnetic pressure along the surface of the inner anode and relatively low magnetic field strength near the outer cathode. It is known, that the primary and pronounced magnetic field penetration occur near the anode even in the case of negative polarity [3]. This suggestion agrees with the experimental studies in plasma accelerators of microsecond range, where during the stationary phase of plasma acceleration (which is similar to conduction phase of the plasma switch performance) the main potential drop took place near the anode. These facts are in good agreement with the suggestion that the development of anode sheath having finite resistance occurs. Our suggestion is also relevant to the earlier appearance of voltage (current) foot of comparatively low amplitude before the main switching began. The anode sheath is inherently more "slow" but it can produce the significant negative impact on the subsequent cathode sheath formation making its

erosion slower.

The cathode sheath dynamics depend on the magnetic field strength in respective region. It was obtained experimentally [4], that at least B > 1 T of magnetic field at cathode surface is needed for effective switching. The poor switch performance in the case of 300 mm cathode diameter substantiates these results. Therefore the maximum cathode diameter accounting B ~ 0.23 T for appropriate switching at "DOUBLE" current level was about 80 mm.

The other limiting condition in positive polarity MPOS experiments is the interelectrode gap dimension limited by secondary electrode plasma expansion. The radial dense plasma motion may result in effective vacuum gap decrease, which can lead to insufficient magnetic insulation or even complete gap closure during the opening. The estimates for a plasma expansion velocity to give approximately 10^6 cm/s, the minimum needed interelectrode gap should be about 3 cm. The experimental run with cathode diameter of 64 mm and anode diameter of 25 mm (24 and 27.5 mm of A-C gap distance respectively) displayed very poor switching characteristics.

Finally there are three competing conditions limiting the acceptable electrode diameters in switch region to achieve the appropriate switching: 1. Early formation of a slow anode sheath; 2. Motion of a dense electrode's plasma through A-C gap; 3. Magnetic field strength in near- cathode region. These factors determined the only pair electrodes diameters (16 and 80 mm), which allowed to achieve the optimum switch performance for given generator parameters.

Basing on the experimental results of MPOS performance with an ion diode for a load, several conditions could be formulated to obtain satisfactory efficiency of energy transfer into ion beam.

1. The minimum inductance between MPOS and MID.
2. The MID current should provide the reliable magnetic insulation of a MPOS gap.
3. The Z_{mid}/ Z_{mpos} impedance ratio should be kept high enough.

These conditions are also competing and determine the optimum existence for diode impedance and its location.

REFERENCES

1. V.M.Bystritskii et. al. Fiz. Plazmy, (in Ruuss), 1986, V. 12, N. 10, p. 1178.
2. P.S.Anan'in et. al, Pribory i Technika Experimenta, (in Russ), 1989, N. 5, p. 149.
3. V.M.Bystritskii et. al. IEEE Trans on Plasma Sci., 1991, V. 19, p. 607.
4. V.A.Kokshenev, Abstr. of 7 All Union Symp. on High Current Electronics, Tomsk, 1988, V, 3, p. 34.

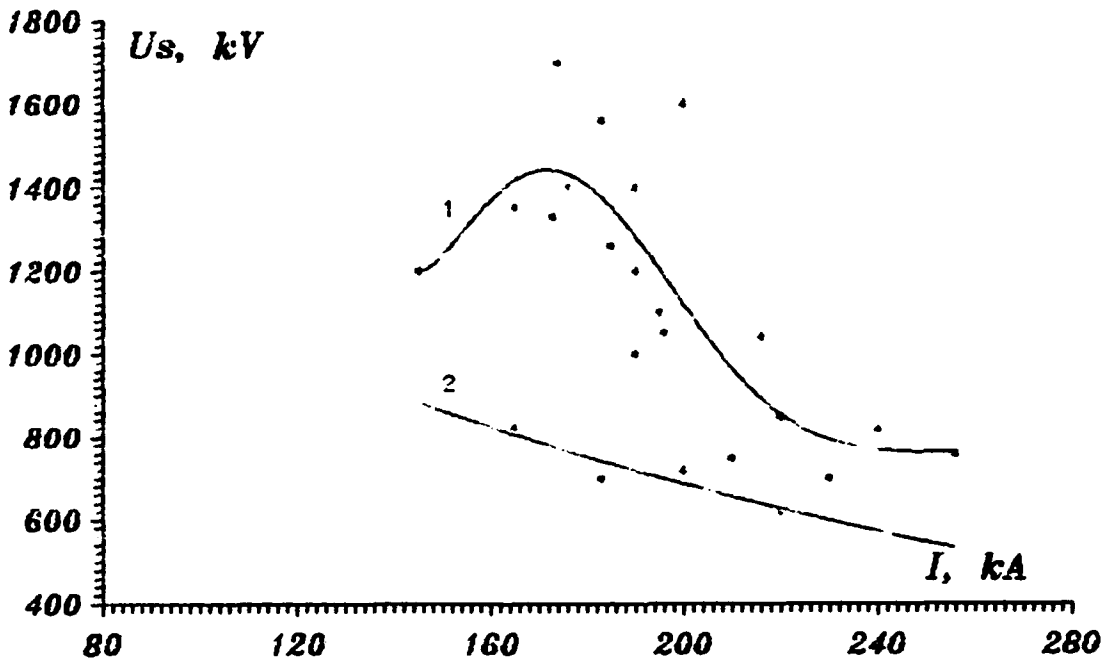

Fig. 1. POS voltage vs switch current.

NUMERICAL SIMULATIONS OF PLASMA DYNAMICS IN A MICROSECOND PLASMA OPENING SWITCH

V.M.Bystritskii, I.V.Lisitsyn, A.A.Sinebryukhov
Institute of Electrophysics, Ekaterinburg, Russia

Abstract. The modified hydrodynamic approach is being used to study the characteristics of plasma motion due to magnetic pressure in plasma opening switch. The simulation code differs from the NRL counterpart with dividing of the plasma filled region into N sections and with using the experimentally measured current penetration parameters. The simulation of the switch opening phase is performed in terms of erosion mechanism of magnetically insulated vacuum gap forming. The code includes the circuit data which are regular for the DOUBLE generator operation regimes in the negative polarity of inner (potential) electrode. In the case of typical duration of the conduction phase (900 ns), the minimum needed plasma density was found to be about 10^{15} cm^{-3}. The best fit of conduction current amplitude vs plasma density is $I \sim n^{0.23}$. The calculated characteristics of the switch opening phase were obtained to be very close to the experimental data.

1. INTRODUCTION

The microsecond plasma opening switch (POS) concept was firstly proposed in [1] to provide direct coupling of the inductive storage with the Marx without use of intermediate pulse forming lines. The first experiments showed such flaws of microsecond POS in comparison with nanosecond counterpart as lesser value of switch impedance and greater POS length. In order to explain the switch characteristics deterioration with increase of conduction phase duration the ion current density [2] and respective plasma density [3] enhancement over the bipolar limits were proposed.

"Hydro- limit" for conduction phase was based on the experimental fact that the plasma displacement due to magnetic pressure was found to be lesser than the initial switch length. Such a low translation to be explained requires at least two orders greater plasma density, that can be derived from bipolar flow conditions, basing on experimentally measured plasma flow velocity. High plasma density in the switch is likely to be the main result of forced ion current enhancement due to considerable electron current lines bending in the plasma (Hall effect), which reaches 25% and more

(compare with 2.3% in case of bipolar flow) [4].

Unlike the bipolar approach hydrodynamic model does not give a reasonable interpretation of the switching phenomena. In the NRL four-phase theory the POS begins to open when magnetic insulation is established in a vacuum gap along the cathode. The vacuum gap formation is connected with erosion process which starts after POS current reaching the bipolar limit.

Accounting for said above the main goal of our work was to combine two different approaches for explaining the features of the microsecond plasma opening switch.

2. SIMULATION ALGORITHM

During the conduction phase 1-D axial plasma motion under magnetic force was considered in the real MPOS geometry used in the "DOUBLE" experiments [4]. The microsecond generator parameters are: output voltage - 480 kV; erection capacity - 0.533 μF; total inductance upstream the POS - 1.3 μH; cathode diameter - 4.5 cm.

The plasma translation was examined near the cathode because this region is the most important in the switching phase. According to plasma erosion theory [5] just near the cathode vacuum gap forms where the main voltage drop and charged particle acceleration occur. The gap erosion rate determines the switch efficiency. Calculated and measured vacuum gap width is 1 cm, what makes 1-D code correct enough for considered range of cathode diameters.

The modeling was performed in the moving frame, which translates with current front. The penetration velocity was taken constant during the conduction phase for a wide range of conduction times, which follows from numerous experiments.

The acceleration of each plasma section was calculated using the approximated experimental current distribution in near- cathode region. The current flowing through given section I_i and total current downstream this section were used to calculate each section acceleration:

$$a_i = \frac{\mu_0 I_i}{4\pi^2 R^2 M_i n_e l_i} \sum_{k=1}^{i-1} I_k \qquad (1)$$

where: R and l_i are cathode radius and section length respectively.

If the resulting plasma section velocity exceeded the experimental current penetration velocity, the plasma density was artificially increased to match these two velocities and avoid the situation when the current front could lag behind the plasma section keeping the pulse value the same:

$$(n_i+\delta n_i)(v_i-\delta v_i)=(n_i v_i) \qquad (2)$$

Therefore even zero plasma density could be taken for initial step: in the calculation process the minimum plasma density profile forms to provide the liable plasma displacement by acceleration.

During the conduction phase the plasma erosion was also calculated. The voltage drop along the switch was estimated using the current distribution. The radial plasma velocity was taken to be equal to zero. The e-i current components were calculated using Child- Langmuir formulas taking into account local magnetic field magnitude.

At the moment when current front reaches the load side of the switch plasma the hydrodynamic part of calculations is stopped, and 1-D erosion model with circuit equations starts. The electric equations for the circuit shown at the Fig. 1 are following:

$$dU_g / dt = I_g / C_g$$
$$dI_g / dt = (U_g - U_s) / L_g$$
$$dI_l / dt = U_s / L_l$$

where: C_g - generator capacity; U_g and U_s are generator and switch voltages; I_g, I_l, L_g, L_l are generator and load current and inductance respectively. The voltage drop along the switch was not taken into account.

3. SIMULATIONS RESULTS

The plasma density dynamics during the conduction phase of switch performance is shown at Fig. 2. It is evident that the initial plasma density (10^{14} cm^{-3}) is not sufficient to provide the current penetration along the switch for 900 ns. This duration of the conduction phase was chosen because it corresponds to the most

efficient switching at the "DOUBLE" generator. The number of ions (average plasma density) increases during conduction phase (Fig. 3). The plasma density profile has a maximum corresponding to the generator side of current channel. FWHM of plasma distribution at the end of conduction is approximately 5 cm.

It should be noted that in the case of long conduction time (900 ns and more) the decrease of initial plasma density below 10^{14} does not result in change of final density shape and total amount of particles. Therefore in this case the minimum plasma density is chosen automatically. The dependence of conduction current vs minimum plasma density is shown at Fig. 4. The nearest fit of this curve is:

$I \sim n^{0.23}$.

The final amplitude of plasma density turned to be maximal in the case of lightest ions. For the initial plasma density of 10^{15} and conduction phase duration of 900 ns, the relative density increase is 3 for H^+, 1.23 for C^{2+} compared with C^+ plasma.

The modeling of the POS parameters in switching phase included the calculation of such switch characteristics as POS voltage and impedance for different conduction times as well as initial plasma densities. The corresponding curves are shown at Fig. 5. The switch voltage has a maximum in the range of conduction times of 600 - 900 ns which is very close to experimental results. Switch impedance decreases monotonously.

Specific time needed for magnetic insulation was found to be approximately equal 100 ns. After this time rapid current switching into load occurs. During this time switch voltage reaches tens-hundred kV, load current - few kA.

4. ASSUMPTIONS AND ANALYSIS

There are several different approaches to determine minimum needed switch plasma density in microsecond range of conduction time durations. The bipolar erosion approach seems to be not valid because the axial displacement in the case of long conduction time for a low plasma density:

$n = (zm_e/m_i)^{1/2} I / SeV$ (estimated value about 10^{13})

is much bigger than experimentally observed and exceed several meters.

In the PI model [6] the other modified bipolar approach is

considered. The electron trajectories bending is accounted for and erosion phase with radial current flow is claimed to be nonexistent. Thus the enhanced erosion phase begins prior the macroscopic gap appearance. This approach gives us the following expression for a plasma density:

$n = 4.543 \cdot 10^{7} I^{2} R^{2}$

The "hydro" approach described shortly in the introduction does not give any switching interpretation despite of many real advantages. It gives the following dependence of plasma density vs conduction current:

$n = 3.97 \cdot 10^{19} I_0^2 (t^2 + (\cos 2\omega t - 1)/2\omega^2) \; / \; (R^2 l^2)$ for sinusoidal and

$n \sim I^4$ for linear current rise.

The model considered in this paper combines partially all these approaches. The plasma density is found basing on the modified hydrodynamic approach; erosion begins during the conduction phase and the considerable part of switch length is magnetically insulated in this phase; and finally the opening is taking place when the current front reaches the downstream side of the plasma simultaneously with the onset of the magnetic insulation along the all switch length.

5.CONCLUSION

The modified hydrodynamic approach has been used to determine the minimum needed plasma density and other characteristics of a microsecond plasma opening switch. The plasma density was found to be approximately equal to 10^{15} cm^{-3} for microsecond conduction phase duration. The calculated voltage and impedance waveforms and dependencies vs conduction time were close to experimental data.

REFERENCES

1. B.M.Koval'chuk, G.A.Mesyats, Sov.Phys.Docl, 1985, V.284, P.857.
2. A.V.Bastrikov et.al, Abstr. of Int. Workshop on Phys. and Tech. of High Power Opening Switches, Novosibirsk, 1989, P. 22.
3. B.V.Weber et.al. BEAMS'90 Proc., Novosibirsk, 1990, P.406.
4. V.M.Bystritskii et.al.IEEE Trans.on Plasma Sci.1991, V.19, P.607.
5. P.F.Ottinger et.al. J. Appl. Phys., 1984, V. 56, P. 774.
6. J.R.Goyer. PI Internal Report PIIR-2-89, 1989.

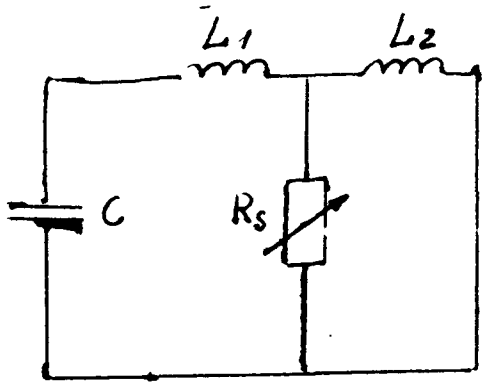

Fig. 1. Scheme of circuit.

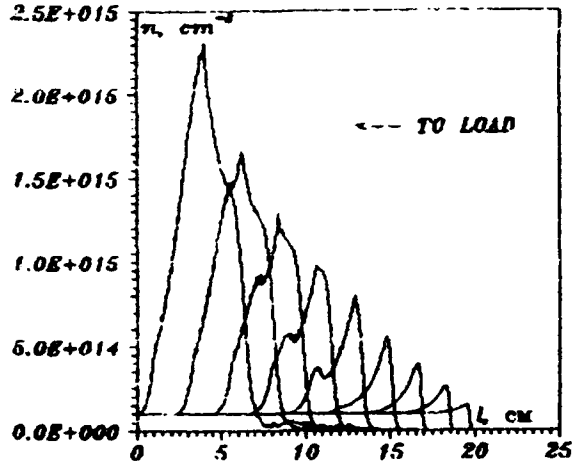

Fig. 2. The plasma density dynamics during conduction phase.

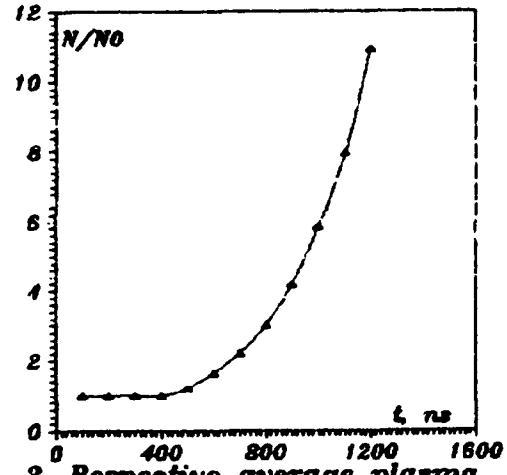

Fig. 3. Respective average plasma density increase during conduction phase.

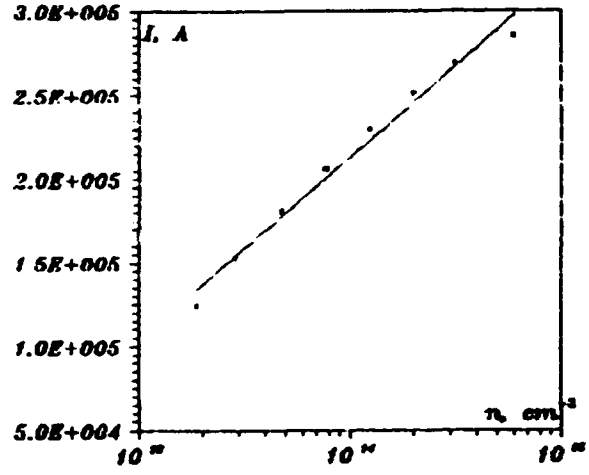

Fig. 4. Conduction current vs plasma density.

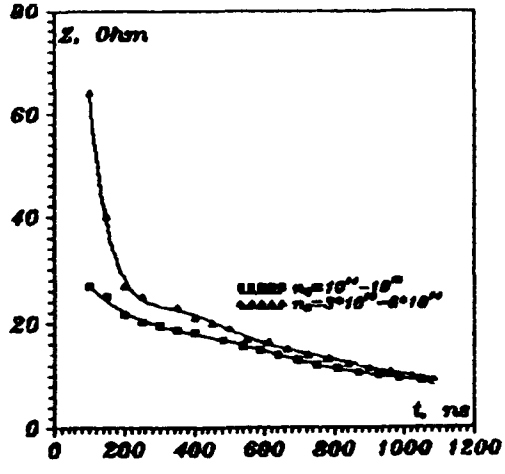

Fig. 5. POS impedance vs conduction phase duration.

A PLASMA OPENING SWITCH WITH A RETAINED PLASMA.

V.L.Gumennyj, Yu.A.Zhdanov, I.N.Naugol'nyj,
A.V.Pashchenko, Yu.V.Tkach

Kharkov Institute of Physics & Technology,
310108 Kharkov, Ukraine

Abstract Studies on the potential theory of a plasma opening switch are briefly surveyed. Equations and results of the theory of ion (electron) current transfer in plasma switches are presented.

Several scenarios have been proposed by the present time for the electrodynamic processes that ensure the current circuit discontinuity in the plasma opening switch (POS) [1-3].The current circuit interruption is either accompanied or provided by the break of the plasma strap in the POS, although its conservation is of primary importance for several applications,as, for example, for frequency types of POS operation, when the POS responce time is much shorter than the time of POS filling with a plasma.This report presents new results of the potential theory for a POS with a retained plasma.

Electrostatic current interruption in the POS is achieved by making zero a self-consistent electric field which arises in the plasma strap due to the external voltage effect and to near-electrode uncompensated charge layers occurring during current transport.In the process, a portion of charge of the opposite sign is carried to the electrodes, but the plasma decay does not necessarily take place in this case. All these effects are described by the potential theory of current interruption in the

POS. Some of its results have previously been reported for the cases of a prescribed external action [4] and a self-consistent POS operation in the external circuit [5]. Below we present the equations for the POS operation in the circuit with a power capacitor bank. The equations allow one to describe the time history of the processes in both the POS and the external circuit. They were derived on solving boundary-value problems for the space inside the POS (Figs.1,2) and on considering the POS switching circuits (Fig.3).

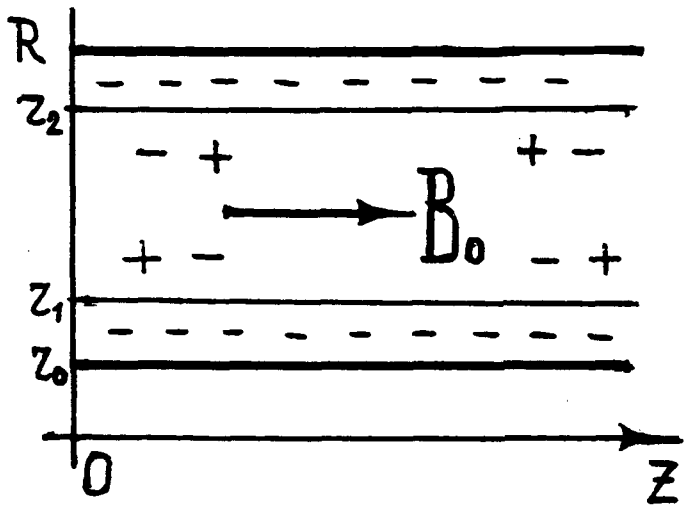

Fig. 1. Schematic diagram of the cylindrical switch.

The equations are written as

$$2\rho \frac{\partial^2 \rho}{\partial \tilde{\tau}^2} + 2\rho \frac{\partial \rho}{\partial \tilde{\tau}} = 1 - \rho^2 + \frac{\zeta_1(\tau)}{y} \quad , \tag{1}$$

$$\zeta_l(\tau) = \frac{1-\beta^2}{\ln \tilde{r}_o^2}\left[-\tilde{a}_l \ln \frac{\tilde{a}_l^2}{e} - \int_{\tilde{r}_o^2}^{\tilde{a}_l^2} \ln \rho^2(y,\tau)dy - 1 - 4k_2\Phi(\tau)\right], \tag{2}$$

$$l = \begin{cases} R \ , & 0 \leqslant \tau \leqslant \tau_m \\ r_2 \ , & \tau \geqslant \tau_m \end{cases}$$

$$\tilde{a}_R = \frac{1}{\rho\,(a_R,\tau)} \quad , \tag{3}$$

$$\tilde{r}_1 = \rho_1 \ (y=\tilde{r}_o, \tau) \cdot \tilde{r}_o \quad , \tag{4}$$

$$I_{\Pi}(\tau) = \frac{\pi}{(1-\beta^2)} k_o \cdot \frac{d\zeta}{d\tau} \quad , \tag{5}$$

$$\frac{dI_1}{d\tau} = -q + k_3 \cdot I_{\Pi} - (k_3 + k_2) I_1 \quad , \tag{6}$$

$$\frac{dq}{d\tau} = I_1 \quad , \tag{7}$$

$$\Phi = k_3 (I_{\Pi} - I_1) \quad , \tag{8}$$

$$I_{H} = I_1 - I_{\Pi} \quad , \tag{9}$$

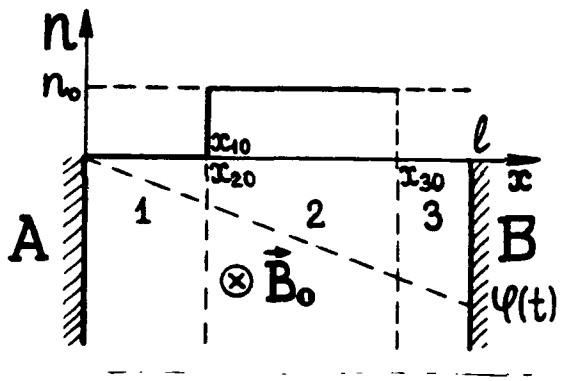

Fig.2.Diagram of the POS as a plasma capacitor.The dashed line between the plates A and B is the potential distribution in vacuum.$x_{10}=x_{20}=0$.

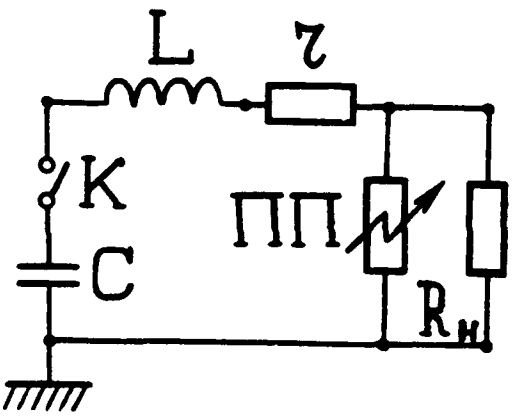

Fig.3.Schematic electric circuit of POS switch-on into the external circuit

where r, a, t are the Lagrange variables (r - radius, a- initial radius, t- time), $\tau = t/\sqrt{LC}$, $\tilde{\tau} = k_1 \tau$,

$$y \equiv \frac{a^2}{R^2} = \tilde{a}^2 ; \quad \tilde{r} = r / R , \quad \rho = \rho \ (y,\tau) = r / a = \tilde{r} / \tilde{a} ;$$

$$k_o = \frac{e n_o R^2}{|u_{co}| C} ; \quad k_2 = \frac{Ze \ |u_{co}|}{m_1 \ \omega_{pi}^2 \ R^2} ; \quad k_3 = R_H / \sqrt{L/C} ;$$

$$k_1 = (\omega_{Bi}^2 + \omega_{Pi}^2)^{1/2} (LC)^{1/2} \quad ; \quad k_r = r / \sqrt{L/C} \; ;$$

$$\beta = \frac{\omega_{Bi}}{(\omega_{Bi}^2+\omega_{Pi}^2)^{1/2}} \quad ; \Phi = \varphi/|u_{co}| ; \quad I = (i/|u_{co}|)\sqrt{L/C} .$$

In the plane geometry case, eqs.(1)-(5) are replaced by the following

$$I_{\Pi} = \frac{1}{k_{01}} \left[- \frac{d\Phi}{d\tau} + \frac{1}{k_{21}} \left\{ \begin{array}{ll} (1-\vartheta) \frac{d\vartheta}{d\tau} , & \vartheta \leqslant \vartheta_m \\ (1-\vartheta_m) \frac{d\vartheta}{d\tau} , & \vartheta \geqslant \vartheta_m \end{array} \right\} \right] , \qquad (5')$$

$$\frac{d^2\vartheta}{d\tau^2} + \nu \frac{d\vartheta}{d\tau} + \left\{ \begin{array}{ll} 1/2 \; \vartheta^2 , & \vartheta \leqslant \vartheta_m \\ \vartheta_m(\vartheta-\vartheta_m/2) , & \vartheta \geqslant \vartheta_m \end{array} \right\} = - k_{21} \Phi(\tau) , \qquad (5'')$$

where $k_{01} = \frac{C\,l}{\varepsilon_0 S}$, $k_{11} = \omega_{Pi} \sqrt{LC}$; $k_{21} = \frac{e\,|u_{co}|}{m_i\,\omega_{Pi}^2\,l^2}$,

l - interelectrode distance; ϑ - ion displacement;
S - electrode area; I_{Π} - the POS current;
Φ - POS voltage; I_1 - inductance L current.

The plot in Fig.4 gives the peak overvoltage in the POS for the plane geometry case.

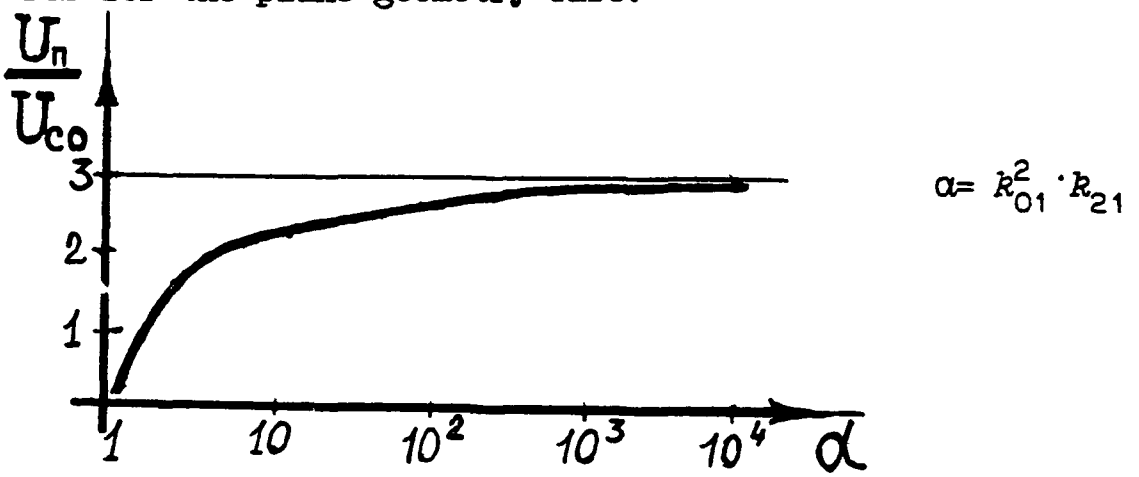

Fig.4.Highest overvoltage of the POS(plane geometry).

It is found that the overvoltage value depends only on the parameter $\alpha = k_{01}^2 k_{21}$ and cannot be higher than 3 for a rather wide range of the POS parameter variation. This conclusion is in agreement with the results of many experiments.

Higher overvoltage values can be attained with the cylindrical geometry by an appropriate choice of geometric sizes [5]. In the plane geometry case, the overvoltage values higher than those shown in Fig.4 can be achieved only through such constructive changes in the POS design which would lead to vanishing of the near-electrode space charge. The relevant theoretical consideration shows that in this case we have a one-fold operation of the POS. As a result of current transport all the plasma is carried away from the POS internal space; the overvoltage is given by the formula

$$\frac{u_{II}}{|u_{CO}|} \approx (k_{21}\sqrt{k_{01}})^{-1}. \qquad (10)$$

As far as best results are obtained for

$$k_{01}k_{21} \approx 1 \quad , \qquad (11)$$

the overvoltage will be

$$\frac{u_{II}}{|u_{CO}|} \approx \sqrt{k_{01}} \quad . \qquad (12)$$

It should be noted, however, that the parameter k_{01} must not be too large, otherwise the degradation of all the functions occurs, and formulas (10)-(12) are no longer valid.

In conclusion we note that the experiments [6] undertaken recently to investigate the processes in the POS, in particular, by spectroscopic methods, and which

have revealed the presence of electric fields of several types, differing in magnitudes, time behaviour and localization, can be explained on a basis of the POS potential theory.

References

1. Chukbar, K.V. and Yan'kov, V.V., Zh. Tekh. Fiz. 58, 2130 (1988).
2. Grossmann,J.M.,Ottinger,P.F.,Neri,J.M. and Drobot,A.T., Phys. Fluids 29, 2724 (1986).
3. Gordeev, A.V., Grechikha, A.V., Gulin, A.V. and Drozdova, O.M, Fiz. Plazmy 17, 650 (1991).
4. Pashchenko, A.V. and Smerdov, B.I., Fiz. Plazmy 13, 999 (1987).
5. Zhdanov, Yu.V.,Pashchenko, A.V. and Tkach, Yu.V., Proc. of the 8th Intern. Conf. "Beams' 90", v.1, 379 (1990).
6. Golovanov, Ju.P., Dolgachev, G.I., Zakatov, L.P. et al., Fiz. Plazmy 17, 799 (1991)

ANTHEM SIMULATIONAL STUDIES OF THE PLASMA OPENING SWITCH*

Rodney J. Mason

Applied Theoretical Physics Division
Los Alamos National Laboratory
Los Alamos, NM 87545

Abstract

For a deeper understanding of the physical processes governing the Plasma Opening Switch (POS) we use the ANTHEM 2D implicit simulation code to study: (1) ion dynamical effects on electrohydrodynamic (EHD) waves propagating along steep density interfaces in the switch plasmas. At radial interfaces where the density jumps toward the anode, these waves can drive a finger of magnetic field into the plasma toward the load. Ion dynamics can open the rear of such fingers into a wedge-like density gap. Then: (2) we examine ion effects in uniform switch plasmas. These first develop potential hill structures at the drive edge of the cathode from the competition between electron velocity advection and EHD magnetic exclusion waves. Magnetic pressure gradients at the hill periphery and EHD effects then establish a density gap propagating along the cathode with radial electron emission from its tip. Similar results are obtained under both multi-fluid and PIC modeling of the plasma components.

Introduction

The Plasma Opening Switch consists of a plasma injected between the anode and cathode of a pulse power transmission line. When a magnetic pulse first arrives at the plasma the associated current is short circuited through the plasma for a "conduction" time, allowing the field to grow to some maximum. Then, optimally, during a much shorter "opening" time the plasma is disrupted, and current and magnetic field propagate further down the line to a load. The length of fill plasma in the switch is typically 4 cm, the inter electrode gap is 2.5 cm, and the field grows to 1.5 T. For 50 ns conduction times the C^{++} fill plasma has a density of 3×10^{13} electrons/cm^3. Such a plasma has a skin depth of 0.1 cm; its initial temperature is 3 eV. It is many Debye lengths in extent. This system has been modeled globally with the ANTHEM 2D implicit simulation code[1-3], which showed opening dependent on a large number of competing physical effects. More recently, the newer effects have been given closer individual scrutiny. Kingsep et al.[4-6] have described electrohydrodynamic field penetration transverse to density gradients that can arise in the POS. Also, electron inertial terms have been shown to contribute to field penetration in uniform plasmas[7]. The competition between field exclusion effects from EHD and electron velocity advection has been related[8] to the development of potential hill structures near the drive end of POS cathodes[9]. These effects arise principally from the electron dynamics. The present work concentrates on modifications of these effects due to the ion dynamics present in a real POS. It is shown that ion motion leads to gap formation along internal

* This work was performed under the joint auspices of of the U.S. Dept. of Energy and the Defense Nuclear Agency

density interfaces in the switch plasma, and above the cathode. Corroborative results are acquired with ANTHEM using both multi-fluid and PIC modeling for the plasma components.

The ANTHEM Model

The code[3] uses a fixed Eulerian mesh in either cartesian or cylindrical geometry. Typically, 50 cells are used in the axial (x or z) direction, and 25 cells describe the interelectrode dimension (y or r). It solves the full set of Maxwell's equations with time advanced current sources obtained from the implicit solution to a set of auxiliary moment equations. These have been adjusted to allow for relativistic electron momenta. The implicitness provides numerical stability to plasma waves with the time step set by a Courant condition on the fastest electrons. This can permit a 100-fold improvement in economy over traditional explicit modeling at high switch densities. Plasma components (emission and background electrons, and ions) are represented on the mesh as either fluids or PIC particles. The fluid updates use Van Leer advection to minimize numerical diffusion. The particle modeling uses divergence conservative current accumulations to guarantee local adherence to charge continuity. External drive circuitry modeling is available to apply a programmed magnetic pulse at the POS vacuum plasma edge.

Ion Dynamical Effects on EHD Waves

In studying EHD field penetration along a density jump interface we return to a test configuration explored in Refs. 6 and 8. We consider cartesian geometry, i.e. plasma between two parallel plates, as shown in Fig. 1. The external driving magnetic field rises to -15 kG over 0.1 ns; thereafter it is constant. A large field has been imposed artificially rapidly to speed the calculation. The plasma starts at 0.6 cm and runs to 5 cm. The A-K gap is 2.5 cm. The plasma density is 3×10^{13} electrons/cm^3 up to 3.75 cm. Over one vertical cell, $\Delta y = 0.1$ cm, it doubles to 6×10^{13}, maintaining this value up to the anode. The plane EHD shock waves studied by Kingsep[4] should penetrate along the density gradient at half the linearized speed u_w given by

$$u_w \equiv \frac{cB_z}{4\pi c}\frac{\partial}{\partial y}(\frac{1}{n_e}). \tag{1}$$

In fact, penetration is about 50% slower than obtained by setting $\partial/\partial y \equiv 1/\Delta y$. This can ascribed to the lack of true planarity, and the presence of effective field diffusion[7] from the electron velocity advection terms, $(\mathbf{v}_e \cdot \nabla)\mathbf{v}_e$, appearing in the magnetic field equation

$$\begin{aligned}\frac{\partial \mathbf{B}}{\partial t} =& \nabla \times [\frac{\partial}{\partial t}(\lambda_B^2 \nabla \times \mathbf{B})] + \nabla \times [\mathbf{v}_e \cdot \nabla(\lambda_B^2 \nabla \times \mathbf{B})] \\ &+ c\nabla \times [\frac{\nabla(n_e \kappa T_e)}{e n_e}] + \nabla \times (\mathbf{v}_e \times \mathbf{B}),\end{aligned} \tag{2}$$

contructed from the electron momentum equation and Faraday's Law. Here

$$\mathbf{v}_e = -\frac{e}{m_e c}\lambda_B^2 \nabla \times \mathbf{B}, \quad \mathbf{B} \equiv B_z \mathbf{k}, \tag{3}$$

in which $\lambda_B \equiv c/\omega_p$, $\omega_p^2 = 4\pi n_e e^2/m_e$.

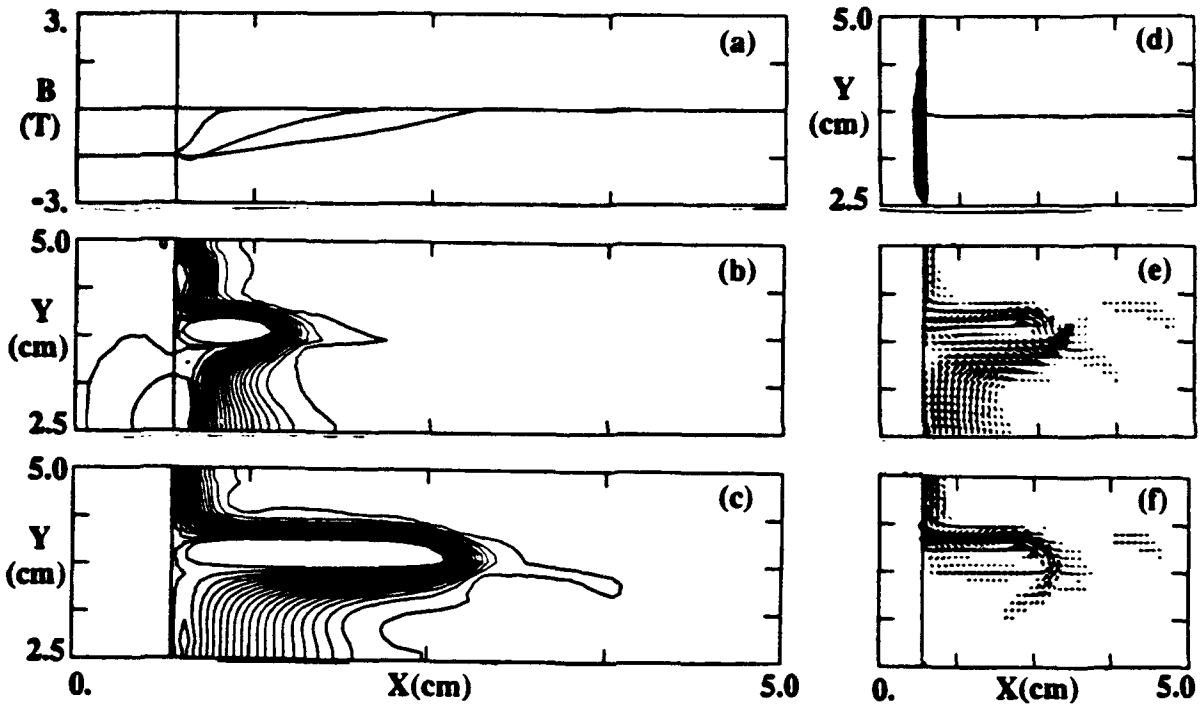

FIG. 1. EHD field penetration along a density jump interface with fixed ions.

Figure 1(a) gives cuts of the penetrating magnetic field at y = 2.8, 3.5 and 4.7 cm at t = 2 ns. Frames (b) and (c) show the field contours at 0.5 and 2.0 ns [so (c) can be calibrated by (a)]. A finger of magnetic field penetrates along the density interface. The fixed ion density is contoured in Fig. 1(d). Left is vacuum, high density is in the upper right region. Finally, (e) and (f) show the emission and background electron flux vector fields $n\mathbf{v}_e$, respectively. Open boundary conditions, forcing $\partial B_z/\partial y = 0$, were employed here in an effort to remove the direct electrode effects to infinity. Clearly, the field penetrates in the center of the switch plasma along the density interface. Other runs[8] have shown that the field leakage at the lower densities near the open boundary ceases when the $(\mathbf{v}_e \cdot \nabla)\mathbf{v}_e$ terms are suppressed in Eq. (2). Note that emission electrons [frame(e)] deliver nearly all the electron flux below the interface, while background electrons (f) carry the dominant flux above it.

Figure 2 collects corresponding results for field penetration when ion motion is permitted. To speed the evolution (and for computational economy) we have lowered the mass of carbon ions by the factor 4.75. Again, frame(a) shows the three cuts in the axial B_z profile at 2 ns. In (b) we see that by 2 ns the the back of the penetrating finger of B_z contours has been torn open into a wedge. Frame (c) shows the concomitant electron density contours. The electron flux vectors, $n_e\mathbf{v}_e$ [frame (e)] and the B_z contours line up along density maximum ridges, just barely evident in (c). The ridge density has tripled to 10^{14} electrons/cm^3; density drops in the center of the wedge to 10^{13}. The last contour to the left is at 10^{12} electrons/cm^3. Frame (e) shows the ion velocity vectors, pushing the wedge further open. Finally, (f) contours the emission electron density, showing its channel along the wedge shaped ridge, but also implying significant streaming toward the load and low density. A return current in the background electrons balances this stream.

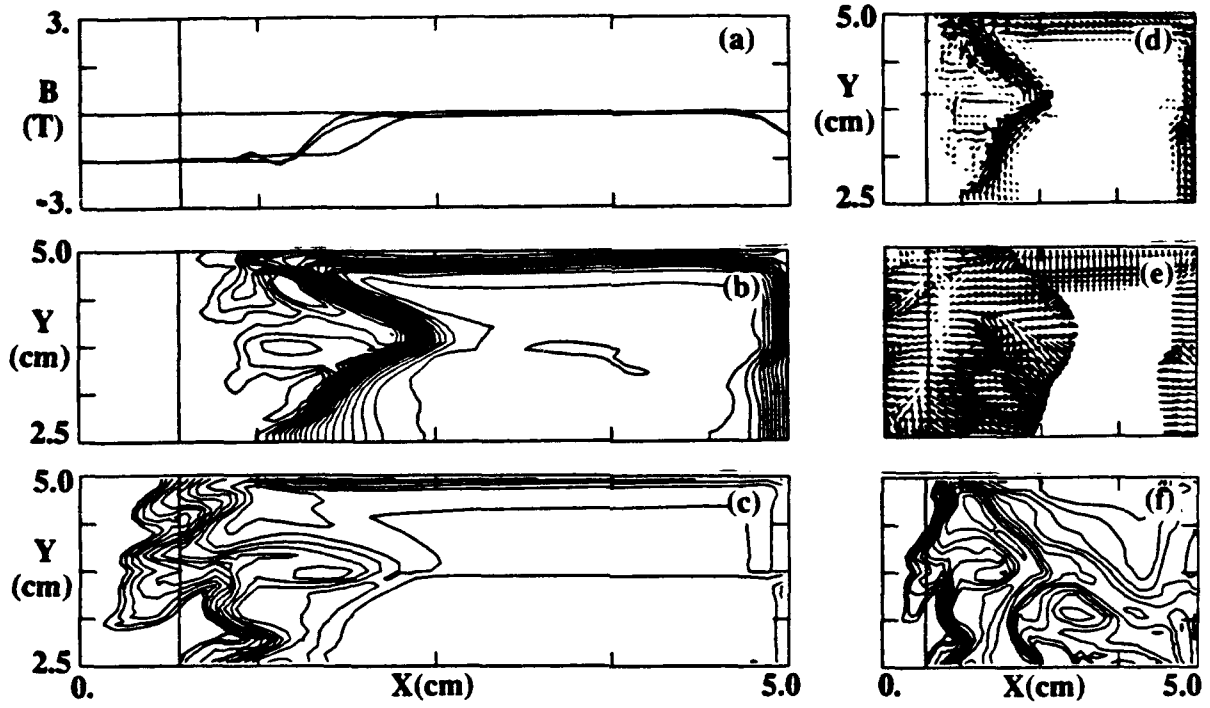

FIG. 2. Wedge-like profile of B-field penetration when the ions move.

From the Fig. 1 and 2 results we see that the coupling of ion motion to EHD magnetic penetration waves can result in significant gap formation in central regions of the switch plasma. With the physical mass of ions restored, such gaps will form more slowly. In Ref. 5 they were evident in global simulations of a cylindrical switch with a pulse rising to 1.6 T over 20 ns. The magnetic wedge penetrated 11 cm of POS plasma during this time. Relatedly, we note that a preestablished field will be removed from POS plasma regions in which the density drops in the direction toward the anode. The field is excluded[8] in accordance with expansion wave solutions to Eq. (2). With moving ions, we can anticipate that magnetic pressure gradients will compress the plasma in such field exclusion regions.

If the density jumps are removed and the ions are again fixed, then at 2 ns the results of Fig. 3 obtain. For the earlier Fig. 2 run the anode and the load were made perfect conductors. This lead to B_z field

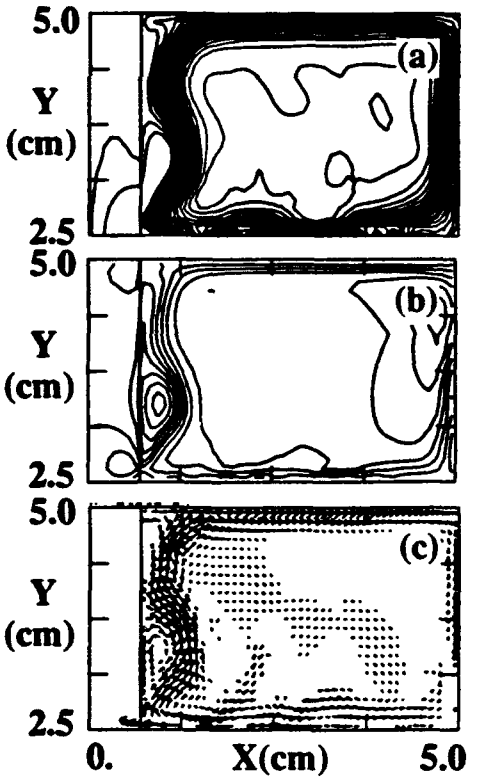

FIG. 3. Limited field penetration of the uniform switch, showing potential hill formation (b).

penetration along the anode by an EHD wave. The anode boundary is essentially the interface below a very dense plasma. For the Fig. 3 calculation both the anode and the cathode boundaries are perfectly conducting. Consequently, again we see rapid penetration along the anode, but now the emission stream is tied to the drive side of the plasma at the cathode. The uniform density permits no EHD central penetration of the plasma. Frame (a) shows the magnetic field contours, (b) electrostatic potential ϕ contours, and (c) plots the emission electron flux stream, $n_e \mathbf{v}_e$. The potential is derived from the ANTHEM solution for the electric field, and the inversion of $\nabla^2\phi = -\nabla \cdot \mathbf{E}$. It has a maximum "potential hill[9]" value of 200 keV just above the electron emission point, with the electron flux vectors circling around it.

Fluid vs. PIC Modeling of Uniform Switch Plasmas with Ion Motion

Finally, when this same Fig. 3 problem is run with ion motion permitted (again, with a 4.75-fold reduction in ion mass for economy), the Fig. 4 evolution ensues. Frames (a) to (c) show the ANTHEM code predictions for fluid modeling of the electrons and ions. Frames (d) to (f) obtain with particles used for the emission electrons and background ions. All the results are for 2 ns. Clearly, the two sets of predictions are quite similar.

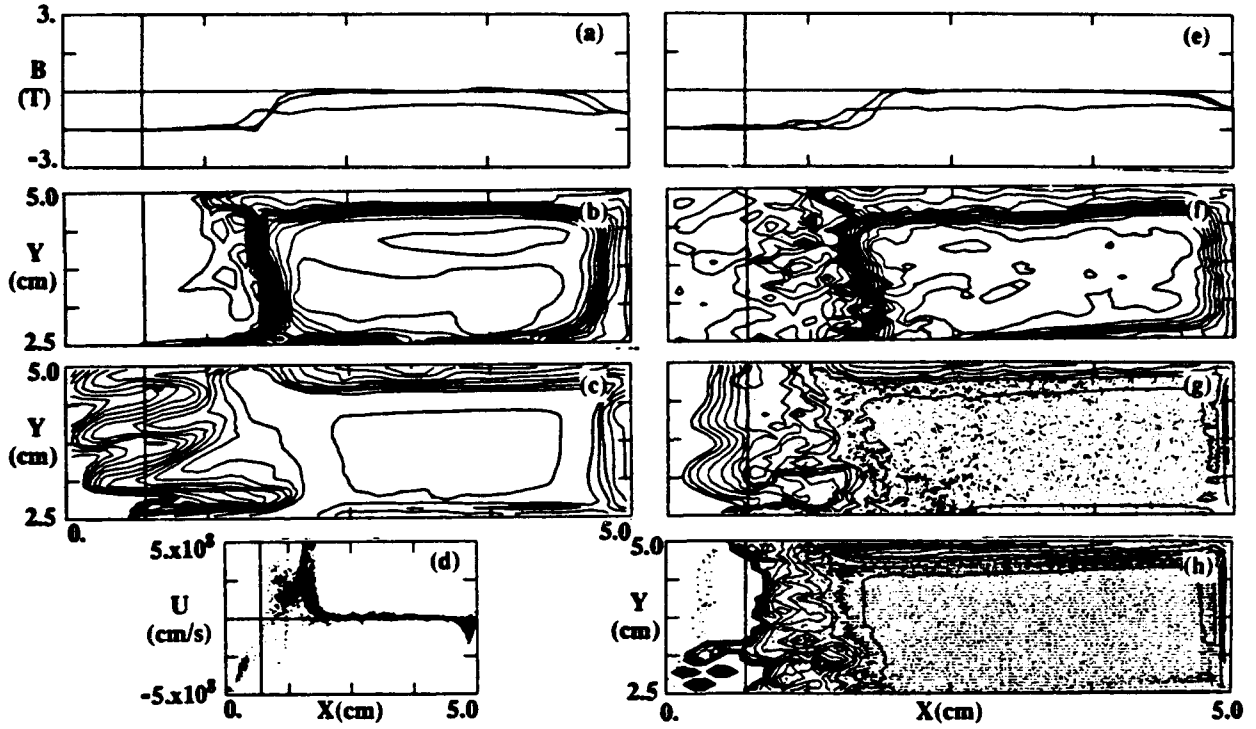

FIG. 4. Multi-fluid modeling (a)-(c); PIC modeling (d)-(h).

The B_z cuts with fluid and PIC modeling are the same, except for sightly deeper field penetration near the cathode. The field contour plot with particles is substantially noisier, but only one particle is emitted per cycle/cathode cell. [Less than 10 K particles are in use; more could readily be employed for smoother results]. The average axial depth of field penetration is nearly identical for the two treatments. The ions seem to push away from the anode somewhat faster than under PIC modeling. Frames (c) and (g) compare the

fluid and particle modeled electron densities. Plotted particles overlay the electron density contours in (g) and the ion density contours in (h). Frame (d) shows the ion phase space. The spike in ion axial velocities implies that a shock has started to form. No significant density perturbation from magnetosonic precursor ions is evident in (h).

The expanding fluid electron flow is more convoluted in the vacuum region near the driver, possibly due to the higher resolution possible with fluids at low densities. [The dynamic density range with particles is low, the minimum being weighted contribution of one particle]. A distinct gap is evident on the electron density contours slightly above the drive end of the cathode. This is under the evolved potential hill of Fig. 3, which shifts right with ion motion. A density ridge starts at the end of this gap, and runs radially (with slight incline toward the driver) up to the anode. This is particularly clear in (c), but also evident in (g). The ridge lies under the radially directed B_z contours in (b) and (f). As in earlier simulations[2], the contours do not twist back to follow the upper vacuum edge of the cathode gap. Field penetrates the plasma axially above such gaps due to an evolved radial density gradient that favors Kingsep wave penetration[4,8]. Effective diffusivity from electron velocity advection[7] also allows for the penetration of field into such plasma – which would remain field-free, if only conventional frozen-in field arguments applied.

The general agreement of our fluid and particle modeled results supports the joint utility of the two methods in POS investigations.

References

1. R. J. Mason, J. M. Wallace, J. M. Grossmann, and P. F. Ottinger, IEEE Trans. Plasma Sci. **15**, 715 (1987).
2. R. J. Mason, M. E. Jones, J. M. Grossmann and P. F. Ottinger, Phys. Rev. Lett. **61**, 1835 (1988); and J. Appl. Phys. **64**, 4208 (1988).
3. R. J. Mason, J. Comput. Phys. **71**, 429 (1987); and R. J. Mason and C. W. Cranfill, IEEE Trans. Plasma Sci. **PS-14**, 715 (1987).
4. A. S. Kingsep, Yu. V. Mohkov, and K. V. Chukbar, Sov. J. Plasma Phys. **10**, 495 (1984); K. V. Chukbar and V. V. Yan'kov, Sov. Phys. Tech. Phys. **33**, 1293 (1988); and A. S. Kingsep, K. V. Chukbar, and V. V. Yan'kov, "Electron Magnetohydrodynamics," in *Reviews of Plasma Physics*, Vol. 16 edited by B. Kadomtsev (Consultants Bureau, NY, 1990).
5. R. J. Mason, M. E. Jones, D. C. Wilson, C. Bergman, and K. Thiem, in *Proceedings of the Eight International Conference on High-Power Particle Beams, Beams' 90*, Novosibirsk, USSR, July 2-5, 1990, Vol. 2, p. 1058.
6. R. J. Mason, P. Auer, R. N. Sudan, B. Oliver, J. Greenly, C. Seyler, and L. Adler, "Theory and simulation of Laboratory Plasma Opening Switches," in *Proceedings of the 8th IEEE Pulsed Power Conference*, San Diego, CA, June 17-19, 1991, IEEE Cat. No. 91CH3052-8, p. 529.
7. B. V. Oliver, L. I. Rudakov, R. J. Mason and P. L. Auer, Phys. Fluids B, **4** 194, 1991.
8. R. J. Mason, P. L. Auer, R. N. Sudan, B. V. Oliver, C. E. Seyler, J. B. Greenly, "Non-Linear Magnetic Field Penetration in Opening Switch Plasmas," submitted to Phys. Fluids B, April 27, 1992.
9. J. M. Grossmann, P. F. Ottinger, and R. J. Mason, J. Appl. Phys. **66**, 2307 (1989).

Two-Dimensional Studies of Current Conduction in Plasma Opening Switches

Donald Parks, Eduardo Waisman, Randall Ingermanson, and Eric Salberta
S-Cubed Division of Maxwell Labs, 3398 Carmel Mountain Road, San Diego, California 92121

Abstract

We summarize our general understanding of the long conduction time (~1 μs) plasma opening switch POS, both in the conduction phase and in the opening phase of POS operation. For long conduction times, the mechanisms dominant in conduction have origins in electron-Hall effect (EHD) and in magneto-hydrodynamics (MHD). These mechanisms are considered in the context of experiments conducted on two different pulsed power accelerators, with concurrent in situ measurements, of plasma density indicating that one of the accelerators is predominantly in the EHD, the other in the MHD regime. In the latter case, with application of a 2-D snowplow model we are able to reproduce with fair accuracy the time variations of line integrated plasma density observed with laser interferometry near the cathode.

For the opening phase, we introduce a theory of magnetically enhanced ion erosion for plasma sheath formation and development of switch voltage. The theory, based on conservation of total momentum flux in the sheath, electromagnetic as well as particle, captures the measured voltage saturation of the switch limited POS operation.

Conduction-Time Models and Their Experimental Verification

Research on opening switches at Maxwell on ACE pulsers[1] and at NRL on HAWK[2] have demonstrated microsecond conduction time and fast opening. At sufficiently high ion densities the ordinary MHD dominates the conduction phase. For a plane geometry, constant density, switch of length d conducting a current which rises linearly with time, the snowplow approximation gives:

$$\rho d^2 = B_c^2 T_c^2 / 48\pi \equiv \rho v_{sp}^2 T_c^2 \qquad (1)$$

relating the conduction time T_c and magnetic field B_c to the plasma density and length, and defining the snowplow speed v_{sp}. Here $\rho = n_e / ZM$ with Z = degree of ionization (2 for C^{++}), M the ion mass, and n_e the electron number density.

At low densities the Hall term dominates. In a cylindrical geometry with $\vec{B} = -\hat{\phi} B(r,z)$, where $\hat{\phi}$ is a unit vector in the azimuthal direction, the propagation speed is: [4,5]

$$v_H = cB / 2\pi ne \ell \qquad (2)$$

For radial propagation in a radial switch (ACE 2 radial) where ℓ is a length scale associated with geometry and ordinary gradients

$$\ell^{-1} = (1/2\, n)(\partial n / \partial z) \qquad (3)$$

and for axial propagation in an axial switch (HAWK, ACE 1, ACE 2 axial)

$$\ell^{-1} = (n/2)\,[-(\partial/\partial r)(1/n) + 2/nr] \qquad (4)$$

Equating v_H to v_{sp} leads to an estimate of the cross-over density

$$n_x(cm^{-3}) = (2/\pi)\left(Mc^2/e^2\ell^2\right) \equiv 4 \times 10^{15} A / \ell^2(cm) \qquad (5)$$

where A is the average atomic weight of the plasma ions. For $n \leq n_x$, Hall effect dominates conduction time, whereas, for $n \geq n_x$ hydro effects (snowplow, e.g.) dominate the conduction.

Figure 1 shows current waveforms obtained with a radial POS on ACE 2, using an inductive short circuit load. The observed peak current and conduction times in Figure 1 are consistent with an electron density of 2.5×10^{14} cm^{-3}, according to the Hall model, and 2 to 4 x 10^{14} cm^{-3}, according to the snowplow model (depending upon assumption of C^+ or C^{++} as the ion species). The interferometrically measured densities were 3 to 4 x 10^{14} cm^{-3} with density ratios of ~ 2:1 over about 5 cm.[1] Thus, in this density range either model is consistent with the observed conduction time, and the ACE 2 POS probably operates in a mixed mode. Figure 2 shows data obtained on HAWK at NRL,[2] using an 8 cm long, coaxial POS, at bank voltage = 640 kV. Density was measured via interferometry. The current at switchout was calculated as a function of density for both the Hall and snowplow models. The data shows that the snowplow model is valid at high densities, and suggests that the Hall model gives better agreement at low densities.

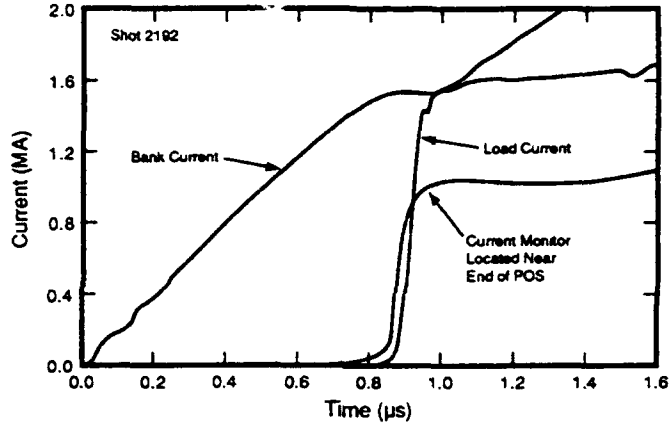

Figure 1. Radial POS results on ACE 2. The flat current reading for Load and Near POS monitors after about 1 μs indicate possible probe shorting by plasma.

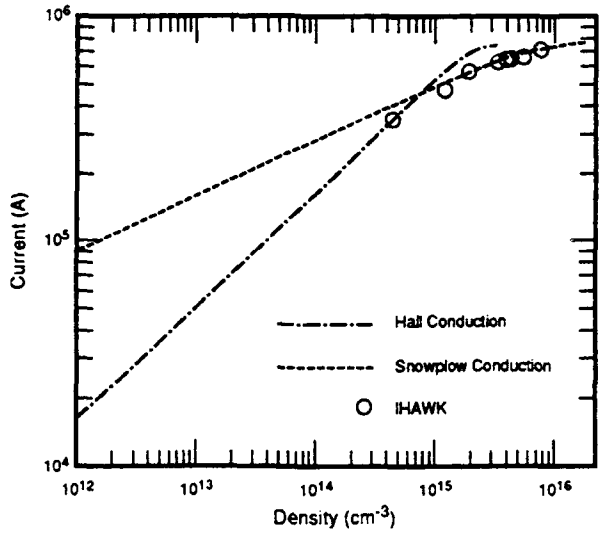

Figure 2. Dependence of current at end of conduction time on the electron density indicates that the snowplow model is confirmed by experiments at high densities.[2]

2-D Snowplow Model and Time Dependent Plasma Density

The 2-D snowplow[6], a generalization of the 1-D snowplow model, accounts for nonuniformities the magnitude of forces driving the system and in the density. Figure 3a shows a snowplow simulation of HAWK shot numbers 738 and 732 using time-dependent density data obtained by interferometry.[7] The unplowed plasma is assumed to be uniform along the axial direction, and to have the time dependence measured when no pulsed power is applied. We also assume that the plasma is moving uniformly toward the cathode at 5 x 10^6 cm/sec. The switch opens at about 930 nsec. We used the ratio of (plasma atomic weight)/ (mean ionization number) = 12/1.5 = 8.

Figures 3b and 3c compare the measured and predicted line-integrals of number density, at positions of 2.5, 5.0, and 7.5 mm from the cathode. Our results agree qualitatively with the measurements, showing a thinning of the density of about the right magnitude.

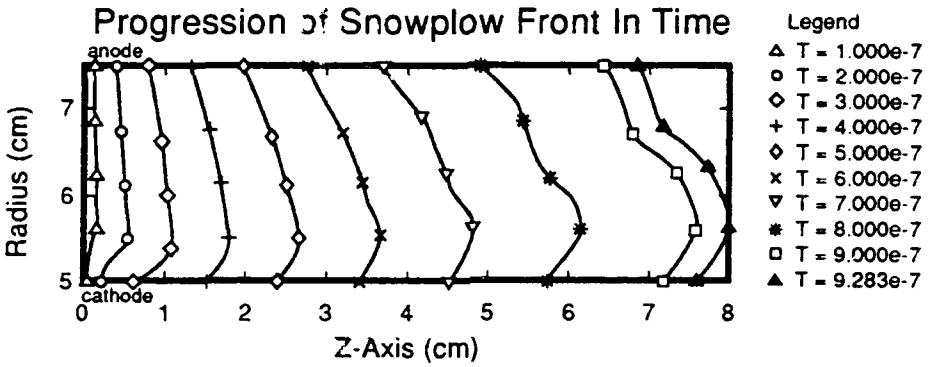

Figure 3a.

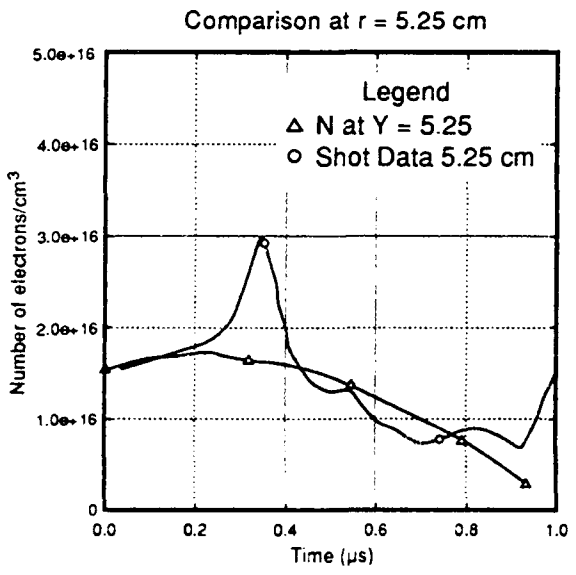

Figure 3b.

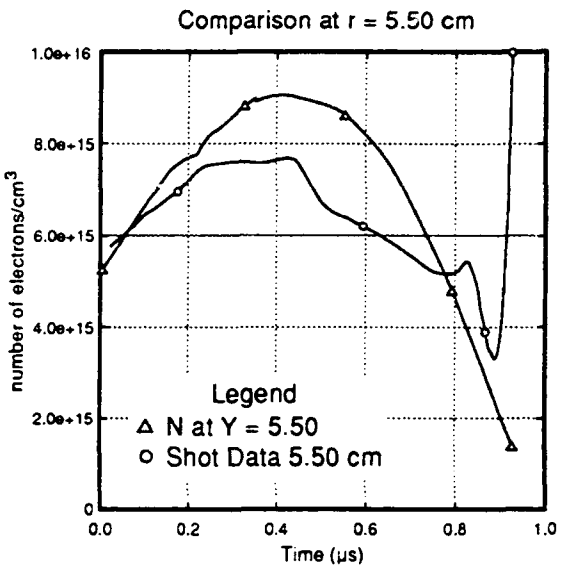

Figure 3c.

Figure 3. Snowplow front at different times, and comparisons of calculated and experimental line-integrated densities near the cathode. Plasma is assumed to have a velocity toward the axis of 5 x 10^6 cm/s, and atomic weight of carbon with effective ionization of 1.5.

The Opening Phase

The physics of the opening phase of the switch is believed to involve the formation of a sheath, or gap, across which the flow of electrons is limited by the magnetic field. The location of the sheath is not known with certainty, it may separate the cathode or anode from the bulk plasma, or it may lie in the interior of the plasma separating regions of widely disparate densities. The voltage V across the sheath of width D is related to the average magnetic field in the sheath by

$$(\gamma^2-1)^{1/2} = e\bar{B}D/mc^2 = D\bar{B}\,(\text{gauss.cm})/(1.70\times10^3) \qquad (6)$$

where $\gamma = 1+eV/mc^2 = 1+V(\text{volts})/5.11\times10^5$

The gap voltage that develops depends on D and the average field $\bar{B}$ in the gap. The gap growth rate $\dot{D}$ is related to the ion current density j_i in the switch,

$$\dot{D} = (j_i/en_iZ) - v_T \qquad (7)$$

where n_i is the effective ion number density at the time and location of opening and Z the state of charge of the ions. The gap growth is assumed to stop when j_i/en_iZ reduces to the ion thermal velocity v_T, taken to be 10^6 cm/sec in all that follows.

Assume now that electrons and ions begin their sheath transit with zero velocity. Neglecting the effect of the magnetic field on ion motion and assuming that the electric field and cross-gap component of electron momentum vanish on both sides of the sheath, it follows from energy and momentum conservation that [3]

$$j_i/Ze = \left(B_A^2 - B_K^2\right)/8\pi\,[2MeZV]^{1/2} \qquad (8)$$

with $B_K < B_A$ because of the diamagnetism of gap electrons. We assume, further, that B_A is from input current to the parallel switch load combination and B_K is due to the current in the load. In any case, the magnetic field leads to substantial electron density in the sheath, and this in turn leads to an enhanced ion erosion represented by eq. (8). This expression differs from earlier formulations of erosion. [8,9]

The theory can be validated by comparison with data from experiments on HAWK and ACE 2. The HAWK data and the comparison to calculations are shown in Figure 4. Peak load voltage and load current HAWK data points are plotted as functions of load impedance at peak power. The curves are our opening model predictions for various constant impedance loads. For ACE 2, experimental results are compared with model predictions for the case of an inductive short circuit load, in Figure 5. Again, the agreement between our model and the experimental data is excellent in both cases.

Our analysis establishes the parametric dependence of opening time and load voltage on the conduction current I, magnetic-field B, switch length l and plasma density n_i. For example, for a charged inductor L discharging a current I_o through the switch at position r in parallel with an open circuit, the peak voltage V_p and time to peak t_p scale as (non-relativistically):

$$V_p = \frac{5.11 \times 10^5}{2^{1/4} e^{1/2}} \lambda^{1/2} (V) = 2.6 \times 10^5 \lambda^{1/2} (V) \quad (9)$$

$$t_p = \frac{13}{12} \frac{1}{2^{3/4}} \lambda^{1/2} \tau(s) = 0.64 \lambda^{1/2} \tau \quad (10)$$

In eqs. (9) and (10), the dimensionless parameters $\lambda = LI_o/(5.11 \times 10^5 \tau)$ (L in H and I_o in A), and $= 1.1 \times 10^2 \sqrt{ZM} \left(n_i / B_o^3\right)$, where n_i is in cm^{-3} and $B_o = 5I_o/r$ is in gauss. In the extreme relativistic case, V_p scales as $\lambda^{2/5}$ and t_p as $\lambda^{3/5} \tau$, As a function of B_o and n_i the scaling is (non-relativistically): $V_p \sim B_o^2 / n_i^{1/2}$ and $t_p \sim n_i^{1/2} / B_o$. The corresponding extreme relativistic case gives $V_p \sim B_o^{8/5} / n_i^{2/5}$ and $t_p \sim n_i^{2/5} / B_o^{3/5}$.

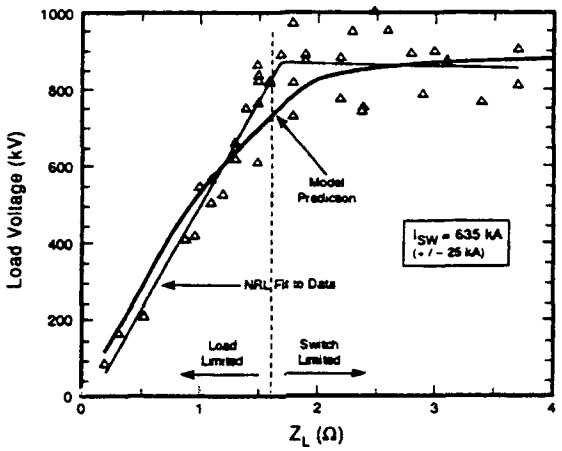

Figure 4. Comparison of HAWK data[2] (5 cm cathode radius) with magnetically enhanced ion erosion model for POS opening. In the calculation Z_L is taken as a constant in time impedance. The values used in eq. (3) for v_T and n_i were 10^6 cm/s and $10^{15}/cm^3$ (Z = 2). The interferometrically observed electron density was approximately between 2-5 x $10^{15}/cm^3$ near the end of the conduction phase at various locations in the interelectrode gap. I_{SW} is the peak switch current.

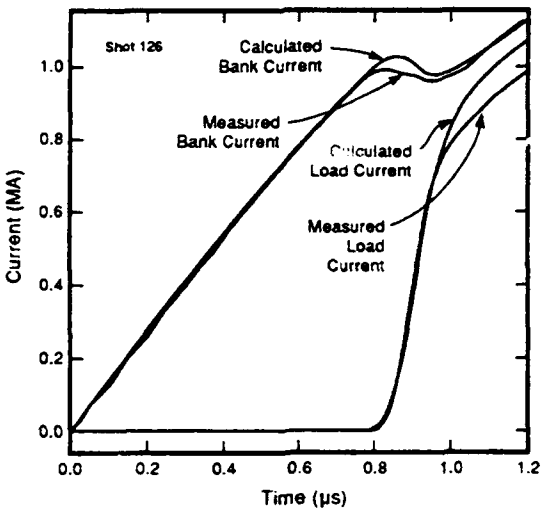

Figure 5. Comparison of magnetically enhanced ion erosion model with ACE 2 radial POS shot 126.[1] The interferometrically observed electron density at mid-gap was approximately 6 x $10^{14}/cm^3$. The values $v_T = 10^6$ cm/s, $n_i = 7 \times 10^{14}/cm^3$, and Z = 2 were used in eq. (3).

Conclusions

Based on the results of theory and experiment presented here, conduction by the POS in the ACE 2 accelerator is EHD dominated, in contrast to the dominance of MHD mechanisms in the HAWK device. In the latter case, a simple 2-D snowplow model accounts for the general features of the spatial-temporal characteristics of electron line density observed with laser interferometry. Finally, the formulation of magnetically enhanced ion erosion reproduces observed switching characteristics, including the voltage saturation of the switch limited regime observed in the HAWK measurement.

References

1. Thompson, John. Private communication, Maxwell Laboratories, San Diego, California, February 20, 1992.

2. Weber, B. V., J. R. Boller, and R. J. Commisso, Plasma Density Measurements in Microsecond Conduction Time Opening Switch Experiments, Poster IP20, 1991 IEEE ICOPS, Williamsburg, Virginia.

3. Parks, D., E. Waisman, and R. Ingermanson, "Magnetically Enhanced Ion Erosion in Plasma Opening Switches", to be submitted for publication to *Applied Physics Letters*.

4. Fruchtman, Ammon, "Penetration and expulsion of magnetic fields in plasmas due to Hall field," *Physics of Fluids B*, 3 (8), p. 1908, August 1991.

5. Kingsep, A. S., K. V. Chukbar, and V. V. Yan'kov, in Reviews of Plasma Physics, edited by B. Kudamtsev, Vol. 16, p. 243. (Consultants Bureau, New York, 1990).

6. E. Salberta, D. Parks, and E. Waisman, "General Solution for Asymmetric Snowplow in Z-Pinch-Like Geometry", submitted for publication in *Physics of Fluids B: Plasma Physics*.

7. Weber, Bruce V., Naval Research Lab, Private Communication, November, 1991.

8. Cooperstein, G. and P. Ottinger, "Guest Editorial: fast opening vacuum switches for high-power inductive energy storage," *IEEE Transactions on Plasma Science*, Vol. PS-15, 6, pp. 629-634, December 1987.

9. Cooperstein, G., J. M. Grossman, D. D. Hinshelwood, D. Mosher, J. M. Neri, P. F. Ottinger, and S. J. Stephenakis, Plasma Erosion Opening Research at NRL, *IEEE Transactions on Plasma Science*, Vol. PS-15, 6, pp 635-648, December, 1987.

ELECTRON AND ION MAGNETOHYDRODYNAMIC EFFECTS IN PLASMA OPENING SWITCHES

J.M. Grossmann*, C.R. DeVore+, and P.F. Ottinger*
Naval Research Laboratory
Washington, D.C. 20375

Abstract

Preliminary results are presented of a numerical code designed to investigate electron and ion magnetohydrodynamic effects in plasma erosion opening switches. The present model is one-dimensional and resolves effects such as the JxB deformation of the plasma, and the penetration of magnetic field either by anomalous resistivity or electron magnetohydrodynamics (Hall effect). Comparisons with exact analytic results and experiment are made.

I. Introduction

Plasma opening switches (POS) are used as power conditioning elements in pulsed power systems. POS's have been shown to suppress prepulse and to compress and multiply the power in such systems by initially shorting the transmission line (during the "conduction" phase) before opening and allowing the current to flow to the load. The POS can carry high currents (300 kA - 1 MA) and open in as little as 5 ns.[1,2] Several physical mechanisms can simultaneously contribute to POS behavior. These mechanisms include sheath formation at electrode/plasma interfaces, gap formation by electrostatic and magnetic forces, magnetic insulation of electrons in these gaps, JxB deformation and translation of plasma, and the penetration of magnetic field into the plasma both by anomalous resistivity and electron magnetohydrodynamic effects (EMH). In this paper, preliminary results are presented of a numerical code designed to investigate the conduction phase in regimes where the level of current carried by the device before it opens is determined by the hydrodynamic deformation of the plasma and/or the penetration of current into the plasma by EMH.[3,4] Tests of the code's performance are conducted and compared to exact analytic solutions. Comparisons with experiment in the short conduction time regime are also made.

II. The Numerical Model

The following are the basic equations that define the present model.

$$\mathbf{E} + \frac{\mathbf{u} \times \mathbf{B}}{c} = \eta \mathbf{J} + \frac{1}{en}\left(\frac{\mathbf{J} \times \mathbf{B}}{c} - \nabla p\right), \tag{1}$$

*Plasma Physics Division
+Laboratory for Computational Physics and Fluid Dynamics

$$\frac{\partial n}{\partial t} + \nabla \cdot (n\mathbf{u}) = 0 , \tag{2}$$

$$\frac{\partial \rho \mathbf{u}}{\partial t} + \nabla \cdot (\rho \mathbf{u}\mathbf{u}) = \frac{(\nabla \times \mathbf{B}) \times \mathbf{B}}{4\pi} - \nabla p , \tag{3}$$

$$\frac{\partial \Lambda}{\partial t} + \nabla \cdot (\Lambda \mathbf{u}) = -p(\nabla \cdot \mathbf{u}) + \eta \mathbf{J}^2 , \tag{4}$$

and

$$\frac{\partial \mathbf{B}}{\partial t} = \nabla \times (\mathbf{u} \times \mathbf{B}) - \frac{\eta c^2}{4\pi} \nabla \times (\nabla \times \mathbf{B}) - \nabla \times \left(\frac{c}{4\pi ne} (\nabla \times \mathbf{B}) \times \mathbf{B}\right) + \nabla \times \left(\frac{c}{ne} \nabla p\right) . \tag{5}$$

In the equations above, the symbols **E**, **u**, η, **J**, **B**, p, n, ρ, and Λ represent respectively the electric field, the plasma fluid velocity, the resistivity, the current density, the magnetic field, the pressure, the plasma number density, the mass density and the internal energy density of the plasma. Equation (5) is obtained by combining Ohm's law, Eq. (1), with Ampere's law (neglecting displacement current) and with Faraday's induction law. The right hand side of Eq. (5) is composed of four sections: a convective term, a diffusive term, a Hall term, and a baroclinic term. In this paper, a 1-D axisymmetric cylindrical system will be examined, so that all parameters depend only on the axial coordinate z. With only the azimuthal component of the magnetic field, $\mathbf{B}=B\mathbf{e}_\theta$, and assuming uniform density, Eqn. (5) reduces to

$$\frac{\partial B}{\partial t} + \frac{\partial}{\partial z}(u_z B) = \frac{c^2 \eta}{4\pi} \frac{\partial^2 B}{\partial z^2} + \frac{cB}{2\pi ner} \frac{\partial B}{\partial z} . \tag{6}$$

The present paper reports on preliminary results obtained from a numerical code designed to solve the 1-D form of the equations above. The mass, momentum, and energy Eqs. (2)-(4) are integrated using a flux-corrected transport (FCT) algorithm. FCT is an explicit, conservative, monotone technique for solving generalized continuity equations.[5-7] A finite-difference representation of the plasma and field variables is used, in which a variety of boundary conditions are flexibly implemented. The FCT algorithm is fourth-order accurate in the grid spacing at long wavelengths, and to achieve second-order accuracy in time, a predictor/corrector (halfstep/wholestep) integration scheme is used.

Equation (6) is integrated using operator-splitting techniques. The convective and Hall terms are treated by a modified FCT algorithm developed for this investigation. The explicitly nonlinear (quadratic) Hall term is handled analogously to the convective term, making their own contributions to the numerical diffusive and antidiffusive fluxes of the standard FCT scheme. The resistive diffusion term in Eq. (6) is treated separately, splitting it away and

integrating it using a fully implicit, three-point diffusion operator. This avoids the severe restriction on the allowed timestep imposed by the use of an explicit diffusion calculation, so that the Courant-Freidrichs-Lewy stability condition for the explicit convective and Hall terms fixes the maximum time increment allowed.[8]

III. Test Cases

For the dual purposes of testing this new computational model and demonstrating the suitability of the treatment of the Hall and resistive terms, several tests were performed on analytically solvable problems. Four of them are briefly described here: Hall penetration into a plasma column of a magnetic field ramped linearly in time at one end [9]; combined Hall and resistive penetration of magnetic field into a plasma column [3]; Hall expulsion of field combined with resistive penetration [3]; and propagation of a dissipationless, magnetoacoustic shock modified by Hall currents.

The first problem demonstrates the Hall penetration of magnetic field into the plasma in the absence of resistive and hydrodynamic effects. An initially field-free plasma column is subjected to a linearly ramped (with time) azimuthal field at one end. The Hall currents cause the field to penetrate in a shock-like solution whose front accelerates uniformly with time [9], with the location of the front determined by a Hugoniot condition derived from Eq. (6).[10] Figure 1 shows the progress of the field as it penetrates the plasma from left to right, at five uniformly spaced times. The solid lines indicate the analytical solution, the circles the numerical solution from the computer model. Clearly, the agreement is excellent, except for the slight staircasing of the sloped field profile behind the front.

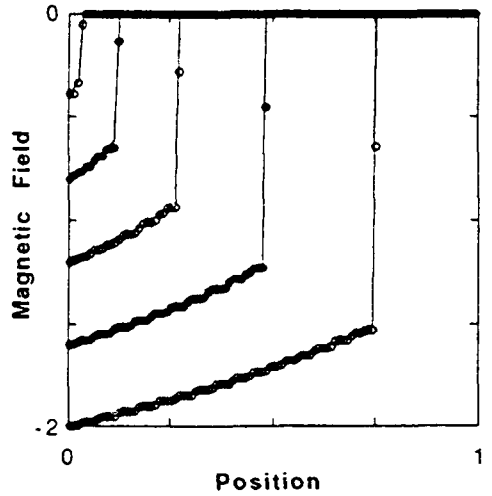

Fig. 1. Hall Penetration w/o Resistivity

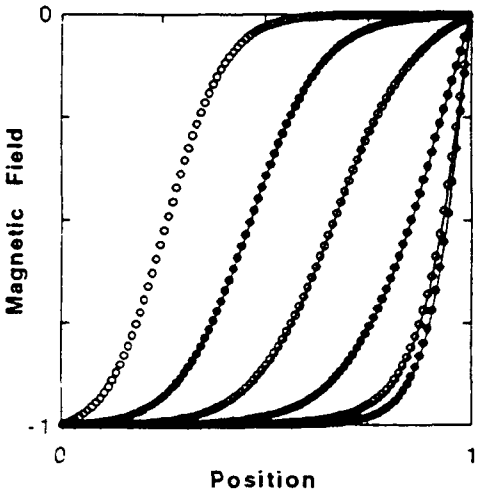

Fig. 2. Hall Penetration w/ Resistivity

The second problem again illustrates the Hall penetration of magnetic field, but this time in conjunction with resistive effects. As in the previous problem, the plasma is initially field-free. But in this instance, the field is suddenly switched on and held at a fixed finite value ($B_o(t)$ = -

1) at the left boundary, and at zero at the right. In Fig. 2, the Hall term leads to penetration of the field from left to right, and the field evolves toward a distribution which is uniform except for the resistive boundary layer at the right end.[3]

Because the Hall term is quadratic in the magnetic field, the Hall current drives a penetration of magnetic field for one sign of the applied voltage, and an expulsion for the opposite sign.[3] In Fig. 3, a plasma is initially suffused with magnetic field (B(z) = 1), and the field is held fixed at $B_o(t) = 1$ at left. The Hall term tends to expel the magnetic field from right to left, except again for a resistive boundary layer, this time at the left end. Both figures show the development of the time-asymptotic profiles at equal time intervals, the analytical solutions as solid lines, the numerical solutions as circles. As before, the agreement between the two is excellent.

The fourth problem combines the effect of the Hall current with convection, in the propagation of a magnetoacoustic shock modified by the Hall term. Here, a shock satisfying the modified Rankine-Hugoniot jump conditions is propagated across the mesh. The results are shown in Fig. 4, in which the solid line is the analytical solution and the initial condition for the computation. The shock profiles after propagation across distances equal to

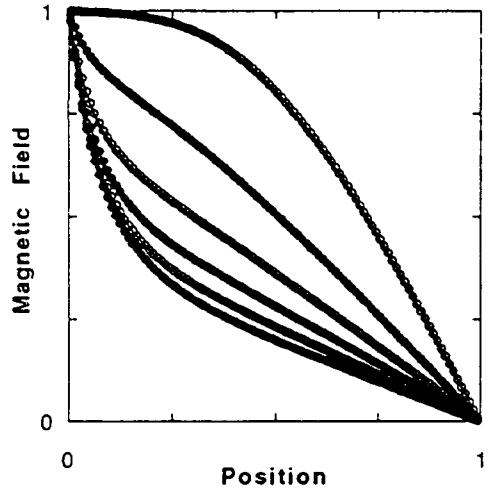

Fig. 3. Hall Expulsion w/ Resistivity

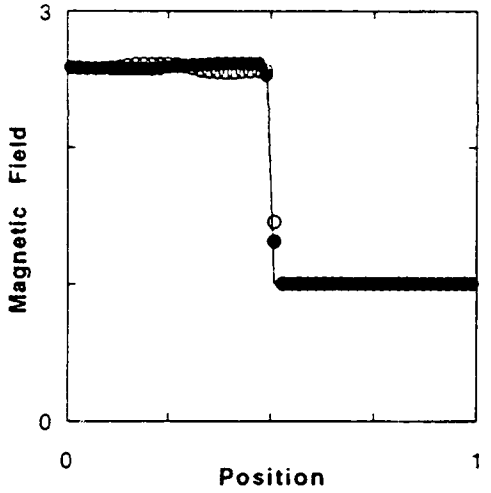

Fig. 4. Hall Modified Shock

the half width and full width of the figure are shown by the open and closed circles, respectively. The discontinuity is resolved over three zones and maintained at its initial value, with a small-amplitude numerical oscillation superimposed on the profile behind the shock front. Profiles of the mass density and total pressure show similar qualitative features, although the oscillations are smaller in magnitude than for the magnetic field.

IV. Comparison with Gamble I Experiments

In this section, the code is compared with experimental results in which the effects of JxB hydrodynamic forces are expected to be small , and Hall or resistivity effects are expected to

dominate. This comparison was made analytically by Fruchtman [9] for Gamble I shot 2197 in the case of zero resistivity, and showed very good agreement. The present code results will be compared with shots 2197 and 2165 and will include resistivity effects.

Two parameters control the degree of agreement between the numerical results and experiment. These are the plasma density and resistivity, or effective collision frequency. Since these parameters are not known exactly in experiment, a certain amount of freedom exists in their choice. In general it is found that, for a given rate of rise of the generator current, the choice of plasma density controls the speed of penetration of magnetic field into the plasma (through the Hall term), while the choice of collision frequency (resistivity) controls the width of the current channel (through the diffusion term). In obtaining the results below, a collision frequency is used that is an order of magnitude lower than the highest value suggested in Ref. [11], and roughly an order of magnitude higher than that associated with a combination of the Buneman, ion acoustic and lower-hybrid drift instabilities.[12] The densities used below were chosen to be reasonable estimates of actual experimental densities based on measurements of plasma source densities made separately from the actual experiment. They were also chosen to give reasonable agreement between experiment and the present model.

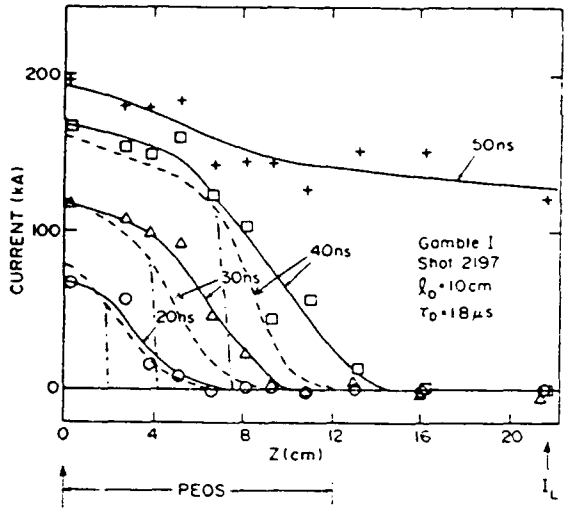

Fig. 5. Shot 2197 Comparison with Model

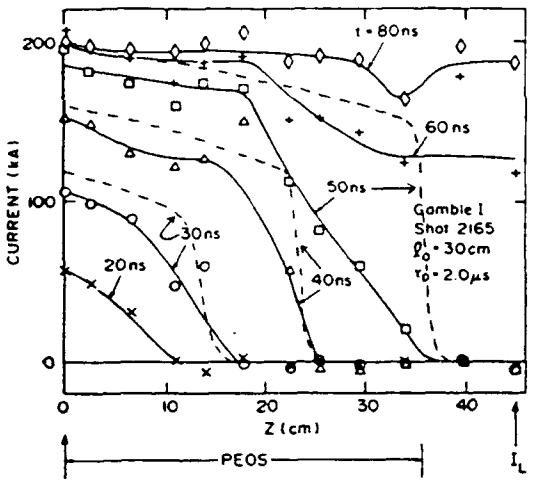

Fig. 6. Shot 2165 Comparison with Model

In Fig. 5, experimental and numerical results are superimposed for Gamble I shot 2197. The experimental (solid) curves show axial profiles of the current enclosed under a magnetic probe located 1.5 cm above the cathode at various times during the experiment.[13] The initial plasma is approximately 10 cm long, has a cathode radius of 2.5 cm and an anode radius of 5 cm. The POS opens after conducting current for about 40 - 50 nsecs. The numerical (dashed) curves show the axial profiles of the current enclosed as predicted by the model. In this case the electron density was chosen to be 2 x 10^{13} cm $^{-3}$ and the effective collision frequency $\nu = \omega_{pe}/12$. The dashed-dot curve shows the predicted current front for zero collision frequency

and shows that the effect of resistivity is to widen the current channels. For these choices of parameters, fairly good agreement is seen between experiment and numerical results. The value of resistivity needed to give good agreement is fairly high compared to the predictions of Ref. [12], which suggests that either another type of instability is active (as suggested in Ref. [11]), or that the magnetic probe signals are misleading.

Figure 6 shows similar results in the case of Gamble I shot 2165. In this shot, the length of the plasma was increased to 30 cm and the number of plasma sources was reduced by a factor of three. Consequently, a value of electron density of 6.67×10^{12} cm $^{-3}$ is used, but the collision frequency is kept at $\nu = \omega_{pe}/12$. As before, the solid curve is a fit to the experimental data, while the dashed curves are the model results. The correspondence between experiment and model is not as good in this case as in the previous one, especially at t = 50 ns, at which point the model predicts much deeper penetration of field. Several factors could contribute to this disagreement. One is that the density of this shot could have been higher than expected, the other is that two-dimensional effects (Hall penetration due to radial density gradients, for example) could be more important. These issues will be examined in later work.

V. Summary

A numerical method has been developed to examine electron and ion magnetohydrodynamic effects in the POS. A 1-D version of the model has been compared with exact analytic solutions and shows excellent agreement. For reasonable choices of physical parameters, good agreement with short conduction time POSs is also found. Further work will investigate regimes where JxB deformation of the plasma and density gradient effects become more important. Two dimensional effects such as the combined radial and axial JxB deformation of the plasma, and the Hall effect with density gradients in both directions will also be included in later work.

References

1 B.V. Weber, et al., Bull. APS **36**, 2456 (1991).
2 D.D. Hinshelwood, et al., Bull. APS **36**, 2456 (1991).
3 A. Fruchtman, Phys. Fluids B **3**, 1908 (1991), and references therein.
4 R.J. Mason, et al., Phys. Rev. Lett. **61**, 1835 (1988).
5 J.P. Boris et al., J. Comput. Phys. **20**, 397 (1976).
6 J.P. Boris, Naval Research Laboratory Memorandum Report No. 3237, (1976).
7 C.R. DeVore, Naval Research Laboratory Memorandum Report No. 6544, (1989).
8 R.D. Richtmyer and K.W. Morton, Diff. Meth. for Initial Value Probs., (Interscience, New York,1967).
9 A. Fruchtman, Weizmann Institute of Science, Rehovot, Israel, private communication, August 1991.
10 J.H. Gardner, Naval Research Laboratory, Washington, DC, private communication, October 1991.
11 R.Kulsrud, et al. Phys. Fluids **31**, 1741 (1988).
12 P.C. Liewer et al., Phys. Fluids **16**, 1953 (1973).
13 R.J. Commisso, et al., Naval Research Laboratory Memorandum Report No. 6057, (1987).

A SELF-CONSISTENT THEORY OF PLASMA FILLED DIODES AND PLASMA OPENING SWITCHES

L.I. Rudakov

I.V. Kurchatov Institute, 123182 Moscow, Russia

Abstract

The theory which is based upon the electron flow in a plasma filled diode can describe the magnetic field penetration into an interelectrode plasma bridge, but the final voltage across the diode gap, $V \leqq 300\, B^2 / 8\pi ne$, derived from this theory is lower by more than one order of magnitude compared to the experimental value. The voltage can increase as a result of the decrease of the plasma density due to ion acceleration towards the cathode by the Hall electric field $eE = 1/n\, \nabla B^2/8\pi$ in the skin layer. Two-dimensional quasi-steady-state flow of electrons and ions of a quasi-neutral plasma is considered. In the theory presented here expressions for erosion / velocity and the voltage drop are derived

1. Introdction

Magnetic field penetration into a homogeneous plasma with stationary ions and infinite condcutivity has been considered in [1]. This paper does not deal with the well-known problem of the anomalous skin $\delta = c/\omega_p$ for the half-space, but rather with the penetration of the magnetic field into the plasma bridge between two electrodes with a gap d much narrower than the displacement of electrons during the characteristic time for the problem. In this case, the flow of electrons may be considered as quasi-steasy-state with the boundary condition that the velocity at which they escape from the cathode is small, compared to the characteristic speed $cB/4\pi en\delta$, where δ is the skin layer thickness in the middle of the diode gap. It has been shown that the quasi-one-dimensional elelctron flow in the skin layer with an amplitude $B_y = B_o$ of the magnetic field imposed at the outer plasma boundary at $z = 0$ and $t = 0$ penetrates into the plasma according to the following law:

$$B = B_o\, b(\xi), \qquad b(\xi) = -1 + \frac{6^{1/3}}{4}\,\xi - \frac{1}{12}\,\xi^3, \tag{1}$$

$$\xi^3 = (\omega_p z/c)^3 \quad (\omega_p x / c\omega_c t) \tag{2}$$

The skin layer gets thinner from the cathode to the anode, and the assumption of quasi-steady-state, quasi-one-dimension flow is valid in the following range of distances from the cathode:

$$\frac{c}{\omega_p}(\omega_c t)^{1/4} < x < Bt/(4\pi nm)^{1/2} \qquad (3)$$

2. Magnetic field penetration in a nonhomogeneous collisionless plasma

It is shown in [2], that a magnetic field can penetrate into the plasma bridge as a shock wave, if the plasma density increases from the cathode to the anode, since the ratio of B/n remains constant along the electron trajectories. In [2] the structure of the wave front is determined by electron friction. We will consider the structure of the front in a collisionless plasma taking into account the electron inertia. The field penetration will be described in terms of the EMHD (electron magnet-hydrodynamics)-equation for cool plasma:

$$rot\left[c\bar{E} + [\bar{v} \times \bar{B}] + \frac{mc}{e}(\bar{v}\nabla)\bar{v}\right] = 0, \quad \text{rot } \bar{B} = -4\pi en\bar{v}/c \qquad (4)$$

Let us suppose for the geometry in Fig. 1 that $n = n_o + n_1 \frac{x}{d}$, $n_1 \ll n_o$

The system (4) can be reduced to the following dimensionless equation:

$$\frac{\partial b}{\partial t} - u_o \frac{\partial b^2}{\partial z} = -(\text{rot}\, b\, \bar{\nabla})\nabla^2 b \qquad (5)$$

where the time, the spatial, and the velocity coordinates have been normalized by $\omega_c^{-1} = mc/eB_o$, $c/(4\pi ne^2/m)^{1/2} = c/\omega_p$, and $u_o = (n_1/2n_o)(c/\omega_p d)$ respectively. If $n_1 = 0$, then (1) and (2) result from (5). If $n_1 \neq 0$, then equation (5) has a solution of the stationary shock wave type.

Assuming $\partial b/\partial z \gg \partial b/\partial x$, the structure of the wave front is described by the following two-dimensional nonlinear equation:

$$-(2bu_o + u)\frac{\partial b}{\partial z} = \left[\frac{\partial b}{\partial z}\frac{\partial}{\partial x} - \frac{\partial b}{\partial x}\frac{\partial}{\partial z}\right]\frac{\partial^2 b}{\partial z^2} \qquad (6)$$

If the self-similar variable $\xi^2 = z^2 x$ is introduced the solution will take the form $b = b(\xi)$.

The operator $\left(\frac{\partial b}{\partial z}\frac{\partial}{\partial x} - \frac{\partial b}{\partial x}\frac{\partial}{\partial z}\right)$

acting on the function of the variable ξ gives zero. Therefore the following equation for $b(\xi)$ results from (6):

$$\left[\frac{d^2 b}{d\xi^2} + \left(u + 2bu_o\right)\right]\frac{db}{d\xi} = 0 \qquad (7)$$

The boundary conditions are:

$$b = 0, db/d\xi = 0; \quad b = 1, db/d\xi = 0. \tag{8}$$

The solution of equation (7), $b + u / 2u_o$, is a periodic function of the variable $\xi(2u_o)^{1/2}$, and the following function meets the boundary conditions:

$$b = -\frac{1}{2}\left[1 + \cos\xi (2u_o)^{\frac{1}{2}}\right] = -\cos^2 \xi(u_o/2)^{\frac{1}{2}} = -\cos^2\left[\frac{2\omega}{c} p\left(x \frac{d\ln n}{dx}\right)^{\frac{1}{2}}\right]$$

$$b = 0, \frac{\xi^2 u_o}{2} > \left(\frac{n}{2}\right)^2, \quad u = u_o = \frac{B}{2(4\pi nm)^{1/2}} \left| \frac{c}{\omega_p} \frac{d\ln n}{dx} \right| \tag{9}$$

In addition to solution (9), equation (8) has the periodic solution $\cos^2\xi (u_o/2)^{1/2}$ in the whole region $\xi > 0$. To exclude this solution, a term with low electron-ion friction is taken into account in the original equation(4).

This yields an additional small non-self-similar term in (7), which changes the behaviour and determines the sign of $db/d\xi$. If $b \Rightarrow 0$, then

$$\frac{db}{d\xi} = -\left(2b + \xi_o^2\right)^{\frac{1}{2}} + \xi_o, \quad \xi_o = \nu_{ei} x^{\frac{1}{2}} / u_o \tag{10}$$

If $b \ll \xi_o^2$, $b \sim \exp(-2u_o \omega^2_p / \nu_{ei} c^2)$

The assumption of quasi-steady-state, quasi-one-dimensional electron flow determines the range of applicability of the solution. The flow becomes quasi-one-dimensional at the distance $\left(d \frac{c^2}{\omega_p^2} \frac{n}{n_1}\right)^{\frac{1}{3}}$.

Unlike the shock wave with ohmic dissipation at the front obtained in [3], where the plasma electrons are heated up to $3/2\ nT \approx 2/3\ B^2/8\pi$, the plasma stays cool in this solution and the energy is entrained by high-energy electron flow.

Thus, a planar solution shock wave like (9) as well as magnetic flux and energy flow is possible only with the plasma density increasing from the cathode to the anode. While this article was prepared I found a shock-wave like solution in collaboration with A Fruchtman from Weizmann Institute for the case of a homogenous plasma /14/. We assumed that the shock-wave velocity u is a function of x:

$$u = \frac{B_0}{(4\pi nm)^{1/2}} \left(\frac{c}{6\omega_p x}\right)^{1/3} \left(\frac{m}{M}\right)^{1/3} \qquad (11)$$

When we obtained solutions (9) and (10) we did not search where the fluxed B and $B^2/4\pi$ were coming from. In a diode filled with plasma up to the metallic electrodes the flux B can be introduced by electrons flowing along the cathode, and the residual flux can leave along the anode. The structure of electron and magnetic field flows in the vicinity of the electrodes with stationary ions and n = const. is described by equation (5). Its solution has the form (1):

$$b = -b_1 + \frac{A}{4}\xi - \frac{1}{12}\xi^3, \quad \xi^3 = x^3 z/t \qquad (12)$$

The constant A must be chosen for the condition that in the plasma b = 1 and $\partial b/\partial x = 0$ if $\xi = \xi_0$.

$$b = -b_1 - \frac{\xi}{4}(6 - 6b_1)^{\frac{2}{3}} + \frac{1}{12}\xi^3, \quad \xi_0^3 = 6(1 - b_1) \qquad (13)$$

Fluxes B and $B^2/8\pi$ in these flows are correspondingly equal to:

$$\frac{c}{8\pi en}(B^2 - B_1^2), \quad \frac{c}{4\pi en}\,\frac{B^3 - B_1^3}{12\pi} \qquad (14)$$

3. Plasma erosion due to Hall electric fields

It should be noted once more that the influx of the field and energy into the plasma filled diode is only possible with electron advection. The plasma does not conduct current any more after field penetration - the Poynting vector becomes zero everywhere except for the layers adjacent to the electrodes. The energy flux is limited by the value (14).

The energy flux can be increased only by decreasing the plasma density in the current layer which may result from acceleration of ions in the skin layer by the Hall electric field [4, 5].

$$eEn = -\nabla \frac{B^2}{8\pi} \qquad (15)$$

In the vicinity of the cathode the ions are accelerated towards the cathode from the plasma with field B_o. The motion of ions through the thin skin layer may be considered quasi-steady-state:

$$n v_i = n_o v_o = I \ , \ MI(v_i - v_o) = (B_o^2 - B^2)/8\pi \qquad (16)$$

Here $v_o = \partial x_o / \partial t$, $x_o(z, t)$ - thickness of the current layer. The flow is quasi-steady-state if the velocity ratio v_i / v_o and the density ratio n_o / n are large.

The following convective term is to be included in equation (4) if ion flow is taken into account:

$$\frac{\partial}{\partial x} v_i B \qquad (17)$$

However, we neglect the contribution of ion current to the magnitude of the magnetic field and assume B_o = const. With this assumption made the equation for the magnetic field in the vicinity of the cathode takes - instead of (5) - the following form:

$$\varepsilon \frac{\partial b}{\partial t} - \varepsilon v_o \frac{\partial}{\partial x}(1 - b^2 + \varepsilon) b = \left(\frac{\partial \bar{b}}{\partial x} \frac{\partial}{\partial z} - \frac{\partial \bar{b}}{\partial z} \frac{\partial}{\partial x} \right) \frac{\partial^2 \bar{b}}{\partial x^2} \qquad (18)$$

$$\frac{\partial \bar{b}}{\partial x} \equiv \frac{n_o}{n} \frac{\partial b}{\partial x} = (1 - b^2 + \varepsilon) \frac{\partial b}{\partial x} \ , \ \varepsilon = \frac{2M}{m} v_o^2 \ll 1$$

This equation in the region $1-b^2 \gg \varepsilon$ can also be reduced to the form:

$$\frac{db}{d\xi} \left[1 - 3b^2 + (1 - b^2) \frac{d^2 (b - b^3/3)}{d\xi^2} \right] = 0 \qquad (19)$$

$$\xi^2 = x^2 z \frac{2M}{m} v_o^3 \qquad (20)$$

Equation (19) has the integral

$$(1 - b^2) \frac{db}{d\xi} = - |2b(1 - b^2)|^{\frac{1}{2}} \qquad (21)$$

This equation describes the monotonous function $b(\xi)$, changing from 1 to 0 in the interval $\xi_o \approx 1$.

The value of $v_o(z, t) = \partial x_o / \partial t$ is determined by the following condition:

$$\xi_o^2 = x_o^2 \left(\frac{\partial x_o}{\partial t} \right)^3 z \frac{2M}{m} = 1, \ v_o = \left(t^2 z \frac{M}{m} \right)^{-\frac{1}{5}} \qquad (22)$$

If we take into account the dependence $v_o(z, t)$ in eq. (18) we should multiply the definition of ξ^2 by 5/2.

Now we can evaluate the value of the magnetic field flux (voltage V on the diode):

$$\frac{B_o^4 (1 - b_1^2)^2}{(8\pi)^2 2M v_o^2 n_o^2} \simeq \frac{B_o^2 (1 - b_1^2)^2}{16\pi n_o} (\omega_c t)^{\frac{4}{5}} \left(\frac{z\omega}{c} p \right)^{\frac{2}{5}} \left(\frac{m}{2M} \right)^{\frac{3}{5}} \qquad (23)$$

The magnetic field flux and voltage in the plasma start to rise just after the magnetic shock reaches the plasma rearside. Therefore, in formula (23) the time should be counted from that moment.

In the range of applicability of the EMHD theory $\omega_c t < M/m$, $z_o \omega_p / c < (M/m)^{3/4}$, the voltage on the diode may reach the value:

$$eV_{max} \leq 300 \frac{B_o^2}{8\pi n_o} \left(\frac{2M}{m} \right)^{\frac{1}{2}} \quad (eV) \qquad (24)$$

The condition for z_o means that the current $en_o v_o z_o$ is minute compared to the electron current. Thus, the reduction in density in the skin layer due to ion acceleration by the Hall electric field yields an up to $(2M/m)^{1/2}$ times voltage increase. This increase should be observed after the magnetic field and current attain the inner side of the plasma bridge.

For the case, in which the original plasma density is homogeneous and there is no input wave, the numerical experiment [6] and linear theory [7] of skin layer stability show, that density valleys with the incoming magnetic flux flowing along these valleys can be generated and grow inside the plasma. These valleys are caused by magnetic pressure; the instability increment is of the order of $\omega_c (m/M)^{1/2}$.

4. Comparison with experiments

Let us see now to what extent the results obtained are consistent with the experimental ones. We will compare our results mainly with those obtained by the team headed by L.P. Zakatov for processes in plasma filled diodes fed by microsecond current generators [8].

We use the experimental parameters and results required for the analysis. The diode, a coaxial system with an outer radius of 18 cm, an inner radius of 3 cm, contained a plasma bridge of 15 - 60 cm length. It was fed by an 2 Ω-impedance gen-

erator supplying for 2 μs a current of 200 kA. A streak camera photograph of the radial gap taken from the load side shows that the luminescence of the plasma in the gap flashes approximately 0.6 μsec after the beginning of current flow, when an amplitude is of 100 kA reached. At the same time a signal appears on the detector, which records the ion flux to the cathode. From this moment on an additional resistance of $\leqq$ 0.5 Ohm from the diode appears in the circuit. After that, the luminescent area moves back from the cathode at a velocity of 10^7 cm,

and according to (22): $$v_o = v_{Ae}\left((\omega_c t)^2 z \frac{\omega_p}{c}\frac{M}{m}\right)^{-\frac{1}{5}} = 10^7 \text{ cm}.$$

The probe measurements of the magnetic fields in the plasma filled diode [9, 10], showing the motion of the current layer through the plasma bridge at a velocity consitstent with (9), confirm the conclusions drawn above.

For some experiments on the generator Kalif [11] the POS had a coaxial geometry with inner and outer radii of 1 and 4 cm, respectively filled by a plasma with a density of $n_e = 5 \times 10^{13}$ cm^{-3} over a length of 15 cm. The voltage rises to an amplitude of 3.5 MV at the diode when the current in the inductor achieved 0.6 MA after 60 ns. In accordance with the described theory this moment should correspond to the end of magnetic field penetration through the POS plasma and to the beginning of the plasma erosion induced by the Hall electric field. As a result a voltage drop given by equation (23) should rise in the plasma.

$$V_{Hall} = \frac{300\,B^2}{16\pi e n(t)} = 0.5\,\frac{MV}{ns}\,(t - t_o)^{\frac{4}{5}}\left(\frac{r_a}{r}\right)^3$$

where r_a = 4 cm is the anode radius and t_o = 60 ns is the time of switching. In the experiment dV/dt = 0.4 MV/ns.

An attempt was made to evaluate the temperature of the diode plasma by the intensity of helium impurity lines [8]. The lines of atomic hydrogen and helium appeared but those of ionized helium were absent. This again is in agreement with the above theory.

6. Hall phenomena in the ion diode

We can use solution (9) and equation (18) with insignificat changes to describe porcesses in magnetically insolated diodes used to obtain high current ion beams in experiments devoted to inertial confinement fusion [11, 12]. Let us consider the v_z electron and v_x ion flows in the vicinity of a plasma cathode at $x \leqq 0$. Here a plasma exists with an electron density n_e which is connected to the ground electrode along B_z field lines, and a flux $n_i v_i$ of ions accelerated in the diode to an energy $eV \gg B_y^2 / 8\pi n_i$ falls on the cathode. Therefore, we can assume that the ion

energy does not change in the j_z current layer in the cathode plasma. Nevertheless, we should remember that a flux of fast ions $n_i v_i$ penetrates into the cathode plasma, and the ion current can be compensated by either the current of accopanying electrons or that of counterstreaming ions. The first possibility is improbable since the electrons have to cross the magnetic field lines of the B_z field. The second possibility means that the ions from the cathode plasma have to reach the cathode current layer with a velocity $v = n_i v_i / n$ to compensate the current of the fast ions. In the j_z skin layer the electrons moving along the z - coordinate must compensate the charge of ions coming from the plasma. Thus, in the range of electron injection into the plasma cathode along B_z at $z > cB_y / 4\pi e n_i v_i$ there must be an area of electron acceleration. The ion flux with a density n_o coming to the cathode is retarded by the Hall field and creates a wave of plasma density moving to the anode at a velocity u, determined from the following equations.

$$un_{max} = n_i v_i = I \qquad \frac{1}{n} = \frac{v}{I} = \frac{B_{oy}^2 - B_y^2}{8\pi M I^2} + \frac{u}{I}$$

Assuming I = const, $v \gg u$, the following equation results from (4):

$$-\frac{d}{d\xi}(1-b^2)^2 = (1-b^2)\left(\frac{db}{d\xi} - b\frac{d}{d\xi}\right)\frac{d}{d\xi}(1-b^2)\frac{db}{d\xi}$$

The asymptotic behaviour of $b(\xi)$ is $b \sim \exp(-\xi^2)$, $\xi \gg 1$; $b = 1 + \xi, -\xi \Rightarrow 0$.
Thus, the present theory satisfactorily takes into account the phenomena observed in a plasma filled diode. As for the vacuum high current ion diode, the above considerations should be compared with the experiment and computer simulations.

Acknowledgement:

The author is grateful to his colleagues from I.V. Kurchatov Institute: A.V. Gordeev, A. Grechiha, A.S. Kingsep and to the colleagues from Cornell University: R.N. Sudan, R.J. Mason, B.V. Oliver, C. Seyler for stimulating discussions and critics, and to H. Bluhm from KfK for discussions and help in the preparation of the manuscript. He also wants to thank the INR-institute at KfK for the hospitality and general support.

References:

1. B.V. Oliver, L.I. Rudakov, R.I. Mason, P.L. Auer, Phys. Fluids B, 4, p. 294, 1992.
2. A.S. Kingsep, Yu. V. Mokhov, K.V. Chukbar, Fizika Plasmy, 10, p. 854, 1984.

3. A. Fruchtman, K. Gomberoff, "Magnetic Field Penetration and Electron Heating in Weakly Nonuniform Plasmas", Preprint WIS-91/41/July-PH, Weizmann Inst., Israel.

R.J. Mason, P. Auer, R.N. Sudan, B. Oliver, J. Greenly, C. Seyer, L. Adler, "Theory and Simulation of Laboratory Plasma Opening Switches", Preprint LPS 91-9, Cornell University, U.S.A.

4. A.V. Gordeev, A.V. Grechiha, A.V. Gulin, O.M. Drozdova, Fizika Plasmy, 17, 1991, pp. 650 - 663.

5. A.I. Morozov, L.S. Solovjev, "Stationary plasma flow in magnetic field" in "Voprosy of Plasma Theory", edited by acad. M.A. Leontovich, vol. 8, Moscow, 1974, pp. 3 - 87.

6. R.J. Mason, M.E. Jones, D.C. Wilson, C. Bergman, K. Thiem, J.M. Grossman, P.F. Ottinger, "Calculated Non-linear Magnetic Field Penetration of Plasma Opening Switches", Proceedings of VIII. Intern. Conf. on High-Power Particle Beams, BEAMS ' 90, Novosibirsk, USSR, 1990, vol. 2, pp. 1058 - 63.

7. A.V. Gordeev, A. Grechikha, Fizika Plasmy, 18, vol. 1, 1992.

8. G.I. Dolgochaev, L.P. Zakatov, A.G. Ushakov, Fizika Plasmy, 17, vol. 1, 1991, 1171 - 82.

9. B.V. Weber, R.J. Commiso, R.A. Merger, J.M. Neri, W.F. Olifant, and P.F. Ottinger, Appl. Phys. Lett., 45, (10), 1984, pp. 1043.

10. V.M. Bystritskyi, Ya.E. Krasik, I.V. Lisitsin, G.A. Mesyats, A.A. Sinebryuhov, "Investigation of the microsecond plasma opening switch conducting phase", Papers presented at the VIII, USSR Symposium on High-Current Electronics, Sverdlovsk, 1990, to be published in Fizika Plasmy.

11. H. Bluhm, K. Böhnel, P. Hoppé, H.U. Karow, D. Rusch, IEEE Transaction on Plasma Science, vol. P5-15, No. 6, 1987.

12. D.L. Cook et al., Proceedings of VII, Intern. Conf. on High-Power Particle Beams, BEAMS'88, Karlsruhe, FRG, 1988, pp. 35.

13. W. Bauer, H. Bluhm, P. Hoppé H.U. Karow, D. Rusch, Ch. Schultheiß, H. Bachmann, L. Buth, H. Laqua, E. Stein, J. Singer, O. Stoltz, "Status and Perspectives of High Power Ion Diodes in Extractor Geometry", ref. 4, vol. 1, pp. 104 - 116.

14. A. Fruchtman and L.I. Rudakov, "Two-dimensional Fast Penetration of a Magnetic field into a homogeneous Plasma", submitted to Phys. Rev. Lett.

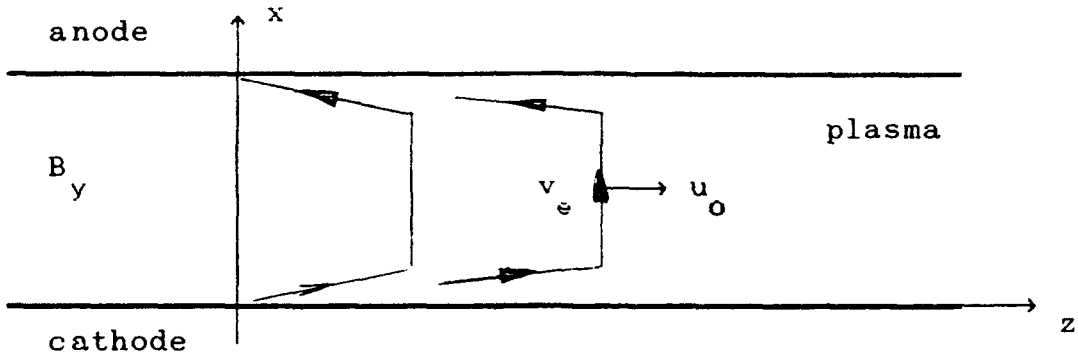

Fig. 1 Magnetic field penetration in an inhomogeneous plasma

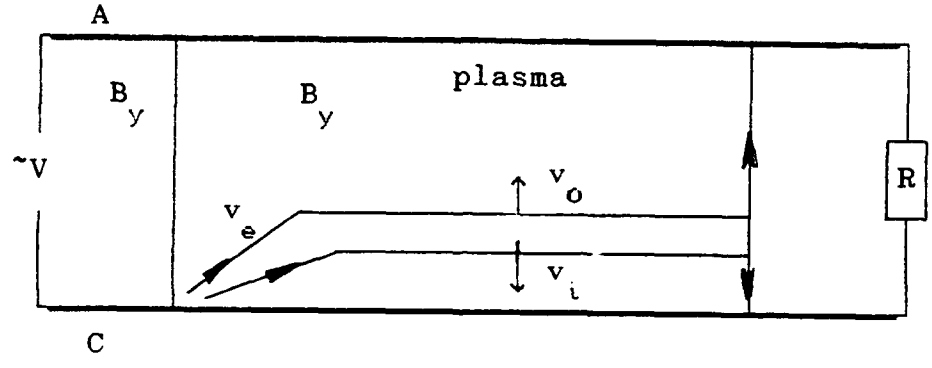

Fig. 2 Electron flow and plasma erosion due to Hall electric fields in the cathode-anode gap.

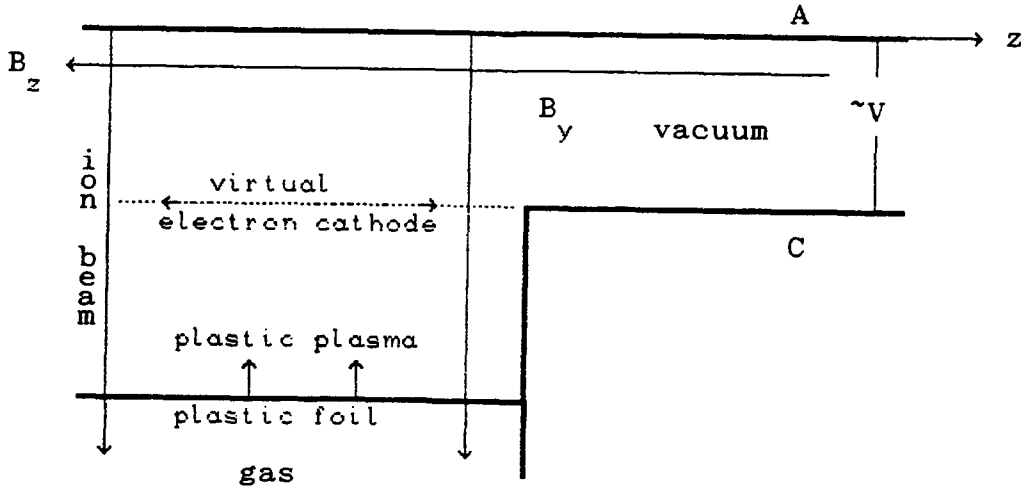

Fig. 3 Counterflow of low energy ions due to inductive electric fields, induced by the ion beam.

OPENING SWITCH MODEL WITH VORTEX STRUCTURES

N.B. Volkov*, T.A. Golub, N.A. Gondarenko, A.M. Iskoldsky*
Institute of High Current Electronics, Tomsk, 634055, Russia
*Institute of Electrophysics, Ekaterinburg, 620219, Russia

Non-linear opening switch model with vortex structures is proposed and discussed. It is shown that the current interruption in opening switch is determined not by the change of electrical conductivity but by breaking of a symmetry in initial laminar flow of conducting fluid and the appearance of vortex structures.

1. Introduction

The dynamics of vortex structures and the states of current in plasma-like fluids is considered under magnetohydrodynamic approximation. In addition, a local thermodynamic equilibrium (LTE) is valid, and local kinetic transport coefficients (σ is the electric conductivity, λ is the thermal conductivity, η is the shear viscosity) are determined by kinetic fluctuations. It is shown in [1] and below, that even with the constant transport coefficients the emergence of vortex hydrodynamic structures results in a spontaneous breaking of symmetry in initial laminar flow of "electron" fluid and the appearance of vortex current structures inside it. As a consequence, current in a cylindrical conductor is interrupted, i.e. an effective resistance of the conductor $R_{eff} \to \infty$ (this fact is interpreted from outside as the result of change of the local kinetic coefficients). This process is singular in time and to realize it the external electric circuit must be overcritical to some extent, which is a characteristic property of a non-equilibrium phase transition (NPT). A simple model of NPT in the cylindrical conductor is designed.

2. The model of a non-equilibrium phase transition.

A homogeneous incompressible liquid with volume of a fixed size (cylinder with the radius r_0 and the length $l \gg r_0$) is considered. Moreover we assume the local kinetic coefficients to be constant. So the system of MHD equations is

$$\vec{\nabla}\cdot\vec{u} = 0 \quad ; \tag{1a}$$

$$\frac{\partial\vec{u}}{\partial t} + (\vec{u}\cdot\vec{\nabla})\vec{u} = -\frac{1}{\rho_0}\vec{\nabla}P + \frac{1}{4\pi\rho_0}[[\vec{\nabla},\vec{H}],\vec{H}] + \nu\Delta\vec{u} \quad ; \tag{1b}$$

$$\frac{\partial\vec{H}}{\partial t} + (\vec{u}\cdot\vec{\nabla})\vec{H} = (\vec{H}\cdot\vec{\nabla})\vec{u} + \nu_m\Delta\vec{H} \ , \tag{1c}$$

where $\nu = \eta/\rho_0$ is the kinematic viscosity, $\nu_m = c^2(4\pi\sigma)^{-1}$ is the magnetic viscosity (c is the light velocity)and Δ is the Laplasian. As follows from Eq. (1a), $\vec{u} = [\vec{\nabla},\vec{A}]$ ($\vec{A}$ is the vector velocity potential, which is known to be accurate within the gradient of a scalar function; used below is Coulomb's calibration of the vector potential: $\vec{\nabla}\cdot\vec{A} = 0$).

We direct the Z axis along the axis of the conductor and use the azimuthal symmetry, setting $\vec{u} = \{u_r(r,z,t), 0, u_z(r,z,t)\}$, $\vec{H} = \{0, H(r,z,t), 0\}$, $\vec{A} = \{0, \Psi(r,z,t), 0\}$. From Eq.(1a) we find $u_r = -\partial\Psi/\partial z$, $u_z = \partial(r\Psi)/r\partial r$. We look for the solution of Eq.(1c) in the form $H(r,z,t) = H_1(r,t) + h(r,z,t)$, where $H_1 = 2i(t)r/cr_0^2$. In this case the boundary conditions for Eq.(1c) are satisfied automatically, and ones are zero for h. Applying the operation $[\vec{\nabla}, \ ]$ to Eq.(1b) and using of the above assumptions, we derive the system describing the dynamics of vortex structures:

$$\frac{\partial(\Delta\Psi - \Psi r^{-2})}{\partial t} = -\frac{\partial(\Psi,\Delta\Psi - \Psi r^{-2})}{\partial(r,z)} + \\ + R\frac{\nu\,\nu_m}{H_0 r_0^3}\frac{\partial h}{\partial z} + \frac{i}{I_0}\nu\,[\Delta(\Delta\psi - \psi r^{-2}) - r^{-2}(\Delta\psi - \psi r^{-2})], \tag{2a}$$

$$\frac{\partial h}{\partial t} = -\frac{\partial(\Psi,h)}{\partial(r,z)} + \frac{H_0}{r_0}\frac{i}{I_0}\frac{\partial\Psi}{\partial z} + \nu_m(\Delta h - \frac{h}{r^2}), \tag{2b}$$

where $\frac{\partial(a,b)}{\partial(r,z)} = \frac{\partial(ra)}{r\partial r}\frac{\partial b}{\partial z} - \frac{\partial a}{\partial z}\frac{\partial(rb)}{r\partial r}$, $R = H_0^2 r_0^2/(2\pi\rho_0\nu_m\nu) =$

$= v_A^2 r_0^2(\nu_m\nu)^{-1}$ is the Rayleigh number, v_A is the Alfven velocity, $Pe_m = v_A r_0 \nu_m^{-1}$ is the magnetic Peclet number, $s = \nu\nu_m^{-1}$; $H_0 = 2I_0(cr_0)^{-1}$; I_0 is the characteristic current value.

The set of Eqs.(2) can be reduced to the set of nonlinear differential equations which describe the interaction of the three perturbation modes: one perturbation mode for Ψ and two modes for h. Following Lorenz [2], we assume free boundary conditions for Ψ: $\Psi(0,z,t) = \Psi(r_0,z,t) = 0$. We use the substitution,

which transforms into the Lorenz substitution [2] in the case of a Cartesian coordinate system:

$$\Psi = 2^{1/2}\,\frac{1 + (\pi k k_1^{-1})^2}{k}\,\nu_m X(t)\sin\left(\frac{\pi k z}{r_0}\right)J_1\left(\frac{k_1 r}{r_0}\right), \qquad (3a)$$

$$h = \frac{R_c H_0}{\pi R}\left\{2^{1/2} Y(t)\cos\left(\frac{\pi k z}{r_0}\right)J_1\left(\frac{k_1 r}{r_0}\right) - 2Z(t)J_0\left(\frac{k_1 r}{r_0}\right)J_1\left(\frac{k_1 r}{r_0}\right)\right\}. \qquad (3b)$$

In (3) $k_1 = 3.83171$ is a zero of the Bessel function $J_1(x)$, $R_0 = 64\,k_1^2\pi^2/(b^2(4-b))$ is the critical Rayleigh number, $b = 4/(1+(\pi k k_1^{-1})^2)$.

On substituting (3) for (2), we find a system of ordinary differential equations for the amplitudes X(t), Y(t) and Z(t) :

$$\dot{X} = -\,s\,X + s\,I\,Y, \qquad (4a)$$

$$\dot{Y} = -\,\pi\,k_1^{-1} X\,Z + (\pi\,k_1^{-1})^2\,r_1 I\,X - Y, \qquad (4b)$$

$$\dot{Z} = -\,\pi\,k_1^{-1}\,X\,Y - bZ, \qquad (4c)$$

where $\tau = 4k_1^2 b^{-1}\nu_m t r_0^{-2}$ is a dimensionless time; $I(\tau) = i/I_0$ is the dimensionless current; $r_1 = RR_c^{-1}$ is the control parameter of the model.

To find the conductor current we specify the voltage as follows:

$$u(t) = u_L + u_R = L_{p0}I_0(\sigma^2 t_0)^{-1}\dot{I} + R_{p0}I_0(I - k_1(\pi r_i)^{-1}J_0^2(k_1)Z),$$

where $R_{p0} = 1(\pi r_0^2\,\sigma)^{-1}$ is the initial conductor resistance, L_{p0} is the external induction of the conductor.

3. Discussion

3.1. Analysis of the dependence of a critical Rayleigh number on the parameter b allows to find a spatial scale of perturbation along the Z axis. We have established that $R_0 \to \infty$ as $b \to 0$ or $b \to 4$. The case $b = 0$ corresponds to a short-wave limit ($k = \infty$ ($\lambda = 0$)). The case $b = 4$ corresponds to a long-wave limit ($k = 0$ ($\lambda = \infty$)) when the perturbation spreads over the whole volume occupied by the matter. In our case a characteristic scale of the task is the conductor radius r_0. Therefore for the most rapidly developed perturbations with $\lambda \propto r_0$, R_0 has a minimum at $b = 8/3$: $R_{0,min}$=

978.08144. This value of R_o corresponds to the perturbation with $\lambda = r_o k_o^{-1} = 1.159 r_o$ and $r_1 = R R_o^{-1} = 1.0224 \cdot 10^{-3} R = 6.5088 \cdot 10^{-4} I_o^2 / (\sigma^2 \rho_o \nu_m \nu)$. A subsequent perturbation evolution is possible in the direction of splitting the spatial scale. In addition, the stratifying process of the conductor into the strates with $l=2\lambda$ (R_o for a perturbation with the wave number $0.5k_o$ is 1650.1966 and for a perturbation with $l=0.5\lambda$, it is 1956.8796) is preferable at first. This analysis is supported by a direct observation of conductor stratification in experiments [3] with 0.58 mm diameter copper conductors, where the mean distance between strates was of 0.78 mm. According to our model $l \cong 2\lambda = 0.672$mm is in good agreement with experiment. The consideration of a larger number of perturbation modes does not significantly change the results of the above analysis, because the modes with a wave number not equal to k_o perturb later than the dominant mode. The fact that $R_{o,min}$ corresponds to $\lambda \cong r_o$ shows the evidence that the model proposed is a model of a non-equilibrium phase transition.

3.2. For practical application of the model (4) the task of identifying of the model parameters has been solved for the explosion wire experiments. The heating stage model [4] was used to calculate the current and voltage at the end of heating stage. One difficulty appears while we transit from the heating model to the vortex one. It deals with a necessity to determine the model parameters as well as the initial amplitudes X, Y, Z. Fig.1 shows the result of model fitting on the experiment where 4 copper wires 54 μm diameter and 4.5 cm length were exploded in RLC-circuit with capacity of 0.5 μF charged up to 22 kV, inductance of 0.6 μH and resistance of 0.14 Ω.

The model is very sensitive to the initial value of X, because in the case of finite energy sources the explosion conditions are determined not only by the parameter r_1 but also by the initial level of non-equilibrium. The model discussed allows to explain so-called anomalies of electrical explosion concerning to the shift of the explosion beginning to the large specific energy region. Hereby it is not necessary to assume the local kinetic

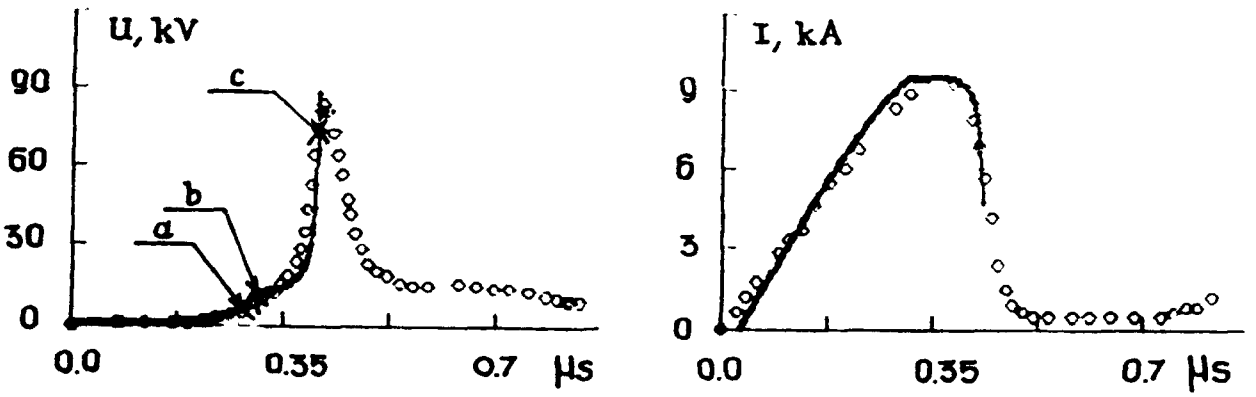

Fig.1.The calculated voltage and current (solid curves), and the experimental ones (points).

transport coefficients change. In particular, the shear viscosity value estimated by means of model fitting on experiment is close to table one for liquid metal. The specific step corresponding to the melting stage is well noted on the experimental voltage trace. The picture of current vortex structures forms just during this interval (these structures are shown on Fig.2. and correspond to the marked point on Fig.1).

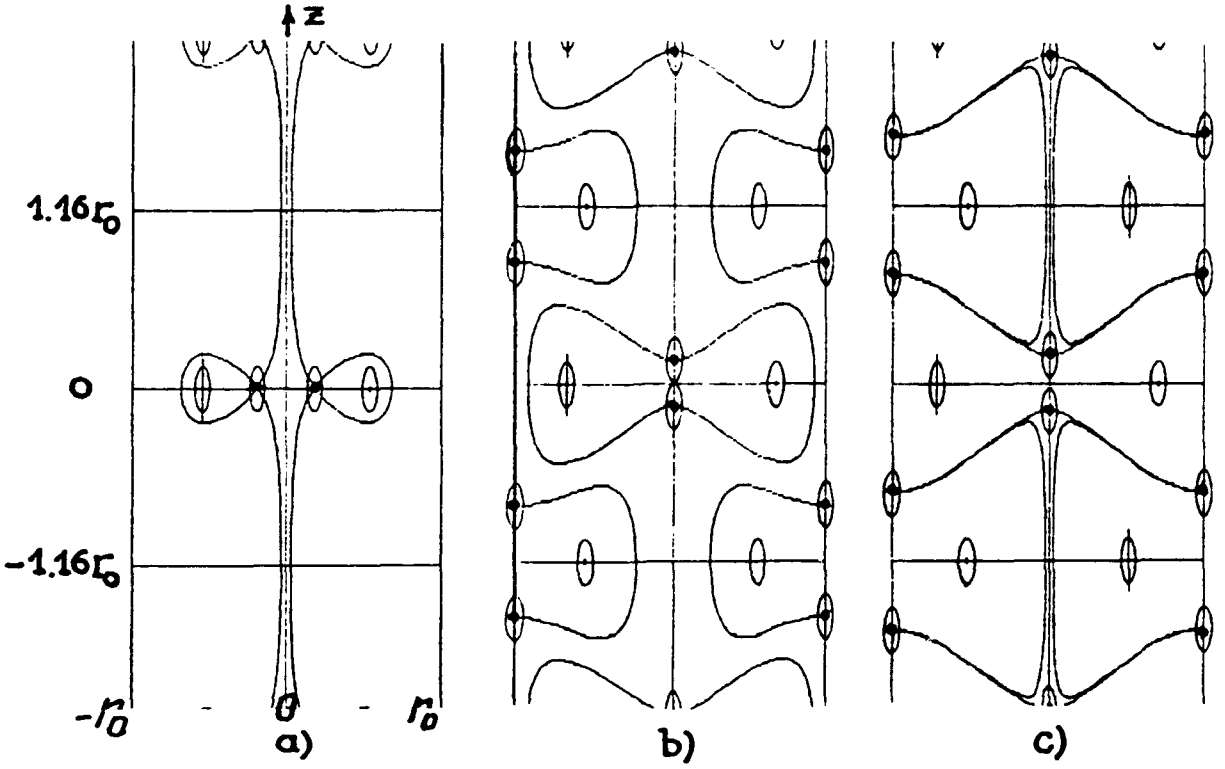

Fig.2 The cross-section of saparatrix surface for conductor in various time moment: a)t=0.301 μs, b)t=0.308 μs, c)t=0.415 μs.

So we can propose the hypothesis that vortex structure formation results in the conductor melting. Figure 2 shows that even while transport coefficients are constant the current interruption occurs and effective conductor resistance has a vortex nature. It should be highlighted that incompressible medium assumption does not decrease the generality of the received results because the vortex component of liquid is always incompressible.

4. Conclusion.

The main results of the present paper are the following:

The model of a non-equilibrium phase transition has been derived where the motion of a laminar component of a heavy liquid is not considered and kinetic coefficients are considered to be constant, i.e. independent of density and temperature. This model can be referred to the class of the Lorenz model [2], the spatial scale of the vortex structure is in good agreement with experiment in [3].

The task of identifying the model parameters has been solved by means of comparison the calculations with the electrically exploding wire experiments. It is shown that the low impedance stage and the interruption are determined not by electric conductivity change but by breaking of symmetry in initial laminar flow of conducting fluid and the appearance of vortex current structures . Consideration of the term describing the thermal expension for the heating stage allows us to reduce the initial level of non-equilibrium (amplitude X).

The results received allows to predict the high-current accelerator behavior in more wide range of circuit and wire parameters compared to [4].

References

[1] Volkov N. B.and Iskol'dskii A. M. 1990 JETP Lett. 51, 634.

[2] Lorenz E. N. J. Atmos. Sci. 1963 20, 130.

[3] Iskol'dskii A. M. Doctoral Dissertation 1985 (Tomsk).

[4] Golub T.A., Gondarenko N.A., Iskoldsky A.M. Abstracts of International Workshop on Physics and Technique of High Power Opening Swightes. (Novosibirsk, USSR), 1989, p.80.

COMPACT GENERATOR WITH PLASMA FLOW OPENING SWITCH

Kablambajev B.A., Poskonin V.A., Ratakhin N.A.
High Current Electronics Institute, Siberian Branch
of the Russian Academy of Sciences, Tomsk, Russia.

The long conduction time plasma opening switch (POS) is a candidate for the last stage opening switch in inductive storage systems. Very fast opening switches have become important for pulsed power. They can provide voltage increase in the largest pulsed power machines. Also, inductive storage using fast opening switches can provide cheaper and more compact pulsed power machines.

There are a variety of inductive storage and opening switch concepts that have been studied and succesfully developed over the last several decades. For an regime, from 10^{-6}-10^{-5}s. input time to 10^{-8}-10^{-7}s. output, the dynamics of a plasma discharge can be utilised to accumulate and transfer magnetic energy to load. One embodimont of such dynamics is the plasma flow opening switshes (PEOS). The generator with plasma flow opening switshes been produced and described in this report.

The geometry of the plasma flow switch is that of a coaxial plasma gun (Fig.2). Magnetic energy accumulates in the vacuum coaxial gun and external circuit inductance as the current rises and the plasma is accelerated axially along the electrodes. The discharge motion is adjusted (by plasma mass, the center conductor length and by JxB force variation) so that peak current is achived just as the discharge reaches the end of the center conductor. The discharge speed remains low during the greater part of the current rise, since the motion energy proportional both to the way from plasma source and as the square of current value. Nevertheless continued acceleration of the discharge plasma expels off the annular plasma to the end of the center conductor at a speed greater than 10^{7}sm s^{-1}. In our case inertia of plasma needs to

expansion it in vacuum when plasma reaches the end of the center conductor. In the time of expansion density of plasma decreases about to the value necessary for erosion and disruption of plasma, voltage increases and energy switched to the load. This combination of dynamics and plasma erosion permits to use this opening switch both for liner implosion and electron beam generation. Experimental system for studying PEOS consists of initial energy storage, vacuum discharging chamber with coaxial conductors, plasma source and monitoring system (Table 1).

Table 1

CIRCUIT PARAMETERS

FIRST SISTEM (imploding load)		SECOND SISTEM (e-beam load)	
11,2μF	Capacitor.	11,2μF	Capasitor.
65nH	Primary circuit inductance.	65nH	Primary circuit inductance.
40-44kV	Charging voltage.	30-32kV	Charging voltage.
1 1.2μs	Primary current risetime	0.7-0.75μs	Primary current risetime
450-500kA	Primary current value	230-250kA	Primary current value
20nH.	Load circuit inductance.	200--20kV	Low inductance voltage
50ns	Load current risetime	200-220kV	High impedance diode voltage
300-320kA	Load current	260-280kV	Bremstrahluhg load voltage

Some typical oscillograms are in Fig.3 and 4.

Experimental results of generator work on thelow inductance load and the electron beam diode shows switch impedance decreasing from $8x10^7$ Ω /s to $2x10^7$ Ω /s. Therefore, the low impedance diode is necessary for increasing of bremsstrahlung. Plasmafulled diode was used. The construction of

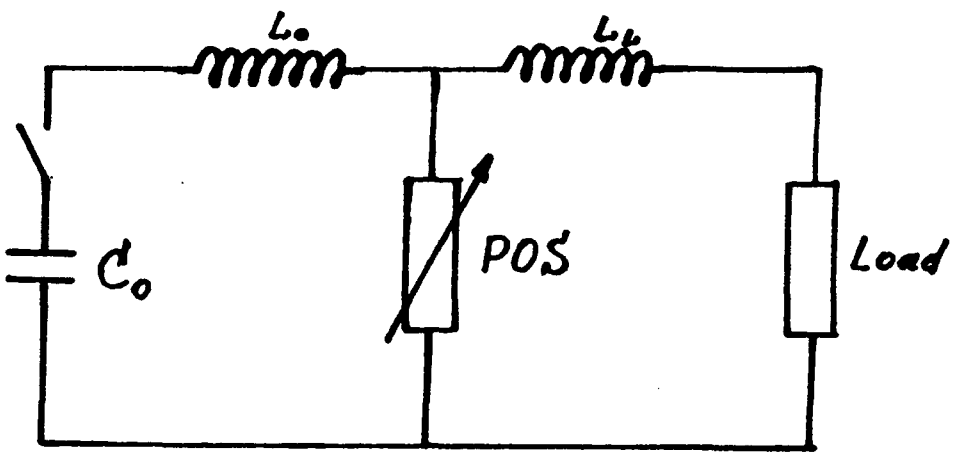

Fig. 1 Electrical circuit scheme.

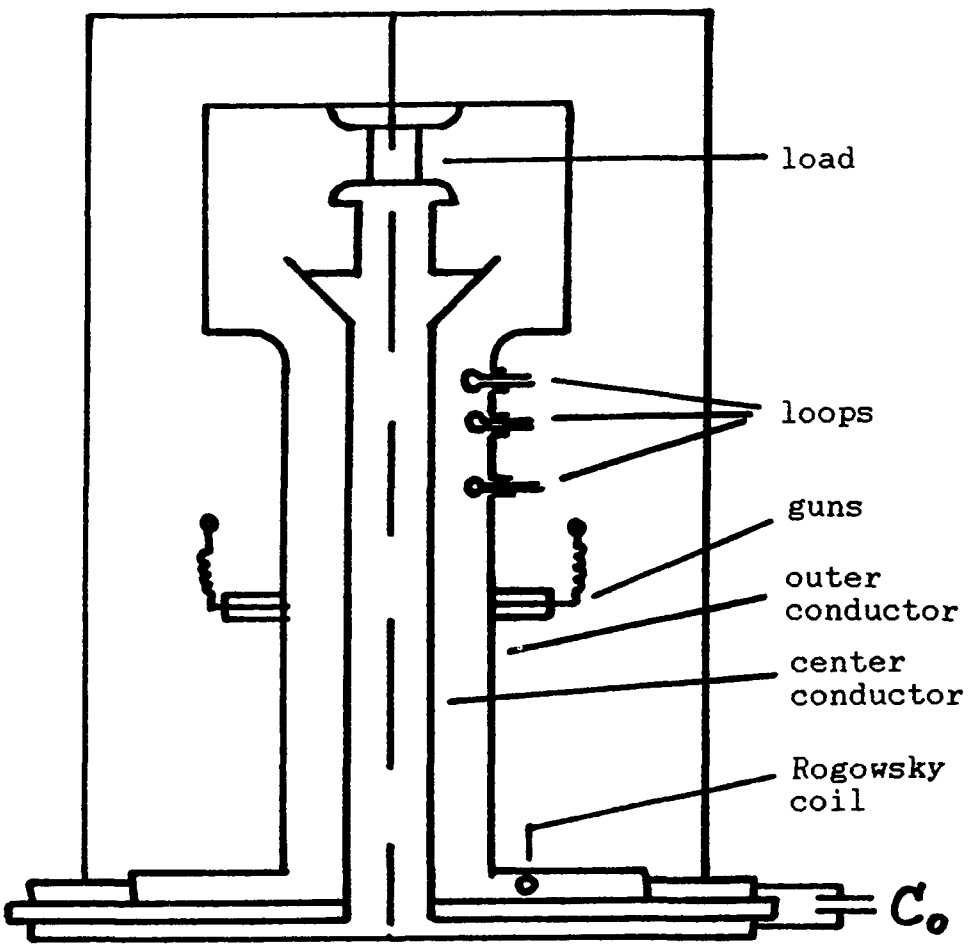

Fig. 2 Plasma opening switch configuration.

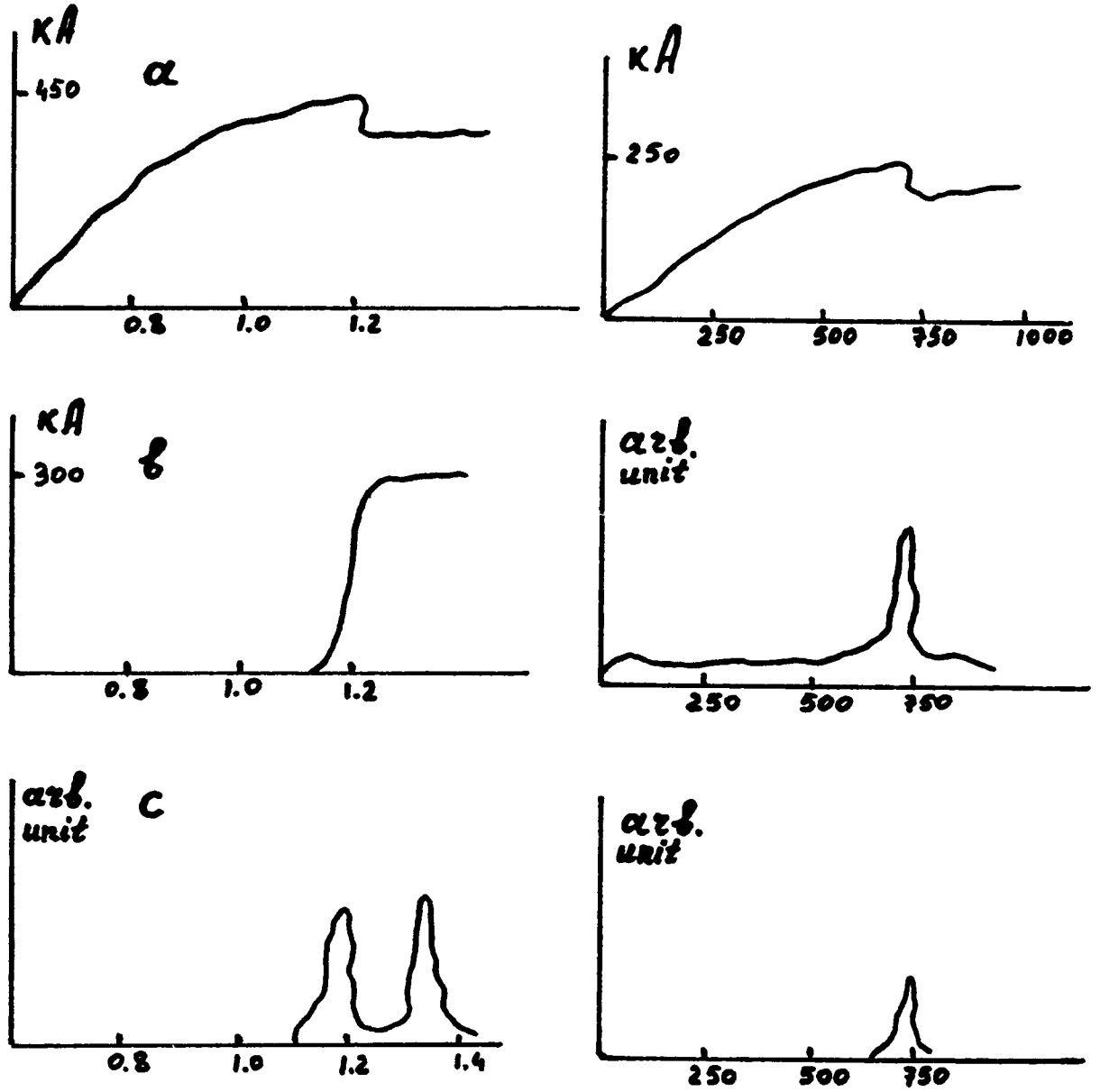

Fig. 3 Imploading load a) Upstream and b) Downstream current measurued by Rogowsky coil; c) Plasma implosion load voltage.

Fig. 4 Electron beam load a) Upstream current, b) Upstream voltage and c) X-ray detector signal.

plasmafulled diode are in Fig. 5. The cathode diameter was 5 sm. The copper anode placed at the angle of 30° to diode axis. The X-ray was measured at the angle of 30° to anode surface with

TLD and a p-n diode. About 2 kJ was stored in circuit inductance and electron beam energy was about 400J.

In conclusion we make a note that an optimization of load parameters may increase beam energy by two.

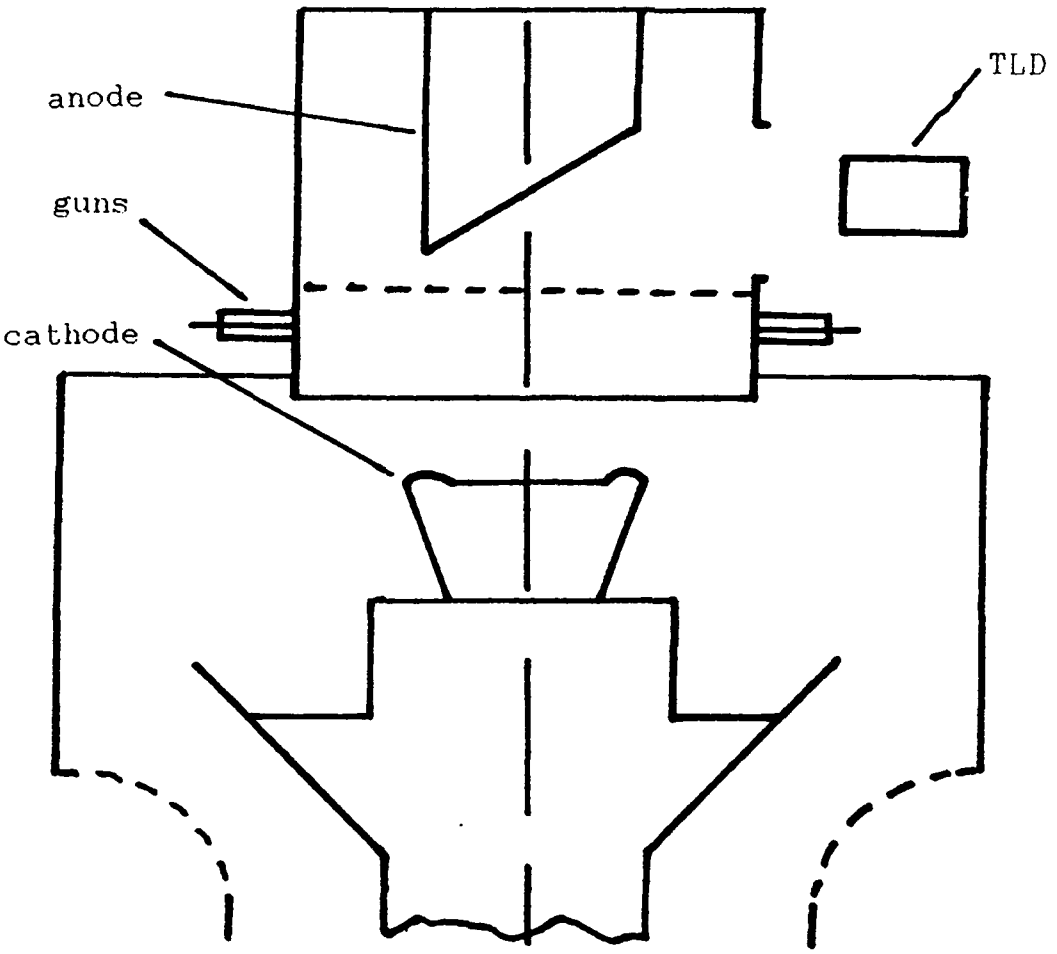

Fig.5 Plasmafulled diode construction

THE INFLUENCE OF THE B_θ FIELD ON MPOS PERFORMANCE

A.A.Kim, D.V.Getman
High Current Electronics Institute, Tomsk 634055, Russia

Introduction

The plasma opening switches (POS) are interesting because of the possibility to create the high power pulse generators with the inductive energy store [1]. The POS with microsecond conduction time (MPOS) are of particular interest allowing to eliminate the water forming lines in generator design. The GIT-4 [2] experience had shown that the further progress in this field would be determined by solving of two major problems [3]. The first is the increase of the conduction time, t_c. At a given output voltage the increase of t_c results in an increase of the power delivering to the inductive storage. The second is the problem with the MPOS resistance at opening. Its value determines the output voltage and power of the generator pulse.

To solve this problems the proper physical understanding of the MPOS operation is necessary. Up to now the complete picture is not clear. The NRL model [4] successfully reproduces short conduction POS results but fails by MPOS analysis. More recently two other papers were published [5,6] with an common idea that the POS operation in two regimes (short and long conduction) is different. In the last one [6] the difference in hydrodynamical plasma displacement under the influence of jxB forces was discussed-when the switch current rises slowly the plasma displacement exceeds many times that of the rapidly rising current. Assuming that the opening occurs when plasma center-of-mass (CM) moves the distance $\sim 0.5l$, where l is the length of the initial plasma fill, the authors successfully explained some important MPOS features. Our work was performed to proof some conclusions of this idea.

Proposition of the experiment

If the MPOS conduction phase is controlled by the switch plasma CM displacement at a given distance z_0 under the influence of $j_r xB_\theta$ force , then the change of B_θ magnetic field should re-

sult in varying of the conduction time t_c. To influence the B_θ field it is possible using the external field $B_{\theta e}$ and/or changing the shape of the switch current self field $B_{\theta s}$.

Let us consider the influence of the $B_{\theta e}$ field on plasma motion along the coax driven by the generator current $I(t)$. The plasma CM equation of motion may be expressed as following

$$\frac{d^2z}{dt^2} = \frac{I^2(t)}{MnSrc^2} + \beta \frac{I(t)B_{\theta e}(t)}{MnSc}, \qquad (1)$$

$$I(t) = I_0 \sin\omega t,$$

$$B_{\theta e}(t) = \frac{2I_0}{rc} \sin(\omega t+\varphi).$$

It is assumed here that the $B_{\theta e}$ field is created by the current flowing through the inner electrode of the coax and having the same amplitude I_0 and period $T = 2\pi/\omega$, as the generator current $I(t)$. The time t starts together with the current $I(t)$, the phase φ (>0) gives the $B_{\theta e}$ value at the moment t=0. The constant β equals 1 or 0 if the field $B_{\theta e}$ is ON or OFF. From (1) the plasma CM displacement may be obtained as

$$z(t) = A\left\{\left[1+2\beta\cos\varphi\right]\left[(\omega t)^2-\sin^2\omega t\right] + 2\beta\sin\varphi\left[\omega t-\sin\omega t\cos\omega t\right]\right\}, \qquad (2)$$

where

$$A = \frac{I_0^2}{8\pi Mc^2nr^2\omega^2 l}.$$

The dependencies $z(t)/z_0$ are given in Fig.1 at different φ. The dashed curve shows the CM displacement without of $B_{\theta e}$ field. The value of z_0 (rel.units) was defined from (2) at β=0 and $t=t_c$ (=0.125 T) obtained in experiment described later. The calculation predicts the ~20% decrease of t_c when the $B_{\theta e}$ field starts together with the generator current (φ=0). The increase of φ first results in an additional plasma acceleration in a "forward" direction, but then the picture of plasma motion changes. At φ=2.83 radian the plasma CM moves first in a "forward" direction but stops before reaching z_0 and begins to accelerate in a "back-

ward" direction reaching the boundary $-z_0$ at a moment t_c = 0.22 T. The further increase of φ results in a plasma motion in "backward" direction only and then a change of motion direction is repeated. The intersection points of the curves shown in Fig.1 with the straight lines z/z_0= ±1 give the conduction time dependence versus φ (Fig.2). It demonstrates the ability to control

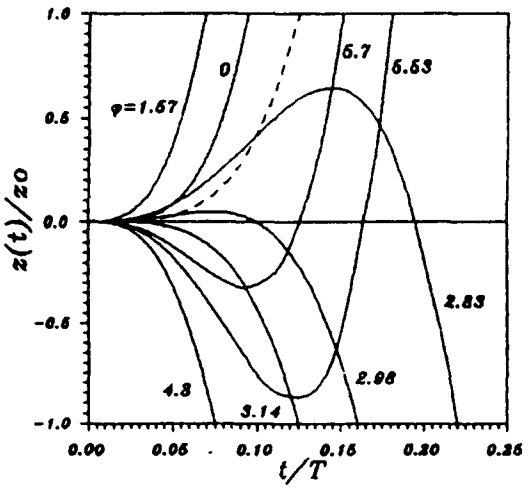

Fig.1.

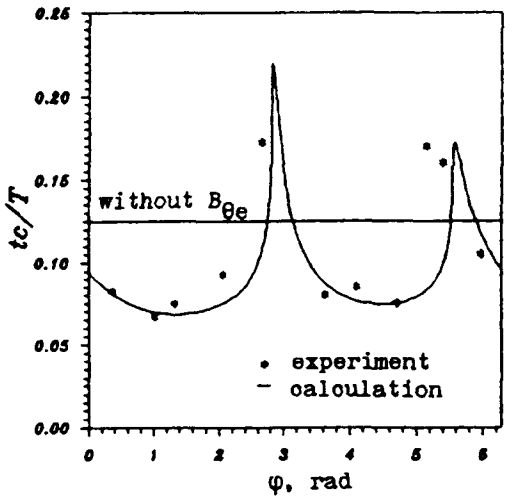

Fig.2.

the MPOS conduction varying the time delay between the $B_{\theta e}$ field and Marx firings.

Experimental setup

The idea of the experiment (Fig.3) is close to that reported elsewhere [7]. The Marx $C1$(0.32 μF, 300 kV) has a positive output pulse, the inductive storage $L1$=9.8 μH. The discharge current rises up to 54 kA in $T/4$ = 2.8 μs. The high voltage MPOS electrode is the outer electrode of the coax (R_a/R_c = 75mm/8mm), the top MPOS cathode end is grounded to the chamber wall and the bottom one through the bushing is connected to the condenser $C2$ used to create the $B_{\theta e}$ field. The inductance $2L2+L3$≈0.7 μH allows to obtain the $B_{\theta e}$ field pulse in the MPOS region close to that of the generator current flowing through the

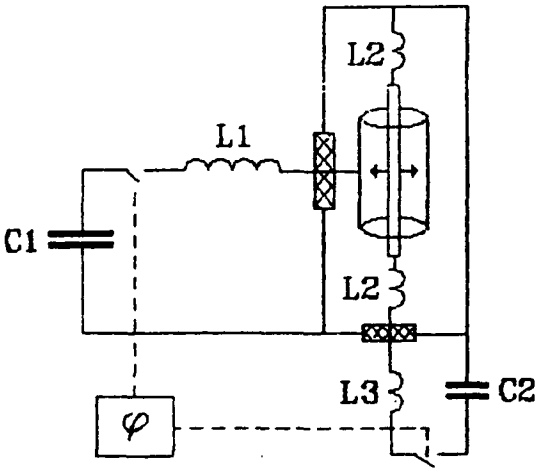

Fig.3.

switch. The peak $B_{\theta e}$ strength equals to 13 kG. Plasma is injected from the cathode in the middle of the cathode vacuum part through the holes located within 10 mm length.

The synchronization scheme provided to fire the Marx and the $B_{\theta e}$ field with arbitrary time delays allowing to study the dependence of the conduction time versus φ. The Rogowsky coils were used to measure the Marx current I_M and the currents I_a and I_b flowing through the cathode. The MPOS voltage was measured by the capacitive divider on the vacuum insulator in oil.

Results

The t_c dependence versus φ was studied at constant time delay of Δt=8.2 μs between the plasma source and Marx firings. In the absence of the $B_{\theta e}$ field the conduction time was of t_c=1.4 μs (t_c/T=0.125), the peak switch current of I_c=40 kA, the switch voltage by opening of U=600 kV. When the $B_{\theta e}$ field was turned on, the conduction time was influenced by the phase φ in a way shown by points in Fig.2. The experiment is very close to calculation. From (2) follows that depending on φ the opening would occur by plasma CM displacement in "forward" or in "backward" direction. This conclusion corresponds to cathode electrode polishing observed in both directions from the plasma injection plane.

The switch voltage by opening depends on φ as well. At φ=0 the switch voltage was ~1.5 times higher then that without of $B_{\theta e}$ field -the result reported previously [7]. This increase is not the result of the conduction time decrease what may be often observed by MPOS operation [2]. In the absence of the $B_{\theta e}$ field the time delay of Δt=2.5 μs resulted in the same t_c decrease but the corresponding switch voltage increase was not so significant. Fig.4 shows the switch resistance versus φ. We shall discuss this dependence later.

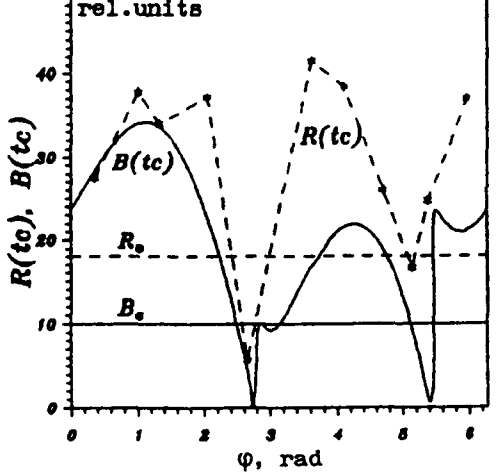

Fig.4.

Another experiment was performed to study the influence of

the self $B_{\theta s}$ field of different shape on the switch conduction. Two regimes were compared: one side feeding and two side feeding.

In one side feeding regime the cathode was connected to the chamber from one side only and its other side was separated from the wall by a 175 mm gap. The generator current after the switch was collected at the grounded end of the cathode creating the self $B_{\theta s}$ field pushing plasma to the opened end of the cathode. Fig.5 shows the traces of the current I_a at the grounded cathode end. In two side feeding regime both cathode ends were connected to the chamber wall. The same generator current was flowing now after the switch in both directions and the self $B_{\theta s}$ field was

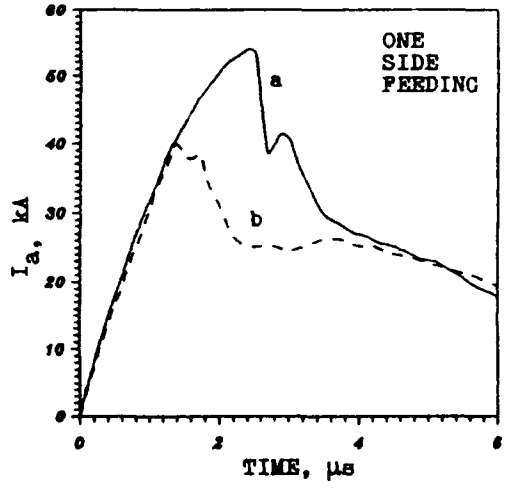

Fig.5.The traces a,b correspond to traces a,b in Fig.7.

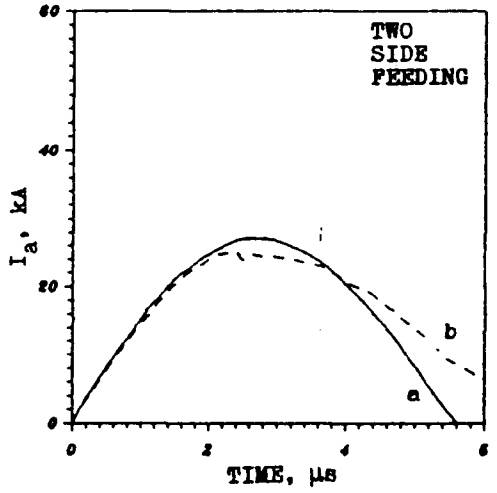

Fig.6.The traces a,b correspond to traces a,b in Fig.7.

pushing plasma to the midplane. The total switch current in this regime was equal to doubled current I_a shown in Fig.6. The traces given in Fig.5,6 demonstrate the influence of the shape of the self $B_{\theta s}$ field on the MPOS conduction. In two feeding regime t_c is much longer than in one feeding regime. The opening in two feeding regime occurs at diminished plasma source current only (shown in Fig.7) with t_c being about two times longer than that in one feeding regime. The voltage by opening was also

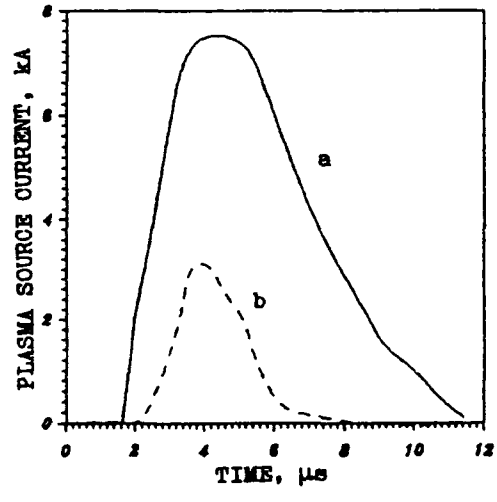

Fig.7.

strongly influenced by the operating regime. In one feeding regime it reaches 650 kV corresponding to the switch resistance of about 16 Ohm. In two feeding regime the switch voltage and resistance were ~20 times lower.

In one feeding regime the 20 cm long cathode surface polishing was shifted from the plasma injection plane to the opened cathode end. In two feeding regime the polishing of 2 cm long was located directly in the midplane of the cathode electrode.

Discussion

Our results support the hydro model [6] demonstrating the ability to control the MPOS conduction by magnetic field in the switch region. Since this model deals with plasma CM displacement one may expect that any action aimed to prevent plasma motion would increase the conduction time and peak switch current.

The important question is the effective switch opening when the conduction is lengthened by such means. If the low density plasma is preferable for effective opening then such lengthening may be the way to increase the output power of MPOS at MA currents. It must be noted however that the requirement of high magnetic field strength in the switch region must be fulfilled as well. Fig.4 shows as well the calculated total B_θ field at the moment $t=t_c$. One may see that the significant resistance decrease corresponds to the case when the magnetic field becomes zero.

References

1. C.W.Mendel, Jr., and S.A.Goldstein, J.Appl.Phys., vol.48, pp.1004-1006, 1977.
2. S.P.Bugaev, et al., IEEE Trans.Plasma Sci., v.18, No.1, pp.115-118, 1990.
3. B.M.Kovalchuk, A.A.Kim, VIII Conf.Low Temperature Plasma, Minsk, 1991.
4. P.F.Ottinger, S.A.Goldstein, R.A.Meger, J.Appl.Phys., v.56, pp.774-784, 1984.
5. J.R.Goyer, PI Internal report, PIIR-2-89, p.10, 1989.
6. B.V.Weber, et al., BEAMS'90, v.1, pp.406-413, 1990.
7. R.V.Chikin, et al., BEAMS'90, v.2, pp.1022-1027, 1990.

POS USE EFFICIENCY IN MULTIMODULE ACCELERATOR WITH SELF-MAGNETIC INSULATION.

V.V. Zajivikhin
TRINITI
142092 Moscow Region, Troitsk, Russia

ABSTRACT. The top value of power enhancement and voltage multiplication in inductive store system with the plasma opening switch (POS) have been studied. Different kinds of loads have been considered. It has been shown that electron losses in vacuum transmission line (VTL) with self-magnetic insulation (SMI) can essentialy change the output pulse parameters. Among issues examined are also the effects of the POS on synchronization condition of the multimodule generator and on the optimum liner parameters used at Angara-5 facility.

I.INTRODUCTION. Systems with current plasma switches are intensely explored both theoretically and experimentally. This interest connected with power sharpening and voltage enhancement in classical pulse power and also with the development of the low-cost inductive store facility. Calculations fulfilled in the framework of lumped circuit model Fig.1a [1,2] showed that the voltage and power increase coefficient (ratio of the actual pulse value in the load to its one in the matched load regime) can achieve ~ 10. The results of such calculation for Angara-5 generator parameters are displayed in fig.2. The ratio of the opening switch time T_{op} to generator time T_g was equal 0.1, L_2/L_1, where L_1 - the storage inductance and L_2 - inductance between the switch and the load, had the same value. The final switch impedance R_s constituted 5 (----) and 30 (——) that of generator R_g. However this simple discription is valid only for low voltage, at high one, arising during the PEOS opening moment, the VTL cathode is exploded and the electron leakage currents appear in the interelctrode gap (see fig.1b). This leakage may essentially decrease the energy transmission efficiency to the load. These questions are considered in Sec.III. Besides PEOS employment with high-impedance loads, it is

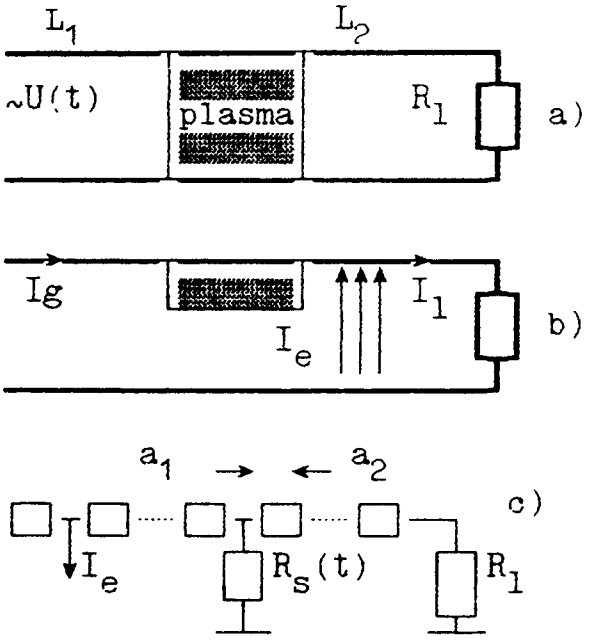

Fig.1 Model circuit of inductive storage pulse compression system (a,b); c) Schematic illustration of mathematical model used for numerical simulation of pulse power generator and vacuum trasmission line.

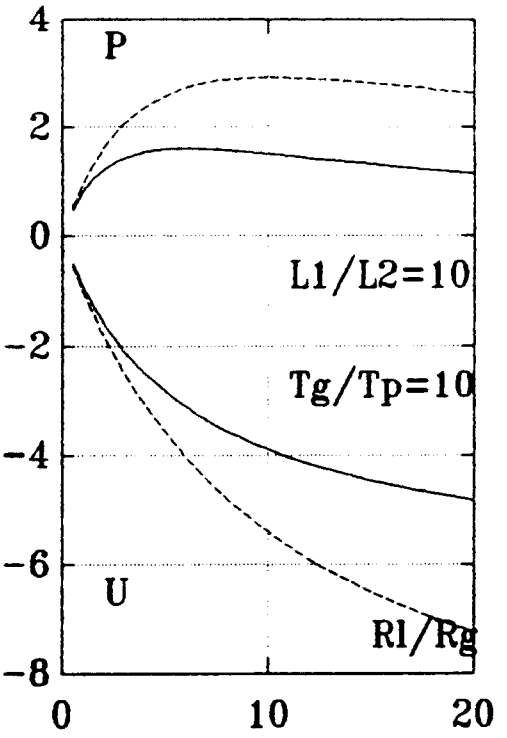

Fig.2 Power P and voltage U amplification factor on normalized load impedance.

highly perspective its utilization for acceleration of the cilindrical shells - liners in pulse power techniques. Usually POS permits to obtain the steeper current front through the liner and as a consequence suppression some instabilities. The possibility to use PEOS for the small liner acceleration are discussed in Sec. IV.

II.NUMERICAL SIMULATION MODEL. Numerical code for electromagnetic processes calculation in VTL with SMI was developed on the base of the telegraph equaticns [3]. In this one VTL have been divided on the separate pieces and a balance between falling a_1 and reflecting a_2 waves in each node have been taken into consideration and SMI condition have been analyzed (see fig.1c) It has been supposed that the current providing magnetic insulation is the minimum one . Electron leakage current was calculated from the relativistic "3/2 law" with the account of magnetized factor. The generator and load were taken into account as boundary conditions. Code permited to consider various loads types: resistance, liner and diode. As far as the POS

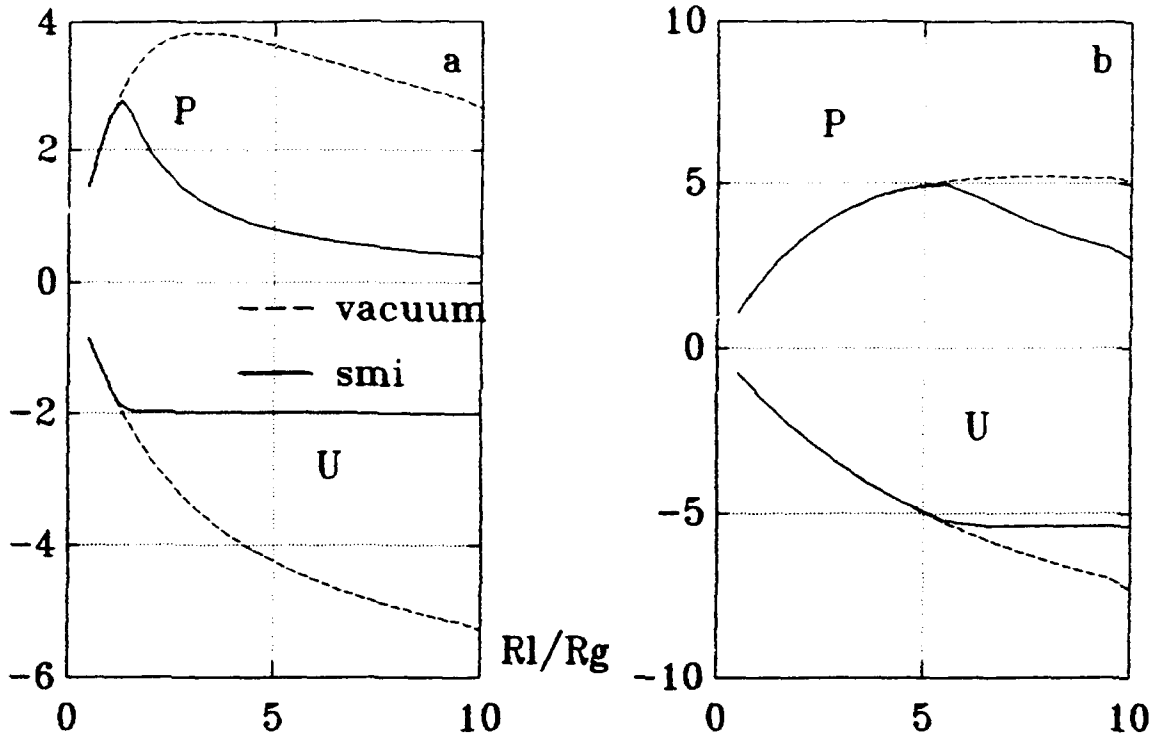

Fig.3 Load power P and voltage U vs load impedance Rl with (a) ρ_w=4 Ohm and (b) ρ_w=12 Ohm VTL wave impedance.

impedance is concerned its value was chosen equal to zero during the conducting phase and then increased up to some final quantity for the typical time T_{op}. The computations on the erosion model of the POS [1] were also fulfilled, however since we considered the processes connected with the electron flow in the VTL and not in the POS and in view of the absence at present an unambiguous physical interpretation of the switching mechanism the main results were obtained in the framework of the simple POS model.

III. RESISTIVE AND DIODE LOADS. Described model was used to simulate perfomance of the Angara-5 facility with POS in its VTL. Angara-5 had the following characteristics: the total generator impedance R_g=0.25 Ohm, the insulator water-vacuum inductance L_p=40 nH at each module. In our calculations it was assumed that voltage pulse had duration 70 ns (FWHM) and aplitude of 1MV for a matched load. Two kinds of the VTL were considered. The first one was the cilinder line with the length ~1.5 m and wave impedance ρ_w=4 Ohm and 12 Ohm, the second one was the real Angara-5 VTL. It consisted of the cilinder line with the length 120 cm, which through the some transition was connected with the disc-shape

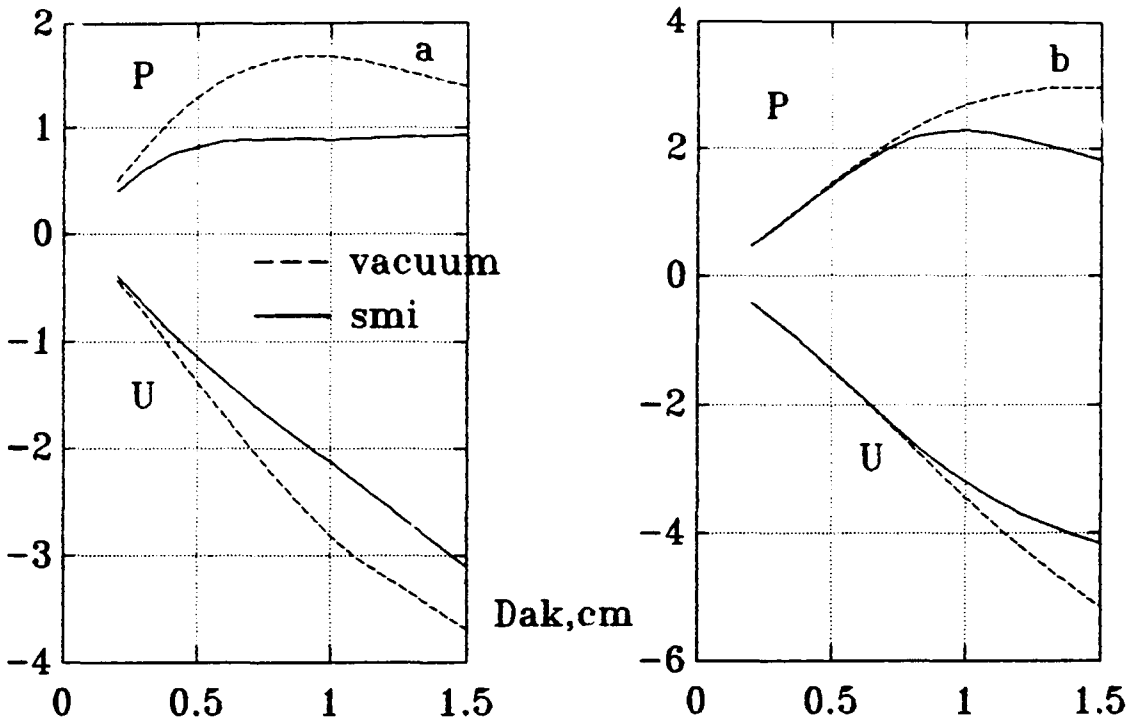

Fig.4 Diode power P and voltage U for various diode gaps Dak with (a) ρ_w=4 Ohm and (b) ρ_w=12 Ohm wave impedance of the VTL.

concentrator. POS was placed in each of eights VTL, such a way that it divided coupling inductance L_2/L_1 (see Fig.1a) in the ratio 1:10. The L_1 charging current was chosen under the condition of the energy maximum delivered from the generator to the L_1 inductance. The final POS impedance R_s was varied from 10 to 30 Ohm with opening time T_{op}=10 ns. The computations results are displayed in Fig.3-4. Dependences of the power P and the voltage U, divided on its matched load values, on load resistance R_l/R_g are presented in fig.3a. The SMI wave with the electron leakage current on its front was propagated to the load. The leakage evolution was defined by the correlation between the "hot line" impedance ρ_h=U(Imin)/Imin and R_l. If $R_l>\rho_h$ the part of the line current was leaked near the load, that is the actual load impedance, which POS "feels", could not ecxeed ρ_h. This leads to the output pulse values falling (see Fig.3). Since $\rho_h \sim \rho_w$, P and U may be enhanced by the increase ρ_w. Corresponding dependences are plotted in fig.3b, where wave impedance is increased in more then 3 times that of Fig.3a. However it's necessary to remember that changing in wave impedance may lead to the opening time changihg.

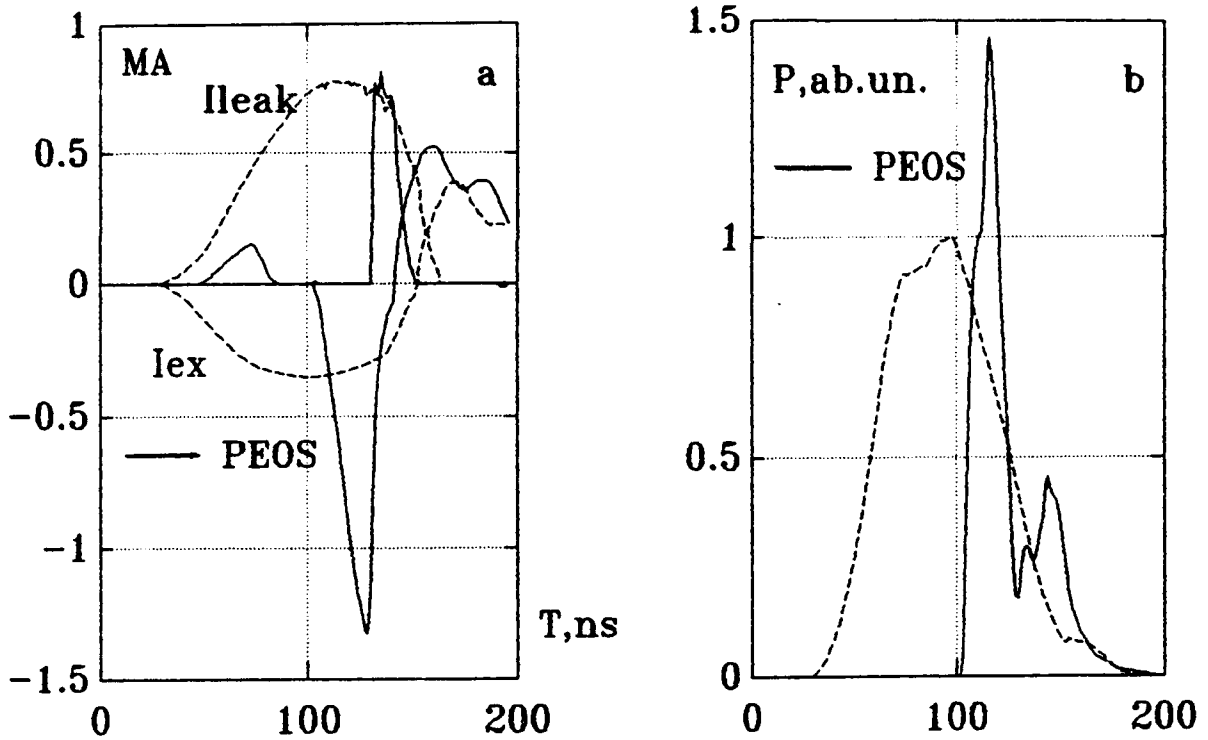

Fig.5 (a) Electron leakage current Ileak and output current Iex of the delayed module; (b) The load power P in abitrary units.

The same dependences are given in Fig.4ab, but the output pulse data were obtained for the Angara-5 VTL coupled with the diode. So far we regarded that all modules of the Angara-5 facility worked synchronously. As was shown in [4] bad synchronization in the generator firing results in high energy losses and perhaps in electrodes destruction. POS utilization can essentially improve situation. For modelling this effect we made calculations with the diode load in Angara-5, when one module delayed at 40 ns. This case is the mostly dangerous for successful accelerator operation [4]. The current at the end of the delayed module and full leakage current in this one are given in fig.5a. The leakage duration in the case with POS is significantly less that without one, and consequantly energy loss is less. As calculations showed there are no any essential changing in the diode output values in jitter regime for system with POS, while in the absence one the nonsynchronization leads to 25% losses of the load energy.

IV. SMALL MASS LINER ACCELERATION. Let's consider situation when VTL with POS is loaded on the liner. It's well known there are optimum conditions which relate $\alpha=mR^2/h$ (m,R,h-liner mass, radius

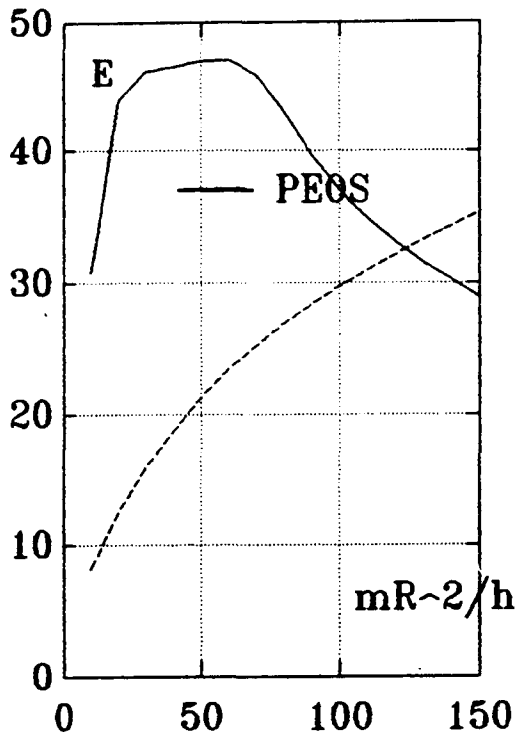

Fig.6 Liner kinetic energy E(kJ) as a function of ratio $\alpha=mR^2/h$ ($\mu g*cm$).

eight) with generator characteristics (U, R_g, T_g *etc*) [5]. For a large α magnetic pressure is insufficient to compress the liner, and for $\alpha<\alpha_0$ liner is compressed before the current maximum. Such current falling could be avoided by the POS employment, as maximum current would be limited by the POS. To demonstrate this effect we used the numerical scheme described in the previous part. The VTL and POS parameters were chosen the same as for the Angara-5 calculations in Sec.III. 0-D model was used for the liner motion and its compression degree was restricted by 10. The results of the computations are given in fig. 6 and show that for the parametres of Angara-5 facility the POS application results in the same liner kinetic energy with $\alpha=50$, as for the liner with $\alpha=200$ without POS. It worth to be noted that contrary to high impedance load case in the liner load one the value of the inductance down the POS should be fairly large to prevent from the negative voltage appearance on the POS before liner motion beginning.

REFERENCES

1. P.F. Ottinger *et al.* J. Appl. Phys. vol.ó ,p.774, (1984).
2. S. Miyamoto *et al.* Jap. J. Appl. Phys. vol.23, p.L109, (1984).
3. V.V. Bulan *et al.* 6th Symp. on high current electronics of USSR. Theses, part II, p.183, 1986, Tomsk,(Rus.)
4. V.V. Bulan *et al.* Proc. of the 8th Int. Conf. on High-Power Particle Beams . Vol.2,p.990,1990, Novosibirsk,USSR.
5. V.V. Zajivikhin *et al.* Pizika Plasmy,vol.14, p.4,(1988),(Rus.)

EXPERIMENTS ON MICROSECOND CONDUCTION TIME PLASMA OPENING SWITCH MECHANISMS

W. Rix, M. Coleman, A.R. Miller, D. Parks, K. Robertson,
J. Thompson, E. Waisman, A. Wilson
Maxwell Laboratories, Inc.
8888 Balboa Avenue
San Diego, CA 92123

Abstract

We describe a series of experiments carried out on ACE 2 and ACE 4 to elucidate the mechanisms controlling the conduction and opening phases on plasma opening switches in a radial geometry with conduction times on the order of a microsecond. The results indicate both conduction and opening physics are similar to that observed on lower current systems in a coaxial geometry.

Introduction

Mechanisms of microsecond plasma opening switch (POS) operation have been studied extensively on the HAWK pulser at the Naval Research Laboratory (NRL). The HAWK POS operates at 500-700 ns conduction time with conduction currents of 600 to 800 kA. Plasma density has been well characterized with interferometry measurements. HAWK experimental results and theoretical modeling have been presented in several papers[1]. Modeling and theory explaining in greater detail the opening characteristics of the HAWK POS have also been developed[2].

POS experiments on the ACE pulsers extend POS operations to different regimes. ACE 2 and ACE 4 use a radial POS geometry in contrast to the coaxial POS geometry on HAWK. ACE 2 operates at a slightly higher current than HAWK (~1 MA) while ACE 4 has conducted currents of 6 MA and has the capability of delivering over 9 MA into the POS. In addition, the radial POS on ACE 4 has been split into top and bottom annuli which operate in parallel.

Despite some differences in ACE and HAWK POS operation, the ACE results can be summarized by the statement that the mechanisms developed to explain HAWK POS data also explain ACE POS data. For the larger area ACE POS, plasma source uniformity is very important to achieving proper operation. Although the individual flashboard plasma sources are very similar for ACE and HAWK, the larger ACE POS area, differences in geometrical convergence, and larger POS anode-cathode gap result in measured ACE POS plasma densities being a factor of 10 below HAWK levels. Conduction currents and times can still be predicted for ACE from the known plasma density by the same theory which explains HAWK POS operation. The plasma density reduction observed in the active region of the POS during the second half of the conduction phase on HAWK is also observed on ACE 2. On HAWK, coupling the POS to varying impedance electron beam loads generates a saturated peak load voltage characteristic which can be explained by postulating that the POS opens via an enhanced erosion mechanism[2]. ACE 4 load voltage and current data for varying impedance electron beam loads can also be explained by this model.

This paper will now present the experimental evidence from the ACE data which supports these conclusions.

POS Configuration and Diagnostics

In Figure 1 a sectional view of the ACE 4 POS radial configuration indicates the layout of the major components and the electrical diagnostics. Figure 2 is a top view of the ACE POS configuration and diagnostics which shows the azimuthal distribution of the flashboards and the diagnostics.

A technique for displaying the data from the 10 individual azimuthal probes has been developed by J. Thompson to characterize the POS opening symmetry. A polar (r, Ø) plot is used where r corresponds to time and Ø corresponds to angular position of an individual probe. A contour is generated by connecting the times when a specified value of load current is reached at each probe. The uniformity of opening around the azimuth of the POS is then apparent. The data

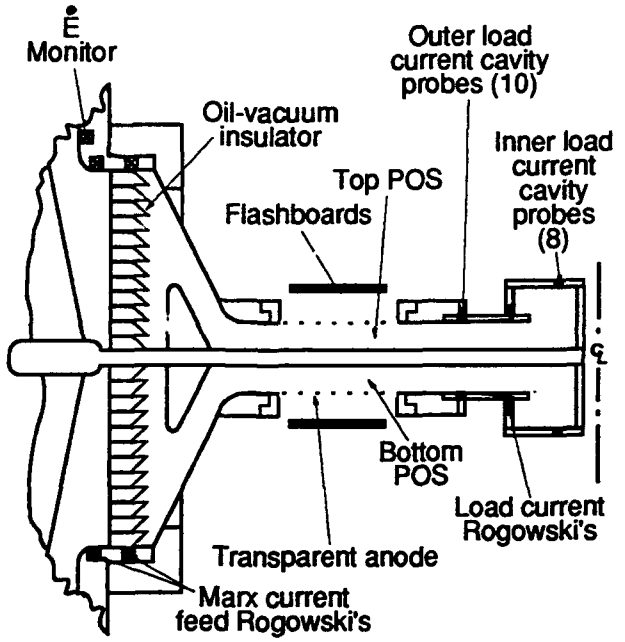

Fig. 1. Sectional view of the ACE 4 POS and short circuit load configuration.

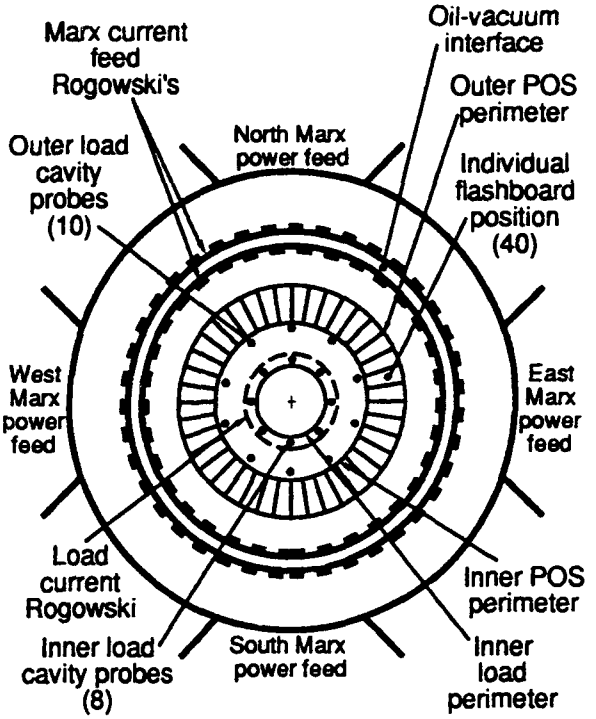

Fig. 2 Top view of the ACE 4 POS diagnostics configuration.

displayed in Figure 3 from ACE 4 shot 352 exhibits poor symmetry due to poor alignment and imprecise triggering of the individual flashboard plasma sources. For this shot the standard deviation in the time when each individual probe passed the threshold for opening was 58 ns. Poor symmetry results in relatively poor opening. Figure 4 shows the current into the short-circuit load for shot 352.

Good symmetry around the azimuth can be achieved by careful alignment of the flashboards and precise triggering as shown in Figure 5 for shot 348. The standard deviation in the time when the individual probes register opening current has been reduced to 9 ns.

Good symmetry results in improved opening as demonstrated by the current waveforms for shot 348 in Figure 6. With proper symmetry in plasma

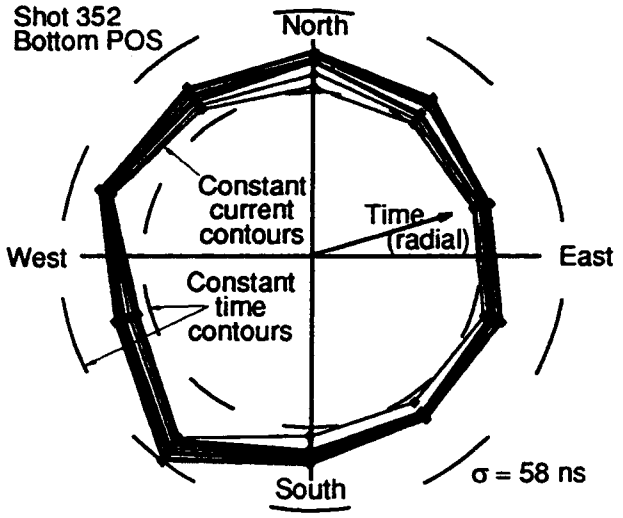

Fig. 3. ACE 4 load current probe contours for a shot with poor opening symmetry.

source operation, the large-area radial POS reproduces POS behavior observed on smaller coaxial configurations.

Plasma Density

Figure 7 indicates good agreement between measured currents on ACE 2 and predicted currents from the POS model developed by Parks [2]. The model used a plasma density of 1×10^{15} cm^{-3} at opening to calculate the currents. The measured plasma density at opening was 8×10^{14} cm^{-3}. The same model accurately predicts HAWK POS behavior.

Direct plasma density measurements as a function of time in the ACE 2 radial POS also exhibit the same qualitative behavior reported on HAWK[1]. As shown in Figure 8, when current from the capacitor bank is flowing through the POS, the density begins to drop about half way through the conduction phase in the same manner observed on HAWK. On ACE 2 the measured plasma density signal is lost just as opening begins.

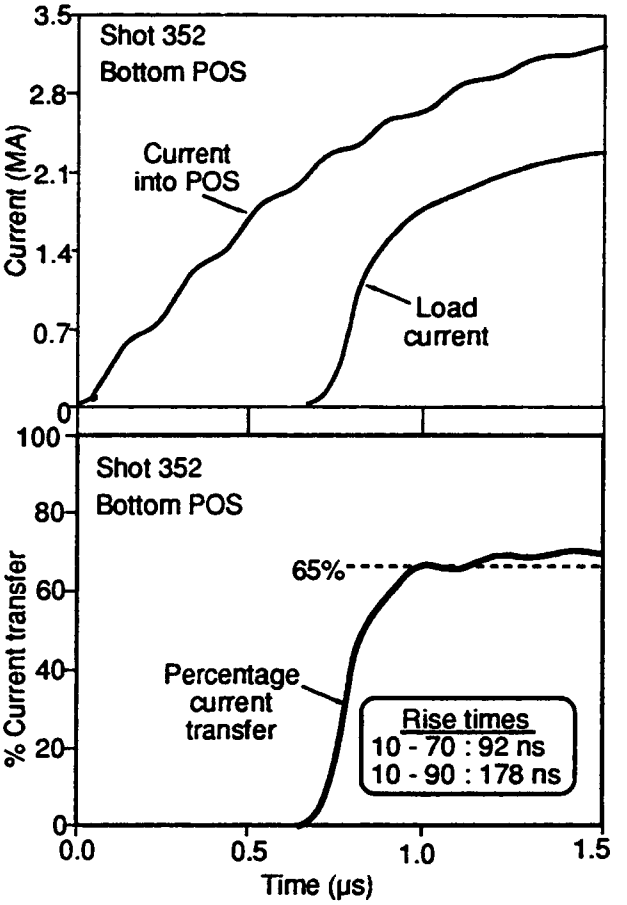

Fig. 4. ACE 4 summed current waveforms for the poor symmetry case.

Peak Power Characteristics

Figure 9 has been extracted from published HAWK data to indicate HAWK POS opening behavior as a function of load impedance[1]. The phenomenological explanation is that a gap of 2 to 3 mm is opened in the switch plasma. This gap can support a peak load voltage determined by the magnetic insulation capability of that gap. If the load impedance generates lower voltages than the peak voltage permitted by the gap, the load performance is "load limited." If the load impedance would generate higher than the gap allowed voltage, the load performance is "switch limited." The "enhanced erosion" model of Parks[2] explains the formation of the 2 to 3 mm switch gap.

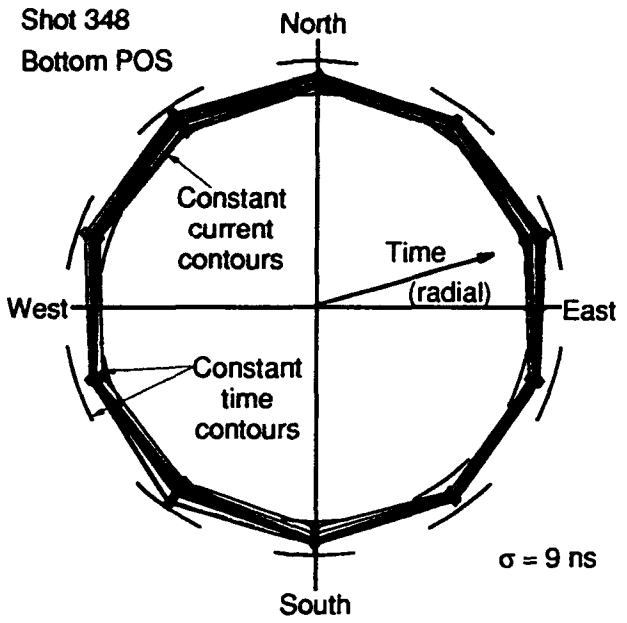

Fig. 5. ACE 4 load probe current contours for a shot with good opening symmetry.

ACE 4 electron beam load characteristics agree with this POS model and display the expected similarities to the HAWK data. ACE 4 data collected while varying electron beam impedances is displayed in Figure 10. The data exhibits "load limited" and "switch limited" regimes with the peak beam voltage at the expected value for the ACE 4 conditions.

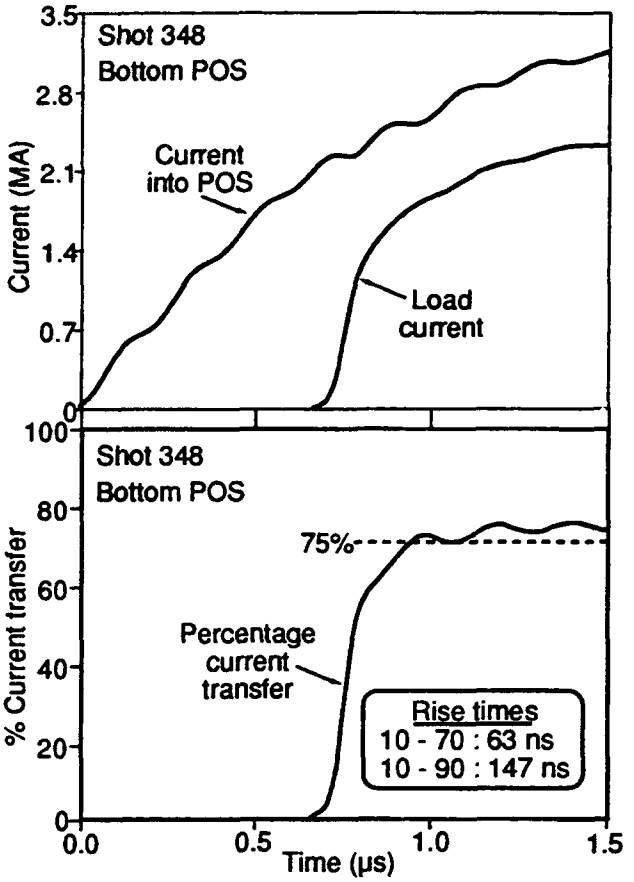

Fig. 6. ACE 4 summed current waveform for the good symmetry case.

Summary

ACE 2 and ACE 4 data extend the parameter space for microsecond conduction time POS experiments to larger currents, radial geometry, and lower plasma density. Models that successfully explain observations on HAWK also explain the data on ACE 2 and ACE 4. The major additional factor in operating the larger ACE POS is the requirement for good symmetry around the azimuth of the large, radial POS.

References

1. R.J. Commisso, P.J. Goodrich, J.M. Grossman, D.D. Hinshelwood, P.F. Ottinger, and B.V. Weber, "Characterization of a Microsecond-Conduction-Time Plasma Opening Switch," accepted for publication in *Physics of Fluids*, **B**, July 1992, and B.V. Weber, J.R. Boller, R.J. Commisso, P.J. Goodrich, J.M. Grossman, D.D. Hinshelwood, J.C. Kellogg, P.F. Ottinger, and G. Cooperstein, "Microsecond-Conduction-Time POS Experiments," these proceedings.

2. D. Parks, E. Waisman, R. Ingermanson, and E. Salberta, "Magnetically Enhanced Ion Erosion in Plasma Opening Switches," submitted to *Applied Physics Letters* and D. Parks, E. Waisman, R. Ingermanson, and B. Salberta, "Two-Dimensional Studies of Current Conduction in Plasma Opening Switches," these proceedings.

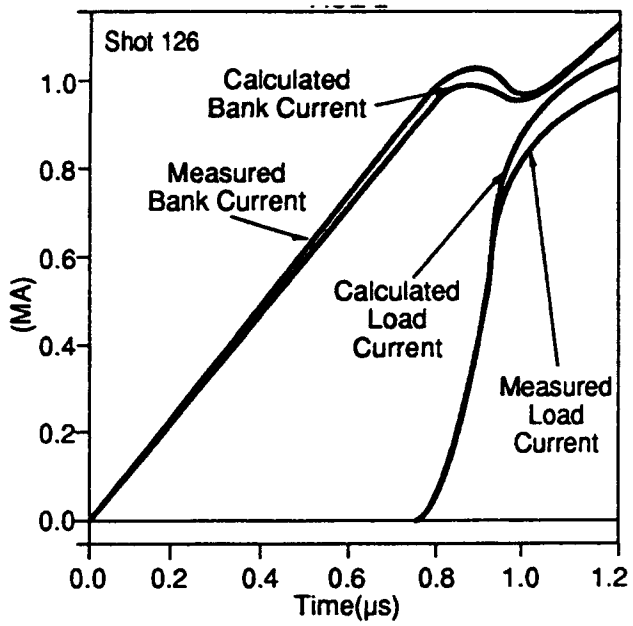

Fig. 7. Comparison of ACE 2 measured and calculated POS currents.

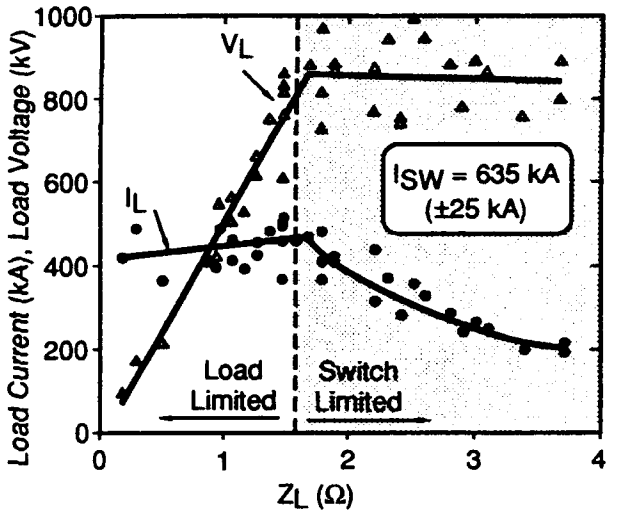

Fig. 9. HAWK data from reference [1] used to characterize POS opening behavior.

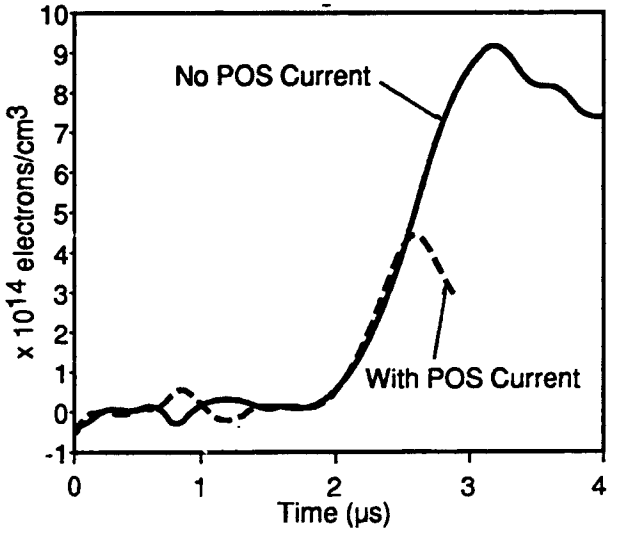

Fig. 8. ACE 2 exhibits POS plasma density "thin-out."

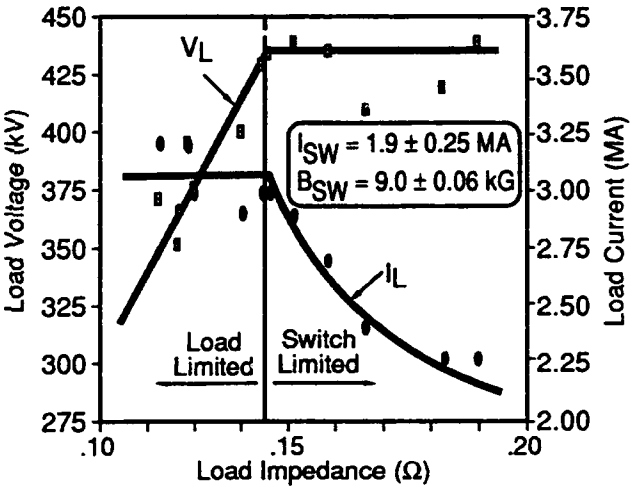

Fig. 10. ACE 4 electron beam load data characteristics.

DENSITY MEASUREMENTS OF MICROSECOND-CONDUCTION-TIME POS PLASMAS

David Hinshelwood,* B. V. Weber, R. J. Commisso,
P. J. Goodrich,* J. M. Grossmann, and J. C. Kellogg.

Plasma Physics Division
Naval Research Laboratory, Washington, DC 20375-5000
*Jaycor, Vienna VA 22182-2270

Abstract: Measurements of the electron density in a coaxial microsecond conduction time plasma opening switch during switch operation are described. Current conduction is observed to cause a radial redistribution of the switch plasma. A local reduction in axial line density of more than an order of magnitude occurs by the time opening begins. This reduction, and the scaling of conduction current with plasma density, indicate that current conduction in this experiment is limited by hydrodynamic effects It is hypothesized that the density reduction allows the switch to open by an erosion mechanism. Initial numerical modeling efforts have reproduced the principal observed results. A model that predicts accurately the conduction current is presented.

Plasma density measurements are critical to the understanding of plasma opening switch (POS) operation. HeNe interferometry is a relatively simple, quantitative, non-perturbing technique for *in situ* electron density measurement during POS operation. The first such measurements were reported recently.[1] A schematic of the arrangement, on the Hawk generator at the Naval Research Laboratory, is shown in Fig. 1. Measurements have been obtained on shots with various cathode and anode radii. A short-circuit load is located 25 cm beyond the switch. A mask outside the anode rods shields all but the (usually) 8-cm-long switch region from the plasma injected by 18 flashboards. The flashboards are typically pulsed 1 to 2 μs before the generator is fired. In the absence of opening, the generator drives 720 kA through the switch in 1.2 μs.

Details of the interferometer are given in Ref. 2 and are only summarized here. An acousto-optic modulator splits a 10-mW cw HeNe laser beam into two beams with a 40-MHz relative frequency shift. A scene beam is directed through the switch region in the axial direction, parallel to the cathode (see Fig. 1). A reference beam traverses an equal path length outside of the vacuum system before combining with the scene beam at a beamsplitter. The intensity of the combined beam exhibits a 40-MHz beat signal whose phase depends on the relative phase shift between the two beams. The zero-crossing times of the beat signal are used to determine the time-varying phase shift of the scene beam, from which the line-integrated density $\int n_e dz$ is calculated. Several null tests were performed to verify that the measured phase shift is caused by electrons in the switch region.[2] Several sources of spurious phase shift have been identified. After taking corrective measures,[2] a measurement limit during shots of less than 2×10^{15} cm^{-2}, or 2° of phase shift, has been achieved. Before each shot the flashboards alone are fired and the density is evaluated for comparison with shots where the POS plasma conducts current.

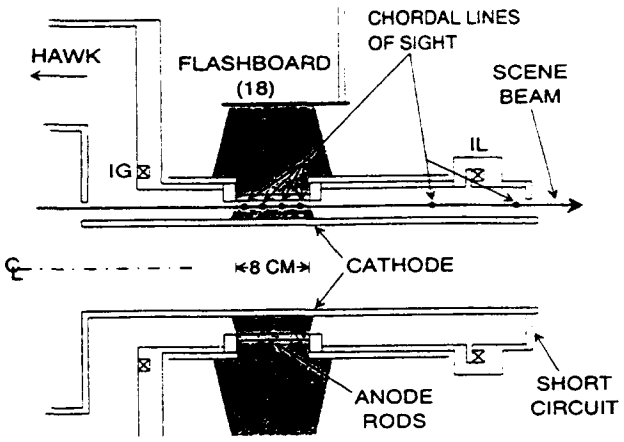

Figure 1: The Hawk POS geometry. Different cathode and anode radii were used during the experiment.

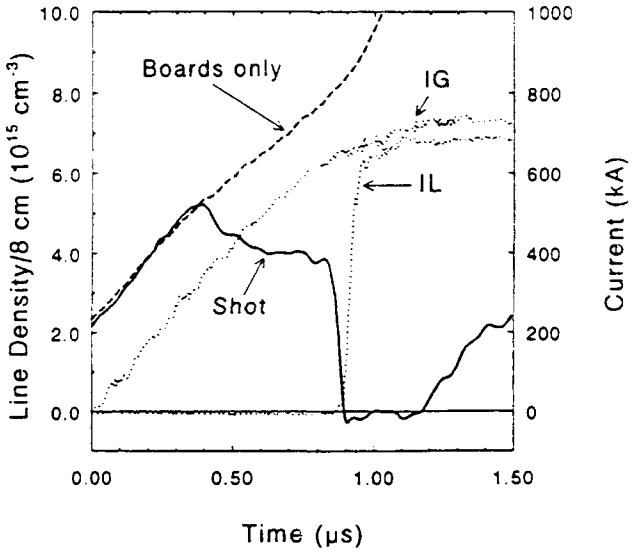

Figure 2: The average electron density at 15 mm from the cathode, with and without firing the generator.

Typical data are shown in Fig. 2. On this shot the switch current rises to 660 kA in 900 ns before the switch opens. The detected portion of the scene beam was located radially 15±0.5 mm from the 5-cm-radius cathode surface, and azimuthally between two anode rods. The measured line density is divided by the assumed switch length to get the average density. At about 350 ns into the conduction phase on this shot, the average density departs abruptly from the flashboard-only behavior. Rather than increasing, the density decreases somewhat until just before the switch opens. At that time it decreases sharply. During opening, the density is less than the measurement limit of 3×10^{14}cm^{-3}. This represents a decrease of over an order of magnitude relative to the value at 350 ns. Later, the density increases again, eventually rising to a level exceeding 10^{17} cm^{-3} for tens of μs (see Ref. 3). We believe that this late time density increase reflects enhanced electrode plasma formation due to bombardment by energetic particles accelerated by the (inductive) switch voltage.

Measurements at other radii, except those within a few mm of either electrode, are qualitatively similar to those in Fig. 2; the average density departs from the flashboard-only value early in the conduction phase and decreases until opening occurs. At 2.5 mm from the cathode the density increases relative to the flashboard-only case during the first few hundred ns. It then decreases, but remains finite at opening. At 1 mm from the anode the density increases sharply toward the end of the conduction phase. The results are similar at different azimuthal locations relative to the anode rods.

Radial density profiles for shots with a 5-cm-radius cathode are shown in Fig. 3. Average densities are plotted for two times, early (300 ns) in the pulse and during opening (900 ns), and compared with data from flashboard-only shots at the same times. The density from the flashboards alone is higher at the cathode because of stagnation

of the injected plasma and/or secondary plasma formation. At 300 ns there is little effect of current conduction other than a further increase in line density at the cathode. This may be indicative of the explosive-emission cathode plasma. By the time of opening, current conduction through the plasma has greatly altered the density profile. Since the interferometer integrates along the axis, and the same results are observed at different azimuths, this alteration must be associated with radial displacement of the plasma. These measurements indicate that plasma is pushed out to the anode radius, and perhaps in to the cathode. The lowest average density immediately prior to opening occurs most frequently at 1.5±0.1 cm from the cathode; opening presumably occurs at this location. Data taken during shots with 2.5-cm-radius and 12-cm-radius cathodes show a strong density decrease over most of the switch gap and the radial location of opening is not as obvious.

The observed radial plasma displacement toward the anode and cathode can be explained by a relatively small axial ($j_z/j_r \sim 10\%$) tilt or bend in the current streamlines. We believe that this axial component arises from a combination of the radial dependence of the magnetic field and the radial variation of the initial plasma line density. A radial variation of B^2/n will result in a radial variation of the axial displacement, and thus a bend in the current streamlines. The different radial density profiles at opening observed with different cathode diameters may result from different initial density and magnetic field profiles.

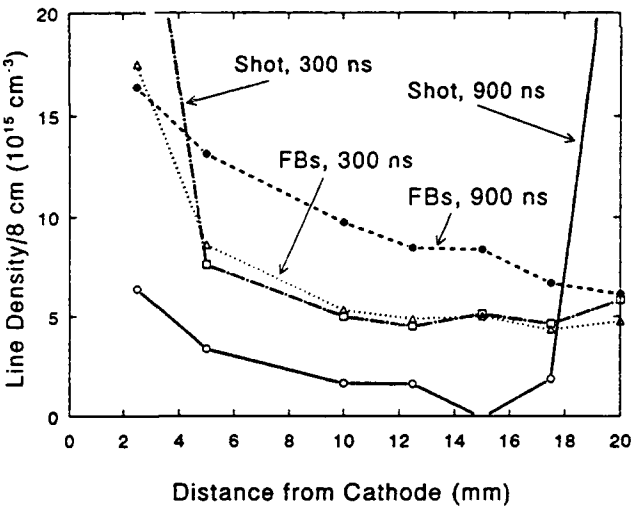

Figure 3: Electron density as a function of radial position early in the conduction phase and just before opening. Flashboard-only data are shown for comparison.

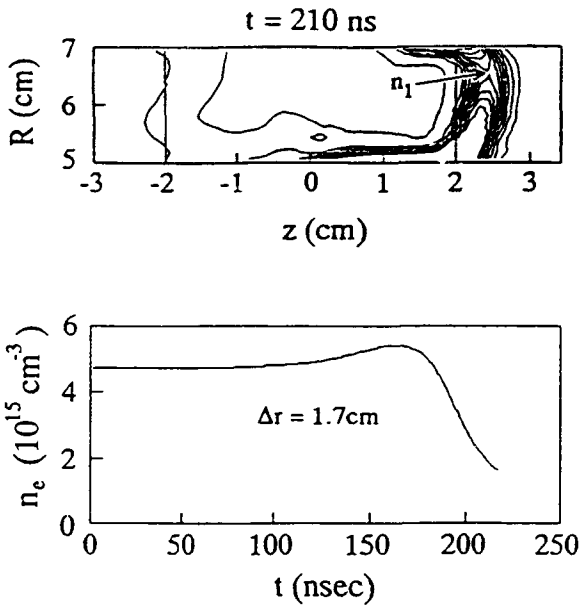

Figure 4: ANTHEM code predictions: (top) Electron density at the end of the conduction phase. The vertical lines indicate the initial plasma location. (bottom) Average density at 17 mm from the cathode.

Hydrodynamic motion of the switch plasma has been modeled with the ANTHEM two-fluid code,[4] using the measured, average electron density profile at 300 ns. To reduce computation time, the plasma mass and length and the current risetime were reduced. A 4-cm-long, H^+ plasma was assumed, with a current risetime of 200 ns.

This risetime was chosen to provide the same calculated center-of-mass translation as the experimental parameters. Results are shown in Fig. 4. Figure 4a shows electron density contours at 210 ns, corresponding to the time of switch opening in the experiment. The current streamlines follow these contours — mostly radial, but bowed. Plasma has been displaced toward the load end of the switch region, albeit in a narrower channel than indicated by previous magnetic field measurements.[5] We believe that the wider current channel indicated by the field measurements could be reproduced by incorporating anomalous resistivity in the modeling.[6] More importantly, the slight bending of current streamlines has led to a radial density redistribution, with a density minimum at 1.7 cm from the cathode. This compares well with the results in Fig. 3. Fig. 4b shows the calculated time history of the average density at this radius. A sharp decrease is seen at the end of the conduction phase, which compares well with the results in Fig. 2.

The ultimate opening of the switch occurs in a (relatively short) few tens of ns. The observed reduction in the average density by more than an order of magnitude at 1.5 cm from the cathode may allow the switch to open by enhanced erosion of the switch plasma. Effective switch gap opening rates are inferred from similar shots with diode loads.[7] Based on magnetic insulation arguments and electrical data from these experiments, gap opening rates of $\sim$5 cm/μs and switch gaps at opening of a few mm are inferred. Faraday cup measurements[5] indicate that the ion current is on the order of 20% of the total current at the time of opening. At the reduced average electron density measured at the end of the conduction phase in these experiments, the value of j_i/en_e exceeds 10 cm/μs. This rate may well exceed the ion injection velocity and can explain the observed, rapid opening.

Data have also been obtained using the chordal lines of sight shown in Fig. 1. Measurements at four locations in the switch region were taken during shots with 2.5-cm-radius cathodes. Tubes shielded the scene beam from plasma outside the switch region. Typical data, from a shot with the line-of-sight located 3 cm from the generator end of the switch region, are shown in Fig. 5. The average density at each location first increases, and then decreases. The density increase is larger toward the load end, as would be expected from axial displacement of the switch plasma. The density decrease at each location is correlated with the arrival of the current front, as determined by dB/dt probe data taken during similar shots, as seen in Fig. 5.

Measurements beyond the switch region were taken during shots with 5-cm-radius cathodes. Typical data are shown in Fig. 6. No significant electron density is observed beyond the switch region until well after opening. This confirms that opening does not arise from a large-scale translation of the switch plasma as it does in a plasma flow switch. An interesting phenomena is observed (see Ref. 3): For conduction currents below 450 kA, no significant plasma is observed beyond the switch, even after opening, while at larger currents plasma is observed. This is suggestive of two different regimes of switch operation.

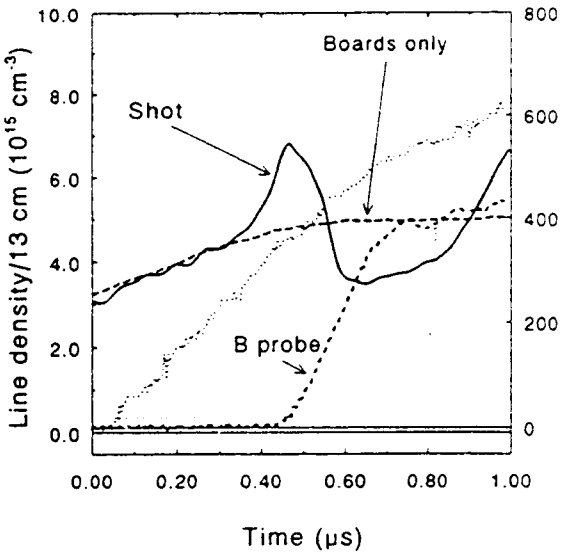

Figure 5: Average density along a chordal line of sight located in the switch region. The signal from a magnetic probe, at the same location on a similar shot, is shown for comparison.

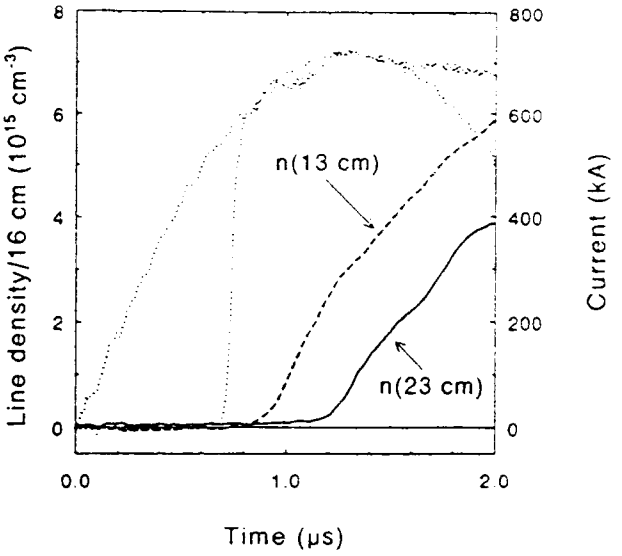

Figure 6: Average densities along lines of sight beyond the initial switch region.

Several models have been proposed to explain the limitations on current conduction in plasma opening switches. Field penetration by the Hall term (EMH)[8] and $\vec{j} \times \vec{B}$ hydrodynamic displacement (MHD)[9] are relevant to the parameters of this experiment. Peak conduction current scaling with density has been studied by taking timing scans using different cathode radii, switch lengths, and current risetimes. Data from timing scans using three cathode radii are compared with predictions in Fig. 7. The peak density at 1.5 cm from the cathode is used in the predictions. In calculating the MHD limit it is assumed that opening occurs when the plasma center-of-mass is displaced by half of the initial switch length. This is consistent with previous magnetic field measurements.[5] Good agreement between the data and the MHD predictions are observed for most shots. Data from a few shots at lower switch currents are suggestive of an EMH mechanism. Data from shots with different switch lengths and current risetimes (see Ref. 3) show agreement with prediction similar to that in Fig. 7.

The MHD calculation has been refined to account for the time-varying density by using a snowplow model.[10] In front of the snowplow, the density is given by data from flashboard-only shots. Behind the snowplow, the self-magnetic field is assumed to prevent further plasma from entering the switch gap. Conduction is assumed to cease when the snowplow reaches the end of the initial switch region. The underlying assumption is that this level of axial displacement is associated with the level of radial displacement necessary to allow opening. Predicted and observed peak conduction currents are shown in Fig. 8 for shots with different cathode radii, switch lengths, and current risetimes. This simple model is seen to have very good predictive capability.

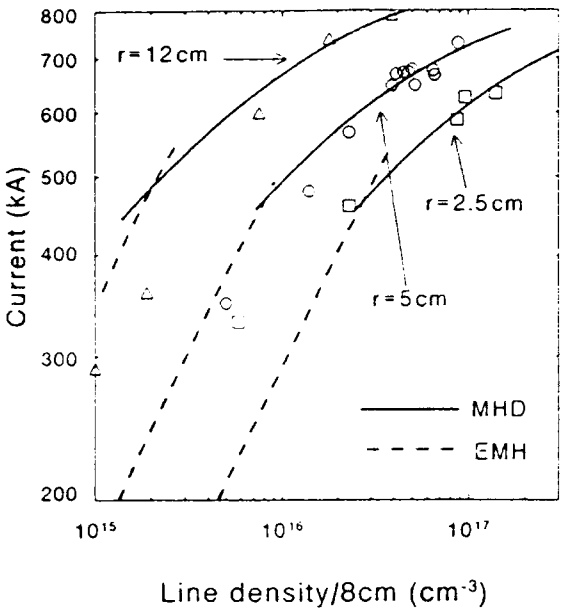

Figure 7: Conduction current as a function of peak density for three cathode radii, compared to that calculated from the MHD and EMH models.

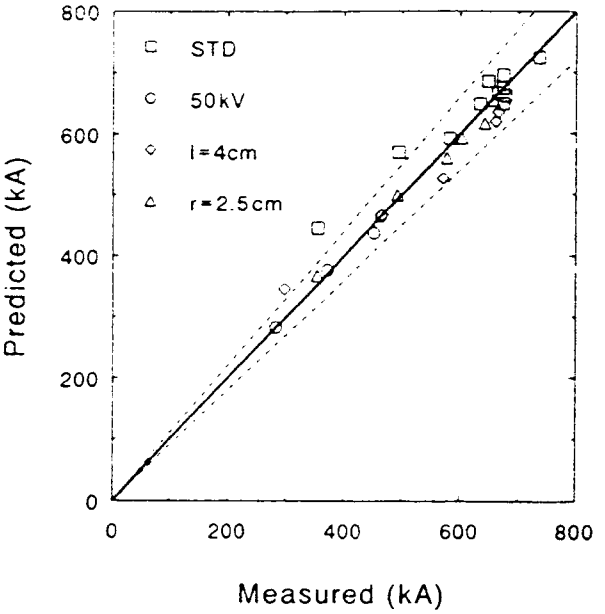

Figure 8: Conduction current versus predictions of the snowplow model, for a range of switch parameters.

In conclusion, electron density measurements during POS experiments have shown new features relating to the conduction and opening mechanisms in a POS. Current conduction causes a density reduction over most of the plasma radial extent, indicating that current conduction in this experiment is limited by hydrodynamic effects. Opening occurs without a large-scale axial displacement. We suggest that a radially-nonuniform axial snowplow gives rise to a radial redistribution of the switch plasma, and that opening occurs by erosion of the rarified region. This picture is supported by axial and chordal line of sight data, fluid code calculations, and the scaling of conduction current with switch parameters. The density measured during flashboard shots can be used to predict accurately the conduction current over a range of switch parameters.

It is a pleasure to acknowledge valuable contributions to this work from Rick Fisher.

References

1. David Hinshelwood, Bruce Weber, R. J. Commisso and J. M. Grossmann, to be published in Phys. Rev. Lett., June 1992.
2. B. V. Weber and D. D. Hinshelwood, to be published in Rev. Sci. Inst., Oct., 1992.
3. B. V. Weber, J. R. Boller, R. J. Commisso, P. J. Goodrich, J. M. Grossmann, D. D. Hinshelwood, J. C. Kellogg, P. F. Ottinger, and G. Cooperstein, these proceedings.
4. R. J. Mason, M. E. Jones, J. M. Grossmann, and P. F. Ottinger, Phys. Rev. Lett. 61, 1835 (1988).
5. D. D. Hinshelwood, R. J. Commisso, P. J. Goodrich, J. M. Grossmann, J. C. Kellogg, P. F. Ottinger, and B. V. Weber, in Proc. 8th Int. Conf. on High-Power Particle Beams Vol. 2, ed. by B. N. Breizman and B. A. Knyazev (World Scientific, New York, 1991), p. 1034.
6. J. M. Grossmann, R. Kulsrud, J. M. Neri, and P. F. Ottinger, J. Appl. Phys. 64, 6648 (1988).
7. B. V. Weber, R. J. Commisso, P. J. Goodrich, J. M. Grossmann, D. D. Hinshelwood, J. C. Kellogg, and P. F. Ottinger, IEEE Trans. Plasma Sci. 19, 757 (1991).
8. K. V. Chukbar and V. V. Yan'kov, Sov. Phys. Tech. Phys. 33, 1293 (1988).
9. W. Rix, D. Parks, J. Shannon, J. Thompson, and E. Waisman, IEEE Trans. Plasma Sci. 19, 400 (1991).
10. Eduardo Waisman, Maxwell Laboratories, personal communication.

MICROSECOND PLASMA OPENING SWITCH EXPERIMENTS ON HAWK WITH AN E-BEAM DIODE LOAD

P.J. Goodrich, R.C. Fisher, D.D. Hinshelwood
Jaycor, Vienna, VA 22182

J.R. Boller, R.J. Commisso, B.V. Weber
Pulsed Power Physics Branch, Plasma Physics Division
Naval Research Laboratory, Washington, DC 20375

Abstract

The Hawk generator is used in plasma opening switch (POS) experiments in the 1-μs conduction time regime to study long conduction time switch physics. Peak load powers of 0.7 TW with 55 kJ delivered to the diode--20% energy efficiency--were achieved with a POS. The data indicate that above a critical load impedance the final switch gap size is limited to about 3 mm. This limits the voltage. Maximum load power is obtained at this critical impedance. Increasing the cathode magnetic field--by conducting more current or by decreasing the cathode radius--allows the fixed-gap POS to remain insulated at a higher voltage. Peak load voltages up to 2 MV were achieved with a 2.5 cm diam cathode, a factor of 2.8 higher than the Marx voltage. Load powers were up to 70% higher with a plasma-filled diode (PFD) used in conjunction with the POS for short POS conduction times. The switch gap may be larger (> 3 mm) on these short conduction PFD shots.

I. Introduction

Pulsed power generators have traditionally used waterline and vacuum transmission line technology for power conditioning of the microsecond output pulses from Marx banks. The emergence of inductive store technology[1] allows the development of more compact pulsed power generators. An opening switch, such as a plasma opening switch (POS), is used for power multiplication and pulse compression of the microsecond Marx output pulse. Hawk[2] uses a 600 nH Marx,[3] with 225 kJ stored and an erected voltage of 640 kV at 80-kV charge to deliver up to 720 kA in 1.2 μs to a POS. By varying the switch plasma density, the switch can be made to conduct from 0 to 1.2 μs. The goal of these experiments was to study the physics of the switch and optimize the switch/e-beam diode performance to generate high power short duration (<100 ns FWHM) power pulses.

II. Experimental Configuration

The front end coaxial vacuum section of the basic configuration is shown in Fig. 1. Different configurations of POS hardware were used, including different switch to load lengths, different cathode center conductor diameters (10 cm diam pictured here), and various cathode tapers--both gradual and abrupt--in the switch and outside the switch. An independent plasma-filled diode (PFD) was also used in some experiments.

The diagnostics consist of a capacitive voltage monitor behind the insulator in oil and several current monitors including a shunt monitor behind the insulator, four B-dot monitors on the vacuum side of the insulator which are added together, a Rogowski monitor just upstream of the switch and two anode B-dot current monitors at the load. A carbon switch plasma was produced by 18 aerodagged flashboards arranged azimuthally around the 8 cm length switch region. The flashboards were 17.75 cm from the axis. This plasma was injected radially through anode rods to the cathode center conductor. The flashboards were driven by 25-kV capacitor banks fired 1-2 μs before current was conducted in the switch. The current in the flashboards rises to 35 kA in 0.6 μs. Typically, the peak switch current density is 2-4 kA/cm^2.

The setup in Fig. 1 with a switch-to-load length of 26 cm is called the standard configuration. In this configuration, for conduction times greater than about 0.6 μs, switch plasma reaches the diode. Some plasma comes directly from the flashboards but most is accelerated to the load by JxB forces during conduction (confirmed by

Faraday cups in the load region). The bulk of the plasma does not reach the load--the center of mass motion of the plasma is only about 4 cm downstream[4,5,6]--however, enough plasma ($n_e \leq 10^{12}$ cm^{-3}) does reach the load for the load to act like a plasma-filled diode with a rising impedance. Also, more plasma (although still low density) reaches the load with smaller radii cathodes at a given conduction time due to the larger JxB force associated with the smaller cathodes. Extending the conductors downstream of the switch to a length of 40 cm or more generally prevented plasma from reaching the load. Two B-dot current monitors were added in this transition section, about halfway between the switch and the load. In this configuration, called the extended configuration, the load looks like a vacuum diode with a falling impedance and the impedance at peak power can be controlled by changing the gap spacing.

III. Experimental Results with Different Cathode Radii

Fig. 2 shows Hawk shot 56 with a 10 cm diam cathode in the standard configuration. The plasma delay is 1.5 μs and the switch conducts for 0.9 μs before opening. The 10-90% load current risetime is 40 ns with an 80% current transfer efficiency and 500 kA delivered to the load. Peak load voltage is 770 kV, peak load power is 0.4 TW. Best switch performance (highest voltage and power and fastest risetimes) for shots with a 10 cm diam cathode occurs for conduction times of ~1 μs, almost the time of peak current.

In this configuration, for conduction times over 0.6 μs, the load acts like a plasma-filled diode. On shot 56 the load impedance rose from 0 Ω to 1.5 Ω at peak power, although with a diode gap of 1 cm the vacuum impedance is 8 Ω. Load impedances of 1.5-2 Ω were the highest possible in this configuration regardless of the gap spacing for conduction times over 0.6 μs, limited by significant switch plasma in the load.

Fig. 3 shows two shots in the extended configuration with 0.95 μs conduction times. Here the load behaves as a vacuum diode with a falling load impedance. Opening the diode gap from 0.5 cm to 1.0 cm increased the impedance at peak power from 2 Ω to over 3 Ω. Note that the voltage generated on these shots was the same, about 800 kV, resulting in more current loss on the overmatched 3-Ω load impedance shot.

The voltage as a function of the load impedance at peak power is shown in Fig. 4 for numerous shots with a 10 cm diam cathode. Below a critical load impedance, ~ 1.7 Ω, the voltage increases linearly with impedance. This is called the "load-limited" regime[6,7]. Above the critical impedance, however, the voltage is constant for a given conduction current. This is called the "switch-limited" regime[6,7]. The voltage limit increases with conduction current.

The current transfer efficiency at peak power for 1 μs conduction is constant at 80% for load impedances less than or equal to the critical impedance, but falls as $(Z_L)^{-1}$ in the switch limited regime. Maximum power is delivered to a load operating at the critical impedance (Fig. 5). Furthermore, the peak load power increases with conduction time up to 1 μs. Thus, the highest power generated, 0.4 TW, occurs for 1 μs conduction at a load impedance of 1.7 Ω.

Fig. 6 shows the peak switch gap, D, derived from magnetic insulation arguments (critical current formula) for these shots plotted as a function of the load impedance at peak power[6,7]. The data indicate that at least above the critical impedance the switch gap is fixed to 2.5-3 mm and is independent of conduction current. The voltage increases with conduction current because the larger magnetic field associated with larger conducted currents allows the fixed-gap POS to remain insulated at a higher voltage.

Current loss in the load limited regime is 100-150 kA, independent of conduction (or plasma density) for conduction currents over ~ 400 kA. Much of the loss could be ion loss in the switch. For example, the 100 kA, or 20% loss on the highest power shots (operating at the critical load impedance and 1 μs conduction) is consistent with single species Child-Langmuir flow of C^{++} ions across a 2.5-3 mm gap. The additional current loss seen when operating above the critical impedance appears to be electron loss downstream of the switch near the load.

Hawk shot 366 with a 5 cm diam cathode in the standard configuration is shown in Fig. 7. The switch conducts for 0.7 μs and opens quickly, delivering 400 kA, 80% of the current, to the load in 20 ns. The voltage generated on this shot is 1.2 MV, well above the ~ 900 kV maximum voltage with the 10 cm diam cathode. The load impedance rises from 0 Ω to about 3 Ω and the peak power is 0.5 TW. Optimum switch performance with this cathode occurs at 0.75 μs conduction times with a ~ 1.5 μs plasma delay, which is also the delay for best opening with the 10 cm diam cathode. For a given plasma density, the switch opens earlier for larger magnetic fields, a consequence of MHD-limited conduction[6,8]. To conduct even slightly longer than 0.75 μs with the 5 cm diam cathode requires a very large increase in plasma timing delay with associated poor switch/load performance (e.g. electrode plasmas may expand into the switch gap and enough plasma reaches the load to limit the load impedance at peak power). This inability to conduct longer may be a consequence of the switch becoming source-limited: the flashboards may not be producing significantly higher plasma densities as the delay is increased above ~1.5 μs.

Voltages as high as 1.7 MV were generated with the 5 cm diam cathode, a factor of 2 higher than the best 10 cm diam cathode shots and 2.7 times higher than the Marx voltage. The data indicate switch opening rates up to 1 Ω/ns or gap opening rates up to 20 cm/μs.

The voltage dependence on the load impedance at peak power for numerous 5 cm diam cathode shots is shown in Fig. 8. Here, the critical load impedance is about 3.5 Ω. Below this value the voltage depends on impedance, above it the voltage is clamped for a given conduction current.

The calculated peak switch gap is shown in Fig. 9 as a function of the load impedance at peak power. The switch gap is limited to the same 2.5-3 mm. The larger magnetic field produced with this smaller radius cathode means a larger voltage can exist across the fixed gap at critical current with the current coupled into a diode operating at a higher impedance, 3.5 Ω. Again, a significant fraction of the current loss in the load limited regime, which is also usually 100-150 kA, could be ion loss in the switch and the additional current loss operating above the critical impedance electron loss near the load.

Voltages up to 2 MV were generated with a 2.5 cm diam cathode (see ref. 4). The optimum switch performance here occurs for conduction times of 0.6 μs with the same ~ 1.5 μs plasma delay. Peak load power was 0.6 TW, at a load impedance of ~ 7 Ω, with a 15 ns load current risetime. Longer conduction requires the similarly large increase in plasma timing delay found with the 5 cm diam cathode, and the subsequent degradation in performance.

The voltages generated with the different cathode radii are shown in Fig. 10 as a function of the cathode magnetic field. The data show the improved switch performance (higher voltage) as the magnetic field increases. The field increases as the conduction current is increased or as the cathode radius is reduced. Also plotted is the calculated effective gap for magnetic insulation. The data suggest a limit to the gap size of about 3 mm. Data points below the D=2.5 mm line are in the load-limited, lower voltage, regime with load impedance less than the critical impedance. Higher power could be achieved if the switch gap size can be increased, as suggested by the PFD data (discussed below).

IV. Experimental Results with Tapered Cathodes

Cathode tapers, abrupt and gradual, were tried in the switch region and upstream and downstream of the switch. The cathode magnetic field is larger in the tapered region which can, in principle, better insulate the electron flow and produce higher load powers. Only tapering in the switch, specifically the axial region from the middle of the switch to the downstream end of the switch, had any effect on performance. Better switch performance resulted using a small radius cathode in this region.

In particular, with a gradual 10 to 2.5 cm diam taper through the 8 cm length switch (the 2.5 cm diam being at the load end of the switch) load power up to 0.7 TW (1.5 MV and 465 kA in Fig. 11) was produced and 55 kJ (20% energy efficiency) was delivered to the load. This taper served as a good compromise between the high voltage with the 2.5 cm diam cathode and the long conduction/high current associated with the 10 cm diam cathode.

V. Experimental Results with Plasma-Filled Diodes

An independent PFD was made with plasma from a flashboard downstream of the diode injected into the diode gap through holes in the anode plate. The PFD was used with a 5 cm diam cathode and with a 10 to 5 cm diam switch taper which also included flaring the cathode at the diode out to a 9.5 cm diam on some shots.

Switch voltages up to 2.2 MV were generated with a PFD. Flaring the cathode at the diode was a convenient way of reducing the load impedance at peak power, operating closer to the critical impedance, and in this geometry load powers approaching 0.7 TW were produced with a PFD. This was about 15% higher than shots without the PFD. However, some switch plasma reached the load--the impedance rises from zero even with no independent PFD on these long conduction time shots--so there are no true vacuum diode shots for comparison.

For short conduction times, where switch plasma does not reach the load and the load with no PFD behaves as a vacuum diode, the enhancement in load power using the PFD was greater. Peak load power on shots with short 0.4 μs POS conduction times was up to 70% higher with the PFD (for similar load impedances at peak power). Both voltage and load current were higher, particularly the current. A possible explanation for this is the tendency toward unsaturated electron flow with a rising load impedance and saturated, hence lossy, flow with a falling load impedance that is seen in simulations[9]. It appears that larger switch gaps, up to 5 mm in size, were produced on the short conduction time PFD shots (see Fig. 10).

VI. Summary

High power pulses have been generated on the Hawk generator using a microsecond conduction time POS. Load power of 0.7 TW with 20% energy efficiency was achieved. The data indicate that an effective gap of 2.5-3 mm was produced in the switch, independent of the load impedance (at least above the critical impedance), conduction current, and cathode radius. Maximum power is obtained at the critical impedance, the transition point from load- to switch-limited operation. The voltage increases with cathode magnetic field. Increasing the field--by conducting more current or decreasing the cathode radius--allows the fixed-gap POS to remain insulated at a higher voltage. Voltages of 2 MV were generated with a small (2.5 cm) diam cathode (cathode magnetic field ~ 70 kG). Load powers were up to 70% higher using a PFD in conjunction with a POS, possibly because of less lossy (unsaturated) electron flow, for POS conduction times short enough that switch plasma does not reach the load. The derived switch gaps are larger than 3 mm on these PFD shots.

References

1. G. Cooperstein and P.F. Ottinger, Guest Editorial, IEEE Trans. Plasma Science, PS-15 (Dec. 1987).
2. J.R. Boller, R.J. Commisso, P.J. Goodrich, D.D. Hinshelwood, J.C. Kellogg, J.D. Shipman, Jr., B.V. Weber, and F.C. Young, NRL Memorandum Report 6748, January 1991.
3. P. Sincerny, D. Drury, J. Goyer, G. James, M. Krishnan, J. Levine, C. McDonald, and I. Roth, 7th IEEE Pulsed Power Conference, Monterey, CA 1989, IEEE Cat. No. 89CH2678-2, p. 275.
4. B.V. Weber, J.R. Boller, R.J. Commissso, P.J. Goodrich, J.M. Grossmann, D.D. Hinshelwood, J.C. Kellogg, P.F. Ottinger, and G. Cooperstein, these Proceedings.
5. D.D. Hinshelwood, B.V. Weber, R.J. Commisso, P.J. Goodrich, J.M. Grossmann, and J.C. Kellogg, these Proceedings.
6. R.J. Commisso, P.J. Goodrich, J.M. Grossmann, D.D. Hinshelwood, P.F. Ottinger, and B.V. Weber, Phys. Fluids B 4, 2368 (1992).
7. P.J. Goodrich, J.R. Boller, R.J. Commisso, D.D. Hinshelwood, J.C. Kellogg, and B.V. Weber, 8th IEEE Pulsed Power Conference, San Diego, CA 1991, IEEE Cat. No. 91CH3052-8, p. 515.
8. B.V. Weber, R.J. Commisso, P.J. Goodrich, J.M. Grossmann, D.D. Hinshelwood, J.C. Kellogg, and P.F. Ottinger, IEEE Trans. Plasma Sci. 19, 757 (1991).
9. J.M. Grossmann, private communication.

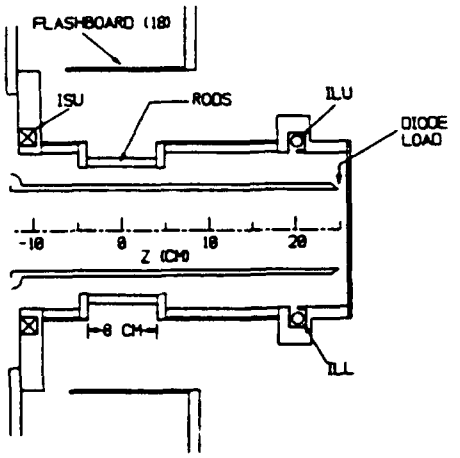

Fig. 1. Hawk switch/load vacuum section in the standard configuration.

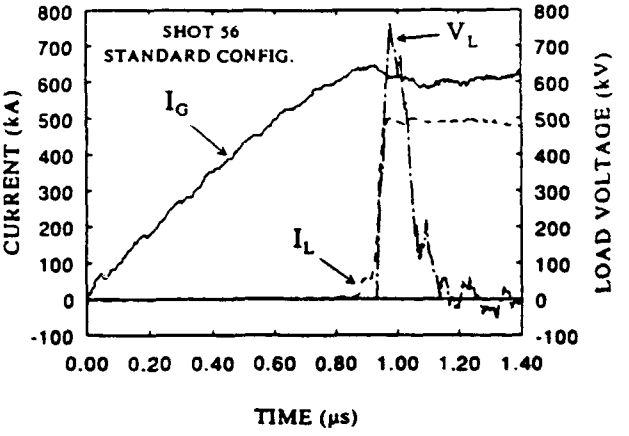

Fig. 2. Current and voltage data for a 0.9 μs conduction time POS shot with a 10 cm diam cathode.

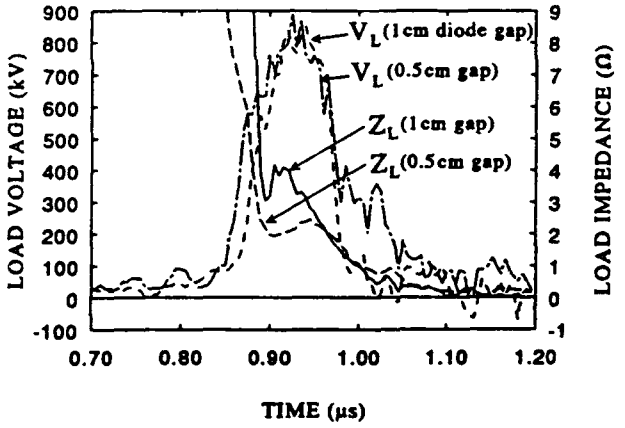

Fig. 3. Load data for two shots in the extended configuration. The diode looks like a vacuum diode with a falling impedance.

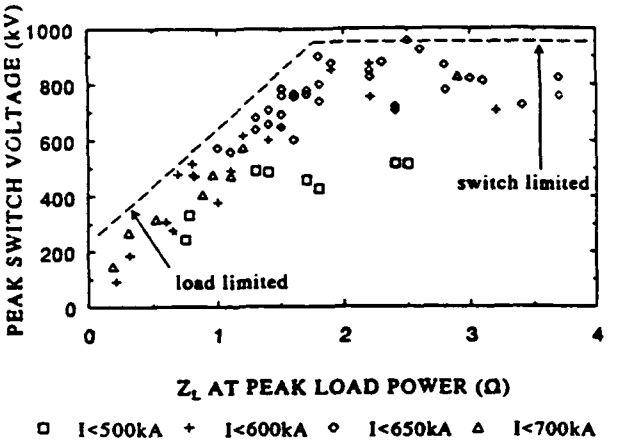

Fig. 4. Peak voltage as a function of load impedance with the 10 cm diam cathode. Above a critical impedance, ~ 1.7 Ω, the voltage is constant for a given conduction current.

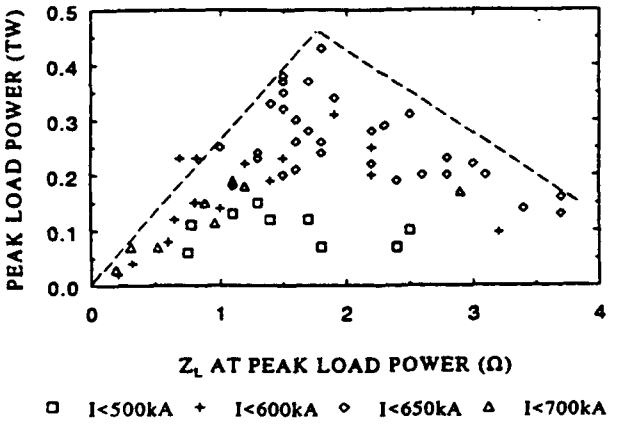

Fig. 5. Peak load power versus load impedance with the 10 cm diam cathode. Maximum power is delivered to a load operating at the critical impedance with ~ 1 μs POS conduction times.

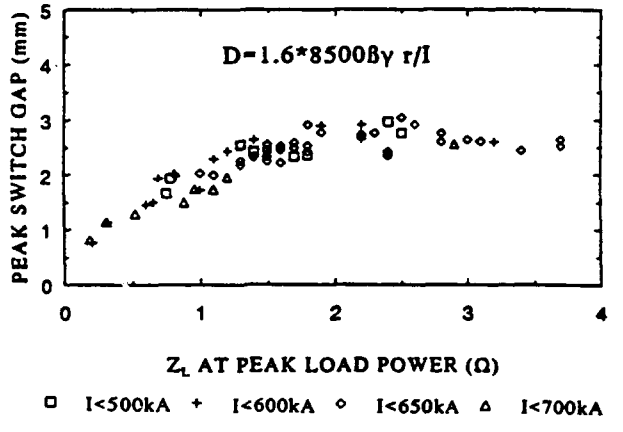

Fig. 6. Switch gap calculated at peak power, assuming the switch is at critical current, versus load impedance with the 10 cm diam cathode. The gap is independent of conduction current and, above the critical impedance, is fixed to 2.5-3 mm.

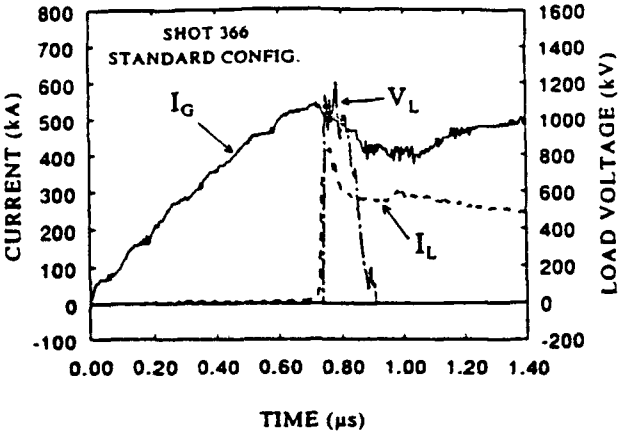

Fig. 7. Curent and voltage data for a 0.7 μs conduction time POS shot in the standard configuration with a 5 cm diam cathode.

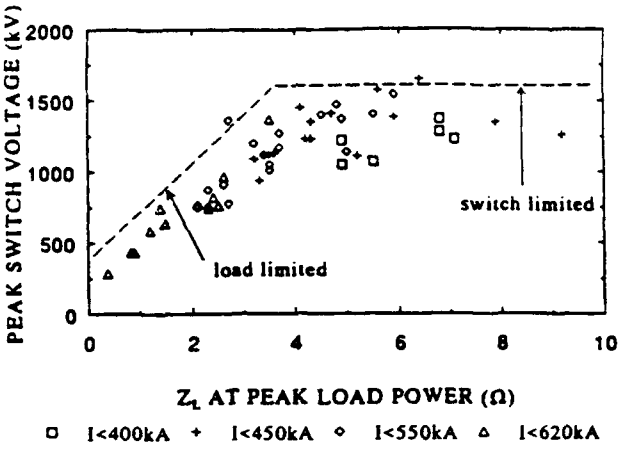

Fig. 8. Peak voltage as a function of load impedance with the 5 cm diam cathode. Above a critical impedance, ~ 3.5 Ω, the voltage is constant for a given conduction current.

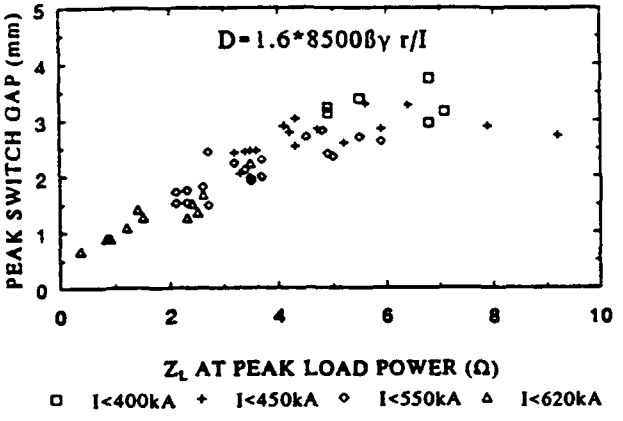

Fig. 9. Derived switch gap at peak power versus load impedance with the 5 cm diam cathode. The gap is also limited, above the critical impedance, to 2.5-3 mm.

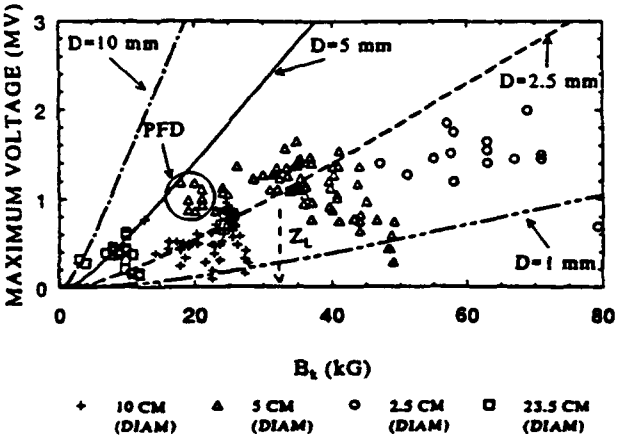

Fig. 10. Maximum voltage generated as a function of cathode magnetic field for different cathode diameters. Here the simple critical current model indicates the ways to increase the switch voltage.

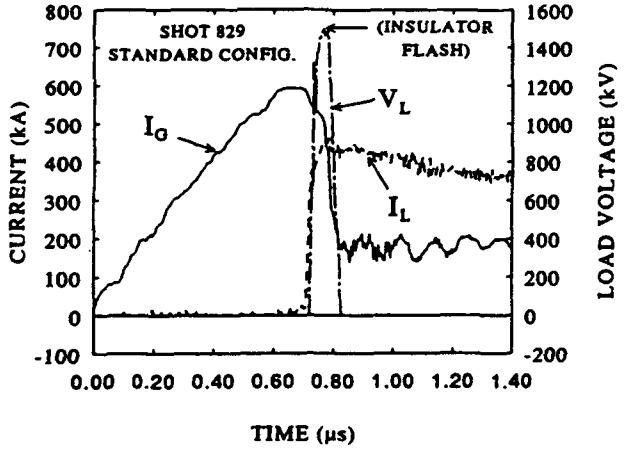

Fig. 11. On this shot with a 10 cm to 2.5 cm diam cathode taper in the switch region, load power was 0.7 TW (1.5 MV and 465 kA) and 55 kJ was delivered to the load.

PLASMA OPENING SWITCH FOR LONG-PULSE INTENSE ION BEAM*

H. A. Davis, R. J. Mason, R. R. Bartsch, J. B. Greenly†, and D. J. Rej
Los Alamos National Laboratory
Los Alamos, NM 87545

Abstract

A Plasma Opening Switch (POS) is being developed at Los Alamos, as part of an intense ion beam experiment with special application to materials processing. The switch must conduct up to 100 kA for 400 ns, and open quickly to avoid premature gap closure in the ion beam diode load. Power multiplication is not a necessity, but prepulse suppression is. A positive central polarity is desirable, since with it an ion beam can be conveniently launched beyond the switch from the central anode toward a negatively charged target. Using traditional scaling rules, a POS was designed with a 1.25 cm radius inner anode, and a 5.0 cm radius outer cathode. This has been constructed, and subjected to circuit, and simulational analysis. The computations are being performed with the 2D ANTHEM implicit code. Preliminary results show a marked difference in switching dynamics, when the central positive polarity is used in place of the more conventional opposite choice. Opening is achieved by the fast development of a central anode magnetic layer, rather than by the more conventional slow evolution of a cathode gap. With the central anode, higher fill densities are needed to achieve desired conduction times. This has suggested switch design improvements, which are discussed.

Introduction

At Los Alamos we are developing a Plasma Opening Switch[1] (POS) for an intense ion beam experiment with application to materials processing. The ion beam will be driven by the Anaconda Marx generator [300 KJ, 1.2 MV open circuit voltage, with $(L/C)^{1/2} = 2.6\ \Omega$]. The magnetically-insulated ion beam load has been designed to operate at approximately 5 to 10 Ω at 500 kV for 1 μs. Significant total beam energy and areal energy density are required for these experiments. Anode-cathode gap closure is expected to limit pulse duration. It is, therefore, imperative to have a fast power rise time, so that significant energy can be delivered to the load before closure terminates the beam pulse. The anticipated voltage rise time delivered directly from the Marx generator is of order 0.6 μs without additional power conditioning. This was thought to be too low for our ion beam application. After consideration of a variety of options, we decided to use a POS ahead of the load. The POS is designed to yield rapid current build up near the load, not to be used for power multiplication as in ICF and radiative output applications. When the switch opens current flows from the POS to the load through relatively low inductance. This leads to faster voltage rise times than in the absence of the switch. A POS, for example, that can conduct for 300 ns and open to a 10 Ω load in 100 ns reduces the net voltage rise time from 600 ns to 100 ns.

* This work was performed under the joint auspices of of the U.S.D.O.E and DNA.
†Permanent Address: Laboratory for Plasma Studies, Cornell University, Ithaca, NY.

The use of a central positive conductor is convenient, since beyond the switch the ions can be fired from the end of this conductor toward a negatively biased target. Some early success was achieved in our materials processing application with the Marx connected directly though a central anode to an ion diode. So, the simplest addition calls for the radial injection of POS plasma between the outer cathode and this central anode. However, central anode (reversed polarity) switches have traditionally performed more poorly[2-4] – with longer opening times – than their conventional counterparts, and so, such use should be approached with caution.

We have studied the possible merits of a fast opening POS though circuit analysis, and we have initiated first principle simulations of the switch plasma dynamics. The circuit studies are encouraging, and the simulations have begun to point the way toward an understanding of polarity effects in POS switches, and their optimization for our applications.

The Proposed Switch and its Circuitry

The switch initially designed for our experiment is shown in Fig. 1. The inner anode radius is 1.25 cm and the cathode sits at 5.0 cm. At 100 kA maximum current the magnetic field at the anode is 1.6 T. This is comparable to the fields driving early Gamble II experiments at the Naval Research Laboratory[1], except that here the inner radius is half that used at NRL. Also, our A-K gap to inner radius ratio, $\Delta R/R = 3.0$, is 3 times larger. The outer cathode is fabricated from 0.6 cm diameter rods. Plasma is injected through the rods ("A" in Fig. 1) by eight to sixteen plasma guns formed from 0.6 cm diameter semi-rigid coaxial cables.

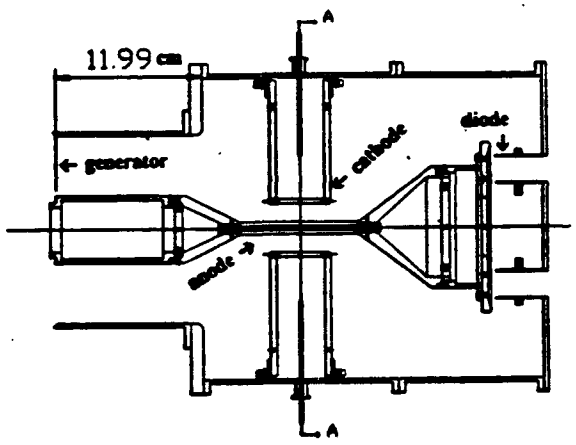

FIG. 1. Switch design for the LANL ion beam experiment.

Our experiments will be performed on the LANL Anaconda Facility, which has a 300 kJ Marx generator that will initially deliver 0.6 MV through the switch. The load is an applied B_r extraction diode connected to the end of the central switch electrode. In Fig. 1 the generator is at the left and the ion diode load is to the right.

In Fig. 2 we display the circuit diagram for this system. Calculations with this representative circuit have been performed assuming various opening characteristics for the switch. The results are collected in Fig. 3. In the absence of the POS we get a long voltage rise of up to 600 kV over 800 ns for a 5 Ω impedance. If the switch can open in 100 ns to the 10 Ω, we calculate that the

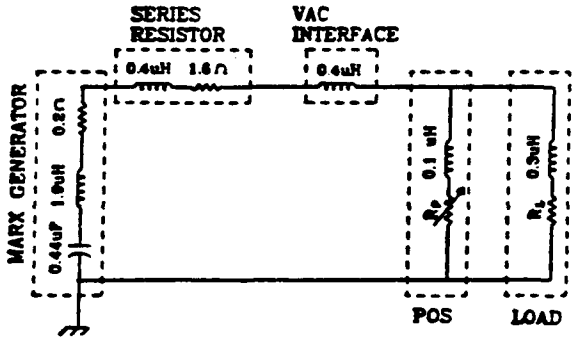

FIG. 2. Circuit representing the POS, driving generator and load.

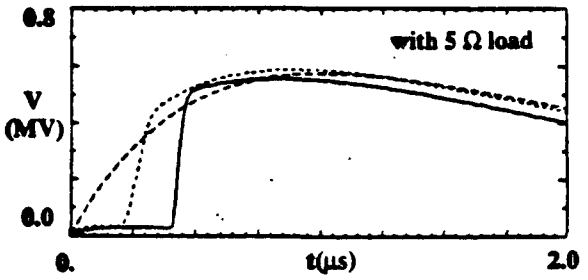

FIG. 3. Calculated load voltage for - - - no POS, - - - poor POS, and — good POS.

conduction time will be 200 ns followed by a steep rise to 500 kV. With a better POS opening in 50 ns, we get the solid line conduction time of 400 ns and then the steeper rise. The "good" switch will certainly meet the needs for our ion beam. Our objective is to see if such good performance can, indeed, be achieved. Our approach is to optimize performance through experiments designed and guided by first principle calculations.

ANTHEM Switch Modeling

The ANTHEM code[5] uses a fixed Eulerian mesh in either cartesian or cylindrical geometry. It solves either fluid or PIC particle equations for the ion and electron plasma components, coupled to the full set of Maxwell's equations. Numerically, it uses time advanced current sources obtained from the implicit solution of a set of auxiliary moment equations. This allows it to treat near vacuum electromagnetic behavior in low density plasmas, and MHD (or electrohydrodynamic[5]) behavior in high densities – avoiding numerical singularity in the first case, and plasma period time numerical time step limitations in the second. The code allows for external drive and load circuitry. More details are given in our companion paper for this conference[6].

To understand wave penetration observed in our switch simulations we note that the electron momentum equation treated in ANTHEM can be rearranged to

$$\mathbf{E} = -\frac{m_e}{e}\frac{\partial \mathbf{v_e}}{\partial t} - \frac{m_e}{e}\mathbf{v}_e \cdot \nabla \mathbf{v}_e - \frac{\nabla(n_e \kappa T_e)}{e n_e} - \frac{\mathbf{v}_e \times \mathbf{B}}{c}. \tag{1}$$

Temporarily assuming fixed ions and neglecting displacement current, we obtain from Ampere's law

$$\mathbf{v}_e = -\frac{e}{m_e c}\lambda_B^2 \nabla \times \mathbf{B}, \tag{2}$$

in which $\lambda_B \equiv c/\omega_p$, $\omega_p^2 = 4\pi n_e e^2/m_e$. These combine with Faraday's law to yield

$$\begin{aligned}\frac{\partial \mathbf{B}}{\partial t} =& \nabla \times [\frac{\partial}{\partial t}(\lambda_B^2 \nabla \times \mathbf{B})] + \nabla \times [\mathbf{v}_e \cdot \nabla(\lambda_B^2 \nabla \times \mathbf{B})] \\ &+ c\nabla \times [\frac{\nabla(n_e \kappa T_e)}{e n_e}] + \nabla \times (\mathbf{v}_e \times \mathbf{B}).\end{aligned} \tag{3}$$

This B-field equation manifests shock-like solutions penetrating axially into the switch plasma along density gradients at a speed

$$u_w \equiv \frac{cB_z}{4\pi e}\frac{\partial}{\partial y}(\frac{1}{n_e}) \tag{4}$$

(cartesian geometry - y in the A-K direction), and in uniform cylindrical switch plasma at the speed

$$u_{wc} = -\frac{cB_\phi}{4\pi e}(\frac{2}{rn_e}), \tag{5}$$

where r measures radial distance from the switch centerline.

Our simulational analysis of the LANL POS has been initiated with studies of the idealized switch geometry of Fig. 4. The bottom central electrode was the anode at 1.25 cm. The outer cathode was set at 4.75 cm. The fill plasma was 10 cm long. We have examined fill densities from 10^{13} to 10^{14} electrons/cm^3; Figure 4 is for the highest density. To economize, we ran the drive pulse up to 1.6 T in just 0.1 ns, and then watched the "end game" of magnetic field penetration. Frames(a) and (b) give B_ϕ contours showing penetration of the whole fill plasma in by 10 ns. The 1/r drop off in field intensity near the generator is clearly evident in frame (b). Frame (c) shows axial B-field cuts taken at r = 1.67, 2.93 and 4.61 cm.

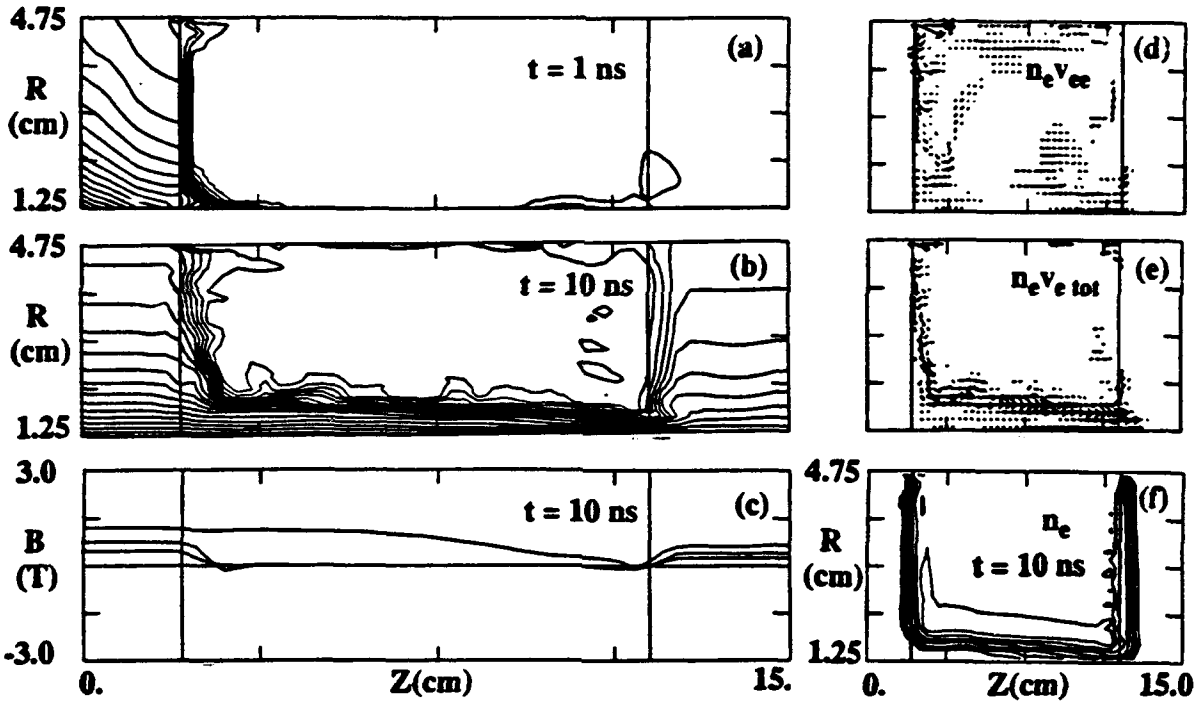

Fig. 4. With positive polarity anode penetration is dominant.

Figure 4(d) shows the emitted cathode electron vector flux, and (e) shows that the total flux runs down along the drive side of the plasma and then out above the anode. Finally (f) shows that the electrons are noticeably pulled away from the anode by 10 ns. The calculations are for a C^{++} fill plasma.

The most significant observation is that penetration occurs extremely quickly for the specified conditions. It proceeds by a density gradient wave obeying Eq. (4), since he anode plasma interface is effectively a layer of steep density rise for entering electrons, and $B_\phi > 0$, so $u_w > 0$. The density gradient waves depend linearly on the field magnitude, so with a more physical linearly rising field over the conduction time, penetration should take 2 times longer. This is still only 20 ns. The wave speed is inversely proportional to density,

so a POS density of 2×10^{15} electrons/cm^3 would be needed for a 400 ns conduction time. Modifications in our plasma source system may be needed to supply this much plasma.

Why is the penetration so rapid? For one thing, the relative field intensity with the cylindrical geometry is three times larger at the inner radius, and the MHD force driving the anode ion gap correspondingly 9 times stronger, than with conventional polarity. Thus, tendencies to form a cathode erosion gap are weaker.

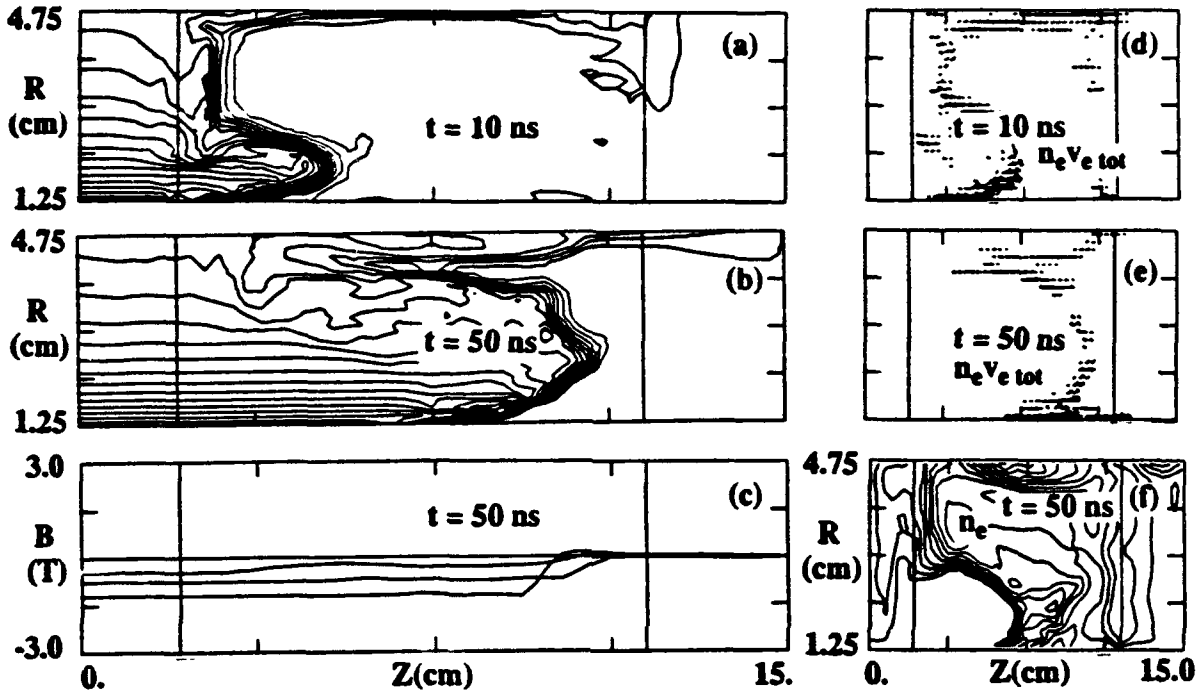

Fig. 5. Opening characteristics with conventional polarity.

Much can be learned from running the same calculation in conventional polarity with the central electrode negative. Results for this case are collected in Fig. 5. Here we see familiar behavior that has been reported elsewhere[7]. The anode penetration is present, but weak (due to the lower field intensity and magnetic pressure). Most of the penetration is associated with a current loop that starts near the cathode, and grows with time to bulge predominantly in the center of the switch. This is evident in the field contours (a,b) and the corresponding electron flux vectors (d,e). By 10 ns, only a third of the plasma has been penetrated. At 50 ns, frames (b) and (c), the current sheet has nearly reached the back side of the plasma. A density gap, with an associated potential hill[6], forms near the cathode, as evident in (g).

So the predicted opening process is at least five time slower with conventional than with reversed polarity. The anode opening from the density gradient waves, Eq. (4), is de-emphasized relative to opening through cathode gap formation and opening through the cylindrical EHD waves of Eq. (5). Note that the electron emission starts at the leading edge of the cathode gap. But by 50 ns the current sheet no longer traces back along the upper edge of the density gap; instead it sweeps forward through the largely uniform collisionless, plasma and through the radial center of the plasma toward the load. By 50 ns the rightmost point on the sheet has penetrated nearly twice as deep as has the density gap. Concomitantly, some penetration has occurred via the anode density layer

mechanism, as evident from frame (b).

Final opening occurs at 62 ns (not shown). We can again assume the opening with a linearly rising pulse would require $2 \times 62 = 124$ ns. The opening consists of a final shift[8,9] of the current sheet to the back side of the fill plasma, encountering progressively less density until relativistic speed limits on the electrons prohibit continuance of a sufficient current to shield against its penetration into the load region. Magnetic insulation ensues as field builds, returning a growing fraction of the electrons to the cathode. Reference 8 showed that the competition between anode layer and cathode gap mechanisms could lead to slow opening. Its scaling studies indicated a conduction time varying as n_e^p, p = 0.5 to 0.33, with conventional polarity. While this should now receive additional scrutiny to account for the detailed combination of opening mechanisms active with various POS geometries, at face value it suggests that a 400 ns conduction time would require a 10 to 33-fold increase in density, i.e. $n_e = 10^{15}$ to 3×10^{15} electrons/cm^3 density fill. This is compatible with the density needed under reversed polarity for a 400 ns conduction time.

Possible access to longer conduction times at relatively lower densities suggests that for ion beam generation some means for conversion to the conventional polarity should be considered. Alternatively, with positive polarity retained, at least the inner anode radius can be increased, for slower wave penetration at achievable fill densities. Further simulational optimization of POS the parameters should prove profitable.

References

1. G. Cooperstein and P. Ottinger, IEEE Trans. on Plasma Science, **PS-15**, 629 (1987).
2. H. Bluhm, et al., ibid., p 654.
3. V. Bystritskii, I. Lisitsyn, and A. Sinebrjukhov, this conference, PI-20c.
4. M. Sarfaty et. al., this conference, PI-41.
5. R. J. Mason, J. Comput. Phys. **71**, 429 (1987); and R. J. Mason and C. W. Cranfill, IEEE Trans. Plasma Sci. **PS-14**, 715 (1987).
6. R. J. Mason, this conference, PI-24.
7. R. J. Mason, M. E. Jones, J. M. Grossmann and P. F. Ottinger, Phys. Rev. Lett. **61**, 1835 (1988); and J. Appl. Phys. **64**, 4208 (1988).
8. R. J. Mason, M. E. Jones, and C. Bergman, "ANTHEM Simulation of Plasma Opening Switches," in *Proceedings of the 7th IEEE Pulsed Power Conference,* Monterey, CA June 11-14, 1989, IEEE Cat. No. 89CH2678-2, p. 255.
9. R. J. Mason, P. Auer, R. N. Sudan, B. Oliver, J. Greenly, C. Seyler, and L. Adler, "Theory and simulation of Laboratory Plasma Opening Switches," in *Proceedings of the 8th IEEE Pulsed Power Conference*, San Diego, CA, June 17-19, 1991, IEEE Cat. No. 91CH3052-8, p. 529; and R. J. Mason, P. L. Auer, R. N. Sudan, B. V. Oliver, C. E. Seyler, J. B. Greenly, "Non-Linear Magnetic Field Penetration in Opening Switch Plasmas," submitted to Phys. Fluids B, April 27, 1992.

LONG CONDUCTION TIME PLASMA OPENING SWITCH EXPERIMENTS AT SANDIA NATIONAL LABORATORIES*

M.E. Savage, W.W. Simpson
Sandia National Laboratories, Albuquerque, NM 87185

G.W. Cooper
University of New Mexico, Albuquerque, NM 87131

M.A. Usher
General Technology Corporation, Albuquerque, NM

Abstract

Sandia National Laboratories has undertaken an ambitious program to reduce the size and cost of large pulsed power drivers. The program basis is inductive energy storage and Plasma Opening Switches (POS). Inductive energy storage has well known advantages, including increased efficiency and reduced stress on the vacuum interface. The Sandia approach is to retain the reliable and efficient Marx generator and the temporal pulse compression of the water dielectric capacitor. A triggered closing switch, developed at Sandia, transfers the capacitor charge into the energy storage inductor. This approach has several advantages, including relaxed requirements on Marx jitter and inductance, and much faster current risetime in the energy storage inductor.

The POS itself is the key to the Sandia program. The switch design uses an auxiliary magnetic field to inject the plasma and hold it in place during conduction. After opening begins, the self magnetic field of the power pulse pushes on the plasma to increase the opened gap. We use magnetic pressure because we desire POS gaps of several cm. Typical plasma opening switches do not achieve large gaps. Improved opening allows more efficient energy transfer to loads.

We will present results from recent experiments at Sandia. Our driver will presently supply 650 kA with a 240 ns risetime to the input of the POS. The storage inductor is a 17 Ohm magnetically insulated transmission line (MITL) that is five meters long. We will discuss the ways in which magnetic fields influence the POS, and the ways in which we control the magnetic fields.

1. Introduction

Plasma Opening Switches (POS) are attractive for pulsed power generators[1-4]. Basically this is because magnetic energy storage can be done at much higher energy densities than can electrostatic energy storage. Electrostatic energy storage is done with voltage-charged pulse-forming lines and closing switches. Magnetic energy storage is done with current-charged pulse-forming lines and opening switches. The lack of efficient opening switches has been the major limitation to the application of inductive storage-based pulsers.

Most plasma opening switch research has been done with direct injection of plasma from flashboards into the transmission line gap. This has the advantage of simplicity, but requires a relatively large mass of plasma for long conduction times. This large mass of plasma tends to slow the opening rate of the switch. For this reason, we have constructed a plasma opening switch that uses magnetic fields to solve some of the problems of simpler switches.

2. The Experiment

Figure 1 shows the major features of the Sandia Long Conduction POS experiment.

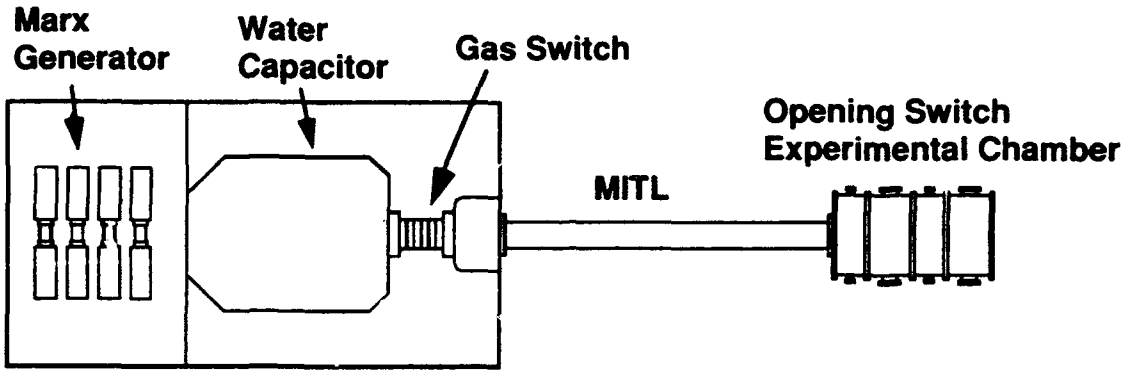

Figure 1. The MITE Opening Switch Research Facility

The Marx generator is 32 stages of 100kV capacitors and is the standard 'PBFA' design[5]. Each capacitor is 3.1 microfarads. The Marx therefore stores roughly 500 kJ at full charge. The inductance of the Marx is 5.5 microhenries. A 600 kV Marx triggers the main Marx[6]. A 100 kV pulse generator fires the trigger Marx.

The Marx charges the water-dielectric intermediate storage capacitor in about 1 microsecond. This capacitor is 42 nanofarads and will tolerate slightly over 2 megavolts in positive polarity. A triggered gas closing switch commutes the intermediate storage capacitor charge into the MITL. The gas switch is the same as those used on PBFA-II[7], except modified for electrical trigger (the PBFA-II switches are laser triggered). A 100 kV pulser triggers the gas switch. The main Marx jitter is less than 10 ns. The jitter of the closing gas switch is about 2 ns.

The energy storage inductor is a MITL 5.2 meters long. The vacuum impedance is 17 Ω. The one-way wave transit time of the MITL is 17 ns. With a perfect opening switch and a load matched to the MITL impedance, the output pulse width would be 34 ns. The equivalent lumped inductance in vacuum is 290 nanohenries. The time to peak current with the POS closed is 240 ns. The POS is near the electron beam load. Eight cathode blades opposite graphite anode blocks make up the electron beam load. The center conductor of the MITL is at positive voltage. A 3 microhenry inductor at the load end of the MITL isolates diagnostic signals from the center conductor.

Diagnostics consist of small derivative-responding magnetic flux loops to detect current, water- and vacuum-voltage monitors, nuclear activation, and ion time-of-flight monitors. We use high-quality passive integrators and software droop correction for the derivative-responding monitors. The current monitors are a standard at Sandia and have GHz bandwidth and typical sensitivities of 10^{12} A/V/s/m. There are three current monitors per axial location, equally spaced. The signals are individually digitized and numerically averaged. There are cathode current monitors at four axial locations, and anode current monitors at 2 axial locations. The voltage monitors consist of standard electric field monitors and Electron Launching Voltage Monitors[8]. A transmission line model[8] corrects voltage measured in the water to the load location.

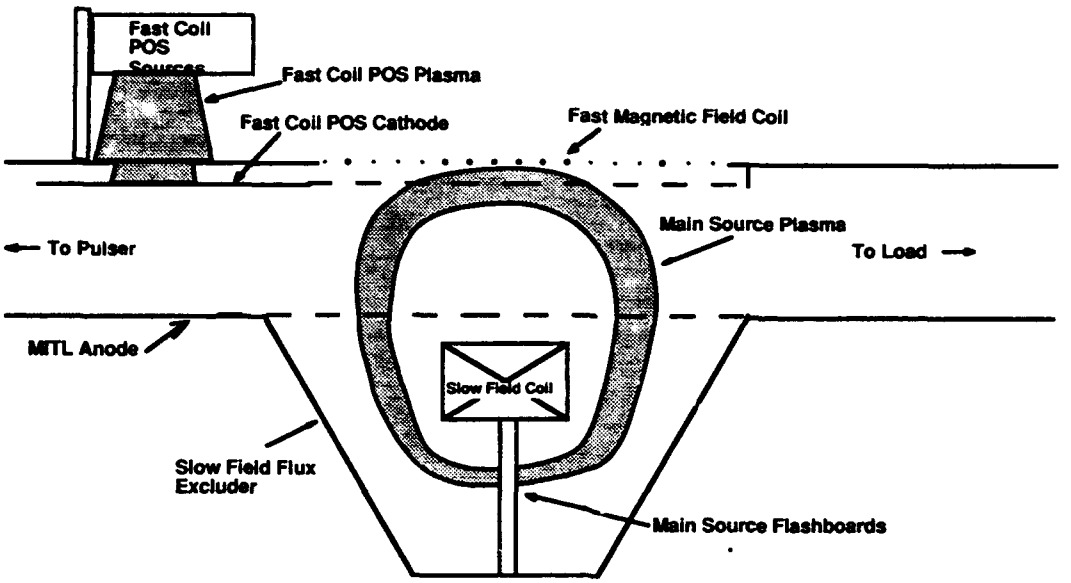

Figure 2. The Sandia Long Conduction Plasma Opening Switch

The switch is shown in Figure 2. Experiments on SuperMITE used a similar POS at 35 ns conduction times[9]. The vacuum impedance in the switch region is 20Ω; the inner conductor diameter is 25 cm and the outer conductor diameter is 36 cm. A 2900 μF capacitor bank energizes the 13 turn slow magnetic field coil to 25 kA on typical experiments. The time to peak magnetic field is 550 microseconds. The plasma source flashboards are etched on fiberglass circuit board. Sixteen each 40 nanofarad pulse charged capacitors near the flashboards provide a fast, high current drive for plasma production. We coat the flashboard gaps with a mixture of graphite and deuterated polystyrene. The polystyrene both increases plasma production by raising the flashboard breakdown voltage and adds deuterium to the plasma for nuclear activation measurements. The D.C. charged plasma source capacitor and switch are inside the hollow center conductor of the MITL. A regulated power supply charges this 2.5 microfarad capacitor to 10 kV, which on firing charges the flashboard capacitors to about 13 kV in 300 ns. At this point, the flashboards break down and plasma is produced. The slow magnetic field guides the flashboard plasma into the transmission line gap. Neutrals do not follow the field lines into the gap. The slow magnetic field also holds the switch plasma in place during conduction. The magnetic field from the slow coil is comparable to the magnetic field from the power pulse current.

The power pulse current energizes the fast magnetic field coil. The fast coil forces an axial component to the power pulse magnetic field. This axial fast field is in the same direction as the slow magnetic field. The vacuum inductance of the fast coil is about 25 nH, or 10 percent of the total MITL inductance. The inductance of the fast coil with plasma fill is lower due to field exclusion from the plasma. A second POS, called the Fast Coil POS, shunts the fast magnetic field coil. Axial vanes connect the Fast Coil POS cathode electrode to the downstream side of the fast coil. These vanes allow axial magnetic field penetration. When the Fast Coil POS opens, the entire machine current flows through the fast magnetic field coil. This fast magnetic field pushes against the slow magnetic field, sweeping the main POS plasma with it. By varying the amount of plasma injected into the Fast Coil POS, it is possible to vary the point at which current starts to flow through the fast coil. In this manner, we can show the effect of the fast magnetic field on the opening of the main POS.

3. Operation of the Opening Switch

The power pulse arrives at the plasma opening switch with the slow magnetic field at peak magnitude and the switch gaps filled with plasma. Plasma mass is controlled by changing the filltime; electrical monitors at the flashboards show when the flashboards actually fire. Typical main plasma filltimes are 2.0 to 2.5 μs; Fast Coil plasma filltimes of 1.2 to 2.0 microseconds are typical. Chamber pressure is normally 10^{-6} Torr at shot time.

Figure 2 shows the POS configuration when the power pulse begins. Both the Fast Coil plasma and main plasma are in place, and the power pulse current flows through both. The slow coil magnetic field is at peak and the fast coil current is zero. Plasma short-circuits the transmission line at this time.

At some point, set by the Fast Coil POS filltime, the Fast Coil POS begins to open. With the Fast Coil POS open, machine current flows through the fast coil before flowing through the main switch plasma. This causes a fast magnetic field in the same direction as the slow magnetic field, and the fast magnetic field pushes on the (flux-excluding) plasma. This opens the switch. The switch also will open with no fast coil current, although later and slower.

With the main plasma pushed from the cathode, load current begins to flow. All load current flows through the fast coil. Load current causes further opening of the switch. Opening a larger gap will allow higher voltage to be supported. We determine the gap that the POS ultimately achieves from the time-dependant inductance of the fast coil and electron flow downstream of the opening switch. If the switch gap is small, there will be a significant difference between anode and cathode currents.

4. Results

The present experiments use 68 kV Marx charge voltage; the Marx energy is therefore about 200 kJ. Figure 3 shows currents measured on an experiment with the POS feeding a 40 nH short-circuited MITL.

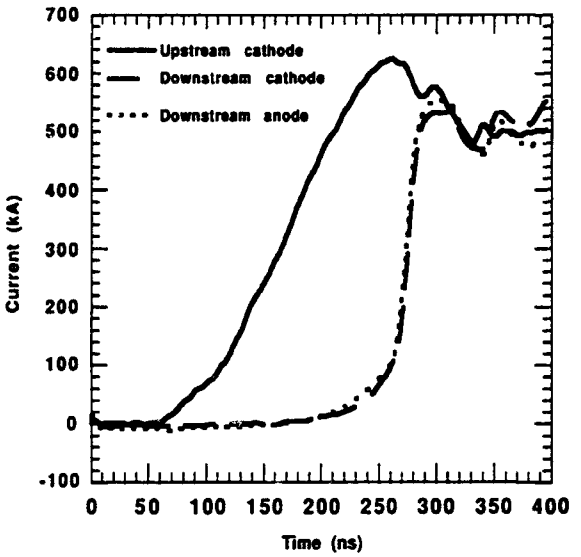

Figure 3. Currents with shorted load.

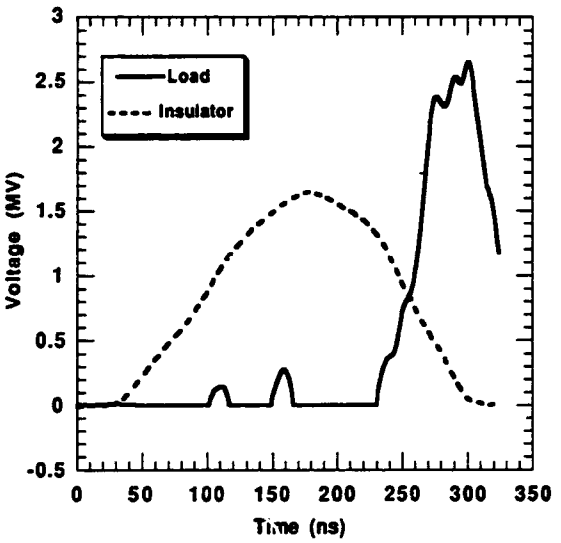

Figure 4. Insulator and load voltage for electron beam load.

The peak POS voltage is 1.7 MV for this inductance. Voltage across the fast coil before the main switch opens

causes the slowly rising foot in the downstream current. On this experiment the Fast Coil POS started to open at 200 ns, and the main POS opened at 260 ns. Given the downstream current measured in a 40 nH inductor, the 100 kA after 60 ns shows about 70 kV across the output of the POS before rapid opening begins. This voltage is not fully understood now, but is related to the onset of current in the fast coil.

Figure 4 shows load voltage for a test with an electron beam load. The voltage monitor is located close to the POS; a 3.7 meter ion time-of-flight monitor corroborates the peak voltage. The time-of-flight monitor sees ions accelerated out of the POS. Peak load voltage is 2.7 MV; peak load voltage occurred when the interface voltage had fallen below 100 kV. The load voltage risetime in Figure 4 is somewhat slow due to inductive drop between the voltage monitor and the switch; this has not been corrected in this Figure.

If magnetic fields control the POS, there is hope for improving the opening characteristics. A switch based solely upon plasma mass is less promising because increasing the conduction time requires raising the plasma mass, and this slows opening and reduces efficiency. Figure 5a shows that the slow magnetic field controls the Sandia switch. Microwave interferometry data[9] show that plasma density is the same for this range of magnetic field values. Notice that two plasma filltimes are shown. The reduced plasma fill tests opened sooner for the same flux; there will always be some dependance on plasma mass.

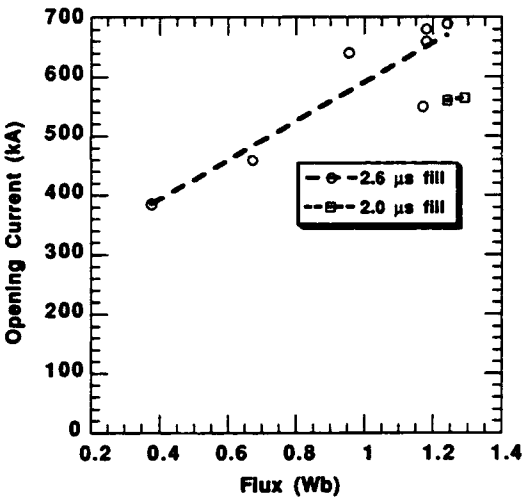

Figure 5a. Opening current vs. slow coil flux.

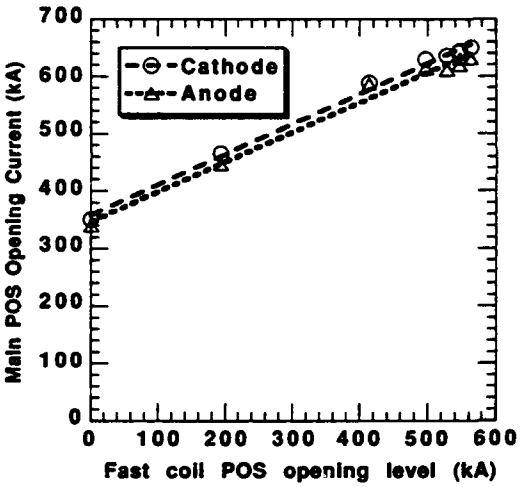

Figure 5b. Opening current vs fast coil POS opening level.

Higher slow coil flux allows higher opening currents with no increase in injected plasma mass. Plasma mass is the major deterrent to rapid and complete opening. As mentioned before, the slow magnetic field also holds the plasma in place during conduction.

Figure 5b shows the effect of fast coil current on main switch opening level, with constant injected plasma mass. The independent variable is the upstream current when current begins to flow in the fast coil. Zero Fast Coil POS opening level is when current always flows in the fast coil. For high value of Fast Coil POS opening level, current does not flow in the fast coil until machine current is high. These data show that the fast coil does push on the main POS plasma. This means opening can be controlled with a fast magnetic

field. Supplying the fast magnetic field with an external pulser would allow command-triggering of the POS opening. This triggering ability makes this POS unique. Unfortunately, Figure 5b shows that the present system would require about one-third of the switched current for a trigger. This means a 250 kA trigger pulser would be needed for MITE. We are presently looking at ways to reduce this requirement.

5. Conclusions

We have presented results from the Sandia Long Conduction Plasma Opening Switch program. The pulser delivers 650 kA peak in 240 ns; the POS conducts this pulse and opens in 30 ns or less. The switch is unique in that we use magnetic fields to supplement plasma mass. Magnetic fields, being massless, are desirable because a high magnetic field will not slow the opening rate. High plasma mass will slow the opening rate. Faster and more complete opening will make a more efficient opening switch. In addition, the Sandia switch is unique in its ability to be command triggered. This may be important for synchronizing multiple modules.

*This work supported by the U.S. D.O.E. under Contract Number DE-AC04-76DP00789.

References.

1. B.V. Weber, R.J. Commisso, G. Cooperstein, J.M. Grossmann, D.D. Hinshelwood, D. Mosher, J.M. Neri, P.F. Ottinger, S.J. Stephanakis; *IEEE Trans. Plasma Sci.*, **PS-15**, Dec. 1987, p. 635.

2. G.A. Mesyats, S.P. Bugaev, A.A. Kim, B.M. Koval'Chuk, V.A. Kokshenov; *IEEE Trans. Plasma Sci.*, **PS-15**, Dec. 1987, p. 649.

3. H. Bluhm, K. Böhnel, P. Hoppé, H.U. Karow, D. Rusch; *IEEE Trans. Plasma Sci.*, **PS-15**, Dec. 1987, p. 654.

4. S. Miyamoto, N. Yugami, K. Imasaki, S. Nakai, C. Yamanaka; *IEEE Trans. Plasma Sci.*, **PS-15**, Dec. 1987, p. 667.

5. L.X. Schneider, *Proceedings of the 4th IEEE Pulsed Power Conference*, (IEEE, Piscataway, NJ, 1983), No. 83CH1908-3, p. 202.

6. B.N. Turman, T.H. Martin, E.L. Neau, D.R. Humphreys, D.D. Bloomquist, D.L. Cook, S.A. Goldstein, L.X. Schneider, D.H. McDaniel, J.M. Wilson, R.A. Hamil, G. W. Barr, J.P. VanDevender, *Proceedings of the 5th IEEE Pulsed Power Conference*, (IEEE, Piscataway, NJ, 1985), No. 85C2121-2, p. 155.

7. B.N. Turman, D.R. Humphreys, C.N. Richards, *Proceedings of the 7th IEEE Pulsed Power Conference*, (IEEE, Piscataway, NJ, 1989), No. 89CH2678-2, p. 555.

8. M.E. Savage, C.W. Mendel, Jr., T.W. Grasser, W.W. Simpson, D.M. Zagar, Rev. Sci. Instrum. **61,** 3812 (1990).

9. C.W. Mendel, Jr., M.E. Savage, D.M. Zagar, W.W. Simpson, T.W. Grasser, J.P. Quintenz, J. Appl. Phys., **71**, 3731 (1992).

PLASMA EROSION OPENING SWITCH USING LASER-PRODUCED PLASMA

H.Akiyama, T.Fukuzawa, S.Ihara, S.Katsuki and S.Maeda
Department of Electrical Engineering and Computer Science
Kumamoto University
Kumamoto 860, JAPAN

Abstract - An opening switch which can repeatedly conduct a large current and then rapidly interrupt this current is necessary to construct a practical inductive energy storage pulsed power generator. Though the plasma erosion opening switch (PEOS) can interrupt a large current rapidly, the effective number of switch operations is limited because of the decrease of the carbon sprayed on the insulator with each shot. Here, a PEOS using a laser-produced plasma, which can possibly be operated for hundreds of thousands of shots without maintenance, is studied experimentally.

Introduction

Practical pulsed power generators with inductive energy storage, which can be made extremely compact and light-weight, would be of great benefit for many pulsed power applications. The opening switch is the key element in developing such a system. The requirements of the opening switch are to conduct large currents, to interrupt those currents rapidly and to operate repeatedly without maintenance. The plasma erosion opening switch (PEOS) [1]-[3] is one of the opening switches that are expected to satisfy these requirements. Plasma guns [4] and flashboards [5] sprayed with carbon have been used as plasma sources, but the lifetimes of these sources are limited to 10's of shots because the carbon decreases with each shot. Moreover, the parameters of the plasmas produced by plasma guns and flashboards change somewhat with every shot. Plasma sources which can produce plasmas with the same parameters repeatedly for many shots are required to make the PEOS practical. A PEOS using a laser-produced plasma, which has the capability of being operated hundreds of thousands of shots without maintenance, was proposed[6].

In this paper, the operation of PEOS using a laser-produced plasma is studied experimentally. The timing between firing the laser to produce the

plasma and discharging the capacitors is changed, and also the inner and outer diameters of conductors in the PEOS region are changed.

Experimental apparatus and method

Figures 1(a) and (b) show a schematic diagram of the experimental apparatus of the PEOS and its equivalent circuit. The experimental apparatus consists of a set of capacitors with C = 0.1 μ F, a triggered spark gap (TSG), the inductor L_s of 436 nH, which is in a coaxial configuration, the PEOS and a short circuit load L_l with an inductance of 24 nH. The polarity of inner conductor is negative, and the charging voltage V_c of the capacitors is 30 kV. The outer conductor in the PEOS region is made of a stainless mesh with 97.5 % transparency. The laser used for producing the plasma is a Q-switched ruby laser (NEC SLG2018) with a peak power and FWHM of 40 MW and 20 ns, respectively. The laser light is focused on the carbon surface by a lens placed outside the vacuum chamber, and the produced plasma enters the switch region from only one direction. The carbon plate can be rotated before each shot.

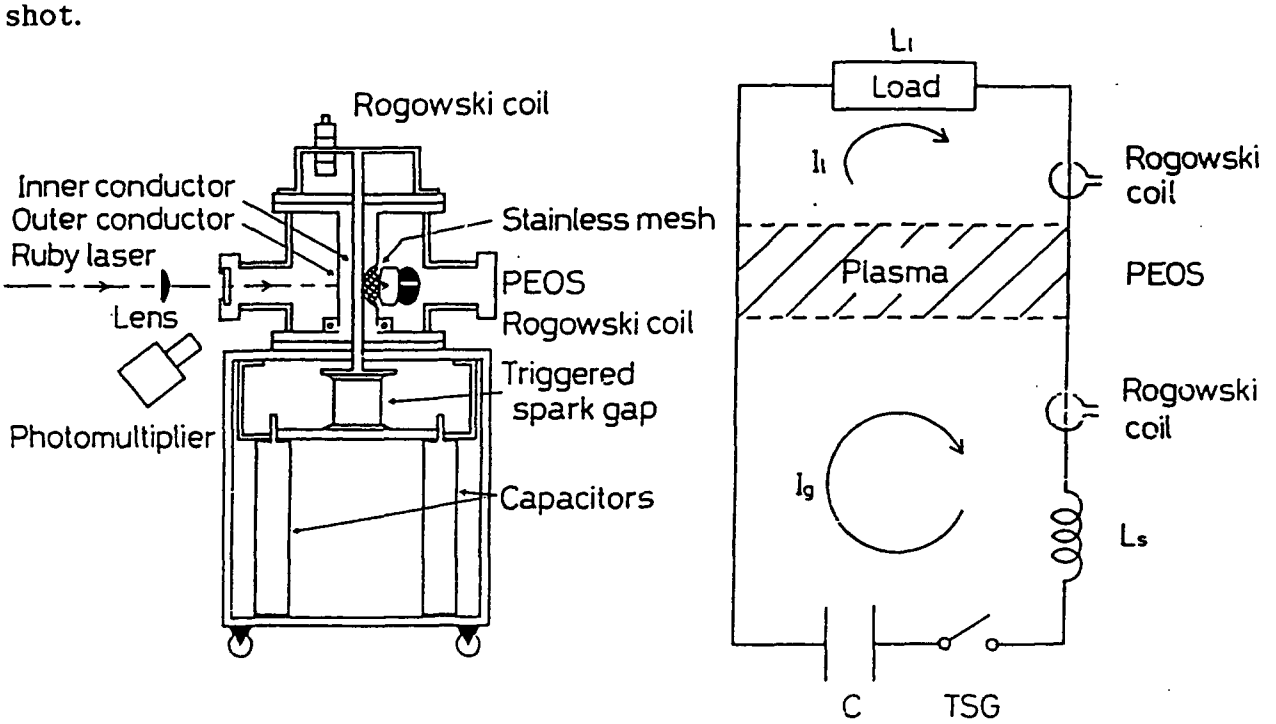

Fig.1. (a) Schematic diagram of the experimental apparatus for the PEOS using laser-produced plasma, (b) equivalent circuit of the apparatus.

During PEOS experiments the TSG was triggered after the ruby laser was fired. The delay time Δ t, measured from the time when the laser begins to oscillate until the time when the source current I_s begins to flow, is varied in the experiments. The load current I_l and the source current I_s are measured with Rogowski coils, and the laser light is observed using a photomultiplier tube set up outside of the vacuum chamber. Ion current densities J_i of the laser-produced plasmas were measured by a single biased Faraday cup placed between 10 cm and 20 cm from the carbon target.

Experimental results

Figure 2 shows waveforms of $z \cdot n_i$ 10cm and 1.95cm (at the cathode surface) away from the carbon target, which are calculated from J_i and the plasma velocity, where z and n_i are the ionic charge state and the ion density. The laser begins to oscillate at t=o.

Figures 3(a)-(d) show typical waveforms of I_l (solid line) and I_s (dashed line) for different Δ t's. For the case of Δ t smaller than about 1 μ s, the rise time decreases with the increase of Δ t. The rise time of the load current then reaches a minimum at around Δ t = 1.085 μ s. As Δ t continues to increase, though, the conduction time becomes longer and the PEOS does not open completely. From Fig.3 the switch region of the PEOS seems to be filled with a plasma having the proper parameters for switch operation when Δ t is about 1 μ s.

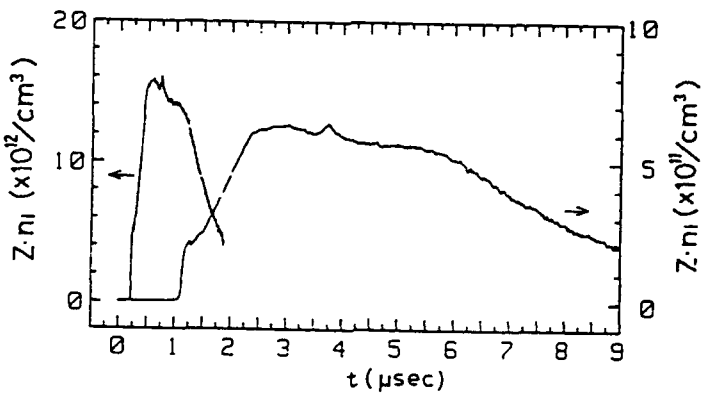

Fig.2. Waveforms of $z \cdot n_i$ at 10cm and 1.95cm away from the carbon target.

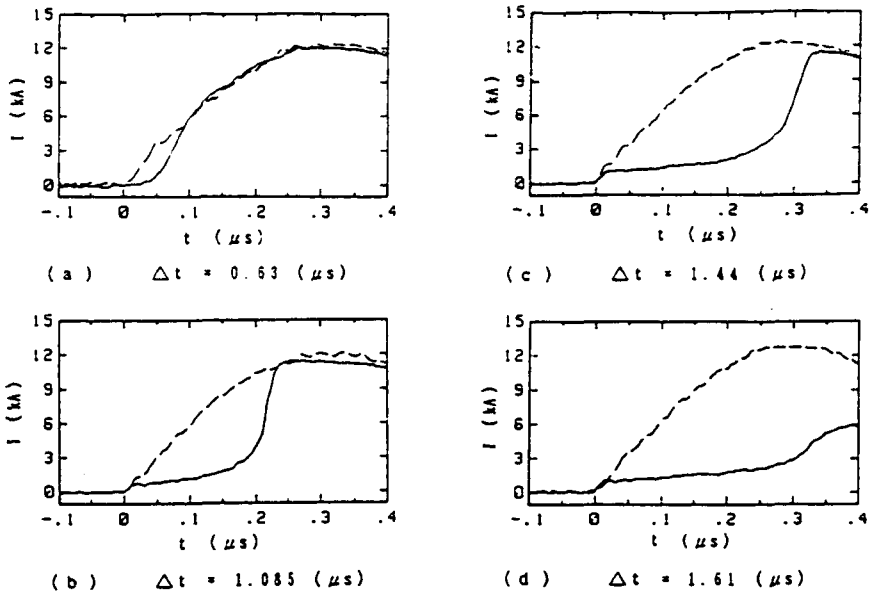

Fig.3.Typical waveforms of I_1 (solid line) and I_σ (dashed line) for different Δ t's.

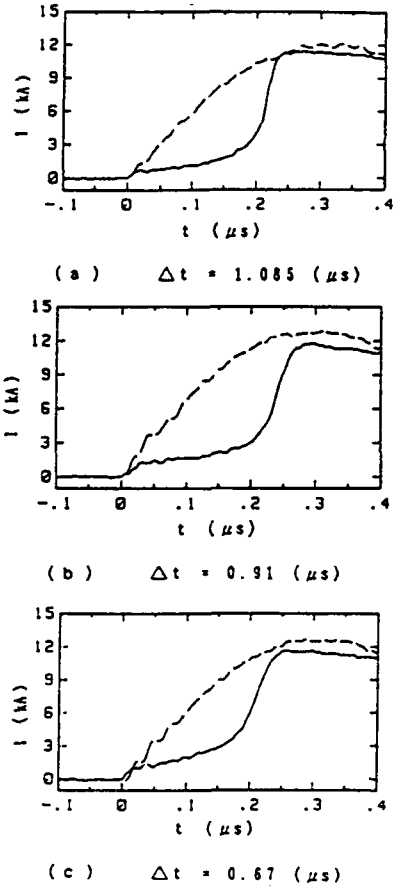

Fig.4. Waveforms of I_1 and I_σ in the inner diameters of (a) 3mm, (b) 6mm, (c) 8mm.

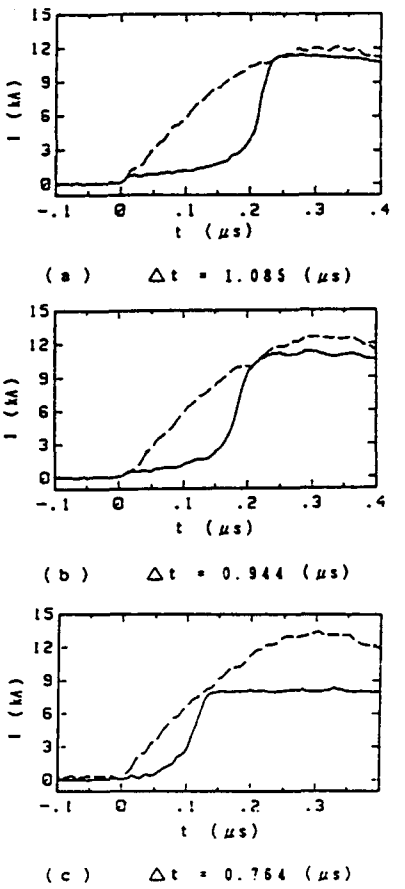

Fig.5. Waveforms of I_1 and I_σ in the outer diameters of (a) 22mm, (b) 18mm, (c) 12mm.

Figures 4(a)-(c) show waveforms of I_1 and I_2 in the diameters 3mm, 6mm, 8mm of inner conductors respectively. The diameter of the outer conductor is 22mm, and the position of carbon target is 10mm away from the outer conductor. The waveform with the minimum rise time is selected from the waveforms in different Δ t's for the same configuration of conductors. The rise time increases with the increase of the diameter of inner conductor.

Figures 5(a)-(c) show waveforms of I_1 and I_2 in the diameters 22mm, 18mm, 12mm of outer conductors respectively. The diameter of the inner conductor is 3mm, and the position of the carbon target is 10mm away from the outer conductor. The conduction time decreases with the decrease of the diameter of outer conductor.

Discussion and conclusion

The lifetimes of conventional plasma sources, such as plasma guns and flashboards, are several shots to several 10's of shots. In addition, several shots are necessary for conditioning after installing the plasma sources. However, the plasma parameters tend to vary from shot to shot even after conditioning the source, since the conditions of carbon sprayed on the surface of the insulator change. Therefore, it is difficult to make a PEOS which can operate repeatedly and give the same performance every shot. The laser-produced plasma as the plasma source for PEOS's has little variation in plasma parameters from shot to shot because the plasma is produced by focusing a laser on a target which can be rotated slightly before each shot. If the diameters of the carbon target and laser beam are 5 cm and 100 μ m, respectively, and the laser beam is focused only once on a particular spot, a plasma can be produced up to two hundred fifty thousand times, which is greater than the lifetime of some capacitors. Thus, a practical opening switch which can operate repeatedly might be obtained by using a PEOS with a laser-produced plasma.

From experiments performed with a PEOS using a laser-produced plasma, it was observed that the rise time of the load current decreased significantly for the proper Δ t between firing the laser to generate the plasma and triggering the TSG to discharge the capacitors. The diameters of inner and outer conductors give the large influence on the performance of PEOS.

The advantages of the PEOS with a laser produced plasma are that it becomes possible to select more suitable plasma species for PEOS operation by

changing the target material, the plasma parameters may be varied by changing the laser power and the PEOS can be operated for many shots under the same conditions. These advantages will help us to compare experimental results with theoretical results for PEOS operation.

References

[1] B. V. Weber, R. J. Commisso, P. J. Goodrich, J. M. Grossmann, D. D. Hinshelwood, J. C. Kellogg, and P. F. Ottinger, "Investigation of Plasma Opening Switch Conduction and Opening Mechanism," IEEE Trans. Plasma Sci., vol.19, No.5, pp. 757-766, 1991.

[2] N. Shimomura, H. Akiyama and S. Maeda, "Compact Pulsed Power Generator by an Inductive Energy Storage System with Two-Staged Opening Switches" IEEE. Trans. Plasma Sci., vol.19, No.6, pp. 1220-1227, 1991.

[3] J. R. Goyer, "A Conduction Model For PEOS Operation Incorporating Simplified Cathode Sheath Effects," IEEE Trans. Plasma Sci., vol.19, No.5, pp. 920-925, 1991.

[4] C. W. Mendel, Jr, D. M. Zagar, G. S. Mills, S. Humphries, Jr., and S. A. Goldstein, "Carbon plasma gun," Rev. Sci. Instrum., vol.51, pp. 1641-1644, 1980.

[5] T. J. Renk, "Flashboards as a plasma source for plasma opening switch applications," J. Appl. Phys., vol.65, pp. 2652-2663, 1989.

[6] T. Fukuzawa, S. Ihara, S. Maeda and H. Akiyama, "Plasma Erosion Opening Switch Using Laser-Produced Plasma," IEEE Trans. Plasma Sci., vol.20, 1992 (in print)

Spectroscopic Investigations of a Plasma Opening Switch using a Novel Gaseous Plasma Source

M. Sarfaty, Ya.E. Krasik, R. Arad, A. Weingarten,
S. Shkolnikova, and Y. Maron.
Department of Physics, Weizmann Institute of Science, Rehovot, 76100, Israel
A. Fisher
Naval Research Laboratories, Washington D.C.

A novel gaseous plasma gun (PG) was developed for spectroscopic investigations of the plasma behavior in a cylindrical Plasma Opening Switch (POS) in the nanosecond time regime. The PG injects the plasma radially outward from inside the high-voltage inner conductor to fill the region between the two conductors. The PG uniformity, reproducibility, electron density and temperature, and plasma flow velocity were determined using floating probes, biased charge collectors, fast photography, and spectroscopic methods. The POS operation was examined for various plasma parameters for a positive polarity of the inner conductor. Eight $\dot{B}$ loops and two Rogowski coils were used to measure the upstream and downstream currents. Ion current flowing during the switch operation from the plasma through the cathode was measured by two arrays of four collimated Faraday cups placed on two opposite sides of the plasma switch. Spectroscopic observations of high spatial and spectral resolutions of various particle velocities in the plasma were made. Excited level populations, velocity distributions, and directed velocities for various ions are discussed. Measurements of a secondary plasma originating from both electrodes are presented.

I. Introduction

Plasma Opening Switches (POS) are largely used to upgrade the nanosecond and microsecond pulsed power accelerators[1-3]. Using the POS, the power on the load exceeds that of an ideal matched load due to a voltage multiplication, a sharper rise time and a shorter pulse duration. The POS operation, based on a rapid increase in plasma resistivity causing the plasma switch to open and to transfer the inductively stored energy to a downstream load, is dominated by the current-carrying plasma properties.

Our studies address the magnetic and electric field distributions during the POS operation, the particle velocity distributions, the temporal evolutions of the plasma density and temperature, and the influence of the secondary plasma formed over the electrodes on the POS operation. We are investigating these phenomena by the use of high resolution, non-intrusive spectroscopic diagnostic methods similar to those described in Refs. 4-7.

II. Experimental Setup

Accelerator and Plasma Opening Switch Configuration

Our POS is powered by a 300 kV, 100-ns-long pulse delivered by a Marx-water-line generator. The experimental setup is shown in Fig.1. A coaxial vacuum inductance (L=120nH) serves as the accelerator upstream load while a short-circuit coaxial line (L=25 nH), with inner/outer diameters of 50 mm/100 mm, serves as the POS load. The maximum current amplitude passing through a short-circuit placed at the center of the POS region was 180 kA with a rise time of 100 ns. Therefore the azimuthal magnetic field at the anode and cathode surfaces are 14.4 kG and 7.2 kG, respectively.

The plasma generated by the plasma gun (PG) is injected radially from inside the inner electrode (anode), short circuiting the inter-electrode gap. The POS chamber has four transverse and one axial optical accesses through U.V. transparent windows, which allow for radial and axial observations.

The current upstream and downstream of the POS is measured by Rogowski coils and by eight $\dot{B}$-loops, four placed downstream and four upstream of the POS. The $\dot{B}$-loops are azimuthaly separated by 90° to test the current flow symmetry. The voltage across the POS is measured by a capacitive voltage divider, corrected for the inductive voltage drop along the coaxial line between the divider and the plasma switch. The ion current density distribution along the POS axis during the conduction and the opening phases is measured by two arrays of four Collimated Faraday Cups (CFC). The CFC are placed on two opposite sides of the plasma switch at several distances from the cathode slits and are axially separated by 1.7 cm.

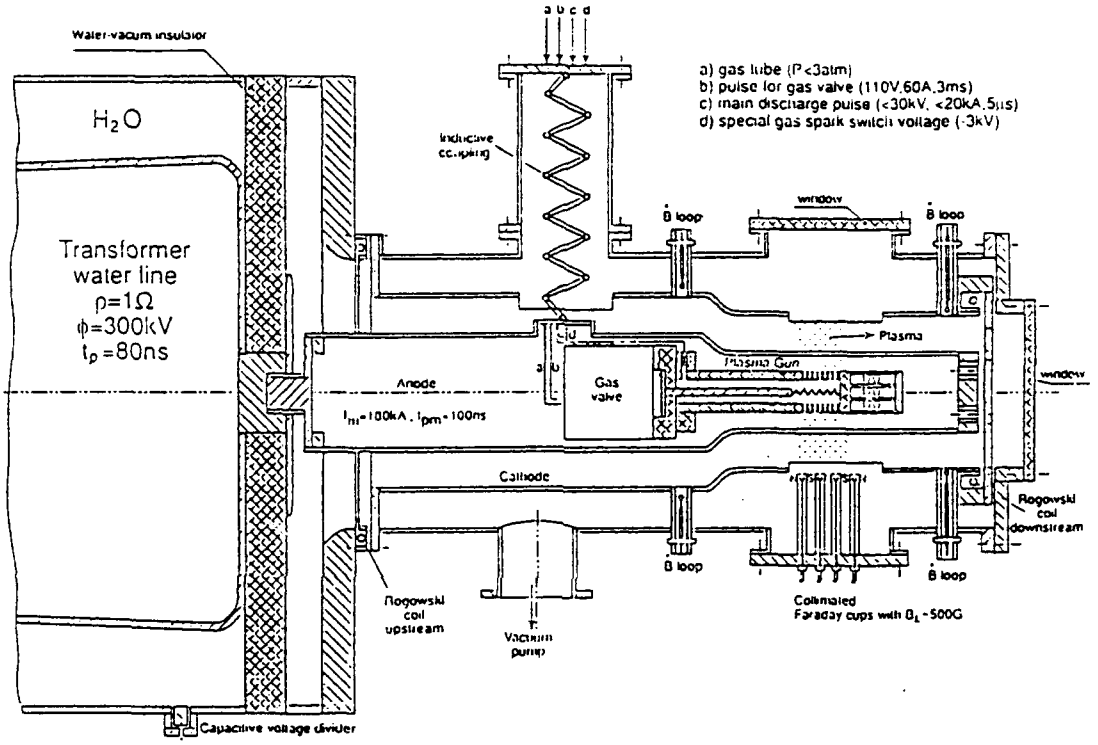

Fig. 1. Schematic of the POS experimental setup.

The Plasma Gun

The PG is composed of a fast gas valve connected to a hollow cylindrical tube with 144 capillary outlets for a radial plasma injection, see Fig.1. The fast opening of the gas valve allows the gas to propagate into the hollow cylinder and fill the capillary channels. The inner coax surface consists of a stainless steel mesh (geometrical transparency of 50%) connected through a 50 Ω resistor to the outer surface of the cylindrical tube. A high voltage pulse of several kV which lasts for few microseconds is supplied to a graphite cathode brush, centered along the hollow cylinder axis, causing gas breakdown inside the cylinder, followed by a gas breakdown inside the Alumina-made capillaries. The high current density in each capillary (a few tens of kA/cm^2) produces a highly ionized plasma which is then injected radially outward.

Spectroscopic System

The plasma light emission was collected in the axial and radial directions by fused silica optics directing the light emission to a 1-meter, 2400 grooves/mm spectrometer. The spatial and spectral resolutions were varied in the experiment between 0.5 mm to 4.0 mm and 0.1 Å to 0.35 Å , respectively. The spectral profile is measured by 10 photomultiplier tubes in a spectral range of 2000-7500 Å and a temporal resolution of 4 ns. An absolute calibration of the spectroscopic system allows for absolute level population measurements.

III. Experimental Results

Plasma Gun

An extensive study has been conducted for optimizing and characterizing the PG. The PG optimal operation regime was investigated by Penning probes for neutral gas measurements, Double Floating Probes (DFP) and CFC for electron (ion) density and temperature measurements, and by framing pictures of the PG light emission. Spectroscopic observations of various particles near the PG surface were used for determining the electron density and temperature, the particle velocity distributions, and the plasma composition. The PG reproducibility was found to be $\pm 20\%$. The PG uniformity measured at the center of the A-K gap is $\pm 10\%$ in the azimuthal direction. The axial plasma density distribution, given in Fig. 2, shows a uniform plasma density over 40 mm at 20 mm from the PG surface. Three operational regimes of the PG were observed depending on the gas pressure inside the capillaries. A capillary surface flashover regime is seen when the PG is operated without gas in the capillaries. A gas discharge regime when the gas pressure inside the capillaries is in the range of 10^{-2} to 10^{-1} Torr, and a volume discharge regime at higher gas pressures. The plasma radial flow velocity measured with DFP, CFC, and inferred from spectroscopic observations of ions and neutral particles is found to be between 1-4 cm/μs. The axial ion velocity distribution gives kinetic energies in the range of 2-15 eV, the energy is higher for higher charge states. Time dependent DFP measurements of the plasma electron density and temperature at 20 mm from the PG surface vary from 10^{12} cm^{-3} to 10^{14} cm^{-3} and from 10 eV up to 30 eV, respectively, depending on the gas mixture, gas pressure, and current density in each capillary.

Spectroscopic time dependent determination of the electron density was performed by observing the H_α and H_β spectral profiles. The Stark broadening was calculated and self-consistently convoluted with the Doppler contribution for the two lines. These calculations were best fit to the data to yield the time dependent hydrogen kinetic energy and electron density, giving 3 ± 1 eV and 5×10^{14} cm^{-3}, respectively, at 2 mm from the capillaries. The time dependent electron density is shown in Fig. 3. The highest charge state of argon, carbon and oxygen was 2. The absolute level populations measurements obtained with the aid of our collisional radiative calculations [4-7], yield the total particle densities in the plasma. Carbon particles, evidently from the electrodes were observed also when an argon gas was used in the PG. However, the amount of CI, CII, and CIII for the argon source was 1, 5, and 10 fold less than when CH_4 was used.

POS Properties

The POS parameters are given in Fig. 4. The prepulse downstream current is observed $\simeq$ 25 ns after the beginning of the upstream current, reaching $\simeq$10 kA at 70 ns, the time at which the current starts to rise. The $\dot{B}$-loops indicate symmetrical current flow.

The ion current density was measured simultaneously on two opposite sides of the POS and at four different axial locations. In all CFC traces shown in Fig. 5, a-5-ns long ion current pulse is observed within 10 ns from the start of the upstream current. The CFCs measurements at various radial distances from the cathode yield a velocity of 4×10^8 cm/s for the ions in this early short pulse. We also measured the start time of the main ion current as a function of distance along the switch. The farther the cup from the generator the later the start time was found to be. The axial dependence of the ion current start time can possibly reflect the axial evolution of the sheath between the plasma and the cathode. Thus, the development of a sheath along the cathode propagates at velocity that increases in time from $5\text{-}7\times10^7$ cm/s up to 2×10^8 cm/s.

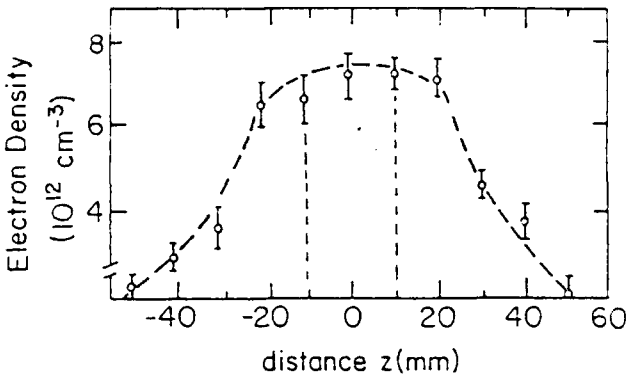

Fig. 2. The plasma density measured in the direction of the PG axis, 3 μs after gas discharge. The DFP measurements are performed at 20 mm from the capillaries. Z=0 is the axial center of the PG. The indicated dashed lines indicate the 20 mm capillaries region. The source gas used is CH_4 at 2.5 Atm. ($j_{cap} = 51kA/cm^2$).

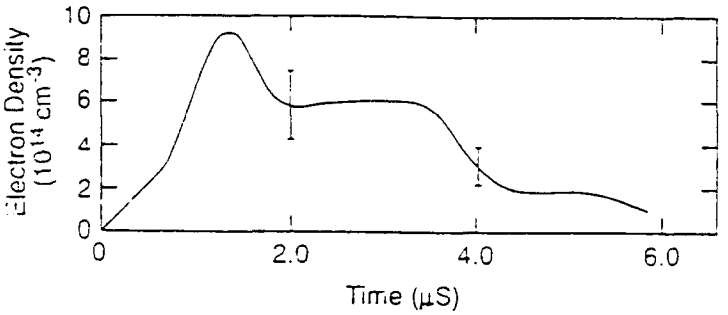

Fig. 3. Time dependent electron density averaged along the PG axis, obtained from H_α and H_β spectral profiles observed in this direction at 2 mm from the capillaries. The uncertainty in the measurements is $\pm$ 30% . The source gas used is Argon at 2.5 Atm. ($j_{cap} = 61kA/cm^2$).

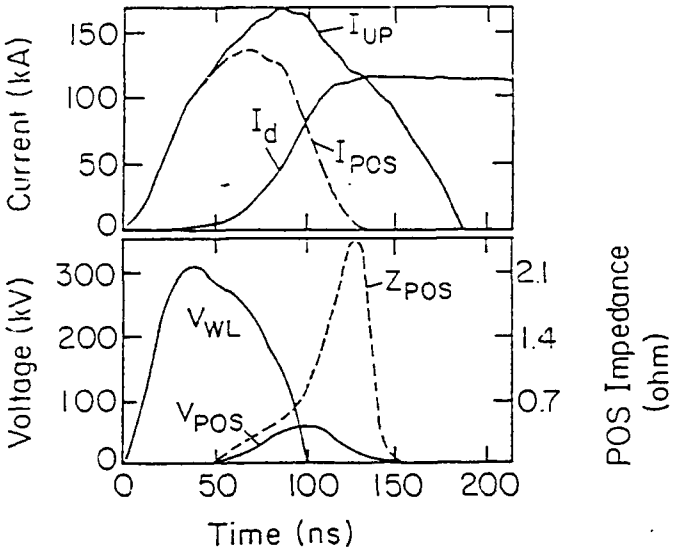

Fig. 4. Typical POS traces illustrating the positive polarity POS parameters. I_{UP}, I_D, and I_{POS} are the the upstream, downstream, and the resulting POS currents, respectively. V_{WL}, V_{POS}, and Z_{POS} are the voltage at the water-line exit, at the POS region, and the switch impedance, respectively.

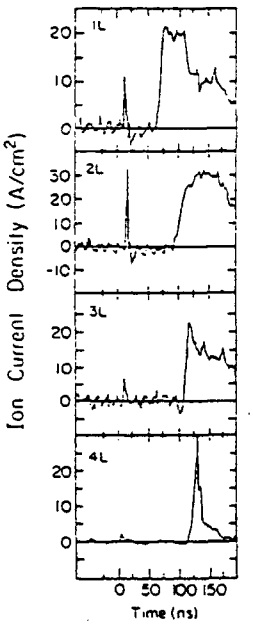

Fig. 5. Time dependent CFC traces measured at four axial locations. The CFC are placed 15 mm from the cathode surface and axially separated by 17 mm between each other. A short and early ion current pulse is observed on both sides of the POS and in all of the CFC. The main ion current pulse at later times ($\geq$ 70 ns) exhibit an axial dependent time delay.

The main spectroscopic observations discussed in the following section concern particle level populations and particle velocity distributions during switch operation, and the secondary plasma formed later in the pulse, after 0.5 μs.

Particle Level Populations

In the POS experiments the PG was operated with argon, CH_4, and CO_2 gases which enabled us to distinguish between the plasma produced from the PG gas and the plasma contributed by the electrodes. Light emission from the PG plasma at the A-K gap was too weak to be observed. The line emission rose by more than 100 times when the switch was powered by the high current. The reproducibility in the line intensities for the various particles was better than $\pm 20\%$.

We determined excited level populations during the switch operation for CI to CV, OII to OVI, and ArII to ArIV. Results for the latter are shown in Fig. 6. The excitations of the high levels of the highly ionized particles observed inside the A-K gap can not be explained by the plasma thermal electrons. These observations suggest the existence of fast electrons in the plasma with energies $\geq$ 300 eV. Radial observations of the plasma switch at different axial positions indicate a $\simeq$ 2 cm long region for the fast electrons. The fast-electron density, participating in the current conduction, estimated from the current density and the lower limit for the electron velocity (300 eV) is $\simeq 3 \times 10^{13}$ cm^{-3}. The absolute densities of the level populations decreased radially from the anode to the cathode as $1/r^2$. This can be explained by the $1/r$ variation of the initial ionic density and the resulting $1/r$ variation in the fast electron density. The axially averaged line intensities in all radial locations increase and decrease simultaneously to within $\pm$ 10 ns. We are presently studying the current channel distribution in the plasma by using various spatially resolved time-dependet line intensities, which we hope to compare in the future with those obtained from the B-field measurements based on Zeeman splitting.

Particle Velocity Distributions

The time dependent directed axial velocity of various particles in the plasma was determined by measuring the Doppler line shifts. The measurements were performed in the direction of the POS axis at various radial positions integrating over the axial extent of the plasma. The axial velocities of CI and CII rise to $\simeq 10^6$ cm/s, of CIII to $\simeq 2 \times 10^6$ cm/s, of CIV to $\simeq 6 \times 10^6$ cm/s, and of CV to $\simeq 12 \times 10^6$ cm/s. The argon axial velocity is shown in Fig. 6. The velocity rise of ArII is $\simeq 1 - 1.5 \times 10^6$ cm/s, of ArIII is $\simeq 2 \times 10^6$ cm/s, and of ArIV is $\simeq 2 \times 10^6$ cm/s. The axial velocities observed are $\simeq$ 10 times smaller than the plasma Alfven velocity. The axial velocities increase during the first 100-120 ns after the initiation of the generator current pulse and then decrease approximately with the decrease in the POS current. This temporal dependence of the axial acceleration and deceleration observed for various plasma species and in all radial positions is presently being studied.

The velocity distributions of the plasma particles are determined by measuring the Doppler spectral line broadenings. The measured spectral profile was unfolded from its instrumental broadening, while the Zeeman and Stark broadenings were estimated to have a negligible contribution to the line widths. The velocity distributions measured are found to depend on the particle mass and charge state. The kinetic energies of neutral Carbon and Hydrogen are found to be relatively low, 10-15 eV, and vary little in time. On the other hand the ionic kinetic energies are found to increase linearly in time to values comparable to their directed axial velocities. The line profile spreads in eV at 120 ns are 30 ± 5 eV for CII, 60 ± 10 eV for cIII, 100 ± 10 eV for CIV, and 140 ± 10 eV for CV. The argon line profiles shown in Fig. 6, given for the ArII, ArIII, and ArIV energies 70 ± 10 eV, 130 ± 10 eV, and 230 ± 20 eV, respectively. Thus, the kinetic energies observed for the ions are due to acceleration and spread in velocity distribution, rather than thermal effects. Ion heating can not occur in our collisionless plasma within $\simeq$ 100 ns.

Secondary Electrode Plasma

The light emission from the switch plasma decays 150-200 ns after the application of the generator current pulse. However line emission from hydrogen and carbon ions starts again about 0.5-1 μs later. No emission from other particles is observed from from this secondary plasma. Also, this plasma does not appear when the PG is operated without the generator current. The secondary plasma line intensities are usually 3-5 times higher than those of the early plasma. The secondary plasma light signals appear at different times in different radial positions in the plasma switch, see Fig. 7. The CII 2512 Å and 4267 Å line intensities measured 5 mm from the anode and 5 mm from the cathode surface appear relatively early and at the same time, while farther from the electrodes, at distances of 10 mm and 15 mm from the anode, they appear at $\geq$ 1μs later. From this we concluded that the carbon and hydrogen particles that comprise the secondary plasma originate at the anode and cathode surfaces. They move away from the surfaces with velocities dependent on the charge and the mass. For CI and CII the radial velocity is $\simeq 10^6$ cm/s, for CIII $\simeq 2 \times 10^6$ cm/s, for CIV$\simeq 3 - 4 \times 10^6$ cm/s, and for HI$\simeq 3 \times 10^6$ cm/s. In the axial direction the secondary plasma velocity is less than 5×10^5 cm/s.

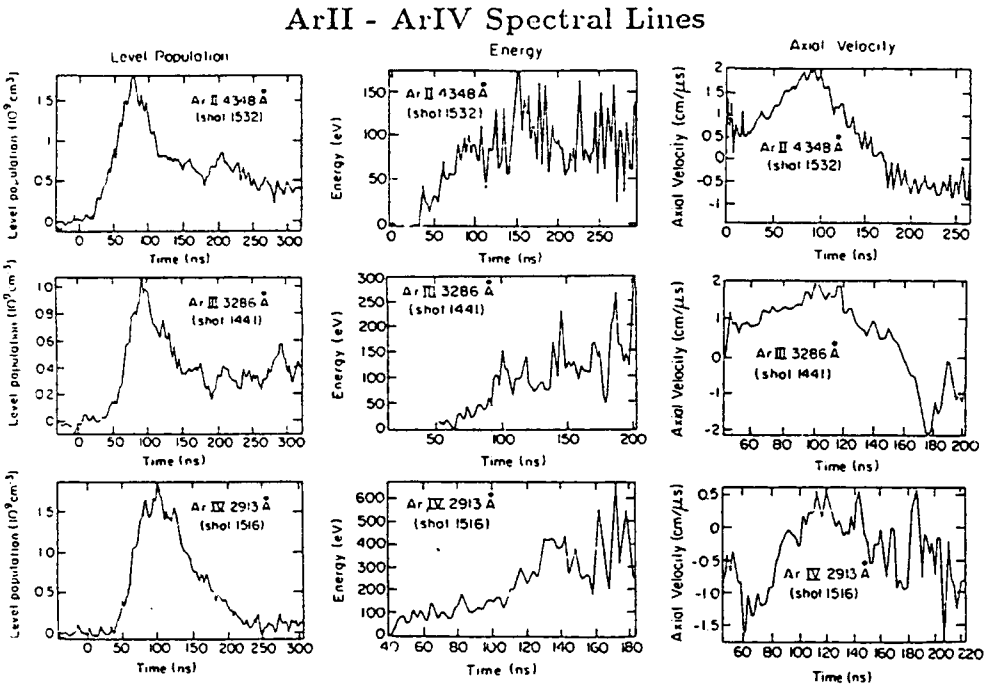

Fig. 6. Time dependent spectral observations of ArII, ArIII, and ArIV at 5 mm from the anode obtained from the 4348 Å , 3286 Å ,and 2913 Å lines, respectively. $t = 0$ is the start of the upstream current. (a) Time dependent absolute level populations of the above particles. (b) Time dependent mean kinetic energies obtained from the Doppler broadenings of the above particles. (c) Time dependent axial velocities obtained from the Doppler shifts of the above particles.

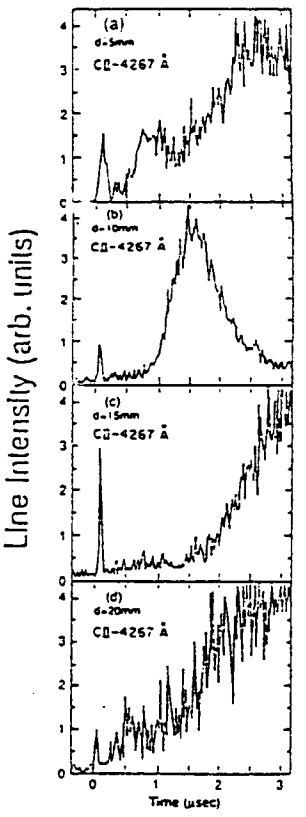

Fig. 7. Time dependent intensity of the CII 4267 Å line measured at radial distances of 5, 10, 15, and 20 mm from the anode. The figure shows the early rise in the line intensity during switch operation followed by a secondary rise at times $\geq$ 0.5 μs.

IV. Summary

A new-type gaseous plasma source was developed for the investigation of cylindrical POS in the 100 ns time regime. The density, temperature, uniformity, reproducibility, and flow velocity of the injected plasma were studied and optimized.

The electrical properties of the POS in the positive polarity were determined.

The line emission from the plasma particles was found to be in correlation with the current through the POS. The presence of fast electrons, ($\geq$ 300 eV), in the plasma was studied as a function of time and location from the excitations of highly-excited levels of highly charged ions. The results suggest that these electrons are associated with the current flow through the plasma.

From the ionic level excitation after the decay of the currents in the plasma it is inferred that the resultant electron heating is relatively small.

The ion axial velocities were found to be much smaller than the Alfven velocity.

The fast electron distribution and the axial acceleration and deceleration of various plasma ions observed during the POS operation are presently being used to study the current distribution in the plasma.

The current flow through the switch produces an electrode plasma that moves into the switch region from both electrodes at an average velocity of $\simeq$ 1 cm/μs. Investigation of the composition and behavior of the secondary electrode plasma is important for developing long-time POS.

References

1. IEEE Trans. Plasma Sci. **PS-15**, (1987).
2. B.M.Koval'chuk, G.A.Mesyatz, Sov. Phys. Dokl. **30**, 879, (1985).
3. P.F.Ottinger, S.A.Goldstein, R.A.Meger, et.al., J.Appl.Phys. **56**, 774, (1984).
4. Y.Maron, E.Sarid, O.Zahavi, L.Perelmuter, M.Sarfaty, Phys. Rev. **A39**, 5842, (1989).
5. Y.Maron, M.Sarfaty, L.Perelmuter, O.Zahavi, M.E.Food, E.Sarid Phys. Rev. **A40**, 3240, (1989).
6. Y.Maron, E.Sarid, E.Nahshoni, O.Zahavi, Phys.Rev. **A39**,5856, (1989).
7. Y. Maron, L. Perelmutter, E. Sarid, M.E. Foord, M. Sarfaty, Phys. Rev. **A41**, 1074, (1990).

THE AURORA ACCELERATOR'S TRIGGERED OIL SWITCH

D. M. Weidenheimer, N. R. Pereira, D. C. Judy,† and K. L. Stricklett‡

Berkeley Research Associates, Inc., Springfield, VA, 22150

†Harry Diamond Laboratories, Adelphi, MD, 20783-1193

‡National Institute of Standards and Technology
Dept. of Commerce, Technology Administration
Gaithersburg, MD, 20899

Abstract

Achieving a radiation pulse with 15 ns risetime using all four of the Aurora accelerator's Blumlein pulse-forming lines demands synchronization of the Blumleins to within 10 ns (in addition to a 15 ns risetime[1,2] for a single line). Timing of each Blumlein is controlled by a triggered 12 MV oil switch. A smaller-than-customary trigger electrode makes the switching time more reproducible.

Time-resolved photography of the oil arcs suggests that triggering occurs simultaneously around the sharp edge of the trigger electrode, perhaps with small deviations that grow into the most prominent arcs characteristically seen in open-shutter photographs. However, many smaller arcs that are usually overlooked in open-shutter pictures may contribute to current conduction in a closed switch.

Introduction

The risetime of the radiation produced by one of the Aurora accelerator's[3] four Blumlein pulse-forming lines can be reduced from a nominal 60 ns to 15 ns by modification of the vacuum diode,[1,4] and can be further reduced to 7 ns with a gas cell.[2] Maintaining the improved risetime using all four Blumleins demands that the radiation pulses arrive within a 10 ns window, and hence requires synchronous Blumlein switching.

The 12 MV oil switch is one element critical to synchronizing the Blumleins. Two switch geometries are investigated: the conventional switch[5] and a switch that has been modified to increase the rate-of-rise of the voltage at the trigger electrode. Other aspects of synchronization, discussed in previous reports,[5,6] have resulted in less than 2% shot-to-shot variation in the radiation dose.[7]

Oil switch triggering

Figure 1 shows Aurora's 12 MV oil switch. After Marx erection, a pulse charge voltage of approximately -10 MV charges the intermediate Blumlein electrode with a 1.8 μs half period. In the switch region, the electrodes are separated by approximately 50 cm, which yields an average electric field strength on the order of 200 kV/cm.

In the conventional switch, the oil trigger electrode is held approximately 5 cm into the gap by a support pipe that is attached to the high potential side of the 1 MV trigatron gas switch. The gas switch's ground electrode is electrically connected to the inner Blumlein electrode through a solid aluminum frame, which also physically supports the trigger assembly. During pulse charging, the voltage on the oil switch trigger reaches a voltage V/n, where the capacitance of the trigger to the inner Blumlein is $n-1$ times the capacitance to the intermediate electrode. Upon closure of the gas switch, the charge on the oil switch trigger flows through the gas switch and support structure to the inner Blumlein, dramatically increasing the electrical stress at the trigger's sharp edge. Prebreakdown streamers originate

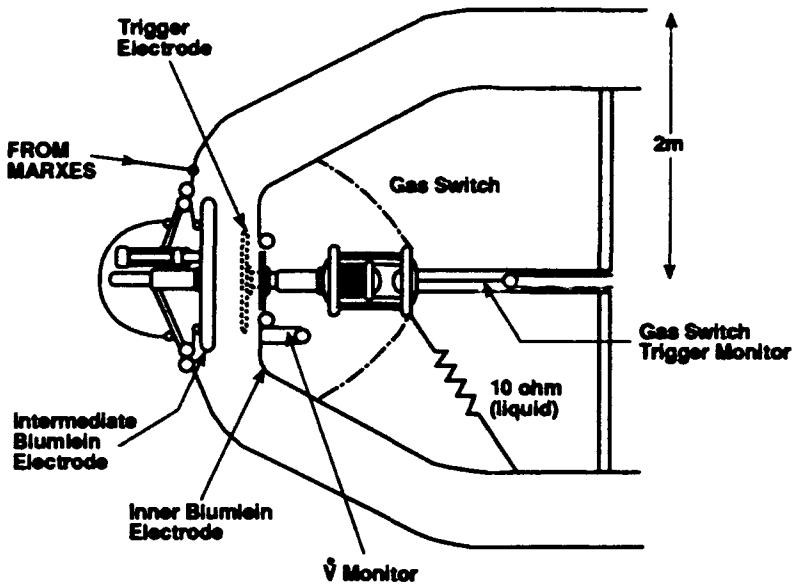

Figure 1. Schematic of Aurora's V/n oil switch. Modifications to the switch include reducing the trigger electrode diameter (the standard trigger electrode is shown by the broken line) and the addition of a low inductance path to ground at the gas switch. Eight conductors, indicated by the dot-dash line, are connected in parallel between the ground electrode of the gas switch and the inner Blumlein.

at the edge of the trigger electrode and propagate across the gap toward the intermediate electrode. Conducting arcs develop along the path of the streamers, connecting first between the oil switch trigger and the intermediate Blumlein and then to the inner Blumlein, thus closing the switch.

The operation of the oil switch is monitored by a capacitive probe mounted within the inner Blumlein, the $\dot{V}$ monitor shown in Figure 1. The $\dot{V}$ signal is proportional to the current from the high-voltage electrode: $I = dQ/dt = d(CV)/dt$, assuming the capacitance of the trigger electrode is constant and that stray current may be neglected.

Figure 2 shows representative data obtained by integration of the $\dot{V}$ signal for the standard trigger. At the beginning of the trace the voltage on the trigger electrode is proportional to the pulse-charge voltage. The gas switch closes at time t_o and produces a rapid change in the trigger electrode voltage. The plummeting voltage at about 200 ns indicates that electrical contact has been made between the high-voltage electrode and the trigger electrode.

The switch run time t_r is the time delay between closure of the gas switch and closure of the oil switch as indicated in the figure. Measurements obtained during operation of the conventional switch[8] give the switch's run time as

$$t_r \simeq t_{1r} \left[\frac{E_{av}}{1\ \mathrm{MV/cm}} \right]^{-\alpha} .$$

Here $t_{1r} = 22\,\mathrm{ns}$ is the run time for an average field E_{av} of 1 MV/cm, and the exponent α is approximately 1.33. In the standard configuration the mean run time is on the order of 130 ns, with a shot-to-shot standard deviation of approximately 5.5 ns:[5] switch closure

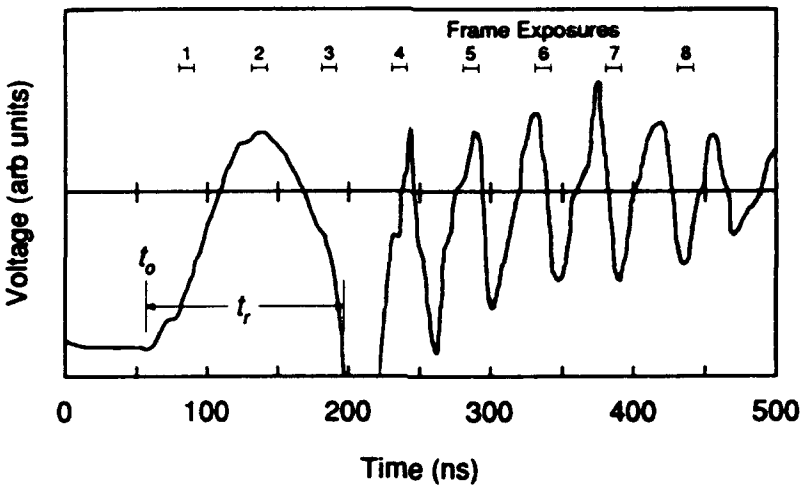

Figure 2. The voltage on the oil switch trigger electrode. The integrated $\dot{V}$ signal is plotted for a single shot using the conventional switch geometry. The gas switch closure time t_o and oil switch run time t_r are shown. The numbered sequence along the top of the figure corresponds to the exposures of the high-speed photograph shown below.

occurs within windows of 13 ns for 9 shots and 28 ns for 95 shots.

The impulse breakdown voltage of insulating fluids depends on the rate of voltage rise: Tests using a small gap and nonuniform fields[9] show that the variance in the time-to-breakdown decreases with increased rate-of-rise. Thus a faster-rising pulse on the trigger electrode should reduce the switch jitter. The trigger network approximates a LRC circuit with the support structure's inductance L, the parallel 10 Ω damping resistor R, and the capacitance C of the trigger electrode. This circuit has a half-cycle time $T = \pi\sqrt{LC}$, and, for the standard switch configuration, $T \simeq 75$ ns. A faster-rising pulse is achieved by adding eight parallel conductors between the gas switch and the inner Blumlein, and by reducing the diameter of the trigger electrode from 95 cm to 60 cm.

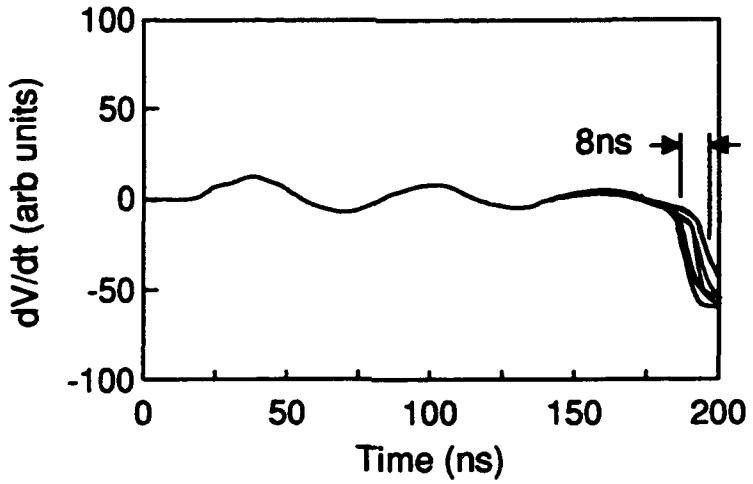

Figure 3. $\dot{V}$ signal for the modified trigger electrode. $\dot{V}$ signal traces obtained from nine consecutive shots are plotted.

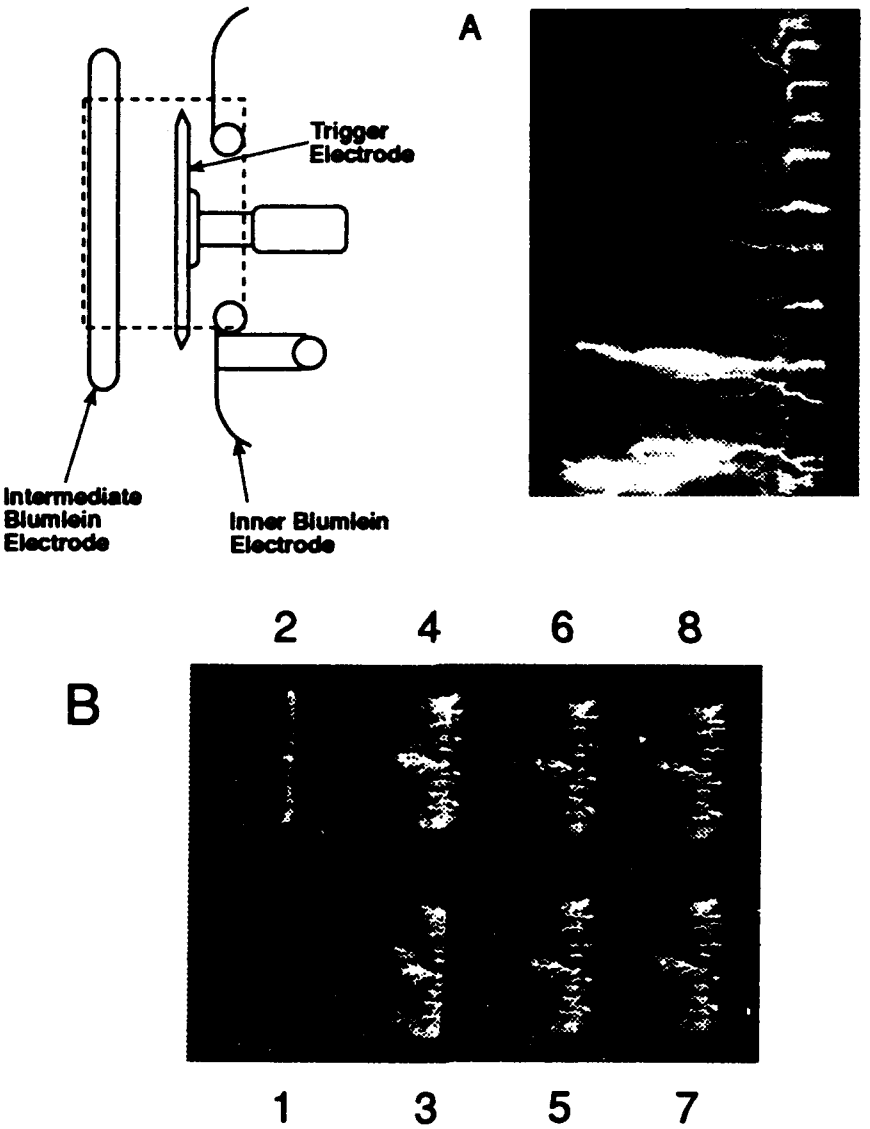

Figure 4. Photographs of switch operation. Open-shutter (A) and high-speed (B) photographs for different shots are shown. The approximate field of view is shown schematically on the upper left. The multi-frame photograph corresponds to the voltage trace shown in Figure 2 where the frame exposure times plotted together with the trigger voltage. Individual frame exposures are 10 ns and the frames are separated by approximately 50 ns.

Oil switch timing is most accurately determined by direct measurement of the $\dot{V}$ signal. Figure 3 shows representative traces of the $\dot{V}$ signal for the small electrode. Compared with the conventional switch, the half-cycle time is nearly halved to 34 ns. It should be noted that, due to the reduction in the trigger electrode capacitance to the intermediate Blumlein electrode, the peak voltage on the trigger electrode is about 60% of that for the conventional switch. Therefore, the voltage rate-of-rise is increased by a factor of 1.2 rather than 2 as indicated by the oscillation frequency alone. The nine consecutive shots shown in Figure 3 have run times that fall within an 8 ns window and an estimated standard deviation of 3 ns.

Optical diagnostics

Two photographic techniques were employed to record light emitted from the oil switch during closure: open-shutter and high-speed photography. Representative photographs of each type for the conventional switch geometry are shown in Figure 4. These pictures provide intriguing information about the switch's operation, such as the number and spatial distribution of the conducting arcs.

In the open-shutter pictures the gap is typically bridged by a few large arcs. It should be noted, however, that the open-shutter photographs emphasize persistent arcs that continue to carry current during late-time ringing of leftover energy in the Blumlein. Therefore these arcs give little information about the pulse forming part of the switch discharge.

In contrast, the multi-frame photographs show many luminous regions close to the trigger electrode. Apparently, the oil switch triggers many channels that are relatively uniformly spaced on the trigger electrode. The first detectable light emission for the sequence shown in Figure 4B appears in the second frame, 75 ns after closure of the gas switch. These data appear to be consistent with the initiation of multiple prebreakdown streamers, the precursors to the fully developed arcs.[10] The streamers start at the sharpened edge of the trigger electrode, presumably when the electric field at the sharp edge exceeds some critical value. The streamers appear to grow uniformly at initiation. However, the photograph suggests that at switch closing only three channels have bridged the gap. In other high-speed photographs, a single channel appears to close the switch.

The photographic data suggest that the detailed temporal development of the streamers may contribute to the variability in the switch run time. Indeed there is some evidence in the photographic data that may explain the "compensation" effect, which is an inverse correlation between switch run time and the rate of discharge of the Blumlein, identified earlier.[5,8] Closure of the oil switch with a single arc, as in the case of runaway growth of a single streamer, seems to reduce the run time and to result in a slightly slower discharge of the Blumlein. However, although light emission is certainly related to currents in the oil, it seems clear that the measurement optics do not fully resolve the structure nor detect the full extent of prebreakdown streamers, and that these photographic data must be evaluated with some care.

It is not yet clear what factors influence arc initiation and the subsequent number of arc channels. Detailed studies of the threshold field and the dependence of streamer initiation on voltage risetime are in preparation.

Acknowledgements

This work is supported in part by the Defense Nuclear Agency, the US Department of Commerce, and the US Department of Energy. The authors thank Aurora's technical staff for

their capable assistance and, in particular, Dennis Lindsay for the open shutter photography.

References

1. M. Bushell, R. Fleetwood, D. C. Judy, G. Merkel, M. Smith, and D. M. Weidenheimer, "Bremsstrahlung risetime shortening by diode geometry reconfiguration," this conference, paper PC-35.

2. G. Merkel, private communication (1990).

3. I. Smith and B. Bernstein, "Aurora, an electron accelerator," IEEE Trans. Nucl. Sci. **NS-20**, 294 (1973); J. Agee, "New capabilities of the Aurora flash x-ray machine," Nucl. Instr. Meth. 1991.

4. T. W. L. Sanford, J. A. Halbleib, W. H. McAtee, K. A. Mikkelson, R. C. Mock, and J. W. Poukey, "Improved flash x-ray uniformity at 19 MeV using a compound-lens diode," J. Appl. Phys. **69**, 7283 (1991), and other papers in this series (including this conference).

5. D. M. Weidenheimer, N. R. Pereira, and D. C. Judy, "Aurora synchronization improvement," Proc. 8^{th} International Pulse Power Conference, San Diego, CA, 924 (1991).

6. D. M. Weidenheimer, D. C. Judy, D. Lindsay, L. E. Salvan, J. Golden, and N. R. Pereira, "Jitter reduction in Aurora," DNA Advanced Pulse Power Conference, Albuquerque, NM, 1990.

7. S. G. Gorbics, private communication (1992).

8. F. T. Warren, H. G. Hammon, B. N. Turman, and K. R. Prestwich, "Jitter improvement on the 12 MV oil switches on Aurora," Proc. 5^{th} IEEE Pulse Power Conference, Arlington, VA (1985), edited by P. J. Turchi and M. F. Rose.

9. E. F. Kelley and R. H. McKnight, "Streamer propagation in transformer oil under the influence of submicrosecond rise-time pulses," in press.

10. For a discussion of electrical breakdown in dielectric fluids see, for example, R. E. Hebner, "Measurement of electrical breakdown in liquids," in *The Liquid State and Its Electrical Properties,* Plenum Press, 1987, edited by E. E. Kunhardt, L. G. Christophorou, and L. H. Luessen.

High-Pressure Gas Switch for a Wideband Source

P. A. Pincosy, P. Poulsen, and W. R. Cravey

Lawrence Livermore National Laboratory
P. O. Box 808, Livermore, California 94551

Abstract

High-power ultrawideband pulses with equivalent center frequencies around 10 GHz require switching in a time scale of about a hundred picoseconds. We are developing a high-pressure gas switch that is designed to store a few joules of energy. Energy is stored in the transmission line upstream of the switch. The switch is a gap in a short transmission line of low impedance. The line is pulse charged to store the desired energy before the electric field across the gap collapses from the avalanche buildup of electrons. To ensure a relatively uniform voltage collapse across the width of the gap, initial electrons are produced by radiation from a bare spark. The switching repeatability is very good when the spark provides the initial electrons. Gap electric fields greater than 1 MV/cm were achieved for a 10-atm switch pressure in air with a voltage collapse less than 150 ps over 6 cm of switch length. The switch was tested with repetitive pulses up to 1 kHz.

In a pulse charging mode, the collapse time of the gap will typically be 5 times less than the charging time. For applications where a switching time of tens of picoseconds is desired, a second switch would be required.

Introduction

An ultrawideband source requires a pulsed power modulator, a fast switch, and a radiating antenna. For broad-band radiation in the GHz range, the pulse energy must be released with a fast rising pulse (i.e., tens of picoseconds). Of the possible pulse sharpening methods in the sub-nanosecond time scale, a high-pressure gas switch[1,2,3] can produce short and high-voltage pulses at energies (joules) of interest resulting in high-power radiation. Although discharge physics are relatively well understood, certain switch issues remain to be determined. In this paper, we present the results of our studies on the attainable electric field at breakdown, the speed of voltage collapse, the voltage collapse phasing along the gap length, and the capability of repetition rate operation. We also discuss scaling for the high-pressure gas switch.

In these studies, we applied nanosecond rising voltage pulses (Marx pulse power supply) to a 50-Ω pressurizable transmission line with an in-line gap and to a plate transmission line. The measurements checked the attainable gap electric field. We also measured the voltage collapse time. The results showing phasing and repetition rate operation were obtained using the plate transmission line.

We present a comparison of simple avalanche physics modeling of the pulse charging and gap voltage collapse to the experimentally measured results. Using the model, we illustrate the calculated pulse waveform for a much higher voltage and pressure switch.

Gas Switch Operation

Two configurations of the switch were tested: a 50-Ω coaxial line and a 17-Ω parallel-plate transmission line. The coaxial transmission line and gap could be pressurized with gas. An initial electron density, n, is produced in the gap by a UV source. The transmission line is charged by the pulsed power supply until the gap voltage collapses and the voltage pulse is propagated down the line. The end of the line was shorted. The development of charge in the gap up to breakdown voltage has been measured[1,4] by the well known E/P vs $P\tau$ relationship for many gases or gas mixtures. The buildup of electron density or formative time, τ, to breakdown is modeled using the Townsend coefficient, a, and the electron drift velocity, v_d, both functions of E/P. The initial

electrons in the gap avalanche from the initial density of between 10^3 to 10^9 to the density of $10^{17}cm^{-3}$ when the voltage collapses. The time for the increase in generations of electron density at constant voltage is termed the formative time. The switching time is so short that electrons will move only a fraction of the gap distance during the voltage collapse. The avalanche process provides an electron density capable of carrying a current density as given by

$$j = n_0 v_d \exp\left[\int_0^t \alpha v_d dt\right],$$

where both α and v_d are functions of E/P. The total current conducted through the gap depends on the transmission line impedance and the gap impedance.

Experimental Setup

The electric field and voltage collapse time was measured in a 50-Ω coaxial line that could be pressurized to 10 atm. The coaxial line had an in-line gap with one chisel-point face and one flat face. The geometry for the parallel plate transmission line is shown in Fig. 1. This geometry was only operated at atmospheric pressure. To observe switch phasing, we used the plate transmission line shown in Fig. 1 with a 2-mm gap (g) across the 10-cm width (w) of the line. The pulse charging supply stores energy in the 10 cm upstream of the gap until voltage collapse occurs, and then launches a pulse down the 20-cm line to a shorted end. The plates were separated by 5 mm (see s) resulting in an impedance of 17 Ω. The voltages were monitored with four D-dot probes. Probe 1 is located 1.5 cm upstream of the gap centerline and probe 3 is 1.5 cm downstream along the transmission line center. Probes 2 and 4 were placed at 3 cm outboard of the downstream probe (see Fig. 1).

To ensure some resident electron density in the gap as the charging pulse is applied, the gap is irradiated by UV[5] from a spark source. The wideband assist pulser (WASP)[6] was used to pulse charge the plate transmission line at repetition rates from 1 Hz to 1 kHz for 1-second duration bursts. The output pulses were measured with a B-dot probe on the output line and the signal was recorded on a SCD5000, 4.5-GHz transient digitizer. The signals from the D-dot probes were also recorded on the SCD5000 transient digitizers. Due to the high frequency of the D-dot signals, and the losses associated with the signal lines, the system frequency response of each signal line was measured using a picosecond pulser and then removed from the pulsed experimental measurements during the data reduction phase.

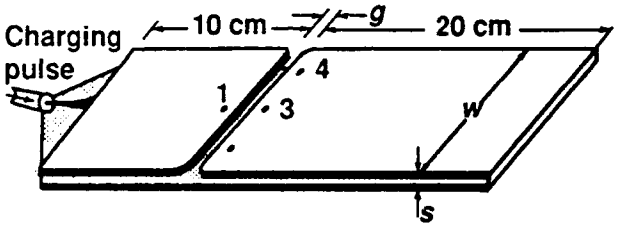

Figure 1. Parallel-plate transmission line; D-dot probe locations 1–4 are noted.

Experimental Results

Gap Electric Field and Breakdown

For the parallel-plate transmission line in atmospheric pressure, the charging pulse developed a peak of 100 kV/cm across the gap as the voltage rose in 1.5 ns. In the 50-Ω coaxial line air gap, pressurized to 10 atm, an electric field of 1 MV/cm was obtained. In the coaxial line at 10 atm of air, the gap voltage (Fig. 2) collapsed to half in less than 150 ps (the time response of the measurement was limited to a rise time of about 150 ps; the signal frequency response was not obtained for these measurements). At 1 atm of air pressure, the gap voltage collapsed to half in 250 ps both for the coaxial line and the plate transmission line (Fig. 3). It follows that with

several tens of atmospheres pressure the voltage collapse will occur in a few tens of picoseconds.

Phasing with a Single Pulse

In order to launch a rapidly rising pulse that is time-phased across the transmission line width, we have required that the switching gap be nearly the full width of the line (Fig. 1). The issue for switching is to have the voltage collapse simultaneously across the full width of the gap. Typical integrated signals for the gap charging voltage (from probe 1) and the launched voltage pulse are shown in Fig. 3.

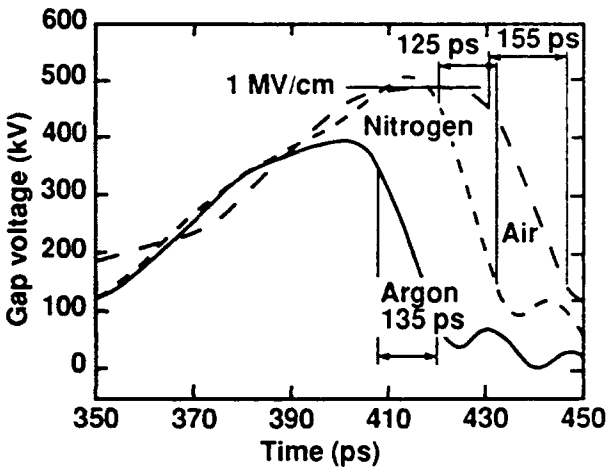

Figure 2. Measured gap voltage wave-forms in a 50-W, coaxial transmission-line gap. Pulse charged from a small Marx generator.

We determined the relative arrival time at the two outboard probes (2 and 4). Without an ionizing spark, the signal arrived at probe 2 an average of 47 ps prior to arriving at probe 4, and the standard deviation of the difference in arrival time was 126 ps, considerably greater than the average difference in arrival time. Because the probes are located 6 cm apart, a variation of 126 ps indicates a significant variation of location of the gap current, thus showing that it is not uniform along the length of the gap. When the UV ionizing spark was applied, the average arrival time difference to probes 2 and 4 was measured to be about 25 ps. The variation in this arrival time was 18 ps (11 shots) or a significant reduction from the 126 ps when no UV spark was used. The estimated instrumental measurement precision was 20 ps.

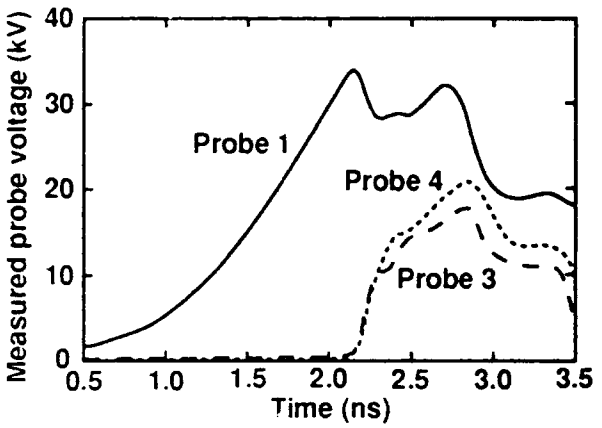

Figure 3. Charging and launched voltage pulses in the parallel-plate transmission line with atmospheric air. UV spark pulse was applied.

The variation in arrival time between probes 2 and 3 was 20 ps or within the instrumental precision. We conclude that with a UV spark source, the gap discharge is uniform along its length to within the measurement accuracy. It was also observed that probes 2 and 4 were typically very similar in wave shape when the phasing was good, and different otherwise. The data from probe 3, as shown in Fig. 3, was typically different for good phasing. We assume this difference from probes 2 and 4 was due to breakdown waves reflecting from the edge of the transmission line and adding to probes 2 and 4 differently than to probe 3.

Phasing and Amplitude with Pulse Repetition

Repetition rate operation was tested up to 1 kHz. The WASP pulser provided a voltage pulse that was about 2 times higher on the first pulse. The UV spark source could not be repeated. The issue was whether there were enough resident electrons from the previous breakdown to uniformly seed the gap with enough electrons for a phased breakdown. On a given burst, we recorded the first breakdown and every one-hundredth breakdown that followed, up to three additional pulses (Fig. 4).

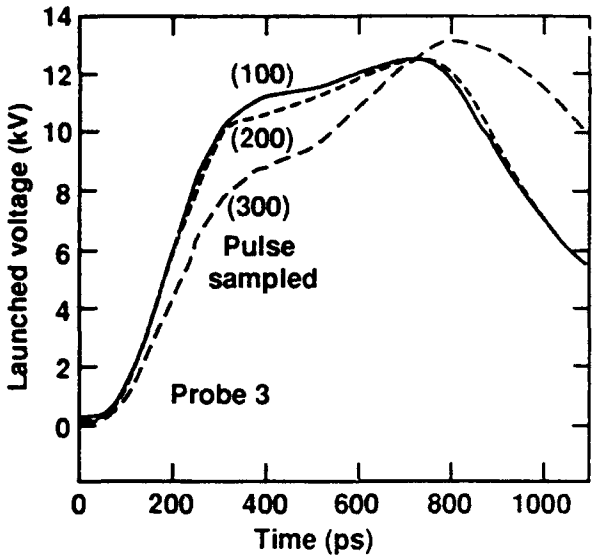

Figure 4. Launched voltage pulse samples at 1 kHz prf with no UV spark. Pulse arrival time differences are unknown.

Unlike these three launched pulses, the wave shape should be almost identical if the gap breakdown is uniform across its length. For repeated breakdowns up to the 1-kHz pulse repetition frequency (prf), the variation in pulse arrival time among probes 2, 3 and 4 was similar to that observed when no UV spark was produced. Fiducial corrections were crucial to making the measurements, and care was taken to determine the relative difference in trigger delays and signal delays between D-dots. For the first pulse in the train when the UV spark was produced, the relative timing among probes 2, 3 and 4 was within measurement accuracy. In Fig. 5, two first pulses with a UV spark illumination are compared. Although the input Marx charging pulse was different in amplitude, the launched wave shape (probe 4) is very similar. We concluded that the first pulse with the UV spark launched a phased pulse but for subsequent pulses the gap breakdown was not uniform. The UV spark will be needed for every pulse up to a 1-kHz prf. In Fig. 4, we observed that the repeated pulses reached the same voltage, 12 kV. The first pulsereaches an amplitude of 20 kV. The difference is because the WASP pulser produces a faster rising and higher voltage pulse on the first pulse, and all subsequent pulses are repeatable with slower rise times and lower amplitudes. With prfs up to 1 kHz, the launched voltage pulses repeated their amplitude. These bursts of pulses were steady for up to one second without degradation in the holdoff voltage or launched amplitude.

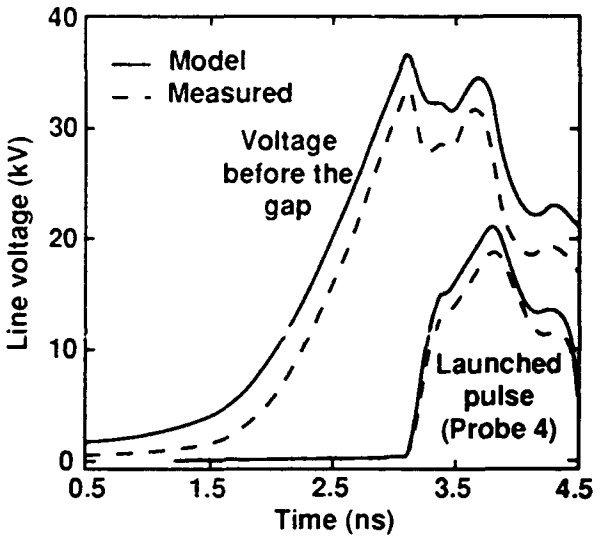

Figure 5. Comparison of the first two charging and launched voltage pulses with the UV spark.

Switch Modeling

When the gap electron density avalanche is modeled using the Townsend coefficient and the drift velocity, it becomes apparent that a difference of several orders of magnitude of initial electron density, n, makes a relatively small change in the formative time to voltage collapse. For example, with an E/P of 50 across the gap, the time of collapse for a 2-ns charge time varied 33 ps per decade of initial electron density charge, going from 10^3 to 10^9 electrons/cm^3. The launched pulse wave rises in 125 ps. Initial electron density variations within a factor of 10 along the length of the gap should have a minor effect on the phase of the propagated wave. Stringent control of the gap electron density during the initial charging time is therefore not necessary.

In Fig. 6, the modeled breakdown in the plate transmission line gap is compared to the measured pulses for air breakdown at 1 atm of pressure. The model assumes a (1 - cosx) charging pulse waveform, which is comparable to the measured charging pulse except for the low voltage foot. The breakdown electric field is closely predicted and can be correctly predicted for higher pressures.

The launched pulse is closely predicted up to the time when the wave propagating back to the input line returns to the gap. The assumed input charging wave in the model does not match the real wave after this time and the model does not include the shorted end of the plate transmission line. Because the gap voltage rise is significantly above the static breakdown voltage, the launched pulse rise time is typically 5 times faster than the pulse charging time To achieve pulses with picosecond rise times a staged switch would be required.

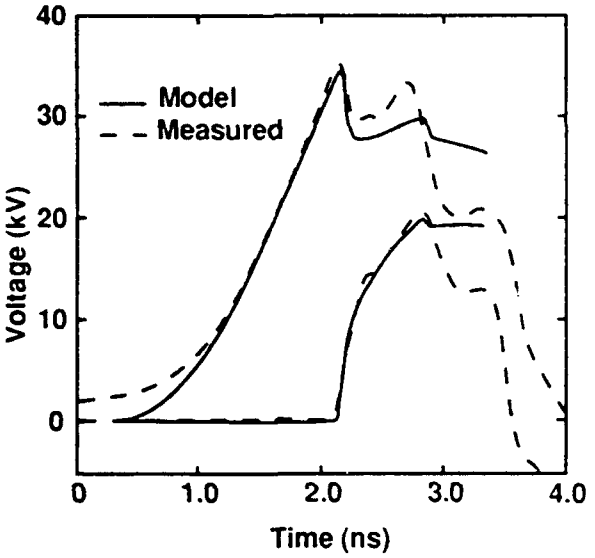

Figure 6. Comparing calculated and measured charging and launched voltage pulses.

The model was capable of using several gases, such as helium, nitrogen, argon, silane, and others. Calculations show that similar electric fields can be obtained but with varying required pressures. The differences lie in the voltage collapse rates, especially as E/P falls to lower values where for some gases, electron attachment plays a role.

The electrical energy stored in the transmission line before switching is dependent on the field volume and the voltage. The E/P scaling indicates that a pressure increase allows a proportionally higher electric field. We have designed a low impedance (0.5 Ω) line 3 cm long with a meter-long gap capable of storing 8.8 J of electrical energy. In helium at 150 atm, the launched pulse is calculated to be 200 ps long (Fig. 7) and the pulse launched energy is 4.4 J.

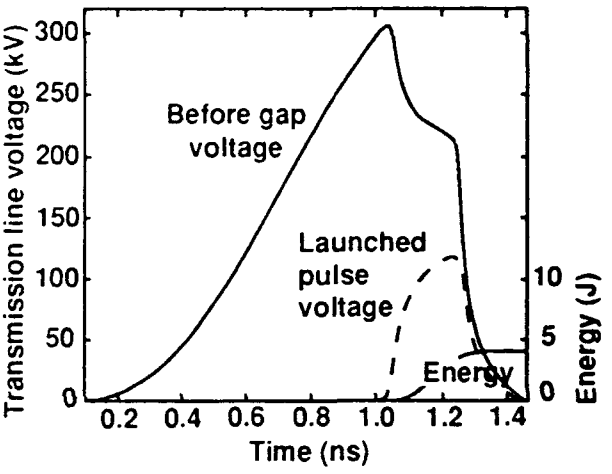

Figure 7. Calculated charging and launched voltage pulses using He at 150 atm pressure. There were 8.8 J stored energy in the 3-cm line at breakdown, and 4.4 J of energy launched in the pulse.

Summary

The high-pressure switch has been shown to be capable of producing sub-nanosecond pulses at high voltages. Electric fields of a few MV/cm are attainable in charging pulses whose duration are of the order of the formative times for electron avalanching. The pulse rise times have been measured as fast as 150 ps (limited by diagnostics) and the pulse can be launched in phase along the gap, provided that a UV source of photons produces seed electrons before the charging pulse arrives. We have demonstrated that a 1-kHz repetition rate can be achieved for this switch during a period of one second. Modeling has been effective in matching experimental results, and should thus be useful in the design of high-voltage and pressure switch configurations.

Acknowledgements

Work performed under the auspices of the U. S. Department of Energy by Lawrence Livermore National Laboratory under Contract W-7405-Eng-48.

References

1. R. C. Fletcher, *Phys. Rev.* **76**, 1501 (1949).

2. R. E. Cassell and F. Villa, High-Speed Switching in Gases, Stanford Linear Accelerator, SLAC-PUB-4858, Feb. 1989: 4th Workshop: *Pulsed Power Techniques for Future Accelerators*, Eric, Trapini Italy, March 4-9, 1988.

3. D. J. Mayhall and J. H. Yee, Computational broadband high-power electromagnetic pulse generation from an air gas avalanche switch, IEEE, *Proceedings of the 1991 Pulsed Power Conference*, 1991.

4. P. Felsenthal and J. M. Proud, Nanosecond-Pulse Breakdown in Gases, *Phys. Rev.* **139**, A1796 (1965).

5. R. Babcock, I. Liberman, and W. Partlow, Volume Ultraviolet Preionizations Bare Sparks, *IEEE J. Quant. Electron*, vol. QE-12, p. 29, 1976.

6. W. R. Cravey, Performance of a 30 kV, 1 kHz Nanosecond Source, IEEE, *Proceedings of the 1992 Power Modulator Symposium*, 1992.

PREDICTION OF ELECTROMAGNETIC PULSE GENERATION BY PICOSECOND AVALANCHES IN HIGH-PRESSURE AIR*

D.J. Mayhall and J.H. Yee
Lawrence Livermore National Laboratory
P.O. Box 808, Mail Code L-156, Livermore, CA 94551

Introduction

The gas avalanche switch is a laser-activated, high-voltage switch, consisting of a set of pulse-charged electrodes in a high-pressure gas.[1–4] Induced electrons from a picosecond-scale laser pulse initiate an avalanche discharge between high-voltage and grounded electrodes. If the voltage, pressure, and dimensions are correct, the rapid avalanche, fueled by the immense number of electrons available in the gas, collapses the applied voltage in picoseconds and generates electromagnetic pulses with widths as short as 1–10 ps and 3 dB bandwidths of 20–120 GHz. With proper voltage or pressure detuning, wider pulses and lower bandwidths occur. In addition to picosecond electromagnetic pulse generation, application of this switch should result in ultra-fast Marx bank pulsers.[5]

A number of versions of the switch are possible. The simplest is a parallel plate capacitor, consisting of a gas between two parallel plate conductors. High voltage is applied across the two plates. A parallel plate, Blumlein geometry features a center electrode between two grounded parallel plates. This geometry emits a single pulse in each direction along the parallel plates. A frozen wave geometry with multiple, oppositely charged center electrodes will emit AC pulses. Series switches consisting of gas gaps between two electrodes are also possible. A recent investigation with an overvolted series gap reported voltage switching times as short as 50 ps.[6]

A Two-Dimensional Electron Fluid Computer Code

For investigation of these switches, we have developed a two-dimensional, electromagnetic, finite difference, electron fluid computer code for ionization in high-pressure gases. This code simultaneously, self-consistently, and implicitly solves Maxwell's curl equations for transverse magnetic modes between perfectly conducting parallel plates. In addition, it solves electron fluid conservation equations for density, momentum, and energy. The coordinates are presently rectangular. Multiple charged, rectilinear, perfect conductors may be situated between the plates. **Figure 1** shows the present geometry.

Differential Equations

The governing Maxwell's curl equations in the MKS system are

* Work performed under the auspices of the U.S. Department of Energy by Lawrence Livermore National Laboratory under Contract W-7405-Eng-48.

$$E_{x,t} = \epsilon_o^{-1}(H_{z,y} - nev_x)\,, \tag{1}$$

$$E_{y,t} = -\epsilon_o^{-1}(H_{z,x} + nev_y)\,, \tag{2}$$

$$H_{z,t} = \mu_o^{-1}(E_{x,y} - E_{y,x})\,, \tag{3}$$

where E_x and E_y are the electric components in the x and y directions, ϵ_o and μ_o are the premittivity and permeability of the gas, H_z is the magnetic component in the z direction, n is the electron density, e is the electronic charge of -1.6×10^{-19}C, and v_x and v_y are the electron velocity components in the x and y directions. The multiple subscript a,b indicates the partial derivative of the a component of a quantity with respect to the b independent variable. The symbol t stands for time.

An approximate set of electron fluid conservation equations is

$$n_t = n\upsilon_i\,, \tag{4}$$

$$(nv_x)_t = n[em^{-1}(E_x + \mu_o v_y H_z) - \upsilon_m v_x]\,, \tag{5}$$

$$(nv_y)_t = n[em^{-1}(E_y - \mu_o v_x H_z) - \upsilon_m v_y]\,, \tag{6}$$

$$(nU)_t = n[e(E_x v_x + E_y v_y) - \upsilon_u(U - U_o) - \upsilon_i \epsilon_i]\,, \tag{7}$$

where υ_i is the neutral molecule ionization rate, m is the electronic mass, υ_m and υ_u are the electron-neutral momentum and energy exchange rates, U is the electron energy, U_o is the time-constant average neutral energy, and ϵ_i is the average neutral ionization potential. The subscript t denotes the partial derivative with respect to time. We use collision rates for air and take U_o = 0.025 eV and ϵ_i = 14 eV to specialize Eqs. (4)–(7) to air. Equations (4)–(7) assume a Maxwellian velocity distribution. In addition, all convective terms, pressure gradients, and heat flows are neglected. All electron number losses are ignored, as is electron generation by photoionization. The collision rates are from previous calculations of high-power microwave pulse breakdown in low-pressure air.[7] These rates are assumed to increase linearly with increasing neutral pressure.

Discretization and Numerical Solution

Figure 1 shows the finite difference discretization of the computational space between the parallel conductors. The partitioning mesh is rectangular with uniform, unequal spacings Δx and Δy. The legend box shows the position of each field component. The electron fluid variables are solved for at H_z grid points. Equations (1)–(3) are centrally differenced in space in the grid interior. Seven ordinary differential equations (ODEs) in time result for each grid cell. The global set of ODEs is solved by numerical time integration with the block-interative, optionally stiff, implicit solver GEARBI.[8]

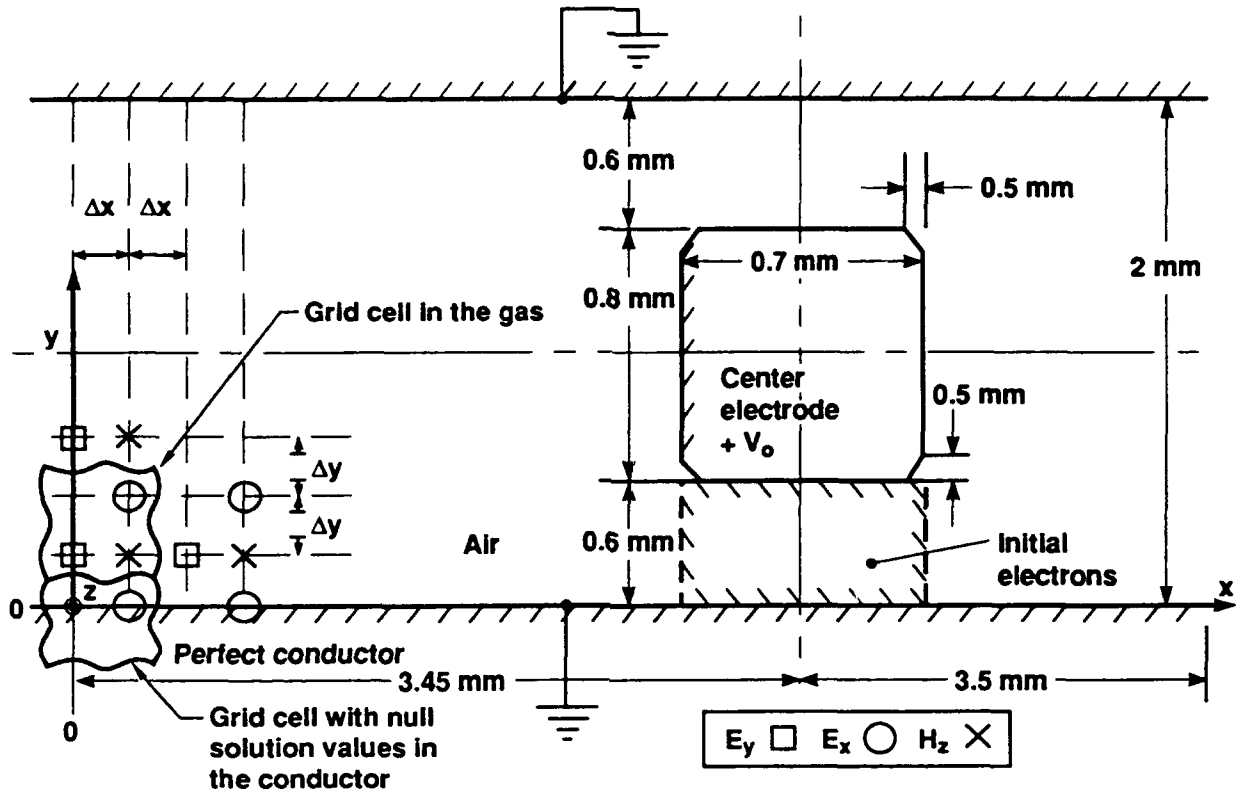

Figure 1. A simple pulse generator switch model.
TEM boundary conditions at left and right.

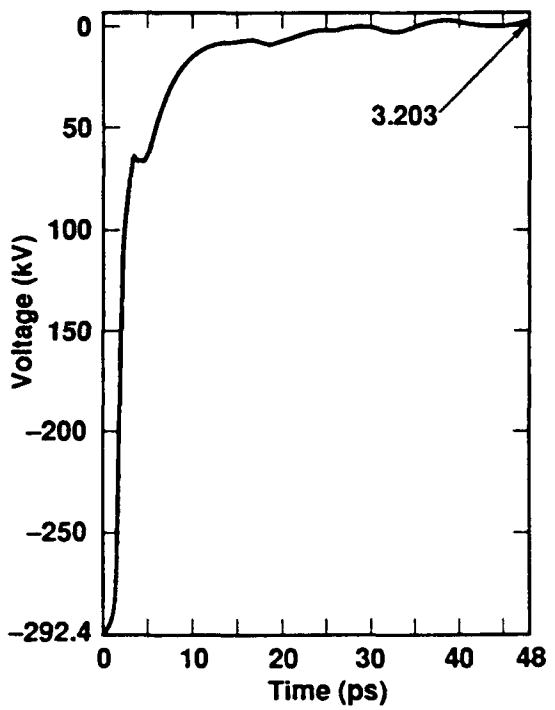

Figure 2. Waveform of the voltage between the electrode and center bottom plate near the center line at 292.4 kV and 27.2 atm.

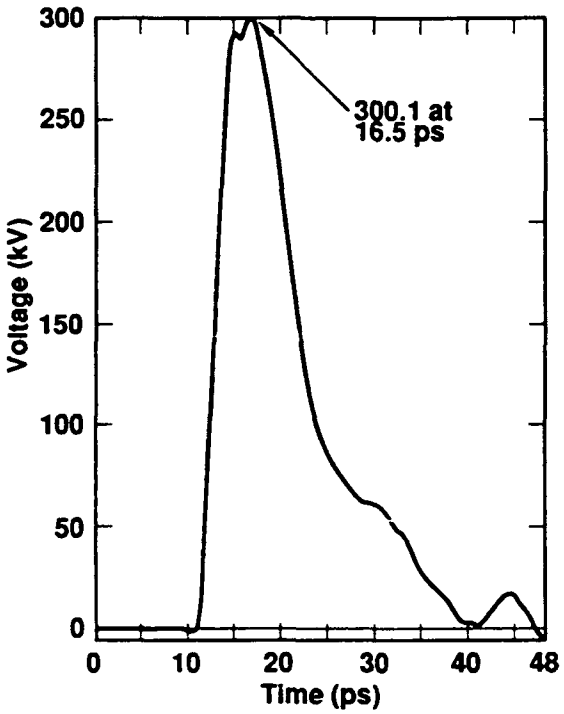

Figure 3. Voltage waveform at right boundary for 292.4 kV and 27.2 atm.

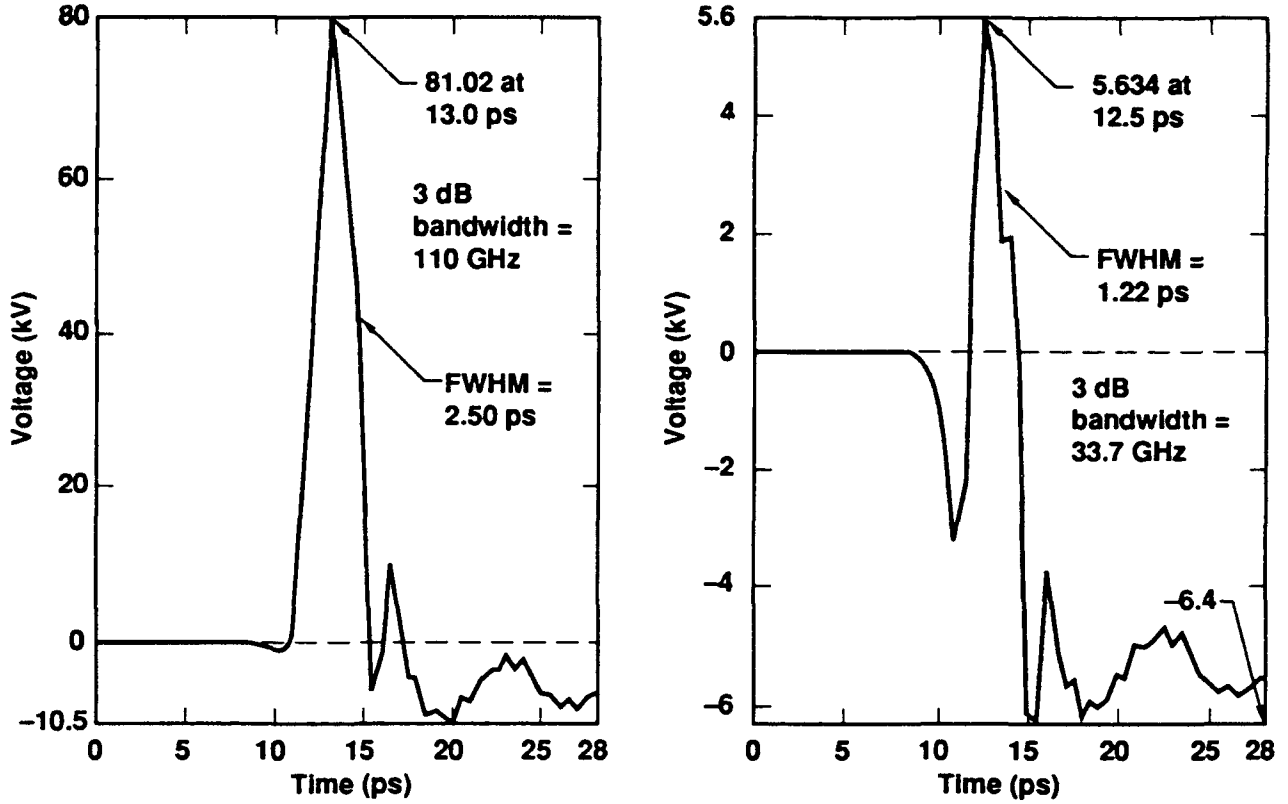

a. Pulse for 0.75 ps delay.

b. Pulse for 0.1 ps delay.

Figure 4. Voltage waveforms at right boundary
from wave interference at 292.4 kV and 27.2 atm.

Pulse Generation in a Three Electrode Air Switch

Switch Geometry

A gas avalanche switch with a strong nonuniformity in its initial electric field consists of a center rectangular electrode between parallel plates. **Figure 1** shows a rudimentary version of this switch. With the proper conditions, this switch computationally generates predominantly transverse electromagnetic waves with picosecond-order rise times and durations. The center electrode is a perfectly conducting rectangle with beveled corners, charged to the positive voltage V_o. The air gap between this electrode and the lower plate is uniformly filled with 1.7×10^{13} laser-induced initial electrons to an assumed depth of 1 m into the plane of the figure. In contrast, the upper gap contains no electrons.

Pulse Generation in the Kilovolt Range

When the simulation begins with a voltage of 292 kV and a pressure of 27.2 atm, the potential difference between the center electrode and the lower plate drops in about 3 ps. **Figure 2** shows the waveform of this potential difference, which occurs close to the vertical center line in **Fig. 1**. The rapid initial voltage collapse is caused by the rapid electron avalanche toward the positively charged center electrode, which generates electromagnetic waves. These waves propagate outward toward

the boundaries at the top, left, and right. **Figure 3** shows the voltage waveform across the parallel plates at the right boundary. The peak induced voltage is 300 kV, the 10–90% rise time is 2.41 ps, and the full width at half maximum (FWHM) is 9.11 ps. The peak pulse voltage is roughly equal to the initial voltage. The initial electrostatic energy is 3.34 J per meter of depth into the switch. By 48 ps, 55.6% of the initial energy has been transported across the boundaries. The pulse in **Fig. 3** has a 3 dB bandwidth of 21.0 GHz. Similar induced voltage pulse shapes occur for megavolts of applied voltage for roughly constant ratios of initial electric field at the center electrode to pressure.

Gross Insensitivity to Reduction of Initial Electron Number

For laser system constraints on the generation of large numbers of initial electrons, the reduction of the number of electrons in the lower gap may be critically important. A series of simulations with uniform illumination under the center electrode, in which the initial electron number dropped from 1.7×10^{13}/m ($4.04 \times 10^{19} m^{-3}$) to 420/m, reveals surprisingly small differences in the induced voltage waveforms at the open boundaries. **Table I** displays some characteristics of the right side voltage pulse for reduction of the initial electron number. The pulse duration is from the initial pulse departure from the zero line to the first zero crossing after the pulse peak.

Gross Insensitivity to Asymmetric, Narrow Column Illumination

When a narrow column of initial electrons is centered under the center electrode, the induced voltage pulses at the two sides of the parallel plates are very similar. With movement of the column to the left side of the center electrode, the two waveforms remain generally similar, but differ more greatly in detail. The greatest difference is in the peak voltage. At 1.21×10^{12} initial electrons/m, the left peak voltage is 19.9% less than the right As the initial electron number drops to 30 electrons/m, this difference drops to 10.6%. More details of these pulses have been previously presented.[9]

Shorter Pulse Generation by Initiation of Two Air Gaps

The FWHM of the induced voltage pulses can be strongly reduced by laser triggering of the upper air gap with a slight delay from the lower gap. For similar avalanches in the gaps, the upper gap generates a wave similar to that from the lower gap, but of opposite polarity. For no time delay between the avalanches, the oppositely polarized waves should exactly cancel each other at each boundary. But with a delay, the wave from the upper gap should annihilate only the tail of the wave from the lower gap. This destructive interference should reduce the width of the induced voltage pulses at each boundary.

Figure 4 shows two induced voltage pulses at the right boundary for different delays in laser initiation of the air gaps. The center electrode voltage is 292 kV, and the pressure is 27.2 atm. The pulse in **Fig. 4a** has a delay of 0.75 ps; that in **Fig. 4b** is for 0.1 ps of delay. The pulse in **Fig. 4a** has a peak value of 81.0 kV, a FWHM of 2.50 ps, and a bandwidth of 110 GHz. The pulse in **Fig. 4b**, has a peak value of 5.63 kV, a FWHM of 1.22 ps, and a bandwidth of 33.7 GHz. The pulse for the

Table I. Induced right side voltage pulse characteristics for reduction of initial electron number at 292 kV and 27.2 atm.

Initial electron number/m	Rise Time (ps)	FWHM (ps)	Duration (ps)	Time to peak (ps)	3 dB bandwidth (GHz)	Peak value (kV)
1.70×10^{13}	2.41	9.11	37.9	16.5	22.0	300
4.20×10^{5}	5.07	8.60	42.3	20.0	21.0	302
4.20×10^{4}	5.47	8.13	42.8	20.5	21.0	296
4.20×10^{3}	5.87	8.13	43.3	22.0	21.0	299
4.20×10^{2}	6.00	8.67	44.2	22.5	21.0	300

Table II. Characteristics of right side induced voltage pulses at 292 kV and 27.2 atm for dual gap initiation.

Delay (ps)	Peak pulse voltage (kV)	FWHM (ps)	Trailing signal amplitude		Rise time (ps)	3dB bandwidth (GHz)
			(kV)	% of main peak		
0.05	–4.32	1.44	6.39	148	1.38	26.9
0.10	5.63	1.22	5.63	114	0.545	33.7
0.25	22.1	2.28	8.02	36.3	0.962	45.9
0.50	56.3	2.53	9.86	18.8	1.28	106
0.75	81.0	2.50	10.5	13.0	1.38	110
1.00	105	2.66	11.3	10.8	1.41	119
1.25	132	2.95	12.0	9.13	1.51	124
1.50	155	3.08	14.1	9.05	1.70	123
1.75	175	3.11	14.6	8.34	1.83	122
2.00	199	3.14	16.2	8.12	1.92	119

shorter delay also has a stronger negative precursor and a stronger trailing negative signal relative to the positive pulse peak.

Table II shows some characteristics of the right side induced voltage pulse as the time delay varies. As the delay increases, the FWHM and bandwidth increase. Beyond 1.25 ps of delay, the bandwidth decreases. The relative strength of the negative trailing noise decreases with increasing delay.

Conclusions

The laser-driven, air avalanche, center electrode switch calculations predict the generation of high-voltage (50–300 kV), very broadband (to ~ 120 GHz) electromagnetic pulses with rise times and widths of the order of picoseconds or tens of picoseconds. The induced voltage pulse characteristics are not strongly affected by reduction of the initial electron number by over eleven orders of magnitude, nor by asymmetric placement under the center electrode. Dual initiation of avalanches in the two air gaps with a slight time delay strongly reduces the induced voltage pulse width and increases its bandwidth.

References

1. F. Villa, "High Gradient Linac Prototype: A Modest Proposal," SLAC-PUB-3875, Jan. (1986).
2. R.E. Cassell and F. Villa, "High Speed Switching in Gases," SLAC-PUB-4858, Feb. (1989).
3. D.J. Mayhall, J.H. Yee, and F. Villa, "Computer Code Prediction of Picosecond Voltage Switching and TEM Wave Generation In Air Gas Avalanche Switches," *7th Pulsed Power Conference*, R. White and B.H. Bernstein, eds., IEEE, New York, 514–517 (1989).
4. D.J. Mayhall and J.H. Yee, "Computation of Broadband, High-Power Electromagnetic Pulse Generation From an Air Gas Avalanche Switch," *8th IEEE International Pulsed Power Conference*, R. White and K. Prestwich, eds., IEEE, New York, 855–858 (1991).
5. M.M. Kekez, "Simple Sub-50-ps Rise Time High Voltage Generator," Rev. Sci. Instrumen. **62**, no. 12, 2923–2930, Dec. (1991).
6. P.A. Pincosy, P. Poulsen, and J.J. Morrison, "Ultrawideband Generators," *Ultrawideband Radar*, Proc SPIE, 1631, to be published.
7. J.H. Yee, R.A. Alvarez, D.J. Mayhall, D.P. Byrne, and J. DeGroot, "Theory of Short, Intense Electromagnetic Pulse Propagation through the Atmosphere," Phys. Fluids **29**, no. 4, 1238–1244, April (1986).
8. A.C. Hindmarsh, "Preliminary Documentation of GEARBI: Solution of ODE Systems with Block-Iterative Treatment of the Jacobian," UCID 30149, Preprint, Lawrence Livermore National Laboratory, Livermore, CA, 94550 (1976).
9. D.J. Mayhall and J.H. Yee, "Two-Dimensional Calculation of Electromagnetic Pulse Generation by Laser-Initiated Air Avalanche Switches," *Laser Interaction and Related Plasma Phenomena*, **10**, Plenum Press, New York, to be published; UCRL-JC-107236, Preprint, Lawrence Livermore National Laboratory, Livermore, CA 94551, Jan. (1992).

HYDROGEN SPARK SWITCHES FOR REP-RATED ACCELERATORS

S. L. Moran, M. G. Grothaus, L. W. Hardesty
Pulsed Power Technology Branch-Code F45
Dahlgren Division, Naval Surface Warfare Center
Dahlgren, Va. 22448-500

Abstract

The Pulsed Power Technology Branch at NAVSWC is investigating high-power switch technologies for use in rep-rated, high-current accelerators. Switches are needed that can handle 10 kJ of energy, 500 kV, 100 kA, while operating with jitter less than 10 ns at repetition rates up to 10 kHz. In-house efforts have concentrated on spark-gap switches because of their high-voltage and high-current capabilities in single-shot devices and because of their simplicity and low cost. We have shown that hydrogen gas, with its high thermal diffusivity, allows an order-of-magnitude improvement in the recovery time (and, therefore, repetition rate) of an unblown spark-gap switch. Recovery of the switch can be made even faster by triggering the switch well below its self-break voltage, allowing voltage to be reapplied while the gas is still hot. Tests have shown that recovery times (to the operating voltage) can be reduced an order-of-magnitude when the gap is undervolted by approximately 50%. The combination of high-pressure hydrogen gas and undervolted triggering provide a factor of 100 improvement over typical air spark gaps. Recent tests have demonstrated 100-μs recovery of an undervolted hydrogen spark gap without gas flow. High energy tests have been performed at 50 kV, 170 kA and 12 kJ with 100 μs recovery times. High voltage tests with a 5-pulse burst at 500 kV are presently underway. Recovery of the switch appears to be largely independent of voltage and energy transferred.

Introduction and Background

The Navy is interested in high-current accelerators *that can* operate at bursts rates up to 10 kHz. Most high-current charged-particle-beam research has been conducted as single-shot tests. Operation at high repetition rates requires repetitive pulsers that achieve all the charging, reset, arming, and firing functions in a time period of 100μs. At present, the major technology limitation for developing these pulsers is a high-repetition-rate switch that can handle the required powers. The Naval Surface Warfare Center, Dahlgren Division, is developing repetitive switch technologies required for compact, recirculating repetitive accelerators. Efforts have concentrated on high-pressure spark gap switches because of their high-voltage and high-current capabilities in single-shot devices. The work has focused on improving the repetition rates of spark gaps without resorting to high gas flow.

Voltage-recovery information has been obtained [1] for triggered spark gaps using a standard center-pin trigatron configuration. Figure 1 shows the percent recovery vs time for triggered spark gaps in hydrogen and other common spark gap gases. For an unblown spark gap triggered near self-break, typical recovery times are about 10 milliseconds for most gases, such as air, nitrogen, argon, and SF_6. We have found that using hydrogen gas, with its high molecular

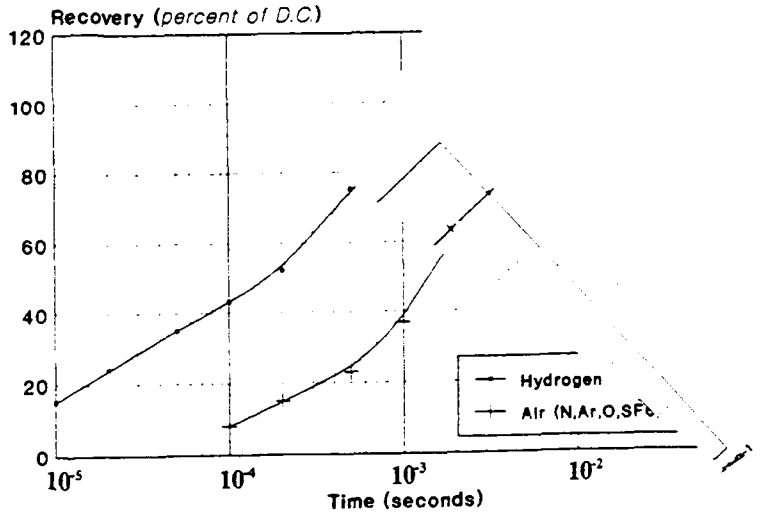

Figure 1. Recovery Curves for Common Gases

speed and thermal diffusivity, allows the recovery time to be an order-of-magnitude faster, or about 1 millisecond.

Recovery of a spark gap switch can also be made faster by triggering the switch well below self-break. Recovery time can be decreased by making the operating voltage significantly less than the static (D.C.) breakdown voltage, allowing voltage to be reapplied before the gas has returned to ambient temperature. Tests with hydrogen have shown that recovery times (to the operating voltage) can be reduced an order-of-magnitude when the gap is "undervolted" by approximately 50%. 100-microsecond recovery has been demonstrated in an unblown spark gap using high-pressure hydrogen in a trigatron configuration.[2] Reapplication of the operating voltage without breakdown verified full recovery. 100-μs recovery of an undervolted hydrogen switch was first demonstrated at low energy (5 Joules) at 120 kV peak voltage and 200 A peak current. Recovery was later demonstrated at 200 Joules using a resonantly charged, sub-ohm, 200-ns pulse-forming-line.[3] Peak current was 35 kA, voltage was 60 kV, and hydrogen gas pressure was 1,000 psi. A drawing of a typical switch is shown in Figure 2. The pressure housing is 20 cm in diameter and made of stainless steel. The insulators are MACOR ceramic, and the electrodes and trigger pin are made from copper-tungsten. Trigger-gap spacings are typically equal to the main-gap spacings of about 0.5 cm.

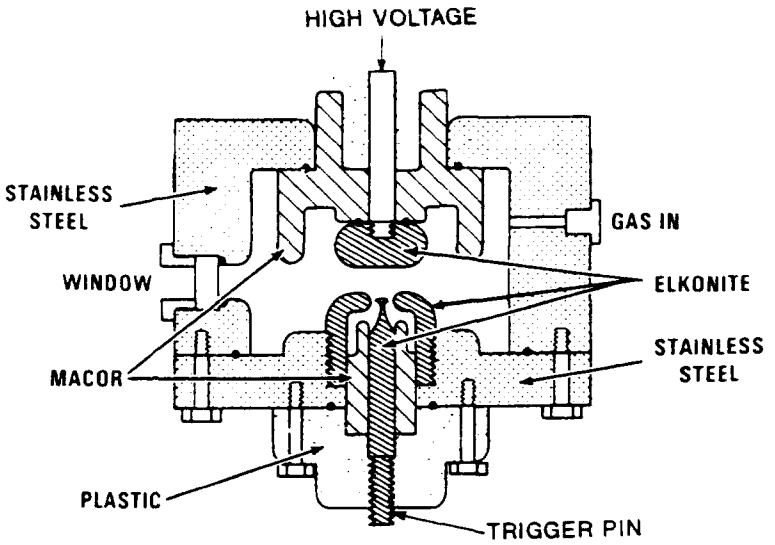

Figure 2. Cross Section of Hydrogen Switch

The hydrogen-switch technology is presently being studied for use in a rep-rated recirculating accelerator using water-dielectric ET-2 cavities under construction at Sandia National Labs. Figure 3 shows a pictorial diagram of a pulsed power train needed for a five-pulse burst. Each prime energy store charges five accelerating cavities in parallel. An identical system powers the five cavities on the other side of the accelerator. Two sets of high rep-rate switches are required. One set is needed at low voltage but high energies and currents to charge the accelerating cavities. The other set is used to switch the accelerating cavities, and operates at less energy but higher voltage. Hydrogen switch technology is being studied for both requirements.

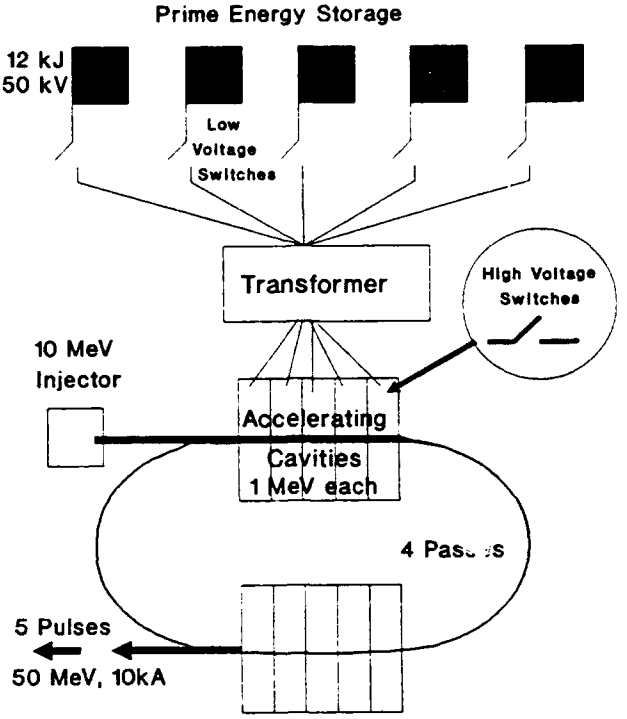

Figure 3. A Pulsed Power System to Drive a Rep-Rated Recirculated Accelerator.

50 kV High-Energy Switches

The current and energy requirements for the low-voltage switches in Figure 3 can be obtained from order-of-magnitude requirements for an accelerator. For a 50 Mev, 10-kA beam 40-ns long (10 accelerating cavities and 4 passes), about 2.5 kJ of energy is required for each cavity without excessive droop. To charge five cavities in parallel, 12.5 kJ of stored energy are needed,

or 10 uF of capacitance at 50 kV. A 15-us charge time would be maximum for a water-dielectric cavity without excessive losses, requiring a peak current of 170 kA. Each switch only needs to recover once.

Hydrogen switches have been successfully tested to the above low-voltage requirements.[4] Two 10-μF capacitor banks were connected via hydrogen switches to a common 0.1-ohm resistive-metal load. Geometric inductance was about 600 nH. Separate single-shot triggers were used to trigger each hydrogen switch at about 50% of self break. The resistive load damped the oscillations after about 1 cycle, giving a current pulse width of about 10 μs and a peak current of 170 kA. Full recovery was achieved in 100 μs at 2.7 MPa (400 psi) at full voltage. The actual time between measurable current flows was less than 80 μs. The system was also operated single-shot into a shorted load at 260 kA peak current for an oscillating pulse 80 μs in duration. There was no gas flow in these experiments.

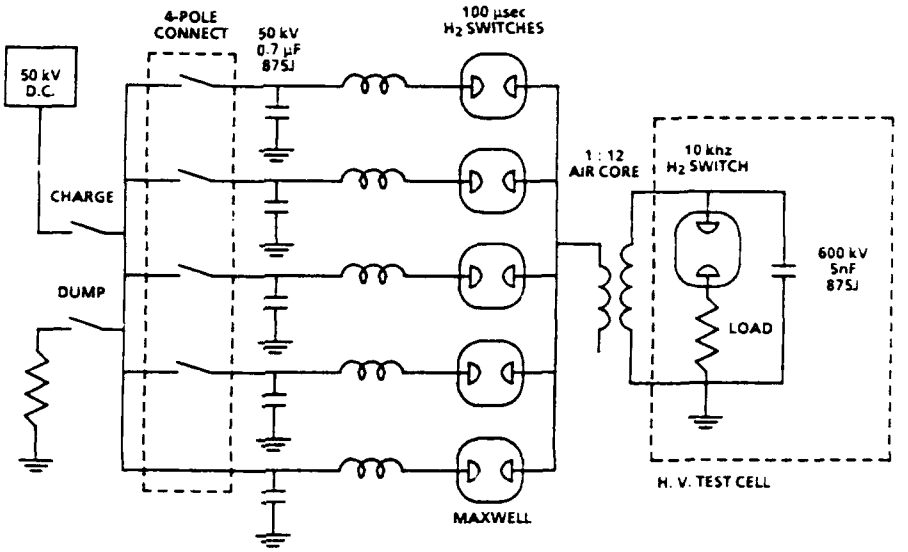

Figure 4. 5-Pulse High Voltage Test Setup.

High-Voltage Switches

The requirements for the high-voltage switches in Figure 3 are given by accelerator requirements. For a 50 Mev accelerator (10 Mev injector) with 10 cavities and four passes, each cavity must average about a megavolt output over four decaying pulses. The ET-2 cavity impedance mismatch provides a step-up of about three, which translates to a cavity/switch voltage requirement of about 500 kV. The effective impedance the ET-2 cavities is less than 1Ω. Since the risetime of the waveform must be about 10 ns or less, the L/R time constant must be less than 5 ns requiring an inductance of 4.5 nH. The present hydrogen switches require twenty switches in parallel to achieve the required inductance. Jitter requirements are very strict for multiple switches, since all must fire together to share the current and energy. Each switch will discharge about 1 nF at 500 kV. Peak current will be about 500 kA going through twenty switches, or 25 kA per switch. Total energy transferred per switch is only 125 J. Since four passes are needed, total current conduction time is about half a microsecond. The high-voltage switch requirements are therefore, 500 kV, 25 kA, 125 J, low jitter, and multiple-pulse operation.

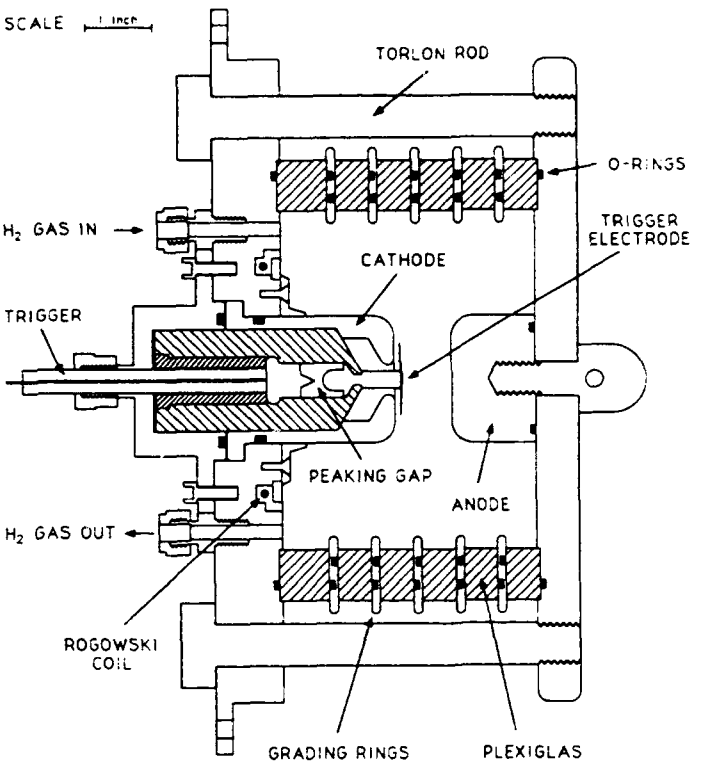

Figure 5. The modified V/N Switch.

High-Voltage 5-Pulse Experimental Setup

An experiment was designed to test the hydrogen switches to 500 kV for multiple pulses. It provides the currents and energies that would flow through a single switch in the accelerating cavity. The 50-kV, 5-pulse system drives a step-up pulse transformer to 500 kV as shown in Figure 4. Each primary capacitor (0.7 μF) is charged through relays to 42 kV D.C. (617 J). Since all switches are connected to a common load, each switch must recover before the next one fires. Individual 100-kV, 100 ns rise, trigger systems are used for each primary switch. The transformer charges a high-voltage capacitor which is discharged by a single, fast-recovery hydrogen switch in a five-pulse burst. The transformer is an air-core, dual-resonant type with a step-up ratio of 12, and for normal operation will provide 500 kV with 42 kV on the primary. The dual-resonant charge time in water is about 13 μs. The high-voltage capacitor is a 4-nF, 500 kV series-stacked set of conventional capacitors and is discharged by a single high-voltage pressurized hydrogen spark gap controlled by a multiple-pulse trigger. The resistive load is adjusted to obtain a ringing decay of about 600 ns to approximate the waveform of an accelerating cavity. Tests ranged from a 2.25-Ω resistor (3 cycles e-fold) to a 9-Ω resistor (about 1 cycle). The inductance of the high-current discharge path was 1.27 μH.

The high-voltage hydrogen switch is a modification of Sandia's V/N switch design [5], which is a single-stage switch with a trigger disk situated within the main gap region near the ground electrode. The spacing ratio of the trigger gap to the main gap is the V/N ratio and also indicates the triggering/voltage ratio. A 1.3-MV V/N switch was converted for use with high-pressure hydrogen. A drawing of the modified V/N switch is shown in Figure 5.

One of the major concerns of this effort was the development of a rep-rated trigger system capable of a 10 kHz-burst of five pulses at voltages over 100 kV. To our knowledge, such a system has never been built. In previous switch experiments, the triggering voltage was typically equal to the working voltage of the switch. This becomes impractical at hundreds of kV. For these experiments, a miniature Marx generator was modified to allow burst-mode operation in hydrogen. The system is based on a single-shot MiniMarx originally designed at Los Alamos.[6] This Marx produces a 200-kV pulse with a 2-ns risetime using a 30-kV D.C. input. We are operating the Marx in a burst mode by using hydrogen gas in the switches and a hard-tube pulser as a trigger source. The Marx is resistively charged from a large capacitor to provide the energy for a 5-shot burst. We have achieved 5-pulse bursts at repetition rates of 2 kHz with this system operating about 85% of self-break at 100 psig of hydrogen. Further improvements are underway using higher gas pressures and increased triggering range to operate at a lower percent of self-break[7].

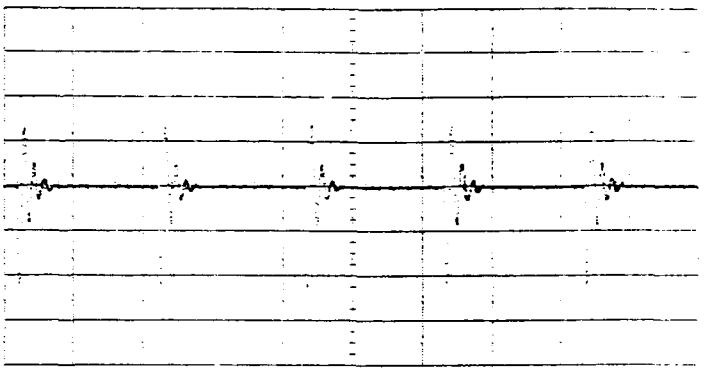

Figure 6. Current from a 5-Pulse Burst into a Resistive load. 10kA/div. vert., 50 μs/div. horiz.

High Voltage Experimental Results

Results of the 5-pulse primary system operating at 45 kV and 10 kHz are shown in Figure 6. This figure shows the 5-pulse burst of current into a 0.375-Ω load. Peak current was 40 kA, stored energy was 700 J per pulse, and hydrogen pressure was 275 psig. The complete 5-pulse system has been fired at half voltage. Figure 7 shows operation at 250 kV with 5 pulses in a 2-kHz burst. The present 5-pulse rep-rate is limited to 2 kHz by the Marx trigger generator.

The high-voltage switch was originally designed for SF_6 with a main gap spacing of 4.4 cm and a trigger-gap spacing of 0.23 cm giving a V/N ratio of 19. The main-gap spacing was reduced for the hydrogen experiments in several steps. The trigger-gap spacing remained constant. The first configuration had a main-gap spacing of 2.9 cm (field strength of 86 kV/cm) and a V/N ratio of approximately 13. The hydrogen pressure range to hold off 250 kV was 120 to 180 psig, allowing operation at almost 70% of self-break. Recovery times of 500 μs were demonstrated. The housing was strengthened with the use of TORLON 4030 polyamide plastic rods, which have double the tensile

strength of nylon. With a main-gap spacing of 1.9 cm and a V/N ratio of 9, the switch operated from 190 to 290 psig, allowing operation down to 65% of self-break. Jitter and delay were also improved over the previous configuration. The gap spacing was then reduced to 1.3 cm to allow operation at 187 kV/cm and a V/N ratio of 5. The switch operated below 60% of self-break at 400 psig with jitters of a few ns. Two-pulse recovery using a single-shot trigger was obtained at 200 μs (shown in Figure 8), which would correspond to 5 kHz in a burst. Further strengthening of the switch, either by more bolts or smaller diameter housing, should allow even more improvement.

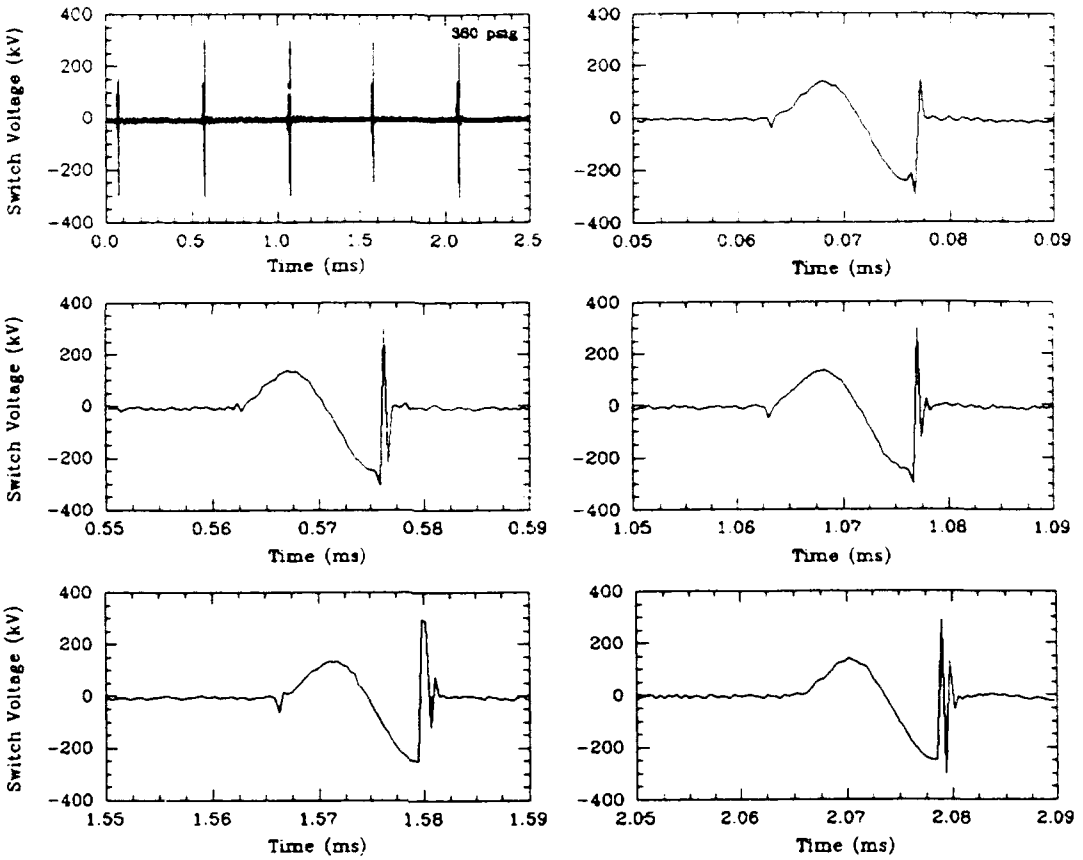

Figure 7. 5-Pulse Burst at 2 kHz and 250 kV.

A crucial test of the hydrogen switch suitability for use in accelerating cavities resides in its delay and jitter characteristics for each pulse in a burst. Experimental tests were performed to determine these quantities for a 1-kHz five-pulse burst at 250 kV. The gap spacing of the switch was 1.3 cm with a V/N ratio of 5 and an average electric field of 187 kV/cm. The results of the measurements are summarized in Figure 9. Only the characteristics for the first four pulses were measured. The raw data is given as a function of switch pressure. Self-breakdown of the switch occurs at approximately 230 psi, so operation at 400 psi represents 60% of self-break operation. The switch delay increases as the switch is more and more undervolted, as one would expect, but does not exceed 16 ns. With the exception of the first pulse, the jitter is below 2 ns and remains so for each of the consecutive pulses.

Tests are underway with a smaller version of the V/N switch which will be operated at pressures up to 800 psi with a gap spacing of 1.7 cm. Tests to 500 kV are planned. Similar, if not better delay and jitter characteristics are anticipated with this switch as the average main-gap field will be increased to 290 kV/cm with a V/N of 7.

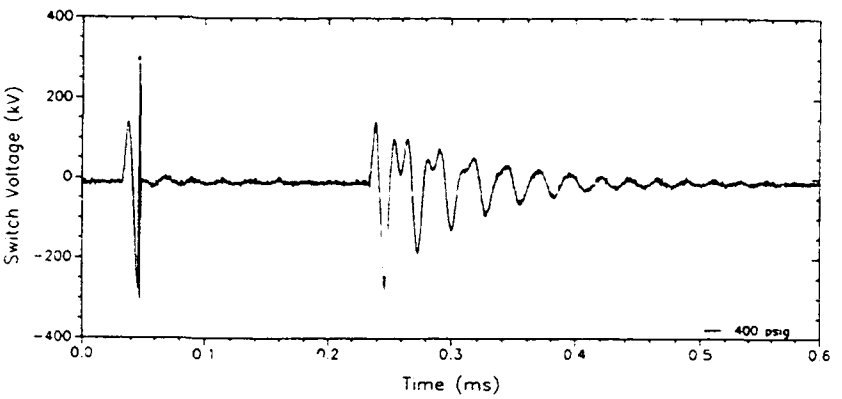

Figure 8. 2-pulse Burst at 5 kHz and 250 kV.

Conclusions

The low-voltage experiments have demonstrated that the hydrogen recovery curve shown in Figure 1 is accurate within a factor of 2 from millijoules of energy to 12 kilojoules. Peak oscillating currents of up to 260 kA have been carried by the hydrogen switch.

The high-voltage experiments have shown that a gap spacing of 3 cm, which was a factor of 6 larger than any previous tests, did not create problems with the recovery of the switch. The recovery curves obtained with small gaps also predict about 500-μs recovery at 60% of self-break. This is a good indication that hydrogen gaps can be scaled to higher voltages while maintaining fast recovery. Gap spacings from 1 mm to 30 mm have been tested at voltages from 20 kV to 250 kV and pressures up to 1,000 psi with similar recovery results.

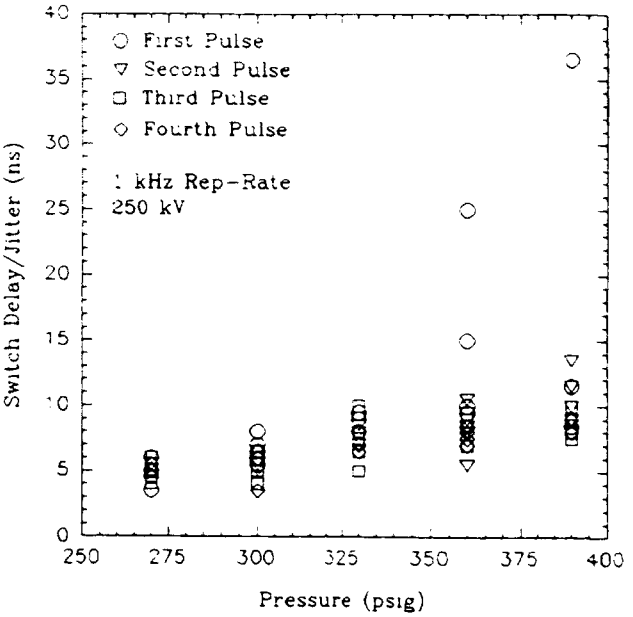

Figure 9. Jitter and Delay Measurements

We have shown that multiple triggered pulses at hundreds of Joules do not degrade switch operation. Two-pulse recovery curves can be applied to bursts of greater length. Multiple pulses do not appear to affect recovery or jitter. However, we have not run experiments where the switch housing was significantly heated. Tests down to 60% of self break show switch jitter in hydrogen can be kept below a few nanoseconds. In a burst, the delay and jitter of each pulse is less than (or equal to) the first pulse.

We have now demonstrated that a 250-kV gas spark-gap switch can operate in a burst mode at a repetition rate of at least two kilohertz with no gas flow with jitters of a few ns. With further improvements in the triggering system, there appears to be no physical reason why a 500 kV spark gap handling kilojoules of energy cannot operate in a burst mode at 10 kHz.

It is important to note the small size of the overall system. The entire system (except for the DC power supply) is only a few cubic meters, and is portable. The system volume could be reduced by half if desired. With high-energy capacitors, two systems this size (plus a third for the injector) would power an entire 50-Mev accelerator for a 5-pulse burst.

References

1. S. Moran and S. Hairfield,"Recovery of Overvolted Spark Gaps," 16th Power Modulator Symposium, Arlington, Va., June 1984, p. 71.

2. R. Hutcherson, S. Moran, and E. Ball, "Triggered Spark Gap Recovery," 6th Pulsed Power Conference, Arlington, Va., June 1987,p. 221.

3. S. Moran, R. Hutcherson, and E. Ball, " A Facility for High-Repetition-Rate Switch Testing at Medium Power,"6th Pulsed Power Conference, Arlington, Va., June 1987, p. 252.

4. S. Moran and L.W. Hardesty, "High-Repetition-Rate Hydrogen Spark-Gap," IEEE Transactions on Electron Devices, Vol. 38, No. 4, April 1991

5. W.K. Tucker, E.E. Jones, T.L. Franklin, L.F. Bennet, and G. Webber, "Compact, Low Jitter, Triggered Spark Gap", Proceedings of the 5th Pulsed Power Conference, Arlington Va., June 1985, p 254.

6. D.A. Platts, "10 Joule High Voltage Trigger Micro-Marx", Proceedings of the 3rd IEEE Pulsed Power Conference. Albuquerque N.M., June 1981, p.485

7. S.L.Moran, L.W. Hardesty, M.G. Grothaus, "Hydrogen Spark Gap for High Repetition Rates", 8th IEEE Pulsed Power Conference, San Diego, Ca., June 1991.

SIMPLE METHODS OF SQUARE PULSE GENERATION BY INDUCTIVE PULSE FORMING LINES AND A FIELD EFFECT TRANSISTOR AS AN OPENING SWITCH

M. J. Rhee and B. N. Ding[a)]
Department of Electrical Engineering and
Laboratory for Plasma Research
University of Maryland, College Park, Maryland 20742 U.S.A.

Abstract

Two simple methods of repetitive square-pulse generation by inductive pulse forming lines with an n-channel enhancement MOSFET as an opening switch are described. The square-pulse output voltages produced by both methods are in good agreement with those predicted for ideal circuits.

I. Introduction

An important merit of the inductive energy pulsed power system is its compactness of size.[1,2] Two inductive pulse forming line (IPFL) systems, the *current charged transmission line* (CCTL)[3-5] and the *dual of the Blumlein line* (DBL),[5] are of particular interest, because of their capability of square pulse generation. Efficient power multiplication can be achieved in these systems by simply narrowing the duration of the square output pulse for a given stored energy. This has been successfully demonstrated[6,7] by producing nanosecond square pulses using a CCTL with a GaAs photoconductive semiconductor switch.

The transistors, which can be easily controlled by a low voltage pulse, have been widely used as variety of switching applications. The n-channel enhancement metal oxide semiconductor field effect transistor (MOSFET), in particular, can be operated as an opening switch at moderate current level of $\sim$100 A/cm^2 and hold-off voltage of $\sim$500 V with a relatively fast opening time of less than 0.1 μs.[8] In this work, using an n-channel enhancement MOSFET as an opening switch in CCTL and DBL, we demonstrate that efficient square pulse generation with high repetition rate can be achieved by such simple methods.

II. Experiment

The experimental realization of the CCTL and DBL is shown schematically in Figs. 1(a) and 1(b) respectively. As the inductive-energy storage element, a 50-m long RG-213 coaxial cable of the characteristic impedance, $Z_0 = 50\Omega$, is used in the CCTL and two of the same cables are used in the DBL. Matched load for CCTL is $R_L = Z_0 = 50\Omega$ and for

DBL is $R_L = Z_0/2 = 25\Omega$ respectively (See Ref. 5). In actual circuits, since the output voltage is measured by a 50-Ω oscilloscope(Tektronix 2440) through a 50-Ω coaxial cable, the load resistance, R_L, is formed by either a series connection of a resistor and the 50-Ω coaxial cable for cases with $R_L > 50\Omega$ or by a parallel connection for cases with $R_L < 50\Omega$ respectively. The charging current is supplied by an initially charged 10 μF capacitor, which approximately acts as a constant voltage source. A simple transmission line analysis dictates that both charging-current waveforms of ideal CCTL and DBL by a constant voltage source are staircase functions. The charging current is monitored by a 0.1-Ω current-viewing resistor (CVR) terminated at the opposite end of the IPFL. An n-channel enhancement-mode MOSFET(NTE67) is employed as a switch, which is controlled by a square wave gate voltage. While the gate voltage is above the threshold voltage, the MOSFET switch is in on-state allowing the charging current to flow through the IPFL(s). As the gate voltage drops below the threshold voltage, the MOSFET switch opens interrupting the current I_0 through

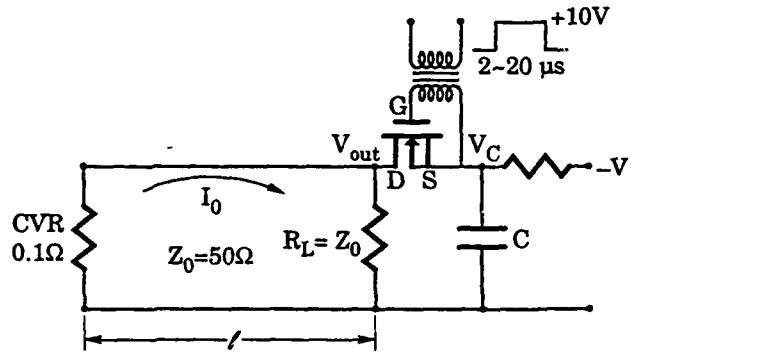

(a) CCTL

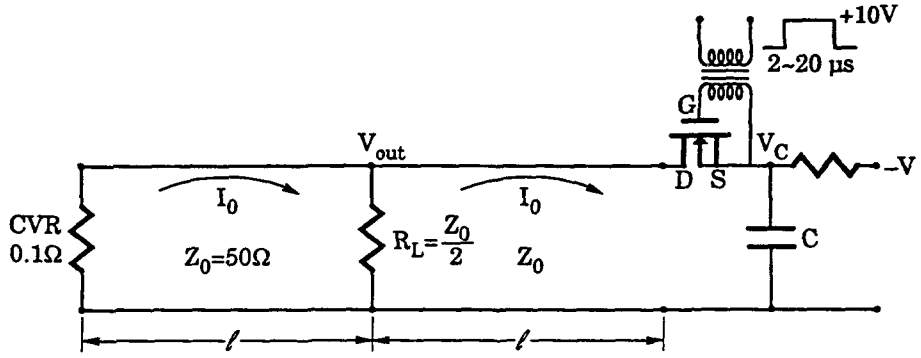

(b) DBL

FIG. 1. Schematic representation of experimental setups, (a) the current charged transmission line (CCTL) and (b) the dual of the Blumlein line (DBL) systems.

the switch. The stored inductive energy in the IPFL(s) is then released to the matched load producing a square pulse.

The output voltage measurements for the both CCTL and DBL are made with the same experimental conditions. The gate trigger pulse of 10-V amplitude, 2-μs duration, and 5-ns rise time and fall time is used. A charging current at the end of the charging period is adjusted to $I_0 = 1$ A by varying the capacitor charging voltage V_c. The measured charging current waveforms of a five- step staircase function and the output waveforms with matched and mismatched loads for both CCTL and DBL are shown in Figs. 2(a) and 2(b) respectively. The mismatched load results in a series of post pulses of amplitudes given by[5]

$$V_{out}^{n} = R_L Z_0 I_0 (Z_0 - R_L)^n / (Z_0 + R_L)^{n+1}, \tag{1}$$

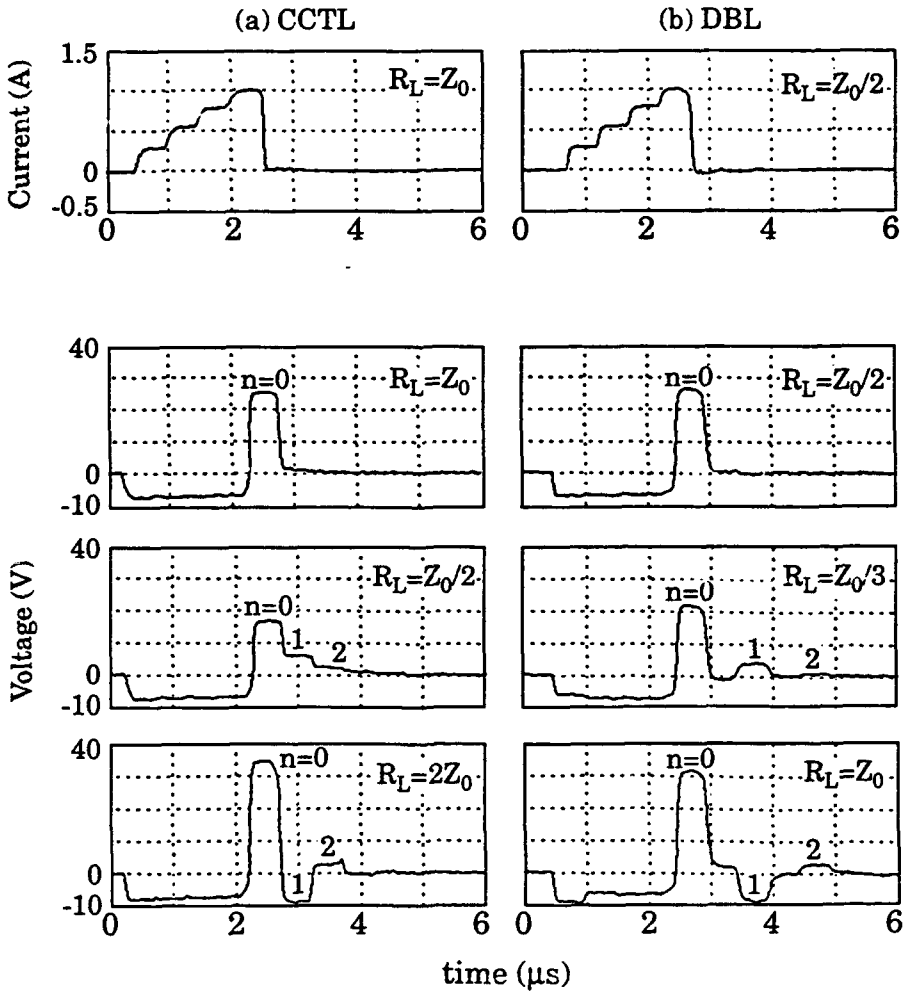

FIG. 2. Typical charging current and output voltage waveforms of (a) the current charged transmission line (CCTL) and (b) the dual of the Blumlein line (DBL).

for the CCTL and

$$V_{out}^{n} = 2R_L Z_0 I_0 (Z_0 - 2R_L)^n / (Z_0 + 2R_L)^{n+1} \qquad (2)$$

for the DBL, where $n = 0$ corresponds to the main pulse. Note that both Eqs. (1) and (2) reduce to $V_{out}^{0} = \frac{1}{2} I_0 Z_0$ for the matched cases. The measured amplitudes of the main and post pulses are in reasonable agreement with the values given by Eqs. (1) and (2). Note that, in the case of DBL, each pulse is separated by an interval which is the same as the pulse duration, $2l/v$, as expected.[5] It is also noted that prior to the main pulse, a prepulse during the current charging is observed. This is the measure of the voltage across the capacitor during the current charging for the case of CCTL and one half of that for the case of DBL with a matched load.

The output voltage may be increased by increasing the charging current, I_0. The charging current can be increased by increasing the capacitor charging voltage or also by increasing the duration of the trigger pulse up to a quarter cycle period of equivalent LC circuit. Figure 3 shows graph of the output voltage for the matched load vs. the charging current I_0 for the both CCTL and DBL cases. Straight-line fit is for $V_{out} = \frac{1}{2} I_0 Z_0$, which is amplitude of the main pulse into the matched load for both CCTL and DBL. It can be shown that the induced voltage across the switch as it opens is $I_0 Z_0/2$ for CCTL and $I_0 Z_0$ for DBL. Thus, the limits of the maximum output voltage for a given switch are approximately equal to the breakdown voltage of the switch for the CCTL and one half of that for the DBL.

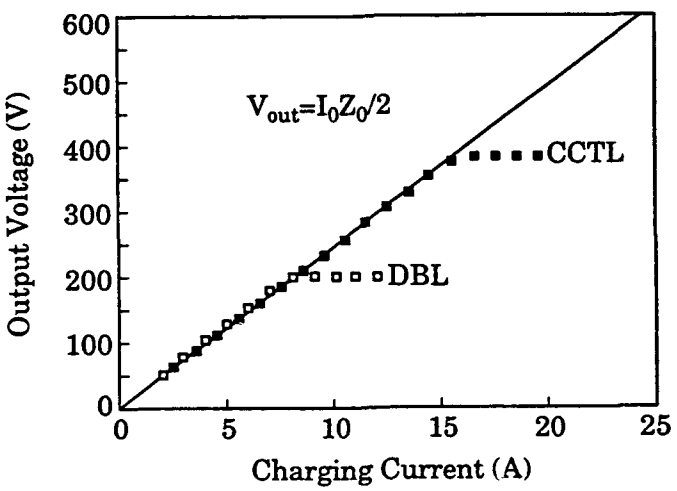

FIG. 3. Graph of output voltage vs the charging current.

This is clearly observed in Fig. 3, and is consistent with the dc breakdown voltage, ~400 V, of the MOSFET. The MOSFET maintains excellent switching characteristics even at a very high repetition rate. It is found in the present setup that the maximum repetition rate corresponds approximately to a frequency for which the current-charging duty cycle is 50%, i.e., the frequency whose period is approximately twice that of the current charging (duration of gate trigger pulse). For example, with a current charging period of 2 μs as in the case mentioned above, the system can be operated at repetition rates up to 250 kHz.

III. Conclusions

Two simple methods of repetitive square-pulse generation by using CCTL and DBL inductive pulse forming lines with an enhancement-mode MOSFET as an opening switch are described. The measured output pulse voltages up to limits by the breakdown voltage of the MOSFET are in good agreement with those predicted for ideal circuits. It is found that the MOSFET switch can be operated at high repetition rates up to a frequency whose period is approximately twice that of the current charging.

Acknowledgment

This work is supported by the U. S. Department of Energy.

Footnote and References

[a]Permanent address: China Academy of Engineering Physics, P. O. Box 523-56, Chengdu, Sichuan, China.

1. K. H. Schoenbach, M. Kristiansen, and G. Schaefer, Proc. IEEE, **72**, 1019 (1984).

2. E. M. Honig, *Opening Switch* (Plenum Press, New York, 1987) edited by A. Guenther, M. Kristiansen, and T. Martin, pp. 1-48.

3. G. N. Glasoe and J. V. Lebacqz, *Pulse Generators*, (McGraw-Hill, New York, 1948), p. 210.

4. M. J. Rhee and R. F. Schneider, IEEE Trans. Nucl. Sci. **NS-30**, 3192 (1983).

5. M. J. Rhee, T. A. Fine, and C. C. Kung, J. Appl. Phys. **67**, 4333 (1990).

6. C. C. Kung, E. A. Chauchard, Chi H. Lee, M. J. Rhee, and L. Yan, Appl. Phys. Lett. **57**, 2330 (1990).

7. E. E. Funk, E. A. Cahuchard, M. J. Rhee, and Chi H. Lee, IEEE Photonic Technology Lett. **3**, 576 (1991).

8. M. Weiner, in Workshop on Solid State Switches for Pulsed Power, edited by W. M. Portnoy and M. Kristiansen (Texas Tech Univ., Lubbock, Texas, 1983) pp. 189-201.

HIGH REPETITION RATE MEGAVOLT MARX GENERATORS

Yu. A. Kotov and S. N. Rukin

Institute of Electrophysics, Russian Academy of Sciences, Ural Division, 620219 Ekaterinburg, Russia

Abstract

We consider problems of developing megavolt Marx generators with a pulse repetition rate of 100 to 1000 pps and with high average power. Principles are proposed for development charge and trigger circuits on the basis of semiconductor elements. The circuits ensure a fast and uniform pulsed-regime charging of capacitor stages within 100 to 200 μs from a thyristor charging unit. In addition, the circuits permit spark gaps to operate automatically without the use of external triggering pulses. A five-stage generator has been developed and tested, which has an output voltage of 0.5 MV and a pulse repetition rate up to 650 pps and whose average load power is as high as 16 kW at an average power density of 150 W/kG.

These principles are embodied in a novel repetitive electron beam accelerator, "RUSLAN". The accelerator developed has the following tentative parameters: electron energy, 1 MeV (an open-circuit voltage of 2 MV); beam current, 10 kA; pulse energy, 0.4 kJ; pulse repetition rate, 100 to 200 pps; average power, 40 to 80 kW in the continuous regime.

Introduction

In contrast to nanosecond-range repetitive pulsed systems based on the use of transformers and forming lines [1, 2], Marx generators are, as a rule, connected directly to the load and perform over a pulse length range between 0,1 and 1 μs. In developing repetitive pulsed generators, the scheme due to Marx is most preferable for practical realization. This is primarily because the Marx circuit does not comprise an output commutator designed for the total voltage and total average power of the setup. The total average power is commutated by a large number of spark gaps, each commutating the power of only one stage. Second, Marx generators have a specific stored energy that is approximately an order of magnitude higher than that of oil-filled megavolt repetitive-duty lines, a feature that permits the specific average power of the setup to be increased substantially.

The present paper discusses problems of developing repetitive Marx generators. Consideration is given to basic components, primary power supply sources, charging circuits, and triggering circuits.

Problems of developing megavolt repetitive Marx generators

Creating compact repetitive Marx generators calls for

developing an appropriate elements base, primarily repetitive capacitors and spark gaps, as well as designing novel charging and triggering circuits.

Generators with an energy reserve of up to 1 kJ employ as storage capacitors low-inductance ceramic capacitors, while generators with a larger energy reserve use special types of film-insulated repetitive capacitors [3] that have an energy reserve of up to 20 J/l at a voltage of 40 to 100 kV, at a pulse repetition rate of up to 400 pps, and with a lifetime of 10^8 pulses. The latter type of capacitors permits developing compact megavolt-range Marx generators that have at a pulse repetition rate of 100 to 1000 pps an average power of 10 to 1000 kW and a power density of 100 to 200 W/kG.

The problems of repetitive commutation in Marx generators are resolved in a conventional way: by using spark-gap electrodes made of erosion-resistant materials, as well as by blowing compressed gas through the gaps [4, 5] to increase the gas cooling rate. Since the spark gaps in the Marx circuit are under a high potential relative to the grounded frame, the problem arises of removing hot exhaust gas when the spark gaps are blown through. With the average power per spark gap being 5 to 10 kW, a metallic cooler is inserted between the spark gap and the dielectric collector to cool the gas and to increase the electrical strength of the entire gas main [6]. The life of the spark gap depends on the power being commutated and ranges between 10^6 and 10^8 pulses [2].

Progress in systems for commutating repetitive generators may be associated with the use of sealed-off hydrogen spark gaps that do not require a blowing system because of substantially lower losses compared to those due to commutation in nitrogen and air. Success can be also achieved owing to the development of novel charging circuit configurations that ensure the supply of charging voltage to capacitors within 0,1 or 1 μs. That would enable one to use as commutating elements magnetic switches with a virtually unlimited lifetime.

The major difference of repetitive-pulse generators from single-pulse generators lies in the way the charging circuits are constructed. Conflicting requirements imposed on charging circuits (low impedance in the charging process and high impedance in the discharging process) manifest themselves in the development of generators with a pulse repetition rate between 10 and 1000 pps, when one has to combine high efficiency in the charging and discharging processes with fast and uniform charging of capacitor stages, which may range from 10 to 20 in number.

The most common way to lower the nonuniformity of charging and to increase the efficiency of the charging process is to make the isolating elements between the stages as inductances [6-11]. Placing an input current-limiting charging inductor with an inductance value much greater than the inductances between the stages ensures a virtually uniform degree of charging of all capacitors. When the generator is energized from an ac voltage charging source, a semiconductor diode is mounted for isolation between the power supply source and the generator, while the generator is triggered during the voltage half-cycle when the diode is not conducting. This method of isolation is used when the pulse repetition rate does not exceed the frequency of the ac

input voltage.

To isolate the generator from the dc voltage charging source and to increase the time span between the Marx discharge and the next charging cycle, the authors of Ref. [10, 11] installed a controllable spark gap. However, mounting in the charging circuit a spark gap that commutates in the repetitive regime the total average power generator and the necessity of using synchronized noise-immune triggering circuits of the charging commutators and of the rest of the spark gaps make the device complicated in design and lower its reliability.

New principles used in the construction of charging and triggering circuits

The transition to the 10^2-10^3 pps range, needed for the creation of compact high-power-density pulsed generators, calls for the development of uniform-capacitor -charging circuits and reliable noise-immune triggering circuits. In the present work, these problems are solved by making the generator's charging elements as unidirectional branches of series-connected semiconductor diodes and by automatically triggering the spark gaps after the capacitor charging process is over [12, 13]. In this case, the nonuniformity in the degree of charging of capacitors C (Fig. 1) does not depend on the value of impedance and on the voltage drop across the isolating element L_c, but is determined only by the performance of the diodes V. Owing to the inversely proportional current dependence of the forward resistance of the diode, the circuit ensures a practically uniform capacitor charging (the nonuniformity of charging does not exceed 0.1% per stage). The elements L_o serve to isolate the discharging and charging circuits during Marx erection. After the spark gaps have been switched on, the diodes V are not conducting and there is no voltage across the coils L_o. The capacitors C are charged in the pulsed regime from a thyristor charging device through a step-up pulsed transformer and the isolating element L_c.

After the charging process is over, the core of the pulsed transformer is saturated and the secondary-winding output voltage reverses its polarity. This process leads to automatic erection of the generator since the half-potential point of the secondary winding is connected, via the circuit R, to the spark-gap triggering electrodes. The absence of external synchronization circuits and controllable switch elements in the triggering circuits renders the commutation system highly reliable when the generator operates in the repetitive mode.

A 0.5 MV repetitive Marx generator

It is on the basis of the principles outlined above that we have developed and studied a repetitive Marx generator with an output voltage of 0.5 MV. The generator comprises 5 stages with a charging voltage of 100 kV and has an energy reserve of up to

50 J. As the generator is charged the energy from the capacitor C_1 with a voltage of 1 kV is transmitted within 100 μs via the pulsed transformer and charging circuits to capacitors C. The transformer has a transformation ratio of 100 and is wound on a permalloy core. In Fig. 2 we show an oscillogram of the voltage across the capacitors when these are being charged; the oscillogram was obtained by superposition of 1200 pulses. Figure 3 presents an oscillogram of the voltage across the transformer secondary winding, demonstrating the triggering pulse of the spark gaps when the charging process is over.

The charging circuits are assembled from diodes with a reverse voltage of 130 kV. The load equivalent R_L and the isolating inductor L_c are combined: the inductor winding is superimposed on a polyethylene pipe whose inner cavity is filled with running water and is a load resistor.

The commutation system contains spark gaps with longitudinal pumping of compressed air along the spark gap axis. To this aim, all electrodes have central holes. The electrodes are fitted out with tapered tips. Mounted at the spark gap outlet is a cooler with a developed surface for cooling the gas before the exhaust main. The range of the controlled operation of the spark gap as a function of pulse repetition rate is shown in Fig. 4.

The generator performs with a pulse repetition rate of 650 pps, gaining an average load power of 16 kW. Ignoring the thyristor power supply source and the pulsed transformer, the generator's power density is 150 W/kG; the efficiency of the generator amounts to 80%.

Megavolt repetitive accelerator RUSLAN

The same principles underlie the design of the megavolt repetitive accelerator RUSLAN. This accelerator has the following tentative parameters: electron energy - 1 MeV (the output voltage of the open-circuit Marx generator is 2 MV), beam current - up to 10 kA, pulse energy - 0.4 kJ, pulse repetition rate - 100 to 200 pps, average power - 40 to 80 kW in the continuous regime. The generator comprises 10 stages with a charging voltage of 200 kV, which are assembled on ceramic capacitors placed in an oil tank of dimensions 1000 x 1300 x 2700 mm^3. The same tank accommodates a pulsed transformer that has a transformation ratio of 210. The charging time of the capacitors is 180 μs. The spark gaps are as three-electrode units with axial pumping by compressed air. Currently the generator is at the stage of alignment and adjustment. A charging thyristor power supply source has been tested for a load equivalent that has a resistance of 0.09 Ω and an inductance of 3 μH. An average power of 86 kW at a pulse repetition rate of 200 pps has been attained in the continuous regime. The spark gaps have been bench-tested with a view to determining the lifetime and optimizing the geometry of interelectrode gaps. With the average power being up to 5 kW and with the pulse repetition rate 330 pps, the spark gap has a resource on the order of 10^8 pulses and permits continuous operation for 8 hours.

Conclusion

New principles of developing the charging and triggering circuits of megavolt repetitive Marx generators have been proposed. These ensure fast and uniform charging of capacitors in the pulsed regime and enable, without using external triggering circuits, automatic operation of spark gaps after the charging process has been completed. The modern elements base (capacitors, diodes, spark gaps) permits developing generators with a pulse repetition rate of 100 to 1000 pps that have an average power of up to 1 MW at a power density of 100 to 200 W/kG. The resource attained, at a level of 10^8, permits such generators to be used as laboratory setups when conducting research that requires high values of both pulsed and average power. Direct application of Marx generators in technological processes calls for increasing the resource to 10^{10} or 10^{11} pulses, an imperative which, in turn, is associated with the necessity of developing fundamentally novel commutation systems.

References

[1] A.S.Eltchaninov, F.Ya.Zagulov, S.D.Korovin et al. High-current electron beam accelerators with high pulse repetition rate. Novosibirsk: Nauka, 1983 (in Russian).
[2] M.T.Buttram and G.J.Rohwein. IEEE Trans. on electron devices, v.ED-26, N 10, p.1503, 1979.
[3] Maxwell Laboratories, Inc. Technical literature on "Repetition- rate capacitors", data sheet MLB-2021 B, 1982.
[4] A.S.Eltchaninov, F.Ya.Zagulov, S.D.Korovin and G.A.Mesyats. "Pribory i Tekhnika Eksperimenta", N4, p.162, 1979 (in Russian).
[5] T.R.Burkes, J.P.Craig, M.O.Hagler et al. IEEE Trans. on electron devices, v.ED-26, N10, p. 1401, 1979.
[6] M.T.Buttram and M.W.O'Malley. Proc. on 6th IEEE Pulsed Power Conf., p. 711, 1987.
[7] V.S.Barantsev, I.I.Kalyatskiy, R.E.Klein. "Pribory i Tekhnika Eksperimenta", N2, p.108, 1964 (in Russian).
[8] I.I.Kalyatskiy, V.I.Kurets, V.N.Safronov at al. "Pribory i Tekhnika Eksperimenta", N 1, p.99, 1974 (in Russian).
[9] K.R.Prestwich, M.T.Buttram, G.J.Rohwein. Proc. 3-rd Int. Conf. on High Power Electron and Ion Beams, Novosibirsk, 1979, p. 198.
[10] N.K.Kapishnikov, V.M.Muratov, V.S.Potapov. "Pribory i Tekhnika Eksperimenta", N5, p.98, 1984 (in Russian).
[11] N.K.Kapishnikov. "Pribory i Tekhnika Eksperimenta", N 2, p.87, 1987 (in Russian).
[12] Yu.A.Kotov and S.N.Rukin. Proc. 7th Simp. on High-current Electronics, Tomsk, pt.3, p.102, 1988 (in Russian).
[13] S.K.Lyubutin, S.N.Rukin, B.G.Slovikovskiy. Proc. 8th Simp. on High-current Electroniks, Sverdlovsk, pt.3, p.29, 1990 (in Rassian).

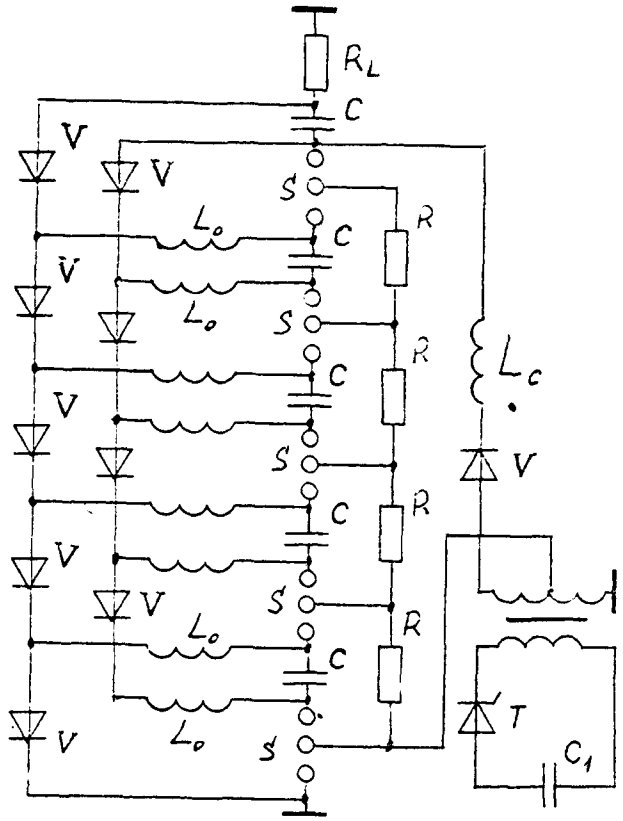

Figure 1

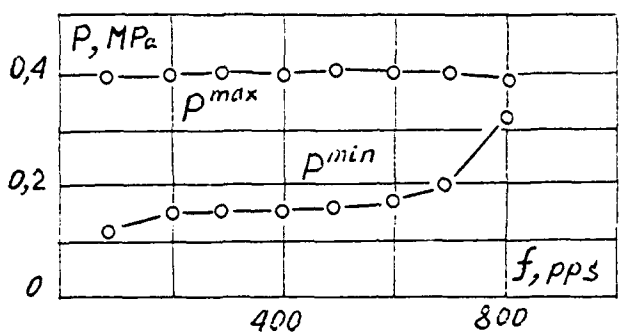

Figure 4

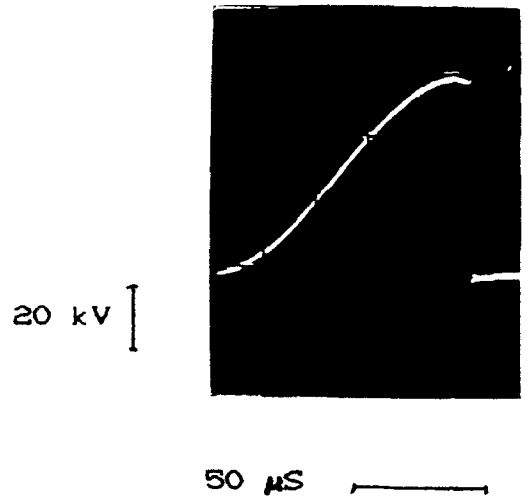

Figure 2

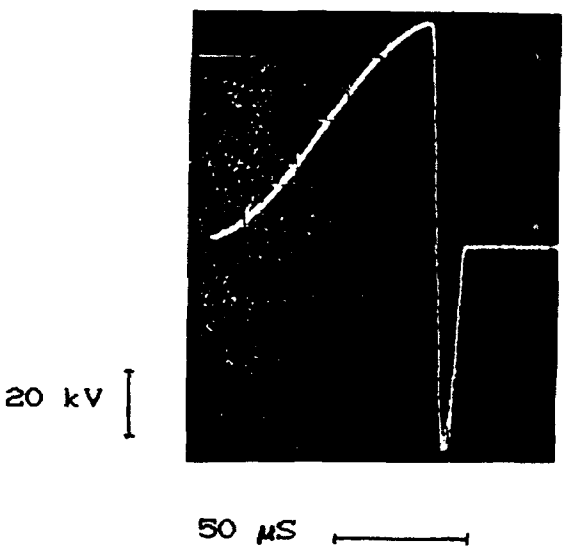

Figure 3

Fig.1. Circuit of a repetitive Marx generator with semiconductor charging circuits, pulsed charging of capacitors and automatic triggering of spark gaps.

Fig. 2. Oscillograms of charging voltage. Superposition of 1200 pulses (pulse repetition rate 300 pps, exposure time 4 s).

Fig. 3. Oscillogram of the voltage across the pulsed transformer secondary winding. Demonstration of the triggering pulse after the capacitor charging process is over.

Fig. 4. Range of control of the repetitive spark gap as a function of the pulse repetition rate. P^{max} is the pressure beyond which the spark gap cannot be triggered, P^{min} the self-breakdown boundary.

150 keV INTENSE ELECTRON BEAM ACCELERATOR SYSTEM WITH HIGH REPEATED PULSE

Zhang Qi, Li Tixing, Tang Hongfang, Xia Nenggiao
Wang Zhigin, Zheng Baohong

Institute of Electronics, Academia Sinica
P.O.Box 2702, Beijing, China

A 150 keV electron beam accelerator system has been developed for wide application of high power particle beams. The new wire-ion-plasma electron gun has been adopted.

The parameters are as follows:

Output energy	130-150 keV
Electron beam density	250 mA/cm^2
Pulse duration	1 μs
Pulse rate	100 pps
Section of electron beam	5 × 50 cm^2

This equipment can be used to study repeated pulse CO_2 laser, to be a preionizer of high power discharge excimer laser and to perform radiation curing process and so on.

The first part contains principle and design consideration. Next is a description of experimental arrangement. The remainder is devoted to describing experimental results and its application.

(I) INTRODUCTION

A small-sized, electron beam accelerator system has been

The project is supported by National Natural Science Foundation of China.

developed for promoting the industrial application of high power particle beams. The main part of this equipment is new Wire-Ion-Plasma (WIP) E-Gun. The principle of WIP E-Gun is very different from thermal electron gun and cold plasma electron gun. The new WIP E-Gun has many advantages over conventional technologies[1], [2]. Important is its flexibility of beam configurations including rectangular, radial and double-sided beams which are scalable to large beam areas. Its demonstrated long life, high reliability, compact design and ease of operation make it suitable for many applications.

There are some papers[3], [4], [5] concerning principle and experimental results of WIP E-Gun in the past. We have designed a WIP E-Gun and conducted series of experiment, the purposes are to explore the possibility of potential application and to lay the foundation of small-sized practical electron beam accelerator system.

(Ⅱ) PRINCIPLE and DESIGN CONSIDERATION

The WIP electron gun concept is illustrated in Fig. 1. Its operation is as follows: the vacuum vessel is filled with helium to a pressure of 10-20 millitorr. By energizing the wire anode with an RF modulator, a helium discharge develops in the plasma chamber. Positive ions extracted from the plasma through the extraction grid enter the high voltage acceleration region where they strike the secondary emitter. Then secondary electrons are accelerated towards the grid and exit the vacuum chamber through a thin metallic window. The plasma distribution thus controls the spatial and temporal characteristics of the emerging electron beam, and since the plasma is at ground potential, no high voltage grid or modulators are necessary.

The working point at the accelerating region of WIP E-Gun are selected as follows. Fig. 2 shows a low-pressure breakdown voltage in the plasma cathode accelerating region as a function of

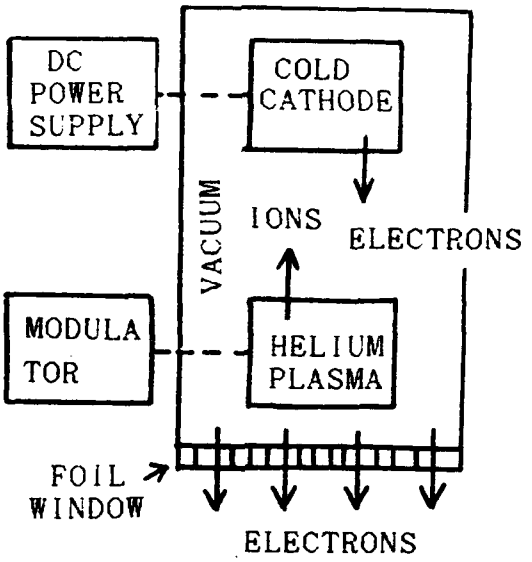

Fig. 1, WIP electron gun concept

gap width. There are two breakdown curves, one is vacuum breakdown, another is Paschen breakdown (15-20 millitorr). The working point will lie between two breakdown curves and nearer to vacuum breakdown characteristics, because the Paschen breakdown is very sensitive to the presence of impurity of the gas. In the present device, the operating voltage is 150 kV, the typical helium pressure is 10-20 mtorr. So selected electrode spacing is about 4 cm.

The maximum ion flux density that can be extracted from a given plate electrode geometry depends on the Child-Langmuir formula. It is as follows:

$$J_i = 2.3 \times 10^{-8} \ (V^{3/2})/d^2 \quad (A/cm^2) \ \text{----------(1)}$$

where: V=voltage of gap (volts); d=electrode spacing (cm), in the present case, J_i=0.106 A/cm^2, where d=4 cm and V=150 kV. The secondary emission coefficient has been measured to be about 14 electrons/ per ion. So the maximum electron beam density for plate electrode configuration are 1.08 A/cm^2.

For cylindrical electrode configuration, we utilize the equation as derived by Langmuir and Compton.

$$I = [3.432 \times 10^{-8} \times V^{3/2} \times L] / [M^{1/2} \times r \times \beta^2] \quad (A) \ \text{----(2)}$$

where M=molecular weight of ion; r=radius of anode (cm);

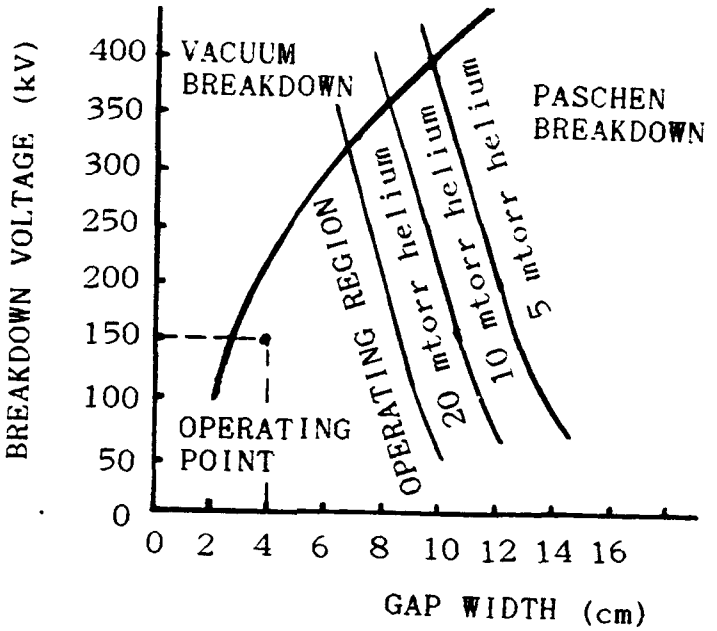

Fig. 2, Low-pressure breakdown voltage in the plasma accelerating region as a function of gap width

V=voltage of gap (volts); β=dimensionless variable; L=length of discharge (cm). β is defined by another variable γ. $\gamma = \ln(r/r_o)$, where r_o is the radius of extraction grid; thus if

$\gamma > 0$, $\beta = 1+0.9769(r_o/r)^{2/3} \sin [1.0854 \log_{10}(r/11.92r_o)]$ --(3)

$\gamma < 0$, $\beta^2 = 4.6712 [(r_o/r) \log_{10}(r_o/1.4142r)]^{3/2}$ ----------(4)

in present case, r_o= 14 cm; r= 18 cm; V=150 kV; helium ion, so γ=0.251, β=0.221. Since we are extracting only over an angle of 25° degrees and the width of electron beam window is 5 cm, so the maximum electron beam density is 2.198 A/cm^2.

In the same case, the electron beam density of coaxial configuration is larger than that of plate configuration.

(Ⅲ) EXPERIMENTAL ARRANGEMENT

Two types of WIP E-Gun configuration have been developed. Fig. 3(a) shows a cross-sectional schematic of the basic coaxial gun design and Fig. 3(b) shows one of plate-electrode E-Gun. Two types of emitter is supported inside the same vacuum vessel by a high voltage cable and is easily to exchange each other. The high voltage cable keeps the cathode (emitter) electrically insulated from ground (the vacuum vessel) and is connected with

high voltage power supply.

The dimensions of plasma chamber are 7 cm width × 4 cm high × 50 cm length. The anode adopted two to six of tungsten filament with ϕ 0.1 - ϕ 0.3 mm and installed in parallel with central plane of the discharge chamber.

Two types of extraction grid have been designed. They are plane and curved surface and the extraction grid have a radius of 14 cm. The extraction grid is made of stainless steel of 1 mm and its transparency is 80%.

The maximum output of high power supply is 100 mA at 150 kV. The high voltage power pack is hermetically sealed and contains high voltage transformer and filter circuit.

The JK-9 oil pump provi[illegible] a vacuum in the electron gun housing. Once vacuum up to 10^{-4} torr, helium was admitted through a fine leak valve until the pressure reached 10-20 mTorr and the system are ready to work.

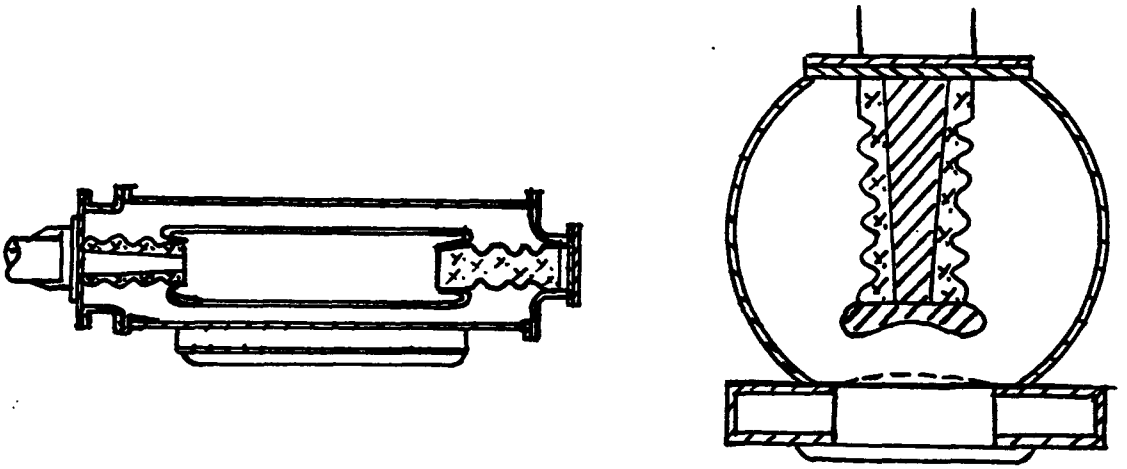

(a) Coaxial gun design; (b) Plate gun design

Fig. 3, Schematic cross section of WIP E-Gun

(Ⅳ) EXPERIMENTAL RESULTS

The WIP E-Gun have been operated with a beam voltage as high as 130 kV, a value limited by the power supply.

The discharge current waveform at different conditions have

been obtained using Pearson Model 410 current transformer. Fig. 4 (a) shows discharge current waveform and the maximum ion flux reached 90 A. The repeatability at 100 Hz have been shown in Fig. 4 (b).

A compact WIP E-Gun system has been constructed and some experiments are just developing in depth. We think that WIP E-Gun will apply to different field in the near future.

(a) single pulse (b) repeated pulse at 100 Hz

Fig. 4, the discharge current waveform

REFERENCES

(1) Li Tixing et al "A new type of low energy electron accelerator system - WIP E-Gun" proceedings of third chinese national conference on High Power Particle Beams, 1988.

(2) G. Wakalopulos and D.K. Conti, "Wire-Ion-Plasma (WIP) - a revolutionary new technology for E-Beam curing" proc. of Finishing'83 conf. Cincinnati, OH, USA.

(3) U.S. patent, No. 4,025,818

(4) W.M. Clark and G.J. Dunniing, "A long pulse high current electron gun for E-Beam sustained Excimer Lasers" IEEE Journal of Quantum Electronics, Vol. QE-14, No. 2, 1973.

(5) D. Pigache et al. "A short pulse secondary emission electron gun for high pressure gas lasers and plasma chemical reactors" proc. of 6th ICPIG. 1983.

QUICK CHARGING BLUMLEIN PFL

K. Masugata, S. Tsuchida, H. Saitou, K. Shibata*, M. Shigeta*,
Y. Sekimoto, and K. Yatsui
Lab. of Beam Tech., Nagaoka Univ. of Tech., Nagaoka, Niigata 940-21, Japan
*TDK Corporation, Chiba 286, Japan

ABSTRACT A new type of compact, discharge-switch free Blumelein PFL has been developed for pulse-power applications. Here, a saturable charging inductor of amorphous cores is utilized to obtain a fast charging of the line. In the initial test, the intermediate conductor of PFL is charged up to +300 kV by a fast Marx generater in ~ 220 ns. After the charging, a magnetic switch of amorphous core is saturated and output of -290 kV, 50 kA, 60 ns is generated. On this phase, charging inductor acts as a step-up transformer and produces a doubled voltage pulse to the load. Output pulse of -580 kV, 24 kA is obtained with current rise time less than 16 ns. The energy transfer efficiency (output pulse energy/charging energy of PFL) is estimated to be more than 92 %.

§1. Introduction

High-voltage pulse-power technology[1] has a wide area of applications including Z-pinch, high power microwave, free electron laser, particle beam fusion, collective ion accelerations, and so on. For these applications, compact and long lived generators with highly repetitive operation are required.

To achieve the requirements, we have developed a new type of pulse power system. Figure 1 shows the cross-sectional view of the system. To obtain quick charging, we have utilized a saturable inductor of amorphous metalic cores as a charging inductor (CI). Thus, quick charging of PFL becomes possible with low prepulse level. In addition, by adding inductive voltage produced in CI to the output pulse, twice the output voltage of PFL can be applied to the load.

Magnetic switch[2] (MS) is suitable to obtain a repetitive operation of PFL. However, since the switching inductance of MS depends on the charging time, it has been difficult to apply to conventional Blumlein lines[3] (BL). This problem is solved in the quick charging BL and fast switching of MS is obtained.

In this paper, the design details of the system and experimental results in the test operation are described with the discussion of the characteristics and performance of each parts.

§2. System description

The fast charging BL is constructed of marx generator, double coaxial, water filled Blumlein PFL, BL switch using saturable inductor, CI using saturable inductor and dummy load. Figure 2 shows the equivalent circuit of the system. High voltage pulse generated by a Marx generator charges a capacitance of the BL (C_i and C_o). Charging C_i is carried out through saturated CI. After the charging, the BL switch is turned on and the charge of C_o is reversed, producing the output pulse. As CI acts as a transformer[3] at the output phase, output voltage of the PFL is doubled and applied to the load (Z_L).

In this sections, design details of each parts are described.

Marx generator (MG) A compact, 3 stage, oil filled MG is used for the charging of PFL. The design values of output voltage, charging energy, charging voltage, and series capacitance are 300 kV, 1.1 kJ, ±50 kV, and 25 nF, respectively. The MG is carefully designed to reduce series inductance (L_s) to be ~ 500 nH.

Pulse Forming Line (PFL) The PFL is a double coaxial, water filled, reversed switching BL. The diameter of the outer conductor is 31 cm and the length is ~ 1 m. The characteristic impedance between inner and intermediate conductor is 3.1 Ω, and that between intermediate and outer conductor is 3.3Ω. The total capacitance of the line in the charging phase is ~ 20 nF. The intermediate conductor is connected to MG and charged by a positive pulse. The BL switch is in the end of PFL and connected between intermediate- and outer-conductor. The design parameters of output pulse are, impedance ~ 6.4 Ω, voltage ~ 300 kV, current ~ 47 kA, and pulse duration ~ 60 ns.

Blumlein Switch MS is used as a BL switch. Table I lists the characteristics of the cores used in MS. Switching inductance (L_c) is calculated to be

Table I. A characteristics of the cores of MS.

Material	iron-based amorphous (AC 10 (TDK))
Inner radius/outer radius/width	155 mm/85 mm/96 mm,
Thickness of amorphous tape	23.1 μm,
Insulation	6-μm thick PET
Space factor	68.3 %
Suturated magnetic flux density (B_s)	1.06 T (DC)
Residual magnetic flux density (B_r)	0.80 T (DC)
Magnetic flux density swing ΔB (=Br+Bs)	1.86 T (DC)
Coercive force (H_c)	3.5 A/m(DC), 2000 A/m(250 ns pulse)
Number of cores	2 + 1/2(half size, width=48 mm)
Total magnetic flux swing (ΔBS)	0.031 Vs

~ 36 nH, which gives switching time of ~ 24 ns for the line of 3.3 Ω. Vτ value, total volume and cross-sectional area of the cores is 0.0372 Vs, 0.013 m^3, and 0.017 m^2, respectively. Hysteresis loss in MS is estimated from B-H loop of same materials in a pulse operation to be 60 J/shot.

Charging Inductor (CI) Figure 3 shows the schematic of CI. Center conductor of the PFL is connected to the outer conductor of the cavity of amorphous core via four spork cross feeders passing through a grounded disk. Charging current of the flows through the outer conductor and inner conductor of CI and grounded. Namely, inner and outer conductor of the PFL are connected through CI. As bias current is applied in advance to the opeation in the same direction as the charging current, CI is saturated in the charging phase with low inductance. In the output phase, direction of the current flow is reversed and CI is unsaturated, having high inductance.

Characteristics of the cores is listed in Table II. Introducing the experimentally obtained values of $\mu_{unsat} \sim 200\ \mu_0$ and $\mu_{sat} \sim \mu_0$, the inductance of CI in the charging phase (L_{ch}) and output phase (L_o) is calculated to be

$$L_0 \sim 5300\ \text{nH}, \quad L_{ch} \sim 41\ \text{nH}.$$

As a result, low impedance in the charging phase as well as high impedance in the output phese are expected.

Table II. Characteristics of the cores of CI.

Material	cobalt-based amorphous(AC 30 (TDK))
Inner radius/outer radius/width	125 mm/57 mm/24 mm,
Thickness of amorphous tape	21.6 μm,
Insulation	6-μm thick PET
Space factor	68 %
Suturated magnetic flux density (B_s)	0.72 T
Residual magnetic flux density (B_r)	0.71 T
Magnetic flux density swing ΔB ($=B_r+B_s$)	1.43 T
Coercive force (H_c)	1.34 A/m(DC), 3000 A/m(60 ns pulse)
Number of cores	7
Total magnetic flux swing (ΔBS)	0.0163 Vs

§3. Experimental results and discussion

Figure 4 shows the typical waveforms of the line. Charging voltage of PFL (V_{ch}) is measured by a capacitive voltage divider and load voltage (V_L) is measured by a resistive voltage divider of $CuSO_4$ solution in the load. Output current of the PFL (I_{BL}), load current (I_L) and switch current of MS (I_{MS}) are measured by Rogowsky coils.

Load voltage of 580 kV has been obtained, which is 97 % of the design

value. The rise time of V_L is limited by the skin effect in the dummy load. The prepulse voltage is about 40 kV, which is 6.9 % of the output pulse. Load current rises up to 24 kA in 20 ns.

From the waveform of V_{ch} in Fig. 4, $V\tau$ value of MS is evaluated to be ~ 0.038 Vs, which well agrees with the design value of ~ 0.031 Vs. From the waveform of I_{MS} before switching, leak current of ~ 2 kA is flowing through MS, which corresponds to H in the core of 2.5 kA/m. After the switching, current rise up to 100 kA with 10-90 % rise time ~ 24 ns. Large value of ~ 50 has been obtained of the ratio of current before and after the switching.

Switching inductance (L_{MS}) is evaluated from the fall time of V_{ch} (24 ns) or the rise time of I_{MS} (24 ns) to be ~ 36 nH by using a equation

$$L_{MS} \sim Z\,\tau/2,$$

where Z is the charactaristic impedance of the line (3.3 Ω) switched by MS.

Figure 5 shows the B-H curve of MS obtained by using the waveform of V_{ch} and I_{MS}. MS is found to be operated with ΔB ~ 2.24 T, H_c ~ 2.1 kA/m. Hysteresis loss in the core is evaluated to be ~ 60 J, which is mainly lost in the charging phase as a leak current of the switch.

The energy loss in CI in the output phase is evaluated to be ~ 25 J by subtracting a load energy from the charging energy of PFL in the case of charging voltage of Marx = 45 kV, where energy loss due to the saturation of CI is ignored. In this case, the leak current is estimated to be ~2.7 kA if output voltage of PFL ~ 270 kV, pulse duration of ~ 60 ns are used.

The energy efficiency of each parts are plotted in Fig. 6 against the charging voltage of MG. Transfer efficiency from PFL to load has a very high value of more than 92 % for V_{ch} = (30 ~ 55) kV, having a peak of ~ 96 % at V_{ch} ~ 45 kV. Energy loss at V_{ch} ~ 45 kV is only ~ 25 J, almost of which is considered to be a hysteresis loss in the charging inductor. In the lower voltage, switching time of MS is delayed from the optimum timing and efficiency decreses. In the higher voltage, the efficiency decreases due to the saturation of CI in the output phase.

On the other hand, transfer efficiency from MG to PFL decreases monotonically from 80 % to 60 % with incresing V_{ch} from 30 kV to 55 kV. As the histerisis loss in MS is evaluated to be only 60 J, main energy loss is considered to be due to the resistance of the gap switch of MG.

§4. Conclusion

A compact, high voltage, discharge-switch free Blumlein PFL has been

successfully developed. The PFL is operated for about 1000 shots without any troubles. In the initial test of the whole system, output pulse of -580 kV, 24 kA is obtained with current rise time less than 16 ns. The energy transfer efficency (output pulse energy/charging energy of PFL) exceeds 90 %.

References

1) J. A. Nation: Particle Accelerators 10, 1 (1979).
2) W. S. Melville: Proc. Institution of Electrical Engineers 98, 185 (1951).
3) J. D. Ivers et al.: IEEE Trans. on Nucl. Sci. NS-28, 3380 (1981).

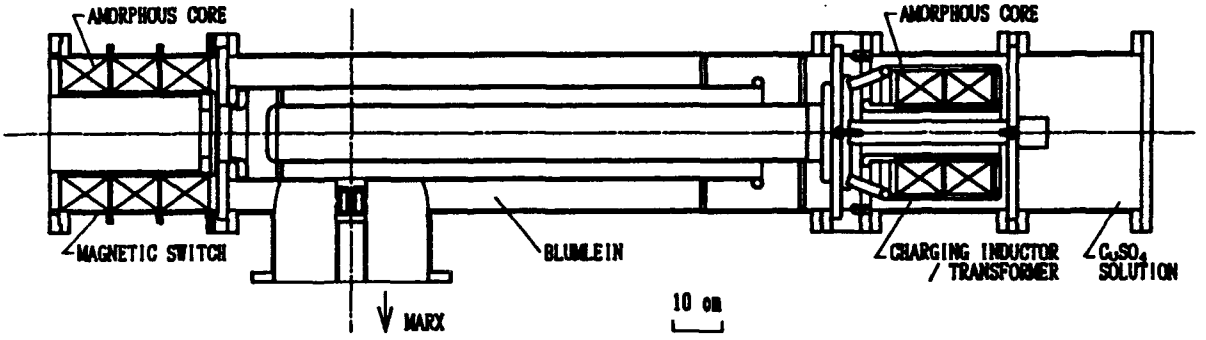

Fig.1 Cross-sectional view the quick charging Blumlein line.

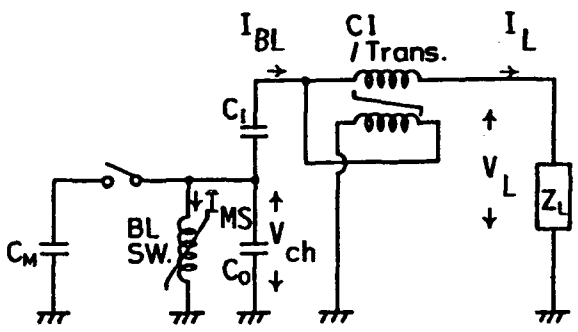

Fig.2 Equivalent circuit of the system.

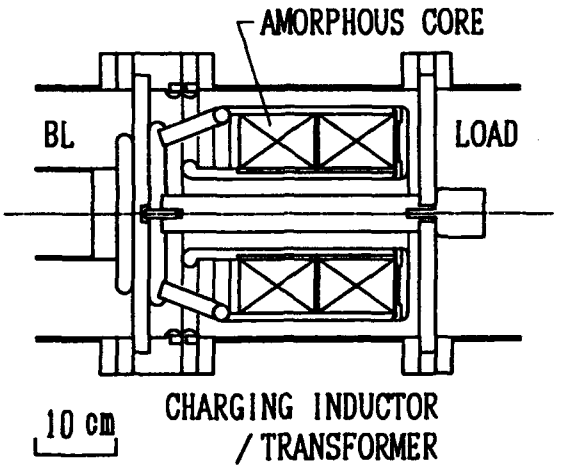

Fig.3 Schematic of the charging inductor.

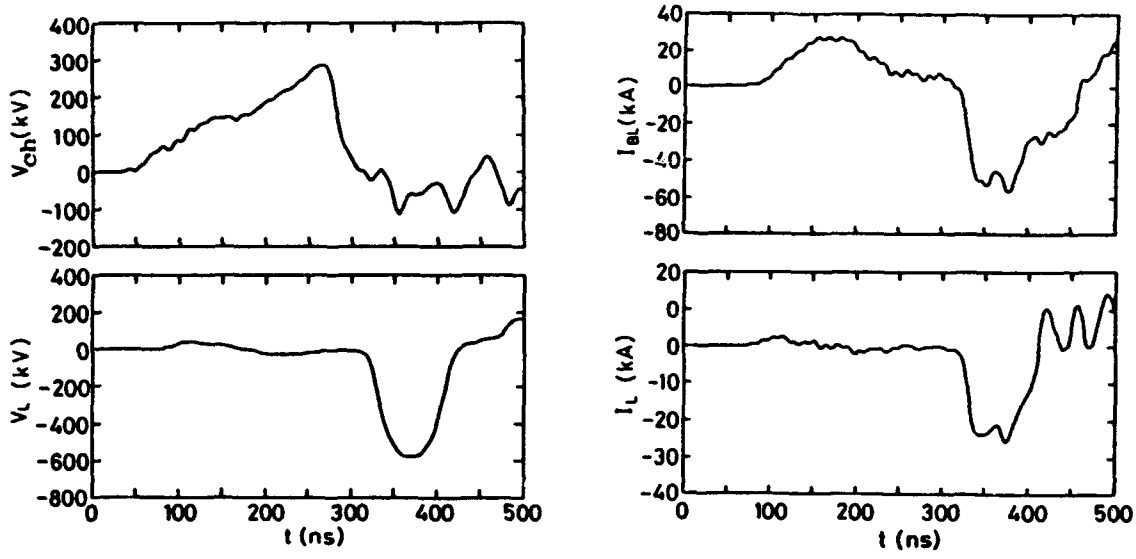

Fig.4 Typical waveforms of charging voltage (V_{ch}), output current of the line (I_{BL}), load voltage (V_L) and load current (I_L).

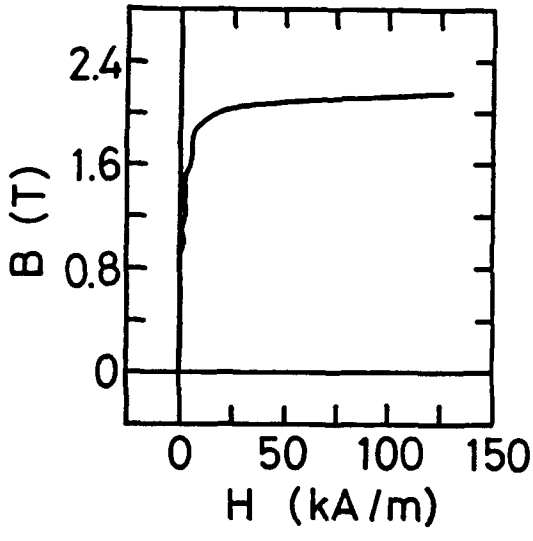

Fig.5 B-H curve of MS.

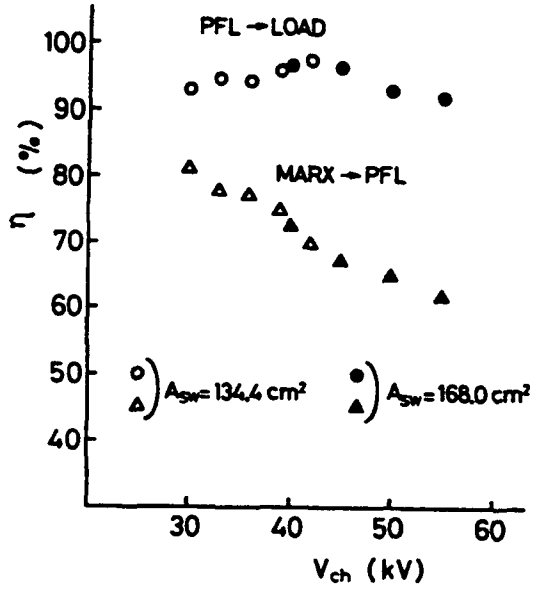

Fig.6 Energy transfer efficiency versus the charging voltage of MG.

THE DEVELOPMENT OF A ONE MICROSECOND PULSE LENGTH, REPETITIVELY PULSED, HIGH POWER MODULATOR AND A LONG-PULSE ELECTRON BEAM DIODE FOR THE PRODUCTION OF INTENSE MICROWAVES[+]

R. M. Stringfield, R. J. Faehl, M.V. Fazio, R. F. Hoeberling, T. J. T. Kwan, D. G. Rickel, F. VanHaaften, R. F. Wasierski, A. Erickson*, K. Rust**

Los Alamos National Laboratory
MS-H851, Los Alamos, NM 87545

* Mission Research Corp.
** Superconducting Supercollider Laboratory

ABSTRACT

This paper discusses the pulse power and explosive emission electron beam diode development effort we have undertaken to power a relativistic klystron amplifier (RKA) microwave source. The pulsed power and electron beam must enable the RKA to produce one kilojoule of 1.3 GHz radiation per pulse at a 5 Hz repetition frequency. These efforts include tests and improvements of a 1 μs pulse length thyratron switched modulator, and the computational and experimental design of a 1-μs-pulse-length explosive emission electron gun. The one microsecond pulse length is almost an order of magnitude beyond what has been achieved heretofore with an RKA. Achieving a peak power approaching 1 GW for 1 μs requires a well behaved electron beam on that time scale. An electron beam diode has been developed that delivers a peak current of 4 to 5 kA for a pulse duration exceeding 1 μs, at a beam kinetic energy above 600 keV. BANSHEE is the high voltage modulator designed for use as an electron beam driver for high power microwave tube development. The BANSHEE output pulse design parameters are 1 MV and 10 kA, with a 1 μs pulse width at a repetition rate of 3-5 Hz, driving a load of impedance of 100 ohms. BANSHEE is a thyratron-switched line-type modulator with a pulse transformer output stage. The modulator design is pushing the state of the art in thyratron technology and capacitor lifetime. The results of the BANSHEE modulator testing are described.

[+]Work supported and funded jointly by the DoD Office of Munitions and the DOE Defense Programs through the joint DoD/DOE Munitions Technology Development Program, and by the Army Harry Diamond Laboratories and Missile Command.

REPETITIVELY PULSED MODULATOR DEVELOPMENT

BANSHEE is the repetitively pulsed, high voltage modulator used to produce a high current relativistic electron beam for high power microwave tube development at microsecond pulse lengths. The design goal for BANSHEE is to achieve a 1 MV, 10 kA pulse, with a 1 μs flat-top, driving a load impedance in the range of 100 ohms at a pulse repetition frequency (prf) of 5 Hz. The long term goal is a prf of 100 Hz. With BANSHEE, thyratron-switched line-type modulator technology is being extended to the megavolt and multi-kiloampere level. Performance to date has achieved 600 kV at 6 kA for 1 μs at a 1 Hz prf. A prf of 5 Hz has been achieved in a different modulator configuration.

A block diagram of BANSHEE is shown in Fig. 1. The prime power source is a 90 KW, variable-voltage dc power supply. An intermediate capacitive energy storage bank of 37.5 μF is used with a small thyratron to command resonantly charge the main pulse forming Blumlein system. The main pulse forming network consists of four lumped element Blumleins. The four Blumleins each consists of two PFNs. Each set

of two Blumleins is switched by a newly developed 120 kV, hollow anode thyratron (EEV CX-1812). The CX-1812 is designed for 100 kA peak current, 10 μs pulse width, and a 500 Hz prf. The Blumleins are discharged through a 10:1 step-up iron core transformer to achieve 1 MV at the 100 ohm load. This modulator design is possible because of the ability of the CX-1812 thyratron to hold off 100 kV and conduct a peak current of 100 kA with a dI/dt of over 10^{11} A/s. The design of the CX-1812 will allow operation of the BANSHEE modulator at 1 MV for a 1 μs pulse length at an ultimate prf of 500 Hz. It must be emphasized that the CX-1812 is still an experimental tube under development, and it has not been tested to its full specifications.

The Maxwell "Type S" capacitors used in the PFN's were selected because of their size, voltage capability, and low self inductance. Low-impedance PFNs require low-stray impedance and therefore need to be compact. The shortcoming of these capacitors is their lifetime which is rated at 10^5 shots at 100 kV. A more expensive version is rated for 10^6 shots. As repetitive pulse modulator operation becomes routine, capacitor lifetime will become a significant issue. The characteristic impedance of a single PFN has been measured to be approximately 1.8 ohms. Each set of two Blumleins is switched by a newly-developed 120 kV, hollow anode thyratron (EEV CX-1812). The CX-1812 is designed for 100 kA peak current, 10 μs pulse width, and a 500 Hz prf. The Blumleins are discharged through a 10:1 step-up iron core transformer to achieve 1 MV at the 100 ohm load. This modulator design is possible because of the ability of the CX-1812 thyratron to hold off 100 kV and conduct a peak current of 100 kA with a di/dt of over 10^{11} A/s. The design of the CX-1812 will allow operation of the BANSHEE modulator at 1 MV and 10 kA for a 1 μs pulse length at an ultimate prf of 500 Hz. It must be emphasized that the CX-1812 is still an experimental tube under development, and it has not been tested to its full specifications.

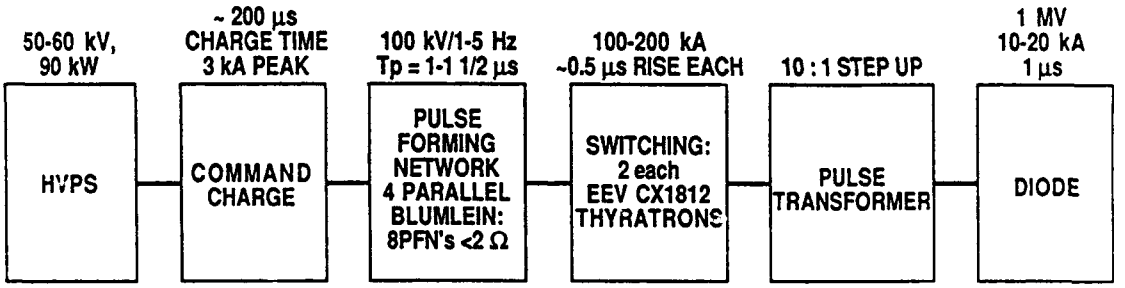

Fig. 1. Block diagram of the BANSHEE modulator.

In the initial modulator testing, four lumped element PFNs were connected in parallel and switched by a single CX-1812 thyratron. Operating at 1 Hz prf for 16 hours, an output voltage pulse of 455 kV into 100 ohms was attained before problems with the CX-1812 tube were encountered. The CX-1812 peak anode voltage was 80 kV and the switched current was 42 kA. Later analysis by EEV personnel determined that welding problems at the metal-metal joints in the tube envelope, performed by vendors to EEV, had contributed to very small vacuum leaks to the outside atmosphere. EEV has now corrected the problem.

The CX 2593 was substituted as the main switch tube in place of the CX-1812, while the CX-1812 was undergoing design improvements. The CX-2593 has a similar peak voltage rating as the CX-1812, but is designed for a lower peak and average powers. The modular nature of BANSHEE allows us to operate only one-half of the modulator consisting of one pair of Blumleins switched by one main thyratron. Using a single CX-2593 tube, we achieved 73 kV and 77 kA at 1 Hz prf for over 10,000 shots without the output pulse transformer in the circuit. These numbers would correspond to about 700 kV and 7.5 kA with the full-up modulator (4 Blumleins with two thyratrons) driving the output pulse transformer with a 100 ohm load. During

the same test period, BANSHEE was operated at a 5 Hz prf at 60 kV and 55 kA, which corresponds to 600 kV and 5 kA in the full-up modulator configuration.

The most recent testing utilized the full-up modulator configuration of four Blumleins with two thyratrons. Each CX-2593 thyratron switched two parallel Blumleins. These tests achieved 600 kV at 6 kA for 1 μs at a 1 Hz repetition frequency into a dummy load. This accomplishment demonstrates the successful operation of two state-of-the-art high power thyratrons (English Electric Valve CX-2593's) in parallel, at a voltage, current, and pulse length appropriate for RKA work at 1 Hz repetition frequency.

We attempted to increase the rep-rate to 3 Hz but encountered a retriggering problem with the small thyratron (EEV CX-1836) used to command resonantly charge (CRC) the main pulse forming network in the modulator. This fault, if uncorrected, could damage the main thyratrons. This full-up modulator configuration with two thyratrons doubles the peak current in the system since each thyratron is conducting 60-70 kA. The electrical noise increases correspondingly. We believe that it is this increased noise environment that has produced the retriggering problem with the CRC thyratron. A remedial plan has been prepared and will be executed during the next phase of the program. Throughout the modulator testing the main thyratrons (CX-2593s) performed flawlessly indicating that we should have no problem achieving 5 Hz once the retriggering problem with the CRC thyratron is resolved. It should be noted that for the single-pulse RKA work, the thyratrons were replaced with one spark gap. This was done to avoid placing the thyratrons at risk when they were not needed. When we begin to do repetitively pulsed RKA development the thyratrons will be used in the modulator.

The progress made on the BANSHEE development has resulted in modulator performance appropriate for the 1 μs, repetitive-pulse development of the RKA. Repetitively pulsed RKA development work awaits the availability of a long pulse, repetitively pulsed electron gun and dc solenoidal magnet.

1 μs Pulse-Length Field-Emission Diode Electron Gun

The major part of the recent experimental effort was directed toward obtaining a stable beam with the desired beam parameters of 500 kV and 5 kA for a 1 μs pulse. Two problems were observed during early RKA research that produced significant beam loss. First, current monitors placed along the length of the vacuum coaxial transmission line feeding the cathode indicated a significant fraction of cathode current loss to the sidewalls of the anode structure, due to the electrons backstreaming along the magnetic field lines from the downstream end of the cathode and from the cathode shank. These field emitted electrons would follow the diverging, fringing magnetic field lines in the upstream direction. The second problem was that only 65% of the cathode current emitted in the downstream direction entered the beam drift pipe. The remainder was instead intercepted by the foilless anode structure, indicating that the beam diameter exceeded the drift pipe diameter, even though the cathode diameter was smaller than the drift pipe diameter. The design of the explosive field emission diode was reexamined to improve the amount of beam current injected into the RKA from 2.5 kA to 5 kA.

Computer simulations of the diode were performed using the Los Alamos National Laboratory 2.5 dimensional PIC code MERLIN [2]. The external magnetic field in the simulation was calculated from the experimental field coil configuration, thereby allowing us to place the cathode in a converging magnetic field.

A simulation with the cathode placed in the converging magnetic field region of the magnet and shaped so that the cathode surface approximately followed the curvature of the magnetic field lines resulted in much improved transmission characteristics. For this simulation the anode was designed to have a smooth transition from the beam drift pipe radius (3.65 cm) to the outer wall of the coaxial anode (radius = 10.6 cm). In the simulation, the cathode tip was located inside the magnet coil so that the magnetic field was nearly uniform in

the axial direction with a magnitude of 0.5 T, while the cathode shank was in the region of diverging field lines. Electron emission occurs over the entire cathode surface and the electrons are radially confined by the external magnetic field. These field-emitted electrons adhere to the cathode surface and execute cycloidal trajectories, causing backstreaming electrons to be mostly reabsorbed by the cathode, particularly when the magnetic field intercepts the upstream portion of the cathode surface. Our computer simulation confirmed the extraction of an electron beam with more than 5 kA of current from such a diode geometry. In Fig. 6a, we show the electron beam cross section in the r-z plane after the electron beam simulation has reached a steady state. The thickness of the electron beam is basically determined by the Larmor radius of the electrons. Electrons emitted from the cathode at radial positions larger than the drift tube radius converge to a smaller radius as they are guided into the drift tube by the converging magnetic field. Consequently, one can avoid the electron beam current interception by the anode by placing the external magnetic field at a position that gives an appropriate final beam diameter. A simulation with the cathode in a uniform magnetic field is seen in Fig. 6b. There is no convergence of the electron beam; and a significant portion of the beam collides with the anode, while the back-streaming component is limited to a small amount of emission from the apex of the cathode. In practice, the magnetic field position is experimentally adjusted between the extremes shown in the two simulations to find the best compromise between reduced backstreaming and high beam transmission into the drift pipe.

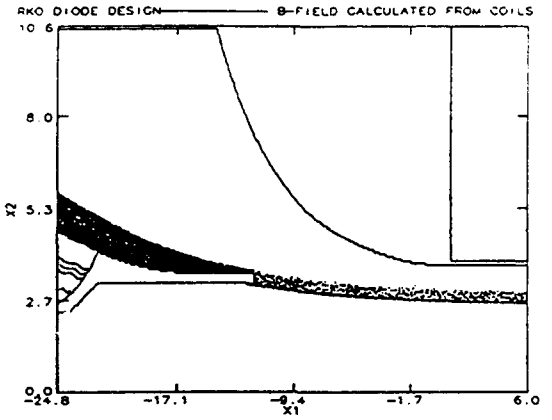

Fig. 2a. MERLIN electron beam simulation with the cathode in a converging magnetic field. The cathode shape diverges slightly less than the magnetic field lines for this simulation. The backstreaming current is ~3 kA, while the forward current is ~5 kA with a diode voltage of 500 kV.

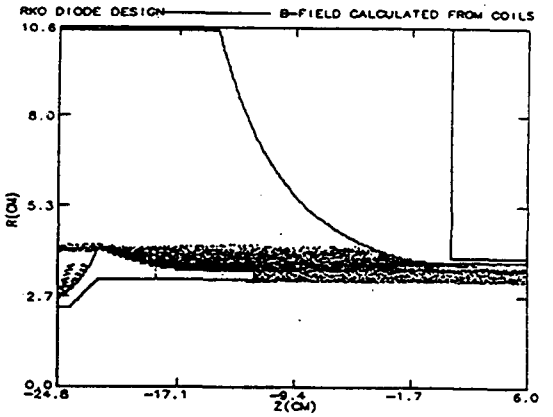

Fig. 2b. MERLIN simulation with the cathode in a uniform magnetic field. The backstreaming current is ~1 kA, while the forward current is ~6 kA.

Fast-framing photographs were taken of the electron beam 50 cm downstream of the cathode. The interframe time of the photographs was 100 ns with a 37 ns shutter open time. A sequence of these pictures is shown in Fig. 3. Note that at early time the diocotron instability is apparent but vanishes as the beam voltage and current increase. The beam thickness does not increase before diode impedance collapse, indicating that we have a well-behaved beam during the pulse. Since the RKA modeling results indicated that we should operate at a somewhat higher voltage and lower current (lower perveance) to improve overall tube efficiency by reducing the kinetic energy lost to the beam's space charge potential energy, we increased the A-K gap to raise the diode impedance. Representative waveforms for modulator voltage and current injected into the drift pipe are shown in Fig. 4. We were able to achieve voltages in excess of 650 kV and currents up to 5 kA during the

pulse. The longer A-K gap also resulted in a slightly longer pulse length due to the increased time before diode closure. The final diode geometry in Fig. 5 is the one that we are now using to produce the electron beam for the RKA microwave development.

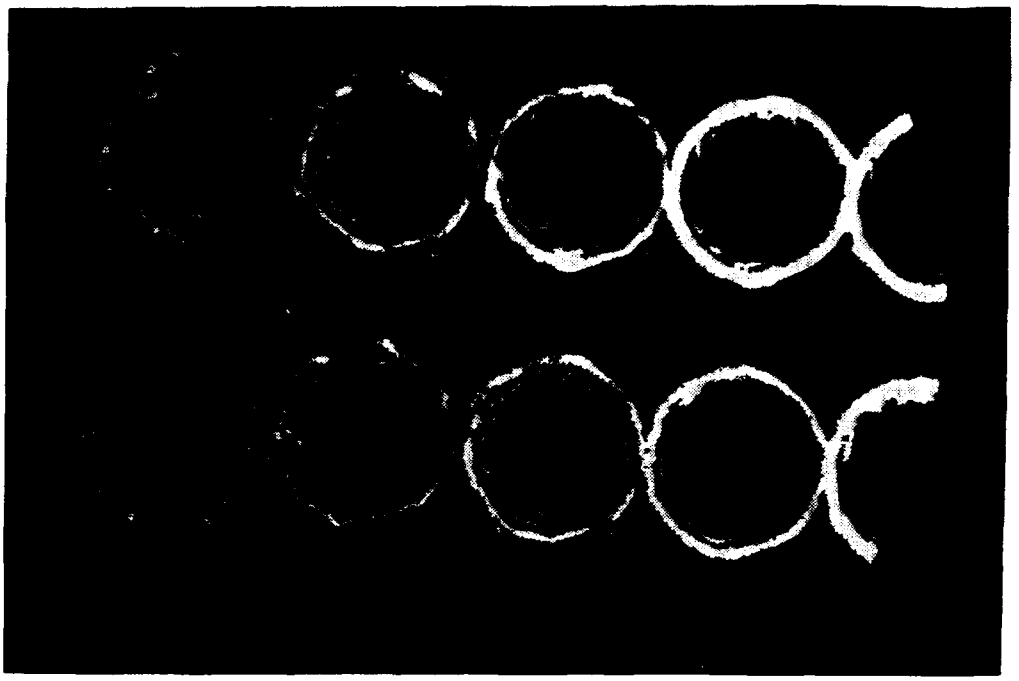

Figure 3. Photograph of a sequence of beam images during one beam pulse. The beam image is created by fluorescence of a glass plate because of the impinging beam. The images are 100 ns apart and each image is a 27 ns exposure. The images proceed in time from left to right and from bottom to top.

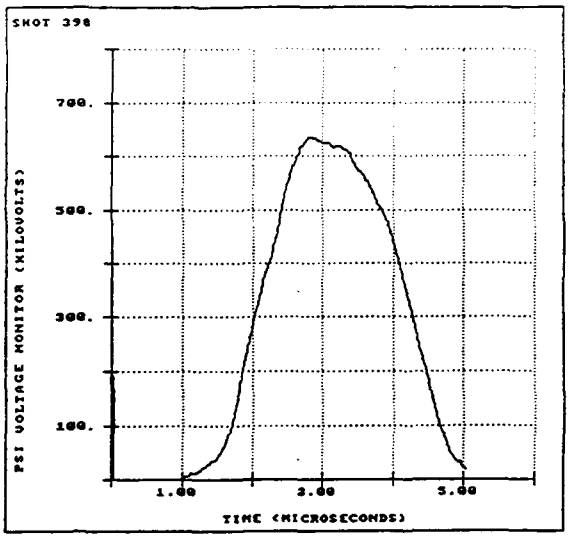

Fig.4a. Diode voltage with final diode configuration. Voltage exceeds 650 kV for 1 μs.

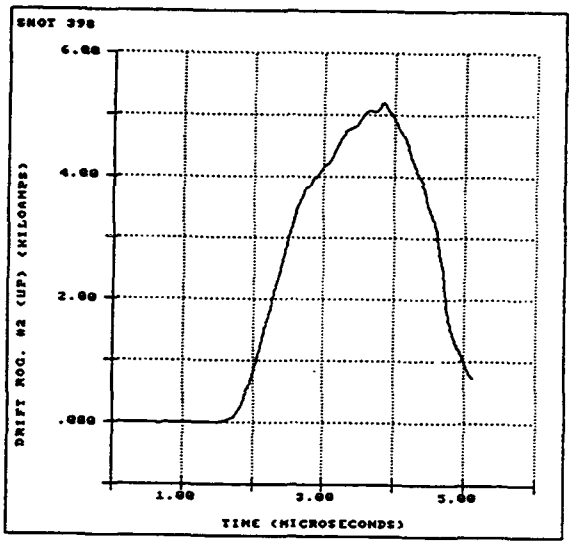

Fig. 4b. Electron beam current measured in the drift pipe from final diode configuration. Current increases from 3.5 to 5 kA during the time that the voltage is at its peak value.

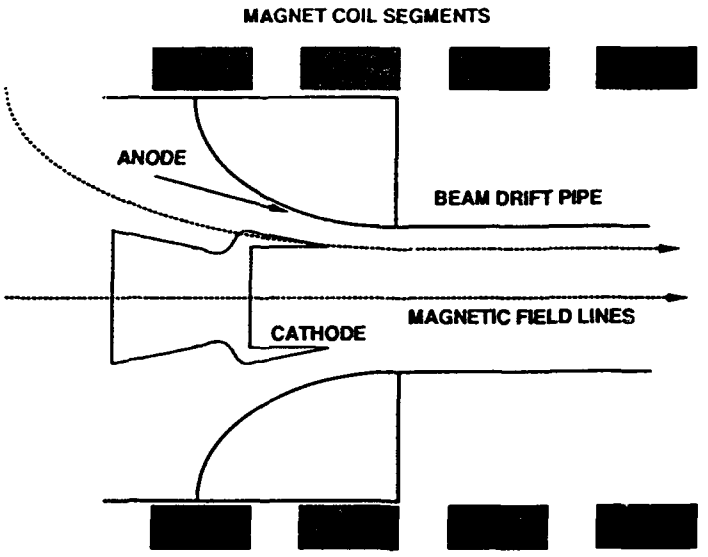

Fig. 5. Final diode configuration with the tapered anode. This configuration is used for all subsequent RKA development. Fig.. 4. Redesigned diode showing cathode with contoured shape to match the fringing magnetic field curvature so as to reduce electron backstreaming and to converge the electron beam for maximum transmission into the drift pipe.

Summary

We have developed a 1 Hz rep-rate capability for the BANSHEE modulator powering our microsecond RKA experiment. The ultmate rep-rate for the system can be as high as 500 Hz, if needed. The present 1 Hz performance delivers pulses of 600 kV and 4 to 6 kA, with ultimate performance anticipated to be 1 MV and 10 kA. An explosive emission diode for microsecond duration also has been developed with computational modelling and experiment.

Author Index

Abdullin E.N. - 419
Abe D.K. - 1607
Abe S. - 1758
Accelerator Physics Laboratory Staff - 1764
Adams R.G. - 800
Adcock J.L. - 333
Aiello N. - 203
Akiba T. - 1403
Akiyama H. - 627
Alberti S. - 1526, 1532
Alef M. - 756
Alexandrovich D.V. - 1574
Alexeev G.I. - 1312
Allen C.K. - 933
Allen S.L. - 247
Allison P. - 283
Alterkop B.A. - 1322
Althaus M. - 51
Ando R. - 1227, 1825
Anthouard P. - 1861
Antoniades J.A. - 99, 1245, 1251, 1257, 1263
Antonsen Jr. T.M. - 1497, 1607, 1613, 1728
Antoshkin M.Yu. - 1690
Aoki T. - 76
Apruzese J.P. - 159
Arad R. - 143, 633
Aragones J.M. - 1001
Armale R. - 890
Arzhannikov A.V. - 127, 431, 1117
Asahina T. - 976
Ashby S.R. - 385, 1855
Astrelin V.T. - 431, 756
Atanassov R. - 1700
Attelan S. - 2008
Averchenkov V.Ya. - 273
Babykin V.M. - 517
Bachmann H. - 51, 68, 735, 963
Bacon L.D. - 31
Bailey J.E. - 31, 788, 794, 903, 1397
Baksht R.B. - 2014
Balakirev V.A. - 1073, 1643
Baranov S.V. - 1574
Baranov V.Yu. - 1930
Bardy J. - 1752, 1861
Barnard J.J. - 297, 951
Bartsch R.R. - 88, 175, 615
Basmanov V.F. - 273, 505
Bastrikov A.N. - 1586
Batskikh G.I. - 449
Bauer W. - 51, 68, 735
Baumung K. - 51, 68, 963
Bayley J.M. - 474
Bekefi G. - 1715
Bell D.E. - 408, 2062
Benage J. - 175
Benford G. - 1631
Benford J. - 203, 341
Bennett L.F. - 1141
Bernard M. - 781
Beruchev N.G. - 436
Bessho I. - 1758
Beyec Y. Le - 939
Bidwell S.W. - 1728
Bieg K.W. - 794
Bishaev A.M. - 1312
Black W.M. - 1479
Bloomquist D.D. - 31
Bluhm H. - 51, 68, 735, 741
Bobylev V.B. - 431, 1117
Bobys M.P. - 1485
Bogachenkov V.A. - 1568
Bohacek V. - 1221
Boller J.R. - 375, 609, 871
Bolshakov E.P. - 1930
Bonnafond C. - 1752
Bossamykin V.S. - 273, 505, 511
Bottollier-Curtet H. - 1752
Boulais K.A. - 1087, 1300
Bourham M. - 1979
Bowers L.A. - 1649
Bowers R. - 175
Bratman V.L. - 1520
Bres M. - 237
Bromborsky A. - 1607, 1613, 1619
Brooks A.L. - 297
Brown D.J. - 1473
Brownell J. - 175
Bruggink D. - 1901
Brunelle A. - 939
Budakov A.V. - 505
Bugaev S.P. - 394, 419, 449, 1099, 1586
Bulan V.V. - 425
Bunkin B.V. - 195
Burdakov A.V. - 127, 1049, 1055
Burns M. - 283
Burtsev V.A. - 1930
Bushell M. - 1215
Buth L. - 51, 68, 735
Butler J.M. - 1637
Butler M.E. - 333
Buzzi J.M. - 237
Bystritskii V.M. - 529, 535, 812, 878
Calico S.E. - 1367
Caporaso G. - 283
Carlson A.L. - 794, 903
Carlson R.L. - 1881
Carlsten B.E. - 227, 1473, 1661
Carmel Y. - 1607
Chandler G.A. - 31
Chang C.L. - 927
Chavez J.R. - 781
Chen C. - 1526, 1807
Chen S.C. - 1135
Chen Y. - 1354
Chen Y.J. - 283
Chen Y.Q. - 1696
Chen Y.S. - 1696
Cherepenin V.A. - 1596
Chernin D.P. - 291, 1294, 1783
Chernobrovin V.I. - 1930
Chernyavsky I.A. - 1586
Chetvertkov V.I. - 1930
Chikin R.V. - 517
Chikunov V.V. - 127, 1043, 1049
Childers F.K. - 385
Ching C.H. - 1789
Chirko K.A. - 1625
Chishiro E. - 847
Chistov A.A. - 419
Chittenden J.P. - 474, 480
Choe J.Y. - 1087
Choi P. - 474, 480, 2008
Chu K.R. - 1491
Chumerin P.Yu. - 1685
Chun S.T. - 1087
Church B.W. - 1795
Chuvatin A.S. - 2008
Clark M.C. - 1649
Clark R.E.H. - 143
Clark R.W. - 2068
Clupek M. - 1221
Coats R.S. - 31, 781

Cochran F.L. - 159, 2050
Cochrane J. - 175
Coffield F. - 297
Coleman M. - 598
Colombant D.G. - 1783
Commisso R.J. - 167, 375, 603, 609
Conde M.E. - 1715
Cook D.L. - 31
Cooksey N. - 203
Cooper G.W. - 621
Cooperstein G. - 375, 871, 1159
Coulter M.C. - 159, 2044
Cravey W.R. - 646
Crawford M.T. - 1367
Cricket C.M. - 1776
Crist C.E. - 109
Cuneo M.E. - 31, 781
Czuchlewski S.J. - 1912
Dadusc G. - 143
Dangor A.E. - 474
Danko J.C. - 1954
Danly B.G. - 1135, 1526, 1532
Datsko I.M. - 2014
Davara G. - 143
Davis C.E. - 1649
Davis H.A. - 88, 615
Davis J. - 2050, 2068
Davis T.J. - 1601, 1667
Deadrick F. - 297
Deeney C. - 159, 167, 385, 2044
Degnan J.H. - 408
Deichuli M.P. - 1586
Denisov G.G. - 1520
Derzon M.S. - 31
Desjarlais M.P. - 31, 775
Destler W.W. - 1728
Deulin Yu.I. - 1015
Deutsch C. - 988
Devin A. - 1752
DeVore C.R. - 559
Didenko A.N. - 219, 1574, 1685, 1690
Ding B.N. - 665, 1176
Ding W. - 1734
Diyankov V.S. - 455, 1165
Dolezal F.A. - 1637
Dolgachev G.I. - 517, 523
Dolgopolov V.V. - 1073
Douglas M.R. - 408, 2062
Downing J. - 283
Drury D. - 1855
Dukart R.J. - 31
Duvall R.E. - 143
Eddy W. - 1979
Efremov A.M. - 419, 1948
Egorov O.G. - 425
Eisenhart R.L. - 1637
Ekdahl C. - 1887
Eliezer S. - 995
Eltchaninov A.S. - 195
Engelko V.I. - 436, 1935
Engelstad R.L. - 1901
Erickson A. - 227, 688
Ershov V.V. - 436
Esarey E. - 313, 1813
Etlicher B. - 2008
Eyharts P. - 1861
Eyl P. - 1861
Faehl R.J. - 88, 227, 688, 762, 1473, 1661
Faillon G. - 237
Failor B. - 159
Fan R.Y. - 1696
Fant K. - 1147
Fayne W.R. - 1649
Fazio M.V. - 227, 688, 1473, 1661
Fedorov V. - 747
Fedotkin A.S. - 273
Fedotov A.V. - 1373
Fedushchak V.F. - 1194
Feher L. - 756
Feng B. - 1721
Fernsler R.F. - 99, 1245, 1251, 1276, 1282
Fidelskaya R.F. - 1930
Filipenko N.M. - 1574
Filippov V.O. - 505
Filippov V.V. - 1015, 1021
Filuk A.B. - 31, 788, 794
Finkelstein K.I. - 1930
Fischer R.P. - 1467
Fisher A. - 143, 357, 633, 812, 1631, 1746
Fisher R.C. - 609
Fisher V. - 143
Fleetwood R. - 1215
Fliflet A.W. - 1467
Fomenko G.P. - 1574, 1690
Foord M.E. - 143
Forman P. - 175
Fortov V.E. - 969
Foster J. - 1789
Fowler W.E. - 781
Freund H.P. - 263, 1709, 1728
Frost C.A. - 109, 492
Fruchtman A. - 143
Fu S. - 1354
Fukuzawa T. - 627
Furman E.G. - 1870
Furuuchi S. - 1971
Furuyama Y. - 841, 976
Gan Y.G. - 1918
Ganguly A.K. - 1514, 1709
Garate E. - 812, 1631
Gardelle J. - 1752
Gardes D. - 939
Gautier D.C. - 88
Gavrilov N.V. - 1105
George M. - 1141
Gerasimov A.I. - 273
Gerbelot N. - 237
Gerber R.A. - 800
Germain G. - 1752
Getman D.V. - 586
Getty W.D. - 1129
Giguet E. - 1526
Gilgenbach R.M. - 1789
Gilligan J. - 1979
Ginzburg N.S. - 1740
Giuliani Jr. J.L. - 159, 167
Glazyring I.V. - 1165
Glidden S.C. - 349
Goebel D.M. - 1093, 1637
Goel B. - 68, 957, 969
Goez M.F. - 68
Goforth J. - 175
Gold S.H. - 1479
Golden J. - 1170
Golovanov Yu.P. - 517
Golub T.A. - 575
Golubev A.A. - 1312
Golubev A.V. - 2020
Goncharenko I.M. - 1948
Gondarenko N.A. - 575
Gonichon J. - 1135
Goodman D.L. - 1526
Goodrich P.J. - 375, 603, 609
Gordeev V.S. - 505, 511
Gorkunov V.S. - 273
Goyer J.R. - 385, 1385
Grabovsky E.V. - 425

Granatstein V.L. - 185, 1449, 1503, 1508, 1728
Green T.A. - 788
Greene A. - 175
Greenly J.B. - 43, 88, 615
Gregorian L. - 143
Grekhov A.V. Gaponov - 195
Gribov A.N. - 425
Gridasov A.P. - 505
Griffith L.V. - 297
Grigoryev V.P. - 1690
Grishin A.V. - 273
Grishin V.K. - 1770, 1776
Gritzina V.P. - 273
Grossmann J.M. - 375, 559, 603, 1159
Grothaus M.G. - 659
Gudovich V.A. - 1312
Guharay S.K. - 933
Gulotta G. - 1532
Gumennyj V.L. - 541
Gundersen M.A. - 1123
Gushenets V.I. - 1099
Guth H. - 68
Haber I. - 945
Hafizi B. - 1479, 1746
Haill T.A. - 31
Haines M.G. - 474
Hakansson P. - 939
Halbleib J.A. - 119
Hallal Jr. M.P. - 1153
Hammer D.A. - 349
Hankins O. - 1979
Hanson D.L. - 31, 781
Harden M.J. - 1141
Hardesty L.W. - 659
Harjes H.C. - 333
Harper-Slaboszewicz V.J. - 486
Harteneck B. - 203
Harvey R.J. - 1637
Hatfield L.L. - 1367
Haworth M.D. - 1649
Hayase H. - 835
Haynes W.B. - 227
Hazelton R.C. - 2032
Henderson J.L. - 1141
Hendricks K.J. - 1649
Henins I. - 88
Herniter M.E. - 1129
Hinshelwood D.D. - 159, 375, 603, 609
Hirshfield J.L. - 1514
Hoeberling R.F. - 227, 688, 1473
Hofmann I. - 969
Hogan B. - 185, 1449
Hogeland S. - 1328
Honrubia J.J. - 1001
Hoppe P. - 51, 68, 735, 741
Horioka K. - 806, 829, 835
Hoshino H. - 1971
Hou W.S. - 1984
Hsu T.Y. - 1123
Hu K. - 1354
Huang D. - 1343, 1349
Hubbard R.F. - 99, 945, 1245, 1251, 1257, 1276, 1282
Huber A.F. - 127, 1049
Hughes T.P. - 1881
Humphries Jr. S. - 1837, 1843, 1887
Hurley J. - 1979
Huseev A.P. - 394
Hushiki T. - 829
Hussey T.W. - 408, 2062
Hyman J. - 1637
Ignatov A.M. - 1373
Ihara S. - 627
Ilily St. - 756
Imada G. - 323
Imasaki K. - 76, 884, 1403, 1758
Ingermanson R. - 553
Irwin K. - 1087
Isakov I.F. - 1966
Ishkhanov B.S. - 1770
Iskoldsky A.M. - 575
Itin V.I. - 1942, 1948
Ivanov I.B. - 1870
Ivanov V.V. - 1655
Ivanov Yu.F. - 1942, 1948
Ivers J.D. - 1081, 1601
Iyyengar S.K. - 1831
Jackson R.H. - 263
Jensen D. - 1147
Jeremkin V.V. - 1930
Jiang B. - 1123
Jiang W. - 323, 859
Jiang X. - 462, 468
Jiangjun S. - 1188
Johnson D.J. - 31, 788, 800, 903
Johnson D.L. - 333
Johnson W.A. - 499
Joyce G. - 313, 945, 1270, 1813, 1849
Judd D.L. - 297
Judy D.C. - 640, 1215
Jungwirth K. - 1337
Kablambajev B.A. - 581
Kadimov A.H. - 1312
Kalantar D.H. - 349
Kamada K. - 1227, 1825
Kanaev G.G. - 1870
Kanavets V.I. - 211, 1586
Kanazawa T. - 1825
Kandaurov I.V. - 1027, 1037
Kanel G.I. - 68, 963
Kang X.D. - 323, 1971
Kapitonov V.A. - 127
Karbushev N.I. - 1643
Karow H.U. - 51, 68, 735, 963
Karyukin A.V. - 127, 1015, 1049
Kasuya K. - 806, 829, 835
Katsuki S. - 627
Kawakita Y. - 829
Kawasaki S. - 255, 1825
Kawata S. - 76
Kazansky L.N. - 449
Keishi T. - 1758
Keller D.V. - 1391
Kellogg J.C. - 375, 603, 1159
Kerslick G.S. - 1081, 1601
Kharchenko I.F. - 1073
Kharlov A.V. - 878
Khomenko A.I. - 449
Khryapov P.A. - 1586
Kiekel P.D. - 333, 1328
Kim A.A. - 394, 586, 2014
Kimura T. - 1532
Kirbie H.C. - 297
Kirichenko Yu.V. - 1073
Kirkman G. - 1123
Kiselev V.N. - 394
Kishimoto Y. - 255
Kitamura A. - 841, 976
Klement'ev A.P. - 505
Klenov G.I. - 1312
Klimov V.I. - 1061, 1067
Knyazev B.A. - 1043
Kobayashi A. - 1758
Kobayashi T. - 255
Koc U.V. - 185, 1455
Koga A. - 1758

Koidan V.S. - 127, 431, 1021, 1049
Kojokhin E.P. - 425
Kokshenev V.A. - 394, 2014
Kolacek K. - 1337
Kolosov Yu.A. - 1643
Komarov O.L. - 436
Kondratiev N.A. - 1033
Kondratyev A.A. - 1165
Konovalov I.V. - 1655
Koontz R. - 1147
Kormilitsin A.I. - 455, 1165
Kornilov V.G. - 1655
Korovin S.D. - 195, 1580
Kortbawi D. - 385, 1385
Koshelev V.I. - 449, 1586
Kostas C. - 291, 1294
Kostin V.V. - 969
Kostov K.G. - 1700
Kotov Yu.A. - 670
Kou C.S. - 1491
Koval T.V. - 1690
Kovalchuk B.M. - 394, 419, 449, 1948
Kovalev N.F. - 1592
Kovalev V.G. - 436
Kovalev V.P. - 455
Kovalev Yu.I. - 517
Kovsharov N.F. - 394
Krall A. - 1087
Krall J. - 313, 1288, 1813, 1849
Krasik Ya.E. - 143, 529, 633
Kreindel M.Yu. - 1111
Kreindel Yu.E. - 1105
Krejci A. - 2020, 2026
Krishnan M. - 159
Kristiansen M. - 1367
Krousky E. - 2020
Kruglyakov Eh.P. - 1027, 1037
Kruse H. - 175
Kuang E. - 1601
Kueny C.S. - 305
Kukharenko I.N. - 425
Kulbeda V.E. - 1033
Kulcinski G.L. - 1901
Kuntz M. - 756
Kuo Y.Y. - 1984
Kurbatov K.V. - 425
Kusse B.R. - 43, 915
Kuznetsov V.E. - 1930
Kwan T.J.T. - 227, 688, 1562, 1661
Labrouche J. - 1752
Laderach G.E. - 333
Ladish J. - 175
Lai S.T. - 1907
Lampe M. - 99, 945, 1270, 1276, 1282
Laqua H. - 51, 741
Larionov V.P. - 1312
Latham P.E. - 185, 1449, 1455, 1461
Latinsky S.M. - 1073
Lats'ko E.M. - 1073
Lau Y.Y. - 1783
Launspach J. - 1752
Lawson W. - 185, 1449
Lazarenko A.V. - 1935
Lazarev S.A. - 273
Lebedev S.V. - 127, 1015, 1021, 1049
Leeper R.J. - 31
Lemke R.W. - 1649
Lenski I.F. - 1776
LePell P.D. - 159, 167, 2044
Les J. - 2068
Levine J. - 203
Levush B. - 1461, 1497, 1607, 1613, 1619, 1728
Li T. - 676
Licht V. - 68, 963
Lin A.T. - 1491
Lin C.L. - 1135
Lindemuth I.R. - 1990
Linton T.W. - 88
Liou R.L. - 1123
Lisenko E.A. - 1073
Lisitsyn I.V. - 529, 535
Litvinov E.A. - 1111
Litwin C. - 143, 143
Litz M.S. - 1170
Liu J.R. - 1918
Lockner T.R. - 31, 788
Loginov S.V. - 419
Lomonosov I.V. - 969
Longcope D.W. - 769
Lopatin V.V. - 1586
Losev M.V. - 1037
Loskutov V.V. - 2014
Lotz H. - 68, 735
Lovberg R.H. - 1990
Lovell E.G. - 1901
Loza O.T. - 1550
Lu Z. - 1721
Luchinsky A.V. - 1194, 2014
Luhmann Jr. N.C. - 1485, 1491
Lujnov V.G. - 425
Lundin C.D. - 1954
Lykov S.V. - 1942, 1948
Ma W. - 1343
MacFarlane J.J. - 903, 1397, 1901
Maeda S. - 627
Maenchen J.E. - 781
Maglich B. - 357
Maidanovskii A.S. - 1574
Main W. - 185, 1449, 1455
Manheimer W.M. - 1467, 1479
Mankofsky A. - 927
Mann G.A. - 333
Markov A.B. - 1948
Maron Y. - 143, 633, 794
Martinez L.E. - 333
Martinez-Val J.M. - 995, 1001
Martynov V.F. - 1318
Maruyama X.K. - 1153
Mascureau J. d. - 1752
Mason R.J. - 547, 615
Masuda W. - 323
Masugata K. - 323, 682, 847, 853, 859, 1971
Masuzaki M. - 1227, 1825
Matsumura N. - 1825
Matsuura N. - 829
Matthews H.W. - 185
Mayhall D.J. - 652
Mazarakis M.G. - 109, 492, 1141
McClenahan C.R. - 333
McDermott D.B. - 1485, 1491
McGuire E.J. - 903
McKay P.F. - 781
McNally J.D. - 1485
Meachum J.S. - 136, 1385
Meek T.T. - 1954
Meger R.A. - 99, 1245, 1251, 1257, 1263
Mehlhorn T.A. - 31, 788
Mekler K.I. - 127, 1049
Melnikov G.V. - 1685, 1690
Melnikov P.I. - 127, 1021, 1043, 1049

Mendel Jr. C.W. - 31, 499
Mendenhall R.S. - 1385
Menge P.R. - 1789
Menninger W.L. - 1526, 1532
Merkel G. - 1215
Meshkov O.I. - 1027, 1037
Mesyats G.A. - 195, 394, 419, 449, 878, 1105, 1942
Mikhailov V.M. - 1322
Mikkelson K.A. - 119, 486
Miller A.R. - 402, 598
Miller J.D. - 1233
Miller R.B. - 1328
Miller S.M. - 1607, 1613
Minguez E. - 1001
Miram G. - 1147
Mitchell I.H. - 474, 480
Mitin L.A. - 1318, 1643
Mix L.P. - 31, 788
Miyai Y. - 829
Miyamoto S. - 76, 884, 1403
Miyauchi Y. - 1758
Miyoshi T. - 829
Mkheidze G.P. - 1061, 1067, 1924
Moats A.R. - 31
Mock R.C. - 119
Mogahed E.A. - 1901
Moir D.C. - 283, 1881
Molina I. - 1328
Mondelli A.A. - 291, 927, 1294
Moran S.L. - 659
Morita H. - 1227
Morunov K.A. - 273
Moschella J.J. - 2032, 2038
Moses G.A. - 1397, 1901
Mosher D. - 60
Moya S.A. - 1141
Mozgovoy A.G. - 818, 824, 1867
Muenchausen R.E. - 88
Muirhead D. - 333
Mulbrandon M. - 167
Mullins B.W. - 408
Munz C.D. - 68
Murphy D.P. - 99, 1245, 1251, 1257, 1263
Musyoki S. - 255
Myers M.C. - 99, 1245, 1251, 1257, 1263
Myers T.J. - 1300
Myskov G.A. - 505
Mytnikov A.V. - 878
Nagai A. - 1758
Nagashima T. - 255
Nakai S. - 76, 884, 1403
Nakajima T. - 841, 976
Nakamura Y. - 255
Nakata K. - 829
Nardi E. - 982
Nash T. - 159, 903
Nation J.A. - 1081, 1601, 1667
Naugol'nyj I.N. - 541
Neau E.L. - 333, 1960
Neely S.M. - 486
Negra S. Della - 939
Neil V.K. - 297
Neri J.M. - 60
Newton M.A. - 297
Ngo M.T. - 1379
Nguyen K.T. - 1233
Ni A.L. - 68, 957, 969
Nianan C. - 1876
Nie L. - 1918
Nifanov A.S. - 211
Nikiforov A.A. - 127, 1049
Nikolaev V.S. - 127, 431, 1117
Nikolov N.A. - 1700
Nishimura E. - 1758
Niu K. - 1895
Nolting E.E. - 1954
Noonan W.A. - 43
Novikov S.A. - 1685
Novikov S.S. - 1574
Novikov V.E. - 1073
Nusinovich G.S. - 185, 1461, 1497, 1503, 1619
Obenschain S.P. - 1912
Oda H. - 255
Ohashi M. - 1971
Ohshita E. - 829
Okano M. - 1758
Oliver B.V. - 921
Olson C.L. - 60, 897, 903
Olson J.C. - 915
Olson R.E. - 31
Olson W.R. - 1141
Oona H. - 175
Oppenheim M. - 1601
Oreshin A.A. - 449
Oreshkin V.I. - 2014
Osipov M.L. - 195
Ostrenskiy Ye.I. - 1643
Ostrovsky A.O. - 1073
Otlivantchik E.A. - 195
Ottinger P.F. - 60, 167, 375, 559, 1159
Ovsyannikov V.A. - 1930
Ozur G.E. - 1111, 1942
Panitz J. - 788
Papadichev V.A. - 818, 824, 1568
Parilis E. - 939
Parker J. - 175
Parks D. - 553, 598
Pashchenko A.V. - 541, 1073
Pasour J.A. - 1379
Paul A.C. - 297
Pavlovskii A.I. - 273, 505, 511, 1655
Pawley C.J. - 1912
Pearce K.D. - 1129
Pearson C. - 1147
Pechacek R.E. - 99, 1245, 1251, 1257, 1263
Pechersky O.P. - 436, 1930, 1935
Pena G.E. - 333
Penn K.J. - 333
Pereira N.R. - 640
Perelmutter L. - 143
Perevodchikov V.I. - 1318
Perlado M. - 1001
Petelin M.I. - 195, 449
Peter W. - 1819
Peterkin Jr. R.E. - 408, 2062
Peterson D. - 175
Peterson R.R. - 909, 1901
Petillo J.J. - 291, 927, 1294
Petin V.K. - 1194
Petukhov A.A. - 436
Peyser T.A. - 99, 1245, 1251, 1257, 1263
Pichugin V.E. - 425
Piera M. - 995, 1001
Piffl V. - 1055, 1221, 2020, 2026
Pikunov V.M. - 1586, 1673
Pincosy P.A. - 646
Platonov Yu.Ya. - 2020
Platt R.C. - 1649
Pointon T.D. - 31, 775
Polevin S.D. - 1580

Polovkov A.I. - 1643
Poskonin V.A. - 581
Postupaev V.V. - 127, 1049, 1055
Poukey J.W. - 109, 119, 492, 781, 897, 1141, 1801
Poulsen P. - 646
Pozdeev V.V. - 1574
Prasad R.R. - 159
Prasol E.A. - 1073
Price D. - 203
Prikhod'ko I.G. - 1655
Prohaska R. - 812, 1631
Prokhorov A.M. - 195
Prokopenko V.F. - 1930
Proskurovsky D.I. - 1111, 1942
Pulsifer P.E. - 2056
Qi N. - 349
Qian M. - 1188
Qiu A.C. - 1918
Quintenz J.P. - 31
Radkevich O.I. - 1312
Rahman H.U. - 1996
Rashchikov V.I. - 219
Ratakhin N.A. - 581, 1194
Raus J. - 1221, 2020, 2026
Razin S.V. - 1685
Reed K.W. - 333
Reginato L.L. - 297
Reinhardt N. - 1123
Reinovsky R. - 175
Reiser M. - 185, 933, 1182
Rej D.J. - 88, 615, 762
Remnev G.E. - 365, 1966
Ren S.Q. - 1918
Renk T.J. - 31, 794, 800
Renner O. - 2020
Renz G. - 1715
Rhee M.J. - 665, 1087, 1176, 1233, 1300
Richter S.H. - 1391
Rickel D.G. - 227, 688, 1661
Riley Jr. R.A. - 1990
Riordan J.C. - 136, 385, 1385
Ripa M. - 1337
Rix W. - 402, 598, 1887
Robertson K. - 598
Rochau G.E. - 31
Rodenz G. - 1473
Roderick N.F. - 175, 408, 2062
Rodgers J. - 1728
Rodiakin V.E. - 1673
Roitman A.M. - 1580
Romanov S.S. - 1073
Roques A. - 1861
Rose D.V. - 60
Rosenthal S.E. - 31, 499, 781
Rostoker N. - 357, 812, 890, 1996
Rostov V.V. - 195, 1580
Roth I.S. - 385, 1385
Rotshtein V.P. - 1942, 1948
Rouille C. - 2008
Roychowdhury P. - 1831
Rudakov L.I. - 565
Rudjak Yu.V. - 1306
Ruiz C.L. - 31
Rukhadze A.A. - 1322, 1556
Rukin S.N. - 670
Rullier J.L. - 1526, 1532
Rusch D. - 51, 68, 735, 963
Russkich A.G. - 2014
Rust K. - 227, 688
Rutledge S. - 1901
Rybak P.V. - 1556
Ryne R.D. - 1661
Ryutov D.D. - 127, 1009
Ryzhov V.V. - 1199
Saddow S.E. - 1087
Saeki K. - 1758
Saitou H. - 682
Sakagami T. - 859
Sakamoto K. - 255
Sakamoto M. - 1825
Salberta E. - 553
Samarsky P.A. - 449
Samsonov S.V. - 1520
Sandalov A.N. - 1673, 1770
Sanford T.W.L. - 119
Sanin A.L. - 1037
Santoru J. - 1637
Santos J. - 99, 1245, 1251
Sapozhnikov A.A. - 1199
Saraev A.P. - 195
Saraph G.P. - 1497
Sarfaty M. - 143, 633
Sarid E. - 143
Sato M - 865
Sato S. - 1758
Savage M.E. - 621
Saveljev Yu.M. - 436
Savin A.A. - 1061, 1067, 1924
Sawan M.E. - 1901
Schachter L. - 1081, 1601, 1667
Schanin P.M. - 419, 1099
Scharlemann E.T. - 247
Schlitt L. - 385, 1855
Schmidt W. - 747, 756
Schneider A.J. - 1637
Schneider R.F. - 1233, 1954
Schuldt R. - 756
Schultheiss Ch. - 735
Schumacher R.W. - 1093, 1637
Schwirzke F. - 1153
Schwoebel P. - 788
Seidel D.B. - 31, 499
Sekimoto Y. - 323, 682
Seldner D. - 756
Selemir V.D. - 1655
Seleznev V.D. - 449
Selivanov I.A. - 1538
Semenov E.P. - 127
Serafim P. - 1746
Sethian J.D. - 159, 1912
Settersten T.B. - 2032
Shan Y. - 1343
Shapiro A.L. - 1318
Sharp W.M. - 297, 951
Shatkus A.D. - 1643
Shay H.D. - 297
Shcheglov M.A. - 127, 431, 1015, 1021, 1049
Sheehey P. - 1990
Shibalko K.V. - 1655
Shibata K. - 682
Shigeta M. - 682
Shiho M. - 255
Shimotori Y. - 1971
Shinmura A. - 841
Shirai N. - 76, 1403
Shiyan V.D. - 1205
Shkolnikova S. - 143, 633
Shkvarunets A.G. - 1538, 1545
Shlapakovskii A.S. - 1625
Shokair I.R. - 1328
Shope S.L. - 109, 492
Shpitalnik R. - 143
Shterbina O.V. - 1312
Shubin O.A. - 1105
Shulov V.A. - 365
Shutov A. - 68

Shvedunov V.I. - 1770
Simpson W.W. - 621
Sincerny P.S. - 385, 1855
Sinebryukhov A.A. - 535, 878
Sinelshikov A.V. - 449
Singer J. - 68, 963
Singh A. - 1508
Sinilshikova I.V. - 1568
Sinitsky S.L. - 127, 431, 1117
Sisakyan I.P. - 195
Skogmo P.J. - 119, 1141
Skopec M. - 1954
Skripka G.M. - 273
Skvortsov V.A. - 969
Slepkov A.I. - 211, 1586
Slinker S.P. - 99, 945, 1270, 1276, 1282
Sloan M.L. - 305
Slutz S.A. - 31, 1801
Smetanin V.I. - 1033
Smirnov A.V. - 431
Smirnov L.V. - 436
Smirnov N.A. - 1194
Smith A.C. - 1960
Smith D.L. - 1141
Smith J.R. - 1328
Smith M. - 1215
Smith O.A. - 1568
Smith R. - 203
Smolenkova O.A. - 425
Smorgonsky A.V. - 195
Sochugov N.S. - 1586
Soln J. - 1211
Sonegawa T. - 323, 1971
Sotnikov G.V. - 1643
Spasovsky I.P. - 1700
Spielman R.B. - 2002
Spindler G. - 1715
Sprangle P. - 313, 1746, 1813
Sprehn D. - 203
Stallings C. - 385
Stark R.A. - 1233, 1954
Stearns W.F. - 781
Stein E. - 51, 735, 756
Stephanakis S.J. - 871, 1159
Stinnett R.W. - 31, 788
Stogov A.A. - 1673
Stoltz O. - 51, 68, 735, 741, 963
Strelkov P.S. - 1545, 1550
Streltsov A.P. - 1930
Stricklett K.L. - 640
Striffler C.D. - 185, 1449
Stringfield R.M. - 227, 688, 1473, 1661
Struckman C.K. - 43
Struve K.W. - 109, 1141, 1328, 1960
Stygar W.A. - 31
Sudan R.N. - 769, 921, 1795
Sugimura H. - 847
Sukhushin K.N. - 1586
Sulakshin A.S. - 1574
Sullivan C.A. - 1479
Sun R.F. - 1918
Sundquist B.U.R. - 939
Sunka P. - 1221, 1337
Suvorov V.A. - 195
Suvorov V.G. - 1655
Sviatoslavsky G. - 1901
Sviatoslavsky I.N. - 1901
Swanekamp S.B. - 1159
Swegle J. - 341
Syomin B.N. - 1360
Syutin O.N. - 273, 505
Tachibana T. - 847
Tahir N.A. - 988
Taillandier P. Le - 1752
Takahashi K. - 841
Tamagawa F. - 1825
Tananakin V.A. - 273
Tang C.M. - 1288
Tang H. - 676
Tantawi S.G. - 185, 1449, 1455
Tao Z. - 1876
Tarakanov V.P. - 1322, 1373, 1538, 1545, 1556
Tarasov A.D. - 273
Tazima T. - 853, 865
Temkin R.J. - 1123, 1135, 1526, 1532
Terry R. - 167
Thevenot M. - 1861
Thompson J. - 402, 598
Thompson J.R. - 305
Thompson L. - 1855
Thornhill J.W. - 159, 2044
Timofeyev V.V. - 1205
Ting A. - 313
Tisone G.C. - 31, 794, 800
Tkach Yu.V. - 541, 1073
Tkachenko K.I. - 436
Tokuda S. - 255
Tolkachev V.S. - 419
Tomimasu T. - 1758
Tomskikh O.N. - 1870
Trainor J. - 175
Trintchouk F.B. - 1924
Trotz S. - 1135
Troyansky L. - 143
Tsang K.T. - 291, 1294
Tskhai V.N. - 1318
Tsuchida S. - 682
Tsvetkov V.I. - 1690
Tukhfatullin A.A. - 1948
Turchi P.J. - 175, 408
Turman B.N. - 109, 492, 1141, 1328
Tzeng C.C. - 1984
Uhm H.S. - 1239, 1679
Ullschmied J. - 1221, 1337
Ushakov A.G. - 517, 523
Usher M.A. - 621
Usov Yu.P. - 1033, 1870
VanDeValde D. - 333
VanDevender J.P - 31
VanHaaften F.W. - 227, 688
Vasilevsky M.A. - 1930
Vasiljev V.V. - 1870
Vatrunin V.Y. - 1655
Vaysburd D.I. - 1360
Velarde G. - 1001
Velarde P. - 1001
Ventzek P.L.G. - 1789
Veresov V.P. - 273
Veron L. - 2008
Vijayan T. - 1831
Villate D. - 1861
Vladyko V.B. - 1306
Vlasov A. - 1619
Vlieks A. - 1147
Vodovosov V.M. - 1930
Volkov A.M. - 394
Volkov N.B. - 575
Volokitenkova I.L. - 1643
Vorobjev O.Yu. - 68, 957, 969
Voronkov S.N. - 1550
Voropaev S.G. - 127, 1015, 1021, 1049
Vyacheslavov L.N. - 1037
Waast B. - 939
Waganaar W.J. - 88
Wagner J.S. - 109
Waisman E. - 402, 553, 598
Walter M.T. - 1789

Wang D.X. - 1182
Warg J.G. - 1182
Wang L.G. - 1918
Wang L.H. - 1918
Wang M.C. - 1721
Wang P. - 903, 1397
Wang Q.S. - 1491
Wang X. - 462, 468, 1343
Wang X.H. - 1918
Wang Y. - 1343
Wang Z. - 676, 1721
Wang Z.X. - 1696
Warn C. - 1887
Wasierski R.F. - 227, 688
Watanabe A. - 255
Watkins R.M. - 1093, 1637
Wavrik R.W. - 333
Weber B.V. - 375, 603, 609, 871, 1159
Weber G.J. - 333
Wei Y.M. - 1918
Weidenheimer D.M. - 640, 1215
Weidman D.J. - 1233
Weingarten A. - 143, 633
Welch D.R. - 109, 119
Wen M. - 1984
Wenger D.F. - 31, 781
Werner P.W. - 1328
Wessel F.J. - 357, 1996, 2008
Westermann Th. - 735, 747, 756
Westfall R.L. - 486
Wheat R.M. - 1473
Whitney K.G. - 159, 2044, 2056
Whittum D.H. - 1270
Wilkinson M. - 402
Willey M. - 203
Wilson A. - 402, 598
Wilson J. - 297
Wittenberg L.J. - 1901
Wong S.L. - 136, 159
Worley J.F. - 474, 480
Wright E.L. - 1147
Wright J. Kinross - 1473
Wurtele J.S. - 1135, 1526
Xia N. - 676
Yadlowsky E.J. - 2032, 2038
Yalovets A.P. - 1165
Yamanaka C. - 76, 884, 1403
Yang D. - 462, 468
Yankovskiy B.D. - 443
Yao D.S. - 1918
Yasuike K. - 76, 884, 1403
Yasuoka J. - 1227
Yatsui K. - 323, 682, 847, 853, 859, 1971
Yee J.H. - 652
Yeh C.K. - 1984
Yeh T.R. - 1984
Yoshikawa M. - 1227
Young F.C. - 159, 871
Yu Q. - 806
Yu S.S. - 297, 951
Yu Y.J. - 1984
Yuan X. - 1918
Yushkov M.V. - 127, 1117
Yushkov Yu.G. - 1685
Zagulov F.Ya. - 195
Zajivikhin V.V. - 425, 592
Zakatov L.P. - 517, 523
Zakharov A.N. - 1586
Zakutayev A.N. - 1966
Zavialov M.A. - 1318
Zcherlitsin A.G. - 1685
Zeng N. - 462, 468, 1343
Zhai X. - 1631
Zhang D. - 1343
Zhang L. - 1721
Zhang M. - 1918
Zhang Q. - 676
Zhang S. - 1876
Zhang Y.M. - 1918
Zhang Z.X. - 1728
Zhao R. - 462, 468
Zhao X.Q. - 1918
Zhdanov V.S. - 1655
Zhdanov Yu.A. - 541
Zheng B. - 676
Zherlitsin A.G. - 1690
Zinamon Z. - 982
Zinchenko V.F. - 1205
Zorin V.B. - 419
Zotkin R.P. - 431, 1117